A survey of the application of soft computing to investment and financial trading

Vanstone, Bruce J; Tan, Clarence

Published in:
Proceedings of the Eighth Australian and New Zealand Intelligent Information Systems Conference (ANZIIS 2003)

QUT

ANZIIS 2003

THE UNIVERSITY OF QUEENSLAND
AUSTRALIA

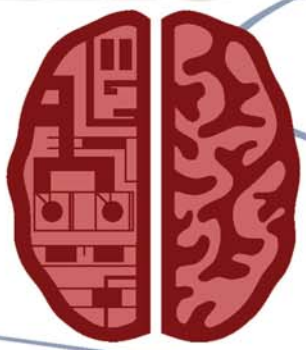

Proceedings of the Eighth Australian and New Zealand Intelligent Information Systems Conference

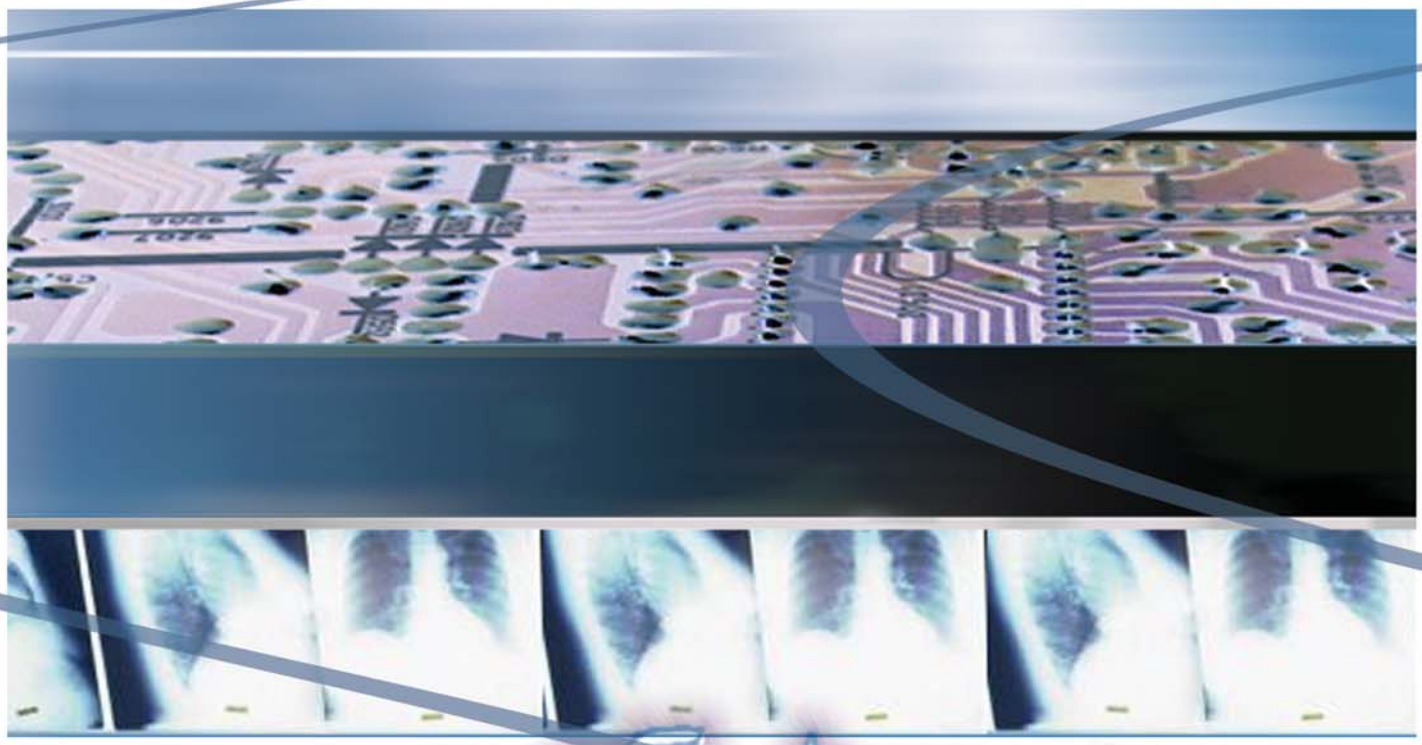

Editors
Brian C. Lovell
Duncan A. Campbell
Clinton B. Fookes
Anthony J. Maeder

Dec 10-12, Sydney Australia

Proceedings of the Eighth Australian and New Zealand Intelligent Information Systems Conference (ANZIIS 2003)

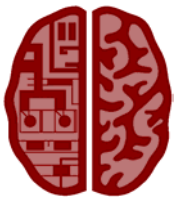

Editors
Brian C. Lovell
Duncan A. Campbell
Clinton B. Fookes
Anthony J. Maeder

Sponsored by
Australian Pattern Recognition Society
IEEE – Institute of Electrical & Electronic Engineers
Queensland University of Technology
The University of Queensland

Published by
Queensland University of Technology
Brisbane, QLD 4001 Australia

First Published in December 2003

Printed in Brisbane

ISBN 1-74107-039-2

Queensland University of Technology

THE UNIVERSITY OF QUEENSLAND
AUSTRALIA

PROCEEDINGS OF THE EIGHTH AUSTRALIAN AND NEW ZEALAND INTELLIGENT INFORMATION SYSTEMS CONFERENCE (ANZIIS 2003)

Organising Committee

General Chair: Anthony Maeder, *Queensland University of Technology*
Technical Chair: Brian Lovell, *University of Queensland*
Treasurer: Joaquin Sitte, *Queensland University of Technology*
Publicity: Duncan Campbell, *Queensland University of Technology*
DICTA Liaison: Len Hamey, *Macquarie University*
Sydney Liaison: Sri Parameswaran, *University of New South Wales*
New Zealand Liaison: George Coghill, *University of Auckland*
Past Chair: Yianni Attikiouzel, *Murdoch University*

Technical Committee

Benjamin Appleton, *The University of Queensland, Australia*
Yianni Attikiouzel, *Murdoch University, Australia*
Henry Baird, *Xerox Parc, USA*
Wageeh Boles, *Queensland University of Technology, Australia*
Laurie Cahill, *La Trobe University, Australia*
Duncan Campbell, *Queensland University of Technology, Australia*
Branko Celler, *University of New South Wales, Australia*
R Chandrasekhar, *Murdoch University, Australia*
Vaughan Clarkson, *The University of Queensland, Australia*
George Coghill, *University of Auckland, New Zealand*
Stuart Crozier, *University of Queensland, Australia*
Kumar David, *Hong Kong Polytechnic University, Hong Kong*
Dennis Deng, *La Trobe University, Australia*
Chris deSilva, *The University of Western Australia, Australia*
Clinton Fookes, *Queensland University of Technology, Australia*
Tom Gedeon, *Australian National University*
Georgy Gimelfarb, *University of Auckland, New Zealand*
Ashantha Goonetilleke, *Queensland University of Technology, Australia*
Reinhard Klette, *University of Auckland, New Zealand*
Peter James Kootsookos, *University of Queensland, Australia*
Murray Loew, *George Washington University, USA*
Brian Lovell, *University of Queensland, Australia*
Anthony Maeder, *Queensland University of Technology, Australia*
Gerard Medioni, *University of Southern California, USA*
Jerry Mendel, *University of Southern California, USA*
Wilfried Osberger, *Tektronix Corp, USA*
Marimuthu Palaniswami, *University of Melbourne, Australia*
Petra Perner, *Inst. Computer Vision & Applied Computer Sci., Germany*
Binh Pham, *Queensland University of Technology, Australia*
Richard Reilly, *University College Dublin, Ireland*
Abdul Sattar, *Griffith University, Australia*
Robert Schowengerdt, *University of Arizona, USA*
Heiko Schroder, *RMIT University, Australia*
Joaquin Sitte, *Queensland University of Technology, Australia*
Orly Yadid-Pecht, *Ben-Gurion University, Israel*
Abdelhak Zoubir, *Darmstadt University of Technology, Germany*

WELCOME FROM THE TECHNICAL CHAIR

Welcome to ANZIIS 2003!

Earlier this year, we decided to hold ANZIIS jointly with DICTA to allow us to reduce costs by sharing infrastructure and prominent invited speakers. We also thought that this would encourage the sharing of ideas and the latest research in a wider community. As the year progressed, we were asked to handle the papers which had been submitted to MEDSIP when this conference was cancelled. As a result of this three-way consolidation, I am certain that the combined conference will be the largest of its kind ever held in Australia.

The organisation of the joint conference itself and the electronic reviewing and submission of papers has been something of a challenge, but I am certain that we now have an exciting technical program embracing the latest international research. Indeed, the number of international participants at ANZIIS 2003 is extremely high by historical standards with participants flying in from Asia, Europe, and North America.

All technical papers were peer refereed by up to four members of our international program committee. We had 110 submissions to ANZIIS, but have accepted only 78 for the proceedings. There are two parallel oral streams and two poster sessions — the oral and poster papers receive equal prominence in the proceedings. Finally, participants at ANZIIS will receive free membership of the Australian Pattern Recognition Society for one year including newsletter subscription and discounts to coming technical events.

I would like to thank Anthony Maeder, Duncan Campbell, and Clinton Fookes for their marvellous organisational and technical support at the Brisbane node. I must also thank the DICTA team in Sydney who have performed remarkably considering the size and complexity of the event.

Hope to catch up with all of you at some stage. Please enjoy ANZIIS 2003.

Brian Lovell
Technical Chair ANZIIS 2003
President of the Australian Pattern Recognition Society

FOREWORD FROM THE PUBLICITY CHAIR

Welcome to ANZIIS 2003!

This year marks the tenth anniversary of ANZIIS and represents a significant milestone for the fledgling conference of 1993 in Perth, Australia. ANZIIS owes its existence to Professor Yianni Attikouzel who, through his dedication and inspiration, brought ANZIIS to life. ANZIIS has since been hosted in Dunedin (New Zealand), Brisbane, Adelaide and three times back in its birthplace of Perth. This brings us to this eighth Australian and New Zealand Conference on Intelligent Information Systems being held at Macquarie University in Sydney, Australia.

This year, we seized upon the opportunity to co-host ANZIIS with DICTA which has given a rich blend of technical topics. We are also pleased to include MEDSIP papers which embed the strong medical theme synonymous with previous ANZIIS conferences.

The organizing committee is delighted with the number of quality paper submissions, the relevance of the papers with the themed technical topics, and the number of delegates in a climate of reduced conference participation given recent global events.

We are fortunate to have Professor Yianni Attikouzel delivering the conference dinner speech. I am sure he will live up to his infamous style of humorous anecdotes threaded within topical research activities and trends. We are also fortunate to have Professor Tony Constantinides, Imperial College, London, delivering his keynote talk, *Hilbert, Poisson and other Relationships* and we look forward to attaining greater insight into that topic.

I would like to acknowledge the organizing and technical committees for their contribution to the conference and in applying the high standards that ANZIIS deserves. It was a privilege to work with Anthony Maeder (General Chair), Brian Lovell (Technical Chair), Clinton Fookes and Andrew Keir who, as a team, tirelessly got the conference up and going. Brian tried out his new on-line paper submission and reviewing system which is a brilliant piece of work in progress. Our gratitude also goes to our DICTA colleagues for their support, hard work and liaison to get the two conferences seamlessly running together.

Finally, and on behalf of the organizing committee, I would like to thank the authors, presenters and conference delegates for their participation and contribution to what promises to be a most successful and productive conference. I look forward to meeting you during this and future ANZIIS conferences.

Duncan Campbell
Publicity Chair ANZIIS 2003

TABLE OF CONTENTS

* Highlighted Technical Papers

(This page left blank intentionally)

ADAPTIVE AND MACHINE LEARNING I

(This page left blank intentionally)

Image Compression Based Upon Independent Component Analysis: Generation of Self-Aligned ICA Bases

Yasuo Matsuyama, Ryo Kawamura, Hiroaki Kataoka, Naoto Katsumata,
Kenzo Tojima, Hideaki Ishijima, and Keita Shimoda

Department of Computer Science, Waseda University
Tokyo, 169-8555 Japan

{yasuo2, ryo@asagi, pp_kataoka@moegi, katsu@ruri,
k-tojima@toki, suzaku@toki, kei215@asagi}.waseda.jp

Abstract

Generation of the ordered set of ICA bases (Independent Component Analysis bases) and its applications to image compression are discussed. The ICA bases have similar properties to existing orthogonal bases. Orthogonal bases generate uncorrelated coefficients, while, the ICA bases bring about independent coefficients. The independence is stronger than the uncorrelatedness. Therefore, the ICA bases can extract source information better. One difficulty using ICA is the permutation indeterminacy among these bases. This paper presents partially supervised learning for generating self-aligned ICA bases. It is observed that: (i) Each basis reflects edges and textures like the early vision. (ii) Bases can be self-aligned in the sense of spatial frequency. (iii) Coefficients of the bases can be used for image compression. Experiments show that (iv) the set of ICA image bases is a well-qualified alternative to existing orthogonal ones.

1. Introduction

Independent Component Analysis (ICA) [1] is a method of multivariate analysis to decompose measured data into independent components. It is a class of learning algorithms from data. Its application is wide including images, speech, music signals and so on. Therefore, ICA has received much attention from communities of adaptive learning and multimedia processing. This paper contributes to these fields by showing a new method to obtain ICA image bases and novel applications to image compression.

Organization of this paper is as follows. In Section 2, the ICA problem is formulated. The role of the ICA basis set is elucidated. The permutation indeterminacy, which essentially exists in the ordinary ICA, is explained. Presentation of the ICA model for image construction is also given. Then, in Section 3, preprocessing, orthonormalization, and ordinary ICA algorithms are explained to assist later explanations on improved methods. In Section 4, The ICA learning with weak guidance is presented. This partial supervision is effective to the reduction of the permutation indeterminacy, whose step is necessary for the application of ICA bases. In Section 5, experiments on digital images are executed. The ICA image bases are successfully aligned by reflecting spatial frequencies. Experiments show that the ICA bases are promising in the image compression as the theory predicts. Section 6 gives concluding remarks with prospects of future studies.

2. Problem Formulation of ICA

2.1. Mixture of Independent Components

In the problem of ICA, a vector random variable

$$\boldsymbol{x} = [x_1, \cdots, x_n]^T \tag{1}$$

is assumed to be generated by another random variable

$$\boldsymbol{s} = [s_1, \cdots, s_n]^T \tag{2}$$

by the following mixture.

$$\boldsymbol{x} = \boldsymbol{A}\boldsymbol{s} = [\boldsymbol{a}_1 \cdots, \boldsymbol{a}_n]\boldsymbol{s} = \textstyle\sum_{i=1}^{n} \boldsymbol{a}_i s_i \tag{3}$$

The matrix $\boldsymbol{A}$ and the vector $\boldsymbol{s}$ are both unknown except for the following information.

(a) The components s_i and s_j are independent each other for $i \neq j$.

(b) The components s_i, $(i = 1, \cdots, n)$, are non-Gaussian except for at most one i.

Under the above conditions, we want to estimate a demixing matrix

$$\boldsymbol{W} = \boldsymbol{\Lambda}\boldsymbol{\Pi}\boldsymbol{A}^{-1} \tag{4}$$

so that the components y_i, $(i = 1, \cdots, n)$, of

$$\boldsymbol{W}\boldsymbol{x} \stackrel{\text{def}}{=} \boldsymbol{y} = [y_1, \cdots, y_n]^T \tag{5}$$

are independent each other. Here, $\boldsymbol{\Lambda}$ is a nonsingular diagonal matrix which decides components' scale, and $\boldsymbol{\Pi}$ is a permutation matrix. These matrices are unknown too. This property is called the indeterminacy, which essentially exists in the ICA formulation. In this paper, such indeterminacy will be carefully avoided.

2.2. ICA bases

Column vectors of $\boldsymbol{W}^{-1} \stackrel{\text{def}}{=} \boldsymbol{U}$ can be interpreted as ICA bases since the following equality holds for the observed data $\boldsymbol{x}$.

$$\boldsymbol{x} = \boldsymbol{U}\boldsymbol{y} = [\boldsymbol{u}_1, \cdots, \boldsymbol{u}_n]\boldsymbol{y} = \textstyle\sum_{i=1}^{n} \boldsymbol{u}_i y_i \tag{6}$$

In order to save notational alphabets, $\boldsymbol{U}$ is re-expressed by $\boldsymbol{A}$ hereafter, and so is $\boldsymbol{y}$ by $\boldsymbol{s}$. This is applied only if there is no confusion.

When an ICA basis $\boldsymbol{a}_i$ is used in image processing, it is interpreted as a two dimensional patch $\{\{a_i(x, y)\}_{x=1}^{m}\}_{y=1}^{m}$. Then, each pixel is modeled by

$$I(x, y) = \textstyle\sum_{i=1}^{n} a_i(x, y) s_i, \tag{7}$$

where $n = m^2$. Once the ICA bases are learned from data, they are *fixed*. Therefore, $\{s_i\}_{i=1}^{n}$ are subject to coding for image compression.

3. ICA Learning Algorithms

3.1. Preprocessing and Orthonormalization

Observed data are preprocessed in the following way so that the estimate of $\boldsymbol{W}$ converges properly.

1. [Mean and variance normalization] Observed data are normalized to have the zero mean and the unit variance.
2. [Whitening] Observed data are then transformed to $\boldsymbol{z} = \boldsymbol{V}\boldsymbol{x}$ so that $\mathcal{E}[\boldsymbol{z}\boldsymbol{z}^T] = \boldsymbol{I}$. Here, $\mathcal{E}$ stands for the expectation. We use $\boldsymbol{V} = \boldsymbol{D}^{-1/2}\boldsymbol{E}^T$ in our experiments. Here, $\boldsymbol{D}$ is a diagonal matrix whose elements are eigenvalues of $\mathcal{E}[\boldsymbol{x}\boldsymbol{x}^T]$. $\boldsymbol{E}$ is the matrix whose columns are corresponding eigenvectors.
3. [Orthonormalization] Another transformation is the orthonormalization: $\boldsymbol{W} \leftarrow (\boldsymbol{W}\boldsymbol{W}^T)^{-1/2}\boldsymbol{W}$. This is an expensive computation, however, the merits of $\boldsymbol{U} = \boldsymbol{W}^T$ and $\boldsymbol{W}^T\boldsymbol{W} = \boldsymbol{I}$ are obtained.

3.2. First-Stage Learning Algorithm

Estimation or learning of $\boldsymbol{W}$ from observed data is performed by the following iteration:

$$\boldsymbol{W}^{\text{new}} = f(\boldsymbol{W}^{\text{old}}), \tag{8}$$

or equivalently,

$$\boldsymbol{W}^{\text{new}} = \boldsymbol{W}^{\text{old}} + \Delta\boldsymbol{W}. \tag{9}$$

The updated vector $\boldsymbol{W}^{\text{new}}$ can be obtained by optimizing statistical measures for the independence [2] $\sim$ [7].

We gave necessary explanations on the first-stage algorithm for $\boldsymbol{W}$ except for the following. We are given sample image patches rather than an abstract random variable in a probability space. Therefore, we need to write down these samples in matrix forms: $\boldsymbol{X} = [\boldsymbol{x}(1), \cdots, \boldsymbol{x}(m)]$, $\boldsymbol{S} = [\boldsymbol{s}(1), \cdots, \boldsymbol{s}(m)]$, and $\boldsymbol{Y} = [\boldsymbol{y}(1), \cdots, \boldsymbol{y}(m)]$. Thus, the data generation model is expressed by

$$\boldsymbol{X} = \boldsymbol{A}\boldsymbol{S}. \tag{10}$$

Then, the first-stage learning algorithm becomes as follows.

[First-stage learning algorithm]

[Step 1 (Preprocessing 1)]
Obtain a sample matrix $\boldsymbol{X}$ as a training data set. Normalize each column vector to be zero mean and unit variance.

[Step 2 (Preprocessing 2: Whitening)]
Obtain Whitening Matrix $\boldsymbol{V}$ from $\boldsymbol{X}$, and compute $\boldsymbol{Z} = \boldsymbol{V}\boldsymbol{X}$.

[Step 3 (Initialization)]
Choose an orthonormalized initial value for $\boldsymbol{W}$.

[Step 4 (Update 1)]
Update $\boldsymbol{W}$ by (8) or (9).

[Step 5 (Update 2)]
Orthonormalize the matrix $\boldsymbol{W}$.

[Step 6 (Convergence check)]

Check to see if convergence is achieved. Otherwise repeat Steps 4 and 5.

[Step 7 (Resulting matrices)]

Resulting matrices are obtained by

$$\boldsymbol{W}_{\text{stage1}} = \boldsymbol{W}\boldsymbol{V}, \tag{11}$$

and

$$\boldsymbol{A}_{\text{stage1}} = (\boldsymbol{W}\boldsymbol{V})^{-1} = \boldsymbol{V}^{-1}\boldsymbol{W}^T. \tag{12}$$

It is necessary to comment here that:

(i) The first-stage algorithm still inherits the permutation indeterminacy. We need further learning algorithms which does not suffer from this indeterminacy.

(ii) In the image compression, the matrix

$$\boldsymbol{Y}_{\text{data}} = \boldsymbol{W}_{\text{stage1}}\boldsymbol{X}_{\text{data}} \tag{13}$$

is encoded to $\hat{\boldsymbol{Y}}_{\text{data}}$. Decoded is then

$$\hat{\boldsymbol{X}}_{\text{data}} = \boldsymbol{A}_{\text{stage1}}\hat{\boldsymbol{Y}}_{\text{data}}. \tag{14}$$

4. Learning Under Weak Guidance

4.1. Indeterminacy Reduction I: Topographic Alignment of ICA Bases

The above $\boldsymbol{A}_{\text{stage1}}$ could be used as a set of image compression bases, if one would dare to check manually the whole matrix pattern, and if high performance is not required. Thus, the bases are more suitable for the image compression if they have ordered by spatial frequencies precisely. Therefore, we consider to use the resulting image bases as an initial set for further learning modification. This is allowed since the image bases need not be computed on-line but to be stored in the encoder-decoder pair. There is one more evidence to support this: All computation in this paper can be carried out by a conventional personal computer, which will be understood in Section 5.

The first step to obtain an aligned image basis set is to modify the matrix $\boldsymbol{W}_{\text{stage1}}$ by using the topographic ICA [8]. In this case, (9) is used with the following computation:

$$\Delta\boldsymbol{w}_i = \eta E[\boldsymbol{z}(\boldsymbol{w}_i^T\boldsymbol{z})r_i], \tag{15}$$

$$r_i = \textstyle\sum_{k=1}^n h(i,k)G'(\sum_{j=1}^n h(k,j)(\boldsymbol{w}_j^T\boldsymbol{z}^2)). \tag{16}$$

On the choices of $G(y)$ and $h(i,j)$, readers are requested refer to [8]. Hereafter, the update matrix by (15) is denoted by $\Delta\boldsymbol{W}_{\text{tp}}$.

4.2. Indeterminacy Reduction II: Weak Guidance

Resulting ICA bases as a topographic map show an intriguing visual pattern. But, a very important indeterminacy is not yet resolved. A human can instantly find the position of the central basis corresponding to the lowest spatial frequency, however, machines can not do so instantly. Therefore, we need a further important mechanism to reduce such indeterminacy. This is the method of *weak guidance* as a partially supervised learning. Such a method was first used in the distillation of brain maps from fMRI data [9], [10].

[Weak Guidance]

First, we prepare a teacher signal, or a reference pattern, as a matrix $\bar{\boldsymbol{R}}$. Then, we compute $\boldsymbol{U} = \boldsymbol{V}^{-1}\boldsymbol{W}^T$. The increment by the teacher signal is

$$\Delta\boldsymbol{U} = \boldsymbol{V}\{\lambda(\bar{\boldsymbol{R}} - \boldsymbol{U})\}. \tag{17}$$

Here, λ is a learning parameter. Then, the update term for the weak guidance is computed by

$$\Delta\boldsymbol{W}_{\text{wg}} = -\boldsymbol{W}\Delta\boldsymbol{U}\boldsymbol{W}. \tag{18}$$

Readers are requested refer to [9] or [10] for the derivation of (17) and (18).

4.3. Total Learning Algorithm

By the preceding preparations, the total algorithm to obtain the ICA bases can be described as follows.

[Step 1 (Learning parameters)]

Control rules of the small learning parameters $\eta > 0$ and $\lambda > 0$ are decided. The rules can be arbitrary as long as (i) η increases and saturates. (ii) λ decreases.

[Step 2 (Weak guidance)]

Compute the updated matrix with the weak guidance

$$\boldsymbol{W} \leftarrow \boldsymbol{W} + \Delta\boldsymbol{W}_{\text{wg}}. \tag{19}$$

[Step 3 (Topographical map)]

Compute the updated matrix with the topographic constraint

$$\boldsymbol{W} \leftarrow \boldsymbol{W} + \Delta\boldsymbol{W}_{\text{tp}}. \tag{20}$$

[Step 4 (Convergence check)]

Check to see if the matrix update is converged. If not, then the iteration is repeated on Steps 2 and 3 after the update of λ, η, and $\boldsymbol{W}$.

5. Experimental Results

5.1. ICA Image Bases with Self-Alignment

All necessary tools were given in the preceding sections. We can now apply them to real images. Training data for the ICA bases contain many images such as natural images, screen text images, and animations. Figure 1 illustrates the ICA bases obtained by the topographic method alone, i.e., without the weak guidance. Each basis is of 8×8 pixels so that the size is compatible with usual JPEG and JPEG2000. As can be observed, the basis of the lowest spatial frequency is located off-centered in the two dimensional array. This position can not be specified in advance. Therefore, the human perception is still necessary to identify where the exact center is. Besides, the obtained ICA bases are inefficient since the center is near the corner of the array.

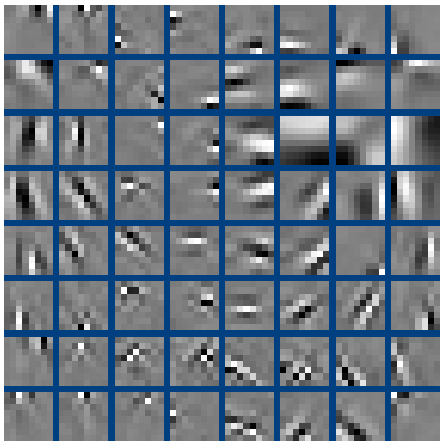

Figure 1. Image bases only by the topographic method.

Figure 2 shows the resulting self-aligned ICA bases by our weak guidance method. The first basis is located at the north west of the four central bases. Low-frequency bases are concentrated around the center of the two-dimensional array. High-frequency bases are located at the corners. This was specified to be so by virtue of the weak guidance. We call such a class of bases the *ICA ripplet set*, or simply the *ripplet set*. The ripplet set is readily applicable to the image compression due to the following properties.

(a) Ordering from low to high spatial frequencies is completed.

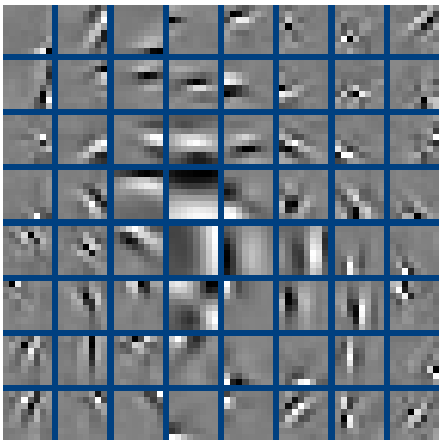

Figure 2. Self-aligned image bases by the weak guidance.

(b) Bases are balanced because of the centering by the weak guidance.

Item (a) can be observed from Figure 3 which was obtained from Figure 2 by the clockwise spiral sorting started from the origin, the north west of the four central bases. This figure clearly shows a self-aligned ordering from low to high spatial frequencies which has the following merit:

(c) Users of this set can understand the role of each basis in a linearly ordered sense. High-frequency bases may correspond to noisy patterns. Such a merit will be utilized in Section 5.3.

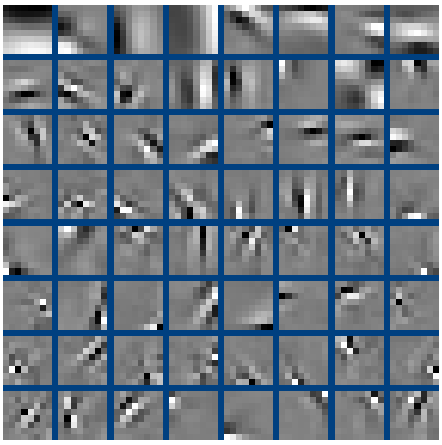

Figure 3. Aligned image bases.

Figures 1 to 3 can claim the similarity to the receptive field properties [11]. Not only appreciating such an intriguing similarity, but we pay attention to the self-aligned ICA bases of Figures 2 and 3 on the use for the image compression.

5.2. Distribution of Coefficients

Source images are reconstructed by using Equation (7). We remind readers here that the relationship on the ICA image bases: $\boldsymbol{A}^{-1} \leftarrow \boldsymbol{W}$. Since the image bases are not altered any more, they are memorized in the encoder and the decoder. In the encoder, coefficients s_i are obtained by $\boldsymbol{S} = \boldsymbol{A}^{-1}\boldsymbol{X}$. Here, each column vector of $\boldsymbol{X}$ corresponds to an image patch. Then, encoded values of elements s_i in $\boldsymbol{S}$ are transmitted (in a two dimensional form, $s_{i,j}$).

The distribution of $\boldsymbol{s}$ is $\{8 \times 8 = 64\}$-dimensional which is unable to illustrate visually. But, the flatness of the distribution can be estimated from the histogram of $s_{i,j}$. If the distribution of $s_{i,j}$ were nearly flat, there would be very little possibility for data compression because of high entropy. Therefore, we have to examine the distribution on real images. Figure 4 is the result-

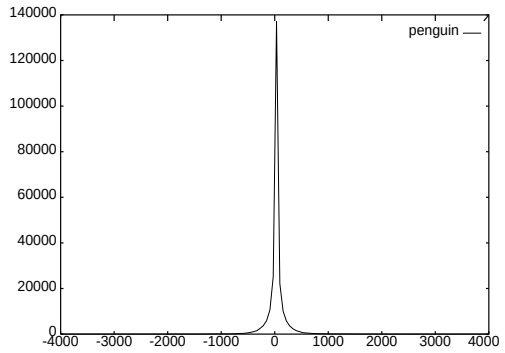

Figure 4. Distribution of coefficients to be encoded.

ing distribution obtained from an image outside of the training data. The horizontal axis shows values of s_i. The vertical axis shows the number of appearances, i.e., the frequency. As can be observed, this distribution is far from flat. It is highly super-Gaussian reflecting the nature of the ICA transformation of images. This means that most of s_i are centered around zero. Few important numbers are distant from zero. Therefore, we can judge that the distribution of $\boldsymbol{s}$ is very sparse. This property encourages us with the anticipation that the encoding for data compression will be effective.

5.3. Image Compression

Here, we discuss the case of variable-length coding based upon the run-length and Huffman coding. The source to be compressed is the matrix

$$\boldsymbol{S} = [\boldsymbol{s}_1, \cdots, \boldsymbol{s}_M]. \tag{21}$$

Here, $\boldsymbol{s}_i$ is the vector coefficient for one patch in the source image. Therefore, $M = 3750$ for a 600×400 pixel image since $(600/8) \times (400/8) = 3750$. The vector $\boldsymbol{s}_i$ is quantized in group. The quantization is set to be granular if a coefficient is for a low spatial frequency. On the other hand, the quantization is rough if the coefficient is for higher frequencies. Quantized zeroes appear frequently because of the sparseness explained in Section 5.2. Then, we denote the resulting coefficient matrix by $\tilde{\boldsymbol{S}}$. We found that quantized zeroes run consecutively if we raster scan this $\tilde{\boldsymbol{S}}$ *vertically* because of the property explained in Item (c) of Section 5.1: High-frequency bases correspond to noisy patterns. Therefore, run-length coding is effective. Huffman coding is used for non-zeroes.

Figure 5. Uncompressed image.

Figure 6. Compressed image 1.

Figures 5 is a source image selected from [12]. Figure 6 is a compressed image by this paper's method. The compressed image has the performance of $\mathrm{SNR}_{\mathrm{pp}} =$

Figure 7. Compressed image 2.

35.2 dB at 1.24 bit/pixel. Figure 7 is another compressed image containing charecters. This image is not a set of outline fonts but is obtained from a computer display. This image has the performance of $\mathrm{SNR}_{\mathrm{pp}} = 34.8$ dB at 1.28 bit/pixel.

More experiments besides Figures 6 and 7 were tried. We can conclude that the image compression based upon the ICA bases designed by this paper's method shows the excellent performance.

6. Concluding Remarks

The main purpose of this paper was to show that

(i) The permutation indeterminacy of the ICA can be avoided. The resulting bases can be used in engineering applications, particularlly for image compression.

(ii) The ICA bases learned from images extract important information. Such bases can be applied to reconstruct unlearned images.

(iii) Coefficients for the reconstruction can be used for the image compression.

It was possible to show that the image compression based upon the ICA bases is promising. We shall have the immediate sophistication of this paper's study as follows:

(a) Incorporation of better lossless coding on coefficients.

(b) Applications to color image compression.

Acknowledgment

This study was supported by the Grant-in-Aid for Scientific Research #15300077 and by the Productive ICT Academia of the 21st Century COE Program granted to Waseda University. The authors are grateful to Mr. S. Imahara of Toshiba Co. for his early contributions.

References

[1] C. Jutten and J. Herault, "Blind separation of sources, part I: An adaptive algorithm based on neuromimetic architecture," Signal Processing, vol. 24, pp. 1-10, 1991.

[2] J-F. Cardoso and A. Souloumiac, "Blind beamforming for non Gaussian signals," IEE Proceedings F, vol. 140, pp. 362-370, 1993.

[3] A. J. Bell and T. J. Sejnowski, "An information-maximization approach to blind separation and blind deconvolution," Neural Computation, vol. 7, pp. 1129-1159, 1995.

[4] H. H. Yang and S. Amari, "Adaptive online learning algorithm for blind separation: Maximum entropy and minimum mutual information," Neural Computation, vol. 9, pp. 1457-1482, 1997.

[5] A. Hyvärinen "Fast and robust fixed-point algorithms for independent component analysis," IEEE Trans. Neural Networks, vol. 10, pp. 626-639, 1999.

[6] Y. Matsuyama, N. Katsumata, Y. Suzuki and S. Imahara, "The α-ICA algorithm," Proc. Int. Workshop on Independent Component Analysis, pp. 297-302, 2000.

[7] Y. Matsuyama, S. Imahara and N. Katsumata, "Optimization transfer for computational learning," Proc. Int. Joint Conf. on Neural Networks, vol. 3, pp. 1883-1888, 2002.

[8] A. Hyvärinen, P.O. Hoyer and M. Inki, "Topographic independent component analysis," Neural Computation, vol. 13, pp. 1527-1558, 2001.

[9] Y. Matsuyama and S. Imahara, "The α-ICA algorithm and brain map distillation from fMRI images," Proc. Int. Conf. Neural Info. Processing, vol. 2, pp. 708-713, 2000.

[10] Y. Matsuyama, N. Katsumata anr R. Kawamura, "Independent component analysis minimizing convex divergence," Proc. ICANN/ICONIP03, Lecture Notes in Computer Science, Springer-Verlag, 2003.

[11] B. A. Olshausen and D. J. Field, "Emergence of simple-cell receptive field properties by learning a sparse code for natural images," Nature, vol. 381, pp. 607-609, 1996.

[12] "Master Photo 75,000," H^2 Soft Co., 1999.

An Improved Neural Tree Classifier with Adaptive Pruning

W. Pensuwon
Faculty of Engineering,
Ubonratchathani University,
Thailand
Wanida.Pe@ubu.ac.th

R.G. Adams
Dept. of Computer Science,
Faculty of Eng & Info. Science,
University of Hertfordshire, U.K.
R.G.Adams@herts.ac.uk

N. Davey
Dept. of Computer Science,
Faculty of Eng & Info. Science,
University of Hertfordshire, U.K.
N.Davey@herts.ac.uk

Abstract
This paper describes an improved Stochastic Competitive Evolutionary Neural Tree (SCENT). Adaptive Pruning algorithm is introduced. The idea is to construct the optimal neural tree structure with a two-phase pruning algorithm, which penalise the incompetent clusterer. The comparative results suggest that the method is fairly efficient in terms of simple structure, fast learning speed and relatively high clustering performances.

Keywords
Stochasticity, Dynamic Neural Tree Network, Hierarchical Clustering, Pruning.

INTRODUCTION

The original motivation and objective for using the adaptive pruning, was mainly trying to optimise the clustering performance by penalise the insufficient clusterer. The improved model is improved the idea of the Stochastic Competitive Evolutionary Neural Tree (SCENT) which provides hierarchical classification of unlabelled data. The network produces stable classificatory structures by repeatedly restructuring the insufficient branch of the classification tree based on internal relation between members.

Stochastic Competitive Evolutionary Neural Tree (SCENT) model [7, 8] attempts to combine the advantages of using a tree structure, and of growing the network. SCENT show promise in their ability to produce stable yet flexible hierarchical structures.

The nature of the hierarchical structure and the quality of the final classification produced by the networks is, however, very strongly influenced by the values given to externally set parameters. The SCENT network does not require externally set parameters, it is therefore able to explore data sets without external influence.

STOCHASTIC COMPETITIVE EVOLUTIONARY NEURAL TREE (SCENT)

Top-Level Algorithm

In SCENT [7, 8], the evolution of the neural tree starts the original root node produces a child group which has 2 randomly positioned children. They have tolerance (the radius of its classificatory hypersphere) set to standard deviation of input vectors and its position is set to the mean of input vectors.

There are two counters, calls inner and outer, which count the number time of classified input vector from distance of within or outside tolerance respectively. These counters defined neural tree should grow children or sibling once. It is decisioned that growth is to be allowed. When a node is allowed to grow, then its inner counter will be greater than its outer counter and it creates two children. Otherwise, it produces a sibling node. The process of growth is illustrated in Figure 1.

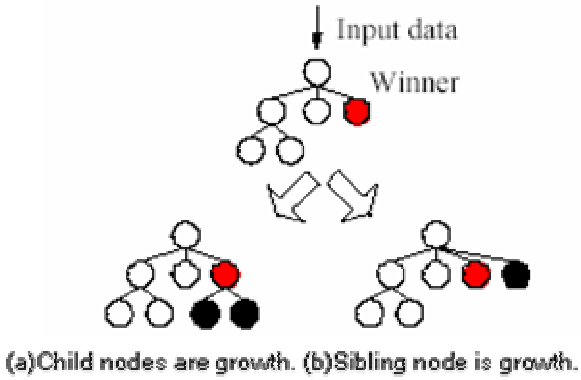

Figure 1. The wining leaf node can grow, (a) children nodes are growth, called downgrowth and (b) sidegrowth in which sibling node is growth.

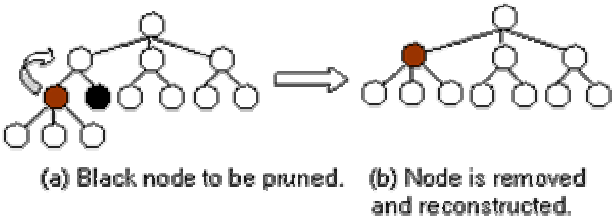

Figure 2. The SCENT models, nodes that are ineffective can be pruned (on the left) when it is also removed (on the right).

This algorithm is called Top-Level Algorithm which a recursive search through the tree is made for a winning branch of the tree. Each node which win of branch is moved top-down towards from input data using the standard competitive neural network update rule. The weight vectors of leaf nodes provide bottom level code-vectors the higher level nodes give representations of the centroids of their corresponding clusters.

Pruning algorithms are divided that two section, short term and long term for efficiently delete. The short-term pruning, nodes are immediately deleted when they are

early life which has error more than set to error acceptance. The long-term pruning delete node when has activity less than a threshold value, illustrated in Figure 2.

Stochasticity

Interest in stochastic method, from the fact that in real world problems, the cost function seldom succeed in defining precisely the real optimality of the solution. The optimality condition is far too complex to be understood by any particular formula, in such cases it is desirable to have methods, which can suggest a set of goods demonstrate such behaviour.

Due to the randomise involved, stochastic method the can handle the cost function and can be considered as promising candidates for solving real world problems.

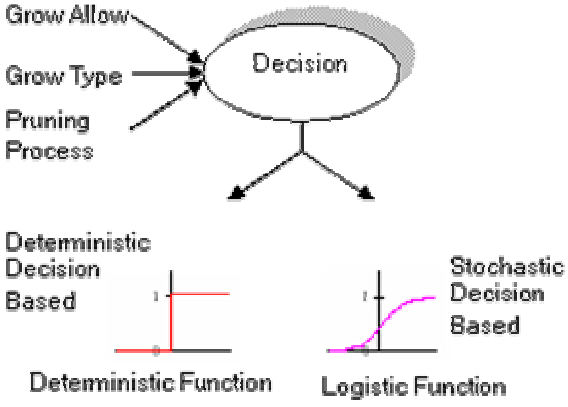

Figure 3. Decision Based Stochasticity. The probability of accepting a decision produced in the left is crisp while the probability of accepting a decision in the right is fuzzy.

One of the main goals of neural network researches has been to build the system the mimic the ability of humans to solve the real world problem. Curiously, tradition approaches in solving have been based on the two valued logic. This is a form of hard computing which based on precision and certainty. It is in sharp contrast to real human reasoning or what is known as common-sense which is based on approximate, rather than precise computing methods.

Adding Stochasticity to a deterministic version (CENT) [1, 2] could have some benefit in helping the model avoid local minima in its implicit cost function. There are two different ways in which stochasticity can be added to the model [8].

Firstly the deterministic decisions relating to growth and pruning can be made probabilistic, it is called Decision Based Stochasticity. The Decision Base Stochasticty has 3 procedures which decisions growth allow, grow type (downgrowth or sidegrowth) and short-term pruning.

Secondly the attributes inherited by nodes when they are created can be calculated with a stochastic element, it is called Generative Stochasticity by changing tolerance values from deterministic function that new tolerance is same every node are created , to stochastic values is randomness effect to new node more flexibility.

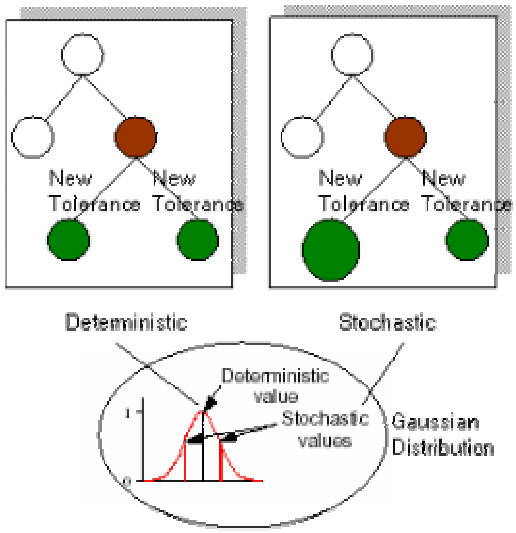

Figure 4. Generative Stochasticity. In deterministic version (CENT) [1, 2] both children have the same value of tolerance (in left crisp). In SCENT a Gaussian is superimposed on the deterministic value to generate 2 different child tolerances (in right crisp).

To both of these approaches a simulated annealing process can be added to mediate the amount of non-determinism in a controlled way, so that a decreasing temperature allows for less randomness later in the life of the network.

The Decision will be deterministic which integration of stochastic decision based and simulated annealing. Deterministic version performed well on artificial training set and adding stochasticity still allowed high quality trees to be produced.

AN IMPROVED STOCHASTIC COMPETITIVE EVOLUTIONARY NEURAL TREE (SCENT)

All dynamic networks have to overcome the problem of creating too many nodes and over classifying the data set. These can potentially be a node produced to classify each input vector. In order to prevent over classification, the technique of adaptive pruning in order to create optimal classification nodes is introduced to the original SCENT model.

The improved SCENT has been reengineered in order to improve the clustering performances. There are a few changes in an updated SCENT model in which the pruning process is repeatedly applied after the final process of the classification has been done.

Every branches of classification of the final tree is evaluated by a flat clustering measure. The inadequate branch is deleted and the process of classification will be repeated once to produce a final optimal classification tree.

Algorithm Description

There are 4 major phases in the program: initialisation, main loop, tidy up loop and adaptive pruning loop. In the initialisation phase, the necessary parameters are set, data files are read and a root node is created. In the second phase, the main loop, the tree is allowed to grow and is systematically pruned. The third phase consists of tidying up the final position of nodes in a tree. The final phase, the worse branch of the root's child is deleted and the remaining tree is restructured by repeating clustering process in order to improve its performance. Each phase is described below using pseudocode.

Initialisation

1. Set maximum epoch and learning rate
2. Read parameter file
3. Set *tolerance* of a root node using standard deviation of input vectors
4. Create *RootNode* and 2 initial children nodes and set their *tolerance*

Main Loop

- ***While*** epoch < maximumepoch ***Do***
  - Shuffle inputvectors
  - ***For*** each input vector ***Do***
    - Set *CurrentNode* ← *RootNode*
    - Increment time
    - Update weights, *activity*, and error of *CurrentNode*
    - ***While*** *CurrentNode* ≠ *NULL* ***Do***
      - Find *WinnerNode* from children of *CurrentNode*
      - Update *inner* and *outer* counter of *WinnerNode*
      - Update weights, *activity* and error of *WinnerNode*
      - ***If*** *WinnerNode* is allowed to grow ***Then***
        - ***If*** *outer* > *inner* ***Then***
          - Create **Side-growth** (*WinnerNode*)
          - Initialise *Winner-Node*
        - ***Else***
          - Create **Down-growth** (*WinnerNode*)
          - Initialise *Winner-Node*
      - ***If*** child of *WinnerNode* is not NULL ***Then***
        - Increment level of a tree
        - Set *Currentnode* ← *Winnernode*
      - ***Else***
        - Set *Currentnode* ← *NULL*
      - ***EndWhile***
      - Calculate Sum of Square Error of a tree
      - Update *activity* and error of a tree
  - ***EndFor***
  - Perform **Short-term Pruning**(*RootNode*)
  - Perform **Long-term Pruning**(*RootNode*)

Tidy up loop

- ***While*** epoch < tidyup epoch ***Do***
  - Shuffle inputvectors
  - ***For*** each input vector ***Do***
    - Set *CurrentNode* ← *RootNode*
    - Increment time
    - Update weights, *activity*, and error of *CurrentNode*
    - ***While*** *CurrentNode* ≠ *NULL* ***Do***
      - Find *WinnerNode* from children of *CurrentNode*
      - Update *inner* and *outer* counter of *WinnerNode*
      - Update weights, *activity* and error of *WinnerNode*
      - ***If*** *WinnerNode*'s child is not NULL ***Then***
        - Increment level of tree
        - Set *Currentnode* ← *Winnernode*

- ***Else***

- Set

Currentnode ← *NULL*

- ***EndWhile***

- Calculate Sum square Error of a tree

- Update *activity* and error of a tree

- ***EndFor***

- Perform **Pruning TidyUp**(*RootNode*)

Adaptive Pruning loop

- ***While*** epoch < adaptivepruning epoch ***Do***

- Root's child: Delete the worse branch performance (minimum Gamma Measure)

- Repeat Step Main Loop

- Repeat Tidy up Loop

- Restructure Tree

Clustering Measures

The general goal in many clustering applications is to arrive at clusters of objects that show small within-cluster variation relative to the between-cluster variation [4]. Clustering is difficult as many reasonable classifications may exist for a given data set, moreover it is easy for a clusterer to identify too few or too many clusters. Suitable cluster criterion measures are therefore needed [3, 4, 5]. There are two types of clustering measure: ones that variety the flat clustering performance of the leaf nodes and ones that variety the hierarchical structure.

The Gamma method [3] , which measures the flat partitioning performance, and the Hierarchical Correlation method [5], that assesses the hierarchical structure in a neural tree network. The methods are as follows:

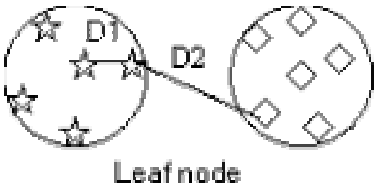

Figure 5. The distance within and between cluster used in calculating Gamma. If D1 is less than D2 then s(+) is incremented and s(-) represents the opposite relationship to s(+).

Gamma: s(+) is number of times when two points not clustered together are further apart than two points which are in the same cluster and s(-) is the number of times when two point not clustered together are closer than two points which are in the cluster. It is compute as,

$$\gamma = \frac{s(+) - s(-)}{s(+) + s(-)}$$

The maximum value indicated the optimal solution. This technique has an upper bound of +1 and a lower bound of -1.

EXPERIMENT

Data Sets

The networks considered in this paper were run over nine different types of data, ranging from a small data set to a large data set. There are two 2-dimensional and two higher dimensional artificial data sets are used. These data sets have cluster structure 4 to 27 classes.

There are nine real world data sets, one example is the well known IRIS data set which consists of 150 instances of 4 attributes describing sepal length, sepal width, petal length and petal width of the iris flower.

RESULTS

In order to know how well the improved SCENT performs over SCENT, the comparative results of improved SCENT, SCENT and CENT (deterministic model) are presented. The corresponding models were applied to all nine data sets three times; the resulting trees were evaluated using the cluster measure.

Table 1. Average gamma measures of the classifications produced by the 3 neural network models tested over 9 data sets. The value closed to 1 representing the best performance.

Neural Classifiers	Average	Standard Deviation
CENT	0.827	0.131
SCENT	0.841	0.171
Improved SCENT	0.850	0.147

Table 1 represents the average and standard deviation of the gamma measure. The performance of the improved SCENT was clearly better than other two networks. The improved SCENT model produced excellent results in terms of flat and hierarchical clustering measures when viewed as a straightforward cluster, illustrated in Figure 6, giving comparable performance to the SCENT and CENT. It also produced useful, compact and repeatable tree structure so represent any hierarchical information in the data.

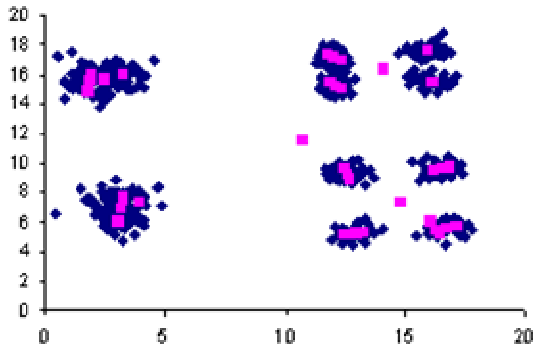

(a) CENT

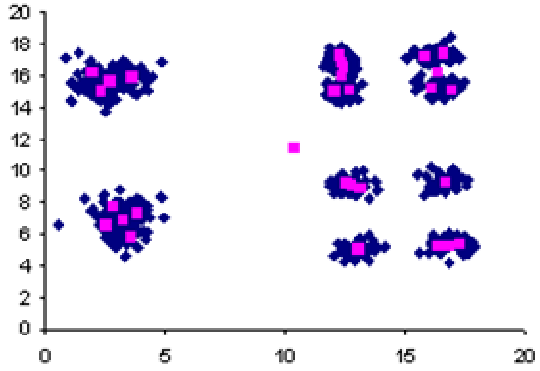

(b) SCENT

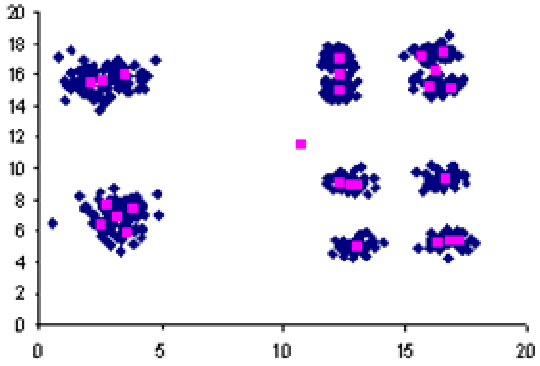

(c) Improved SCENT

Figure 6. Leaf node positions of 3 models tested over a representative data set.

CONCLUSIONS

Using neural networks to perform data exploration is difficult; most models require the preimposition of a maximum number of clusters, and will normally classify the data to utilise all classificatory units. There is a question of when to stop training and so when to stop pruning.

Therefore, introducing adaptive pruning by penalise the insufficient classification nodes could balance the scale factor of the misclassification and it can be controlled dynamically.

Using Adaptive Pruning is an interesting and promising approach as a way of taking advantage of the learning advantages of larger systems while avoiding their over fitting problems.

The performance of the propose network (improved SCENT) over a wide range of data sets has been presented and it has been shown to provide a good interpretation of the real world data set, and to produce better classifications compared to the SCENT and the CENT over the nine data sets. The network has shown also that it can handle large data sets.

The improved SCENT model has produced a consistently good performance over all of the data set presented, has maintained the quality of performance and has improved reliability. Further work is being carried out to determine the best combination of restructuring mechanisms for measuring both flat and hierarchical clustering on the stochastic model.

REFERENCES

[1] R.G. Adams. K. Butchart. And N. Davey, "Classification with a Competitive Evolutionary Neural Tree," Neural Networks J, Vol. 12, pp. 541-551, 1999.

[2] N. Davey, R.G. Adams. and S. G. George, "The Architecture and Performance of a Stochastic Competitive Evolutionary Neural Tree," Journal of Applied Intelligence, Vol. 12, No. 1/2, pp. 75-93, 2000.

[3] A. D. Gordon, Classification, Chapman & Hall, London, 1999.

[4] J. A. Hartigan, Clustering Algorithms, John Wiley & Sons, USA, 1975.

[5] G. W. Milligan. and M. C. Cooper, "An Examination of Procedures for Detemining the Number of Clusters in a Data Set," Psychometrika Journal, Vol. 50, No. 2, pp 159-179, 1985.

[6] M. Mitchell, An Introduction to Genetic Algorithms, MIT Press, USA., 1998

[7] W. Pensuwon, R. G. Adams. and N. Davey, "Comparative Performances of Stochastic Competitive Evolutionary Neural Tree (SCENT) with Neural Classifiers," Proceedings of the 8th International Conference on Neural Information Processing - ICONIP-2001., pp.121-126, 2001.

[8] W. Pensuwon, R. G. Adams. and N. Davey, "The Analysis of the Addition of Stochasticity to a Neural Tree Classifier," Journal of Applied Soft Computing, Vol. 1, No.3, pp 189-200, 2002.

(This page left blank intentionally)

Agent-Based Modelling of House Price Evolution

Siti Amri
School of Information Technology,
Charles Sturt University
Bathurst, NSW, Australia
samri@csu.edu.au

Terry Bossomaier
School of Information Technology,
Charles Sturt University
Bathurst, NSW, Australia
tbossomaier@csu.edu.au

Abstract

Housing prices result from many factors, from government control to individual needs. Yet they seemingly take on a will of their own, booming rather than crashing and so defying all analysis and expectation. We discuss a comprehensive agent-based model of housing prices, in which real data is embedded from a variety of sources. Much of the data is spatial collected from Geographical Information Systems (GIS). The variety of different stakeholders, costs, formats and infrastructure presents considerable challenges in developing a general model. This paper describes the preliminary design work towards such a general model of the way house prices evolve. A number of initial simulations are developed in MATLAB to examine the impact of real-estate agents and fuzzy inference of the vendor's agent on house price evolution.

INTRODUCTION

House Prices are determined by the interaction of supply and demand factors [8]. These factors have a different temporal lag and may have positive or negative effects on house prices. For example, an increase in population will result in increasing demand on housing consumption and consequently will increase housing price. However, an increased construction of new houses will add to the "for sale" stock and will decrease price. These housing factors have a positive or negative feedback loop and are dynamic in nature. Historical observation of house prices indicates a cyclical trend with distinctive regional variations.

The housing market is in a perpetual state of disequilibrium due to the inelasticity of supply [8] [18]. The construction rate of new houses is relatively low proportional to the overall stock. Durability of houses lead to a housing market which is determined by existing homes. Harvey argued that house prices are less affected by supply but more demand driven. The housing market also functions inefficiently due to, amongst other factors, imperfect knowledge of buyers and sellers, the uniqueness of each site and building, and high legal and transaction costs, which prevent the asset from transferring smoothly to its most profitable use.

These market inefficiencies allow speculation of houses for short term gain [2] [13] [9]. Other researchers have also identified the speculation sentiment on house price and term it the "frenzy effect" [3] [13] [20]. This speculation sentiment explains the expectation that once house prices rise, the rise is continuing thus reinforcing the upward trend of house prices. These studies confirmed that house prices are generally too volatile to be driven by economic fundamentals alone. The varying sentiment of buyers and sellers' behaviour contribute to the volatility as well. Balchin et. al [18] summarised the housing market as "disorganised with no central buying or selling place, comprised of a vast number of housing transactions involving heterogeneous houses".

Knowledge of how house prices evolve is useful for investors, banks, institutions, and private purchasers as it allows them to make informed decisions about a purchasing strategy. This is particularly important in Australia, where real estate is the greatest component of household wealth. For most households, the family home constitutes the single most important investment and the most expensive. Being able to model the evolution of house prices has the potential to have a significant impact.

The general model of house prices is that they have been on the rise over time. However, the pattern of the rise has not been continual and includes a high number of fluctuations [4]. In general, house prices are determined by the interaction of demand and supply factors within the housing market. There are both global and local factors that impact on pricing. In addition, the housing market is driven by the expectation of buyers and vendors about future price growth [5]. Varying levels of market knowledge and cycles of buyer-vendor sentiment add further complexity to the way house prices evolve.

Because of the number of factors at different levels, producing a model of the way house prices evolve has proved extremely difficult. Using an agent-based model is an alternative approach to modelling such complex systems. Such systems have proved successful in many other diverse and complex domains such as stock market trading and petroleum exploration. In this paper we describe an agent-based model to incorporate the various temporal, spatial and human factors that impact on the evolution of house prices.

The paper reviews methodological issues on house price estimation. This paper also proposes a simulation model to capture the adapting cognitive processes of vendors, buyers, and real-estate agents and the impact of their changing sentiments upon prices. A simulation has been developed in MATLAB [14] to further investigate this aspect of the model. The implementation and results from this simulation

are described before the paper concludes with a summary of outcomes and directions for future work.

METHODOLOGICAL ISSUES

There are 3 distinct groups of methodologies to calculate house prices:

- Statistical Methods
- Preference Methods
- Artificial Intelligence Methods

Statistical Methods

Of the statistical techniques, Multiple Regression Analysis is by far the most commonly used method to forecast house prices. In this method, the dependent variable, house price, is regressed against a set of predictors (or independent variables), as illustrated in the equation below. These predictors are comprised of variables such the housing structure (size and features) and location.

$$Y = \beta_1 + \beta_2 X_2 + \beta_3 X_3 + \beta_4 X_4 + \ldots + \beta_n X_n + \mu$$

where:

Y = dependent variable

$\beta_1, \beta_2, \ldots, \beta_n$ = unknown parameters to be estimated

$X_1, X_2, \ldots, X_n$ = independent variables

μ = error term

In many studies, past values of house prices are used to predict its future price [7] [19]. A further extension of this model created market segments based on spatial factors [17][19]. These spatial factors adjusted prices for different areas. This allows different regression functions to be computed for each of the market segments.

Another extension of this method is to apply factor analysis, principal component analysis (PCA) or multidimensional scaling (MDS) to segment the data. The data with reduced dimensions are then grouped into submarkets using cluster analysis [19].

Critics of these statistical methods argue against the generalisation of aggregate price indices from regression results [7] [10]. This model assumed a uniform appreciation rate for all housing units in a given locality and they claimed that this contradicted with their own findings. Seward et. al found that higher price housing appreciates at a more rapid rate than low and medium price housing during a growth phase yet there is no difference in a down trend. The difference in the market behaviour of the housing unit is lost in the regression approach due to the averaging effects over available data. The question of sample bias has been raised in the way regression techniques use previous sales prices [7]. Jud and Seales determined that the sample included only homes that were sold and not all the houses in a given area. Thus, in an economic downturn, bias is largest when fewer houses are sold [7]. The dependence of this technique on secondary datasets is also a problem because variable selection tends to be based on what is available rather than on what is sensible [19].

Kauko further questioned the use of a partitioning technique, explaining that "heterogeneity of dwellings and households can imply not necessarily the existence of several submarkets, but rather the same diversified markets". This argument raises doubt about whether a locally partitioned dataset with multiple regression functions or a single hedonic price function is more appropriate for forming house price estimation.

The strongest counterargument against this technique is that it ignores the importance of household and institutional preferences [6] [19]. Parker et. al [6] criticised this technique as it failed to represent feedbacks and capture a dynamic process. They argued that this top-down modelling approach is only suitable when analysing with a very coarse temporal and spatial resolution. If there is strong local heterogeneity and interactions then this type of modelling is not considered appropriate.

Preference Methods

The second group of modelling techniques on house forecasting is focusing not on prices but on housing preference. This stream of research activity includes conventional stated preferences (interview surveys, experimental choice design, contingent valuation) and analytic decision tools. These studies generate house price estimates associated with value differences from information collected through interview. The argument against this method is that it is based on hypothetical rather than actual behaviour and reflects consumer tastes and not house price formation [19].

Artificial Intelligence Methods

The final group of methods, from Artificial Intelligence (AI), has recently emerged offering a simple approach to simulating market behaviour and house price estimation. These approaches have qualitative underpinnings and simulate market behaviour with the aim not to generate perfect accuracy but to simulate judgemen [11] [19].

In the house price application, Rossini [15] [16] and Kauko [19] both employed an artificial neural networks (ANN) together in comparison with multiple regression analysis (MRA). Kauko provides an extensive review of ANN use in house price research and discusses the issues surrounding the relative poor "take up" of this technique. The consensus from these researchers is the results from ANN are superior to the MRA. However, Rossini, who applies ANN to develop a mass appraisal valuation of property in South Australia, finds that ANN produces superior results when the data set is small.

In summary, the MRA technique requires the exclusion of outliers and homogeneous data to prevent large error margins and to trace average dependencies respectively. It assumes equilibrium and linear data trend. The ANN technique used together with the genetic algorithm provides an

excellent data grouping but assumes rational choice with perfect knowledge.

Existing methodologies of calculating house prices assumes rational choice, complete knowledge, and optimal solution. These models often fail to predict and explain the reality of the housing system. The nature of housing is influenced not only by its location and associated structural attributes but also by its relative value reflected by individual or institutional preference. These individuals and institutions have incomplete knowledge of the market and are boundedly rational i.e. they have evolving choices that move toward achieving their goals.

THE AGENT-BASED MODEL

The housing system can be viewed as an evolving complex system. Supply and demand factors may have linear or non-linearity tendency. Furthermore, in the urban areas the housing system can generate surprising complexity and often ordered pattern in aggregate form. These emergence and self-organisation phenomena are reflected in the pricing cycle and in the spatial clustering of socio-economic groups by housing markets in the urban landscape. In the complex system framework, house price distribution and dynamics are the result of interactions from multiple independent entities or agents, which may be individuals (buyers, sellers, real-estate agents) or institutions (banks, property developers, government).

The agent-based modelling approach is a technique derived from complexity. It captures non-linearities and emergent behaviour from cycle to chaos. It represents the housing economics as a decentralised collection of interacting, adaptive, autonomous agents with no global control. It focuses on the simulation of agents' behaviour and how they interact. This research proposes the construction of the computational model of the housing system. This model will be used as a test bed to examine alternative agents' traits eg. pricing strategies. This computational model enables simulation of the house price evolution and the testing of its processes. Validation of model results will be compared with existing house price data.

1.1 The Agents

There are 3 types of agents considered in this study; vendor, buyers and real-estate agents (Figure 1). These agents have imperfect knowledge of the housing market and may rely on information from past decisions, their own and those of other agents to update decision-making strategies. This process leads to temporal interdependencies among agents. These decisions will likely have temporal dynamic impacts on the house price distribution and market environment.

Figure 1: Agents Relationship

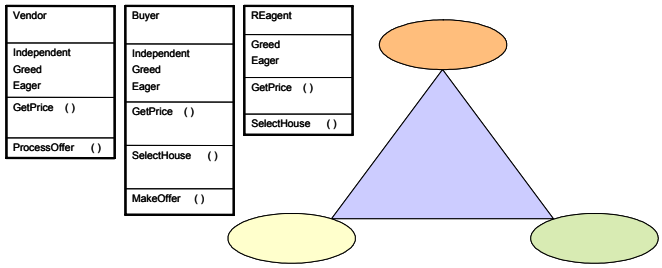

In this study, the agents have simple adaptive traits for speculating house price strategies. Each agent constructs a probability measure of house price based on their knowledge of housing factors and level of access to sales history information. In this study, the varying level of knowledge is represented by the different methods of estimating house prices employed by the agents. The vendor and buyer agents adapt their pricing and transaction strategies according to their personal attributes. In this initial set-up the agent strategy is reflected by how it speculates the house price estimate. Also, house price is determined by the cost of acquiring the house plus the speculation of its appreciation over time. The price function of the agents has to ensure that the vendors or real estate agent never sells a house for less than it paid to acquire it.

The vendor agent perceives the house estimate through a limited scope of comparing recent property sales in their neighbourhood. The vendor deduces its house projection based on a subset of previous sale records. In this example, it is a list comprising of 20 houses which make up the recent sales. The vendor then locates the 2 nearest houses and calculates the sale mean value of the prices. This value will be the vendor's perception of its house value and constitutes the asking price.

$$Dist(x) = \sum_{i=1}^{n} (r_1 - r_n)^2 + (c_1 - c_n)^2$$

$$P_v = \frac{P_{\min_1} + P_{\min_2}}{2}$$

where:

P_v = Vendor's price

$P_{\min_1}$ = Price at 1st closest

$P_{\min_2}$ = Price at 2nd closest

$r_1, c_1 \ldots r_n, c_n$ = House locations

The real estate agent is assumed to have a better knowledge of the sale price variations of a given area [12]. The real estate agent constructs an estimate of house prices in a current year based on a comprehensive list of sold prices using the following equation:

$$P_{y_c} = \frac{n}{i=1} P_{y_s}(1+r)^{y_c - y_s}$$

where:

P = house price

y_c = the year current

y_s = the year sold

r = inflation rate

When a vendor approaches a real estate agent for a valuation on a property, the following steps are executed

1. Start with vendor's house location and search recent sales record;
2. Calculate the distance of sold houses to vendor's location, sort the distance table;
3. Take the first n values(n=8); The estimate is sum of the new list divided by n

The buyer agent is by far the simplest in terms of estimating their offer price. Buyer uses the same recent sale record as the vendor agent but employs the median price to set its price range. Buyer bid should be as low as possible without failing to win the house. If a bid fails, the buyer agent increases the price it will bid at the next offer. Buyer preference to particular neighbourhood and associated amenities constrain their housing search behaviour. This behaviour is encapsulated in buyer's eagerness index randomly assigned to each of the buyer agent. Buyer agent behaviour is characterised by an upgrading of their housing situation, thus stimulating the higher quality housing market. This behaviour is set by its choice of houses with high desirability index. The second attribute of the buyer is confidence.

$$P_b = P_{median}(b_{eager}(i)+1)$$

where:

P_b = Buyer Price

P_{median} = Median Price

b_{eager} = Buyer's eagerness index between 0 and 1

The vendor is given 3 personal attributes to determine their behaviour and interactions with other agents (independent, greed, and eager). The vendor with high independent values will conduct the sale of their house directly to the buyer agent. If the vendor independent attribute is less than the given threshold values than the vendor will employ the real estate agent to provide a valuation of the vendor's property.

The vendor's decision to accept or reject buyer's offer employs the fuzzy logic to map input of the vendor's attribute (*eager* and *greed*) to the decision space (*accept* or *reject*). Eager has a positive relationship with accept while greed has an inverse relationship with accept. Membership function of the vendor's attribute follows the asymmetrical polynomial function for greed input and sigmoidal function for eager input (Figure 2) [14].

Figure 2: Membership Functions

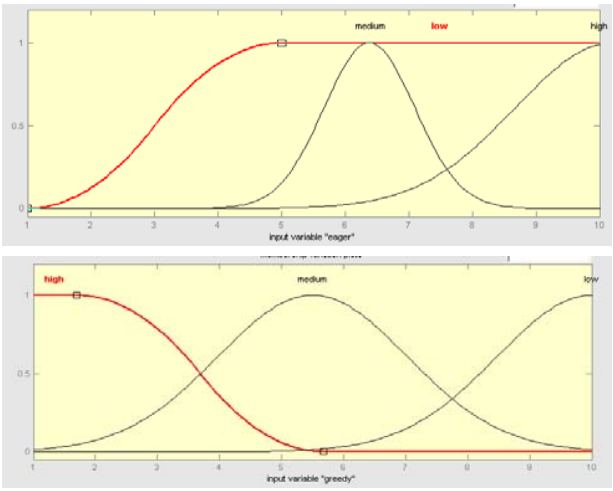

The fuzzy relationship is summarised in Figure 3. The decision rules for determining the vendor's decision is as follows:

If (*eager* is low) or (*greed* is high) then decision is reject

if *(eager* is medium) the decision is accept

if (*eager* is high) or (*greed* is low) the decision is accept

Figure 3: Fuzzy Logic Decision Space

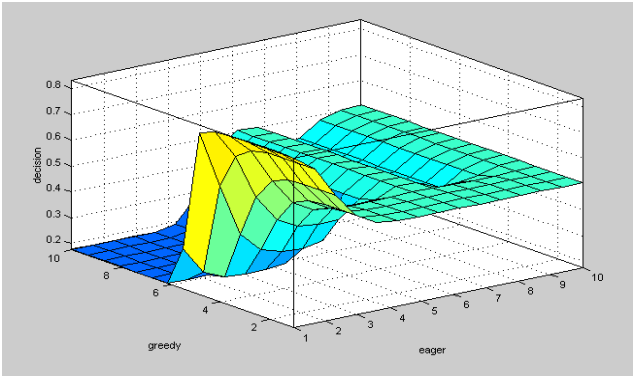

The defuzzification method is a decision set represented by a number between 0 and 1 (Figure 4). A threshold value is set to determine the final decision to accept or reject.

Figure 4: Defuzzification Method

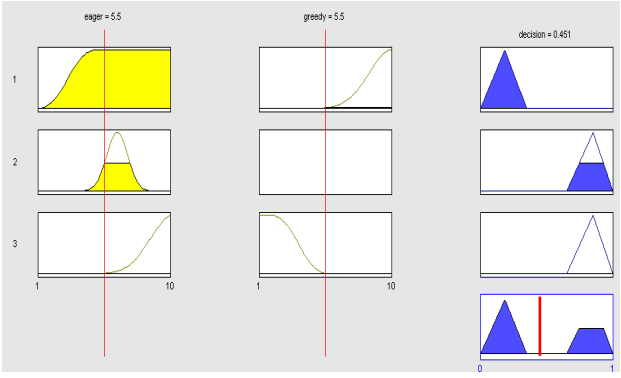

SIMULATING HOUSE PRICES

In this study an artificial environment of 10x10 grid is selected to provide the model framework. In future developments, this grid will be replaced with the actual cadastre data of the study area. Each grid will correspond to the parcel boundary and will have specific structural and locational attributes.

In this simulation, each cell is assigned initial price and a random desirability value.

$$P = 1000(d^2 + 1)$$

where:

P = House Price

d = desirability index between 0 and 1

The desirability index encapsulates the neighbourhood quality or some special features of the house such as view or aspect. The total number of houses in the simulation is 100. The number of houses for sale is fixed at 10 and the same number is set for buyer and vendor agents. These initial settings provide a framework to test dynamics of house price through agents' interactions.

The problem in this study is considered as a dynamic housing simulation. Given a set of buyers-vendors, all agents fixed with initial house estimates, the task is to find speculation strategies for each buyer/vendor to optimize their housing options.

The model works as follows

Initialization:

- each cell is given a random value of house price
- each vendor agent sets an initial price
- each buyer agent sets an initial price
- set number of buyer, vendors, house for sale
- set speculation rate, r

one time step:

Run the simulation for 12 time steps and until all buyer list is exhausted. If house is sold, another house is randomly added to the list for sale. Each buyer will have a fixed set of 10 houses to select from. Buyer and vendor agents are given an independent value which determines whether they will negotiate directly with one another or use the real estate agent to mediate. In the current setting the agents have varying levels of memory, to simplify the model implementation. Later developments will increase agent intelligence.

DISCUSSION

In this study, 3 models of agent pricing strategies are examined. In model 1, the housing simulation has no real-estate agent and buyers and vendors agents conduct direct transaction in the sale process. Buyers and vendors have no speculation strategy in their house price estimate. In model 2, the vendors and buyers' independence attributes are integrated in the pricing and house selection decisions. In this model, the vendors and buyers are assigned a confidence attribute randomly between 0 and 1. In model 2, vendors and buyers with confidence less than .50 per cent will rely on the real-estate agent to calculate the selling price and select house respectively. Model 2 inclusion of the real-estate agent adds a simple speculation element in the house price evolution. In model 2, the real-estate agent sets a uniform price increase of 5 per cent. Model 3 is similar to model 2 but with a speculation rate of 10 per cent. Figure 5 summarizes the results of the 3 models

Figure 5: All models

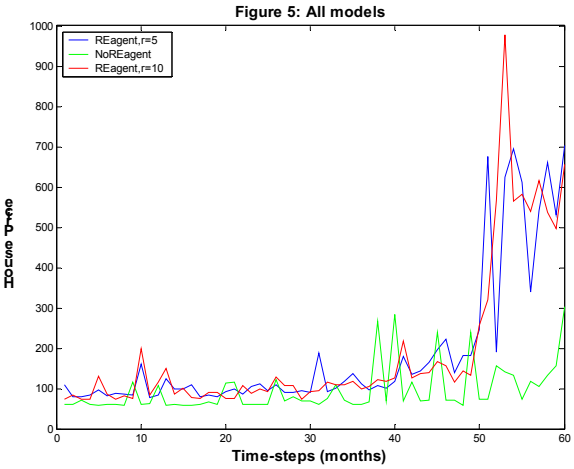

Using a log-linear plot, the speculative inflation attempted by the real-estate agent shows a straight line. The simulation shows that inflation occurs at 5 per cent level but does not follow the 10 per cent speculation so well.

Figure 6: Logarithm Analysis

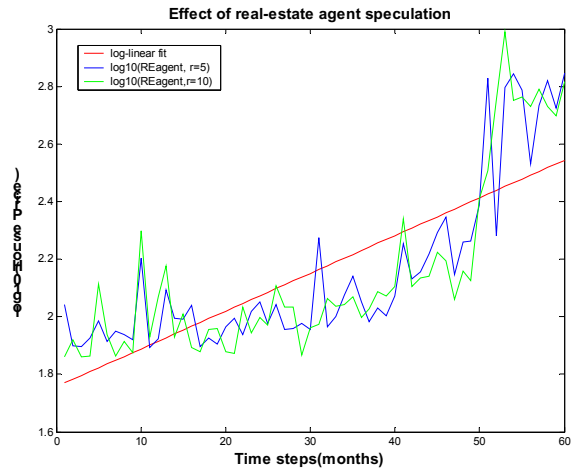

OUTCOMES AND FUTURE WORK

There are various applications of agent-based simulation ranging from environmental system, financial markets to

social systems. Agent-based modelling is unique because of the focus on behaviour of adaptive agents. In this project, research questions on how agents form their house price speculations and whether or not asset prices are predictable are explored. Initially, the agents deduce house price estimates based on their information processing of housing factors. The agents adapt their property pricing and transaction strategies based on their personal traits. In this model, the interpretation of the emergent behaviour may lead to new strategies and tactics that will benefit household in making housing investment decision.

The housing market has been characterized by strong cyclical and regional price variations. Previous housing studies confirmed that the housing market is not only driven by economic fundamentals but also by individual speculation. The motivation behind this study is to understand house price dynamics and its associated spatial distribution in the study area. This research has constructed buyer-seller behavior to investigate agent-based modeling approach in simulation of house price evolution. Comparative analysis of existing housing models and the agent-based approach will be carried out. Finally, extension of this study will integrate the model results with Geographic Information System (GIS) for the purpose of capturing the spatial dynamics of house price variations.

ACKNOWLEDGMENTS

This project was sponsored by Australian Research Council Linkage Grant no. LP0212023

REFERENCES

[1] A. Karantonis, *An Empirical Study of Demand Factors Affecting the Segmented Sydney Housing Market*, 7 th Pacific Rim Real Estate Society Conference, Brisbane 2003

[2] A.M.Zarestsky, *Asset Prices and Market Speculation*, Regional Economist, http://www.stls.frb.org/publications/re/1999/b/re1999b3.html, 1999

[3] B. Badcock, *Snakes or Ladders? The Housing Market and Wealth Distribution in Australia,* International Journal of Urban and Regional Research, 18(4):609-627

[4] Bized, *House Price Simulation*, http://www.bized.ac.uk/virtual/vla/house_prrices/resource_pack, 2003

[5] Charter Keck Cramer, *Housing Gets That Cyclical Feeling*, http://www.charterkc.com.au, 2003

[6] D. C. Parker, S.T. Manson, M.A. Janssen, M.J. Hoffmann, and P. Deadman, *Multi-Agent Systems for the Simulations of Land-Use and Land-Cover Change: A Review*, Annals of the Association of American Geographers,2002

[7] G.D. Jud and T.G. Seaks, *Sample Selection Bias in Estimating Housing Sales Prices*, The Journal of Real Estate Research,9(3):289-298,1994

[8] J. Harvey, Urban Land Economics 4th Edition, Macmillan Press Ltd., 1996

[9] J. Muellbauer and A. Murphy, *Booms and Busts in the UK Housing Market,* Economic Journal, 107(445):1701-1727,1997

[10] J.A. Seward, C.J. Delaney, and M.T. Smith, *An Empirical Analysis of Housing Price Appreciation in a Market Stratified by Size and Value of the Housing Stock*, The Journal of Real Estate Research,7(2):195-205,1992

[11] K. Nagel, *Truly Agent-Based Strategy Selection For Transportation Simulations* http://www.sim.inf.ethz.ch/papers/agdb/html/agdb.html , 2002

[12] L. V. Zumpano, K.H.Johnson and R.T. Anderson, *Internet Use and Real Estate Brokerage Market Intermediaries*, Journal of Housing Economics,12:134-150,2003

[13] M. Riddel, *Fundamental, Feedback Trading, and Housing Market Speculation: Evidence from California*, Journal of Housing Economics, 8:272-284,1999

[14] MATLAB, http://www.mathworks.com

[15] P. Kershaw and P. A. Rossini, *Using Neural Networks to Estimate Constant Quality House Price Indices* ,5th Pacific Rim Real Estate Society Conference, Kuala Lumpur,1999

[16] P. A. Rossini, *Application of Artificial Neural Networks to the Valuation of Residential Property* , 3rd Pacific Rim Real Estate Society Conference, New Zealand, 1997

[17] P.A. Waddell, A. Borning, M. Noth, N. Freir, M. Becke, and G. Ulfarsson, *UrbanSim Reference Guide*, version 0.9, http://www.urbansim.org, 2003

[18] P.N. Balchin, G.H. Bull and J.L. Kieve, Urban Land Economics and Public Policy 5th edition, Macmillan Building and Surveying Series, 1995

[19] T.J. Kauko, *Modelling the Locational Determinants of House Prices: Neural Networks and Value Tree Approaches*, PhD thesis, University Utrecht, http://www.library.uu.nl/digiarchief/dip/diss/2002-1204-091756/inhoud.htm

[20] Yates, J. *A Spatial Analysis of Trends in Housing Markets and Changing Patterns of Household Structure and Income*, Australian Housing and Urban Research Institute (AHURI), http://www.ahuri.gov.au,2002

BIOMEDICAL INFORMATION TECHNOLOGY

(This page left blank intentionally)

Numerical Evaluation of an 8-element Phased Array Torso Coil for Magnetic Resonance Imaging

Feng Liu, Joe Li, Ian Gregg, Nick Shuley and Stuart Crozier
School of Information Technology and Electrical Engineering,
University of Queensland, Brisbane, QLD 4072, Australia
stuart@itee.uq.edu.au

Abstract

Recently, parallel imaging using multiple RF coils has excited great interest in magnetic resonance imaging (MRI). To help the design of some novel flexible array coils for the human torso, we theoretically investigate the RF field of an 8-element array coil loaded with an anatomically accurate model of the human torso. The RF behaviour is predicted based on a hybrid FDTD/MoM approach. The primary results are reported and simulations demonstrate the feasibility of torso imaging using array coils.

1. Introduction

Radio-frequency (RF) coils are used in MRI as near-field antennas transmitting RF pulses and receiving the nuclear magnetic resonance (NMR) signal. In MRI, a phased array coil generally refers to a set of surface coils whose signals are combined to obtain a uniform image over a region larger than any individual coil could cover while taking advantage of the high signal-to-noise ratio (SNR) available from the smaller individual coils [1-3]. Over the last few years, several parallel imaging strategies such as simultaneous acquisition of spatial harmonics (SMASH) and sensitivity encoding (SENSE), have been proposed, which have the potential to revolutionize the field of fast MR imaging by enabling parallel acquisition [4]. These techniques employ spatial information of individual coils of an array to partially replace spatial encoding which is usually be achieved using magnetic field gradients, and hence reducing scan time [5]. Phased array technology is now having a major impact on standard MR methodologies. Besides the SNR advantage, array coils may also help to reduce the geometrical distortion that occurs due to variation of sample susceptibility. Most studies on mid-high frequency volume coils to date have been limited to the human head, as the shorter wavelength at high frequencies makes it very difficult to produce large volume coils with reasonable homogeneity. This makes array technology an attractive alternative for RF resonators for high field MR imaging of the human body. It is anticipated that at high fields an array can be designed to operate in the transceive mode and provide adequate homogeneity with a higher SNR while reducing power levels and safety concerns [6].

Since the development of the NMR array in the late 1980s, multicoil arrays have been designed to image almost every part of the human anatomy [2]. The aim of this study was to assess the feasibility of parallel MRI for the human torso using array coils. In theory, volume array coils offer increased SNR over standard body coils. However, there are many technical problems that remain to be addressed. To help the design of some novel array coil structures, we theoretically investigate the RF field of an 8-element torso coil loaded with an anatomically accurate model of a human torso. In the literature, the quasistatic approach based on Biot-Savart's law is widely used to verify the coil design [2,7]. However, this method fails when used with arrays because it does not properly allow for mutual coupling. Also the quasi-static approach assumes a current distribution on the coils and thus fails when coils are used in high-field imaging where the current distribution is less likely to be well characterized [8]. This paper presents a full-wave analysis method, that is, the combination of the finite difference time domain (FDTD) method with method of moment (MoM), to determine the currents of the coil and RF fields inside the body generated by array coils [9]. The simulation explored several imaging related parameters such as B_1 distribution, signal intensity (SI), wave polarization, and energy absorption rate (SAR) inside the biological body. The preliminary results are reported and demonstrate the feasibility of the design concept of array imaging of the human torso.

2. Methods

In order to model the field/object interactions, a voxel-based human torso model has been incorporated into the

numerical simulations. The model data was obtained from the U.S. Air Force Research Laboratory (http://www.brooks.af.mil/AFRL/HED/hedr/), which represents a large male. Frequency dependent dielectric properties were obtained using a volume-averaging method and the proton density of body tissues were adapted from low-field image data.

The evaluated array geometry is shown in Fig.1. It is an array of 8 similar sized rectangular coils wrapped laterally around the chest. Recognising that the patient's size and torso geometry could vary significantly, the simulated general array does not conform too closely to the torso model. The coil elements are located about 2-4 cm from the human torso model. The capacitors were distributed at equal intervals in each single coil element to maintain uniform current and reduce dielectric interaction and losses from loading effects [10]. The coils were tuned to 85 MHz and matched to 50 ? . Eight sinusoidal sources were used to excite the coils with quadrature phasing to achieve a circularly polarized field. This proposed model could be applied for coils as either transmitters or receivers according to reciprocity theory.

In designing array coils, one of the most important things is to minimize the mutual inductance between the coils [2]. The cancellation of the coupling could be achieved by overlapping neighbouring coils. However, for a flexible torso array, overlapping is not such an attractive choice. Overlapping can only cancel coupling between adjacent coils and the coupling between these coils will vary as the structure flexes. Especially for SENSE imaging, adjacent coil elements should not overlap [11]. Therefore, we use a capacitor network to achieve coil decoupling. In theory, this method has no constraint in geometric arrangement of the coils thereby allowing placement of coils that could optimize parallel spatial encoding without concern for coupling between the coils.

The numerical analysis of the RF field produced by the array was based on a full-wave solution of Maxwell's equations. The MoM was applied to evaluate the current density distribution on the coils and the FDTD method was employed to find the steady-state electromagnetic fields (EMFs) inside the torso, which were then used to calculate the B_1 field, SI, and SAR map, etc.

For the current density calculation, quadrature voltage sources were applied, and current $\mathbf{J}$ was induced on the coils to satisfy the boundary condition of zero tangential electrical field. In the MoM discretization, all the coils were divided into small segments, and then the current on each segment was decomposed into a linear combination of basis functions and formulated into a matrix equation in which the unknowns are the currents, obtained by multiplying the inversed impedance matrix by the voltage vector using iteration techniques. Once the currents of the coil were obtained, FDTD was employed to investigate the RF fields in the presence of the inhomogeneous torso model excited by the calculated currents. To allow for RF radiation a three dimensional perfectly matched layer (PML) was applied as an absorbing boundary condition. The FDTD outputs were the magnitudes and phases of the steady-state EMFs, which were combined using a peak detection method.

The parameters, such as SI and SAR were derived on the basis of the FDTD results. The strategy of assessing NMR signal strength was based on the principle of reciprocity and the formulation [12] was

$$SI = iwM_0 \sin^n\left(kgt\left|\hat{B}_{1t}^{+}\right|\right)\left|\hat{B}_{1r}^{-*}\right| \qquad (1)$$

where, w is the operating frequency, M_o is the initial magnetization, g is the gyromagnetic ratio, t is the RF pulse duration of the transmission field, k is a dimensionless constant to adjust the flip angle. $\hat{B}_{1t}^{+} = (\hat{B}_x + i\hat{B}_y)/2$ is the positive circularly-polarized component of the transmission B_1 field, and $\hat{B}_{1r}^{-} = (\hat{B}_x - i\hat{B}_y)^*/2$ is the negative circularly-polarized component of reception B_1 field. The integer n is sequence-dependent, and is equal to 3 for a SE sequence and 1 for a GE sequence respectively. It is assumed that the magnetization is constant over each FDTD cell and the effect of relaxation times and other factors similar factors have been neglected. In order to evaluate the potential safety problem, the SAR value is evaluated as $SAR = s|E|^2/2r$, where $\mathbf{E}$ was the electric field and r was the local mass density. The simulated image is constructed by combining the images of individual coils using the sum of the squares method.

3. Simulation and Results

To implement the FDTD calculation, the cell size was 4 mm and the entire computational domain was divided into a $x \times y \times z = 139 \times 119 \times 143 \approx 2.4 \times 10^6$ box region and the torso model was embedded within this (see Figure 1). The 8 array coil elements were placed around the torso centred at the position of the heart. Twelve PML layers with a parabolic conductivity profile were located on the six open sides which effectively absorbed any radiated EMF energy. The results of the FDTD calculation show that the array of coils can achieve higher SNR than standard volume coils. With decoupling the coils in the array provide distinct, high SNR images of the regions adjacent to each coil. These distinct images can be combined to produce an image of a complete section such as would be produced by a volume coil but with higher SNR. Fig.2 shows the magnitude of transverse magnetic field component B_1 and it can be seen that the array coils

perform much better than a single surface coil. It can also be seen that the predicted RF field behaviour is very dependent on the geometry of the sample and the array coils.

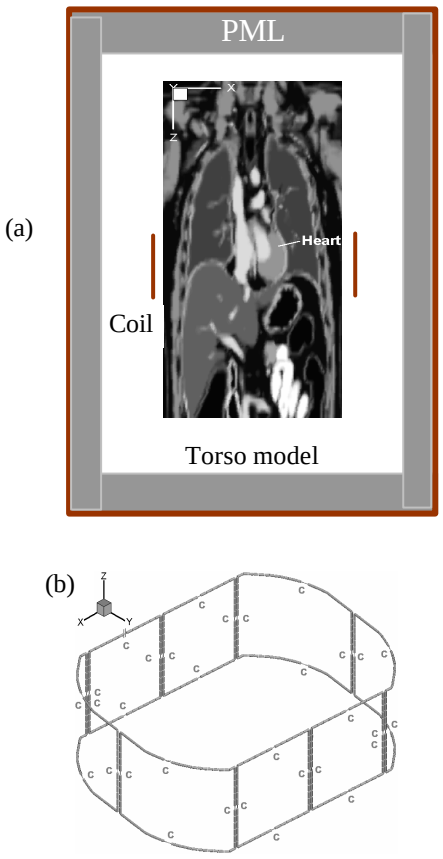

Figure 1. The 8-element array and its FDTD model loaded with human torso (shown the xz section)

The simulation also showed that the homogeneity of the B_1 field could be improved by optimizing the phase of the currents in the coils. Different combinations of phase were simulated and one was selected which best approximated a circularly polarized field, which has a theoretical advantage of $\sqrt{2}$ in SNR over linearly polarized coils [11]. Introduction of a non-homogeneous load disturbs the uniformity of the field as shown in Fig.2 (c,d). As the non-uniform load causes the flip angle to vary over the region of interest (see Figure 2(b)), an RF power level was chosen that resulted in an averaged 90^0 flip for the imaging zone with a 3-ms rectangular pulse. Two modes of operation were simulated, one where the transmit field is produced by a body coil which is assumed to produce a uniform B_1 field and a second where the array of surface coils is used to both transmit and receive. Figure 3 shows the high local signal intensity adjacent to each coil that decreases toward the centre of the region and Figure 4 shows the simulated images that result. Although the signal intensity is low in each individual image the combined images of Figure 5 show that a reasonably uniform image of the whole region can be achieved. These preliminary simulated results on human torso model are encouraging. Some small bright and dark artifacts can be seen close to the coil conductors due to the rapid changes in B_1 and hence SI and flip angle in these regions.

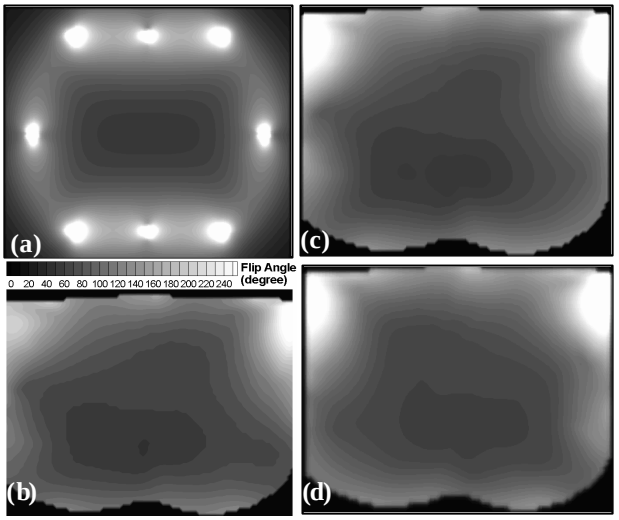

Figure 2. (a) The simulated field in the plane z=0(a) $|B_1|$ map without load; (b) The flip angle map with load; (c) Transmit $|B_1|$ map with load; (d) receive $|B_1|$ map with load

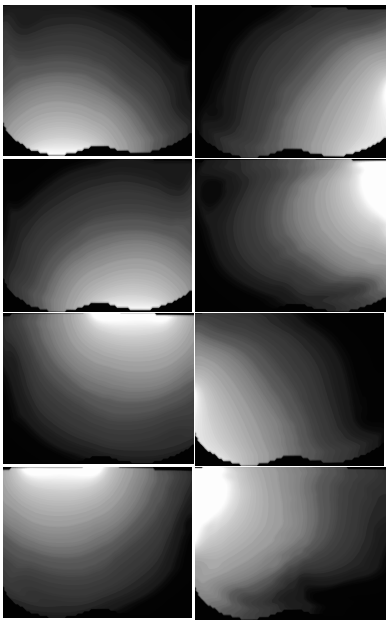

Figure 3. The signal intensity (SI) of each coil in the phased array

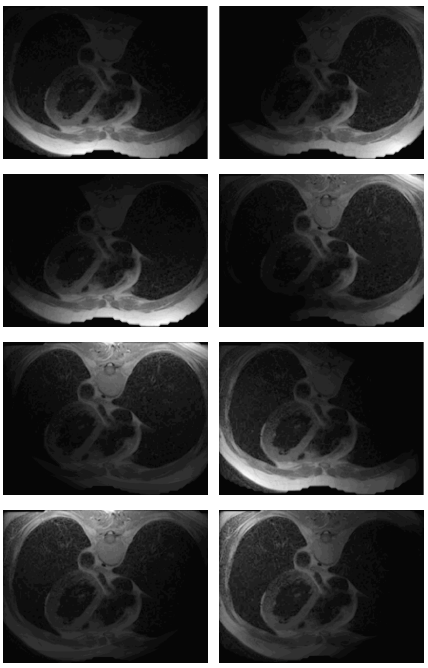

Figure 4. The simulated GE image of each coil in the phased array

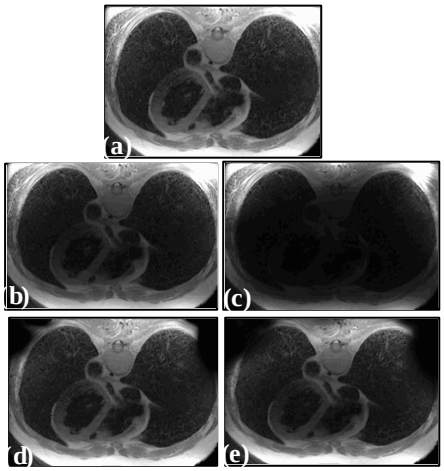

Figure 5. The combined GE image (a)Receive Only; (b,d) Tranceive GE sequence; (c,e) Tranceive SE sequence. Plane Averaged flip angle: (b,c) 45^{o}(a,d,e) 90^{o}

Figure 6 shows the variation of SAR across the imaging plane and shows that relatively larger values of SAR are located in the skin/muscle near the torso surface due to the large strength of the RF field in the skin and the high conductivity of the muscle.

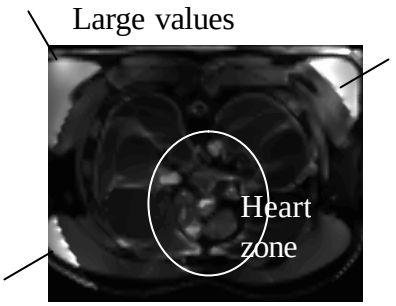

Figure 6. SAR map in the z=0 plane

4. Discussion

Single surface coils can be used to image surface tissues but to acquire images of regions in the interior of the torso requires a combination of sensitivity and magnetic field homogeneity over a larger field of view (FOV). This cannot be realised with a single surface coil because if the size of the coil is increased to improve the magnetic field homogeneity then the sensitivity is reduced. Similarly, small coils achieve high sensitivity at the expense of reduced magnetic field homogeneity. As shown by these simulations, an array of surface coils can achieve a combination of sensitivity and homogeneity that will allow imaging of complete torso sections.

This study investigated the RF field of volume-array coils by numerical evaluation of the Maxwell's wave equations at 2T (85 MHz). The basic limitation of the FDTD method was recognized and hybrid approaches were developed to overcome this. The coil currents were calculated by MoM and the RF field inside the body were evaluated by the full wave approach based on the finite difference approximation of the Maxwell's Equations. This approach should generate much more realistic information of the RF behaviour inside the body than the conventional quasi-static assumption for the current distribution and also the B1 field in the tissues. The problem of EMF interaction with the biological object in high field MRI has been studied for over a decade. Accurate assessment of the field-sample interaction phenomenon will help to find the optimal coil structure. Circuit theory and other quasi-static approaches do not handle interactions between coils in an array and do not even give accurate results for single coils in high frequency cases where the coil elements represent significant fractions of a wavelength. The high frequency case has to be addressed using full-wave approaches such as FDTD. Future work will extend this approach to higher field strengths and frequencies with the aim of overcoming the problems of volume coils in these situations.

From these simulated results it is seen that the RF field is disturbed by the sample even at 2T (85 MHz) and it is known that this effect becomes worse at higher field strengths and frequencies. This is because the wavelength is reduced by both the increased frequency and the dielectric properties of the body to a scale where the interactions become much more complex. Although the array interactions are complicated they hold the promise of overcoming some of the problems associated with imaging with volume coils at high field strengths [5-7,10]. Aside from image quality concerns there are safety concerns that non-uniform fields can cause localised hotspots where SAR limits are exceeded. This is a concern with volume coil imaging at high fields but these simulations show that the distance from surface coils to the body need to be monitored to avoid the high fields that exist in close proximity to the conductors. SAR limits will be more of a concern with fast imaging sequences and care needs to be taken that guidelines are not exceeded. Compared with volume coil the array of surface coils still has the advantage of lower global SAR and higher SNR [6,10].

Arrays of surface coils can be used to yield a circular polarized field, giving a theoretical advantage of $\sqrt{2}$ in SNR versus linear polarized coils[11]. At higher frequencies, the stronger interaction between the field and sample could compromise circular polarization and may decrease potential SNR gains.

Although the MoM simulations did not show a large effect of the sample on the currents in the coils at 2T, this effect will increase at higher frequencies. The method employed here should properly account for the more complex interactions and this will be investigated as this project progresses

In this theoretical study a specific array was simulated and seems to be an effective method for torso imaging. It is a promising RF coil structure for torso imaging at high field with or without a body coil. Cardiac imaging is a specific area in the torso to be explored using a volumetric transceiver phased array. This could also be applied to other parts of the body.

5. Conclusion

Accurate modelling of the interactions between coils and the body is needed to design arrays of surface coils for acquiring images of specific regions of interest in MRI at high frequencies. In this work, we present a hybrid MOM/FDTD computational model that was used to investigate the RF characteristics of an array of 8 surface coils loaded with an anatomically-accurate multi-tissue model of the human torso. The numerical studies showed that the array can provide a field of view similar to a body coil but allows for the possibility of using parallel imaging techniques. Using this kind of torso array will allow a large field of view for high resolution imaging with reduced scan times. The next step is to determine the optimum configuration of an array of coils for human torso/cardiac applications. It is also anticipated that these kinds of concepts and implementations will help to design of MR RF coil at higher field strengths.

Acknowledgement

Financial support for this project from the Australian Research Council is gratefully acknowledged.

References

[1] Roemer P.B. et al. The NMR phased Array. *Magn. Reson. Med*., 16:192-225, 1990.

[2] Wright S.L. et al. Theory and application of array coils in NMR spectroscopy. *NMR in Biomed*., 10: 394-410, 1997.

[3] Haacke E.M. et al. *Magnetic resonance imaging: physical principles and sequence design*. Wiley_Liss, NY 1999.

[4] Wang Y. et al. Description of parallel imaging in MRI using multiple coil. *Magn. Reson. Med*., 44:495-499, 2000.

[5] Griswold M.A. et al. Generalized antocalibrating partially parallel acquisitions (GRAPPA). *Magn. Reson. Med*., 47: 1202-1210, 2002.

[6] Peterson D.M. et al. An MR Transceive phased array designed for spinal cord imaging at 3 Tesla: preliminary investigations of spinal cord imaging at 3 T. *Invest. Radio*., 38:428-435, 2003.

[7] Lin F.H. et al. Quantitative spectral/spatial analysis of phased array coil in magnetic resonance imaging based on method of moment. *IEEE Trans. Med. Imag*, 18: 1129-1137, 1999.

[8] Wright S.M. et al. Full-wave analysis of planar radiofrequency coils and coil arrays with assumed current distribution. *Concept Magn. Reson*., 15(B): 2-14, 2001.

[9] Chen J. et al. Numerical simulation of SAR and – Field inhomogeneity of shielded RF coils loaded with the human head. *IEEE Trans. Biomed. Eng*., 45: 650-659, 1998.

[10] Kim H.W. et al. In vivo prostate magnetic resonance imaging and magnetic resonance spectroscopy at 3 Tesla using a Transceive Pelvic phased array coil Preliminary results. *Invest. Radio*. 38: 443-451, 2003.

[11] Weiger M, et al. Specific coil design for SENSE: a six-element cardiac array. *Magn. Resona. Med*., 45: 495-504: 2001.

[12] Wang J. et al. Polarization of the RF field in a human head at high field: a study with a quadrature surface coil at 7.0 T. *Magn. Reson. Med*., 48:362-369, 2002.

Numerical Simulation of the Field and Frequency Limits for Volume coils in MRI

Bin Xu, Ian Gregg, Stuart Crozier and Feng Liu
School of Information Technology and Electrical Engineering,
University of Queensland, Brisbane, QLD 4072, Australia
Email: stuart@itee.uq.edu.au

Abstract

As signal to noise ratio in magnetic resonance imaging (MRI) improves with increasing static magnetic field strength there is a strong incentive to develop the technology to acquire images at higher fields. While magnet technology has made it possible to generate fields of 10 Tesla and more, limitations of the radio frequency (RF) hardware prevent the acquisition of high quality images over full regions of interest in clinical applications. Since its introduction, the birdcage coil [1] has become a very popular choice for volume imaging and this paper investigates the high frequency limits of several different sizes and designs of birdcage coils. Unloaded coils are simulated using commercial Method of Moments (MoM) software (FEKO [12]) and the capacitances and radii of the conductors are varied within practical limits to determine a maximum frequency of operation for each coil. Results show that practical birdcages are frequency limited to about 400 MHz for a typical head coil (27cm inside diameter, 30cm shield diameter and 25cm length); 128 MHz for a small whole body coil (60cm inside diameter, 64cm shield diameter and 70cm length) and 100 MHz for a large whole body coil (60cm inside diameter, 64cm shield diameter and 100 cm length). These limits are reduced when interactions with the load are taken into account and experience shows that a typical head coil is limited to about 200 MHz in practical experiments.

1. Introduction

Magnetic Resonant Imaging, known as MRI, is a powerful, non-invasive imaging technology that has played and will continue to play an important role in the Biomedical Imaging community. A key element in a MRI system is the radio-frequency (RF) coil, a resonant device used for transmitting and receiving electromagnetic energy at the Larmor frequency of a given nucleus of interest. The quality of the image depends upon the homogeneity of the RF magnetic field generated by the coil. The current generation of clinical MRI systems employ primary magnetic field intensities for human head at 3T, 4T, 7T and even 9T, and for the whole body MRI up to 4T [1, 2, 9 and 11] for which the Larmor frequencies are roughly 128 MHz, 174 MHz, 300 MHz and 400 MHz.

Today, nuclear MRI technologies are moving inexorably toward higher field strength in search of improved signal-to-noise ratio (SNR), spectral resolution and spatial resolution. As MRI moves to higher field and higher frequencies, the size of RF coils relative to the wavelength of operation becomes larger. The high magnetic field (frequency) technology has brought considerable challenges in engineering in the form of ancillary hardware, e.g., the radio frequency (RF) resonator [3, 4]. Current and past design procedures for RF coils, which have been quasi-static at lower frequencies, become inaccurate and full wave methods must be used. At higher frequencies wave-like phenomena become more important.

The birdcage coil was first developed by Hayes et al. for whole body NMR imaging at 1.5T [1,2]. While birdcage coils have been used very successfully at up to 200 MHz, their physical structure makes it impossible to them to operate in the same mode at higher frequencies. Higher resonant frequencies are achieved by reducing the inductance and capacitance of the components of the coil. However, a limit is reached where the conductors cannot be made larger and even without any lumped capacitors the stray capacity of the coil causes it to self resonate. As the stray capacity is not well controlled self resonant coils tend not to produce homogeneous field distributions.

As coils approach wave length dimensions, the performance of conventional lumped element designs and conventional birdcage coils encounter several problems [5] and do not achieve good performance. The transverse electromagnetic (TEM) resonator design [7, 8,and 9] has been proposed as a superior replacement for the standard birdcage coil in high-field applications. Some other volume coils such as cavity coils and re-entrant cavity (recav) coils have demonstrated better field homogeneity and a higher quality factor than an equivalent birdcage

coil at higher frequencies resulting in improved image quality [9, 11].

To obtain practical volume coils for clinical/experimental applications or design some novel coil types, however, it is still necessary to investigate the field and the frequency limits of conventional volume coil technology and here three different sized birdcage coils are simulated: a typical head coil (27cm inside diameter, 30cm shield diameter and 25cm length); a small whole body coil (60cm inside diameter, 64cm shield diameter and 70cm length) and a large whole body coil (60cm inside diameter, 64cm shield diameter and 100 cm length). The maximum frequency, field homogeneity and current distributions are determined for each to assist with selection of coils for higher frequency applications.

2. Theory and Methods

Analytic methods

A birdcage coil with N rungs has (N/2+1) modes and will resonate at (N/2+1) different frequencies. In these modes there is a dominant mode that produces the best B_1 field. In this dominant mode the currents on the rungs are sinusoidally distributed and hence the field closely approximates the homogeneous magnetostatic field produced by a sinusoidally distributed cylindrical surface current.

RF coils are usually made of conducting wires or conducting strips and discrete capacitors. At low frequencies where the size of the coil elements is small relative to the wavelength of the resonant frequency simple equivalent circuit models can be utilized [2]. The simplest equivalent circuit, ignoring mutual inductance, gives the following analytical solutions for the resonant frequencies for high pass and low pass birdcage coils:
For the high pass coil this is:

$$\omega_m = \left[C \left(L + 2M \sin^2 \left({}^{\pi m}/_{N} \right) \right) \right]^{-0.5} \tag{1}$$

and for the low pass birdcage coil it is:

$$\omega_m = \left[C \left(M + \frac{L}{2 \sin^2 \frac{\pi m}{N}} \right) \right]^{-0.5} \tag{2}$$

Where N is the number of rungs of the birdcage coil; M is the inductance of a rung of the coil, L is the inductance of each segment of the end ring, C is the capacitance on the rungs or end rings and m is the mode number.

Although these results are not very accurate they can be employed to examine the general effect of various parameters on the resonant frequencies. As the number of rungs is increased the resonant frequency of the dominant mode (m=1) of high pass coils will increase and the resonant frequency of low pass coils will decrease. To investigate the maximum frequency of operation the number of rungs should be chosen to be as large as is practical for the high pass coil and as low as practical for the low pass coil.

This method can be extended to take into account the mutual inductance between conductors and is highly efficient, reasonably accurate and thus very practical for low frequency cases. However, the analytic method does not provide accurate results for higher frequencies such as those investigated here where the length of the conductors become significant when compared to the wavelength.

Method of Moments (MoM)

A simulation approach based on method of moments (MoM) [2] as implemented by the commercial software package FEKO (EM Software & Systems) [12] is used here. This method does not require any assumptions regarding the current distribution on the conductors to be made. By providing a full wave solution of Maxwell's equations for both the currents and the fields it accurately models wavelength effects and coupling between conductors. It is very efficient for unloaded cases or cases where there is a simple, symmetrical load.

The simulation is set up as a conventional scattering problem where the unknown current distribution on the RF coil is solved by decomposing the problem into two parts. One is the impressed voltage source regarded as an incident electric field. Second is the scattered field due to an RF coil which functions as an object of scattering. [2]

A voltage source applied to the model is equivalent to an incident electrical field, E_i. To satisfy the boundary condition of zero tangential electrical field on the resonator conductors, the scattered field, E_s can be derived from

$$(\mathbf{E}_i + \mathbf{E}_s)\,|_{tangential} = 0 \tag{3}$$

The scattered field can be expressed as

$$\mathbf{E}_s(\mathbf{J}) = -jw\mathbf{A} - \nabla\Phi \tag{4}$$

where J is the current density induced on the surface of the objects, w is the operating frequency, A, Φ are the magnetic vector potential and electric scalar potential, respectively. These potentials can be expressed by using Green's functions G.

$$\begin{cases} \mathbf{A}(r) = \mu_0 \left(\iint_{S_1+S_2+S_3} \mathbf{J}(r')G(r,r')ds' \right) \\ \Phi(r) = \dfrac{-1}{jw\varepsilon_0} \left(\iint_{S_1+S_2+S_3} \nabla' \cdot \mathbf{J}(r')G(r,r')ds' \right) \end{cases} \tag{5}$$

Where S_1, S_2, S_3 denote the surfaces of the resonator, RF shield or cavity wall and head model, respectively.

In the MoM discretization the wires are divided into segments and the surfaces are divided into small triangular patches. The maximum dimension of these elements is chosen to be a small fraction, typically 1/10, of a wavelength at the highest frequency to be simulated. The currents on these elements are then decomposed into a linear combination of basis functions. After performing testing for each basis function, the integral equations are finally transformed into MoM matrix equations in the form of

$$[Z][I]=[V] \tag{6}$$

Where [Z] is the impedance matrix, [I] is the current to be determined and [V] is the voltage vector including the excitation source. The impedance matrix can incorporate terms representing lumped elements such as the capacitors in the birdcage coil. The impedance matrix is dense and hence equation (6) is solved using iterative techniques in conjunction with preconditioning.

Simulation parameters

Making the conductors thicker or using wide, thin strips minimizes the inductance and maximizes the resonant frequency as can be seen from the following formulae for self inductance:
For wire

$$L = 0.002l\left(\ln\frac{2l}{a}-1\right) \tag{7}$$

where l is the length and a is the radius of the wire.
For strips

$$L = 0.002l\left(\ln\frac{2l}{w}+\frac{1}{2}\right) \tag{8}$$

where l is the length of the strip and w is its width.
Here only wires are used in the simulation but combining (7) and (8) gives a simple conversion from wire radius to an equivalent strip width

$$w = 4.482\ a \tag{9}$$

Hence performing simulations with wire of different radii should be sufficient for the characterization of the maximum frequency of operation of these coils. For detailed design at the highest frequencies the differences between wires and strips should be taken into account.

Six different cases were simulated; both are high pass and low pass for each of the three sizes of coil. The high pass coils all have 16 rungs with lumped capacitors added to the centre of the rungs. The low pass coils all have 4 rungs with lumped capacitors added to the centre of each end ring segment. See Figure 1.

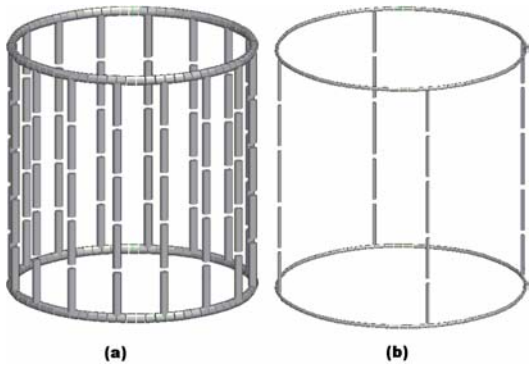

Figure 1 (a) 16 rung high pass birdcage coil
(b) 4 rung low pass birdcage coil
(The shield is not shown here)

Coils with wires of radius 0.5mm, 1mm, 2mm and 5mm and capacitors of 15pF, 10pF, 5pF, 2.5pF and 1pF were simulated. As with the number of rungs these values were chosen to represent a practical range for these parameters. The series of values allows trends to be easily discerned from the results. Although the value of 1pF for capacitance could be difficult to achieve in practice when stray capacitance is taken into account, this value was included to approximate the self resonant frequency of each coil.

3. Results

Figure 2 shows the resulting dominant mode resonant frequency when the wire radius and lumped capacitance are varied as mentioned above.

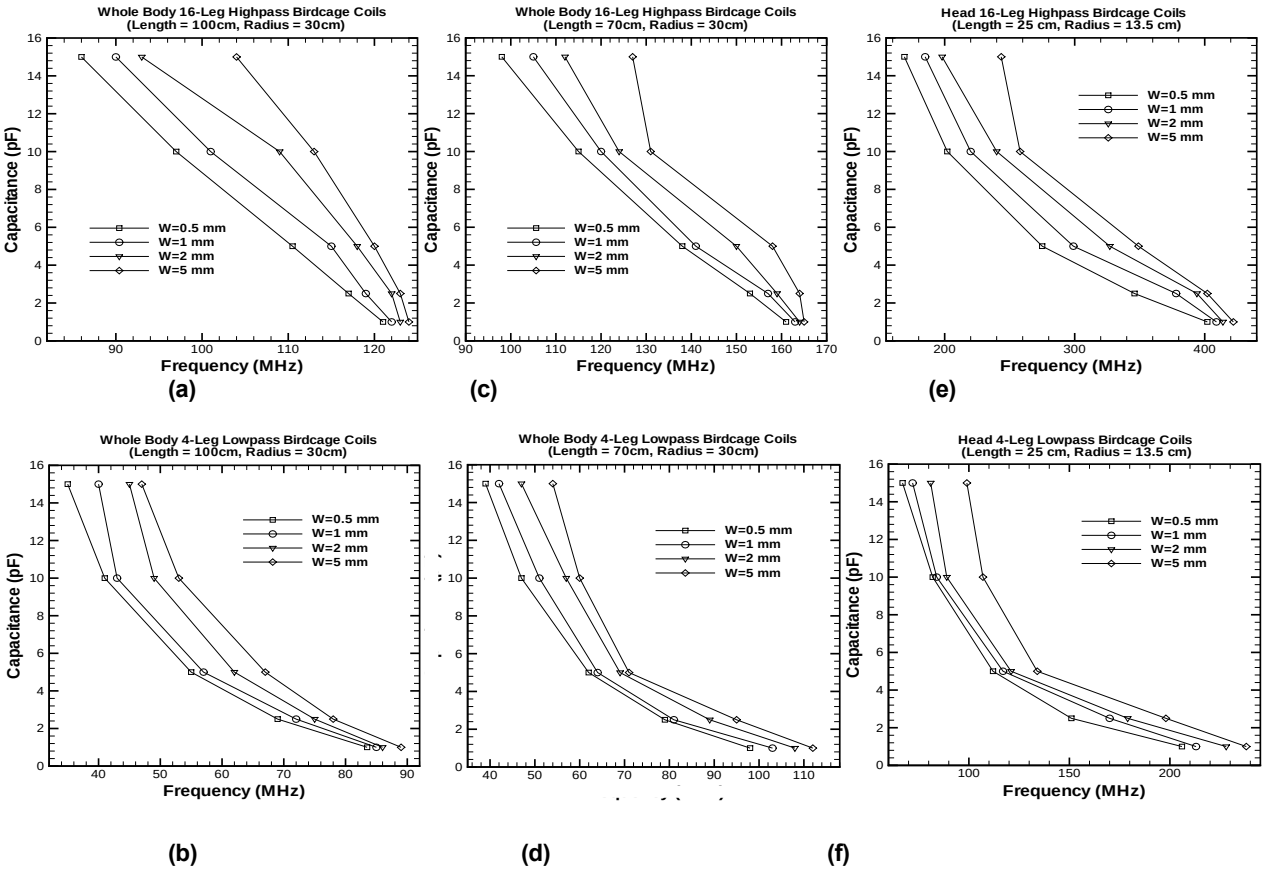

Figure 2 The resonant frequencies for six different coils.
(a) large, high pass (16 rung) body coil (b) large, low pass (4 rung) body coil
(c) small, high pass (16 rung) body coil (d) small, low pass (4 rung) body coil
(e) high pass (16 rung) head coil (f) low pass (4 rung) head coil

Knowing that the current on the rungs should be distributed sinsusoidally, the currents were plotted to give an indication of how the distribution changed with frequency. Figure 3 shows the current distribution on the rungs of the large, high pass, 16 rung body coil at three different frequencies. As there are 11 segments on each of the 16 rungs the x axis range is from 1 to 176.

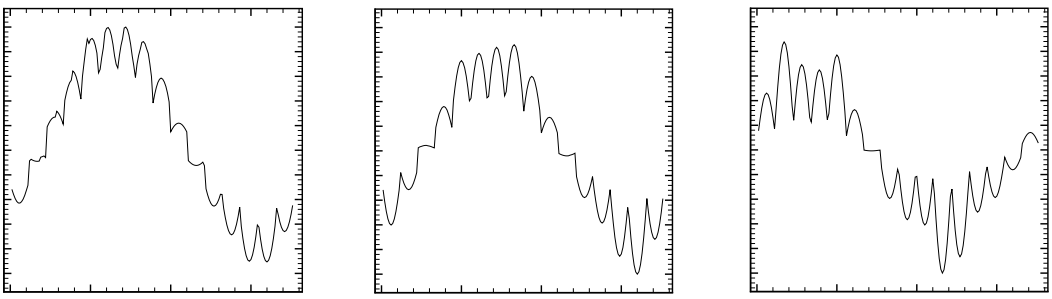

Figure 3. Current distribution on the rungs of the large, high pass, 16-leg Whole body coil
(a) 86 MHz; (b) 104 MHz; (c) 124 MHz

The B1 magnetic field homogeneity was investigated by plotting the magnitude of this field across a section through the centre of the coil. Figure 4 shows the current distribution and field profile for the 16 rung, high pass head coil at three different frequencies.

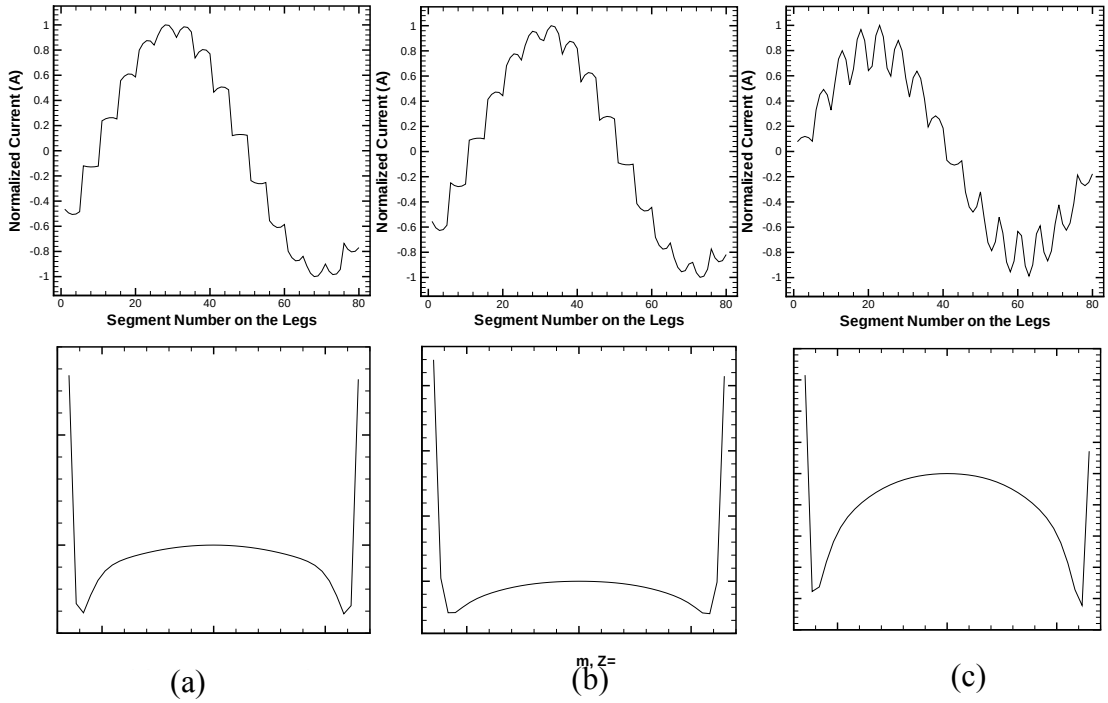

Figure 4 Current distributions (top) and the corresponding B1 field (bottom) for 16-rung, high pass head coil. (a) 169 MHz (b) 275 MHz (c) 402 MHz

4. Discussion and Conclusion

Frequency limits for empty coils

Figure 2 indicates the following approximate self resonant frequencies for the six coils that were simulated:

large, high pass (16 rung) body coil	124 MHz
small, high pass (16 rung) body coil	165 MHz
high pass (16 rung) head coil	422 MHz
large, low pass (4 rung) body coil	89 MHz
small, low pass (4 rung) body coil	112 MHz
low pass (4 rung) head coil	238 MHz

The resonant frequency increased with decreasing capacity and increasing wire radius (decreasing inductance) as expected. From these results it can be seen that the resonant frequency is inversely proportional to the size of the coil. For coils of the same size it demonstrates that the low pass configuration has a lower resonant frequency than the high pass configuration.

Current distributions on the rungs

The plots of current distribution on the segments shows that there is significant departure from the ideal of current that is constant along the length of each rung but varies sinusoidally around the coil even at frequencies well below the maximum. This indicates that the practical limits will be less than those given above as the field will also vary along the axis of the coil and the useful, homogeneous region will be reduced. As shown in Figure 4 the field also varies across the coil at the higher frequencies and reduces the useable volume even further. For these reasons practical limits of approximately half the above values for simulated self resonance will probably be more appropriate when selecting birdcage coils for high field use.

Sample interactions

While only unloaded coils have been considered in these simulations it is known that the introduction of a practical sample with high relative permittivity, conductivity and asymmetry will cause further problems. Even when using TEM or Recav coils with excellent unloaded field distributions, large variations in intensity appear in both experimental and simulated images with

bright spots in the centre at very high fields and frequencies (11.7 T, 470 MHz.). From Figure 5, it can be seen that the homogeneity of the loaded volume coil is getting worse as the frequencies goes higher. In addition, we have also conducted some simulation work on these sample/field interactions and obtained similar conclusion [10]. Therefore, the loading effect is another factor to be taken into account when assessing the upper frequency limit of a particular coil design.

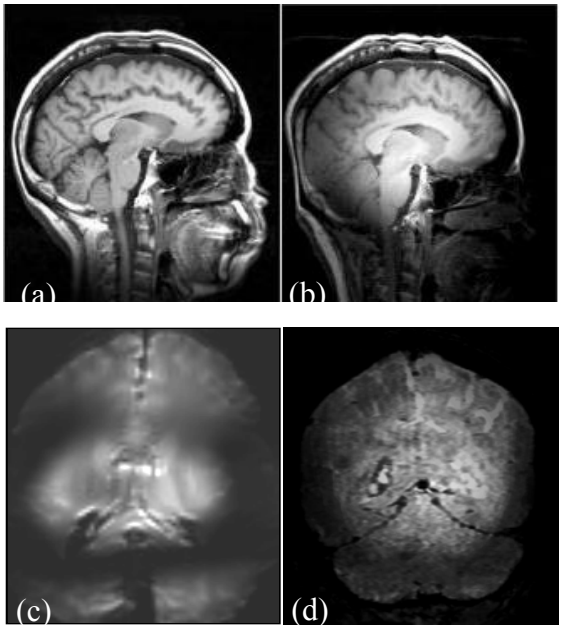

Figure 5
(a) Experimental head image in a TEM coil at 4 T [11];
(b) Experimental head image in a TEM coil at 7 T[11];
(c) Experimental had image in a Recav coil at 11.7 T[10];
(d) Simulated head image in a Recav coil at 11.7 T [10].

References

[1] C.E. Hayse, W.A. Edelstein, J.F. Schenck, O.M. Mueller, M. Eash, An Efficient Highly Homogeneous Radiofrequency Coil for Whole-Body NMR Imaging at 1.5T, J. Magn. Reson. 63: 622-628, (1985).

[2] J.M. Jin, Electromagnetic design and analysis in magnetic resonance imaging, Boca Raton, FL: CRC, (1999).

[3] C. Chin, S. Li, C.M .Collins and M. B. Smith, Mutual inductance Calculation between Ending-Ring Segments for Elliptical Birdcage Coils, ISMRM 5th Scientific Meeting,Vancouver, (1997)

[4] D.I. Hoult, The sensitivity and power deposition of the high field imaging experiment, J Magn. Reson. Imag., 12: 46-67, (2000).

[5] J.T. Vaughan, H.P. Hetherington, J.O. Out, J.W. Pan, G.M. Pohost, High-frequency volume coils for clinical nuclear magnetic resonance imaging and spectroscopy, Magn. Reson. Med., 32: 206-218, (1994).

[6] E.C Wong , E. Boskamp, and J.S Hyde, A volume optimized quadrature elliptical end-cap birdcage brain coil, 11th Annu. Sci. Mtg .Sco .Magn .Reson.Med., 4015, (2002).

[7] P. Röschmann, "High-frequency coil system for a magnetic resonance imaging apparatus," U.S. Patent 4 746 866, 24, (1988).

[8] J. F. Bridges, Cavity resonator with improved magnetic field uniformity for high frequency operation and reduced dielectric heating in NMR imaging devices, U.S. Patent 4 751 464, June 14, (1988).

[9] B.A., Baertlein, O. Ozbay, T. Ibrahim, R. Lee, Y. Yu; A. Kangarlu; P.-M.L. Robitaille, Theoretical model for an MRI radio frequency resonator**,** IEEE Trans. Biomed. Eng., 47(4): 535-546, (2000).

[10] Feng Liu , Bin Xu, Barbara L. Beck , Stephen Blackband and Stuart Crozier, 11T MRI and Numerical Modelling of the Excised, Fixed Human Head, submitted to IEEE Trans. Med. Imag., (2003)

[11] J.T. Vaughan, M. Garwood, C.M. Collins, W. Liu, L. DelaBarre, G. Adriany, P. Andersen, H. Merkle, R. Goebel, M.B. Smith, K. Ugurbil, "7T vs. 4T: RF power, homogeneity, and signal-to-noise comparison in head images," Magn. Reson. Med., 46: 24-30, (2001).

[12] EM Software & Systems. FEKO User's Manual, South Africa, (2000).

Multiple Regression and Statistical Analysis on SEMG of Lumbar Muscles

S C Ragupathy, D K Kumar
Biomedical Research Laboratories,
RMIT University, Melbourne, Australia
Email: dinesh@rmit.edu.au

K Kamei, B I Polus
Complementary Medicine Clinical
Neuroscience Research Group, RMIT
University, Melbourne, Australia.

Abstract

SEMG has been used as a tool over the past few years for analysing paraspinal muscle function in normal and low back pain populations. Within the group of paraspinal muscles the role of the multifidus muscles is to stabilise the spine. The Relative Strength of Contraction (RSC) of each lumbar segmental multifidus muscle was analysed in order to classify postures. Multiple Regression Analysis (MRA) was used to predict the relationship between the different levels of multifidus muscles in the lumbar region using different regression equations for different postures. In the model the least square fit method was used to make a best fit of the coefficients in the equation.. Analysis of Variance (ANOVA) was used to find the level of confidence (p values) of lumbar multifidus left L2-3 and lumbar multifidus left L4-5 as a combined factor in determining lumbar multifidus right L4-5 activity levels. Results indicate that the relationship between pattern of activity of muscle (multifidus) between the left and right sides can be predictable for a pre-defined static posture.

1. Introduction

There is a high incidence of episodes of acute low back pain (ALBP) of mechanical origin in Australia with a significant proportion (up to 80%) of these suffering further acute episodes within the next twelve months [1]. The mechanism of recurrent acute episodes of low back pain and the development of chronic Low Back Pain (CLBP) is suspected to be lumbar spine instability caused by an increased laxity of the spinal joints secondary to injury of spinal tissues, degenerative changes in spinal joints, disease or muscle weakness[2]. Muscle weakness may occur because of deterioration in the muscle stability function of the intrinsic lumbar paraspinal muscles[2,3]. Surface Electromyography (SEMG) is a measure of muscle activity and may be used to measure the properties of muscles supporting spinal segments. SEMG of lumbar erector spine muscles (LESM) has been used frequently in applied physiology for the assessment of back muscle function during various activities[4, 5]. Researchers have attempted to use the magnitude of the SEMG for the analysis of the relative strength of contraction of the paraspinal muscles for the diagnosis of lumbar back ailments[6].

1.1 Electromyography

Surface Electromyography (SEMG) is the electrical recording from the surface and represents the summation of the electrical activity from all the muscle fibers and thus the summation of all motor unit action potentials (MUAP) in the region of the electrodes. The origin of each of the MUAP is inherently random, non-stationary, and the electrical characteristics of the surrounding tissues are non-linear. Thus EMG is a very complex signal. The amplitude of the EMG recorded from the surface (non-invasive) is stochastic in nature and ranges from peak-to-peak 0 to 10mV or a Root Mean Square (RMS) value ranging between 0 to 1.5mV.

SEMG is also a useful indicator of the strength of contraction of muscles. It may be used to assess the overall functional status of muscles and can be done simultaneously on identical contra-lateral muscles in a number of functional conditions. Researchers have attempted to use SEMG for the analysis of paraspinal muscle function for various lumbar back-related conditions[7]. However SEMG of paraspinal muscles is a noisy signal for example the presence of ECG artifact[8].

SEMG may be affected by various factors. The anatomical/ physiological processes such as properties and dimensions of tissues, and force and duration of contraction of the muscle are known to influence the signal. Peripheral factors such as

spacing, type and size of electrodes may also have an influence on the signal[9, 10] and to obtain reliable information, considering such factors is critical. Some of these factors may be handled through careful skin preparation, and by choosing proper anatomical landmarks for the placement of electrodes.

1.2 Static Posture and SEMG

Epidemiological studies have identified work intensity, static work postures, frequent bending and twisting, lifting and repetitions as occupational risk factors associated with LBP[10]. Spine related pain causes hardship to a large section of population. The lack of understanding of the behaviour/relationship between muscle groups (i.e., with muscles located at different vertebral levels) for a given posture can be a barrier for the assessment of back muscle function[11].

Lumbar paraspinal muscles, and in particular the multifidus muscles are responsible for stabilising spinal joints during movement and in the maintenance of posture. Atrophy and dysfunction of the multifidus could permit spinal instability and could be an important factor that contributes to the high recurrence rate in CLBP. Since a recent focus in conservative management of patients with ALBP has been the specific training of the stabilizing muscles, there is a need for quantifying and qualifying the activity patterns of the multifidus before and after training [12].Static posture testing using SEMG has been used for patient education[13], and to provide information to clinicians about the balance of activity of spinal muscles. It is assumed that the technique may also help determine whether muscles are in spasm, or have "shut down" due to fatigue.

SEMG provides a method to estimate the degree of muscle activation that occurs during the execution of a specific movement/posture. However, SEMG of lumbar paraspinal muscles may record the activity from several different muscles during specific postures. Before the clinical and research utility of the SEMG for this task can be assessed it is essential that issues of reliability and validity of the SEMG of lumbar paraspinal muscles be addressed. The ability of the SEMG to reliably record the relative strength of contraction of specific lumbar paraspinal muscles during the maintenance of a specific static posture is an important preliminary step in the validation procedure. Researchers [14]comparing SEMG activity between CLBP subjects and pain free controls have arrived at conflicting results possibly because of failure to measure subjects in different postures and to categorize different types of back pain as cited by Ambroz [11]. Despite the use of SEMG for the assessment of patients with CLBP [11], the effect of different static postures on the SEMG parameters of the lumbar multifidus muscles has not yet been reported.

During SEMG recordings of multifidus muscle activity in different static postures the reliability of the SEMG signal is a major concern with issues such as electrode placement and high noise content in the recordings needing to be addressed. The development of a reliable objective measure of muscle activity would allow investigation into treatment outcomes and the role of muscle dysfunction in the maintenance or generation of LBP[16]. There is also a need to accurately and reproducibly define specific static postures before the utility of SEMG can be assessed.

Based on normalized RMS values this paper has studied the relative strength of SEMG and reports a regression model for analysing posture. The purpose is to explore the functional relationship between the activity levels of the multifidus at different segmental levels of the lumbar spine during specific static postures for normal healthy subjects. The statistical significance for the regression coefficients is found using ANOVA method and the standard error of estimate coefficients is examined for each segmental level. Based on this model, differences of healthy and CLBP patients will be studied in the future.

2. Methodology

The aim of this study is to determine the relative strength of contraction of multifidus muscles as measured by the RMS of SEMG during pre-defined static postures. For this purpose, experiments were conducted and the results were statistically analysed to determine the relationship and thus generate a model. The experimental details are below:

2.1 Experiments

Experiments were conducted on human subjects performing a series of pre-defined static postures during which time the SEMG of lumbar paraspinal muscles was recorded. The experiments were

repeated twice for the each subject for each of the postures. Details of the experimental procedure is below:

2.2 Subjects

A total of 20 experiments were conducted on 10 healthy (no history of low back pain) volunteer subjects and in accordance with the University human research ethics committee approved experimental protocol. The subjects were from both genders and their age ranged from 20 to 60 years.

2.3 Electrode Placement

Four pairs of surface EMG electrodes were positioned symmetrically on either side of the spine along the landmark line linking the L1 spinous process and the ipsilateral posterior superior iliac spine (Figure 1). Self-adhesive electrodes were placed at the levels of the L2-3 and the L4-5 interspinous spaces[17]. These electrode sites were considered to represent activity recorded from the underlying superficial fibers of the multifidus muscle[18]. A ground was placed on the upper part of the back midline. Lumbar vertebral interspaces were located through palpation by using the iliac crest as a landmark to the L4-5 interspace.

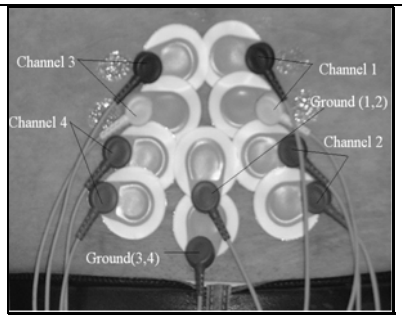

Figure 1: Four channel recording of Multifidus muscles

2.4 Choice of Postures

SEMG recordings were made while subjects maintained standardized sitting, standing and four point kneeling positions looking forward. Specific postures were chosen on the assumption that these specific postures preferentially activated the multifidi muscles of the lumbar spine. The postures also represented steady, static contractions of the lumbar multifidi muscles. Each participant was asked to assume a relaxed position when sitting, standing and during four point kneeling. For the standing posture, participants were asked to stand against a vertical support with their feet approximately shoulder width apart. Each participant was directed that they should position themselves with their back against the support so that the anatomical point most convex from the body (scapulae and/or thoracic spine) lightly touched the vertical support. The back of the head and the buttocks also lightly touched the vertical support. For the sitting posture each subject was asked to sit unsupported and erect .A flat chair was used, the height of which was adjustable so that the angle formed between the thigh and calf measured 90 degrees. Custom-built pointers were positioned against anatomical landmarks at the head (mastoid process), shoulder (greater tubercle of the humeral head) and pelvis (lateral aspect of the iliac crest).

In four point kneeling subjects were asked to kneel down and support the back using both hands and knees. The position of the hands and knees was determined by each participant and recorded by the examiners for reproducibility. Two sets of adjustable space bars were used to ensure consistent spacing between the two knees and the two hands. Solid wooden support ensured the reproducibility of the thigh position. Between the calf and thigh 90-degree angle was maintained. The distance between the thigh and arms was maintained using an adjustable bar placed on the wooden board. A visual focus point was used for all sitting, standing and four point kneeling postures, so that the subject would not make any neck movements.

A total of 11 postures were studied including Sitting Normal (SitN), Sitting Left Arm Up (SitL), Sitting Right Arm Up (SitR), Sitting Both Arms Up (SitB), Standing Normal (StaN), Standing Left Arm Up (StaNL), Standing Right Arm Up (StaNR), Standing Both Arms Up (StaNB), Four Point Kneeling Normal (4PN), Four point kneeling left arm (4PL) and Four Point Kneeling Right Arm Up (4PR) were done. The postures were maintained such that arm flexion was at 90 degrees. A vertical and horizontal scale was used in order to reproduce arm positions during repeated trials.

2.5 Recording of SEMG

The SEMG signal was recorded using the Powerlab data acquisition system (AD Instruments, Castle Hill, NSW, Australia) at a sampling rate of 1000 samples/second. The signal was denoised using spectral filters consisting of an anti aliasing filter with 3db cut-off at 200 Hz, high pass filter of 3 Hz and a 50 Hz notch filter to remove the power line noise. Particular attention was paid to ensure an identical inter electrode distance and good contact between electrode and skin at the recording sites, because poor contact can produce high erroneous readings[19]. For each subject a template was created using a transparent sheet placed on the iliac crest bones to reproduce the electrode placement during repeated experiments. Recordings were monitored on-line for any motion artifacts and those readings that had any motion artifacts were discarded.

3 Analysis of signals

Signals were normalised to overcome differences between different recordings. The recorded signals were processed using Matlab software. A statistical analysis of the SEMG parameters was carried out using MINITAB (Statistical software) to calculate regression equations, Analysis of Variance (ANOVA) and residual coefficients.

3.1 Normalization

Magnitude of SEMG is known to have intra and inter subject variability. To permit comparison between SEMG recordings the RMS-SEMG was normalised with respect to right L2-3 segmental level. This represents the relative strength of contraction (RSC). This method of RSC normalisation is most appropriate when lower levels of activation are studied or assessed compared to percentage Maximum Voluntary Contraction (%MVC). The regression coefficients were calculated and using least square fit algorithm, equations were modelled to determine the relationships between different muscle activations for different static postures.

3.2 Multiple Regression Analysis (MRA) and Analysis of Varience (ANOVA):

Regression analysis is a multivariate analysis used to summarize data and study relations between different variables[20].Regression has been used in many fields for estimation and fore casting. Traditionally multiple regression analysis (MRA) has been used to model the functional relationship between anthropometric measurements[21].A multivariate model of the data is given by Equation 1.

$$y = a_0 + a_1 \times x_1 + a_2 \times x_2 \quad (1)$$

Multiple regression solves for unknown coefficients a_0, a_1, a_2 by performing a least square fit. Thus, the relationship between the RMS of the SEMG for right L4-5 multifidus, left L2-3 multifidus and left L4-5 multifidus was found for each posture. The equation output of this multivariate process gives the correlation coefficients between segmental levels of muscle activity and the standard error estimate (SE) of each segmental level contributing to the regression equation.

Taking the average absolute deviation between the original and the derived values, the cross-validation of the model is achieved. The outcome of this cross-validation is the average error. Confidence in generalizing the regression equation is based on the error coefficients. In order to analyse postures and determine the relationship between the segmental levels of muscle activity assuming ch3 (Left L2-3 multifidus) and ch4 (Left L4-5 multifidus) as responses and ch2 (Right L4-5 multifidus) as predicted, MRA was performed.

4. Results

Multiple regression modelling provides the values of the correlation coefficients and the relationship between various segmental levels by providing the general equation for each posture. From Table 1 we can observe that the standard error of the estimate (SE) is composed of three values including the error constant (δ), left L2-3 multifidus (Ch 3) and leftL4-5 multifidus (Ch 4. δ represents the error occurrence by the constant in the equation.

Posture	Regression Equation	SE			ANOVA
		δ	Ch3	Ch4	P
4PL	$Ch2 = 1.06 + 0.51 \times Ch3 - 0.65 \times Ch4$	0.2738	0.3410	0.4304	0.302
4PN	$Ch2 = 0.33 + 0.80 \times Ch3 - 0.04 \times Ch4$	0.3487	0.4414	0.1822	0.072
4PR	$Ch2 = 0.99 - 0.05 \times Ch3 - 0.14 \times Ch4$	0.2071	0.1054	0.09468	0.227
SitB	$Ch2 = 0.48 - 0.14 \times Ch3 + 0.57 \times Ch4$	0.1169	0.1384	0.2001	0.030
SitL	$Ch2 = 0.44 + 0.03 \times Ch3 + 0.20 \times Ch4$	0.0824	0.0936	0.1004	0.004
SitN	$Ch2 = 0.31 - 0.05 \times Ch3 + 0.71 \times Ch4$	0.2236	0.1932	0.2245	0.013
SitR	$Ch2 = 0.42 - 0.07 \times Ch3 + 0.47 \times Ch4$	0.1415	0.1638	0.1833	0.008
StaN	$Ch2 = 0.68 - 0.34 \times Ch3 + 0.60 \times Ch4$	0.1335	0.1315	0.1201	0.0001
StaNB	$Ch2 = 0.60 - 0.21 \times Ch3 + 0.50 \times Ch4$	0.1160	0.1037	0.0902	0.001
StaNL	$Ch2 = 0.49 + 0.02 \times Ch3 + 0.42 \times Ch4$	0.1100	0.0862	0.1110	0.001
StaNR	$Ch2 = 0.89 + 0.39 \times Ch3 - 0.16 \times Ch4$	0.5244	0.2718	0.2782	0.360

Table 1: Regression equations showing relationships between segmental levels of muscle activity and their corresponding Error coefficients. (SE=Standard Error of Estimate). Ch2 = Right L4-5 multifidus, Ch3 = Left L2-3 multifidus, Ch4 = Left L4-5 multifidus. δ =Error constant.

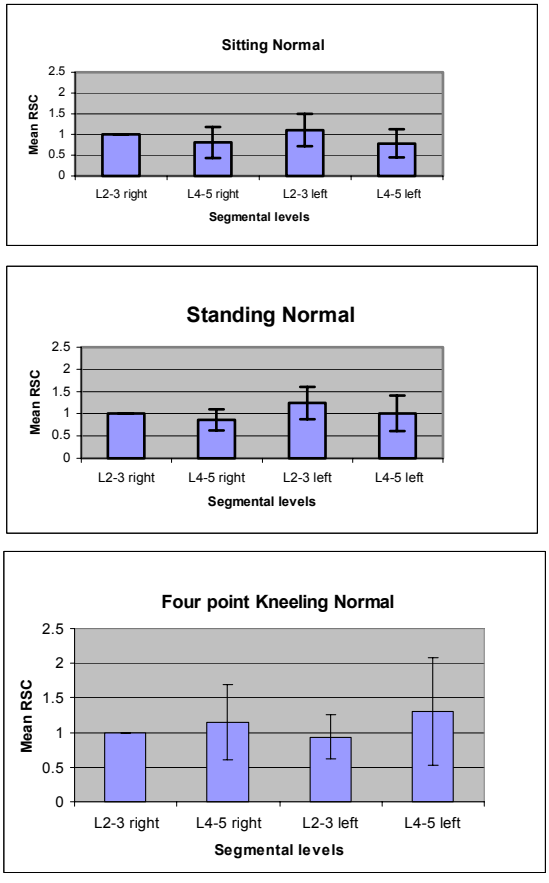

Figure 2: Bar graphs of Mean RSC vs. segmental levels for each static posture.

The values in column *Ch*3 and *Ch*4 provides the error caused by left L2-3 multifidus and left L4-5 multifidus in modelling the equation respectively. The P values given in Table 1 for each posture represents the statistical significance of the predicted value of right L4-5 multifidus activity, given the left L2-3 multifidus, left L4-5 multifidus and right L2-3 multifidus. The mean RSC and the deviation in error are observed from Figure 2. This illustrates the level of activity at different vertebral levels for a given posture.

5. Discussions

The strength (magnitude) of each segmental level can be observed from the graphs and the hierarchy of muscle activity from high to low is determined by the mean RSC of each segmental level for a given posture. Inspection of the mean RSC in Figure 2 shows the extent of exertion (or extent of contraction) for the multifidi muscles at different segmental levels for the static postures we examined.

From the results of regression analysis, it is observed that the relationship between segmental level muscles for sitting and standing postures is stronger while this relationship is weak for kneeling. The average error rate observed from Table 1 shows that the relationship between

segmental muscles is strongest for predicting the sitting posture. This suggests that normal human subjects have well defined muscle contraction behaviour pattern for the muscles of the lumbar back for the postures they are familiar with such as sitting and standing, while the muscle contraction pattern for postures they are not familiar with is weaker.

6. Conclusion

In conclusion it is clear that the MRA has an application in assessment of postures based on lumbar multifidus activity, although some models should not be used without a good clinical understanding. In particular extreme caution has to be taken while dealing with four point kneeling postures because of unstable muscle activity. This model will form a ground basis for analysing of Low Back Pain (LBP) caused by multifidus muscles due to different postures and also provide insight about the functionality of the muscles during different daily activities in normal healthy subjects.

References

1. Hides, J., G. Jull, and C. Richardson, *Long-term effects of specific stabilizing exercises for first-episode low back pain.* Spine, 2001. **26**(11): p. E243-248.
2. Panjabi, M.M., *The stabilizing system of the spine. Part I. Function, dysfunction, adaptation, and enhancement.* J Spinal Disord, 1992. **5**(4): p. 383-9.
3. Panjabi, M.M., *The stabilizing system of the spine. Part II. Neutral zone and instability hypothesis.* J Spinal Disord, 1992. **5**(4): p. 390-6.
4. Mannion, A.F., et al., *The use of surface EMG power spectral analysis in the evaluation of back muscle function.* J Rehabil Res Dev, 1997. 34(4): p. 427-39.
5. Koumantakis, G.A., et al., *Paraspinal muscle EMG fatigue testing with two methods in healthy volunteers. Reliability in the context of clinical applications.* Clin Biomech (Bristol, Avon), 2001. 16(3): p. 263-6.
6. LeVeau, B. and G.B.J. Andersen, *Output Forms: Data Analysis and Applications Interpretation of the Electromyographic Signal*, in *Selected Topics in Surface Electromyography for Use in the Occupational Setting: Expert Perspectives*, G.L. Soderberg, Editor. 1992, National Institute for Occupational Safety and Health Publication 91-100.
7. Cram, J.R., J. Lloyd, and T.S. Cahn, *The reliability of EMG muscle scanning.* Int J Psychosom, 1994. 41(1-4): p. 41-5.
8. Bluthner, R., H. Seidel, and B. Hinz, *Myoelectric response of back muscles to vertical random whole body vibration with different magnitudes at different postures.* Journal of Sound and Vibration, 2002. 253(1): p. 37-56.
9. Elfving, B., et al., *Influence of interelectrode distance and force level on the spectral parameters of surface electromyographic recordings from the lumbar muscles.* J Electromyogr Kinesiol, 2002. 12(4): p. 295-304.
10. Zedika M, K.S., Narayan Y, *Comparison of surface EMG signals between electrode types, interelectrode distance and electrode orientations in isometric exercise of erector spinae muscle.* Electromyogr.Clin.Neurophysiol, 1997. 37(7): p. 439-447.
11. Andersson, G.B., *Epidemiologic aspects on low-back pain in industry.* Spine, 1981. 6(1): p. 53-60.
12. Ambroz, C., et al., *Chronic low back pain assessment using surface electromyography.* J Occup Environ Med, 2000. 42(6): p. 660-9.
13. Julie A.Hides, C.A.R., *Multifidus Muscle Recovery Is Not Automatic After Resolution of Acute,First -Episode Low back Pain.* Spine, 1996. 21(23): p. 2763-2769.
14. Marcarian, D., *Surface EMG: Static vs Dynamic Testing*, MyoVision. Retrieved 22/July, 2003, from Precision Biometrics, Inc.(http://www.myovision.com/)
15. Arena, J.G., et al., *Electromyographic recordings of 5 types of low back pain subjects and non-pain controls in different positions.* Pain, 1989. 37(1): p. 57-65.
16. Watson, P.J., et al., *Surface electromyography in the identification of chronic low back pain patients: the development of the flexion relaxation ratio.* Clin Biomech (Bristol, Avon), 1997. 12(3): p. 165-171.
17. De Foa, J.L. and W. Forrest, *Muscle fiber direction of longissimus, ilicostalis and multifidus: landmark derived reference lines.* Journal Anatomy, 1989. 163: p. 243-7.
18. Arokoski, J.P., et al., *Back and hip extensor muscle function during therapeutic exercises.* Arch Phys Med Rehabil, 1999. 80(7): p. 842-50.
19. Merletti, R., L.R. Lo Conte, and C. Orizio, *Indices of Muscle fatigue.* J Electromyogram Kinesiol, 1991. **1**(2): p. 20-33.
20. Norusis, M.J., *SPSS base system user's guide.* 1990, Chicago, Ill.: SPSS Inc. 250.
21. Kaya, M.D., et al., *A new approach to estimate anthropometric measurements by adaptive neuro-fuzzy interface system.* International Journal of Industrial ergonomics, 2002. Article in press.

BIOMETRICS & AUTOMATION

(This page left blank intentionally)

High Speed Pupillometry

Shiau Shing Sammy Phang, D. Robert Iskander, and Michael J. Collins
Contact Lens and Visual Optics Laboratory, School of Optometry,
Queensland University of Technology, Australia.
(s.phang)(d.iskander)(m.collins)@qut.edu.au

Abstract

Measuring the parameters of the pupil in the human eye has become increasingly important in customised refractive surgery and other eye care applications. High-speed and high-resolution CMOS cameras can be used to study the dynamics of eyelids and their interaction with the pupil at different illumination levels. We consider the problem of measuring the pupil size from a high-speed video. In particular, we develop a novel algorithm for setting intra-lid sectors for the detection and estimation of the pupil and iris outlines from a sequence of digital images. An application of the proposed methodology to the estimation of the pupil parameters during an eye blink is given.

1. Introduction

In the past, the pupil size was often measured with a ruler or a special gauge. However, in the era of advanced refractive surgery and contact lens fitting, the traditional measurement techniques are not sufficient [1]. In many optometry and ophthalmology applications, it is important to determine the location of the pupil with respect to other features of the anterior eye such as the limbus (iris outline). For example, determining the relation between the pupil and limbus centres is crucial in corneal transplantation [2]. Also, in some surgical procedures there is a need to determine the pupil and limbus outlines as well as the position of the eyelids [3]. Nowadays, these parameters are often estimated from digital images or video sequences utilising image processing techniques.

Most of the pupillometers that are commercially available do not posses the capability of estimating the limbus. Relating the pupil to the limbus is possible in videokeratoscopy [4], although this technique is not reliable for eyes that have dark irides [5]. In customised refractive surgery, on the other hand, there are some commercial eye-trackers that can determine the pupil parameters and relate them to the limbus [6]. However, their accuracy has not been fully established. Also, since they are integral parts of the excimer laser systems, they cannot be used independently.

With the introduction of high resolution CMOS imaging devices and the developments in high-speed filming it is now possible to observe the changes in pupil size during an eye-blink or sudden changes in the lighting conditions. It is known that the pupil changes its size under different lighting conditions. However, with changes in pupil dimension the pupil centre often moves in relation to other ocular landmarks [7, 8]. Such detailed observations provide clinicians and vision scientists with valuable information on eye dynamics.

Several image processing techniques devoted to pupillometry have been reported [9, 10]. Recently, a robust method for estimating the considered parameters of the anterior eye has been proposed [11]. The procedure utilises several customised image processing techniques and is reported to perform well for a wide range of clinical images. In summary, the procedure first finds the initial centre of the eye [12]. Then the limbus outline algorithm is performed in which it is crucial to determine the so-called *limbus sectors*, the area of an image that contains the transition from the limbus to the sclera. The limbus sectors depend on the characteristics of the individual eye and its direction of gaze. Figure 1 shows an example of this for a natural gaze. Next, a pupil outline algorithm is performed. The detected candidate points of the limbus and pupil are then used to estimate the parameters of the pupil and limbus models. A circle and an ellipse are the most popular models. In some cases, however, more detailed analysis of the pupil may be necessary for which one can utilise a model based on the Fourier series [13]. The whole procedure is iterated until the estimates of the pupil and limbus centers converge to stationary values.

Our goal was to extend the methodology from [11] to high speed pupillometry. In particular, we are interested in the determination of the limbus sectors that may change from one frame to the other during an eye blink.

The paper is organised as follows. In the next section, we provide details on high-speed image acquisition and intro-

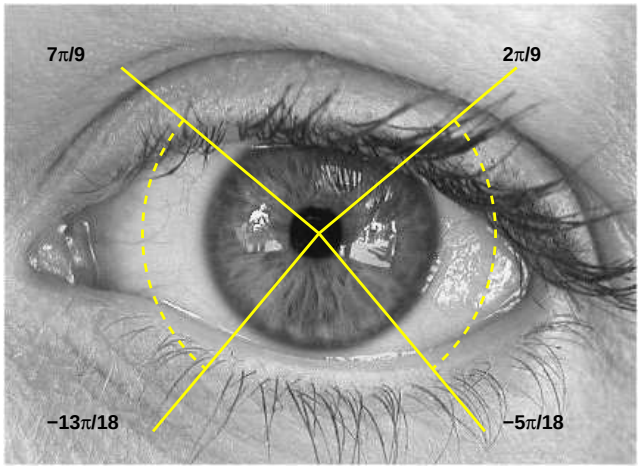

Figure 1. The image of the eye with two initial limbus sectors superimposed. The initial origin $\left(x_0^{(0)}, y_0^{(0)}\right)$ is determined by the QSI detector.

duce the proposed algorithm for setting the limbus sectors. Section 3 presents an example of high-speed pupillometry during an eye blink.

2. Methodology

The high-speed camera that is used in the study is a CMOS sensor type Redlake MotionPro with a full resolution of 1280×1024 pixels. During image acquisition, the subject was asked to blink. The images were taken with the sampling rate set to 250 frames per second (FPS) under powerful 300W back-light that has been diffused through a white board. This was necessary because the CMOS camera requires a significant amount of light for image capture. A total number of 64 frames (256ms) for a full blink were then edited from the video sequence. This corresponds to the length of a typical blink. An example of eight consecutive frames taken during the first phase of the blink is shown in Figure 2. It is clear that the information on the pupil and limbus significantly change from one frame to the next. Thus, it is crucial to estimate the limbus sectors individually for each of the images in the video sequence.

2.1. Algorithm for Limbus Sector Detection

The automatic pupillometry algorithm from [11] together with our proposed automatic limbus sector estimation for high-speed digital images is used. The procedure starts with the acquisition of the first image of the eye. It is assumed that the first image from the set of considered

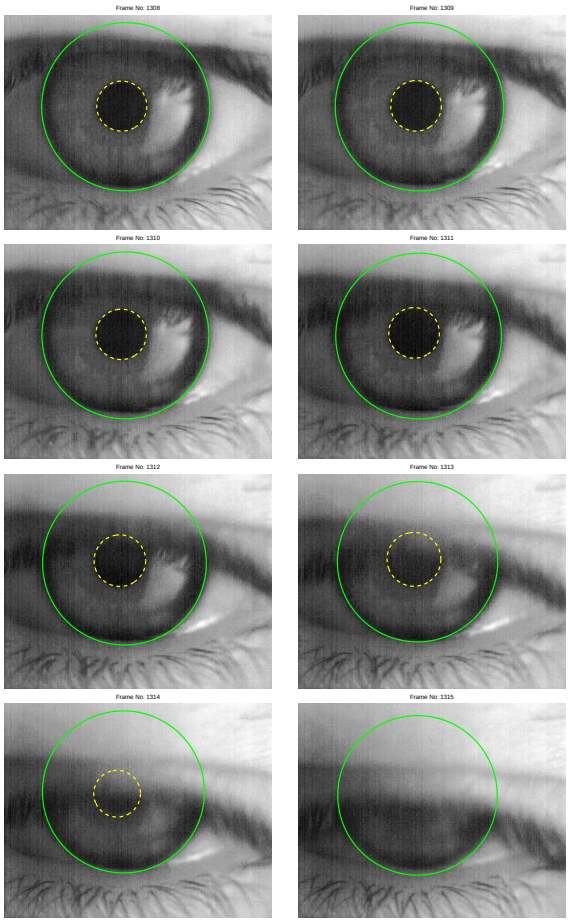

Figure 2. Eight consecutive frames in the first phase of the blink with the estimated pupil (dashed line) and limbus (solid line) outlines.

frames depicts an open eye and that it contains at least partial information on both iris and pupil.

The initial centre of the pupil $\left(x_0^{(0)}, y_0^{(0)}\right)$, is determined by applying the QSI detector proposed in [12]. During the eye-blink, the eye moves slightly. However this movement does not significantly affect the performance of the QSI detector. Thus, in order to reduce the computational expense, the initial estimated centre location from the first frame is used for the rest of the 63 frames in the image preprocessing stage.

In this stage, each image is cropped to a maximum possible square inscribed in the original image and centred at $\left(x_0^{(0)}, y_0^{(0)}\right)$. The cropped image should contain the whole area of the pupil and iris, and partial information on the sclera and eyelids.

Let $I(x, y)$, $x = 1, \ldots, n_x$, $y = 1, \ldots, n_y$ be the intensity of a grey scale image, where n_x and n_y denote the

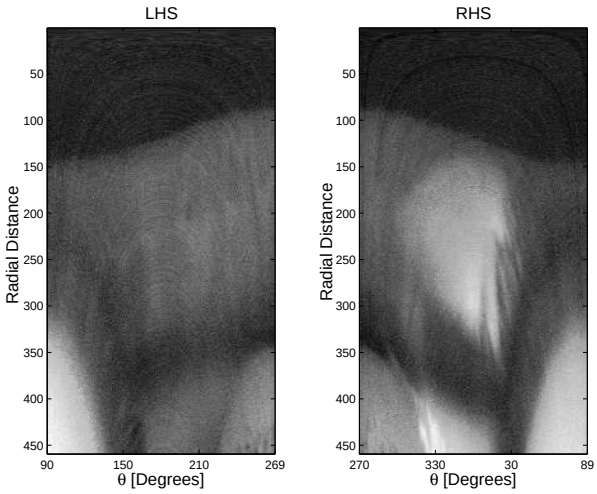

Figure 3. The polar image representation for the left and right hand sides of a typical image depicting an open eye.

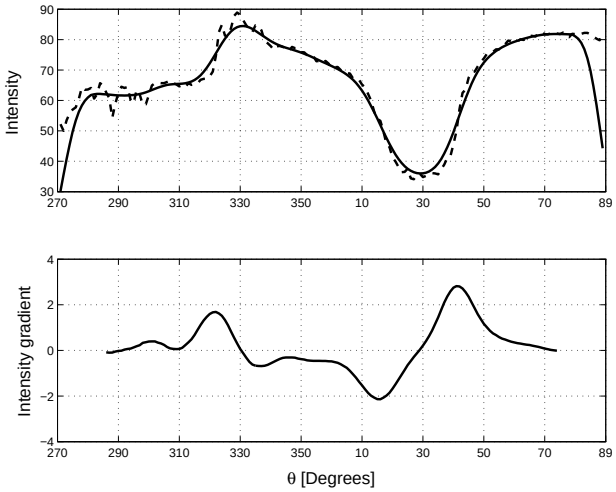

Figure 4. The average angular intensity profile before and after smoothing (top) and its derivative (bottom).

number of pixels in the cropped image in the x and y directions respectively. We define a radial image profile $I_p(r,\theta)$, $r = 1,\ldots,r_{\max}$,$\theta = \theta_{\min}, \theta_{\min}+\delta_\theta, \theta_{\min}+2\delta_\theta,\ldots,\theta_{\max}$, where δ_θ is a predetermined angular step (1 degree). We can then form an $n_r \times n_\theta$ polar-grid matrix (image) with columns corresponding to sampled radial profiles

$$\boldsymbol{I}_p = \begin{bmatrix} I_p(1,\theta_{\min}) & \cdots & I_p(1,\theta_{\max}) \\ I_p(2,\theta_{\min}) & \cdots & I_p(2,\theta_{\max}) \\ \vdots & \vdots & \vdots \\ I_p(r_{\max},\theta_{\min}) & \cdots & I_p(r_{\max},\theta_{\max}) \end{bmatrix}$$

where $n_r = r_{\max}$ and $n_\theta = (\theta_{\max} - \theta_{\min})$ [4, 11].

In the next step, two polar images are generated for the left (from 270^o to 89^o) and right (from 90^o to 269^o) hand side of each of the cropped images. An example of the polar image representation is shown in Figure 3. We note that the eyelid information appears only at the bottom of the polar image. To detect the upper and lower eyelid, we only process the section of the image that possibly contains the eyelids. Let $\boldsymbol{I}_s$ be the considered section of the polar image $\boldsymbol{I}_p$,

$$\boldsymbol{I}_s = \begin{bmatrix} I_s(r_s,\theta_{\min}) & \cdots & I_s(r_s,\theta_{\max}) \\ \vdots & \vdots & \vdots \\ I_s(r_{\max},\theta_{\min}) & \cdots & I_s(r_{\max},\theta_{\max}) \end{bmatrix}$$

where r_s to $r_{\max}$is a predetermined radial section that includes significant amount of the eyelid information, normally chosen to be $r_s > 0.9 r_{\max}$.

To detect the angular location of upper and lower eyelid, we first average the angular intensity

$$\bar{\boldsymbol{I}}_s = \frac{1}{r_{\max} - r_s}\left[\sum_{r=r_s}^{r_{\max}} I_s(r,\theta_{\min}) \cdots \sum_{r=r_s}^{r_{\max}} I_s(r,\theta_{\max})\right],$$

an example of which is shown by a dashed line in Figure 4. This is further smoothed with an n-point Hamming window (typically $n = 21$). The solid lines in Figure 4 show the corresponding average angular intensity profile after smoothing and its derivative. The two highest peaks are the angular location for lower θ_1 or upper θ_2 eyelid respectively. From this, the start sector and the sector size for the pupil and limbus estimation can be calculated. In this case, we determined $\theta_1 = 324^o$ and $\theta_2 = 42^o$, which are around the angular positions of the upper and lower eyelids of the right hand side of the polar image from Figure 3. We check whether the image does contain a sufficient amount of information for estimating the pupil and limbus outlines by comparing the difference of θ_1 and θ_2 with a certain threshold.

In the case where there are more than two peaks detected, the angular location that produces a smaller sector size is selected. This is done because for automatic pupillometry, it is preferable to select the part of the image without too much obstruction from the eyelashes. Further detail of automatic pupillometry can be found in [11].

3. Results

Consider the sequence of images shown in Figure 2. We run the pupillometry procedure of [11] enhanced by the au-

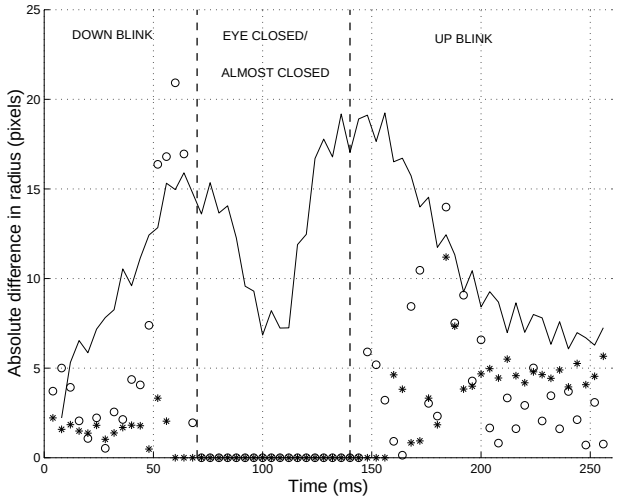

Figure 5. The absolute difference between the manual and automatic pupil ($*$) and iris ($\circ$) radii. The image time gradient is superimposed with the solid line.

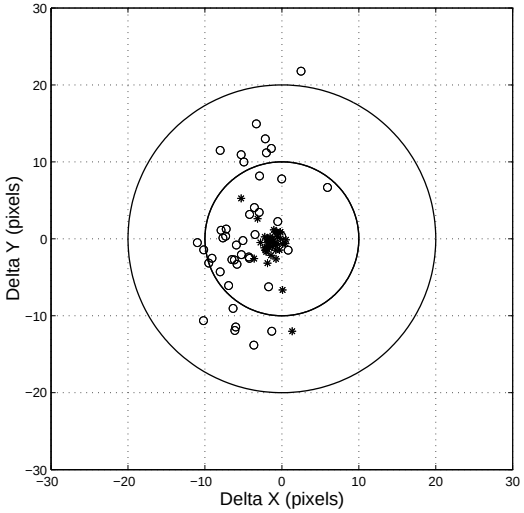

Figure 6. The difference between the manually and automatically estimated pupil ($*$) and limbus ($\circ$) centers.

tomatic detection of limbus sectors as outlined in the previous section. The result of the estimated pupil and limbus outlines is superimposed in Figure 2 with a dashed line and a solid line, respectively.

To determine the relative accuracy of the proposed automatic methodology, we have developed a graphic user interface to assist manual fitting of the limbus and pupil. A single frame is displayed at a time and an operator is instructed to click with the mouse on 16 points that are believed to constitute the limbus outline and a further eight points for the pupil outline. The algorithm uses the manually selected points to estimate the parameters of the best-fit circle (Least Squares) for both the limbus and the pupil.

The results of two experienced operators have been averaged and compared to the fully automatic procedure. In Figure 5, we show the absolute difference between the manually and automatically estimated pupil (asterisks) and iris (circles) radii. The averaged and scaled image time gradient, i.e.

$$s \sum_{(x,y)} [I(x,y;t) - I(x,y;t-1)], \quad 0 < s < 1,$$

is superimposed with the solid line, showing the dynamic changes in the video sequence. Note that the down phase of the blink is faster than the up blink phase (76ms vs 100ms). From Figure 5, we can note that the standard deviations of the estimated limbus parameters are around three times larger than the corresponding standard deviations of the pupil parameter estimators. The deviation of limbus estimate becomes more significant towards the end of down blink phase and the beginning of the up blink phase.

One may expect higher standard deviation for the limbus parameter estimators because, in general, the transition from the iris to sclera is not as clear as the transition from the pupil to the iris. Also, other factors such as shadowing caused by eyelashes and build-up of the tear film at the eyelid margins may contribute to a larger variability in the parameter estimates.

In Figure 6, we show the difference between the manually and automatically estimated pupil and limbus centers, denoted by asterisks and circles, respectively. Most of the pupil centres were estimated both manually and automatically within ± 4 pixels. This corresponds to approximately 100 microns. For limbus center estimation, most of the result were within ± 15 pixels (375 microns). Note however, that these results are relative to subjective measurements and show only how closely the automatic pupillometry procedure can mimic a human operator.

It is clear that both centers are slightly biased to the left. This is because the images from Figure 2 were taken with a setup consisting of a back-light located to the right of the subject. This resulted in irregular illumination of the acquired images and an unwanted reflection in the iris.

4. Conclusions

We have developed a novel procedure for estimating the limbus sectors. The proposed procedure is used with the recently proposed automatic pupillometry algorithm for the study of pupil dynamics in high speed filming. It was found

that the procedure closely mimics an experienced human operator and provides, in most cases, consistent results. It should be emphasised that the proposed methodology will be significantly hindered if the acquired images are taken with a low resolution camera. The procedure could be significantly enhanced if colour images were available [14]. In such a case, separation of features not related to the eye in the image can be achieved.

5. Acknowledgment

The project was supported by the QUT Strategic Collaborative Program scheme.

References

[1] Holladay, J. T. "The high cost of inaccurate pupillometry," *Review of Ophthalmology*, vol. 9, no. 3, pp. 47–49, 2002.

[2] Langenbucher, A., Seitz, B., Kus, M. M., Vilchis E. and Naumann, G. O. H. "Graft decentration in penetrating keratoplasty: nonmechanical trephination with the excimer laser (193 nm) versus the motor trephine," *Ophthalmic Surgery and Lasers*, vol. 29, no. 2, pp. 106–113, 1998.

[3] A. D. A. Souza, E. E. S. Ruiz, and A. A. V. Cruz. "Palpebral fissure morphology segmentation and measurement using image processing," *IEEE Engineering in Medicine and Biology Magazine*, pages 114–119, January/February 2000.

[4] Morelande, M. R., Iskander, D. R., Collins, M. J., and Franklin, R. "Automatic estimation of corneal limbus in videokeratoscopy," *IEEE Transactions on Biomedical Engineering*, vol. 49, no. 12, pp. 1617–1625, 2002.

[5] Fogla, R. and Rao, S. K. "Pupillometry using videokeratography in eyes with dark brown irides," *Journal of Cataract and Refractive Surgery*, vol. 26, no. 9, pp. 1266–1267, 2000.

[6] Schwiegerling, J. and Snyder, R. W. "Eye movement during laser in situ keratomileusis," *Journal Cataract and Refractive Surgery*, vol. 26, no. 3, pp. 345–351, 2000.

[7] Walsh, G. "The effect of mydriasis on the pupillary centration of the human eye," *Ophthalmic and Physiological Optics*, vol. 8, no. 4, pp. 178–182, 1988.

[8] Wilson, M. A. and Campbell, M. C. W. "Change of pupil ccentration with change of illumination and pupil size," *Optometry and Vision Science*, vol. 698, no. 24, pp. 129–136, 1989.

[9] Barry, J. C., Pongs, U. M., and Hillen, W. "Algorithm for Purkinje images I and IV and limbus centre localization," *Computers in Biology and Medicine*, vol. 27, no. 6, pp. 515–531, 1997.

[10] Miro, I., Lopez-Gil, N., and Artal, P. "Pupil-meter and tracking system based in a fast image processing algorithm," *Proceedings of SPIE*, vol. 3591, pp. 63–70, 1999.

[11] Iskander, D. R., Collins, M. J., Mioschek, S., and Trunk, M. "Automatic pupillometry from digital images," *IEEE Transactions on Biomedical Engineering*, (in review).

[12] Iskander, D. R., Mioschek, S. Trunk, M. and Werth, W. "Detecting eyes in digital images," In *Proceeding of Seventh International Symposium on Signal Processing and Its Applications*, Vol. II, pp. 21–24, Paris, France, July 2003.

[13] Wyatt, H. J. "The form of the human pupil," *Vision Research*, vol. 35, no. 14, pp. 2021–2036, 1995.

[14] Chai, D. and Ngan, K. N. "Face segmentation using skin-color map in vediohone applications," *IEEE Transactions on Circuits and System for Video Technology*, vol. 9, no. 4, pp. 551–564, 2002.

(This page left blank intentionally)

Hardware Design, Development and Evaluation of a Pressure-based Typing Biometrics Authentication System

Wasil Elsadig Eltahir
Mechatronics Dept,
International Islamic University Malaysia (IIUM),
Jalan Gombak, 53100
Kuala Lumpur. Malaysia
d_jwasel@hotmail.com

W. K. Lai
MIMOS Technology Research Group
lai@mimos.com

Ahmad Faris Ismail
Faculty of Engineering,
International Islamic University Malaysia (IIUM),
Jalan Gombak, 53100
Kuala Lumpur. Malaysia
faris@iiu.edu.my

Momoh Jimoh Salami
Faculty of Engineering,
International Islamic University Malaysia (IIUM), Jalan Gombak,
53100 Kuala Lumpur.
Malaysia
momoh@iiu.edu.my

Abstract

The hardware design of a pressure based typing biometrics authentication system (BAS) is discussed in this paper. The dynamic keystroke is represented by its time duration (Δt) and force (F) applied to constitute a waveform, which when concatenated compose a complete pattern for the entered password. Hardware design is the first part in designing the complete pressure-based typing (BAS) in order to ensure that the best data to represent the keystroke pattern of the user is captured. The system has been designed using LabVIEW software. Several data preprocessing techniques have been used to improve the acquired waveforms. An experiment was conducted to show the validity of the design in representing keystroke dynamics and preliminary results have shown that the designed system can successfully capture password patterns.

1. Introduction

In the strictest sense, biometrics refers to the application of a statistical analysis to biological data and phenomena. The security community, however, widely uses the term to describe technologies for personal identity verification. Biometric devices fall into two categories: those that use physical characteristics, such as fingerprints and hand geometry, and those that use behavioral characteristics, such as signature dynamics and keystroke dynamics. Although a variety of authentication, devices to verify a user identity are in use, password mechanisms have been and probably will remain the preferred method. Password authentication is an inexpensive, familiar paradigm that most operating systems support. Confidence in its ability to provide adequate authentication is, however, waning. This is largely due to the wrongful use of passwords by many users, methods are needed, therefore, to extend and enhance the life of password techniques. One can develop a methodology that improves security by using typing biometrics to reinforce password-authentication mechanisms. Typing biometrics is the analysis of a user keystroke patterns. Each user has a unique way of using the keyboard to enter a password; for example, each user types the characters that constitute the password at different speeds. Fuzzy logic, SVM or Neuro-fuzzy can be implemented to measure the user typing biometrics. This reinforcement is transparent—indiscernible to the users while they are entering the normal authentication information (user ID and password), [1, 4, 5 and 10].

This paper discusses the hardware design of BAS, in such a system it is necessary to determine the dynamics of keystroke typing. One have to identify the parameters of importance that can constitute a convenient pattern or dynamic signature of the user. These parameters can be identified by:

1. The duration of pressing a key, in other words the amount of time a user takes to press and release when typing (Δ t).
2. The amount of force exerted on each button pressed (F).

The application of force (F) over duration of time (Δ t) produces a wave pattern which could be recognized as the typing-template for a sequence of keys pressed.

In [1], a good algorithm for the password authentication is outlined. Here, when a new user requests access to the computer system, or when an existing user password is to expire, the access-control system asks the user to type in the user ID and a new password. The system then asks the user to reenter the user ID and password to verify the previous inputs. Based on the typing patterns displayed on entering and reentering the

information, the typing-biometrics methodology computes a typing template for the user. The access-control system then saves the user identification with the associated template, along with the normal user ID and password pair. On subsequent attempts to access the system, the user goes through the normal password-authentication procedure that is, entering the user ID and password. At the same time, the system monitors the user typing patterns and computes a typing template based on the user ID and password just entered. It then compares this template with the template previously determined for this user. If the new password and typing template match those saved in the database, the system grants access to the user. However, if the password does not match, the normal password-authentication mechanism (without consulting the biometrics component) will reject the user or ask the user to reenter the authentication information. If the password does match, BAS will provide a supporting recommendation that verifies that the user is legitimate.

If the user ID and password are correct, but the new typing template does not match the reference template, the security system has several options, which will be devised accordingly. A typical scenario might be that BAS advises a security or net-work administrator that the typing pattern for a newly entered user ID and password is not what the system expects it to be and that a security breach might be possible. The security administrator then closely monitors the session to ensure that the user does nothing he or she is not authorized to do. A practical situation applies on ATM subscribers where if the user password and pattern don't match restriction is placed on the amount of money that can be withdrawn [1].

The hardware design of BAS has been carried out to achieve desired results with minimal hardware component utilization. The DAQ capture system constitutes of sensors, DAQ hardware, interface card and signal conditioning circuit in addition to the PC unit.

The biometric sensors of the system are force sensors which are needed to give a precise inspection of the amount of force that each user applies while typing. Force sensors can also provide more specific information than just the force applied, hence using data acquisition and analysis one can examine each signal pattern and monitor the time duration (Δt), this will enhance the systems sensitivity and precision.

Flow chart of BAS has been reported in [1]. An important issue to discuss here is the learning stage that the user undergoes when creating a new password.

Initially the system assumes that a user typing undergoes gradual learning curve. The system adjusts the reference typing template for a user when the newly displayed pattern closely resembles the previously saved template. His or her reference typing template has to be updated to reflect the current typing pattern. When the newly typed pattern substantially deviates from the saved template, the system assumes that the user is an impostor, and will not adjust the saved template. However, soon it becomes clear that simultaneously matching patterns and learning new patterns is very difficult, if not impossible, hence it is recommended to separate learning and matching for a prototype system. When a user registers new authentication information by entering the user ID and password, the system monitors when the user pattern stabilizes into a recognizable pattern. The user must therefore repeatedly enter the password until the pattern becomes recognizable. The number of retries before the pattern stabilizes varies from 10 to 20.

The hardware design is divided into two main sections in this paper:

1. The drive and filter circuit, these are external to the main PC unit.
2. The Front panel and block diagram of the LabVIEW VI (virtual instrument).

In the first section the amplifier circuit and the corresponding filter were designed. The sensors were attached to the drive circuit and then from the drive circuit to the A/D interface card.

The overall system block diagram is shown in Figure 1.

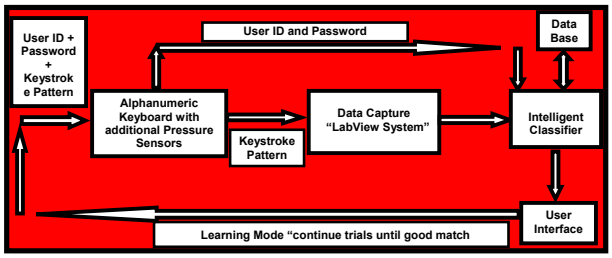

Figure 1. Overall system Block diagram.

Two main authentication frames are emphasized during the overall design of the BAS:

1. The alphanumeric password representing the normal password entered by the user, it consists of alphanumerical combination created by the user or the system administrator and saved by the system.
2. The typing biometrics associated with the user "typing template", this is the second authentication frame needed to study the typing pattern of the user and classify it according to certain parameters associated with typing patterns.

The analysis of BAS is the focus of this paper. However, the overall system as depicted by Figure 1 is currently

being integrated and tested. The overall system will be discussed separately in the future.

2. Hardware design

2.1 Force sensors arrangement

The sensor is an ultra-thin (0.005") flexible printed circuit. It is 0.55" (14 mm) wide and 8" (203 mm) in length. The active sensing area is a 0.375" diameter circle at the end of the sensor. The sensors are attached to the bottom (below) each keyboard key, a plastic spring is fixed on the sensing area of the sensor to insure that the key does not push on the sensing area and cause error pulse. This fabrication allows the template to have a normal distribution for the voltage waveform for each pulse (key pressed), the waveform pulse will hence have a shape similar to half a sine wave cycle.

2.2 System design in LabVIEW

The DAQ system has been designed with LabVIEW based on the following specifications:

1. The data captured must be saved continuously into a file format that would be transferred to the database and the intelligent classifier.
2. The system must have an independent trigger to start the acquisition

The main objective is to continuously acquire and save data to text file readable by spreadsheet programs. Each row is a scan and each column is a channel; columns are separated by commas and rows by an end-of-line character.

The system uses the circular buffer technique for data acquisition whereby data is continuously acquired into a circular acquisition buffer at the same time that the VI reads the acquired data and processes it. After the program creates the file, it initializes and starts the acquisition. It converts the scan rate to a string ending with an end of line character and writes it as the first line in the file. In each iteration, it reads "number of scans to write at a time" scans from the acquisition buffer, converts the data to a spreadsheet string, and writes it to the file. When one presses the STOP button, the program stops the acquisition and closes the file. The scan backlog indicates how much data remains in the buffer after each retrieval, and is an indication of how well the application is keeping up with the acquisition rate. If the backlog increases with time, that means scanning is too fast and will eventually overwrite the circular buffer [8].

There are inputs for setting the channels, size of the circular buffer, scan rate, and the number of samples to retrieve from the circular buffer each time. For example if a VI has an input buffer size of 2,000 samples and 1,000 number of scans to read at a time, which means the VI reads in half of the buffer's data while the VI fills the second half of the buffer with new data.

Analog trigger signal is connected to one analog input channel. The DAQ device monitors the analog trigger channel until trigger conditions are met. The DAQ hardware has been configured in LabVIEW to begin taking data when the incoming signal is on the rising slope and when the amplitude reaches 1.2V, signal is initiated by a special button on the keyboard.

2.3 Signal preprocessing

The first stage of signal preprocessing is to pass the acquired waveform over a lowpass filter which eliminates any undesirable high frequency components or noise before the sampler and ADC.

After applying the filter one can observe in (Figure 2 and Figure 3) the elimination of noise and the improvement in the waveform signal.

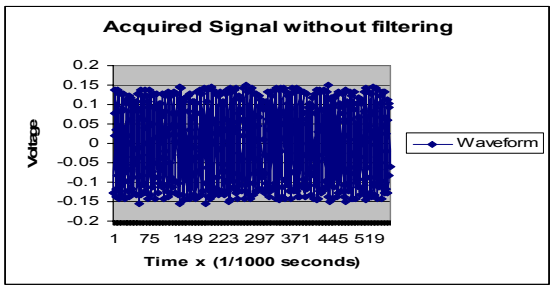

Figure 2. Acquired signal without filtering.

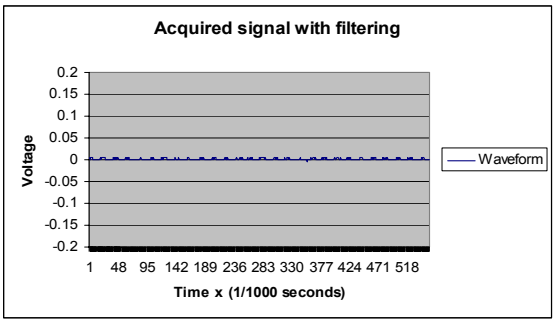

Figure 3. Acquired signal with filtering.

3. Experimental setup

According to the system specifications, the data captured for the password pattern should comply with the type of classifier to be used; the classifier in this case is

SVM (support vector machine). Here are the main criteria for the experiment.

1. The experiment aims at proving the consistency of the design in capturing, representing and analyzing the keystroke pattern of a certain password.
2. The keystroke waveform pattern for each individual keyboard button pressed should be appended (attached) to make up one continuous waveform for all the buttons together; this continuous waveform is the dynamic keystroke pattern that will be passed to the classifier. Appending the waveforms can be done externally (before entering the DAQ terminals) or internally (with the LabVIEW software). The results of both external and internal appending were compared, and it was found that external appending is better. Waveforms were appended externally by superimposing them to one channel in a parallel connection, by this way it is possible to save extra processing on the LabVIEW software.
3. The number of data points for each time a user enters his/her password should be consistent, otherwise the classifier will arbitrarily insert small values (or zeros) as replacement for the missing points (to make up the maximum number of points which is 540). It is required to collect only a fixed number of data points for each key pressed or find a way to concise the graph and reduce the number of data points without altering the trend of the data points acquired. This was achieved by applying the moving average algorithm with interpolation in the LabVIEW data processing. The consistency of such approach is shown in the results.

The experiment was done by asking a volunteer to key in a 7 digit password and verifying whether one can constitute a recognizable pattern for the password entered. The experiment showed that password pattern has a very high degree of precision and sensitivity, making it to have the following advantages and disadvantages.
The advantages are:

1. Data is more accurate and more descriptive to keystroke dynamics of the user.
2. Easiness in identifying different patterns of different users.
3. More into fulfilling the real-time dynamic response of password pattern.

While the disadvantages are:

1. Patterns for a certain user can never match completely; this puts a burden on the classifier module.
2. The effect of external factors on the user (his emotional state, his physical position while typing) can greatly affect the keystroke pattern typed

For these reasons one should adjust the sensitivity of DAQ system, the aim is to find the optimal sensitivity for the system. Sensitivity can be adjusted by changing the amplifier gain or by changing the LabVIEW waveform parameters, such as the sampling rate or the numbers of scans to read at a time.

In the experiment results one can notice the effects of using the moving average algorithm in compressing keystroke patterns without altering the trend of the waveforms.

3.1 Data acquisition and processing

The moving average is a simple mathematical technique used primarily to eliminate aberration and reveal the real trend in a collection of data points.

$$y_M[n] = \frac{1}{M}\left(\sum_{k=0}^{M-1} x[n-k]\right) \qquad (1)$$

The algorithm was written so as to make average for (M) number of points and represent them with one point, for convenience an interpolation algorithm has been applied, the interpolation was done to get the average between each two consecutive data points, the scope was to reduce the data points without distorting or losing any significant information in the signal. Simple test on the algorithm have shown that this can improve patterns [9].

1. Data before applying the moving average algorithm

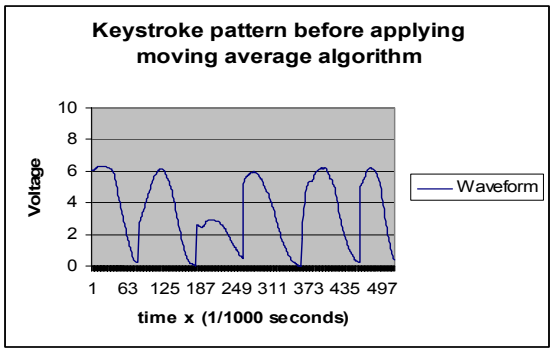

Figure 4. Keystroke pattern without moving average and interpolation.

As one can see the number of points is around 400 to 500 points for each password pattern, the error (difference in number of points for successive password trials) will be high (20-100 points) which is not recommended for the SVM classifier. Therefore it is mandatory to reduce the number of points representing each pattern in order to comply with design specifications

2. Data after applying the moving average algorithm.

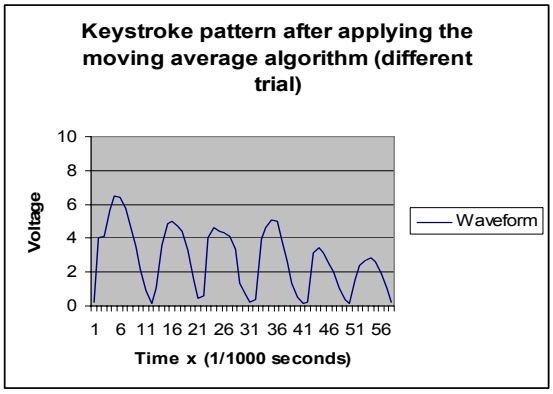

Figure 5. Keystroke pattern with Moving average and interpolation.

It is observed that the 5 moving average has greatly reduced the number points without altering the overall shape and trend of the keystroke pattern, in the 7 digit experiment it will shown that the error in that case was only 5 data points for all trials in the experiment.

3.2 Experiment results and discussion

The experimental results for keying a 7 digit password for one user is shown in figure 6, 7 and 8 respectively.

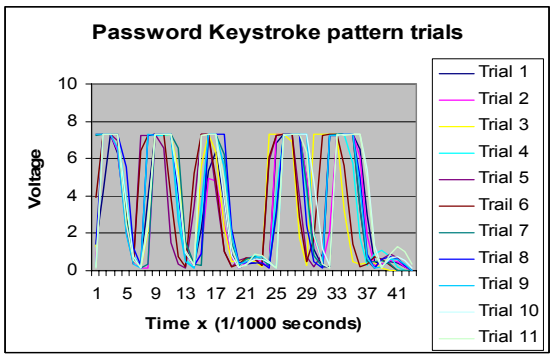

Figure 6. Keystroke pattern trials for single user and 7 digit password.

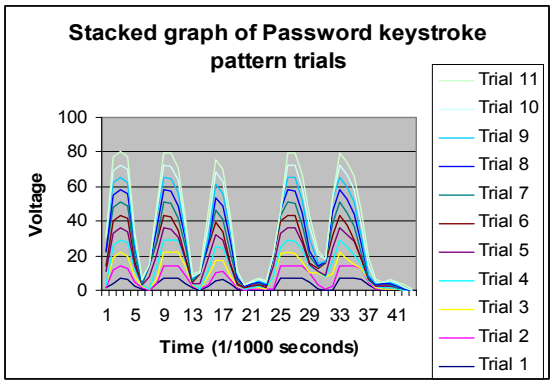

Figure 7. Keystroke pattern trials for single user and 7 digit passwords (stacked graph).

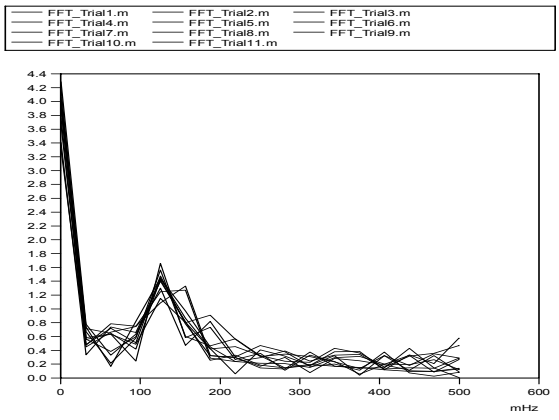

Figure 8. FFT of keystroke pattern trials for single user and 7 digit password.

In Figure 6, it is evident that the user is following distinct stroking rhythms, a general pattern is easily recognizable from the graph. This proves that the hardware has been successful in capturing a recognizable

pattern for the password, justifying that the approach of designing the dynamic keystroke pattern is correct.

The difference in the number of data points for each password pattern is only 5 for all 11 trials, this is confirmation with the SVM requirements of the system.

Figure 7 shows the stacked graph for the 7 digit password trials, this graphs is more descriptive to the degree of compatibility between each password trial, it is clear that there is a lot of similarity between keystroke patterns.

It is also possible to examine the frequency analysis of the concatenated waveform. This can be achieved by computing the discrete Fourier transform (DFT) of $y[n]$ using the FFT algorithm. This would produce the energy spectral density (ESD) of $y[n]$ which is directly related to the pattern of keystroke typing (it is expected that different users should produce different ESD). However, information about the latency is lost due to the procedure of acquiring the data.

Figure 8 shows the ESD graph for the 7 digit password trials. FFT algorithm calculates the discrete spectrum of a particular waveform. from the graph it is noticed that the ESD for the patterns are very similar, it is also noticed that the FFT estimates of the keystroke patterns are very similar too.

4. Conclusions and recommendations

This paper is aimed at proving the consistency of the hardware design for BAS. The approach was to represent the keystroke by its force and duration so as to constitute a waveform pulse, the addition of several waveforms for several keystrokes (appending) makes the password pattern of the user.

The experiment was conducted to prove that this approach is reliable and that the overall design for the BAS is feasible and valid. This result gives the green light to proceed to the second stage of the design which involves the classifier testing and the construction of the keystroke pattern database.

The second stage will emphasize on the inference options that can be implemented to classify the keystroke pattern templates. Currently SVM classifier (support vector machines) is being implemented and tested for; other classifier techniques such as Neuro-fuzzy and ARMA (auto regressive moving average) are going to be tested as well.

For several password trials, the degree of matching between each keystroke pattern entered can vary. However, the general keystroke harmonics preserves this variation within a limited range. In the design one has to emphasize on ways to increase the matching degree of patterns for a distinct user, while passwords for different users must not match. This is somehow related to the sensitivity of the hardware when measuring the voltage waveform; it was experimented that if one increases the sensitivity the waveforms of keystroke patterns will reach the threshold voltage for most of the keys pressed when typing a certain password, this is not desired as it increases the possibility of match between patterns of different users. To solve this problem one have to attain the optimal settings for the sensitivity which can only be achieved by conducting more random experiments for many users and passwords.

The FFT was used to prove the analogy between the ESD of keystroke patterns; this is a good criteria to include in further analysis of pattern classification.

References

[1] Willem G. de Ru, Jan H. P. Eloff, "Enhanced Password Authentication through Fuzzy Logic", IEEE Expert 12(6): 38-45 (1997).

[2] P. Conn, J.H. Parodi and M. Taylor, "The Place of Biometrics in a User authentication Taxonomy," Proc. 13th Nat'l Computer Security Conf., Nat'l Inst. Standards and Technology/Nat'l Computer Security Center, Gaithersburg, Md.,1990.

[3] Sajjad Haider, Ahmed Abbas and Abbas K.Zaidi, "A multi-technique Approach for User Identification through Keystroke Dynamics", Proc.IEEE SMC Society Conference 2000. ,8 Oct 2000.

[4] D.L. Jobusch and A.E. Oldehoeft, "A Survey of Password Mechanisms, Weaknesses and Potential Improvements, Part 1," Computers & Security, Vol. 8, 1989, pp. 587–604.

[5] W.G. de Ru and J.H.P. Eloff, "Improved Password Mechanisms through Expert System Technology," Proc. Ninth Ann. Computer Security Applications Conf., IEEE Computer Society Press, Los Alamitos, Calif., 1993, pp. 272–280.

[6] D. Russell and G.T. Gangemi, Sr., "Computer Security Basics", O'Reilly and Associates, Sebastopol, Calif., 1991.

[7] O. Coltell, G. Torres, and J. M. Badía, "Biometric Identification System Based in Keyboard Filtering". Proc. of 33rd Annual 1999 International Carnahan Conference on Security Technology, IEEE Publisihng Services, pp. 203-209, Piscataway (USA), 1999.

[8] "LabVIEW measurement manual", National Instrument, July 2000 edition.

[9] James H.Mcllellan, Ronald W.Schafer and Mark A. Yoder, "DSP First a multimedia approach", Prentice-Hall, international edition 1998, PP 119-155.

[10] Brigitte Wirtz, "Biometric systems 101 and beyond, an introduction to and evaluation of the technology and an overview on current issues", Infineon Technologies AG.

A Visual Attention Approach to Personal Identification

Anthony Maeder and Clinton Fookes
School of Electrical & Electronic Systems Engineering
Queensland University of Technology
GPO Box 2434 Brisbane, 4001 QLD Australia
{a.maeder,c.fookes}@qut.edu.au

Abstract

This paper describes the use of visual attention characteristics, monitored by gaze tracking during presentation of a known visual scene to a viewer, as a biometric for distinguishing between individual viewers. The positions and sequences of gaze locations during viewing may be determined by overt (conscious) or covert (sub-conscious) viewing behaviour. Methods to quantify the spatial and temporal patterns established by the viewer for a particular image are proposed, and distance measures between these are established. Experimental results suggest that both types of gaze behaviours can provide simple and effective biometrics for this application.

1. Introduction

Establishing the identity of a person when validating a request for access to a secure environment is an important and challenging application in the world of today. To complement the widespread practice of data-based authentication using private information (such as passwords) which is prone to attack or theft, some physical aspects of the human individual known as "biometrics" may also be used (such as fingerprints) [2]. While these are harder to violate than purely data-based methods, it is not impossible. Safer forms of biometrics would be based on non-visible and non-physiological information hidden within the person, such as behaviour or thought processes. Here we propose to exploit the personal aspects of visual attention processes determined by means of monitoring eye movements, in an attempt to develop such a biometric.

2. Visual Attention and Eye Movement

It has been estimated that approximately 80% of the information a human receives comes from visual inputs [13]. Visual information therefore plays a major role in our everyday life activities and also in our ability to make decisions based on this information. Visual attention is a complex and expanding research field which investigates aspects of human vision and how it relates to higher cognitive, psychological and neurological processes. The concept of attention, or conscious selecting and directing of perceptual information intake, arises because finite physical human limitations prevent us from perceiving all things at once. Rather, attention is used to focus our mental capacities on small portions of the sensory input gamut so that we can successfully assimilate the stimulus of interest [6].

The human visual system relies on positioning of the eyes to bring a particular component of the visible field of view into high resolution. This permits the person to view an object or region of interest near the centre of the field in much finer detail. In this respect, visual attention acts as a "spotlight" effect [9]. The region viewed at high resolution is known as the foveal region and is much smaller than the entire field of view contained in the periphery. Viewing of a visual scene consists of a sequence of brief gaze periods (typically 100-500ms) of visual concentration (fixations) at specific locations in the field of view, interspersed with sudden movements of the eyes (saccades) to reposition the foveal region at the next point of attention. This process provides the brain with detailed visual information over a succession of these fixation-saccade events covering a few comparatively small areas in the field of view, from which a "conceptual" image of the visual scene is constructed by combining these with the large area of low resolution information gained from the periphery. The fixation-saccade events may be consciously directed by the viewer to visit a sequence of specific points in the scene (overt), or else may be allowed to be directed sub-consciously by the brain according to its choice of points of interest (covert) [8].

In order to understand visual attention processes better, methods have been devised to track gaze location through eye movements: a simple approach uses a video camera image to recover the 3D orientation of the eye. By observing where and when a person's gaze is directed, it is possible to establish the fixation-saccade path followed by the viewer. This provides insights about what the viewer found interesting (i.e. what captured their attention) and perhaps reveal how that person perceived the visual scene they were viewing [6]. If the viewer is undertaking a defined task, such

as following a prescribed sequence of gaze locations, this is equivalent to providing a password. If a task is not specified, the path denotes the pattern of visual interest for that individual, corresponding to the scene being viewed. Either of these situations can provide a suitable foundation for a biometric, and both are explored here.

3. Biometric Gaze Measurements

Biometric research is a rapidly evolving field due to the increased demand on modern society to identify or authenticate an individual [11]. Whether for the purpose of entering a restricted room or building, or for credit card payments, there are numerous needs to validate identity. Biometric identification has adopted a wide range of human features and characteristics which may be used to identify or authenticate an individual with much stronger certainty. Typical examples include the fingerprint, iris and retina scan, voice print [12], face geometry [4, 10], DNA, handwriting, or even a person's typing style which can be used as a keyboard behavioral signature [1]. An identification system is also often formed as a combination of different traditional identification and biometric measures [5]. This paper describes another such biometric measure based on distinguishing between visual attention patterns for individual viewers.

As described earlier, a viewer will build up a perception or "conceptual image" of the visual scene by a sequence of fixation-saccade events. The spatial and temporal pattern of these events for a given visual scene varies widely between different people and accordingly can be used to compute a visual attention "signature" of each individual. These signatures can be formulated by quantitative analysis of the individual's gaze data [7]. Two possible ways that such signatures could be constructed are as follows.

1. The viewer could be presented with a known picture for which they had decided upon a personal sequence of fixation points, already informed to the authentication system in a training phase. The viewer would consciously (overtly) direct their gaze to these points in the order established, while the authentication system tracked the sequence of points.

2. The viewer could be presented with a known picture for which their unconscious (covert) pattern of gaze points when inspecting the picture had previously been captured by the authentication system in a training phase. The viewer would simply view the picture passively and allow the authentication system to collect the pattern of gaze points occurring naturally.

Both methods require some assumptions about the properties of eye movement and gaze tracking, as follows:

1. The operating characteristics of the tracking device need to be sufficient to allow the necessary detail in spatial and temporal resolution. A sampling rate of approximately 50ms or less will achieve the temporal requirement for detecting fixations generally. Spatial localisation to around 10% of the overall scene linear dimensions is judged sufficient to establish fixation points appropriate to this application.

2. A sufficient number of successive gaze points is required to allow unique characterisation of an individual within the population, and to override the effect of involuntary errors in gaze location and sequence, without requiring too many points or too long a gaze duration for practical purposes. A comfortable maximum viewing time for an image is approximately 20 secs, after which some fatigue/boredom effects typically occur. This allows for at least 40 fixations to be measured.

3. The gaze pattern followed by a viewer needs to be reasonably similar on different occasions. Substantial evidence from experiments with numbers of viewers indicates this expectation is realistic [14].

4. The covert viewing gaze patterns for different viewers of the same scene need to differ significantly and consistently from each other to allow effective detection. Evidence in the literature [6] suggests that this is the case.

5. An efficient and unbiased technique is needed to establish the distance between two gaze patterns, to allow easy decision-making for establishing similarity. A signature of relatively few numerical values representing a compacted form of the gaze pattern would be appropriate, and can be compared using ranking or matching type procedures.

6. A distance measure between gaze patterns also needs to make allowance for involuntary errors, such as sequence or duration variations. The signature should therefore be constructed to constrain the effects of same viewer variations.

Our approach to developing the biometrics described above, and establishing their viability subject to the above assumptions, is described in the sections below.

4. Methodology & Outcomes

The experimental methodology adopted consisted of recording gaze data of three different viewers for a particular image of an outdoor scene. This image is shown in Figure 1. For each image, the viewer was directed to examine the scene both consciously (overtly) and unconsciously

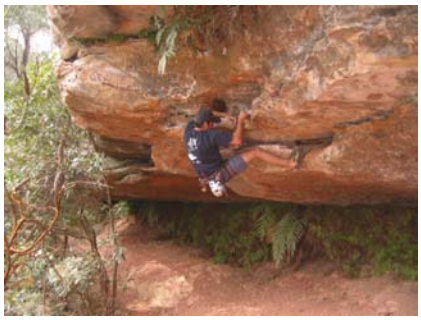

Figure 1. Rockclimb image used in the gaze-tracking experiments.

(covertly). The former approach relied on the observer to gaze at a select number of points and in a particular sequence known only to them. In the latter approach, the viewer was free to examine the image in their natural manner, i.e. as directed by their personal visual attention processes. For each case, the gaze-tracking experiment was repeated three times, each occasion being separated from the others by some other visual tasks to reduce the influence repetition.

4.1. Gaze-Tracking Device

The device used to record eye movements during these experiments was an EyeTech video-based corneal reflection eye tracker. This device is normally used for point-of-regard measurements, i.e. those that measure the position of the eye relative to 3D space rather than relative to the head [15]. The method of operation relies on tracking the corneal reflection from an infra-red light source, as it is invisible to the human eye and non-distracting. Although four separate reflections are formed during the reflection of a light source, referred to as Purkinje reflections [3], only the first Purkinje reflection is utilized in the video-based tracker and is located relative to the location of the pupil center using image processing techniques.

The gaze-tracker utilized operated at 15 frames per second, resulting in a sample of the observer's gaze direction approximately every 67ms. The experiments were conducted using an image and screen resolution of 1024×768 pixels.

4.2. Overt Experiment

For the overt experiments, each viewer was directed to look at six specific points in the Rockclimb image. As only a small number of people were utilised, the same six points were used in each case, however, the viewing sequence was re-arranged substantially for each person. This essentially provided a unique pattern which could be used to distinguish very clearly between the different individuals.

For both the overt and covert approaches to developing a biometric measure, the system may be considered to have two operating modes. The first mode consists of the off-line training wherein the library of gaze "signatures" is compiled for each individual. The second mode is the actual online operation of the authentication system. In this mode, an observer's gaze data is recorded online and compared against the database of signatures to identify or authenticate an individual. The off-line training mode for the overt experiment consisted of building the database of points to be viewed and their sequences manually. The recorded gaze data gathered during the online mode was then compared against the database to authenticate the individual.

For the given Rockclimb image, the observer was directed to gaze at each of the six specific points for approximately one second each and in their prescribed sequence. The gaze data (sampled at 15fps) was then passed through a spatial clustering algorithm to extract any fixations with an approximate viewing time of 1.0 secs and a tolerance of 0.3 secs, i.e. containing roughly 10 to 19 samples of gaze data. The locations of these fixations were then compared against the database, along with their viewing sequence, to authenticate the individual.

Figure 2 shows the original gaze data and fixations extracted for all subjects viewing the Rockclimb image, for comparison purposes. After clustering the original gaze samples with a constraint on the time of fixation, only six fixations were obtained and are plotted against the Rockclimb image. These fixations correspond to the six points the observer was directed to examine. Similar fixation plots were also obtained across the three repeat experiments from the same people.

For the overt experiment, a successful authentication is the case when the location of the fixations extracted from the clustering algorithm (subject to a time constraint of approx one second) is within a small threshold of the locations stored in the database. The sequence of viewing these fixations also had to correspond to those stored for each individual. The authentication process was successful in all cases.

4.3. Covert Experiment

Comparing the recorded gaze signatures of a person with those in a database is a straight forward procedure for the overt experiments. A valid authentication is simply the case when the location of the clustered fixations, and their viewing sequence, matches those stored in the database. However, the comparison of the gaze patterns for the covert experiments is a much more complicated and problematic endeavour. This is due to the inherent variations that exist not only between viewing patterns of different people, but more significantly, between different scans of the same person. This inter- and intra-variability makes the development of a simple authentication process extremely difficult. Consequently, more sophisticated measures need to be developed in order to truly identify commonalities, if any, that exist

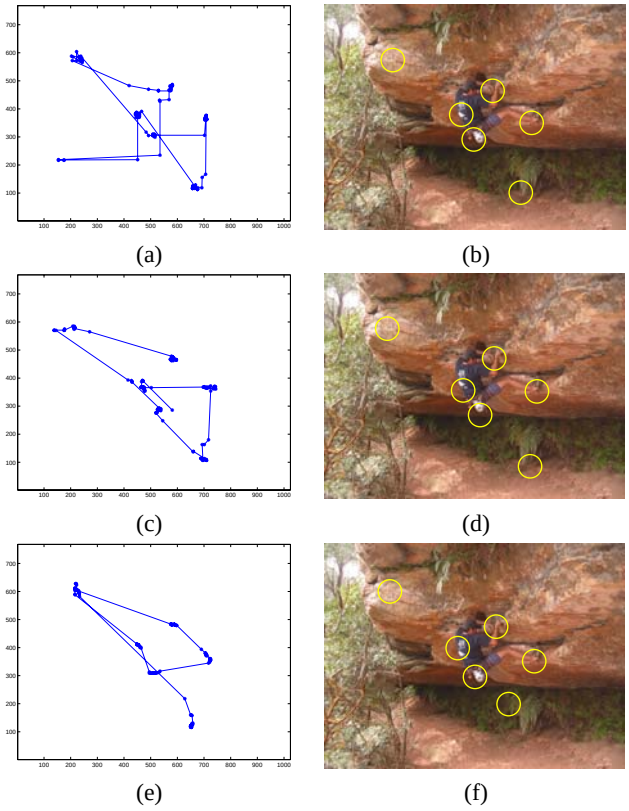

Figure 2. Overt Experiment: (a,c,e) show the original gaze samples while (b,d,f) show the extracted fixations plotted against the Rockclimb image for all three viewers.

between different scans of the same observer and between observers. The measures and data that will be discussed in this section are presented to ascertain if any patterns exist across the same observers and/or different observers. The existence of any such patterns will determine if a person's covert visual attention processes can in fact be used as a successful biometric. At this stage, no authentication procedure has been implemented on these measures.

Figure 3 presents some sample data for the covert experiments. Plots (a), (b) and (c) show fixations of Scan 1 for Person 1, Person 2, and Person 3 respectively, plotted against the Rockclimb image. The variations between observers in these cases are quite apparent. Figures (d), (e) and (f) represent the three repeated scans for Person 1 on the Rockclimb image. These three scans do appear to have many similarities after a visual comparison, however, there is still obviously some diversity between the three repeated scans, i.e. intra-viewer variation. Moreover, the plots in Figure 3 do not contain any information about the sequence these points were viewed in.

The measures employed to determine the similarities between different scans in this experiment are outlined below.

- $\mathbf{D}$: is used to measure or count the number of common fixations between any two scans. A common fixation is one which coincides spatially (within a given threshold) with another fixation in the second scan.

- $\mathbf{D}'$: encompasses the order information between two scans. It is a measure or count of the number of position changes in order for the common fixations viewed in both scans. This count is also normalised by the square of the number of common fixations, i.e. $\mathbf{D}^2$.

- $\mathbf{D}^*$: is used quantify the difference in visit periods of the first five fixations in two scans. This is achieved by the computation of a SAD score between the number of gaze samples in each of the first five fixations, $\mathbf{D}^* = \sum_{i=1}^{N} \left| p(F_i^1) - p(F_i^2) \right|$, where $N = 5$, F_i^1 and F_i^2 are the ith fixations of scan 1 and scan 2, and $p(.)$ is the number of gaze samples in each fixation.

- $\mathbf{D}^+$: quantifies the difference between the number of revisits of each of the first five fixations. The revisits is represented as a count of the number of times a viewer "revisits" one of the first five fixations during the entire viewing duration. This measure is implemented with another SAD score, $\mathbf{D}^+ = \sum_{i=1}^{N} \left| r(F_i^1) - r(F_i^2) \right|$ where $N = 5$, and $r(.)$ is the number of revisits for each fixation.

The first two distance measures are used to assess the commonality of the fixations and their viewed sequence between any two scans. $\mathbf{D}$ simply counts the number of common fixations while $\mathbf{D}'$ counts the number of position changes in the order of the fixation viewing sequence. This count is normalised by $\mathbf{D}^2$ to penalize those counts with a small number of common fixations. Thus, viewing sequences with a certain number of sequence changes and a large number of common fixations will be more significant than those with the same count for sequence changes and a small number of fixations.

The second two distance measures described above are used to quantify slightly different aspects of the visual attention process. $\mathbf{D}^*$ measures the difference between the period (or the number of sample points) of the first five fixations via a SAD score. Empirical evidence has shown that the most prominent of all fixations generally occur within the first five viewed. Later fixations as a general rule contain a much smaller period. These is the reason for only comparing the first five fixations. Note however, that these first five fixations can be revisited during the entire viewing duration (10 secs). Thus, $\mathbf{D}^*$ computes the SAD score between the total number of sample points between the first five fixations obtained over the entire viewing sequence. The last distance measure $\mathbf{D}^+$ quantifies the difference between the revisiting habits of the viewers. Different viewers will have different

underlying psychological and cognitive process which direct them in to revisit points or regions of interest to them in various manners. Thus, $\mathbf{D}^+$ measures the differences in the number of revisits of the first five prominent fixations via another SAD score.

Table 1 presents the $\mathbf{D}$ distance measures calculated between all possible scan combinations. The larger the value, the more similar the scans as they share a larger number of common fixations. The diagonal values in this table signifies comparison between a scan and itself, which simply yields the total number of fixations in that person's scan. From a simple visual inspection of the table, there is evidence that the $\mathbf{D}$ scores of intra-viewer comparisons (not including the diagonals) are generally larger than inter-viewer comparisons, except for a few cases. This measure however, is by no means sufficient enough to adequately distinguish between different viewers.

		P1			P2			P3		
		S1	S2	S3	S1	S2	S3	S1	S2	S3
P1	S1	14	9	9	6	8	7	5	5	3
	S2		10	8	3	7	5	3	3	2
	S3			11	3	5	5	4	4	3
P2	S1				15	7	9	4	3	3
	S2					13	6	2	2	2
	S3						13	4	5	3
P3	S1							9	7	6
	S2								10	4
	S3									7

Table 1. Quantitative measures: $\mathbf{D}$ calculated between scans of all viewers.

Table 2 presents the $\mathbf{D}'$ scores which signify the differences in order of the fixation viewing sequence, normalised by the square of the number of common fixations. In this case, the smaller the $\mathbf{D}'$ score, the more similar the scan. The diagonal values in this table are all zeros as a scan compared with itself will obviously have the exact same viewing sequence, so the changes between them will be zero. From a visual inspection of the table, it can be scene that the intra-viewer comparisons (not including the diagonals) are almost all smaller than inter-viewer comparisons, except for five distinct cases which the score is zero. These are cases when the viewing sequence of the common fixations are the same. However, from a cross-comparison with Table 1, it is clear that these instances generally only contain two or three common fixations between the two scans, so the possibility of having the same sequence is significantly higher. Future work will look at penalizing these instances rather than assigning it a zero value which would suggest similar scans, when in actual fact they are far from similar due to the small number of common fixations.

Table 3 presents the $\mathbf{D}^*$ SAD scores which measures the difference in the visit period (or number of gaze samples) between the first five fixations of any two scans, whatever location those fixations may be. This measure essentially compares how long a person views each of the first five fixations, which have been shown empirically to be the most prominent fixations. Similarly Table 4 presents the SAD scores between the number of revisits of the first five fixations. For the values in both Table 3 and 4, the smaller the score, the more similar the scans. Once again, from a visual inspection of both of these tables, there is an obvious trend where the intra-viewer comparisons are generally smaller than inter-viewer comparisons, except for a few cases.

		P1			P2			P3		
		S1	S2	S3	S1	S2	S3	S1	S2	S3
P1	S1	0	37	37	83	0	61	80	80	111
	S2		0	16	111	41	80	0	0	0
	S3			0	111	40	80	63	63	111
P2	S1				0	82	37	63	111	111
	S2					0	28	0	0	0
	S3						0	125	80	222
P3	S1							0	25	41
	S2								0	40
	S3									0

Table 2. Quantitative measures: $\mathbf{D}' \times 10^3$ calculated between scans of all viewers.

		P1			P2			P3		
		S1	S2	S3	S1	S2	S3	S1	S2	S3
P1	S1	0	27	56	65	45	72	87	85	59
	S2		0	53	80	54	81	80	78	48
	S3			0	63	69	82	69	85	49
P2	S1				0	38	31	76	108	82
	S2					0	51	78	72	68
	S3						0	95	115	83
P3	S1							0	36	44
	S2								0	54
	S3									0

Table 3. Quantitative measures: $\mathbf{D}^*$ calculated between scans of all viewers.

		P1			P2			P3		
		S1	S2	S3	S1	S2	S3	S1	S2	S3
P1	S1	0	3	8	8	7	9	8	8	4
	S2		0	5	9	10	12	7	5	3
	S3			0	10	11	13	8	6	4
P2	S1				0	3	3	8	8	8
	S2					0	4	7	9	7
	S3						0	9	11	9
P3	S1							0	6	4
	S2								0	4
	S3									0

Table 4. Quantitative measures: $\mathbf{D}^+$ calculated between scans of all viewers.

From the preliminary results presented thus far, there are some obvious trends in the data to suggest that a scan from one person is in actual fact more similar to other scans from that same person than to scans from other people. Future work will repeat these experiments on a greater range of images and subjects to provide a richer set of base data. Investigation will also be carried out on various statistical approaches to extract more concrete conclusions from these results, as well as examining more advanced comparative measures.

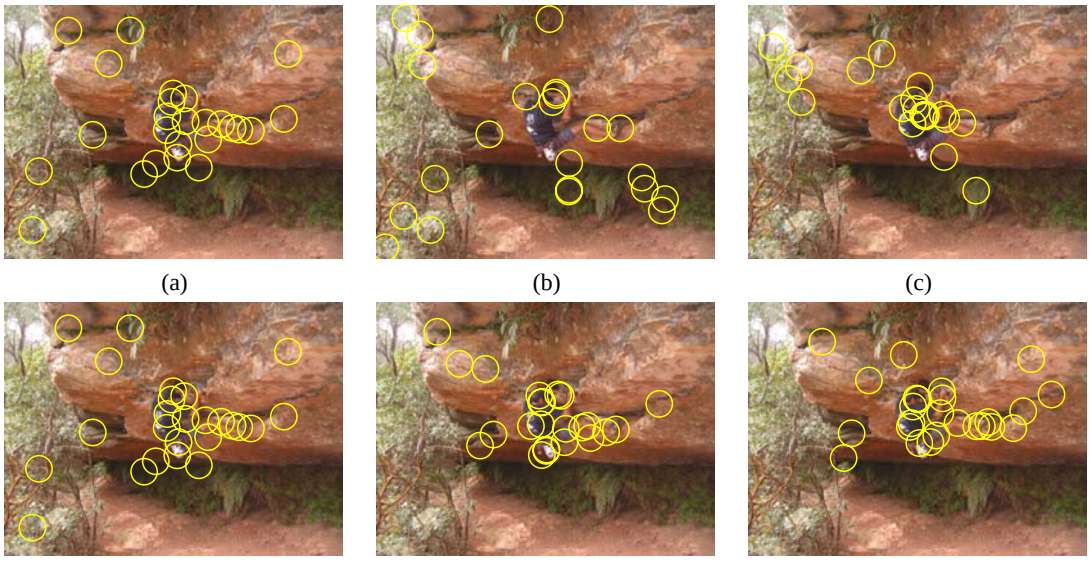

(a) (b) (c)

(d) (e) (f)

Figure 3. Covert Gaze Data: Fixations for Scan 1 of (a) Person 1, (b) Person 2, and (c) Person 3, for the Rockclimb image. Figures (d), (e) and (f) represent the three repeated scans for Person 1, i.e. intra-viewer variation.

5. Conclusion

The above experimental results would be enhanced by increasing the number of subjects tested, and refining the resolution of performance parameters associated with the complexity of the gaze tracking data and the corresponding compacted signature information. The simple visual attention biometrics described here could be extended in a number of ways, to increase the sophistication of the signatures extracted, or to introduce sufficient variability to make attacks harder: for example, expanding the number of different images available to a single viewer for the covert gaze method. The applicability of the method under highly constrained circumstances such as exist for present PC or PDA systems, using typical cheap camera technology for eye tracking and allowing no choice of images, is currently being investigated.

References

[1] T. Alexandre. Biometrics on smart cards: An approach to keyboard behavioural signature. *Future Generation Computer Systems*, 13:19–26, 1997.

[2] J. Ashbourn. *Biometrics: Advanced Identity Verification: The Complete Guide*. Springer, London, 2000.

[3] H. Crane. The purkinje image eyetracker, image stabilization, and related forms of stimulus manipulation. In D. Kelly, editor, *Visual Science and Engineering: Models and Applications*, pages 13–89, New York, NY, 1994. Marcel Dekker, Inc.

[4] J. Crowley. Vision for man-machine interaction. *Robotics and Autonomous Systems*, 19:347–358, 1997.

[5] U. Dieckmann, P. Plankensteiner, and I. Wagner. Sesam: A biometric person identification system using sensor fusion. *Pattern Recognition Letters*, 18:827–833, 1997.

[6] A. Duchowski. *Eye Tracking Methodology: Theory and Practice*. Springer, London, 2003.

[7] J. Goldberg and X. Kotval. Computer interface evaluation using eye movements:methods and constructs. *International Journal of Industrial Ergonomics*, 24:631–645, 1999.

[8] L. Itti and C. Koch. A saliency-based search mechanism for overt and covert shifts of visual attention. *Vision Research*, 40:1489–1506, 2000.

[9] L. Itti and C. Koch. Feature combination strategies for saliency-based visual attenion systems. *Journal of Electronic Imaging*, 10(1):161–169, January 2001.

[10] A. Nikolaidis and I. Pitas. Facial feature extraction and pose determination. *Pattern Recognition*, 33:1783–1791, 2000.

[11] N. Ratha, J. Connell, and R. Bolle. Biometrics break-ins and band-aids. *Pattern Recognition Letters*, 24:2105–2113, 2003.

[12] C. Rebman, M. Aiken, and C. Cegielski. Speech recognition in the human-computer interface. *Information and Management*, 40:509–519, 2003.

[13] C. Roux and J.-L. Coatrieux, editors. *Contemporary Perspectives in Three-Dimensional Biomedical Imaging*, volume 30 of *Studies in Health Technology and Informatics*. IOS Press, Netherlands, 1997.

[14] A. Yarbus. *Eye Movements and Vision*. Plenum Press, New York, NY, 1967.

[15] L. Young and D. Sheena. Survey of eye movement recording methods. *Behavior research methods and instrumentation*, 7(5):397–439, 1975.

MEDICAL IMAGE ANALYSIS

(This page left blank intentionally)

Three-dimensional Bone Shape Sonography System Aided by Fuzzy Logic

Tadashi Kimura[†], Kouki Nagamune[†], Syoji Kobashi[†], Katsuya Kondo[†], Yutaka Hata[†],
Yuri T. Kitamura[‡], and Toshio Yanagida[‡]

[†]Graduate School of Engineering
Himeji Institute of Technology
2167, Shosha, Himeji, 671-2201, Japan

[‡]Graduate School of Frontier Biosciences
Osaka University
2-2, Yamadaoka, Suita, 565-0871, Japan

kimura@comp.eng.himeji-tech.ac.jp

Abstract

This paper describes a sonography system that enables us to recognize three-dimensional (3D) bone shape by using ultrasonic technique. Conventional ultrasonic technique can visualize soft tissue of human body (e.g. heart and liver). However, it cannot apply to hard tissue (i.e. bone) because of the difficulty in inserting the ultrasonic wave to the bone caused by significant attenuation of the ultrasonic wave in it. To overcome this problem, we employ fuzzy logic, which can deal with ambiguous information. This method consists of two stages. First, a degree of bone surface is calculated from knowledge of bone surface. Second, a degree of bone bottom is calculated from knowledge of bone bottom. This method could visualize 3D bone shape by using each degree based on fuzzy logic. It applied to artificial bones. As a result, the error of the determined thickness was less than approximately 1.0 mm.

1. Introduction

For diagnosing and curing fracture or osteoarthritis, information of bone shape is essential to check the current state of human bone. X-ray Computed Tomography (CT) scanners are widely used for visualizing bone shape. CT systems cannot visualize bone shape in real time, and it requires high cost and large equipment, in comparison with ultrasonic systems. In addition, bone shape visualizing system in real time is required because physician would like to understand bone shapes on operation table, especially, under orthopedic surgery such as total knee arthroplasty and intramedullary nail locking.

Ultrasonic technique is well known for real time visualizing technique. The ultrasonic technique is used in many fields (e.g. diagnostic technique [1]-[3] and non-destructive evaluation [4]) due to its low cost and non-invasiveness. Moreover, ultrasonic technique helps us to diagnose the human body. However, since a bone is layer structure constructed of the cortical bone, the cancellous bone, and so on, the ultrasonic wave is significantly attenuated in bone tissue. Several researchers studied about visualizing bone tissue using ultrasonic technique [5][6]. However, because of pulse transit-time method or fixed specific region, it was not enough to visualize bone shapes. Development of pulse echo ultrasonic techniques that propagates bone tissue enables us to visualize bone shapes in real time.

Fuzzy logic [7][8] provides a high robustness scheme to control or manipulate ambiguous information. Especially, fuzzy inference technique is employed for various medical fields, such as image processing [9][10] and signal processing [1][3]. This paper therefore employs fuzzy inference technique to develop the sonography system.

The developed ultrasonic system consists of a composite probe whose center frequency is 1 MHz. The ultrasonic wave with frequency of 1 MHz penetrates bone practically. The system acquires several A-scope waves by moving the probe using a scanner. These A-scope waves comprise three-dimensional (3D) ultrasonic data. These waves have characteristics of the ultrasonic wave such as amplitude and frequency. This paper aims to determine surface and bottom points of a bone. We realize the bone sonography system that consists of two stages by considering these characteristics on fuzzy logic. First, we determine bone surface from the degrees of the surface echo. Second, we determine bone bottom from degrees of the bottom echo. We applied our method to artificial bones. As a result, the error of the determined thickness was less than 1.0 mm.

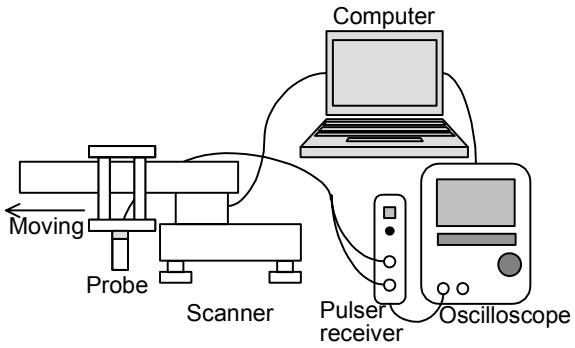

(a) Model of our method

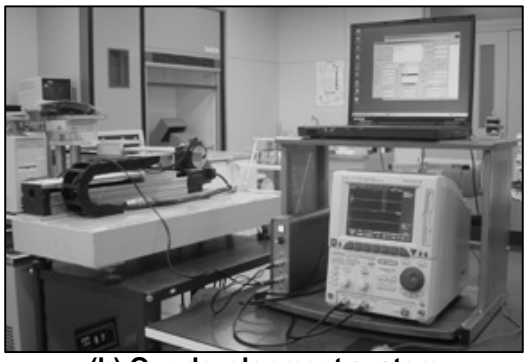

(b) Our development system

Figure 1. Ultrasonic data acquisition system.

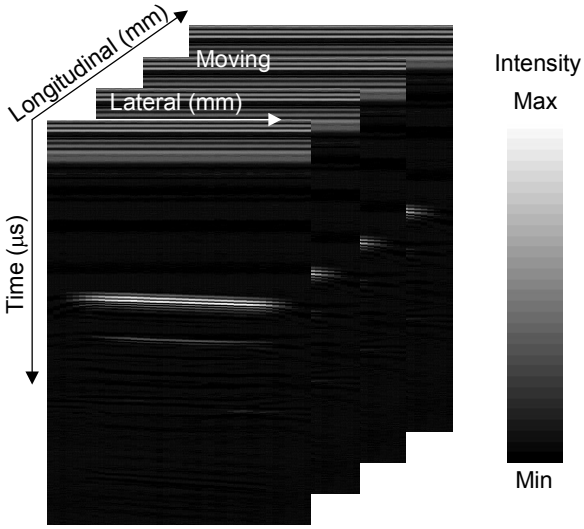

Figure 2. Ultrasonic data.

2. Preliminaries

2.1 Ultrasonic data acquisition system

Figure 1 shows an overview of the developed ultrasonic data acquisition system. We use a low frequency probe (KGK, 1K14I/6I-F20) whose center frequency is 1 MHz. This probe is a doughnut-type probe that means to be arranged (a transmit probe and a receive probe) in concentric circle shape. In this experiment, the outside probe transmits ultrasonic waves, and the inside probe receives it. The ultrasonic pulser receiver (New Sensor Inc., NSI-PR2000L) transmits and receives ultrasonic waves via this probe. The oscilloscope (Yokogawa Electric Corp., DL1720) obtains A-scope waves that are displayed as amplitude value vs. propagation time. By moving the probe using a scanner, A-scope waves at several lateral and longitudinal locations are obtained. These waves convert into 3D ultrasonic data (shown in Figure 2). The scanner and the oscilloscope are handled using a personal computer. The sampling interval of data is 10 ns. In our experiment, the ultrasonic data is obtained in a thermostat water bath (Thomas Kagaku Co. Ltd., T-22L) that keeps the target at a fixed temperature of 20 degrees Celsius.

2.2 Characteristics used in our method

We focus on four characteristics (i.e. *Amplitude*, *Quadrature*, *Frequency*, and *Distance* between bone surface and bottom) with respect to the ultrasonic wave in our method.

First, *Amplitude* indicates ultrasonic wave power. In general, ultrasonic wave oscillates between a positive value and a negative value. Since, we need to deal with ultrasonic wave power, we do rectifying ultrasonic waves and smoothing them.

Second, *Quadrature* indicates ultrasonic wave spectrum for a frequency. When $y(t) = A\sin(\omega t + \theta)$ is given as a wave, *Quadrature* is calculated by following equation. The sine component of the wave S is calculated by Equation (6).

$$\begin{aligned} S &= \int_0^T y(t)\sin(\omega t)dt \\ &= \int_0^T A\sin(\omega t+\theta)\sin(\omega t)dt \\ &= A\int_0^T \{\sin(\omega t)\cos\theta + \cos(\omega t)\sin\theta\}\sin(\omega t)dt \\ &= A\cos\theta\int_0^T \sin^2(\omega t)dt + A\sin\theta\int_0^T \sin(\omega t)\cos(\omega t)dt \\ &= \frac{A}{2}\cos\theta \end{aligned} \tag{6}$$

The cosine component of the wave C is calculated by Equation (7).

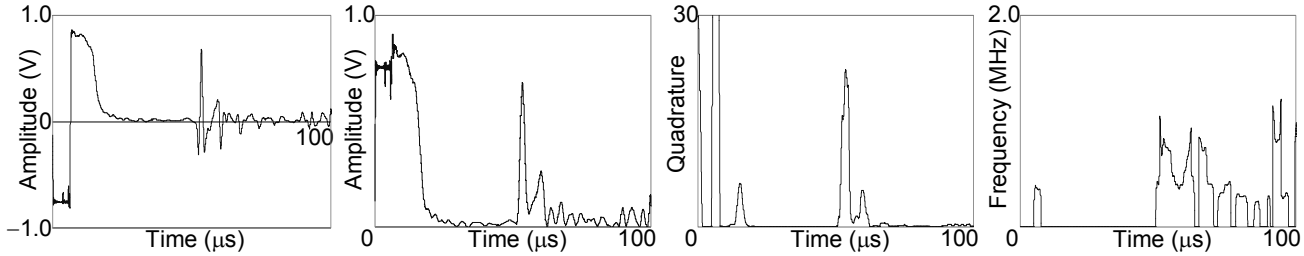

(a) Raw wave **(b) *Amplitude*** **(c) *Quadrature*** **(d) *Frequency***

Figure 3. Characteristics of ultrasonic wave.

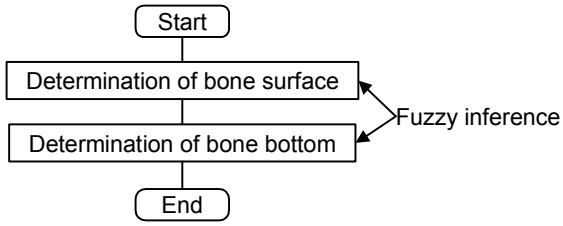

Figure 4. Procedure of our method.

$$C = \int_0^T y(t)\cos(\omega t)dt = \frac{A}{2}\sin\theta \tag{7}$$

Consequently, *Quadrature* is calculated by Equation (8).

$$A = 4(S^2 + C^2) \tag{8}$$

Third, generally, the ultrasonic wave has fixed frequency range. The fixed frequency is calculated from spectrum of the echo. Peak spectrum indicates the highest power for a frequency. In this paper, frequency with the highest peak magnitude is called by *Frequency*.

Finally, all materials have distance between surface and bottom. The ultrasonic wave is reflected from surface and bottom of the material. *Distance* is calculated from both acoustic velocity in the material and time lag between surface and bottom echoes.

Example of raw wave data is shown in Figure 3(a). These *Amplitude*, *Quadrature*, and *Frequency* are shown in Figures 3(b), (c), and (d), respectively.

3. Bone shape visualization

3.1 Bone shape visualization method

We employ fuzzy logic technique to determine bone surface and bottom. Fuzzy logic proposed by Zadeh facilitates us to handle uncertain and imprecise information. Our method employs fuzzy knowledge derived from characteristics of echoes. Figure 4 shows the procedure of this method. This method consists of two stages. First stage determines bone surface from the degrees of the surface echo at each measured point. Second stage determines bone bottom from degrees of the bottom echo at the each point. On the basis of determined bone surface and bottom, the 3D bone shape is visualized. The detail of each process is described in the following section.

3.2 Bone surface determination

First, bone surface is determined. Bone has high acoustic impedance compared with other region of body. The echo from the bone is higher amplitude value than other echoes, i.e. higher amplitude value is the echo from the bone. Moreover, because no region of body has high attenuation except for bone, peak frequency of the echo from the bone is close to center frequency of the probe. From these facts, we can obtain three knowledge as follows,

- **Knowledge 1:** Higher amplitude implies the higher degree of bone surface,
- **Knowledge 2:** Higher quadrature implies the higher degree of bone surface, and
- **Knowledge 3:** The peak frequency of bone surface is close to center frequency of the probe.

The following fuzzy if-then rules are derived from these knowledge,

- **Rule 1:** IF *Amplitude* is high, THEN degree of bone surface is *High*,
- **Rule 2:** IF *Quadrature* is high, THEN degree of bone surface is *High*, and
- **Rule 3:** IF *Frequency* is close to center frequency of the probe, THEN degree of bone surface is *High*.

These knowledge can be usually translated to a fuzzy inference mechanism by min-max-center-of-gravity method. However, in this case, simple fuzzy calculation using membership functions is enough to manipulate it. The membership functions are shown in Figure 5, where Th_a and Th_q, are thresholds of *Amplitude* and *Quadrature*, respectively. They are determined by target region,

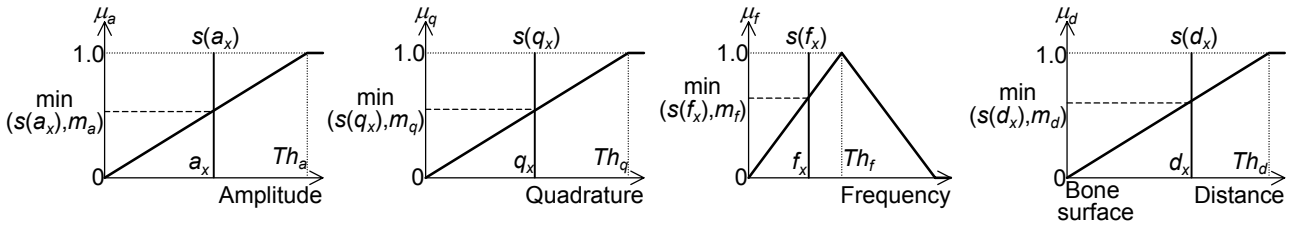

(a) *Amplitude* **(b) *Quadrature*** **(c) *Frequency*** **(d) *Distance***

Figure 5. Membership functions.

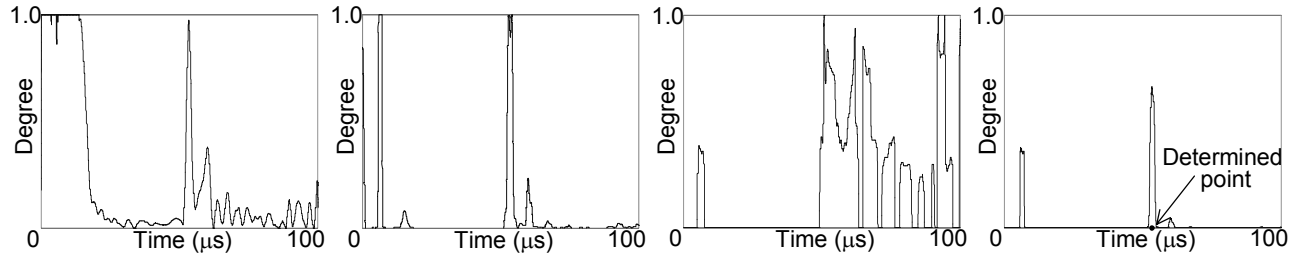

(a) *Amplitude* **(b) *Quadrature*** **(c) *Frequency*** **(d) Total**

Figure 6. Fuzzy degrees of surface.

ultrasonic wave power, and so on. Th_p is a threshold of *Frequency*, which is determined by center frequency of the probe. The total degree $\mu_s(x)$ of a point x (= a_x, q_x, f_x) is calculated by arithmetic product of three degrees as follows,

$$\mu_s(x) = \min\left(s(a_x), \mu_a\right) \times \min\left(s(q_x), \mu_q\right) \times \min\left(s(f_x), \mu_f\right) \quad (9)$$

where $s(a)$ is a singleton function: $s(a) = 1$ if $x = a$; $s(a) = 0$ otherwise. The $\mu_s(x)$ expresses the fuzzy membership degree of bone surface The point with the highest degree is determined as bone surface.

[Example 1] Bone Surface Determination: Consider the raw wave data in Figure 3(a). Three fuzzy degrees, *Amplitude*, *Quadrature*, and *Frequency* are calculated and are shown in Figures 6(a), (b), and (c), respectively. Here, in *Quadrature* and *Frequency* parameter, we use center frequency of the probe for ω and Th_f. In *Amplitude* and *Quadrature* parameter, Th_a and Th_q are determined the probe characteristics. From these three degrees, the total degree of bone surface $\mu_s(x)$ is calculated by Equation (6). This result is shown in Figure 6(d).

[End of example]

3.3 Bone bottom determination

In case of heterogeneous materials such as bone, the ultrasonic wave is almost attenuated in regard of amplitude and frequency. The echo from bone bottom is low amplitude and low frequency in comparison with the echo from bone surface. A bone has almost fixed distance between bone surface and bottom at several regions. From these facts, we can obtain knowledge 4,

Knowledge 4: Bone bottom is not close to bone surface.

The following fuzzy if-then rules are derived from this knowledge,

Rule 4: IF *Distance* between bone surface and bottom is not small, THEN degree of bone bottom is *High*.

In the similar way in bone surface determination, the membership functions are shown in Figure 5, where Th_d is a threshold of *Distance*. Rule 4 plays a role to divide the region into bone surface and bone bottom regions. Therefore, Th_d satisfies $\mu_t = 0$ before the bone surface point determined. The total degree $\mu_b(x)$ of a point x (= a_x, q_x, f_x, d_x) is calculated by arithmetic product of four degrees.

$$\mu_b(x) = \min\left(s(a_x), \mu_a\right) \times \min\left(s(q_x), \mu_q\right) \times \min\left(s(f_x), \mu_f\right) \times \min\left(s(d_x), \mu_d\right) \quad (10)$$

The $\mu_b(x)$ expresses the fuzzy membership degree of bone bottom. The point with the highest degree is determined as the bone bottom.

[Example 2] Bone Bottom Determination: Consider the raw wave data in Figure 3. Four fuzzy degrees, *Amplitude*, *Quadrature*, *Frequency* and *Distance* are calculated shown in Figures 6(a), 7(a), (b), and (c),

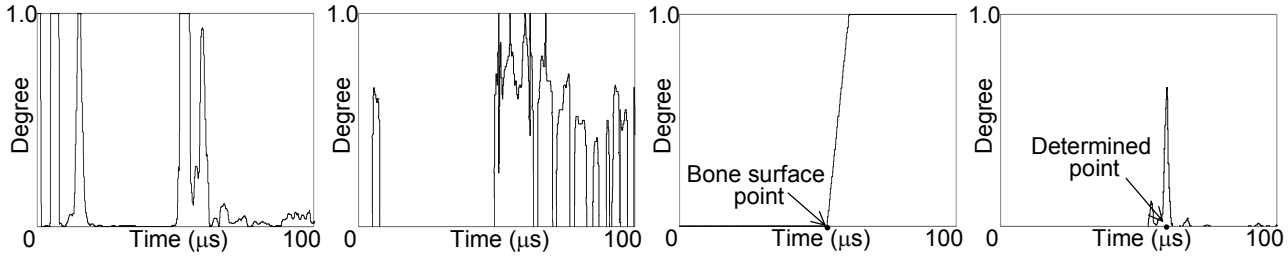

(a) *Quadrature* **(b) *Frequency*** **(c) *Distance*** **(d) Total**

Figure 7. Fuzzy degrees of bottom.

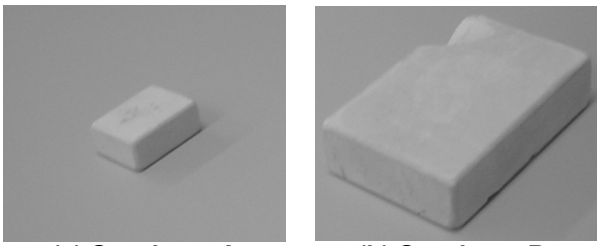

(a) Specimen A **(b) Specimen B.**

Figure 8. Bone specimens.

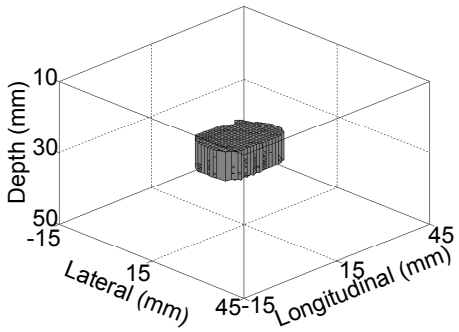

(a) Specimen A

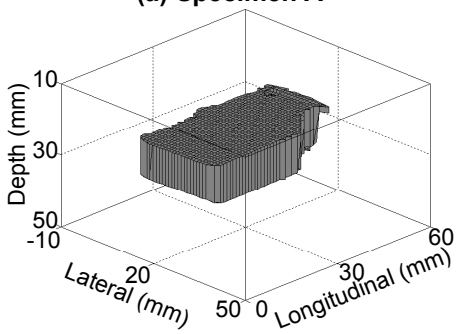

(b) Specimen B

Figure 9. 3D images of our results.

respectively. Here, in *Amplitude* and *Quadrature* parameter, we use thresholds of Example 1. In *Quadrature* and *Frequency* parameter, we use lower frequency compared with ω and Th_f of Example 1. Th_d is determined as the surface point calculated in Example 1.

From these four degrees, the total degree of bone bottom $\mu_b(x)$ is calculated by Equation (10). This result is shown in Figure 7(d).

[End of Example]

4. Results

We prepared two specimens (the artificial bone made by hydroxyapatite) shown in Figure 8. These specimens are cuboid shape: Specimen A has 8.20 mm of thickness, 15.20 mm of lateral length, and 20.15 mm of longitudinal length. Specimen B has 12.30 mm of thickness, 30.25 mm of lateral length, and 45.25 mm of longitudinal length. Here, we set that acoustic velocities in water and an artificial bone are 1500 m/s and 3300 m/s, respectively. The value 3300 m/s can be known experimentally. We applied our method to these specimens. These 3D images are shown in Figure 9. Because specimens are cuboid shape, the determined thickness should be of same in several lateral and longitudinal locations. Figure 10 visualized the overlapped image (lateral view) of 3D shapes by our method and real shapes. The dotted line represents the real shape. In this method, the lateral error is higher than the depth error because lateral resolution is coarser than depth resolution. We compare the real bone shape with our shape. The result is tabulated in Table 1. In it, the mean ± SD (standard deviation) for thickness of the bone at each lateral and longitudinal location is shown. The mean ± SD is shown for the error (= |real value – our method|). Our method provides that the mean error of bone thickness was less than 1 mm in both cases. The small specimen A (the mean error of thickness: 0.27 mm) was determined more precisely than big specimen B (0.67 mm).

5. Conclusions

This paper has proposed a sonography system for visualizing 3D bone shape using ultrasonic wave. Our method has visualized 3D bone shape aided by fuzzy

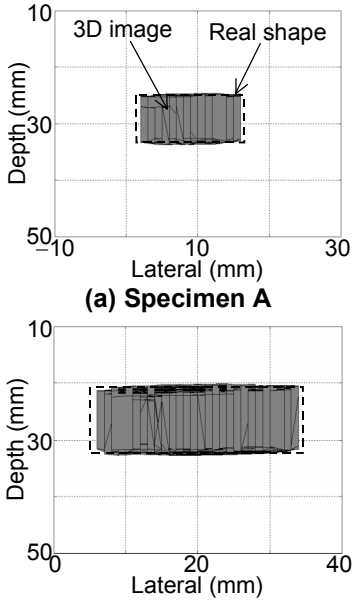

Figure 10. Overlapped image of our method shape and real shape.

Table 1. Comparison of thickness between our method and real value

	(a) Specimen A	(b) Specimen B
Our method (Mean ± SD)	8.30 ± 0.31	11.63 ± 0.23
Real value	8.20	12.30
Error (Mean ± SD)	0.27 ± 0.19	0.67 ± 0.22

(unit: mm)

logic from ultrasonic data acquired by pulse-echo method. Bone surface and bottom were correctly identified from knowledge of surface and bottom echo of bone based on fuzzy logic. As the result of applying our method to two artificial bones, the error of thickness between determined value and real value was less than 1 mm in both cases. We cannot compare our method with other method because there is no works to provide 3D bone shape using ultrasonic wave. It remains as future works to improve visualizing accuracy by adding new knowledge and to apply our method to human bone.

Acknowledgement

This work was supported in part by and the Ministry of Education, Culture, Sports, Science and Technology, Grant-in-Aid for Scientific Research (B) (KAKENHI 14370284).

References

[1] T. Kimura, K. Nagamune, S. Kobashi, K. Kondo, Y. Hata, and K. Taniguchi, "A Fuzzy Inference System for Identifying Tissue Elasticity Using Ultrasound," *Journal of Advanced Computational Intelligence and Intelligent Informatics*, 7(1): 31-39, 2003.

[2] Y. M. Kadah, A. A. Farag, J. M. Zurada, A. M. Badawi, and A. M. Youssef, "Classification Algorithms for Quantitative Tissue Characterization of Diffuse Liver Disease from Ultrasound Images," *IEEE Trans. Med. Imag.*, 15(4): 466-477, 1996.

[3] T. Shimizu, K. Nagamune, S. Kobashi, K. Kondo, Y. Hata, Y. T. Kitamura, and T. Yanagida, "An Automated Ultrasound Discrimination System of Tissue under an Obstacle by Fuzzy Reasoning," *Joint 1st International Conference on Soft Computing and Intelligent Systems*, (CD-ROM), 2002.

[4] K. Nagamune, K. Taniguchi, S. Kobashi, and Y. Hata, "Ultrasonic Nondestructive Evaluation for Embedded Objects in Concrete Aided by Fuzzy Logic," *IEICE Transactions on Information & Systems*, E86-D(1): 79-88, 2003.

[5] P. Laugier, G. Berger, P. Giat, P. Bonninfayet, and M. Lavaljeantet, "Ultrasound Attenuation Imaging in the Os Calcis: An Improved Method," *Ultrasonic Imaging*, 16(2): 65-76, 1994.

[6] Y. Minakuchi, K. Tachi, and T. Ide, "Ultrasonic Measurement of Bone and Bone Marrow Thickness in Femur Covered with Flesh by Inserting a Hip Prosthesis Stem," *JSME International Journal A*, 38(4): 494-499, 1995.

[7] L.A. Zadeh, *Fuzzy Sets and Applications*, John Wiley and sons, New York, 1987.

[8] A. Kandel, Fuzzy Expert System, Boca Raton, F1: CRC, 1992.

[9] Y. Hata, S. Kobashi, S. Hirano, H. Kitagaki, and E. Mori, "Automated Segmentation of Human Brain MR Images Aided by Fuzzy Information Granulation and Fuzzy Inference," *IEEE Trans. Syst. Man Cybern. C*, 30(3): 381-395, 2000.

[10] Y. A. Tolias and S. M. Panas, "Image Segmentation by a fuzzy clustering algorithm adaptive spatially Constrained Membership Functions," *IEEE Trans. Syst. Man Cybern. A*, 28(3): 359-369, 1998.

Segmentation of Cerebral Lobes in 3.0 T IR-FSPGR MR Images Using Fuzzy Inference

Yuji Fujiki, Syoji Kobashi[1], Mieko Matsui[2], Noriko Inoue[2], Katsuya Kondo[1], Yutaka Hata[1], and Tohru Sawada[2]

[1]Graduate School of Engineering, Himeji Institute of Technology, 2167, Shosha, Himeji, 671-2201, Japan

[2]BF Research Institute, Inc., c/o National Cardiovascular Center, 5-7-1, Fujishirodai, Suita, Osaka 565-0873, Japan

fujiki@comp.eng.himeji-tech.ac.jp

Abstract

This paper proposes a computer-aided system for segmenting the frontal, parietal, temporal, and occipital lobes from 3-D human brain 3.0 T IR-FSPGR MR images. Because there is no conventional definition about the cerebral lobes inside the cerebrum, the first work of this research is to define the cerebral lobes using anatomical landmarks, which are the central sulcus, Sylvian fissure, parieto-occipital sulcus, and anterior and posterior commissures. The proposed system finds the boundary by using a fuzzy rule-based active contour model with respect to the anatomical landmarks. For investigating the ability of the reproducibility of the proposed system, MR images of three healthy subjects were analyzed by three beginners and one expert using the proposed system. Each operator segmented ten times per one serial dataset for each subject. Experimental results showed that the system segmented the cerebral lobes with high reproducibility for any subjects and any users.

1. Introduction

Diffuse brain atrophy is observed across the whole cerebrum as the progress of dementia such as the Alzheimer's disease (AD) and the frontotemporal dementia (FTD), but the atrophy doesn't occur at the same rate across the cerebrum [1][2]. The medial temporal and parietal lobes, for example, atrophy mainly in early stage of AD. In FTD, atrophy is particularly severe around the frontal lobe and the temporal tip. To quantitatively validate the difference of the rate of atrophy across the cerebrum, we should measure the volume and surface area of each cerebral lobe.

The cerebrum is composed of the frontal, parietal, temporal, and occipital lobes. Generally, the cerebral lobes are classified on the cerebral cortex (e.g., [3]). For example, the frontal lobe is surrounded by the Sylvian fissure and the central sulcus. However, we cannot measure the volume and surface area according to the conventional definition of the cerebral lobes because the boundary inside the cerebrum is not defined.

A few approaches to define the cerebral lobes inside the cerebrum have been discussed. Zeng *et al.* defined the cerebral lobes inside the cerebrum [4]. In this definition, the boundary between the parieto-temporal and the occipital lobes is inadequate, because the boundary varies with the subject. In addition, because these definitions were given to manually measure the volume of the cerebral lobes, they are still not enough for designing a computer-aided segmentation method. We also showed a definition of the frontal lobe [5]. However, the other cerebral lobes, which are the parietal lobe, temporal lobe, and occipital lobe, are not discussed.

There are two approaches for segmenting cerebral lobes using three-dimensional (3-D) volumetric data. One is a manual delineation and the other is an automated segmentation. Manual delineation has low reproducibility due to the lack of rules for segmenting lobes, especially inside the cerebrum. Because it is time-consuming and needs much effort, it is impossible to analyze the large numbers of subjects. In contrast, although automated segmentation can analyze the large numbers of subjects with few operators' effort, there are a few studies on segmentation of cerebral lobes. Ref. [6] and [7] showed a method using a statistical parametric mapping (SPM) software. SPM is the commonly used software for analysis of the brain function [8]. They prepare some MRI templates that are labeled manually into four cerebral lobes. The MRI templates are transformed to the subject's brain using a normalization process of SPM. The cerebrums of the subject are segmented into each lobe using the transformed MRI template. Performance of this

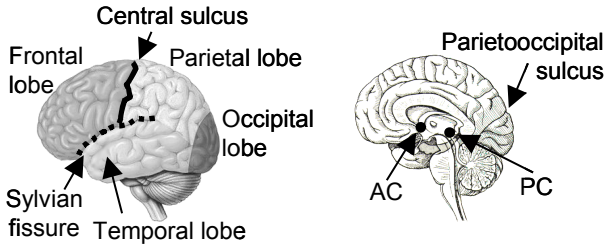

(a) Cerebral surface. (b) Interior cerebrum.
Figure 1. Anatomical atlas of the cerebrum.

method depends on the accuracy of normalization by SPM, which often causes estimation errors. We have proposed a method using a fuzzy rule-based active contour model (ACM) and user-given anatomical landmarks [5]. The method could segment the frontal lobe with high reproducibility (variability of the frontal lobe's volume among ten trials for a given dataset is within 0.95 %.). However, the method was not applied to segment the parietal lobe, temporal lobe and the occipital lobe.

In this paper, we propose a computer-aided segmentation system of the cerebral lobes in 3.0 T inversion recovery fast spoiled GRASS (IR-FSPGR) MR images using fuzzy rule-based ACM. Our system has original landmarks, which are the central sulcus, Sylvian fissure, parieto-occipital sulcus, anterior commissure (AC) and posterior commissure (PC). For investigating the ability of the reproducibility of the proposed system, MR images of three healthy subjects were analyzed by one expert and three beginners using the proposed system.

2. Materials

Two healthy female subjects (Subject 1, and 2, ages 40.5±7.8 years old, mean ± SD) and one healthy male subject (Subject 3, 42 years old) were recruited. They all gave informed consent according to the guidelines approved by the local Ethical Committee at the BF Research Institute, Inc.

MRI studies were performed on a 3.0 T Signa LX VH/i Scanner (GE Medical Systems, Milwaukee, WI) with a circularly polarized head coil as both transmitter and receiver. Images were acquired by a coronal 3-D IR-FSPGR with a repetition time (TR) of 10.7 ms, an actual echo time (TE) of 1.9 ms, and an inversion time (TI) of 600 ms. The field of view (FOV) was 220 mm square. The matrix was 256 by 256. Each volume dataset consisted of 124 separated slices whose thickness was 1.5 mm with no gap. Voxel size was $0.86\times0.86\times1.5$ mm^3.

We constructed the MR volume of the brain, which consisted of 256×256×124 voxels. In our system, the MR images appeared and were treated as intensity images. The intensity for all voxels of all intracranial structures ranged between 0 and 4095. The acquired datasets were classified into the left and right cerebral hemispheres, cerebellum, and brain stem by the automated human brain MR image segmentation algorithm [10].

3. Definition of the cerebral lobes

The cerebrum consists of the frontal lobe, parietal lobe, temporal lobe, and occipital lobe illustrated in Fig. 1 (a) [3]. Generally, the cerebral lobes are classified on the cerebral cortex. The frontal lobe is segmented by the central sulcus and Sylvian fissure. The parietal and temporal lobes are classified by Sylvian fissure. The central sulcus is the boundary between the frontal and parietal lobes, and the Sylvian fissure is the boundary between the fronto-parietal and temporal lobes. However, this classification can be achieved only on the cerebral cortex. That is, there is no index to classify the cerebral lobes inside the cerebrum. In this paper, we define the cerebral lobes using the anatomical landmarks not only on the cerebral surface but also inside the cerebrum.

The frontal lobe is defined to be a region whose section is formed by the union of all line segments composed of the middle point of the AC-PC line and the points on the closed curve derived from the central sulcus and the Sylvian fissure [5]. AC and PC are well-known anatomical points denoted in Fig. 1 (b).

In this paper, the occipital lobe is defined to be a posterior region segmented by a section, which is formed by extending the parieto-occipital sulcus so that the sulcus crosses the longitudinal fissure of cerebrum vertically.

After segmenting the frontal and the occipital lobes from the cerebrum, the remaining region is divided into the parietal lobe and the temporal lobe by using the Sylvian fissure. The boundary is determined by projecting the Sylvian fissure to the longitudinal fissure of cerebrum vertically. Because the posterior tail of the Sylvian fissure is often unclear, the fissure should be extended so that it reaches the parieto-occipital sulcus.

4. Segmentation of the cerebral lobes

Segmenting the cerebral lobes is performed with the following four steps:

1) Set the anatomical landmarks.
2) Segment the frontal lobe [5].
3) Segment the occipital lobe.
4) Segment the parietal and temporal lobes.

Because the proposed method segments the cerebral lobes according to the anatomical landmarks, which are the central sulcus, the Sylvian fissure, parieto-occipital sulcus, AC and PC, users manually give these landmarks at the first step. To make users easily set the landmarks we have developed a graphical user interface (GUI). The second step segments the frontal lobe by means of the

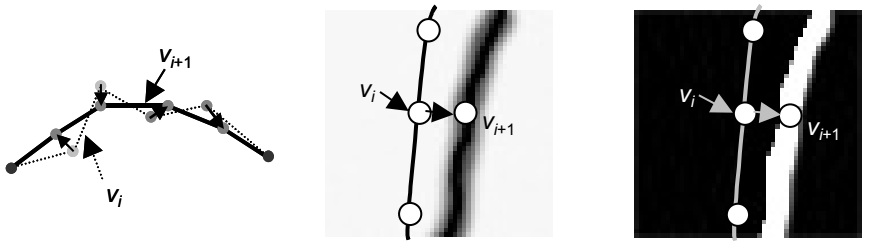

(a) Feature value f_{int}. (b) Feature value f_{line}. (c) Feature value f_{edge}.

Figure 2. Feature values. In (b) and (c), the smaller values of intensity and gradient are appeared as the black.

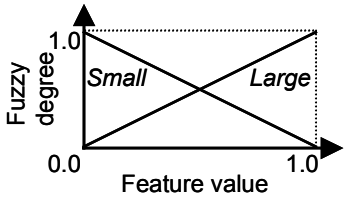

Figure 3. Membership functions.

algorithm described in Ref. [5]. The algorithm uses the AC, PC, central sulcus, and Sylvian fissure as the landmarks for segmentation. Third step generates a section using the parieto-occipital sulcus, and then segments the occipital lobe at the section. Finally, we remove the segmented the frontal and occipital lobes from the cerebrum, and decompose the remaining region into the parietal and temporal lobes according the Sylvian fissure. In the following, we describe the details of the developed GUI, and the algorithms for segmenting the occipital, parietal and temporal lobes.

4.1 Graphical user interface to set the landmarks

Our system runs according to the anatomical landmarks given by users. This enables it to process any data like postoperative/atrophied brains. In this work, we develop a GUI so that users easily set the anatomical landmarks. The GUI consists of two interfaces using a shaded surface display (SSD) and a multi-planar reconstruction (MPR). Using the SSD interface, users can set the 3-D sulcus by drawing lines on the 2-D SSD images. Although sulci are structurally complex, there are some proper angles where users easily recognize them on the cerebral surface. Because these angles vary by user and by subject, the interface should be configured so that the user can select proper angles to recognize the sulci on the SSD image. Using this interface, the Sylvian fissure and the central sulcus are given. The MPR interface consists of three sectional images, which are a coronal, a sagittal, and an axial images. Using this MPR interface, the user can set any point on 3-D space. The AC, PC and the parieto-occipital sulcus are given by using this interface.

4.2 Segmentation of the occipital lobe

We segment the occipital lobe according to the parieto-occipital sulcus given by the user. Because the user-given curves are not set at the deepest point of the parieto-occipital sulcus, our system drops the curves into the deepest point using the fuzzy rule-based ACM (the details are described in the following paragraph). Then the detected parieto-occipital sulcus is extrapolated so that the sulcus crosses over the whole cerebrum. The boundary surface of the occipital lobe inside the cerebrum is determined by projecting the extended parieto-occipital sulcus to the longitudinal fissure of cerebrum vertically.

The parieto-occipital sulcus is detected by fitting the user-given curve into the deepest point using the fuzzy rule-based ACM. The fuzzy rule-based ACM, which is proposed in Ref. [5], is a fuzzy logic based extension of the conventional ACM [9]. The principal advantage of the fuzzy rule-based ACM is that it can easily implement physicians' anatomical knowledge with fuzzy if-then rules.

In the fuzzy rule-based ACM, a fitting curve is given by $v(t) = (z(t), y(t))\ (1 \le t \le n)$, where n is the number of nodes composing the curve. At first, initial nodes of $v(t)$ are determined by selecting the points at the 2 pixel interval. Then the nodes of the curve are moved so that the curve detects the parieto-occipital sulcus. We then evaluate whether the curve detects the parieto-occipital sulcus or not by estimating a fuzzy degree belonging to the parieto-occipital sulcus. The fuzzy degree is estimated by a mean of fuzzy degrees of every node, and it is given by

$$\mu = \frac{1}{n}\sum_{t=1}^{n}\mu_t \ , \tag{1}$$

where μ and μ_t are fuzzy degrees belonging to the parieto-occipital sulcus for the curve of interest and for node t, respectively. The fuzzy degree for the node of interest, μ_t, is estimated by using knowledge about the parieto-occipital sulcus:

(1) The parieto-occipital sulcus runs smoothly.
(2) The parieto-occipital sulcus has low intensity.
(3) The parieto-occipital sulcus has high gradient of intensity.

To evaluate a node of interest with respect to this knowledge, we define three features of the node, f_{int}, f_{line} and f_{edge}. The first feature, f_{int}, estimates the smoothness of the curve at the node of interest, and is given by:

$$f_{int} = \left(\left|\frac{dv(t)}{dt}\right| + \left|\frac{d^2v(t)}{dt^2}\right|\right) \Big/ f_{int\_max} \ . \tag{2}$$

This feature gives the lower value when the node v_i moves to node v_{i+1} as shown in Fig. 2 (a). The second

feature, f_{line}, evaluates the intensity at the node, and is given by:

$$f_{line} = I(x,y) \big/ f_{line\_max} \ . \quad (3)$$

This feature takes the lower value when the node moves to a voxel with the lower intensity as shown in Fig. 2 (b). The third feature, f_{edge}, estimates the strength of edge, and is given by:

$$f_{edge} = \left|\nabla I(x,y)\right| \big/ f_{edge\_max} \ , \quad (4)$$

where ∇ is a gradient operator. This feature gives the lower value when the node moves to a voxel with the higher gradient of intensity as shown in Fig. 2 (c). In the above definitions, f_{int_max}, f_{line_max} and f_{edge_max} are normalization parameters given by the user. Using these three features, we derive the following two fuzzy IF-THEN rules from the knowledge about the parieto-occipital sulcus:

[Rule 1]
IF (f_{int} is *Small*) AND (f_{line} is *Small*) AND (f_{edge} is *Large*)
THEN μ_t is *Large*.
[Rule 2]
IF (f_{int} is *Large*) AND (f_{line} is *Large*) AND (f_{edge} is *Small*)
THEN μ_t is *Small*.

Small and *Large* are fuzzy languages defined by membership functions shown in Fig. 3. The fuzzy IF-THEN rules are carried out by a MIN-MAX implementation technique. The consequent fuzzy degree, $\hat{\mu}_t$, is the center of gravity of the obtained fuzzy sets. The fuzzy IF-THEN rules are applied to every node, and then the fuzzy degree belonging to the parieto-occipital sulcus of the curve of interest is calculated by Eq. (1) for each node. By iterating with moving nodes so that the fuzzy degree, μ, is maximized, the parieto-occipital sulcus will be detected.

The detected parieto-occipital sulcus is not still enough for segmenting the occipital lobe because the sulcus does not cross over the whole cerebrum. For example, because the superior tail of the sulcus is often unclear, it is impossible to detect the whole sulcus. Therefore, we extrapolate the detected sulcus so that the sulcus crosses over the whole cerebrum.

Using the obtained parieto-occipital sulcus that completely crosses over the cerebrum from the inferior to the superior, we determine the boundary between the occipital lobe and both the parietal and temporal lobes. According to our definition about the occipital sulcus, the boundary is formed by projecting the obtained parieto-occipital sulcus to the longitudinal fissure of cerebrum vertically. To estimate the longitudinal fissure of cerebrum, we first find the contact points of the right and left cerebral hemispheres by raster scan on axial planes (x-z plane). Secondly, the contact points are projected on 2-D plane and a line approximating the contacting points is calculated by using a linear least square method (LSM). Then, the longitudinal fissure of cerebrum is obtained by extending the approximated line for y-direction. Consequently, a section is obtained by projecting the parieto-occipital sulcus to the longitudinal fissure of cerebrum, and then the occipital lobe is segmented at the obtained section.

4.3 Segmentation of the parietal and temporal lobes

The remaining region after removing the frontal lobe and the parietal lobe from the cerebrum is composed of the parietal and temporal lobes. Therefore, the parietal and temporal lobes can be segmented by determining the boundary between them. According to our definition, the boundary is determined by projecting the Sylvian fissure to the longitudinal fissure of cerebrum.

However, because the Sylvian fissure does not reach the parieto-occipital sulcus in almost of cases, we extrapolate the Sylvian fissure so that the sulcus crosses the cerebrum from the anterior to the parieto-occipital sulcus. The extrapolation is done for each cerebral hemisphere separately, and the details are described below. At first, the Sylvian fissure detected by fuzzy rule-based ACM is projected on a 2-D plane. Second, the Sylvian fissure is extrapolated by means of the LSM using a quadratic function on the 2-D projection plane. Third, the extrapolated Sylvian fissure is projected on the 3-D cerebral surface. Finally, we drop the projected Sylvian fissure on the cerebral surface into the deepest point of the sulci by the fuzzy rule-based ACM. The fuzzy IF-THEN rules and conditions are the same as those used to detect the parieto-occipital sulcus.

The boundary between the parietal and temporal lobes are found by projecting the extrapolated Sylvian fissure to the longitudinal fissure of cerebrum, and the parietal and temporal lobes are segmented at the obtained boundary.

5. Experimental results and discussion

MR images acquired from Subject 1 were analyzed by the proposed system for demonstrating the ability of segmenting the cerebral lobes. A screenshot of the configured GUI system is shown in Fig. 4. This figure shows a screenshot of the SSD interface. Using this GUI system, a user gave the central sulcus and Sylvian fissure. Then, the user gave the AC and PC points, and the parieto-occipital sulcus using the MPR interface. For running the fuzzy rule-based ACM, three parameters, which are f_{int_max}, f_{line_max} and f_{edge_max}, were set at 20, 100 and 50, respectively. The same parameters were used across all of our experiments. The computation time for segmentation (not including pre-processing, i.e., segmen-

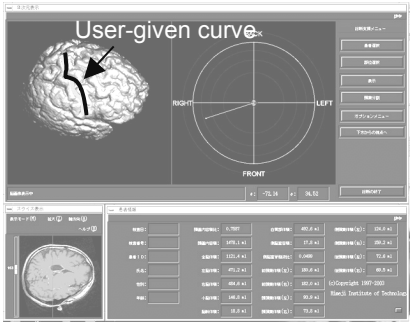

Figure 4. Configured system.

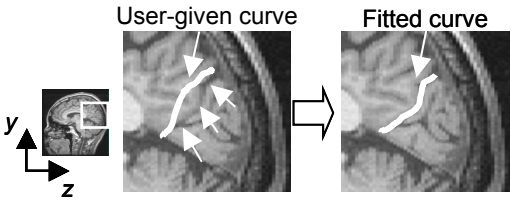

Figure 5. User-given curve is matched to the parieto-occipital sulcus by fuzzy rule-based ACM.

tation of the brain, and decomposing the brain portions) was less than 15 s running on a workstation (Silicon Graphics Fuel™, R14000, 500MHz, 1024MB, SGI). Fig. 5 shows a part of the cerebrum. In this figure, a user-given curve and the fitted curve are described in white solid lines. The user-give curve was fitted at the parieto-occipital sulcus. Coronal and sagittal images of the labeled volume data are shown in Fig. 6. The cerebral lobes were correctly segmented at the proper sulci. In this figure, we can confirm the Sylvian fissure (A) between the parietal and the temporal lobes, and parieto-occipital sulcus (B) between the occipital and the temporal lobes. 3-D SSD images of the segmented cerebral lobes are shown in Fig. 8. These images are visually appropriate compared with Fig. 1 (a). As shown in Fig. 7, the boundaries between the parietal and temporal lobes of the right and left cerebral hemispheres are not same shape because the shape of the Sylvian fissure of the right and left cerebral hemispheres are not same.

We weighed the variability of volumes of cerebral lobes when the system was operated by an expert and three beginners. The expert got well used to our system and could easily detect the central sulcus and Sylvian fissure on the SSD interface, and the parieto-occipital sulcus and the AC and PC points on the MPR interface. Beginners were collected who were not familiar with our system and the location of the anatomical landmarks. Therefore, the beginners were trained on how to use the system about ten minutes, and were instructed on the anatomical landmarks before testing our system. Both of the expert and the three beginners segmented individually ten times per one dataset of the subject.

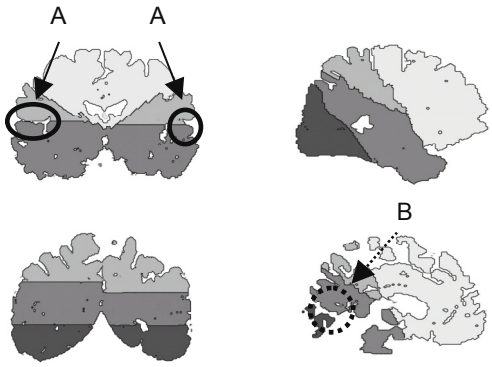

(a) Coronal images. (b) Sagittal images.

Figure 6. The result of segmentation (2-D). (A): the Sylvian fissure, and (B): the parieto-occipital sulcus.

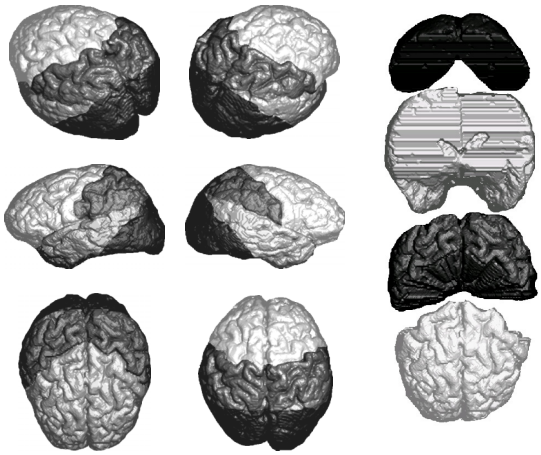

Figure 7. Segmentation results. The cerebrum is segmented into the frontal lobe (light gray), parietal lobe (dark gray), temporal lobe (gray), and occipital lobe (dim gray).

The variabilities of the volumes within a user and across inter users were investigated. Fig. 8 shows mean and SD of volume (block graph) of the cerebral lobes that were segmented by four users. The graphs showed that for any subjects and for all cerebral lobes, (1) the variabilities of the volumes within a user were small, and (2) those across the users relatively were small, however, is larger than those within a user. These results confirmed that by using the proposed system we could segment the cerebral lobes with high reproducibility even if the user is beginner.

6. Conclusion

We have proposed a computer-aided system for segmenting the cerebral lobes from 3.0 Tesla IR-FSPGR MR images. To design the system, we first defined the cerebral lobes geometry using the anatomical landmarks. To our knowledge, this will be the first approach to define the cerebral lobes inside the cerebrum.

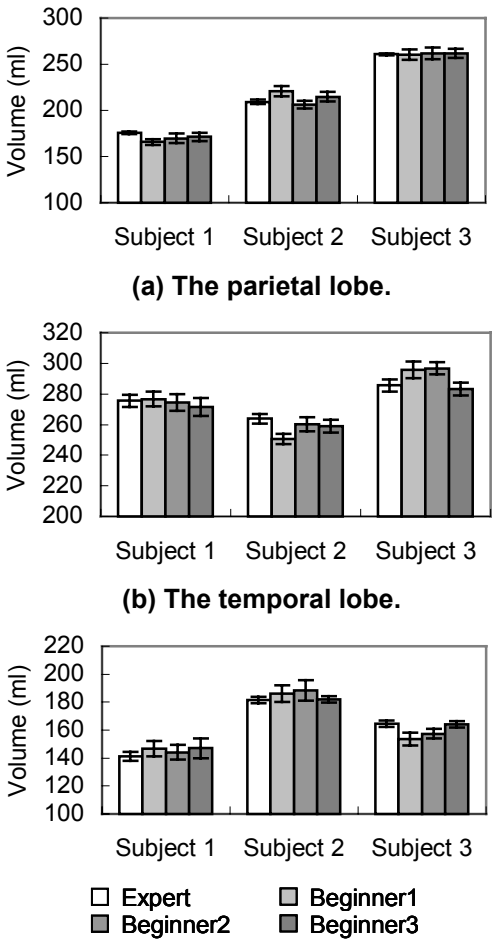

Figure 9. Variability of the volumes within a user and among the users.

The segmentation of the cerebral lobes was performed with the fuzzy rule-based ACM according to the anatomical landmarks, which are given by a user on the SSD and MPR interfaces. The algorithm drops the user-given sulci into the deepest point. This leads the system to produce stable segmentation results. The ability of the reproducibility of the proposed system was evaluated by applying the system to three healthy subjects in which four users operated. The experimental results confirmed that our system could segment the cerebral lobes with high reproducibility even if the user is a beginner, and even if the user differs by each experiment.

There are a few differences between the boundaries segmented by the proposed system and the conventional wisdom at the posterior cerebrum. In the future, we will apply another definition of the occipital lobe so that the system segments the cerebral lobes more stably and more adequately to the conventional wisdom. In addition, a method for automatically detecting the Sylvian fissure and parietooccipital sulcus will be studied.

Acknowledgments

We thank PhD candidates M. Umeda (Dept. of Medical Informatics, Meiji University of Oriental Medicine) and M. Fukunaga (BF Research Institute, Inc. and Dept. of Medical Informatics, Meiji University of Oriental Medicine) for their advice on MRI. We also thank Mr. S. Itoi (BF Research Instituted. Inc.) for his assistance in MR studies. This work was supported in part by Ministry of Education, Culture, Sports, Science and Technology, Grant-in-Aid for Encouragement of Young Scientists, 15700198, 2003, and the BISC Program of UC Berkeley.

References

[1] D. Wang, J. B. Chalk, S. E. Rose, G. Zubicaray, G. Cowin, G. J. Galloway, D. Barnes, D. Spooner, D. M. Doddrell, and J. Semple. MR Image-Based Measurement of Rates of Change in Volumes of Brain Structures. Part II: Application to a Study of Alzheimer's Disease and Normal Aging. *Magn. Reson. Imaging*, 20:41-48, January 2002.

[2] R. I. Scahill, J. M. Schott, J. M. Stevens, J. M. Rossor, and N. C. Fox. Mapping the Evolution of Regional Atrophy in Alzheimer's Disease: Unbiased Analysis of Fluid-Registered Serial MRI. *Proc. Natl. Acad. Sci*, 7:4703-4707, 2002.

[3] H. J. Kretschmann, W. Weinrich. *Klinische Neuroanatomie und Kranielle Bilddiagnostik*. Thieme, 1999.

[4] X. Zeng, L. H. Staib, R. T. Schultz, and J. S. Duncan. Segmentation and Measurement of the Cortex from 3D MR Images Using Coupled Surfaces Propagation. *IEEE Trans. Med. Imag.*, 18(10):100-111, October 1999.

[5] Y. Fujiki, S. Kobashi, M. Matsui, N. Inoue, K. Kondo, Y. Hata, and T. Sawada. Interactive 3-D Segmentation of the Frontal Lobe in 3.0T IR-FSPGR MR Images Using Fuzzy Rule-Based ACM. *J. of Advanced Computational Intelligence and Intelligent Informatics*, 7(2):189-199, 2003.

[6] S. Kanekiyo, H. Toyama, K. Uemura, K. Ishii, and A. Uchiyama. Development of a Method to Divide Brain Lobes Automatically. *Proc. of 40th Japan Soc. ME & Be*, 39:443, 2001. (In Japanese)

[7] D. L. Collins, N. J. Kabani, and A.C. Evans. Automatic Volume Estimation of Gross Cerebral Structure. *4th Int. Conf. on Functional Mapping of the Human Brain*, June 1998.

[8] K. J. Friston, J. Ashburner, J. B. Poline, C. D. Frith, J. D. Heather, and R. S. J. Frackowiak. Spatial Registration and Normalization of Images. *Human Brain Mapping*, 2:165-189, 1995.

[9] M. Kass, A. Witkin, and D. Terzopoulou. Snakes: Active Contour Models. *Int. J. of Computer Vision*, 1(4):321-331, 1987.

[10] Y. Hata, S. Kobashi, S. Hirano, H. Kitagaki, and E. Mori. Automated Segmentation of Human Brain MR Images Aided by Fuzzy Information Granulation and Fuzzy Inference. *IEEE Trans. Syst., Man, Cybern. C*, 30(3):381-395, August 2000.

An Efficient Method for Kidney Segmentation on Abdominal CT Images

Daw-Tung Lin[1], Chung-Chih Lei[1], and Shiao-Yun Hsiung[2]
1. Department of Computer Science, Chung-Hua University, Hsin Chu, Taiwan
2. Radiology Department, Taichung Veterans General Hospital, Taichung, Taiwan

Abstract

This paper describes an effective method for kidney segmentation on abdominal CT images. This segmentation system is expected to assist the physicians on clinical diagnosis and educational training. The proposed method is partitioned into two processes. First, the ROI is extracted using the statistics of geometric location of kidney on the abdomen area. In addition, the noise is removed by applying the conditional median filter and performing the primary pixel aggregation. In the following stage, the kidney is identified by the proposed operations including adaptive region-growing, efficient filling operation, labeling, and mathematical morphology operation. Furthermore, in order to show different view for physicians, we have implemented a visualization tool to show the renal segmentation contour automatically.

1 Introduction

Image segmentation is one of the most popular topics for computer aided medical image analysis and diagnosis such as segmentation of liver, lung, kidney, and so on. Generally speaking, there are two main reasons for the need of computer aided segmentation: to improve user-guided segmentation [12], and to acquire segmentation prior to visualization or quantification [2]. In the recent years, many computer- aided diagnostic (CAD) systems have been developed to assist physicians to diagnose symptoms in the fields of lung cancer, brain tumor and breast diseases diagnosis. However, there are less literatures and researchers on the kidney segmentation. This is because that understanding the various aspects of kidney by using computer technologies is difficult.

There were three categories methods for kidney segmentation: region-based, knowledge-based and snake-based approaches. Pohle and Toennies[2][3][4] developed a region growing algorithm that learns its homogeneity criterion automatically from characteristics of the region to be segmented. Wang, et. al.[5] proposed a constrained optimization approach in which region information can be computed as extra constraints within the contour energy minimization framework. Kobashi and Shapiro [6] described a knowledge-based procedure for identifying and extracting organs from normal CT imagery. Based on the above consequences, we attempt to combine the advantages of the above-mentioned works and develop a more promising method for kidney segmentation on abdominal CT images, and then exhibit the exploited system for the ease of kidney observation. The rest of this article is organized as following: the pre-processing is illustrated in Section 2, the detailed methodology of kidney segmentation is stated in Section 3, the experimental results and conclusion are mentioned in Sections 4 and 5, respectively.

2 Pre-processing and ROI Extraction

In this section, we will describe the pre-processing approach for the ROIs extraction for left and right kidney. In order to simplify the question of different slice thickness of CT images and machine setting resulted from various hospitals and patients, we start to proceed from the i_{th} slice which is approximately in the middle of the sequence where $i = \lfloor \frac{n}{2} \rfloor$, and n is the total number of slices of one patient case. The middle slice shows the obvious kidney image, and easy to review for each datasets. The spine is one important landmark in our work, which is used to allocate the reference position of kidney. The spine (denoted as "**X**" in Fig. 1) is approximately located at the position

∗ This work was supported in part by the National Science Council, Taiwan, R.O.C. (NSC91-2213-E-216-007). Acknowledgement also due to Dr. Bai-Lu Shih at the Radiology Department, Chungli Li-Shin Hospital, for invaluable discussions and suggestions.

∗ Corresponding author: Daw-Tung Lin, Department of Computer Science and Information Engineering, Chung-Hua University, 30 Tung Shiang, Hsin Chu, Taiwan 30067 (email:dalton@chu.edu.tw).

(0.5 l_1 ,0.56 l_2) where l_1 is the length of horizontal axis and l_2 is the length of vertical axis of the abdominal boundary. The abdominal boundary is obtained by the following algorithm:

For all pixels f(i,j) in the CT image

Do

For each direction (f(i±7, j), f(i,j±3))

if the total number of nonzero pixels on that direction is less than 1

then set f(i, j) = 0

The initial ROI of left kidney is then located by the following rules: 1. the distance between spine and the right boundary of ellipse is 25 pixels; 2. the distance between the upper boundary of ellipse and the border of abdominal boundary is 22 pixels; 3. the distance between the lower boundary of ellipse and the border of abdominal boundary is 25 pixels; 4. the distance between the left boundary of ellipse and the abdominal boundary is 45 pixels. The ROI of right kidney can be determined in the same way. Therefore, the initial ROI ellipse center X_0, Y_0 can be decided. Both of the kidneys usually appear in the range of a specific inclined angle. To obtain more meaningful ROIs, we rotate the preliminary ROIs and represent the new result in Equation (1).

$$\begin{pmatrix} X' \\ Y' \end{pmatrix} = \begin{pmatrix} \cos\theta & -\sin\theta \\ \sin\theta & \cos\theta \end{pmatrix} \begin{pmatrix} X - X_0 \\ Y - Y_0 \end{pmatrix} + \begin{pmatrix} X_0 \\ Y_0 \end{pmatrix} \qquad (1)$$

where (X', Y') denotes the final coordinates of the center of ROI ellipse, (X_0, Y_0) is the coordinate of the center of the initial ROI, θ =60 ^{0}. The relationship between (X', Y') and (*X, Y*) can be obtained by geometric transformation of translation and rotation. Consequently, the ROIs of the left and the right kidney can be found and located as plotted in dotted line in Fig. 1. One of the results of ROI extraction is shown in Fig. 2. This transformation possesses high flexibility for positioning a large variety of objects. The ROIs include two parts which are true kidney region and non-kidney region such as liver, spleen, fat and so on. To eliminate the preliminary noises, we applied the smooth filtering operation as shown

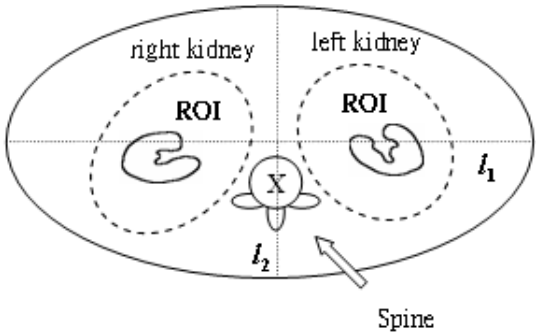

Figure 1: ROIs are plotted in dotted lines.

in Equation 2:

$$\mu_{left\_ROI} = \frac{\sum\sum f_{left\_ROI}(i,j)}{n_{left\_ROI}} \qquad (2)$$

where $f_{left\_ROI}(i,j)$ denotes the intensity of pixel (*i, j*) and n_{left_ROI} shows the number of pixels on the left ROI, μ_{right_ROI} is the filtering operation for the right ROI. It seems trivial and ordinary, but still contributes to facilitate the follow-up process. In addition, the mean values μ_{left_ROI}, μ_{right_ROI} just need to be calculated once for the entire dataset, because the rest of slices remain approximately equal intensity distribution on kidney images for one patient [8].

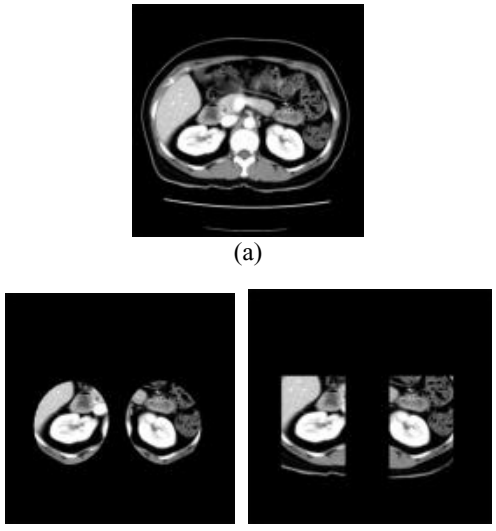

(a)

(b) (c)

Figure 2: (a) Original image, (b) ROIs image extracted by the proposed technique, and (c) ROIs image obtained by Tsagaan[1].

The median filter [11] is particularly effective for the noise pattern consisting of strong spikelike components. The gray level of each pixel is replaced by the median of the gray levels in its neighborhood, instead of using the average. We try to apply median filter of the size of 7*7 in terms of renal size excluding those of pixels with zero. The results of the proposed ROI extraction are shown in Fig. 2(b). We can observe from Fig. 2 that the resultant image after noise removal is more clear then that of the original one (Fig. 2(a)) . The ROIs are more attractive compared to that of Tsagaan's method (Fig. 2(c)).

3 Kidney Segmentation

Now, we would begin to segment the right and left kidney from two extracted ROIs on each slice. We utilized a series of image processing techniques including region growing, labeling, filling and mathematical morphology such as erosion and dilation. In addition, we have modified those techniques to fulfill the segmentation requirement.

3.1 Adaptive Region Growing

There are three problems in the region growing process including initial seeds selection, similarity criterion of growing, and the formulation of termination criterion. To conquer these problems, we proposed the adaptive criteria for region growing by constructing a model of direction (see Fig. 3) in terms of five frequent locations of kidneys within ROIs. In this step, we search the right kidney related to directional sequence that is less different from that of left one. Besides, to enhance the learning effect, we choose an adaptive interval of threshold θ_1 that allows to be updated by each processing iteration or each direction is discontented with gray level criterion. The search operation will not be terminated until uniform mesh is found in all directions, meanwhile the threshold θ_1 will be also updated. Thus, we provide a more formal formulation of this approach.

- Initial seeds: A new initial search point is segmented in terms of renal trend in different slice, as

$$\begin{aligned} x^{'} &= x^{'}_{center} - \rho(a_i - a_0) \\ y^{'} &= y^{'}_{center} - \rho(a_i - a_0) \end{aligned} \quad (3)$$

$$\begin{aligned} x^{''} &= x^{''}_{center} + \rho(a_i - a_0) \\ y^{''} &= y^{''}_{center} - \rho(a_i - a_0) \end{aligned} \quad (4)$$

where ρ is a threshold (ρ=2.2), $x^{'}$, $y^{'}$, and x'', y'' are coordinates of left ROI and right ROI, respectively, ($x^{'}_{center}, y^{'}_{center}$) and ($x^{''}_{center}, y^{''}_{center}$) are the center points for those ROIs, a_i is an index of slice i being processed and a_0 is the index of starting slice in a dataset. Since the kidney is a homogeneous located inside the ROI, we constructed a model of direction where the search path is illustrated by d_4, d_1, d_5, d_3, and then d_2 in turn (shown in Fig. 3). We compute the difference between the maximum and minimum pixel values in a 7*7 mesh along a direction of d_i, if the value is lager than a threshold (20), it would be not suitable as an initial seed (i.e. non-homogeneous area). The search procedure lasts until an appropriate seed is found.

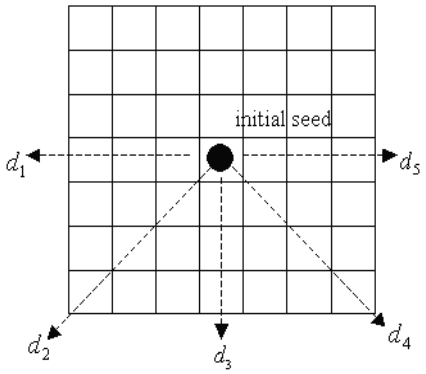

Figure 3: Direction finding for initial seed.

- Kidney growing criterion: Once the initial seed is located, we start to perform the region growing from this seed by the following equation:

$$\left|\Psi(i,j) - \Theta_{local}\right| \le t_0 \quad \forall (i,j) \subseteq R_{ROIs} \quad (5)$$

and

$$\Theta_{local} = (\Re_{\max} + \Re_{\min})/2 \quad (6)$$

where $\Psi(i,j)$ is a pixel which satisfies 8-connected condition for the initial seed, t_0 is a heuristic threshold, $\Re_{\max}$ and $\Re_{\min}$ denote

maximum and minimum of intensity in the mesh, respectively. According to the growing criterion, the growing would be terminated when $\Psi(i,j) - \Theta_{local} > t_0$.

3.2 Region Modification

Once the binary image has been obtained by the adaptive region growing, there are still trivial and irregular objects with concaves scattering in the candidate kidney region. For this, the region modification technique is essential to improve the segmentation accuracy under various conditions such as the contrast media injection time and rate, image intensity variations, and blood flow rate. We implemented the region modification by utilizing a series of image processing skills including: pixels filling, erosion, labeling, and dilation [9]. The details will be presented in this section. To identify those irregular objects, an efficient filling algorithm is proposed which is modified from the point containment technique[10]. Let R_1 and R_2 are two regions in one ROI in the binary images, namely, pixels in R1 are with gray level 0 and pixels in R2 are with gray level 255. Given a transformation represented for the following equation:

$$f^{'}(x,y) = \begin{cases} 1, if\ f(x,y) = 0, \forall (x,y) \in R_1 \\ 0, otherwise \end{cases} \quad (7)$$

where $f^{'}(x,y)$ is an inverse image of the binary image $f(x,y)$. Then we apply the region growing once again by selecting the pixels in the ROIs as the initial seeds. During the process of region growing, all pixels in R1 will be inverted and constituted the final image:

$$H(x,y) = F(x,y) + G(x,y)\ \forall x,y \in R_1, R_2 \quad (8)$$

where $H(x,y)$, $F(x, y)$, and $G(x,y)$ represent the resultant filled image, original binary image, and the image obtained from the second region growing, respectively. However, some problems may be found. For example, the threadlike region would belong to non-kidney. In addition, a bridge between two regions may also occur. We used the conventional erosion technique as the following equation to solve this problem.

$$A \ominus B \cap_{b \in B} (A)_{-b} \quad (9)$$

	1	1	1	
1	1	1	1	1
1	1	1	1	1
1	1	1	1	1
	1	1	1	

Figure 4: The designed structure element *B*.

where A denotes the current binary image, B denotes the structuring element, b denotes the individual elements of B, and $-b$ denotes the inverse of b. The designed structuring element B (Fig. 4) is not as same as the common 3x3 mask. A circle structure element is applied instead. The result of this operation indulges region separation and retains more smooth object boundary. Once the erosion operation has been applied, the region will be separated into two or more sub-regions. It is indeed to apply a labeling approach to size up each sub-regions.

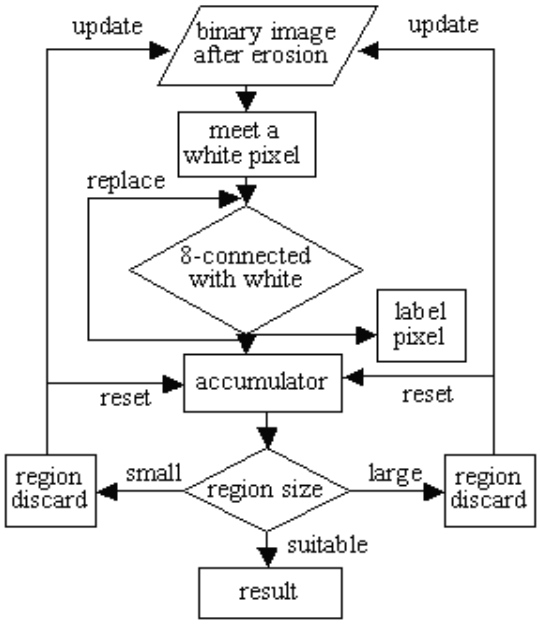

Figure 5: Labeling procedure of our method.

For this, we introduce a fine method to evaluate the region size directly by an accumulation and the recursive process illustrated in Fig. 5. Furthermore, it is necessary to apply the dilation operation to compensate for the above-mentioned erosive region. A formal definition of dilation is presented as below:

$$A \oplus B = \cup_{b \in B} (A)_b \quad (10)$$

where the definition of A, B, and b is same as those of erosion operation. The relationship between erosion and dilation can be understood by comparing their operation. Finally, we will display the segmentation image of kidney by pasting the resulting area of region growing and modification from the original CT images. The main consideration is that the precise location of kidneys display may change slice by slice or patient by patient on abdominal CT image.

3.3 Contour Visualization and Edge Detection

To provide better visualization for physicians on the CT image, the second-order neighborhood edge detection technique is applied to depict the contour of kidney on the abdominal CT images. The second order neighborhood is applied to distinguish the relationship between the current pixel (i,j) and its neighboring pixels $\hat{N}(i,j)$. An edge may pass through the second-order neighborhood of a pixel in one of the four various masks, namely horizontal, vertical, northeast diagonal, and northwest diagonal[7]. In Equations 11 and 12, the values of $HE(i,j)$, $VE(i,j)$, $NE(i,j)$ and $SE(i,j)$ as well as "*edge strength*" are induced by the horizontal, vertical, northeast diagonal, and northwest diagonal edge masks, respectively.

$$\begin{cases} HE(i,j) = | G(i,-1j+1) + 2G(i,j+1) \\ \qquad + G(i+1,j+1) - G(i-1,j-1) \\ \qquad - 2G(i,j-1) - G(i+1,j-1) | \\ VE(i,j) = | G(i+1,j-1) + 2G(i+1,j) \\ \qquad + G(i+1,j+1) - G(i-1,j-1) \\ \qquad - 2G(i-1,j) - G(i-1,j+1) | \end{cases} \tag{11}$$

$$\begin{cases} NE(i,j) = | G(i+1,j) + 2G(i+1,j+1) \\ \qquad + G(i,j+1) - G(i-1,j) \\ \qquad - 2G(i-1,j-1) - G(i,j-1) | \\ SE(i,j) = | G(i,j+1) + 2G(i-1,j+1) \\ \qquad + G(i-1,j) - G(i,j-1) \\ \qquad - 2G(i+1,j-1) - G(i+1,j) | \end{cases} \tag{12}$$

where $G(i+1,j+1)$ denotes the gray level of the pixel at the coordinate $(i+1,j+1)$. $ME(i,j)$ is defined as the maximum of four edge strengths for evaluating the "*local maximum edge strength*" of pixel (i,j),

$$ME(i,j) = max\{HE(i,j), VE(i,j), NE(i,j), SE(i,j)\} \tag{13}$$

The contour is formed by connecting pixels with $ME(i,j) \geqq 255$.

4 Experimental Results

The kidney CT data used in this study was obtained from three CT scanners including HiSpeed LX/i by GE, PQ2000 by PICKER, and Aquilion Multi 16 by TOSHIBA. Thirty cases of abdominal CT images sequence were collected in the dataset. Each case contains around 7 to 20 slices due to different cross-section thickness protocol of different CT scanners. One particular viewpoint of this research domain is that there is no precise ground rule of truth. Conventionally, most professional physicians make diagnosis on the CT slices directly by observation. They may make around 5 to 10 pixels width of mismatch by drawing the contours of complex regions in an image of size 512x512. In the worst case, there will be even more than 10 pixels width mismatch [6]. In the proposed segmentation system, we evaluated the performance objectively by the attending physicians. Moreover, the evaluation was made based on the accuracy of the outermost contours only. The segmentation result on each slice is graded as "*G*"(Good), "*A*"(Acceptable) or "*B*"(Bad), namely, "*G*" denotes the CAD system is comparable to surgical work and the width of mismatch is less than 15 pixel, "*A*" denotes the result is worse than "G", however the correct segmented kidney region or under- segmentation region is at least 75 percentage overlapped with the entire true area. "*B*" denotes the detected kidney region is smaller than 75% of the true area. The proposed system was examined on 291 images with better image quality (B.Q.) from 20 patients and examined on 90 testing images with poor quality (P.Q) from 10 patients. The result of computer-aided segmentation of half of the data (10 B.Q. and 5 P.Q) was graded by the author, and the other was graded by two physicians. We concluded the examination results in Table 1 and Table 2. In Table 1, the evaluation of the system performance by the author achieves to 94.95% correct segmentation above the grade "*G*" and "*A*". The ratio of poor segmentation is as low as 5.5%. Table 2 shows the evaluation from two professional physicians. Since the criteria of physicians is more restrict and conservative, the segmentation performance is not as good as that evaluate by the author (70.3% v.s. 82.55% in grade "*G*", 27.1% v.s. 13.7% in grade "*A*"). Nevertheless, the evaluation of the part of "*B*" grade is much less than that of author. In other words, physicians agree that the proposed system can maintain the

segmentation quality above certain level. Judging by comparing Figure 2(b) and (c), we learn that our technique emphasizes the relaxation of ROIs setting better than that of Tsagaan [1], et. al. whose ROIs are fixed. Besides, the performance has been improved by considering the relation of 3D structure of consecutive slices. From the above-mentioned statistics, the performance evaluations show a satisfactory segmentation result.

Grade	Left kidney		Right kidney		Average
	B.Q.	P.Q.	B.Q.	P.Q.	
"G"	85.3%	86.1%	80.3%	78.5%	82.55%
"A"	10.5%	11.9%	13.8%	18.6%	13.7%
"B"	4.2%	2%	5.9%	2.9%	3.75%

Table 1: Performance evaluation by author: 10 B.Q. and 5 P.Q cases.

Grade	Left kidney		Right kidney		Average
	B.Q.	P.Q.	B.Q.	P.Q.	
"G"	69.3%	70.1%	70.3%	71.5%	70.3%
"A"	27.5%	26.5%	27.8%	26.6%	27.1%
"B"	3.2%	3.4%	1.9%	1.9%	2.6%

Table 2: Performance evaluation by physicians: 10 B.Q and 5 P.Q. cases.

5 Conclusions

In this paper, an efficient method for kidney segmentation on abdominal CT images has been proposed systematically. The kidney ROIs is first obtained based on a priori anatomical knowledge of kidney. Furthermore, mean and conditional median filtering are integrated to perform preliminary noise removal. Such a flexible ROIs extraction scheme as we introduced should be very attractive for various kidney location appeared on abdominal CT image. Next, we develop an adaptive region growing for kidney segmentation and provide a strategy of region modification for the consideration of accurate extraction. For supplying user with better visualization, the concept of second-order neighborhood is used for edge extraction.

References

[1] B. Tsagaan, A. Shimizu, H. Kobatake and K. Miyakawa, 2002, "An Automated Segmentation Method of Kidney Using Statistical Information", *Proceedings of Medical Image Computing and Computer Assisted Intervention, 1*, 556-563.

[2] R. Pohle and K. D. Toennies, 2001, "A New Approach for Model-Based Adaptive Region Growing in Medical Image Analysis", *9th International Conference on Computer Analysis of Images and Patterns, 2124,* 238-246.

[3] R. Pohle and K. D. Toennies, 2001, "Segmentation of Medical Images using Adaptive Region Growing", *Proceedings of SPIE, 4322*, 1337-1346.

[4] R. Pohle and K. D. Toennies, 2001, "Self-Learning Model-Based Segmentation of Medical Images", *Image Processing and Communications, 7*, 97-113.

[5] X. Wang, L. He, C. Y. Han and W. G. Wee, 2002, "Deformable Contour Method: A Constrained Optimization Approach", *British Machine Vision Conference*, 183-192.

[6] M. Kobashi and L. G. Shapiro, 1995, "Knowledge-Based Organ Identification from CT Images", *Pattern Recognition, 28*, 475-491.

[7] J. Fan, D. K. Y. Yau, A. K. Elmagarmid and W. G. Aref, 2001, "Automatic Image Segmentation by Integrating Color-Edge Extraction and Seeded Region Growing", *IEEE Transactions on Image Processing, 10*, 1454-1466.

[8] S. H. Kim, S. W. Yoo, S. J. Kim, J. C. Kim and J. W. Park, 2000, "Segmentation of Kidney without using Contrast Medium on Abdominal CT Image", *5th International Conference on Signal Processing, 2*, 1147-1152.

[9] J. S. Hong, T. Kaneko, S. Sekiguchi and K. H. Park, 2001, "Automatic Liver Tumor Detection from CT", *IEICE Transactions on Information and System, E84-D*, 741-748.

[10] A. E. Fabris, L. Silva and A. R. Forrest, 1997, "An Efficient Algorithm for Non-simple Closed Curves using the Point Containment Paradigm", *SIBGRAPI'97,* http:// mirror.impa.br/sibgrapi97/ anais/pdf/art17.pdf.

[11] R. C. Gonzalez and R. E. Woods. 2002, "Digital Image Processing", *Addision-Wesley*, 2nd edition.

[12] J. Z. Chen, G. S. Tracton, M. Rao, S. Joshi, E. L. Chaney and S. M. Pizer 2002, "Comparison of Automatic and Human Segmentation of Kidneys from CT Images", *International Journal of Radiation Oncology*Biology*Physics, 54*, 82.

INTELLIGENT IMAGE PROCESSING & COMPUTER VISION I

(This page left blank intentionally)

Face Recognition with One Sample Image per Class

Shaokang Chen
Intelligent Real-Time Imaging and Sensing (IRIS) Group
The University of Queensland
Brisbane, Queensland, Australia
shaokang@itee.uq.edu.au

Brian C. Lovell
Intelligent Real-Time Imaging and Sensing (IRIS) Group
The University of Queensland
Brisbane, Queensland, Australia
lovell@itee.uq.edu.au

Abstract

There are two main approaches for face recognition with variations in lighting conditions. One is to represent images with features that are insensitive to illumination in the first place. The other main approach is to construct a linear subspace for every class under the different lighting conditions. Both of these techniques are successfully applied to some extent in face recognition, but it is hard to extend them for recognition with variant facial expressions. It is observed that features insensitive to illumination are highly sensitive to expression variations, which result in face recognition with changes in both lighting conditions and expressions a difficult task. We propose a new method called Affine Principle Components Analysis in an attempt to solve both of these problems. This method extract features to construct a subspace for face representation and warps this space to achieve better class separation. The proposed technique is evaluated using face databases with both variable lighting and facial expressions. We achieve more than 90% accuracy for face recognition by using only one sample image per class.

1. Introduction

One of the difficulties in face recognition (FR) is the numerous variations between images of the same face due to changes in lighting conditions, view points or facial expressions. A good face recognition system should recognize faces and be immune to these variations as mush as possible. Yet, it is been reported in [19] that differences between images of the same face due to these variations are normally greater than those between different faces. Therefore, most of the systems designed to date can only deal with face images taken under constrained conditions. So these major problems must be overcome in the quest to produce robust face recognition systems.

In the past few years, different approaches have been proposed for face recognition to reduce the impact of these nuisance factors. Two main approaches are used for illumination invariant recognition. One is to represent images with features that are less sensitive to illumination changes such as the edge maps of the image. But edges generated from shadows are related to illumination changes and may have an impact on recognition. Experiments in [19] show that even with the best image representations using illumination insensitive features and distance measurement, the misclassification rate is more then 20%. The second approach presented in [21] and [22], is to prove that images of convex Lambertian objects under different lighting conditions can be approximated by a low dimensional linear subspaces. Kreigman, Belhumeur and Georghiades proposed an appearance-based method in [7] for recognizing faces under variations in lighting and view point based on this concept. Nevertheless, these methods all suppose the surface reflectance of human faces is Lambertian reflectance and it is hard for these systems to deal with cast shadows. Furthermore, these systems need several images of the same face taken under different lighting source directions to construct a model of a given face. However, sometimes it is hard to obtain different images of a given face under specific conditions.

As for expression invariant recognition, it is still unsolved for machine recognition and is even a difficult task for humans. In [23] and [24], images are morphed to be the same shape as the one used for training. But it is not guaranteed that all images can be morphed correctly, for example an image with closed eyes cannot be morphed to a neutral image because of the lack of texture inside the eyes. It is also hard to learn the local motions within the feature space to determine the expression changes of each face, since the way one person express a certain emotion is normally somewhat different from

others. Martinez proposed a method to deal with variations in facial expressions in [20]. An image is divided into several local areas and those that are less sensitive to expressional changes are chosen and weighed independently. But features that are insensitive to expression changes may be sensitive to illumination variation. This is discussed in [19] which says that "when a given representation is sufficient to overcome a single image variation, it may still be affected by other processing stages that control other imaging parameters".

It is known that performance of face recognition systems is acutely dependent on the choice of features [3], which is thus the key step in the recognition methodology. Principal Component Analysis (PCA) and Fisher Linear Discriminant (FLD) [1] are two well-known statistical feature extraction techniques for face recognition. PCA, a standard decorrelation technique, derives an orthogonal projection basis, which allows representation of faces in a vastly reduced feature space — this dimensionality reduction increases generalisation ability. PCA finds a set of orthogonal features, which provide a maximally compact representation of the majority of the variation of the facial data. But PCA might extract some noise features that degenerate performance of the system. For this reason, Swets and Weng [8] argue in favor of methods such as FLD which seek to determine the most discriminatory features by taking into account both within-class and between-class variation to derive the Most Discriminating Features (MDF). However, compared to PCA, it has been shown that FLD overfits to the training data resulting in a lack of generalization ability [2].

We propose a new method Affine Principle Component Analysis (APCA) that can deal with variations both in illumination and facial expression. This paper discusses APCA and presents results, which show that the recognition performance of APCA greatly exceeds that of both PCA and FLD when recognizing known faces with unknown changes in illumination and expression.

2. Review of PCA & FLD

PCA and FLD are two popular techniques for face recognition. They abstract features from training face images to generate orthogonal sets of feature vectors, which span a subspace of the face images. Recognition is then performed within this space based on some distance metric (possibly Euclidean).

2.1. PCA (Principal Component Analysis)

PCA is a second-order method for finding the linear representation of faces using only the covariance of data and determines the set of orthogonal components (feature vectors) which minimise the reconstruction error for a given number of feature vectors. Consider the face image set $I = [I_1, I_2, \ldots I_n]$, where I_i is a p×q image, $i \in [1..n]$, $p, q, n \in Z^+$, the average face Ψ of the image set is defined by:

$$\Psi = \frac{1}{n}\sum_{i=1}^{n} I_i \,. \tag{1}$$

Normalizing each image by subtracting the average face, we have the normalized difference image:

$$\tilde{D}_i = I_i - \Psi \,. \tag{2}$$

Unpacking $\tilde{D}_i$ row-wise, we form the N ($N = p \times q$) dimensional column vector d_i. We define the covariance matrix C of the normalized image set $D = [d_1, d_2, \ldots d_n]$ by:

$$C = \sum_{i=1}^{n} d_i d_i^T = DD^T \tag{3}$$

An eigendecomposition of C yields eigenvalues λ_i and eigenvectors u_i which satisfy:

$$Cu_i = \lambda_i u_i \,, \tag{4}$$

$$DD^T = C = \sum_{i=1}^{N} \lambda_i u_i u_i^T \,, \tag{5}$$

where $i \in [1..N]$. Since those eigenvectors obtained looks like human faces physically, they are also called eigenfaces. Generally, we select a small subset of $m < n$ eigenvectors, to define a reduced dimensionality facespace that yields higher recognition performance on unseen examples of faces. Choosing $m = 10$ or thereabouts seems to yield good performance in practice. Although PCA defines a face subspace that contains the greatest covariance, it is not necessarily the best choice for classification since it may retain principle components with large noise and nuisance factors [2].

2.2 FLD (Fisher Linear Discriminant)

FLD finds the optimum projection for classification of the training data by simultaneously diagonalizing the within-class and between-class scatter matrices [2]. The FLD procedure consists of two operations: whitening and diagonalization [2]. Given M classes S_j, $j \in [1...M]$, we denote the exemplars of each class by $s_{j,k} = [s_{j,1}, s_{j,2}, \cdots, s_{j,K_j}]$ where K_j is the number of exemplars in class j. Let μ_j denote the mean of class j

and $\bar{\mu}$ denote the grand mean for all the exemplars, then the between class scatter matrix is defined by:

$$B = \sum_{j=1}^{M} K_j (\mu_j - \bar{\mu})(\mu_j - \bar{\mu})^T , \quad (6)$$

and the within class scatter matrix is defined by:

$$W = \sum_{j=1}^{M} \sum_{k=1}^{K_j} (s_{j,k} - \mu_j)(s_{j,k} - \mu_j)^T \quad (7)$$

$$W_{FLD} = \arg\max_A \frac{|A^T BA|}{|A^T WA|} \quad (8)$$

In other words, FLD extracts features that are strong between classes but weak within class. While FLD often yields higher recognition performance than PCA, it tends to overfit to the training data, since it relies heavily on how the within-class scatter captures reliable variations for a specific class [2]. In addition, it is optimised for specific classes, so it needs several samples in every class and thus can determine only a maximum of *M*-1 features.

3. PROPOSED METHOD

An Affine PCA method is introduced in this section in an attempt to overcome some of the limitations of both PCA and FLD. First of all, we apply PCA for dimensionality reduction and to obtain the eigenfaces U. Every face image can be projected into this subspace to form an *m*-dimensional feature vector $s_{j,k}$, where $m < n$, denotes the number of principal eigenfaces chosen for the projection, and $k = 1,2,...K_j$, denotes the k[th] sample of the class S_j, where $j = 1,2,...M$. We often use the nearest neighbor method for classification, where the distance between two face vectors represents the energy difference between them. In the case of variable illumination, lighting changes dominate over the characteristic differences between faces. It has also been proved in [19] that the distance between face vectors with facial expression variations are generally greater than that with face identity. This is the main reason why PCA does not work well under variable lighting and expression. In fact, not all the features have the same importance in recognition. Features that are strong between classes and weak within class are much more useful for the recognition task. Therefore, we propose an affine model (Affine PCA) to resolve this problem. The affine procedure involves three steps: eigenspace rotation, whitening transformation and eigenface filtering.

3.1. Eigenspace Rotation

The eigenfaces extracted from PCA are Most Expressive Features (MEF) and these are not necessarily optimal for face recognition performance as stated in [8]. Applying FLD we can obtain the Most Discriminating Features but overfits to only training data lacking of generalization capacity. Therefore, in order not to lose generalization ability while still keep the discrimination, we prefer to rotate the space and find the most variant features that can represent changes due to lighting or expression variation. That is to extract the within class covariance and apply PCA to find the best eigen features that maximally represent within class variations. The within class difference is defined as:

$$D_{Within} = \sum_{j=1}^{M} \sum_{k=1}^{K_j} s_{j,k} - \mu_j , \quad (9)$$

and the within class covariance become:

$$Cov_{Within} = D_{Within} D_{Within}^T , \quad (10)$$

which is a *m* by *m* matrix. Applying singular value decomposition (SVD) to within class covariance matrix, we have,

$$Cov_{Within} = USV^T = \sum_{i=1}^{m} \sigma_i v_i v_i^T .$$

Then the rotation matrix M is the set of eigen vectors of covariance matrix, $M = [v_1, v_2, ...v_m]$. Then all the vectors represented in the original subspace are transformed into new space by multiply by *M*.

3.2. Whitening Transformation

The purpose for whitening is to normalize the scatter matrix for uniform gain control. Since as stated in [3] "mean square error underlying PCA preferentially weights low frequencies", we would need to compensate for that. The whitening parameter Γ is related to the eigenvalues λ_i. Conventionally, we would use the standard deviation for whitening, that is: $\Gamma i = \sqrt{\lambda_i}$, $i = [1...m]$. But this value appears to compress the eigenspace so much that class separability is diminished. We therefore use $\Gamma_i = \lambda_i^p$, where the exponent *p* is determined empirically.

3.3. Filtering the Eigenfaces

The aim of filtering is to diminish the contribution of eigenfaces that are strongly affected by variations. We want to be able to enhance features that capture the main differences between classes (faces) while diminishing the contribution of those that are largely due to lighting or

expression variation (within class differences). We thus define a filtering parameter Λ which is related to identity-to-variation (ITV) ratio. The ITV is a ratio measuring the correlation with a change in person versus a change in variations for each of the eigenfaces. For an *M* class problem, assume that for each of the M classes (persons) we have examples under *K* standardized different variations in illumination or expression. In case of illumination changes, the lighting source is positioned in front, above, below, left and right as illustrated in Figure 2. The facial expression changes are normal, surprised and unpleasant as shown in Figure 3. Let us denote the ith eigenface of the kth sample for class (person) S_j by $s_{i,j,k}$. Then

$$ITV_i = \frac{\text{Between Class Scatter}}{\text{Within Class Scatter}} = \frac{\frac{1}{M}\sum_{j=1}^{M}\frac{1}{K}\sum_{k=1}^{K}\left|s_{i,j,k} - \varpi_{i,k}\right|}{\frac{1}{M}\sum_{j=1}^{M}\frac{1}{K}\sum_{k=1}^{K}\left|s_{i,j,k} - \mu_{i,j}\right|}, \quad (11)$$

$$\varpi_{i,k} = \frac{1}{M}\sum_{j=1}^{M} s_{i,j,k},$$

and $$\mu_{i,j} = \frac{1}{K}\sum_{k=1}^{K} s_{i,j,k}, \quad i = [1 \cdots m].$$

Here $\varpi_{i,k}$ represents the ith element of the mean face vector for variation k for all persons and $\mu_{i,j}$ represents the ith element of the mean face vector for person j under all different variations. We then define the scaling parameter Λ by:

$$\Lambda_i = ITV_i^q \quad (12)$$

where q is an exponential scaling factor determined empirically as before. Instead of this exponential scaling factor, other non-linear functions such as thresholding suggest themselves. These possibilities have been explored, but so far the exponential scaling perform best. After the affine transformation, the distance d between two face vectors $s_{j,k}$ and $s_{j',k'}$ is:

$$d_{jj',kk'} = \sqrt{\sum_{i=1}^{m}\left[\omega_i (s_{i,j,k} - s_{i,j',k'})\right]^2}, \quad (13)$$

$$\omega_i = \Gamma_i \Lambda_i / \left|\Gamma \Lambda^T\right|.$$

The weights ω_i scale the corresponding eigenfaces. To determine the two exponents *p* and *q* for Γ and Λ, we introduce a cost function and optimise them empirically. It is defined by:

$$OPT = \sum_{j=1}^{M}\sum_{k=1}^{K}\sum_{m}\left(\frac{d_{jj,k0}}{d_{jm,k0}}\right), \forall m \in d_{jm,k0} < d_{jj,k0} \quad (14)$$

where $d_{jj,k0}$ is the distance between the sample $s_{j,k}$ and $s_{j,0}$ which is the standard image reference for class S_j (typically the normally illuminated image). Note that the condition $d_{jm,k0} < d_{jj,k0}$ is only true when there is a misclassification error. Thus *OPT* is a combination of error rate and the ratio of between-class distance to within-class distance. By minimizing *OPT*, we can determine the best choices for *p* and *q*. Figure 1, shows the relationship between *OPT* and *p*, *q*. For one of our training database, a minimum was obtained at $p = -0.2$, $q = -0.4$.

From the above, our final set of transformed eigenfaces would be:

$$u_i' = \omega_i u_i M = \frac{1}{\sigma_i}\omega_i D v_i M \quad (15)$$

where $i = [1 \cdots m]$. After transformation, we can apply PCA again on the compressed subspace to further reduce dimensionality (two-stage PCA).

4. EXPERIMENTAL RESULTS

The method is tested on an Asian Face Image Database PF01 [6] for both changes in lighting source positions and facial expressions. The size of each image is 171×171 pixels with 256 grey levels per pixel. Figure 2 and 3 show some examples from the database. To evaluate the performance of our methods, we performed a 3-fold cross validation on the database as follows. We choose one-third of the 107 subjects to construct our APCA model, one-third for training. Then we just add the normally faces (pictures in the first column in Figure 1 and 2) of the remaining one-thirds of the data into our recognition database. We then attempt to recognize these faces under all the other conditions. This process is repeated three-fold using different partitions and the performance is averaged. All the results listed in this paper are obtained from experiments only on testing data. Table 1 is the comparison of recognition rate between APCA and PCA. It is clear from the results that Affine PCA performs much better than PCA in face recognition under variable lighting conditions. The proposed APCA outperforms PCA remarkably in recognition rate with 99.3% for training data and 95.6% for testing data with negligible reduction in performance for normally lit faces. Figure 3 displays the recognition rates against numbers of eigenfaces used (m). It can be seen that selecting the principal 40 to 50 eigenfaces is sufficient for invariant luminance face recognition. This number is

somewhat higher than is required for standard PCA, where selecting m in the range 10 to 20 is sufficient — this is possibly a necessary consequence of the greater complexity of the APCA face subspace compared to standard PCA.

Figure 1. Examples of illumination changes in Asian Face Database PF01.

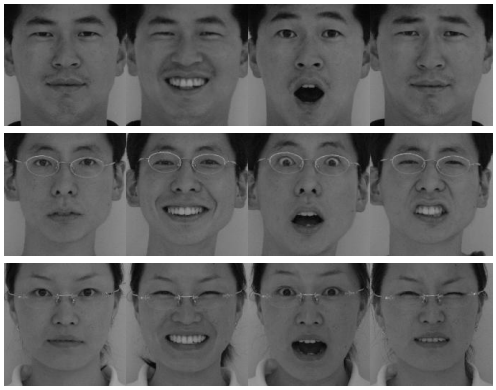

Figure 2. Examples of expression changes in Asian Face Database PF01.

As for variations in facial expression, APCA achieves higher recognition rate than PCA with an increase of 10%. For changes in both lighting condition and expression, APCA always performs better than PCA despite of the change in number of eigenfaces. The gain is almost stable with high dimension of subspace. It can also be seen from Figure 3, that recognition rate of expression changes does not decrease dramatically with the reduce of number of eigen features compared to illumination variations. Therefore, only as low as 20 features is enough to recognition faces with facial expression variations.

We also test the performance of APCA on variations on illumination and expression simultaneously. The recognition rate of APCA is less than 5% lower than that of illumination changes and expression changes, but it is obviously higher than the recognition rate of PCA. Thus it shows that performance of APCA is stable in spite of the complexity of variations. However, PCA is not as robust as APCA with different variations. For illumination changes, PCA only achieve less than 60% accuracy while the accuracy increase to more than 80% for expression variations. It drops back to 60% with changes combining illumination and expression. This phenomenon has also been reported in [19] as any given representation is not sufficient to overcome variations in both illumination and expression.

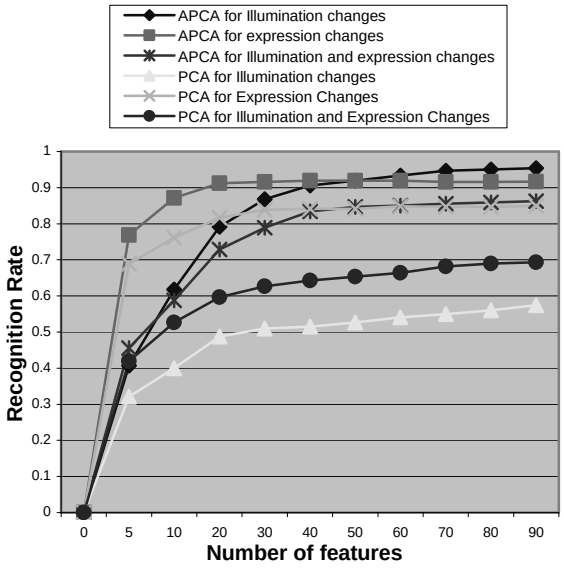

Figure 3. Recognition Rate Vs. Number of features.

Method	Recognition rate		
	Illumination Variation	Expression Variation	Illumination and Expression Variations
PCA	57.3%	84.6%	70.6%
Affine PCA	95.6%	92.2%	86.8%

Table 1. Comparison of recognition rate between APCA and PCA.

Conclusion

We have described an easy to calculate and efficient face recognition algorithm by warping the face subspace constructed from PCA. The affine procedure contains three steps: rotating the eigen space, whitening Transformation, and then filtering the eigenfaces. After affine transformation, features are assigned with different weights for recognition which in fact enlarge the between

class covariance while minimizing within class covariance. There only have as few as two variable parameters during the optimization compared to other methods for high dimensionality problems. This method can not only deal with variations in illumination and expression separately but also perform well for the combination of both changes with only one sample image per class. Experiments show that APCA is more robust to change in illumination and expression and have better generalization capacity compared to the FLD method.

A shortcoming of the algorithm is that we can not guarantee that the weights achieved are the best for recognition since we only rotate the eigen space to the direction that best represent the within class covariance. Future work will be to search the eigen space and find the best eigen features suitable for face recognition.

References

[1] P.Belhumeur, J. Hespanha, and D. Kriegman, “Eigenfaces vs. fisherfaces: Recognition using class specific linear projection”, IEEE Trans. Pattern Analysis and Machine Intelligence, Vol.19, No.7, 711-720, 1997.

[2] Chengjun Liu and Harry Wechsler, “Enhanced Fisher Linear Discriminant Models for Face Recognition”, 14th International Conference on Pattern Recognition, ICPR’98, Queensland, Australia, August 17-20, 1998.

[3] Chengjun Liu and Harry Wechsler, “Evolution of Optimal Projection Axes (OPA) for Face Recognition”, Third IEEE International Conference on Automatic face and Gesture Recognition, FG’98, Nara, Japan, April 14-16,1998.

[4] Dao-Qing Dai, Guo-Can Feng, Jian-Huang Lai and P.C. Yuen, “Face Recognition Based on Local Fisher Features”, 2nd Int. Conf. on Multimodal Interface, Beijing, 2000.

[5] Hua Yu and Jie Yang, “A Direct LDA Algorithm for High-Dimensional Data-with Application to Face Recognition”, Pattern Recognition 34(10), 2001, pp. 2067-2070.

[6] Intelligent Multimedia Lab., “Asian Face Image Database PF01”, http://nova.postech.ac.kr/.

[7] Georghiades, A.S. and Belhumeur, P.N. and Kriegman, D.J., "From Few to Many: Illumination Cone Models for Face Recognition under Variable Lighting and Pose", IEEE Trans. Pattern Anal. Mach. Intelligence, vol.23, No. 6, 2001, pp. 643-660.

[8] Daniel L. Swets and John Weng, “Using discriminant eigenfeatures for image retrieval”, IEEE Trans. on PAMI, vol. 18, No. 8, 1996, pp. 831-836.

[9] X.W. Hou, S.Z. Li, H.J. Zhang. "Direct Appearance Models". In Proceedings of IEEE International Conference on Computer Vision and Pattern Recognition. Hawaii. December, 2001.

[10] Z. Xue, S.Z. Li, and E.K. Teoh. "Facial Feature Extraction and Image Warping Using PCA Based Statistic Model". In Proceedings of 2001 International Conference on Image Processing. Thessaloniki, Greece. October 7-10, 2001.

[11] S.Z. Li, K.L. Chan and C.L. Wang. ``Performance Evaluation of the Nearest Feature Line Method in Image Classification and Retrieval". IEEE Transactions on Pattern Analysis and Machine Intelligence, 22(11):1335-1339. November, 2000.

[12] G.D. Guo, H.J. Zhang, S.Z. Li. "Pairwise Face Recognition". In Proceedings of 8th IEEE International Conference on Computer Vision. Vancouver, Canada. July 9-12, 2001.

[13] S. Mika, G. Ratsch, J.Weston, and K. R. M. B. Scholkopf, “Fisher discriminant analysis with kernels”, Neural networks for Signal Processing IX, 1999, pp.41-48.

[14] M. A. Turk and A. P. Pentland, “Eigenfaces for recognition”, Journal of Cognitive Neuroscience, vol. 3, No. 1, 1991, pp.71-86.

[15] Jie Zhou and David Zhang **“**Face Recognition by Combining Several Algorithms”, ICPR 2002.

[16] Alexandre Lemieux and Marc Parizeau, “Experiments on Eigenfaces Robustness”, ICPR 2002.

[17] A. M. Martinez and A. C. Kak, “PCA versus LDA”, IEEE TPAMI , 23(2):228–233, 2001.

[18] A. Yilmaz and M. Gokmen, “Eigenhill vs. eigenface and eigenedge”, In Proceedings of International Conference Pattern Recognition, Barcelona, Spain, 2000, pp.827-830.

[19] Yael Adin, Yael Moses, and Shimon Ullman, “Face Recognition: The problem of Compensating for Changes in Illumination Direction”, IEEE PAMI, Vol. 19, No. 7, 1997.

[20] Aleix M. Martinez, “Recognizing Impercisely Localized, Partially Occluded and Expression Variant Faces from a Single Sample per Class”, IEEE TPAMI, Vol. 24, No. 6, 2002.

[21] Ronen Basri and David W. Jacobs, “Lambertian Reflectance and Linear Subspaces”, IEEE TPAMI, Vol. 25, No.2 2003.

[22] Peter W. Hallinan, “A Low-Dimensional representation of Human faces for Arbitrary Lighting Conditioins”, Proc. IEEE Conf. Computer Vision and Pattern recognition, 1994.

[23] D. Beymer and T. Poggio, “Face Recognition from One Example View”, Science, Vol. 272, No. 5250, 1996.

[24] M. J. Black, D. J. Fleet and Y. Yacoob, “Robustly estimating Changes in Image Appearance”, Computer Vision and Image Understanding, Vol. 78, No. 1, 2000.

[25] Shaokang Chen, Brian C. Lovell and Sai Sun, “Face Recognition with APCA in Variant Illuminations”, Workshop on Signal Processing and Applications, Australia, December, 2002.

Object Recognition in Image Sequences and Robust Associative Image Memory using the Multilevel Hypermap Architecture

Henning Hofmeister
Leibniz Institute for Neurobiology
Magdeburg, Germany
hofmeister@ifn-magdeburg.de

Bernd Brückner
Leibniz Institute for Neurobiology
Magdeburg, Germany
brueckner@ifn-magdeburg.de

Abstract

The introduced system for object recognition and tracking uses an associative memory for storing prototypes of objects. The Multilevel Hypermap Architecture (MHA), a self-organizing neural network approach, is used, to construct a robust system. To process form variant objects the MHA is extended to work with masked input data.

Because of using scaled input objects, the system is invariant to translation. The invariance to rotation is realized by the associative memory, which is able to learn different instances of the same input object.

In our tests we obtained a robust system behavior, because the associative memory is able to minimize disturbances in feature extraction with the learned and recalled features of an object prototype.

Keywords

Multilevel Hypermap Architecture, MHA, figure-ground-separation, image sequence analysis, object recognition, object tracking

1. Introduction

From the point of machine vision the key to interpret the real world is to extract object information from it. One of the problems is to separate the objects from the background and to find their real boundaries. This is a condition for automated object recognition and object tracking on long image sequences in image analysis systems. Such systems are from great interest, not only in the field of traffic and security.

Classical methods of signal and image analysis are successfully used to solve especially low dimensional problems. For high dimensional problems artificial neural networks become more important nowadays. These adaptations to the biological signal processing system (brain) try to control the complexity of recognition tasks. There is a wide range of usable neural network learning algorithms and of applications in the field of object recognition [1, 8, 13, 14, 16].

Our research in the field of image analysis pursues the goal first to adapt principles of biological vision to computational algorithms for improving machine vision and second of a large use of artificial neural networks. Especially we are dealing with Learning Vector Quantization (LVQ) [11] and Adaptive Resonance Theory (ART) [6].

Our development of the Multilevel Hypermap Architecture (MHA) led to applications in speech recognition, analysis of fMRI data sets and generation of hypotheses. ART we were using for classification of high dimensional data sets and color segmentation in images [9].

Both neural network types use self-learning algorithms. So they are qualified for automated systems.

In this paper an algorithm for figure-ground-separation in long image sequences is described and the ability of the MHA to store objects robustly as an associative memory is shown**.**

2. Image Sequence Analysis system

In this paper we present a system for analyzing monocular image sequences, which autonomously describes and stores complex objects in an associative memory structure.

The structure of the technical system is motivated by a simplified biological model of vision.

The processing of visual stimuli takes place in two functional paths with clear anatomical differentiation. The magnocellular “where”-path analyses simple form and motion parameters, has high contrast sensitivity, transient responses and lack of overt wavelength selectivity. The parvocellular “what”-path extracts features like color, colorbased forms or texture by having lower contrast sensitivity, sustained responses and pronounced wavelength

selectivity [7]. The striate cortex V1 has a modular structure and each module is capable of analyzing the pattern, wavelength, luminance, movement and depth of stimuli appearing in different portions of visual space [15]. In the higher areas of visual cortex like medio- and inferotemporal cortex (MT, IT) and V4 topographical context will be lost and perception and recognition of a stimulus happens. MT analyses motion and depth, IT is responsible for the recognition of complex forms, like faces, and V4 for the experience of color. Object features described by the visual stimuli are distributed spatially over the matrix of feedback connections of the neurons in the brain [10].

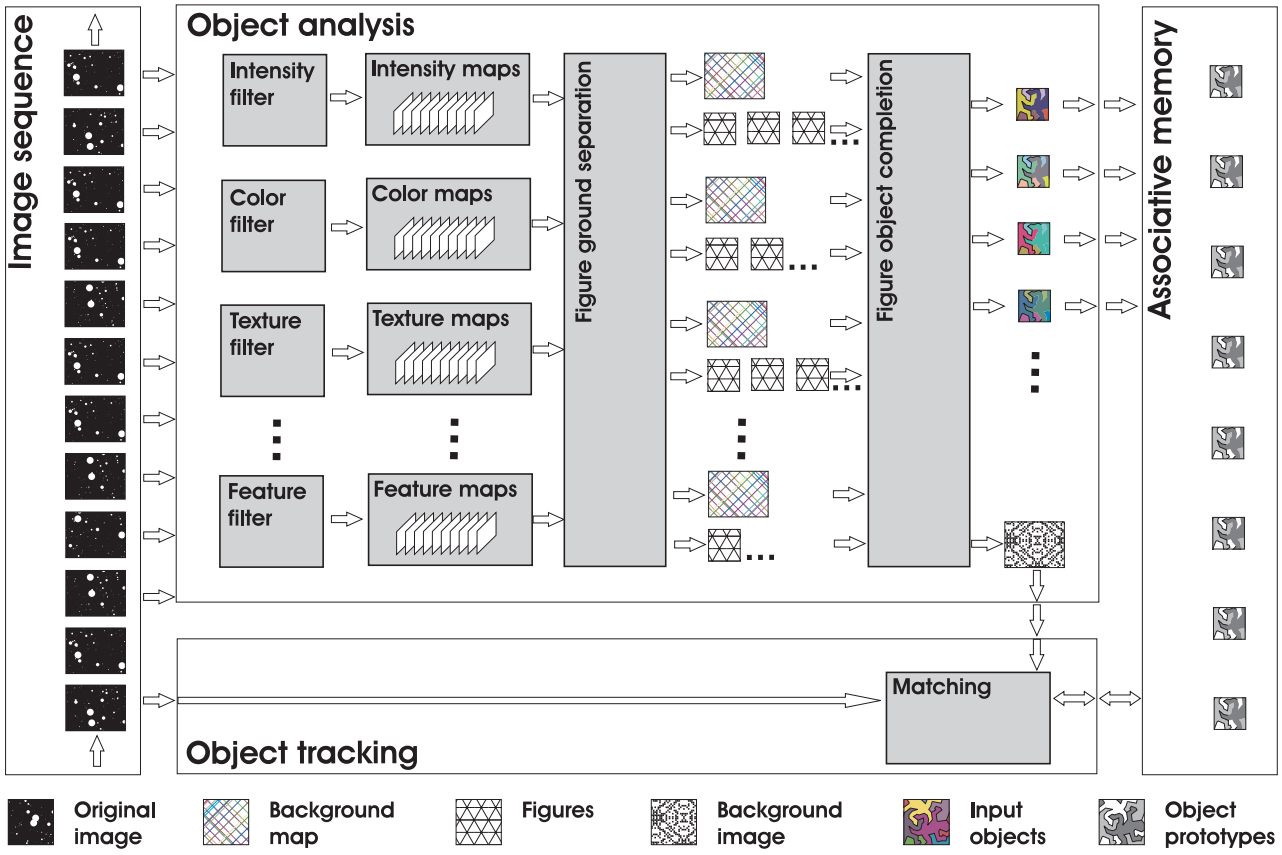

Figure 1: System model

Inspired by the biological model we developed the following technical analysis system shown in Fig. 1 to recognize and track unknown and form variant objects. As input we use a monocular sequence of trichromatic images (RGB) from a stationary camera. Over a time of *n* images a stack is created representing the history of the object movement. The history is necessary for the suggested figure-ground-separation. The first step is a feature extraction. The filter modules extract in parallel different features from each image of the stack. So a stack of feature maps is generated. After that figure-ground-separation for each feature take place resulting in a set of featured figures from the object and a map from the background. For further processing the figures must be scaled to the same size. They are superimposed by a map, so that pixels not belonging to the object are marked. For improving the robustness of the object extraction it is meaningful to combine the separation results of several filter modules. Therefore next step is an object completion and we get as result scaled and masked images from the objects, which occurred in the sequence. The contour of the input objects for the associative memory follows the contours of the moving objects in the image sequence. Background pixels are marked as such. For robust learning of an input object we suggest a multi-level scaling like in cortical neurons coding differently large ranges of visual space. So it is possible to get an input object with different spatial scales by a determined size and to get a more or less detailed view on the objects. Therefore the input objects are translation invariant.

The associated memory is able to learn the input objects unsupervised and creates prototypes. Each prototype

represents a moving object from the image sequence by all the features analyzed by the filter modules.

For an easy object tracking we suggest to locate the objects by a matching algorithm between the prototypes and the figures from the current image of the sequence separated from the ground. Conditions for the object tracking are prototypes and a background image. But after initial analyzing of the first few images of the sequence the system fulfils these conditions. Then the object recognition and tracking tasks are running in parallel.

In the proposed application we use long sequences of 576*720 images. For a three-level spatial scaling input objects of sizes 4x4, 16x16 and 64x64 are created.

3. Figure ground separation

By image acquisition with a stationary camera we can assume stable background pixels and varying pixels over a sequence if changes happen. So, for detection of moving objects the pixel difference between successive images is usable. In the analysis system the history (a number of previous images) is considered and for each pixel a vector is created only from the stable feature values of the considered sequence, which describe the background. Changing feature values are faded out. In Fig. 2 an intensity map of a traffic scene and the background map belonging to it are shown. The background is calculated from a sequence of twenty images. The three moving objects on the road (two cars and a cyclist) are suppressed.

Figure 2: Intensity map and background map

The figures of the moving objects are selected by subtraction the calculated background map from the current feature map. Figures are separated by labeling connected pixels and each of them is scaled to the size of the input object images (4x4, 16x16, and 64x64). In these images all pixels not belonging to the object are marked with a special value. So the objects are masked by their real contour boundaries. As result of the figure-ground-separation we get a background map for each filter module (see Fig.1, 2) and a set of three images for each figure of a moving object (Fig. 3).

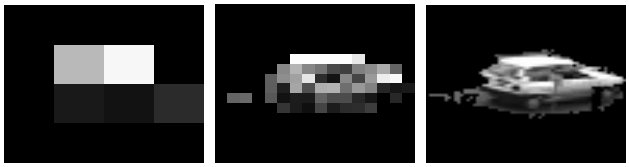

Figure 3: Masked figures of an object in 3 scales (4x4 pixel, 16x16 pixel, 64x64 pixel)

4. Associative Memory

4.1 The Multilevel Hypermap Architecture

One type of Learning Vector Quantization (LVQ) is the Hypermap principle introduced by Kohonen [11]. This principle can be applied to both LVQ and SOM algorithms. In the Hypermap the input pattern is recognized in several separate phases: the recognition of the context around the pattern to select a subset of nodes is followed by a restricted recognition in this subset. This architecture speeds up searching in very large maps and may carry out stabilizing effects, especially if different inputs have very different dynamic ranges and time constants [2].

The modification and extension of the Hypermap, the Multilevel Hypermap Architecture (MHA), are described in [2], the system model is shown in Fig. 4.

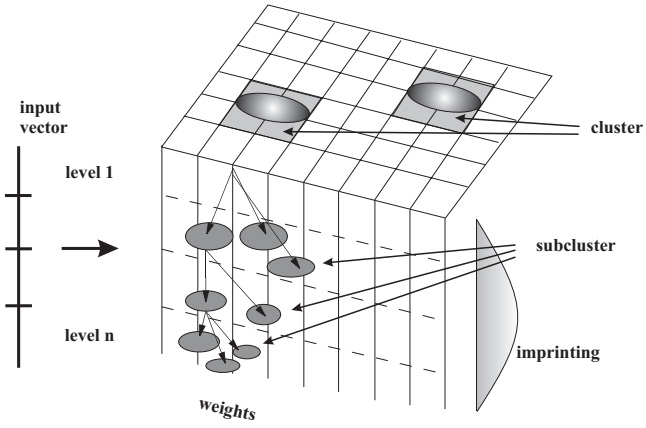

Figure 4: The Multilevel Hypermap Architecture (MHA)

Instead of two levels proposed in the Hypermap [12], the data and the context level, the MHA supports several levels of data relationship and a hierarchical unsupervised clustering. Therefore the input vector consists also of an arbitrary number of levels. In the MHA there is the same number of levels in the weight vector of each unit and these levels are related to the corresponding levels of the input vector. A varying number of levels for the units of the map is supported.

The MHA is trained with the different levels of the input vector whose representation is a hierarchy of encapsulated subsets of units, the so called clusters and subclusters, which define different generalized stages of classification.

Classification is achieved by finding the best matching node for each level of the hierarchy and by determining the square mean error of matching. In principle the algorithm handles different numbers of levels in the input vector.

One advantage of the MHA is the storage of hierarchical relationships of data. This will be useful for the generation of hypothetical relationships, i.e. relations that are not trained by input data. The MHA find it by itself by analyzing trained data.

By means of MHA it is possible to analyze structured or hierarchical data, i.e.

- o data with priorities, e.g. projection of hierarchical data structures in data bases
- o data with context (data bases, associative memories)
- o time series, e.g. speech, moving objects
- o data with varying degrees of exactness, e.g. sequences of measured data.

One advantage of the MHA is the support for both, the classification of data and the projection of the structure in one unified map. The resulting hierarchy has some redundancy like in biological systems.

An overview of our last works about MHA and further details on the algorithm gives [2, 4, 5]. Also in the previous years some real world applications using the MHA were reported in the literature [3, 5].

4.2 Adaptation for an Associative Image Memory

To use the MHA for the described object tracking system some extensions and definitions are needed. First of all the MHA is now able to learn masked data. With this feature the scaled and masked input objects (see Fig. 5) are learned. The different input objects (images) are assigned to the levels of the MHA, especially the 4x4 image is assigned to the 1. level, the 16x16 image to the 2. level and so on.

Therefore we get a generalization depending on the resolution of the image. The better the resolution, the more disturbances are expected and the higher is the number of the used level of the MHA (obviously with less generalizing effects). With learning the input objects the MHA creates prototypes of objects. These prototypes are used from the tracking system to find and track an object in a scene. The associative memory is unsupervised and self-organized, i.e. learning and recall of learned objects happened at the same time.

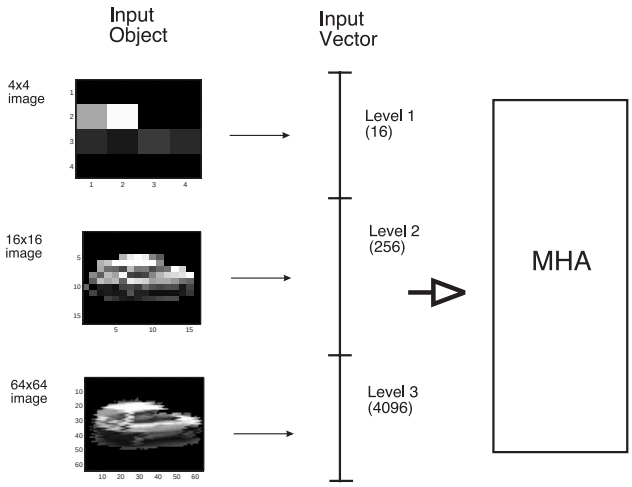

Figure 5: The scaled input objects are transformed into the input vector for training the MHA. The different image resolutions are assigned to the corresponding levels of the input vector (in summary 4368 elements).

To be invariant to the rotation of an object the associative memory (MHA) builds instances of the object prototypes, which are all learned views of an input object. Because of the hierarchical structure of the MHA similar instances are clustered, i.e. are assigned to the object prototype.

In the matching process of the object tracking the recalled object prototypes are combined with the background image and labeled as known objects. For these known objects the tracking is processed.

5. Results

The ability of the MHA as an associative memory should be demonstrated by the results of a simulation experiment of the suggested object recognition system.

Figure 6: Image 36 from traffic sequence

A video sequence from a camcorder with 67 images was presented to the system. The first twenty images were used for creating the initial background image for the figure-ground-separation. From the following 47 images the object figures were separated and the input objects were created. Also the background image was updated continuously. In the sequence there were five moving objects (four cars and a cyclist). A MHA with 25x25 nodes was trained with the input object images. In the traffic sequence (one image from it is shown in Fig. 6) we observed a disturbance. The object of the cyclist (in the center of the image in Fig. 6) covers partially the object of the car. The effect on the prototype is shown below.

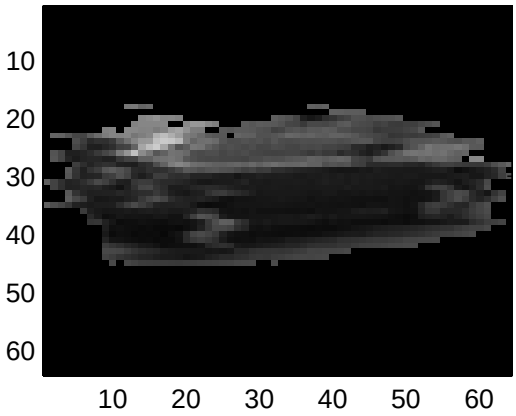

Figure 7: 64x64 image of input object

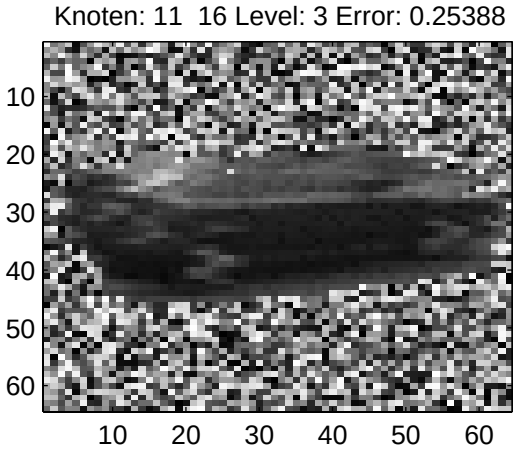

Figure 8: 64x64 image of object prototype

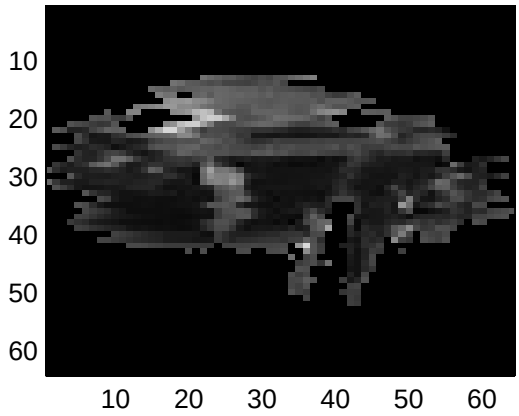

Figure 9: 64x64 image of disturbed input object

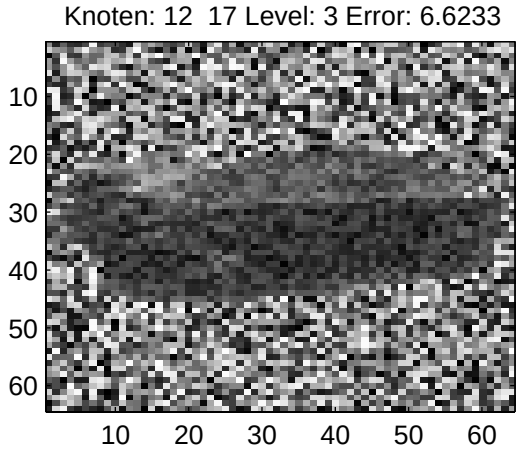

Figure 10: 64x64 image of disturbed object prototype

Fig. 7 shows the 64x64 feature image of the input object from an image of the sequence before the disturbance occurs.

We use here the 64x64 images for presentation, because they are better to view then the smaller images. The results of the first two levels of the MHA are comparable to the results of level 3, but with a higher significance (generalization effect of the MHA's hierarchical structure).

Fig. 8 shows the level 3 prototype of the object 'car' generated by the MHA. It's clearly to be seen that only the masked object is learned. Pixels from the surrounding lead to coincident values. The shown prototype is represented by node {11,16} from the 25x25 MHA.

Fig. 9 shows the input object created from the car covered by the cyclist resulting from image 36 (see also Fig. 6).

In Fig. 10 the result of the recall for the disturbed input object (from Fig. 9) is shown. The resulted prototype is represented by node {12,17}. This means that the prototype of the disturbed object belongs to the same cluster like the undisturbed. The MHA has learned an instance of the object. The similarity of both recalls is obviously

comparing Fig. 8 and Fig. 10, and the generalization effect of the MHA, too.

In spite of the disturbance by another object the tracking continuous uninterruptedly. So the robustness of the associative memory stabilizes object tracking.

6. Summary and Conclusions

In the last years we were dealing with block matching for motion detection. Because of problems by using it for separating objects from a scene we are now using a new figure-ground-separation algorithm for motion detection.

To construct a robust system, the object tracking is combined with an associative memory, where prototypes of objects are stored. The associative memory is an adaptation of the Multilevel Hypermap Architecture (MHA), a self-organizing neural network approach. To process form variant objects, which are constructed as masked images, the MHA is extended to work with masked input data.

The introduced system for object recognition and tracking is invariant to translation because of using scaled input objects. Different image resolutions of object features are used for classifying and storing objects in the associative memory in form of prototypes.

The system is invariant to rotation, because the associative memory is able to learn different instances of the same input object and the hierarchical structure guarantees the consistency of all instances of an object prototype.

In our tests we obtained a robust system behavior, because the associative memory is able to minimize disturbances in feature extraction (e.g. shadow or partly covered objects) with the learned and recalled features of an object prototype.

Further works are going to implement more feature filters in the system, especially for texture features of the input objects. Also improvements in the history mechanism of the scene analysis and optimization of speed are planned.

Acknowledgements

This work was supported by the LSA grant 3133B/0089B.

References

[1] Bhandarkar, S.M., Koh, J., and Suk, M., Multi-scale Image Segmentation using a Hierarchical Self-Organizing Feature Map. *Neurocomputing*, **vol. 14**, No. 3, pp. 241-272 (1997).

[2] Brückner, B., Improvements in the Analysis of Structured Data with the Multilevel Hypermap Architecture. In: Kasabov et.al.: Progress in Connectionist-Based Information Systems, vol. 1, Springer-Verlag, Singapore, 342-345 (1997).

[3] Brückner, B., Gaschler-Markefski, B., Hofmeister, H., and Scheich, H., Detection of Non-Stationarities in Functional MRI Data Sets using the Multilevel Hypermap Architecture. In: Proceedings of the IJCNN'99, Washington, pp. 1–4 (on CD), ISBN: 0-7803-5532-6 (1999).

[4] Brückner, B., and Hofmeister, H., Generating Hypotheses Using the Multilevel Hypermap Architecture. In: Proceedings of the ICONIP2001, Fudan University Press, Vol. 1, pp. 58-62, Shanghai (2001).

[5] Brückner, B., and Wesarg, T., Modeling Speech Processing and Recognition in the Auditory System using the Multilevel Hypermap Architecture. In: Seiffert, U. and Jain, L.C. (Eds.), Self-Organizing Neural Networks. Recent Advances and Applications, Springer Series on Studies in Fuzziness and Soft Computing, Vol. 78, Springer-Verlag, Heidelberg, pp. 145-164 (2001).

[6] Carpenter, G.A., Grossberg, S., A Massively Parallel Architecture for a Selforganizing Neural Pattern Recognition Machine. *Computer Vision, Graphics, and Image Processing*, **vol. 37**, pp. 54-115 (1987)

[7] De Yoe, E.A., and van Essen, D.C., Concurrent processing streams in monkey visual cortex. *Trends Neurosci.*, **11**, 219-226 (1988).

[8] Grossberg, S., and Wyse, L., A neural network architecture for figure ground separation of connected scenic figures. *Neural Networks*, **vol. 4**, pp. 723-742 (1991).

[9] Hofmeister, H., Brückner, B., Color Classification to Improve Block Based Motion Estimation in RGB-Image Sequences. Proceedings of 6th ICONIP 1999, vol. 3, pp.1224-1229 (1999)

[10] Kohonen, T., Self-Organization and Associative Memory (Third edition). Springer-Verlag, Berlin (1989).

[11] Kohonen, T., Selforganizing Maps (Second Edition). Springer-Verlag, Berlin (1997).

[12] Kohonen, T., The hypermap architecture. In: Kohonen et. al.: Artificial Neural Networks, Elsevier Science Publishers, Helsinki, 1357-1360 (1991).

[13] Konen, W.K., Maurer, T., and von der Malsburg, C., A Fast Dynamic Link Matching Algorithm for Invarainat Pattern Recognition. *Neural Networks*, **vol. 7**, Nos. 6/7, pp. 1019-1030 (1994).

[14] Mel, B.W., SEEMORE: Combining Color, Shape, and Texture Histogramming in a Neurally Inspired Apporach to Visual Object Recognition. *Neural Computation*, **9**, 777-804 (1997).

[15] Schiller, P.H., Striate cortex. In: Encyclopedia of Neuroscience, ed. Adelman, G., Birkhäuser, Boston Basel Stuttgart, pp. 1148-1149 (1987).

[16] Wöhler, C., and Anlauf, J.K., An Adaptable Time Delay Neural Network Algorithm for Image Sequence Analysis. *IEEE Transactions on Neural Networks*, **vol. 10**, no. 6, pp. 1531-1536 (1999).

Remarks on Human Body Posture Estimation From Silhouette Image Using Neural Network

Kazuhiko Takahashi
Faculty of Engineering
Yamaguchi University
Tokiwadai Ube, Yamaguchi, Japan
kylyn@yanaguchi-u.ac.jp

Abstract

This paper proposes a human body posture estimation method using neural network. The input feature vector of the neural network is composed with the result of analyzing a human silhouette extracted from camera image and the output vector of the neural network indicates the 2D coordinates of the human body's significant points. The proposed method is implemented on a personal computer and runs in real-time. Experimental results show both the feasibility and the effectiveness of the proposed method for estimating human body postures.

1 Introduction

Artificial neural network (ANN) originated from studies on the mechanisms and structures of the brain has excellent capabilities, such as nonlinear mapping and learning. Studies on biological systems have led to the development of new computational models with application to complex problems such as pattern recognition, fast information processing, learning, and adaptation. In the field of computer vision, ANN is often utilized in many applications since the capabilities of ANN provide very powerful tools for solving pattern classification and/or recognition problems [10]. While computer vision technologies have widely been studied in various engineering fields, recent expectations have been for them to find application in sensing human information [2, 9]. To recognize non-verbal information, such as gestures and sign language, and to understand actions or motions, awareness has been growing on the importance of being able to measure the human body posture or motion parameters. More specifically, human body posture estimation is important for a number of applications including advanced human-machine interface systems, visual communications, virtual reality applications, and video game systems.

Human body posture estimation based on computer vision can lighten the burden and stress of users since they no longer need to utilize contact methods such as magnetic sensors. Therefore, several studies have been undertaken on estimation methods using computer vision [1, 3, 5, 7, 8, 14, 15]; they often lack the ability for real-time performance, have limits on the body parts able to be detected, and require large computational costs. The authors have also proposed real-time human body posture estimation methods [4, 12, 13]. The methods are based on both a contour analysis of human silhouette and their characteristics are: (1) high-speed and robust processing, (2) no markers on the human body, and (3) a small computing power requirement. However, the range of acceptable postures is still limited and a priori knowledge about the relationship between the analysis results and the human body parts is required.

This paper proposes a human body posture estimation method using ANN. In the proposed method, a human silhouette image extracted from camera image is analyzed to compose of input feature vector to the ANN and the ANN outputs the 2D coordinates of the human body's significant points in the image. By using the learning ability of the ANN to obtain the relationship between the human silhouette and the significant points, no a priori knowledge is necessary to achieve the human body posture estimation. Section 2 describes our human body posture estimation method in detail. Section 3 presents the experiments that tested how well the proposed method could estimate human body postures and the results are summarized in section 4.

2 Posture Estimation Method

Figure 1 shows the outline of our method for estimating human body postures. It is composed of two processes: feature extraction which uses image processing and significant

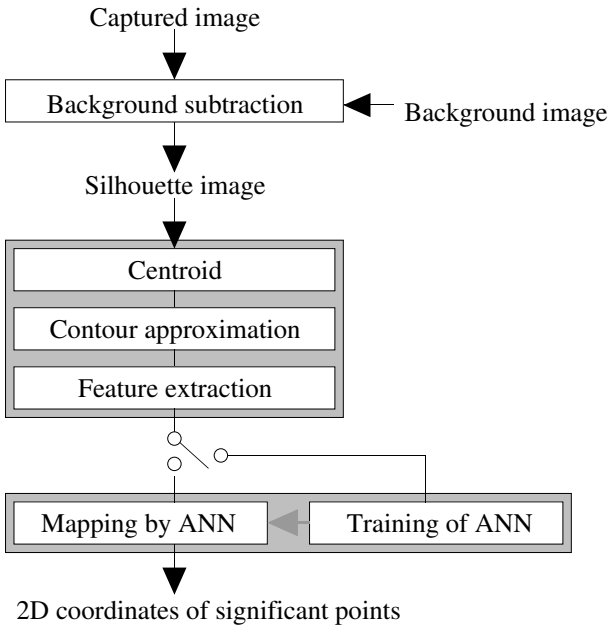

Figure 1. Outline of estimation method.

point estimation which uses ANN. To simplify the process, we use the following assumptions: (1) no other moving object exists within the field besides the human, and (2) the camera is facing the front of the human.

2.1 Feature extraction from silhouette image

Here, we describe how to compose an input feature vector from a human silhouette image obtained from camera images. As a preprocess, the human silhouette is extracted by calculating the difference at each pixel between the background image and the input image and then thresholding the difference at that pixel. First, the centroid of the human silhouette, $[x_g\ y_g]$, is located as follows.

$$x_g = \frac{M_d(1,0)}{M_d(0,0)} \tag{1}$$

$$y_g = \frac{M_d(0,1)}{M_d(0,0)} \tag{2}$$

$$M_d(m,n) = \sum_x \sum_y x^m y^n d_{xy} \tag{3}$$

Here, d_{xy} is the silhouette image, x and y are the vertical and horizontal coordinates of the image, respectively. Next, an intersection of the human silhouette's contour and an axis that is projected outwards from the centroid is obtained [11]. The intersection point is the furthest contour

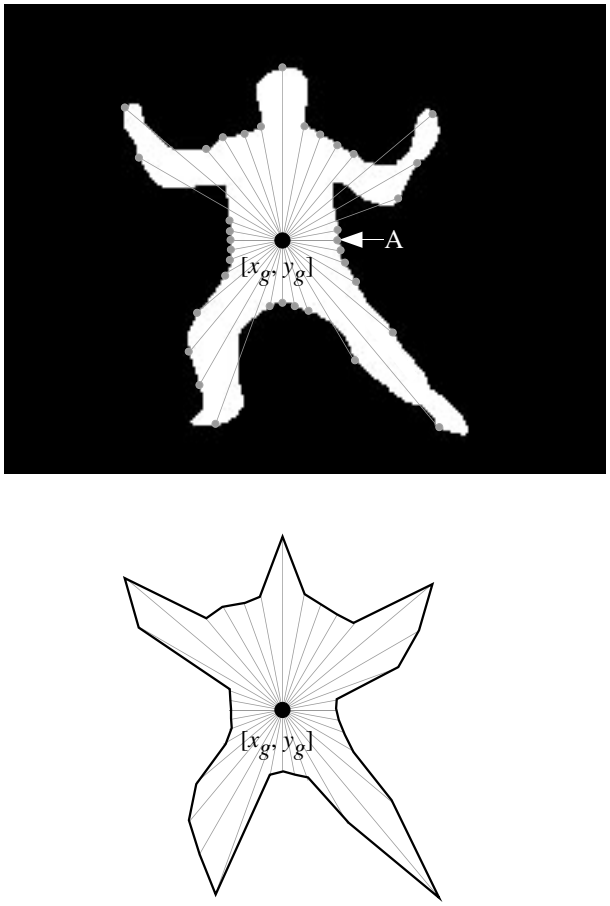

Figure 2. Extracting feature vector from human silhouette image (top: axes projected at specific angles on silhouette image, bottom: contour image approximated by furthest contour edge from the centroid).

edge along the axis. As shown in the top of Fig. 2, the intersection points are located at every Θ_0 degrees around the centroid with the clockwise direction from point A on the contour pixel. As shown in the bottom of Fig. 2, a figure which connected each intersection point sequentially is a circumscribed polygon of the silhouette image. This approximated contour has similar characteristics to active shape models [6].Then, the distance between the intersection point $[x_{p_i}\ y_{p_i}]$ and the centroid is calculated as follows.

$$D_i = \sqrt{(x_{p_i} - x_g)^2 + (y_{p_i} - y_g)^2} \tag{4}$$

The distance D_i can be considered as a feature from the human silhouette. However, it is hard to find mathematical model that defines the relationship between the feature and the part of the human body. Therefore, we estimate the re-

lationship by using ANN. The feature vector can be defined as follows.

$$\boldsymbol{z}^T = \left[\begin{array}{cccccc} D_1 & D_2 & D_3 & \ldots & D_N \end{array} \right] \tag{5}$$

The feature vector is normalized in order to have zero mean and unit variance and is scale, location and rotation invariant. The normalized feature vector $\boldsymbol{z}^*$ is used as a feature input vector in the stage of estimating significant points of the human body using ANN.

$$z_i^* = \frac{z_i - \mu_z}{\sqrt{\sigma_z}} \tag{6}$$

Here μ_z and σ_z are the mean and the variance of the element of the feature vector $\boldsymbol{z}$, respectively.

2.2 Significant point estimation using ANN

In this section, we describe how to design ANN for estimating significant points of the human body. The ANN is a three-layer PDP model with no inner feedback loops and no direct connections from the input layer to the output layer. The following sigmoid function, f, is used as an activation function of neurons in the hidden and output layers.

$$f(u) = \frac{1 - exp(-au)}{1 + exp(-au)} \tag{7}$$

Here a is the parameter of the sigmoid function. The relationship between inputs and outputs of the ANN is given by the following equation.

$$v_l = f(\sum_{j=1}^{M} w_{2_{lj}} f(\sum_{i=1}^{N} w_{1_{ji}} z_i + \theta_{1_j}) + \theta_{2_l}) \tag{8}$$

where z_i is the input to the ith neuron in the input layer, v_l is the output of the lth neuron in the output layer, $w_{k_{ji}}$ and θ_{k_j} $(k = 1, 2)$ are the weight and threshold, and N and M are the number of neuron unit in the input and hidden layer. The learning of the ANN is carried out according to the generalized δ-rule with an adaptive learning rate to minimize the cost function J.

$$\begin{left} \left[\begin{array}{c} w_{k_{ji}}(t+1) \\ \theta_{k_j}(t+1) \end{array} \right] = \left[\begin{array}{c} w_{k_{ji}}(t) \\ \theta_{k_j}(t) \end{array} \right] \\ -\eta(t) \left[\begin{array}{c} \frac{\partial J}{\partial w_{k_{ji}}(t)} \\ \frac{\partial J}{\partial \theta_{k_j}(t)} \end{array} \right] + \alpha \left[\begin{array}{c} \Delta w_{k_{ji}}(t) \\ \Delta \theta_{k_j}(t) \end{array} \right] \end{left} \tag{9}$$

$$\eta(t) = \left\{ \begin{array}{ll} (1+\gamma)\eta(t-1) & \text{if } J(t) < J(t-1) \\ (1-\beta\gamma)\eta(t-1) & \text{if } J_(t) > J(t-1) \\ \eta(t-1) & \text{otherwise} \end{array} \right. \tag{10}$$

$$J(t) = \frac{1}{2} \sum^{P} \sum_{l=1}^{L} (v_{d_l} - v_l(t))^2 \tag{11}$$

where η is the learning factor, α is the momentum factor, $\Delta w_{k_{ji}}(t)$ is the weight increments at the tth iteration, $\Delta \theta_{k_j}(t)$ is the threshold increments at the tth iteration, γ and β are the adaptive factor in the learning, v_{d_l} is the teaching signal, L is the number of neuron unit in the output layer, and P is the total number of the training data.

3 Estimation Experiment

In this study, 9 significant points of human body (head, hands, feet, elbow joints, and knee joints) are considered. Thus we define the relationship between the ANN's outputs and the significant points as follows.

$$\begin{aligned} \boldsymbol{v}^T \quad = \quad & [\, x_H \; y_H \; x_{e_L} \; y_{e_L} \; x_{h_L} \; y_{h_L} \; x_{k_L} \; y_{k_L} \; x_{fL} \\ & y_{f_L} \; x_{f_R} \; y_{f_R} \; x_{k_R} \; y_{k_R} \; x_{h_R} \; y_{h_R} \; x_{e_R} \; y_{e_R} \,] \end{aligned}$$

Here, the subscript H is the index of the top of the head, e_L is the index of the left elbow joint, h_L is the index of the left hand tip, k_L is the index of the left knee joint, f_L is the index of the left foot tip, f_R is the right foot tip, k_R is the index of the right knee joint, h_R is the index of the right hand tip, and e_R is the right elbow joint.

In order to achieve the relationship between the input feature vector and the significant points of human body part by learning of the ANN, various patterns of body posture are necessary as a teaching data of the ANN. However it is hard to collect everything of every body posture even if the posture is limited to only front view. In our experiment, the teaching data is made by extracting postures from the teaching materials video of Chinese shadow boxing (Tai Chi Quan) because the movements of Chinese shadow boxing have various combinations with complexity of hands and feet. The total amount of 1064 teaching data ($P = 1064$) was extracted manually from the Chinese shadow boxing instruction video with a 320-by-240 pixel resolution. Thus the teaching vector $\boldsymbol{v}_d$ is defined by normalizing with respect to the centroid of the human silhouette $[x_g \; y_g]$ as follows.

$$\begin{aligned} \boldsymbol{v}_d^T \quad = \quad & [\, \frac{x_{d_H} - x_g}{x_g} \; \frac{y_{d_H} - y_g}{y_g} \; \frac{x_{d_{e_L}} - x_g}{x_g} \; \frac{y_{d_{e_L}} - y_g}{y_g} \\ & \frac{x_{d_{h_L}} - x_g}{x_g} \; \frac{y_{d_{h_L}} - y_g}{y_g} \; \frac{x_{d_{k_L}} - x_g}{x_g} \; \frac{y_{d_{k_L}} - y_g}{y_g} \\ & \frac{x_{d_{f_L}} - x_g}{x_g} \; \frac{y_{d_{h_L}} - y_g}{y_g} \; \frac{x_{d_{f_R}} - x_g}{x_g} \; \frac{y_{d_{f_R}} - y_g}{y_g} \\ & \frac{x_{d_{k_R}} - x_g}{x_g} \; \frac{y_{d_{k_R}} - y_g}{y_g} \; \frac{x_{d_{h_R}} - x_g}{x_g} \; \frac{y_{d_{h_R}} - y_g}{y_g} \\ & \frac{x_{d_{e_R}} - x_g}{x_g} \; \frac{y_{d_{e_R}} - y_g}{y_g} \,] \end{aligned} \tag{12}$$

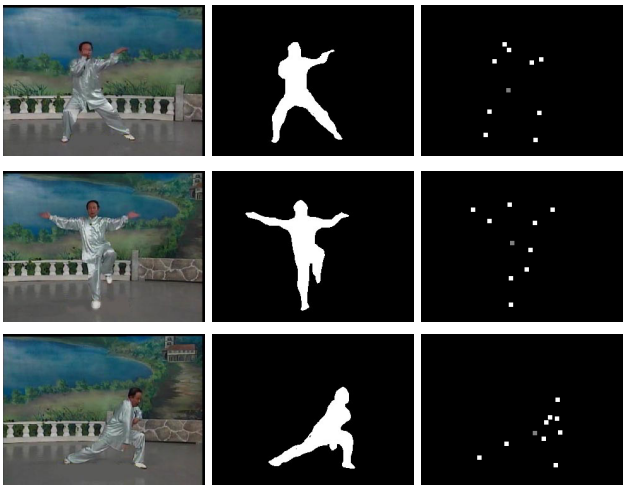

Figure 3. Examples of estimating significant points in close testing (left column: original image, middle column: human silhouette image, right column: estimated human body's significant point image).

The dimension of the feature input vector was 36 since the intersection points are located at every 10 degrees ($\Theta_0 = 10$). The number of neuron in the hidden layer was defined by trial and error in order to converge the ANN learning. In the experiment, the ANN structure was a 36-76-18 network ($N = 36$, $M = 76$, and $L = 18$). The initial weight matrices were randomly selected from the interval $[-1, 1]$. The parameters were $a = 1$, $\eta(0) = 10^{-4}$, $\gamma = 10^{-2}$, $\beta = 10$, and $\alpha = 0.9$. The maximum allowable error in each output unit was 10^{-2} while the learning iteration was limited to 10^5 for each training data. After the learning of the ANN was completed, the weight matrices were fixed and the ANN was used in the significant point estimation process. Figure 3 shows examples of the estimation result in the close testing. Here the silhouette images are manually obtained in the middle of Fig.3 and the estimated significant points of human body are shown with small squares in the right of Fig.3. As shown in the right figures, the significant points and the centroid are located successfully.

To evaluate the feasibility of our estimation method, we carried out experiments using real camera images. The proposed method was coded in the C language and implemented on a personal computer (Gateway GP7 Pentium III 800MHz, Windows 98). The images from the CCD camera (SONY EVI-D30) were digitized into the computer with a 160-by-120 pixel resolution via flame grabber (MATROX METEOR-II). The background subtraction was carried out by using the statistical background modeling, threshold selection, subtraction operation, and pixel classification [3] and an image processing of noise cleaning was also applied. The entire process for estimating human postures ran in real time (approximately 20 frames/sec).

Figure 4 shows examples of estimation results and Table 1 shows the estimation error that is defined as follows.

$$\epsilon_i = \sqrt{(x_{i_m} - x_i)^2 + (y_{i_m} - y_i)^2}$$

Here the real locations of significant points, $[x_{i_m}\ y_{i_m}]$, were obtained manually from images and the estimated locations of significant points, $[x_i\ y_i]$, were the outputs from the ANN (i = H, e_L, h_L, k_L, f_L, f_R, k_R, h_R, e_R). Fig. 4(a) is the captured images, Fig. 4(b) is the human image extracted by using the background subtraction, Fig. 4(c) is the significant points that are intersections of the human silhouette's contour and axes that are projected outwards from the centroid, and Fig. 4(d) is the significant points estimated by the ANN. In Fig. 4(d), the estimated significant points of human body are indicated with small squares. In each estimation result, the significant points are indicated with small squares (white: significant point, gray: centroid). As shown in Fig. 4, all of the significant points could be extracted successfully without depending on the posture, position where the person was standing, background condition, and image resolution. Although the ANN was trained using only the limited data extracted from the Chinese shadow boxing video and the human image extraction with the background subtraction is not always completely successful, the proposed method could achieve robust estimation of the significant points with the ANN's generalization ability. These experimental results indicate both the feasibility and effectiveness of our proposed method for estimating human body postures. However the estimation of the significant points is not good enough accurate as shown in Table 4. In order to improve the estimation accuracy, the learning or network topology of the ANN should be redesigned and the human extraction method from image should also be improved.

4 Conclusions

This paper has proposed a real-time human body posture estimation method using ANN. The input feature vector of

Table 1. Estimation error of the posture shown in Fig. 4.

	posture 1	posture 2	posture 3
$\min \epsilon_i$ [pixel]	1.00	5.83	5.39
$\max \epsilon_i$ [pixel]	10.03	21.59	15.62
$\sum \epsilon_i$ [pixel]	47.78	112.75	88.23
$\sum \epsilon_i/9$ [pixel]	5.31	12.53	9.80

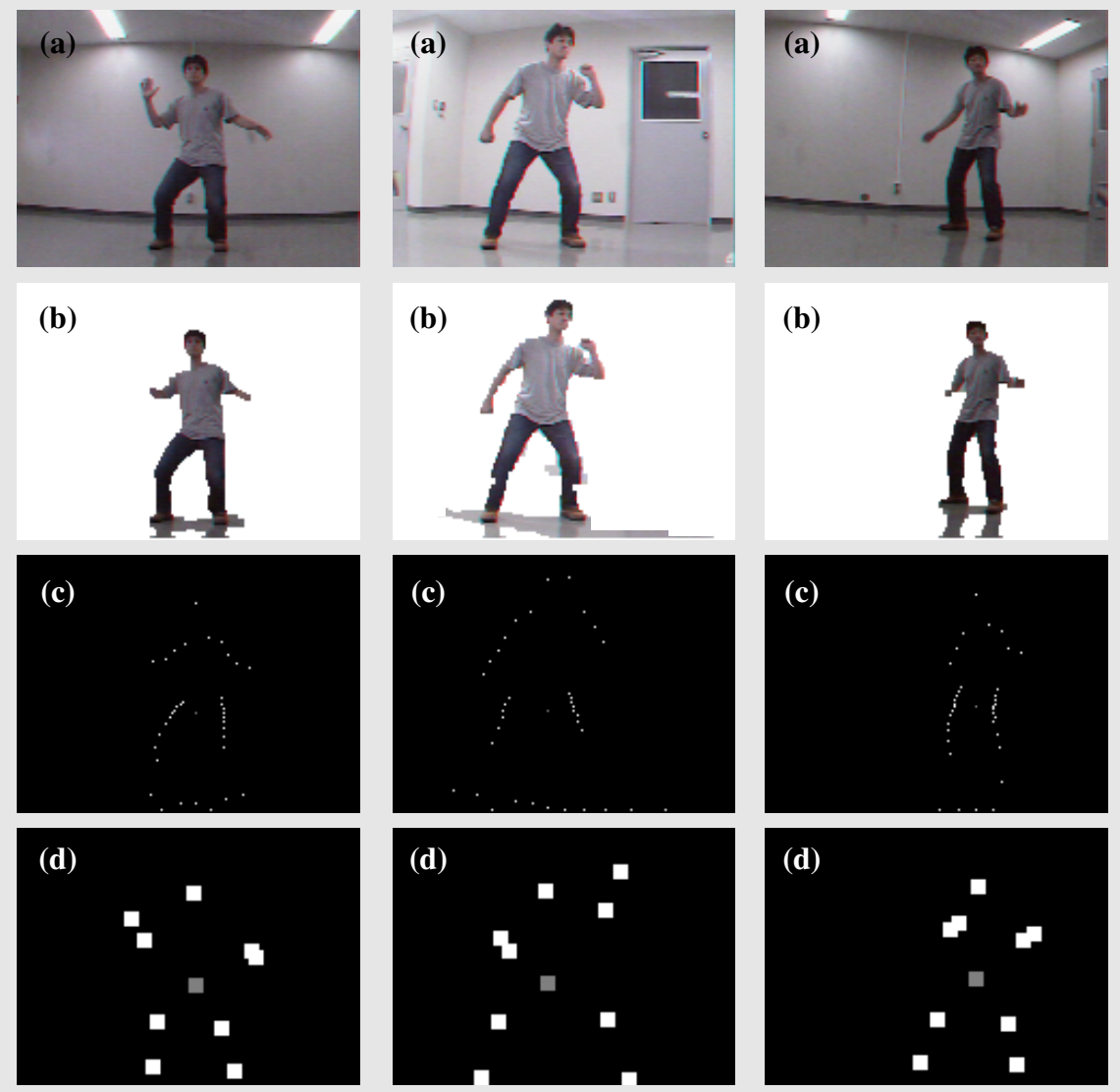

Figure 4. Examples of estimating significant points(left column: posture 1, middle column: posture 2, right column: posture 3). (a) original camera image, (b) human image obtained by background subtraction, (c) extracted significant point image, and (d) estimated human body's significant point image

the ANN is extracted from a human silhouette's contour image, and the output of the ANN indicates the 2D coordinates of the human body's significant points. Using image data extracted from Chinese shadow boxing video, the ANN is trained. The proposed method is implemented on a personal computer and runs in real time. Experimental results confirm both the feasibility and the effectiveness of the proposed method for estimating human body postures.

Acknowledgment

This work was supported by JSPS Grant-in-Aid for Young Scientists (B) 15700160.

References

[1] A. Bottino and A. Laurentini. A silhouette based technique for the reconstruction of human movement. *Computer Vision and Image Understanding*, 83(1):79–95, 2001.

[2] D. M. Gavrila. The visual analysis of human movement: A survey. *Computer Vision and Image Understanding*, 73(1):82–98, 1999.

[3] I. Haritaoglu, D. Harwood, and L. S. Davis. W4: Who? when? where? what? a real time system for detecting and tracking people. In *Proc. of Third IEEE Int. Conf. on FG'98*, pages 222–227, 1998.

[4] S. Iwasawa, J. Ohya, K. Takahashi, T. Sakaguchi, S. Kawato, K. Ebihara, and S. Morishima. Real-time, 3d estimation of human body postures from trinocular images. In *Proc. of Int. Workshop on mPeople*, pages 3–10, 1999.

[5] I. A. Kakadiaris and D. D. Metaxas. Three-dimentional human body model acquisition from multiple views. *Int. Journal of Computer Vision*, 30(3):191–218, 1998.

[6] A. Koschan, S. Kang, J. Paik, B. Abidi, and M. Abidi. Color active shape models for tracking non-rigid objects. *Pattern Recognition Letters*, 24:1751–1765, 2003.

[7] M. K. Leung and Y. H. Yang. First sight: A human body outline labeling system. *IEEE Trans. on PAMI*, 17(4):359–377, 1995.

[8] Y. Li, A. Hilton, and J. Illingworth. A relaxation algorithm for real-time multiple view 3d-tracking. *Image and Vision Computing*, 20(12):841–859, 2002.

[9] T. B. Moeslund and E. Granum. A survey of computer vision-based human motion capture. *Computer Vision and Image Understanding*, 81(3):231–268, 2001.

[10] M. S. Obaidat. Editorial: Artificial neural networks to systems, man, and cybernetics: Characteristics, structures, and applications. *IEEE Trans. on SMC – Part B:Cybernetics*, 28(4):489–495, 1998.

[11] K. Tabb, N. Davey, S. George, and R. Adams. Detecting partial occlusion of humans using snakes and neural networks. In *Proc. of 5th Int. Conf. on EANN'99*, pages 34–39, 1999.

[12] K. Takahashi, T. Sakaguchi, and J. Ohya. Remarks on no-wear, non-contact, 3d real-time human body posture estimation method. *Systems and Computers in Japan*, 31(14):1–10, 2000.

[13] K. Takahashi and T. Uemura. Real-time human body posture estimation using neural networks. *JSME Int. Journal (C)*, 44(3):618–625, 2001.

[14] C. Wren, A. Azarbayejani, T. Darrel, and A. Pentland. Pfinder: Real-time tracking of the human body. *IEEE Trans. on PAMI*, 19(7):780–785, 1997.

[15] M. Yamamoto, T. Kondo, T. Yamagiwa, and K. Yamanaka. Skill recognition. In *Proc. of Third IEEE Int. Conf. on FG'98*, pages 604–609, 1998.

Improvement of Fast Circle Detection Algorithm Using Certainty Factors

Ali Ajdari Rad
Computer Engineering Department, Amirkabir University of Technology, Tehran, Iran
alirad@aut.ac.ir

Karim Faez
Professor of Electrical Engineering Department, Amirkabir University of Technology, Tehran, Iran
kfaez@aut.ac.ir

Navid Qaragozlou
Computer Engineering Department, Amirkabir University of Technology, Tehran, Iran
eavidq@aut.ac.ir

Abstract
The Circle Hough Transform (CHT) has become a common method for circle detection in numerous image processing applications. Because of its drawbacks, various modifications to the basic CHT method have been suggested. In this paper, an algorithm is presented to find circles which are totally brighter or darker than their backgrounds. The method is size-invariant, and such circular shapes can be found very fast and accurately called Fast Circle Detection (FCD). Though Fast Circle Detection (FCD) method loses the generality of the CHT, there are many applications that can use this method after a simple preprocessing and gain a considerable improvement in performance against the CHT or its modified versions. In this paper, we present a method based on certainty factor concept to improve the FCD performance. The improved version of the FCD has been evaluated in some famous industrial and medical fields, and the results show a significant improvement.

Keywords
Circle Detection, Hough Transform, Certainty Factors.

INTRODUCTION

Detecting lines and circles in an image is a fundamental issue in image processing applications. Extracting circles from digital images has received more attention for several decades because an extracted circle can be used to yield the location of circular object in many industrial applications. So far many circle-extraction methods have been developed. The Circle Hough Transform (CHT) [1] is the best-known algorithm and aims to find circular shapes with a given radius r within an image. Usually the edge map of the image is calculated then each edge point contributes a circle of radius r to an output accumulator space. For circles with unknown radiuses, the algorithm should be run for all possible radiuses to form a 3-dimensional parameter space, where two dimensions represent the position of the center, and the third one represents the radius. The output accumulator space has a peak where these contributed circles overlap at the center of the original circle.

In spite of its popularity owing to its simple theory of operation, the CHT has some disadvantages when it works on a discrete image. The large amount of storage and computing power required by the CHT are the major disadvantages of using it in real-time applications. Some modifications have been reported to increase the CHT performance so far. Tsuji and Matsumoto decomposed the parameter space by using the parallel property of circle [2]. Several methods use randomized selection of edge points and geometrical properties of circle instead of using the information of edge pixels and evidence histograms in the parameter space. Xu et al. [3] presented an approach that randomly has selected three pixels. The method selects three noncollinear edge pixels and votes for the circle parameters which are found by using the circle equation. Chen and Chung [4] improved Xu et al.'s method by using the randomized selection of four pixels. However, the randomized selection method has its own problems such as probability estimation, accuracy and speed that are dependent on the number of edge pixels. Yip et al. [5] proposed a method which has reduced the parameter dimension, but estimated the parameters of the circles based on local geometrical properties which often have suffered from poor consistency and location accuracy due to quantization error. To overcome these disadvantages, Ho and Chen [6] used the global geometrical symmetry of circle to reduce the dimension of the parameter space. The UpWrite method used the spot algorithm to produce the local models of the chosen edge pixels [7]. The chosen edge pixels are those in a circular neighborhood of the parameter radius r centered on the chosen edge pixels. Also there has been many works to make the CHT size-invariant [8]. Though these approaches reduced heavy computational burden, other problems have still remained.

With some prior knowledge about an image, we can simplify the CHT and reduce the algorithm's difficulties according to especial features of the problem. Use of edge orientation information was first suggested by Kimme et al. [9], who noted that the edge direction on the boundary of a circle points towards or away from the circle's center. This modification reduced computational requirements as only an arc needed to be plotted perpendicular to the edge orientation at a distance r from the edge point. In the limit, arcs may be reduced to a single point in the accumulator space. Minor and Sklansky [10] extended the use of edge orientation by plotting a line in the edge direction to detect circles over a range of sizes simultaneously. This has an additional advantage of using a two rather than a three-dimensional parameter space. The method can be further extended to the detection of circle-like shapes (compact convex objects, or blobs).

The FCD method [11] got the main idea of edge orientated methods, and presented an algorithm to find circular shapes that were totally brighter or darker than their background. According to the edge oriented methods, the edge direction on the boundary of a circle points towards or away from the circle's center. The condition of being totally darker or brighter than background forces all edge directions of a circle to be outward or inward, so the FCD can use the symmetry property of the gradient vectors to find vector pairs. These founded vector pairs are used to improve the circle detection algorithm. In this paper, we present a method based on certainty factor concept to improve the FCD performance. For each founded vector pair, some certainty factors are considered and final decision about location of founded circles is made according to these parameters. Using such certainty factors, the FCD is speed up with more accuracy and more robustness against noise.

The rest of the paper is organized as follows. Section 2 describes the FCD algorithm in details and section 3 presents improved method. Section 4 shows experimental results comparing with the CHT and original version of the FCD. Finally, in section 5, we describe the conclusion and our plans for future work.

FAST CIRCLE DETECTION USING GRADIENT VECTOR PAIRS

In this section, we present a fast circle detection algorithm based on gradient vector pairs. Suppose that we have a dark circle on a bright background[1], as shown in Figure 2.a. The following paragraphs describe the major steps of our algorithm.

The first step is calculating the gradient of the image. The gradient vectors of the circle we search for are in the form shown in Figure 2.b. These vectors' directions are outward the circle, because the circle is darker than its background. Due to the symmetry of circle, for each gradient vector there is another gradient vector in its opposite direction. We call these vectors vector pair. As shown in Figure 3.a, a specific vector V_1 is paired with a vector V_2 if the following two conditions are satisfied:

(i.) Angle α, defined as the absolute difference between directions V_1 and V_2, should be nearly 180 degrees.

(ii.) Angle β between the line connecting P_2 to P_1 (the bases of V_2 and V_1) and the vector V_1 should be nearly 0 degree[2] (This means $\overrightarrow{P_2P_1}$ that should be in the same direction as V1).

The second step of the algorithm is applied to find all vector pairs according to the above conditions in the gradient image. The second condition considerably removes noise by filtering useless vectors. As Figure 3.b shows, vectors V1 and V2 are not assumed as a vector pair due to condition (ii); however they satisfy condition (i).

To increase the speed of pair matching, vectors are sorted according to their directions. So, for each specific vector, vectors with opposite direction can be found fast and easily.

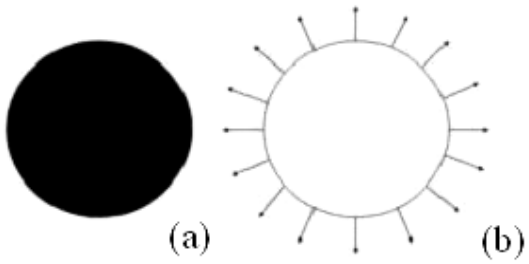

Figure 2. (a) A black circle in white background, (b) Gradient vectors of (a)

In the third step, a candidate circle is considered for each pair of vectors. Such a circle has its center at the midpoint of P_1 and P_2, and its radius is equal to half of the distance between P_1 and P_2. Figure 3.a shows such a candidate circle in dashed lines. In special cases, if the approximate radius of the desired circle is known, a third condition can be used to filter out those vector pairs whose distances are outside the range of the expected values. This can improve the performance of algorithm significantly.

In the fourth and final step, the desired circles are extracted from the candidate circles produced in the previous step. There are two ways to do this. One way is employing a 3-dimensional accumulator matrix to count the occurrence of quantized circles. Then, the desired circles can be found by searching for local maxima in such a space. This is just like the classic CHT approach.

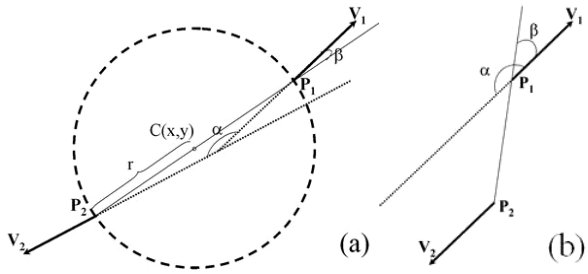

Figure 3. (a) Pair vectors (V_1 & V_2) and their candidate circle, (b) vectors rejected by condition (ii)

As the candidate circles are known, a second and easier approach can be used to find the desired circles. Candidate circles are saved as a set of triples (C_x, C_y, r). These triples are then clustered using Euclidian distance between them. The means of clusters then specify the desired circles. The method reduces the space complexity and optimizes the entropy of the saved data. Also, prior knowledge about the number of the circles in the image can be used to get better results. In our algorithm, we use the second approach.

[1] We can assume this without loss of generality because if the circle is brighter than its background, we can work on the negative image or simply reverse the direction of vectors.

[2] Or it should be in the opposite direction of V_2, because they are nearly parallel according to condition (i.)

Adjusting parameters of algorithm is critical and depends on image features and statistics. By increasing α and β, more pair vectors will be found. This may lead to better result (robustness against noise) or worse result (Finding more wrong pair vectors). So adjusting these parameters is an art in each application.

To improve the algorithm performance in real applications, some preprocessing on the input image may be necessary. As mentioned earlier, the algorithm searches for circles that are brighter or darker than their background. To obtain such image, some preprocessing can be done based on the problem features. Figure 4 shows an output result of the original FCD when 25% pepper-salt noise is applied to the image.

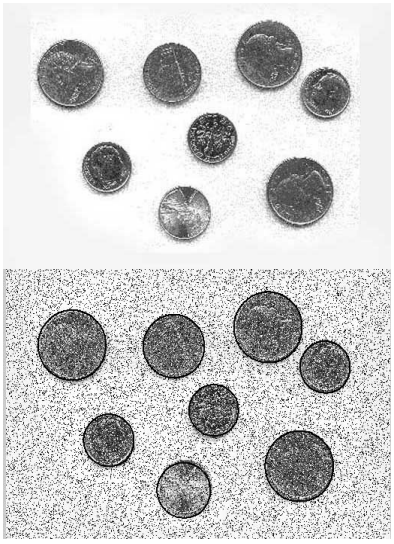

Figure 4. Output result of the FCD when 25% pepper-salt noise is applied to the image

THE FCD IMPROVEMENT USING CERTAINTY FACTORS

In this section, we describe how the performance of the FCD algorithm can be improved using certainty factors.

According to the original FCD, two vectors make a pair if they satisfy conditions i and ii of previous section. In real applications, these conditions are rarely satisfied. So a range of acceptable values should be used for α and β. If the deviations of α or β from their ideal value (180 and 0 degrees) become more than a threshold value, the vector pair is omitted and if both parameters place in range, the candidate circle is considered. In contrast with this binary decision, two certainty factors can be considered according to mentioned angles:

$$C_\alpha = \exp(-\frac{(\alpha-180)^2}{\sigma_\alpha^2}) \text{ and } C_\beta = \exp(-\frac{\beta^2}{\sigma_\beta^2}).$$

These factors show the rate of satisfaction of i and ii conditions and can be used to control the behavior of the algorithm. Parameter σ can be used to adjust the effect of acceptable tolerance according to problem attributes.

Also, symmetry property of circle can be used to improve the performance of the FCD. By increasing the noise in the image the probability of matching of two random vectors as a vector pair increases. These wrong vector pairs increase error rate. Also, when the number of candidate circles is increased the clustering time is growth as well. Without loss of generality assume that the center of the candidate circle produced by v1 and v2 is placed at origin. According to figure 5, if a vector pair founded (suppose the bases of this vector pair are p1(x,y) and p2(-x,-y)), then 6 other points p3(y,x), p4(-y,x), p5(-x,y), p6(-y,-x), p7(y,-x) and p8(x,-y) should be placed on the same circle as well.

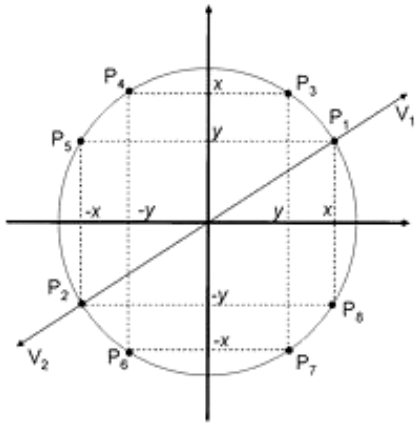

Figure 5. The pair vector and its related 6-points

To reduce the effect of noise, we can verify the existence of other 6 points in edge map of the image. If number of founded points is less than a specified threshold then the vector pair is omitted. In this way, random vectors that are not really placed on a circle are discarded. By omitting wrong candidate circles the number of candidate circles is reduced so the clustering step can be execute faster. If number of founded edge points is more than specified threshold then a candidate circle is considered just like the standard FCD. The number of founded points (n) also used to produce another certainty factor for the candidate circle denoted by C_8:

$$C_8 = \exp(-\frac{(n-8)^2}{\sigma_8^2})$$

In implementation, if either C_a, C_b, or C_8 become negative we omit the vector pair otherwise tree certainty factors used to make a final certainty factor according to the following formula:

$$CF = iC_\alpha + jC_\beta + kC_8$$

Parameters i, j, and k can be used to form different formulas according to problem features. For example for almost hidden circles, k parameter should considered near zero and for finding circles in noisy images, i parameter should be

decreased. For the best adaptation to special problems, parameters, i, j, and k can be learned.

In clustering phase, to extract the desired circles, a weighted averaging is used based on certainty factors. Using weighted averaging causes more accuracy for the algorithm.

RESULTS

To test our proposed method, a database of about 100 different images is used. Each image contains one or more circles with different radiuses and some cases contain corrupted circles. The test images are collected from various real applications, with various subjects and also contain few hand made samples.

We structured our samples of database into four groups evaluate our algorithm more effectively than using random samples. The first group contained 100 original images. In the second group, binary images were produced from the original images by a simple gray level thresholding. Some pepper and salt noise and standard Gaussian noise were added to the original images to produce the third and the fourth categories. Two datasets with the same images (in the four groups) and with different image sizes (256 X 256 and 512 X 512) were produced and the evaluation was done on both of them to measure the effects of the increasing image size on the algorithm's performance. Also, the CHT (improved version) and the FCD algorithms were implemented to compare them with our proposed algorithm. The CHT is not a fast method, but it is a standard method. Almost all papers that presents a circle detection algorithm, implements the CHT and compare presented method with it. For the FCD versions both α and β parameters are set to 5 degree and gradient vectors are calculated using sobel operator and averaged in 5x5 windows and finally threshold by 30%. The All algorithms were implemented in Matlab 6.1, and the experiments were performed using a PC equipped with 1.8MHz Pentium IV processor and 512MB RAM. The average time of 10 trails that each algorithm used to produce the result for each image size and each image group is shown in Table 1.

Table 1. The results of execution time of the circle detection approaches (time is in second)

Image size				
256×256	Original	Binary	Pepper-Salt	Gaussian
CHT	205	172	319	262
FCD	0.30	0.26	0.32	0.33
FCD-CF	0.21	0.18	0.21	0.21
Image size				
512×512	Original	Binary	Pepper-Salt	Gaussian
CHT	1711	1567	2073	1932
FCD	1.58	1.44	1.66	1.60
FCD-CF	1.25	1.19	1.30	1.30

From Table 1, we find out that for 256x256 images, the proposed method is about one thousand times faster than the CHT and nearly 1.2 times faster than the original FCD. For 512x 512 size images, the proposed method still 1.2 times faster than the original FCD, and for the CHT it becomes more than 1600 times faster.

To compare accuracy of the FCD and proposed method, fifty different images were selected and the circle boundaries on them were determined manually. The error rate was calculated in three ways: Distance of the estimated centers from actual centers, difference between estimated radius and actual radius, and percentage of overlap of circles' surfaces.

Table 2 shows the final result of accuracy tests. Distance between centers and difference of the radii are normalized by the actual radius.

Table 2. The results of accuracy tests of the FCD

	Centers	Radii	Overlap
FCD	0.04	0.07	0.93
FCD with CF	0.02	0.04	0.96

Another evaluation is done to comparison the resistance of the FCD and proposed algorithm against noise. In this evaluation, the density of the pepper and salt noise was increased from 0 to 80 percent for each input image. Then error rates of these three approaches were calculated.

Results of this experiment show that proposed method resists against noise until 30% but the FCD error rate increases before 25% density. In this case the CHT just resists until 10%. After this threshold, the error rate increases exponentially for each approach. The CHT and FCD are totally failed after 30% and 52% noise but the improved method resists against noise until 70%. Figure 6 draws the error rates versus noise density for each approach.

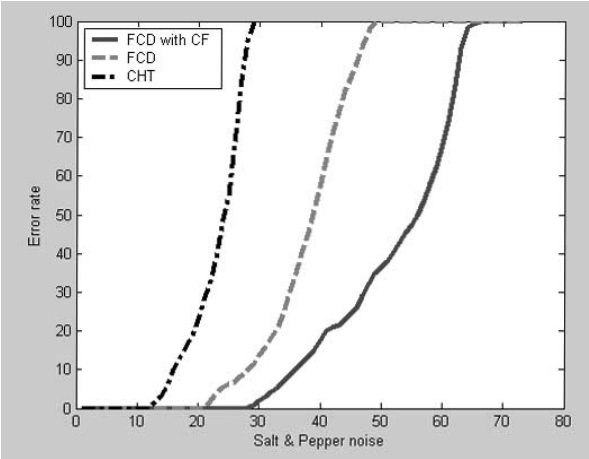

Figure 6. Resistance of the FCD and proposed algorithm against pepper-salt noise

CONCLUSION AND FURTHER RESEARCH

In this paper, we presented an improved version of a size invariant method to find circles that are totally brighter or darker than their backgrounds called Fast Circle Detection (FCD) method. The original idea is based on the symmetry of the gradient pair vectors on such circles. The improved method uses certainty factors for each vector pairs based on the parameters of the algorithm (α, β, and predicted edge points) to increase accuracy of the FCD algorithm.

The experimental results show that the proposed method is 1.2 times faster than the FCD and about a 1600 times faster then the CHT in case of 512x512 resolution images. The proposed method has better resistance against noise in comparison to the FCD and its accuracy is not affected until 30% pepper-salt noise is applied to the image (5% improvement in comparison to the original FCD). Also, the proposed method is more accurate than the original FCD. The improved method used for iris localization step in iris recognition applications, and the results show a significant improvement. Figure 7 shows an output proposed method for iris localization purpose [12].

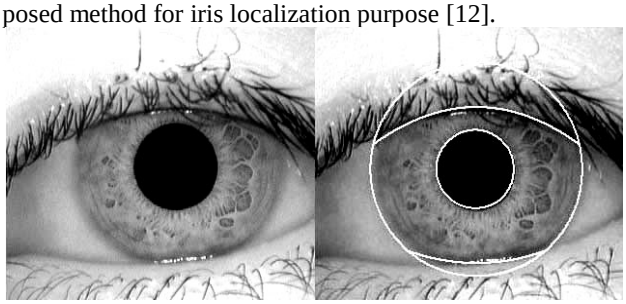

Figure 7. Output result of the FCD with certainty factors for iris localization

We plan to use the FCD and its improved version in other industrial and medical applications. Also, we plan to use the proposed algorithm to find known ellipses which have known ratio of diameters and directions. Figure 8 shows a simple result of the FCD to detect a known ellipse in MRI images of brain for fast brain boundary detection purpose.

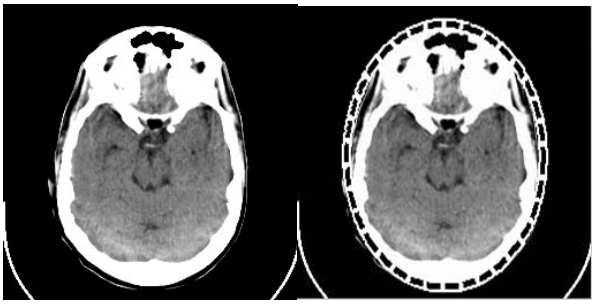

Figure 8. An example of ellipse detection for fast brain boundary detection in MRI images

REFERENCES

[1] Duda, R., and Hart, P., "Use of the Hough Transform to Detect Lines and Curves in Pictures", Communications of the ACM 15, pp: 11–15, 1975.

[2] Tsuji, S., and Matsumoto, F., "Detection of ellipses by a modified Hough transformation", IEEE Transactions on Computers, vol.C-27, no.8, pp: 777-781, 1978.

[3] Xu, L., Oja, E., and Kultanan, P., "A new curve detection method: randomized Hough transform (RHT)", Pattern Recognition Letter, vol.11, no.5, pp: 331-338, 1990.

[4] Chen, T., and Chung, K., "An efficient randomized algorithm", Computer Vision and Image Understanding, vol.63, no.83, pp: 172-191, 2001.

[5] Yip, R., Tam, P., and Leung, D., "Modification of Hough transform for circles and ellipse detection using a 2-dimensional array", Pattern Recognition, vol.25, no.9, pp: 1007-1022, 1992.

[6] Ho, C., and Chen, L., "A fast ellipse/circle detector using geometric symmetry", Pattern Recognition, vol.28, no.1, pp: 117-1995.

[7] McLaughlin, R., and Alder, M., "The Hough transform versus UpWrite," IEEE Trans, PAMI, vol.20, no.4, pp: 396-400, 1998.

[8] Atherton, T., and Kerbyson, D., "Size invariant circle detection", Image and Vision Computing, volume 17 pp: 795–803, 1999.

[9] Kimme, C., Ballard, D., and Sklansky, J., "Finding circles by an array of accumulators", Proc. ACM 18, pp: 120–122, 1975.

[10] Minor, L., and Sklansky, J., "Detection and segmentation of blobs in infrared images", IEEE Trans. SMC 11, pp: 194–201, 1981.

[11] Ajdari Rad, A., Faez, K., Qaragozlou, N., "Fast Circle Detection Using Gradient Pair Vectors", to be appear in 7th International Conference on Digital Image Computing: Techniques and Applications (DICTA'03), 2003.

[12] Ajdari Rad, A., Safabakhsh, R., Qaragozlou, N, "Fast Iris Localization Using Gradient Vector Pairs", submitted to First International Workshop on Biologically Inspired Approaches to Advanced Information Technology, Lausanne, Swizerland, 2004.

(This page left blank intentionally)

MACHINE VISION & ROBOTICS

(This page left blank intentionally)

Intelligent Image Processing Constraints for Blind Mobility Facilitated through Artificial Vision

Jason Dowling, Anthony Maeder, Wageeh Boles
School of Electrical and Electronic Systems Engineering, Queensland University of Technology
GPO Box 2434 Brisbane 4001, Queensland Australia
email j.dowling@qut.edu.au a.maeder@qut.edu.au w.boles@qut.edu.au

Abstract
This paper examines intelligent image processing constraints which may need to be considered for visual prosthesis development and proposes a display framework which incorporates context, task and alerts related to a scene. A simulation device to investigate this framework is also described. Mobility requirements, assessment, and devices are discussed to identify the functions required by a prosthesis, and an overview of state of the art visual prostheses is provided. Two main computer vision approaches are discussed with application to a visual prosthesis: information reduction and scene understanding.

Keywords
Visual prostheses, blind mobility, artificial human vision, image processing, computer vision.

1. Introduction

The partial restoration of sight for the blind is an exciting opportunity currently being pursued by a number of international research teams. Partial restoration can be achieved by the use of a camera to capture images, image processing, and then delivery of an electrical impulse to a component of the visual pathway in the human brain. In each case, when this signal is received the subject may perceive multiple points of light ('*phosphenes*'). Because it provides the link between camera and implant, image processing is an integral part of all clinical visual prostheses [1].

Most current mobility devices for the blind provide information in either tactile or auditory form. The two most widely used devices are the *long cane* and *guide dog*. However these devices have limitations: the long cane is only effective over a short range and a guide dog requires expensive training and maintenance. A number of *electronic travel aids (ETA's)* have also been developed over the past thirty years. Early versions of these devices relied on reflected ultrasound to detect obstacles. Later devices have also used laser and image information.

In sighted people, vision usually provides the important functions of mobility (such as avoiding obstacles), therefore it is reasonable to assume that an intelligent image processing (IIP) approach may also provide good mobility information. There are two broad classes of computer vision approaches which could be useful to the development of a visual prosthesis system: information reduction and scene understanding.

The purpose of this paper is to summarise mobility requirements and devices for the vision impaired, before identifying some IIP techniques and constraints that may be important for mobility requirements. A display framework and proposed simulation device are then described.

2. Mobility

Mobility is a person's ability to travel between locations "gracefully, safely, comfortably and independently" [2]. Blind mobility requires skill, effort and training. Mobility problems for a blind person can be caused by changes in terrain and depth (stairs, kerbs); unwanted contacts (bumping); and street crossings (which involve judging the speed and distance of vehicles and may involve identifying traffic light colour) [3]. The most dangerous events for a blind or partially sighted person are drop offs (sudden depth changes, such as on the edge of a subway platform) and moving vehicles [4]. Making unwanted contact with pedestrians is also undesirable as it can be socially awkward and may pose a threat to a persons safety [5].

The assessment of mobility provides information on the effectiveness of different training techniques and also provides information for developers and consumers of mobility devices. The three main methods for assessing mobility are *self report questionnaires*, *field experiments* (such as walking through a shopping mall) and *artificial laboratories* (such as walking through an artificial maze). The latter two methods usually involve a count of the frequency of obstacle contacts by a subject and their walking speed (usually the percentage of preferred walking speed).

3. Mobility information presentation modes

Mobility devices generally provide information by tactile or auditory methods. A visual prosthesis approach is different as it uses a functioning component of the visual pathway, and does not overload another sense. These two presentation modes are summarised in table 1.

Table 1: Summary of blind mobility devices

Presentation Mode	Mobility Device	Sensory method
Conventional	Electronic Travel Aids	Most auditory, some tactile
	Guide dog	Tactile feedback
	Long Cane	Tactile and echolation
	Mobility Robot	Tactile/auditory
	Human Guide	Tactile/auditory
Visual Pathway	Retinal, Cortical and optic nerve prosthesis	Phosphene perception in subject

3.1. Conventional presentation

The most useful devices for mobility are the guide dog and the long cane. However, ambient sound is still important in blind mobility (as it is in sighted mobility). Ambient sound might be directional traffic noise, pedestrian crossing signals or voices. Non-visual information may also be tactile or olfactory.

The long cane provides a blind person with sufficient information for safe movement in the immediate environment. Mobility enhancement in a blind person after long cane training is often dramatic [6]. An additional benefit is the high visibility of the cane to drivers and other pedestrians. The most significant problem with the long cane is that it only provides two paces of preview. Because there is limited preview, a long cane user needs fast reaction times. A cane does not protect against obstacle collision to the upper part of the body (such as wall-mounted public telephones). There is also a risk of tripping other pedestrians with a cane [7].

Guide dogs also provide good mobility assistance by pulling in the same way that a human guide would. They are able to respond to hand and voice signals and are trained to avoid obstacles, prevent veering in street crossings, stop if there is a dangerous situation and intelligently disobey commands that are not safe. A dog may remember common landmarks (such as a particular shop door). However guide dogs are expensive (~AUS$25,000) and require a person to be comfortable with dogs. A guide dog user also needs to be physically fit and prepared to maintain the dog [8].

Although a number of ETA's have been developed, none has achieved widespread market penetration. These devices often provide little benefit in mobility, require a long period of training are expensive and are cosmetically unattractive [6]. Ultrasound based devices (which generally provide auditory information) include the SonicTorch, SonicGuide and SonicPathfinder. More recent ultrasonic devices include the Navbelt and the Guidecane [9]. A laser cane ETA has also been developed, which uses reflected light energy to provide both tactile and auditory information [10]. The Guide Dogs for the Blind Association of Queensland provide a low cost, handheld ultrasound device, the Miniguide, to visually impaired clients. A promising new ultrasound device, the UltraCane, acts as a standard cane while providing tactile information about head and chest level obstacles in the environment.

The vOICe is the only commercially available ETA which uses an image processing approach. This ETA presents an acoustic representation of images to a blind person [11]. This portable device captures image data using a head mounted camera, processes this information (using a 64x64 pixel array) and provides an auditory representation once per second.

Another approach to blind mobility and navigation involves adjusting the environment to provide useful information. Environmental accessibility for blind and the partially sighted can involve using a logical design layout (for example, stairs should be next to lift), assisting with visibility (for example, hand rails should have high contrast) and adequate lighting (which should be 50-100 % greater than that required for normally sighted) [12]. Useful mobility and navigation information can be provided by locating transmitters at strategic locations in the environment; a blind person can then use a handheld receiver to receive directional information about the landmark. This approach has been used in the 'Talking Signs' program which has been implemented in many locations in San Francisco [13].

3.2. Visual Pathway presentation

Human vision involves the focusing of light by the lens and cornea in the eye and the absorption of this light by photoreceptors in the retina. Electrical signals from these photoreceptors are then processed through a layer of bipolar and ganglion cells within the retina, before passing to the optic nerve [14]. The amount of information entering the eye is reduced considerably: there are over 120 million photoreceptors and only about 1 million ganglion cells. Most signals from the optic nerve pass through the lateral geniculate body to the visual cortex, where a spatial representation of the retinas appears to exist [15].

A visual pathway approach promises to provide significantly more information than a conventional mobility aid, without overloading another sensory channel. The three main approaches to visual prostheses involve a retinal implant (subretinal or epiretinal), an optic nerve cuff electrode and a cortical implant. Each approach has advantages and

disadvantages, and all have been successful in providing phosphene perception to subjects [16]. All methods share a common constraint: due to limitations of current technology there is a limited number of phosphenes that can be generated. Therefore it is necessary to develop methods for the optimal use of these phosphenes.

4. Relevant Intelligent Image Processing techniques

An image processing approach requires an image to be *captured* by a sensor and digitized. This image is then usually *pre-processed* to reduce noise. After these stages we can use an *information reduction* approach to provide essential environmental information, and/or attempt to *understand* objects in the environment. We provide a review of IIP as any visual prosthesis system will need to satisfy the same constraints.

4. 1. Information Reduction (low level vision)

Most existing visual prosthesis efforts are aimed at this level, which is concerned with the reduction or collapse of visual information. Operations on images at this level are designed to improve image saliency, or to emphasize features of particular importance or relevance, for example kerbs or walls. Cortical prosthesis research by the Dobelle Institute has found that *edge detection* and *image reversal* enhance the ability of subjects to recognize important scene components (such as doorways) [1].

Low level computer vision techniques commonly involve image filtering, edge detection and *segmentation* to identify objects within the image. At the information reduction level, a real world scene can be processed and presented in a more visually recognizable form, like a picture or cartoon. It might be sufficient for mobility purposes to have the outline and basic shapes of objects displayed. The reduction of visual information to cartoons, which typically use approximations of features to convey information, can be useful in representing objects using little information [17].

Another low level technique is *motion analysis*. The motion of a person provides visual information about movement relative to the environment and information about the depths of observed scene points [18]. Therefore the analysis of image sequences is desirable in a mobility device. One monocular method of judging depth is *motion parallax* which is used when objects are moving at equal speed: those which are closer to the observer seem to move faster. This information is used for mobility in sighted people (for example, when approaching a subway platform). The detection and location of *moving objects* (such as another person, car or dog) is also important for mobility.

In deciding on the most important features of a scene, it may be useful to consider which parts of a visual scene receive attention from sighted people. Models of the human visual attention have been developed to predict regions of interest in image sequences [19]. Moving objects, people and foreground/centrally located objects have been found to influence subject's attention.

Information reduction ranges from high quality images through to the lowest level of information (binary, low pixel resolution). Previous work at our facility [20], [21], has examined the use of various image processing techniques (such as enhancing edges, using different grey scales and extracting the most important image features) to identify a recognition threshold for low quality stationary images. These images are used to represent the limited number of phosphenes available to the subject (typically a 25x25 array). This research aims at providing a means of determining which parts of a visual scene to represent, and a model for inherent information to determine which visual elements of the scene should be presented for maximum perceptual intelligibility by the subject.

An early visually impaired mobility device which used an information reduction approach was developed during the 1980s. This system [22] used spoken output to describe the current scene. Two modes were provided: the first attempted to identify a safe route for the traveler, using an analysis of gray levels within the image. The second mode used scene analysis in an 'object-identification' mode. This mode attempted to use the aspect ratio of identified objects to categorize an object into three classes: long thin objects (such as a pole or mail box), square or circular objects (such as a pot hole), and large objects (such as a car or wall). When an obstacle was detected, the system provided a warning and asked the user to walk slowly. If object identification was required, the blind person would need to stop walking and wait while this processing took place. An image correspondence technique was used to identify drop-offs.

More recent research [23] has explored the use of edge detection to determine the positions of lines in an image. The grouping of these lines was then used to classify the object (such as a doorway). Paths were also identified using edges and the Hough transform was used to group these into straight lines. A clustering technique, similar to the Hough transform, was then used to find the dominant vanishing point to indicate the subject's direction of travel. A similar approach for a blind mobility device was investigated by the same authors in [24]. This device used stereo vision, combined with sonar for obstacle detection and kerbs. Once an image was captured, edge points were detected and the Hough transform used to locate parallel line

clusters (which were assumed to represent kerb or path information).

4.2 Scene Understanding (high level vision)

This level is concerned with *identifying features* and *extracting information*. The scene structure is still there to a degree, but it is idealised or reduced. An example application might be to identify a bus stop, fire hydrant or traffic light. It may also be useful to know the distance to the object (number of steps, or time at current walking speed).

Due to the limited number of phosphenes that can be generated by current technology, it may be better to present a symbolic representation. For example a small part of the grid (perhaps 5x5) could be used for information on obstacle locations in the current environment. Auditory information could also be provided in natural language. A scene description mode could be useful (similar to [22]).

Object interpretation depends on knowledge of possible objects, and might also depend on context (for example, an outdoor scene versus a home environment. For orientation, it would be useful if a prosthesis system using a scene understanding approach could 'learn' to recognize new objects – for example, an image of a particular type of building (tram stop) could be added to the existing object knowledge base.

Some recent blind mobility research has attempted to recognize particular objects in a scene. The identification of stair cases was addressed in [25]. This research used a texture detection method (using Gabor filters) to locate distant stair cases. Once a person had moved close enough to the stairs, they were then detected by searching for groups of concurrent lines. The intensity variation was then used to partition the convex and concave lines. Homography with some search criteria was then employed to recover the vertical rotation and slope of the located stair case. Although reasonable results were achieved, the approach was found to be slow and not suitable for real-time applications.

5 Visual prosthesis constraints

This section identifies a number of constraints which affect visual prosthesis development:

Number of Phosphenes. Current technology limits the number of phosphenes that can be provided to a patient. Additionally, the size, shape and brightness of phosphenes are not predictable, although recent work in a 4 x 4 retinal prosthesis shows promise in overcoming these problems [26]. The information reduction associated with a 25 x 25 image is demonstrated in figure 2a.

Figure 1a: Original street scene image

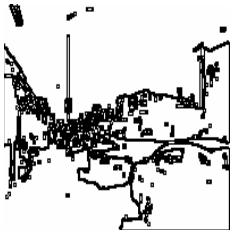

Figure 1b: Street scene with edges detected and binary

Figure 2a: Subsampled 25 x 25 representation of the street scene in figure 1b.

Figure 2b: The reduced 25 x 25 representation with an 'obstacle on right hand side' alert activated.

Real-time processing: A visual prosthesis system needs to perform in real-time. However, this has been problematic for other image based mobility systems, particularly those that are stereo-vision based. One way of providing real-time processing may be to restrict the field of view of the camera, although this would restrict the amount of preview (or time to anticipate problems) available to a blind traveler. Movement of the subject (egomotion) is an additional image processing overhead, as the camera will need to be attached to the person's body.

Integration/Prioritization : The integration of different functions is a challenge. Dangerous features of the environment, such as moving objects, obstacle detection and sudden changes in depth, should be displayed before less important information. Figure 2b shows a sample obstacle warning in a display, where the right half of the display is highlighted.

Scene type: Scene understanding depends to a large extend on context. An intelligent image processing approach would consider the type of context in recognizing objects. Context information is often defined by previous images, which suggests an image sequence approach. Different display and processing modes will probably be required for a prosthesis system to cope with differences in operational environments.

Device simulation. Currently it is necessary to use a visual prosthesis simulation with normally sighted subjects to test the effects of different IIP approaches on mobility. The results of these investigations may not generalize to actual visual prosthesis patients.

Standard set of image sequences: A constraint on the development of both the information reduction and scene understanding approach for mobility is the lack of a standard set of images/image sequences for evaluation and comparability of methods: an approach which has been successfully applied in the field of Information Retrieval [27]. The benefit of a standard is that different algorithms could be objectively tested against each other and measured for efficiency and effectiveness. Sample image sequences might be captured from a subject walking at normal pace towards different obstacles, over different drop-offs or towards a door. Different environments (such as indoors/outdoors) and lighting conditions could also be included.

6. Proposed mobility display framework

The display from an 'intelligent' visual prosthesis (or simulation) should process different information reduction and scene understanding information depending on the type of scene. For mobility purposes this display depends on three main dimensions (see figure 3) of the current scene:

- ***Context:*** The type of scene can affect the type of IIP required. For example, there may be a greater need for information reduction in a crowded shopping mall than a suburban street.
- ***Task:*** Different information is required depending on the current task. A road crossing task may emphasize a straight path to the opposite kerb (to prevent veering), whereas a task involving identifying a set of keys on a cluttered table may involve zooming or object recognition.
- ***Alert:*** The system needs to continually investigate any hazardous features of the current scene. These alerts, such as an approaching tree branch (obstacle detection) or descending stairs (drop off) need to run as background tasks, and interrupt the current display when required.

Common abstract classes for these dimensions could be developed to reduce decision processing requirements. For example an indoor home and indoor office context could both be assigned to an 'indoor room' class.

7. Simulation system

To investigate the mobility display framework, we are developing a visual prosthesis simulation. This portable head mounted device which consists of a Personal Digital Assistant (PDA) and an attached digital camcorder. Currently the PDA display is used to present the phosphene simulation. A normally sighted subject can then wear the device and be assessed on various mobility tasks under different contexts, alert scenarios and IIP conditions. A sheet of cloth is used to limit the subject's visual information to the PDA display. The proposed simulator components are listed in figure 4.

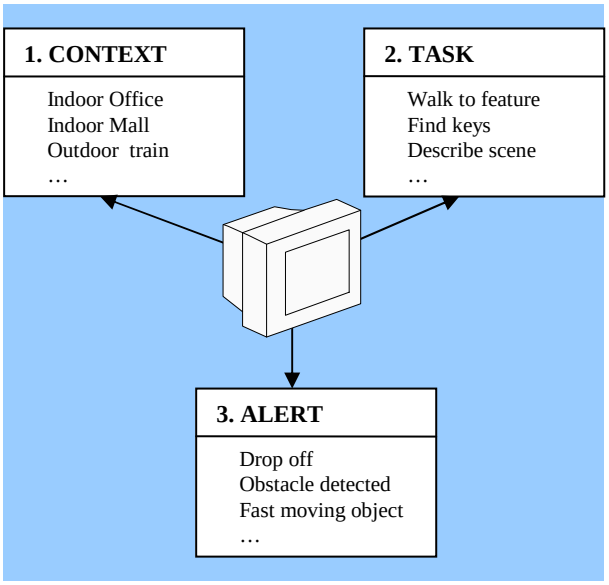

Figure 3: Proposed mobility display framework

Input: PDA digital camera (LifeView FLYCAM-SD)
Processor: Intel XScale PXA255 400 Mhz. (HP iPAQ H5550)
Operating System: Microsoft PocketPC 2003
Simulation display: PDA display (HP iPAQ H5550)
Software Development: MS embedded visual C++, Intel Integrated Performance Primitives

Figure 4: Proposed simulation components

A similar simulation approach was used in [28] where the minimum number of phosphenes required for adequate mobility was investigated. The 'pixelised vision simulator' device consisted of a video camera connected to a monitor in front of the subject's eyes. A perforated mask was placed on the monitor to reproduce the effect of individual phosphenes. The artificial environment consisted of an indoor maze which contained paper column 'obstacles'. Walking speed and frequency of contact were used as dependant variables. This research found that a 25x25 array of phosphenes, with a field of view of 30^{o} would be required for a successful device.

6. Conclusion

A successful visual prosthesis should result in increased mobility performance. Evidence from previous research suggests that the objective assessment of mobility is important in developing and comparing different devices and techniques. In this paper we have described IIP techniques and constraints related to visual prosthesis development. We have also presented a framework and simulation device for further investigation into how IIP techniques can en-

hance the effectiveness of visual prostheses. Experimental work exploring the benefits of this framework is currently under way.

ACKNOWLEDGMENTS

This research was supported by the Australian Research Council and Cochlear Ltd.

REFERENCES

[1] W. Dobelle, "Artificial Vision for the Blind by Connecting a Television Camera to the Brain," *ASAIO Journal*, vol. 46, pp. 3-9, 2000.

[2] C. A. Shingledecker and E. Foulke, "A human factors approach to the assessment of mobility of blind pedestrians," *Human Factors*, vol. 20, pp. 273-286, 1978.

[3] D. Geruschat and A. J. Smith, "Low vision and mobility," in *Foundations of Orientation and Mobility*, B. B. Blasch and W. R. Weiner, Eds., 2nd ed. New York: American Foundation for the Blind, 1997.

[4] D. G. Pelli, "The visual requirements of mobility," in *Low Vision: Principles and Applications*, G. C. Woo, Ed. New York: Springer-Verlag, 1986, pp. 134-146.

[5] D. Geruschat, K. A. Turano, and J. W. Stahl, "Traditional Measures of Mobility Performance and Retinis Pigmentosa," *Optometry and Vision Science*, vol. 75, pp. 525-537, 1998.

[6] A. Dodds, *Mobility Training for Visually Handicapped People: A Person-Centred Approach*. London: Croom Helm, 1988.

[7] L. W. Farmer and D. L. Smith, "Adaptive technology," in *Foundations of Orientation and Mobility*, B. B. Blasch and W. R. Weiner, Eds., 2nd ed. New York: American Foundation for the Blind, 1997.

[8] R. H. Whitestock, L. Frank, and R. Haneline, "Dog guides," in *Foundations of Orientation and Mobility*, B. B. Blasch and W. R. Weiner, Eds., 2nd ed. New York: American Foundation for the Blind, 1997.

[9] S. Shoval, I. Ulrich, and J. Borenstein, " Computerized Obstacle Avoidance Systems for the Blind and Visually Impaired," in *Intelligent Systems and Technologies in Rehabilitation Engineering*, H. N. L. Teodorescu and L. C. Jain, Eds.: CRC Press, 2000, pp. 414 - 448.

[10] A. Dodds, *Rehabilitating Blind and Visually Impaired People*. London: Chapman and Hall, 1993.

[11] P. B. L. Meijer, "Vision technology for the totally blind," http://www.seeingwithsound.com/, 2003.

[12] B. L. Bentzen, "Environmental accessibility," in *Foundations of Orientation and Mobility*, B. B. Blasch and W. R. Weiner, Eds., 2nd ed. New York: American Foundation for the Blind, 1997.

[13] Talking Signs Inc, "Talking Signs Infrared Communications System," http://www.talkingsigns.com/, 2003.

[14] T. N. Cornsweet, *Visual Perception*. New York: Academic Press, 1970.

[15] R. L. Gregory, *Eye and Brain: The Psychology of Seeing*, 5th ed. Tokyo: Oxford University Press, 1998.

[16] E. Margalit, M. Maia, J. D. Weiland, et al., "Retinal Prosthesis for the Blind," *Survey of Ophthalmology*, vol. 47, pp. 335-356, 2002.

[17] M. C. Fairhrust, *Computer Vision for robotic systems*. New York: Prentice Hall, 1988.

[18] V. S. Nalwa, *A guided tour of computer vision*. Reading, Massachusetts: Addison-Wesley, 1993.

[19] W. Osberger and A. Rohaly, "Automatic Detection of Regions of Interest in Complex Video Sequences," in *Human Vision and Electronic Imaging VI*, vol. 4299. Bellingham, USA: SPIE - The International Society for Optical Engineering, 2001, pp. 361-372.

[20] J. Boyle, A. Maeder, and W. Boles, "Static Image Simulation of Electronic Visual Prosthesis", Proceedings of the 7th Australian and New Zealand Intelligent Information Systems Conference, Perth, pp 85-88, 2001.

[21] J. Boyle, A. Maeder, and W. Boles, "Can environmental knowledge improve perception with electronic visual prostheses?" Proceedings of the 4th World Congress on Medical Physics and Biomedical Engineering, Sydney, 2003.

[22] J. T. Tou and M. Adjouadi, "Computer Vision for the Blind," in *Electronic Spatial Sensing for the Blind*, D. H. Warren and E. R. Strelow, Eds. Dordrecht: Martinus Nijhoff Publishers, 1985, pp. 83-124.

[23] M. Snaith, D. Lee, and P. Probert, "A low-cost system using sparse vision for navigation in the urban environment," *Image and Vision Computing*, vol. 16, pp. 223-292, 1998.

[24] N. Molton, S. Se, M. Brady, D. Lee, and P. Probert, "Robotic Sensing for the Partially Sighted," *Robotics and Autonomous Systems Journal*, vol. 26, pp. 185-201, 1999.

[25] S. Se and M. Brady, "Vision-based Detection of Staircases," Proceedings of the Fourth Asian Conference on Computer Vision ACCV 2000, pp. 535-540, Taipei, January 2000.

[26] M. S. Humayun, J. D. Weiland, G. Y. Fujii, R. Greenberg, R. Williamson, J. Little, B. Mech, V. Cimmarusti, G. Van Boemel, and G. Dagnelie, "Visual perception in a blind subject with a chronic microelectronic retinal prosthesis," *Vision Research*, vol. 43, pp. 2573-2581, 2003.

[27] National Institute of Standards and Technology, "Text Retrieval Conference (TREC)," http://trec.nist.gov/, 2003.

[28] K. Cha, K. Horch, and R. Normann, "Mobility Performance with a Pixelised Vision System," *Vision Research*, vol. 32, pp. 1367-1372, 1992.

An Efficient Strategy for Implementing Iterative Area Openings Using the Max Tree

Xiaoqiang Huang, Mark Fisher, Yanong Zhu, Richard Aldridge, Dan Smith,
School of Computing Sciences, University of East Anglia
Norwich, United Kingdom, NR4 7TJ
Email: xq.huang@uea.ac.uk, {mhf, yz, rva, djs}@cmp.uea.ac.uk

Abstract

Area opening is an important morphological connected set operator that features in removing upper level sets from an image whose area properties are smaller than a threshold λ. Existing algorithms found in the literature that implement the area opening operator are based on either priority queues, the max tree or the union-find approach. In this paper we explore the advantages of using the max tree based approach for iterative area opening. Iteratively applying an area opening is the central idea underpinning all scale based image decompositions. An efficient implementation strategy for iterative area opening is therefore very important if scale based image processing algorithms are to be successfully applied in real time computer vision applications. This paper builds on recently published work comparing approaches for implementing area openings, and improves on the method proposed for image reconstruction via a max tree. Experimental results are presented that show the new approach proposed in this paper obtains a performance gain of 25% with images of reasonable big size (320×256).

1 Introduction

Connected set operators [9, 8, 1] are fundamental to many non-linear morphological image filters having a number of desirable properties, most importantly preservation of shape or the scale casualty [4]. A connected set operator only deals with flat zones (largest connected set of the space where the image grey-level is constant) in the image. When a connected operator is applied to an image, each flat zone will either be merged to one of its neighbouring flat zones or be left intact. As this does not introduce any new contour, it simplifies the image as well as preserving the scale casuality.

Area opening [11] (area closing as its dual operator) is one such operator that features in removing connected upper level sets (brighter intensity image objects) whose area properties are smaller than a threshold λ. Examples of applying the area opening operator to both a binary and a gray scale image are shown in figure 1 and figure 2, respectively. Figure 1 illustrates the area opening operator removes only those flat zones whose area properties are smaller than seven pixels, leaving the other larger regions untouched. From a signal processing point of view, area opening and area closing operators form a pair of non-linear filters.

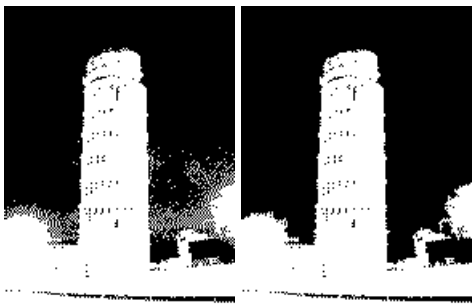

(a) the original image (b) the image after area opening

Figure 1. An example of binary area opening: image size = 144 $\times$ 192, λ = 7

Binary area opening is based on binary connected opening. Let the set $X \subseteq M$ denote a binary image with domain M. The binary connected opening $\Gamma_x(X)$ of X at point $x \in M$ yields the connected set of X containing x if $x \in X$ and $\emptyset$ otherwise. Thus Γ_x extracts the connected set to which x belongs, discarding all others.

The binary area opening can now be defined as:

(a) the original image (b) the image after area opening

Figure 2. An example of gray scale area opening: image size = 160 $\times$ 128, λ = 100

Definition 1. Let $X \subseteq M$ and $\lambda \geq 0$. The binary area opening of X with scale parameter λ is given by

$$\Gamma^a_\lambda(X) = \{x \in X | Area(\Gamma_x(X)) \geq \lambda\}. \quad (1)$$

The binary area closing can be defined by duality

$$\Phi^a_\lambda(X) = [\Gamma^a_\lambda(X^c)]^c. \quad (2)$$

The definition of an area opening of a gray-scale image f is usually derived from binary images $T_h(f)$ obtained by thresholding f at h. These are defined as

$$T_h(f) = \{x \in M \mid f(x) \geq h\}. \quad (3)$$

Definition 2. The area opening for a mapping $f : M \rightarrow \bar{R}$ is given by

$$(\gamma^a_\lambda(f))(x) = sup\{h | x \in \Gamma^a_\lambda(T_h(f))\}. \quad (4)$$

The gray-scale area closing ϕ^a_λ is defined by using a duality relationship similar to equation (2).

$$\phi^a_\lambda(f) = -(\gamma^a_\lambda)(-f). \quad (5)$$

The above definitions of area opening and closing are both adopted by Vincent et. al. [11] and Meijster et. al. [5]. Although morphological opening and closing are usually applied in the context of level sets the concept has been extended and generalised by Breen et. al. [2] to operate on other image attributes including length, diameter, radius, perimeter and other shape features.

Existing algorithms found in the literature that implement the area opening operator are based on either priority queues [11], the max tree [7] or the union-find approach [10]. Recently, Meijster et. al. [5] published a comprehensive comparison of these three algorithms and concluded that the union-find approach outperformed the other two algorithms in terms of CPU execution time and memory efficiency. However, this conclusion was based on the assumption that only one area opening/closing (at predefined λ) needs to be performed. In another words, the threshold λ should be known a-priori. In most scale based image decompositions one is interested in applying the area opening operator iteratively at varying scale λ to the same image. The experiments reported in section 4 concludes that in this case the method of area opening used by the max tree is a better option. This is because no matter how many times one wants to apply the area opening operator to the same image , the tree only needs to be constructed once. However, with the other two approaches area openings need to be re-computed whenever λ changes.

This paper discusses several issues relating to how to implement more efficiently iterative area openings via the max tree. The paper is organised as follows: Section 2 briefly describes the max tree and introduces an efficient way of building a max tree from an image. Section 3 describes two different strategies for iterative area openings in the context of a max tree and compares these two strategies theoretically. Experimental results, shown in section 4, confirm that the strategy adopted in this paper is more efficient than that proposed by other researchers. Conclusions are drawn in the final section.

2 The Max Tree

The max tree proposed by Salembier et. al. [7] is a multi-scale image representation formed by considering a hierarchy of connected upper level sets of pixels in an image. This representation was developed to deal with classical anti-extensive connected operators (such as area opening), as well a new ones, in an efficient manner. The max tree has been applied to image filtering, segmentation, tracking and information retrieval [6].

To understand the tree, the image is considered to be a 3D relief. The nodes of the tree represent the connected upper level sets for all possible gray-level values. The leaves of the tree correspond to the regional maxima of the image. The links between the nodes describe the inclusion (father-child) relationship of the connected sets. An example of a max tree created from a simple image is shown in figure 3 [1].

Three sub-problems need to be addressed before the max tree can be successfully constructed:

A. Find all possible tree nodes from the original image

B. Create the father-child relationships (links) between each possible pair of tree nodes

C. Create an efficient data structure to store information (region attributes) at nodes in the max tree.

[1] This figure is reproduced from [6]

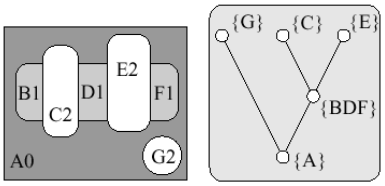

Figure 3. left: a simple image only with seven flat zones, right: the max tree for the image on the left

The first sub-problem has been successfully addressed by a recursive flooding algorithm proposed in [6], however a number of approaches to the remaining sub-problems have been described. The max tree built by Meijster et. al. adopted an array as the underlying data structure for the tree. The advantage of using the array is that it provides direct access to its elements i.e. the complexity of visiting a random element in an array is $O(1)$. However, there are two major problems in using an array as the underlying data structure. Because the size of a max tree is unknown before the tree is built using a static array is not memory efficient. For example, Meijster el. al. used the image size (number of pixels) to parameterise the length of their array. This approach is very wasteful of memory as in most cases the number of max tree nodes is far less than the number of pixels in the image. Secondly, when a node is deleted from the tree its corresponding element must also be removed from the array. Maintaining the array structure can become very cumbersome.

A more efficient data structure using a linked list associated with a hash table has recently been proposed by the authors of this paper [3]. The linked list provides dynamic allocation of computer memory thus the memory allocated for the max tree is just enough. However, the nodes in a linked list must be accessed serially so the complexity of visiting a random node in a linked list is $O(N)$. To overcome this problem a hash table is built immediately after the recursive flooding step. Using this table, the elements in the linked list are accessed directly so that the complexity is reduced to $O(1)$. The linked list structure also allows more flexible management of the tree nodes, they can be easily deleted and the memory recovered. Further details and experimental results comparing the efficiency of the technique to other published implementations may be found in [3].

Once the underlying data structure of the max tree has been decided, one needs to consider what information should be stored at a tree node. A minimal set of attributes should include

A. ID: node identification number

B. father's ID

C. a list of children IDs

D. a list of pixel coordinates

E. area: number of pixels belonging to a node

Obviously, each node in a tree needs a unique identification number. As a tree is a hierarchical data structure, each node is linked to its father and children nodes. The area attribute records the total number of pixels belonging to a node (i.e. the size of a granule or region). A node would also need to store information of pixels belonging to its support region so that an image can be reconstructed from a tree. Note that the list of children's ID and the list of pixel coordinates are also implemented by the linked list.

During the recursive flooding step of the creation of the max tree, Salembier et. al. use a number of arrays to store information important in later steps. The remainder of this section provides a brief overview of these attributes, however we refer the reder to [7] and [6] for a more complete description.

Salembier et. al. has proposed a very efficient way of finding scale tree nodes using a recursive flooding algorithm. The flooding algorithm begins at the root node of the tree (this is, the lowest gray value of the image) and recursively constructs each of the branches of the tree. They use hierarchical first-in-first-out queues of NG levels, with NG the possible number of gray levels (usually $NG = 255$). These queues are used to define the scanning and processing order of pixels comprising the image. An array $STATUS$ of the same size as the image is used to determine to which node a pixel belongs to. A pixel p with gray-level h belongs to the node C_h^k if $STATUS[p] = k$. Initially, all elements in $STATUS$ are set to $NOTPROCESSED(< 0)$. One array of G integers called $Number - Nodes(h)$ is used to store the number of max tree nodes detected so far at each gray level h. The values of Number-Nodes is updated whenever new nodes are created at gray-level h. A further array of G Boolean $Node - at - Level(h)$ stores at which levels below the current gray-level nodes have been detected in the path from current node to the root.

A node in a max tree is presented uniquely by C_h^k. For instance, a node presented by C_{20}^3 means this node's gray value is 20 and it is the third node found in the level of 20 during the recursive flooding algorithm. Note that a node C_h^k corresponds to a connected component P_h^k. However, C_h^k contains only those pixels in P_h^k which have gray-level h for the purpose of memory efficiency. In the next section, we proceed to explain why and how efficient iterative area openings can be achieve using the max tree.

3 Iterative Area Opening via the Max Tree

Both Salember [7] and Meijster [5] claimed that once a max tree of an image has been constructed, computing

an area opening at scale λ reduces to removing all nodes representing regions which have an area smaller than λ from the tree, and then reconstructing the image at the new scale.

The area opening operator is often applied as a non-linear filter for preprocessing an image. In most cases, one is interested in applying an area opening operator at different scales λ to the same image. In this case, it is beneficial to retain the max tree structure unchanged after computing an area opening operation. Thus, once a max tree of an image has been constructed, computing an area opening reduces to analysing the max tree nodes and reconstructing the opened image only by those tree nodes which have an area greater than or equivalent to λ.

The strategy proposed by Meijster et. al. to reconstruct the opened image is described as follows. Here, as stated earlier in section 2, a node C_h^k corresponds to a connected component P_h^k. However, C_h^k contains only those pixels in P_h^k which have gray-level h. For each node, Meijster et. al. check whether its area is smaller than λ. If so, its output gray level is set to that of its parent (which has already been assigned the correct gray). The output image O is made by visiting all pixels in the image, determining its node from the input image $I[p]$ and $STATUS[p]$, and assigning the output gray level of that node to $O[p]$. Their strategy actually consist of two steps. First, they assign the correct value for the output gray level of each node according to their area properties. Second, they assign each pixel the correct gray value according to the node the pixel belongs to. These two steps are processed serially.

We use different strategy to reconstruct the output image. The area property of a node is always smaller than that of its father (except the root node as it does not have a father node). Thus if a node is determined to have a smaller area value than the threshold λ, there is no need to check its descendant nodes at all. Therefore, we start checking the root node and proceed to recursively check each of its children nodes. During each check, the pixel in the output image O is assigned the gray level value of the node it belongs to as long as the area property of the current node is smaller the λ. When a node whose area property is greater than the λ is found, the current checking stops and all the pixels belonging to this node and its descendant nodes are output directly into the reconstruction image with the gray level value of the father node of the current node. With the help of the father-child relationships embedded in the tree, the descendant nodes of the current node can easily be visited in a recursive way.

The main differences between our strategy and that of Meijster et. al. 's is firstly not all max tree nodes are checked and secondly the checking and the reconstruction of the output image are done in a parallel way. Also the strategy is more memory efficient. Both strategies are data structure independent. In another words, both the strategies could work either using the array [5] or using the linked list combined with hash table [3] as the underlying data structures.

4 Experiments

Both the above strategies are evaluated in our experiments. The max tree is implemented by combining the linked list and the hash table as the underlying data structure [3]. The max tree and the iterative area opening operator are implemented in C++ using Microsoft Visual C++ IDE (version 6). The specification of the computer in which all experiments are carried out is as follows: OS: Windows 2000, CPU: Pentium 1.7GHZ, Memory: DDR 1.0G Bytes. The multi-resolution test images used in our experiments are shown in figure 4. Here, image 5 in figure 4 is the original image and the others are the resized versions of it. The time costs associated with area openings of these images that are reported as mean values found by repeating the experiment 100 times.

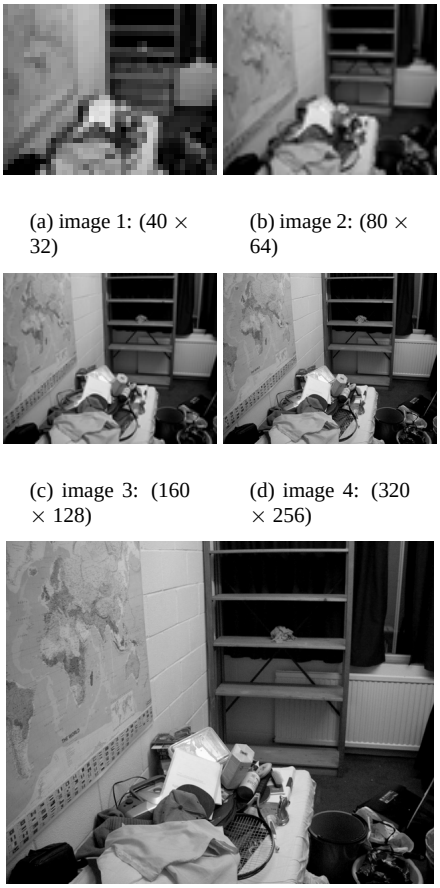

(a) image 1: (40 × 32) (b) image 2: (80 × 64)

(c) image 3: (160 × 128) (d) image 4: (320 × 256)

(e) image 5: (640 × 512)

Figure 4. The first group of our test images

Three sets of experiments have been conducted. The

aim of the first experiment is firstly to compare the performance of the two filtering strategies described in section 3 and secondly to find out if the iterative area opening via the max tree is scale independent. Image 4 in figure 4 is chosen for this experiment as its size ($320 \times 256 = 89920$) is reasonably large. The time cost for building the max tree and then computing an area opening ($\lambda = 100$) is 265 milli-seconds and 12.82 milli-seconds respectively (approximately 4 milli-seconds faster than that (16.7) by the strategy from Meijster et. al).

For a more comprehensive evaluation of the two strategies all the possible values for λ (from 1 to 81920) are computed (in steps of 10). For each of the 8191 different values of λ, area openings are found using both strategies and 9 time cost averages computed from blocks of 1000 results (the final group contains 191 samples). The nine values from each strategy are plotted in figure 5.

Each point in the plot stands for the average time cost of applying the area opening to the image with a limited range of λ. The range is defined between the values of a pair vertical lines, one is the line that the point just sits on, another is the nearest line to the left side of the first line. The mean time cost is shown in the Y axis of figure 5.

These experiments clearly show the strategy for implementing the iterative area opening reported in this paper runs about 25 percent faster than that from Meijster et. al. This is because the Meijister's strategy requires extra work to assign the correct output gray level to a pixel in the output image. In the new strategy the checking and reconstruction of the output image are done in a parallel way. In addition, we used a recursive approach to identify the descendant nodes of the current node, which is also very efficient. The iterative area opening implemented by both strategies is *almost* scale independent. However, there is a small (almost unnoticeable) variation of the time cost using either of the two strategies (see figure 5. Investigating the underlying reasons for these variations is part of our further work.

The comparison work done by Meijster et. al. showed that the union-find approach is the fastest algorithm to implement a one-off area opening and runs no more than two times faster than the max tree based approach (using their filtering strategy) for real images. However, when a max tree is built up, the time cost of recovering an area opening using the tree is almost negligible. For example it costs 265 milli-seconds to build the max tree for image 4 and the average time cost of recovering an area opening to image 4 takes no more than 13 mil-seconds. Thus we conclude that the max tree approach outperforms the union-find approach is the case of iterative area opening.

The aim of the second experiment is to see, if the value of λ is kept the same, how the time cost varies when the image size changes. Table 1 showed the results of our second experiment using the test images from figure 4 and λ set

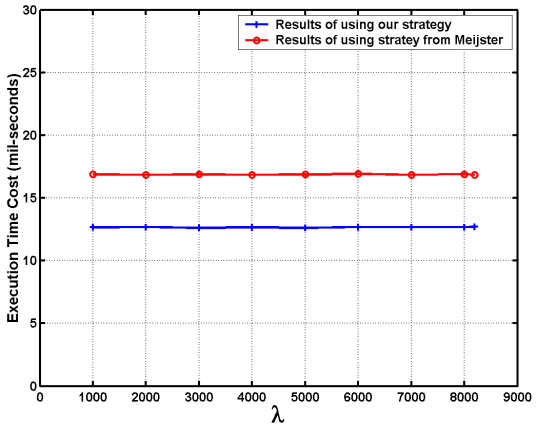

Figure 5. Our first experimental results

equal to 100. The results clearly show that both the strategies are not linear in terms of image size. However, our strategy is more linear than that from Meijster. This means that the performance gain of our strategy compared to that from Meijster et. al. should increase against image size. For instance, 25% performance gain is achieved with image 4 and 31% with image 5 using our filtering strategy (see table 1). Investigating the non-linearity is also part of our future work.

Strategy	Image Number				
	1	2	3	4	5
Ours	N/A	N/A	2.97	12.82	59.37
Meijster's	N/A	N/A	3.75	16.70	86.40

Table 1. Time cost (in term of milli-seconds) of applying area opening with $\lambda = 100$ to all images from figure 4.

More images (see figure 6) have been evaluated with different value of λ. The results also show that our strategy runs about 25% faster than Meijster et. al's strategy.

5 Conclusions and Further Work

In this paper, the term 'iterative area opening' has been developed to describe the operation that is at the heart of many morphological scale based decompositions. Based on our experiments, we proposed a new strategy for reconstructing the image at scale λ and compared this to that recently published by Meijster. The experiments show that our strategy runs about 25 percent fast than that from Meijster with images of reasonable big size.

Fast implementation of iterative area opening is impor-

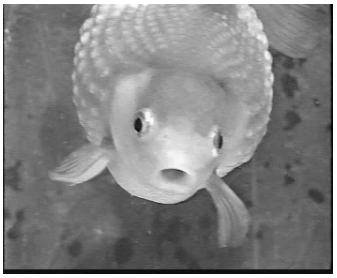

(a) image 1: (352 × 288)

(b) image 2: (384 × 256)

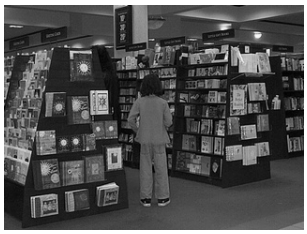

(c) image 3: (320 × 240)

Figure 6. The second group of our test images

tant for a number of real time application in the field of computer vision. These might include non-linear image filtering, image segmentation, and object based image coding.

So far only a small number of image sets have been tested in our experiments. We are planing to use more synthetic and real images of different complexities for our further experiments. Investigating the underlying reasons for those small variations in figure 5 and the non-linearity in table 1 is also worthy of further work.

References

[1] J. Bangham, R. Harvey, and P. Ling. Morphological scale-space preserving transforms in many dimensions. *Electronic Imaging*, 5(3):283–299, 1996.

[2] E. J. Breen and R. Jones. Attribute openings, thinnings, and granulometries. *Computer Vision and Image Understanding*, 64(3):377–389, 1996.

[3] X. Huang, M. Fisher, and D. Smith. An efficient implementation of max tree with linked list and hash table. In *Proceedings of International Conference on Digital Image Computing-Techniques and Applications (Accepted)*, Macquarie University, Sydney, Australia, December 2003.

[4] T. Lindeberg. *Scale-Space Theory in Computer Vision*. Kluwer Academic Publishers, 1994.

[5] A. Meijster and M. Wilkinson. A comparison of algorithms for connected set openings and closings. *IEEE Transactions on Pattern Analysis and Machine Intelligence*, 24(4):484–494, 2002.

[6] L. G. Ostermann. *Hierarchical Region Based Processing of Image and Video Sequences: Application to Filtering, Segmentation and Information Retrieval*. PhD thesis, Department of Signal Theory and Communications, Universitat Politecnica de Catalunya, Barcelona, Spain, April 2002.

[7] P. Salembier, A. Oliveras, and L. Garrido. Anti-extensive connected operators for image and sequence processing. *IEEE Transactions on Image Processing*, 7(4):555–570, 1998.

[8] P. Salembier and J. Serra. Flat zones filtering, connected operators and filters by reconstruction. *IEEE Transactions on Image Processing*, 3(8):1153–1160, 1995.

[9] J. Serra and P. Salembier. Connected operators and pyramids. In *Proceedings of SPIE Conference on Image Algebra and Mathematical Morphology*, volume 2030, pages 65–76, 1993.

[10] R. E. Tarjan. Efficiency of a good but not linear set union algorithm. *J. ACM*, 22:215–225, 1975.

[11] L. Vincent. Grayscale area openings and closings: Their efficent implementation and applications. In *Proceedings of the International Workshop on Mathematical Morphology and its Applications to Signal Processing*, pages 22–27, 1993.

Convolutional neural networks for robot vision: numerical studies and implementation on a sewer robot

Saeed Shiry, Matthew Browne
GMD-Japan Research Laboratory,
Collaboration Center,
2-1 Hibikino, Wakamatsu-ku,
Kitakyushu-city
saeed.shiry@gmd.gr.jp

Abstract

Convolutional neural networks (CNNs) impose constraints on the weights, and the connectivity of a standard neural network, providing a framework well suited to the processing of spatially or temporally distributed data. Although CNNs have been applied to face and character recognition, they have still received relatively little attention. The present paper applies the CNN architecture to an artificial test problem and to an application in robot vision. Autonomous sewer robots must independently navigate the sewer pipe system using information from sensors. One required component is robust detection of pipe joints and inlets using data from the omnidirectional sensor. A simple CNN is shown to robustly classify 36x36 pixel normalized video frame data on a limited validation set. The study indicates that machine learning methods for robot vision are feasible in terms of classification accuracy and online implementation.

1 Introduction

The goal of sewer robotics is to construct an autonomous robot capable of autonomously conducting sewer inspection tasks in sewerage systems [13]. Autonomous sewer robots are robots designed to perform automated inspection of sewer pipe systems. These robots must navigate independently the sewer pipe system using only available information from sensor systems. The task of accurately detecting and classifying relevant landmarks and features in the environment is an essential part of the navigation routines. Because video is often used for the inspection work, performing detection of cracks and other faults, it is useful if the same data can be utilized for landmark detection.

Paletta, Rome and Platz [13] used a multi-stage system for landmark detection based on video data. This involved an attention controller, pre-processing, feature extraction, probabilistic interpretation, and final classification. Early components of the system operate according to fixed *a priori* rules while latter components are data-driven and adaptive. A related work for sewer pipe navigation include procedures for navigating under uncertainty [12].

Other pattern recognition approaches designed for use in autonomous sewer inspection include application of neural architecture to segmentation of pipe joints [7] and reconstruction of a 3D model of the interior of the pipe based on video data [6].

In this work we follow the general viewpoint of [13], holding that interpretation of sensor images should be learnt from experience, and modeling of features of interest takes place in terms of their appearance to the agent. This is therefore a strong data-based perspective: analytical approaches towards constructing an objective model of the objects in question are rejected in favor of methods that directly learn from experienced sensor data. The present work attempts to take this perspective further, in attempting to implement an entirely trainable system. Thus, pre-processing and feature detection, transformation and classification modules are integrated into a single adaptive neural architecture. Convolutional neural networks (CNNs) form the theoretical basis that makes such an approach possible.

2 Convolutional Neural Networks

The term *convolutional network* (CNN) is used to describe an architecture for applying neural networks to two-dimensional arrays (usually images), based on spatially localized neural input. This architecture has also been described as the technique of shared weights or local receptive fields [16, 5, 14] and is the main feature of Fukushima's *neocognitron* [11, 10]. Le Cun and Bengio [4] note three ar-

chitectural ideas common to CNNs: local receptive fields, shared weights (weight averaging), and often, spatial downsampling. Processing units with identical weight vectors and local receptive fields are arranged in an spatial array, creating an architecture with parallels to models of biological vision systems [4]. A CNN image mapping is characterized by the strong constraint of requiring that each neural connection implements the same local transformation at all spatial translations. This dramatically improves the ratio between the number of degrees of freedom in the system and number of cases, increasing the chances of generalization [15]. This advantage is significant in the field of image processing, since without the use of appropriate constraints, the high dimensionality of the input data generally leads to ill-posed problems. To some extent, CNNs reflect models of biological vision systems [9]. CNNs take raw data, without the need for an initial separate pre-processing or feature extraction stage: in a CNN the feature extraction and classification stages occur naturally within a single framework.

In the CNN architecture, the 'sharing' of weights over processing units reduces the number of free variables, increasing the generalization performance of the network. Weights are replicated over the spatial array, leading to intrinsic insensitivity to translations of the input - an attractive feature for image classification applications. CNNs have been shown to be ideally suited for implementation in hardware, enabling very fast real-time implementation [17]. Although CNNs have not been widely applied in image processing, they have been applied to handwritten character recognition [5, 17, 3, 1] and face recognition [15, 9, 8]. CNNs may be conceptualized as a system of connected feature detectors with non-linear activations. The first layer of a CNN generally implements non-linear template-matching at a relatively fine spatial resolution, extracting basic features of the data. Subsequent layers learn to recognize particular spatial combinations of previous features, generating 'patterns of patterns' in a hierarchical manner. If downsampling is implemented, then subsequent layers perform pattern recognition at progressively larger spatial scales, with lower resolution. A CNN with several downsampling layers enables processing of large spatial arrays, with relatively few free weights.

To sum, CNNs perform mappings between spatially / temporally distributed arrays in arbitrary dimensions. They may be applied to time series, images, or video. CNNs are characterized by:

- translation invariance (neural weights are fixed with respect to spatial translation)
- local connectivity (neural connections only exist between spatially local regions)
- an optional progressive decrease in spatial resolution (as the number of features is gradually increased).

Often when applying CNNs we wish to progressively reduce spatial resolution at each layer in the network. For example, a CNN may be used for classification where an image is mapped to a single classification output. Given fixed filter sizes, reducing spatial resolution has the effect of increasing the effective spatial range of subsequent filters. In a CNN with subsampling in each layer, the outcome is a gradual increase in the number of features used to describe the data, combined with a gradual decrease in spatial resolution. Because the change in coordinate system is accomplished in a nonlinear, incremental, hierarchical manner, the transformation can be made insensitive to input translation, while incorporating information regarding the relative spatial location of features. This provides an interesting contrast to methods such as principle components analysis, which make the transition from normal coordinate space to feature space in a single linear transformation.

In the present paper we shall restrict ourselves to a graphical illustration of the architecture. Fig. 1 shows an elementary network that maps 8x8 input arrays to a single output array via three layers, each consisting of a 2x2 weight vector. The feature arrays are formed by convolving the weights vectors with the previous array, using a step size of 2. The network has 64 inputs and 84 connections, but due to the constraint of translation invariance, there are only 12 free weights. The reader may refer to [2] [1] for a formal description of a CNN.

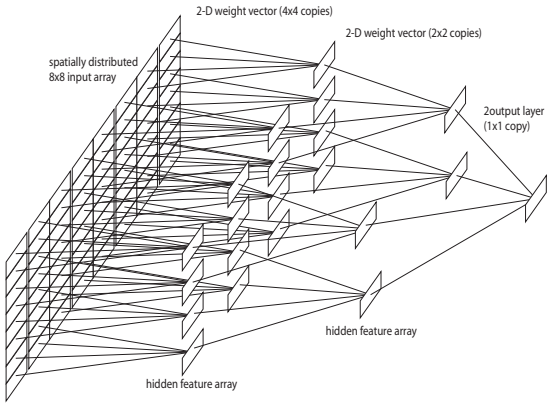

Figure 1. An elementary CNN architecture

3 Numerical tests

Although impressive applied applications of CNNs have been reported (e.g. [1]), less work has been done to specify the theoretical performance of CNN networks, either analytically or through numerical tests. Previous work [2] has

[1] preprint available at http://www.gmd.gr.jp/html/ matthew.browne/

defined and detailed the formal structure of a CNN. Here we shall detail a numerical experiment that is used partly to elucidate the essential properties of CNNs, and partly in order to confirm that CNNs can learn spatially invariant, non-linear filtering systems.

Small 4x4 pixel input arrays were considered. Each input array considered of two 'micro features', either two pixels in top-left to bottom-right (type A) diagonal arrangement, or two pixel in bottom-left to top-right diagonal arrangement (type B). Each micro-feature was allowed to vary independently over all possible spatial locations in the input space. Considering input arrays of two micro-features, four combinations are possible: AA, BB, AB, BA. Figure 2 displays class AA and class BB while figure 3 displays the combined class AB / BA.

The first numerical experiment was to test that a CNN could correctly differentiate between classes AA and BB. Casual inspection of figure 2 would indicate that the various permutations and interference between the micro features creates a non-trivial and perhaps challenging problem for a normal neural network. It was expected that a CNN with 2 neurons in the hidden layer was sufficient to differentiate between the two classes.

A CNN with the properties shown in table 1 was used

Table 1. Architecture of CNN used for spatial XOR.

feature maps	1	2
filter size	2	3
map size	3	1
downsampling	no	no
transfer fun.	log	log

The network successfully classified all inputs except those shown in the lower section of figure 2. In these cases, interference between the micro features creates identical patterns. Although the CNN can theoretically learn purely spatial differences, sensitivity to pure translation would have violated the underlying decision rule required to classify the rest of the data set, namely orientation differences.

The second numerical experiment was more challenging: the CNN was required to differentiate between class AB/BA and class AA/BB. This represents a kind of spatial X-OR problem, with the added difficulty of interference between features. 100% performance was obtained on this problem, demonstrating that a minimal CNN architecture can learn a non-linear translation-invariant mapping in two dimensional feature space.

The key property of the first layer of the CNN is that only a single template is learnt for all possible translations. The following layer integrates information across different templates and spatial translations, enabling approximation of the X-OR function.Thus, *CNN units de-couple detection of a feature's shape and a feature's location*. In conventional spatial feature extraction (principle component 'eigenfaces' are a prominent example) shape and location are clamped. Thus, a separate representation of a feature must be learnt over the entire of range spatial locations where it may occur. Although the artificial problem is highly stylized, realistic detection of complex objects in spatially or temporally distributed data usually involves uncertainty in the absolute and relative position of sub-features.

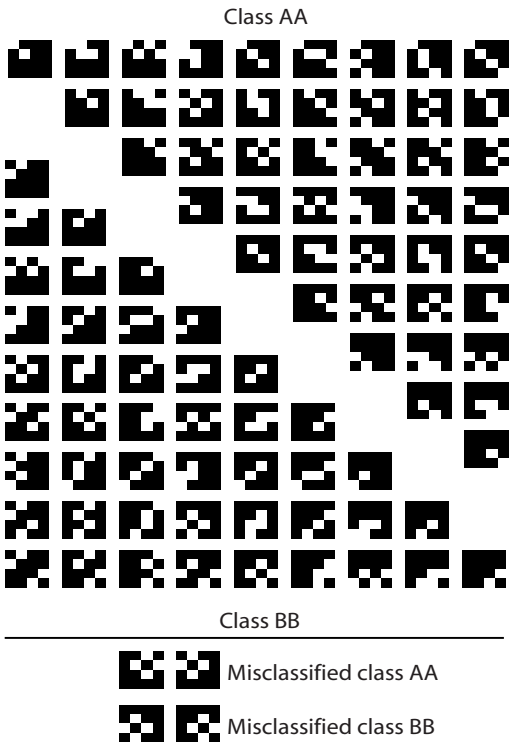

Figure 2. Differentiation of classes 1 and 2 requires translation invariance and tolerance of interference between features.

4 Application in service robotics

The current project involves video data gathered from a robot fitted with an omnidirectional camera with the task of navigating and inspecting civil sewer pipe systems. Ef-

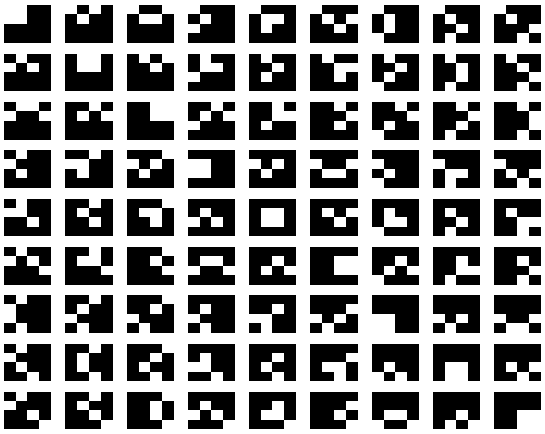

Figure 3. Differentiation of of class 3 from classes 1 and 2 represents a spatial X-OR problem requires implementation of a translation invariant non-linear spatial filter system.

fective navigation requires that the robot be capable of detecting pipe inlets and pipe joints using the same sensor data used for fault detection, namely the omnidirectional data. Figure 4 displays examples of each sensor data class. The CCD original camera image frames were truncated and down sampled to arrays of 36x36 pixels. It was found that this was approximately the maximum amount of downsampling that could be achieved while preserving enough resolution for detection of the relatively finely structured pipe joints. Standard 1:255 valued black and white pixel intensities were normalized across frames to lie within a range of 0:1.

Dirt, reflections, and changes in reflectance represented a challenge in this classification task. However, the objects to be detected had a relatively simple structure. The main challenge for classification of this kind of spatial input by machine learning methods is the size of the input ($36^2 = 1296$ inputs) and variability in the scale and location of features as they pass through the robot's visual field [2].

Table 2 shows the relatively simple architecture used for classification of the camera frames. Only one feature map

[2] A conventional neural network would require a correspondingly large number of free weights. Pre-processing methods such as PCA would decrease the number of free weights required, but generally create features highly sensitive to translation and scale

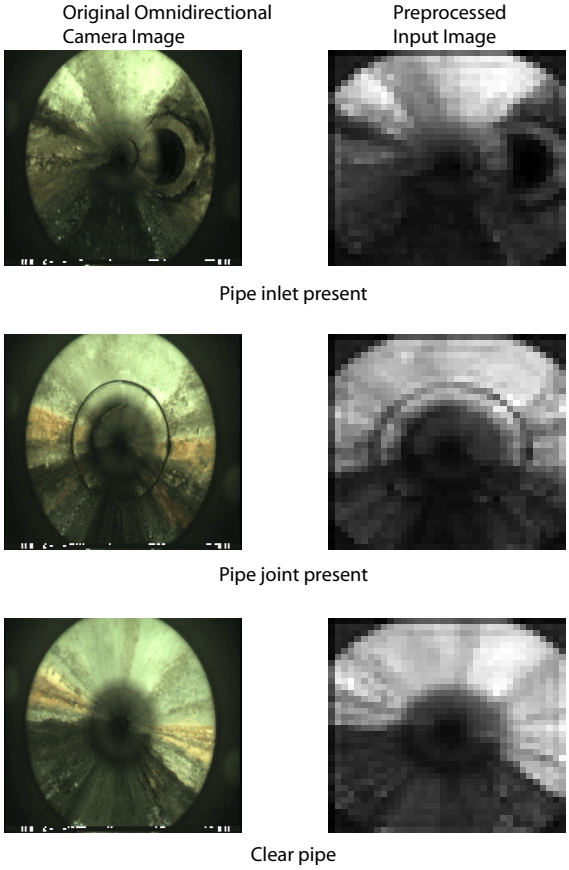

Figure 4. Examples of three classes of omnidirectional camera images for classification by the CNN.

per layer was used to detect pipe joints and pipe inlets, respectively. The 'inlet detector' and the 'joint detector' subnetworks each consisted of a total 51 free weights, including biases to each 2D weight vector. We note that the input size of the 36x36 was somewhat tailored to the architecture, since application of a 5x5 convolution filter without downsampling results in a 32x32 array, which is convenient for subsampling to a single 1x1 array, corresponding to the class prediction. Tan-sigmoid and log-sigmoid transfer functions were used.

Table 2. Architecture of CNN used for omnivision camera processing.

layer	1	2	3	4	5	6
filter size	5	2	2	2	2	2
map size	32	16	8	4	2	1
downsampling	no	yes	yes	yes	yes	no
transfer fun.	tan	tan	tan	tan	tan	log

The networks were trained using 160 manually classified video frames drawn from a sample run through the test pipe, consisting of an approximately equal number of 'joint present', 'inlet present', and 'nothing present' class samples. Training was performed for 1000 epochs, using backpropagation, with momentum and an adaptive learning rate. After training, mean square error rates of 0.0022 and 0.0016 were obtained.

Validation was performed on a second 840 frame, 42 second video sample through the same pipe. For classification of continuous video data, subsequent frames are not statistically independent, and there also exists some 'grey area' where one class stops and the next starts. Thus, calculation of an overall correct classification rate is rather misleading. A more accurate description of the performance of the network is provided in fig. 5, which displays the output of the CNN, along with the actual state of the sewer pipe within the visual field of the robot.

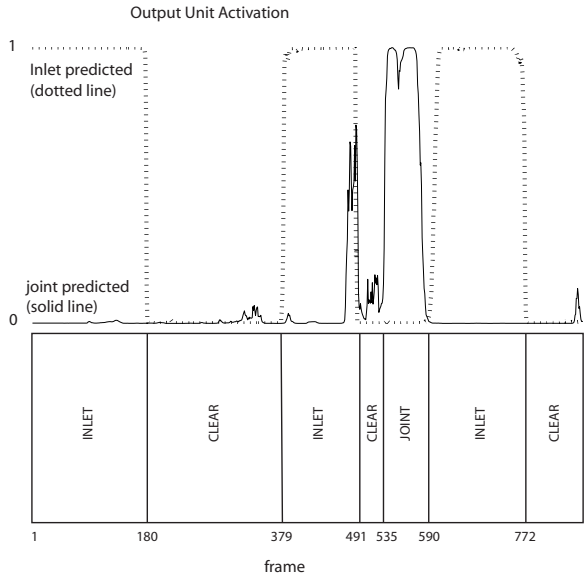

Figure 5. Predicted and actual objects in the visual field of the omnidirectional camera for validation of CNN network.

5 Discussion

The present paper has presented a demonstration of the properties of CNNs using artificial data, and the application of the architecture to an applied problem in robot vision. CNNs are shown to implement non-linear mappings of features with invariance to spatial translation. More precisely, CNNs decouple the learning of feature structure and feature location, and are therefore well suited to problems where the relative or absolute location of features has a degree of uncertainty. It is the contention of the authors that this is a general rule, rather than a special case, in classification of spatially or temporally distributed data.

CNNs have been studied with a view to application in robot vision, where we have found the properties of spatial invariance and weight constraints are necessary for application of machine learning methods to high dimensional image input, where features of interest may occur at a variety of spatial locations. The validation results in figure 5 show that the CNN are very positive indication that CNNs may be effectively applied to detecting navigational landmarks in the sewer-pipe environment. With appropriate thresholding, the activations of the 'inlet detector' and 'joint detector', would result in perfect landmark detection for the validation data. We note the uncertainty of the 'joint detector' around frame 491 is due to a slightly unusual inlet construction that bears some similarity to a normal pipe joint. The system is computationally efficient, capable of processing image frames using an on-board processor in real time.

With respect to the development of an industrial-standard landmark-detection system, much work is required to train and test the network with a wider variety of environments and lighting conditions. We emphasize that the present results should be treated only as a promising indication of the effectiveness of CNNs for robot vision in sewer robots.

The CNN architecture also requires further development. Although basic gradient descent with an adaptive learning rate is adequate, implementation of more advanced optimization techniques (such as Levenburg-Marquardt or conjugate-gradient optimization) is a priority. The basic CNN framework allows a wide variety of possible network architectures: are currently investigating pruning and growing algorithms for specification of the various network parameters. Finally, although CNNs are an efficient method of applying neural networks to image processing, real-time processing of high definition images with a sophisticated architecture would appear to be computationally infeasible without the use of specialized hardware implementation.

References

[1] Y. Bengio, Y. Le Cun, and D. Henderson. Globally trained handwritten word recognizer using spatial representation, convolutional neural networks, and Hidden Markov Models. In J. D. Cowan, G. Tesauro, and J. Alspector, editors, *Advances in Neural Information Processing Systems*, volume 6, pages 937–944. Morgan Kaufmann Publishers, Inc., 1994.

[2] M. Browne and S. Shiry. Convolutional neural networks for image processing: an application in robot vision. In *to appear at Australian Joint Conference on Artificial Intelligence*, 2003.

[3] Y. L. Cun. Generalization and network design strategies. Technical Report CRG-TR-89-4, Department of Computer Science, University of Toronto, 1989.

[4] Y. L. Cun and Y. Bengio. Convolutional networks for images, speech, and time series. In M. Arbib, editor, *The Handbook of Brain Theory and Neural Networks*, pages 255–258. MIT Press, Cambridge, MA, 1995.

[5] Y. L. Cun, J. Boser, D. Denker, R. Henderson, W. Howard, W. Hubbard, and L. Jackel. Backpropagation applied to handwritten zip code recognition. *Neural Computation*, 4(1):541–551, 1988.

[6] T. P. D. Cooper and N.Taylor. Towards the recovery of extrinsic camera parameters from video records of sewer surveys. *Machine Vision and Applications, 11*, pages 53–63, 1998.

[7] J. R. del Solar and M. K-pen. Sewer pipe image segmentation using a neural based architecture. *Pattern Recognition Letters, 17*, pages 363–368, 1996.

[8] B. Fasel. Facial expression analysis using shape and motion information extracted by convolutional neural networks. In *Proceedings of the International IEEE Workshop on Neural Networks for Signal Processing (NNSP 2002), Martigny, Switzerland*, 2002.

[9] B. Fasel. Robust face analysis using convolutional neural networks. In *Proceedings of the International Conference on Pattern Recognition (ICPR 2002), Quebec, Canada*, 2002.

[10] K. Fukushima. Neocognitron: A hierachical neural network capable of visual pattern recognition. *Neural Networks*, 1(2):119–130, 1988.

[11] K. Fukushima, S. Miyake, and T. Ito. Neocognitron: a neural model for a mechanism of visual pattern recognition. *IEEE Transactions on Systems, Man, and Cybernetics*, 13:826–834, 1983.

[12] J. Hertzberg and F. Kirchner. Landmark-based autonomous navigation in sewerage pipes. In *Proc. First Euromicro Workshop on Advanced Mobile Robots (EUROBOT '96)*, pages 68–73. Kaiserslautern. IEEE Press, 1996.

[13] E. R. L. Paletta and A. Pinz. Visual object detection for autonomous sewer robots. In *Proc. 1999 IEEE/RSJ International Conference on Intelligent Robots and Systems (IROS '99), vol. 2*, pages 1087–1093. IEEE Press, Piscataway, NJ, 1999. ISBN 0-7803-5184-3.

[14] K. Lang and G. Hinton. Dimensionality reduction and prior knowledge in e-set recognition. In D. Touretzky, editor, *Advances in Neural Information Processing Systems*, pages 178–185. Morgan Kauffman, San Marteo, CA, 1990.

[15] S. Lawrence, C. L. Giles, A. C. Tsoi, and A. D. Back. Face recognition: A convolutional neural network approach. *IEEE Transactions on Neural Networks*, 8(1):98–113, 1997.

[16] D. E. Rumelhart, G. E. Hinton, and R. J. Williams. Learning internal representation by error propagation. In D. E. Rumelhart and J. L. McClelland, editors, *Parallel Distributed Processing: Explorations in the Microstructure of Cognition*, volume 1, pages 318–362. Cambridge, MA: MIT Press, 1986.

[17] E. Sackinger, B. Boser, J. Bromley, and Y. LeCun. Application of the anna neural network chip to high-speed character recognition. *IEEE Transactions on Neural Networks*, 3:498–505, 1992.

DATA MINING & INTELLIGENT DATABASES

(This page left blank intentionally)

Parallel Sequence Mining on Cycle Stealing Networks

Calum Robertson
Centre for IT Innovation,
Queensland University of Technology,
Queensland, Australia
cs.robertson@student.qut.edu.au

Shlomo Geva
Centre for IT Innovation,
Queensland University of Technology,
Queensland, Australia
s.geva@qut.edu.au

Wayne Kelly
Centre for IT Innovation,
Queensland University of Technology,
Queensland, Australia
w.kelly@qut.edu.au

Abstract

Cycle stealing networks can convert a network of computers into a virtual supercomputer. However, harnessing this power for sequence mining is not a simple process. Most parallel sequence mining algorithms suffer from high inter-process communication costs which we effectively eliminate with our data partitioning algorithm. We show that this solution, running on the G2 [1] cycle stealing network, offers substantial performance gains, finds nearly all maximal sequences, with only a small percentage of false positives.

1 INTRODUCTION

Cycle stealing applications such as SETI@HOME allow the unutilized compute power of PCs spread across the Internet to be exploited. Data mining applications such as sequence mining are computationally intensive and therefore could benefit from parallelisation in such an environment. Unfortunately, existing data mining algorithms, such as (CD, DD, IDD) [2], pSPADE [3] and (DPF, STPF) [4], require all or at least some candidates to be passed between the nodes. While this works well on a traditional supercomputer or on a dedicated cluster computer, it doesn't work well when utilising PCs spread across the Internet. This is because direct communication between fellow "volunteers" is extremely difficult if not impossible, due to the presence of firewalls and the fact that volunteers can come and go during the computation without notice.

We propose a new approach to parallelising sequence mining problems that requires no communication between fellow volunteers and therefore results in much better performance in an Internet environment. The algorithm is based on a sampling heuristic and so in general will produce only an approximation of the results obtained by an exhaustive approach, but we show that in practice only a small percentage of incorrect results are produced, which we believe is acceptable for most applications.

In this paper we will briefly define the sequence mining problem, and outline our serial algorithm, before introducing the G2 [1] grid computing environment in Section 4. We will then briefly outline our parallel algorithms, and evaluate their performance, before presenting our conclusions.

2 PROBLEM DEFINITION

The sequence mining problem introduced by Agrawal and Srikant [5] processes large transaction datasets to find frequent sequential patterns with minimum support. A sequence mining dataset contains a history for a number of customers, each of which consists of a time ordered sequence of transactions. Each transaction consists of a set of individual items. The same items can appear in multiple transactions. An itemset is a subset of the items that make up a transaction. A sequence is an ordered list of itemsets that derive from successive transactions of a given customer. A sequence is said to have p% support if it exists in at least p% of all customers. A sequence is said to be maximal if no super-sequence exists with enough support.

3 SERIAL ALGORITHM

Our aim is to divide the sequence mining problem up into manageable parts and allow each to operate independently prior to combining results. We decided to partition the dataset into several small sub-datasets and perform a complete sequence mining operation on each. This approach not only reduces the memory requirement but also reduces I/O costs as the entire dataset doesn't need to be shifted in and out of memory. We chose the Apriori [5] algorithm for processing the data, as it is a widely known algorithm with well documented performance.

3.1 Apriori

The Apriori algorithm solves the sequence mining by finding all itemsets, converting the dataset so each transaction represents the itemsets it contains, and finally finding all sequences. Itemsets and Sequences are both found by recursively generating candidates of increasing length, counting their support and then subsequently pruning all candidates that don't have support.

A candidate containing n items/itemsets is called an n-length candidate. All 2-length candidates are formed by appending 1-length candidates. As items within an itemset have to be ordered, items are appended in order, though itemsets within a sequence can be appended in any order. A n-length candidate is formed by finding two patterns

with the same (n-1)-length prefix and combining, such that (0,1,2,3) and (0,1,2,4) make (0,1,2,3,4). Agrawal and Srikant [6] propose that it is cheaper to validate that (1,2,3,4) exists than it is to count the support of (0,1,2,3,4), so we incorporated this into our implementation.

Support for a given itemset/sequence is only counted once per customer to ensure that the minimum support requirement is met.

3.2 DPA

The Data Partitioning Apriori (DPA) algorithm divides the dataset into various equally sized sub-datasets that are processed independently before all results are combined. Partitioning is constrained because the size of the dataset partitions must not be so small that even a single instance of a sequence satisfies the minimum support constraint. Therefore there is a strict limit to the number of times the dataset can be partitioned.

The DPA algorithm requires that a percentage of partitions (β) support a sequence for it to be included. This condition ensures that sequence that is prominent in only a minor partition does not appear in the overall results.

4 THE G2 CYCLE-STEALING FRAMEWORK

G2 [1] is an application framework, also developed at QUT, for creating parallel applications that exploit the idle cycles of networked PCs. The framework is designed to make it both easy to develop simple new parallel applications (such as the sequence mining application described in this paper) and easy to deploy such applications.

The G2 framework is designed for use on the new Microsoft .NET platform. This allows application programmers to choose from a number of implementation languages, while still providing a managed runtime environment in which the operations attempted by user code can be carefully vetted so as to prevent malicious or accidental damage to volunteered workstations (this is typically referred to as "sand-boxing").

4.1 The G2 Programming Model

The G2 framework presents the application programmer with a programming model directly analogous to the implementation and use of web services using ASP.NET. To implement a section of code that is to be executed in parallel, a G2 application programmer simply creates a method and annotates it with a WebMethod attribute as shown in the trivial example in Figure 1:

```
using System.Web.Services;

public class Math
{
    [WebMethod]
    public int Multiply(int a,int b)
    {
        return a * b;
    }
}
```

Figure 1: Sample G2 Method

This code is then used as input to a G2 utility program that generates a proxy class that allows clients to make multiple invocations of the designated Web Methods in parallel (on volunteered machines). This is exactly analogous to how proxy classes are generated in ASP.NET from WSDL specifications. Client programs simply create an instance of the automatically generated proxy class and invoke its methods (asynchronously) in exactly the same manner that they would invoke a regular local method. The methods are invoked asynchronously in order to provide the possibility for them to be evaluated in parallel. The standard .NET design pattern for asynchronous method invocation is followed, so it should again be familiar to many .NET programmers.

4.2 G2 Internal Architecture

Each G2 Web Method invocation is transparently converted by the client-side proxy class into a SOAP message, which is then transported using HTTP to a G2 server machine. There the SOAP message is stored in a job repository (a relational database) until a volunteer machine becomes available to execute it (see Figure 2).

Volunteered machines, when they would otherwise be idle, request a job from the G2 server machine, de-serialize the SOAP message, execute the method and send a SOAP encoded result back to the server. The result is then fetched by the client machine where it is used to provide a result for the original asynchronous method call.

With the wide spread use of firewalls, we assume, pessimistically, that clients and volunteers may be located on opposite sides of a firewall. We require only that the G2 Server is universally accessible by all clients and volunteers. Note that all communication is initiated by either the clients or the volunteers; the clients push jobs to the server and pull down results, while the volunteers pull down jobs and push back results. This arrangement is mandated by the assumption that the server cannot "push" data to either the clients or the volunteers.

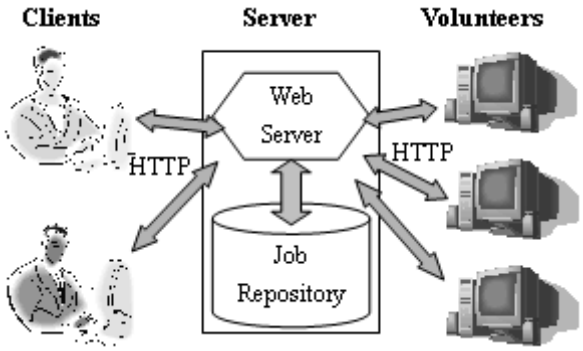

Figure 2: G2 Internal Architecture

4.3 G2 Application Deployment

Normally with ASP.NET web services, the software components (referred to as assemblies in .NET) that implement a web service need to be pre-deployed on a web server. In our case, the "Web Methods" are actually executed on a large collection of volunteer machines that are owned by various individuals that may have no particular relationship with the people wishing to run client applications. We cannot therefore hope to pre-deploy all client applications to all volunteers, so we instead adopt a lazy (and transparent) deployment strategy. All of the code, both the portion to execute on the client machine and the portion ultimately intended to execute on volunteer machines, initially resides only on the client machine. At runtime, it is dynamically uploaded to the server machine (if it is not already present) and from there dynamically downloaded to the volunteer machines and stored in their download assembly caches.

4.4 Isolated Storage

The same is true of any large data files that need to be read by the code executing on the volunteers. They are lazily uploaded to the server and then downloaded to the volunteer machines where they stored in a special part of the volunteer's local file system called isolated storage that is strictly managed by the .NET runtime environment. Application code executing on the volunteer machines is able to access files in this isolated storage, but are otherwise unable to read or write to the local file system.

4.5 Volunteer Host

All of the G2 code that executes on the volunteer, including the framework code that fetches jobs from the server is hosted within a web browser. Volunteers simply need to start their web browser and point it at a G2 Server and they are instantly volunteering. Absolutely no code needs to be pre-deployed on the volunteer machines apart from a web browser and the (free) .NET framework SDK. All G2 and application code that needs to execute on the volunteer is automatically downloaded as required inside a security context set up by the browser. If a volunteer wishes to stop volunteering, they can simply shutdown or kill the web browser process. If the volunteer was in the middle of executing a job, that job will be automatically picked up and re-executed (from the beginning) by some other volunteer – i.e. the system is intrinsically fault tolerant to volunteers disappearing without notice.

5 PARALLEL ALGORITHMS

The G2 client program for DPA sequence mining will create a number of jobs to be executed in parallel on the volunteers. Each job consists of performing the standard Apriori algorithm on a subset of the customers. Each volunteer needs therefore only part of the total dataset in order to perform its task. We investigate two alternative approaches to distributing this data to the volunteers.

The first approach involves sending to each volunteer (using isolated storage) only the part of the data (PDDPA) that it needs to complete the job it has currently been assigned. This requires the client to perform some initial processing in order to create individual files for each job, however, it minimizes the amount of data sent over the network.

The second approach involves sending to each volunteer (again using isolated storage) the entire dataset (EDDPA). This requires a lot more data to be sent over the network initially, but since this data is cached on the volunteers, subsequent mining operations on the same dataset will require no data to be sent to those volunteers. In other words, we pay a high once off cost which is then (hopefully) amortized over a number of sequence mining operations.

When a volunteer receives the job it initially needs to pre-process the data to extract the part it needs. In our implementation we first calculate all items, within the subdataset, with minimum support. We then transform the data so that each transformed transaction contains at least one supported item, and each customer contains at least one transformed transaction. This process effectively reduces the search space, as there is no need to search through items that don't have support.

In our early work with PDDPA we attempted to transfer the data to volunteers via a string SOAP variable in the method call. Whilst this process requires none of the I/O costs associated with isolated storage, it places unacceptable loads on the client, server and volunteer, due to the serialization process. The variable to be serialized must be memory resident, as must the generated XML. Deserialization normally requires the XML to be memory resident, along with the created variable. For small datasets this is not a major concern, though our 1,000,000 customer DS4

takes up 350MB in its base format. For a string variable this effectively means 700MB of data must exist in memory simultaneously, which caused problems with the 512MB machines we tested on. Therefore isolated storage is the most efficient solution for transmission of large datasets.

6 RESULTS

The results section is divided into two distinct sections. The first analyses the loss rate of the DPA algorithm, whilst the second examines the performance gains obtained on G2.

6.1 Lossy Performance

To analyse the effect of β we produced four synthetic datasets, using software provided by the IBM Quest group [5], defined in Table 2 (refer to Table 1 for parameter definitions). For all our tests we set N = 10,000, N_I = 25000, and N_S = 5000.

Table 1: Synthetic Dataset Paramters

D	Number of Customers
C	Av. Transactions per Customer
T	Av. Items per Transaction
S	Av. Potentially Maximal Sequence Length
I	Av. Potentially Maximal Itemset Length
N	Number of Items
N_S	Number of Maximal Sequences
N_I	Number of Maximal Itemsets

Table 2: Dataset Definitions

	Dataset			
Parameter	DS1	DS2	DS3	DS4
C	10	10	10	20
T	2.5	5	5	2.5
S	4	4	4	4
I	1.25	1.25	2.5	1.25

The results in Figure 3 show the percentage of maximal sequences found for 100,000 customer datasets partitioned 100 times at 1% support. This is close to the limit for partitioning yet it highlights that requiring too many sub-datasets to support the sequence reduces the number of maximal sequences found.

On the other hand Figure 4 shows that as β is reduced, more false positives are found. This in turn reduces the number of maximal sequences found, as false positives tend to be supersets of actual maximal sequences. Therefore, it seems that a value of β=60% is near optimal.

We tried reducing the minimum support requirement for each partition, in an attempt to find more sequences, but found that too many false positive results were found.

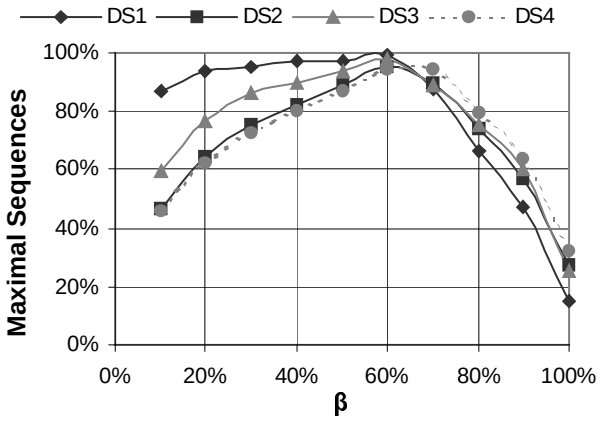

Figure 3: Results Vs β

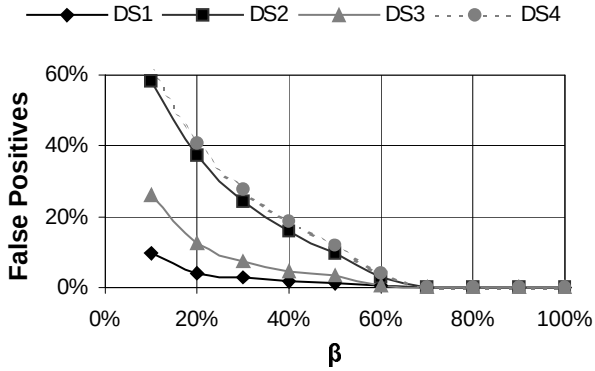

Figure 4: False Positives Vs β

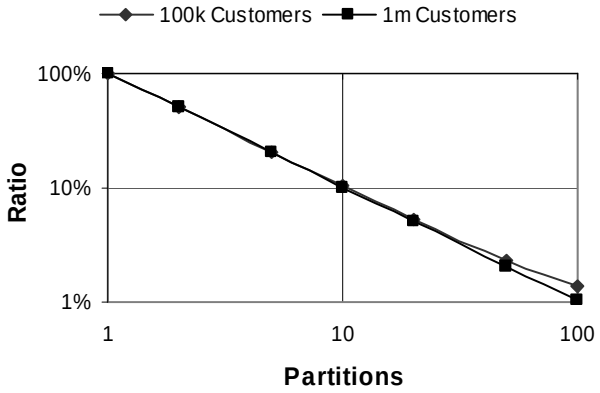

Figure 5: Candidates Checked Vs Partitions

To analyse the benefits of the DPA algorithm, we ran it on the four datasets with both 100,000 and 1,000,000 cus-

tomers at 1% support. We measured the number of candidates generated, and the number of candidates that were counted for support (the two major costs in the Apriori algorithm). The results in Figure 5 show that for more partitions there is a linear reduction in the number of candidates checked for support. This is due to the linear decrease in customers.

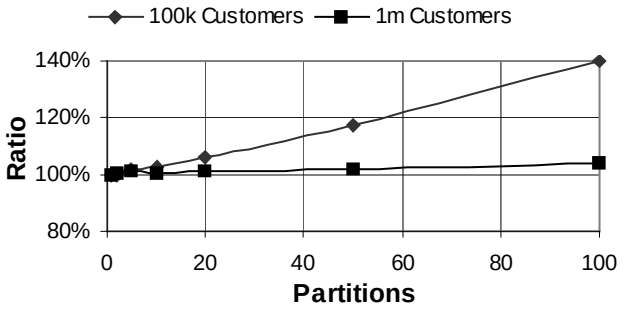

Figure 6: Candidates Vs Partitions

Figure 6 shows that the number of candidates generated starts to increase as the data is partitioned more. The effect on the 100,000 customer dataset is very prominent because at 100 partitions the 1% support requirement means that only 10 customers must contain the candidate for it to be significant. This emphasises our earlier statement that there is a strict limit to the number of times the dataset can be partitioned.

6.2 Parallel Performance

These algorithms were written in Microsoft C# .NET using the Microsoft .NET 1.1 Framework. All tests were performed on 800MHz Intel Pentium 3 PCs with 512MB of memory. A 100Mb/s switching network was used, though not exclusively for these tests.

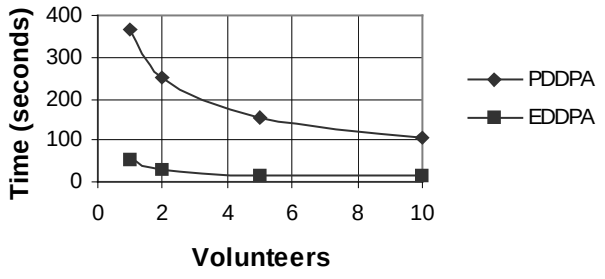

Figure 7: EDDPA Vs PDDPA

The process times in Figure 7, for the 100,000 customer DS1 at 1% support, demonstrates that, when data has been pre-deployed, EDDPA is a lot cheaper than PDDPA. However PDDPA speeds up reasonably well, so if only one sequence mining operation needs to be performed, PDDPA is preferable to EDDPA. Note that by speedup we refer to the time taken to execute the code on a single volunteer versus multiple volunteers.

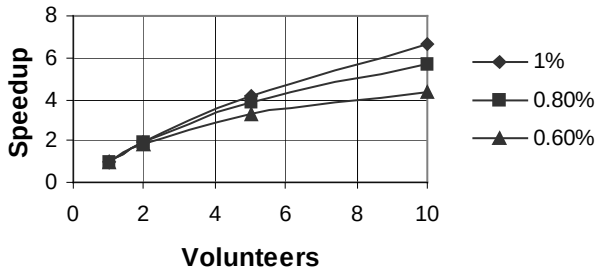

Figure 8: Mean EDDPA 100k customer Speedup

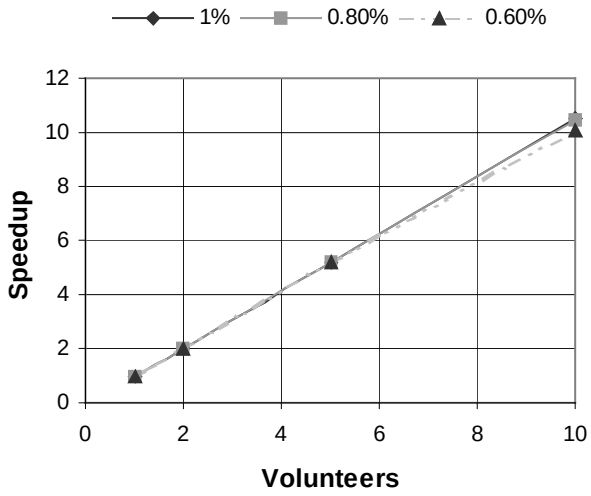

Figure 9: DS1 EDDPA 1m customer Speedup

The results in Figure 8 show the mean speedup for all datasets with 100,000 customers, whilst Figure 9 shows the speedup for the 1,000,000 customer DS1, with varying supports. They demonstrate that decreasing the support, also decreases the speedup, though the effect is less significant for larger datasets.

To analyse this effect we recorded the Fixed (candidate generation, and pruning) and Dynamic (pre-processing, transmission, support counting, and dataset conversion) costs for each volunteer. The costs in Figure 10 show that fixed costs become more significant, as the number of partitions increase. The results in Figure 5 highlight that the support count cost reduces proportionally to the number of partitions, and obviously the other dynamic costs reduce with more partitions, as there is less data. Also results in Figure 6 demonstrate that the candidate generation cost remains relatively constant.

Therefore these results indicate that the performance of parallel DPA algorithms are limited by the ratio of fixed to dynamic costs. If the fixed costs are equivalent to the dynamic costs at a 100,000 customer partition, then there is no benefit in creating smaller partitions.

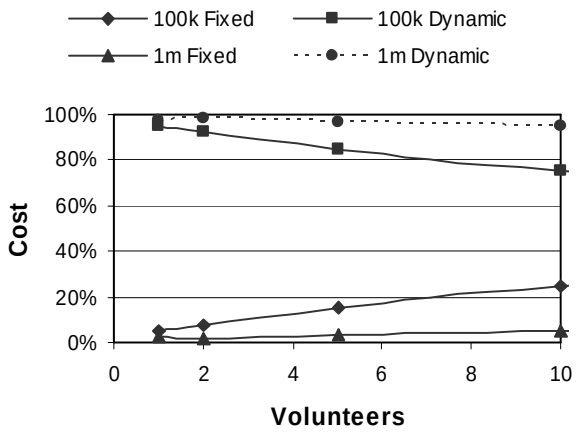

Figure 10: DS1 EDDPA at 1% Costs Per Volunteer

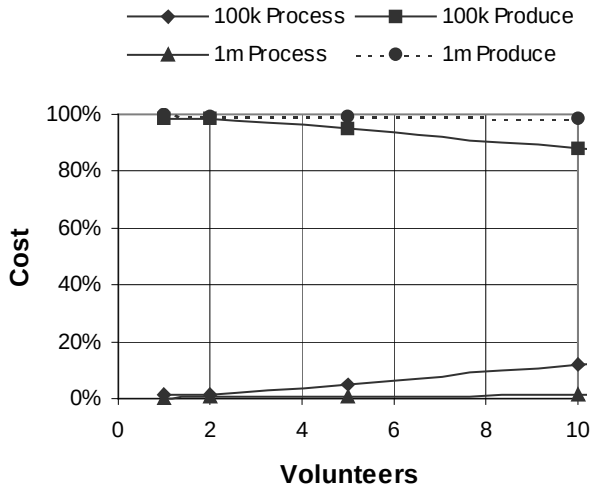

Figure 11: DS1 EDDPA at 1% Process Vs Produce

However, to verify this effect, we measured the cost of result processing versus production. Result production costs are the costs associated with producing all the jobs, and having the volunteers process them all. Result process costs are the costs associated with retrieving the volunteers' results, combining them and finally eliminating all but those with β% support amongst the partitions. The results shown in Figure 11 indicate that process costs start to increase with more partitions. This is due to an increase in the number of results, as each partition, no matter the size, will produce a similar number of results to that produced by processing the whole dataset. Of course Figure 6 shows that the more times the data is partitioned, the more candidates are generated, and therefore there is a higher chance of there being more results.

Interestingly the result process versus result production costs is not nearly as severe as the volunteer fixed versus dynamic costs. This effect can be attributed to the asynchronous nature of the G2 environment, where jobs are not created simultaneously, and therefore results are not submitted simultaneously. With this in mind it is possible to predict when an individual job will be inefficient, though is it is not as easy to predict when the whole process will become inefficient.

7 CONCLUSIONS

We have shown that the DPA algorithm can find the majority of maximal results, with a very small percentage of false positives. Our results show that substantial performance gains can be achieved for large datasets for EDDPA, though gains are limited by the complexity of the dataset. We have also shown that the PDDPA algorithm offers good gains for situations where EDDPA is not preferable. Though we used the Apriori algorithm, other algorithms could provide better gains, which we hope to establish in future work.

The G2 framework, outlined in this paper, enables the power of local intranets, and the internet, to be harnessed for parallel computing. Its application to the sequence mining problem has shown its benefits, and in future we will demonstrate its effect on other problems.

8 REFERENCES

[1] Kelly, W.A., P. Roe, and J. Sumitomo, *G2: A Grid Middleware for Cycle Donation using .NET.* In Proceedings of *The 2002 International Conference on Parallel and Distributed Processing Techniques and Applications*, Las Vegas. June 2002.

[2] Joshi, M.V., E. Han, K. G., and V. Kumar, *Efficient Parallel Algorithms for Mining Associations.* Lecture Notes in Artificial Intelligence, 2000: p. 83-126.

[3] Zaki, M., *Parallel Sequence Mining on Shared-Memory Machines.* Journal of Parallel and Distributed Computing, 2001(61): p. 401-426.

[4] Guralnik, V. and G. Karypis, *Parallel Formulations of Tree-Projection-Based Sequence Mining Algorithm.* Technical Report 03-0003, University of Minnesota, Minneapolis, 2003.

[5] Agrawal, R. and R. Srikant, *Mining Sequential Patterns.* In Proceedings of *11th International Conference on Data Engineering*, Taipei, Taiwan. 1995: p. 3-14.

[6] Agrawal, R. and R. Srikant, *Mining Sequential Patterns: Generalizations and Performance Improvements.* In Proceedings of *5th International Conference on Extending Database Technology*, Avignon, France. 1996. Springer-Verlag: p. 3-17.

Data Mining Fault Information Reports for Prediction

Ramesh K. Rayudu
Transpower NZ Ltd,
New Zealand.

Ajay Maharaj
Transend Networks Pty Ltd,
Australia.

C-fACS
Lincoln University
New Zealand
Ramesh.Rayudu@transpower.co.nz
Phone: +64 3 3253623
Fax: +64 3 325 3839

Abstract

The paper discusses an application of datamining techniques for analysis of fault information data of transmission network in New Zealand. The analysis is mainly aimed to provide necessary prediction knowledge of a fault after an event. This prediction could be a reason for fault, faulted equipment, estimated loss of supply and estimated time for restoration. Our data used for this paper contains transmission faults of approximately 342 events spanning over three years.

In this paper, we introduce the general datamining procedure and discuss its application to analyse the fault information reports. Our solution methodology, pre-processing data selection, analysis algorithms are also discussed. Finally we present and analyse some of the results.

INTRODUCTION

Information technology has developed rapidly over the last three decades contributing towards the formation of data warehouses. The growth of this 'soft' data in computers is now leading towards the so-called 'knowledge' era. To analyse the data and identify useful information, several data analysis techniques have been proposed.

Data mining is one such process of data analysis that could be employed in extracting valid, previously unknown, and ultimately comprehensible information from large databases and use it to make crucial decisions [1]. It involves the application of several statistical and soft-computing techniques to identify meaningful relationships between data. Since the advent of SCADA systems in electric power transmission control, a large amount of data is acquired and stored in data warehouses. Several online tools

Such as state estimation, contingency analysis, and security analysis use this data. However, the data can also be used for other analysis that would assist in better management and control of power systems.

Our motivation behind this research is to device a datamining strategy to analyse power system fault information reports (FIRs). FIRs are reports that are prepared after extensive analysis of and unplanned event that occurred on the power system. Each event is analysed by engineers at a later stage and the conclusions are recorded in the reports. Since considerable amount of resources are spent on analysing and preparing these reports, our aim was to use this documented knowledge and information to provide a reasonable prediction of information in real-time to system co-ordinators when an event occurs in the future.

Data mining has been successfully proven to be effective in applications such as on-line intruder detection [2], rule discovery in alarm processing [3] and prediction of black-outs [4]. In this paper we discuss our experience of applying datamining to predict the unplanned outage information.

DATA MINING PROCESS

The general datamining process has five stages [1]:

- *Data selection* is a process where the required data is identified and gathered into a central repository.
- *Data Cleansing* is a process where the data is pre-processed and possible errors and dubious values are eliminated.
- *Feature extraction* is a process where all the attributes that are deemed to be 'interesting' are selected.

- *Model learning* involves the application of datamining techniques to discover the 'patterns'.
- *Model analysis and evaluation* is a process of visualising the 'mined' information and evaluation of the results based on the identified relationships and accuracy of prediction output.

Based on the above stated stages our datamining process has the generalised input-output patterns as shown in the following Figure 1. The input attributes depict the data available for input in real-time and the output attributes are prediction values required. The process of our research towards the illustrated mechanism is discussed below.

Data Selection

Initially we have selected around 470 events spanning over three years. Each event is described in terms of 42 attributes. Some attributes have no values in them and some have more than one value. Some attributes also include English sentences that provide descriptions of the event. Since FIR data was not configured for real-time usage and datamining, we had to go through multiple iterations of data pre-processing to extract meaningful dataset for datamining.

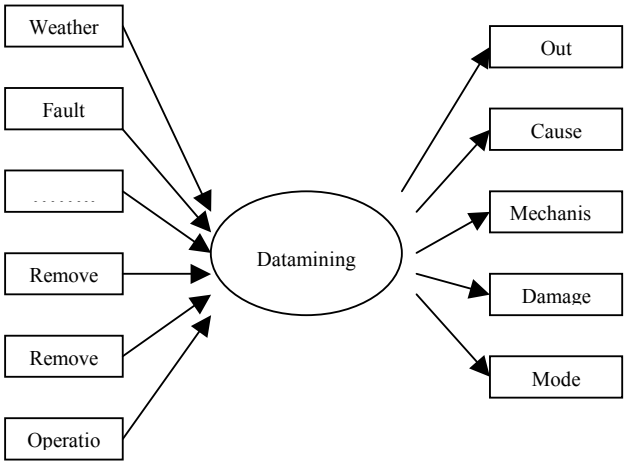

Figure 1. General input-output patterns for FIR datamining.

Data Cleansing

Our main motivational attribute of the FIR data is the time it took to restore the supply after an event. Hence, all the events that had 'no' loss-of-supply were deleted from the data. This has reduced the events to 394 out of which 52 events were used for testing and the rest were used in datamining process.

Secondly, since the original dataset had a combination of discrete, continuous and linguistic data, we also had to normalise the data based on our FIR analysis knowledge. One example is the following Table 1 that depicts the classification of loss-of-supply duration.

Table1. Loss of supply time classification

Duration time(min)	Class label
1- 5	1
6-10	2
11-20	3
21-50	4
51-100	5
101-500	6
Over 500	7

.

Feature Extraction

This process involves the identification of appropriate input and output attributes. We have selected five output attributes. These are outage duration classification, cause of the fault or event (rain snow, wind, and pollution), mechanism of the fault (error by staff, error by contractor or wilful damage), damage analysis (equipment damage and injury to humans or animals), and finally the mode of the fault (red-earth, phase to phase etc.). For inputs selection, we have analysed the data based on our experience and then by performing sensitivity analysis on the data. By this process we could delete 12 attributes that had 10% or less effect on the output prediction.

342 events with 30 attributes were used for training phase of our datamining process.

Model learning

We have used three algorithms for datamining the training data. These algorithms are:

- SSV decision tree: Decision trees algorithms are usually quite efficient and therefore worth attempting first on the data. They are preferred over other kinds of adaptive models when a logical description of collected data is required. Decision trees are built in a recurrent process by splitting the feature space into two or more parts. The splits aim for the best separation of objects belonging to

different classes. At each step, they use information gain to decide separation rules.

- K nearest neighbours algorithm (KNN): This algorithm assumes all instances correspond to points in the n-dimensional space R^N. The nearest neighbours of an instance are defined in terms of the standard Euclidean distance. KNN remembers all training data and selects most similar vectors at the moment it is asked to make a prediction.
- Feature Space Mapping (FSM): FSM adopted here is a neuro-fuzzy network is based on multidimensional separable functions. The main idea is simple: components of the input and output vector define features, and combinations of these features define objects in the feature spaces. These objects are described by the joint density probability of the input/output data vectors using a network of properly parameterised transfer functions.

Model Analysis and Evaluation

The following table, Table 2, displays the accuracy of the prediction output results. For this analysis, we have chosen the threshold accuracy rate of above 50% as the average percentage of accurate prediction of these events by humans is around 50%. It is evident from the above results that no single algorithm performed well against all the outputs. Exception is the 'mode' of fault identification where all the algorithms performed reasonably well.

There are several reasons to explain the above accuracy results. Some of these are:

- Data pre-processing: It can be estimated that some of the accuracy can improved if we re-iterate the data pre-processing phase to identify other information requirements.
- Physical location of operation: The circuit breaker and equipment trips have been generalised in the experiment. It is possible that the geographical location of the equipment information could contribute towards better accuracy.
- Extensive code inputs: Each attribute has an extensive list of sub-categories. For example, the cause and mechanisms have 274 different descriptions. Since we had a set time limit for the experiment, we could not code all the descriptions.
- Some important information such as the English sentence input needs to be input in a machine-readable format.

CONCLUSION

We have presented a process to perform datamining on electric power fault information reports. We have followed the five stages of datamining and then analysed the results. We have used three different algorithms for analysis. The prediction (outputs) parameters were Outage duration in minutes, Cause and Mechanism of the fault, Expected damage to the equipment, and Mode of the fault. No single algorithm had performed well against all outputs. All algorithms for all predictors had an average accuracy of about 66.7%. We analysed some accuracy contributors for further research.

REFERENCES

1. I. H. Witten, E. Frank, Data Mining: Practical Machine Learning Tools and Techniques with Java Implementations, Morgan Kaufmann, San Francisco, CA, 2000.
2- K. Ilgun, R. A. Kemmerer, and P. A. Porras, "State transition analysis: A rule-based intrusion detection approach.", *IEEE Transactions on Software Engineering*, 21(3):181-199, March 1995.
3- K. Hatonen, M. Klemettinen, H. Mannila, P. Ronkainen, H. Toivonen, "Rule Discovery in Alarm Databases", Report number C. No. C-1996-7, University of Helsinki, 1996.
4- P. Geurts & L. Wehenkel, "Early Prediction of Electric Power System Balackouts by Temporal Machine Learning", Technical Report WS-98-07, AAAI Press, 1998.

Table 2. Accuracy Results.

	KNN		SSV		FSM	
	Training	Test	Training	Test	Training	Test
Out duration	57.4%	37.7%	55.8%	21.4%	**63.9%**	**58%**
Cause	100%	46.8%	**76%**	**74%**	87%	35%
Mechanism	100%	45.7%	**78.7%**	**74.2%**	82.1%	48.8%
Damage	79.8%	42.8%	79%	42.3%	**86%**	**42.8%**
Mode	**74%**	**71%**	**65%**	**64%**	**97%**	**57%**

A Grammar for the Specification of Forensic Image Mining Searches

Ross Brown
Faculty of IT, Queensland University of Technology,
GPO Box 2434 Brisbane
AUSTRALIA
r.brown@qut.edu.au

Binh Pham
Faculty of IT, Queensland University of Technology,
GPO Box 2434 Brisbane
AUSTRALIA
b.pham@qut.edu.au

Olivier De Vel
Information Networks Division,
Defense Science and Technology Organisation,
PO Box 1500 Edinburgh
AUSTRALIA
Olivier.DeVel@dsto.defence.gov.au

Abstract
There has been much research into the use of similarity measures to facilitate content-based image retrieval. However, there are other application areas where the user will wish to retrieve images that contain objects in specified arrangements. This has particular application in the area of Image Forensics, where legal investigations require the ability to perform search queries on images containing suspicious objects in relevant spatial organisations. In this paper we present a grammar which augments a body detection system by allowing arbitrarily arranged detectors.

Keywords
Intelligent Image Mining, Pattern Recognition, Image processing, Support Vector Machines

INTRODUCTION

Computer forensics is the application of computer analysis techniques to determine potential legal evidence of computer crimes or misuse that are caused by unauthorised users or by unauthorised activities generated by authorised users. It covers a wide range of applications such as law enforcement, fraud investigation, theft or destruction of intellectual property. Techniques used for such investigations are varied and may include data mining and analysis, timeline correlation, information hiding analysis, etc. Data for evidence are of various types and come from different sources, e.g. storage devices, networks, etc. Since multimedia format is widely used and readily available via the Internet, there are increasing criminal activities in the last few years, which involve the transmission and usage of inappropriate material in this format. Hence, much forensic evidence comes in the form of images or videos which contain objects and/or scenes that may be related to criminal behaviours. A typical investigation in computer forensics can generate large image and video data sets. For example, a disk can easily store several thousands of images and videos in normal files, browser cache files and unallocated space (i.e., non-file system areas on the disk which may contain fragments of files). This can make the task of searching for, and retrieving, images/videos very time consuming. Digital image forensics efficiently seeks for evidence by using appropriate techniques based on image analysis, retrieval and mining. The use of such techniques for investigative purposes have only recently emerged, although they have been intensively researched over the last three decades for many other important applications: medical diagnosis, mineral exploration, environmental monitoring and planning, aerial surveillance, etc.

Image mining is a specific area of image analysis in which images of certain characteristics are detected and retrieved from a large set of images. The goal of image mining is to combine image retrieval techniques with the ability to learn and model specific objects of interest found in an image. Earlier approaches to image retrieval rely on the retrieval of associated text strings which provide some descriptions of the images such as name, place, date and annotation. Content-based approaches which came much later allow searches based on some general low-level visual features such as colour, shape, texture e.g. [1]. Search-by-example is a common practice whereby an image is supplied and the system would return images which have features similar to those of the supplied image. The similarity of images is determined by the values of similarity measures which are specifically defined for each feature according to their physical meaning. For example, a similarity measure for colour can be defined as the sum of square of the difference in red, green and blue components. Retrieved images can be ranked according to these similarity measures. Users are allowed to select specific features and their weights to add subjective bias based on preferences or previous experience. Since the quality of the retrieval results relies on the choice of features and their similarity measures, much research has been focused on identifying features with strong discriminatory power and similarity measures which are meaningful and useful. In addition, we would ideally want a more "intelligent" system which can include high-level knowledge, deal with incomplete and/or uncertain information, and learn from previous experience. Such systems could include, for example:

- methods that develop a model of each object to be recognised (called *model-based* methods). These objects are classified using their constituent components that in turn are characterised in terms of their primitives,

- methods that use statistical techniques to assign semantic classes to different regions/objects of an image (called *statistical modelling* methods), and
- methods that require user feedback to drive and refine the retrieval process (called *user relevance feedback* methods). The system is thus able to derive improved rules from the feedback and consequently generate better semantic classes of images [2].

Image mining in computer forensics would ideally use a combination or hybridization of these methods. For example, the inherently interactive and continually changing nature of a forensic investigation would favour a user relevance feedback approach together with either a model-based or statistical approach that would capture knowledge about the objects in the image and better retrieve images with specific types of objects (rather than just similar images).

For general image forensics, investigators often identify certain objects or scenes in an image which might suggest a criminal activity by their co-occurrence or relationships with each other. For example, the presence of firearms and maps of an important building might suggest a potential armed hold-up. Thus, our aim is to look for a generic method of image mining which is capable of detecting objects and/or scenes that are made up of components, where components can be nominated by investigators. These components can also be constrained by spatial or non-spatial relationships and might be deformed by various standard transformations. We also wish to provide a system that can be trained by examples, and furthermore can be iteratively improved by using relevance feedback supplied by investigators on retrieval results.

We now elucidate a prototype mining system [3], in order to provide a basis for the later grammar which we use to describe scenes in more complex search queries. The prototype system is for detecting partially clad humans in swimwear.

PROTOTYPE SYSTEM OVERVIEW

The system is composed of two main parts: training and querying. The training process involves the setting up of object models which includes the specification of the parameters for image features used by the component classifier, and the constraints on the position and orientation of the components to make up an object. The model trainer who performs this task should have some understanding of the principles underlying the classifiers as well as insight into the types of objects required for forensic evidence. The system performs segmentation on a sample set of images (called the training set) to obtain: image patches which contain those components of interest; the feature parameters of these components (e.g. arm, leg); and their position and orientation constraints (e.g. above, behind). These will be used as input to train the classifier. The training process gradually refines the models through the modification of parameters and the addition of false positives and false negatives resulting from test runs. Once the models have been specified and the classifier has been trained, the query operator can set up a query based on the components of interest and the constraints to be placed on them to form an object of interest. The system will then perform the classification and return those images that contain the object of interest.

Image Component Detectors

We achieve improvements on the performance of image component detectors in a number of aspects. The detectors are sensitive over the problem of scaling caused by relative size of the image, object and object components. We also find that the detection accuracy is improved when HSV colour space is used instead of RGB. In particular, YCbCr colour space gives better discrimination for human skin tone. Mohan et al. [4] dealt with the translation of objects and their components by traversing the wavelet decomposition space to crop certain regions of coefficients used for classification. We deal with in-plane rotation by rotating the wavelet space coefficients to search for a match. We find that the out-of-plane rotation does not cause a problem if fairly coarse scale coefficients are used. We use low coefficients in addition to high wavelet coefficients in order to add more discrimination for areas of low contrast.

Hierarchical Classifier

The component detectors are integrated into a hierarchical system in the following way. The patches that contain object components are constrained to locations based on knowledge obtained from the training sets. The results of the component detectors at constraint locations are then fed into a trained SVM for the whole object. While a quadratic SVM is used for component detectors, a linear SVM is used for the object detector because of its robustness for partial detection.

Feature Vectors

Each vector is made up of two main groups of information edge coefficients defining the outline of body parts and regions defining areas of continuous tones. The number of entries for each vector depends on the number of coefficients making up the two components of the component detector. Therefore, the feature vector varies for each component detector generated. Each vector thus contains two levels of the wavelet pyramid at the 16x16 and 32x32 pixel coefficients – except in the case of faces which are 8x8 and 16x16 due to the smaller patch size. That is, the region and edge information is repeated for each level within the final feature vector.

Edge Coefficients

Figure 1 shows the high threshold coefficients for the ensemble images (white squares are above an arbitrary threshold set to obtain a nice outline). These represent consistently high Haar wavelet coefficient values throughout the training set of pelvis images. The image at the bot-

tom is the vertical wavelet coefficients, while the image at the top is the horizontal wavelet coefficient image.

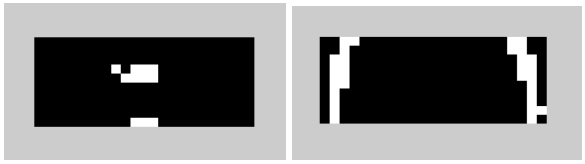

Figure 1 Horizontal and vertical wavelet coefficients for a pelvis.

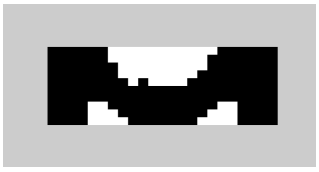

Figure 2 Threshold image of a pelvis.

Each of the white coefficients forms a variable in the feature vector. The maximum of the YCbCr components is written out from the actual image being processed. Therefore, in short, the white squares are the most important coefficients in the process of recognising the *outline* of a pelvis with a bikini. So the first component of each feature vector is a list of the most important coefficients from the vertical and horizontal wavelet coefficients.

Region Information

Figure 2 illustrates the threshold images from the same ensemble image set. Here, the white regions indicate coefficients below an arbitrary threshold. Therefore, these are regions of consistent colour across all the images in the training set. For the pelvis example, this indicates the presence of regions of skin that identify the shape of a pelvis.

Figure 3 illustrates an example image found by the detector. The white rectangles indicate the discovery of a body component (pelvis, torso, face). The results of the component detectors are then assessed by a whole body detector.

SEARCH DESCRIPTION GRAMMAR

From the basic system described, a grammar can be constructed to enable arbitrary scene descriptions to be devised for search queries. This grammar allows the search to be specified as a hierarchy of detectors, working at different structural resolutions. The grammar is made up of component detectors and object detectors and their related spatial relationships and position data.

Object detectors and component detectors are an abstraction of the detection mechanisms used to find components. The object detectors themselves are hierarchies of other component detectors and/or other objects. An entire scene description can be used in another object detection scene, and so on. The hierarchies can be at varying levels of precision. The high layers may implement rough detectors to find regions of interest for the lower levels to apply finer level detectors in a multi-resolution manner. Thus, the grammar allows the encapsulating system to store the resolution of the search at either a broad structural level (e.g. skin detection) down to fine grain informational detection (e.g. face, pelvis, torso).

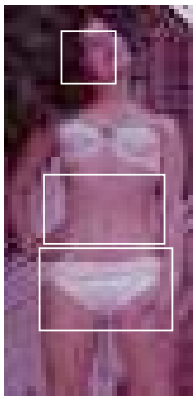

Figure 3 Example illustrating the locations of detectors on a possible positive image.

Relationships encapsulate relative spatial arrangements between the object detectors within the query description. This is specified in a multi-precision manner: from rough linguistic terms like up, down, above, below; to more precise terms like north, south, east, west; and then to orientation and absolute position specifications. Each of the absolute position measurements is specified in normalised image-space coordinates [0..1]. The orientation angle, specified in degrees relative to the horizontal axis, is also stored within each node. Each of these values have intervals attached which allow for deviation from the original positions. These terms, values and deviations facilitate the complete 2D specification of the arrangements of the detectors at levels of resolution relevant to the search task.

We describe the grammar in two sections. One for static scenes, and one for dynamic scenes. The static scene grammar will be implemented in full, to provide support for image query specifications across many application areas.

Static Scenes

The following diagram and text outlines the grammar for static search scenes. Figure 4 illustrates the n-ary tree data structure [5] for an example detector finding the co occurrence of human bodies and tanks in images. The human detector has been implemented, while the tank detector is hypothetical, but based upon the work developed for the partially-clad human body detector.

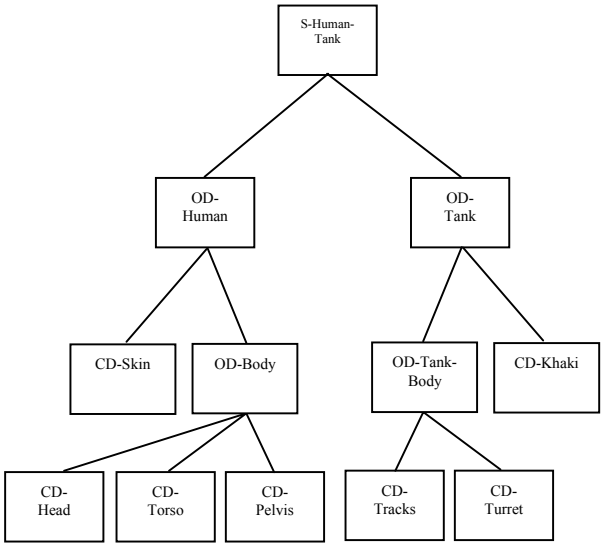

Figure 4 Diagram illustrating the hierarchical nature of the search grammar.

As can be seen in the diagram, the image mining query is described as a scene (marked S)to be searched for using a number of object detectors (marked OD) and component detectors (marked CD). Each node contains the relevant information to fully specify the spatial attributes of the object or component detector. Note that an object detector can be a collection of components and/or other object detectors, giving complete freedom to use predefined scenes as object detectors in other scenes. The object and component detector attributes are listed in Table 1 and Table 2.

Table 1 Table listing of Component Detector attributes

Component Detector Attributes	*Description*	*Constraints*
Comp-Detector-ID	Identification string for component detector.	Unstructured string of characters.
Comp-Detector-Loc	Directory location for detector.	Unstructured string of characters.
Displacement	2D motion displacement vector for detector from previous frame.	2 floats [0.0..1.0]
Orientation	Angle in degrees that the detector is rotated relative to vertical axis.	Float [0.0..360.0)
Relation-List	List of relationships to other objects/components in the scene.	Array

Table 2. Table listing of Object Detector attributes

Object Detector Attributes	*Description*	*Constraints*
Object-Detector-ID	Identification string for component detector.	Unstructured string of characters.
Object-Detector-Loc	Directory location for detector.	Unstructured string of characters.
Displacement	2D motion displacement vector for detector from previous frame.	2 floats [0.0..1.0]
Orientation	Angle in degrees that the detector is rotated relative to vertical axis.	Float [0.0..360.0)
Relation-List	List of relationships to other objects/components in the scene.	Array
Detector-List	List of object/component detectors making up the object detector.	Array must contain at least one component detector.

File Grammar

This hierarchy has been encapsulated into a file grammar to support the storage and manipulation of the data structure for future use by a user. This has been described using the following grammar, semi compatible with lex and yacc [6]. Comments are inserted to illustrate more obscure constructs. Some of the more atomic definitions have been elided in order to save space, e.g. the definitions for *free-form strings*.

```
Forensic-Scene:
    Scene
        Scene-Detector-ID
        Comp-Detector-ID
    End-Scene
    Scene
        Scene-Detector-ID
        Object-Detector-ID
    End-Scene

Comp-Detector:
    Component
        Comp-Detector-ID
        Comp-Detector-Loc
        Displacement_opt
        Orientation_opt
        Relation-List_opt
    End-Component
```

```
Object-Detector:
    Object
        Object-Detector-ID
        Object-Detector-Loc
        Displacementopt
        Orientationopt
        Relation-Listopt
        Detector-List
    End-Object

Detector-List:
    Detector-List, Gen-Detector-ID

Gen-Detector-ID: one of
    Object-Detector-ID, Comp-Detector-ID, Scene-Detector-ID

Scene-ID:
    S Freeform-String

Comp-Detector-ID:
    CD Freeform-String

Object-Detector-ID:
    OD Freeform-String

Comment:
# Freeform-String

Relation-List:
    Relation-List, Relation

Displacement:
    (Integer Integer)
    Compass-Dir
    Ling-Term

Relation:
    Compass-Dir Object-Detector-ID
    Abs-Pos
    Ling-Term Object-Detector-ID

# These compass terms cover a number of
# direction specifications, e.g. North and North West.

Compass-Dir:
    Compass-Term
    Compass-Term Compass-Term

Ling-Term: one of
    Above Below Left Right Up Down
```

The following lists the file format generated for the example scene detector in Figure 4. Note how the detectors are defined once and then referred to with an ID number.

```
Scene S-Human-Tank
    OD-Human
    OD-Tank
End-Scene

Object OD-Human
    CD-Skin
    OD-Body
End-Object

Object OD-Body
    /usr/CFIT/objects/body.svm
    CD-Head
    CD-Torso
    CD-Pelvis
End-Object

# The directory locations are just arbitrary
# examples, and are not representative of
# actual detectors.

Component
    CD-Skin
    /usr/CFIT/objects/skin.exe
End-Component

Component
    CD-Head-Detector
    /usr/CFIT/objects/head.svm
    90
    Above CD-Torso-Detector
End-Component

Component
    CD-Torso-Detector
    /usr/CFIT/objects/torso.svm
    90
    Above CD-Pelvis-Detector
End-Component

Component
    CD-Pelvis-Detector
    /usr/CFIT/objects/pelvis.svm
    90
End-Component

Object OD-Tank
    CD-Khaki
    OD-Tank-Body End-Object  Object OD-Tank-Body
    CD-Tracks
    CD-Turret
End-Object
# Tank components are defined similarly to the body detector.
```

Dynamic Scene Grammar

The previous static image search query grammar requires augmentation to model changes in the structure and relationships of the detectors when searching motion videos. The grammar needs to model the following dynamic effects:

- appearance/disappearance of objects – implemented via insertion and deletion operations on the n-ary tree;
- changes in the attributes of objects – implemented via searching for the appropriate tree node and then modifying contents;
- changes in spatial relationships between objects – implemented via the attribute modification operation;
- changes in the structure of the tree hierarchy – implemented as a deletion and insertion of sub-trees within the n-ary tree.

The appearance of a new object is handled by insertion of the new object detector into the hierarchy. This will facilitate the tracking of objects in motion scenes. Similarly, the disappearance of an object is handled by the deletion of a node from the n-ary tree.

Changes in the attributes of the objects include transformations such as: scale, shear, translation, rotation, and related modifications to linguistic spatial relationships to other objects and occlusion effects. This is accommodated by searching the n-ary tree for the object detectors in question, and then modifying the tree node contents. An additional displacement field stores the frame to frame 2D displacement of the detector in question.

Changes in the n-ary tree organisation, which may or may not indicate changes in the actual scene being searched for, are handled by standard sub-tree deletion and reinsertion operations. This may occur due to user modification of the search specification upon receipt of search results in a *user in the loop* feedback query scenario.

Each node can also have an additional co occurrence field to record the number of occurrences of the object within a scene. This allows the setting up of queries which seek to find more than one occurrence of the object in the scene without specifying the actual number of objects.

In the case of objects which become occluded in the scene, a visibility flag is used to indicate occlusion of an object, and not disappearance. Occlusion occurs when the detectors tracking objects in the scene overlap other detectors and one of the objects disappears.

The adaptive features of the data structure can be used to provide data mining facilities for the system. In particular, the number of occurrences of objects within an image database can be used to search for patterns that show likely relationships. The search engine may not specify a structure, but may contain a number of detectors which find occurrences of the objects and simply report back their number and spatial locations for use by rule induction techniques.

CONCLUSION

We have described a grammar for the specification of forensic image mining queries that facilitates the specification of arbitrary scenes using different detection systems at differing structural resolutions. Examples have been shown for the grammar that illustrates its power in describing a search query. This grammar will be implemented for the static scenes and in the future will be modified to accommodate motion scenes in videos. The adaptive nature of the search query grammar allows for other data mining applications, which may infer rules from searches of the image database.

We expect the applications of this grammar to be in the law enforcement, homeland security and web search facility areas. In general, the grammar can be used where a search specification requires a particular spatial arrangement of objects.

ACKNOWLEDGEMENTS

The authors wish to acknowledge the assistance of the Australian Defence Science and Technology Organisation in the development of this project.

REFERENCES

1. Niblack, W., et al. *Updates to the QBIC System*. in *Storage and Retrieval for Image and Video Databases*. 1997.
2. Muller, H., et al. *Strategies for positive and negative relevance feedback in image retrieval*. in *Proc. International Conference on Pattern Recognition ICPR2000.* 2000.
3. Brown, R., B. Pham, and O. de Vel, *Image Mining for Computer Forensics*. Submitted to IEEE Security and Privacy, 2003.
4. Mohan, A., C. Papageorgiou, and T. Poggio, *Example-Based Object Detection in Images by Components.* IEEE TRANSACTIONS ON PATTERN ANALYSIS AND MACHINE INTELLIGENCE, 2001. **23**(4): p. 349-361.
5. Gonzalez, R. and M. Thomason, *Syntactic pattern recognition : an introduction*. 1978, Reading, USA: Addison-Wesley.
6. Kernighan, B. and D. Ritchie, *The C Programming Language*. 2nd ed. 1988, Murray Hill: Prentice Hall.

Automated and Perceptual Data Mining of Stock Market Data

Keith V. Nesbitt
School of IT, Charles Sturt University
Bathurst, NSW, Australia
knesbitt@csu.edu.au

Abstract

Data mining large abstract data sets for useful patterns is an attractive proposition. It may, for example, reveal useful trading rules in stock market data. There are two basic types of data mining, Automated data mining tools use algorithms that allow the computer to search the data. Perceptual data mining tools present the data to the user's senses (vision, hearing, touch) in a way that the user can search for useful patterns. The two methods are not disjoint, as rules discovered with the user's perception can then be automated. This paper describes a case study, where a visual-auditory interface was used to uncover patterns in stock market data. Results from a formal evaluation are reported. The paper also includes a discussion on how to incorporate these results into an automated tool using an agent framework.

INTRODUCTION

A problem facing many areas of industry is the rapid increase in the amount of data and how to deal with it. However, these large amounts of data could also be considered a resource. The term *data mining* has been used to describe the diverse methods used to explore abstract data in the search for valuable and unexpected patterns [8].

The available tools for *data mining* can be considered in two broad categories, *Automated Intelligent Tools* and *Human Perceptual Tools* (see figure 1). *Automated Intelligent Tools* implement well-defined strategies for finding rules or patterns in data. These systems take advantage of a computer's capability to perform error-free, repetitive tasks and to process large amounts of data efficiently. *Human Perceptual Tools*, on the other hand, display the data to the user and allow the user to search for patterns. These systems take advantage of the human capability to perform subtle pattern matching tasks.

In fact the two types of data mining are closely related. New rules discovered by users of *Human Perceptual Tools* can be automated. These new patterns thus then form the basis of a new *Automated Intelligent Tool* (see figure 1). The primary motivation of this paper is to illustrate this close relationship with a real world case study.

The are a number of different approaches to developing *Automated Intelligent Tools* [17]. These include supervised methods, such as, Neural Networks and Linear Regression Models. They also include unsupervised methods, such as, K-means and self-organising maps. Because the idea of a Human Perceptual Tool is less familiar this paper reviews in more detail work in this area. In particular the review concentrates on the design of multi-sensory displays for virtual environments.

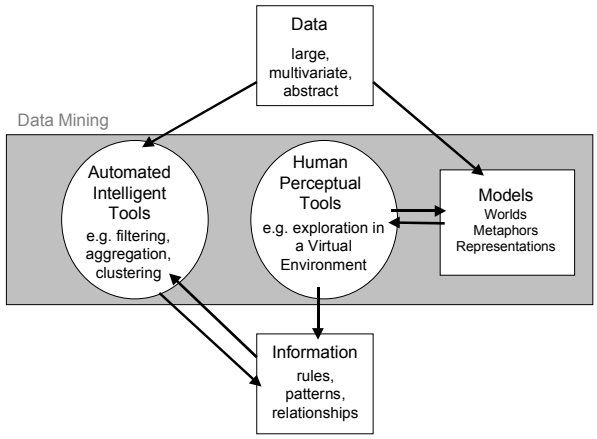

Figure 1. The two categories of data mining and the relationship between them.

The case study described in this paper is from the domain of stock market trading. The abstract data in this case uses *bid* and *ask* data from the Australian Stock Exchange. This data is also described as depth of market data. It is gathered in real time and captures offers made by potential buyers (bids) and sellers (asks) of a particular stock. The design of a auditory-visual display for predicting the direction of the stocks price is described. The results from a formal evaluation are detailed. The null hypothesis of the experiment was that "non-experts could not predict the direction of the stock price using this tool". Surprisingly the null hypothesis was proved false.

This motivates the possibility that useful patterns have been detected in the display. The reasoning used by each user to make decisions was also captured during the experiment. These "heuristics" are sometimes in conflict or competition. Even single users perceived conflicting sensory information when using the multi-sensory displays. One way to handle such complexity is to use an agent model. Such models have proved successful for modelling complex domains [7] and could provide a useful framework for implementing an automated tool. The preliminary design for such a tool is discussed. The paper concludes with an outline of further work.

PERCEPTUAL DATA MINING

It can be expected that *Human Perceptual Tools* are particularly useful where:

- Unpredictable exceptions may occur in the data.
- Heuristics are required to filter subtle variations.
- The target is unknown or cannot be precisely formalised by rules.
- The problem requires intuitive knowledge that is hard to formalise, such as, past experience.

During the 1990s, the accent for Human Perceptual Tools was on designing visual displays of data. This approach is called *Visual Data Mining* [17]. A number of example applications have been described and the field of Information Visualisation [4] has emerged. There are also some good examples using sound display [9] for finding patterns. Haptic (touch) displays are still relatively uncommon although they have been employed in novel ways to investigate force fields [3] and fluid flow fields [14].

To implement a Human Perceptual Tool typically requires a Virtual Environment. There have been a number of descriptions of Virtual Environments that define their properties [6]. These properties include immersion in a three-dimensional, synthesised world and multi-sensory interaction within that world [6]. One goal of Virtual Environments is to widen the bandwidth between human and computer. With multi-sensory interfaces the user can potentially perceive and assimilate multi-attributed information more effectively. By mapping different attributes of the data to different senses, such as the visual, auditory and haptic sense, it may be possible to better understand large data sets.

Displaying more data to the user makes perceptual data mining an enticing approach to searching large data sets. Designing a display using multiple displays is particularly difficult as sensory interactions can occur [15]. Previously the design space itself was not well enumerated. However, recent attempts have been made to better categorise the design space, gather guidelines and also provide a process for designing these displays [15].

TECHNICAL ANALYSIS

Stock market data contains many attributes, far more than traders can readily comprehend. Yet traders attempt to determine relationships between the data attributes that can lead to profitable trading of financial instruments. Predicting the market has some obvious rewards. However, the complex dynamics and interactions that drive the stock market are very difficult to model. Although a number of agent based systems have been developed to predict aspects of the market none of these have been proved successful in a all types of market conditions [1][10][11] [12].

Market traders make use of two types of complementary analysis. They are known as *technical analysis* and *fundamental analysis* [16].

Fundamental analysis studies the underlying factors that determine the price of a financial instrument. For example, factors such as, a company's profit, market sector, or potential growth can influence the share price. These factors can be considered against more global considerations such as the general economic trend. Fundamental analysis is the more traditional form of analysis used to trade the market.

Technical analysis is defined as "the study of behaviour of market participants, as reflected in price, volume and open interest for a financial market, in order to identify stages in the development of price trends" [16]. Unlike fundamental analysis, technical analysis ignores the underlying factors that determine price and makes the assumption that the price of a financial instrument already quantifies all these underlying factors. Technical analysis is based on patterns that can be found directly in the data. This case study is based on Technical Analysis.

CASE STUDY – DEPTH OF MARKET TRADING

This case study focuses on the search for short term trading rules based on *depth of market data*. Short-term players of the market, such as day traders, may wish to make minute by minute decisions from live feeds of stock data. The *depth of market* refers to the number of buyers and sellers currently trying to trade a financial instrument. A buyer may make a *bid* to purchase a specified volume of shares while at the same time a seller may *ask* a price for some specified volume. The balance of bids and asks determines the state of the current market. The difference between the highest bid and lowest ask is known as the *spread*.

Table 1. Traditional table used to display depth of market data.

Buyers		Trade 12.03	*Sellers*	
Volume	Price		Price	Volume
40,230	12.03	1	12.04	20,000
1,000	12.02	2	12.06	68
34,000	12.02	3	12.07	450
500	11.99	4	12.09	12,000
2300	11.98	5	12.10	6,000
10	11.97	6	12.11	10,200

The task of buying and selling shares to make a profit on short-term variations in market prices is called *discretionary trading*. The emphasis is on making a small profit many times during the period of trading. A trader may decide to sell when the volume of bids around the last trade price outweighs the volume of asks, or conversely sell if asks outweigh bids.

Traditionally the depth of market data is displayed in a table (see table 1), which updates every 30 seconds or so. The bids and asks are sorted so that highest bid and lowest ask are shown at the top. The difference between the highest bid and lowest ask indicates the spread. A wider spread usually indicates a lower likelihood that a trade will occur. The price of the last trade is shown for comparison with the

current spread. Other more peripheral information includes the volume of stock in bid and ask quotes, and the context provided by lower bids and higher asks.

CASE STUDY – DESIGN

The visual part of the multi-sensory display was designed to provide extra context and historical information that is not easy to interpret from a conventional tabular display. The data is represented by a series of surfaces formed by the volume of bids, asks and trades at each price (see Figure 2). Price is on the X axis, volume on the Y axis and updates in time are appended on the Z axis. Bids are coloured yellow and asks are coloured green to separate them. The highest bid and lowest ask are next to each other close to the centre of the display while less important data spreads to the periphery. The trades are shown as a red river that also tracks the market spread (the difference between highest bid and lowest ask).

Note that as new data is used to update the display the visualisation takes on the form of an evolving 'landscape' that looks like a valley between two hills with a river flowing through it. It is proposed that this 'ecological' metaphor may help users interpret the visualisation from familiar natural properties such as 'steepness' of cliffs or 'height' of the hills.

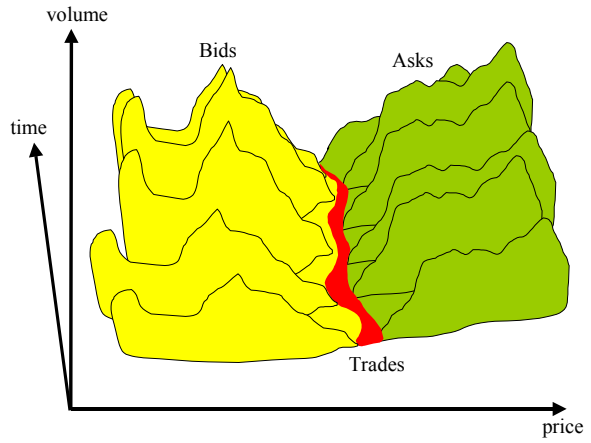

Figure 2. A conceptual model of the depth of market visualisation.

The sound display design method has two levels - a schema level and a perceptual level [2]. At the schema level a 'market place' metaphor is adopted. In this market place sellers shout the price of produce and buyers reply with offers or agree to trade. It is proposed that listeners using the display may interpret 'direction' of the next trade from this familiar experience. At the perceptual level we map information from the data attributes onto perceptually scaled auditory variables. This mapping considers issues of perceptual grouping and segregation in the auditory scene. While the final display is quite simple to interpret the full mapping is very complex and has been described elsewhere [15].

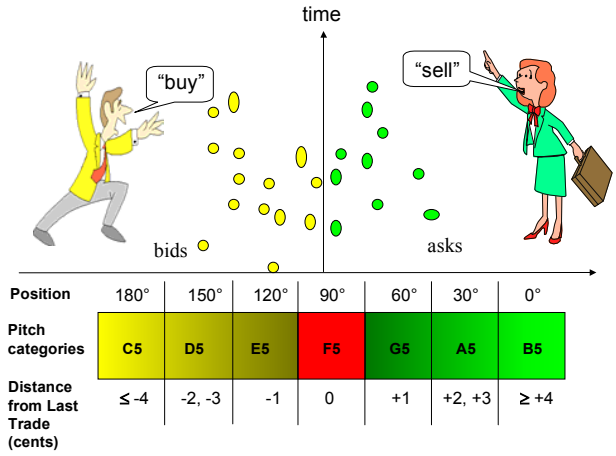

Figure 3. A conceptual model of the depth of market sound display.

Bids and asks are heard as they are made and come from the left or right as though from a crowd (see figure 3). If the bid or ask is lower than the last trade it is heard to the left, if it is the same then it comes from the centre and if it is higher it comes from the right. A flurry of bids to the right could indicate demand to buy at a higher price than the last trade and could indicate upward movement in trade price. A pattern of bids to the left mixed with asks to the right might indicate equilibrium in the market.

The resulting display should enable quick, confident and accurate answers to the global question "what is the direction of the next trade?" - either up or down. It should also enable answers to intermediate questions about relations between data elements such as "how wide is the current spread between bids and asks?" and "where is the current activity relative to the last trade?". At the local level it should allow answers to questions about individual elements such as "are there any bids?" or "what is the volume of the most recent ask?"

CASE STUDY – EVALUATION

The experiment was designed to answer the questions:

- Can people use the visual (V), auditory (A) and combined multi-sensory (M) displays to predict the direction of the next trade from depth of market data?
- What differences are there in performance with the visual, auditory and multi-sensory displays?
- Do people find consistent patterns in the data?
- How do people make decisions from these displays?

The multi-sensory depth of market display was implemented and evaluated on a BARCO stereo Projection Table, (see figure 4), in the CSIRO Virtual Environment Lab, Canberra. The null hypothesis for the evaluation was that

subjects cannot predict the direction of the next trade from these displays. The alternative hypothesis that subjects can predict market direction depends critically on the technical trading hypothesis that all the information needed is contained in the data. Since it relies on this premise the data was recorded from real trading data for two shares over a day of trading on the Australian Stock Exchange. The data were divided into 6 subsets, three for training and three for evaluation. These subsets were randomly allocated to visual training, visual evaluation, auditory training, auditory evaluation, multi-sensory training and multi-sensory evaluation for each Subject. The Order of presentation of the different Modes of display (Visual, Auditory, Multi-sensory) was also randomised.

Figure 4. The Barco Projection Table at the CSIRO VE Lab being used during the evaluation.

Each Subject carried out the experiment one at a time with the researcher. At the start the Subject was given a written introduction to trading with depth of market stock data, and allowed to ask questions. They then carried out a training session followed by an evaluation session for each Mode. In the training session the Subjects were shown a display of historical data which was paused at 10 random points where they were told the direction of the next trade - up or down. In the evaluation the Subjects were asked to predict the direction of next trade at 10 random pause points as either up or down. The up and down movements were between 1 and 7 cents, with 80% of the decision points involving only 1 or 2 cent changes. After each evaluation the Subjects were asked for comments.

The Subjects comprised 13 males and 2 females between the ages of 20 and 42. Only one subject had any familiarity with depth of market data and none had traded on the stock market. For each Subject 10 predictions were recorded for each of the 3 Modes (V, A, M). At the end of the evaluation subjects were interviewed and asked how they made decisions using each display. Each Subject typically took 45 minutes to complete the training and evaluation.

CASE STUDY – RESULTS

The analysis was separated into 'total' predictions and predictions of price increase ('up') and predictions of a price decrease ('down'). Analysing totals correct out of 10 by regression analysis showed no significant effect for variation in Subject, Mode or Order. (see table 2). Next the analysis considered proportions of correct predictions for trades that went up in price separately from trades that went down using generalised linear models [5]. In the up direction there were no significant effects, for Subject Mode or Order. However, in the down direction some Subjects performing significantly better than others (P=0.014), and there was also a significant variation with Mode (P=0.029). However the Order was still not significant.

Table 2. P values for significance (P<0.05) of main variables in experiment.

Direction	*Subject*	*Mode*	*Order*
all (up+down)	0.884	0.397	0.953
up	0.981	0.812	0.793
down	**0.014**	**0.029**	0.653

Table 3. Experimental analysis for prediction groups (all, up, down).

G	M	#	T	%	PC	s.e.	P
all	V	92	150	61.3	0.613	0.047	**0.000**
	A	105	150	70.0	0.070	0.047	**0.000**
	M	105	150	70.0	0.070	0.047	**0.000**
up	V	50	85	58.8	0.583	0.077	0.128
	A	46	78	59.0	0.595	0.079	0.141
	M	42	64	65.6	0.658	0.085	**0.017**
down	V	43	64	67.2	0.649	0.050	**0.008**
	A	59	72	81.9	0.831	0.036	**0.000**
	M	63	86	73.3	0.734	0.046	**0.000**

Table shows: prediction group(G), Mode (M), number of correct predictions (#), total number of predictions (T), percentage correct prediction (%), estimate of mean proportions correct (PC) and standard error (s.e.) for one binomial trial, and the exact two-tailed binomial of calculated probability (P).

Next we compared how well the Subjects were actually predicting the direction of the next trade, using the regression model to estimate mean proportions correct (PC) and standard error (s.e.) for one binomial trial, and using an exact two-tailed binomial to calculate probability (P) of the result occurring by chance. This analysis shows Subjects predict the direction of the next trade at levels significantly above chance in all three Modes, with A (70%), M (70%) and V (61.3%) (see table 3).

Subjects were best at predicting down trades from A (83.1%) followed by down trades from M (73.4%), up trades from M (65.8%), and down trades from V (64.9%). The prediction of up trades from V (58.8%) and A (59.0%) separately was not significantly above chance. The effectiveness of M in the up direction where the individual V and A are not so effective indicates that complementary information from both Modes is needed to predict up trades. Subjects predict down trades much better than up trades, at levels so far above chance that the overall analysis shows significant prediction for all 3 Modes despite the up results. The prediction of down trades was best with the A (81.9%), followed by M (73.3%), and then V (67.2% correct). These results suggest that A is the best source of information for predicting down trades, and that the combination of A with V reduces performance in the M display.

CASE STUDY – TOWARDS AN AGENT MODEL

The results from this evaluation are quite complex and further discussion of the issues raised about perceptual displays and predicting stock market direction are discussed elsewhere [13]. The results are encouraging but a great deal of caution is required. Many stock market prediction systems are highly dependent on the current market and the particular stock being predicted. Hence it would be desirable to automate the predicting process so a broader array of conditions could be analysed.

The first question that needs to be addressed is: Do people find consistent patterns in the data? The frequency for the proportion of correct responses at each decision point was analysed (see figure 5). While there were too few predictions made at each decision point to statistically validate the presence of patterns. However, indications are promising, with 10 points consistently predicted and 1 point consistently mis-predicted.

The second question that is addressed is: How do people make predictions? The comments from each Subject were recorded after the evaluation in each Mode. In the Visual display nine Subjects commented that they made decisions based on 'size, height, slope and steepness of cliffs', 'how close the peaks were to the centre', and 'bending and trends in the river or valley'. Three said they could not understand how to make decisions. One commented that it was not clear whether the 'forces shown by hills' were pushing or pulling against each other. Overall three Subjects said they preferred the Visual display.

In the Auditory display the Subjects made decisions from 'frequency of calls', 'closeness to the centre', and 'loudness'. Six said they found it easy to understand the Auditory display. One commented that the words 'buy' and 'sell' could be interpreted as commands rather than labels which could lead to a prediction in the opposite direction. One commented that information about the last trade price was missing from the Auditory display.

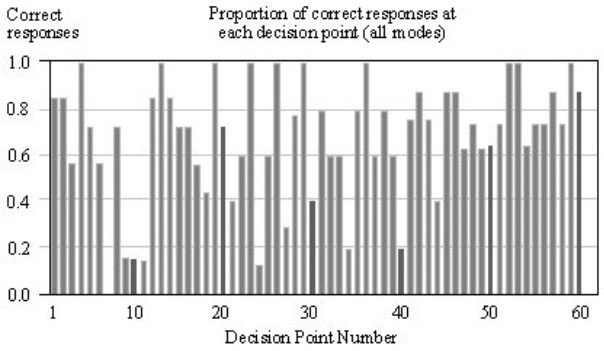

Figure 5. Proportion of correct predictions at the 60 decision points in the data.

In the Multi-sensory display Subjects commented that the combined display contained more information than the Visual or Auditory alone, and that the Visual display provided 'context, history, past and general trends', while the Auditory display provided 'most recent trends', 'focus', 'eagerness' and 'presence'. Four mentioned that if the Visual display was not clear they used the Auditory display to make the decision. Four commented that Visual and Auditory displays were sometimes in conflict, and 3 of these relied on the Auditory while the other relied on the Visual in this situation. One found the conflicts in Multi-sensory display made it more ambiguous and preferred the Auditory alone. Another found the Auditory display distracting and preferred the Visual over the Multi-sensory display.

What is interesting about the comments recorded from Subjects is the different heuristics used to predict trade direction and also their level of confidence. In effect the Subject's approach to interpreting the display provides a way of generating rules to automate the data mining process. The Subjects are in fact intelligent agents and we have tried to capture their beliefs, desires and intentions. What is interesting is that Subjects do not have an agreed approach and even find there own senses in disagreement. Sometimes the information from the Auditory and Visual displays conflict and at other times they collaborate. Some Subjects are strongly biased to the visual patterns while others favour the auditory information. This complex system indeed suggests that an Agent framework might be best suited to automate the data-mining.

A simple hierarchical model is proposed (see figure 6). At the lowest level there are two main families of agents. One family predicts on the basis of 'Auditory' rules. This in effect incorporates shorter-term fluctuations in the data. The second family uses 'Visual' rules that capture longer-term trends in data. Agents may collaborate or disagree within these families.

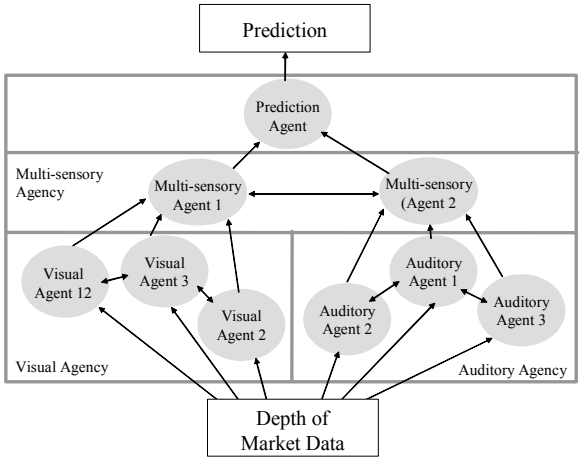

Figure 6. A proposed agent model for automating the prediction process.

At a higher level the results of the 'Auditory' and 'Visual' agents are processed by an agency of 'multi-sensory' agents. These agents incorporate longer-term and shorter-term information. In fact it is quite normal to incorporate longer term trading information into shorter-term trading rules [16]. For example, a bull market is a long-term up trend. In such a market it is expected that short-term trends are more likely to go up then down. It is likely that many agents with different policies will generate an array of predictions with different levels of confidence. A top-level agent, the 'Prediction' agent must resolve any conflicts and arrive at a final prediction.

FURTHER WORK

The Agent model needs to be implemented and tested. Work is under way to formalise the 'Visual' and 'Auditory' patterns that have been detected in the perceptual tool. The flexibility of an agent system makes the task of adding and removing 'rule' agents quite simple.

An automated tool will allow better testing of the results from the perceptual data-mining tool. However, the perceptual tool has already yielded promising results and more work is also ongoing to test the multi-sensory display in 'live' trading situations.

What this case study shows is that the two types of data-mining, perceptual and automated can in fact work together to yield cooperative benefits to the individual in search for patterns in abstract data.

ACKNOWLEDGMENTS

This work was carried out in collaboration with staff at the CSIRO Virtual Environment Laboratory in Canberra. I would like to thank Stephen Barrass and Warren Muller who provided major contributions to this work. Stephen's expertise is in the area of sound displays and he was instrumental in the design of the sound displayed used in this work. Warren provided invaluable help with experimental design and analysis.

REFERENCES

[1] Arthur, W. B. Holland, B. LeBaron, R., Tayler, P. Asset pricing under endogenous expectations in an artificial stock market. In W. B. Arthur, S. Durlauf, and D. Lane, editors, The Economy as an Evolving Complex System II, pages 15-44. Addison-Wesley, Reading, MA, (1997).

[2] Barrass, S. "Auditory Information Design". Ph.D. Thesis, Australian National University, Canberra, Australia (1997).

[3] Brooks, F. P., Ouh-Young, J. M. et al. "Project GROPE– Haptic Displays for Scientific Visualization." *Computer Graphics* 24(4): 177-185. (1990)

[4] Card, S. K., J. D. Mackinlay, et al., Eds. *Information Visualization. Readings in Information Visualization*. San Francisco, California, Morgan Kaufmann Publishers, Inc. (1999).

[5] Dobson, A. J. "An Introduction to Generalized Linear Models", Chapman and Hall, London, (1990).

[6] Durlach, N. I. and A. S. Mavor, Eds. *Virtual Reality: Scientific and Technological Challenges*. Washington, D.C., National Academy Press. (1995)

[7] Gallimore, R J., Jennings, et. al. "Cooperating Agents for 3D Scientific Data Interpretation"., IEEE Transactions on Systems, Man and Cybernetics, (1996).

[8] Groth, R. *Data mining: a hands-on approach for business professionals*. Upper Saddle River, N.J., Prentice Hall. (1998).

[9] Kramer, G. *An Introduction to Auditory Display. Auditory Display:Sonification, Audification and Auditory Interfaces*. G. Kramer, Addison-Wesley Publishing Company. (1994).

[10] Lettau, M. Explaining the facts with adaptive agents: The case of mutual fund flows. Journal of Economic Dynamics and Control, 21:1117-1148. (1997).

[11] T. Lux. The socio-economic dynamics of speculative markets: interacting agents, chaos, and the fat tails of return distributions. *Journal of Economic Behavior and Organization*, 33:143-165. (1998).

[12] Lux, T. and Marchesi, M. Scaling and criticality in a stochastic multi-agent model of a financial market. *Nature*, 397:493-500, 1999.

[13] Nesbitt, K. and Barrass, S. (2002) "Evaluation of a Multimodal Sonification and Visualisation of Depth of Market Stock Data", Proceedings of the International Conference of Auditory Display. Kyoto, Japan, pp 233-238. (2002).

[14] Nesbitt, K. V., Gallimore, R. et al. "Using Force Feedback for Multisensory Display". *2nd Australasian User Interface Conference AUIC 2001*, Gold Coast, Queensland, Australia, IEEE Computer Society. (2001)

[15] Nesbitt, K. V., "Designing Multi-sensory Displays for Abstract Data", PhD Thesis, University of Sydney, Sydney, Australia (2003).

[16] Nicholson, C. *Technical Analysis*. Course Notes E114. Sydney, Australia, Securities Institute and Australian Technical Analysts Association. (1999).

[17] Soukup, T. *Visual data mining: techniques and tools for data visualization and mining*. New York, John Wiley & Sons. (2002).

EXPERT, FUZZY & NEURAL SYSTEMS I

(This page left blank intentionally)

Comparison of Recognition Methods for Emotions Involved in Speech

Kazuhiko Takahashi
Faculty of Engineering
Yamaguchi University
Tokiwadai Ube, Yamaguchi, Japan
kylyn@yanaguchi-u.ac.jp

Ryohei Nakatsu
Faculty of Science and Engineering
Kansaigakuin University
Sanda, Hyogo, Japan
nakatsu@ksc.kwansei.ac.jp

Abstract

This paper investigates the characteristics of recognizing emotions contained in human speech. The concept of artificial neural network (ANN) is adopted for a recognition algorithm. An approach based on the support vector machine (SVM) or hidden markov model (HMM) is also investigated as an alternative recognition method. Using a large database of phoneme-balanced Japanese words, three recognition systems are trained and tested. To evaluate the emotion recognition results, emotion recognition testing is carried out with human subjects. The obtained average emotion recognition rates are 51% using ANN, 51% using SVM, 32% using HMM, and 55% with humans. Experimental results confirm that the emotion recognition rate achieved by using the ANN or SVM in the speaker- and context-independent mode is feasible and that ANN and/or SVM are well suited to this task.

1 Introduction

Speech involves a great deal of information: verbal information that conveys the speaker's will, personal information that expresses aspects of the speaker's personality such as age and gender, and emotional information that expresses the speaker's emotion or mood. In speaking text, several different meanings can be expressed depending on how it is said. For example, with the word "really" in English, a speaker can ask a question, express either admiration or disbelief, or make a definitive statement. An understanding of text alone cannot successfully interpret the meaning of such a spoken utterance. Therefore, it is clear that nonverbal information such as emotions plays an important role in communication.

Emotion recognition in speech has many potential applications. One possible use is as an aid to speech understanding. Speech understanding has traditionally treated emotion as noise, however, it is possible that by recognizing the emotions in speech one could subtract them from the speech and improve the performance of speech understanding systems. Another possibility is that an emotion recognition system could serve as a kind of 'emotional translator'. Emotions are often portrayed differently in different cultures and languages (e.g., one type of intonation that indicates admiration in Japanese can indicate disbelief in English). A method of translating emotions between languages can help improve international communication. Moreover, in order to make interactions between humans and machines more natural, the capability of communicating with humans by using both verbal and non-verbal communication channels will be essential on man-machine interfaces [13].

Although the importance of non-verbal aspects of communication has been recognized, most research has involved nonverbal information for images (e.g., facial expression [12] and gesture [16]) while little research has been done in the recognition of emotions involved in human speech [2, 3, 5]. With this and its potential uses in mind, we studied the recognition of emotions involved in speech and developed an emotion recognition system using an artificial neural network (ANN) [10]. A recognition rate of approximately 50% was achieved for speaker- and context-independent mode, however, it was not clear whether the emotion recognition rate of our system is satisfactory or not.

In order to evaluate the emotion recognition system, this paper investigates the characteristics of emotion recognition methods based on ANN, support vector machine (SVM), hidden markov model (HMM), and human subjects. First we explain the recognition of emotion involved in speech. Next, we describe how to design a recognition system using ANN, SVM or HMM. We then carry out recognition experiments with the ANN, SVM, HMM, and human subjects. Finally, we discuss the emotion recognition characteristics.

2 Emotions Involved in Speech

In this study, emotion recognition experiments were carried out with the following assumptions.

- Consciously and purposefully expressed emotions are treated since they are easier for humans to recognize [9] and significantly easier to gather data on.

- Eight emotional states (joy (J.), teasing (T.), fear (F.), sadness (Sa.), disgust (D.), anger (A.), surprise (Su.), and neutral (N.)) are selected by considering several works of emotion classification systems [4, 7, 8, 14].

- By carrying out training with a number of different speakers and a large set of phoneme-balanced words, a recognition system achieves speaker- and context-independence.

- A combination of two kinds of speech features, phonetic features and prosodic features, is considered because it is difficult to express emotions by only controlling prosodic features as these two kinds of features are tightly combined in uttering speech.

Recognizing emotions is a difficult task because people mainly rely on meaning recognition in daily communication. This is why speech recognition research has long treated emotions contained in speech as simply fluctuations or noise. What makes the situation more complicated is that emotional expressions are consciously or unconsciously intertwined with the meaning of speech. In the unconscious state, context plays a more important role than emotional features. As a result, the intensity of emotional expression varies dramatically depending on the situation. Our final target is to recognize emotions in speech even if emotional expression is unconsciously mixed with the meaning of speech. However, for the time being, this is not our research target for the above reasons. Instead, the strategy adopted here is to treat speech intentionally uttered with specific emotional expressions but not speech with unconscious emotion expressions.

2.1 Speech database

In gathering data, we adopted 100 phoneme-balanced Japanese words (e.g., "daidokoro (kitchen)", "ikioi (force)", "jyuuichigatsu (November)", etc.) because our target is context-independent emotion recognition. Since we utter most of these words without any special emotion in our daily life, it is difficult for ordinary people to intentionally utter them with emotions. Therefore, we first recorded the utterance of 100 words with each of the eight emotions by two voice actors (male and female). Then each of our subjects listens to the recordings of the voice actors and tries to imitate them. A total of 100 speakers, 50 male and 50 female native Japanese speakers, served as subjects. Each subject uttered a list of 100 Japanese words eight times, one time for each of the eight emotions.

2.2 Feature Extraction

As the phonetic features, we adopted linear predictive coding (LPC) parameters [6], which are typical speech feature parameters often used for speech recognition. The prosodic features consist of three factors: amplitude structure, temporal structure, and pitch structure. Speech power and pitch parameters are used to express amplitude structure and pitch structure, respectively, and each can be obtained in the LPC analysis. In addition, a delta LPC parameter, which is calculated from the LPC parameters and expresses a time variable feature of the speech spectrum, is adopted since it corresponds to temporal structure.

The speech feature is obtained in the following way. Analog speech is first transformed into digital speech by an A/D converter at an 11 kHz sampling rate and 16 bit accuracy. The digitized speech is then arranged into a series of frames, where each is a set of 256 consecutive sampled data points. LPC analysis is carried out and the following feature parameters are obtained for each of these frames.

$$\boldsymbol{f}^T = \left[\begin{array}{ccccccc} P_w & p & \delta & c_1 & c_2 & \cdots & c_{12} \end{array} \right], \qquad (1)$$

where P_w is speech power, p is pitch, δ is delta LPC parameter, and $c_j (j = 1, 2, ..., 12)$ is LPC parameter. These speech features are extracted from each utterance as shown in Fig. 1. First, the period where speech exists is extracted based on the information of speech power. Speech power is compared with a predetermined threshold value; if the speech power exceeds the threshold value for a few consecutive frames, the speech is determined to be uttered. After the beginning of the speech period, the speech power is also compared with the threshold value; if the speech power is continuously below the threshold value for another few consecutive frames, the speech is determined to no longer exist. Once the period of an utterance has been determined, the utterance is divided into 20 intervals of equal length in time. Let these 20 intervals be expressed as the vectors $\boldsymbol{f}_k (k = 1, 2, ..., 20)$. Each of the vectors has the 15 feature parameters of Eq. (1) for that interval.

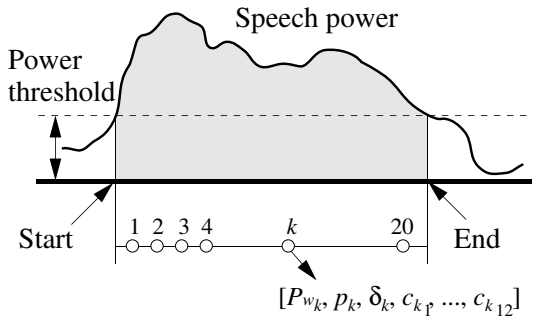

Figure 1. Speech feature extraction.

3 Emotion Recognition Methods

3.1 Emotion recognition by ANN [10]

The configuration of the ANN for emotion recognition is shown in Fig. 2. The network is composed of eight sub-ANNs, with one network for each of the eight emotions that are examined. The feature vector which is composed by the 20 speech vectors of 15 parameters, $\boldsymbol{F}_v^T = [\ \boldsymbol{f}_1^T \quad \boldsymbol{f}_2^T \quad \cdots \quad \boldsymbol{f}_{20}^T\ ]$, is simultaneously fed into all sub-ANNs. The output from each sub-ANN is a value (v_1, v_2, ..., v_8) representing the likelihood that the utterance corresponds to that sub-ANN's emotion. Decision logic selects the best emotion based on these values.

Each sub-ANN is a four-layer PDP model (300-M_1-M_2-1 network) and is trained by a back-propagation algorithm. The number of nodes in the intermediate layers, M_1 and M_2, varies depending on the specific emotion. A sigmoid function was used as an activation function of the nodes.

3.2 Emotion recognition by SVM

The SVM is a learning algorithm based on statistical learning theory [15]. Originally the SVM is designed for two classes classification by finding the optimal hyperplane where the expected classification error of test samples is minimized. There are several approaches to apply the SVM for multiclass classification. In this study, the one-vs-all method [1] is implemented.

Figure 3 shows the processing flow of the emotion recognition using SVM. Eight SVMs that correspond to each of the eight emotions were used. The ith SVM is trained with all of the training data in the ith class with positive labels, and all other training data with negative labels. Given a labeled set of N training data ($\boldsymbol{x}_i$, y_i), where $\boldsymbol{x}_i \in R^n$, $i = 1, 2, ..., N$, and y_i is the class of $\boldsymbol{x}_i$ ($y_i \in 1, 2, ..., 8$), the optimal hyperplane of the ith SVM can be found by solving the following problem:

$$\min_{w^i, b^i, \xi^i} \quad \frac{1}{2}(\boldsymbol{w}^i)^T \boldsymbol{w}^i + C \sum_{j=1}^{N} \xi_j^i (\boldsymbol{w}^i)^T$$

constrained by:

$$(\boldsymbol{w}^i)^T \phi(\boldsymbol{x}_j) + b^i \geq 1 - \xi_j^i \quad (if \quad y_j = i)$$

$$(\boldsymbol{w}^i)^T \phi(\boldsymbol{x}_j) + b^i \leq -1 + \xi_j^i \quad (if \quad y_j \neq i)$$

$$\xi_j^i \geq 0 \quad (j = 1, 2, ..., N)$$

where the training data $\boldsymbol{x}_i$ are projected to high dimensional feature space by the function ϕ, $\boldsymbol{w}^i$ is the weight vector, ξ_j^i is the slack variable that is introduced to account for non-separable data, C is the margin parameter that quantifies the trade-off between training error and system capacity. Solving the dual formulation of this problem, the optimal hyperplane can be defined by decision functions $y_i = (\boldsymbol{w}^i)^T \phi(\boldsymbol{x}) + b^i (i = 1, 2, ..., 8)$. The feature vector $\boldsymbol{F}_v^T$ is simultaneously fed into all SVMs ($\boldsymbol{x} = \boldsymbol{F}_v^T$) and the output from each SVM (y_1, y_2, ..., y_8) represents the likelihood that the utterance corresponds to that SVM's emotion. Decision logic selects the best emotion; the SVM that gives the largest value is chosen, and the class C_s (where $s = \arg\max_i y_i$) indicates the recognition result.

3.3 Emotion recognition by HMM

HMM is an nondeterministic state machine that, given an input, moves from state to state according to various transition probabilities. In each state, HMM generates output symbol probabilistically; this needs to be related to pattern features in an application-dependent manner. HMM, which is particularly suitable if the structure of the object sought is relatively clear, is commonly used in speech recognition

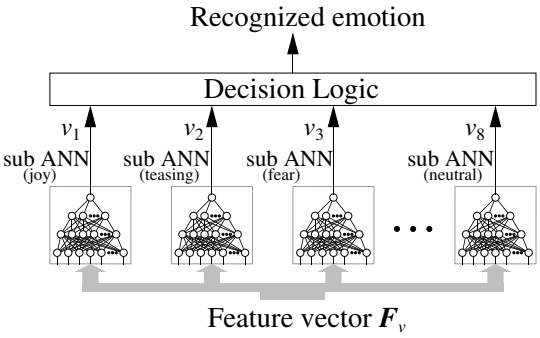

Figure 2. ANN-based emotion recognition system.

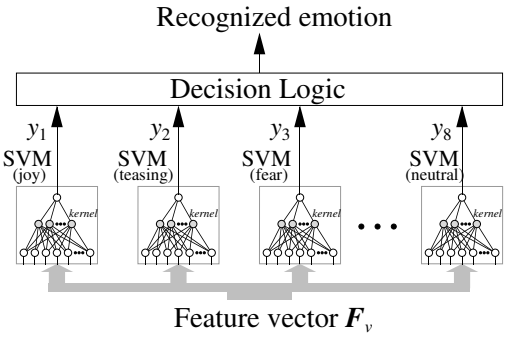

Figure 3. SVM-based emotion recognition system.

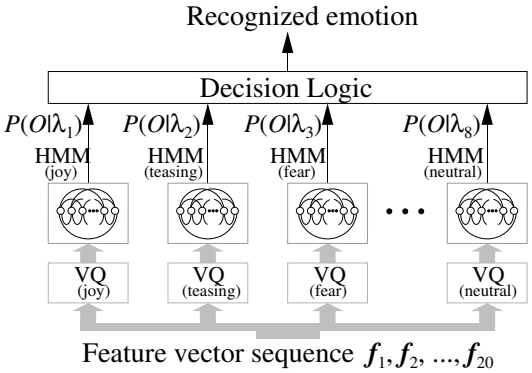

Figure 4. HMM-based emotion recognition system.

[11]. Since phoneme structures are the basis for the content of words or sentences, HMM is appropriate in speech recognition. The structure of emotions is not clear, however, we test HMM as an alternative recognition method.

Figure 4 shows the processing flow of the emotion recognition using HMM. Eight HMMs that correspond to each of the eight emotions were used. In this study, a discrete HMM modeled with an ergodic model was used. The input to the recognition system is the sequence of the feature vector $F = \boldsymbol{f}_1^T, \boldsymbol{f}_2^T, ..., \boldsymbol{f}_{20}^T$. First, a vector quantization (VQ) is carried out to transform the sequence of the feature vector F to a symbol sequence, $O = O_1, O_2, ..., O_{20}$. We used the category-separated VQ [17] in which the codebook B_i corresponds to category C_i and HMM λ_i ($i = 1, 2, ..., 8$). The codebook was created by using the LBG algorithm with the regular Euclidian norm. Next, each symbol sequence was fed into each HMM, which has been trained and re-estimated with the Baum-Welch algorithm using each emotional category's teaching data. The HMM then calculates the probabilities $P(O|\lambda)$ between the input symbol sequences and the teaching data with the Viterbi algorithm. Since category-separated VQ is adopted, a penalty function based on the distance between the input feature vector and the code word is considered in the probability calculation. Finally, the HMM that gives the highest probability is chosen in the decision logic, and the category C_s (where $s = \arg\max_i P(O|\lambda_i)$) indicates the recognition result.

4 Emotion Recognition Experiment

We used the large speech database for training ANN, SVM or HMM and carried out the following two types of recognition experiments to evaluate the performance of the recognition systems. In closed testing, utterances spoken by the speakers included in the training sets (#1-#30) are used for the recognition experiment. In open testing, utterances spoken by the speakers not included in the training sets (#31-#50) are used for the recognition experiment. The ANN, SVM, and HMM were trained and tested separately for male data and for female data.

Table 1. Recognition rates using ANN for male data [%].

	J.	T.	F.	Sa.	D.	A.	Su.	N.
J.	**31.00**	13.00	6.17	5.59	7.68	7.39	11.95	16.62
T.	10.36	**42.03**	8.05	4.99	11.50	5.48	8.78	8.81
F.	5.87	8.62	**40.18**	11.60	13.15	6.06	5.30	9.22
Sa.	2.65	2.17	10.96	**66.13**	4.50	2.65	1.18	9.76
D.	4.56	6.28	8.89	3.75	**63.30**	3.17	2.30	7.75
A.	5.42	2.94	4.11	3.40	2.94	**70.05**	4.11	7.03
Su.	10.31	10.55	4.02	2.90	5.09	9.14	**55.12**	2.87
N.	12.63	8.77	9.17	16.80	9.16	10.86	3.29	**29.32**

Table 2. Recognition rates using ANN for female data [%].

	J.	T.	F.	Sa.	D.	A.	Su.	N.
J.	**30.45**	14.67	4.84	0.34	2.82	24.37	12.78	9.73
T.	9.91	**45.21**	14.19	1.25	8.20	7.55	7.60	6.09
F.	2.06	4.21	**47.79**	29.32	6.73	2.82	0.39	6.68
Sa.	0.42	1.22	17.02	**75.35**	2.83	1.09	0.04	2.03
D.	1.90	6.04	12.53	4.74	**71.60**	1.16	0.58	1.45
A.	5.59	3.60	4.46	2.15	2.35	**72.68**	2.74	6.43
Su.	9.82	14.68	3.74	0	3.03	14.58	**52.60**	1.55
N.	13.88	6.99	17.42	16.56	5.85	11.56	0.81	**26.93**

In the training of the ANN, each ANN's network topology is first optimized using a small database composed of ten speakers. The optimization results were: (300-32-8-1) network topology for joy, teasing, fear and neutral sub-ANN, and (300-16-4-1) network topology for sadness, disgust, anger, and surprise sub-ANN. Then ANN was trained using 30 speakers where the maximum allowable error was 10^{-3} and the training epoch was limited to 1.6×10^4. In the closed testing, the averages of the recognition rates for all eight emotions were 57.4% for male data and 56.9% for female data. In the open testing, the recognition rates were 49.5% for male data and 52.8% for female data. The details of the open recognition results are shown in Table 1 for male data and Table 2 for female data. Here the row and column are the input and recognized class, respectively.

In the training of the SVM, we carried out tests with various kernel functions (Gaussian $\phi(\boldsymbol{x}_1)^T\phi(\boldsymbol{x}_2) = K(\boldsymbol{x}_1, \boldsymbol{x}_2) = exp(-\gamma|\boldsymbol{x}_1 - \boldsymbol{x}_2|^2)$, polynomial $K(\boldsymbol{x}_1, \boldsymbol{x}_2) = exp(-\gamma|\boldsymbol{x}_1 - \boldsymbol{x}_2|^d)$, and sigmoid function $K(\boldsymbol{x}_1, \boldsymbol{x}_2) = tanh(a\boldsymbol{x}_1\boldsymbol{x}_2 - h)$) and parametric studies of the margin parameter C to find the

Table 3. Recognition rates using SVM for male data [%].

	J.	T.	F.	Sa.	D.	A.	Su.	N.
J.	**32.33**	6.34	7.56	3.22	0.80	18.6	6.52	21.62
T.	11.26	**45.73**	11.19	2.80	7.48	5.73	6.43	9.37
F.	1.92	6.29	**60.03**	11.25	8.59	2.44	1.63	7.85
Sa.	1.12	1.12	15.83	**61.62**	2.80	6.72	0.14	10.64
D.	1.05	8.16	15.70	2.16	**67.06**	3.49	0.35	2.02
A.	9.44	1.82	7.41	3.36	1.54	**51.05**	1.61	23.78
Su.	20.57	8.12	3.50	0.70	2.24	6.58	**52.76**	5.53
N.	11.34	5.25	13.45	10.36	1.96	16.60	0.63	**40.41**

Table 4. Recognition rates using SVM for female data [%].

	J.	T.	F.	Sa.	D.	A.	Su.	N.
J.	**29.07**	10.57	3.24	1.76	2.96	19.80	15.47	17.12
T.	9.81	**41.92**	10.67	3.10	10.87	7.57	6.91	9.15
F.	1.57	1.96	**48.48**	33.01	5.68	2.60	1.91	4.80
Sa.	1.12	1.86	18.04	**66.89**	3.57	1.61	2.98	3.91
D.	1.41	5.57	6.93	4.87	**78.25**	1.08	0.60	1.30
A.	7.14	4.57	4.80	2.33	2.61	**59.93**	5.32	13.29
Su.	11.96	12.99	4.79	0.41	3.51	15.05	**44.28**	7.01
N.	9.76	5.50	12.15	19.78	3.86	11.35	2.53	**35.08**

optimal SVM. As a result, a maximum rate of the closed testing was reached with the Gaussian kernel function ($\gamma = 0.1$) under the margin parameter of 10. In the closed testing, 100% and 99.6% averages of the recognition rates for all eight emotions were achieved for male and female data, respectively. Table 3 and Table 4 show the details of the open recognition results, where the averaged recognition rates were 51.4% for male data and 50.5% for female data.

In the training of the HMM, we conducted tests with various codebook sizes (16, 32, 48, 64, and 128) for the LBG algorithm and various numbers of HMM states (8, 16, 32, and 48) to obtain the optimal HMM. As a result, a maximum rate of the closed testing was reached with a codebook size of 48 and 16 HMM states. In the closed testing, 49.5% and 44.5% averages of the recognition rates for all eight emotions were achieved for male and female data, respectively. Table 5 and Table 6 show the details of the open recognition results, where the averaged recognition rates were 32.2% for male data and 32.6% for female data.

Emotion recognition testing by human subjects was carried out as follows. A total of 28 subjects (22 males and 6 females native Japanese) were served. In this experiment, each of them first listened to correctly classified examples of speech uttered by the voice actors, where the examples were shown four times from each emotion category. The

Table 5. Recognition rates using HMM for male data [%].

	J.	T.	F.	Sa.	D.	A.	Su.	N.
J.	**27.07**	12.36	7.00	2.01	4.14	17.92	10.00	19.50
T.	18.00	**25.14**	10.43	3.65	8.93	8.50	5.71	19.64
F.	3.28	10.78	**37.64**	14.14	15.79	4.57	1.09	12.71
Sa.	2.79	3.29	19.43	**51.36**	8.93	6.86	0.41	6.93
D.	6.86	9.78	22.43	14.78	**21.76**	4.68	1.28	18.43
A.	14.00	5.78	8.86	2.57	6.78	**37.50**	2.58	21.93
Su.	27.36	13.50	4.64	1.15	2.64	8.71	**32.50**	9.50
N.	12.43	13.71	15.86	8.36	8.86	15.00	1.14	**24.64**

Table 6. Recognition rates using HMM for female data [%].

	J.	T.	F.	Sa.	D.	A.	Su.	N.
J.	**21.31**	20.68	4.79	2.22	7.63	16.21	10.16	17.00
T.	15.95	**18.63**	11.26	4.42	16.00	9.58	7.00	17.16
F.	1.31	1.58	**44.31**	37.53	7.74	1.21	0.21	6.11
Sa.	1.31	2.27	26.00	**55.74**	6.47	0.79	2.00	5.42
D.	9.37	7.32	18.26	18.89	**28.74**	3.37	1.42	12.63
A.	7.10	10.63	5.47	2.02	6.95	**46.10**	10.26	11.47
Su.	14.79	16.79	4.00	1.57	6.741	20.79	**22.95**	12.37
N.	9.31	12.31	13.74	16.68	18.42	6.21	2.22	**23.11**

subjects then listened to 450 voice data samples randomly selected from the large speech database and classified each of them into one of the eight emotion categories. The recognition results for male and female voice data are shown in Table 7 and Table 8, respectively. The averaged recognition rates were 58.2% for male data and 51.7% for female data.

Comparing the results leads to the following observations.

- In each recognition method, the open recognition results are similar between male and female data.
- The recognition results of the HMM are worse than those of the ANN and SVM, however, all methods show similar recognition characteristics: negative emotions, such as anger or sadness, are easy to recognize, while positive emotions, such as joy, are harder to recognize.
- Human subjects easily classify negative emotions but seem to have some difficulty in classifying positive emotions.
- The recognition rate of the 'neutral' emotion is low when using ANN, SVM, or HMM, while human subjects show a good recognition rate for this emotion.
- The emotion recognition capability of either ANN or SVM is almost the same as that of the human subjects.

Table 7. Recognition rates by human subjects for male data [%].

	J.	T.	F.	Sa.	D.	A.	Su.	N.
J.	**18.57**	3.51	0.88	1.46	1.02	5.99	7.46	61.11
T.	7.74	**61.61**	2.43	4.40	4.86	4.70	5.46	8.80
F.	0	1.55	**58.74**	30.25	3.52	1.32	1.03	0.59
Sa.	0	1.52	17.96	**70.62**	4.26	0.91	0.30	4.41
D.	0	7.92	1.47	1.91	**86.66**	0.88	1.03	0.15
A.	1.32	1.76	2.94	7.65	6.18	**53.82**	2.35	23.97
Su.	13.03	8.20	1.90	1.90	0.73	19.33	**45.39**	9.52
N.	1.61	1.46	1.46	15.47	3.07	5.99	0.58	**70.36**

Table 8. Recognition rates by human subjects for female data [%].

	J.	T.	F.	Sa.	D.	A.	Su.	N.
J.	**26.54**	4.11	0.59	0.88	0.44	6.60	3.67	57.18
T.	20.00	**39.86**	1.82	4.76	6.01	4.90	9.23	13.43
F.	0	1.54	**42.42**	48.88	5.06	0.84	0.14	1.12
Sa.	1.97	1.13	9.99	**71.87**	8.16	3.23	0.70	2.95
D.	0.15	7.78	0.15	0.59	**90.16**	0.59	0.44	0.15
A.	6.74	4.78	0.70	3.37	7.30	**37.78**	4.21	35.11
Su.	25.00	6.14	2.19	5.70	3.36	9.50	**30.99**	17.11
N.	3.23	2.67	1.69	8.85	3.09	6.04	0.70	**73.74**

These results indicate that an emotion recognition rate of approximately 51% by using either ANN or SVM in the speaker- and context-independent mode is feasible and it is possible for machines to communicate with people by using nonverbal communication capabilities.

5 Conclusions

This paper investigated the characteristics of recognizing emotions contained in human speech. We adopted ANN for a recognition algorithm. For comparison, a system based on SVM or HMM was tested as an alternative recognition method. Using a large database of phoneme-balanced Japanese words uttered by speakers consciously trying to portray an emotion, we trained and tested the recognition systems. To evaluate the emotion recognition results, we also carried out emotion recognition testing using human subjects. The obtained emotion recognition rates were 51% using ANN, 51% using SVM, 32% using HMM, and 55% using human subjects. Experimental results confirmed that the emotion recognition rate achieved by using ANN in the speaker- and context-independent mode is feasible and the SVM is also well suited to emotion recognition task.

References

[1] O. Chapelle, P. Haffner, and V. Vapnik. Support vector machines for histogram-based image classification. *IEEE Trans. on Neural Networks*, 10(5):1055–1064, 1999.

[2] F. Dellaert, T. Polzin, and A. Waibel. Recognizing emotion in speech. In *Proc. of 4th IEEE Int. Conf. on Spoken Language Processing*, volume 3, pages 1970–1973, 1996.

[3] L. C. DeSilva and P. C. Ng. Bimodal emotion recognition. In *Proc. of FG2000*, pages 332–335, 2000.

[4] G. Klasmeyer and W. F. Sendlmeier. Objective voice parameters to characterize the emotional content in speech. In *Proc. of ICPhS'95*, volume 1, page 182, 1995.

[5] K. Kostov and S. Fukuda. Emotion in user interface, voice interaction system. In *Proc. of SMC2000*, volume 2, pages 798–803, 2000.

[6] J. D. Markel and A. H. Gray. *Linear Prediction of Speech*. Springer-Verlag, 1976.

[7] S. McGilloway, R. Cowie, and E. D. Cowie. Pitch variations and emotions in speech. In *Proc. of ICPhS'95*, volume 1, page 178, 1995.

[8] S. Mozziconacci. Prosodic signs of emotion in speech: Preliminary results from a new technique for automatic statistical analysis. In *Proc. of ICPhS'95*, volume 1, page 250, 1995.

[9] I. R. Murray and J. L. Arnott. Toward the simulation of emotion in synthetic speech: A review of the literature on human vocal emotion. *J. of Acoustical Society of America*, 93(2):1097–1108, 1993.

[10] J. Nicholson, K. Takahashi, and R. Nakatsu. Emotion recognition in speech using neural networks. *Neural Computing and Applications*, 9(4):290–296, December 2000.

[11] L. R. Rabiner and B. H. Juang. An introduction to hidden markov models. *IEEE ASSAP Magazine*, pages 4–16, January 1986.

[12] M. Rosenblum, Y. Yacoob, and L. Davis. Human expression recognition from motion using radial basis function network architecture. *IEEE Trans. on Neural Networks*, 7(5):1121–1120, 1996.

[13] J. Sato and S. Morishima. Emotion modeling in speech production using emotion space. In *Proc. of RO-MAN'96*, pages 472–477, 1996.

[14] K. R. Scherer. How emotion is expressed in speech and singing. In *Proc. of ICPhS'95*, volume 3, page 90, 1995.

[15] V. Vapnik. *The Nature of Statistical Learning Theory*. Springer, 1995.

[16] C. R. Wren and A. Pentland. Dynamic modes of human motion. In *Proc. of FG'98*, pages 22–27, 1998.

[17] J. Yamato, S. Kurakake, A. Tomono, and K. Ishii. Human action recognition using hmm with category-separated vector quantization. *IEICE Trans.*, J77-D-II(7):1131–1318, 1994.

The Parameter-Less SOM algorithm

Erik Berglund
Smart Devices Lab, QUT
e.berglund@student.qut.edu.au

Dr. Joaquin Sitte
Smart Devices Lab, QUT
j.sitte@qut.edu.au

Abstract

One of the biggest problems facing practical applications of Self-Organising Maps (SOM) is their dependence on the learning rate, the size of the neighbourhood function and the decrease of these parameters as training progresses, all of which have to be selected without firm theoretical guidance. This paper introduces a simple modification to the SOM that completely eliminates the learning rate, the decrease of the learning rate and the decrease of the neighbourhood size. This is done by making the learning rate and neighbourhood size dependant on a variable calculated from the internal state of the SOM, rather than on externally applied variables.

Keywords: Self-Organising Map, SOM, Parameter-Less, PLSOM, learning rate, neural network, neighbourhood function, neighbourhood size, unsupervised learning.

1. Introduction

Training of many Artificial Neural Networks, including the SOM [6], depends on learning rates to converge. The learning rate is a variable that governs how much the weights of a network are altered in response to an input. For SOMs the learning rate must be decreased according to some algorithm as learning progresses, this process is referred to as annealing in this document. The update of the weight vector in the standard SOM depends on the error of that particular weight vector, but to make sure the SOM converges towards a stable state a learning rate is required. The learning rate is large in the beginning of the training, when the map is unordered and fits the input space poorly, and small the end of the training when there is only need for small changes to the map.

Learning rates present a two-sided problem to users and researchers of Self-Organising Maps:

1. There exists no theoretical way of estimating the starting learning rate, nor the rate at which it should decline (the annealing scheme). There exist general guidelines and heuristics, but in the last instance the learning rate has to be adapted to a specific task by empirical methods.

2. Explaining the learning rate from the perspective of the SOM as a model of biological neural networks is difficult: While the human brain loses some of its flexibility over time, learning is much more rapid than the reduction of flexibility and learning is still possible after the reduction. Even complex neural networks like mammalian brains are capable of drastically changing their mapping if the input changes suddenly, such as after an amputation [5].

The choice of learning rate and annealing schemes greatly affects the network's ability to reach a stable and well-ordered state and the time it takes to reach this state [8]. This led to the search for a method by which the optimal learning rate and decay can be determined with mathematical certainty given a specific problem, for example [7]. Unfortunately, this has not produced a universally valid, simple and computationally effective algorithm. Some previous works include the Generative Topographic Mapping (GTM) algorithm [1, 2] which eliminates the neighbourhood function entirely, but relies on other variables and choice of prior distribution and basis functions. The Maximum Entropy learning Rule (MER) algorithm [4] achieves global ordering without use of a neighbourhood at all, but is slower and still relies on a learning rate. The Growing Neural Gas (GNG) algorithm [3] is similar to the algorithm proposed in this paper in the way it computes the error and in that it eliminates the annealing schemes, but instead of scaling neighbourhood size and learning rate with the error, it uses the accumulated error per neuron to determine where to insert a new cell in the network, in addition it introduces new variables that must be pre-determined with no firm theoretical grounding. Many supervised learning algorithms feature the idea of scaling the learning rate according to the error (Newton's method could be seen as an early example of this) - however the error in a supervised learning scheme is readily available, which is not the case in unsupervised

learning schemes like the SOM. This still leaves us with a SOM algorithm that relies on empirical testing to determine the annealing scheme - a poor choice of learning rate, learning rate annealing scheme or neighbourhood size annealing scheme can result in knotting, folding, a poor input space fit or later inputs destroying what was learned by earlier inputs.

The solution we propose in this paper is to let the scaling of the weight vector update function and/or the size of the neighbourhood depend on internal conditions in the map, instead of or in combination with externally enforced scaling variables such as the learning rate. The internal condition we selected for scaling these variables is the least error ϵ, i.e. the normalized euclidean distance from the input to the closest weight vector, see Section 3.1. It is intuitive that if this variable is large, the map needs to change more to accommodate future inputs of this class, but if it is small the fit is already good and there is no need for large alterations of the map. In this paper we will examine two variants of the standard SOM algorithm, we will demonstrate the Parameter-Less SOM (PLSOM) and compare its performance to the performance of a widely used SOM algorithm, namely the variant implemented in the Matlab neural networking package, and discuss some of their relative merits.

2. Background

2.1. The standard SOM algorithm

The SOM we will be modifying in this paper is the gaussian-neighbourhood, euclidean distance, rectangular topology SOM, given by equations (2)-(5). The algorithm is, in brief, as follows: An input $x(t)$ is presented to the network at epoch (or timestep, iteration) t. The 'winning neuron', i.e. the neuron with the weight vector that most closely match the input, is selected using equation (1).

$$c = \arg\min_i(||x(t) - w_i(t)||_2) \tag{1}$$

$w_i(t)$ is the weight vector of cell i at epoch t. $||.||_2$ denotes the l_2-norm or n-dimensional Euclidian distance. There are other ways of computing the distance than the Euclidian distance given in equation (1) that can be used in the SOM, for example Manhattan or link distance. The weight update is calculated using equations (2) and (3).

$$w_i(t+1) = w_i(t) + \alpha(t)h_{ci}(t)[x(t) - w_i(t)] \tag{2}$$

$$h_{ci}(t) = e^{\frac{-d(i,c)^2}{\beta(t)^2}} \tag{3}$$

$h_{ci}(t)$ is referred to as the neighbourhood function, and is a scaling function centred on the winning cell c decreasing in all directions from it. $d(i, c)$ is the euclidean distance from cell i to the winning cell c. $\alpha(t)$ is the learning rate at epoch t, $\beta(t)$ is the neighbourhood size at epoch t.

Lastly the learning rates are decreased in accordance with the annealing scheme. We have chosen the annealing scheme given by equations (4) and (5) for the decrease of the learning rate and the neighbourhood size, respectively.

$$\alpha(t+1) = \alpha(t)\delta_\alpha, \qquad \delta_\alpha < 1 \tag{4}$$

$$\beta(t+1) = \beta(t)\delta_\beta, \qquad \delta_\beta < 1 \tag{5}$$

Here δ_β and δ_α are scaling constants determined beforehand, typically around 0.9999.

These steps are repeated until some preset condition is met, usually after a give number of epochs or when some measurement of error reaches a certain level.

It should be noted that one of the most widely used implementations of the SOM algorithm differs in some respects from this. The overall algorithm is the same, but the annealing scheme is different: It is divided into two phases, phase 1 (ordering phase) and phase 2 (tuning phase). Matlab also uses a step-based neighbourhood function, equation (6). Equations (7) and (8) govern the annealing by reducing the learning rate and the neighbourhood size, respectively.

$$h_{ci}(t) = \begin{cases} 1 & \text{if } d(i,c) = 0 \\ 0.5 & \text{if } d(i,c) < \beta(t) \\ 0 & \text{otherwise} \end{cases} \tag{6}$$

$$\alpha(t+1) = \begin{cases} \alpha(0) + ((\alpha(0) - \alpha(\tau))(1 - \frac{t}{\tau})) & \text{if } t < \tau \\ \alpha(\tau)\frac{\tau}{t} & \text{otherwise} \end{cases} \tag{7}$$

$$\beta(t+1) = \begin{cases} \beta(0) + ((\beta(0) - \beta(\tau))(1 - \frac{t}{\tau})) & \text{if } t < \tau \\ \beta(\tau) & \text{otherwise} \end{cases} \tag{8}$$

τ is the number of epochs in phase 1 (default: 1000), $\alpha(0)$ is predefined (default: 0.9) and $\beta(0)$ is calculated based on the network size, for the two dimensional case this is given by (9). $\alpha(\tau)$ is predefined (default: 0.02) and $\beta(\tau)$ is 1.00001.

$$\beta(0) = \sqrt{(w-1)^2 + (h-1)^2} \tag{9}$$

w and h is the number of cells in the vertical and the horizontal directions, respectively.

The difference between these two variants of the SOM is that while the Matlab version achieves basic ordering quicker, it does not fit the data as well as the other variant.

3. The Parameter-Less SOM

The PLSOM relies on the idea that the learning rate and neighbourhood size should not vary according to the iteration number, but rather vary according to how well the map represents the topology of the input space.

3.1. Algorithm

The scaling variable depending on how good the fit of the weight vector of the winning neuron is to the last input, ϵ, is defined in equations (10) and (11).

$$\epsilon(t) = \frac{||x(t) - w_c(t)||_2}{\rho(t)} \tag{10}$$

$$\begin{aligned} &\rho(t) = \max(||x(t) - w_c(t)||_2, \rho(t-1)), \\ &\rho(0) = ||x(0) - w_c(0)||_2 \end{aligned} \tag{11}$$

$\epsilon(t)$ is best understood as the normalized euclidean distance from the input vector at time t to the closest weight vector. If this variable is large, the network fits the input data poorly, and needs a large readjustment. Conversely, if ϵ is small, the fit is likely to already be satisfactory for that input.

The algorithm for the PLSOM uses a neighbourhood size determined by ϵ, thus replacing the equation governing the annealing of the neighbourhood with $\beta(t) = constant \ \ \forall t$. Furthermore it uses equation (14) for weight updates and equation (13) for the neighbourhood function.

$$\Theta(t) = \beta(t)\epsilon(t), \qquad \Theta(t) >= \theta_{min} \tag{12}$$

$$h_{ci}(t) = e^{\frac{-d(i,c)^2}{\Theta(t)^2}} \tag{13}$$

$$w_i(t+1) = w_i(t) + \epsilon(t)h_{ci}(t)[x(t) - w_i(t)] \tag{14}$$

As we can see from equation (14) the learning rate $\alpha(t)$ is now completely eliminated, replaced by $\epsilon(t)$. All examples in this paper are based on 2-dimensional input spaces and maps. Since the Euclidean distance can be calculated in n-dimensional space it is likely that the PLSOM algorithm can be adapted to any number of input- and output dimensions.

3.2. Advantages

The PLSOM completely eliminates the selection of the learning rate, the annealing rate and annealing scheme of the learning rate and the neighbourhood size, which have been an inconvenience in applying SOMs. It also markedly decreases the number of iterations required to get a stable and ordered map. The PLSOM also covers a greater area of the input space, leaving a smaller gap along the edges.

3.2.1 Comparison to the SOM variants

We trained the Matlab SOM variant, the SOM and the PLSOM with identical input data, for the same number of iterations. The input data was pseudo-random, 2 dimensional and in the $[0, 1]$ range. This was chosen because a good pseudo-random number generator was readily available, eliminating the need to store the training data. Since the training data is uniformly distributed in the input space the perfect distribution of weight vectors would be an evenly spaced grid, with a narrow margin along the edges of the input space. That way, each weight vector would map an evenly sized area of the input space.

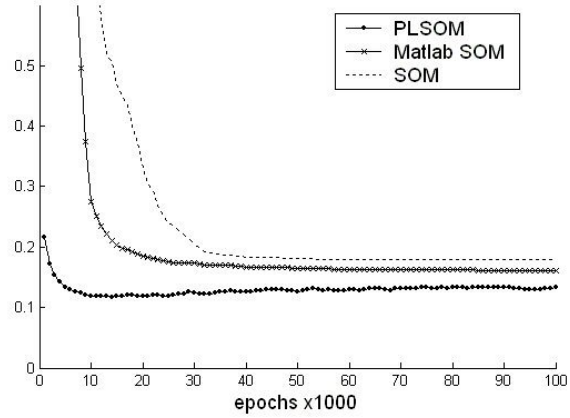

Figure 1. Graph of the decrease of uncovered space as training progresses for the PLSOM, the SOM and the Matlab SOM implementation. Note the quick expansion of the PLSOM and that it consistently covers a larger area than the SOM variants.

In comparing the two SOM implementations we used 3 separate metrics, which are all based on the shape and size of the cells. A cell is the area in the input space spanned by the weight vectors of four neighbouring neurons.

Unused space We summarized the area covered by all the cells, and subtracted this from the total area of the input space. The resulting graph clearly shows how the PLSOM spans a large part of the input space after only a small number of iterations and maintain the lead throughout the simulation (figure 1). Please note that this metric will be misleading in situations where cells are overlapping.

Average skew For each cell we calculate the length of the two diagonals in a cell and divide the bigger by the smaller and subtract one, thus getting a number from 0 to infinity, where 0 represents a perfectly square cell. Again, we see that the PLSOM outperforms the SOM in the early stages of simulation but after ca. 24000 epochs the SOM surpasses the PLSOM. After 100000 epochs the difference is still small, however. See figure 2.

Deviation of cell size We calculate the absolute mean deviation of the cell size and divide it by the average cell

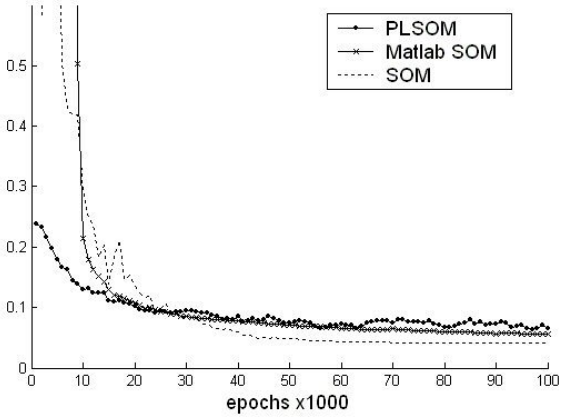

Figure 2. Graph of the average skew for the PLSOM, the SOM and the Matlab SOM implementation. For the first 24000 iterations the PLSOM is more ordered, before the SOM variants narrowly overtakes it.

size to get an idea of how much the cells differ in relative size. Here the SOM is superior to the PLSOM after ca. 10000 epochs, mainly because of the flattened edge cells of the PLSOM, see figure 3.

If we ignore the cells along the edge, the picture is quite different: the PLSOM outperforms the SOM with a narrow margin, see figure 4.

All experiments was carried out using Matlab and the JRobot package [9]. Thanks to Dr. Mark Hale for his contribution to JRobot, and to Dr. Steffen Log.

3.2.2 Plasticity preservation

The illustrations in this section shows the positions of the weight vectors, connected with lines, in the input space. When a SOM has been trained, it will not adapt well to new data outside the range of the training data, even if a small residual learning rate is left. This is illustrated by figures 5 and 6, where a SOM has been presented with pseudorandom, uniformly distributed 2-dimensional data vectors in the $[0, 0.5]$ range for 50000 iterations. Thereafter the SOM was presented with 20000 pseudorandom, uniformly distributed 2-dimensional data vectors in the $[0, 1]$ range, after which the SOM has adapted very little to the new data. In addition the adaptation is uneven, creating huge differences in cell size and distorting the space spanned by the weight vectors. If we subject a PLSOM to the same changes in input range, the difference is quite dramatic; it adapts to the new input range almost immediately, as seen in figures 7 and 8.

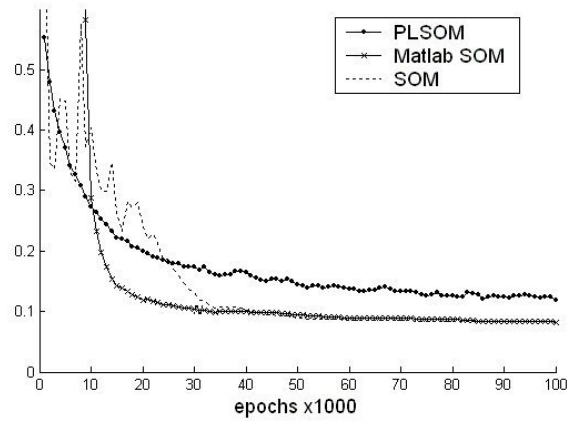

Figure 3. Graph of the absolute mean deviation of cell size for the PLSOM, the SOM and the Matlab SOM. The PLSOM is more regular up until ca. epoch 10000.

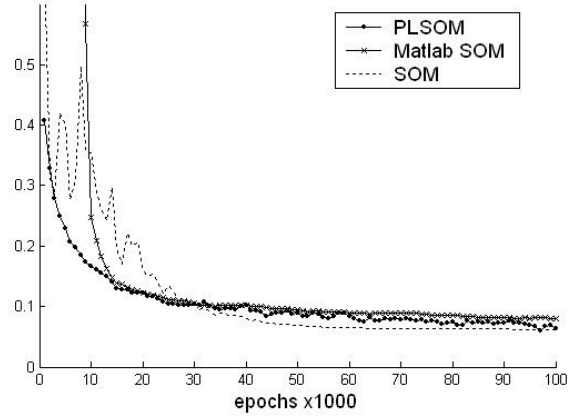

Figure 4. Graph of the absolute mean deviation of cell size for the PLSOM, the SOM and the Matlab SOM, excluding the edge cells. Compare to figure3. The PLSOM outperforms the Matlab SOM in both adaption time and accuracy, and the SOM needs until ca. epoch 30000 to reach the same level of ordering.

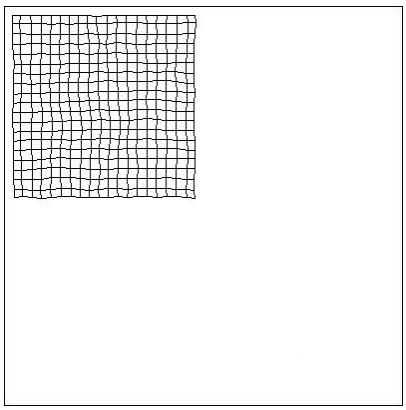

Figure 5. SOM weight vector position in input space after training for 50000 iterations with uniformly distributed pseudorandom 2-dimensional input, ranging from 0 to 0.5.

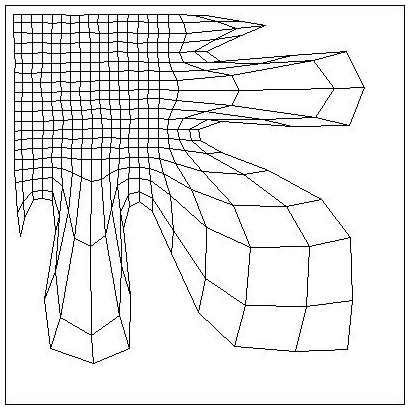

Figure 6. Same SOM as in figure 5 after 20000 further training steps with inputs ranging from 0 to 1.0.

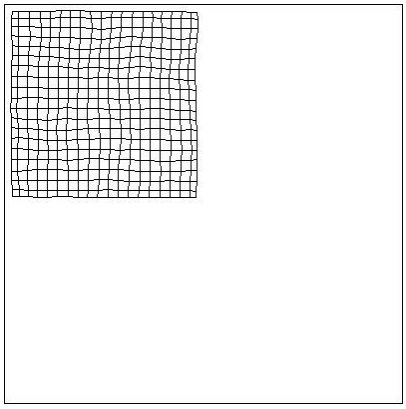

Figure 7. PLSOM weight vector position in input space after training for 50000 iterations with uniformly distributed pseudorandom 2-dimensional input, ranging from 0 to 0.5.

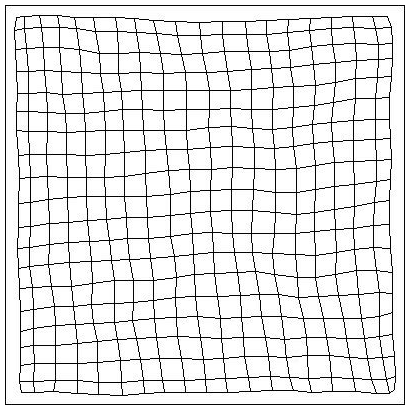

Figure 8. Same PLSOM as in figure 7 after 20000 further training steps with inputs ranging from 0 to 1.0. Note the difference between this figure and figure 6.

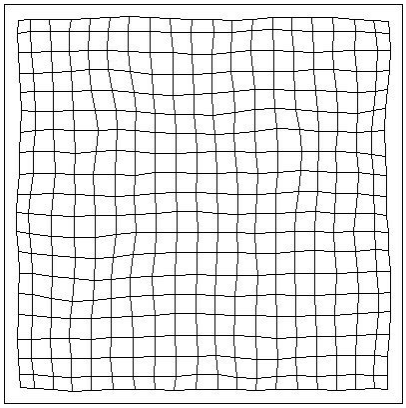

Figure 9. PLSOM weight vector position in input space after training for 50000 iterations with uniformly distributed pseudorandom 2-dimensional input, ranging from 0 to 1.0.

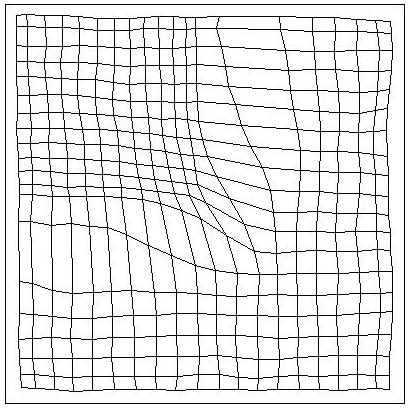

Figure 10. Same PLSOM as in figure 9 after 20000 further training steps with inputs ranging from 0 to 0.5. Note that while the weights have a higher density in the new input space, the same area as before is still covered, i.e. none of the old input space has been left uncovered.

3.2.3 Memory

If the opposite is the case, that the SOM is presented with a sequence of inputs that are all restricted to a small area of the training input space, it would be preferable if the SOM maintains its original weight vector space, in order to not 'forget' already learned data. Figures 9 and 10 demonstrate what happens to a PLSOM if it is trained with pseudorandom, uniformly distributed 2-dimensional data in the $[0, 1]$ range for 50000 iterations and then presented with inputs confined to the $[0, 0.5]$ range for 20000 iterations. This leads to an increase of the density of weight vectors in the new input space, yet maintains coverage of the entire initial input space, resulting in distortions along the edge of the new input space. Both these effects are most pronounced in the PLSOM.

3.3. Drawbacks

The PLSOM is measurably less ordered than a properly tuned SOM and the edge shrinking is also more marked in the PLSOM. The PLSOM doesn't converge in the same manner as the SOM (there is always a small amount of movement).

4. Conclusion

The PLSOM provides a simplification of the overall application process, since it eliminates the problems of finding a suitable learning rate and annealing schemes. The PLSOM also reduces the training time and preserves generality. This is achieved without inducing a significant computation time or memory overhead.

References

[1] C. M. Bishop, M. Svensén, and C. K. I. Williams. Gtm: A principled alternative to the self-organizing map. *Advances in Neural Information Processing Systems*, (9), 1997.

[2] C. M. Bishop, M. Svensén, and C. K. I. Williams. Gtm: The generative topographic mapping. *Neural Computation*, 10(1):215–235, 1998.

[3] B. Fritzke. A growing neural gas network learns topologies. In G. Tesauro, D. S. Touretzky, and T. K. Leen, editors, *Advances in Neural Information Processing Systems 7*, pages 625–632. MIT Press, Cambridge MA, 1995.

[4] M. M. V. Hulle and K. U. Leuven. Globally-ordered topology-preserving maps achieved with a learning rule performing local weight updates only. *Neural Networks for Signal Processing [1995] V. Proceedings of the 1995 IEEE Workshop*, pages 95–104, Sep 1995.

[5] J. H. Kaas. Plasticity of sensory and motor maps in adult mammals. *Annual Review of Neuroscience*, 14:137–167, Mar 1991.

[6] T. Kohonen. *Self-Organizing Maps*. Springer-Verlag, 1997.

[7] F. Mulier and V. Cherkassky. Learning rate schedules for self-organizing maps. In *Computer Vision & Image Processing., Proceedings of the 12th IAPR International. Conference on*, volume 2, pages 224–228. IEEE, 1994.

[8] D. R. Wilson and T. R. Martinez. The need for small learning rates on large problems. In *Neural Networks, 2001. Proceedings. IJCNN '01. International Joint Conference on*, volume 1, pages 115–119. IEEE, IEEE, July 2001.

[9] J. Zhu and E. Berglund. Jrobot. http://blog.no/erik.berglund/jrobot, 2002.

An Experiment with Approximate Reasoning in Site Selection using 'InfraPlanner'

David Bailey, Duncan Campbell and Ashantha Goonetilleke
Queensland University of Technology, GPO Box 2434 Brisbane QLD 4001
d2.bailey@qut.edu.au

Abstract

This paper discusses an application of an intelligent information system for decision-makers involved in multiple criteria group site selection problems under uncertainty. The fuzzy algorithm behind the system was developed by the authors for use in large-scale infrastructure site selection, and is validated here using a site selection problem at Brisbane Airport. The 'InfraPlanner' Spatial Decision Support System (SDSS) was created by customising ArcView GIS, and operates on raster data files. The tightly coupled system features linguistic interaction, multiple decision-maker input, uncertainty assessment, and a linguistically controllable aggregation function capable of a variety of compensatory and non-compensatory outcomes. Feedback from decision-makers involved in the experiment indicated a high level of satisfaction with outputs from the system, whilst noting some areas for future development.

1. Introduction

Site selection for facilities such as airports, highways, and heavy industry is often extremely complex. As multiple stakeholders are usually involved in the selection of a given location, there is a strategic need to take into account multiple criteria, which are often conflicting, incommensurate and subject to uncertainty. Also, the spatial variation of suitability and the weighting of each criterion is often hard to measure, and may be the basis of disagreement amongst a group of heterogeneous decision-makers. Such problems are often described as 'surprisingly difficult' [1]

The use of Geographical Information Systems (GIS) in site selection has a long history, with most approaches being based on a multiple criteria evaluation (MCE) framework. There has been much literature on MCE embedded in GIS [2-4], however most GIS-based MCE methods have inherent difficulties and limitations. Embedded MCE approaches generally assume consensus among decision-makers [5] and have little capacity for dealing with conflicts between affected parties, thereby losing potentially important information in the aggregation phase. Many authors have also noted that there is a need for accuracy measures to be incorporated into spatial datasets upon which decisions are to be made [6-8], however the nature of data uncertainty is not always easily fitted to a probability distribution, and measures of accuracy may themselves be hard to quantify. Perhaps most importantly, the use of MCE in computer-based decision support systems is limited by the fact that highly capable analytical systems are often used as simple visualization tools, primarily due to difficulties in use and understanding of the systems by strategic decision-makers [9].

'InfraPlanner' is a SDSS, developed using a fuzzy algorithm to mitigate these difficulties. Specifics of the algorithm are given in [10]. Broadly speaking InfraPlanner is an intelligent information system based on approximate reasoning that offers the following capabilities:

- Linguistic interaction: *Linguistic interaction is provided using primary term sets semantically defined by parameter-based fuzzy numbers, which may be enhanced via a hedging procedure to add more terms. Both input and feedback is accomplished linguistically.*
- Multiple decision-maker capability: *The system accepts linguistic inputs from each party involved in the decision-making process. Conflict between parties is assessed based on differing suitability and weighting judgments and factored into overall site suitability.*
- Uncertainty assessment: *There are two types of uncertainty inherent in decision-maker suitability assessments: linguistic and quantitative. Linguistic uncertainty is represented by the fuzziness of the primary suitability term, whereas quantitative uncertainty is represented using the concept of a type-2 fuzzy set and its footprint of uncertainty (FOU)* [11]. *Quantitative uncertainty is the term used here to represent uncertainty in the source data and/or its relationship with site suitability.*
- User controllable aggregation: *Users have the ability to choose an aggregation that minimizes uncertainty, risk or conflict, or maximizes compensatory suitability. A variety of compensatory and non-compensatory linguistically defined outcomes may be delivered.*
- Real-time interaction: *In raster GIS the decision area may contain millions of cells, with each cell representing an alternative that will ideally be analyzed in a real-time interactive environment. The computationally efficient fuzzy algorithm of InfraPlanner utilizes a scoring function when dealing with fuzzy quantities that minimizes calculation time and makes real-time interaction possible.*

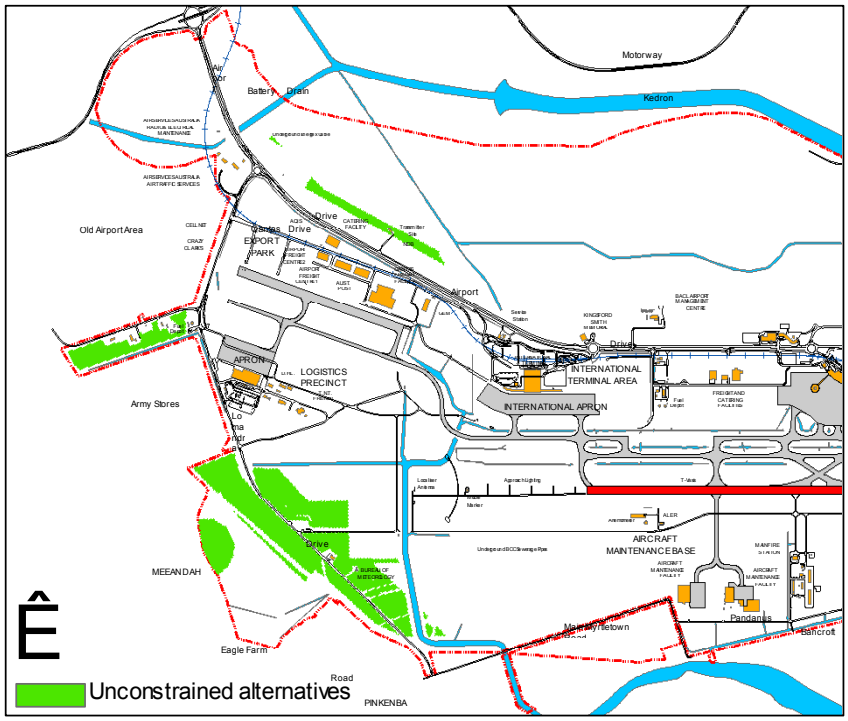

Figure 1. Unconstrained alternatives

This paper follows from existing work in development of the algorithm by discussing its application to a real world site selection task at Brisbane Airport, Australia. The remainder of the paper is structured as follows: Section 2 provides an overview of the site selection problem used in the experiment: Section 3 details input from decision-makers: Section 4 covers exploration of alternatives, Section 5 is a discussion of the outcomes of the experiment and Section 6 draws conclusions.

2. The problem

The problem worked through here concerns the location of a new construction and demolition (C&D) facility, at Brisbane Airport, Australia. The Airport occupies 2700ha of land, located 13km north east of the Brisbane CBD, adjoining Moreton bay. The site is flat and low lying, occupying part of the original Brisbane river delta, which has undergone extensive changes since the 1830s, with most of the original network of tidal waterways being replaced with constructed drains. Much of the vegetation on the site has been planted in the last 15 years, and was chosen to reduce the attraction of birds. There are, however, some environmentally sensitive areas to consider when locating new developments, as well as issues associated with airport facilities, Government legislation and the effects of airport operations on local communities.

A Construction and Demolition facility inputs masonry from demolished buildings and, via crushing and grinding, turns out various grades of landfill material. The main impacts of such an operation on its immediate vicinity are noise and dust emissions. The Brisbane Airport Corporation (BAC) is considering leasing a parcel of land on its site to a C&D facility operator primarily because of the flow on benefit of easily accessible fill material for other development sites on the Airport grounds.

Three separate groups are to be engaged in the decision-making process: The Brisbane Airport Corporation, The Commonwealth Government, and the Pinkenba residential community. The three groups differ considerably in their priorities and suitability assessments, creating a rich decision-making environment.

3. Decision-maker input

Data input primarily consists of the creation of a set of maps detailing the suitability and uncertainty assessments of each group. The first step in the process is the definition of constraints (Boolean criteria) that serve to limit the number of alternatives under consideration. After an initial consultation with decision-makers, a set of five constraints emerged:

1. Airport Boundary: The site must lie within the airport boundary
2. Existing Buildings: Sites already occupied are excluded
3. Road access: The site must be within 200m of selected access roads.
4. Zoning: The site must lay in a zone designated ‘General Industry’ or ‘Light Industry’ as defined by the BAC 1998 Master Plan.
5. Conservation: The site must not occupy an area of high conservation value.

The map of unconstrained alternatives is derived using standard GIS Boolean overlay functionality and is shown in Figure 1.

The next step in the process involves the definition and linguistic assessment of criteria that vary on a suitability scale from 'Totally Unsuitable' to 'Perfect'. These criteria (referred to as factors) are represented as a set of suitability maps, created using specially designed interfaces that convert linguistic inputs from each decision-maker to a spatially explicit format as shown in igure 2 and 3. To illustrate how the linguistic input is structured factor definition from BAC is provided below:

1. Environmental value is 'important': It is 'moderately certain' that sites of moderate conservation value are 'good' whilst it is 'very certain' that all others are 'perfect'.
2. Zoning is 'very important': It is 'very certain' that general industry zones are 'perfect' whilst it is 'moderately certain' that light industry zones are 'good'.
3. Tenant Amenity is 'important': It is 'very certain' that sites less than 50m from sensitive tenants are 'totally unsuitable'. It is 'moderately certain' that sites 100m from sensitive tenants are 'good'. It is 'certain' that sites 500m from sensitive tenants are 'perfect'.
4. Community Impact is 'important': It is 'very certain' that sites less than 500m from Pinkenba are 'totally unsuitable'. It is 'uncertain' that sites 1000m from Pinkenba are 'good'. It is 'very uncertain' that sites 2000m from Pinkenba are 'perfect', and 'certain' that sites 4000m from Pinkenba are 'perfect'.
5. Proximity to BAC Landfill Requirement is 'moderately important': It is 'very certain' that sites on Lomandra Dr are 'perfect'. It is 'moderately certain' that sites on Randle Rd, Sugarmill Rd and Viola Pl are 'good'. It is 'moderately certain' that sites on Airport Dr are 'indifferent'.
6. Traffic impact is 'important': It is 'very certain' that sites on Airport Drive are 'bad'. It is 'moderately certain' that sites on Lomandra Drive and Viola Pl are 'good'. It is 'certain' that sites on Randle Road and Sugarmill Rd are 'perfect'.

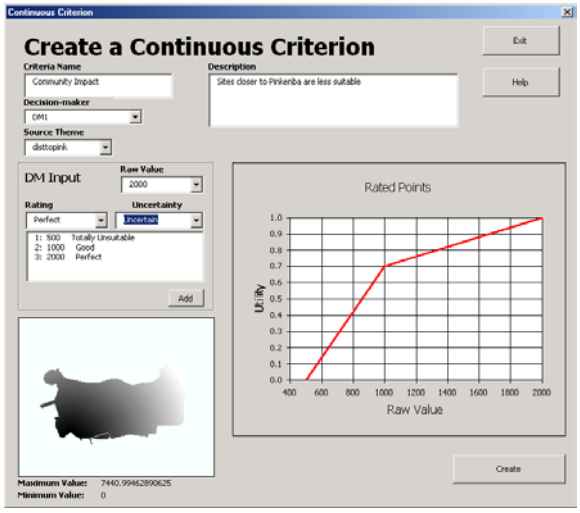

Figure 2: Creating a suitability map from a continuous variable (the charted utility function is a guide only as values are fuzzified)

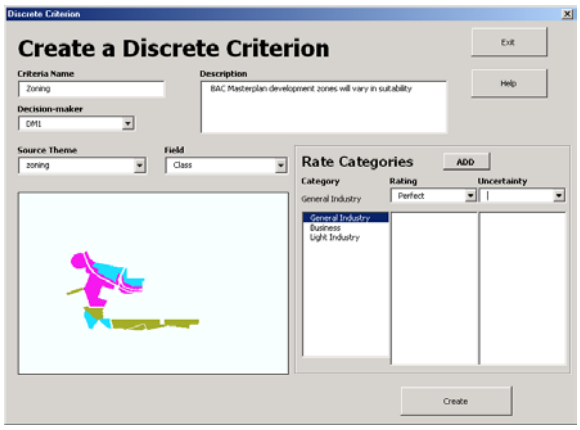

Figure 3: Creating a suitability map from a discrete (categorical) variable

InfraPlanner takes the linguistic assessments and generates raster maps, where each raster cell has a fuzzy number representative of the suitability and uncertainty assessment for each criterion from each decision-maker. Figure 4 illustrates the type-2 fuzzy concept used to accomplish this. When all maps are generated a fuzzy aggregation is performed, enabling decision-makers to interactively explore alternatives as discussed in the next section.

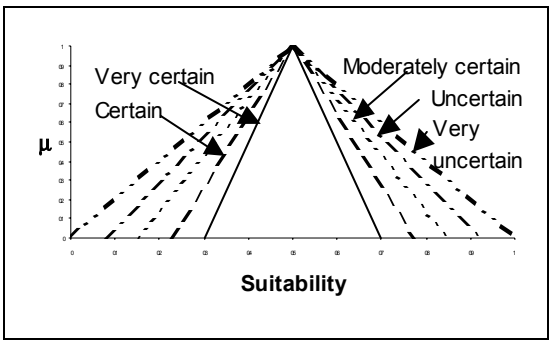

Figure 4. The effect of uncertainty assessments on the primary MF of 'indifferent'

4. Alternative exploration

The initial aggregation provides four linguistic parameters for each alternative cell: Compensatory suitability, uncertainty, risk, and conflict. Compensatory suitability is derived from a fuzzy weighted combination of individual criterion outcomes, importance values and a relevance value representing the ability of each decision-maker to assess each criterion, as shown in Equation 1.

$$S_i = \sum_{j=1}^{J}\sum_{k=1}^{K} O_{ijk} \times R_{jk} \times W_{jk} \mid \quad i = 1 \ldots I \quad (1)$$

Where:

S_i is the suitability of alternative i.

O_{ijk} is the criteria outcome for alternative i with relation to criterion j and decision-maker k, including quantitative uncertainty.

R_{jk} is the relevance of decision-maker k's opinion with respect to criterion j.

W_{jk} is the weight assigned to criterion j by decision-maker k

Uncertainty is derived from the support of the triangular fuzzy number, as this will vary with the individual uncertainty assessments via a Type 2 scaling procedure. Risk is a measure of how each criterion outcome compares to a specified minimum, and conflict is a measure of disagreement amongst decision-makers, as shown in Equation 2.

$$R_c(i) = \frac{\bigvee_{j=1}^{J}\left(\bigvee_{k=1}^{K}(R_s(O_{ijk}) - w_{jk}) - \bigwedge_{k=1}^{K}(R_s(O_{ijk}) - w_{jk})\right)}{2} \quad (2)$$

Where:

$R_c(i)$ is the conflict score for alternative i

$R_s(i)$ is the suitability score for alternative i

$\wedge$ is the minimum operator

$\vee$ is the maximum operator

Decision-makers can now decide which parameters are most important as they explore and reduce the set of feasible alternatives in an interactive, point and click environment as shown in Figures 5a and 5b. Alternatives are gradually reduced by selecting minimum standards for each of the four parameters or creating an overall adjusted suitability value by combining them as shown in Equation 3.

$$A(i) = \frac{R_s(i)w_s + (1 - R_u(i))w_u + (1 - R_r(i))w_r + (1 - R_c(i))w_c}{w_s + w_u + w_r + w_c} \quad (3)$$

Where:

$A(i)$ is the adjusted suitability value of alternative i

$R_r(i)$ is the risk score for alternative i

$R_u(i)$ is the uncertainty score for alternative i

w_s is the weighting of the suitability score

w_u is the weighting of the uncertainty score

w_r is the weighting of the risk score

w_c is the weighting of the conflict score

The adjusted suitability score is then used to generate an adjusted linguistic suitability rating. Weighting of the four parameters is via consensus, or a non-weighted averaging of each decision-maker's preferences, which enables a variety of non-compensatory outcomes to be generated.

As expected the system easily identified the preferred sites for each decision-maker individually. The three sites varied in location, and thus contained high levels of conflict. The best compensatory solution was acceptable to only two of the parties, and performing a second aggregation to minimise conflict found a slightly different solution that the third party also rejected. It was quickly ascertained that disagreement was primarily due to the third decision-maker placing primary importance on satisfying a single criterion. Unfortunately this left no locations available that were completely satisfactory to all, and the primary benefit gained in from the system was the clear identification of the source of conflict, which has become the subject of negotiation between parties.

5. Discussion

The nature of the site selection problem presented here is typical of many real world situations. A fundamental problem in designing systems to solve such problems is that there is often no universally accepted solution to find, and it is not always possible to derive the best compromise from initial assessments. Most GIS based decision-making methods assume that crisp numerical suitability assessments can be processed according to a pre-determined algorithm to derive a solution. However the complex nature of many site selection decisions make such assumptions unrealistic. It was noted during the experiment that decision-makers were reluctant to place their faith in a derived solution without fully understanding how that solution was obtained. This creates a significant hurdle for system designers whose aim is to replicate, and by default replace, the decision-making process. Using a pre-determined optimization algorithm is standard procedure in many areas of problem solving, and works particularly well when the exact utility of a solution can be precisely measured and used as feedback to improve performance. However the exact utility of a solution in site selection is seldom known. Multiple, conflicting criteria, and the added human element of conflicting opinions of measurement and importance create an ill-structured problem that is often dynamic, in that assessments may change as the solution space is examined. It is also relevant to note that problem-solving strategies vary from person to person, making the group situation a particularly dynamic environment.

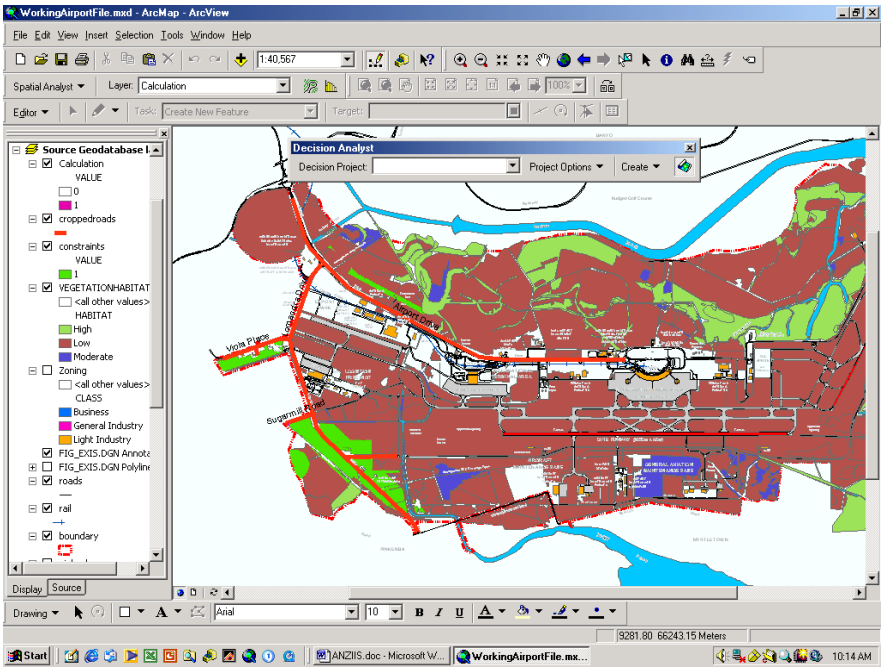

Figure 5a: Choosing alternatives

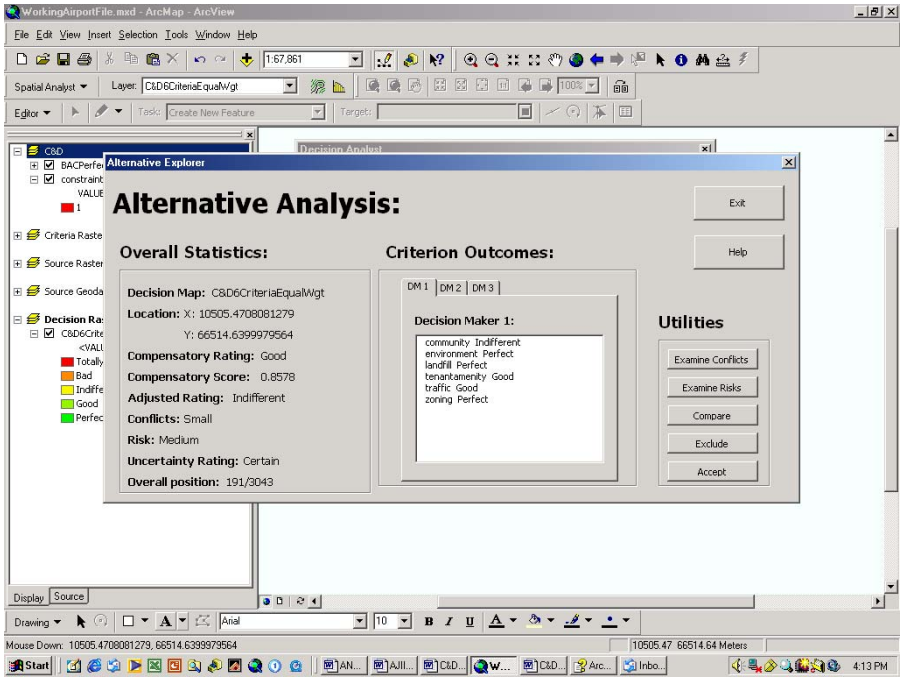

Figure 5b: Alternative exploration and feedback

InfraPlanner was designed as an intelligent information system to provide decision-makers with relevant, understandable processed information, whilst leaving them in control of the decision-making process. To this end it was noted that decision-makers expressed a high level of satisfaction with outputs, as they enabled the group to find the core elements behind their conflicting assessments. In a real world situation, where political issues can dominate operational concerns, it is often most beneficial to identify these core areas as they may be traded off for concessions outside the sphere of the site selection task. Outcomes from the experiment discussed in this paper confirm this point of view.

Giving decision-makers the ability to generate a variety of solutions that maximized aggregated suitability or minimized risk, conflict and uncertainty provided an easily understandable way for decision-makers to take more control of the analysis, rather than accepting imposed heuristics. Moreover, whilst the system makes computationally deriving a solution from input data possible, it's major strength was the high information value of outputs. The experiment confirmed that a focus on a meaningful, interactive exploration of alternative outcomes is a valid way to support decision-makers in their task.

The experiment also confirmed some important limitations of the system: Firstly, the method used is limited to analyzing problems with a single objective, which makes it unsuitable for situations where multiple facilities are to be located simultaneously or multiple land uses considered. Secondly, the use of single cells as alternatives does not accurately represent the true size and spatial configuration of a proposed development, which has been surprisingly seldom noted [12]. Lastly, utilizing linguistic terms for data input may unnecessarily limit the accuracy of results in those cases where hard quantitative data is available.

Another difficulty noted in the group experiment was the requirement to define discrete criteria. As an example, some decision-makers noted overlap in their perception of community impact versus environmental impact. Some authors have described multicriteria decisions, particularly those with multiple objectives, in terms of a hierarchical structure, whereby some criteria encompass others, eg [13]. In a group situation this provides another area for disagreement and/or misunderstanding.

6. Conclusions

The experiment confirmed the validity of an approximate reasoning approach to group site selection problems under uncertainty. The InfraPlanner system enabled decision-makers to express their assessments linguistically and receive meaningful linguistic feedback, whilst taking more control of the process than other methods allow, and a high level of satisfaction with outputs was expressed.
The results indicated a definite benefit from utilizing a multi-decision-maker framework, as the identification of conflicts between parties could be easily accomplished. An emphasis on providing meaningful processed information, rather than offering a heuristically derived solution was also found to be beneficial.

Further work is needed to design site selection algorithms that are capable of handling multiple facility problems, and explicitly include the size and spatial configuration of the required land parcels. Genetic algorithms offer a promising method to explore feasible alternatives without resorting to the massive number of calculations required to fully examine the solution space of such problems.

Acknowledgements

We gratefully acknowledge the contribution of The Brisbane Airport Corporation, The Australian Commonwealth Government and Queensland University of Technology, who have funded this research.

References

1. Carlsson, C. and R. Fuller, Fuzzy multiple criteria decision making: Recent developments. "Fuzzy Sets and Systems", 1996. 78(2): p. 139-153.
2. Jankowski, P., Integrating geographical information systems and multiple criteria decision-making methods. "Int. J. Geographical Information Systems", 1995. 9(3): p. 251-273.
3. Eastman, J.R., et al., Raster procedures for multi-criteria/multi-objective decisions. "Photogrammetric Engineering and Remote Sensing", 1995. 61(5): p. 539-547.
4. Pettit, C. and D. Pullar, An integrated planning tool based upon multiple criteria evaluation of spatial information. "Computers, Environment and Urban Systems", 1999. 23(5): p. 339-357.
5. Malczewski, J., A GIS-based approach to multiple criteria group decision-making. "Int. J. Geographical Information Systems", 1996. 10(8): p. 955-971.
6. Beard, M.K. Accommodating uncertainty in query response. in "6th International Symposium on Spatial Data Handling". 1994. London: Taylor & Francis.
7. Hunter, G.J. and M. Goodchild, Dealing with error in spatial data sets: a simple case study. "Photogrammetric Engineering and Remote Sensing", 1995(61): p. 529-537.
8. Kyriakidis, P.C. and M. Goodchild, Geostatistics for conflation and accuracy assessment of digital elevation models. "Int. J. Geographical Information Science", 1999(13): p. 677-707.
9. Klosterman, R., Planing support systems: a new perspective on computer aided planning, in "Planning support systems: integrating geographic information systems, models and visualisation tools", R. Brail and R. Klosterman, Editors. 2000, ESRI Press: Redlands, California.
10. Bailey, D. and A. Goonetilleke. A decision support system for site selection of large-scale infrastructure facilities using natural language. in "ASOR03". 2003. Noosa, Australia: Australian Society for Operations Research.
11. Mendell, J.M. and R.I. John. Footprint of uncertainty and its importance to type-2 fuzzy sets. in "Sixth international conference on artificial intelligence and soft computing". 2002. Banff, Canada: IASTED.
12. Brookes, C.J., A genetic algorithm for locating optimal sites on raster suitability maps. "Transactions in GIS", 1997. 2: p. 201-212.
13. Saaty, T.L., "The Analytic Hierarchy Process". 1980, New York: Macgraw Hill.

ADAPTIVE AND MACHINE LEARNING II

(This page left blank intentionally)

Highlighted Technical Paper A

Generalization of Kernel PCA and Automatic Parameter Tuning

Takahide Nogayama, Haruhisa Takahashi, Masakazu Muramatsu
The University of Electro-Communications
Chofugaoka 1–5–1, Chofu-shi, Tokyo, 182-8585, Japan
noga@ice.uec.ac.jp

Abstract

We propose a generalized kernel PCA which provides much more accurate information of kernel space. Calculating partial derivatives of eigenvalues with kernel parameters, we can obtain the optimal kernel parameters. The criterion for optimal parameters are given by a quadratic cost function with respect to eigenvalues. We compared our method with SVM for face recognition, and showed that our method works efficiently as expected.

1. Introduction

Kernel based methods work by mapping data into a high dimensional feature space defined by the kernel function that computes inner product of two input images. There are several related methods such as support vector machine (SVM)[1], kernel principal component analysis (KPCA)[7] [6], and kernel Fisher's discriminant analysis (KFDA)[3].

Kernel based methods potentially provide a proficient approach to pattern recognition. KPCA proposed by Schölkopf [7] [6] can extract nonlinear component by performing PCA on the kernel feature space. It is expected for effective application to pattern recognition, and recently draws intensive attention in the face recognition society [9] [8].

A particular application generally requires sensible choice of a specific kernel function, and in pattern recognition the classification performance largely depends on this choice. In some application such as face recognition, radial basis function is in popular use, and so the choice of kernel function reduces to the problem of choosing of kernel parameters. If the parameters are appropriately chosen, one can extract optimal performance. Unfortunately there have been no effective methods so far for this issue.

Usually the parameters are determined empirically, or with auxiliary experiments, but in some cases such as multi-class problems and multi-parameter cases, it would be unreasonable for huge computational effort. In this paper we generalize Schölkopf's method and apply it to automatic determination of semi-optimal parameters for Gaussian kernel. The method makes use of the derivatives of kernel matrix eigenvalues to obtain iterative methods for optimal values using.

The following notation of the gaussian kernel is used through this paper

$$K(\boldsymbol{x}, \boldsymbol{z}) = \exp\left(-\frac{\|\boldsymbol{x} - \boldsymbol{z}\|^2}{2\sigma^2}\right) \tag{1}$$

where σ is called kernel parameter.

2. Generalization of kernel PCA

As was mentioned in Introduction, KPCA proposed by Schölkopf performs PCA for features on the kernel space. PCA usually put the median point at the average vector of features. Since Schölkopf performed the analysis assuming that the fiducial point is at the origin in the kernel feature space, but it does not reflect the true distribution of variances in the kernel space. In this section we review his analysis setting the fiducial point at the average vector of features. We call this generalized KPCA.

2.1. Kernel method

Let $\boldsymbol{x} = (x_1, \ldots, x_n)^t$ be an observed feature vector, and let the set of vectors be $S = \{\boldsymbol{x}_1, \ldots, \boldsymbol{x}_l\}$. We assume that $\boldsymbol{x}$ is mapped to p dimensional kernel feature space F by $\boldsymbol{\phi}(\boldsymbol{x}) \in F$.

$$\boldsymbol{x} = (x_1, \ldots, x_n)^t \mapsto \boldsymbol{\phi}(\boldsymbol{x}) = (\phi_1(\boldsymbol{x}), \ldots, \phi_p(\boldsymbol{x}))^t \tag{2}$$

Kernel method computes inner product

$$k(\boldsymbol{x}, \boldsymbol{z}) = \langle \boldsymbol{\phi}(\boldsymbol{x}), \boldsymbol{\phi}(\boldsymbol{z}) \rangle = \boldsymbol{\phi}(\boldsymbol{x})^t \boldsymbol{\phi}(\boldsymbol{z}) \tag{3}$$

without referring the feature ϕ_i $(i = 1, \ldots, p)$ directly. Let K be $K_{ij} = \langle \boldsymbol{\phi}(\boldsymbol{x}_i), \boldsymbol{\phi}(\boldsymbol{x}_j) \rangle = k(\boldsymbol{x}_i, \boldsymbol{x}_j)$, then $K = \Phi^t \Phi$ with $\Phi = (\boldsymbol{\phi}(\boldsymbol{x}_1), \ldots, \boldsymbol{\phi}(\boldsymbol{x}_l))$ (sample matrix).

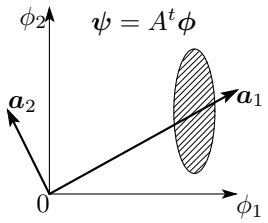

Figure 1. KPCA

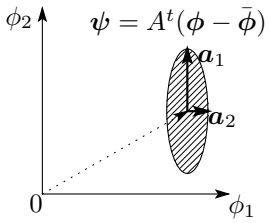

Figure 2. GKPCA

2.2. Kernel PCA with fiducial point at the mean vector

There are two methods for determining principal component axis : variance maximization criterion and mean square error minimization criterion. In this paper we adopt the former criterion. This criterion maximize the variances in feature space which is linearly transformed by some orthonormal system.

Performing PCA in kernel space, we assume that p dimensional linear space is transformed to d dimensional linear space. Let $\boldsymbol{a}_i$ be an orthonormal vector of the d-dimensional linear sub-space, and let $A = (\boldsymbol{a}_1, \ldots, \boldsymbol{a}_d)$. We assume $\boldsymbol{\phi}(\boldsymbol{x})$ is transformed to $\boldsymbol{\psi}^t(\boldsymbol{x}) = (\psi_1(\boldsymbol{x}), \ldots, \psi_d(\boldsymbol{x}))$ by $\boldsymbol{a}$ $(i = 1, \ldots, l)$, where

$$\boldsymbol{\psi}(\boldsymbol{x}) = A^t\left(\boldsymbol{\phi}(\boldsymbol{x}) - \bar{\boldsymbol{\phi}}\right) \tag{4}$$

and where $\bar{\boldsymbol{\phi}} = \frac{1}{l}\sum_{i=1}^{l}\boldsymbol{\phi}(\boldsymbol{x}_i)$ (see Figure 2). Let $\mathbf{1}$ be the $l \times 1$ vector, where all entries equal unity. Now let $p \times p$ covariance matrix in kernel space be Σ_ϕ. Then

$$\Sigma_\phi = \frac{1}{l}\Phi\left(I_l - \frac{1}{l}\mathbf{1}\mathbf{1}^t\right)\left(I_l - \frac{1}{l}\mathbf{1}\mathbf{1}^t\right)\Phi^t. \tag{5}$$

Σ_ψ is $d \times d$ covariance matrix in the d-dimensional subspace given by eq. (4) or

$$\Sigma_\psi = A^t\Sigma_\phi A. \tag{6}$$

Because orthonormal bases $\boldsymbol{a}_i$ $(i = 1, \ldots, d)$ that we want to obtain are in the kernel space, we can represent them as a linear combination of $\left(\boldsymbol{\phi}(\boldsymbol{x}_i) - \bar{\boldsymbol{\phi}}\right) \in F$, $(i = 1, \ldots, l)$. Assuming $\boldsymbol{b}_i = (b_{i1}, \ldots, b_{il})^t$ be the coefficient vectors

$$\boldsymbol{a}_i = \sum_{j=1}^{l} b_{ij}\left(\boldsymbol{\phi}(\boldsymbol{x}_j) - \bar{\boldsymbol{\phi}}\right). \tag{7}$$

Further $B = (\boldsymbol{b}_1, \ldots, \boldsymbol{b}_d)$

$$A = \Phi\left(I_l - \frac{1}{l}\mathbf{1}\mathbf{1}^t\right)B. \tag{8}$$

Now we can formalize PCA as an optimization problem. Let $G = \left(I_l - \frac{1}{l}\mathbf{1}\mathbf{1}^t\right)\Phi^t\Phi\left(I_l - \frac{1}{l}\mathbf{1}\mathbf{1}^t\right)$. Then maximizing sum of variances in subspace using orthonormal bases is

$$\text{maximize} \quad : \quad tr\left(\Sigma_\psi\right) = \frac{1}{l}tr\left(B^tG^2B\right) \tag{9}$$

$$\text{subject to} \quad : \quad A^tA = B^tGB = I_d. \tag{10}$$

To obtain the solution, We can use Lagrangian function

$$L(B, \Lambda) = \frac{1}{l}tr\left(B^tG^2B\right) - tr\left(\left(B^tGB - I_d\right)\Lambda\right). \tag{11}$$

Then setting

$$\frac{\partial L}{\partial B} = \frac{2}{l}G^2B - 2GB\Lambda \tag{12}$$

be zero, we obtain Karush-Kuhn-Tucker(KKT) condition

$$\frac{1}{l}G^2B = GB\Lambda \tag{13}$$

$$B^tGB = I_d. \tag{14}$$

Solving this KKT condition for B, we can obtain the solution.

Let the ith eigenvalue of G be μ_i with corresponding eigenvector $\boldsymbol{v}_i$. Assume that $\boldsymbol{v}_i^t\boldsymbol{v}_i = 1$ $(i = 1, \ldots, l)$, and $\mu_1 \geq \ldots \geq \mu_d \geq 0$. Since G is a symmetric matrix, eigenvectors constitute orthonormal set. Thus letting $\boldsymbol{b}_i = \frac{1}{\sqrt{\mu_i}}\boldsymbol{v}_i$, we obtain $\boldsymbol{b}_i^tG\boldsymbol{b}_j = \delta_{ij}$ which satisfy eq. (14). We denote $V = (\boldsymbol{v}_1, \ldots, \boldsymbol{v}_l)$, the diagonal matrix M as $M_{ii} = \mu_i$, and $M^{-\frac{1}{2}}$ as

$$[M^{-\frac{1}{2}}]_{ij} = \begin{cases} \frac{1}{\sqrt{\mu_i}} & \text{if} \quad i = j \\ 0 & \text{if} \quad i \neq j \end{cases}. \tag{15}$$

Then

$$B = VM^{-\frac{1}{2}}. \tag{16}$$

And eq. (13) can be transformed to

$$\text{(left side)} \quad = \quad \frac{1}{l}G^2B = \frac{1}{l}VM^2M^{-\frac{1}{2}} \tag{17}$$

$$\text{(right side)} \quad = \quad GB\Lambda = VMM^{-\frac{1}{2}}\Lambda \tag{18}$$

by using $GV = VM$. Since V, M are non zero matrix ,

$$VM\left(\frac{1}{l}M - \Lambda\right)M^{-\frac{1}{2}} = O \tag{19}$$

results in $\Lambda = \frac{1}{l}M$ or $\lambda_i = \frac{\mu_i}{l}$ $(i = 1, \ldots, d)$.

One can easily check $\Sigma_\psi = \Lambda$ is substituting B and Λ into Σ_ψ and using eq.(6) , eq.(8). This means the variance on ith axis in the d-dimensional subspace is λ_i, and each axes are uncorrelated.

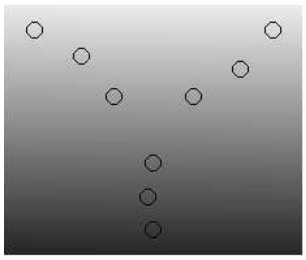

Figure 3. Linear PCA 1st principal component

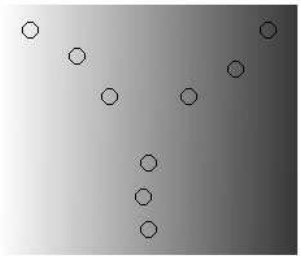

Figure 4. Linear PCA 2nd principal component

Finally $\psi(\boldsymbol{z})$ is represented by

$$\begin{aligned}\psi(\boldsymbol{z}) &= A^t\left(\phi(\boldsymbol{z})-\bar{\phi}\right)\\ &= B^t\left(I_l-\frac{1}{l}\mathbf{1}\mathbf{1}^t\right)\Phi\left(\phi(\boldsymbol{z})-\frac{1}{l}\Phi\mathbf{1}\right)\\ &= M^{-\frac{1}{2}}V^t\left(I_l-\frac{1}{l}\mathbf{1}\mathbf{1}^t\right)\left(\boldsymbol{k}(\boldsymbol{z})-\frac{1}{l}K\mathbf{1}\right)\end{aligned} \quad (20)$$

using $\boldsymbol{k}(\boldsymbol{z})=(K(\boldsymbol{x}_1,\boldsymbol{z}),\ldots,K(\boldsymbol{x}_l,\boldsymbol{z}))^t$.

2.3. Illustration via artificial data

Now we illustrate the generalized KPCA using artificial data. Consider a data of Figure 3 and 4 which shows stellately distributed data on two dimensional space having three actinoid wings.

If we apply linear principal component analysis for this data, we obtain only two principal components which are clearly unable to represent the data. The results are shown in Figure 3,4. Thus KPCA would be an efficient tool in this example.

Figure 5 shows the result of applying the generalized KPCA for this data. In this example one can see that a small parameter can give only features neighbor of the data, and large parameter is too crude to represent precise features. In a later section we will see that the optimum parameter in this case is $\sigma = e^{0.7}$.

In Figure's 6, 7 the landscapes of variance for each principal component axis scanned with kernel parameter are shown for KPCA and the generalized KPCA (GKPCA), respectively. From Figure 7 (GKPCA), one can see that small parameters give equal variance for each axis, thus each component is equally important. On the other hand the large parameters give zero variance for each axis meaning the distribution of data is concentrated on data points. KPCA (Figure 6), on the other hand, can not represent this, because the center point is not appropriately set.

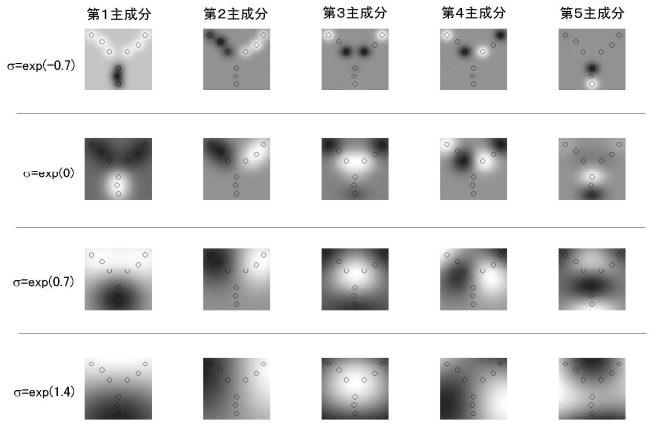

Figure 5. Kernel parameter and principal component of GKPCA

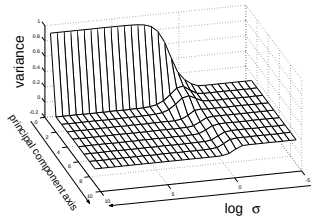

Figure 6. Variance vs. principal component and kernel parameter (KPCA)

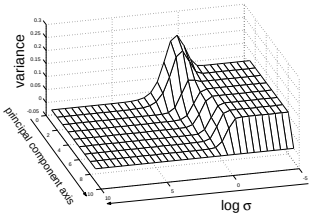

Figure 7. Variance vs. principal component and kernel parameter(GKPCA)

3. Automatic parameter tuning

As was mentioned in the previous section, when the kernel parameter is too large, each axis in the kernel space has similar variance. On the contrary when the kernel parameter is too small, all axes have zero variances losing data information. The optimal parameter should be in the middle of these extremes. Thus the optimal kernel space should consist of a few principal component axes with large variance and remaining large number of principal component axes with small variance. This is illustrated in Figure 8. We require that the optimal kernel parameter should be maximizing the deviation of variances distribution.

Let kernel parameter be θ, and let variance of ith principal component axis be λ_i. According to our request, optimal kernel parameter maximizes following cost function (see Figure 8).

$$E(\theta) \quad = \quad \frac{1}{l}\sum_{i=1}^{l}\left(\lambda_i-\bar{\lambda}\right)^2$$

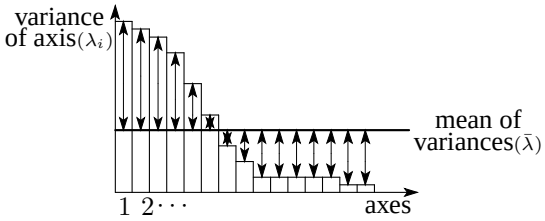

Figure 8. Deviation of variances

$$= \frac{1}{l}\boldsymbol{\lambda}^t \left(I_l - \frac{1}{l}\mathbf{1}\mathbf{1}^t \right) \boldsymbol{\lambda} \tag{21}$$

Eq.(21) can be optimized by the following steepest descent gradient method:

$$\theta_{t+1} = \theta_t + \eta \frac{\partial E}{\partial \theta}. \tag{22}$$

In eq.(23), the derivative of cost function with θ is given by

$$\frac{\partial E}{\partial \theta} = \frac{2}{l}\boldsymbol{\lambda} \left(I_l - \frac{1}{l}\mathbf{1}\mathbf{1}^t \right) \frac{\partial \boldsymbol{\lambda}}{\partial \theta} \tag{23}$$

$$= \frac{2}{l^3}\boldsymbol{\mu} \left(I_l - \frac{1}{l}\mathbf{1}\mathbf{1}^t \right) \frac{\partial \boldsymbol{\mu}}{\partial \theta}. \tag{24}$$

To obtain $\frac{\partial \mu_k}{\partial \theta}$, we apply the implicit function theorem and the derivation of determinant. Since μ_k is an eigenvalue of $G(\theta)$, it satisfies characteristic equation $\det\left(\mu_k I_l - G\left(\theta\right)\right) = 0$. Thus there exists implicit function $f_{\mu_k}\left(\cdot\right)$ such as $f_{\mu_k}\left(\theta\right) = \mu_k$. Let C be the transposed cofactor matrix of $\mu_k I_l - G$. Then if $\sum_{i=1}^{l} C_{ii} \neq 0$,

$$\frac{\partial f_{\mu_k}}{\partial \theta} = -\frac{\frac{\partial \det(\mu_k I_l - G)}{\partial \theta}}{\frac{\partial \det(\mu_k I_l - G)}{\partial \mu_k}} \tag{25}$$

$$= \frac{\sum_{i=1}^{l}\sum_{j=1}^{l} C_{ij}\frac{\partial G_{ij}}{\partial \theta}}{\sum_{i=1}^{l} C_{ii}}. \tag{26}$$

To avoid much computational effort for calculating the transposed cofactor matrix, we refer the following theorem without proof.

Theorem 1 *Let eigenvalues and eigenvectors of G be $\mu_i, \boldsymbol{v}_i$ $(i = 1, \ldots, l)$, respectively. Then transposed cofactor matrix of $(\mu_k I_l - G)$ is given by*

$$\prod_{\substack{i=1 \\ i\neq k}}^{l} \left(\mu_i - \mu_k\right) \boldsymbol{v}_k \boldsymbol{v}_k^t. \tag{27}$$

This theorem can be proved by a regularization method of a cofactor matrix and inverse matrix.

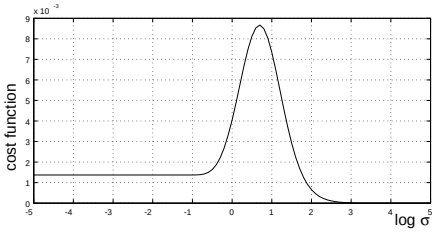

Figure 9. Cost function

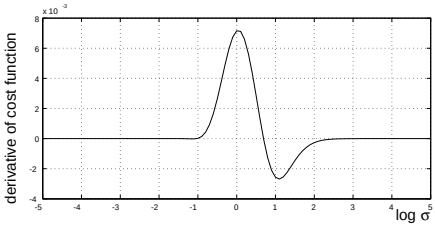

Figure 10. Derivative of cost function

Using Theorem 1, $\frac{\partial \mu_k}{\partial \theta}$ is calculated

$$\frac{\partial f_{\mu_k}}{\partial \theta} = \frac{\prod_{\substack{i=1 \\ i\neq k}}^{l}\left(\mu_i - \mu_k\right)\sum_{i=1}^{l}\sum_{j=1}^{l}(\boldsymbol{v}_k \boldsymbol{v}_k^t)_{ij}\frac{\partial G_{ij}}{\partial \theta}}{\prod_{\substack{i=1 \\ i\neq k}}^{l}\left(\mu_i - \mu_k\right)\sum_{i=1}^{l}[\boldsymbol{v}\boldsymbol{v}^t]_{ii}}$$

$$= \frac{\prod_{\substack{i=1 \\ i\neq k}}^{l}\left(\mu_i - \mu_k\right)\boldsymbol{v}_k^t \frac{\partial G}{\partial \theta}\boldsymbol{v}_k}{\prod_{\substack{i=1 \\ i\neq k}}^{l}\left(\mu_i - \mu_k\right)}$$

$$= \boldsymbol{v}_k^t \frac{\partial G}{\partial \theta}\boldsymbol{v}_k. \tag{28}$$

The following Learning algorithm gives the optimizing procedure.

- $t = 1, \quad \theta_t := \theta_0$
- repeat
  - $G := \left(I_l - \frac{1}{l}\mathbf{1}\mathbf{1}^t\right) K(\theta_t) \left(I_l - \frac{1}{l}\mathbf{1}\mathbf{1}^t\right)$
  - $\frac{\partial G}{\partial \theta} := \left(I_l - \frac{1}{l}\mathbf{1}\mathbf{1}^t\right) \frac{\partial K(\theta_t)}{\partial \theta} \left(I_l - \frac{1}{l}\mathbf{1}\mathbf{1}^t\right)$
  - $\boldsymbol{\mu} :=$ eigenvalues of G
  - $V :=$ eigenvectors of G
  - for $i := 1$ to l
    - $\frac{\partial \mu_i}{\partial \theta} = \boldsymbol{v}_i^t \frac{\partial G}{\partial \theta}\boldsymbol{v}_i$
  - $\frac{\partial E}{\partial \theta} := \frac{1}{l^3}\boldsymbol{\mu}^t \left(I_l - \frac{1}{l}\mathbf{1}\mathbf{1}^t\right) \frac{\partial \boldsymbol{\mu}}{\partial \theta}$
  - $\theta_{t+1} := \theta_t + \eta \frac{\partial E}{\partial \theta}$
- until $(\theta_{t+1} \simeq \theta_t)$

Figure 9, 10 illustrate the cost function and its derivative as functions of the kernel parameter for the data used in section 2.3. One can easily see that the cost function gives its maximum at $\sigma = e^{0.7}$ where the derivative is zero.

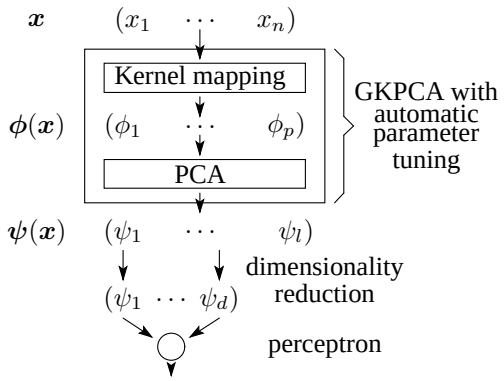

Figure 11. GKPCA-plus-perceptron

4. Experimental results

4.1. Learning with GKPCA-plus-perceptron

Since PCA is the preprocessing step for classification task, we use perceptron(single layer) as a classifier. Because GKPCA prepare powerful nonlinear mapping and enabling appropriate dimensionality reduction, such simple classifier is sufficient for classification tasks. To enable to learn weakly nonlinearly separable problem, we employ the sigmoidal function for the output function.

$$f(u) = \frac{1}{1+\exp(-u)} \quad , \quad \left(u = \boldsymbol{w}^t \boldsymbol{x} + b\right) \tag{29}$$

Perceptron has only one parameter called learning rate η. Since perceptron learning approximately converges to the same solution without regard to a value of the learning rate, it has no heuristic parameters. Optimizing the kernel parameter by our method, "GKPCA-plus-perceptron" also has no heuristic parameter. (see Figure 11).

4.2. Face recognition

To test our method, we applied it to face images of the HOIP database [1] . The data consist of 300 images of 150 males and 150 females, and each image is normalized to 46×44 pixels having real number from 0 through 1. Thus the input vector has 2024-dimensions. We classified male and female into two categories (see Figure 12). We performed 10-fold-cross-varidation with randomly divided data, and took average of five 10-fold-cross-validations. Perceptron's learning rate was set to $\eta = 0.1$. The landscape of variance for each principal component axis scanned with kernel parameter σ are shown in Figure 13.

[1]The facial data in this paper are used by permission of Softopia Japan, Research and Development Division, HOIP Laboratory. It is strictly prohibited to copy, use, or distribute the facial data without permission.

Figure 12. Face images used in experiment

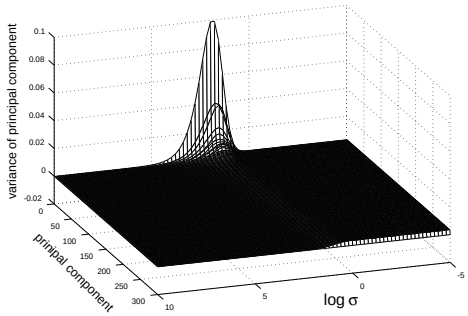

Figure 13. Variances scanned with kernel parameter

In Figure 14, 15, the training error and the testing error are shown for the parameter and the number of principal components. The experiments were done for each parameter σ, changing the number of principal components (Note that principal components are sorted in descending order). Optimal parameter determined by our method is near $\sigma = e^{1.8}$ in this case (see Figure 13). One can observe that both errors become small near the optimal parameter, although we use only few principal component axes (see Figure 16). The minimal value of average testing error was 7.53% for the optimal parameter and for the number of principal component $d = 155$. The true minimal value of average testing error was 6.13% obtained for the parameter scan with $\sigma = [e^{-5}, e^{-4.8}, \ldots, e^{9.8}, e^{10}]$ for $d = 155$ (see Figure 15, 16). Both errors were averaged over 50 times simulation-runs.

The optimal parameter was computed by eq.(22) setting $\eta = 10000$, and setting σ_0 randomly from [1.0, 20.0]. The average computational time for the optimal solution is 8.01 sec. [2]

We compared our method with support vector machine using gaussian kernel. SMO algorithm [5] was used for training SVM. We performed exhaustive search for the optimal parameters σ and C, setting $\sigma = [e^{-5}, e^{-4}, \ldots, e^{10}]$, $C = [e^{-5}, e^{-4}, \ldots, e^{10}]$. Note that to find out the optimal parameter, we need to take an average of several experiments, e.g. of 50 times. The average computational time for the search was 39.58 sec / experiment, and totally it takes

[2]The programs were run on Pentium4(2.53GHz) with 512MB RAM.

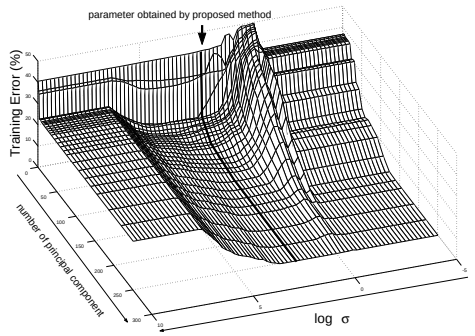

Figure 14. Average training error

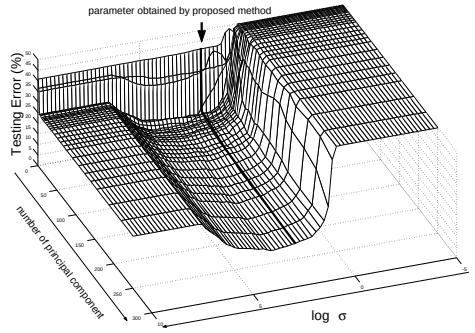

Figure 15. Average testing error

1979 sec to obtain the optimal kernel parameters. The minimal value of average testing error is obtained as 5.86% with $\sigma = e^5, C = e^7$.

We conclude from the experiments that the kernel parameter is near optimal. Although, we employ the perceptron algorithm, generalization errors are different only 2% from SVM.

We characterized the relationship between kernel parameter and eigenvalues about the data sets (iris, wine, glass, baberman, bupa-liver-disorders, ionosphere, breast-cancer-wisconsin, vehicle, vowel, segment) collected from UCI Repository of machine-learning-databases(http:// www.ics.uci.edu /˜mlearn /MLRepository.html). Therefore the data set which has distribution of eigenvalues similar to Figure 7 or Figure 13 seems to avoid the local minimum problem with our optimization method. All of the data sets indicates that each distribution of the eigenvalues resembles the used face data.

5. Conclusion

In this paper, we proposed a method which can tune the kernel parameter automatically. Furthermore the merit applying GKPCA-plus-perceptron is that we can solve any classification problem without heuristically determined parameters. We showed GKPCA-plus-perceptron can attain enough classification performance which is comparable to SVM.

The extention to the multi-class problem would have some merits because each class can have different parameter by our method.

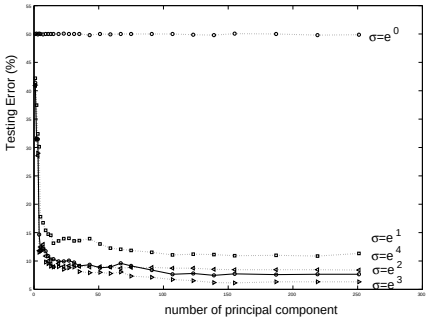

Figure 16. Average testing error

6. Acknowledgements

The helpful comments of the Prof. Kazuhiro Hotta on preliminary versions of the article are gratefully acknowledged. and the helpful proofreading of Mr. Yasuhide Miura is also gratefully acknowledged.

References

[1] N. Cristianini and J. Shawe-Taylor. *An Introduction to Support Vector Machines and othe kernel-based learning methods*. Cambridge University Press, 2000.

[2] G. F. Hughes. On the mean accuracy of statistical pattern recognizers. *IEEE transactions on information theory*, IT-14:55–63, 1968.

[3] S. Mika, G. Ratsh, J. Weston, B. Scholkopf, and K.-R. Muller. Fisher discriminant analysis with kernels. *Neural Networks for Signal Processing IX*, pages 41–48, 1999.

[4] R. O.Duda, P. E.Hart, and D. G.stork. *Pattern Classification Second Edition*. John Wiley & Sons,. Inc, 2000.

[5] J. C. Platt. Fast training of support vector machines using sequential minimal optimization. *Advances in Kernel Methods*, pages 185–208, Dec 1998.

[6] B. Scholkopf, A. J. Smola, and K.-R. Muller. Kernel principal component analysis. *Advances in Kernel Methods*, pages 327–353, Dec 1998.

[7] B. Scholkopf, A. J. Smola, and K.-R. Muller. Nonlinear component analysis as a kernel eigenvalue problem. *Neural Computation*, 10(5):1299–1319, July 1998.

[8] T. Takahashi and T. Kurita. Robust de-noising by kernel pca. *Lecture Notes in Computer Science*, pages 739–744, 2002.

[9] M.-H. Yang. Kernel eigenfaces vs. kernel fi shrefaces: Face recognition using kernel methods. *Fifth IEEE International Conference on Automatic Face and Gesture Recognition*, pages 215–220, May 2002.

A Hybrid Network for Input that is both Categorical and Quantitative

Roelof K. Brouwer
Department of Computing Science
University College of the Cariboo
Kamloops, BC, Canada, V2C 5N3
rkbrouwer@ieee.org

Abstract

The data on which a MLP (multi-layer perceptron) is to be trained to approximate a continuous function may include inputs that are categorical in addition to numeric or quantitative inputs. An approach examined in this paper is to train a hybrid network consisting of an MLP and a encoder with multiple output units; a separate output unit for various combinations of values of the categorical variables. Input to the feed forward sub network of the hybrid network is restricted to truly numerical quantities.

Results show that the method discussed here of separating numerical from quantitative is quite effective.

1 Introduction

Often the data on which a multiplayer *perceptron (MLP)* is to be trained to approximate a continuous function has inputs that are categorical rather than numeric or quantitative. A MLP [1,2] with connection matrices that multiply input values and sigmoid functions that further transform values however represents a continuous mapping in all input variables. The values of categorical variables even if they are ordinal should not be passed through the MLP as if they were continuous in nature since Kolmogorov's theorem is only proven for a network that is used to represent a continuous mapping. The underlying function to be represented may really be several distinct functions with the values of the categorical variable labeling these functions. As an alternative then we could consider a separate MLP for various combinations of values for the categorical variables found in the training data and expected during prediction.

Another method that makes use of several networks in combination is the mixture of experts [3]. Other work using neural networks in case where categorical variables are present is by Barton and Burgess [4]. Burgess [5] describes a methodology, based upon the statistical concept of analysis of variance (ANOVA), which can be used both for non-linear model identification and for testing the statistical significance of categorical inputs to a neural network Bishop [6,7] introduces a new class of neural, network models obtained by combining a conventional neural network with a mixture density model. The complete system is called a Mixture Density Network. Lee and Lee [8] also address the problem of multi-value regression estimation with neural network architecture.

This paper is organized as follows. It commences with a description of a neural network construction and its amended training algorithm. This is followed by the results of simulations that demonstrate the validity of the approach suggested in this paper.

2 Alternative Approach

2.1 Introduction

A commonly used approach is to convert the categorical values into real numbers and to feed them together with the other numerical input into a single MLP without distinction from the numerical input. Let us instead consider a more general approach as shown in Figure 1. In this case the categorical input is treated separately from the numerical input.

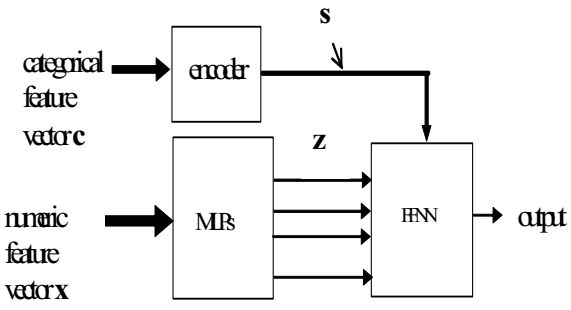

Figure 1 General network with categorical input treated seperately

If we represent the output of the neural network by **z** then the complete network calculates the output as

$$y = f(\mathbf{z}, \varphi(\mathbf{w},\mathbf{s})) \quad (1)$$

with $\varphi(\mathbf{w},\mathbf{s}) = (\varphi_i(\mathbf{w},\mathbf{s}_i) \quad i = 0,1..h-1)$ and where $\varphi_i(\mathbf{w},\mathbf{s}_i)$ could be Boolean functions with values from {0,1} . The parameter vector **w** would be trainable. $\mathbf{s}_i$ $i = 0,1..h-1$ are elements of {0,1} and are the components of output of the encoder network. We may now consider various options since we have choices regarding the φ function performed by the FFNN, the encoder and the MLPs.

2.2 The FNNN

The first simplification is to set $\varphi_i(\mathbf{w},\mathbf{s}_i) = \mathbf{s}_i$ and let f be the dot product. The output of the combined network is the dot product of the output of the MLP, **z**, with the output of the encoder, **s** i.e

$$y=\mathbf{z}.\mathbf{s} \quad (2)$$

If **s** is a 1 of n vector with the position of the 1 identifying the output unit of the MLP then **s** behaves like a selector by selecting the ouput that applies.

2.3 The MLPs

As far as the MLPs are concerned we could consider a separate MLP for each combination of values for the categorical variables, **c**, found in the training data and expected during prediction. In statistical terms the ANN consists of several MLP's with a dedicated MLP for each regression equation as shown in Figure 2. Each regression equation corresponds to a subset of different combination of values of categorical variables.

$$y=(\mathbf{W}^{(1)}.(f(\mathbf{W}^{(0)}.\mathbf{x})).\mathbf{s} \quad (3)$$

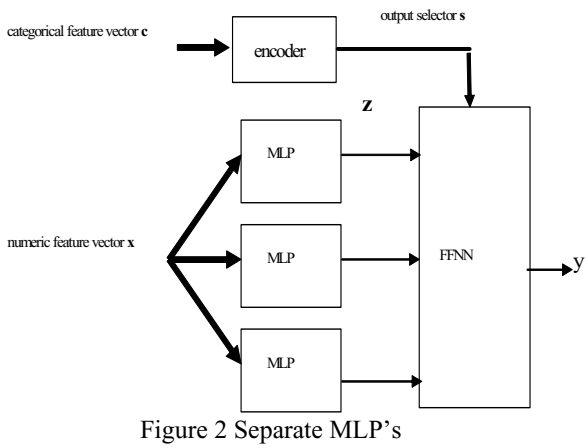

Figure 2 Separate MLP's

The nominal input through selector, **s**, then determines which MPL has the correct result for the continuous input. The encoder will generate a 1 of n binary vector, **s**, that is combined with the output of the MLP in a dot product. The FNN selects the MLP that provides the correct output. For example each of the three MLP's in Figure 2 represents a different regression equation. This means that the categorical feature vectors are used as function identifiers rather than as values of a quantitative variable. In the case of one category variable with 3 values 3 separate networks each with a single output unit would be trained. In case of the Boston housing data discussed in this paper up to 12 networks would be required depending upon the allowable number of combinations of categorical values.

The problem with the preceding method of including categorical input separately is that the number of output units required for the network is equal to the number of categorical feature values or even combinations of feature values (not the number of categorical features). The training data is effectively segmented with a segment for each categorical feature value. This may leave some segments with very few training elements and some with no training elements at all. It is quite possible that some categorical feature value combinations do not occur in the training data set because they are not at all possible in reality.

However a collection of MLPS, each with the same input and each with one output unit is equivalent to a single MLP that is not fully connected between the hidden layer and the output layer. Each output unit will only be connected to the subset of hidden units that correspond to the same component MLP.

If we now allow the single MLP to be fully connected from hidden layer we get a MLP with more expressive power, because of additional degrees of freedom, to represent each of the two regression equations We may reduce the number of hidden units. Based on this the approach examined in this paper is to train a single MLP with multiple outputs; a separate output unit for each rule or condition.

The transfer function corresponding to the complete feed-forward network that accepts both the quantitative and categorical input is then

$$y=(\mathbf{W}^{(1)}.(f(\mathbf{W}^{(0)}.\mathbf{x})).\mathbf{s} \quad (4)$$

The matrices $\mathbf{W}^{(0)}$ and $\mathbf{W}^{(1)}$ correspond to the connection matrices for the first and second layer respectively in the MLP. For simplicity sake the additional unit in the input layer and hidden layer of the MLP sub-network that has a constant input of –1 to be multiplied by a weight representing bias has been left out.

2.4 The Encoder Network

Next the encoder network operation will be described. The encoder network accepts the categorical input portion of the total input and produces a selector vector, **s**. The dot product of this 1 of n selector vector with the output of the MLP, **z**, produces the final output, y. The encoder network converts the categorical input into a partitioned 1 of n code as illustrated in (5). The coded categorical input is then compared to entries in a table, **S**.

For a particular categorical variable a category is represented by a binary vector using 1-of-n encoding. (n is the number of categories). Each category for a category variable is then represented by a position in a binary vector. These 1 of n arrays are combined to form a 1-dimensional array of 1-dimensional arrays. The benefit of this representation is that conditions for rules are easier to express as subsets of coded inputs. An example is shown in (5).

$$[(0, 1, 0), (1, 0), (1, 0)] \tag{5}$$

A condition for selection an output unit would then be expressed as

$$[(1, 1, 0), (0, 1), (1, 0)] \tag{6}$$

There may be several conditions or rules like this with each condition corresponding to a regression equation. Each rule consists of a condition and the identifier of a regression equation. An example of a set of rules, **S**, is in Table 1.

Table 1 An example of S

Condition	1 of n representation of output unit identifier and selector **s**
[(1,0,0), (1, 1), (0, 1)]	0 0 1
[(0,1,0), (0, 1), (1, 0)]	0 0 1
[(0,0,1), (1, 0), (0, 1)]	0 0 1
[(1,0,1), (0, 1), (1, 0)]	0 1 0
[(0,1,0), (1, 0), (0, 1)]	0 1 0
[(0,0,1), (1, 0), (1, 0)]	0 1 0
[(1,1,0), (1, 0), (1, 0)]	1 0 0
[(0,1,1), (0, 1), (0, 1)]	1 0 0

2.5 Training

Training is done by using gradient descent as is normally done on a feed forward network with some additional operations that will be described next.

There are several output units for the MLP while in the training data there is only one scalar output value for each input. To obtain an error value for training, the output unit of the MLP that produces the value closest to the target output for the given training pattern is used to update the connection matrices, $\mathbf{W}^{(0)}$ and $\mathbf{W}^{(1)}$, of the MLP. It is important to note that the connection matrix, $\mathbf{W}^{(1)}$, between the hidden layer and the output layer has only the row corresponding to the winning output unit modified. The categorical input concatenated with the identifier of the output unit producing the smallest error, through selector **s**, is then either added to a table, **S**, or replaces an entry in the table or does nothing to the table. Note that this in general will be a many to one mapping. As a final step in training, table, **S**, is reduced by combining rows that contain the same value for **s** whenever possible. The entries in the first column will then be conditions.

Formally let t be the target output of the entire network, y the output of the entire network and **z** the output of the MLP. Then

$$e=y-t \tag{7}$$

and

$$\mathbf{e} = (\mathbf{z} - t) \tag{8}$$

Note that bolded **e** is a vector and un-bolded e is a scalar.

$$e= y-t = \mathbf{s}.\mathbf{z}-t = \mathbf{s}.(\mathbf{z}-t) = \mathbf{s}.\mathbf{e} \tag{9}$$

A performance measure we may use during training is as in eqn. (10)

$$C = \frac{(y-t)^2}{2} = \frac{e^2}{2} \tag{10}$$

Then

$$\nabla_{\mathbf{U}} C = e\nabla_{\mathbf{U}} y \tag{11}$$

U represents any parameter of the network to be learned. Now

$$\nabla_{\mathbf{U}} y=\mathbf{s}.\nabla_{\mathbf{U}}\mathbf{z}+\mathbf{z}.\nabla_{\mathbf{U}}\mathbf{s} \tag{12}$$

U is replaced by the connection matrices $\mathbf{W}^{(0)}$ and $\mathbf{W}^{(1)}$. **s** is a function of the categorical input, **q**, and does not depend on the connection matrices in the trained network even if it does during training as we will see later. Therefore the second term on the right side in (12) can be dropped. Then

$$\nabla_{\mathbf{W}^{(0)}}\mathbf{z} = (\mathbf{W}^{(1)} \quad \mathbf{W}^{(0)}.\mathbf{x} \times \mathbf{I} \otimes \mathbf{x} \tag{13}$$

$$\nabla_{\mathbf{W}^{(1)}}\mathbf{z} = \quad \otimes \quad ^{(0)} \tag{14}$$

We get

$$\mathbf{s}.\nabla_{\mathbf{W}^{(0)}}\mathbf{z} = (\mathbf{s}.\mathbf{W}^{(1)} \times \quad ^{(0)} \quad \otimes \mathbf{x} \tag{15}$$

$$\mathbf{s}.\nabla_{\mathbf{W}^{(1)}}\mathbf{z} = \mathbf{s} \quad \otimes \quad ^{(0)} \tag{16}$$

$$= \mathbf{s} \otimes \quad ^{(0)} \tag{17}$$

f(x) is equal to tanh(x). Note that component-wise multiplication of arrays is defined as long as the dimensions of one of the arrays form a prefix of the dimensions of the other array. Thus the component wise multiplication between a 3*4 array and a 3*4*6 array is defined. **I** is the identity matrix with the same rank as **s**.

The complete training algorithm consists of applying the following:

$$\mathbf{z}=\mathbf{W}^{(1)}.f(\mathbf{W}^{(0)}.\mathbf{x}) \tag{18}$$

$$\mathbf{s}_{\text{pmin}(\mathbf{z}\text{-}t)}=1 \quad \text{and} \quad 0 \quad \text{otherwise} \tag{19}$$

pm in (**z**-t) means position of maximum in **z**-t.

$$\Delta\mathbf{W}^{(0)} = -\mu_0 \times e \times (\mathbf{s}.\mathbf{W}^{(1)} \times \quad ^{(0)} \quad \otimes \mathbf{x} \tag{20}$$

$$\Delta\mathbf{W}^{(1)} = -\mu_1 \times e \times \mathbf{s} \otimes \quad ^{(0)} \tag{21}$$

In addition to the above the table **S** is updated at each step.

3 Simulations

Following are the results of carrying out simulations to permit comparisons of the approaches discussed previously.

3.1 Simulation 1 -Boston Housing Data

The data for this simulation is from the StatLib library that is maintained at Carnegie Mellon University. The creator is Harrison, D. and Rubinfeld, D.L. 'Hedonic prices and the demand for clean air', J. Environ. Economics & Management, vol.5, 81-102, 1978. Date: July 7, 1993. The data set is available at http://www.ics.uci.edu/~mlearn/ MLRepository.html**.** It is concerned with housing values in suburbs of Boston. The feature vectors consist of 12 continuous attributes, one non-ordered binary-valued attribute and one ordered categorical attribute. Thus we have two kinds of categorical features. The value to be predicted is the median value of owner-occupied homes in $1000's.

The first categorical variable has the values 0 and 1 while the second has the values 1, 2, 3, 4, 5, 6, 7, 8, and 24. Using 1 of n encoding the first variable requires 2 bits and the second 9 bits for a total of 11 bits. The total number of combinations for categorical input is 2*9=18 although only 15 show up in the simulation. The number of hidden units per output unit is set at 5. The mean square error on training data before training was 1051.2. While the mean square error on test data before training was 1034.8.The learning rate was 0.0001 for both connection matrices. The number of output units made available is 15 while the number actually used is 11. Figure 3 shows the progress in training. The error on the test data is very close to the error on the training error at each epoch.

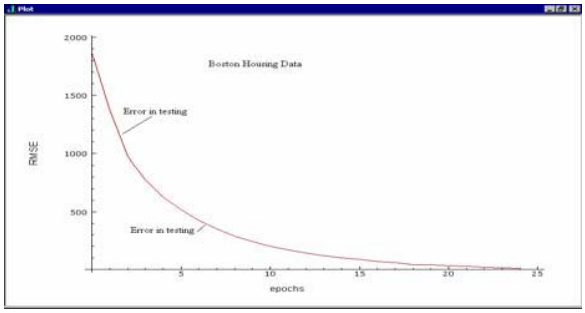

Figure 3

The table, **S**, obtained by training and sorted by the last column is

Table 2 Categorical input versus selector

R	Categorical input	s
1	[(0 1), (1 0 0 0 0 0 0 0 0)]	0 0 0 0 0 0 0 0 0 0 0 0 0 0 1 0
2	[(1 0), (0 0 1 0 0 0 0 0 0)]	0 0 0 0 0 0 0 0 0 0 0 0 0 0 1 0
3	[(1 0), (0 0 0 0 0 0 1 0 0)]	0 0 0 0 0 0 0 0 0 0 0 0 0 1 0 0
4	[(0 1), (0 0 0 0 1 0 0 0 0)]	0 0 0 0 0 0 0 0 0 0 0 0 1 0 0 0 0
5	[(0 1), (0 0 0 0 0 1 0 0 0)]	0 0 0 0 0 0 0 0 0 0 0 1 0 0 0 0 0
6	[(1 0), (0 1 0 0 0 0 0 0 0)]	0 0 0 0 0 0 0 1 0 0 0 0 0 0 0 0
7	[(1 0), (0 0 0 0 0 0 0 0 1)]	0 0 0 0 0 0 1 0 0 0 0 0 0 0 0 0
8	[(1 0), (0 0 0 1 0 0 0 0 0)]	0 0 0 0 0 1 0 0 0 0 0 0 0 0 0 0
9	[(0 1), (0 0 0 0 0 0 0 0 1)]	0 0 0 0 1 0 0 0 0 0 0 0 0 0 0 0
0	[(0 1), (0 0 1 0 0 0 0 0 0)]	0 0 0 0 1 0 0 0 0 0 0 0 0 0 0 0
1	[(1 0), (0 0 0 0 0 0 0 1 0)]	0 0 0 1 0 0 0 0 0 0 0 0 0 0 0 0
2	[(0 1), (0 0 0 1 0 0 0 0 0)]	0 1 0 0 0 0 0 0 0 0 0 0 0 0 0 0
3	[(1 0), (1 0 0 0 0 0 0 0 0)]	0 1 0 0 0 0 0 0 0 0 0 0 0 0 0 0
4	[(0 0), (0 0 0 0 0 1 0 0 0)]	1 0 0 0 0 0 0 0 0 0 0 0 0 0 0 0
5	[(0 0), (0 0 0 0 1 0 0 0 0)]	1 0 0 0 0 0 0 0 0 0 0 0 0 0 0 0

The first column is there to identify the rows for the purpose of the reader. This table is reduced to

Table 3 Condition versus selector value

Condition	Selector
[(1 0), (0 0 0 0 1 1 0 0 0)]	1 0 0 0 0 0 0 0 0 0 0
[(1 1), (1 0 0 1 0 0 0 0 0)]	0 1 0 0 0 0 0 0 0 0 0
[(1 0), (0 0 0 0 0 0 0 1 0)]	0 0 1 0 0 0 0 0 0 0 0
[(0 1), (0 0 1 0 0 0 0 0 1)]	0 0 0 1 0 0 0 0 0 0 0
[(1 0), (0 0 0 1 0 0 0 0 0)]	0 0 0 0 1 0 0 0 0 0 0
[(1 0), (0 0 0 0 0 0 0 0 1)]	0 0 0 0 0 1 0 0 0 0 0
[(1 0), (0 1 0 0 0 0 0 0 0)]	0 0 0 0 0 0 1 0 0 0 0
[(0 1), (0 0 0 0 0 1 0 0 0)]	0 0 0 0 0 0 0 1 0 0 0
[(0 1), (0 0 0 0 1 0 0 0 0)]	0 0 0 0 0 0 0 0 1 0 0
[(1 0), (0 0 0 0 0 0 1 0 0)]	0 0 0 0 0 0 0 0 0 1 0
[(1 1), (1 0 1 0 0 0 0 0 0)]	0 0 0 0 0 0 0 0 0 0 1

3.2 Simulation 2-Abalone Data

The source of the data for this experiment is the Marine Resources Division, Marine Research Laboratories – Taroona, Department of Primary Industry and Fisheries, Tasmania GPO Box 619F, Hobart, Tasmania 7001, Australia. The data set is available at http://www.ics.uci.edu/~mlearn/MLRepository.html. The data is for predicting the age of abalone from physical measurements. The number of attributes is 8 with all but one being continuously valued. The output data is normalized before training. Of 4177 feature vectors 1/2 were used for training and the other 1/2 was used for testing.).

The simulation was done with 3 output units and 3 hidden units per output unit. The mean square error based on training data before training commenced was 2.328320995 and the mean square error on test data before training commenced was 2.502301048. The number of epochs allowed was 25. he learning rates for the two connection matrices was 0.0001. The actual number of output units used was 3. The training error and testing error at the end of 25 epochs was 0.232212 and 0.247859.

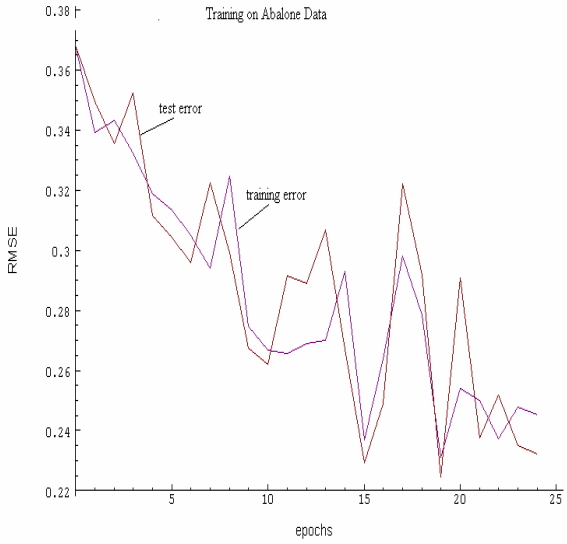

Figure 4 Training on Abalone Data

The table identifying the output unit corresponding to a category value is as shown in Table 4. Three output units were made available and 3 were utilized with one unit for each category variable

Table 4 Selector of output unit

Category	Category in 1 of n	Output unit	Output unit in 1 of n
M	0 0 1	1	0 1 0
F	0 1 0	0	1 0 0
I	1 0 0	2	0 0 1

4 Conclusion

We have shown how the categorical features may be segregated from the numeric features when using an MLP for prediction. The numeric feature vector is processed by an MLP with several outputs that are then combined with the coded form of the categorical feature vector. This is somewhat similar to the statistical approach except that non-linearities are used instead of linearities [9]. The only correct way is to have a separate function and separate MLP for each categorical feature vector but this is not feasible unless there is sufficient data for feature vector instance. Including several outputs in the MLP is an attempt to approximate the method of having a separate function approximator MLP for each categorical feature vector instance. Since the connection matrix from the input layer to the hidden layer is fixed this approximation

is limited. Further work includes finding a Boolean function to replace the table, **S**.

5 References

[1] P. J. Werbos, *Beyond Regression: New Tools for Prediction and Analysis in the Behavioral Sciences*, Doctoral Dissertation, Appl. Math., Harvard University, Mass. 1974.

[2] D. E. Rumelhart, G. E. Hinton, and J. L. McClelland. A general framework for parallel distributed processing. In *Parallel Distributed Processing*, pages 45-76, D. E. Rumelhart, J. L. McClelland, and the PDP Research Group, Editors, The MIT Press, Cambridge, MA, 1986.

[3] R. A. Jacobs, M.L. Jordan S. J. Nowlan and G. E. Hinton Adaptive Mixtures of Local Experts *Neural Computation* 3/1 (1992) 79-87.

[4] J. G. Barton and A. Lees. "Comparison of shoe insole materials by neural network analysi"s. *Medical-and-Biological-Engineering-and-Computing.* 34 (6) Nov 1996, p 453-459.

[5] A. N. Burgess, "Non-linear model identification and statistical significance tests and their application to financial modeling" IEE, Stevenage, Engl. p 312-317 Proceedings of the 4th International Conference on Artificial Neural Networks 1995. Cambridge, UK

[6] C. M. Bishop "Mixture Density Networks" NCRG/94/004 Available from http://www.ncrg.aston.ac.uk

[7] C. M. Bishop *Neural Networks for Pattern Recognition* Clarendon Press Oxford 1995.

[8] K. Lee and T. Lee. "Design of Neural Networks for Multi_value Regession. *International Joint Conference on Neural Networks* (2001) 93-98.

[9] J. Neter, William Wasserman, W. and Michael H. Kutner, M. H. *Applied Linear Statistical Models* Irwin 1990 pp 349- 385.

ANALYSIS & CLASSIFICATION

(This page left blank intentionally)

Using a Neural Network and Genetic Algorithm to Extract Decision Rules

Karen Blackmore
School of IT,
Charles Sturt University
Bathurst, NSW, Australia
kblackmore@csu.edu.au

Terry Bossomaier
School of IT,
Charles Sturt University
Bathurst, NSW, Australia
tbossomaier@csu.edu.au

Abstract

Rule extraction from neural networks often focusses on exact equivalence and is often tested on relatively small canonical examples. We apply genetic algorithms to the extract approximate rules from neural networks. The method is robust and works with large networks. We compare the results with rules obtained using state of the art decision tree methods and achieve superior performance to straight forward application of the WEKA implementation of the C5 algorithm, J48.PART.

Keywords

Neural networks, rule extraction, genetic algorithms, rule based classifiers.

INTRODUCTION

It seems somewhat strange to extract rules from artificial neural networks (ANN), when neural solutions were thought to be distinctive. The huge growth of activity in neural networks from the mid-80s occurred because they seemed to be able to solve problems intractable by conventional logic-based artificial intelligence. In fact a series of seminal papers [1], Abu Mostafa asserted that neural networks were particularly effective on problems of high algorithmic complexity [12], common in many pattern recognition. Such problems intrinsically require very many complex rules for their solution.

However, the success of ANNs in many areas led to a deeper understanding of how they work and detailed comparisons with statistical and other methods, such as the classic book by Ripley [16]. But the ease of use, resilience to lack of understanding of search space, and the ready availability of good software ensures the continuing use of ANN methods.

But in some situations where an ANN solution is to be distributed to a large client base, with little background in ANNs, for extended use in safety critical applications, some intuitive support is highly desirable. In such situations a set of rules is very valuable because of its greater ease of comprehension and its link to common sense and experience.

In earlier work [5] we showed that neural networks outperform state of the art decision tree methods on a human classification problem. In the present paper we apply genetic algorithms to extract rules from the network which themselves are superior to those we obtained from decision tree analysis.

BACKGROUND TO RULE EXTRACTION

A wide variety of methods are now available, recently reviewed by Andrews et al. [2]. Tickle et al [20] revisits the Andrews classification of rule extraction methods and emphasise distinction between decompositional and pedagogical approaches. Rule extraction methods usually start by finding a minimal network, in terms of number of hidden units and overall connectivity. Setiono [18] for example adds penalty terms to the error function to bias back-propagation like training towards such sparse networks. The next simplification, the key feature of the method, is to quantize or cluster the hidden unit activations. It is then possible, link by link, to extract combinations of inputs which will activate each hidden unit, singly or together and thus output generate rules. This unit by unit analysis characterises the decompositional approach. Although it can yield exact representations, the computational time may grow exponential with number of inputs (attributes) as noted by Tickle et al. [2] for decompositional algorithms such as Subset and KT.

Taha and Ghosh [19] suggest for binary inputs such as our data generating a truth table from the inputs and simplying the resultant Boolean function. But this simplification is itself combinatorially nasty and thus the method works only for small networks. They also refine the Liu and Setiono [13] methods using linear programming. The test networks have just a few inputs.

The growth of computational time with number of attributes makes minimising the size of the neural network essential and some methods evolve minimal topologies. Santos et al [17] use genetic algorithms in combination with the Setiono rule extraction to optimise network topology using quality indices on the rules extracted as a fitness function to guide network evolution.

The pedagogical approaches treat the neural network as a black box [20] and use the neural network only to generate test data for the rule generation algorithm. Keedwell et al.[11] use genetic algorithms to evolve rules directly. They use a wild-card like representation where each input to the

neural network is represented explicitly in the chromosome by one or more bits with zeros for don't care inputs. Our method is broadly similar, but since the number of inputs we have is very high, we use a different encoding scheme as discussed below. The Keedwell approach requires a specific term in the fitness function to make the rules as small as possible, since each chromosome admits every possible attribute. In our approach, we enforce maximum size predicates and number of rules thus reducing the size of the search space.

METHODOLOGY

The following methodology was employed:

1. Format dataset for training.
2. Generate random splits of the dataset for cross-validation.
3. Perform classification using rule based classifier.
4. Train the neural network
5. Extract rules from neural network using a genetic algorithm
6. Assess and compare the predictive accuracy of the rules from the neural network with those obtained using the rule based classifier.

Formatting of the Dataset

The data for analysis was provided by Foy as part of a larger study [8]. The data set contained 24 mulit-value categorical input and 3 output variables for 357 human profiling cases (see [4,5] for a detailed discussion and description). For classification using *J48.PART*, the data was converted to *ARFF* format [21], which provides the attribute definitions and the data instances without specifying the attribute for prediction. Selection of the prediction attribute and filtering of any unwanted attributes is carried out within the Weka scheme.

For neural network training, the dataset was converted to numeric binary values. This resulted in 96 inputs and 3 outputs due to the conversion of the multi-value categorical inputs.

Random Splits for Cross-Validation

Evaluation of an algorithm's predictive ability is best carried out by testing on data not used to derive rules [21], thus all training was carried out using tenfold cross-validation. Cross-validation is a standard method for obtaining an error rate of the learning scheme on the data [21]. Tenfold cross-validation splits the data into a number of blocks equal to the chosen number of folds (in this case 10). Each block contains approximately the same number of cases and the same distribution of classes. Each case in the data is used just once as a test case and the error rate of the classifier produced from all the cases is estimated as the ratio of the total number of errors on the holdout cases to the total number of cases. Overall error of the classification is then reported as an average of the error obtained during the test phase of each fold.

Variations in results for each iteration in a cross-validation occur depending on the cases used in the training and hold-out folds, which can lead differences in overall results. Thus, rather than use the cross-validation function, which is part of the rule based classifier, the cases in the dataset were randomized and split into ten separate train and test sets. Using this method, both the rule based classifier and the neural network were trained using the exact same fold splits.

Rule Based Classifier

Algorithms that derive rule sets from decision trees first generate the tree, then transform it into a simplified set of rules [9]. Based on results from previous research [3], the *WEKA J48.PART* [21] algorithm was selected to derive and evaluate rules sets from the training data.

Neural Network Training

The ANN was feed-forward, and one hidden layer was found to be sufficient [5], with 6 hidden units. Training was carried out using the neural network toolbox from Matlab [14], with the Levenberg-Marquardt algorithm and log-sigmoid transfer function [16].

Genetic Algorithm

Genetic algorithms [15], [10] are now a mature optimisation technique, achieving good results on NP hard problems in practical times. We employed a simple genetic algorithm with a single population, no self-adaptation of parameters, and a variety of conventional cross-over mechanisms.

The genetic code is of fixed length and encodes a maximum number of rules and conditions per rule. Binary represented integers are used to describe each condition in the rule with a further bit setting this condition to true or false. The networks have 90 inputs, so 7 bit integers are used for each predicate. 38 values are thus unused, but they serve an important function. If input values appear in this high range, they do not generate a condition. Thus, the genetic code can describe rules with fewer conditions in the predicate than the maximum allowable.

After the predicate comes the rule outcome. Together this chunk of predicate and outcome is repeated to the maximum number of rules allowed. Since the data has three outcomes, a fourth outcome (from 2 bits) is available. This could be used to indicate a null rule, but in the work presented herein, has a different function. The neural networks seem to generalise well and were tested with extensive cross-validation [5]. However, if we now generate random inputs and observe the neural network output, we can sometimes get inconsistent outputs. Thus there are regions of the search space, which would not occur in practice, in which

the neural network is less secure. This fourth bit encodes the ``don't know'' case.

As an illustration, suppose we have two rules each with three conditions. The chromosome will have 136 bits as shown in Figure 1. Square brackets denote the number of bits in each gene.

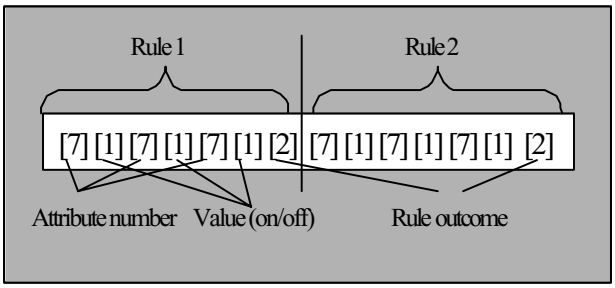

Figure 1. Example chromosome for a two rule, three condition set.

The fitness function is simply the aggregate performance of the rule set measured against the neural network outputs. No majority voting on rules is imposed, so rules giving erroneous classification feed through to the fitness function. The approach is holistic. No one rule, regardless of number of cases it classifies, is given explicit preference over any other. This holistic approach avoids the brittleness of other methods, since the rules are optimised as a set rather than determined in sequence according to some criterion.

The genetic algorithm methods were implemented using the Genetic Algorithm Toolbox [6]for Matlab [14].

RESULTS

The predictive accuracy of the rule based classifier and the ANN, using both random and fixed initial weights and biases, were compared. As can be seen in both Table 1 and Figure 2, the ANN, regardless of starting conditions, achieved superior accuracy over the rule based classifier (WEKA). These results are consistent with previous research [5].

The rule based classifier achieved 70% predictive accuracy, whereas the ANN was able to, on average, correctly predict outcomes 99% of the time. Additionally, as each fold contained exactly the same train and test cases for all methods, it can be seen that classification errors vary randomly, with high error rates not linked to specific folds For example, the Weka method had the highest error on the sixth fold, whereas the ANN with random starting conditions had the highest error on the fourth fold. From the results of this ten-fold cross validation, the ANN with fixed starting conditions would appear to be most stable.

Table 1. Error Comparison

Fold	Weka	NN_Random	NN_Fixed
1	31.4	0.00	0.84
2	31.4	1.40	1.40
3	14.3	0.00	0.56
4	30.5	5.04	2.24
5	36.1	1.68	1.40
6	41.7	2.24	2.24
7	19.4	0.56	1.12
8	22.2	0.56	0.56
9	38.9	0.84	1.40
10	33.3	1.68	2.52
Avg Err	29.9	1.40	1.43

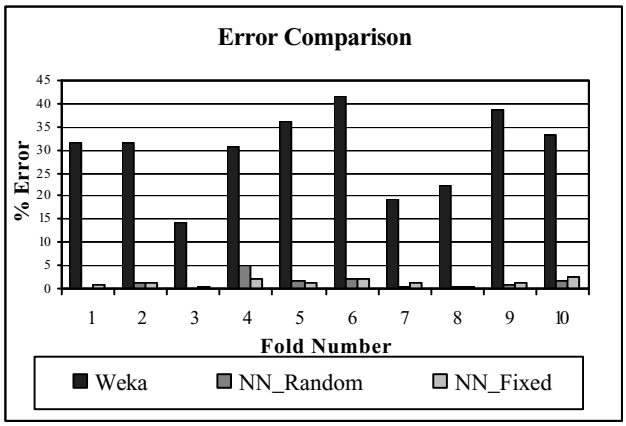

Figure 2. Graph Comparing Errors

Genetic Algorithm Parameters

The genetic algorithm initialized with the following parameters:

i. Number of individuals in the population: 40

ii. Maximum number of generations: 1000

iii. Generation gap: 1

iv. Selection function: 'sus' (stochastic universal sampling)

v. Maximum number of conditions: 3

vi. Number of rules: 18

Variations in the values of the initialization parameters were used, however, best results were achieved with the values above. The genetic algorithm converged quickly within the first 100 generations, with minimal improvement in fit in the following 900 generations (Figure 3).

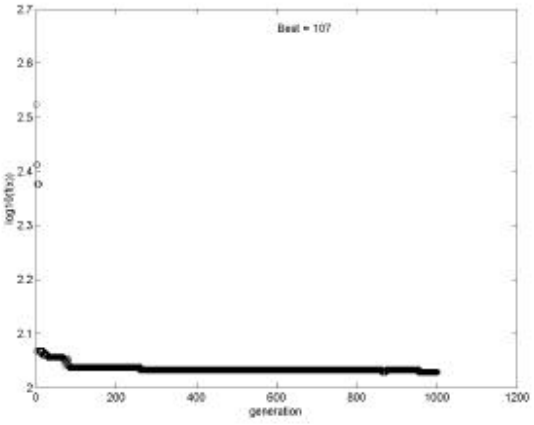

Figure 3. Convergence over 1000 generations

Rule set from the Genetic Code

The following ruleset was derived from the neural network using the genetic algorithm.

1. IF behavioural = Condition3, on, AND region = Condition 1, off, AND Age = Condition3, on, THEN =outcome1
2. IF mn_problems = Condition3, off, AND reporter = Condition1, on, AND Marital_status = Condition2, on, THEN =outcome1
3. IF longterm_stressors = Condition2, on, THEN =outcome2
4. IF time = Condition2, on, AND risk = Condition8, on, THEN =outcome2
5. IF Age = Condition3, on, THEN =outcome2
6. IF reporter = Condition2, off, AND dependen = Condition2, off, AND time = Condition4, off, THEN =outcome4
7. IF occupation = Condition2, off, THEN =outcome1
8. IF time = Condition4, off, AND last_seen = Condition2, off, AND day = Condition4, off, THEN =outcome1
9. IF day = Condition1, off, THEN =outcome2
10. IF mn_problems = Condition6, on, AND longterm_stressors = Condition4, off, AND day = Condition3, on, THEN =outcome2
11. IF risk = Condition4, off, AND character = Condition1, off, THEN =outcome1
12. IF Age = Condition2, on, THEN =outcome2
13. IF season = Condition3, off, AND day = Condition1, on, THEN =outcome2
14. IF occupation = Condition6, on, AND longterm_stressors = Condition2, off, AND reporter = Condition1, off, THEN =outcome3
15. IF mn_problems = Condition2, on, AND longterm_stressors = Condition1, off, THEN =outcome3
16. IF occupation = Condition2, off, AND occupation = Condition7, on, THEN =outcome2
17. IF urban = Condition2, off, AND history = Condition2, on, AND season = Condition1, off, THEN =outcome2
18. IF appearance = Condition1, off, AND ph_outcome2 = Condition2, on, AND reporter = Condition4, on, THEN =outcome3

Although the maximum number of conditions per rule is set at three, as mentioned previously, the genetic code can describe rules with fewer conditions in the predicate than the maximum allowable. The ruleset generated by the genetic algorithm produced 8 rules with the maximum three clauses, 5 rules with two clauses and 5 rules with one clause (Figure 4). The rules were valid for 306 or 86% of cases in the dataset. This represents a significant improvement over the 70% accuracy achieved by the rule based classifier. Importantly, this improvement in accuracy was achieved using fewer rules (18 as apposed to 22 for the rule based classifier) with fewer clauses (see Figure 4), thus abiding by the minimum description length principle [7].

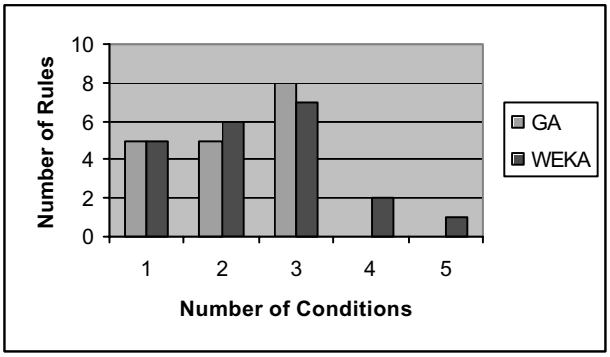

Figure 4. Comparison of Number of Rules and Conditions

DISCUSSION

Keedwell et al. [11] also find on manufactured test data with varying amounts of noise. They found a slight advantage for their GANN method when noise levels are high. Their technique uses additional heuristics after a set of rules has been generated by the genetic algorithm. The rules obtained may be contradictory and a voting system is used for choosing the classification in the event of conflict. Our fitness function explicitly penalises rules which generate incorrect outputs in some cases, thus the rule sets we evolve do not need further refinement or heuristics. Pedagogical methods of this kind may behave quite well with increasing size of neural network and number of attributes. The computation time for the neural network generation of test classifications grows approximately linearly with the number of connections, which is favourable. The complexity of the genetic algorithm depends on the size of the rule set, each iteration depending linearly on the number of rules and depends only weakly on the number of conditions in the current implementation. But, most significantly, it is most effective, when regardless of the size of neural network, a small number of rules capture the important characteristics of the

data, i.e. where the data is essentially of low algorithmic complexity [12]. It is in such cases that the rule extraction process will be of most value to the end user.

CONCLUSION

The genetic algorithm approach described here determines rules better than those found from various decision tree based methods. It is simple to implement, but requires considerable computing resources for the large neural networks of the present paper. As such its greatest value is for determining heuristic rules for medium term use by practitioners who welcome the intuitive description that rules provide.

REFERENCES

[1] Abu-Mostafa, Y. Complexity of random problems. In: *Complexity in Information Theory*, Anonymous Springer-Verlag, 1986.

[2] Andrews, R., Diederich, J., and Tickle, A. B., A survey and critique of techniques for extracting rules from trained artificial neural networks *Knowledge Based Systems*, vol. 8, pp. 373-389, 1995.

[3] Blackmore, K. and Bossomaier, T. R. J., "Comparison of *See5* and *J48.PART* Algorithms for Missing Persons Profiling," *ICITA2002,* Bathurst, 2002.

[4] Blackmore, K. L., Bossomaier, T. J. R., Foy, S., and Thomson, D., "Data mining of missing persons data," *1st International Conference on Fuzzy Systems and Knowledge Discovery,* Orchid Country Club, Singapore, 2002.

[5] Blackmore, K. L. and Bossomaier, T. R. J., "Soft Computing Methodologies for Mining Missing Person Data," *submitted to 2002 IEEE International Conference on Data Mining,* Maebashi TERRSA, Maebashi City, Japan, 2002c.

[6] Chipperfield, A. J., Fleming, P. J., Pohlheim, H., and Fonseca, C. M., "A genetic algorithm toolbox for MATLAB," *Proceedings of the International Conference on Systems Engineering,* Coventry, UK.

[7] Domingos, P. , The role of Occam's razor in knowledge discovery *Data Mining and Knowledge Discovery*, vol. 3, pp. 409-425, 1999.

[8] Foy, S. *PhD Thesis, forthcoming.*, (UnPub)

[9] Frank, E. and Witten, I. H., "Generating accurate rule sets without global optimization," *Machine Learning: Proceedings of the Fifteenth International Conference,* Madison, Wisconsin, pp. 144-151, 1998.

[10] Holland, J. H., Genetic algorithms *Scientific American*, vol. pp. pp. 45-50, Jul, 1992.

[11] Keedwell, E., Narayanan, A., and Savic, D., Creating rules from trained neural networks using genetic algorithms *International Journal of Computers, Systems and Signals (IJCSS)*, vol. 1, 2000.

[12] Li, M. and Vitanyi, P. *An Intorduction to Kolmogorov Complexity and its Applications*, 1997: Springer-Verlag,

[13] Liu, H. and Setiono, R., Incremental feature selection *Journal of Applied Intelligence*, vol. 9 , pp. 217-230, 1998.

[14] Mathworks Inc., Matlab Student Version , ver. 6.1 Release 12.1, rel. 2001. Mathworks Inc.

[15] Mitchell, M. *An Introduction to Genetic Algorithms (Complex Adaptive Systems)*, MIT Press, 1996.

[16] Ripley, B. D. *Pattern Recognition and Neural Networks*, UK: Cambridge University Press, 2001.

[17] Santos, R., Nievola, J. C., and Freitas, A. A., "Extracting comprehensible rules from neural networks via genetic algorithms," *Proceedings of the 2000 IEEE Symposium on Combinations of Evolutionary Computation and Neural Networks (ECNN-2000),* San Antonio, TX, USA.

[18] Setiono, R., A penalty-function approach for pruning feedforward neural networks *Neural Computation*, vol. 9, pp. pp. 185-204, Jan, 1997.

[19] Taha, I. and Ghosh, J., Three techniques for extracting rules from feedforward networks *Intelligent Engineering Systems Through Artificial Neural Networks*, vol. 6, 1996.

[20] Tickle, A., Andrews, R., Golea, M., and Diederich, J., The truth is in there: directions and challenges in extracting rules from trained artificial neural networks *IEEE Transactions on Neural Networks*, vol. 9, pp. 1057-1068, 1998.

[21] Witten, I. and Frank, E. *Data mining: practical machine learning tools and techniques with Java implementations*, San Francisco: Morgan Kaufmann, 2000.

(This page left blank intentionally)

Bayesian Decisions on Differentially Fed Hyperplanes

Bangalore University
Manjunath.R, Dr K.S.Gurumurthy
Dept of EC & CSE, UVCE, Bangalore, INDIA
manju_r_99@yahoo.com

Abstract: Generally the neural networks employing Bayesian decision do not output one simple hypothesis, but a manifold of probability distributions. This throws out the bayes posterior coefficients as a large number of classifiers. Here a novel method based on differential feedback is explored to merge these classifiers. The experimental results confirm affine transportation of these classifiers. Also, it has been shown that the differentially fed Artificial Neural Networks (ANNs) learn in much the same way as Bayesian learning and are hence resistant to over fitting

1 INTRODUCTION

In Information geometry, a family of probability distributions are made use to compute quantities related to pdf including mutual interactions. It was used to study multilayer perceptrons [1]. A family of distributions called exponential family has the pdf

$$P(y,\theta)=\exp\{\Sigma\theta_i k_i(y)-\psi(\theta)\} \quad (1)$$

Where θ is the cosystem, $k= k_i(y)$ are adequate functions of y, ψ the offset. The exponential family forms $\alpha=\pm1$ flat manifold. For this Riemann-christoffel curvature vanishes identically. This is non Euclidean space. For this manifold, there exists $\alpha=\pm1$ affine cosystem. This is because log of pdf is linear in θ . For any two distributions p (y) and q (y) the geodesic connecting them is given by

$$\log (p(y, t))=(1-t)\log p(y)+t \log q(y)-\psi(t) \quad (2)$$

A family of Divergence measures namely α-divergence is associated with the manifold of pdf [2]. The $\alpha=-1$ divergence is known as Kullback divergence. These divergence functions give a Reimannian metric to the manifold of pdf.

The networks are represented by a set of parameters called weights $\theta=w_{ij}$ .A family of networks parameterized by θ forms a manifold, θ playing the role of a cosystem.. In this paper, it is shown that they form hyperplanes for different choices of feedback. The amount of feedback is proportional to Kullback divergence distance i.e., planes are Kullback distance apart. The kullback divergence of pdf p from pdf q is given by

$$p*\log(p/q) \quad (3)$$

In this paper, different orders of differential feedback form a manifold of hyperplanes and are related to manifolds of pdfs. The distance between them and the trajectory of a point on these planes is explored. In section 2 differentially fed ANNs are introduced. In section 3 the superposition of hyperplanes is explained. The simulation results are given in section 4 section 5 concludes

2. FORMALISM OF DIFFERENTIALLY FED ANN

The output y of a neural network except for the nonlinearities can be written as

$$y=\Sigma wixi. \quad (4)$$

Where xi are the inputs wi, the corresponding weights. The thing to be noted is weight cannot span the entire input space, whatever may be the training mode. Again the linearity of the output (1) may be viewed as a particular case of ARMA

$$y(n+1)=b0y(n)+b1y(n-1)+\ldots..+a0xn+\ldots \quad (5)$$

Where b0.. and a0.. are constants. The auto regressive terms b0…bn may be realized using inherent differential feedback [3]. With differential feedback it has been found out [3] that the no of iterations required for training is reduced as shown in the table I.XOR gate is considered for simulation. Gaussian distributed random input with seed value 1000 is taken as input. With I order different feedback, the output may be written as:

$$\Sigma Wixi+b1y1 \quad (6)$$

y1 being the I order differential. This equation once again represents a plane parallel to Σwixi. Thus the set of differentially fed ANNs form a manifold of parallel planes, with ∞ order feedback being the plane with zero error.

Table 1. Performance with feedback

Order of differential	Square error	Iterations
No feedback	18	1156
I order	18	578
II order	18	289

Table 2..Performance with II order feedback

Order of differential	Square error	Iterations
II order Feedback	18	578
Equivalent Output	18	578

Also, simulation results of table 2 show that two terms of II order differential feedback i.e., y2-y1 and y1-y0 can be replaced by a single equivalent plane represented by

Weq=(w1*iextra+w2*iextra1)/y0 (7)
In II order differential feedback system, the two differential terms can be replaced by a single term. Extending this principle, the ∞ terms of ∞ order differential feedback can be replaced by a single term.

This is termed as eigen plane which is the practical way of generating lowest error. Now the differential feedback becomes

$dy/dt+d^2y/dt^2+\ldots$ (8)

Taking Z transform, & then the inverse,

yeq = IZT{Y (z)/(1-z)} (9)

2.1. Information geometry of differential feedback

For less error, the plane spanned by the weight vectors should be as close as possible to the eigen plane. When I order differential feedback is given, the new plane is given by

ynew =∑wixi+a*yold (10)

Which is a parallel plane. To start with, set Yold=0.So, y = ∑wixi. Since error varies asymptotically with order, the gap between parallel planes decreases and the infinite order Plane coincides with the eigen plane. If still more feedback is given, error increases further as shown in fig.2

To show that the entropy is minimum on the eigen plane, consider the exponential family as given in [4] . The error may be assumed to be Gaussian distributed. In Gaussian distribution with Zero mean, the pdf can be written as

$p(x)=\exp((\text{energy of } x)/\sigma^2)$ (11) .

The error energy of a plane x may be written as $(x-d)^2$. (x-d) being the distance of x from eigen plane d (or the actual value). The entropy of such a distribution takes minimum value when (x-d)=0. i.e. entropy is min when the plane reaches the eigen plane The Natural learning algorithm is given by [5]

$\theta(t+1)=\theta(t)-\eta G^{-1}$ (12)

i.e.,newplane=oldplane+deviation This shows that the repeated learning in gradient descent algorithm shifts the planes towards the eigen plane in the same way the diff feed back will do ,but fails to reach it because eigen plane does not belong to the space spanned by inputs alone.

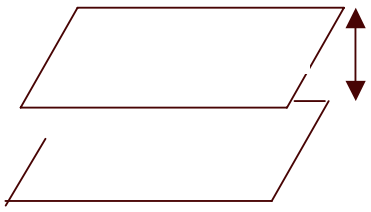

Figure.1.Differential feedback planes

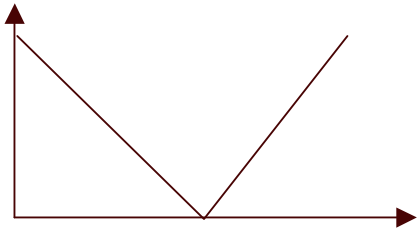

Figure2. Feedback v/s error

3. SUPERPOSITION OF HYPERPLANES

Bayesian learning [6] is a pdf over hypothesis (parameterized) space, expressing degree of belief in a specific hypothesis. A neural network trained with Bayesian learning algorithm outputs entire distribution of probabilities over hypothesis set rather than a single hypothesis. Such a distribution is Bayes' aposterior and depends up on the training data and on the prior distribution. This dependency on the aprior distributions make it a memory system where previous outputs take a role in deciding the present output. In the present context each hypothesis corresponds to one hyper plane i.e., different orders of feedback. Alternative perspective is that each hyperplane may be taught of as a classifier with an associated probability density function. Degree of belief is 0 for no feedback and increases towards 1 for infinite feedback or when all classifiers merge. In such a classifier the actual output may be thought of as superposition of beliefs [7] i.e., addition of different feedbacks. As the order of differential feedback increases, the number of estimators considered in the sum increases by the same amount and hence the degree of belief moves towards 1.The addition is not simple but weighted by belief or pdf. In [1]. it has been proved that the n number of differential terms with a feedback of degree n may be replaced by a single n^{th} degree differential term. It follows that, a single equivalent or effective distribution will be thrown out with n^{th} degree differential feedback. It may be seen that equation. 13 runs in much the same way as that of equation.7.Finally we arrive at the eigen plane. I.e. the superposed effect of all classifiers is the eigen plane. This gives

P0*no feedback+p1*I order differential feedback=p2*II order differential feed back (13.a)

P1* I ordered differential+…infinite order =Eigen plane (13.b)

I.e. weighted sum of different ordered differentials.

P1*distance between I order and nofeedback+p2*II order and no feedback+…=1*distance between no feedback and Eigen plane (13.c)

The equations show that the learning algorithms with differential feedback do indeed resemble Bayesian learning algorithms and are hence resistant to over fitting [7]. It may be attributed to the hidden Auto regression associated with differential feedback

3.1. Resistance for over training

The posterior has two components-a data independent Gaussian prior part and a data dependent term. Logically, the Gaussian part may be attributed to the previous or differential terms of the output since the weighted sum of any probability distribution function in general turns towards Gaussian, by central limit theorem. Such a Gaussian classifier is known to resistant to over fitting

3.2..Bayesian learning

The result of Bayesian learning is a pdf over the hypothesis space each expressing the degree of belief in a specific hypothesis as an approximation to the target function. The aprior distribution $P(\lambda)$ generally encodes some prior knowledge. With the arrival of data pattern D the aprior distribution gets updated using Baye's rule as $P(\lambda|D) \propto P(D|\lambda)\, P(\lambda)$.Taking Logarithm both sides, we get

$$\text{Log}\,(P(\lambda|D)) \propto \log(P(D|\lambda)) + \log(P(\lambda)) \quad (14)$$

The equation has two terms-one current data dependent term and one data independent term where the prior or previous outputs (Gaussian as a result of superposition) are considered.The posterior distribution so obtained hence encodes information coming from the training set and prior knowledge.

Consider the example of II order feedback which makes use of two previous or priori terms $P(\lambda 1)$ and $P(\lambda 2)$. With this the equation may be rewritten as $P(\lambda|D) = P(D|\lambda 1)^* P(\lambda 1) + P(D|\lambda 2)^* P(\lambda 2)$Which leads to the equation

p2*II order differential feed back =P0*no feedback+p1*I order differential feedback (15)

This is analogous to the famous equation

$$P(y|x, D) = \int_{\lambda} f(x,\lambda)\, p(\lambda \mid D)\, dP(\lambda) \quad (16)$$

in probability space.As can be seen here, the probabilities are proportional to the weights. The equation tries to expand the $(k+1)^{th}$ order differential feedback plane with0,1..K th order differential feedback planes. The weighing factors may be taught of as the projection or dot product of the hyper plane over lower order hyper planes.

3.3.Hilbert space

The set of probabilities form Hilbert space

H={z:Λ→ℜ| such that $\int_{\lambda\in\Lambda} z(\lambda^2)dp(\lambda) < \infty\}$

with the inner product

<z1.z2>= $\int_{\lambda\in\Lambda} z1(\lambda)\, z2(\lambda)\, dp(\lambda)$ (17)

Since the same constraints are also satisfied by the hyper planes, they form Hilbert space.The output of a neural network is subjected to nonlinearity or fair quantization. Let sk be the number of points or planes which go wrong because of this nonlinear round off. The fractional error ek is defined as sk/l , l being the number of hyperplanes considered. Because of the uniform nature of this error, the probability of this error equal to r/l is

$\frac{\ell!}{2^{l}(l\varepsilon)!(\ell-\ell\varepsilon)!}$ which gives average probability of realizing different patterns of r errors.Now mapping the hypothesis space to error shells or differential feedback hyperplanes, We get

$$\sum_{j\in J} p_j \varepsilon_j = \frac{1}{2^l}\sum_{r=0}^{l}(\frac{r}{l}) * B \qquad (18)$$

Where B=(r,l). Hence the error in classification has to vary asymptotically as a power of 2 with increase in the order of differential feedback. This is indeed the case as given in table I. But for the nonlinearity, any hyperplane or the k+1 th degree feedback happens to be a linear weighted sum of the k hyperplanes found in H. This threshholding makes the output a subset C (H) the convex hull of H rather than H itself. It can be shown that the bias term or the datum or reference depends just up on the instantaneous data and independent of the feedback inputs. I.e. it remains the same for all orders of the feedback. Here also, P (D|λ1) and P (D|λ2) are the same and independent of λ or the feedback but depends only up on D the data. Hence the above equation may be rewritten as

P (λ|D)=P (D){P (λ1)+ P (λ2)} (19)

I.e., Output without feedback or the bias term*Gaussian like pdf. especially with higher Orders of the feedback

.

4. SIMULATION

The differentially fed Artificial neural networks are made to learn the psd of random data .The Normal distributed data is generated using Matlab.The error after learning and the differentials of the error are stored The probability distribution of each of them is computed using Parzen equation p (x)= $1/\sqrt{2\pi\sigma}$ exp (-($\frac{(mean - x)^2}{\sigma^2}$)).The weighted sum of the zero th order feedback and I order feedback data with their corresponding pdfs is found identical to the weighted second ordered differential feedback with the corresponding pdf as given in the equation In fig.3 signals of I and zero order weighed with pdf and weighed II order signal are shown.

5. CONCLUSIONS

From the simulation results it is clear that the classifier represented by a certain hyper pane is the weighted sum of the hyper planes o classifiers below. This way, ideal classifier is the weighted sum of all the classifiers.

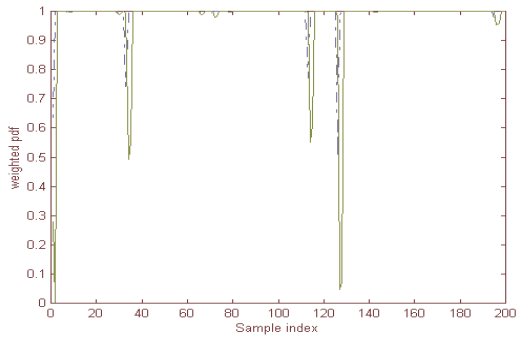

Figure.3.signals of I and zero order weighed with pdf and weighed II order signal

Legend: - Weighted second ordered feedback. -. Sum of weighted zeroth and first ordered FB

REFERENCES

1. S.Amari, 1995, Information Geometry of the EM and em algorithms for neural networks, Neural networks, 8, No.9

2. 7.S.Amari and H.Nagaoka, 2000, Methods of information geometry, AMS and Oxford University press.

3. Manjunath.R and K.S.Gurumurthy, oct2002, System design using differentially fed Artificial Neural networks, TENCON'02

4. S.Amari, 1995, Information Geometry of the EM and em algorithms for neural networks, Neural networks, 8,No.9

5 Aarts, E.H.L. and Korst, J.H.M, 1989,.Simulated Annealing and Boltzmann Machines, Chichester: Wiley.

6.D.J.C.Mac Kay, 1992, A practical Bayesian framework for back propagation networks Neural computation 4:448-472

7. Radford Neal, 1996, Bayesian learning in neural networks springer verlag

INNOVATIVE APPLICATIONS

(This page left blank intentionally)

Application of Machine Learning Techniques to Design Style Classification

Aruna Lorensuhewa
s.lorensuhewa@qut.edu.au

Binh Pham
Center for Information Technology Innovation,
Faculty of Information Technology, QUT
Brisbane, Australia.
b.pham@qut.edu.au

Shlomo Geva
s.geva@qut.edu.au

Abstract

Fuzzy knowledge exists in domains such as medicine, law and design as it is difficult to retrieve all knowledge and experience from experts. Machine learning and data mining techniques can be used to automatically extract knowledge from unstructured information sources. The aim of this research is to develop a generic framework and methodologies that will facilitate knowledge extraction automatically by using machine learning and data mining techniques and integrating with expert knowledge. We show that classification accuracy can be improved by integrating expert knowledge with other machine learning classifiers, SVM and Nearest Neighbour.

Keywords
Data Mining, Feature selection, Classification, Support Vector Machine, Decision Trees, C4.5, Design Style.

1 INTRODUCTION

Fuzzy knowledge exists in domains where it is difficult to retrieve all knowledge and experience from experts. For instance, expertise may not be easily expressible, it may be incomplete, or may exist at a subconscious level. Experts have often gained or improved their expertise from experience, by dealing with concrete cases, reading literature. Sometimes no one has a complete understanding of the domain. In such cases we can gather information from experts through questionnaires, domain specific databases and literature. The challenge is to derive structured knowledge in an automatic fashion from unstructured sources and augment this with available expert knowledge.

Machine learning and data mining techniques have been used to automatically extract knowledge from unstructured information sources. Commonly used algorithms are C4.5 [1], Support Vector machine (SVM) [2], Nearest Neighbour [5] and Neural Networks.

On Design, some experts believe that design style is an intangible concept and that its knowledge is difficult to present in a formal way. So far, there has been no computer supported automatic technique to assist novice designers in learning to distinguish design styles or judge how similar a design is to a specific style.

The aim of this research is to develop a generic framework and methodologies that will enable knowledge extraction in an automatic fashion by using machine learning and data mining techniques, then integrating expert knowledge with extracted knowledge. Furniture Design style has been selected as the domain for the evaluation of the framework.

Data is collected for seven different styles: Chippendale, Classical, Jacobean, Early Victorian and Queen Anne. A Web based questionnaire (Figure. 1) is used to collect data from users and domain experts. In total fifteen different features were examined, including appearance, chair arms, back shape, leg type, seat shape, etc. Most of the features are categorical. For example, Foot can have options such as lion, ball, pad, drake and block etc. The Connectedline Furniture Design Style Guide database [3] is commercially available software for the Windows platform. This guide identifies and dates about 20 furniture styles and their distinctive features. This database is used to create an expert classifier for this research.

The dataset collected from the experiment has categorical data fields characterized by a number of distinct values. On the other hand, the dataset we collected has characteristics such as uncertainty, incompleteness and imprecision.

The total framework is divided into three main phases: selecting an encoding scheme and classifiers, feature reduction and weight assignment, and integrating expert knowledge with knowledge extracted from machine learning techniques.

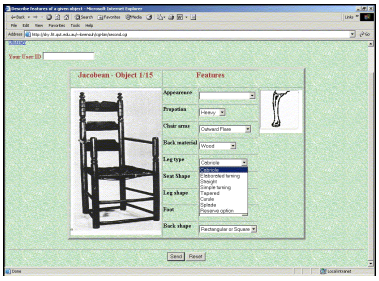

Figure 1. Web based questionnaire of the experiment

The remainder of the paper is organized as follows: Section 2 provides the methodology for selecting a suitable coding scheme and suitable classifiers for the selected encoding scheme. Section 3 provides the process of selecting a suitable feature reduction and weight assignment scheme. The method of integrating expert knowledge by combning multiple classifiers to raise total accuracy is presented in section 4. The conclusion is given in the final section.

2 ENCODING SCHEME AND CLASSIFIERS

The collected furniture design style dataset consists of Categorical data fields characterized by a large number of distinct values. It represents a serious challenge for many classification and regression algorithms that require numerical inputs. Classification and pattern recognition techniques such as neural networks, linear regression and support vector machines (SVM) [2] require numerical input. However some machine learning algorithms, like decision trees and other rule-induction methods (CART, C4.5, etc.), can handle high cardinality categorical attributes without the need for external pre-processing. We tested different coding schemes with different classifiers and selected the most promising encoding and best classifiers for the selected encoding scheme.

Different Encoding Schemes

The Following encoding schemes were found to be suitable for converting our original categorical dataset for use with regression type classifiers.

Binary Scheme: For low cardinality categorical attributes the most widely used numerical representation method is N binary derived inputs, one for each possible value of the original attribute. This scheme represents each value of the original categorical feature by a binary vector with the i^{th} component set to one, and the rest set to zero. When N is relatively small, this 1 to N mapping can be used. This technique is not suitable for a data set with attributes having hundreds of distinct values.

Categorical Encoding using target statistics scheme: This scheme was introduced by Daniele [4]. The basic idea is to map individual values of the high-cardinality categorical independent attribute to an estimate of the probability of the dependent attribute. In the case of binary target attribute $Y \in \{0,1\}$, the transformation maps individual values X_i of a high-cardinality categorical attribute X to a scalar S_i representing and estimating of the probability of Y=1 given that X= X_i:

$$X_i \rightarrow S_i \equiv P(Y|X = X_i) \qquad (1)$$

This scheme can be extended to m-valued categorical targets, $Y \in [y_1, y_2, ,.. y_m]$ in the following way. For each possible value Y_j of the dependent attribute a derived input attribute X_j^* is created in substitution of the original high cardinality categorical independent attribute X. Each derived attribute X_j^* will represent an estimate of $P(Y = Y_j \,|\, X = X_i)$ using the formula 1.

Different Classification Techniques

The original categorical dataset, binary coded dataset and statistical based coded dataset were tested with C4.5 [1], SVM [2] and Nearest Neighbour [5] classifiers. Brief descriptions of each of the methods are given below.

Nearest Neighbour: In the instance based learning, all the real work is done when the time comes to classify new instances, rather than when a training set is processed. In instance-based learning, each new instance is compared with existing ones using a distance metric, and the closest existing instance is used to assign the class to the new one. Sometimes more than one nearest neighbour is used, and the majority class of the closest k neighbours (or the distance-weighted average, if the class is numeric) is assigned to the new instance: this is termed the k-nearest neighbour method. With nearest neighbour we can use different distance metrics to measure similarity between two vectors. Exact matching, hamming distance and Euclidian distance matrices were used for the three encoding schemes.

Support Vector Machines (SVM): SVM [4] recently gained popularity in the learning community. SVM techniques for classification and regression provide powerful tools for learning models that generalize well even in sparse, high dimensional settings. It is directly applicable for binary classification tasks. Multi class categorisation has to be treated as a series of dichotomous classification problems [2].

The SVM method is defined over a vector space. In its simplest linear form, SVM is a hyperplane that separates a set of positive and examples from a set of negative examples with maximum interclass distance, the margin. The hyperplane is determined by only the training instances on the margin, the support vectors. The SVM is extended to nonlinear models by mapping the input space into a high dimensional feature space. In this space, an optimal separating hyperplane is constructed. After the optimal hyperplane is found, new examples can be classified by checking which side of the hyperplane they on.

Decision tree based classifier (C4.5): Quinlan's C4.5 [1] is a modified version of ID3 which addresses many of the deficiencies of ID3. These includes pruning, ability to deal with continuous data and built in facility to extract rules by tracing a path from the root to leaf. C4.5 is an algorithm that summarises the training data in the form of a decision tree. To build a decision tree from data, C4.5 employs a greedy approach that uses an information theoretic measure (gain ratio) as its guide. Choosing an attribute for the root of the tree divides the training instances into subsets corresponding to the values of the attribute. If the entropy of the class labels in the subsets is less than the entropy of the

class labels in the full training set, then information has been gained through splitting on the attribute. C4.5 chooses the attribute that gains the most information to be at the root of the tree. The algorithm is applied recursively to form sub-trees, terminating when a given subset contains instances of only one class.

Generalisation

Cross validation is often used to estimate the generalization ability of classifiers (i.e. performance on previously unseen data) where the amount of available data is insufficient to form the training, validation and test partitions. Under cross validation, the available data is divided into k disjointed sets, k models are then trained, each one with a different combination of k-1 partitions and tested on the remaining partition. The k-fold cross-validation estimate of a given performance statistic is then simply the mean of that statistic evaluated for each of the k models over the corresponding test partitions of the data. Cross validation thus makes good use of the available data as each pattern used both as training and test data. The most extreme form of cross-validation, where k is equal to the number of training patterns, is known as leave-one-out cross validation and has been used widely when the data set is very small..

Experimental Details

The experiments were conducted with three encoding schemes: the original categorical dataset with numerical labels, binary and statistically encoded dataset. Results are given in Table 1.

Original dataset (nominal dataset): The original data set with nominal attributes was tested with Nearest Neighbour and C4.5 classifiers. Nearest neighbour classifier used simple attribute wise exact matching as a distance metric. A Windows based software implementation of C4.5 (See 5) was used as decision tree classifier. In both cases ten-fold cross validation is used for validation.

Binary coded dataset: The original categorical (nominal) dataset with 16 attributes is converted to a binary dataset with 100 binary attributes excluding class attribute which has 7 different class numbers. Nearest Neighbour and SVM classifiers are used to classify design style. In this case, Nearest Neighbour classifier used Hamming distance as the distance metric because of the binary dataset. In the case of SVM, seven different classifiers were trained to classify seven different styles separately. Each classifier determined only if a given style attributes belonged to the corresponding style or not (binary classification). The classification decision for the entire ensemble of classifiers was based on the classifier giving the maximum output value (largest margin). In both cases ten-fold cross validation was used for validation

Table 1. Summary of Results for different encoding schemes and classification techniques

Method used	Categorical data	Binary encoded data	Statistically Encoded data
SVM	Not applicable	88.75±5.73	83.30±8.10
NN	85.59±9.49	85.68±9.47	77.5±12.24
C4.5	76.50±3.70	Not applicable	Not applicable

Statistically encoded dataset: The original dataset is converted to dataset with numerical attributes using the technique "categorical encoding using target statistics for multi-casts datasets" discussed earlier. Nearest Neighbour and SVM classifiers are used to classify design style. In Nearest Neighbour classifier, the distance between input and an instance of a training data is measured by using Euclidian distance metric. Ten-fold cross validation is used for validation in both cases.

Conclusion

On average, the binary coded dataset gave higher level of overall accuracy when compared to the original categorical dataset and statistically encoded dataset. Nearest Neighbour and SVM classifiers gave the best classification accuracy over C4.5. In addition, the binary coded and statistically encoded datasets can be used with neural networks, regression type techniques and support vector machines. Therefore, it is useful to proceed to further analysis using the binary encoded dataset and Nearest Neighbour and SVM classifiers.

3 FEATURE REDUCTION & WEIGHT ASSIGNMENT

Feature selection is a useful process when dealing with high dimensional input patterns. When the numbers of features are potentially quite large classification is very expensive computationally. Also features may sometimes have certain amount of noise that leads to low accuracy of classification. So it is better to eliminate such features or set low weights.

The problem of feature selection is to take a set of candidate features and select a subset that performs the best under some classification system. An important question in the field of machine learning, pattern recognition and knowledge discovery is how to select the best subset of features. A good set of features may not only help to improve performance accuracy, but also to find a small model for data, resulting in better understanding and interpretation of the data. It also reduces the cost of extracting features.

When selecting a best subset of attributes, there are two fundamentally different approaches:

Filter (Scheme-independent selection): Make an independent assessment based on general characteristics of data before learning commences.

Wrapper (Scheme-dependent selection): Evaluate subset of features using machine learning algorithm that will ultimately be employed for learning. This is called wrapper because learning algorithm is wrapped into the selection scheme. We experimented with two approaches, one from

the each specific scheme: discriminative analysis based and genetic algorithm based.

Discriminative Analysis Based Scheme

We have used a scheme-independent approach to select the best subset of features and weights to improve the accuracy and efficiency of the design style classification. In this method, the discriminative power of features in the data set itself was used to construct a feature subset, where the discriminative power E (Entropy) for a particular feature is calculated from the following equation

$$E_{feature} = \frac{-\sum_{i=1}^{i=n}\left(\frac{x_i}{\sum_{i=1}^{i=n} x_i} \times \log\left(\frac{x_i}{\sum_{i=1}^{i=n} x_i}\right)\right)}{\log_2(n)} \quad (2)$$

where n is the number of styles and x_i is the number of times a feature occur in a style i.

High E values (close to 1) mean that features uniformly occur among all styles. Low E values mean features are more selective. This scheme allows you to find the correct subset of features for a given problem and set different weights for each attribute based on the relevant E value of each feature.

Calculating E value: The dataset is split into two parts to remove bias of E calculation from the classification process. The first part is used for calculating E and the other half is used for training and validating a classifier. As the dataset is limited (˜100 instances), it is important to know the splitting ratio to obtain maximum accuracy and highest feature reduction. The size of the dataset for training and validation is reduced due to splitting and this will decrease the accuracy of the classifier. Figure 3 shows how the Nearest Neighbour classifier is sensitive to the size of the dataset. According to Figure 3, if the dataset is in the range of 50% or less then the accuracy drastically decreases.

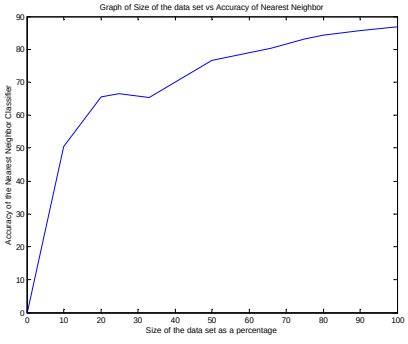

Figure 2 Graph of size of the dataset as a % Vs Accuracy of the nearest neighbour classifier as a %

Figure 3 shows a comparison of Nearest Neighbour classifier and Nearest Neighbour classifier with different weighting for the feature based on E value. The X axis of Figure 4 represents data proportion used for training and validation. If the training proportion is x%, the data proportion for calculating E is (100-x)%. Leave one out cross validation is used because of the smaller training dataset. Figure 4 also shows, when the training data proportion is in the range between 25% and 60% (proportion for E 75% and 40%) the weighted Nearest Neighbour gives significant higher accuracy over Nearest Neighbour.

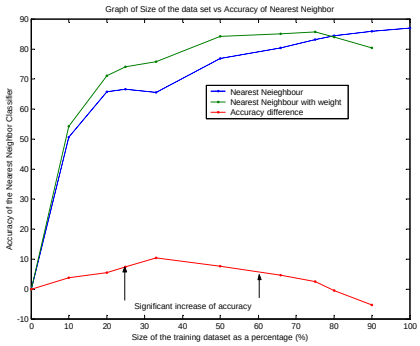

Figure 3 The Graph of size of the dataset as a percentage Vs Accuracies of Nearest Neighbour classifiers

Figure 4 shows how the accuracy of the Nearest Neighbour classifier changes when low significant attributes are dropped, one at a time. These low attributes are selected based on E value. The experiment is repeated for three selected cases and three different curves represent the results of the experiment.

Accuracies of Nearest Neighbour Classifiers: According to the results in Figure 4, maximum accuracy goes beyond 85% when 10% of the dataset is used for E calculation. However, only 10-20 features (low significant) are dropped based on the E value. Maximum feature reduction (about 50-60 features) and classification accuracy around 85% can be achieved when 30% of the dataset is used for E calculation and 70% of the dataset for validation and training

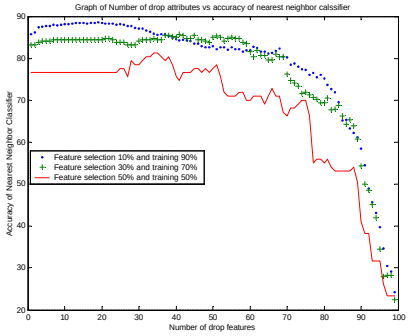

Figure 4 The Graph of numbers of drop features Vs Accuracies of Nearest Neighbour clssifires

Feature Selection Using GA

Genetic Algorithm is an optimization tool which can be used to solve various optimization problems. GA maintains

a population of members, usually called "genotypes" and classically represented by binary strings, which can be mutated and combined according to a measure of their "fitness", as measured by a task-dependent evaluation function.

GA can be used for feature selection and weight assignment.

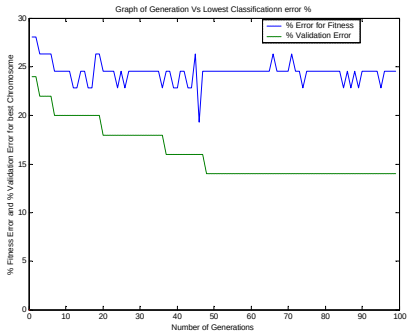

Fig. 5: The Graph of the number of generation Vs Fitness value and Validation error for best chromosome

We used GA-based technique for feature selection and weight selection for furniture style classification system. This is achieved by using GA to select binary/real number weight feature vectors for the population and Nearest Neighbour algorithm to find fitness values for each chromosome in the population based on the classification error. The binary weights are used for optimum feature selection and real weight chromosomes are used for best weight vector selection. The complete data set split into two segments, for training and validation. The training dataset is used to find a fitness values for a population in each cycle. The chromosome with best fitness value (lowest classification error) is tested with the validation set. By comparing the validation and training error for each generation the termination point and the best solution is found. Leave one out cross validation was used throughout the experiment.

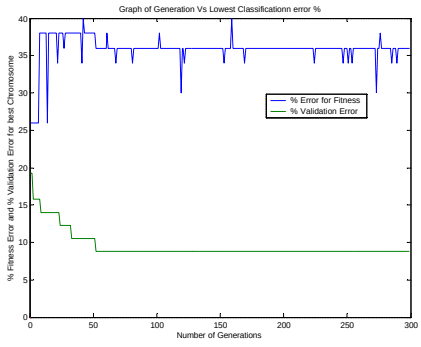

Fig. 6: The Graph of the number of generation Vs Fitness value and Validation error for best chromosome

Figure 5 shows the experimental results for binary feature selection using GA. According to the graph, the validation error stabilises around 24% after approximately ten generations. The best chromosome after ten generations is selected as the best binary weight vector. This chromosome is used for feature selection. The features relevant to 1s in the binary stream are selected and others are dropped.

Figure 6 shows the experimental results for real number feature selection using GA. According to the graph, validation error becomes stable at around 37% after fifty generations. The best chromosome after fifty generations is sleeted as the best weight vector for weight assignment.

Conclusion

We have experimented with two different schemes: scheme independent and scheme specific. The discriminative analysis based (scheme independent) outperformed the GA based scheme (scheme specific) for feature selection and weight assignment for furniture design domain. Discriminative analysis based technique presented the best classification accuracy of (80-85) % for feature selection and weight assignment. The GA based technique presented the best accuracy of (70-75) % for feature selection and (60-65) % accuracy for weight selection.

4 INTEGRATING EXPERT KNOWLEDGE

Multiple approaches have been developed for improving predictive performance of a system by creating and combining various learned models. D. Bahler and L. Navarro [6] are proposed that the combination of classifiers has long been proposed as a method to improve the accuracy achieved in isolation by a single classifier. There are two main approaches to creating model ensembles. The first is to create a set of learned models by applying an algorithm repeatedly to different training sample data; the second applies various learning algorithms to the same sample data. The predictions of the models are then combined according to a particular scheme. The reason for combining the outputs of multiple classifiers are compelling, because different classifiers may implicitly represent different useful aspects of a problem, or of the input data, which no one classifier represents all useful aspects.

Combining Multiple Classifiers

There are several methods of combining multiple classifiers. Two most commonly used techniques are voting and Bayesian ensemble.

Voting: Generally speaking, the voting principle is just what we know as majority voting. Several variations of this idea have been proposed: unanimity, majority and threshold plurality. Combining classifiers with this method is simple; it does not require any previous knowledge of the behaviour of the classifier. It only counts the number of classifiers that agree in their decision and accordingly decided the class to which the input pattern belongs. This simplicity has a drawback, however: the weight of the decision of all the classifiers is equal, even when some of the classifiers are much more accurate than others.

Bayesian Ensemble method: Voting methods are based solely on the output label computed by each classifier. No expertise or accuracy is considered. In these methods the decision of each classifier is treated as one vote, but what happens if one of the classifiers is much more accurate than any other? To address this problem we can establish weights proportional to each expert's accuracy, so each classifier's output is considered according to its past performance and combining them using Bayes' theorem.

Combining SVM, Nearest Neighbour and Expert classifiers using simple rules

The main purpose of this experiment is to determine how we can combine expert knowledge acquired from Connected line database to improve the overall accuracy of the individual classifiers. Three different classifiers were used in this phase. The first two classifiers were based on Nearest Neighbour and SVM. The third one was created from the Connectedline database.

Expert Classifier: Expert classifier is built from knowledge available in the Connected line database. All the features in a specific style were represented in one specific rule. For all seven styles (classes), seven different binary rules were constructed based on information of Connectedline database. The expert classifier is evaluated with the binary encoded dataset. In this approach, the distance between instance of the dataset and each of the expert rules was measured using exact matching metric. The rule provides maximum overlap is the best rule to explain the data instance. The style that belongs to this rule is the predicted style or class.

Table 2. Class wise accuracies for three classifiers

Class	% Accuracy of classifiers			Selected Classifier
	SVM	N-Neighbour	Expert	
1	84.21	73.68	5.26	SVM
2	85.71	85.71	14.29	SVM/NN
3	95.65	95.65	17.39	SVM/NN
4	96.55	96.55	79.31	SVM/NN
5	82.35	82.35	100.00	Expert
6	90.00	80.00	10.00	SVM
7	0.00	0.00	0.00	None

```
If (SVM Prediction=NN Prediction)
        Final Prediction=SVM Prediction
Else If (SVM Prediction~=NN Prediction) & (Expert Prediction=5)
        Final Prediction=Expert Prediction
Else If (SVM Prediction~=NN Prediction) & (Expert Prediction~=5)
        Final Prediction=SVM Prediction
End
```

Rule set 1: Simple rule set to combine classifiers

According to results in Table 2, different styles in furniture design domain are giving different accuracy for different classifiers (SVM, Nearest Neighbour and Expert). SVM classifier provides highest accuracy for class 1 and class 6. SVM and Nearest Neighbour classifiers are giving similar accuracy for class 2, 3 and 4. Expert rule classifier is giving highest accuracy for class 5. Based on the results on the Table 2 (passed performance), we have constructed simple rules to combine three different classifiers to get maximum accuracy. The set of rules is given in Rule set 1.

By combining three different classifiers with simple rules we have achieved overall accuracy of design style recognition around 90% which is higher than the individual accuracy of each of the different classifiers

FINAL CONCLUSION

We have found that furniture design style can be recognized by using SVM and Nearest Neighbour classifiers with an accuracy above 85%. The classification accuracy has been further increased (90%) by integrating expert knowledge with other data driven classifiers: SVM and Nearest Neighbour. The binary encoding scheme is more suitable for encoding for the selected furniture style domain. Accuracy of the furniture design classifier has been further improved though the use of feature reduction and weight assignment. The discriminative power of feature analysis based scheme gave more accurate results compared to GA based scheme for feature selection and weight assignment. This total frame work can be used in other similar domains.

BIBILIOGRAPHY

[1] Quinlan, J.R., C4.5: Programs for Machine Learning. 1993: Morgan Kaufmann.

[2] Schlkopf, B. and A.J. Smola, Learning with kernels 2002, Cambridge: MIT University Press.

[3] Connectedlines, The On-Line Furniture Style Guide. 1998, http://www.connectedlines.com/styleguide/index.htm.

[4].Daniele, M.B., A Pre-processing Scheme for High-Cardinality Categorical Attributes in Classification and Prediction Problems. SIGKDD Explorations, 2001. 3(1): p. 27-32.

[5] Theodoridis, S. and K. Koutroumbas, Pattern Recognition. 1999, England: Academic Press.

[6] Bahler, D. and L. Navarr. Methods for Combining Heterogeneous Sets of Classifiers. in 17th Natl. Conf. on AI (AAAI 2000), Workshop on New Research Problems for Machine Learning. 2000. Austin, Texas.

Artificial Intelligence: a Promised Land for Web Services

D. Richards[1], M. Sabou[2], S. van Splunter[2], F.M.T. Brazier[2],

[1] *Department of Computing*
Macquarie University
Sydney, Australia
richards@ics.mq.edu.au

[2] *Department of Computer Science*
Vrije Universiteit Amsterdam
Amsterdam, The Netherlands
< marta, sander, frances>@cs.vu.nl

Abstract

This paper considers the possibilities offered by the application of techniques from the field of artificial intelligence (AI) to the newer field of web services (WS). Current commercial and research-based efforts are reviewed and positioned within the two fields. Particular attention is given to the application of AI techniques to the important issue of WS composition. Within the range of AI technologies considered, we focus on the work of the Semantic Web and Agent-based communities to provide WSs with semantic descriptions and intelligent behaviour and reasoning capabilities. Re-composition of web services is also considered and a number of adaptive agent approaches are introduced, including our own, to achieve this.

1. Introduction

Research in the web service (WS) and artificial intelligence (AI) communities is coming together to develop solutions that will take us to the next and more mature generation of the WWW. The composition of web services to create a value-chain greater than the sum of the parts is a key part of what can be expected. The fulfillment of the vision of the web as an *information-providing* and *world-altering* provider of services [29] is not far away. More futuristic is the notion of *serendipitous interoperability* which Lassila [27] defines as "the ability of software systems to discover and utilize services they have not seen before, and that were not considered when the systems were designed". In both visions the services and outcomes may be the same. However, the difference between the two visions is that the first can be achieved through static and manual solutions and the second requires dynamic and automated solutions. While helpful for the first, the addition of semantic content on the web is essential to enable automatic discovery and composition of multiple services. It is natural that earlier work in the field of AI will assist in realization of the (artificially) intelligent web.

The work on the Web Services Modeling Framework[1] (WSMF) is an example of AI being applied to this new field. WSMF offers the combined use of ontologies, goal (problem-type) repositories, web service descriptions and mediators to handle interoperability issues. The agent community, which is primarily AI-based, have also been actively conducting WS related research. Examples are the FIPA-led work that allows agents to use web service infrastructure and the inclusion of a web services track at the recent AgentCities [26].

Our own distributed agent-based work and the Agent Factory [6], originates from our earlier AI research into complex knowledge based systems and generic task based configuration. On the one hand, our work on planning and automated configuration offers a way of composing web services. On the other hand, WSs potentially provide us with components needed to achieve an implementation of our design. Through the addition of techniques from the Semantic Web community, the benefits of combining our agent technology with WSs has been mutual.

This paper offers a review of research that overlaps the fields of WS and AI. In the following section we describe web services and the need for semantics to be added. In section 3 we look at how the Semantic Web community, within the field of AI, are offering semantics. In section 4 we present AI-based research to address the discovery of WSs. In section 5 we consider both commercial and AI-based techniques for WS composition. In section 6, the notion of re-composition of WS is considered and how adaptive agent technology, including our own, can address this problem. We conclude with future directions for the role of AI in the web services field.

2. Web Services

As is typical in new fields, there are a number of definitions of a web service. According to the W3C, "a web service is a software application identified by a URI, whose interfaces and binding are capable of being defined, described and discovered by XML artefacts and supports direct interactions with other software applications using XML based messages via Internet-based protocols" [46]. We find this definition overly-focused on the technical aspects of a web service. A more business-oriented definition which supports the idea of services as providing a value-chain is "a self-contained, internet-enabled application capable not only of performing business activities on its own, but also possessing the ability to engage other web services in order to complete higher-order business transactions" [48]. The definition that most fits with our intended use of WSs as components in the Agent Factory is given by the Stencil[2] group who define a WS as "loosely coupled, reusable software components that semantically encapsulate discrete functionality and are distributed and programmatically accessible over standard

internet protocols". The three definitions offered differ in their emphasis on technology, business and software engineering but all encapsulate the self-contained, modular,

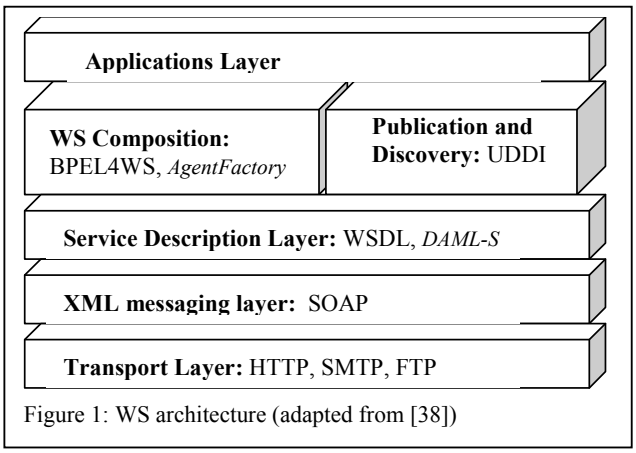

Figure 1: WS architecture (adapted from [38])

composable and distributed nature of WS.

These four characteristics of WS are well supported by a layered-architecture where the base is a well-established transport layer, as shown in Figure 1. In each layer we give an example of a major standard. In italics we position the work reported in this paper. The next layer up uses the Simple Object Access Protocol (SOAP) which is an XML-based communication protocol for exchanging data in decentralized and distributed environments via typed message exchange and remote calls. The service description layer includes the XML-based Web Service Description Language (WSDL). The next layer is split into two main types of WS technologies: ones that support single service advertising and discovery and ones that support service composition. For service registration and discovery there is the Universal Description, Discovery and Integration (UDDI) (by IBM, Microsoft and Ariba) standard service repository. To provide some very basic semantics (such as identification via a product classification code) one or more tModel descriptions may be attached to a service. For service composition there are a myriad of possible solutions. Figure 1 just includes the Business Process Execution Language for Web Services (BPEL4WS)[3] which has grown out of the early offerings WS Flow Language (WSFL) (IBM) [28] and XLANG (Microsoft) [41] (an extension of the W3C's Web Services Description Language (WSDL)).

3. Semantic description of Web Services

WSDL, SOAP and UDDI are seen as steps in the right direction but ones that will fail to achieve the goals of improved automation and interoperability, because they rely on *a priori* standardisation and require humans in the loop [27]. To support automated reasoning, knowledge representations (such as markup languages) will be needed that express both data and rules for reasoning. The ability to dynamically locate and compose web services based on their semantic description will rely on the richness of the description and the robustness of the matching techniques used. Ontologies will be used to enable definition and comprehension of meaningful content. These are the concerns of the Semantic Web community. Additionally, agents will be needed to interpret the content and transform user requests into optimized delivered solutions.

The Intelligent Brokering Service for Knowledge-Component Reuse on the WWW (IBROW)[4] can be seen as a forerunner of the Semantic Web. In IBROW problem solving methods (PSMs) and ontologies were the components being configured, the current focus is on WS configuration. PSMs and ontologies when used together are also capable of delivering services.

The most significant work that has been done to describe web services has been conducted by the DAML-S coalition [40]. The matching of service providers and service requesters via semantic descriptions of the services are key goals of this work. DAML-S uses the DAML+OIL specification language (which extends the weak semantics of RDF(S)) to define a number of ontologies that can be specifically used to describe web services. DAML-S is built on the AI-based action metaphor where each service is either an atomic/primitive or composite/complex action. Knowledge preconditions and knowledge effects are handled via the inputs and outputs of the web service [29]. The DAML-S coalition are providing solutions to work with current WS standards. For example, a DAML-S service grounding definition can be mapped to a WSDL definition of the service. A number of approaches to service discovery and composition that we discuss in the following sections use or extend the DAML-S web service ontologies.

4. Discovering Web Services

Discovery involves locating and/or matchmaking against some selection criteria. An earlier AI system, Lark [39], which involved annotation of agent capabilities to enable them to be located and brokered, clearly solved a problem similar to the discovery of WS by a middle agent. This work has developed into the DAML-S Matchmaker[5]. To support matchmaking a number of filters may be configured by the user to achieve the desired tradeoff between performance and matching quality. These filters include: word frequency comparison, ontology similarity matching, ontology subsumption matching, and constraint matching.

[11] offer an alternative to sequential searching when matchmaking an agent with a service request. They point out that finding possible partners via matching of service advertisements with requests is not enough. To support runtime interactions we need smarter behaviour to handle components that are not quite what was requested and combining several partial components to meet the original request. The solution to overcome sequential searching is the conversion of the concepts into number intervals and

the use inheritance hierarchies to determine subclass and equality relations. A generalised search tree is used to handle partial matches.

The feasibility of matchmaking largely depends on the annotation of web services. AI can also be applied to this problem. A number of markup tools have been developed for document markup and these could be applied to the semantic description of WSs. The SHOE Knowledge Annotator [19] uses ontologies to guide knowledge annotation. To produce RDF-based markup, COHSE [1] or AeroDAML [24] can be used. These approaches start with descriptions in DAML+OIL and DAML, respectively. These approaches support automatic conversion of markup languages but do not support information extraction or automatic markup. OntoMat [18] does support some form of automated extraction of semantics. OntoMat combines the resource with its DAML-S markup. The MnM [44] approach additionally stores the annotations in a knowledge base. Automated markup in MnM is achieved using techniques from knowledge engineering, machine learning and natural language processing.

[22] have developed a query language that is used to find services. The solution to finding services is to first describe the service using the process ontology with the assistance of the MIT Process Handbook. The Handbook is large and allows reuse to assist in ontology definition. Next, the ontology is indexed by breaking it down into its components such as attributes, ports, dependencies, subtasks and exceptions. The requester can form a query in the query language that will use the index to find matches.

Clearly AI is already contributing solutions for locating, matchmaking, querying and annotation of WS to facilitate their discovery. Discovery of web services is an important issue as it is a prerequisite to their use. However, the real value of web services lies in their composition.

5. Composing Web Services

Web service composition can be simply defined as: "the problem of composing autonomous services to achieve new functionality" [33]. WS composition is not just an alternative to application development but a means of reducing the application backlog problem because: many services are moving online; integration is easier since WSs conform to the HTTP protocol and many independent providers have related services that need to be combined to satisfy user requirements. The rigidity and lack of intelligence of current solutions has spawned a number of research projects from a number of other research fields.

The work by [42] has arisen from experience in the distributed systems and networking fields. They have developed the Infrastructure for Composability at Runtime of Internet Services (ICARIS). They have extended WSDL to develop the Web Services Offerings Language (WSOL). They offer flexibility and adaptability but their approach is very alternative. Instead of trying to solve the problem of how to find services dynamically and combine them, they focus on the situation where providers and requestors are already matched but will at times either make changes to their services or requests. A service is seen to have numerous offerings. The functionality will be the same but the constraints will differ such as authorisation rights and QoS. They suggest that a limited number of classes of services be offered and described. Then using WSOL they are able to specialise the classes into offerings. Their solution offers dynamic switching between offerings. From a commercial point of view the notion of offerings makes sense as customers probably prefer to do business with companies they already know and businesses want to maintain their existing client base.

The work at Hewlett Packard laboratories on *eFlow* [9] is similar in that dynamic composition involves automatic adaptation of the configuration at runtime according to the requests of the individual customer. The approach is driven by the view that composition adds value but to stay competitive, composition needs to be dynamic as services offered need to adapt to stay competitive. Their goal is to allow dynamic change in service processes with no or minimal human intervention. While they take a business process perspective they point out that web services are less static, predictable or repetitive compared to "traditional" business processes. Similar to most current commercial solutions, dynamic composition is made possible due to the use of a central repository that has clients and providers already attached to it.

The notion of generic solutions that are customized according to user constraints is a recurring theme in much of the literature. [37] also look at composition as the selection of possible services based on user specified criteria. They offer a centralized, pipes and filters architecture with two main components: a composer (user interface) and an inference engine (IE) component (which includes a knowledge base of known services). The inference engine is an OWL reasoner and includes axioms to find all relevant entailments, such as the inheritance relation between two classes which may not have been made explicit. The user identifies some criteria that the service must satisfy. The matchmaker (IE) selects services that might be suitable based on those criteria and the composer shows them to the user. Suitable services for composition are ones whose output can be an input to a selected service. While execution of WS may be performed automatically, the actual task of composition is performed by a human using the services suggested by the system.

Model-based reasoning is a common technique employed in AI approaches. In SWORD [33] entity-relationship modeling of services is performed by "base service modelers" to produce a "world model". After building a world model for each service, a composition model is developed that models each service as an action. An expert system is used to automatically determine if the composite service can be created with existing services and if so a plan of execution is generated.

In summary, a number of solutions are offered to provide web service composition. The approaches described in this section show that composition can be assisted through the use of class definitions, inheritance hierarchies and model and rule-based reasoning. In many cases, decision making is left to humans. The only automated composition offered is in limited situations where a central repository is used and the requestor and provider are part of the same system. However, the web is distributed in nature. Intelligent reasoning and collaboration between services is needed to handle this complexity. Agents are capable of both.

6. Agents and Web Services

The autonomous and reasoning capabilities of agents make them well suited for handling cross-organisational decision making. For example, agents can be used to (re)negotiate contracts which would then require: determination of which processes are needed to fulfil the contract; creation of new business processes; and adaptation of existing business processes. Two main agent-oriented approaches exist: use wrappers to make WS behave like agents and; using agents to orchestrate WS.

6.1 Adding Behaviour to WS via Agents Wrappers

WS are componential, independent, software applications similar to agents. However, agents are also reactive, social and capable of reasoning [47]. If we wish web services to work together, we need to give them social and reasoning capabilities. This can be achieved by wrapping a service in an agent. In the work of [8], a composition language is used to create an agent wrapper which allows services to collaborate. The created agent has first–order reasoning abilities that have been derived from the DAML-S description of the service. This then allows one agent-wrapped service to know what other agent-wrapped services are capable of doing and whether they can assist in the service/agent meeting its goals. [23] also offer an agent-based wrapper approach to web services. They have developed a tool for creating wrappers so that web sources can be queried in a similar manner to databases. They then use an interactive, hierarchical constraint propagation system to perform integration. As in [37], the end-user interacts via a GUI to manage the orchestration. The Racing project[6] offers a mediator architecture also using agent wrappers that are structured into a hierarchy. A number of different agent wrappers are supported: user, query translation, query planning, resource wrapper, ontology, matchmaking, cloning and coordination agents. The use of agent wrappers is a way of allowing multi-agent system technology to be applied to web services.

6.2. Composing Web Services using Agents

The work of [29] combines ideas from the Semantic Web, Knowledge Representation and Agent communities to allow WSs to be composed. Their goal is to "construct reusable, high-level generic procedures, and to archive them in shareable (DAML-S) generic-procedures ontologies so that multiple users can access them". In the approach, WSs and user constraints are marked up in DAML-S. A generic task procedure is selected by the user and given to the DAML(-S) enabled agent, who customises the procedure according to the user specific constraints. The generic procedures are written in an extended version of ConGolog, a situation calculus agent programming language, and executed using a Prolog inference engine. Others provide agent-oriented languages for web service description. [10] propose an Agent Service Description Language (ASDL) and Agent Service Composition Language (ASCL). ASDL is an extension to WSDL and captures external behaviour via a finite state machine. Their work is based on the argument that composition requires more than description of the data, but also requires a strong representation of actions and processes. A number of approaches are focused on the design of agent systems with web services as the components. [3] has developed WARP (Workflow Automation through Agent-based Reflective Processes) that uses the XML and WSDL standards. The goal is automatic configuration and management of low-level services (components). The software engineering development process that has been developed is semi-automatic involving multiple software agents and a human workflow designer. They support visualisation of the process based on activity diagrams in UML.

Niersatz [31] argues that (re-)composability is a distinguishing feature of open systems. We have considered some approaches which support the use of agents to reason about and coordinate services over the ultimate open system, the web. In some of these approaches, composition involves reuse and specialization of generic components. As [29] point out, services often provide multiple outputs, only some of which may be needed as inputs to a subsequent service. Sometimes additional services will be needed to overcome a mismatch in inputs and/or outputs. Such shortcomings in the original configuration may require recomposition of WSs. To achieve this may involve adapation of the agent's behaviour, since web services are by nature closed and immutable.

6.3 (Re-)composition and Adaptable Agents

The ability of agents to adapt according to changes in system requirements and the environment is important to enable dynamic and reactive behaviour.

Agents may be adapted in a number of different ways. The knowledge and facts that an agent uses may be adapted for example the agent may use a client profile that changes according to the clients activities (e.g. [45]. This type of adaptation typically involves machine learning, e.g. [25]. An agent may also adapt its interface according to the platform on which it is being used (e.g. [brand]. A third type of adaptation, and the type of adaptation we are concerned with, is adaptation of the agent's functionality. There is limited work in this area. Semi-automatic agent creation tools such as AGENTBUILDER [34], D'AGENTS/ AGENT/TCL [17], ZEUS [32] and PARADE [2] could possibly be extended to support agent adaptation.

Following the use of compositionality in the major software engineering paradigms (e.g. functional programming [21], object-oriented programming [4], component-based programming [20] and the Factory design pattern [16], we have developed an Agent Factory [6]. The approach is based on the use of components, the general agent model (GAM) and the DESIRE formal knowledge-level modelling and specification framework for multi-agent systems [7]. Our agent (re-)structuring approach allows an agent to automatically adapt by reusing existing components. Our approach is a combination of process-oriented and object-oriented approaches by treating processes as the 'active' parts of our agent, which are our agent components, and classes as the 'passive' part of our agent, which are the data types used in the agent components. We are currently exploring whether DAML-S descriptions of web services are adequate for automated configuration of web services by the Agent Factory. Our initial report on how the Agent Factory can be used to perform this task

is found in [43]. Our observations and recommendations regarding DAML-S are given in [35].

The work by [12], which is also called the Agent Factory and based on the notion of design patterns, assists human designers in functional design, and the configuration of software components to fulfil the conceptual design specified by the designers, depending on the agent platform that is to be used. Our approach does more: it automates the creation and redesign of both the conceptual and operational design based on the requirements on function, behaviour and state of an agent. Our use of web services as components is a further distinguishing feature.

While not currently working in the WS area, the AdaptAgent [30] approach, bring together adaptive workflow and agent research. They consider how agents can be used to collaborate to perform a workflow and make workflow more intelligent and how workflow can be used to organise a set of agents and coordinate interaction between people and agents.

The reuse of knowledge has also been a widely researched topic and the creation of libraries of problem solving methods [36] and generic task models [7] offer a similar idea to the functional components in our agent factory. The IBROW project, mentioned earlier, has even more in common with our approach by semi-automatically configuring intelligent problem solvers using problem solving methods as building blocks. They use mappings to act as glue between the components which are modeled as CORBA objects. Unlike our approach, their architecture is restricted to specific languages and architectures, they only support semi-automation and they do not distinguish between conceptual and implementation level designs.

7. Discussion and Future Directions

An interesting phenomena of AI research is that when a problem becomes solved it no longer holds any mystery and moves from being called AI to being just another part of information processing. This phenomena was first noted by Donald Michie and is thus known as *the Michie effect* [15]. Examples of the assimilation of AI concepts into mainstream data processing are the use of machine learning techniques in knowledge discovery from databases, the inclusion of business rules in database technologies and the use of ontologies for information systems development.

Similarly, AI-based research will benefit B2B, e-commerce and internet applications requiring knowledge-level interoperability of information systems and intelligent processing by agents. Advances in natural language technology research will assist discovery of web services and agents will play an important role in using web services to satisfy user requests.

The current trend towards interoperability of systems and integration of technologies will continue and increase the need for standards. Standards, as mentioned in section 2, are emerging for web services. As the roles of agents on the web increases, further work is required in the area of communication standards between agents and web services. For invocation, the Java Agent Services (JAS) project is developing an industry standard and API for network agent and service architectures. JAS does not, however, specify how an ACL message can be translated into the format needed by the web service. HP BlueJade also does not describe how agents can use SOAP, UDDI, WSDL, etc, or say how services and agents can communicate [26].

Existing agent platforms may need to be adapted to handle the specific requirements of web services. In this direction, CMU have proposed the RETSINA[7] agent architecture for web-based agents. The RETSINA functional architecture includes four basic types of agents: interface, task, information and middle agents who communicate via a special agent communication language. Each of these agents includes four reusable modules: communication and coordination, planning, scheduling and monitoring. The middle agent plays a critical role in matching providers with requesters and is offered as a solution to the heterogeneous nature of agents over the web.

The work of the Semantic Web community to provide semantic description of web services will play a key role in enabling agents to automatically compose web services. We are more than interested onlookers in these developments. While it is still early days, the incorporation of ideas from AI is already proving to be mutually beneficial.

10. References

[1] Bechhofer, S. and Goble, C. Toward Annotation Using DAML+OIL, 1st Int. Conf. on Knowledge Capture (K-CAP'2001), W'shop on Semantic Markup and Annotation, Victoria, BC, Canada, Oct. 2001

[2] Bergenti, F., Poggi A.: A Development Toolkit to Realize Autonomous and Inter-Operable Agents. In: Proc. of Fifth Int. Conf. of Autonomous Agents (Agents 2001), Montreal (2001) 632-639

[3] Blake, M.B. An Agent-Based Cross-Organizational Workflow Architecture in Support of Web Services, WETICE 2002: 176-181

[4] Booch, G.: Object oriented design with applications. Benjamins Cummins Publishing Company, Redwood City, 1991

[5] Brandt, R., Hörtnagel, C., Reiser, H.: Dynamically Adaptable Mobile Agents for Scaleable Software and Service Management. Journal of Communications and Networks 3:4 (2001) 307-316

[6] Brazier, F.M.T., Wijngaards, N.J.E.: Automated Servicing of Agents. AISB Journal 1 (1), Spec. Issue on Agent Tech. (2001) 5-20

[7] Brazier, F.M.T., Jonker, C.M., Treur, J.: Principles of Component-Based Design of Intelligent Agents. Data and Knowledge Engineering 41 (2002) 1-28

[8] Buhler, P. A. and Vidal, J. M. (b) Semantic Web Services as Agent Behaviors. In B. Burg, J. Dale, T. Finin, H. Nakashima, L. Padgham, C. Sierra, and S. Willmott, editors, Agentcities: Challenges in Open Agent Environments, pages 25-31. Springer-Verlag, 2003

[9] Casati, F., Ilnicki, S. and Jin, L Adaptive and Dynamic Service Composition in eFlow. HP Technical Report, HPL-2000-39, March, 2000, www.hpl.hp.com/techreports/2000/HPL-2000-39.pdf

[10] Cheng, Z., Singh, M.P. and Vouk, M.A., Composition Constraints for Semantic Web Services. WWW2002 Workshop on Real World RDF and Semantic Web Applications, to appear in the proceedings, May 7, 2002

[11] Constantinscu, I. and Faltings, B. Efficient Matchmaking and Directory Services. Technical Report No IC/2002/77, 18 Nov 2002, Laboratoire d'Intelligence Artificielle, Department Informatique, Swiss Federal Institute of Technology, IN (Eculbens), 2002

[12] Cossentino, M. Burrafato, P., Lombardo, S. and Sabatucci, L. Introducing Pattern Reuse in the Design of Multi-Agent Systems. AITA'02 workshop at NODe02 - 8-9 October 2002 - Erfurt, Germany

[13] Dumas, M., O'Sullivan, J., Heravizadeh, M., Edmond, D. and ter Hofstede, A. Towards a semantic framework for service description In Proc. of the IFIP Conference on Database Semantics, Hong Kong, Kluwer Academic Pub., April 2001

[14] The DAML Services Coalition (alphabetically Anupriya Ankolenkar, Mark Burstein, Jerry R. Hobbs, Ora Lassila, David L. Martin, Drew McDermott, Sheila A. McIlraith, Srini Narayanan, Massimo Paolucci, Terry R. Payne and Katia Sycara), DAML-S: Web Service Description for the Semantic Web, The First International Semantic Web Conference (ISWC), Sardinia (Italy), June, 2002

[15] Gaines, B. (2000) Knowledge Science and Technology: Operationalizing the Enlightenment In P. Compton, A. Hoffmann, H. Motoda and T. Yamaguchi (eds) Proceedings of the 6th Pacific Knowledge Acquisition Workshop, Sydney Dec. 11-13,2000, 97-124
[16] Gamma, E., Helm, R., Johnson, R., Vlissides, J.: Design Patterns: Elements of reusable object-oriented software. Addison Wesley Longman, Reading, Massachusetts, 1994
[17] Gray, R.S., Kotz, D., Cybenko, G., Rus, D.: Agent Tcl. In: Cockayne, W., Zypa, M. (eds.): Itinerant Agents: Explanations and Examples with CD-ROM. Manning Pub. (1997) 58–95
[18] Handschuh, S., Staab, S. and Maedche, A. CREAM- Creating Relational Metadata with a Component-Based, Ontology-Driven Annotation Framework, 1st Int. Conf. on Knowledge Capture (K-CAP'2001), Workshop on Semantic Markup and Annotation, Victoria, BC, Canada, October 2001
[19] Heflin, J. and Hendler, J. A Portrait of the Semantic Web in Action, IEEE Intelligent Systems, 16(2), 2001
[20] Hopkins, J.: Component primer. Communications of the ACM 43:10 (2000) 27–30
[21] Kernighan, B.W., Ritchie, D.M.: The C Programming Language. 2nd edn. Prentice Hall Software Series, 1988
[22] Klein, M and Bernstein, A. Searching for Services on the Semantic Web using Process Ontologies. In The Emerging Semantic Web - Selected papers from the first Semantic Web Working Symposium, Isabel Cruz, S. Decker, J. Euzenat, and D. McGuinness, Eds. Amsterdam: IOS press, 2002, pp. 159-172
[23] Knoblock, C., Minton, S., Ambite, J..L., Muslea, M., Oh, J. and Frank, M. Mixed-initiative, multi-source information assistants,In Proceedings of the World Wide Web Conference, pages 697--707, ACM Press, New York, NY, May 2001
[24] Kogut, P. and Holmes, W. AeroDAML: Applying Information Extraction to Generate DAML Annotations from Web Pages, 1st Int. Conf. on Knowledge Capture (K-CAP'2001), Workshop on Semantic Markup and Annotation, Victoria, BC, Canada, October 2001
[25] Kudenko, D., Kazakov, D., Alonso, E.: Machine Learning for Multi-Agent Systems. In: V. Plekhanova, V.(ed.): Intelligent Agents Software Engineering, Idea Group Publishing, 2002
[26] Kuno, H. and Sahai, A. My Agent Wants to Talk to Your Service: Personalizing WSs through Agents. HP Tech. Rep., HPL-2002-114, www.hpl.hp.com/techreports/2002/HPL-2002-114.html
[27] Lassila, O. Serendipitous Interoperability, in Eero Hyvönen (ed.): "The Semantic Web Kick-Off in Finland - Vision, Technologies, Research, and Applications", HIIT Publications 2002-001, University of Helsinki, 2002
[28] Leyman, F. Web Service Flow Language (WSFL) 1.0, IBM, Armonk, NY, www-4.ibm.com/software/solutions/webservices/pdf/WSFL.pdf, 2001
[29] McIlraith, S. and Son, T., Adapting Golog for Composition of Semantic Web Services, Proceedings of the Eighth International Conference on Knowledge Representation and Reasoning (KR2002), Toulouse, France, April, 2002
[30] Narendra, N. C. AdaptAgent: Integrating Adaptive Workflows and Multi-Agent Conversations for B2B E-Commerce. Proceedings of International Conference on Artificial Intelligence, Special Session on Agent-Oriented Workflow Architecture for B2B, 2001
[31] Nierstrasz, O. and Meijler, T. D.Requirements for a Composition Language. Object-Based Models and Langages for Concurrent Systems, Paolo Ciancarini, Oscar Nierstrasz and Akinori Yonezawa (Eds.), 147—161, Springer-Verlag, 1995
[32] Nwana, H.S., Ndumu, D.T., Lee, L.C.: ZEUS: An Advanced Tool-Kit for Engineering Distributed Multi-Agent Systems. Applied AI 13:1/2 (1998) 129-185
[33] Ponnekanti, S.H. and Fox, A. SWORD: A Developer Toolkit for Web Service Composition. In The Eleventh WWW Conference (Web Engineering Track), Honolulu, Hawaii, May 7-11, 2002
[34] Reticular: AgentBuilder: An Integrated Toolkit for Constructing Intelligent Software Agents. Reticular Systems Inc, white paper edition. http://www.agentbuilder.com, 1999
[35] Sabou, M., Richards, D. and van splunter, S. An experience report on using DAML-S , Workshop on E-Services and the Semantic Web, Budapest, Hungary, May, 2003 (submitted)
[36] Schreiber, G., Akkermans, H., Anjewierden, A., de Hoog, R., Shadbolt, N., van de Velde, W., Wielinga, B.: Knowledge Eng. and Management, the CommonKADS Methodology. MIT Press, 2000
[37] Sirin, E., Hendler, J. and Parsia, B. Semi-automatic Composition of Web Services using Semantic Descriptions. Accepted to "Web Services: Modeling, Architecture and Infrastructure" workshop in conjunction with ICEIS2003, 2002
[38] Staab, S., Benjamins, R., Bussler, C., Gannon, D., Sheth, A. and van der Aalst, W., Web services: Been there, Done that? IEEE Intelligent Systems, Trends & Controversies, 18(1), Jan/Feb 2003
[39] Sycara, K., Widoff, S., Klusch, M. and Lu, J., LARKS: Dynamic Matchmaking Among Heterogeneous Software Agents in Cyberspace, Autonomous Agents and MAS, 5 (2): 173-203, June, 2002
[40] The DAML Services Coalition (alphabetically A. Ankolekar, M. Burstein, J. Hobbs, O. Lassila, D. Martin, S. McIlraith, S. Narayanan, M. Paolucci, T. Payne, K. Sycara, H. Zeng), "DAML-S: Semantic Markup for Web Services", in Proceedings of the International Semantic Web Working Symposium (SWWS), July 30-Aug. 1, 2001
[41] Thatte, S. XLANG: Web Services for Business Process Design, www.gotdotnet.com/teaml/xml_wsspecs/xlang-c/default.htm, 2001
[42] Tosic, V., Pagurek, B. Esfandiari, B. and Patel, K. :On the Management of Composition of Web Services position paper at the Workshop on Object-Oriented Web Services - OOWS (at OOPSLA 2001), Tampa, USA, October 15, 2001. Also published as: Technical Report OCIECE-01-10, Ottawa-Carleton Institute for Electrical and Computer Engineering - OCIECE, October, 2001
[43] van splunter, S., Sabou, M., F.M.T. Brazier and Richards, D. Configuring Web Services, using Structuring and Techniques from Agent Configuration, EEE/WIC International Conference on Intelligent Agent Technology (IAT 2003) (submitted)
[44] Vargas-Vera, M, Motta, E., Domingue, J, Lanzoni, M., Stutt, A. and Ciravegna, F. MnM: Ontology Driven Tool for Semantic Markup. European Conference on Artificial Intelligence (ECAI 2002). In proceedings of the Workshop Semantic Authoring, Annotation & Knowledge Markup (SAAKM 2002). Lyon France, July 22-23, 2002
[45] Wells, N., Wolfers, J.: Finance with a personalized touch. Comms of the ACM, Issue on Personalization 43:8 (2000) 31–34
[46] W3C Web Services Architecture Working Group. Web Services Architecture Requirements, Working Draft 29 April 2002, http://www.w3.org/TR/2002/WD-wsa-reqs-20020429
[47] Wooldridge, M. and Jennings, N. (1995), Agent Theories, Architectures, and Languages: a Survey, in Wooldridge and Jennings Eds., Intelligent Agents, Berlin,:Springer-Verlag, 1-22.
[48] Yang, J and Papazoglou, M. Web Component: A Substrate for Web Service Reuse and Composition. in Procs of the 14th International Conference on Advanced Information Systems Engineering (CAiSE02), May, Toronto, Lecture Notes in Computer Science, Vol. 2348, p21-36, Springer, 2002

[1] http://informatik.uibk.ac.at/c70385/wese.
[2] www.stencilgroup.com/ideas_scope_200106wsdefined.html
[3] http://xml.coverpages.org/bpel4ws.html
[4] www.ibrow.org
[5] http://www-2.cs.cmu.edu/~softagents/daml_Mmaker/daml-s_matchmaker.htm
[6] http://www.zsu.zp.ua/racing/
[7] http://www-2.cs.cmu.edu/~softagents/retsina_agent_arch.html

A Survey of the Application of Soft Computing to Investment and Financial Trading

Bruce Vanstone
School of IT, Bond University
Gold Coast, Queensland, Australia
bvanston@bond.edu.au

Clarence Tan
School of IT, Bond University
Gold Coast, Queensland, Australia
ctan@bond.edu.au

Abstract

This paper surveys recent literature in the domain of applying Soft Computing to Investment and Financial Trading. It analyses the literature according to the style of soft computing used, the investment discipline used, the successes demonstrated, and the applicability of the research to real world trading. This papers contribution is to expose the key areas where research is being undertaken, and to attempt to quantify the degree of successes associated with the different research approaches.

1 Introduction

This paper surveys the literature on the utilization and successes of Soft Computing techniques in the Investment arena. Where applicable, it suggests improvements to the methodologies used to increase their practicality.

Investment trading is normally divided into two major disciplines, Fundamental Analysis, and Technical Analysis. Papers concerned with applying Soft Computing to these two disciplines are reviewed.

The papers reviewed are assessed and categorized according to the style of soft computing used, their investment discipline, the degree to which they demonstrate their success, as well as their practicality for use as real world trading models.

2 Analysis of Methodologies Used

2.1 Analysis by Soft Computing Technique

Soft computing represents that area of computing adapted from the physical sciences. Artificial Intelligence techniques within this realm attempt to solve problems by applying physical laws and processes. This style of computing is particularly tolerant of imprecision and uncertainty, making the approach attractive to those researching within 'noisy' realms, where the signal-to-noise ratio is quite low. Soft computing is normally accepted to include the three key areas of Fuzzy Logic, Neural Networks, and Probabilistic Reasoning (which includes Genetic Algorithms, Chaos Theory, etc).

The arena of investment trading is one such field where there is an abundance of noisy data. It is in this area that traditional computing typically gives way to soft computing, as the rigid conditions applied by traditional computing cannot be met. This is particularly evident where the same sets of input conditions may appear to invoke different outcomes, or there is an abundance of missing or poor quality data.

There are a number of approaches within the literatures which deal with applying soft computing techniques to investment and trading. Although there appears to be no formal segmentation of these different approaches, this paper classifies the literature into the topics proposed by Tan [1], and augments these classifications with one more category, namely, Hybrid. These categories of soft computing, then, are:

- Time Series – forecasting future data points using historical data sets. Research reviewed in this area generally attempts to predict the future values of some time series. Possible time series include: Base time series data (e.g. Closing Prices), or time series derived from base data, (e.g. Indicators - frequently used in Technical Analysis).
- Pattern Recognition and Classification – attempts to classify observations into categories, generally by learning patterns in the data. Research reviewed in this area involved the detection of patterns, and segregation of base data into 'winner' and 'loser' categories.
- Optimization – involves solving problems where patterns in the data are not known, often non-polynomial (NP)-complete problems. Research reviewed in this area covered the optimal selection of parameters, and determining the optimal point at which to enter transactions.
- Hybrid – this category was used to distinguish research which attempted to exploit the synergy effect by combining more than one of the above styles.

There is a wide acceptance of the benefit of the synergy effect, whereby the whole is seen as being greater than the sum of the individual parts. This can be easily seen by inspecting Table 1, which clearly shows that Hybrid techniques account for more than one-third of the research reviewed.

Further, the bias in this style of research towards technical analysis techniques (see below) is also evident from the table, with one-third of the research pursuing the area of Pattern Recognition and Classification. Technical analysis particularly lends itself to this style of research, as a large focus of technical analysis concerns the detection of patterns in data, and the examination of the behavior of market participants when these patterns are manifest.

Table 1. Reviewed papers classified by style of soft computing used

Research Classification	Number of papers	Paper References
Time Series Prediction	6	[2], [3], [4], [5], [6], [7]
Pattern Recognition & Classification	11	[8], [9], [10], [11], [12], [13], [14], [15], [16], [17], [18]
Optimization	2	[19], [20]
Hybrid	11	[21], [22], [23], [24], [25], [26], [27], [28], [29], [30], [31]

2.2 Analysis by Investment Discipline

There are predominantly two schools of thought concerning investment trading, namely Fundamental Analysis and Technical Analysis.
Fundamental Analysis provides a framework for examining the underlying forces that affect the price of an investment. Fundamental analysis techniques give rise to investment approaches like Value Investment. This style of investment espouses the view that investing is the process of determining the fair value of an individual investment, and purchasing that investment at or below that fair value.

The other main school of thought concerning investment trading is Technical Analysis. This style of trading is concerned primarily with the study of past trading data, believing this is reflecting the behavior of market participants. Such trading data includes prices, volume and open interest.

Both disciplines are concerned with attempting to predict likely future prices movements, and seek to capitalize on these predictions with trading models.

This paper classifies the reviewed literature in one of three categories, namely Fundamental, Technical, or Combined, with Combined representing some mix between the two techniques. Table 2 presents the results of this classification for the papers reviewed.

Table 2. Reviewed papers classified by Investment Discipline

Research Classification	Number of papers	Paper References
Fundamental Analysis	3	[29], [7], [13]
Technical Analysis	23	[20], [19], [28], [27], [26], [25], [24], [23], [22], [21], [31], [30], [5], [4], [2], [18], [16], [15], [14], [12], [10], [9], [8]
Combined	4	[6], [3], [11], [17]

Although many practitioners feel a strong divide between Fundamental techniques, and Technical techniques, there appears to be a growing acceptance amongst the investment community that the techniques may be viewed as complementary. Indeed, as earlier as 1992, Taylor and Allen conducted a survey on behalf of the Bank of England, and their findings indicated that a high percentage of chief foreign exchange dealers already considered fundamental and technical techniques as complementary strategies, preferring fundamental analysis for long-term horizons, and technical analysis for shorter term horizons [32].

Research using soft computing techniques is particularly data intensive, as soft computing techniques generally require a large set of data on which to learn. This may go some way towards explaining the apparent large bias of the research of this nature to focus on technical analysis. Typically, the technical analysis data used in the majority of research is daily data, which is easily obtained and available in large quantities. Conversely, the data normally used for fundamental analysis is yearly data, often sourced from company balance sheets, or other accounting publications.

3 Analysis of Investment Performance

There are a number of measures of success in common use throughout the research reviewed. Soft computing achieves its benefits from a learning process, which generally allows the specific soft computing techniques the ability to repeatedly assess their own learning using some form of feedback mechanism. This lends itself to the creation of an error function, and most forms of soft computing attempt to minimize this error function. As the value of the error function is decreased, the soft computing technique is

said to be learning the relationship between the various inputs and outputs provided.

Although this is an excellent way of providing a soft computing technique with the ability to assess its own degree of learning, it does not necessarily deliver results consistent with the expectations of the trainer. In the area of investment trading, a trainer typically wants to maximize returns, or minimize time in the market, or some other specific attribute of the domain being studied. This leads to something akin to an impedance mismatch, which may result in a trained process delivering a poor outcome in its specific domain. This problem may also result from the trainer attempting to predict something too specific, such as the price of an individual investment, when the trainer may well have achieved a far better result by attempting to predict only the direction of the price movement, as suggested by Tan [1].

It should be mentioned that much of the work in the area of applying soft computing to investment trading has been of an evolutionary approach. That is, much of the earlier work was concerned only with establishing whether a particular soft computing approach could outperform some corresponding regression technique. It was some time before soft computing firmly established itself, and the research involving forecasting was mature. Until this point had been reached, it was not common to continue on and implement the particular technique as a trading mechanism.

For the purposes of this review, the research is classified according to what is assumed to be the most likely desired criteria of success, namely, the ability to increase investment returns above and beyond that achieved by using a buy-and-hold naïve approach. Table 3 shows whether the papers reviewed outperformed the naïve strategy, or whether their performance was classified in another way.

Table 3. Benchmark performance against the buy-and-hold approach

Research Classification	Number of papers	Paper References
Outperforms Buy-and-Hold	4	[27], [6], [12], [18]
Does not outperform Buy-and-Hold	1	[9]
See Table 4	25	[19], [20], [29], [30], [21], [31], [22], [23], [24], [25], [26], [28], [4], [7], [2], [3], [5], [8], [10], [13], [14], [15], [16], [17], [11]

In the case of Mizuno, Kosaka et al. [9] which did not outperform the buy-and-hold strategy overall, the results presented demonstrate that the system developed did exceed the buy-and-hold strategy for buy situations. However, performance achieved during sell situations was less than optimal. Overall, the combined results achieved a slightly lower rate of profit for the soft computing approach (1.20) compared with a rate of profit (1.21) for the buy-and-hold strategy. The authors propose that this could be due to the increasing upward trend in price change throughout the simulation period.

Table 4 below categorizes those papers which do not lend themselves to the primary classification of increasing investment returns. These papers occasionally rate their own performance by comparison to statistical techniques, or by comparison to the results which would be obtained without the use of soft computing, for example, by applying technical analysis or fundamental analysis alone. More often, however, there is a tendency to conclude with statements of a broadly positive nature.

Table 4. Benchmarking performance using a comparator other than Buy-and-Hold

Research Classification	Result[1]	Number of papers	Paper References
Comparison to Statistical Technique	1	1	[7]
Comparison to same technique without soft computing	8	8	[19], [20], [29], [22], [25], [26], [2], [3]
Other	N/A	16	[30], [21], [31], [23], [24], [28], [4], [5], [8], [10], [13], [14], [15], [16], [17], [11]

4 Analysis of Applicability to Non-Academic Community

The final categorization of the papers reviewed concerns the applicability of the research results to the non-academic investment community. This section briefly outlines the requirements of the non-academic community in the form

[1] Number of Papers that Outperformed relative to the basic comparison technique

of two major constraints, namely Money Management, and Trading Costs.

Money Management techniques are directly related to the methods by which traders control their capital. Every trader has restrictions not only on the amount of capital that can be employed, but also how that capital is to be expended in trading activities. Typically, this relates to various position sizes that a trader can control, and also the restrictions on holding those positions in the event of price moving against the trader. These restrictions placed on a trader would be rigidly enforced, in terms of position size, equity invested in specific positions, and the amount of drawdown which could be tolerated before trading was halted. None of the papers reviewed implemented money management techniques. For a detailed explanation of money management techniques, the reader may wish to refer to Elder [33].

Trading costs refers to the amount of cost expended to earn a given return. Traders are subject to a variety of costs, such as:

- transaction costs (brokerage),
- gaps (potentially large price changes, outside of trading hours),
- bid-ask spreads

For a detailed explanation of the costs involved in the trading process, the reader may wish to refer to Babcock [34].

Accounting for these costs can easily turn a system with a positive return into one with a negative return. For example, a system which has a high number of trades, each generating very little profit would appear as a successful system in terms of rate of return. However, taking transaction costs into account could see the profit earned quickly eroded in paying transaction costs. Only five of the papers reviewed accounted for trading costs, and these papers specifically only accounted for transaction (brokerage style) costs. Typically, these papers allowed 1% of the cost of the trade as expended on brokerage. Table 5 demonstrates the degree to which the reviewed papers implemented real-world trading constraints.

Table 5. Reviewed papers classified by implementation of real-world trading constraints

Research Classification	Number of papers	Paper References
Money Management	0	None
Trading Costs		
- transaction costs	5	[23], [25], [30], [2], [4]
- other	0	
Not applicable[2]	6	[21], [31], [7], [14], [15], [16]

5 Conclusions

This paper has surveyed recent and key literature in the domain of applying Soft Computing to Investment and Financial Trading. It categorized the papers reviewed according to their investment discipline, the style of soft computing they used, the degree to which they demonstrated their success, and finally, their applicability as real world trading models.

Within the context of investment discipline, the survey shows that the majority of this type of research is being conducted in the field of Technical Analysis. As discussed in the survey, soft computing is particularly data intensive, and it is suggested that this observation goes someway to explaining this obvious bias in research.

Within the area of soft computing styles, the survey finds that the majority of research is within the area of both Hybrid systems, and Pattern Recognition and Classification. It is suggested the reason for this is that the technical analysis approach lends itself towards the pattern recognition and classification areas. Also, many hybrid systems include pattern recognition and classification as one of their constituents.

Perhaps the greatest difficulty in surveying this style of literature is to be found in classifying successes. Very few papers measure success in terms of outperforming a buy-and-hold approach. This measure is extremely important in this domain, as the majority of implementations can only be compared to each other in this way. There are a number of papers which demonstrate success within a very narrow time frame, or small data window, or indeed, propose several alternative models, and demonstrate one model to be superior to the other alternatives.

No research was found to be directly transferable to the non-academic arena, due to the lack of trading constraints implemented. Further, it was clear that a number of papers demonstrated results that could not be captured in practice. This was found, for example, in papers that demonstrated a superior return, but only in the absence of transaction costs. Earning a small return per transaction without taking transaction costs into account demonstrates a successful result. The effect of transaction costs upon such a system would be catastrophic. It is felt that this situation could be improved by implementing simple constraints such as ac-

[2] These papers did not implement trading systems, thus they had no need for money management techniques, or accounting for cost.

counting for transaction costs, and simple money management techniques to control position sizing.

REFERENCES

1. Tan, C.N.W., *Artificial Neural Networks: Applications in Financial Distress Prediction and Foreign Exchange Trading*. 2001, Gold Coast, QLD: Wilberto.
2. Chan, K.C.C. and K.T. Foo. *Enhancing Technical Analysis in the Forex market using Neural Networks.* in *IEEE International Conference on Neural Networks*. 1995.
3. Quah, T.-S. and B. Srinivasan. *Utilizing Neural Networks in Stock Pickings*. in *Proceedings of the International Conference on Artificial Intelligence*. 2000.
4. Yao, J. and H.-L. Poh. *Forecasting the KLSE index using Neural Networks*. in *IEEE International Conference on Neural Networks*. 1995.
5. Hobbs, A. and N.G. Bourbakis. *A Neurofuzzy Arbitrage Simulator for Stock Investing*. in *Computational Intelligence for Financial Engineering (CIFER)*. 1995. New York.
6. Austin, M., C. Looney, and J. Zhuo, *Security Market timing using Neural Network Models.* New Review of Applied Expert Systems, 1997. **3**: p. 3-14.
7. Falas, T., A. Charitou, and C. Charalambous. *The Application of Artificial Neural Networks in the Prediction of Earnings*. 1994. Orlando: IEEE.
8. Yamaguchi, T., *A Technical Analysis Expert System in the Stock Market.* Future Generation Computer Systems, 1989. **5**(1): p. 21-27.
9. Mizuno, H., et al., *Application of Neural Network To Technical Analysis of Stock Market Prediction.* Studies in Informatics and Control, 1998. **7**(2): p. 111-120.
10. Leus, M., et al. *GAs and Financial Analysis*. in *14th International Conference on Industrial Engineering Applications of Artificial Intelligence and Expert Systems*. 2001. Berlin.
11. Baba, N., et al. *Knowledge-Based Decision Support Systems for Dealing Nikkei-225 by Soft Computing Techniques*. in *Knowledge-Based Intelligent Information Engineering Systems and Allied Technologies KES 2001*. 2001: IOS Press, Netherlands.
12. Skabar, A. and I. Cloete. *Discovery of Financial Trading Rules*. in *Proceedings of the IASTED International Conference on Artificial Intelligence and Applications*. 2001.
13. Suh, Y.-H. and J.E. LaBarre, *An Application of Artificial Neural Network Models to Portfolio Selection.* Journal of Computer Information Systems, 1995. **36**(1): p. 65-73.
14. Fu, T.-C., et al. *Evolutionary Segmentation of Financial Time Series into Subsequences*. in *Proceedings of the 2001 Congress on Evolutionary Computation*. 2001.
15. Yasunobu, C., et al. *A Knowledge-Based Technical Analysis System for Financial Decision-Making*. in *Proceeding of Artificial Intelligence in the Pacific Rim*. 1991.
16. Kamijo, K. and T. Tanigawa. *Stock Price Pattern Recognition: A Recurrent Neural Network Approach*. in *Proceedings of the International Joint Conference on Neural Networks*. 1990.
17. Baba, N. and H. Handa. *Utilization of Neural Network for Constructing a User Friendly Decision Support System to Deal Stocks*. in *IEEE International Conference on Neural Networks*. 1995.
18. Baek, J. and S. Cho. *"Left Shoulder" Detection in Korea Composite Stock Price Index using an Auto-Associative Neural Network*. in *Intelligent Data Engineering and Automated Learning - IDEAL 2000: Data Mining, Financial Engineering and Intelligent Agents*. 2000.
19. Chen, A., C. Chianglin, and H. Chung, *Establishing an Index Arbitrage model by applying Neural Networks method - A case study of Nikkei 225 Index.* International Journal of Neural Systems, 2001. **11**(5): p. 489-496.
20. Tan, P.-Y. *Using Genetic Algorithm to optimize an oscillator-based market timing system*. in *Proceedings of the Second Singapore International Conference on Intelligent Systems SPICIS'94*. 1994. Singapore.
21. Lee, R.S.T. and J.N.K. Liu, *NORN Predictor - Stock Prediction using a neural oscillatory-based recurrant network.* International Journal of Computational Intelligence and Applications, 2001. **1,4**: p. 439-451.
22. Lam, K.P., K.C. Chiu, and W.G. Chan. *An embedded fuzzy knowledge base for technical analysis of stocks*. in *Neural Networks in Financial Engineering. Proceedings of the Third International Conference on Neural Networks in the Capital Markets*. 1996.
23. Liu, N.K. and K.K. Lee, *An Intelligent Business Advisor System for Stock Investment.* Expert Systems, 1997. **14**(3): p. 129-139.
24. Leigh, W., R. Purvis, and J.M. Ragusa, *Forecasting the NYSE composite index with technical analysis, pattern recognizer, neural network, and genetic algorithm: a case study in romantic decision support.* Decision Support Systems, 2002. **32**(4): p. 361-377.
25. Dourra, H. and P. Siy, *Investment using Technical Analysis and Fuzzy Logic.* Fuzzy Sets and Systems, 2002. **127**: p. 221-240.
26. Chou, S.-C.T., et al., *A Stock Selection DSS combining AI and Technical Analysis.* Annals of Operations Research, 1997. **75**: p. 335-353.
27. Baba, N., N. Inoue, and Y. Yanjun. *Utilization of Soft Computing Techniques for Contructing Reliable Decision Support Systems for Dealing Stocks*. in *IJCNN'02: Proceedings of the 2002 International Joint Conference on Neural Networks*. 2002. Honolulu, Hawaii.
28. Jang, G., et al. *An Intelligent Trend Prediction and Reversal Recognition System using Dual-Module Neural Networks*. in *First International Conference on Artificial Intelligence Applications on Wall Street*. 1991.
29. Wong, F. and D. Lee. *Hybrid Neural Network for Stock Selection*. in *The Second Annual International Confer-*

ence on Artificial Intelligence Applications on Wall Street. 1993. New York.

30. Chenoweth, T., Z. Obradovic, and S. Lee. *Technical Trading rules as a Prior Knowledge to a Neural Networks Prediction System for the S&P 500 Index*. in *IEEE Technical Applications Conference and Workshops*. 1995. Portland, Oregon.

31. Abdullah, M.H.L.b. and V. Ganapathy. *Neural Network Ensemble for Financial Trend Prediction*. in *Tencon 2000: Proceedings: Theme: Intelligent Systems and Technologies for the new millennium*. 2000.

32. Taylor, M.P. and H. Allen, *The Use of Technical Analysis in the Foreign Exchange Market.* Journal of International Money and Finance, 1992. **11**: p. 304-314.

33. Elder, A., *Trading for a Living*. 1993: John Wiley & Sons.

34. Babcock Jr., B., *The Dow Jones-Irwin Guide to Trading Systems*. 1989, Homewood, Illinois: Dow Jones-Irwin.

MEDICAL APPLICATIONS I

(This page left blank intentionally)

Highlighted Technical Paper B

Computer-Aided Diagnosis of Cerebral Aneurysm Based on Fuzzy Expert System: MR Angiography Study

Mika Ninomiya[1], Syoji Kobashi[1], Katsuya Kondo[1], Yutaka Hata[1], and Tomoharu Nakano[2]
[1]Graduate School of Engineering, Himeji Institute of Technology
2167, Shosha, Himeji, Hyogo, 671-2201, JAPAN
[2]Cancer and Thoracic Surgery, Graduate School of Medicine, Okayama University, JAPAN
ninomiya@comp.eng.himeji-tech.ac.jp

Abstract

MRA (magnetic resonance angiography) is a commonly used method for diagnosing unruptured cerebral aneurysms. In this paper, we introduce a novel computer-aided diagnosis (CAD) system for the cerebral aneurysm using MRA images. The proposed CAD system automatically finds candidates of the cerebral aneurysm, and then evaluates a fuzzy degree belonging to aneurysm whose size is more than a user-specified size. To find the aneurysm candidates, the normal model, which has no aneurysm, is estimated by using the cerebral arteries segmented from MRA images. Then the candidates are characterized by four features; variance, hemi-sphericity, mean MR signal value, and directional gradient concentration. The system then estimates the fuzzy degrees by using a feature value map generated by reference datasets. In the experiments, the proposed system was applied to eight patients with cerebral aneurysms. The four patients were used to make reference datasets, and the four patients were used to test the ability of finding cerebral aneurysms. The experimental results showed that our system gave the highest fuzzy degree for the cerebral aneurysm among the candidates in all cases except one case with small aneurysm.

1. Introduction

Cerebral aneurysms occur in the blood vessels (usually arteries) in the brain. Finding the aneurysms before they rupture is essential for prophylaxes of the subarachnoid hemorrhage, the cerebral infarction and so on. Wilcock et al. showed that magnetic resonance angiography (MRA) reliably detected aneurysms greater than a diameter of 5 mm [1]. According to Wiebers et al.'s findings, mean diameter of ruptured aneurysm was 7.5 mm [2]. It has been reported that long-term risk of rupture for aneurysm whose size is more than 10 mm is between 1 % and 2 % [3]. In addition, the risk of rupture correlates with the aneurysm size [4]. Thus, it is important to detect cerebral aneurysm with respect to the size of the aneurysm.

Several studies have been conducted on a computer aided-diagnosis (CAD) of aneurysm. They can be classified into (1) blood vessel segmentation [5][6], (2) volume rendering [7], (3) evaluation of blood velocity [8], and (4) automated detection of aneurysm. Especially, there are the related methods for detecting aneurysms. Kawata et al. have proposed a method for detecting the abdominal blood vessel disease [9]. An automated method for detecting the retinal microaneurysm has been proposed [10]. As related study to our interest, automated polyp detection has been studied [11]. However, they have not been applied to detecting cerebral aneurysms in MRA images. Moreover, there is no work on a CAD system to assist radiologists in finding cerebral aneurysms using MRA images.

The aim of this paper is to develop a CAD system, which supports radiologists to find the cerebral aneurysm. Because aneurysm is unspecified in size, shape, or location, it is difficult to realize a fully automated detection system. Therefore, our method detects aneurysm candidates and assigns the fuzzy degree belonging to various size of aneurysm. The aneurysm candidates are found by using a normal model, which is composed of normal arteries of the given subject before the aneurysms occur. The normal model is constructed by using the cerebral arteries segmented from MRA images. Assigning the fuzzy degrees is carried out on a feature value map generated by reference datasets. In the experiments, the proposed system was applied to eight patients.

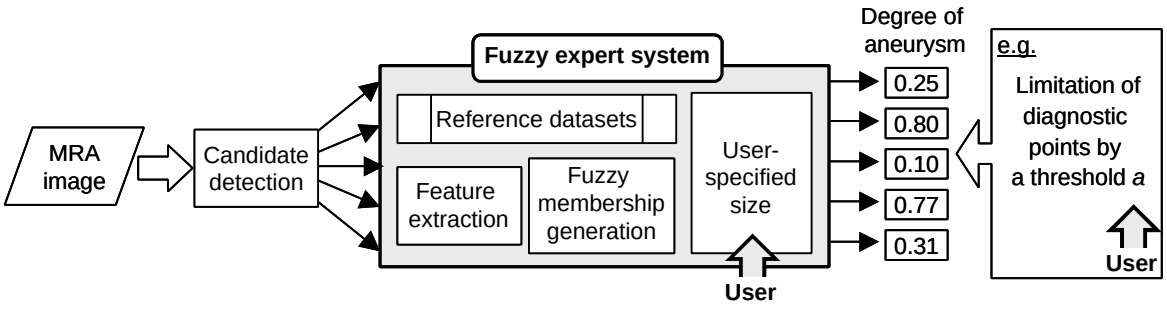

Figure 1. The proposed CAD scheme.

2. Materials

MRA images used in this study were acquired using a Genesis Signa 1.5 tesla MRI scanner (General Electric Medical Systems). The image acquisition method was 3-D time-of-flight (TOF) angiography with a repetition time (TR) of 25.0 msec and an echo time (TE) of 6.9 msec. A field of view was 160 mm. A matrix was 512 by 512, and the thickness of the slice was 1.2 mm. The dimension of the given voxel was 0.3125×0.3125×0.6 mm^3. Each of the volume data was composed of about 100 separated and volumetric slices taken from the axial plane. The intensity value for all voxels of all intracranial structure ranged between 0 and 4095. The subjects were eight volunteers with aneurysms. MRA datasets used in this experiment was converted into cubic voxels, that is, filled between axial slices by linear interpolation.

3. Methods

The risk of rupture of the aneurysm depends on its size. We propose a system to help radiologists find cerebral aneurysms whose size is greater than an arbitrary size that the radiologists want to find. The proposed CAD scheme is illustrated in Figure 1. This CAD system finds aneurysm candidates from MRA images of a given subject. For each candidate, the degree of aneurysm is assigned in the range of 0 to 1 by a fuzzy expert system. One means that the aneurysm candidate is completely the cerebral aneurysm. In the example illustrated in Figure 1, the system finds five aneurysm candidates, and assigns fuzzy degree for each candidate. Thus, users can diagnose only the aneurysm candidates with respect to the fuzzy degrees. This makes the users easily find the aneurysm because it is not necessary to observe the whole cerebral arteries. And the number of points to diagnose can be limited. For example, the number of points to diagnose can be controlled by changing a threshold value. That is, the users diagnose the aneurysm candidates whose fuzzy degree is higher than the threshold. In addition, the system estimates the fuzzy degrees belonging to the aneurysm whose size is more than an arbitrary size decided by the user. For example, when the user tries to find the aneurysms whose size is greater than 3.0 mm, our system gives the low fuzzy degree for the aneurysm whose size is smaller than 3.0 mm. In the following, we describe (1) finding of aneurysm candidates, (2) feature extraction, and (3) fuzzy expert system.

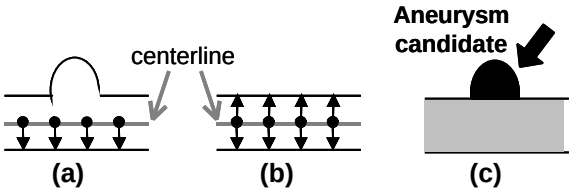

Figure 2. (a) Segmented arteries image and the centerline is described in the gray line. (b) The normal model by dilating the centerline. (c) Aneurysm candidate obtained by subtracting the normal model (a) from the segmented arteries (b).

3.1. Aneurysm candidates

We assume a normal model to extract aneurysm candidates. The normal model is composed of normal arteries of the given subject before the aneurysms occur. Thus, the normal model is generated for the individual subject. Finding the aneurysm candidate from an MRA dataset is performed with four steps. At the first step, arteries are extracted by means of an automated artery extraction method proposed by Kobashi et al. [5]. The method gives 3-D binary images in which the voxels of segmented arteries are 1 and the others are 0. The second step skeletonizes the 3-D binary image using Saito and Toriwaki's method [12], and then gives the centerlines of arteries. At the third step, the normal model is genelated using the centreline and radius of the arteries. Assume an example of constructing the normal model illustrated in Figure 2. For each voxel of the centrelines, we define the radius of the arteries to be the Euclidean distance from the voxel to the nearest background voxel as shown in Figure 2(a). So, in the case of the aneurysm, the normal radius before the aneurysm occurs can be approximated. Next, the centrelines are dilated so that the radius of centrelines becomes the approximated normal radius for

each voxel of the centrelines as shown in Figure 2(b). We call the dilated centrelines as the normal model. Finally, aneurysm candidates are found by subtracting the normal model from the arteries segmented at the first step as shown in Figure 2(c).

3.2. Feature Extraction

To characterize the aneurysm candidates, we introduce four features, *variance*, *hemi-sphericity*, *mean MR signal value*, and *directional gradient concentration*. Each feature value is normalized by

$$z_i = \frac{F_i - a_i}{s_i}; \quad (i = 1,\ldots,4) \tag{1}$$

where F_i, a_i, and s_i are the ith extracted feature value, the average value and the standard deviation, respectively.

[Feature 1] ***Variance*****:** All voxels of the candidate are assigned the Euclidean distance from the voxel to the nearest voxel of normal model. The method then constructs Euclidean distance histogram of aneurysm candidate. Using the histogram, we define the *variance* of the histogram as a feature value. To demonstrate the effectiveness of this feature value, assume three candidates shown in Figure 3. In this example, the first candidate shown in (a-1) is the aneurysm that is called as true-positive (TP), the second and the third candidates shown in (b-1) and (c-1) are quasi aneurysms that are called false-positive (FP). In the case of the second candidate, *variance* is too small (b-2). This is due to errors of the normal model assumption. In contrast, in the case of the third candidate, *variance* is too large (c-3). This is due to an overextraction in the artery extraction process.

[Feature 2] ***Hemi-sphericity*****:** The shape of the aneurysm should be like a hemisphere. We define a feature of hemi-sphericity as:

$$HS = \sqrt[3]{\frac{V_C}{V_{CHS}}} \tag{2}$$

where V_C is the volume of the aneurysm candidate. V_{CHS} is the volume of a hemisphere, which circumscribes the aneurysm candidate.

[Feature 3] ***Mean MR signal value*****:** The voxels of aneurysm have similar intensity to the voxels of the arteries because aneurysm is a part of the arteries. Mean intensity value of the aneurysm candidate of interest is calculated as the third feature.

[Feature 4] ***Directional gradient concentration*****:** Generally, the shape of aneurysms appearing on the arteries wall is hemispherical. In the hemisphere, gradient vectors of the intensity map point toward the center of a sphere, which is estimated by using the hemisphere as shown in Figure 4. Therefore, we employ the *directional gradient concentration* (*DGC*) feature [11]. The *DGC* feature is computed by

$$DGC(p) = \frac{1}{2N}\sum_{i=1}^{N/2}\begin{cases}\left|e_i^{\max}(p) - e_{i+N/2}^{\max}(p)\right|; & e_i^{\max}(p), e_{i+N/2}^{\max}(p) > 0 \\ e_i^{\max}(p) + e_{i+N/2}^{\max}(p); & \textit{otherwise.}\end{cases}, \tag{3}$$

$$e_i^{\max}(p) = \max_{R_{\min} \le n \le R_{\max}}\left\{\frac{1}{n - R_{\min} + 1}\sum_{j=R_{\min}}^{n}\cos y_{ij}(p)\right\},$$

where p is a voxel of the aneurysm candidate, and N is the number of the 3-D symmetric directions that is used for computing the response. The value $e_i^{\max}(p)$ is the maximum gradient concentration between $R_{\min}$ and $R_{\max}$. As illustrated in Figure 5, the angle $y_{ij}(p)$ is the angle between the direction vector $\overrightarrow{D_i}$ and a gradient vector $\vec{g}_j$ located at distance j from p. Also, $e_i^{\max}(p)$ and $e_{i+N/2}^{\max}(p)$ are computed from the opposite directions, $\overrightarrow{D_i}$ and $\overrightarrow{D_{i+N/2}}$. In comparison with the second feature, *hemi-sphericity*, this feature value gives the information about a hemisphere like based on the intensity values.

3.3. Fuzzy expert system

In this section, we propose a fuzzy expert system. The

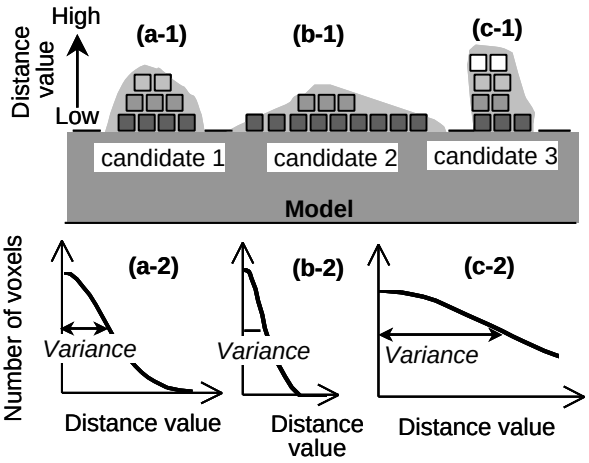

Figure 3. (a) TP candidate. (b) FP candidate due to overextraction. (c) FP candidate due to errors of the normal model assumption.

Figure 4. An example of gradient vector distribution in a hemispherical density.

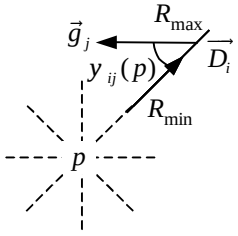

Figure 5. The angle between $\overrightarrow{D_i}$ and $\vec{g}_j$ for computation of in each direction.

fuzzy degrees are given by evaluating the similarity of the candidate to the reference datasets.

The reference datasets, which are constructed by an expert preliminary, are a set of feature values, the size, and the labeled instance (TP or FP) of the aneurysm candidates. The instance, TP, means an expert instructs that the candidate is the aneurysm. In contrast, the instance, FP, means the expert instructs the candidate is NOT the aneurysm. In the following, we call the reference datasets of TP and FP are TP object and FP object, respectively. The reference datasets are obtained from MRA images by candidate detection, feature extraction, and instance labeling. The instance of each candidate is given by the expert. Note that there are various sizes of TP objects.

For each candidate, a fuzzy degree belonging to each TP object is calculated as below. First, Euclidian distance values from the feature vector of the candidate to that of each reference data are computed. For explanation of estimating the fuzzy degree, consider a feature vector map of the reference data illustrated in Figure 6. This is an example of the feature map in the case of 2-D space. In this figure, the values d_{T1}, …, d_{Tn} (n: the number of TP objects) are the distances to each TP object, and d_F is to the nearest FP object. Using the distance values, we estimate a fuzzy degree belonging to the ith TP object, m_{T1}, …, m_{Ti}, (i = 1, …, n) by:

$$m_{Ti} = \frac{1}{1+e^{-c_1(r_{Ti}-0.5)}}, \quad r_{Ti} = \frac{d_F}{d_F + d_{Ti}}, \qquad (4)$$

where c_1 is a parameter that controls fuzziness (c_1 = 10 is used in this experiment). Figure 7 gives an example of Eq. 4. As shown in this figure, if the distance from the candidate to the ith TP object is d_{Ti}, the fuzzy degree is m_{Ti}. That is, the shorter distance gives the higher fuzzy degree. By applying Eq. 4 for all TP objects, we can obtain fuzzy degrees belonging to for each TP object.

Using the fuzzy degrees, a membership function illustrated in Figure 8 is given by:

$$f_T(D) = f_{T1}(D) \cup f_{T2}(D) \cup \cdots \cup f_{Ti}(D),$$
$$f_{Ti}(D) = m_{Ti} \cdot \exp\left(\frac{-(D - D_{Ti})^2}{b^2} \right), \qquad (5)$$

where D_{Ti} is the size of the ith TP, and b is a parameter for fuzziness (b = 30 in this experiment). This membership function gives a change of fuzzy degree according to the size of aneurysm. Thus, using the membership function, we can obtain a fuzzy degree belonging to an arbitrary size of the aneurysm.

Finally, this system calculates a fuzzy degree, $m_{aneurysm}$, belonging to the aneurysm whose size is greater than a user-specified size. For a candidate of interest, the aneurysm degree $m_{aneurysm}$ is given by:

$$m_{aneurysm} = \max\left(f_T(D) \times g(D) \right),$$
$$g(D) = \begin{cases} \exp\left(\dfrac{-(D - D_{object})^2}{b^2} \right); & 0 \le D \le D_{object} \\ 1; & D_{object} < D \end{cases}. \qquad (6)$$

where D_{object} is a size specified by the users. The example is illustrated in Figure 9. The difference between this

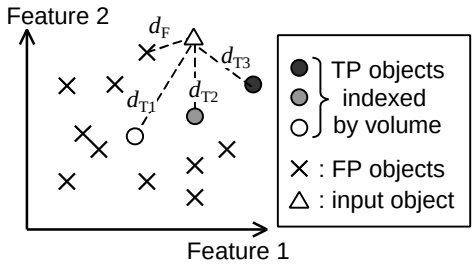

Figure 6. An example of the feature values map of the reference data.

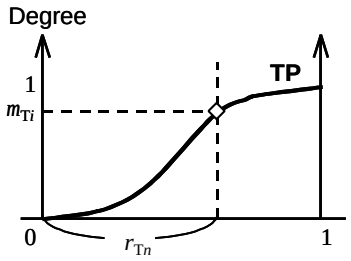

Figure 7. The degree of the *i*th TP.

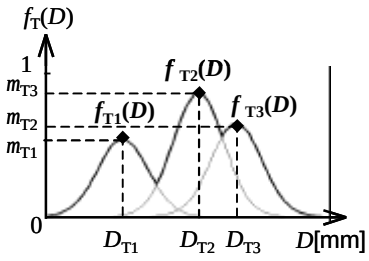

Figure 8. The membership function of the degree of TP.

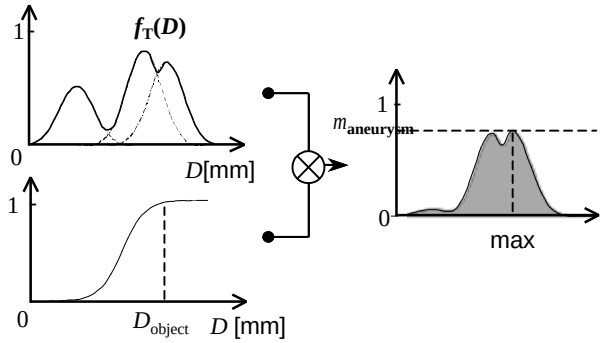

Figure 9. The aneurysm degree.

Table 1

(a) The TP feature values.

TP#	*Variance*	*Hemi-Sphericity*	*Mean MR value*	*DGC*
1	4.20	0.771	199.2	0.144
2	6.40	0.904	182.5	0.143
3	11.4	0.661	194.5	0.141
4	11.9	0.703	175.8	0.139

(b) Normalization parameters.

	Variance	*Hemi-Sphericity*	*Mean MR value*	*DGC*
a	4.91	0.608	154.6	0.135
s	5.15	0.173	24.22	0.008

fuzzy degree, $m_{aneurysm}$, and the fuzzy membership function defined above is that $m_{aneurysm}$ gives a fuzzy degree belonging to the aneurysm whose size is greater than a given by a user, and the membership functions give a fuzzy degree belonging to the aneurysm for each size.

4. Results and discussion

We applied the proposed method to MRA datasets of eight patients with aneurysms. The four MRA datasets were used to make reference datasets, and the another four MRA datasets were used to test the ability of finding cerebral aneurysms. 22 reference datasets were obtained from four MRA datasets by candidate detection and feature extraction. The reference data consisted of 4 TP objects and 18 FP objects. Table 1 tabulates the feature values of TP objects and the normalization parameters. Table 1 showed that the feature values of TP objects were obtained within a constraint range.

The MRA datasets of the four patients (subject 1, 2, 3, and 4) for testing were analyzed by the proposed system. Figure 10 shows a part of results of candidate detection for subject 1. In this case, three candidates including one aneurysm (candidate 3) and two mis-findings (candidates 1,2) were obtained. The membership function f_T for each candidate is shown in Figure 11. As shown in these figures, we found that the f_T of the aneurysm (candidate 3) was higher than that of the other mis-finding (candidates 1,2). Figure 12 shows the maximum fuzzy degree distribution of all aneurysm candidates for each subject. The ground-truth aneurysms in the candidates were given by a radiologist for evaluation. The fuzzy degree of the ground-truth aneurisms are denoted by a white allow in the maximum fuzzy degree distribution. In this result, our system gave the highest fuzzy degree for the ground-truth aneurysms among the candidates in all cases except the subject 2. In the case of subject 2, the fuzzy degree of the ground-truth aneurysm was poorly estimated because the number of the reference datasets used in this experiment is very small and there is no reference dataset corresponding to the aneurysm in the subject 2.

Figure 13 shows the aneurysm candidates whose fuzzy degree is the highest in the candidates for subject 1 and 4. The size to derive the resultant fuzzy degree was set at 4 mm. The aneurysm candidates with the highest fuzzy degree were equal to the ground-truth aneurysms given by the radiologist. The size of the candidate in subject 1

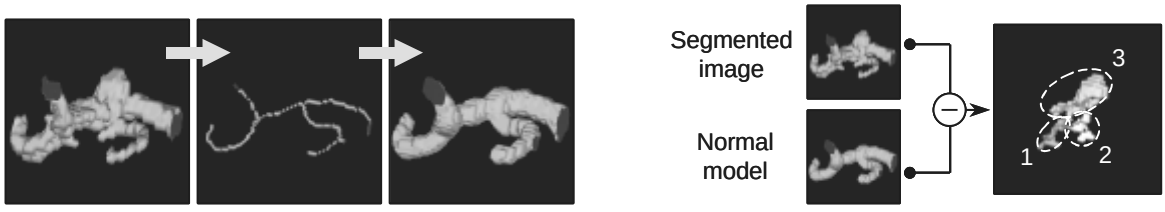

Figure 10. (a) Segmented arteries. (b)Skeletonized image. (c) Normal model. (d) Three aneurysm candidates were found.

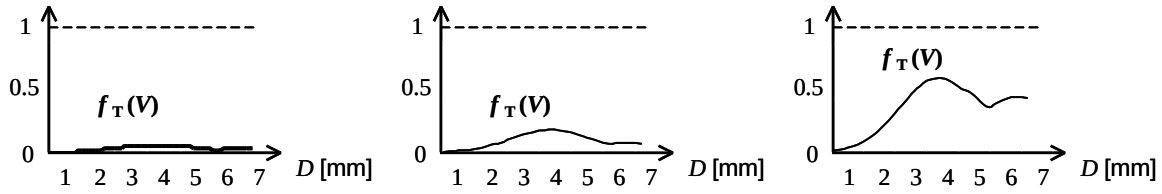

(a) Candidate 1. **(b) Candidate 2.** **(c) Candidate 3.**

Figure 11. The membership function f_T. (a) and (b) are the FP candidates. (c) is the TP candidate.

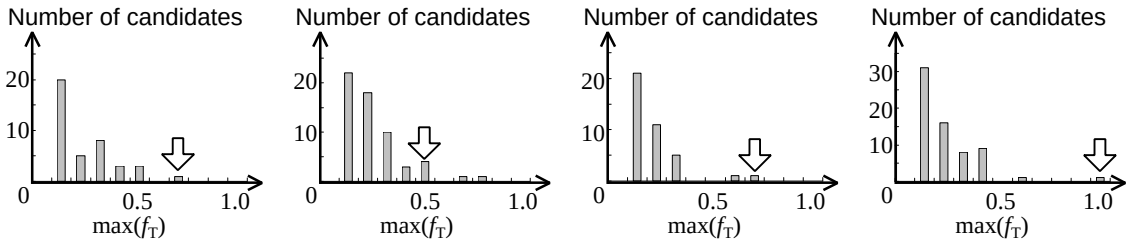

(a) Subject 1. **(b) Subject 2.** **(c) Subject 3.** **(d) Subject 4.**

Figure 12. Fuzzy degree distribution of aneurysm candidates.

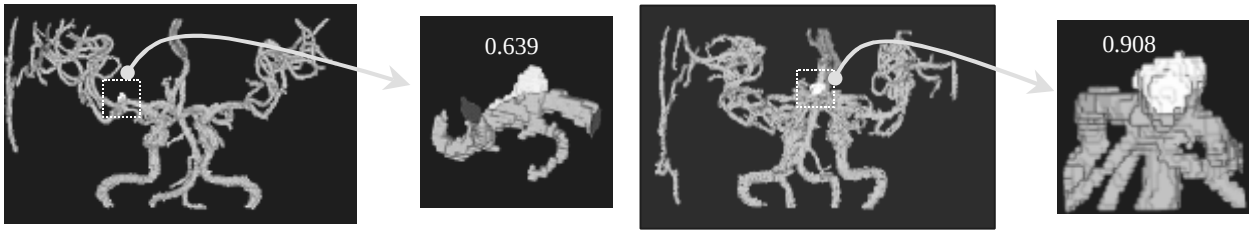

(a) Subject 1 **(b) Subject 4.**

Figure 13. Illustration of the detection of aneurysm.

and 4 are 4.1mm and 6.0mm, respectively. These results indicate that the proposed system gave high fuzzy degrees for the aneurysm in spite of little number of the reference datasets. The accuracy will be more improved with an increase in the number of the reference datasets.

5. Conclusions

We have proposed a novel CAD system for finding aneurysms using MRA images. The CAD system estimates a fuzzy degree belonging to aneurysms whose size is greater than a user specified size by using reference datasets. The experimental results confirmed that high fuzzy degrees were given for the ground-truth aneurysms. Thus, the proposed system strongly assists radiologists to find the cerebral aneurysm from the MRA images but the radiologists investigates the all sectional images or all points of the arteries. The feature of the proposed system is that it can be applied to entire cerebral arteries independent of the shape, and can limit the aneurysm candidates on the size of user's demand. It should be noted that our method is efficient to assist diagnosis of cerebral aneurysm. It remains us to evaluate the proposed system using the large number of subjects.

Acknowledgement

This work was supported in part by a grant from Ishikawa Hospital Grant, a grant from the Ministry of Education, Culture, Sports, Science and Technology, a Grant-in-Aid for Encouragement of Young Scientists (15700198, 2003), a research grant from Telecommunications Advancement Foundation, and the Berkeley Initiative in Soft Computing (BISC) Program of the University of California at Berkeley.

References

[1] D. Winlock, T. Jaspan, I. Holland, G. Cherryman, and B. Worthington, "Comparison of magnetic resonance angiography with conventional angiography in the detection of intracranial aneurysms in patients presenting with subarachnoid hemorrhage." *Clin Radiol*, 51:330-334, 1996.

[2] DO. Wiebers, JP. Whisnant, TM. Sundt Jr and WM. O'Fallon "The significance of unruptured intracranial saccular aneurysms," *J Neurosurg*, 66:23-29, 1987.

[3] "Unruptured intracranial aneurysms--risk of rupture and risks of surgical intervention. International Study of Unruptured Intracranial Aneurysms Investigators." *N Engl J Med*, 339:1725-33, 1998.

[4] J. Rosenorn and V. Eskesen, "Does a safe size limit exist for unruptured intracranial aneurysms?," *D Acta Neurochir (Wien)*, 121:113-118, 1993.

[5] S. Kobashi, N. Kamiura, Y. Hata and F. Miyawaki, "Volume Quantization Based Neural Network Approach to 3D MR Angiography Image Segmentation," *Image and Vision Computing*, 19(4):185-193, 2001.

[6] A. C. Chung, J. A. Noble, and P. Summers, "Fushing speed and phase information for vascular segmentation of phase contrast MR angiography," *Medical Image Analysis*, 6(2):109-128, 2002.

[7] A. Huber, M. Matzko, B. J. Wintersperger, and M. Reiser, "Reconstruction methods in postprocessing of CT- and MR-angiography of the aorta," *Radiologe*, 41(8):689-694, 2001.

[8] N. Fatouraee, and A. A. Amini, "Regularization of flow streamlines in multislice phase-contrast MR imaging," *IEEE Transaction on Medical Imaging*, 22(6):699-709, 2003.

[9] Y. Kawata, N. Niki, and T. Kumazaki, "Measurement of blood vessel characteristics for disease detection based on cone-beam CT images," *IEEE Transactions on Nuclear Science*, 43(6):3348-3354, 1996.

[10] S. Abdelazeem, "Micro-aneurysm detection using vessels removal and circular Hough transfer," *Radio Science Conference, Proceedings of the Nineteenth National*, 421-426, 2002.

[11] J. Nappi and H. Yoshida, "Automated detection of polyps with CT colonagraphy: Evaluation of volumetric feature for reduction of false-positive findings," *Academic Radiology*, 9(4):386-397, 2002.

[12] T. Saito and J. Toriwaki, "A sequential thinning algorithm for three dimensional digital pictures using the Euclidean distance transformation," *Proceedings of 8th Scandinavian Conference, Image Analysis*, 507-516, 1995.

Heart-Beat Signal Extraction From Phonocardiograms

A. Bouzerdoum, M. A. Tinati*

Edith Cowan University, Perth, WA, Australia
*University of Tabriz, Iran

Abstract: This article introduces a method for constructing a heart-beat signal from a long record of phonocardiogram (PCG). The method comprises a series of algorithms that decompose a long data record of heart sound to its heart-beat cycles using the simultaneously recorded electrocardiogram (ECG). First the cardiac cycles are identified using the synchronized ECG signal. The corresponding heart-beat cycles are then extracted from the PCG signal and used to construct a template signal. Using the correlation of the heart-beat signals with the template signal, the heart-beats corrupted by noise are identified and discarded. The remaining heart-beats are then used to construct a heart-beat signal which is free of artefacts and can be used for various heart sound analysis purposes.

1 INTRODUCTION

A phonocardiogram (PCG) is a recording of an acoustic wave produced by periodical contractions and relaxation of the heart muscles along with acceleration and deceleration of blood within the cardiac structure. The sequence of events occurring during such activities is called the cardiac cycle. Each cardiac cycle is categorized into four basic groups: first, second, third, and forth heart sounds [1]. Phonocardiograms have been studied for diagnostic purposes for various heart diseases [2]-[5]; and also for better understanding of heart sounds [6]-[8].

The PCG signals are oscillatory in nature; although it may not be exactly periodic in strict mathematical sense. Observation of the evolution of these signals reveals that there are similar events or periods, but they may not exactly reproduce themselves. Furthermore, phonocardiograms are quasi-stationary signals; consequently, their characteristics do not change drastically within few minutes of recordings.

However, analyzing long data records of PCG signals using some signal processing techniques such as time-frequency or wavelet methods imposes a huge computational burden. The heart-beat signal extraction technique presented herein can be used to obtain a single heart-beat signal encapsulating the characteristics of the PCG signal. The extracted heart-beat signal can then be used for analysis or diagnostic purposes.

The proposed heart-beat signal extraction technique is explained in the succeeding two sections. First the electrocardiogram beat cycle detection algorithm is introduced in Section 2. In Section 3, the segmentation of the PCG signal and the reconstruction of a single heart-beat signal are explained. Then in Section 4 experimental results are presented, followed by a concluding remarks in Section 5.

2 HEART-BEAT CYCLE DETECTION

The central idea of the proposed heart-beat separation scheme is the decomposition of phonocardiograms into heart-beat signals through the detection of the heart-beat cycles of the synchronized electrocardiograms; beat cycle detection is easier using ECG signals. In order to accomplish this, first the QRS peaks of the ECG signal are detected, and then the corresponding beat cycles are identified.

2.1 QRS Peak Detection

QRS detection is one of the important tasks in ECG analysis; a great deal of research effort has been devoted to this task [2]. Most of the QRS detectors described in the literature are aimed for analysis of the ECG signal itself. Our aim, however, is to find the temporal location of the peaks of the QRS complexes and use them to separate the heart-beat cycles from the PCG signal. Our QRS detection scheme is divided into two sub-systems: the preprocessor and the decision rule system, as shown in Figure 1. The main concern in the QRS detector is to avoid detection of false peaks, if any.

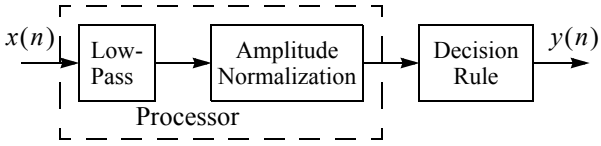

Figure 1 QRS peak detector.

Figure 2 shows the QRS detection algorithm. The input signal, $S_{ecg}(t)$, is initially normalized in amplitude. This is essential since a thresholding scheme is employed for detection of peaks of the QRS complexes. There are usually some fluctuations in the QRS amplitudes, hence the threshold level is set to a value V_{th} given in Eq. (1).

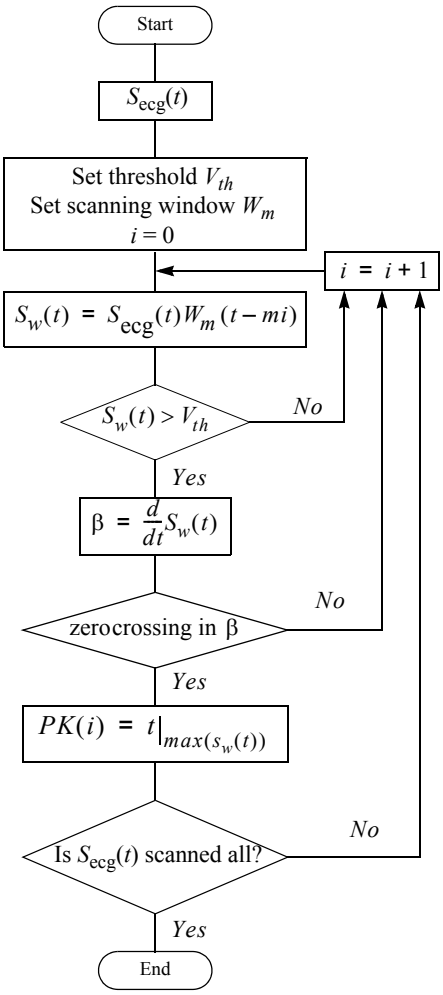

Figure 2 QRS peak detection algorithm.

$$0.8 \le V_{th} \le 1 \tag{1}$$

The input data is scanned with a rectangular window the width of which is much less than a heart-beat period, whose length could vary from about half a second to more than one second depending on the person. A small window size reduces the possibility of missing any QRS peaks during the scanning process. Within each window the parts of the data that are above threshold are selected and their maximum value is found. The thresholding scheme ensures that only regions of the signal that are in the vicinity of the peak of the QRS complex are considered for peak detection. In Figure 3 shows one cycle of an ECG signal with threshold level V_{th} and a scanning window W_m of length m.

In order to distinguish and locate the position of the actual QRS peak, the slope of the signal above threshold is calculated within each window. Let $W_m(t - mi)$ be the ith window and $S_{ecg}(t)$ be the portion of the QRS

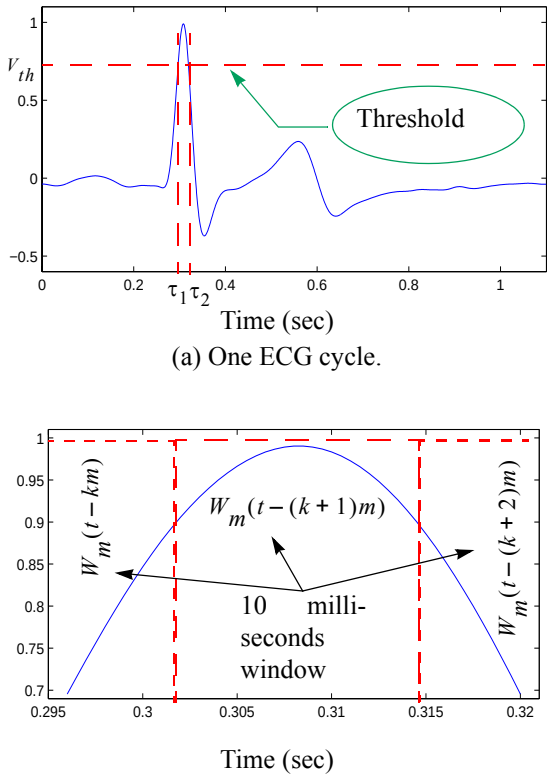

(a) One ECG cycle.

(b) Peak of QRS Complex.

Figure 3 The process of thersholing and windowing the ECG signal.

complex above threshold. The slope of the windowed ECG signal above threshold level is

$$\beta_i(t) = \frac{d}{dt}[S_{ecg}(t)W_m(t - mi)] \tag{2}$$

The zero crossing in $\beta_i(t)$ represents a local maximum in the ECG signal, i.e., a potential QRS peak.

2.2 True QRS Interval Detection

The primary objective of the true QRS interval detection is to ensure that the peaks detected with the algorithm of Figure 2 are real QRS peaks; that is, we want to identify any false detections and remove them. There are two situations in which a false detection may occur: a presence of an artefact whose height is higher than the threshold level, or the presence of small fluctuations (due to noise) near the QRS peak.

The mean interspike (i.e., QRS peak-to-peak) interval is calculated as

$$T = \frac{1}{M-1}\sum_{j=1}^{M-1} PK(j+1) - PK(j) \tag{3}$$

where M is the number of detected QRS peaks, and PK is a vector containing the locations of the QRS peaks. We define the minimum and the maximum acceptable time interval between two consecutive QRS peaks as:

$$\Delta T_{\text{mn}} = T - 0.1T \tag{4}$$

$$\Delta T_{\text{mx}} = T + 0.1T \tag{5}$$

The average interval between the ith peak and its nearest neighbours is calculated as follows:

$$\delta t_i = \frac{\Delta t_i + \Delta t_{i+1}}{2} \tag{6}$$

where Δt_i and Δt_{i+1} are the time intervals between the ith peak and its preceding and succeeding peaks, respectively; that is,

$$\Delta t_i = PK(i) - PK(i-1) \tag{7}$$

$$\Delta t_{i+1} = PK(i+1) - PK(i) \tag{8}$$

The interval, δt_i, for every detected peak is compared with ΔT_{mx} and ΔT_{mn}. If it is within the interval $[\Delta T_{\text{mn}}, \Delta T_{\text{mx}}]$, it is accepted as a true QRS peak, otherwise it is considered to be a false peak, and hence rejected. That is, for a true QRS peak, Eq. (9) must be satisfied.

$$\Delta T_{\text{mn}} \le \delta t_i \le \Delta T_{\text{mx}} \tag{9}$$

When a false QRS peak occurs at position i, the value of its average interval δt_i, and possibly those of adjacent peaks, will not satisfy Eq. (9). In particular, there will be a local valley centred on i in the values of the vector δt, the vector whose elements are the intervals δt_i. In order to find the location of the false QRS peak, it is necessary to find the position of the bottom of the valley. This is accomplished by calculating the derivative of the vecotr δt and finding the position at which the derivative becomes zero. The proposed QRS interval detection algorithm is shown in Figure 4.

2.3 ECG Beat Cycle Detection

In order to detect the beat cycles, the beginning of each cardiac cycle with respect to QRS peaks must be identified. The P-wave is chosen as the beginning of the cardiac cycle. If the time interval between two consecutive QRS peaks is divided into three sections, the P-wave occurs in the third section. The onset of the third section of the ith QRS peak is given by Eq. (10).

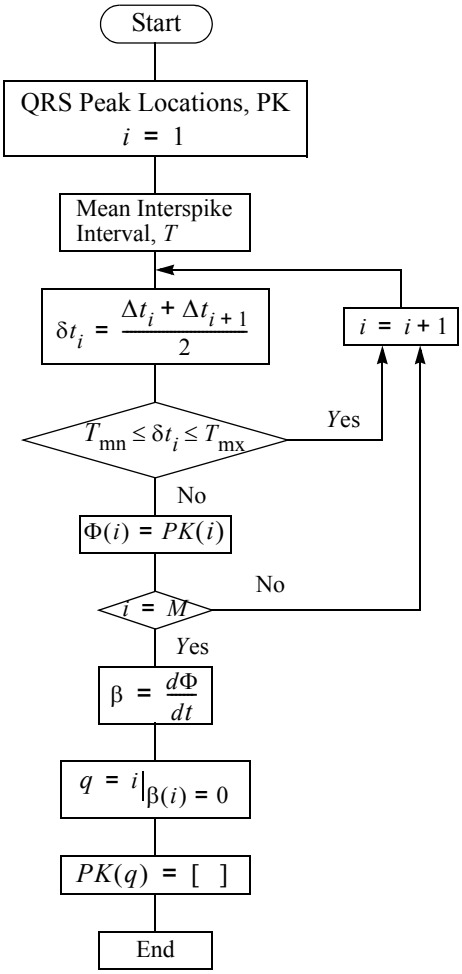

Figure 4 QRS interval detection algorithm.

$$tr_i = PK(i) - \frac{1}{3}[PK(i) - PK(i-1)] \tag{10}$$

where its offset time is the ith entry in the vector PK. This is illustrated in Figure 5.

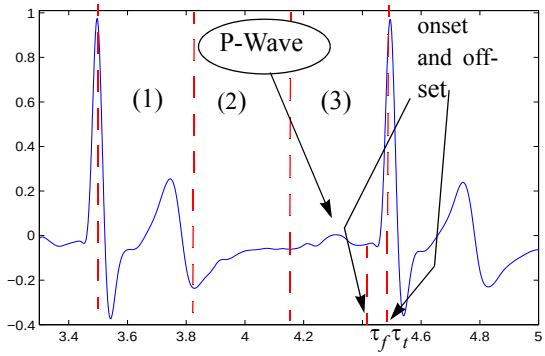

Figure 5 Two consecutive cycles of ECG signal for P-wave recognition.

Since we are going to use the QRS peak detector to find the peaks of the P-waves, it is essential to remove the portion of the QRS complex that falls within section three. This is the part of the signal between τ_f and τ_t in Figure 5. This is accomplished by calculating the slope of the signal from tr_i to PK_i as:

$$\text{mp}_i = \frac{d}{dt} S_{\text{ecg}}(t) \quad \text{for} \quad tr_i \le t \le PK(i) \tag{11}$$

The signal mp_i is scanned in a bottom-up fashion; that is, scanning starts from the end and proceeds towards the beginning. When the first zero crossing is encountered, the scanning is stopped. This point corresponds to the first minimum in the signal just before the QRS complex. The part of the signal to the right of the zero crossing is discarded. In order to detect the peak of the P-wave, the algorithms of Figure 2 and 4 are applied to the remaining part of the signal. This process is repeated for all detected QRS intervals. The final outcome is a vector the same size as the ECG signal $S_{\text{ecg}}(t)$, the elements of which are all zeros except at the locations of the P-wave peaks, where a value of one is recorde. The flow chart of this algorithm is shown in Figure 6.

3 SEGMENTATION OF PCG SIGNAL

The prime purpose for developing the QRS detection algorithm was to devise a scheme which would enable us to decompose the PCG signal into its beat cycles with minimum error of miss-detection. As was mentioned earlier, the ECG and PCG signals must be recorded simultaneously. Therefore, the decomposition process of the PCG signal into its constituent beat cycles can be accomplished by simply aligning it with the signal obtained by the algorithm of Figure 6, $v_{\text{ecg}}(t)$, which is a train of impulses located at the starts of the cardiac cycles.

3.1 Identification of Artefact-Free Beat Cycles

Among the separated heart-beat cycles, it is necessary to identify and discard those cycles that contain artefacts. Let each PCG heart-beat signal be denoted by $S^i_{\text{pcg}}(t)$, where i is the order of the beat cycle within the PCG signal. A correlation scheme is devised to distinguish the artefact-free heart-beat cycles within the PCG signal. A template signal is constructed for this purpose, and every beat cycle is compared with it. The template signal, $S_{\text{tmp}}(t)$ is constructed by taking the ensemble average of all the beat cycles.

$$S_{\text{tmp}}(t) = \frac{1}{M} \sum_{i=1}^{M} S^i_{\text{pcg}}(t) \tag{12}$$

where M is the total number of heart-beat cycles.

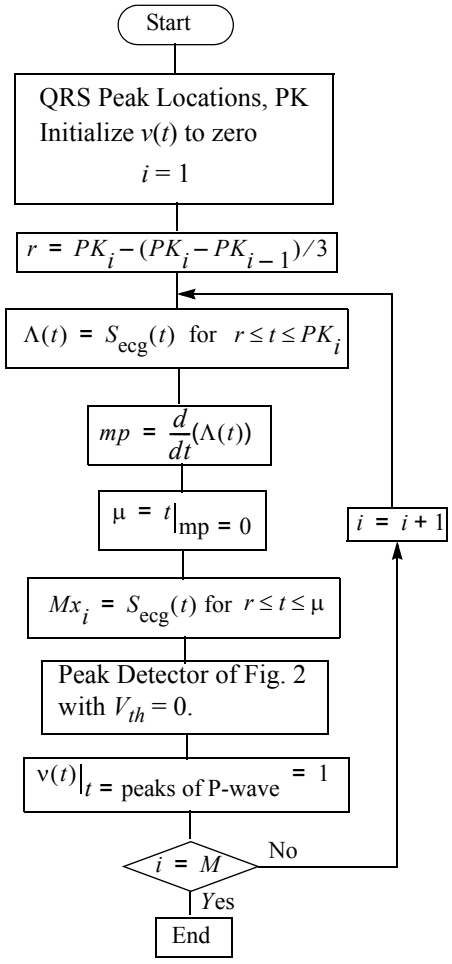

Figure 6 ECG beat cycle detection.

The degree of similarity between the beat cycle waveforms and this template signal is measured by calculating the correlation coefficient of the template signal with each of the beat cycles. The correlation coefficient between the template signal and a given beat cycle is defined as

$$\rho = \frac{C_{\text{tmp, btc}}}{\sqrt{C_{\text{tmp}} \times C_{\text{btc}}}} \tag{13}$$

where $C_{\text{tmp, btc}}$ is the cross-covariance between the template signal and the beat cycles, C_{tmp} and C_{btc} are, respectively, the covariances of the template signal and the beat cycle.

In order to obtain the maximum correlation coefficient possible, the beat cycle is shifted with respect to the template signal. In other words, the correlation coefficient is computed at the smallest time-lag which yields maximum cross-correlation between the two signals.

The cross-correlation of the template signal with the beat cycle is defined as

$$X(\tau) = \sum_{n=0}^{N} S_{\text{tmp}}(n) S_{\text{btc}}(n-\tau) \qquad (14)$$

where N is the length the template signal, which is equalt to the length of the beat cycle.

In order to identify the beat cycles corrupted with artefacts, a threshold level for the correlation coefficients is set to 0.9; that is, those beat cycles that have their correlation coefficient below 90% of the maximum correlation coefficient are rejected.

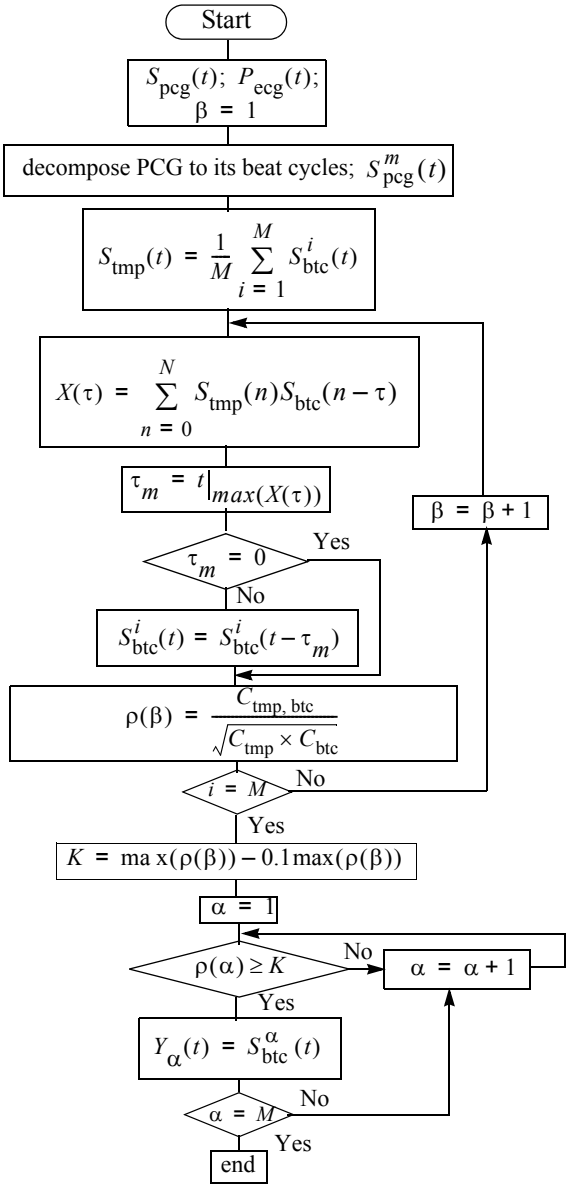

Figure 7 Heart-beat construction algorithm.

3.2 The Heart-beat signal

The final heart-beat signal is reconstructed using only the artefact free beat cycles. The mean signal of the beat cycles is computed in the frequency domain. Frequency domain averaging is used to avoid errors that may occur due to small miss-alignments of the beat cycles in the time domain. To obtain the time domain signal, the averaged frequency domain signal is converted back to the time domain using the inverse discrete Fourier transform (IDFT). The heart-beat cycle reconstruction algorithm is presented in Figure 7.

4 RESULTS

In this section we present the results of applying the algorithms presented in this article to real signals recorded from patients suspected with coronary artery disease. Thirty seconds of synchronously recorded PCG and ECG signals are shown in Figure 8 below; clearly the PCG signal contains some artefacts.

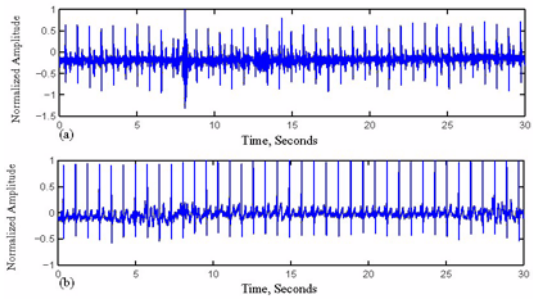

Figure 8 Synchronously recorded PCG (a) and ECG (b) signals.

The ECG signal was scanned with a 10 millisecond long rectangular window. A threshold level of 0.8 was selected, and the QRS detection algorithm was applied. The detected QRS peaks were examined with the algorithm of Figure 4 for false detections. Then the starting points of the cardiac cycles were detected using the ECG beat-cycle detection algorithm (Figure 6). The output of the ECG cycle detection algorithm, the signal $\nu_{\text{ecg}}(t)$, is shown in Figure 9.

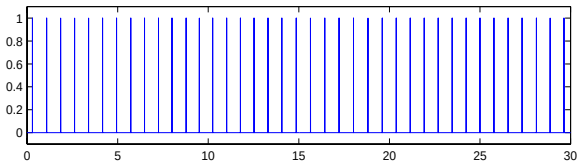

Figure 9 The signal $\nu_{\text{ecg}}(t)$ obtained from the ECG beat-cycle detection algorithm.

The PCG cardiac cycles were separated by aligning the PCG signal (Figure 8(a)) with the signal $v_{ecg}(t)$ of Figure 9. These extracted PCG cardiac cycles, shown in Figure 10(a), were then used to reconstruct the PCG template signal presented in Figure 10(b).

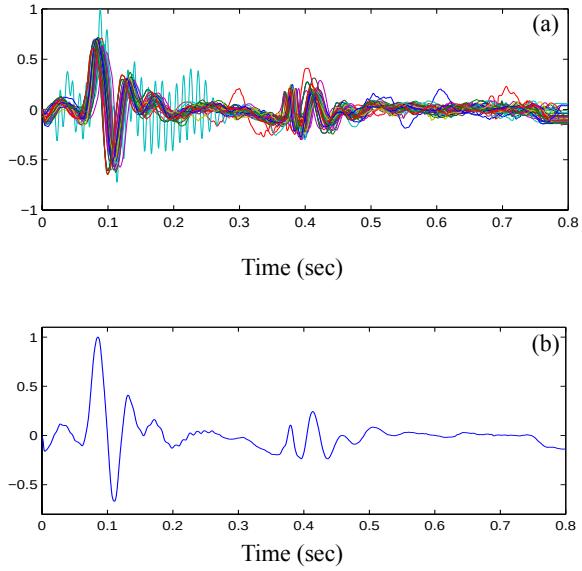

Figure 10 (a) Beat cycles of PCG signal of Figure 8 (a). (b) PCG template signal.

The correlation coefficients of the template signal of Figure 10(b) with each beat cycle of Figure 10(a) were calculated; the computed correlation coefficients are tabulated below (TABLE 1) and plotted in Figure 11. In Table 1, four correlation coefficients fall below 0.9, but one of them is equal to 0.8946), very close to 0.9. If the threshold level is set at 0.88, as shown in Figure 10, only tree beat cycles that have their correlation coefficients below the threshold level, and hence are rejected. Figure 12 illustrates the accepted and rejected PCG beat cycles. The final heart-beat cycle is constructed using only the artefact free beat cycles as described in Section 3.2. The final PCG beat signal is presented in Figure 13. It is an artefact free signal, which represents the typical heart-beat cycle of the person from who the signal was recorded.

TABLE 1 – Correlation coefficients of PCG template signal with individual beat cycles.

0.9660	0.9625	0.9395	0.9505	0.9375
0.9634	0.9482	0.9387	0.9170	0.6944
0.6568	0.9181	0.8946	0.9060	0.8681
0.9194	0.9455	0.9198	0.9322	0.9323
0.9613	0.9400	0.9172	0.9359	0.9490
0.9405	0.9400	0.9278	0.9448	0.9669
0.9645	0.9394	0.9500	0.9389	0.9658
0.9485	0.9386	0.9171		

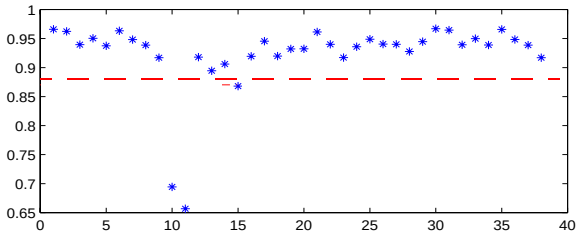

Figure 11 Correlation coefficients for signals of Fig. 10(a) with the template signal of Fig. 10(b).

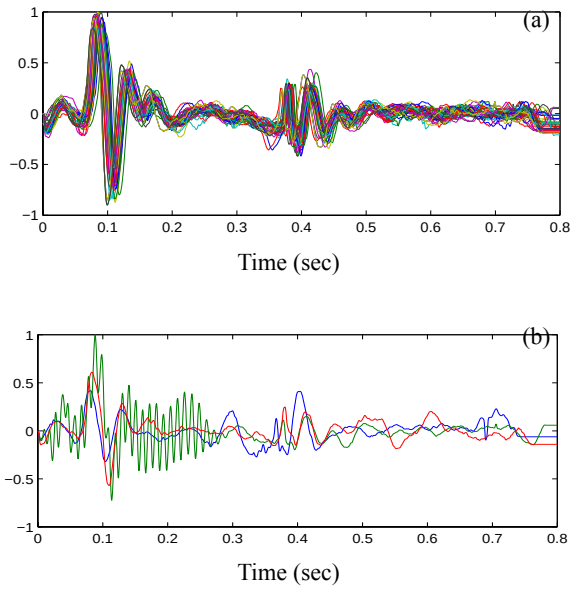

Figure 12 (a) Accepted beat cycles, and (b) rejected beat cycles for PCG signal of Figure 8 (a).

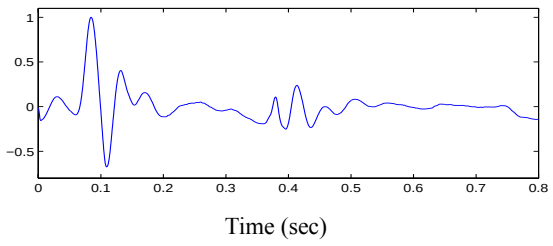

Figure 13 Final PCG heart-beat signal.

5 Conclusions

In this article a method was described which decomposes the PCG signal into its constituent heart-beat cycles using the ECG signal. Five algorithms have been devised to carry out this task. These algorithms are summarized in TABLE 2.

TABLE 2 – Algorithms used to decompose the PCG signal and reconstruction of an artefact-free heart-beat signal.

1) QRS peak detector.
2) QRS interval detector.
3) ECG beat cycle detector.
4) PCG beat cycle detector.
5) Heart-beat signal reconstruction algorithm.

First the QRS peaks are detected in the ECG signal, then the false peaks are identified and removed using the true QRS interval detector. The third algorithm is used to isolate the cardiac cycles from the ECG signal. This is done by detecting the peak of the P-wave as the beginning of the cardiac cycle. The starting points of the cardiac cycles are then used to decompose the PCG signal into beat-cycles. A template signal is formed from the PCG beat cycles. The correlation coefficients of the template signal with the individual beat cycles are used to identify the artefact free heart-beat cycles. Using frequency domain averaging, the mean of the heart-beat cycles is found and converted back to the time domain as the final heart-beat signal. These algorithms were successfully applied to real signals recorded from patients suspected with coronary artery disease.

REFERENCES

[1] Rushmer, R. F., 1970, "Cardiovascular dynamics," W. B. Sanders Company, Philadelphia, PA.

[2] Akay, M., Welkowitz, W., Semmlow, J. L., et al., 1991, Med & Biol. Eng. & Computing, 29, 365-372.

[3] Tinati, M. A., Bouzerdoum, A, Mazumdar, J., and Mahar, L., 1997, "Time-Frequency analysis of heart sounds before and after angioplasty", Proc. IEEE Int. Conf. on Digital Signal Processing (DSP' 97), 75-79, July, 1997, Santori Greece.

[4] Tinati, M. A., Bouzerdoum, A, Mazumdar, J., and Mahar, L., 1998, "Short time Fourier analysis of phonocardiograms before and after angioplasty", Proc. of Third Biennial Eng. Math. and Application Conf., (EMAC' 98), 495-498, July 1998, Adelaide Australia.

[5] Benetley, P. M., Grant, P. M., and McDonnell, J. T. E., 1998, IEEE Trans. Biomed. Eng., 45, 125-128.

[6] Friensen, G. M., Jannett, T. C., Jadallah, M. A., et. al., 1990, IEEE Trans. Biomed. Eng., 37, pp. 85-98.

[7] Wood, J. C., and Barry, D. T., 1994, Med. Biol. Eng. Comput., 32, S71-S78.

[8] Zhang, X., Durand, L.-G., et. al, 1998, IEEE Trans. Biomed. Eng., 45, 972-979.

(This page left blank intentionally)

Application of the Fuzzy C-Means Clustering Method on the Analysis of non Pre-processed FTIR Data for Cancer Diagnosis

Xiao Ying Wang, Jon Garibaldi, Turhan Ozen
Department of Computer Science and Information Technology
The University of Nottingham, United Kingdom
{xyw,jmg,txo}@cs.nott.ac.uk

Abstract

Fourier-transform infrared spectroscopy (FTIR) is an efficient, sensitive and computer operated technique that can detect changes in cellular composition that may reflect the onset of a disease. As such, it is being investigated as a method for automatic early detection of pre-cancerous changes. In previous work, FTIR spectral data was first empirically pre-processed and then classified using various data clustering techniques in order to compare to manually obtained classifications. It was found that accurate clustering could only be achieved by manually applying pre-processing techniques that varied according to the particular sample characteristics. In this paper, two data clustering techniques, Hierarchical Cluster Analysis (HCA) and Fuzzy C-Means (FCM) clustering, are used to classify sets of oral cancer cell data without a pre-processing procedure. The performances of these two techniques are compared and their differences are discussed. The FCM method was found to perform significantly better.

1. Introduction

As a major health problem to human, cancer has become a main research area for science researchers in all over the world. There are over 200 different cancer types that have been found so far. In Britain, the lifetime risk of developing cancer is more than one in three. The detection of early invasive cancer is essential in reducing mortality rate. Fourier-transform infrared spectroscopy (FTIR) technology has been recently developed to study biomedical conditions and used as a diagnostic tool for various human cancers and other diseases [1-5]. This technology is based on Fourier-transform infrared spectroscopy. Different functional groups of chemical compounds absorb infrared radiation (IR) at characteristic frequencies and the intensities of IR bands depend on their concentration. This technology can detect changes in cellular composition that reflect the onset of a disease and changes in intermolecular interactions in cells. This makes it a potentially powerful tool in cancer diagnosis, as it can help detecting abnormal cells at molecular levels that occur before the change in morphology seen under the light microscope. An advantage of the FTIR technique is that it may be fully automated and hence be less time-consuming than visual inspection. For one sample, measuring the spectrum on FTIR equipment only takes approximately one minute. In addition, it is a sensitive, computer-operated system. Very small amounts of samples are adequate and they can be studied regardless of the sample's form and physical state. These attributes make the technique of significant potential interest to large scale screening procedures, such as routine screening of cervical smears [6].

The FTIR technique is based on spectral parameters that reflect the structural changes at the molecular level. If the characteristic spectrum of an abnormal and normal tissue component is known, it may be possible to compare the spectra in each cluster to these reference spectra and hence achieve accurate diagnosis.

In previous work [12], FTIR spectral data was first empirically pre-processed and then classified using various data clustering techniques in order to compare to manually obtained classifications. It was found that accurate clustering could only be achieved by manually applying pre-processing techniques that varied according to the particular sample characteristics. In this paper, two data clustering techniques, Hierarchical Cluster Analysis (HCA) [7] and Fuzzy C-Means (FCM) [8] clustering, are used to classify sets of oral cancer cell data without a pre-processing procedure. The performance of these two techniques is presented and their differences are discussed. The results are presented in comparison with a previous study on the same data where the data was pre-processed empirically before a diagnosis analysis. The aim of this research is to develop an advanced cancer diagnosis system that is easy to use, reliable and efficient.

2. Materials and Methods

The HCA method is a statistical method for finding relatively homogeneous clusters of cases based on measured characteristics. It starts with each case in a separate cluster and then combines the clusters sequentially, reducing the number of clusters at each step until only one cluster is left. The Figure 1 shows an example of a dendogram for HCA classification.

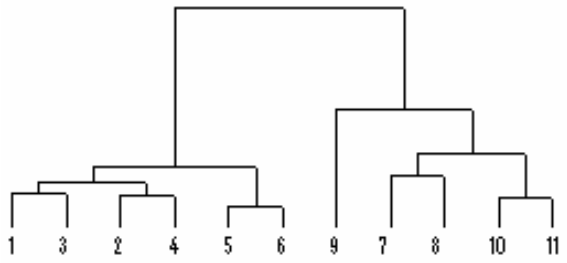

Figure 1: A sample of dendogram for HCA for classifying a set of data points in a plane.

FCM method, also known as Fuzzy ISODATA, which was originally introduced by Bezdek in 1981 as an extension to Dunn's algorithm [9] is the most widely used fuzzy clustering algorithm in practice.

FCM is a data clustering technique based on optimising the objective function:

$$J(U,V)=\sum_{j=1}^{C}\sum_{i=1}^{N}(\mu_{ij})^{m}\parallel x_i-v_j\parallel^{2} \quad (1)$$

It requires every data point in the data set to belong to a cluster to some membership degree. The purpose of the FCM is to group data points into different specific clusters. Let $X=\{x_1,x_2,...x_N\}$ be a collection of data. By minimising the objective function (1), *X* is classified into c homogeneous clusters. Where μ_{ij} is the membership degree of data x_i to a fuzzy cluster set v_j, $V=\{v_1,v_{2,...}v_C\}$ are the cluster centres. $U=(\mu_{ij})_{N*C}$ is a fuzzy partition matrix, in which each μ_{ij} indicates the membership degree for each data point in the data set to the cluster j. The value of *U* should satisfy the following conditions:

$$\mu_{ij}\in[0,1],\quad \forall i=1,...N,\forall j=1...C \quad (2)$$

$$\sum_{j=1}^{C}\mu_{ij}=1,\quad \forall_i=1,...N \quad (3)$$

The $\parallel x_i-v_j\parallel$ is the Euclidean distance between x_i and v_j. The parameter *m* is called fuzziness index, which control the fuzziness of membership of each datum. The goal is to iteratively minimise the aggregate distance between each data point in the data set and cluster centres until no further minimisation is possible.

The whole FCM process can be described in the following steps.

Step 1: Initialise the membership matrix *U* with random values, subject to satisfying conditions (2) and (3).
Step 2: Calculate the cluster centre *V* by using following equation

$$v_j=\frac{\sum_{i=1}^{N}(\mu_{ij})^{m}x_i}{\sum_{i=1}^{N}(\mu_{ij})^{m}},\forall j=1,...,C \quad (4)$$

Step 3: Get the new distance:

$$d_{ij}=\parallel x_i-v_j\parallel,\forall i=1,...,N,\forall j=1,...C \quad (5)$$

Step 4: Update the Fuzzy partition matrix *U*:
If $d_{ij}\neq 0$ (means $x_i\neq v_j$)

$$\mu_{ij}=\frac{1}{\sum_{k=1}^{C}(\frac{d_{ij}}{d_{ik}})^{\frac{2}{m-1}}} \quad (6)$$

Else $\mu_{ij}=1$

Step 5:
If the termination criteria have been reached, then stop.
Else go back to step 2.

The suitable termination criteria can be set by checking whether the objective function is below a certain tolerance value or if its improvement compared to the previous iteration is below a certain threshold. Moreover, the maximum number of iteration cycles can be used as a termination criterion as well. [11]

In this study, HCA and FCM clustering techniques were applied to a number of previously obtained clinical data sets with 'gold-standard' classifications by obtained through conventional cytology. Seven sets of FTIR data containing tumour (neoplasm), stroma (connective tissue), 'early keratinisation' and 'necrotic' specimens from three oral cancer patients were provided by Derby City General Hospital to carry out this study. Figure 2 shows an example of FTIR spectra for one of the data sets. A separate analysis of the same data had previously been

carried out at Derby City General Hospital. In the report [12] of the previous study, the FTIR data analysis was performed by using Infometrix Pirouette, multivariate analysis software (Infometrix, Inc.). Pre-processing on the spectra was carried out empirically; all spectral range in this study was limited to the 900-1800cm^{-1} interval. The HCA and FCM clustering results obtained during the research presented in this paper are compared with the results presented in the report mentioned above and number of disagreements of classifications is used to compare the performances of HCA and FCM techniques.

In this study, HCA and FCM analysis were performed using MATLAB (version 6.5.0, release 13.0.1).

3. Results

The tumour, stroma, early keratinisation and necrotic specimens were classified using HCA and FCM clustering techniques on seven FTIR data sets. At this stage of our study, we are concerned with asserting spectral characteristic of essentially distinct classes of tissue cells, rather than gradation process or mixed types. So the boundary region points are excluded from the data sets 4 and 7 because the stroma region is invaded by tumour within the vicinity of the boundary between two layers.

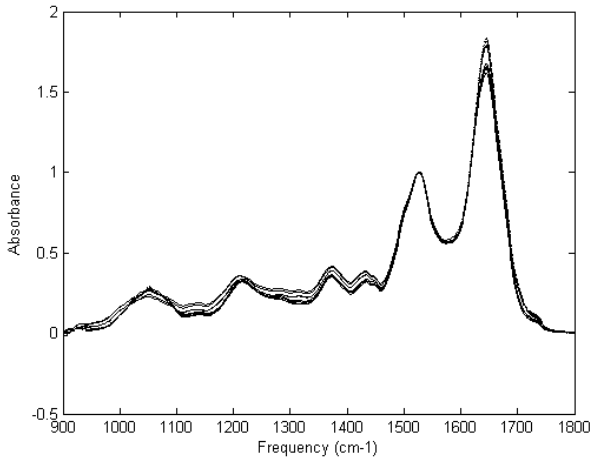

Figure 2: FTIR spectra for data set 1

The comparison results shown are based on the numbers of classifications that are different than those identified in a previous clinical study carried out at Derby City General Hospital. From data set 1 to data set 4, all the data is taken from the first patient, the corresponding data series number is from #001-#092. Data in set 5 and set 6 is taken from the second patient, the corresponding data series number is from #101-#145. Data set 7 is taken from the third patient, the corresponding data series number is from #201-#255. The number of data in each data set (after excluding the boundary data points in data set 4 and 7) is 15, 18, 11, 31, 30, 15 and 42 respectively. Tables 1a -7a show the number of actual data samples of tumour, stroma, early keratinisation and necrotic, and the numbers obtained by using each of the different analysis methods. For instance, in data set 2, 10 data samples were clinically identified as tumour and 8 data samples were identified as stroma. By using the HCA technique, the number of data deemed to be tumour is 17, and 1 is stroma. By using the FCM technique to classify the same data set, the number of data in the cluster deemed to be tumour is 9, in stroma 9, and so on.

Tables 1a - 7a give a general view on the FCM and HCA classification results. In most of data sets, the numbers of data points belonging to tumour, stroma, early keratinisation and necrotic do not exactly match the results from the clinic study. Some HCA classification results even get extreme differences with the clinical results in some data sets (such as in data set 2, 5 and 7). The reason to make the difference is some data points which should be considered in tumour cluster are missed, and at the same time, those missed data points are misclassified into the stroma cluster as extra data points, and vice versa. For example, in data set 2, by using HCA technology, the numbers of data points considered as tumour is 17, while 1 is considered as stroma. Actually, in the stroma cluster, 7 data points are missed, meanwhile these missed data points are misclassified into tumour cluster as extra data points. We will regard these extra data points from HCA and FCM cluster technologies as the number of disagreement of classification to compare with the results from previous clinic study results. Tables 1b - 7b show the comparison results of FCM and HCA classifications based on the disagreements with the results of the previous clinical study at the Derby City General Hospital.

4. Discussion

From the results presented in the previous section, it can clearly be observed that the number of disagreements of classification by the FCM technique is less than that by the HCA technique. In simple terms, the FCM technique appears to achieve better classification than HCA. Table 8 shows the total number of disagreement of classifications by HCA and FCM methods. Over all the data sets, the HCA incorrectly classifies more than twice as many data samples as FCM. Nevertheless the FCM technique can produce a fairly high number of disagreements of classifications in some data sets (i.e. data set 3 and 4). Based on experimental results, we have obtained, we can put forward two hypotheses.

Table 1a: Data set 1 - distribution number of tumour, and stroma in clinic study, HCA and FCM.

Data set 1	Clinic Study	HCA	FCM
Tumour	10	10	10
Stroma	5	5	5

Table 1b: Data set 1 - comparison results based on number of disagreement of classifications by HCA and FCM techniques.

Data set 1	HCA	FCM
Tumour	0	0
Stroma	0	0

Table 2a: Data set 2 - distribution number of tumour, and stroma in clinic study, HCA and FCM.

Data set 2	Clinic Study	HCA	FCM
Tumour	10	17	9
Stroma	8	1	9

Table 2b: Data set 2 - comparison results based on number of disagreement of classifications by HCA and FCM techniques.

Data set 2	HCA	FCM
Tumour	7	0
Stroma	0	1

Table 3a: Data set 3 - distribution number of tumour, and stroma in clinic study, HCA and FCM.

Data set 3	Clinic Study	HCA	FCM
Tumour	8	4	4
Stroma	3	7	7

Table 3b: Data set 3 - comparison results based on number of disagreement of classifications by HCA and FCM techniques.

Data set 3	HCA	FCM
Tumour	0	0
Stroma	4	4

Table 4a: Data set 4 - distribution number of tumour, stroma and early keratinisation in clinic study, HCA and FCM.

Data set 4	Clinic Study	HCA	FCM
Tumour	12	19	11
Stroma	7	5	8
Early Keratinisation	12	7	12

Table 4b: Data set 4 - comparison results based on number of disagreement of classifications by HCA and FCM techniques.

Data set 4	HCA	FCM
Tumour	7	3
Stroma	5	4
Early Keratinisation	0	0

Table 5a: Data set 5 - distribution number of tumour, and stroma in clinic study, HCA and FCM.

Data set 5	Clinic Study	HCA	FCM
Tumour	18	1	14
Stroma	12	29	16

Table 5b: Data set 5 - comparison results based on number of disagreement of classifications by HCA and FCM techniques.

Data set 5	HCA	FCM
Tumour	0	0
Stroma	17	4

Table 6a: Data set 6 - distribution number of tumour, and stroma in clinic study, HCA and FCM.

Data set 6	Clinic Study	HCA	FCM
Tumour	10	10	10
Stroma	5	5	5

Table 6b: Data set 6 - comparison results based on number of disagreement of classifications by HCA and FCM techniques.

Data set6	HCA	FCM
Tumour	0	0
Stroma	0	0

Table 7a: Data set 7 - distribution number of tumour, stroma and necrotic in clinic study, HCA and FCM.

Data set 7	Clinic Study	HCA	FCM
Tumour	21	28	18
Stroma	14	13	16
Necrotic	7	1	8

Table 7b: Data set 7 - comparison results based on number of disagreement of classifications by HCA and FCM techniques.

Data set7	HCA	FCM
Tumour	7	0
Stroma	0	2
Necrotic	1	1

Table 8: Total number of disagreement of classifications by HCA and FCM techniques.

	HCA	FCM
Total	48	19

First in HCA, each observation represents a single cluster initially, and then clusters are merged at each until only one cluster remains. The number of clusters is determined subjectively. If one of the observations is erroneous (e.g. that section cell is damaged), then the whole classification will be affected. For instance, in data set 2, if we eliminate 33rd datum and do HCA analysis again, the number of disagreements of classification in that data set becomes zero. That is, the HCA method is very sensitive to what is probably erroneous data.

Secondly, the FCM technique appears to achieve better classification when the cluster's size and shape are approximately the same. In the given data sets, some clusters sizes have big differences. For example, in data set 3. The number of data belonging to tumour is 8, belonging to stroma is 3; FCM gets 4 disagreements compared with the gold-standard classification. However in data set 2, the number of data belonging to tumour is 10, belonging to stroma is 8; FCM gets 1 disagreement compared with the known classification. Dae-Won et al [10] propose a fuzzy cluster validation index based on inter-cluster proximity for solving this problem.

Overall, these results indicate that FCM is a promising clustering technique for analysing the non pre-processed FTIR data. In work currently underway, we are investigating methods to extend the clustering process into a classification (diagnostic) process. The result of the clustering process is simply to split the data into two or more unlabelled categories. In the results presented above, the clusters were mapped to the actual known classifications in such a way as to minimise mis-classifications in each case. In a true diagnostic process it is necessary to be able to give the clinical user a predicted class for a novel (previously unseen) data sample. The ability to accurately cluster data samples according to the known classifications is the first step in establishing whether the FTIR technique is likely to be clinically useful.

The ultimate goal of this research is to establish the techniques necessary to develop clinically useful tools in a number of clinical domains: e.g. oral cancer, cervical smear test screening, etc. Currently, this ambitious goal remains a long way off. Further research for improving the FCM technique in order to create an advanced cancer diagnosis system is ongoing. We are attempting to obtain significantly larger numbers of samples of known classification from a wider range of patients, and are also in the process of extending the type of samples to sources other than the oral samples presented here. In particular, we are actively engaged on a research programme to obtain FTIR spectral data from cervical smear test samples. Other research challenges include developing the experimental techniques necessary to obtain reliable

spectra from the nucleus of a single cell, and the development of the analytical techniques necessary to aggregate the classifications of multiple single nucleus spectra from a given patient into an overall diagnosis.

5. Conclusion

FTIR technology based on detecting abnormal cells at molecular levels has become a prominent technology in cancer diagnosis in recent years. In previous work, the FTIR spectral data has been first empirically pre-processed prior to classification using various data clustering techniques. In order to avoid the extra tools, time and expertise necessary for the pre-processing procedure, it is desirable to avoid pre-processing. In this study, HCA and FCM techniques are used to classify sets of oral cancer cell data without a manual pre-processing procedure. The performance of these two techniques is presented and their results, which are based on the numbers of classifications that are different than those identified in a previous clinical study, are shown. The FCM method was found to perform significantly better and further research on improving this method is on going.

Acknowledgements

The authors are grateful to John Chalmers et al for providing the FTIR spectral data used in this study, and for making available their internal report on the clinical study carried out at Derby General City Hospital.

References

[1] Wong PTT, Rigas B. Infrared spectra of microtome sections of human colon tissues. *Applied Spectroscopy*, 44:1715–8, 1990.

[2] Rigas B, Morgello S, Goldan IS, Wong PT. Human colorectal cancers display abnormal Fourier-transform infrared spectra. *Proceedings of the National Academia of Science USA*, 87(20):84–8, 1990.

[3] Wong PTT, Goldstein SM, Grekin RC, Godwin TA, Pivik C, Rigas B. Distinct infrared spectroscopic patterns of human basal cell carcinoma of the skin. *Cancer Research*, 53(4):762–5, 1993.

[4] Morris BJ, Lee C, Nightingale BN, Molodysky E, Morris LJ, Appio R. Fourier transform infrared spectroscopy of dysplastic, papillomavirus-positive cervicovaginal lavage speciens. *Gynecological Oncology*, 56(2):245–9, 1995.

[5] Malins DC, Polissar NL, Nishikida K, Holmes EH, Gardner HS, Gunselman SJ. The etiology and prediction of breast cancer. Fourier transform-infrared spectroscopy reveals progressive alterations in breast DNA leading to a cancer-like phenotype in a high proportion of normal women. *Cancer*, 75(2):503–17, 1995.

[6] Lowry SR. The analysis of exfoliated cervical cells by infrared microscopy. *Cellular and Molecular Biology*, 44(1):169-77, 1998.

[7] Gong, X., and M. B. Richman, 1995: On the application of cluster analysis to growing season precipitation in North America east of the Rockies. *Journal Climata*, 8:897-931, 1995.

[8] Bezdek J, *Pattern Recognition with Fuzzy Objective Function Algorithms*, Plenum Press, USA, 1981.

[9] Dunn JC, "A fuzzy relative of the ISODATA process andits use in detecting compact, well separated clusters", *Journal of Cybernetics*, 3(3):32-57, 1974.

[10] Dae-Won Kim, Kwang H. Lee, Doheon Lee, Fuzzy cluster validation index based on inter-cluster proximity. *Pattern Recognition Letters*, 24: 2561-74, 2003.

[11] Lampinen T, Koivisto H, Honkanen T, Profiling Network Applications with Fuzzy C-Means Clustering and Self-organizing Map. *Proceeding of 1st International Conference on Fuzzy Systems and Knowledge Discovery. Orchid Country Club, Singapore*. 1:300-4, 2002.

[12] Allibone R, Chalmers JM, Chesters MA, Fisher S, Hitchcock A, Pearson M, Rutten FJM, Symonds I, Tobin M, FT-IR microscopy of oral and cervical tissue samples. *Internal Report*, Derby City General Hospital, 2002.

POSTER SESSION I

(This page left blank intentionally)

A Novel Generic Higher-order TSK Fuzzy Model for Prediction and Applications for Medical Decision Support

Qun Song
Knowledge Engineering & Discovery Research Institute
Auckland University of Technology
Private Bag 92006, Auckland 1020 New Zealand
email qsong@aut.ac.nz

Tianmin Ma
Knowledge Engineering & Discovery Research Institute
Auckland University of Technology
Private Bag 92006, Auckland 1020 New Zealand
email mmaa@aut.ac.nz

Nikola Kasabov
Knowledge Engineering & Discovery Research Institute
Auckland University of Technology
Private Bag 92006, Auckland 1020 New Zealand
email nkasabov@aut.ac.nz

Abstract

This paper introduces a higher-order Takagi-Sugeno-Kang (TSK) neuro-fuzzy inference system and its applications in medical decision support systems. Different from most TSK fuzzy systems that utilize first-order TSK type fuzzy rules, the proposed system is composed of higher-order TKS fuzzy rules that have functions in their consequent parts of the following type: $y = b_0 x_1^{b1} x_2^{b2} \ldots x_p^{bp}$. The type of the non-linear function has been chosen based on the rationale that it is well established in the medical practice, for example the MDRD formula and many other formulas for Glomerular Filtration Rate (GFR) evaluation used in the area of renal research and practice [8]. The proposed approach consists of three steps: (1) Apply Fuzzy C-means clustering to partition the input space; (2) Initialize a higher-order TSK fuzzy rule set according to the clustering results. For each fuzzy rule, a non-linear function of the defined type (e.g. the MDRD formula) is used in the consequent part; (3) Train the system on training data with the use of the steepest descent algorithm (Back-propagation learning algorithm) to optimize the parameters of the fuzzy rules. We illustrate the performance of the proposed system on a real case study data for GFR evaluation. For a comparison, we also present the predicted results on the same data by three other models: (i) the MDRD formula; (ii) the MLP network; and (iii) the Adaptive Neuro-Fuzzy Inference System (ANFIS) [2, 4]. The proposed system outperforms the rest as it takes into account some existing knowledge - the type of the function already developed in the past and the variables used in it, along with applying a new method for training the system.

1. Introduction

The TSK fuzzy inference system was proposed by Takagi and Sugeno in 1985 [14]. Since then, a lot of research and applications have been developed [1, 13, 15]. The TSK fuzzy model is now established as one of the most powerful fuzzy models and has been widely and successfully used in different research areas such as: adaptive control; classification; prediction; and system identification [3, 6, 7, 10, 16].

A typical TSK fuzzy model consists of If-Then rules that have the following form:

R_l: if x_1 is F_{11} and x_2 is F_{12} and … and x_P is F_{1P},

then y is $g_1(x_1, x_2, \ldots, x_P)$ (1)

where "x_j is F_{lj}", $l = 1, 2, \ldots m$; $j = 1, 2, \ldots P$, are $m \times P$ fuzzy propositions that form m antecedents for m fuzzy rules respectively; x_j, $j = 1, 2, \ldots, P$, are antecedent variables defined over universes of discourse X_j, $j = 1, 2, \ldots, P$, and F_{lj}, $l = 1, 2, \ldots m$; $j = 1, 2, \ldots, P$ are fuzzy sets defined by their fuzzy membership functions μ_{Flj}: $X_j \rightarrow [0, 1]$, $l = 1, 2, \ldots m$; $j = 1, 2, \ldots, P$. In the consequent parts of the fuzzy rules, y is the consequent variable, and functions g_l, $l = 1, 2, \ldots m$, are employed.

If $g_l(x_1, x_2, \ldots, x_q) = C_l$, $l = 1, 2, \ldots m$, and C_l are constants, we call this inference a zero-order TSK fuzzy inference system. The system is called a first-order TSK fuzzy inference system if $g_l(x_1, x_2, \ldots, x_q)$, $l = 1, 2, \ldots m$, are linear functions. If these functions are non-linear functions, it is called a higher-order TSK inference system [5].

For an input vector $\boldsymbol{x}^i = [x_1^i\ x_2^i\ \dots\ x_P^i]$ the result of the inference, y^i, or the output of the system, is the weighted average of each rule's output value indicated as follows:

$$y^i = \frac{\sum_{l=1}^{m} w_l g_l(x_1^i, x_2^i, ..., x_p^i)}{\sum_{l=1}^{m} w_l} \qquad (2)$$

$$where\ \ , \ w_l = \prod_{j=1}^{P} F_{lj}(x_j);\ \ l = 1, 2, \dots m;\ \ \ j = 1, 2, \dots, P.$$

Because the fuzzy inference systems are considered as an effective aggregation of interconnected subsystems, described with simple models, the first-order TSK models are mostly used so far. In some cases, however, certain kind of non-linear functions would be more appropriate and more effective to use in a TSK system. In our research, we use the following type of a function: $y = b_0\, x_1^{b1}\, x_2^{b2} \dots x_p^{bp}$. This type is very much used in many medical areas, such as renal function evaluation through GFR estimation with the use of the MDRD formula [8]. The function above is used as the consequent part of fuzzy rules to build a higher-order TSK fuzzy system. The system is trained on training data to optimize the parameters in both antecedent and consequent parts of the fuzzy rules.

2. The problem of accurate estimation of GFR in advanced renal impairment

The accurate evaluation of renal function is fundamental to the nephrology practice. The early detection of renal impairment will allow for the institution of appropriate diagnostic and therapeutic measures, and potentially maximise preservation of intact nephrons.

Glomerular filtration rate (GFR) [8] is traditionally considered the best overall index to determine renal function in healthy and diseased patients. Most clinicians rely upon creatinine clearance (CrCl) as a convenient and inexpensive surrogate for GFR. CrCl can be determined by either timed urine collection, or from serum creatinine using equations developed from regression analyses such as that by Cockcroft-Gault formula, but the accuracy of CrCl in terms of GFR prediction is limited by methodological imprecision and the systematic bias.

Recently, the Modification of Diet in Renal Disease (MDRD) study developed a new formula to more accurately evaluate the GFR. The formula uses the following variables: age, sex, gender, height, serum creatinine (Screat), serum albumin (Salb) and blood urea nitrogen concentrations (Surea) and is defined as follows:

$$GFR = 170 \times Screat^{-0.999} \times Age^{-0.176} \times 0.762(\text{if sex is female}) \times 1.18\ (\text{if race is black}) \times Surea^{-0.17} \times Salb^{0.318} \qquad (3)$$

However, the formula can be misleading as to the presence and progression of renal disease in new patients. Therefore a method to improve the estimation of GFR in advanced renal impairment is to be investigated.

Using a higher-order TSK fuzzy model, here we obtain more accurate results for the GFR prediction than with the use of the MDRD formula. In the next section a novel learning algorithm of higher-order TSK fuzzy model is described. In section 4, the model is applied to real data for GFR prediction and the result is compared with some results obtained by other models.

3. A generic higher-order TSK Fuzzy model

3.1. Model Initialization

To partition the input space for creating fuzzy rules and obtain initial parameter values of the fuzzy rules, a *Fuzzy C-means clustering* method [2] is applied. The cluster centres are taken as initial values of the centres of *Gaussian* fuzzy membership functions and in each cluster, the maximum distance between the cluster centre and samples is taken as the initial value of the width of the corresponding *Gaussian* membership function.

As the consequent part of each higher-order TSK fuzzy rule, the non-linear function is a MDRD formula like function that can be expressed in the following form:

$$y = b_0 x_1^{b1}\, x_2^{b2} \dots x_p^{bp} \qquad (4)$$

We apply a logarithm transformation to Eq. (4) and obtain Eq.(5):

$$\ln(y) = b_0 + b_1 \ln(x_1) + \dots + b_p \ln(x_p) \qquad (5)$$

We then use *least-square estimator* (LSE) on the samples in each cluster to obtain initial values of the parameters b_j , j = 0, 1, 2, … , P, where P is the number of inputs.

3.2 Learning and parameter optimization through the steepest descent algorithm

In the higher-order TSK fuzzy model training algorithm, described below, the following indexing denotation is used:

- Training data pairs: i = 1, 2, … , N;
- Input variables: j = 1, 2, … , P;
- Fuzzy rules: l = 1, 2, …, M;
- Training epochs: k = 1, 2, ….

The training procedure consists of the following steps. Consider the system is having P inputs and one output. Suppose that it has M fuzzy rules, where the l-th rule has the form of

R_l: if x_1 is F_{11} and x_2 is F_{12} and … and x_P is F_{1P},

$$\text{then } y_l = b_{l0} x_1^{b_{l1}} x_2^{b_{l2}} \cdots x_p^{b_{lp}}$$

$$l = 1, 2, \ldots, M \tag{6}$$

Here, F_{lj} are fuzzy sets defined by the following *Gaussian* type membership function

$$GaussianMF = \alpha \exp\left[-\frac{(x-m)^2}{2\sigma^2}\right] \tag{7}$$

When the model is given an input-output pair ($\boldsymbol{x}_i$, d_i), it calculates the following output value:

$$f(\boldsymbol{x}_i) = \frac{\sum_{l=1}^{M} y_l \prod_{j=1}^{P} \exp\left[-\frac{(x_{ij}-m_{lj})^2}{2\sigma_{lj}^2}\right]}{\sum_{l=1}^{M} \prod_{j=1}^{P} \exp\left[-\frac{(x_{ij}-m_{lj})^2}{2\sigma_{lj}^2}\right]} \tag{8}$$

The goal is to design the system from (8) so that the following objective function is minimized:

$$E = \frac{1}{2}\left(f(\boldsymbol{x}_i) - d_i\right)^2 \tag{9}$$

Below, the steepest descent algorithm (BP) [5, 9, 15,] is applied to optimize the parameters b_{lj}, m_{lj}, α_{lj} and σ_{lj} in the fuzzy model:

$$b_{l0}(k+1) = b_{l0}(k) - \frac{\eta_b}{b_{l0}(k)} y_l(k)[f(\boldsymbol{x}_i) - d_i]\Phi_l(\boldsymbol{x}_i) \tag{10}$$

$$b_{lj}(k+1) = b_{lj}(k) - \eta_b y_l(k)\ln(x_{ij})[f(\boldsymbol{x}_i) - d_i]\Phi_l(\boldsymbol{x}_i) \tag{11}$$

$$\alpha_{lj}(k+1) = \alpha_{lj}(k) - \frac{\eta_\alpha}{\alpha_{lj}(k)}[f(\boldsymbol{x}_i) - d_i][y_l(k) - f(\boldsymbol{x}_i)]\Phi_l(\boldsymbol{x}_i) \tag{12}$$

$$m_{lj}(k+1) = m_{lj}(k) - \eta_m [f(\boldsymbol{x}_i) - d_i][y_l(k) - f(\boldsymbol{x}_i)]\frac{[x_{ij} - m_{lj}(k)]}{\sigma_{lj}^2(k)}\Phi_l(\boldsymbol{x}_i) \tag{13}$$

$$\sigma_{lj}(k+1) = \sigma_{lj}(k) - \eta_\sigma [f(\boldsymbol{x}_i) - d_i][y_l(k) - f(\boldsymbol{x}_i)]\frac{[x_{ij} - m_{lj}(k)]^2}{\sigma_{lj}^3(k)}\Phi_l(\boldsymbol{x}_i) \tag{14}$$

where,

$$\Phi_l(\boldsymbol{x}_i) = \frac{\prod_{j=1}^{P} \alpha_{lj} \exp\left\{-\frac{[x_{ij}(k) - m_{lj}(k)]^2}{2\sigma_{lj}^2(k)}\right\}}{\sum_{l=1}^{M}\prod_{j=1}^{P} \alpha_{lj} \exp\left\{-\frac{[x_{ij}(k) - m_{lj}(k)]^2}{2\sigma_{lj}^2(k)}\right\}} \tag{15}$$

η_b, η_m, η_α and η_σ are learning rates for updating the parameters b_{lj}, m_{lj}, α_{lj} and σ_{lj} respectively.

4. Experimental results for the GFR prediction and a comparative analysis with other techniques

A real data set is used here for experimental analysis. The data set has 447 samples, collected at hospitals in New Zealand and Australia. Each of the records includes 6 variables (inputs): age, sex, gender, serum creatinine, serum albumin, and blood urea nitrogen concentrations, and one output - the Glomerular Filtration Rate (GFR) value. All experimental results reported here are based on 10 experiments with the same model and parameters and the results are averaged. In each experiment 70% of the whole data set is randomly selected as training data and another 30% as testing data. The results are listed in Table1. They include the number of fuzzy rules (for ANFIS and for the proposed TSK fuzzy model) or neurons in the hidden layer (for the MLP model), the test RMSE (root mean square error), and the test AAE (average absolute error). Figure.1 shows spot-graphs for each prediction result by different models.

Table 1. Experimental Results with Different Models

Model	Rules or Neurons	RMSE	AAE
MDRD	-	5.88	7.74
MLP	16	5.75	8.44
ANFIS	27	5.48	7.49
Higher-order TSK Model	12	5.08	6.97

5. Conclusions and directions for further research

The paper presents a higher-order TSK fuzzy model for prediction tasks. The higher- order function is of the type of: $y = b_0 x_1^{b1} x_2^{b2} \ldots x_p^{bp}$ which is used in the medical practice, and especially for the prediction of the Glomerular Filtration Rate (GFR) in many renal clinics all over the world. The proposed model demonstrates superiority when compared with the widely popular MDRD formula [8], the MLP neural network model, and the ANFIS neuro-fuzzy model.

Further directions for the research include: (1) self-optimization of the learning parameters of the introduced TSK model, such as learning rate, number of fuzzy rules, etc.; (2) optimal selection of input variables for better prediction results

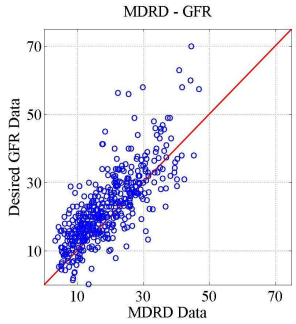

Figure1a. MDRD vs GFR

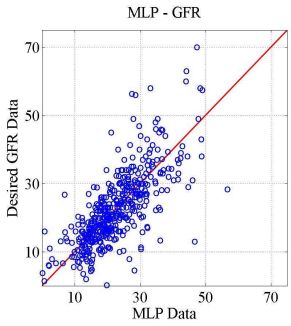

Figure1b. MLP vs GFR

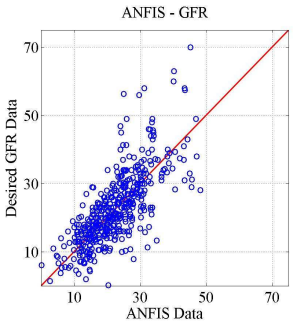

Figure1c. ANFIS vs GFR

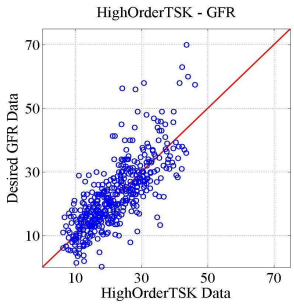

Figure1d. Higher-order TSK model vs GFR

6. Acknowledgements

This research is part of a research programme funded by the New Zealand Foundation for Research Science and Technology, contract NERF-AUT-02001. The GFR data used in the paper includes New Zealand and Australia data, collected by AUS-14 Study Group and Middlemore hospital with the participation of Dr Mark Marshall.

References

[1] Chuang, C.C., Su, S.F. and Chen, S.S., "Robust TSK Fuzzy Modelling for Function Approximation With Out-Liers", *IEEE Trans. on Fuzzy Systems*, vol. 9, pp. 810 – 821, 2001.

[2] *Fuzzy Logic Toolbox User's Guide*, The Math Works Inc., ver. 2.01, 2000.

[3] Guerra, M.T. and Vermeiren, L., "Control Laws for Takagi-Sugeno Fuzzy models", *Fuzzy Sets and Systems*, vol.120, pp. 95-108, 2001.

[4] Jang, J.S.R., "ANFIS: adaptive network-based fuzzy inference system", *IEEE Trans. on Systems, Man, and Cybernetics*, vol. 23, pp. 665-685, 1993.

[5] Jang, J.S.R., Sun, C. and Mizutani, E., *Neuro-Fuzzy and Soft Computing*, Prentice Hall, Inc., 1997.

[6] Juang, C.F., "A TSK-Type Recurrent Fuzzy Network for Dynamic Systems Processing by Neural Network and Genetic Algorithms", *IEEE Trans. on Fuzzy Systems*, vol. 10, pp. 155 – 170, 2002.

[7] Kasabov, N. and Song, Q., "DENFIS: Dynamic, evolving neural-fuzzy inference systems and its application for time-series prediction," *IEEE Trans. on Fuzzy Systems*, vol. 10, pp. 144-154, 2002.

[8] Levey, A.S., Bosch, J.P., Lewis, J.B., Greene, T., Rogers, N., Roth, D., for the Modification of Diet in Renal Disease Study Group, " A More Accurate Method To Estimate Glomerular Filtration Rate from Serum Creatinine: A New Prediction Equation", *Annals of Internal Medicine*, vol. 130, pp.461-470, 1999.

[9] Lin, C.T. and Lee, C.S.G., *Neuro Fuzzy Systems*,. Prentice Hall (1996).

[10] Mastorocostas, P.A., Theocharis, J.B. and Petridis, V.S., "A Constrained Orthogonal Least-squares Method for Generating TSK Fuzzy Models: Application to Short-term Load Forecasting", *Fuzzy Sets and Systems*, vol. 118, pp. 215 – 233, 2001.

[11] Mendel, J.M., *Uncertain Rule-Based Fuzzy Logic Systems: Introduction and New Directions*. Prentice Hall, 2001.

[12] *Neural Network Toolbox User's Guide*, The Math Works Inc., ver. 4, 2001.

[13] Papadakis, S.E. and Theocharis, J.B., "A GA-Based Fuzzy Modelling Approach for Generating TSK Models", *Fuzzy Sets and Systems*, vol. 131, pp. 121 – 152, 2002.

[14] Takagi, T. and Sugeno, M., "Fuzzy identification of systems and its applications to modeling and control", *IEEE Trans. on Systems, Man, and Cybernetics*, vol. 15, pp. 116-132, 1985.

[15] Wang, L.X., *Adaptive Fuzzy System And Control: Design and Stability Analysis*. Englewood Cliffs, NJ: Prentice Hall, 1994.

[16] Wang, L.X. and Langari, R., "Sugeno Model, Fuzzy Discretization, and the EM Algorithm", *Fuzzy Sets and Systems*, vol. 82, pp. 279 – 288, 1996.

(This page left blank intentionally)

Efficient Enterprise Integration Solutions Using Web Services for Hospital Management System

Savitri Bevinakoppa Kaushik Hegde
School of Computer Science and Information Technology, RMIT University
Melbourne – 3001, AUSTRALIA
savitri@cs.rmit.edu.au khegde@cs.rmit.edu.au

Abstract

Distributed oriented businesses are moving towards mergers and tie-ups with other businesses, so as to provide value to their customers and thereby increase their revenue etc. They are facing problems of efficiency in integrating their heterogeneous software applications with each other. The evolution of Web services has simplified the problem of Integrating Enterprise (IE) applications. Web services use technologies, which are Simple Object Access Protocol (SOAP), used for messaging, Web Services Description Language (WSDL) used for description and Universal Description, Discovery and Integration (UDDI) used for discovery. These technologies improve transactional integration and add value to the business workflow. However the core technologies involved in Web services like SOAP are riddled with problems of performance and slow response time.

This paper gives the development of a Hospital Management system, which is dynamically integrated to external and internal online hospital services. The services include patient registry, pathology, radiology and radiotherapy, using web services with SOAP, WSDL and UDDI. The performance and response times are improved by caching SOAP requests and responses. From the experimental results, it was found that caching SOAP messages helps in improving the performance of the web services infrastructure. This research establishes the fact that web services can be effectively used for integrating applications dynamically.

1. Introduction

Web Services is a new revolution in the field of enterprise applications having program-to-program interactions such as Business-2-Business portals [1]. It reduces the costs for business moving towards e-business help in deploying applications very fast and dynamically discovering new opportunities. These advantages resulting from web services are due to the fact, that they are built on commonly used and emerging standards like HTTP, Extensible Markup Language (XML) [2], Web Services Description Language (WSDL) [3] and Universal Description, Discovery and Integration (UDDI) [3]. It allows applications to be integrated economically, fast and easily because integration of business is not based on network protocol semantics, but on messages generated based on service semantics, thus inducing loose coupling between business applications [4]. It provides a uniform approach to integrate external applications as well as internal applications and evolve electronic business towards just in time integration of business over the Internet.

The objective of this research is to build efficient web-based Hospital Management system. This solution enables doctors to interact with various internal and external services that are dynamically integrated using the concepts of web services. The various services may include patient details service, pathology service, radiology service and radiotherapy service. A service provider such as the radiology department registers a service with the UDDI registry of hospital management. The service functionality is exposed using a WSDL file, which is registered in the hospital management UDDI registry. The performance of transmission of request and response SOAP messages between the service requestor (Hospital Management solution) and the service provider (radiology etc) is improved by caching these SOAP request and responses.

2. Web Services

The web services model consists of three main roles namely service provider, service registry and service requestor and three main operations namely publish, find and bind. The conceptual web service stack is made up of 5 layers namely service discovery, service publication, service description, XML messaging and network. These layers are guided or have to satisfy the factors of security, management and quality of service.

Service Discovery and Service Publication layers of the web service stack are involved with service discovery and service publication functionality of the web service model and they are implemented using Universal Description, Discovery and Integration (UDDI). It is also responsible for describing the service operation and also gives binding information. It is implemented using web services Description Language (WSDL).

XML Messaging and Network layers of the web service stack are responsible for transportation of request and responses between service initiator and service provider. The XML messaging is implemented using Simple Object Access protocol (SOAP), which is transported over HTTP or SMTP or FTP in the network layer [5].

2.1 Simple Object Access protocol (SOAP)

Simple Object Access protocol is a standardized XML based object invocation protocol [5]. SOAP [6] was initially developed so that distributed applications could communicate with each other over HTTP which is one of the standard ways to communicate over the internet and through corporate software security systems like firewalls, other distributed protocols like RMI, IIOP and COM were ineffective in these regards. Since SOAP is defined in XML and is based over HTTP it is platform independent. SOAP does not define its own application semantics in terms of programming model and implementation specific semantics rather it defines a simple mechanism for expressing application semantics by providing a modular packaging model and encoding mechanisms for encoding data within modules. This enables SOAP to be used in a variety of applications ranging from messaging and remote procedure calls (RPC).

3. Hospital Management System

A Hospital Management system has been taken as a case study in this paper. The solution provided for a Hospital Management system proves that web services are an efficient integration solution. The Hospital Management solution shows how caching improves the performance of SOAP.

3.1 Hospital Management Solution Description

A Hospital Management solution will provide a revolutionary single point of access, to many external and internal Hospital services like radiology service, pathology service, hospital management service etc, to its clients mainly the doctors. The doctor will be able to access patient details such as patient personal information, diagnostic information etc belonging to various hospitals from a single access point. The Hospital Management solution will be making use of functionalities of already existing software solutions of various departments like radiology department, pathology department etc, which may be under different hospitals to achieve its functionality. An integration framework has to be applied to the Hospital Management solution for its successful interaction with heterogeneous software applications of various departments. In this minor project a web services integration framework is selected for the Hospital Management solution due to the advantages of web services over other existing integration solutions.

3.2 Main Functionalities of Hospital Management Solution

The doctor can view patient contact details of a patient belonging to various hospitals that have exposed their services as a web service to the Hospital Management system. The doctor records patient clinical exam details using the Hospital Management system.

3.2.1 Stakeholders involved in the Hospital Management system

Doctor: -A doctor uses the Hospital Management system to view and record patient contact details and diagnostic details.

The doctor uses the Hospital Management system to record patient clinical exam details.

Radiology Department: uses the Hospital Management system to expose its services such as treatment and its outcome.

Radiotherapy Department: uses the system to expose its services such as dosage, location etc.

Pathology Department: uses the system to expose its services such as MRI, PET images.

Toxic/Follow-up Department: uses the system to expose its services such as consultation and its outcome. Architectural view of Hospital Management system is shown in the figure 1.

3.3 Deployment view of Hospital Management system

SOAP cache is used to cache SOAP requests and responses. UDDI registry is used for registration and dynamic discovery of services. The deployment view of Hospital Management System is shown in figure 2.

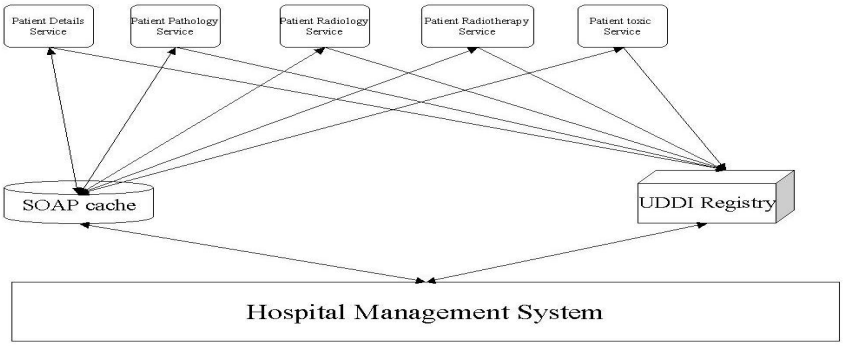

Figure 1 Architectural View of Hospital Management System

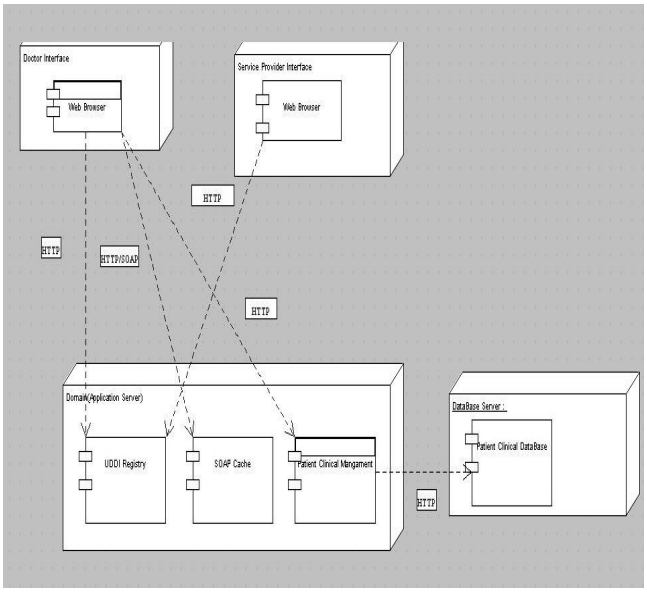

Figure 2 A Deployment View of the Hospital Management System

The top level indicates the client view of the doctor and the service provider. The client view interacts with the application through the web browser. The domain layer hosts the UDDI registry, SOAP cache and clinical management component of the Hospital Management system. The data server layer is used to host the database used to store patient clinical details. The protocol used for transmission between the layers is HTTP coupled with SOAP.

4. SOAP Cache

In Distributed software applications using a web services infrastructure, the default protocol used for transmission of requests and responses is Simple Object Access Protocol (SOAP). The performance of SOAP compared to other Distributed binary protocols like RMI, IIOP and COM is very poor. As SOAP is an XML based protocol, assembling and disassembling a SOAP request and response involves a lot of overhead. Caching a SOAP request and its corresponding response locally on the client end helps in improving the performance of SOAP bypassing the time required to assemble and disassemble a SOAP message. Only read SOAP request are cached as caching of write SOAP request leads to inconsistency and failure of the entire software application. The following section gives details of the architecture of caching component, design details involved in eviction of SOAP objects from the cache and maintaining consistency of SOAP messages in the cache, the implementation of the SOAP cache and the test results regarding the performance of SOAP by caching SOAP requests and responses locally at the client end [7], [8].

4.1 The Main Components of SOAP Caching Architecture

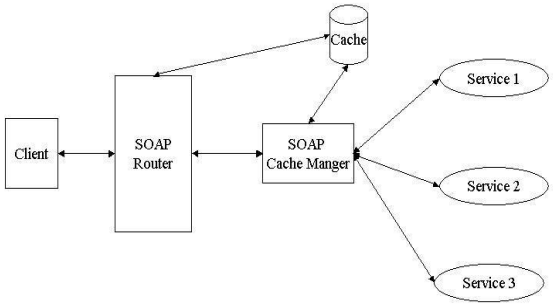

Figure 3 SOAP Caching Architecture

Cache is an abstraction of physical memory used for storing SOAP requests and responses. In this architecture (figure 3), client is responsible for invoking SOAP requests and receiving SOAP responses. SOAP Router is responsible for receiving requests from a client and redirecting these requests to the SOAP cache. The SOAP router receives SOAP responses from the SOAP cache and the SOAP router sends the responses to the client. The SOAP router is also responsible for performing administration functions like maintaining the size of the cache repository and writing cache contents from the run time memory in to a persistent storage on the hard disk when the application server on which the SOAP cache is mounted is being shutdown.

SOAP Cache Manger is responsible for storing requests and response SOAP messages in the cache. It is responsible for generating cache keys, which is used to index cached data. It is responsible for maintaining consistency of data in the cache.

4.1 Cache Keys

A cache key is used to easily locate cache data. The use of cache key simplifies the process of searching data in the cache and also helps in decreasing the time needed to search data in the cache. Two types of cache keys have been used to index cache data in the caching solution provided in this minor project. They are as follows.

Service Key: - A service key is used to reference data belonging to a particular web service. It is extracted from a SOAP request message. It is made up of the web service name.

E.g.

```
<SOAP-ENV:Envelope>
 <SOAP-ENV:Body>
  <ns1:getPatientDetailsByURNO
xmlns:ns1="urn:PatientDetails">
  <name
xsi:type="xsd:string">001100006</name>
 </ns1:getPatientDetailsByURNO>
 </SOAP-ENV:Body>
</SOAP-ENV:Envelope>
```

In the above SOAP message the service key is "urn:PatientDetails" which is used to reference the web service named by Patient Details.

Message key: -A message key is used to reference data belonging to a particular method in a web service. It is extracted from a SOAP request message. It is made up of the method name and the parameter values of that method.

```
E.g.  <SOAP-ENV: Envelope>
        <SOAP-ENV:Body>
    <ns1:getPatientDetailsByURNO
xmlns:ns1="urn:PatientDetails">
    <name
xsi:type="xsd:string">001100006</name>
   </ns1:getPatientDetailsByURNO>
   </SOAP-ENV:Body>
</SOAP-ENV:Envelope>
```

In the above SOAP message the message key is "getPatientDetailsBy URNO 001100006" which is used to reference the function getPatientDetailsByURNO with parameters 001100006 under the web service named by PatientDetails.

4.2 The Hierarchy and Structure of the Cache data structures

The cache data structure is maintained in the form of a linked list. The ServiceContainer is a serializable java class used to store details of all the published web services. The ServiceContainer is made up of ServiceElements. A ServiceElement is a serializable java class used to store details of a particular web service. The ServiceElement is made up of CacheElements. Each ServiceElement is indexed by a service key. The CacheElement is a serializable java class used to store method details under the particular web service and SOAP requests and responses to that particular method. Each CacheElement is indexed by a message key (figure 4, 5). Figure 6 indicating the Hierarchy of a Cache data Structure.

4.2 Basic Workflow of the SOAP Cache

The following sequence diagram depicts the basic workflow of the SOAP cache.

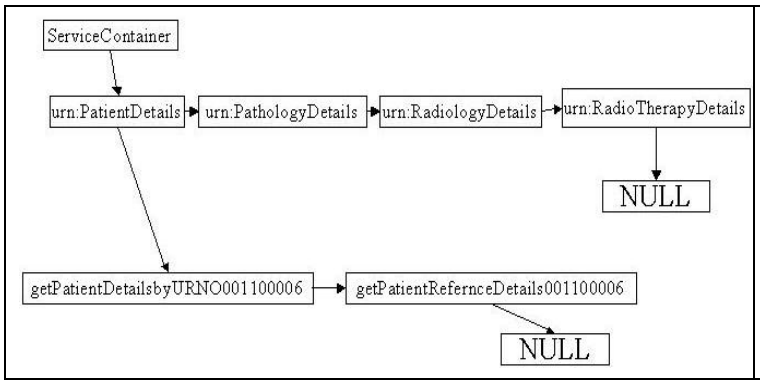

Figure 4 Example SOAP Cache Hospital Management Linked List Structure

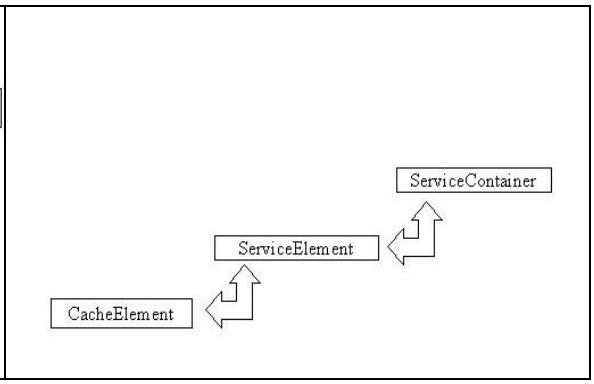

Figure 5 Sequence Diagram Showing SOAP Cache workflow

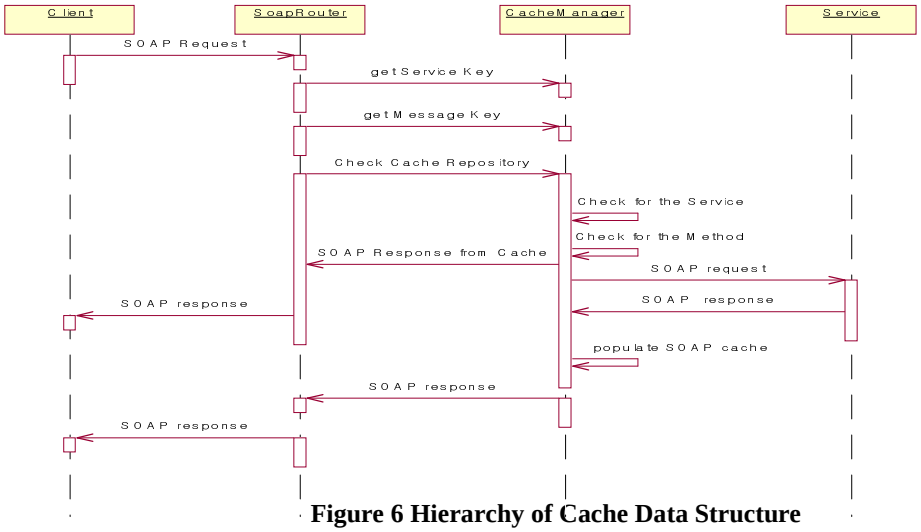

Figure 6 Hierarchy of Cache Data Structure

A client issues a SOAP request to a published service. This SOAP request is passed to a SOAP router and generates a service key, which identifies the published service and a message key, which identifies the method under the particular published service from the SOAP request message. The SOAP router invokes a function on the cache manager to check if a SOAP response is stored for the corresponding service key and message key. If present the stored SOAP response is sent to the SOAP router, which in turn is sent to the client. If not, specific entries of the service key and message key are made in the cache data structure to identify the service, the method under the service and a SOAP request is sent to the corresponding service, the SOAP response from the service is stored in the cache data structure under the corresponding service key and message key of the SOAP response and the SOAP response is sent to the SOAP router, which in turn is sent to the client.

4.3 Eviction from the SOAP cache

Eviction from the SOAP cache is carried out to decrease the size of the cache repository. Decreasing the size of cache repository results in fast retrieval of required cache objects and also prevents from storing invalid cache objects.

The Eviction policy used in the caching component of this minor project is Least Recently Used (LRU) policy and size policy. When cached SOAP objects have to be evicted, the cache repository is initially searched for cached SOAP object, which have been used less frequently used, and these cached SOAP objects are evicted. If two or more cached SOAP objects have the same least frequency of usage, then the sizes of the cached SOAP objects are compared. The cached SOAP object having the maximum size is evicted from the SOAP cache repository.

4.4 Maintaining Consistency of the SOAP cache

Figure 7 depicts, the workflow consistency of SOAP cache is maintained by using time policy. The administrator of the SOAP cache sets the expiry time for the SOAP objects to be cached. When a new SOAP object is cached, the last access time attribute of the SOAP cache object is set to the current time. When a cached SOAP object is fetched from the cache repository the difference between the current time and the last access time is calculated and compared to expiry time. If the difference is greater than the expiry time a fresh SOAP response is fetched from the web service. This SOAP response is cached. Setting the time attributes of the cached SOAP object to current time and the SOAP response is returned to the client or if the difference is less than the expiry time the cached SOAP response is returned to the client (figure 5.6.b, 5.6.c).

6. Experimental Results

The test environment consisted of three terminals. The first terminal hosted the client. The second terminal acts as an intermediate between the client and the web service. The cache module is loaded on the second terminal. The third terminal hosted the web service. The three terminals were connected in a local LAN network. The three terminals communicated with each other over HTTP. The three terminals run on a Pentium 3 500MHZ processor and a 256 MB RAM.

6.1 Testing Approach

Two types of testing methodologies were used. The first test procedure involved comparing response times for retrieving a character array of varying sizes with and without cache. The second test procedure involved comparing response times for hospital management web services workflow with and without cache. For each test data, the response time of 1000 SOAP messages were tested with and without a cache, so as to minimize the effect of external factors like network latency, IO latency etc.

The fig 8 indicates the test results for a varying size character array with and without cache. The fig 9 indicates the test results for a varying size SOAP inputs in kilobytes with and without cache. The graphs in 8 and 9 indicate that the performance of SOAP improves drastically by the use of cache. By caching SOAP requests and responses locally on the client side the overhead time involved in the construction and parsing SOAP message is avoided.

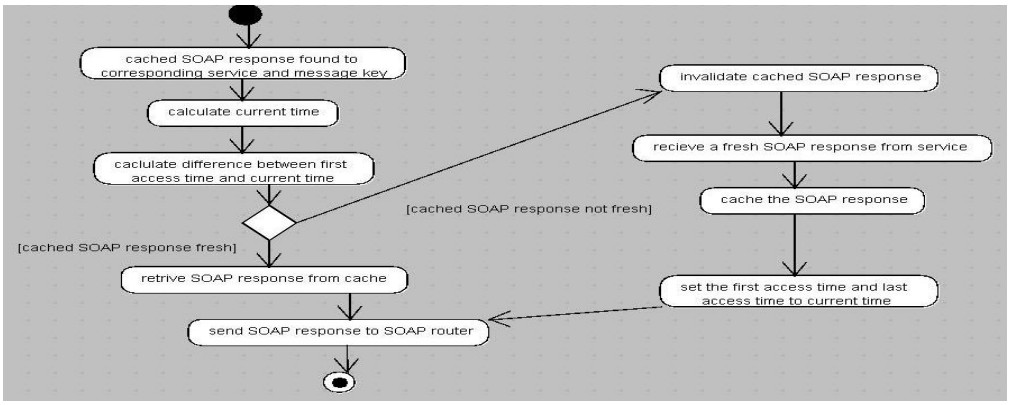

Figure 7 Consistency of SOAP Cache Activity Diagram

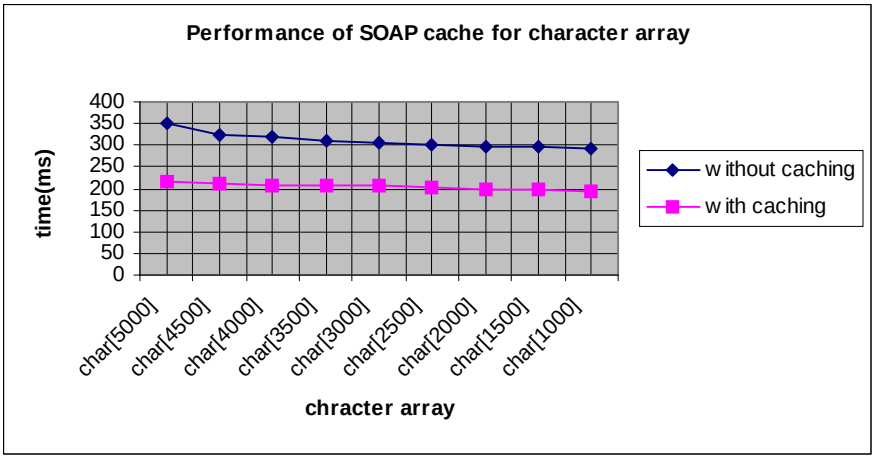

Figure 8 SOAP Performance Graph 1

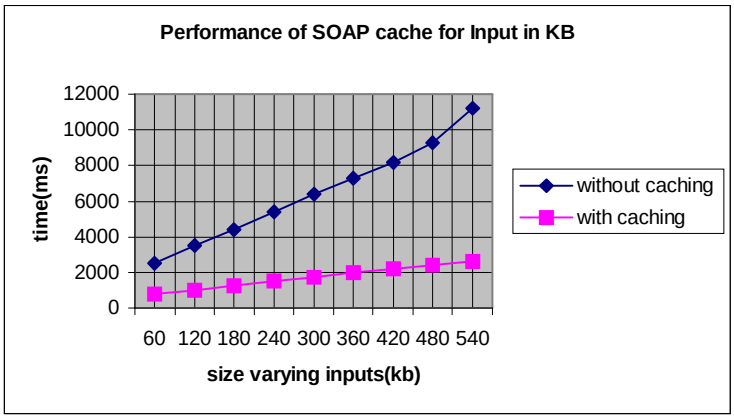

Figure 9 SOAP Performance Graph 2

6. Conclusion

This paper dealt with how caching SOAP messages can help improve the performance of SOAP. The architecture of the SOAP caching component is used in hospital management system. The data structure is used to cache SOAP objects. The eviction and consistency policies used in the SOAP cache and the testing methodology and results used to gauge the performance of SOAP by using caching.

References

[1] Meng, J. Krithivasan, R. Su, Helal, S.Y.W. S.: Flexible Inter-enterprise Workflow Management Using E-services, *Advanced Issues of E-Commerce and Web-Based Information Systems*, 2002. (WECWIS 2002). Proceedings. Fourth IEEE International Workshop on , 2002

[2] Garshol, L.: *Definitive XML Application Development*, Prentice Hall, 2002.

[3] Walsh, A. E.: *UDDI, SOAP, and WSDL: The Web Services Specification Reference Book*, Prentice Hall, 2002.

[4] Aoyama, M. Sullivan, K.: *Web services Engineering promises and challenges*, University of virgina USA, IEEE publication March 2002

[5] Chester, T. .M.: *Cross-platform Integration with XML and SOAP*, IT Professional, Volume: 3 Issue: 5, Sept.-Oct. 2001,IEEE.

[6] Box, D. Ehnebuske, D. Kakivaya, G. and et al: *Simple Object Access Protocol*, W3C Note 08 May 2000

[7] Davis, D. and Prashanth, M.: *Latency Performance of SOAP Implementation*, *Cluster Computing and the Grid* 2nd IEEE/ACM International Symposium GRID2002.

[8] Chiu, K. Govindaraju, M. and Bramley, R.: *Investigating the Limits of SOAP Performance for Scientific Computing*, Bloomington, Indiana University.

[9] Chandra, S.: *Performance Analysis of Soap*, New Jersey institute of technology, March 2002.

A Student-Adaptive System for Driving Simulation

I. Weevers, A. Nijholt, B. van Dijk & J. Zwiers
Dept. of Computer Science, University of Twente
Enschede, the Netherlands
i.weevers@tm.tue.nl, {anijholt,
bvdijk,zwiers}@cs.utwente.nl

J. Kuipers, A.O. Brugman
Green Dino Virtual Realities
Wageningen, the Netherlands
{jorrit, arnd}@greendino.nl

Abstract

Driving simulators have to be student-oriented. We created the Virtual Driving Instructor (VDI), an intelligent tutoring multiagent system, which provides student-adaptivity. The VDI enhances the interaction between the driving simulator and the student. It uses regressive instruction and feedback, which are adapted to the student, presentation context and task, to help the student improving his driving skills. Collaborative agents realize this. Each agent deals with a sub domain of driving education.

1. Introduction

Driving simulators, such as the Dutch Driving Simulator developed by Green Dino Virtual Realities, offer useful opportunities for training to control and drive a car in traffic situations. With simulators objective measurements can be carried out on the student's driving behavior. The obtained values can be used to adapt the learning environment to the student.

To become a proficient driver, a person needs to acquire various skills, varying from simple to complex levels. This acquisition needs to be guided by a driving instructor. An intelligent tutoring system becomes an innovative technique to create a student-adaptive learning environment by using the individual measurements. The system evaluates the user's driving behavior in relation to the current situation and responds by providing feedback and adapting the simulated environment to the user's needs. For this, the system needs to understand the interaction between the user's and the environment's knowledge and respond to each individual user. In this paper, we present the Virtual Driving Instructor (VDI), an intelligent tutoring system that adapts the evaluation and feedback about the driving behavior to the current user of the driving simulator.

The goal of the VDI is to transfer expert knowledge of driving a car to a student. The VDI is successful if the following conditions are met:

- *Driving Skills*. The performance on all driving skills is sufficient. That means the student drives safe, smooth, and economical.
- *Procedural Skills*. The performance on all procedural skills is sufficient. That means no steps in any driving task procedure are skipped or swapped.
- *Traffic Insight*. The performance on traffic insight is sufficient. The student performs the right driving task at the right time.

In this paper we will discuss the interaction between the VDI and the student and focus on instruction and feedback to the student.

2. Interaction in the simulator

Driving involves an extensive interaction between the driver and the driving environment. As Norman [5] stated, part of the knowledge is in the world, and part of the knowledge is in the head. To responds appropriate to events, the driver has to perceive and understand what is happening in the world and apply his own driving skills and knowledge for that. An instructor has to look at the interaction of and gap between the two knowledge domains, for improving the student's knowledge and skills. Figure 1 shows the interaction between the driving simulator system and the student by data flows. The figure shows two important interaction elements of the system, the 'simulated world' and the VDI. The first concerns presenting visual and auditive information, such that the student perceives the world in which he is driving. The second responds to the student's driving behavior.

The student perceives what is happening in the simulated world (1). Subsequently, he responds to the perceived situation according to his own goals (2). This response may be instinctive or rationalized, and wrong or good. The VDI recognizes the student's driving behavior and relates it to the current situation (5) and previous behaviors. The VDI than may choose for action. If action is required, the system may either adapt the simulated world according to the student's needs (3), give educational feedback to the student (4), or do both.

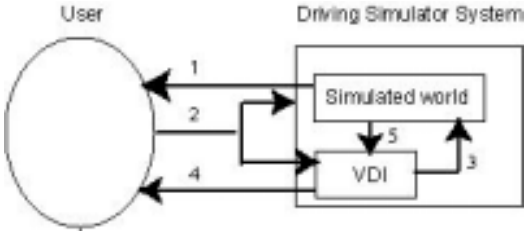

Figure 1. Interactions between driving simulator and the user

Weevers et al. [8] discussed the issues involved with the VDI's architecture and the techniques used to create an understanding of the current situations and performed driving tasks. In this paper, we will discuss how the VDI establishes student-adaptive interaction to improve the education of the learning environment.

3. Regressive instruction

Learning how to drive can only be achieved in practice. We think this is especially true for the last phase of the driver's development from a novice to an advanced level. A novice driver comes across many stages of acquiring different skills, in order to become a skilled driver. Each stage involves different driving tasks. A simulated environment offers opportunities to focus specifically on certain tasks. Michon [4] discerned three levels of driving tasks:

- Strategic level: This is the highest (abstract) level at which one may think of route planning and higher goals determination.
- Tactical level: At this level the driver selects and achieves short-term objectives. One may think of overtaking, merging and crossing an intersection. This level deals with driving maneuvers that can be decomposed in more basic skills
- Operational level: This level holds the most elementary operations, the basic car control operations like using the clutch, steering and accelerating.

In addition, there are different phases in which instructions about a certain task may be provided:

1. Motivating phase. The instructor may give the student a preliminary instructions about the approaching task
2. Mentoring phase: The instructor guides the student, while he performs the task
3. Evaluating phase: The instructor gives feedback after the student carried out the task.

Depending on the current student's driving skills and knowledge, these levels have to be embedded into the current state of the learning environment. A novice driver will start with operational tasks, while a proficient driver is applying tactical and strategic tasks. The levels will be reflected on the simulated world: Operational skills cannot be practiced at crowded intersections and tactical tasks, such as overtaking, require situation opportunities to actually practice that.

The feedback and instructions of the VDI to the student have to adapt to the three levels and the current student's level. We introduce *regressive instruction*: The VDI reduces the frequency of feedback and instruction with increasing skill levels of the student. As the student improves his driving skills the tasks become bigger and more comprehensive; the focus shifts from tasks at operational level, to tactical and strategic level. Therefore, the number of tasks will decrease. Furthermore, the improving student requires less guidance. The novice driver needs continuous instructions, while he is performing driving tasks. Feedback and instructions in all phases are important. However, as the student develops his skills he needs less task preparation from the motivating phase, less guidance from the mentoring phase, and less evaluation from the correcting phase.

The acquisition and training potential of skills in an Intelligent Tutoring System relies heavily on the ability to provide the students with extensive practice on various training exercises in conjunction with adequate instruction (Dong Mei Zhang [1]). Regressive instruction is applied to all (non-predetermined) situations. Since the simulation is partly unpredictable, which results in various situations, the driving exercises combined with the instruction result in good training capabilities of the VDI.

4. A student-adaptive system

Each novice driver has his own specific learning process. Amongst others, this depends on the student's personality, skills and intelligence. A driving instructor adapts the learning environment to the individual student. He may adjust the driving curriculum and feedback to suit the individual needs. Since the driving simulator provides a learning environment in which the student is the focus of attention, the system has to be able to adapt to each individual student. We developed a multiagent system to realize the adaptivity.

The VDI needs to possess and apply different types of awareness. According to Smiley and Michon [5], awareness is the domain-specific understanding to achieve goals for this domain. Within the domain of driving and instruction different sub domains with different goals exist. Each of these sub domains includes its own specific tasks. The VDI needs to recognize the driving behavior of the student and relate it to the observed current situation. Then, the VDI evaluates the performed driving tasks and

decides whether feedback to the student about the performances is needed. In addition, all decisions have to be made within a framework of task focus. The VDI should guide the student to accomplish a complete driving curriculum step-by-step. We created agents that each deal with an awareness type.

4.1. The Situational Agent

The VDI needs to conduct analysis on the driving tasks and occurring traffic situations. The Situational Agent implements situation awareness, which recognizes and evaluates the student's driving behavior. It can only accomplish when it knows the possible occurring driving tasks and situation elements. The agent uses an adapted version of the extensive McKnight' and Adams' task analysis [3] on car driving. The integration of this listing with the various situational elements gives the VDI the understanding for contextual relations in the current situations (see Weevers et al. [8] for a more elaborate discussion).

Additionally, the Situational Agent keeps track of each student's performances on each (sub)task. By maintaining records on the current student level and progress for specific tasks, the agent can point out specifically to which aspect the VDI, and therefore the student, should pay attention.

Situations consist of different type of elements. Currently, the agent deals with one continuous (speed control), one dynamic (car following) and one static (approaching and crossing an intersection) aspect, which show promising results.

4.2. The Presentation Agent

Presentation awareness concerns presenting natural feedback to the student. This involves formulating and timing utterances in a natural and educational style. We implemented this awareness type into the VDI by creating the Presentation Agent. It schedules, formulates and presents the feedback and instructions.

4.3. The Curriculum Agent

Curriculum awareness relates to achieving goals for the driving curriculum, such as offering the student the exercises that suits his current driving skills. We made a first step by embedding the structure of the recently introduced new Dutch driving program the RIS (Driving Education in Steps) into the agent. Although dynamic curriculum regulation is still a next step, storing each student's performance in relation to specific driving aspects provides a good overview of each individual. Incorporating the RIS makes the Driving Simulator also attractive for the market, which will stimulate future developments and research.

5. Feedback to the student

Instructions and feedback to the student are one of the pillars of driving education. As we discussed, the feedback concerns different driving tasks at different skill levels and in three phases. For understanding the interaction between the driving instructor and the student, we carried out a two days empirical research on the practical experience of professional driving instructors at the Dutch national police school. This research provided insights into educational aspects, such as feedback timing and the formulation of utterances. The most important results, which are also used by the VDI, were that:

(1) The feedback usually is positively expressed. For example, the VDI should express that something will go better next time instead of stating that the student did something wrong;

(2) The student is being prepared for approaching complex situations by instructions. For example, when the student approaches an intersection, the VDI will tell this and point out the aspects to which attention should be paid;

(3) The instructor mainly focuses on the aspects the exercise is meant for. For example, in case the student is practicing overtaking behavior for the first time, the VDI should not start to complain about gear shifting mistakes. The student pays attention to just the overtaking process. Therefore, feedback should not confuse him to stay aware of other less important things.

5.1. Auditive instructions and feedback

As opposed to real driving lessons, the driving simulator may use different media, such as visual display and audio generation, for presenting the instructions and feedback. Wickens developed the multiple resource theory [9], which states that each type of data perception relates to its own resource with its own capacity. Therefore, different tasks, which utilize different resources, can be well executed concurrently. However, Verweij [7] revealed that auditory tasks may attract the full attention at the cost of the visual tasks.

An important aspect of driving instruction is that the student needs to perceive the feedback as soon as it is provided. This may not be accomplished by visual presentation, since humans only perceive visual data by looking at it. Since the student should be focused on the traffic situations, he should not have to shift his attention to an-

other display. We think that feedback display in the windshield of the simulator also will be too distractive. To guarantee the feedback perception we chose for auditive feedback. To avoid distraction by memory consuming auditive data, the feedback should be as short, but informative, as possible.

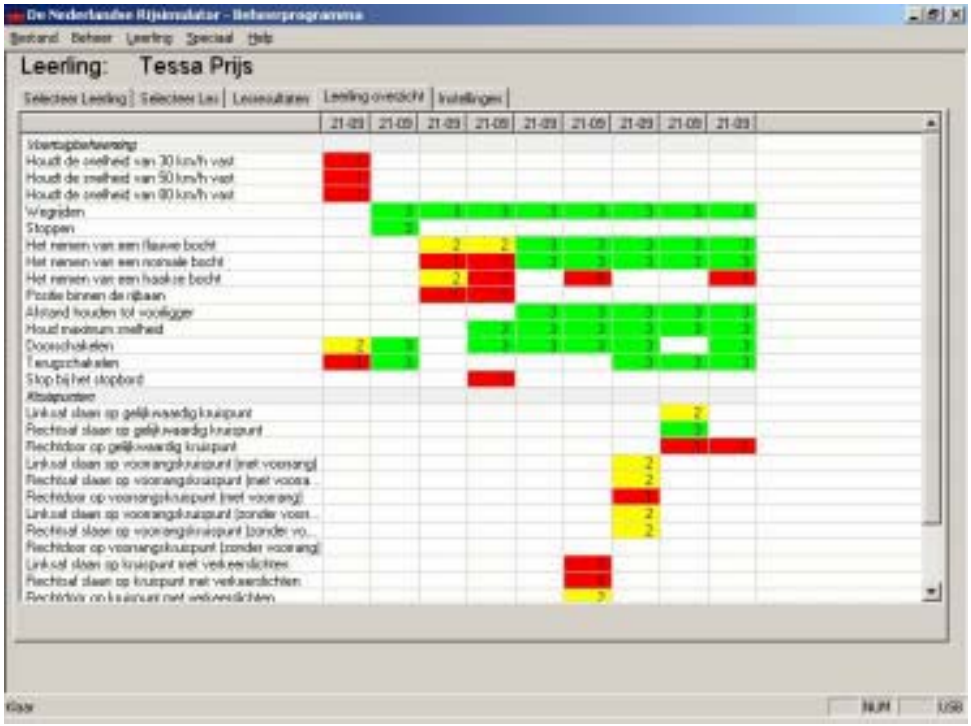

Figure 2. Resume of driving tasks and overview of instruction levels

5.2. Context and task related feedback

Holding [2] stated that providing the driver with feedback about the quality of his performance is useful for motivating and correcting, and improving his performance on tasks. Consequently, the VDI has to provide clear direct feedback on specific driving tasks.

The previous feedback system of the driving simulator provided the same feedback utterance within a predefined time period all over again (For example, "You are driving too fast" every five seconds with the same intonation). Experiences show that students perceived this as irritating and certainly not benefiting the learning process. To overcome this problem, the VDI needs to consider timing and utterance issues for feedback and instructions.

The collaborative processes of the Situation Agent and the Presentation Agent showed good solutions. The Situation Agent decides which tasks require most attention and therefore possible feedback. Furthermore, it keeps track of the feedback provided on specific tasks. The Presentation Agent considers the presentation context. It makes decisions independent from the instruction's and feedback's contents. It changes the utterances and intonation of task-related comments depending on related feedback within a given time period.. In addition, the Presentation Agent looks at the priority of the feedback. The student needs to perceive important comments, such as possible life threatening situations, immediately. However, the VDI may refrain from presenting less important feedback. Continuous feedback is irritating and causes mental overload. Priority scheduling solves this issue. McKnight and Adams [3] assigned priorities to the tasks in different situations. The Presentation Agent uses this task information to decide on feedback in the current presentation context.

All timing parameters were determined empirically. Users and our results from the research with the driving instructors indicated desirable moments of feedback.

6. Global performance and application

The VDI has the capability to adapt its comments to the performance of the student. The beginner will be treated different from the more advanced user. The student's progress is tracked per driving task. In case the performance of the student drops after a while, the comments may revert to an earlier stage. For every driving task, the student goes through three phases. Each of these phases is handled differently by the VDI:

- *Conscious*. The student's attention is mainly focused on the driving skills. The VDI takes the student by the hand and names each step in the procedure. This is called introducing and mentoring. The performance of the driving skills is evaluated by the VDI.
- *Semi-conscious*. The student has a reasonable control of the driving skills and procedure, but may have fallbacks. The VDI does not mention each step of the procedure any more, but still makes corrections if the student makes a mistake.

- *Autonomous*. The student does not make mistakes in the procedure and has acquired the driving skills. At that point traffic insight becomes more important. Does the student apply the driving task at the appropriate time? The VDI does not even command the driving task any more, to see if the student performs it on his own.

Green Dino, developer of VDI, has implemented the instructor in the Dutch Driving Simulator. At driving schools we tested the VDI on 17 years old students with no driving experiences. The students started with a module on vehicle procedures. In 5 lessons they learnt how to handle throttle, breaks, clutch, steering wheel, and so on. In the second module they learnt how to handle crossings procedures and give right. Each lesson took 30 minutes including an introduction and an evaluation. The introduction describes the drive tasks and procedures. The evaluation showed the performance on the task and the progression in instruction level. All the results are collected in an administration system and can be used for further analysis of the performance of students and system.

Students followed the 10 driving lessons at one day. At the end of the day the VDI gave 'green light' for driving in a real car. The VDI showed to be a perfect driving task and procedure trainer without the help of an instructor. These first results showed the strength of virtual instruction and the working of the VDI.

7. Conclusions

We have presented the Virtual Driving Instructor that realizes student-adaptivity in a driving simulator. The VDI implements several sub domains of driving instruction by the Situational, Presentation and Curriculum Agent. Since each agent takes some specific student related information into account, the collaborating processes emerge adaptation to each individual.

The VDI observes the interaction between conducted driving tasks by the student and the simulated situations. To bridge the gap between the student's and the environment's knowledge, it provides instructions and feedback to improve the student's driving skills. This follows the strategy of regressive instruction: the frequency of feedback and instructions reduce with improving skills. The presentation depends on the relation of the feedback to the actual task and the context of presentation. To avoid distraction from the actual tasks, the VDI provides the comments brief and auditively.

8. Future directions

One of the next steps in the VDI's development is functionality for user modeling. A good user model will influence the decision-making processes of the agents positively and enhance the student-adaptiveness of the VDI.

Currently, the input by the user is active and is realized by mechanic controls, such as steer, gas and throttle. There are many passive opportunities for additional input. We think of observing the user by measuring devices, such as eye trackers. They will provide important eye gaze behavior, which is essential for driving behaviors.

Future research includes feedback and instruction timing issues. The current parameters were determined empirically. Timing values depending on a student's personality and skill level have to be determined more accurately.

Acknowledgements

We thank Rob van Egmond and Ronald Docter of the Dutch national police driving school, LSOP, for their support with the research.

References

[1] Dong Mei Zhang, From task sequencing to curriculum planning, Proceedings AI ED 97, 1997.

[2] Holding, D.H., In: G. Salvendy (ed.), Handbook of human factors, New York, USA, Wiley, 1987.

[3] McKnight, J., Adams, B., Driver education and task analysis volume 1: Task descriptions. *Technical report, Department of Transportation*, National Highway Safety Bureau, 1970.

[4] Michon, J., A critical view of driver behavior models: What do we know, what should we do?. In Evans, L., and Schwing, R. (eds.), *Human Behavior and Traffic Safety*, Plemum, 1985.

[5] Norman, D. A., Cognition in the head and in the world: an introduction to the special issue on situated action, *Cognitive Science*, 17, 1-6, 1993.

[6] Smiley, A. and Michon J.A., Conceptual framework for generic intelligent driving support. *Deliverable GIDS/I*, Haren, The Netherlands, Traffic Safety Centre, 1989.

[7] Verwey, W.B., Adaptable driver-car interfacing and mental workload: a review of literature, *Deliverable GIDS/DIA/I*, Haren, the Netherlands, Traffic Safety Centre (1990).

[8] Weevers, I., Kuipers, J., Brugman, A.O., Zwiers, J., Van Dijk, E.M.A.G., Nijholt, A., The Virtual Driving Instructor, Creating Awareness in a MultiAgent System, In *Proceedings of AI 2003, Canadian Conference on Artificial Intelligence*, Halifax, Canada, 2003.

[9] Wickens, C.D. , The structure of attentional resources, In: Nickerson R. (ed.) *Attention and performance* VIII, Hillsdale, USA, Erlbaum, 1980.

(This page left blank intentionally)

Web Services Based Single Sign-on for Hospital Management System

Savitri Bevinakoppa Ravi Sankar Tripuramallu
School of Computer Science and Information Technology, RMIT University
Melbourne – 3001, AUSTRALIA
savitri@cs.rmit.edu.au rtripura@cs.rmit.edu.au

Abstract

The potential of Internet has been credited with the ability to communicate and collaborate among the partners and transact among multiple organizations. Thus companies are fast moving in the direction of collaborative Business-to-Business (B2B) e-commerce providing the customers and business partners more flexibility and efficiency. Web services are fast replacing the traditional Enterprise Application Integration (EAI) solutions that suffer from interoperability issues. Securing web services is important and difficult as the services and clients span disparate platforms and security domains.

The aim of this paper is to implement efficient and secured single sign-on service for a Hospital Management System (HMS). The HM system consists of various web services like pathology, radiology, clinics etc. These services are exposed to other internal and external entities through registries. The user or doctor once authorized to use one of the services is entitled to access any of the other services based on the type of authentication performed and the privileges acquired.

1 Introduction

The collaboration among businesses has led to necessity in minimizing the number of hurdles the user has to go through to avail the co-operating services. This gives the user the overall liberty to browse a federation of services once authorized at one of the services. Since Web services allow loose coupling of applications unlike traditional distributed computing models like COM [1] and CORBA [2], allow the incrementing of systems. Web services are simpler to design and develop when compared to other EAI solutions [3].

Web services are based on open standards unlike other EAI solutions that are based on proprietary protocols. Web services allow dynamic integration based on the service-oriented architecture. This allows the consumers to bind at runtime based on the business logic rather on technology platform of the service [5]. This section gives the software and protocols used for developing single sign-on service for Hospital Management System.

1) Web logic server 7.0 – This application server is used to host the various services that collaborate.
2) Windows 2000 Professional – Operating system for hosting the Application Server.
3) IBM XSS4J- security suite for Encrypting XML Documents

Section 2 gives description of the web services components that are used for the implementation. Design and analysis of the HMS single sign-on services are explained in section 3 and 4 respectively. Section 5 gives the implementation of the service and conclusion of the paper is given in section 6.

1.1 Web services Components

Software/Protocols used for HMS are

Apache XML Security Project – for generating XML Digital Signatures

2 Web services

Web services can be defined as network accessible interfaces to applications exposing functionality. The applications exposed by web services are accessible with protocols such as HTTP and open standards like XML that are driving the Internet. The following terms/protocols used for Hospital Management Systems (HMS).

1. Interface: Every UDDI registry is provided with interfaces that allow consumers or providers to retrieve the information or browse the registry.
2. Web Services Description Language (WSDL): A web service exposes functionality and the operations that can be invoked. These operations are invoked with certain parameters or specific information.
3. Security in Web Services: SAML is a standard used in this application. This project implements secured single sign on system for an existing federation of hospital web services taken as a case study.
4. Security Assertion Mark-up Language (SAML): SAML is used to implement single sign on for web services at application level. SAML works over the existing security technologies and is a solution for open, web-based interoperable single sign-on service. SAML is a combination of S2ML and AuthXML.

3 Design of Hospital Management System

A Hospital management system is taken as a case study for the project. This was chosen because of the underlying service oriented architecture. This single sign-on enabled service oriented architecture allows the authenticated end users to access the exposed services. This section details

design of the hospital management system and the steps involved in design and various components that make up hospital management system. While the initial sections cover high-level deployment diagram and component diagrams, later sections cover in depth of the use cases and scenarios involved.

3.1 Hospital Management System Components

The system comprises various web services – pathology, radiology, radiotherapy, clinical details etc. The goal of the system is to expose all the available services to the end users such as doctors who have the access rights to one of the services. Various departments in the hospital play the role of service providers. The service providers register with the Universal Description Discovery and Integration registry. The web services architecture allows all these registered services on disparate systems to form a federation.

3.2 Roles or Actors in the system

The doctor: Doctor is the end user of the system who avails the services. Authenticated doctor is given the access to the available services for which he is authorized.

The service: Service is the functionality offered to the end user and in this case to a doctor.

Pathology service: Pathology department records the pathology details of the patients and makes them available to the doctor in the form of service.

Radiology service: Radiology department maintains the records of the patients referred to the radiology department.

Clinical Centres: keeps the record of patients details such as patients personal information, consultations, referral doctors, details of diagnosis and treatment outcome etc.

3.3 Functionality of Hospital Management Solution

Every doctor accessing a service belongs to one of the security domains in which each service is hosted. The doctor authenticated at one of the services

has the capability to add, alter, view or delete patient details. The authenticated doctor when crosses the security domain to access a remote service, the doctor have the capability to view patient details provided by the remote service.

The single sign-on capability integrated into the system gives the doctors authenticate once and only once to avail any of the exposed services that form a federation. The doctor interacts with the system while authenticating or while availing the services.

4 Analysis of Single Sign-on Service for Hospital Management System

Authorization is the act of granting privileges based on the credentials. This act involves exchanging information about the authentication act carried out.

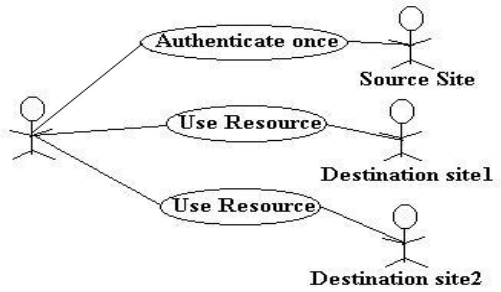

Fig. 1: Use case for single sign-on using SAML

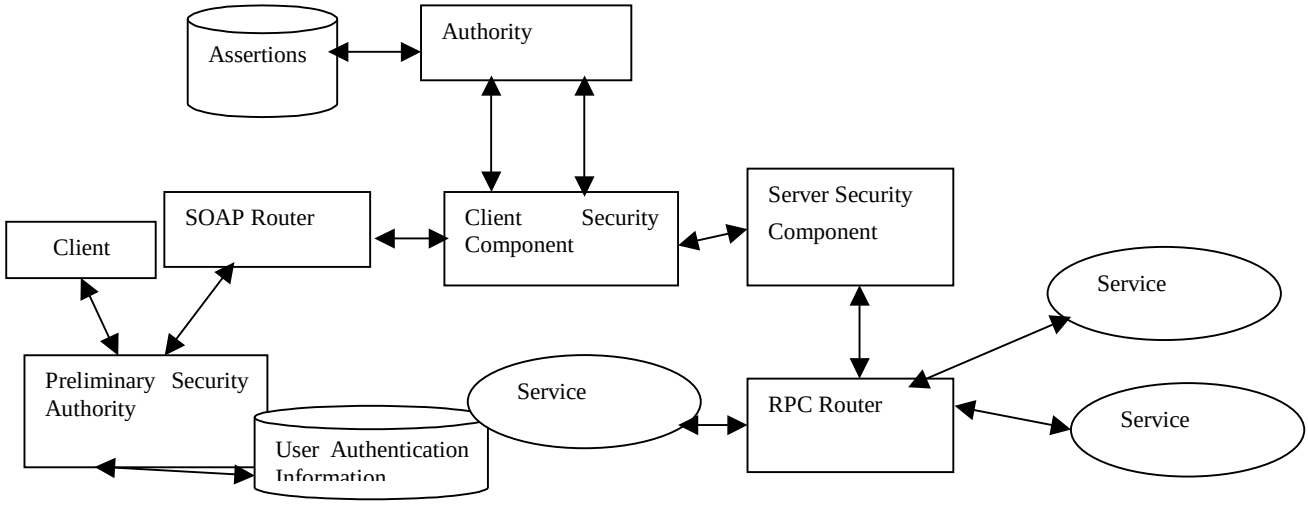

Fig. 2 Components of SAML enabled Single Sign-On Web services Framework

In a federation, the user achieves the capability to roam around the federation server with out re-authenticating. The use case for single sign-on is depicted in figure 1. The user only needs to authenticate to one of the services of the federation and is granted permission to any other services of the federation. The source site is the site at which the user visits first and authenticates. A destination site is a site that the user accesses further on his authentication at the source site. Security Assertion Markup language (SAML) is about writing assertions and exchanging them. Assertions are nothing but the facts about the authentication events that have taken place. These assertions are exchanged to enable single sign-on in a web services infrastructure. The assertions are passed along with service requests.

4.1 Architectural Overview of single sign-on

Architectural overview is shown in figure 2. Preliminary Security Authority is responsible for initial authentication process for the end users. This authority is supported by a database, which holds the authentication information. This authority permits the users with proper id and password.

User Authentication Information Database assists preliminary security authority in basic authentication implementation. This holds the information about the users intend to login to the hospital management system.

SOAP Router is responsible for processing the SOAP requests and dispatching them to the services. SOAP Routers are also responsible for delivering the responses from the services back to the clients or request makers. SOAP Router takes the responsibility for browsing UDDI registry, WSDL descriptions of the services and association of requests to services.

The client security component is responsible for SAML requests. The client security component creates SAML requests depending on the type of assertion needed. These requests are then passed on to the authority. The client security component is also responsible for maintenance of artifacts for each login. The client security component also dispatches the artifacts to the server security component for further processing.

Server security component is the component that requests the processes the assertions. It is the responsibility of server security component to fetch the assertions from the authority. Server security component acts as the Policy Decision Point. It takes decision on permitting the requests to the services based on the assertions.

Authority is typically a third party entity that is trusted by the services that are forming a federation. The authority is the entity that issues the assertions based on the users method of authentications scheme and information. Authority is supported by a database for assertions.

Assertion database holds assertions for each login. This database provides the backend for authority. RPC Router dispatches the SOAP requests to the services. A service is the information provider for the authenticated users of the hospital management system. Services register themselves with UDDI registry to participate in the federation and also trust the authority and the assertions that are vouched by authority.

4.2 Steps Involved in Service Access

The following sequence diagram figure 3 depicts the time line sequence of steps involved in accessing a remote service. The steps involved initial authentication to a local service that is carried out of band and eventually accesses the desired target service.

As we can see in figure 3, the client security component initiates the SAML message flow: The client security component gets the requests only from the users that are authenticated by basic password authentication technique. The client security component provides the authority with the details of the authenticated user who is making request. The authority checks if the authenticated user is eligible to access the service as requested. Authority builds an assertion based on the authorization information and a reference to the assertion or so-called *artifact*. The artifact is passed back to the client security component as a response to the details submitted. The client security component holds the artifact for future access to other services. The artifact is passed to the server security component along with the service request. Server security component acts the gateway to the services hosted by the server. The authority security component builds the assertion request along with the artifact and dispatches it to the authority. Authority on attaining the artifact and the assertion request fetches the assertion that was built corresponding to the artifact. This assertion is dispatched as SAML Response to the server security component. The server security component processes the assertion received from the authority, analyzes the authorization and conditions. The server security component then decides whether to allow the access to the services.

Security of SAML messages is out of scope of SAML in this paper. Messages can be secured using XML digital signatures or SOAP Security Extensions.

5. Key Elements for Implementation of Single Sign-on for HMS

This section gives the protocols used and testing approach.

5.1 Protocols

SAML Artifact:

```
<SOAP-ENV:Envelope xmlns:SOAP-
ENV="http://schemas.xmlsoap.org/soap/env
elope/">
<SOAP-ENV:Body>
```

```
<samlp:AssertionArtifact Type-
Code="0x0001"
xmlns="urn:oasis:names:tc:SAML:1.0:cm:ar
tifact-01"
xmlns:samlp="urn:oasis:names:tc:SAML:1.0
:protocol">
```

```
<SourceID>AU_AUTHORITY</SourceID>
<AssertionHan-
dle>1291c9e5</AssertionHandle>
</samlp:AssertionArtifact>
</SOAP-ENV:Body>
```

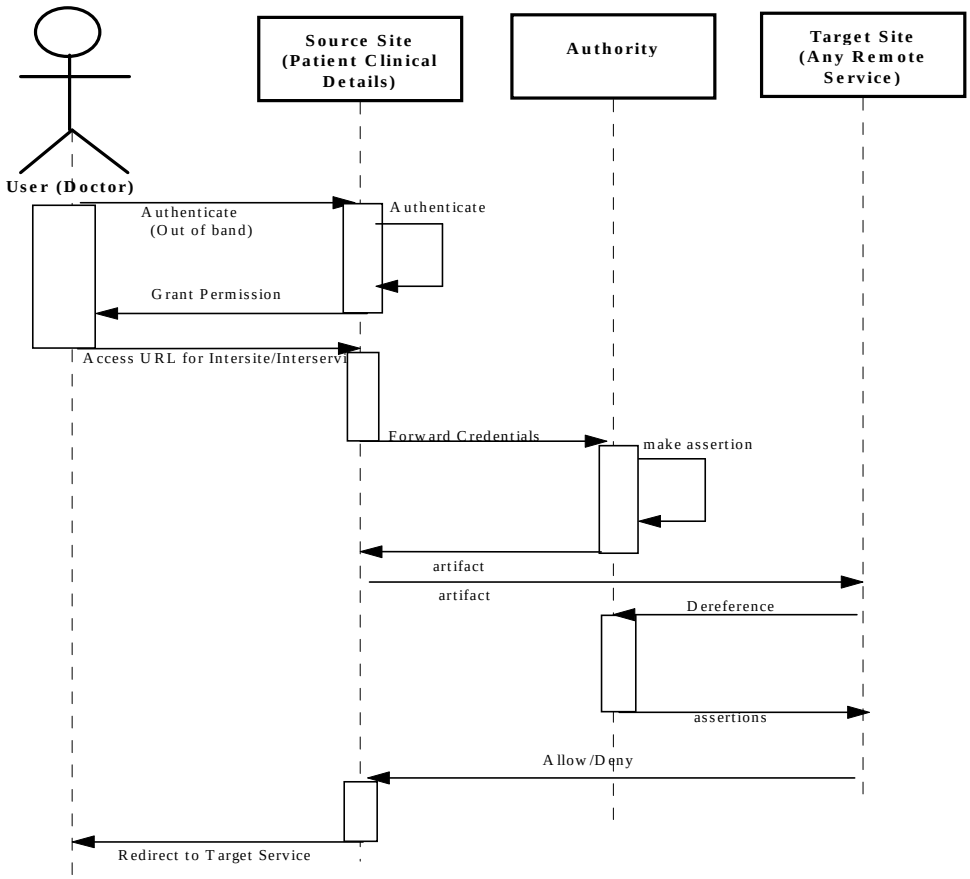

Fig. 3: Sequence Diagram to Access Remote Service – SAML message flow

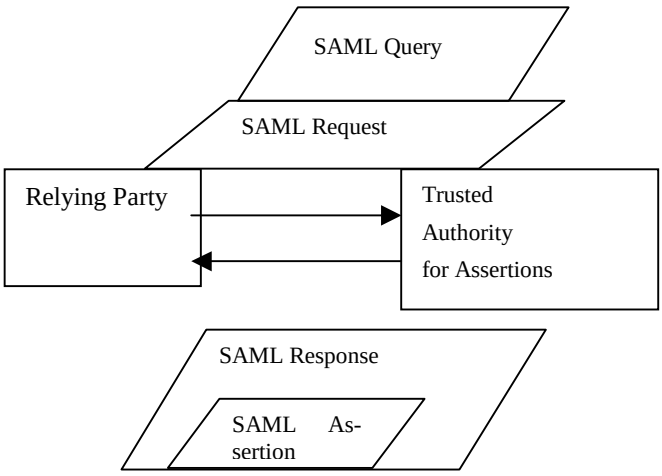

Fig. 4: Protocol underlying SAML

```
</SOAP-ENV:Envelope>
```

Every SourceId element refers to an URI. AU_AUTHORITY represents the URI of authority. The service maintains a list of SourceID and the corresponding URIs. The AssertionHandle is a randomly generated 64-bit string by the authority. The authority holds an assertion for each corresponding AssertionHandle. The assertion is returned when assertion handle is de referenced.

SAML Assertion

```
  <saml:AuthenticationStatement Authen-
ticationInstant="Sun Apr 14 15:09:02EST
2002" AuthenticationMethod="password" />
   <saml:AttributeStatement>
   <saml:Subject>
```

```
      <saml:NameIdentifier          For-
mat="urn:oasis:names:tc:SAML:1.0:asserti
on
    #emailAddress">doctor@hope.com
   </saml:NameIdentifier>
  </saml:Subject>
  <saml:Attribute               Attribu-
teName="Designation">
 <saml:AttributeValue>DOCTOR</saml:Attri
buteValue>
  </saml:Attribute>
<saml:Attribute                 Attribu-
teName="AllowedServices">
  <saml:AttributeValue>Pathology
</saml:AttributeValue>
  </saml:Attribute>
  </saml:AttributeStatement>
  </saml:Assertion>
  </SOAP-ENV:Body>
  </SOAP-ENV:Envelope>
```

The value of the element, `AttributeName="Designation"` asserts that the user for which the assertion belongs is a doctor. The value of the element `AttributeName="AllowedServices"`, asserts that the user has right to access Pathology service.

5.2 Securing of SAML messages: XML Encryption:

XML Encryption provides end-to-end security for XML data that is exchanged. The XML Encryption has certain advantages over Transport Layer Security (TLS) which is based on Secure Socket Layer (SSL). XML Encryption can encrypt the parts of XML documents that are exchanged.
An XML Encrypted document can carry both the secured and unsecured XML/binary data. In the case of securing SOAP/SAML messages through XML Encryption, only parts of SAML message are encrypted [13].
Symmetric key encryption assumes a key known as 'secret key' known only to both the sender and receiver. The sender uses this key for encryption and eventually for decryption by the receiver. SAML messages are exchanged in this fashion among the security components.

SOAP message header and body that envelop SAML message pass through intermediaries unencrypted. The <urn> element in SAML Artifact is encrypted using triple DES Security needs for web services are similar to that of typical web based applications [12]. Securing of SAML messages is out side the scope of SAML. XML Encryption and XML Digital Signatures ensure confidentiality and non-repudiation aspects of securing SAML messages in an inter-operable fashion.

key and the key itself if encrypted with sender' s RSA key. It is assumed that keys are exchanged out of band and are available to the sender and receiver

Xml digital signatures:
An XML Digital signature ensures the integrity and authenticity of origin for XML messages. Unlike traditional signature mechanisms, with XML Digital signature, a sender has the capacity to sign only the portion of the document for which the sender is liable. This granularity is important as XML based SAML messages tend to pass several intermediaries on the way to destination. Each SAML message that is exchanged in implementing single sign-on service needs to be digitally signed. This ensures that each security component in the application has the confidence on any incoming SAML message.

5.3 Testing

Testing environment:
Application server: BEA Web logic version 7.0 hosts the services
The server runs on Pentium III processor with 128 MB RAM.
The client is a web browser, Internet Explorer 5.0
Operating System for Application Server is Windows 2000Professional

Testing Approach
The aim of the testing is to establish that the application developed enables single sign-on for the services in a secure fashion.

Opportune scenario
A Doctor logs in into Patient Clinical Details Service. Once he is logged in, the doctor should be able to browse the other services available.

Access to multiple services (Single sign-on)
Doctor logs into Patient Clinical Details service at the URL,
http://distributed28:7001/examplesWebApp/doctorlogin.jsp
.
The doctor is challenged to produce user id and password. The system allows only the doctor with correct user id and password with respect to the security domain in which Patient Clinical Details services is hosted.
The doctor is provided with Patient Clinical Details and also the links to other services. The doctor is not challenged for user id and password when he accesses the links to the other services. The doctor can browse through other services at will. This proves that the services are single sign-on enabled.

Accessing Individual Services.

An end user can access any individual service. The access is restricted to the users who have credentials with respect to that particular security domain. The authenticated users have the access only to the individual service.
In this case, when doctor logs into Patient Clinical Details Service, he has the access to the Patient Clinical Details Service. The doctor is restricted to that particular security domain or in other words, to that service alone. The doctor when tries to access the other services individually, access is denied. This is because the doctor does not possess the access rights to any other service other than Patient Clinical Details. Any user with access permission to any of the service can access that particular service alone.
The above test cases prove that access to the services is obtained only when the services participate in the federation and participate in single sign-on.

6. Conclusions and Future Work

This research demonstrated an implementation of a single sign-on feature for web services. It includes technologies that are used to accomplish the task. Traditional security technologies like Transport Layer Security, Encryption techniques have to go hand in hand with up-coming XML security standards like S2ML, SAML and XKMS to achieve total security for single sign-on enabled web services. Implementing the support security services using traditional security technologies is out side the scope of this project. SAML does not alone guarantee the security of single sign-on enabled web services.
The future work includes LDAP directories can be used for maintenance of assertions, Public Key infrastructure can be implemented to achieve over all security for a web services infrastructure. Currently signing and verification of SAML messages is painfully slow process. Work can be done in reducing the delays in message processing.

Acknowledgement

Authors would like to acknowledge Dr Kailash Narayan, Head of the Radiation, Peter MacCallum Cancer Institute for providing the information for Hospital Management Systems.

References

1. Nathan, A., *NET and COM: The Complete Interoperability Guide*, Sams Publisher; 1st edition (January 31, 2002), ISBN: 067232170X
2. Cerami, E., *Web Services Essentials (O'Reilly XML)*, O'Reilly & Associates; 1st edition (February 2002), ISBN: 0596002246
3. Graham, S., Simeonov, S., Boubez, T., et. Al.: *Building Web Services with Java: Making Sense of XML, SOAP, WSDL and UDDI*, Sams Publisher; 1st edition (December 12, 2001) ISBN: 0672321815
4. Oellermann, W.: *Architecting Web Services*, APress; 1st edition (October 15, 2001) ISBN: 1893115585
5. http://www.w3.org/TR/wsa-reqs
6. Ray, E., Maden, C.: *Learning XML*, O'Reilly & Associates; 1st edition (February 2001) ISBN: 0596000464
7. Zuffoletto, J., Wells, G., Gill, B., et. Al.: *BEA Weblogic(R) Server Bible*, John Wiley & Sons; 1st edition (February 21, 2002) ISBN: 0764548549
8. http://www.ptsdirect.co.uk/saml.cfm
9. Steelman, A., Murach, J.: *Murach's Java Servlets and JSP*, Mike Murach & Associates; Book and CD edition (January 2003) ISBN: 1890774189
10. http://www.javaworld.com/javaworld/jw-12-1998/jw-12-servletapi.html
11. *Simple Object Access Protocol (SOAP) 1.1* W3C Note 08 May 2000 http://www.w3.org/TR/2000/NOTE-SOAP-20000508/
12. Krishnamurthy, B., Mogul, J., Kristol, D.: *Key Differences Between HTTP/1.0 and HTTP/1.1*, WWW8 Conference Refereed Papers, Compiled from Authors' Original Papers by E. Tang, Foretec Seminars 1999

On the Implmentation of a Fuzzy CMAC

Yu Changbin and Abdul Wahab
School of Computer Engineering
Nanyang Technological University
Singapore 639798
{Brad, Abdulwahab}@pmail.ntu.edu.sg

Abstract

This paper presents a Novel Fuzzy Cerebellar Model Articulation Controller (CMAC) implementation using Field Programmable Gates Array (FPGA) available in a flexible software/hardware co-design platform. The novel fuzzy quantization technique used for reducing CMAC memory requirement is similar to Discrete Incremental Clustering (DIC), with modifications to meet the hardware constraint.

The objective of the project is therefore twofold: to propose a hardware-friendly fuzzy clustering technique based on DIC, to implement the Fuzzy CMAC in hardware cost-saving manner and exploit realization of its inherent parallelism in FPGA architecture.

Test result for classification of 2-spiral problem is presented, which demonstrates the validity and generalization capability of proposed architecture and its advantage of reduced memory requirement.

I. Introduction

Inspired by how brain works: artificial neural networks (NN) have attracted the growing interest of researchers, scientists, engineers and students in many different scientific and engineering areas. Many NN architectures were proposed over the years, among which we will look at the Cerebellar Model Articulation Controller (CMAC) [1, 2], first developed by Albus in an attempt to develop an efficient computational algorithm for use in manipulator control. Functionally, CMAC is a generalized Look-Up Table which able to perform multivariable approximation. Structurally, it is a three-layer feed-forward associative memory neural network. These features enable the CMAC very unique characteristics such as fast speed training and local generalization, which makes it particularly suitable for control applications, signal processing and pattern recognition.

The performance of CMAC is largely dependent on quantization of each input dimension, fine resolution is desired to ensure satisfactory performance, but results in large size of memory to be used and naturally, higher cost incurred. In many cases, CMAC are made impracticable due to its high memory requirement, such as for small-embedded systems, in which both space and/or cost of memory are of major concern.

Motivation to make CMAC used in embedded system such as commercialized electronics has come into sight of many researchers. Producing an affordable yet storage efficient FPGA based Novel CMAC hardware is the main objective of this project.

In order to exploit the parallel processing capability of the CMAC net, the CMAC can be implemented by means of FPGA chips, together with banks of RAM chips. In previous works, emphasis had been made on efficient migration of CMAC from software simulation to hardware realization [3, 4] without the fundamental changes to CMAC structure itself. It was concluded that more memory to be used to increase the input resolution, then better performance could be achieved. The CMAC input quantization and memory size dilemma still exist and yet to be solved. For small-embedded system, addition of RAM chips means both increase in cost and space, which may again yield CMAC-based application impracticable. Instead of reducing input resolution to avoid high memory requirement, we could be solved the problem in a different approach: non-linear quantization of input, which is used to make better memory utilization without lost to dynamic resolution.

Many clustering techniques can be used for non-linear quantization. A novel fuzzified quantization technique based on Discrete Incremental Clustering (DIC)[5] was chosen for its simplicity and effectiveness demonstrated in CVT control application [6]. However, DIC itself is a complicated algorithm with full real numbered arithmetic and requires large hardware for implementation. Hence, this project is specially addressed the problem and proposed the modified algorithm named Sim-DIC which is more suitable for hardware implementation. Finally, Sim-DIC clustering and CMAC are integrated to a Fuzzy Novel CMAC, which is highly hardware realizable and allows on-chip learning and flexible configuration. The proposed architecture is also implemented on low-end FPGA chip and benchmarked by classification problem.

Section II briefly presents the neural network model -CMAC, which maybe implemented in a hash mapping method or conventional Look-Up Table (LUT). Both

methods are briefly introduced and compared. Section III explains how fuzzy quantization is achieved through discrete incremental clustering (DIC) and why it cannot directly prototyped to FPGA. Implementation is presented in section IV with special addressing to multiplier-free implementation for fast processing as well as testing Result for 2-spiral classification problem. The paper is concluded in Last Section.

II. The neural network model

The CMAC architecture can be considered as consisting of a single layer of memory locations, a memory addressing unit, weights adjusting unit and an output-summer. Simply speaking, the content of addressed memory locations (i.e. weights) are summed to provide network response to the input. Some applications might require input signals to be transformed to CMAC Input Space. CMAC is then defined by a series of mappings,

$$X \Rightarrow M \Rightarrow W \Rightarrow y$$

Where X is transformed input vector from external CMAC environment, M is the set of addressed memory locations, W is the set of contents (weights) of M, y is an one dimensional output. A function of

$$y = h(X)$$

is a well representation of overall mapping $X \Rightarrow y$. In the case CMAC nets consisting set of N CMACs operating on the same input to produce a vector mapping

$$X \Rightarrow Y$$

This, similarly, has all properties of the vector function

$$Y = H(X).$$

Hash Mapping

For Albus proposed CMAC, hash mapping scheme is used for indexing multiplayer CMAC, i.e $X \Rightarrow M$ mapping. To explain the concept of Hash Mapping, the case of a single input and single output (SISO) is considered. The variable of the transformed input space is denoted by *x*.

In the first layer, the input space is parted into five divisions, which division is the so-called *Cell*. Now, five weights from *W*11 to *W*15 are allocated to each *Cell*. Then, the second layer can be added by shifting the first layer to *S*21. The *Slk* means the amount of shift in the direction of the *k*th degree of freedom (DOF) on the *l*th layer. Therefore, *S*11 necessarily becomes zero because the first layer is the basis. Subsequent layer can be added in a similar manner. The result to input *x* would be summation of weights of all indexed cells, one from each layer.

The more layers are used, the better the output resolution can be achieved; but the required size of memory increases according to the number of layers. One should be careful when adds in more layers so that none of the shifted layers coincide with one another.

Multiple Layers of weight matrix also enables generalization property and hence speed up learning process. This is easy to see as one weight in a specified layer can be indexed by a number of different inputs close to each other, or neighborhoods.

Conventional Look-Up Table

Since the basic idea of CMAC is to store information in a Look-Up Table (LUT) manner, one can simply use conventional LUT scheme, which simply has one cell for each and every possible input index in every dimension. To compare the memory requirement of both approaches, we have the ratio of the two memory structures,

$$\delta = \frac{N_{(TLU)}}{N_{(hash)}} = (R/C)^{N-1} = K^{N-1}$$

with the assumption that the *N* input dimensions are of the same resolution, each can produce *R* different outputs, the number of layers is *K,* assume that the number of cells in each layer is the same:

$$C = C_1 = C_2 = \Lambda = C_k$$

One can easily know from this ratio that the hash mapping becomes more effective as the dimensionality of the input space increases. It is also worth to point out that memory requirement for hash mapping is further reduced when more layers are used (increasing *K*), but this also increases the complexity of the addressing algorithm, which makes it hardware expensive. In addition, such an algorithm is usually topologically non-adaptable to hardware implementation, when number of layers changes, the whole addressing scheme need to be changed.

Thus LUT scheme was chosen for its simplicity and flexibility in hardware realization. And the indices could be calculated as follows[10]:

Given a two-dimensional input (x_i, x_j), the winning neurons' locations can be calculated in

$$(a_i^k, a_j^k) = \left(\left\lceil \frac{(i_{\max} - K)}{x_{i\max}} x_i + k \right\rceil, \left\lceil \frac{(j_{\max} - K)}{x_{j\max}} x_j + k \right\rceil \right)$$

Where (a_i^k, a_j^k) are the calculated index for the i and j axis for layer *k*, $x_{i\max}$ and $x_{j\max}$ are the maximum value of the inputs in respective dimension, $k = \{1, 2 \ldots K\}$ is the Layer number, $i_{\max}$ and $j_{\max}$ are the maximum addressable memory locations in respective axis, K is the number of Layers used, $\lceil x \rceil$ is the ceiling function, denotes least integer that is greater than or equal to x

It is important to point out that the expressions $(i_{\max} - K)$ and $(j_{\max} - K)$ ensure when the input (x_i, x_j) is at maximum, the addressing scheme will not allow any memory overflow. The overflow problem can also be solved from hardware prospective, by adding the memory locations in each axis to

$$R' = R + K - 1$$

Then the calculation for determining winner neurons is further simplified to

$$\left(a_i^k, a_j^k\right) = \left(\left\lceil \frac{x_i}{x_{i\max}} + k \right\rceil, \left\lceil \frac{x_j}{x_{j\max}} + k \right\rceil \right)$$

The number of layers and localization topology can simply be adapted by varying the value of *K* and how it is selected. Therefore In this project, the LUT addressing scheme with multiple winning neurons is used for its simplicity in hardware implementation.

III. Fuzzy quantization

The *uniform quantization* problem remains in the conventional CMAC presented in previous section. It can be described such that the CMAC input space is quantized into equal-size regions while inputs at problem space are not necessarily uniform. When problem inputs appear with uneven degree of variation, or clustering effect, then uniform quantization of such inputs could be associated with large quantization error and not efficient for storage.

Moody [7] uses multiple CMACs with different resolution to resolve the quantization error problem. His idea is to start learning with Low Resolution CMAC, and CMAC with higher resolution is then used in same input space if the result is unsatisfied. This expansion process stops only when error rate is reduced to an acceptable level, and output of this structure is the summation of all CMACs' outputs. This approach solved minimum acceptable resolution problem but fundamentally the uniform quantization characteristic remains unchanged, further more, memory requirement increases and becomes unpredictable at first instance when problem is given.

Kim and Lin [8] proposed an adaptive quantization technique for input space by using *mapping function*. In this approach, training of CMAC stills starts with uniform quantization, and subsequently input intervals with large variation are compressed and those with small variation are extended. Hence learning accuracy is improved and storage requirement is reduced. However, the mapping function used to convert inputs is globally adjusted and it requires prior knowledge of the problem inputs in order to determine which are the intervals to be compressed or extended.

A fuzzified MCMAC (Modified CMAC) proposed by Shu [6] employs Fuzzy Quantization to replace uniform quantization. This is achieved by the use of a novel clustering technique named Discrete Incremental Clustering (DIC) [5], which dynamically forms the fuzzy clusters by using only input information from same neighborhood (or intervals). The theory is stated as:

"The input space is divided into several regions, and quantization ratio in that region is proportional to the number of fuzzy sets that covers the region."

It can be illustrated using figure 1.

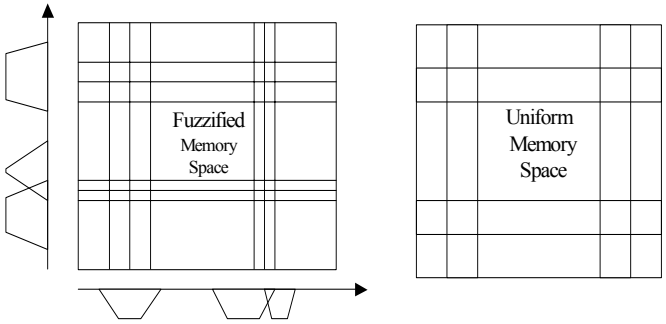

Figure 1. Memory Space Structures

Note the trapezoidal-shaped fuzzy sets for both input dimension are created as indexing rule base by DIC. The DIC is a novel clustering techniques that requires only raw numerical values of training inputs without any pre-processing. In most DIC implementations, trapezoidal-shaped fuzzy sets are used and each fuzzy set belonging to the same input dimension has little or no overlapping in kernels with its immediate neighbors. The DIC performs clustering on a local basis, that is, the number of fuzzy sets created is dimensional specific. This concept is similar to ART clustering techniques but in DIC will not "recreate" any existing fuzzy set for a particular dimension. Hence, DIC ensures that fuzzy set can uniquely identify fuzzy labels which formulate a consistent rule base for Fuzzy CMAC.

DIC technique overcomes several limitations encountered in many other partition-based clustering techniques. It does not require prior knowledge about number of clusters to be created for a given set of data. DIC performs clustering on a local basis and can significantly increase the memory efficiency yielding reduced the memory requirement. Moreover, DIC provides a platform for Fuzzy CMAC to formulate consistent fuzzy rule base.

However, DIC itself is NOT a hardware friendly algorithm, for it has large computational overhead and difficult-to-implement non-linear functions. With limited precision, limited computational resources and restricted arithmetic that can be performed on FPGA, it is really challenging to have DIC, or rather, DIC-like algorithm to be implemented from a hardware prospective.

There are many costly computations (other than addition, subtraction and bit-wise operations) involved in DIC algorithm, to name a few, non-linear sinusoidal function, division, multiplication. One of the major problems of FPGA implementing Neural Networks, affecting both performance and number of gates used, is the presence of multiplier. Thus the preliminary feature of proposed Sim-DIC is that it must be multiplier free.

- Some multiplication can be replaced by bit-wise operation, such as bit shift which equivalent to multiply (or divide) a Power of 2 Number.
- The nonlinear functions are implemented using Look-Up Tables (LUT) with proper discretization of entries.
- The Membership Function is also implemented in LUT with consideration for data precision.

Three major effects of these simplifications and modifications are founded in the testing result. They are:

- Reduced Accuracy and precision
- Reduced flexibility in fine tuning of parameters
- Increased Learning Speed on very small circuit

We shall address these effects again in next section.

IV. Implementation & Result

The Fuzzy CMAC with Sim-DIC was implemented on Student RC100 Development Board (Celoxica) featured with one Spratarn II 20K gates FPGA chip from Xilink[9]. The project was conducted in software/hardware co-design manner, as in, the proposed novel architecture was first implemented using C language, tested and tuned for performance; then the C code was migrated to Celoxica Handle-C language, which is a C-like High Level Language can subsequently be compiled and translated into HDL; then the Bitmap is generated from HDL file by Xilink Design Manager for running in specific FPGA.

Note that this project is to demo the novelty and feasibility of implementing a Fuzzy CMAC on FPGA, so the data transfer from PC to RC100 Board was not of main concern. Thus we prepared the input data in raw file and pre-load to onboard Flash RAM for use. And for the result, which is also in raw format, is loaded to PC and converted to Text file for easy viewing and analysis.

The Sim-DIC clustering Phase and CMAC Learning Phase of Fuzzy CMAC is performed by FPGA, however, due to large hardware created for both Sim-DIC and CMAC, two phases are *time-partitioned* in the design. So FPGA is first configured for creating clusters and store them back into RC100 onboard Flash RAM, and the re-configured to a CMAC enabled Fuzzy Quantization which is realized by indexing through clusters. This way we enhanced the functional density of FPGA, which is effective for further cost saving

Note that this project is to demo the novelty and feasibility of implementing a Fuzzy CMAC on FPGA, so the data processing was not of main concern. Thus we prepared the input data in raw file and pre-load to onboard Flash RAM for use. And the result, also in raw format, is loaded to PC and converted to Text file for easy viewing and analysis. Figure below illustrates the overall implementation strategy in block diagram (Figure 2).

Our implementation of Sim-DIC uses 73% of slices (logic elements) of the Spartan II (FG456) with a highest frequency at 21.44MHz. The Fuzzy CMAC (learning phase) with indexing through clusters is made up 41% of slices and runs at 31.74MHz. In contrast, conventional CMAC with uniform quantization can be implemented using only 36% slices but runs at close frequency of 33.05MHz. Table 1 below shows a summary of important implementation statistics running on a P4-2.4 512M PC

Table 1. Statistic of Current Implementation

	Sim-DIC	Fuzzy CMAC	CMAC (pure)
Size (# of Gates)	74,132	34,946	29,037
Device utilization (%slices)	73%	41%	36%
Max clock	21.439 MHz	31.736 MHz	33.050 MHz
Period	46.643 ns	31.510 ns	30.257ns
Build Time	47.1 sec	23.6 sec	20.5 sec
Netlist->.BIT time	1 min 28.4 sec	42.5 sec	40.2 sec

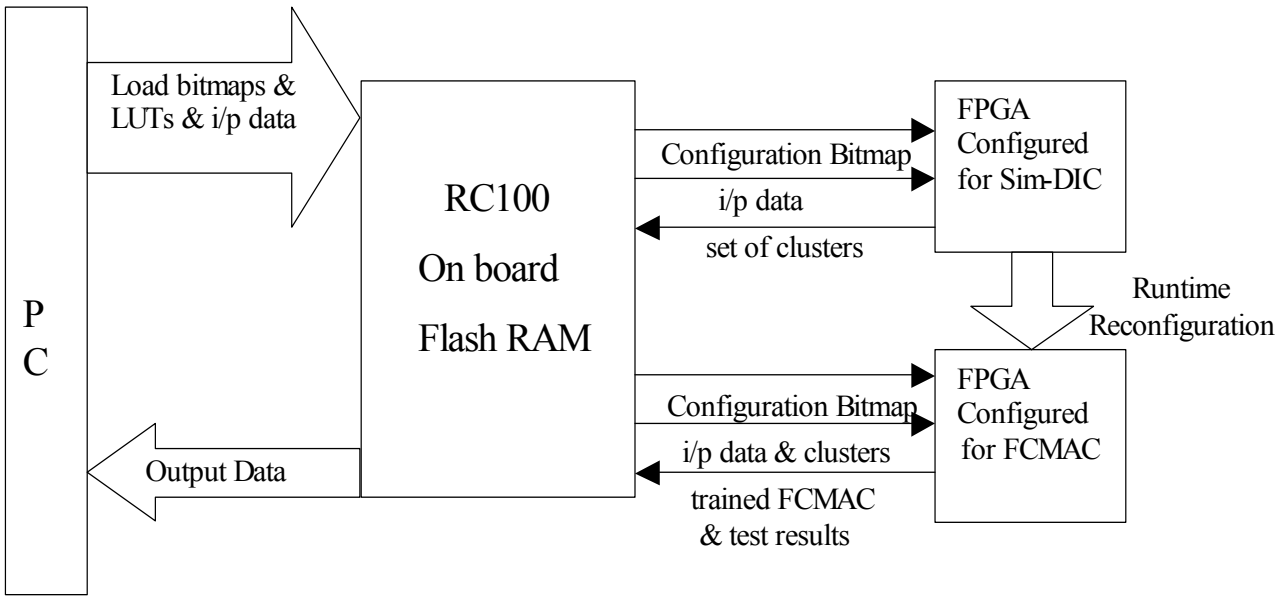

Figure 2. FCMAC Implementation Diagram

Table 2. Test Result on Recall Performance

	Test Set A (194)			Test Set B (770)		
Architecture	Correct	Errors	Classification Rate	Correct	Errors	Classification Rate
FCMAC on PC (double precision)	194	0	100%	770	0	100%
64X64, CMAC	194	0	100%	770	0	100%
40x40 , CMAC	188	6	96.91%	766	4	99.48 %
30x30 , CMAC	189	5	97.42%	766	4	99.48 %
20X20, CMAC	180	14	92.78%	675	95	87.66 %
12x12 , CMAC	154	40	79.38%	625	145	81.17%
11x13, FCMAC	178	16	91.75%	691	79	89.74%
17x20, FCMAC	191	3	98.45%	769	1	99.87%
28x27, FCMAC	194	0	100%	770	0	100%

The classification of two intertwined spirals problem, first developed by Alex Wieland, is a complex task for neural networks. We adopted this problem as a validation benchmark for feasibility of using FPGA implemented Fuzzy CMAC for practical applications with defined error rate. The standard training set contains 194 points (set A) with 97 points for each spiral and testing set consists of 770 points (set B) with 385 each. The recall capability of proposed novel FCMAC is investigated. We conducted Supervised Training for CMAC or Fuzzy CMAC with desired value to be either 0 (for class 0) or 1 (for class 1).

We first benchmark the problem using an FCMAC simulated on P4-2.0G Personal PC, with precision set to Double. In this case, both set can be classified correctly, but both running time and memory consumption are relatively large. Then we tested the FPGA implemented CMAC and found out that using 16bit integer representation, the problem can be solved using 64x64 CMAC. Since the purpose is to further reduce the memory requirement on FPGA, and such a reduction will become more significant as input dimensions increases. We then reduced the CMAC size, by having 40, 30, and 20 cells in each dimension, and as predicted, the classification rate drops. And if the problem requires a classification rate above 95%, the minimum CMAC size required is 30x30.

With aid of Sim-DIC, the proposed Novel Fuzzy CMAC is able to classify the data correctly when cells drop to maximum 30 per input dimension, and still sustain a classification rate above 98% when cells were further reduced to max 20 per input dimension. We can see that Fuzzy CMAC still functions when cells go as low as 11x13, given classification rate about 90%. In same case for 12x12 CMAC, only about 80% data can be classified due to poor resolution (Table 2).

More experiments are now in progress. To further demonstrate the viability of proposed Fuzzy CMAC and its advantage over conventional CMAC in clustering effect, hardware cost saving and reduced memory requirement. Test for higher dimensional problems will also be conducted.

V. Conclusion

In this paper, we proposed a hardware-friendly fuzzy clustering technique based on DIC, namely Sim-DIC. We also implemented a novel Fuzzy CMAC in FPGA using simple prototyping platforms. Handle-C is used for fast migration of C-simulation on PC to hardware. The architecture and implementation is tested using two-spiral problem and proved to be of better performance over conventional CMAC of same size. The FPGA implementation of Fuzzy CMAC proved that the integration of Fuzzy Techniques and Neural Network can be realized in simple hardware form (Student RC100 Development Board). And such hardware FNN can subsequently be used in real-time, embedded systems and/or for the sole purpose of fast processing through FPGA's internal true parallelism.

Refernces

[1] J.S.Albus, "A new approach to manipulator control: The cerebellar model articulation controller (CMAC)," *Transaction of ASME, Journal of Dynamic System, Measurement, and Control*, Vol. 97, pp. 220-227, 1975

[2] J.S.Albus, "Data Storage in the Cerebellar Model Articulation Controller(CMAC)". *Transaction of ASME, Journal of Dynamic System, Measurement, and Control*, Vol 97, pp.228-233, 1975

[3] G.Horváth & F.Deák, "Hardware Implementation of Neural Networks Using FPGA Elements", *Proc. of The International Conference on Signal Processing Application and Technology*. Vol. II. pp. 56-63, Santa Clara, Ca. 1993.

[4] G.Horváth & T.Szabó, "Higher order CMAC and its efficient hardware realization " *, Proc. of the International ICSC/IFAC Symposium on Neural Computation*, pp. 72-78, Vienna, 1998.

[5] W.L.Tung & C.Quek, "DIC: a novel discrete incremental clustering technique for the derivation fuzzy membership functions", *Proc. Of 7th Pacific Rim International Conference on Artificial Intelligience*, Tokyo, 2002.

[6] Z.G.Shu, "Fuzzy Associative Memory for the automatic control of a CVT control in an Automobile", *HYP report*, SCE, NTU, 2002.

[7] J.Moody, “Fast Learning in Multi-resolution hirecharies”, *Advances in Neural Information Processing System*, Vol. 1, pp.29-38, D.S Touretzky, Morgan Kaufmann Publishers, 1989.

[8] H. Kim & C.S Lin, “ use of adaptive resolution for better CMAC Learning”, *International Joint Conference on Neural Networks, IJCNN*, 1, pp.517-522, 1992

[9] S.M, R.G & S.B, "RC100 Hardware Manual", Ver. 1.2, Celoxica Ltd., 2001.

[10] A. Wahab and C. Quek, “Novel Noise Modeling Using AI Techniques ”, in *Intelligent Systems: Technology and Applications*, Cornelius T. Leonades, N.W: CRC press, 2003, III, ch.9, pp.297-327.

Wavelet Based Techniques for the Processing of Physiological Signals

Adrian Diery
Griffith University
Biomonitioring Group
Kessels Rd, Brisbane, Qld.
Adrian.diery@student.gu.edu.au

David Grevell
Griffith University
Biomonitioring Group
Kessels Rd, Brisbane, Qld
david.grevell@student.gu.edu.au

Daniel A James
Griffith University
Biomonitioring Group
Kessels Rd, Brisbane, Qld.
Daniel.james@gu.edu.au

Yvette Hill
Griffith University
Biomonitioring Group
Kessels Rd, Brisbane
Yvette.hill@gu.edu.au

Abstract

In this paper we concentrate on the field of physiological signal processing and demonstrate how non-linear processing techniques, in particular wavelet transforms, can be applied to physiological signals. We have chosen also to focus upon two commonly used and studied physiological signals; namely the Electrocardiogram and Electroencephalogram. These physiological signals are commonly recorded in continuous monitoring conditions and require relatively high sampling rates to accurately record their high frequency components. This results in large volumes of data being acquired which presents problems for storage, retrieval and transmission of the electronic recordings.

1 INTRODUCTION

Patient monitoring via the internet is quickly becoming a reality with new technologies being created to allow patients to be continuously monitored from home [1]. This ease of access and low cost of the technology also implies that large numbers of patients will be able to be monitored by a single hospital system which would have to cope with enormous amounts of data being continuously collected and stored. Therefore a vital requirement of any such patient monitoring system would be the efficient storage of this data. This study investigates the compression, recognition and simulation of two of the most commonly used physiological signals, Electrocardiogram (ECG) and Electroencephalogram (EEG). ECG and EEG are recorded over extended periods of time at high sampling frequencies therefore requiring large databases for storage. A suitable compression algorithm will minimise the storage while not compromising the characteristics of the signals and the reduction in file size also means that speed retrieval and transmission of the recordings will be increased.

The compression of both ECG and EEG signals has been a topic of research for the past 20 years. In recent years new life has been given to the topic by the application of wavelet transforms to the problem. Wavelet processing of ECG and EEG signals has proven quite flexible and along with compression has been adapted to perform not only compression of the signals but feature detection [2] and classification [3]. Previously the ECG/EEG compression problem had been approached using classical direct data compression methods such as linear prediction and interpolation, these gave way to direct ECG and EEG data compression algorithms such as FAN, AZTEC, Turning Point, and peak picking which were variants on classical data compression modified specifically for the ECG signal [9].

Large amounts of data can also present problems to analyse and classify. The signals are frequently analysed via visual inspection by a cardiologist or electroencephalographer. This imposes considerable time constraints upon reviewers and how many patients they can assess within a given timeframe. Therefore automated recognition of the waveforms would be valuable in the scoring procedure. To do this an understanding of the signals must first be achieved.

A subset of physiological signals from the human body can be measured via surface electrodes. For example the ECG and EEG are indirect measurements of the electrical activity produced by the heart and brain respectively.

1.1 Electrocardiogram - ECG

The Electrocardiogram is a recording of the electrical activity in the heart. It is typically represented by 12 perspectives called leads that are recorded and derived from 10 electrodes placed around the torso and limbs of the patient. The ECG is comprised of several characteristic waveforms which represent the various stages of conduction of electrical activity through the myocardial tissue. This gives rise to a series of 6 potentials labelled with the letters P through U. Atrial depolarization is represented by the P wave, Ventricular depolarization by the QRS complex and repolarization of the ventricles by the T wave, the exact origin of the U wave is unknown. The ECG data used in this study was in MIT-BIH format, available from Physionet, sampled at 360Hz and also provided by the Griffith University School of Applied Psychology EEGLAB, which is sampled at 500Hz with a 16bit precision.

1.2 Electroencephalogram - EEG

The Electroencephalogram (EEG) measures the electrical potential between different locations on the scalp [4] or between cortical locations and a neutral reference. The electrical potential observed on the scalp is generated by population of neurons, and transmitted through the intervening tissue. As the signal is not taken directly from the brain, and brain activity itself is a low-power signal, the voltage measured at the various locations on the scalp is typically in the range of 1-300 μV [5].

1.3 Wavelet Transform

In this study the wavelet transform is used to compress and perform recognition on the physiological data. The Wavelet Transform (WT) is a very powerful time-frequency analysis method, because it provides excellent control of time frequency trade-off compared to traditional techniques such as the Short Time Fourier Transform (STFT) [6], [7], [8]. The Fourier Transform gives a representation of all the frequencies present in a signal, for the entire duration of the signal being analysed however, the temporal resolution is fixed by the selected frequency resolution. The Wavelet Transform is similar to the Fourier Transform in that it gives a representation of all the frequencies present in a signal; however it also shows at what times in the signal the frequency was present [6] and indicates that this varies across the frequency spectrum. A wavelet is defined in time as a small, narrow band, multi frequency waveform, the wavelet is said to be supported for the interval in which the majority of the energy of the wavelet is contained. If the entire wavelet energy is contained within that interval the wavelet is said to be compactly supported, this property also allows for the perfect reconstruction of a decomposed signal, which will be discussed in more detail later.

1.4 Mother Wavelet

The Mother Wavelet is the initial characteristic wavelet type and shape from which the wavelet family or basis set is derived. The set of wavelets used to represent the original signals (also known as basis functions), "$g_{a,b}(t)$" is defined by Eq. 1.

$$g_{a,b}(t) = \frac{1}{\sqrt{a}} g\left(\frac{t-b}{a}\right)$$

Eq. 1 Derivation of basis functions from mother wavelet

The scaling factor "a" dilates or compresses each basis function, hence focusing on a particular bandwidth with a centre frequency related to the scaling factor. The translation factor "b" shifts each function in time. The power of the mother wavelet is maintained throughout the basis set by the normalization factor; "$1/\sqrt{a}$". The basis set is then used to perform wavelet transformation, as can be seen in Eq. 2 and is shown in figure 3 of [6].

$$c_{a,b} = \int_{-\infty}^{+\infty} E(t) g^{*}_{a,b}(t) dt,$$

Eq. 2 Continuous Wavelet Transform of E(t)

In Eq. 2 "$c_{a,b}$" represents the continuous wavelet coefficients and "$E(t)$" is the temporal signal being transformed. The choice of Mother Wavelet for the transformation of the physiological signals is based upon the characteristic shape of the signals.

$$E(t) = k \int_{-\infty}^{+\infty} \int_{0}^{+\infty} \frac{c_{a,b}}{a^2} g_{a,b}(t) da\, db$$

Eq. 3 Reconstruction of Signal E(t)

The choice of mother wavelet can have dramatic effects on the results achieved as will be shown later for the case of the processing of the EEG.

1.5 Discrete Wavelet Transform DWT

The Discrete Wavelet Transform (DWT) is similar to CWT in that it generates coefficients based on the correlation between the wavelet of certain scales and the original signal. However, DWT uses orthogonal wavelets, such that a signal can be represented by a number of wavelet coefficients generated by distinct scales [6], respecting the number of degrees of freedom in the sampled signal. The mother wavelet is used as the original scale of the wavelet, with each level of decomposition representing a doubling of the scale. DWT also requires a companion function called a scaling function, which is "a combination of mother wavelets from all DWT scales larger than the scale of the first detail function" (Samar et al., 1999, page 23) [6].

2 REVIEW

To ensure that this study was not simply repeating work previously completed by other studies, an extensive review of applicable techniques for compression, recognition and simulation was undertaken.

2.1 Compression

In general ECG compression techniques may be classified as one of three types [9]; significant feature extraction, linear predictive coding or orthogonal transform. It is in the latter of these three that the wavelet based transform methods fall. Typical results for linear prediction and significant feature extraction methods range between Compression ratios of 2.0/2.5 (Turning Point/DPCM Linear Prediction) – 10 (AZTEC) with NRMSE values of 5.3% and 28.0% respectively. Several Orthogonal transform based ECG compression algorithms are compared in Table 1. The methods discussed in [10] & [11] are for all intensive purposes the same with the only difference being the number of bits allocated to the ECG recording.

The algorithms discussed in [12] make use of standard image processing methods and transforms in this case a 2 dimensional discrete cosine transform. The method from [13] is our won which makes use of a biorthogonal wavelet transform, zero-run length coding and recursive splitting Huffman Coding [20]. The advantage of the wavelet transform over the discrete cosine transform is its superior resolution at lower frequency levels which enables further dimensionality reduction but eliminating extraneous low frequency components which might not be resolved by the DCT. The advantageous properties of recursive Huffman coding over standard Huffman coding are discussed later.

EEG compression has been performed in many instances, however primarily for ambulatory monitoring, not long-term storage of sleep signals. Several different techniques have been used to compress EEG data, with varying levels of compression ratio (CR) as can be seen in Table 2.

Table 1 Orthogonal Transform based compression methods (review section)

Compression Technique	CR	Sampling Frequency	Precision	NRMSE %
Wavelet Based Transform [10]	14	500	8	4.85
Wavelet Based Transform [11]	16.8	500	7	5.25
Cut and Align Beats approach [12]	12	360	12	7.03
As above	24	""	""	18.14
2D Transforms [12]	12	""	""	6.16
As above	24	""	""	10.08
As above	48	""	""	15.78
Biorthogonal Wavelet Based Transform with recursive Huffman coding [13]	21.42	500	8	2.94
As Above for 14 MIT-BIH files.	24.56	360	12	3.56

The lossless techniques allow perfect reconstruction of the signal after compression, whereas lossy techniques will give better compression at the expense of the signal integrity. It is apparent that lossless encoding will give lower compression ratios than lossy encoding, as more information is retained, however generally, the main limit for the lossy compression of a signal is the amount of error that can be tolerated.

Table 2: Compression techniques applied to EEG data

	Technique	**CR**
Lossless	Commercial Arithmetic Coders	2.5 - 3.8
Lossy	DWT [14]	8
	Iterative Function System w GA [15]	6.8-13.7
	AR prediction [16]	2.3-3.3

The Discrete Wavelet Transform (DWT) was implemented for EEG compression, as this study required the signal to have only the same sleep stage classification after compression as before, not a set limit of error. This meant that compression could be improved by removing the frequencies that are not needed for sleep stage classification (generally frequencies above 32Hz), which is simple using DWT denoising.

2.2 Recognition

Automated analysis of physiological signals is also of great necessity in a continuous patient monitoring environment. Most analysis of the ECG occurs with relation to the QRS complex as it is the most characteristic and easily identifiable wave in the ECG. QRS complex detectors can be described as either syntactic or non-syntactic. Syntactic detectors require an analysis of the entire data record from which an average beat template is derived. These methods can be slow and are susceptible to noise and changes in beat morphology. Non-syntactic methods do not generate average beat models but rely on heuristic criteria to identify the QRS; they also employ some form of preprocessing transformation or paradigm. Approaches to QRS by software algorithms were well summarized in [17] which compares the preprocessing stages of many QRS detection algorithms. The categories of algorithms include:

- Signal derivative and Digital Filter approaches
- Wavelet Based Algorithms
- Neural Network Approaches
- Additional Approaches; which covers many varied approaches to the QRS detection problem including Hidden Markov models, Matched Filters and Genetic Algorithms.

Once the QRS complexes have been identified then specific beat classification can be performed. The variety, number and means of classifying cardiac arrhythmia would require a much more in depth discussion then can be afforded here.

Table 3 Comparison of QRS detection methods

System	**False +**	**False -**	**False Detection**
Wavelet Based [18]	0.056%	<0.001%	0.152%
Syntactic Template [19]	0%	0.577%	0.577%

Detection of the position each beat within an ECG recording can be of great diagnostic benefit by providing an accurate measure of the heart rate and providing a beat to beat comparison. Accurate detection is complicated by anomalous changes in the morphology of the ECG and changes in heart rate. These two factors are particularly difficult for the syntactic detection methods to deal with.

3 SOLUTION

3.1 Compression

The nature of continuous monitoring means that a lot of data is collected quite quickly, therefore the compression algorithm has to be quick enough to work within a real-time system (compresses data faster than it is collected). From Figure 1 it can be seen that the majority of the ECG's energy is concentrated in the lower frequency levels therefore faithful reproduction of these levels is of upmost importance. However it should not be forgotten that diagnostically important information is still contained in the higher frequency component such that they can not be discounted altogether. The wavelet transform provides an excellent platform to address these concerns. The

compression method discussed in [13] is our own and works as follows:

1. The signal is blocked into smaller segments.
2. The blocks are decomposed using a biorthogonal wavelet transform.
3. The individual transform levels are normalized and a hard threshold is applied to them.
4. The transform levels are zero-run length encoded.
5. Each level is assigned a specific quantization precision and is quantized.
6. Finally a recursive splitting Huffman Coder [20] is applied to the quantized coefficients.

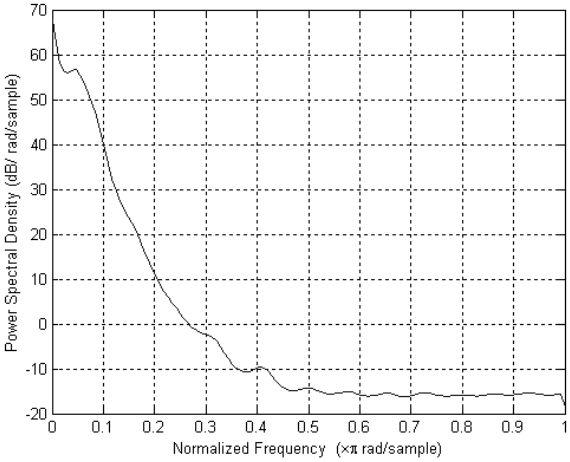

Figure 1 Power Spectral Density of an ECG

The EEG data processed was in European Data Format, available from Physionet, and was sampled at 100Hz. For sleep stage classification (using only EEG), the information needed is generally in the frequency range of 0.5-32Hz, so the data was filtered using finite impulse response techniques, to fit this range. If Wavelet Packet Transform had been used instead of DWT, filtering would have been performed as part of denoising. Sleep stage classification is often performed by analysing epochs of 30 seconds; the EEG data was therefore compressed in 30 second periods or windows, to allow precise extraction of the data of interest. After bandpass filtering and windowing the signal was transformed to generate the wavelet coefficients. The power of the discrete wavelet transform in compression is its characteristic of breaking up the signal into coefficients resembling discrete frequency bands. Frequencies that are characteristic of unwanted information can therefore be easily removed. This is called denoising, and uses thresholding to actually remove the coefficients. Thresholding was performed on ECG and EEG by zeroing out the coefficients in the unwanted frequency band less than a certain magnitude, and then performing Zero Run-Length Encoding (ZRLE) to reduce the amount of data.

Huffman encoding was performed on top of this reduced data set to improve the compression ratio again, without increasing the error of the compressed signal with respect to the recorded EEG signal. The entropic coding scheme employed was a Huffman coder using recursive splitting, developed by K. Skretting [20]. The Huffman coder made use of recursive splitting of the wavelet coefficients so that greater coding gain, and hence bit rate, could be achieved. This is due to the fact that the wavelet coefficients aren't independent of each other, they infact exhibit some correlation, and therefore can be split such that each new sequence of coefficients has statistically different information. This allows different Huffman coding schemes to be applied to each sequence which means that code symbol length is minimized. For further explanation it is recommended that the reader refer to the paper by Skretting, et al.

3.2 Recognition

The simplest approach to automated ECG analysis is to begin by identifying and locating each beat which would then allow for beat to beat analysis. The easiest characteristic to identify in each beat is the QRS complex, by locating the position of each QRS complex the R-R interval can also be calculated which means that we can assess basic heart rate. The next step is then to examine the associated waveforms of every beat. The relatively high frequency and energy content of the QRS complex means that it will be clearly visible in the first few levels of a DWT, by using a low order DWT we can highlight each QRS complex and correlate the information from each level to produce a robust means of locating the QRS. This is achieved by applying a frame square average to each level and then searching for the peaks which will correspond to the high energy QRS complexes. In addition to this a set of decision rules is used to improve the robustness of the detector to interferences such as movement artefact. These heuristics can be used once each beat is detected and can also improve the accuracy of the QRS detection. Typical rules include defining a timeframe in which only one QRS complex should occur. This timeframe can be adaptable to compensate for changes in heartrate. Other characteristics can then be searched for within the defined timeframe, these can include the P wave and T wave and various segments of the ECG.

4 RESULTS

4.1 Compression

As wavelets were used for both ECG and EEG compression, and are based on denoising, an intrinsically lossy technique, the amount of compression gained is determined by how much information is lost – that is, less data stored will give better compression. Due to this, the results are shown as compression vs. error, although the best compression is likely to be irrelevant due to a loss in signal characteristics of interest. Two parameters were used to evaluate the level of compression of the signal, and the error caused by compression, Compression Ratio (CR) and Normalised Root Mean Square Error (NRMSE) respectively.

4.1.1 Compression Ratio

The Compression ratio is defined as the ratio between the original file size and the compressed file size. A higher compression ratio indicates better compression.

4.1.2 Normalized Root Mean Squared Error

Normalized Root Mean Squared Error (NRMSE) indicates the error in the final signal as a percentage of deviation from the original signal, as can be seen in Eq 4. The NRMSE is the numerical evaluation of the error of the signal and is used in this paper to find the maximum compression ratio possible without loss of vital information from the signal. This ranges between 0% and 100%.

$$NRMSE\% = \sqrt{\frac{\sum_{i=1}^{n}[x_{org}(i) - x_{rec}(i)]^2}{\sum_{i=1}^{n} x_{org}^2(i)}} * 100\%$$

Eq. 4 Normalized Root Means Squared Error

4.2 Experimental results

The results of our compression algorithms and comparisons of them with other orthogonal transform based compression algorithms are shown below. In Figure 2 the effect of the order used in the DWT on the compression ratio achieved and the NRMSE suffered is shown, from these results the effect of changing the global threshold level was determined using standard 9th order DWT decomposition. Figure 3 shows the NRMSE and Compression Ratio achieved using our Wavelet Based compression algorithm and its performance as the threshold level of the wavelet transform was varied between 0.2 and 10% of each transform level's dynamic energy range, the hard thresholding method was used.

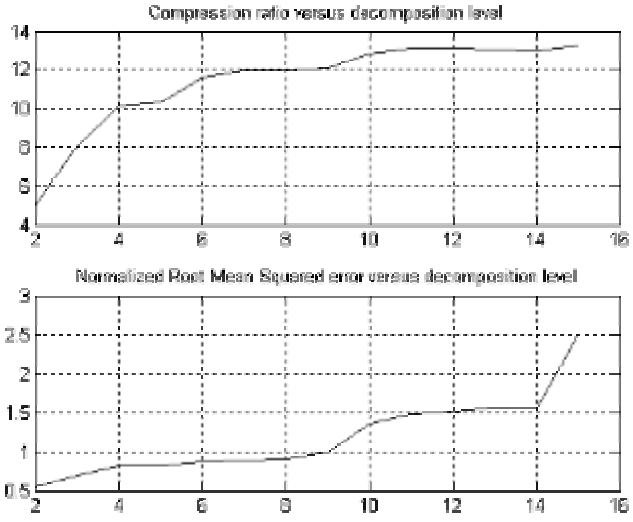

Figure 2 Compression Ratio and NRMSE vs. level of DWT decomposition for ECG data.

When wavelet based compression was applied to the EEG signals, it could be seen that again the error intrinsic in the signal was the limit for the compression ratio that could be achieved. All the results presented for EEG compression use wavelet techniques, and Huffman encoding. The wavelet used generated significantly different levels of error, with wavelets such as Biorthogonal 5.5 and Symlet 10 giving the best CR/NRMSE ratio, as can be seen in Table 4 below, while other wavelets such as Haar gave a much lower CR/NRMSE. It can be observed from Figure 4 that the wavelet chosen often has little effect on the NRMSE of the generated file, but can increase the CR substantially (each point refers to a different mother wavelet used in the algorithm). There are however several exceptions to this rule, with the NRMSE for most 1st order models of wavelets above 10%.

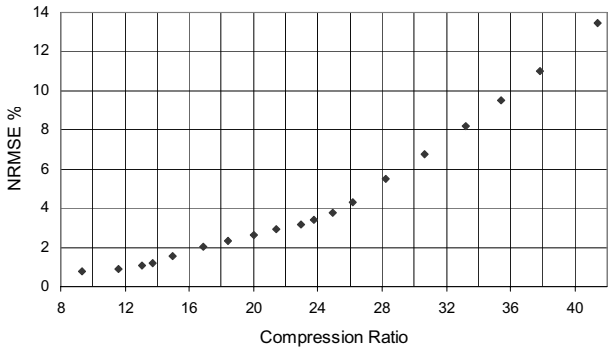

Figure 3 Compression Ratio vs NRMSE for ECG using Biorthogonal 2.8 with varying thresholds.

Wavelet Used	CR	NRMSE (%)	CR / NRMSE	Wavelet Used
Biorthogonal 5.5	7.9	4.9	1.7	Biorthogonal 5.5
Symlet 10	7.8	4.7	1.6	Symlet 10
Daubechies 10	7.8	4.7	1.6	Daubechies 10
Coiflet 5	7.5	4.7	1.6	Coiflet 5
Discrete Meyer	6.7	4.6	1.5	Discrete Meyer

Table 4: Effect of Mother Wavelet used on Compression Ratio and NRMSE for EEG compression

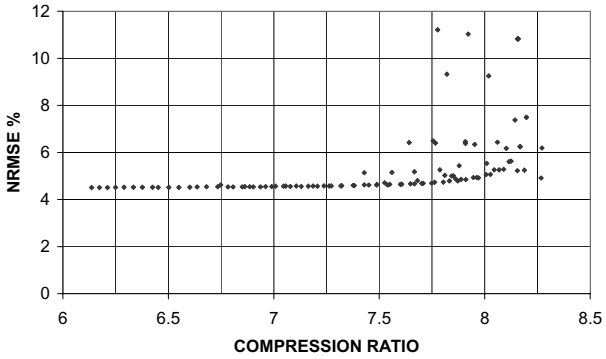

Figure 4: Effect of different types of wavelets on CR and NRMSE for EEG

The relationship between the error of the signal and the compression that can be achieved can be seen in. High compression ratios can be achieved easily by increasing the level of thresholding (retaining less information), and applying additional techniques, such as storing the wavelet coefficients as n-bit integers instead of floating point values, on top of the wavelet techniques. These techniques will however increase the error substantially. Lossless techniques such as Huffman encoding or arithmetic encoding may also be applied, and may increase the compression with no increase in error. Similar studies have achieved compression ratios and errors as shown in Table 5. It should be noted that this table is a composite of ECG and EEG parameters, and that the amount of compression possible on both of these is dependent primarily on the error. Because of this the results of all the techniques are presented for a similar level of error where available, as well as the maximum CR and error reported by those studies.

Technique	**ECG / EEG**	**CR with lowest NRMSE**	**Max. CR reported**	**NRMSE for Max. CR**
Entropic Coding (lossless)	ECG	2.6	2.6	2.6
Biorthogonal DWT with Recursive Huffman coding [13]	ECG	12.42 (NRMSE = 0.93)	41.38	13.49
2D Transforms [12]	ECG	12 (NRMSE =6.16)	48[1]	15.78

Table 5: Comparison of this study to compression results for similar studies

4.3 Recognition

As mentioned previously, the major constraint for EEG compression was for the compressed data to receive the same classification as the original data. A major reason for this is the development of an automated sleep stage classification program that will ultimately be able to score EEG data as well as, or more accurate than, current manual scoring following Reschtaffen and Kales criteria.

ECG compression has a smaller range of error that is suitable due to the wider range of anomalies that can be identified, however currently an automated QRS detection routine has been implemented successfully. The routine utilizes the DWT and signal averaging over several transform layers to improve the accuracy of the detector. Testing of this system on a selection of MIT-BIH recordings showed a 100% positive detection accuracy however a small percentage of false positives still occurred.

[1] A compression ratio of 96 was also reported in [12] however testing results were not complete.

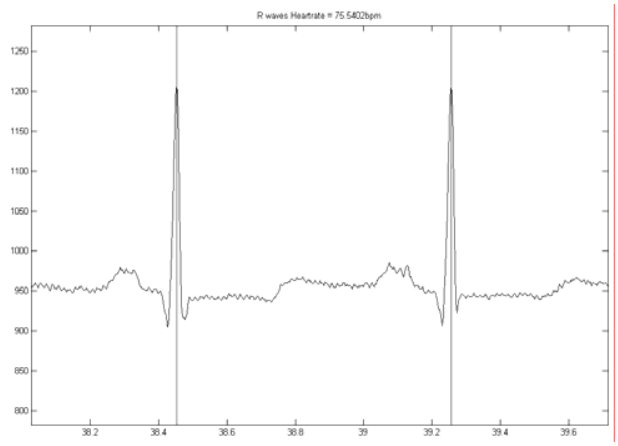

Figure 5 QRS detection via DWT for MIT-BIH 108

5 Discussion

5.1 Compression

The results for the compression investigated in this study indicate a higher level of compression than achieved in similar studies. This study has improved on results from other studies using the wavelet transform by implementing entropic coding techniques on top of the denoised wavelet coefficients.

5.1.1 ECG

As shown in the review section the Orthogonal transform approaches to ECG compression performed significantly better than the classical and direct methods. The comparison of orthogonal transform methods also showed that the Wavelet transform offered an advantage over the discrete cosine transform due to its superior low frequency resolution properties. The use of Huffman Coding with recursive splitting improved compression ratio and bitrate over the standard Huffman coders used in [10][11].

5.1.2 EEG

The main feature of wavelet-based EEG compression that this study has identified is the effect of using different mother wavelets. It is apparent from Figure 4 that the mother wavelet chosen can effect the level of compression and the amount of error present significantly - two different wavelets can give different amounts of compression for the same error. Additionally, the wavelet suitable for a particular application will depend on the amount of computational power available. For instance the higher order symlets are not suitable for real-time due to their complexity requiring over 30 times more time than the average. The wavelets used for the EEG component of this study were the pre-existing wavelets available in the Wavelet toolbox for MATLAB.

5.2 Recognition

Wavelet based recognitions techniques offer improved performance over syntactic methods in their robustness against noise and morphological changes in the QRS. The advantage that the syntactic method developed in [19] has is its low incidence of false positive detection. However

with a thorough set of heuristics the Wavelet transform approach can be improved.

6 CONCLUSIONS

ECG and EEG compression are implemented in this study for the storage of data recorded by an automated sleep monitoring device that has been developed, and will allow long term storage of the ECG and EEG data generated by these techniques. As ECG and EEG have the highest sampling frequencies, the compression of this data is most crucial. However, due to the similarities between implementation for ECG and EEG, it is believed these techniques can be modified slightly for use with other physiological signals recorded such as EMG and EOG.

This study has also shown that it is likely that Wavelet based EEG compression is not as powerful as ECG compression. This is not unexpected as EEG is such a chaotic signal in comparison to the ECG which can be generally characterised by an appropriately shaped mother wavelet such as the biorthogonal wavelets. This characterisation means that the original signal can be efficienctly represented in terms of time-frequency coefficients with minimal residual detail coefficients. As EEG for sleep studies are generally only interested in frequencies beneath 40Hz, the NRMSE may not be as suitable in determining the effective error present as a professional sleep scorer's opinion. For instance, if the NRMSE represents primarily higher frequency components of the EEG, which are not used for sleep monitoring purposes, the effective error of the compression technique will be much less than this value. The error that can be tolerated and therefore the maximum possible compression ratio will hence depend on the application.

The superior performance of the wavelet based methods over classical methods and their ease of implementation make them ideal for clinical applications. The flexibility of the discrete wavelet transform is highlighted by its ability to be the basis of compression and recognition algorithms for physiological signals. This gives rise to the possibility of amalgamating both processes so that, in the case of the ECG, beat recognition data could be stored with the compressed data. This would significantly improve analysis by aiding the reviewer as well as reducing the time for retrieval and transmission.

References

[1] D. James, et al., "Internet Based ECG Medical Information System", Australasian Physical & Engineering Sciences in Medicine, Vol 26, No. 1, 2003

[2] S. Kadambe, T. Murray, G. F. Boudreaux-Bartels, "Wavelet Transform-Based QRS Complex Detector" IEEE Transactions on Biomedical Engineering, Vol 46 No 7 July 1999

[3] A Prochazka, M Storek, "Wavelet Transform use for signal classification by self organizing neural networks", Artificial Neural Networks, 26-28 June 1995, Conference Publication No. 409, IEE 1995.

[4] M. Browne, "Wavelet Methods for Analysis of Event-Related Potentials", Griffith University, October 2001

[5] H-J Park et al., "Automated Detection and Elimination of Periodic ECG Artifacts in EEG Using the Energy Interval Histogram Method", IEEE Transactions on Biomedical Engineering, Vol. 49, Issue. 12, December 2002

[6] Samar et al. "Wavelet Analysis of Neuroelectric Waveforms A Conceptual Tutorial", Brain and Language 66, pp 7-60, 1999

[7] J. Raz et al., "A Wavelet Packet Model of Evoked Potentials", Brain and Language Vol. 66, pp 61-88 (1999)

[8] V. Samar, "Multiresolution Analysis of Event-Related Potentials by Wavelet Decomposition", Brain and Cognition, Vol. 27, pp398-438, 1995

[9] S. Jalaleddine, C.G. Hutchens, R.D Strattan, W.A. Coberly, "ECG Data Compression Techniques – A Unified Approach", *IEEE Transactions on Biomedical Engineering,* Vol. 37, NO.4, April, 1990, pp 329-343

[10] I. Provazník, J. Kozumplík, "Wavelet-Based Compression of ECG signals", Department of Biomedical Engineering, Faculty of Electrical Engineering and Computer Science, Technical University of Brno, Czech Republic

[11] I. Provazník[1], J. Kozumplík[1], J. Bardonová[12], M. Nováková[2], Z. Nováková[2], "Wavelet Transforms in ECG Signal Processing", [1] Department of Biomedical Engineering, Brno University of Technology, [2] Institute of Physiology, Masaryk University Brno, Euro Conference, 2000

[12] H. Lee, K.M. Buckley, "ECG Data Compression Using Cut and Align Beats Approach and 2-D Transforms", *IEEE Trans On Biomed Eng*., Vol 46, No. 5 May 1999

[13] A.Diery, "Digital Electrocardiogram Processing Techniques and Applications", Thesis, School of Microelectronic Engineering, Griffith University, 2002

[14] A. Folkers et al., "Realtime bioelectrical data acquisition and processing from 128 channels utilizing the wavelet-transformation", Neurocomputing, Vol. 52-54, June 2003, pp247-254

[15] S. Cerutti, et al., Non-linear algorithms for processing biological signals, Computer Methods and Programs in Biomedicine, Volume 51, Issues 1-2, October 1996, Pages 51-73

[16] N. Memon, "Context-based lossless and near-lossless compression of EEG signals", IEEE Transactions on Information Technology in Biomedicine, Volume: 3 Issue: 3 , Sep 1999 pp231-238

[17] B.U. Köhler, C. Hennig, R. Orglmeister, "The Principles of Software QRS Detection", IEEE Engineering in Medicine and Biology, 0739-5175/02, January/February, pp 42-57, 2002

[18] C.Li, C. Zheng, C. Tai, "Detection of ECG Characteristic Points Using Wavelet Transforms", pp 21-28, IEEE transactions on Biomedical Engineering, Vol 42, No1, Jan, 1995.

[19] T.R.H. Cutmore, "Matlab QRS detection for the electrocardiogram using a template approach", Unpublished algorithm, School of Applied Psychology, Griffith University, (2002)

[20] K. Skretting, J. H. Husøy, and S. O. Aase: "Improved Huffman coding using recursive splitting," in Proc. of Norwegian Signal Proc. Symp., Oslo, pp. 92-95, September 1999. Available at http://www.ux.his.no/~karlsk/proj99/

(This page left blank intentionally)

Autonomous Sports Training from Visual Cues

Andrew W. B. Smith and Brian C. Lovell
Intelligent Real-Time Imaging and Sensing Group,
The School of Information Technology and Electrical Engineering
The University of Queensland
Brisbane, Qld 4072, Australia
{awbsmith, lovell}@itee.uq.edu.au

Abstract

Computer driven biometric analysis of athlete's movements have proven themselves as effective sports training tools. Most current systems rely on the use of retro-reflective markers or magnetic sensors to capture the motion of the athlete, so the biometric analysis can be performed. Video based training tools have also proved to be valuable instructional aids, however most require significant human interaction for analysis to be performed. This paper outlines an ongoing project focussed on capturing posture without the use of any markers or sensors, while still capturing enough information for an automated analysis to be performed. The approach taken to solving this problem is presented, as well as the current state of development of a an instructional aid for golfers.

1. Introduction

Biometric analysis has established itself as an effective training tool for athletes. Currently most techniques rely on the use of retro-reflective markers or magnetic sensors to be placed on an athlete before such analysis can be performed. An example of this is the 3D-GOLF^{TM}system[11], where posture is obtained from magnetic sensors and then professionally analyzed. There is an inherently large setup time involved with the use of these systems, increasing the cost and inconvenience to the athlete. Were the athletes postural information captured visually, this setup time could be greatly minimised. Furthermore, vision based systems have the potential to be produced at much lower cost than magnetic sensor systems due to the mass production of cheap cameras sensors. A final advantage of obtaining posture from visual cues is that recorded video of the actual athlete can be shown to provide feedback, instead of a 'stickman' representation or an animated model.

Video based analysis tool have been widely used as instructional aids. Systems such as Swingcam[14] and the GolfTek®Video Swing Analysis System[12] record footage of a golf swing for the player to view. Analysis is left to be done by the player in these systems. Other systems can perform limited analysis, however many require human processing to determine the position of important features. Motion Coach^{TM}[13] is one example of this.

With continuous developments in the image processing field and increases in the computational power of PC's, visual motion capture and analysis applications have become quite feasible. An example of such a system is the virtual personal aerobics trainer[4], which provides feedback on exercise activities from purely visual cues.

The aim of the project is the development of a system which uses visual cues to obtain an athlete's postural information, and analyzes this with respect to a learned ideal motion. Completely automated feedback can then be given based on differences between the athlete's motions and the technically correct motion. No human interaction is required in this process, giving it an advantage over other systems. Golf has been chosen as the sport of focus as there is a well defined technically correct swing, and because of the golfer's limited motion in space (a camera can see the whole swing without moving). The visual system can also be integrated with golf swing analyzer mats, which provide data that the visual system cannot detect.

2. System Overview

The system envisaged is one where the golfer addresses a ball situated on a swing analyzer mat. The swing analyzer mat is a commercially available product that has been used as a golf instruction aid for over 20 years, and is discussed in section 2.1. The golfer will be facing a single camera (current focus is on a purely 2D system) with a display monitor mounted above. This system is illustrated in

figure 1. Once the golfer has completed their swing, information collected from both the camera and the golf mat will be combined to provide both audio and visual feedback on the monitor for the golfer to observe. The project can be though of as a fusion of the measurements from the analyzer mat and the visual system. Analyzer mats have been used to determine what happens around impact time, but not why this has occurred. We are adding analysis of the postural variation which caused the given swing. It is envisaged that training booths equipped with this system could be incorporated into driving ranges as instructional aids.

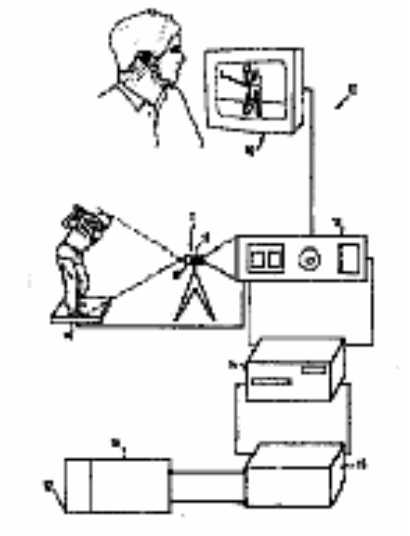

Figure 1. Original concept of Golf Swing Personal Trainer from Hi-Tech Video's 1991 Patent Application [15]

The camera used in this system is the dragonfly firewire camera from Point Grey Research[10]. This camera is capable of 30 frames per second, at a resolution of 640x480 pixels.

2.1. The Swing Analyzer Mat

Golf swing analyzer mats use an array of sensors to detect the club passing overhead. Top of the line units use around 53 infrared sensors which measure:

1. club head path
2. club face angle
3. club speed
4. impact location
5. tempo
6. ball carry
7. ball trajectory (push, pull, slice, straight, draw etc)

and then determine the result of the shot — either fairway or rough.

The golf analyzer mat adds extra capabilities for feedback as it can detect small changes in the club head angle which are infeasible to detect via visual means. For example, if the visual analysis detects no significant deviations from the correct swing, yet the predicted path of the ball is not straight, the mistake can be asserted to be caused by an incorrect rotation of the wrist. Imagine this rotation causes the club to be rotated about its axis, something the visual analysis will not detect but will result in a poor shot. The program can infer this and provide feedback showing the frame where the club impacts the ball, appropriately zoomed, allowing the player to perform their own comparison between their wrist and the professional's.

We have modified a GolfTek®Pro III Golf Swing Analyzer for use with our system. Details on this analyzer are given at [12]. Data is sent to an Atmel AT90S8515, which interfaces with a PC using the RS232 protocol. Consideration is being given to making this a wireless link.

2.2. Off site processing

It is envisaged that analysis performed using this system will be performed at a central site. Sensor data will be transmitted to a central site via technology such as broadband communications, the analysis performed, and the result transmitted back to the user.

2.3. Intended Application

It is intended that this system would be used by social, rather than professional, players. As such it is aimed at players looking to improve their game — this would occur by either supplementing coaching from a golf professional, or developing a level of prowess that allows them to take full advantage of the professional's advice. It is not intended that this system should provide the in-depth analysis required by professionals.

2.4. Adding expert players to the learned set

While the initial design will focus on providing feedback based on a technically correct swing, it is intended that expert golf professionals' swings will be added to this database. Professional golfers swings are not always what is considered technically correct. An example of this is Jim

Furyk's swing, which is considerably different from a technically correct swing. Despite not being technically correct, Furyk's swing was good enough to win the 2003 U.S. Open. A player could try to replicate his swing, or another of their favorite players.

3. Visual Tracking Overview

In this application we need an algorithm capable of robustly tracking the human body through the range of motion encountered during a golf swing. It should use minimal knowledge of the background as we expect the background to change as people move behind the golfer.

For the algorithm to track robustly, we assert that it should search a wide range of the search space, as opposed to simply finding the nearest local maxima in the search space. This will enable tracking through cluttered environments. Algorithms such as AAMs[3] or Kalman filtering [9] do not satisfy this conditions, as they both seek out the nearest local maxima in the search space to the expected position. This can just as easily be an artifact of clutter as the true object. Isard and Blake's condensation[5] algorithm was designed to meet just these criteria, and not rely on assumptions about the background, though they can prove useful.

Condensation is a stochastic algorithm which uses a particle filtering approach to determine the most probable target configuration. Each particle is a spline based contour constrained to lie in a configuration space. The sampling nature of the particle filter attempts to search the entire configuration space, not just a local region of it. Considering the case where the number or particles, $n = \infty$. In this case the entire configuration space will be searched. Although the amount of samples must be restricted to a practical number, condensation provides the ability to search a wide area of the configuration space, and not just find the nearest local maxima. This gives it the ability to track in applications where the posterior distribution is multi-modal, i.e., any cluttered environment.

3.1. An Overview of the condensation algorithm

The steps of the condensation algorithm from [5] are as follows for each time step t:

1. Starting with a set of particles $\mathbf{s}^{(t-1)} = (s_1^{(t-1)}, ..., s_n^{(t-1)})$ with prior probabilities $\boldsymbol{\pi}^{(t-1)} = (\pi_1^{(t-1)}, ..., \pi_n^{(t-1)})$, a new set of samples are randomly drawn via a weighted sampling operation.

2. Dynamics are then applied to each particle in the set, giving the new sample set $\mathbf{s}^t$.

3. The posterior $\boldsymbol{\pi}^t$ for the sample set $\mathbf{s}^t$ is constructed by finding the observational likelihood of each particle

4. Estimates of the object position are calculated.

The dynamics used in this project are currently a learnt 2nd order auto-regressive process, as described in [2]. Observational likelihoods are constructed by drawing an evenly spaced set of measurement lines along curve normals of each contour (remember each particle is a contour). MacCormick [7] gives a number of methods to calculate probabilities based on the set of features on each measurement line of a contour. Currently the Poisson method with robust color detection is being used. The spline position can be calculated using MAP, MLE or MMSE estimates. As in [5] we are using a MAP estimate of the target position, obtained by an average of all the particles weighted by their probabilities.

3.2. Modelling the golfer

For the initial development of this application a principal component approach has been used to determine the configuration space. This is due to uncertainty in the nature of the articulated model we wish to use. An example to show why this uncertainty exists focuses on the players shoulders. Take for example, a 26 DOF (degrees of freedom) articulated model. This model would assume the shoulder carapaces are in a fixed position relative to the top of the spine. During a movement like shrugging however, the shoulder carapaces violates this assumption. Consider trying to swing a golf club with your shoulders in a raised position like when shrugging. Clearly a posture like this will lead to a poor swing, necessitating the need detect such postural variations. Another two degrees of freedom need to be added to model this. Figure 2(a) shows a 26 DOF model, while figure 2(b) shows the incorporation of 4 DOF to model the movement of the shoulder carapace, which models both the shrugging motion and the hunching of the shoulders.

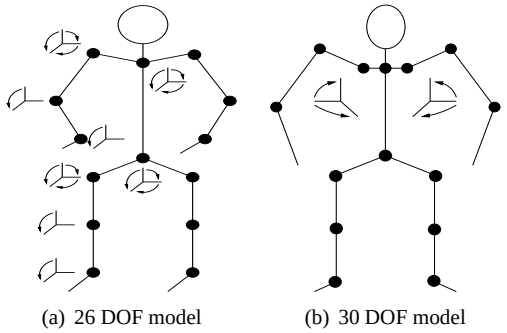

(a) 26 DOF model (b) 30 DOF model

Figure 2. Modelling the articulated body

Once data from a training set has been analyzed, the articulated model which best explains the variation can be chosen.

With the articulated model chosen, a surface must be fitted to each link. This presents another reason why we are starting with the principal component approach as the surface must represent the clothes and not just the skin. This causes variability in the shape of each surface during the swing, to be investigated at a later stage.

3.3. Coping with the high dimensionality configuration space of the human body

One problem associated with tracking the human body is the high dimensionality of the configuration space. The higher dimensionality of the configuration space, the more particles that are required, and hence the higher the computational cost. MacCormick and Blake [8] showed that the number of particles required, N, can be found by

$$N \geq \frac{D_{min}}{\alpha^d} \tag{1}$$

where D_{min} and $\alpha \ll 1$ are constants, and d is the dimensionality of the search space. Clearly a large number of dimensions (around 26 for an articulated human) creates the need for a impractical number of samples. To make tracking in high dimensional spaces tractable, methods such as annealed particle filtering [1] have been proposed. This method allows tracking in high dimensional spaces assuming no knowledge of motion, angle of view, or availability of labelling cues. The condensation algorithm propagates the conditional density $p(X|Z)$ using $p(Z|X)$, where Z is the image and X the configuration space, whereas annealing finds the maximum value of a weighting function $w(Z, X)$. The benefit of this is that $w(Z, X)$ is computational cheaper and requires fewer evaluations, however this comes at the cost of not being able to work within a robust Bayesian framework. In the case of the golf tracking application these assumptions can be relaxed, the angle of view is known and importantly we can assume that the head is never occluded during the swing from this angle. This allows a hierarchical search to be performed using the knowledge that:

1. the head will not be occluded
2. the only object which occludes the arms and club is the head
3. the only objects which occlude the legs are the arms and club

MacCormick and Isard [8] develop a method of partitioned sampling, whereby the configuration space is decomposed into multiple partitions to be search in a hierarchical order. Dynamics are applied to the first partition, the result being multiplied by the observational density of this partition. A resampling operation is then performed, and the dynamics of the second partition applied. Now we multiply by the observational density of the second partition. The process is repeated until all partitions have been calculated. It was shown in [8] to reduce the number of particles required to

$$N \geq \frac{D_{min}}{\alpha}. \tag{2}$$

Another advantage of this method is that the number of particles used in each partition can be varied.

Considering two partitions in this application, we have one which contains the head, and another which contains the arms. The partitions meet at the tops of the shoulders. These are drawn as individual contours in figure 3. The observational density of the head partition is independent of the arms partition, and hence can be found with no knowledge of the location of the arms. The prior can the be resampled weighted by this observational density. This concentrates the search in areas of the arms partition which correspond to high observational densities in the head partition.

(a) The head partition

(b) The arm partition

Figure 3. Different partitions of the configuration space, manually annotated

3.4. Smoothing the output

The nature of this application allows for post processing of the tracking results, as the analysis occurs after the golfer has completed their swing. Because of this, a backwards optimization phase can be added to the algorithm to improve results. Isard and Blake [6] present a framework for a output smoothing filter. From section 3.1 the output of a time step of the condensation algorithm consists of a set of state vectors $\mathbf{s}^t = (s_1^t, ..., s_n^t)$ with associated probabilities $\boldsymbol{\pi}^t = (\pi_1^t, ..., \pi_n^t)$ at time t. The smoothing algorithm

can be thought of as finding the best path through a Hidden Markov Model, where the transitional probabilities are derived form the dynamic model.

This smoothing framework provides a powerful tool when multiple hypotheses of the object position are present. In this case, the prior for the time step will be multi-modal. Should the posterior reflect the same peaks as the prior, we conjecture that a MAP estimate of the object position will be not be useful. The MAP estimate will average the competing hypotheses, producing a result in the middle of them that does not necessarily represent a probable object position. The tradeoff however is the restriction upon the type of dynamic model which can be used, i.e it must be first order to fulfill the Markov criteria. A less accurate dynamic model will increase the number of particles required for successful tracking. At the same time it is worth remembering that as this is a training aid, deviation from the dynamic model is exactly what we are looking for. Although strong multiple hypotheses are not expected in this application, it will be determined at a later stage if this smoothing technique proves beneficial.

4. Providing feedback to the golfer

Once the results from the visual tracking have been obtained, feedback can be provided to the golfer. To do this, the system will have a learned set of swings from technically correct professional golfers. Areas where the players swing varies significantly from the mean of the learnt set can then be highlighted. The correct postural position can be superimposed onto the video of their swing, or shown alongside the video. Audio advice will also be provided, again from a learnt set, on causes of the problem and the expected result of the shot as determined by the analyzer mat.

4.1. Matching the timing

To match the timing of the players swing and the learned set, the swing is broken into two parts. These are the back swing and the down swing. By detecting when the player is at the top of their back swing, indicated by a change in direction of arms, the learned set data can be interpolated or extrapolated to match the time taken for the player to reach that point. A rule of thumb is that the down swing should be twice as fast as the back swing and is referred to as the tempo of the swing. The down swing from the learnt set can also be interpolated or extrapolated to match the player's swing speed, or the player can try to match the learnt set to improve their tempo.

5. Current state of the project

Contours outlining the head and arms have been successfully tracked throughout the golf swing. These result are shown in figure 4. Tracking here was achieved using the condensation algorithm, with the Poisson observational likelihood function function described in [7]. The hierarchical tracking algorithm described in section 3.3 was not used in this test, meaning each contour was tracked independently of the other.

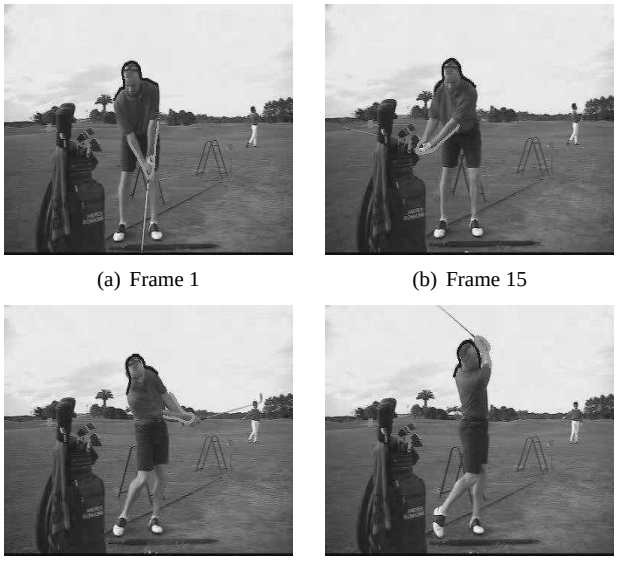

(a) Frame 1 (b) Frame 15

(c) Frame 30 (d) Frame 38

Figure 4. Results of tracking

6. Future Work

The focus of the project now is on creating a concept demonstration version of the product to arouse interest in the golfing community. To achieve this a small set of swings taken from available golf players will be learnt, allowing for rudimentary feedback to be given. This feedback is envisioned to be simple suggestions such as advising a player not to lift their head or to keep their arms straight. It is hoped that this concept demonstrator version can be completed around January 2004.

References

[1] A. Blake, J. Deutscher, and I. Reid. Articulated body motion capture by annealed particle filtering. *Proceedings of Computer Vision and Pattern Recognition Conference*, 2:126–133, 2000.

[2] A. Blake, and M. Isard. *Active Contours*. Springer-Verlag, London, 1998.

[3] T.F. Cootes, G.V. Wheeler, K.N. Walker and C. J. Taylor. View-based active appearance models. *Image and Vision Computing*, (20).

[4] J. Davis and A. Bobick. Virtual pat: a virtual personal aerobics trainer. *MIT Media Lab Perceptual Computing Group Technical Report*, (436), 1998.

[5] M. Isard and A. Blake. Visual tracking by stochastic propagation of conditional density. *Proc. 4th European Conf. Computer Vision*, pages 343–356, April 1996.

[6] M. Isard and A. Blake. A smoothing filter for condensation. *Proc 5th European Conf. Computer Vision*, 1:767–781, 1998.

[7] J. MacCormick. *Stochastic Algorithms for Visual Tracking*. Springer-Verlag, London, 2002.

[8] J. MacCormick and A. Blake. Partitioned sampling, articulated objects and interface quality hand tracking. *Accepted to ECCV*, 2000.

[9] R. Szeliski and D. Terzopoulos. Tracking with kalman snakes. *Active Vision*, pages 3–20, 1992.

[10] "Dragon Fly at Point Grey Research". [Online] Available at http://www.ptgrey.com/products/dragonfly/dragonfly.pdf, last accessed 25/8/2003.

[11] "Golf Bio Dynamics". [Online] Available at http://www.golfbiodynamics.com/html/GAS.htm, last accessed 20/8/2003.

[12] "GolfTek". [Online] Available at http://www.golftek.com, last accessed 20/8/2003.

[13] "Motion Coach". [Online] Available at http://motioncoach.com/mp_rmvbck.htm, last accessed 22/8/2003.

[14] "Swing Cam". [Online] Available at http://www.swingcam.co.uk/index.htm, last accessed 20/8/2003.

[15] International Patent Classification(s)A63B 069/36 G06F 015/62, Application No.:WO92/21412, Application Date:01.06.92, PCT Publication Number:WO92/21412, Priority Data Number: PK6405, Date: 30.05.91, Country: AU AUSTRALIA, Publication Date: 08.01.93, Applicant: Richard John Baker, Inventor(s): Richard John Baker.

Weighted Data Normalization and Feature Selection for Evolving Connectionist Systems Proceedings

Qun Song
Knowledge Engineering &
Discovery Research Institute
Auckland University of Technology
Private Bag 92006, Auckland 1020
New Zealand
email qsong@aut.ac.nz

Nikola Kasabov
Knowledge Engineering &
Discovery Research Institute
Auckland University of Technology
Private Bag 92006, Auckland 1020
New Zealand
email nkasabov@aut.ac.nz

Abstract

This paper introduces a method for weighted data normalization (WDN) that optimizes the normalization ranges for the input variables of an evolving connectionist system (ECOS). ECOS perform incremental, local area learning based on clustering. A genetic algorithm is used as part of the WDN method. The derived weights have the meaning of feature importance and are used to select a minimum set of variables (features) that optimize the performance of the ECOS. The method is illustrated on two types of ECOS. The first one is for time series prediction and the second one is an original ECOS for classification, proposed in this paper.

1. Introduction

In some applications raw (not normalized) data is used. This is appropriate when all the input variables are measured in the same units. Normalization, or standardization, is reasonable when the variables are in different units or when the variance between them is substantial. However, a general normalization means that every variable is normalized in the same range, e.g. [0,1] and therefore has the same importance for the output of the system.

For many practical problems, variables have different importance and make different contribution to the output. Therefore, it is necessary to find an optimal normalization and assign proper importance factors to the variables. Such a method can also be used for feature selection or reducing the size of the input vectors through keeping the most important ones. This is especially applicable to a special class of neural networks, evolving connectionist systems (ECOS), where nodes and connections evolve from an input stream of data to capture clusters and to allocate a local output function for each cluster [1, 2, 3]. Distance between existing nodes and new input vectors are measured as Euclidean distance, so that variables with a wider range will have more influence on the learning process and vice versa.

The paper is organized as follows. Section two presents the main principles of ECOS, while section three introduces a new ECOS model for classification, called Evolving Clustering Method for Classification (ECMC). Section four introduces a method for weighted data normalization (WDN) based on genetic algorithms (GA). Section five illustrates the method on a known ECOS for prediction, as well as on the introduced ECMC method. Conclusions are drawn in section six.

2. Principles of evolving connectionist (ECOS)

Evolving connectionist systems (ECOS) are multimodular, connectionist architectures that facilitate modelling of evolving processes and knowledge discovery [1, 2, 3]. An ECOS may consist of many evolving connectionist modules.

An ECOS is a neural network that operates continuously in time and adapts its structure and functionality through a continuous interaction with the environment

and with other systems according to: (i) a set of parameters that are subject to change during the system operation; (ii) an incoming continuous flow of information with unknown distribution; (iii) a goal (rationale) criteria (also subject to modification) that is applied to optimise the performance of the system over time. The evolving connectionist systems have the following characteristics [1]:

1) They evolve in an open space, not necessarily of fixed dimensions.

2) They learn in on-line, incremental, fast learning - possibly through one pass of data propagation.

3) They learn in a life-long learning mode.

4) They learn as both individual systems, and as part of an evolutionary population of such systems.

5) They have evolving structures and use constructive learning.

6) They learn locally and locally partition the problem space, thus allowing for a fast adaptation and tracing processes over time.

7) They facilitate different kind of knowledge representation and extraction, mostly - memory based, statistical and symbolic knowledge.

ECOS are connectionist structures that evolve their nodes (neurons) and connections through supervised incremental learning from input-output data pairs. One of the ECOS models, evolving fuzzy neural network (EFuNN), is shown as a simple version in Figure1 [2]. It consists of five layers: input nodes, representing input variables; input fuzzy membership nodes, representing the membership degrees of the input values to each of the defined membership functions; rule nodes, representing cluster centers of samples in the problem space and their associated output function; output fuzzy membership nodes, representing the membership degrees to which the output values belong to defined membership functions; and output nodes, representing output variables.

ECOS learn local models from data through clustering of the data and associating a local output function for each cluster. Rule nodes evolve from the input data stream to cluster the data, and the first layer W_1 connection weights of these nodes represent the co-ordinates of the nodes in the input space. The second layer W_2 represents the local models (functions) allocated to each of the clusters.

Clusters of data are created based on similarity between data samples either in the input space (this is the case in some of the ECOS models, e.g. the dynamic neuro-fuzzy inference system DENFIS [3], and the zero instruction set computer ZISC [4]), or in both the input space and the output space (this is the case in the EFuNN models [2]). Samples that have a distance to an existing cluster center (rule node) *N* of less than a threshold *Rmax* (for the EFuNN models it is also needed that the output vectors of these samples are different from the output value of this cluster center in not more than an error tolerance *E*) are allocated to the same cluster *Nc*. Samples that do not fit into existing clusters, form new clusters as they arrive in time. Cluster centers are continuously adjusted according to new data samples, and new clusters are created incrementally.

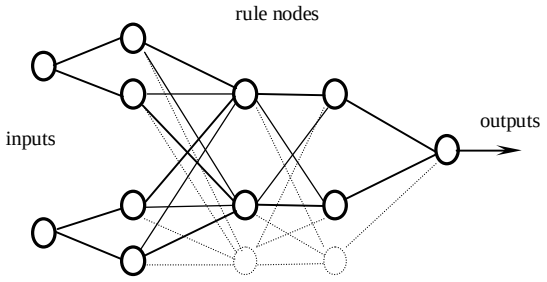

Figure 1: A simple version of an ECOS – EFuNN (from [2])

The similarity between a sample $S = (\boldsymbol{x}, \boldsymbol{y})$ and an existing rule node $N = (W_1, W_2)$ can be measured in different ways, the most popular of them being the *normalized Euclidean distance*:

$$d(S, N) = \frac{1}{n}\left[\sum_{i=1}^{n} \left| x_i - W_{1N} \right|^2\right]^{\frac{1}{2}} \quad (1)$$

Where *n* is the number of the input variables.

ECOS learn from data and automatically create a local output function for each cluster, the function being represented in the W_2 connection weights, thus creating local models. Each model is represented as a local rule with an antecedent – the cluster area, and a consequent – the output function applied to data in this cluster, e.g.:

IF (data is in cluster *Nc*) THEN (the output is calculated with a function *Fc*) (2)

In case of DENFIS [3], first order local fuzzy rule models are derived incrementally from data, for example:

IF (the value of x_1 is in the area defined by a *Gaussian function* with a center at 0.7 and a standard deviation of 0.1) AND (the value of x_2 is in the area defined by a *Gaussian function* with a center at 0.5 and a deviation of 0.2) THEN (the output value *y* is calculated with the use of the formula $y = 3.7 + 0.5x_1 - 4.2\ x_2$) (3)

In case of EFuNNs [2], local simple fuzzy rule models are derived, for example:

IF [x_1 is High (0.7) and x_2 is *Low* (0.9)] THEN y is *High* (0.8) [radius of the input cluster 0.3, number of examples in the cluster 13] (4)

where: *High* and *Low* are fuzzy membership functions defined on the range of the variables for x_1, x_2, and y (see Figure1). The number and the type of the membership functions can either be deduced from the data through learning algorithms, or can be predefined based on human knowledge.

3. Evolving clustering method for classification (ECMC)

The ECMC method introduced in this section classifies a data set into a number of classes in the *n*-dimensional input space by evolving rule nodes. Each rule node is associated with a class through a constant. Its receptive field covers a part of the *n*-dimensional space around the rule node. Usually, such an influence field in the *n*-dimensional space is a hyper-sphere and a number of rule nodes may be associated to a same class [1, 2, 3].

There are two distinct phases of ECMC operation. During the first, learning phase, data vectors are dealt with one by one with their known classes. The learning sequence is described as the following steps:

1) If all learning data vector have been entered into the system, complete the learning phase; otherwise, enter a new input vector from the data set.
2) Find all existing rule nodes with the same class as the input vector's class.
3) If there is not such a rule node, a new one is created[*] and then go to step 1; otherwise:
4) For each of these rule nodes, if the input vector dose not lie within the associated field, increase this field if possible [**].
5) If the field increment is successful[***] or the input vector lies within an associated field, go to step 1; otherwise, a new node is created [*]. Go to step 1.
6) End of the learning procedure.

[*] Create a new rule node: the position of the new rule node is the same as the current input vector in the input space and the radius of its influence field is set to the Min-radius parameter.

[**] Suppose that the field has a radius of R^0 and the distance between the rule node and the input vector is d; the increased radius is $R^{new} = (R^0 + d) / 2$ and the rule node moves to the new position that is situated on the line connecting the input vector and the rule node before it changed its position and has the distance R^{new} to the input vector.

[***] If the new field does not include any input vectors from the data set, which belong to a different class, the increment is successful; the rule node changes its position and the field increases; otherwise, it is failed, both rule node and its field do not chang.

The learning procedure takes only one iteration (epoch) but all input vectors are retained in the system at their position in the input space.

The classification of new input vectors is performed in the following way:

1) The new input vector is entered and the distance between it and all rule nodes is calculated. If the new input vector lies within the field of one or more rule nodes associated with one class, the vector belongs to this class.
2) If the input vector does not lie within any field, the vector will belong to the class associated with the closest rule node.

To compare the performance of the ECMC method we conducted the following experiments. We used ECMC, ECF [13], ZISC [4], and a multiplayer perceptron MLP on the benchmark *Iris* data for classification. *Iris* data set has four input variables and each input vector belongs to one of three classes [6]. 50% of the whole data set is randomly selected for training data and another 50% for testing data. The parameters of each model are set as follows and the average test results of 50 experiments are shown in Table 1.

Parameters for ECMC: Min-radius = 0.02, one epoch. Parameters for ECF: Max-field = 1; Min-field = 0.2; MF = 2; MofN = 1; 5 epochs.

Parameters for ZISC: Max-field = 4096; Min-field = 1; 5 epochs.

Parameters for MLP: number of hidden layer 1; number of neurons in the hidden layer 12; learning epochs 100 with *Levenberg-Marquardt* learning algorithm [7].

Table 1. Comparison between ECMC and other models on the *Iris* classification data

	Rule nodes (or neurons)	Average number of test errors
ECMC	9.8	4
ECF	12.7	4
ZISC	14.4	6.1
MLP	12	4.6

The results from Table1 show that ECMC compares favorably with other classification methods. The ECMC method is distance-based. As it changes the influence field in an eccentric manner, ECMC will have less rule

nodes than the ECF or the ZISC models, which change their influence fields in a concentric manner.

4. Weighted data normalization (WND) and feature selection based on genetic algorithm

The WDN method described here makes use of *evolutionary computation* (EC) techniques [8, 9, 10] and of *genetic algorithms* (GA) in particular [8]. A GA algorithm applies a multi-point, probabilistic search in the whole search space to discover a global optimum subject to an objective (fitness) function. Methods based on EC techniques for optimizing parameters of MLP and other traditional neural network models are published in [11, 12]. In [13, 14], a GA is used to optimize some of the parameters of ECOS models.

The WDN method proposed here optimizes the normalization intervals (ranges) of the input variables and allocates weights to each of the variables from a data set. The method consists of the following steps:

1) The training data is preprocessed first by a general normalization method. There are several ways for this: a) normalizing a given data set so that they fall in a certain interval, e.g. [0, 1], [0, 255] or [-1, 1] etc [9]; b) normalizing the data set so that the inputs and targets will have means of zero and standard deviations of 1 [9]; c) normalizing the data set so that the deviation of each variable from its mean normalized by its standard deviation [10]. In the WDN, we normalize the data set in the interval [0, 1].
2) The weights of the input variables $x_1, x_2,\ldots, x_n$ represented respectively by $w_1, w_2,\ldots,w_{n,,}$ with initial values of 1,1,…1 , form a chromosome for a consecutive GA application. The weight w_i of the variable x_i defines its new normalization interval $[0, w_I]$.
3) A GA is run on a population of connectionist learning modules for different chromosome values, over several generations. As a fitness function, the root mean square error RMSE of a trained connectionist module on the training data or on a validation data is used, or alternatively – the number of the created rule nodes can be used as a fitness function that needs to be minimized. The GA runs over generations of populations and standard operations are applied such as binary encoding of the genes (weights); roulette wheel selection criterion; multi-point crossover operation for crossover.
4) The connectionist model with the least error is selected as the best one, and its chromosome – the vector of weights $[w_1, w_2,\ldots,w_n]$ defines the optimum normalization range for the input variables.
5) Variables with small weights are removed from the feature set and the steps from above are repeated again to find the optimum and the minimum set of variables for a particular problem and a particular connectionist model.

The above WDN method is illustrated in the next section on two case study ECOS and on two typical problems, namely EFuNN for a time series prediction, and ECMC for classification.

5. Case study examples ofpplying the WND method to ECOS

5.1 EFuNN with WDN for Prediction

In the present paper, EFuNN is applied to the time series prediction. Improved learning with the WDN method is demonstrated on the Mackey-Glass (MG) time series prediction task [6]. The MG time series is generated with a time-delay differential equation as follows:

$$\frac{dx(t)}{dt} = \frac{0.2x(t-\tau)}{1+x^{10}(t-\tau)} \qquad (5)$$

To obtain this time series values at integer points, the *fourth-order Runge-Kutta method* was used to find the numerical solution to the above MG equation. Here we use the following parameter values: a time step of 0.1, $x(0) = 1.2$, $\tau = 17$ and $x(t) = 0$ for $t < 0$. From the input vector $[x(t-18)\ \ x(t-12)\ \ x(t-6)\ \ x(t)]$, the task is to predict the value $x(t+6)$. In the experiments, 1000 data points, from t = 118 to 1117, were extracted for predicting the 6 steps ahead output value. The first half of the data set was taken as a training data, and another half as the testing data.

The following parameters are set in the experiments for the EFuNN model: *Rmax*=0.15; *E*=0.15; 3 membership functions. The following GA parameter values are used: for each input variable, the values from 0.16 to 1 are mapped onto 4 bit string; the number of individuals in a population is 12; mutation rate is 0.001; termination criterion (the maximum epochs of GA operation) is 100 generations; the *root-mean square error* RMSE on the training data is used as a fitness function. The resulted weight values, the number of the rule nodes created by EFuNN with such weights, the training RMSE and testing RMSE are shown in Table 2. For a comparison, EFuNN results with the same parameters, the same training data and testing data, but without WDN are also shown in Table 2.

Table 2: Comparison between EFuNN without WDN and EFuNN with WDN

	Normalization Weights	Number on Rule Nodes	Training RMSE	Testing RMSE
EFuNN without WDN	1, 1, 1, 1	87	0.053	0.035
EFuNN with WDN	0.4, 0.8 0.28 0.28	77	0.05	0.031

With the use of the WDN method, a better prediction results is obtained for a significantly less number of rule nodes (clusters) evolved in the EFuNN model. This is because of the better clustering achieved when different variables are normalized differently and the normalization reflects on their importance.

5.2 ECMC with WDN for Classification and Feature Extraction

In this section, the ECMC with WDN is applied on the *Iris* data for both classification and feature selection. The same as the experiments in the section 3, all experiments in this section are repeated 50 times with the same parameters and the results are averaged. 50% of the whole data set is randomly selected as training data and another 50% as testing data. The following parameters are set in the experiments for the ECMC model: *Min-radius* 0.02; each of the weights for the four normalized input variables is a value from 0.1 to 1, and is mapped into a 6-bit binary string.

The following GA parameters are used: number of individuals in a population 12; mutation rate 0.005; termination criterion (the maximum epochs of GA operation) 50; fitness function - the number of created rule nodes. The resulted weight values, the number of rule nodes created by ECMC with such weights and the number of errors on the testing data are shown in Table 3. For comparison, ECMC classification results with the same parameters, the same training data and testing data but without WDN are also shown in Table 3.

From the results, we can see that the weight of the first variable is much smaller than the weights of the other variables. The weights can be used as a measure of the importance of the variables and the least important variables can be removed from the input. Same experiment is repeated without the first input variable and the results have improved as shown in Table3. If another variable is removed, and the total number of input variables is 2, the test error increases, so it can be assumed that for the particular ECMC model the optimum number of input variables is 3.

Table 3: Comparison between ECMC without WDN and ECMC with WDN

	Normalization Weights	Number of rule nodes	Number of test errors
4 Inputs without WDN	1, 1, 1, 1	9.8	3.8
4 Inputs with WDN	0.25, 0.44 0.73 1	7.8	3.1
3 Inputs without WDN	1, 1, 1	8.8	3.7
3 Inputs with WDN	0.50, 0.92, 1	8.1	2.9
2 Inputs without WDN	1,1	7.7	3.2
2 Inputs with WDN	1, 0.97	7.4	3.1

6. Conclusions

The proposed method for weighted data normalization (WDN) is a generic one and can be applied to any connectionist models, but it is especially efficient when applied to *evolving connectionist systems* (ECOS) as the latter use local, clustering-based learning algorithms. The WDN method is also efficient when used for feature selection. Further development of the method includes using linear along with non-linear normalization, using different types of normalization across variables and across areas of the problem space for achieving a better performance of the system.

The proposed evolving clustering method for classification ECMC uses clusters of different shapes rather than hyper-spheres, as it is the case in other ECOS methods, and results in a less number of rule nodes and less error. New ECOS methods are being developed at present that will have all the parameters and the features optimised together.

7. Ackonwledgements

The research presented in the paper is funded by the New Zealand Foundation for Research, Science and Technology under grant NERF/AUTX02-01.

References

[1] Kasabov, N. *Evolving connectionist systems: Methods and Applications in Bioinformatics, Brain study and intelligent machines*, Springer Verlag, London, New York, Heidelberg, 2002.

[2] Kasabov, N. "Evolving fuzzy neural networks for on-line supervised/unsupervised, knowledge–based learning", IEEE Trans. SMC – part B, Cybernetics, vol.31, No.6, 902-918, December 2001.

[3] Kasabov, N. and Song, Q. "DENFIS: Dynamic, evolving neural-fuzzy inference systems and its application for time-series prediction," IEEE Trans. on Fuzzy Systems, vol.10, No.2, 144-154, April 2002.

[4] ZISC Manual, Silicon Recognition, www.silirec.com, 2001.

[5] Song, Q. Kasabov, N.,"ECM - A Novel On-line, Evolving Clustering Method and Its Applications", ANNES 2001, Dunedin, New Zealand, 22 - 24, November, 2001, 87 – 92.

[6] Blake, C. and Merz, C. (1998) Repository of machine learning databases. http://www.ics.uci.edu/~mlearn/MLRepository.html Irvine, CA: University of California, Department of Information and Computer Science.

[7] Baeck, T. *Evolutionary algorithm in theory and practice: evolution strategies, evolutionary programming, genetic algorithms*, Oxford University Press, New York (1995)

[8] Holland, J. H. *Adaptation in natural and artificial systems*, The University of Michigan Press, Ann Arbor, MI (1975)

[9] Koza, J. R. *Genetic Programming*, MIT Press (1992)

[10] Goldberg, D. E. *Genetic Algorithms in Search, Optimization and machine Learning*, Addison-Wesley, Reading, MA (1989).

[11] Fogel, D., Fogel, L. and Porto, V. (1990) Evolving neural networks, Biological Cybernetics, vol.63, 487-493

[12] Yao, X. (1993) Evolutionary artificial neural networks, Int. Journal of Neural Systems, vol.4, No.3, 203-222

[13] Kasabov, N. and Song, Q. "GA-Optimisation of evolving connectionist systems for classification with a case study from bioinformatics," Proc. of ICONIP'2002, Singapore, November, 2002, IEEE Press, 602-605.

[14] Kasabov, N., Song, Q. and Nishikawa, I, "Evolutionary computation for parameter optimisation of on-line evolving connectionist systems for prediction of time series with changing dynamics",. in Int. Joint Conf. on Neural Networks IJCNN'2003. 2003. USA.

EXPERT, FUZZY & NEURAL SYSTEMS II

(This page left blank intentionally)

Rule Extraction from Images Using Neural Networks

Hiroshi Nishiyama
Faculty of Engineering, The University of Tokushima
2-1,Minami-Josanjima,Tokushima,770-8506 Japan
lark@is.tokushima-u.ac.jp

Minoru Fukumi and Norio Akamatsu
Faculty of Engineering, The University of Tokushima
2-1,Minami-Josanjima,Tokushima,770-8506 Japan
fukumi@is.tokushima-u.ac.jp
akamatsu@is.tokushima-u.ac.jp

Abstract

*In this paper, as a method of extracting keywords, feature data is extracted from an image and a method using a Back-Propagation neural network for learning and classifying them is proposed. First, a bit map image in the RGB color space is transformed into the L*a*b* color space. Next, it clusters image pixels using the c-means method and domains are extracted by Labeling. Features, such as area of the obtained domain, color information, and coordinates of the center of gravity, are then calculated, which are input attributes to a neural network. Moreover, rule generation is carried out by extracting values in the hidden layer of each keyword after the learning of the neural network. The method of generating keywords using the rules is proposed and a comparison experiment is performed. Finally the validity of this method was verified by means of computer simulations.*

1. Introduction

In recent years, it has become the multimedia society where images play an important role, and the use of the Internet and image input apparatuses have spread. Nowadays, there is huge image data in our personal appearance with its spread. It is not easy to find an image suitable for one's purpose out of such a huge image data. Therefore, the technique of searching images is desired. For image retrieval from image database, suitable keywords are necessary in each image [1].

There is a technique of adding keywords to images beforehand, and searching by using a keyword based on them as a method of images retrieval. However, this can cause a problem that it is unmanageable if there is an immense quantity of images. In this case, automatic keyword extraction from images is important for image retrieval and to construct a large scale image archive. In this paper, therefore, a technique of performing keyword addition automatically to images is proposed.

First, in Section 2, a technique used is this paper is explained, and an experimental method which uses a neural network in Section 3 is described, and Section 4 shows a simulation result and consideration and conclusion in Section 5.

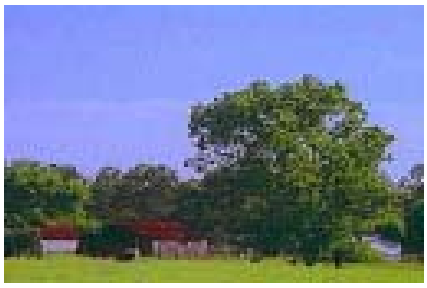

Figure 1. Sample of scenery image.

2. Feature extraction

2.1 L*a*b* color space

A L*a*b* color space is a front color system currently used for expressing an objective color most popularly in all fields. By the L*a*b* color space, intensity is expressed with L* and the degree of color which shows hue and saturation is expressed with a* and b* [2].

A conversion formula is shown below.

$$L^* = 116(Y/Y_n)^{1/3} - 16$$

$$a^* = 500[(X/X_n)^{1/3} - (Y/Y_n)^{1/3}]$$

$$b^* = 200[(Y/Y_n)^{1/3} - (Z/Z_n)^{1/3}]$$

$$X = 0.49000R + 0.31000G + 0.20000B$$
$$Y = 0.17697R + 0.81240G + 0.01063B$$
$$Z = 0.01000G + 0.99000B$$

($X_n = 95.045$ $Y_n = 100$ $Z_n = 108.892$)

$$X/X_n > 0.008856$$

However, $Y/Y_n > 0.008856$

$$Z/Z_n > 0.008856$$

When there is a value of 0.008856 or less in $X/X_n, Y/Y_n, Z/Z_n$, the term of the cubic root which corresponds to it in the upper formula is calculated by transposing it to the following formulas, respectively [9].

$$(X/X_n)^{1/3} \to 7.787(X/X_n) + 16/116$$
$$(Y/Y_n)^{1/3} \to 7.787(Y/Y_n) + 16/116$$
$$(Z/Z_n)^{1/3} \to 7.787(Z/Z_n) + 16/116$$

2.2 C-means method

The c-means method is a technique of clustering performed by adding a membership function to the k-means method [3][4][5][6].

Let $X = \{x_1, ..., x_n\}$ be n individuals with a p-dimensional vector to be clustered. Moreover, the number of clusters is set to c, the representative point of Cluster $i (i = 1, ..., c)$ is set to v_i, and it is decided with the membership function u_{ik} whether Individual x_k belongs to the Cluster i. Then, it is regarded as a problem which makes the criterion function J_m minimum by properly choosing Matrix $U = (u_{ik})$ and the representative point $V = (v_1, ..., v_c)$ for the problem of clustering.

In this technique, the membership u_{ik} is defined as the following.

In $x_k \neq v_i$

$$u_{ik} = 1 / \left[\sum_{j=1}^{c} \left(\frac{(d_{ik})^2}{(d_{jk})^2} \right)^{1/(m-1)} \right]$$

In $x_k = v_i$

$$u_{ik} = 1 \quad u_{jk} = 0 \quad (j \neq i)$$

Moreover, the center v_i of a cluster is computed as

$$v_i = \sum_{k=1}^{n} (u_{ik})^m x_k / \sum_{k=1}^{n} (u_{ik})^m .$$

The fundamental Algorithm is shown below.

FCM1. Initial values of U and V are decided suitably.

FCM2. U is fixed to the last value, the optimal

solution from $\min_{V \in R^p} J_m(U,V)$ is calculated, and it is referred to as a new V.

FCM3. V is fixed to the last value, the optimal solution from $\min_{V \in R^p} J_m(U,V)$ is calculated, and it is referred to as a new U.

FCM4. If this process converges on a proper value, it stops, otherwise, return to Step FCM2.

2.3 Labeling

Labeling is used to search for the coordinates of the area of each domain, an average RGB values, and the center of gravity in the image where domain division was carried out [7]. It is a operation which assigns a different label to a non-connected region and which assigns the same label to the same connected region. The processing procedure of Labeling used in this research is shown below.

<Algorithm>

Step.1. Label attachment is carried out using neighboring 8 pixels in each pixel.

Step.2. About the neighboring 8 pixels of a standard center, if it has the same pixel value as the standard pixel, the same label “i” is assigned.

Step.3. If there is a pixel with the same pixel value in the eight pixels, the same operation is carried out for the pixel with Label “i” and it is repeated.

Step.4. The whole image is operated until the same element is not found in neighboring eight.

Step.5. $i = i + 1$

Step.6. It is carried out to eight kinds of all quantization values in the same way.

3. Experimental method using a neural network

Conversion from a RGB color space to a L*a*b* color space is carried out by performing L*a*b* conversion to a bit map image. Five levels quantization using the c-means method to a* and b* which were obtained by the L*a*b* conversion is carried out (Figure.2). Next, three domains are extracted in order with the largest area by performing Labeling. The coordinates of the area of the domain obtained from this, color information, and the center of gravity were calculated, and they were made into a neural network's input signals.

Moreover, this technique uses a feed forward neural network as shows in Figure.3, and a Back-Propagation (BP) method as a learning algorithm. The model of the BP method has 6 units in the input layer, 10 units in the hidden layer, and units of the number of keywords in the output layer, as shown in Figure.3. Teacher data use 48 domains from a total of 43 scenery images, and the keywords in this study are "sky", "sea", "clouds", "plain", "dark green", and "rocks."

Next, the newly proposed if-then rule is explained. An If-then rule is a method of classifying based on the hidden layer's values at the time of classification. First, the values of a hidden layer of each key word are taken out from a trained neural network. Rule generation is performed to them. A rule in this case is based on combination of the hidden outputs. Each output unit can produce such a combination for each input. For instance, IF $H_1 = 1$ and $H_3 = 0$, then $class = 1$, where Hi indicates the output value of the first hidden unit. Based on generated rules, feature data are classified into each keyword in classification. That is, it is the

technique of classifying according to the hidden layer outputs. By this technique, the 1st place of a decimal is rounded off for every keyword, and the ten hidden layer's values are binarized to 0 or 1.

Comparison experiments between the neural network and the rules are performed.

Figure2.The quantization result by the C-means method.

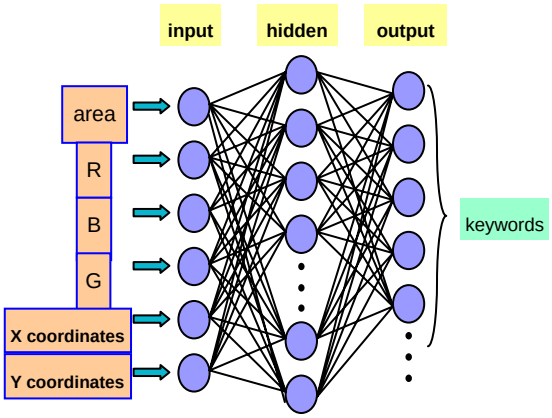

Figure3. A Neural Network Model.

4. Simulation and Consideration

The result classified into keywords using the BP method is shown in Table 1. Those rate shows accuracy which the neural network produced accurate keyword using the features of each region in images.

Table 1.BP method

sky	clouds	sea	plain	dark green	rocks
90%	67%	75%	70%	75%	80%

Next, the result obtained using If-Then rule for the hidden layer's values for every keyword is shown in Table 2.

Table 2.If-Then rule

sky	clouds	sea	plain	dark green	rocks
60%	45%	40%	50%	42%	58%

Compared with the results using a BP method, as for the rate of recognition, the results using the If-Then rule become worse in every keyword. This is due to approximation which transformed hidden layer's values into binary values simply.

However, although the sea can be incorrectly-recognized to be a sky by the BP method this time, the sea was not much incorrectly-recognized to be a sky using an If-Then rule. That is, when you want images of a sky, it is thought that only the image of a sky can be retrieved in many cases. However, more keywords and more kinds of images are necessary to construct a practical.

5. Conclusion

In this paper, the technique of keyword extraction from landscape images as the first phase which performs image retrieval was proposed. First, the feature domain was chosen by giving L*a*b* conversion, quantization by the C-means method, and labeling to the images, and the amount of features was extracted. Moreover,

the If-Then rule was generated and compared with the rate of recognition in the BP method.

Rule extraction method is improved in order to raise the rate of recognition in the If-Then rule from now on. Moreover, although the C-means method is used in domain division, it is considering a technique which can be divided still better.

References

[1] James Z. Wang, Integrated Region-Based Image Retrieval, 2001, Kluwer Academic [2] Mikio Takagi, Image Analysis Handbook, 1991, University of Tokyo Press, in Japanese

[3] The handbook of soft computing and fuzzy., Japan Society for Fuzzy Theory and Systems (2000)

[4] Sadaaki Miyamoto, A Guide to Cluster Analysis, 1999, Morikita Publishing, in Japanese

[5] Takeshi Agui and Tomoharu Nagao, Processing and Recognition of a Picture, 1992, Syokodo, in Japanese

[6] Hisoshi Ozaki and Keiji Taniguchi, Image Processing, 1988, Kyoritsu Publishing Company, in Japanese

[7] Hideyuki Tanaka and Japan Industry Engineering Center, A Guide to Computer Image Processing, 1985, Soken Publishing Company, in Japanese

[8] J. Dayhoff, Neural Network Architecture, 1990, Van Nostrand Reinhold

[9] http://www005.upp.so-net.ne.jp/fumoto/

(This page left blank intentionally)

An Expert System for Preventing Emergencies in Power Systems

Mark Jyn-Huey Lim
School of Engineering
University of Tasmania
GPO Box 252-65 Hobart TAS 7001 AUSTRALIA
mjlim@utas.edu.au

Michael Negenevitsky
School of Engineering
University of Tasmania
GPO Box 252-65 Hobart TAS 7001 AUSTRALIA
Michael.Negnevitsky@utas.edu.au

Abstract

A Java-based prototype expert system is developed for advising system operators in a power system operations control centre on how to prevent selected emergency situations. The expert system is implemented on IBM PC's in the operations control centre of Transend Networks Pty Ltd in Tasmania. This paper discusses the methods used for solving power system contingencies and the development and implementation of the Java-based expert system. The case study also demonstrates how advice is presented to the system operators.

1. Introduction

In a power system operations control centre, a Supervisory Control and Data Acquisition (SCADA) system receives measurements from different equipment that make up the power system grid. The data received by the SCADA system is automatically analysed and the system operators are informed about the current status of the power system. Equipment failure, unexpected load demand variations or catastrophic events (eg. lightning strikes, bushfires) may drive the system into an emergency state of operation. In this state some transmission equipment (eg. power transmission lines, busses and transformers) may have their voltage limit or loading ratings violated. In such cases, to avoid a failure or damage of the system equipment as well as collapse of the entire system, the system operators must take some control actions to remove these violations.

However, making decisions on the appropriate control actions to return the power system to a normal state during emergency situations is a difficult task where useful tools of artificial intelligence can be applied [1]. In a power system operations control centre, a program called the Contingency Analyser, analyses data stored in the SCADA system and runs power flow simulations of different emergency situations to predict whether the power system would be able to cope with a given emergency. If the Contingency Analyser finds any voltage limits or loading violations' while running the power flow simulation, outputs a list of these violations informing a system operator of a possible problem if a particular emergency should occur. A flow diagram of the programs and their outputs is shown in Figure 1. It is then up to the system operator to decide on what type of preventative control actions to take to prevent the power system from reaching an emergency state of operation.

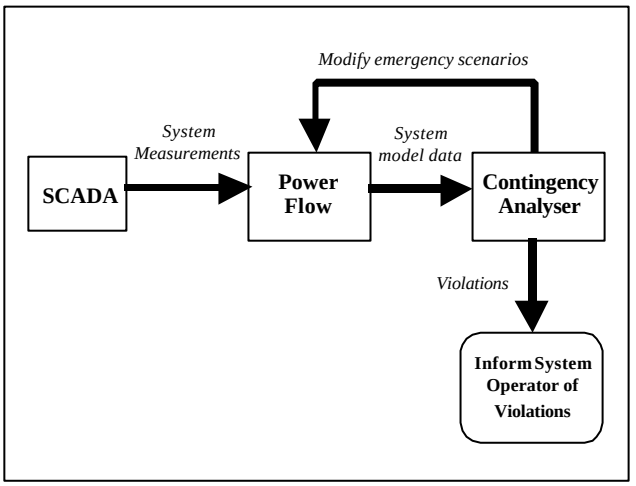

Figure 1. Flow diagram of power system operations control centre programs and their outputs.

Successful execution of these preventative control actions largely depends on an operator's skills and experience to recognise the problem and apply appropriate actions to solve it. System operators that have little experience in solving these types of problems often have great difficulty in deciding on the appropriate preventative control actions. The role of a prototype expert system in providing decision support for preventative control actions is described in this paper.

2. Power System Security Control

The type of control actions used by the system operators for preventative control is dependent on violations that are found by the Contingency Analyser. These violations can be divided into two types: bus voltage violations and equipment overloads.

Bus voltage violations occur when the voltage level on a bus is above or below specified limits. The allowance for variation in voltage level is usually ±5% of the bus rating. Control actions that can be applied to remove bus voltage violations are [2]:

- Adjusting generator excitors to change the voltage at the generation busbar.
- Adjusting in-phase transformer taps.
- Switching in-phase transformer taps.
- Switching on/off shunt reactive (capacitors/reactors) sources.
- Performing emergency load shedding at selected locations.
- Switching the transmission network.

For the case of equipment overloading, this occurs when the power flow through transmission equipment exceeds the equipment's loading rating. Power transmission equipment that can become overloaded includes transmission lines and transformers. Control actions that can be applied to remove such overloads are [3]:

- Provide full loading of the power stations and other power sources in the receiving part of the power system.
- Provide unloading of the power stations in the sending part of the power system.
- Adjust phase-shift transformers and switch capacitor banks and reactors.
- Transfer the load from one part of the system to another.
- Increase output of the active and reactive power of generators and synchronous compensators in the receiving part of the power system via their permissible short-term overloading.
- Adjust bus voltages in order to decrease the power demand.
- Curtail loads of the lowest priority.
- Switch off radial transmission lines.
- Perform emergency load shedding at selected locations.

However, determining which preventative control action to use is dependent on the effectiveness of a particular action. To determine the effectiveness of a particular action requires the use of network sensitivity methods [4].

3. Network Sensitivity Calculations

Network sensitivity methods are based on calculating a set of values (network sensitivity factors), which relate the sensitivity between a change in a control device and its effect on each element of the given power system. The control devices are generators, tap transformers, and shunt reactive sources. The elements affected by a change in the control devices are busses, transmission lines and transformers. It can be demonstrated that network sensitivity factors represent a fast way of determining the most effective control device for changing the bus voltage or power flow through transmission equipment [4].

Calculation of the network sensitivity factors takes the following form [4]:

$$\Delta C_k = C_k' - C_k^o \tag{1}$$

$$\Delta E_j = E_j' - E_j^o \tag{2}$$

$$S_{kj} = \Delta E_j / \Delta C_k \tag{3}$$

where:

- C_k^o is the original value for the control device C_k; C_k' is the value for control device C_k after a small change is applied; ΔC_k is the percentage change for control device C_k.
- E_j^o is the original value for element E_j; E_j' is the value for element E_j after a change is applied from control device C_k; ΔE_j is the percentage change for element E_j due to a small change applied from control device C_k.
- S_{kj} is the sensitivity factor relating the change in value for element E_j to a small change from control device C_k.

Using the above sensitivity factors, a sensitivity matrix is built. It relates the sensitivities between all control devices to all elements in the power system.

4. Expert System Development

The Java programming language was used to develop a prototype expert system. The preference for choosing Java rather than an expert system shell for developing the prototype expert system was Java's flexibility which allows the expert system better interaction with external programs and databases. The Java-based system also is better suited for on-line use.

4.1 Overview of the Expert System

The following diagram in Figure 2 shows an overview of how the expert system interacts with external programs in an operations control centre.

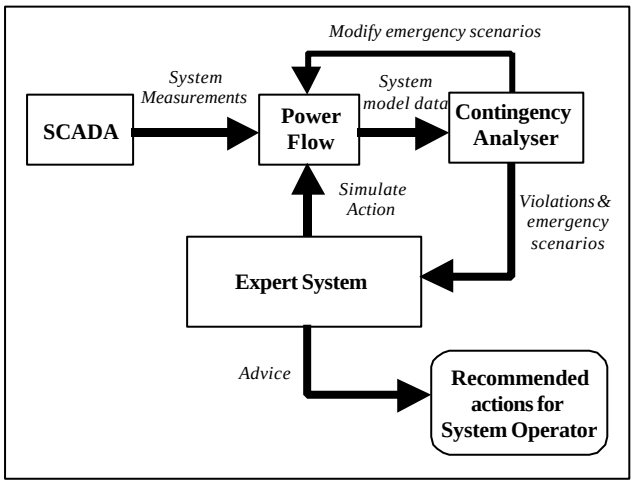

Figure 2. Diagram of interaction between external programs and the expert system.

4.2 External Programs

The Contingency Analyser is used in power system operations control centres to simulate different contingencies and inform the system operators of any violations resulting from the contingencies. The expert system is using the output of the Contingency Analyser to obtain the list of violations resulting from a simulated emergency situation. Contingency Analyser is also used by the expert system to rerun the emergency simulation after a corrective action has been applied.

The Power Flow program uses a model of the power system grid and performs calculations of power flow and bus voltages, based on a set of parameters of the power system elements. Power Flow is used by the expert system to calculate network sensitivity factors and to build up the network sensitivity matrix. It is also used by the expert system to simulate effects of a particular control action.

4.3 Database

The expert system for preventing emergencies interacts with a power system database. This database provides on-line data and is used for:

- Obtaining information on the type of emergency situations that is to be simulated.
- Checking on the violations given by the Contingency Analyser.
- Obtaining and changing the data computed by the Power Flow program.
- Obtaining information on voltage limits for busses and obtaining information on loading ratings for transmission lines and transformers.

4.4 Rule-base and Inference Engine

A rule-base is used for selecting the most appropriate control device from the network sensitivity matrix for a particular situation.

The expert system can be used in either off-line or on-line modes. In the off-line mode the inference engine performs the following steps (generating an advice – the first stage of the inference process):

- Allow the system operator to select an emergency situation being simulated by the Contingency Analyser.
- Check the database for violations generated by the Contingency Analyser for the selected emergency situation.
- If no violations are found, then stop the inference process. Otherwise select the most serious violation, based on the selection rules in the rule-base.
- Build a list of recommended actions, using rules from the rule-base and network sensitivity factors from the network sensitivity matrix.

- Calculate the effectiveness of each recommended control action by using the network sensitivity matrix.
- Sort the list of recommended actions based the effectiveness of each action and find the most effective control device.

After the inference engine selects the most serious violation and generates a list of recommended actions to deal with that violation, the system operator can then choose to simulate one of the recommended actions to see its effect. When the system operator chooses to simulate one of the recommended actions, the inference engine performs the following steps (control action simulation – the second stage of the inference process):

- Apply the selected control action to the database.
- Run Power Flow to predict the new state of the power system.
- Run Contingency Analyser to check for new violations.
- Check the database for violations generated by the Contingency Analyser after applying the selected control action.
- If there are no more violations, end the inference process. Otherwise do the first stage of the inference process again to select the most serious violation from the new list of violations and form a new list of recommended control actions.

After finishing the second stage of the inference process, the inference engine builds a list of control actions that have been simulated. The system operator can view this so that they have a complete record of the control actions that have been used.

The first and second stages of the inference process are repeated until either no violations occur or the system operator chooses to stop simulations.

4.5 User Interface

The screen dialogs shown in figures 5 to 8 show the graphical user interfaces that are presented to the system operators. Figure 5 shows the main screen interface that is shown to the system operator in off-line mode. This screen allows the system operator to view a list of contingency cases simulated by the Contingency Analyser and to select an emergency scenario to view the violations that would occur. When the system operator clicks on the "Advice..." button, the advice screen is displayed as shown in Figure 6, allowing the system operator to view advice on how to remove a violation for the selected contingency case. If the system operator wishes to view more information about a recommended control action, the system operator can select a recommended action from the list and click on the "More Information..." button. A dialog then appears as shown in Figure 7 revealing more detailed information about the selected control action.

Once the system operator has selected a recommended control action from the list in Figure 6, they can tell the expert system to simulate the effect of applying that control action by pressing the "Simulate Action" button. The expert system will then perform the simulation and refresh the advice dialog. If the system operator has requested the expert system to perform several control action simulations, a record of the actions previously simulated by the expert system can be displayed by clicking on the "Previously Simulated Actions..." button in the advice dialog. A dialog showing the list of control actions previously simulated by the expert system is then shown as in Figure 8.

5. Case Study

The prototype expert system is to be implemented on IBM personal computers in the Network Operations control centre of Transend Networks Pty Ltd, a Tasmanian company that manages and operates the electricity transmission system for Tasmania. The expert system's performance is tested on a part of the Tasmanian power transmission network, comprising of Sheffield, George Town, Hadspen and Palmerston substations. A diagram of the 220 kV network is shown in Figure 3.

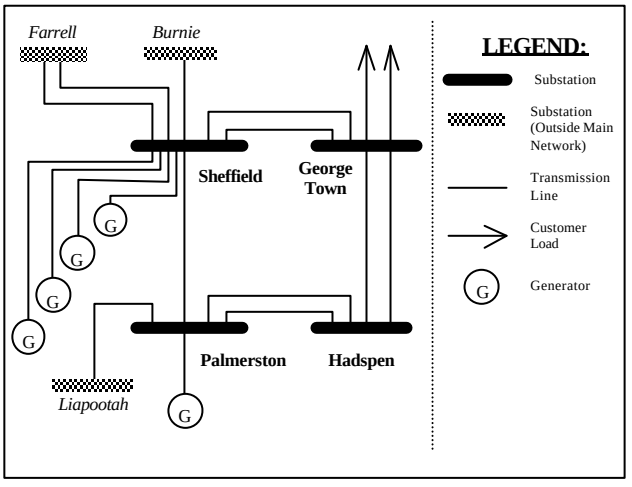

Figure 3. Diagram of the 220 kV network comprising of Sheffield, George Town, Hadspen and Palmerston substations.

The case study examines a contingency of two of the Sheffield-George Town transmission lines (i.e. the lines are disconnected from the rest of the power system). In this study, there is a large amount of power being produced by power stations on the west coast of Tasmania in comparison with the power produced by power stations in the south of the state. A diagram of the emergency situation is shown in Figure 4.

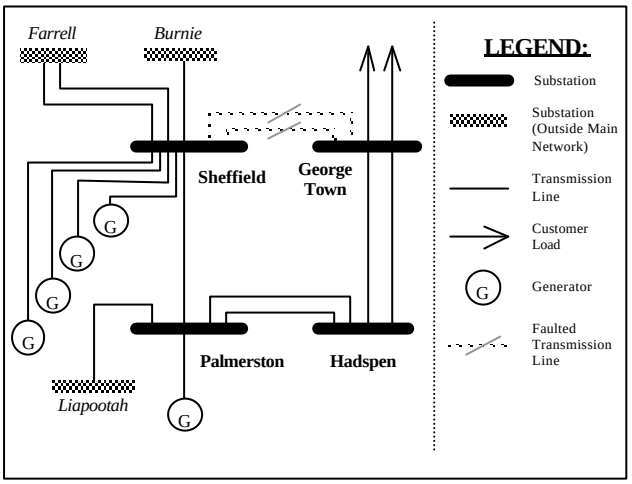

Figure 4. Diagram of 220 kV network when the two transmission lines connecting Sheffield and George Town substations are faulted.

The simulation by the Contingency Analyser found that there was one violation for this emergency scenario, shown in Figure 5. Advice given to the system operator for this scenario produced a list of four recommended actions, all sorted by the percentage expected improvement as shown in Figure 6. After selecting the first recommended action in the advice dialog, a more detailed explanation for increasing the generation at Fisher power station is given in Figure 7, showing how the control action relieves the overloading on the Palmerston-Sheffield transmission line.

After performing four control action simulations to clear all the violations, the dialog displaying the list of the simulated actions and details of their outcomes can be seen in Figure 8.

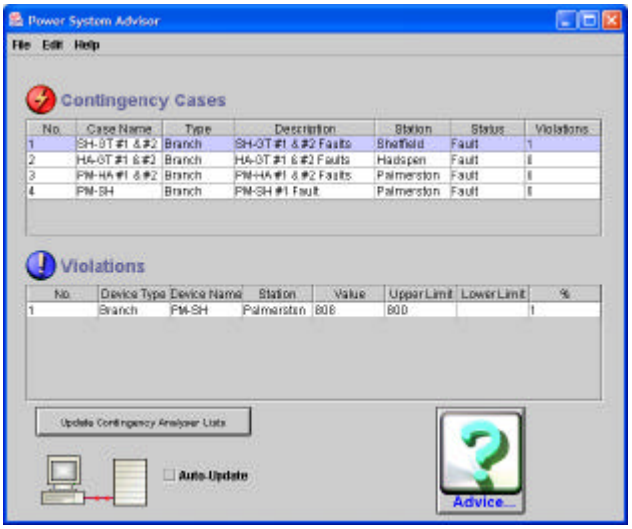

Figure 5. Main screen that displays the simulated contingency cases and violations found by the Contingency Analyser.

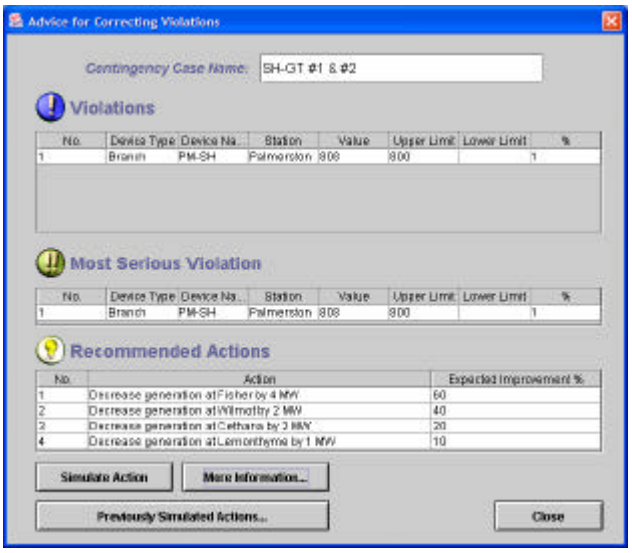

Figure 6. Advice dialog for the violations resulting from the Sheffield-George Town transmission line faults.

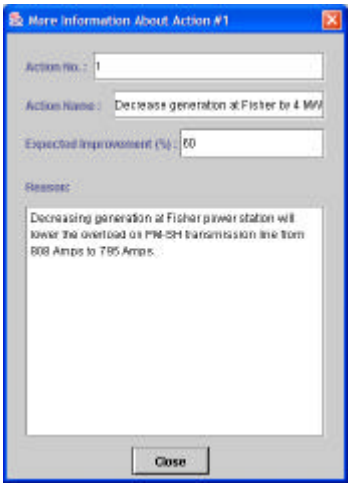

Figure 7. Dialog for explaining the reason for a recommended action.

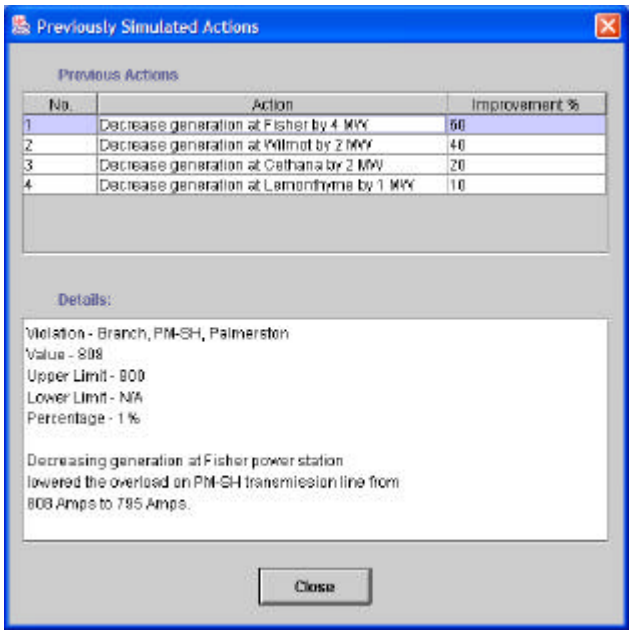

Figure 8. A dialog listing all the control actions previously simulated by the expert system.

6. Conclusion

This paper has demonstrated the development of a Java-based prototype expert system for preventing emergencies in power systems. Feasible solutions were provided to the system operators and simulated in the operations control center of Transend, Tasmania.

Currently, the prototype expert system can operate in off-line mode for simulation purposes only. Further work on the development of the Java-based expert system will include the on-line operation and providing advice to system operators in real-time during actual emergency situations.

7. Acknowledgements

This project was supported by Transend Networks Pty Ltd. Thanks to Richard Power, Mat Hosan, Michael Verrier of Transend Networks. Special thanks goes to Michael Whitehead, Craig Collins, Jan Dittmann and Stewart Sayer for contributing their invaluable knowledge towards the project.

8. References

[1] M. Negnevitsky, *Artificial intelligence : a guide to intelligent systems*. New York: Addison Wesley, 2002.

[2] C. S. Chang, "Application of pattern recognition techniques for online security-economy and reactive control of power systems," *IEE Proceedings - Part C*, vol. 138, no. 1, pp. 1-10, Jan 1991.

[3] M. Negnevitsky, "An Expert System Application for Clearing Overloads," *International Journal of Electrical Power & Energy Systems*, vol. 15, no. 1, pp. 9-13.

[4] I. Hano, Y. Tamura, S. Narita, and K. Matsumoto, "Real time control of system voltage and reactive power," *IEEE Transactions on Power Apparatus and Systems*, vol. Pas-88, no. 10, pp. 1544-1559, Oct. 1969.

Development of a Parameter-Based Control System using Neural-Fuzzy Approach

H.C.W. Lau
Dept. Industrial & Systems Engineering
Hung Hom, Kowloon, Hong Kong
mfhenry@inet.polyu.edu.hk

A. Ning
Dept. Industrial & Systems Engineering
Hung Hom, Kowloon, Hong Kong
mfandrew@inet.polyu.edu.hk

Abstract

The capabilities of the two computational intelligence technologies including neural network and fuzzy logic can be synergized through the formation of an integrated and unified model which capitalizes on the benefits and concurrently offsets the flaws of the involved technologies. In this paper, a neural-fuzzy model, which is characterized by its ability to suggest the appropriate change of process parameters in a relatively complex parameter-based control situation involving multiple parameters, is presented. This model is particularly useful in multiple input and multiple output situations where complex mathematical calculations are required if conventional control approach is adopted. In particular, it serves to acquire knowledge from the information base for extracting rules which are then fuzzified based on fuzzy principle. To validate the feasibility of this approach, a test has been conducted based on the neural-fuzzy model with the objective to achieve heat transfer enhancement in rectangular ducts using transverse ribs. This paper describes the roadmap for the deployment of this hybrid model to enhance machine intelligence of a complex system with the description of a case study to exemplify its underlying principles.

Keywords

Machine Intelligence, Neural Network, Fuzzy Logic, Heat Transfer.

INTRODUCTION

In industrial and engineering applications, parameter-based control systems are normally employed in situations where parameters such as heating temperature, injection pressure and cooling time need to be adjusted to achieve the required outcome of the overall condition. Traditionally, Proportional-Integral-Derivative (PID) control algorithms are adopted to deal with these parameter-based control situations albeit complex mathematical equations need to be used to analyze the operating conditions. However, the mathematical analysis based on relevant algorithms may become more complex when dealing with Multiple-Input Multiple-Output (MIMO) control situations where more than one input is used with more than one output. A typical example of MIMO is the control of flow rate (e.g. gallons/hour) and temperature (e.g. degrees C) of a certain liquid (e.g. water) by adjusting the hot tap and the cold tap of that particular liquid (in this case it is water) for a specific industrial or engineering process. The complexity of this type of control (two inputs and two outputs) is that a slight change of either one of the taps (hot or cold) affects both the temperature and flow rate of the output liquid. The mathematical equations involved in the PID control algorithms of such a MIMO situation are rather complex. By the same token, the level of complexity can be visualized if more than two inputs and two outputs are involved, noticing that this is not uncommon in actual engineering processes and operations. The analysis of MIMO control using PID algorithms can be found in a number of publications (such as Driankov et al [1]) and therefore not to be covered in this paper.

To address this MIMO situation, a model incorporating computational intelligence technologies such as fuzzy logic, neural network and genetic algorithms, can be employed. It is known that a system with the inclusion of the artificial intelligence elements is able to enhance the performance, reliability and robustness of control by incorporating knowledge which cannot be accommodated in the analytic model upon which the design of the control algorithm is based [1]. This paper presents a neural-fuzzy model, which is featured by its ability to recommend the adjustment of process parameters in a MIMO parameter-based control situation involving multiple parameters. This model is particularly useful in situations where complex mathematical calculations are required if conventional control algorithm is adopted. In particular, it serves to acquire knowledge from the information base for extracting rules which are then fuzzified based on fuzzy principle. A case study has been conducted related to the heat transfer situation where multiple parameters, such as rate of radiation and rate of conduction, are involved. Most importantly, this paper outlines the roadmap for the deployment of this hybrid model to deal with complex control situations in various engineering and industrial applications.

THE NEURAL-FUZZY MODEL WITH PRACTICAL EXAMPLE

The neural-fuzzy model proposed in this article is focused on the approach to find the required results without involving too many mathematical calculations. To exemplify the procedures and steps of this non-mathematical approach, a

practical example is employed to illustrate how it can be used to deal with a real life MIMO problem.

Description of the case

An overview of the thermal system under test is shown in Figure 1. The main portion to be discussed in this paper is the "Test Section" of the system, which is further explained in Figure 2.

In the present study, experiments are conducted for six repeated ribs to investigate the overall heat transfer from the tip portion as well as the sides of the ribs. The experimental apparatus was a long rectangular duct of 1.22 m length, with the test section at 50 cm from the inlet. The cross sectional area of the test section was 190(W) x 170(H) cm^2. The test geometry comprised six rectangular aluminum ribs of various cross sections and 190 cm long. A suction fan with variable speed control was connected to the exit of the duct. A 13mm thick aluminum plate was placed on the bottom of the duct and it was heated with an electric heater (input power rating: 1000W). The backside of the heater was insulated with glass wool to minimize the heat losses. Mica and insulation wood were used to insulate the aluminum and electric heater to avoid short circuit. The electric heater was controlled by means of a variable transformer. K-type thermocouples (1-mm diameter) were used to detect the temperature at the top and sides of each rib by inserting them in a small groove along the top surface and the upstream and downstream sides. These thermocouples were connected to a thermocouple scanner for simultaneous temperature measurements. An XYZ table was used to maintain the instruments in the correct position.

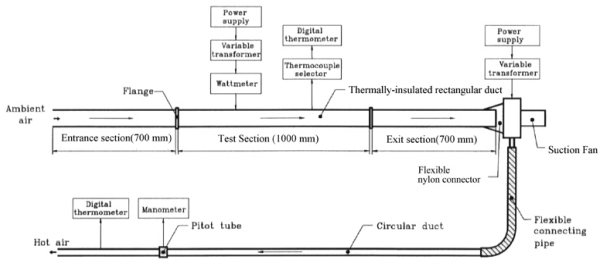

Figure 1. An overview of the thermal system under test showing the heat transfer process within the system of the case.

The geometry of the rectangular duct with transverse ribs of equal spacing is illustrated in Figure 2. The following additional assumptions are also made:

- Laminar flow
- Newtonian and incompressible fluid
- Constant fluid properties
- Steady-state

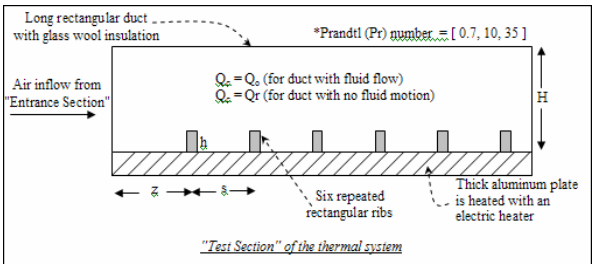

Figure 2. Side view of the long rectangular duct with transverse ribs of equal spacing, showing all the essential parameters for heat transfer study within the "Test Section" of the thermal system.

The air velocity inside the duct was maintained at 9.75 m/s. The average room temperature and pressure were 22 ^oC and 757 mm respectively. Measurements of rib temperature were taken an hour after the commencement of each experiment to allow for stability of readings. It can be seen that for each experimental investigation a new aluminum plate of different rib dimensions and spacing would be required.

A rib zone is defined as the area along the contour of the ribs and inner duct surface between the midpoints on the tips of adjacent ribs. The first rib zone is the area from the inlet of the duct to the midpoint on the tip of the first rib. The last rib zone is the area from the midpoint on the tip of the last rib to the exit of the test section. The values of Q/Qo are relative measures of performance representing the ratio of heat transfer from the inner wall for a rib zone to the heat transfer from the corresponding zone on an unribbed duct. The values for Q/Qr represent the amount of heat conducted from the zonal area to outer wall of an otherwise unribbed duct with no airflow.

The steady-state convection heat transfer, Q, from the rib surfaces to the fluid flow was deduced from the input power (E) as follows:

$$Q_c = E - Q_{rad} - Q_l \qquad (1)$$

Where Q_{rad} = the rate of radiation loss through both ends of the duct to its environment and it can be estimated by means of the following equation i.e.

$$Q_{rad} = \varepsilon\sigma(Tc^4 - Ta^4) \qquad (2)$$

Where ε = emissivity of duct surface

σ = Stefan-Boltzmann constant (W/m^2-°K)

Tc = Average rib side temperature (°K)

Ta = Average air temperature measured upstream of the test section (°K)

And Q_l = the rate of conduction heat loss through the external surface of the rectangular duct assembly to the surroundings and it can be estimated by using the Fourier's Law, i.e.

$$Q_l = kA(Tc - To)/L \quad (3)$$

Where k = thermal conductivity of duct material

A = internal surface area of duct

To = ambient air temperature

L = thickness of duct

Hence in the case of a ribbed duct with fluid flow, $Q_c = Q$; whereas in the case of an unribbed duct, $Q_c = Qo$ (for duct with fluid flow) and $Q_c = Qr$ (for duct with no fluid motion). The Prandtl (Pr) number is a dimensionless quantity depends solely on the physical properties of the fluid, irrespective of flow conditions.

METHODOLOGY FOR DESIGNING A NEURAL-FUZZY MODEL

As depicted in the above context, the two different values (Q/Qo and Q/Qr) are the outputs affected by the four input parameters (Pr, z/H, s/H and h/H). The dimensions of ribs and their spacing (i.e. z/H, s/H and h/H) depend mainly on the magnitude of the overall heat transfer. This is considered to be a parameter-based control situation where complex mathematical analysis is required if conventional control theory is used. The proposed neural-fuzzy model consists of a neural network for acquiring the knowledge between the input and output data, and a fuzzy logic reasoning mechanism for generating a more reliable suggestion for modifying the induced output values from the trained neural network.

A methodology with a step-by-step approach has been developed for those who would like to tackle a MIMO parameter-based control problem using a hybrid neural-fuzzy approach which is able to significantly simplify the tedious analytical work of a conventional PID approach. In particular, this proposed hybrid approach does not require the prior knowledge of the theoretical aspects of neural network and fuzzy logic and therefore is meant to be used by novice users. The following steps provide guidelines for the development of such model.

Step 1 - Determine the input and output parameters of the neural network

The first step of the methodology is to determine the input and output values of the neural network with the purpose to obtain data for training purpose. The two key parameters of heat transfer are Q/Qo and Q/Qr with required performance as shown in Table 1:

Table 1. The two key parameters of the heat transfer model (Q/Qo and Q/Qr)

	Q/Qo	Q/Qr
Experimental heat transfer ratio	1.4698	5.7974
Deviation of heat transfer ratio (%)	0	0

$$Heat\ Transfer\ Performance(\%) = \frac{(Design\ Output - Experimental\ Output) \times 100}{Experimental\ Output}$$

The number "0" for the "Heat Transfer Performance (%)" indicates that the performance are within the tolerance limit or in this example referred as experimental values. Any value more than or less than "0" of "Deviation of heat transfer ratio (%)" indicates that certain degree of dimensional inconsistency has occurred.

In this test, the heat transfer model parameters that may affect the outputs have been identified. The values of parameter that are able to maintain the nominal values of Q/Qo and Q/Qr are specified below.

z/H = 3.75

s/H = 0.50

h/H = 0.10

Pr = 10.00

Obviously, the target is to keep the "Deviation of heat transfer ratio (%)" at "0" for the two values (Q/Qo and Q/Qr). As mentioned before, it is important that the neural network learns the relationship between data sets mapped to the nodes of the input and output layers. To meet this requirement, 108 sets of data were obtained by varying the values of the depicted heat transfer model parameter, which would subsequently affect the dimensional outcome.

Step 2 - Recall the trained neural network due to changed variables

Technically, there should not be any dimensional changes occurred in Q/Qo and Q/Qr if the four parameters remain unchanged. However, as in real industrial environment, there can be many reasons for creating such changes. In this test, it happened that the two dimensions of the heat transfer model changed slightly after a few days of production though the heat transfer model conditions have remained unchanged. It was found that the dimensions have been changed as shown in Table 2:

Table 2. The dimensional deviation of the heat transfer model

	Q/Qo	Q/Qr
Design Heat Transfer Ratio	1.4793	5.7202
Experimental Heat Transfer Ratio	1.4698	5.7974
Heat Transfer Deviation (%)	0.65	-1.33

Neural network recall is the processing of new inputs through a trained network to obtain the outputs based on the correlation acquired during the data training process. The two new "Design Heat Transfer Ratio" data for "Q/Qo" and "Q/Qr" were mapped to the input nodes of the trained network. The network's outputs were as below:

Output node 1 (Pr) = 10.261

Output node 2 (z/H) = 4.137

Output node 3 (s/H) = 0.500

Output node 4 (h/H) = 0.098

The outputs from the trained network as indicated above suggest the deviations of the heat transfer conditions that subsequently cause the dimensional inconsistencies. For example at output node 1 (Pr), the output value is 10.261. This means that the deviation of the 'Pr' partly contributes to the dimensional deviations of the heat transfer model.

Step 3 - Determine fuzzy sets representation for output variables

The third step is to determine the fuzzy sets for the output variables [2, 3]. At this stage, the input and output data are all in crisp value (exact numeric values) and it is necessary that the data should be fuzzified prior to the fuzzy inference process. Figure 3 shows the fuzzification of the two key dimensions. The membership functions for dimension Q/Qo and Q/Qr, taking the higher values, are 0.87 and 0.74 respectively. The product of two membership function values is 0.64 (0.87 * 0.74) which will be used for the fuzzy inference with the output fuzzy set [4, 5]. In Figure 3, the fuzzy sets are represented by S (small), RS (relatively small), N (normal), RL (relatively large) and L (large). The detail about this fuzzification technique can be found in relevant publications and not to be covered here.

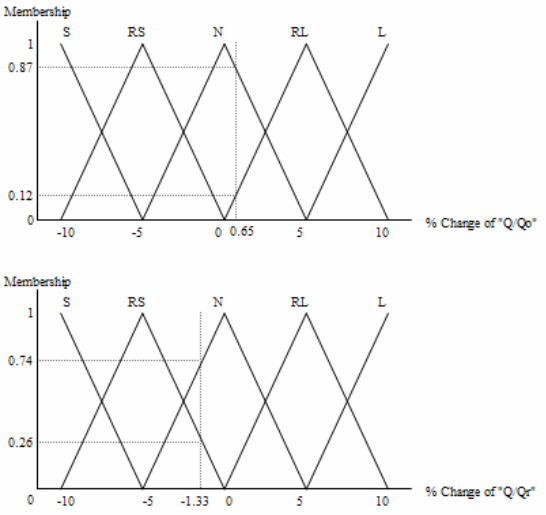

Figure 3. The fuzzification of dimensions Q/Qo and Q/Qr, where the fuzzy sets are represented by S (small), RS (relatively small), N (normal), RL (relatively large) and L (large).

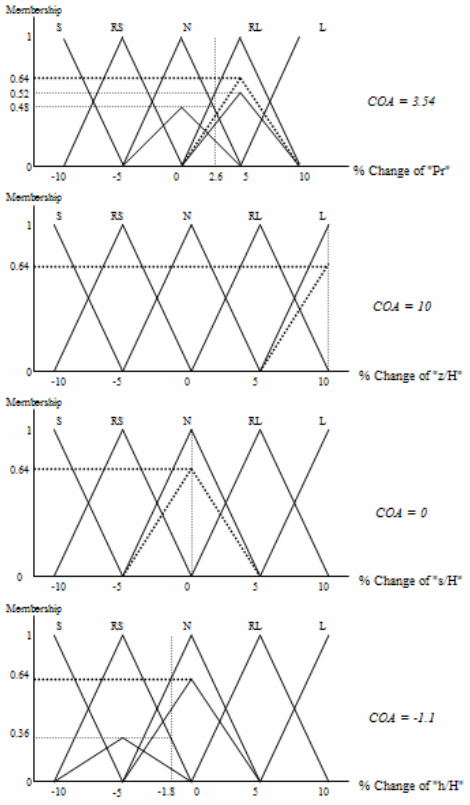

Figure 4. The COA defuzzification of process model parameters.

Step 4 - Specify the setting of fuzzy rules

The fourth step is to set up the fuzzy rules that are to be used by the rule (inference) engine to provide the desired answer. The fuzzy rules are set based on experience from field experts, experimental results and theoretical derivation. Unlike conventional expert systems, fuzzy rules allow the use of imprecise, uncertain and ambiguous terms. In this practical example, the parameter values of the output nodes need to be fuzzified as well. As shown in Figure 4, the output fuzzy sets are represented by S (small), RS (relatively small), N (normal), RL (relatively large), L (large). Using the output node 4 (h/H), the output value is 0.0098, which is -1.8% of the nominal value 0.1. As shown in Figure 3, it cuts N at 0.64 and RS at 0.36. Based on this result, the fuzzy rule can be specified as:

If dimension Q/Qo is relative small (RS) and dimension Q/Qr is normal (N)

Then adjust the h/H to a higher value as it is relative small now.

Step 5 - Determine fuzzy rules for firing and defuzzification process

The fifth step is to determine the rules to be fired based on the given conditions, then obtain the results using the graphical techniques, and defuzzify the results from the inference process. Since the outcome of the fuzzy inference process is likely to be another fuzzy set, it is essential that only a single discrete action is applied and so a single point that reflects the best value of the set needs to be specified eventually.

Based on Figure 4, the Max-dot reasoning strategy and COA defuzzification using triangles with membership function values 0.64, 0.64 and 0.36 evaluated that the value of h/H is -1.1 (%) lower that the nominal value or is 0.001 lower and should be adjusted. As the actual h/H was 0.1, it should be adjusted to 0.099 (0.098 + 0.001). The same technique is also applied to the other 3 parameters.

The second parameter is at output node 3 (s/H) with the value of 0 which is 0 (%) of the nominal value 0.5. Referring to the diagram shown in Figure 4, the value of s/H is 0 (%) or the same as the nominal value. As the actual s/H was 0.5, there should be no adjustment required.

The third parameter is at output node 2 (z/H) with the value 4.137 which is 10.3 (%) of the nominal value 3.75. The same approach will be repeated as the Pr. Referring to the diagram shown in Figure 4, the value of z/H is 10 (%) or 0.41 higher that the nominal value and should be adjusted back to normal. As the actual z/H was 3.75, it should be adjusted to 3.72 (4.13 - 0.41).

The fourth parameter is at output node 1 (Pr) with the value of 10.261 which is 2.6 (%) of the nominal value 10. Referring to the diagram shown in Figure 4, the value of Pr is 3.54 (%) or 0.36 higher than the nominal value. As a result the recommended adjustment is 9.90 (10.26 - 0.36).

Table 3. The comparison of test results after each iteration

	Heat Transfer Deviation of "Q/Qo" (%)	Heat Transfer Deviation of "Q/Qr" (%)	Root Mean Square (RMS) value
Original deviation	0.65	-1.33	0.11
1st iteration result	0.22	-0.59	0.07
2nd iteration result	0.13	-0.23	0.04
3rd iteration result	0.10	-0.18	0.03

The parameters of the heat transfer model were adjusted in accordance with these new parameter values evaluated based on the neural-fuzzy model. The subsequent dimensional outcome was obtained with obvious sign of improvement. The process was repeated twice to find the trend of dimensional performance through iteration of the heat transfer model. The test results are shown in the Table 3 with the root mean square errors calculated to compare the results after each iteration. And according to Table 3, it can be observed that the dimensional output has achieved significant improvement after each iteration, from the first root mean square error of 0.11 to 0.03 after third iteration.

HOW THE NEURAL-FUZZY MODEL WORKS

Neural network

The responsibility of the neural network model element is to provide the desire change of parameters based on what the network has been trained on. Intrinsically, a sufficient amount of data sample is a key factor in order to obtain accurate feedback from the trained network. In actual situations, recommended action about the required change of parameters to cope with the dimensional inconsistency is essential. In view of this situation, neural network can be regarded as a better option, if the dimensional values are mapped to the nodes of the input layer and heat transfer parameters are mapped to the output layer nodes, thus resulting in a control model that is the reverse of the heat transfer model. In the light of the fact that in an actual thermal system design, the required overall heat transfer is first determined from the system analysis. Then the rib geometry is chosen according to the nearest overall heat transfer performance determined from experimental investigations. Very often the difference between the designed overall heat

transfer and the experimental performance data can be quite significant.

With a neural network, the correlation between the deviations of heat transfer parameters in response to the deviations of the occurring dimensional values can be trained based on a wide spectrum of actual sample data. As neural network is intended to learn relationships between data sets by simply having sample data represented to their input and output layers [6], the training of a network with input and output layers mapped to dimensional deviation values and heat transfer deviation values respectively with the purpose to develop the correlation between these two groups of data will not contradict the basic principle of neural network.

With a trained network available, it is possible that recommended action about the change of parameters can be obtained with the purpose to optimize the design of rib geometry, should that occur at a later stage. Therefore, in the training process of the neural network, the nodes of the input layer of the neural network represent the deviation of the dimensional values and those of the output layer represent the deviation of the heat transfer parameters.

Fuzzy logic reasoning

If there is dimensional inconsistency on the heat transfer model, the values at the nodes from the neural network (representing the parameter deviations) may provide some hints for possible dimensional correction. With the availability of this information, a fuzzy logic approach can then be employed to provide a modified set of recommended parameter change based on the original output values from the neural network. The motive for using fuzzy logic reasoning in this model is to take advantage of its ability to deal with imprecision terms which fit ideally in the parameter-based control situations where terms such as "rib spacing could be increased slightly" are used. Furthermore, the vagueness and uncertainty of human expressions is well modeled in the fuzzy sets, and a pseudo-verbal representation, similar to an expert's formulation, can be achieved.

During fuzzy reasoning process, the input and output values of the neural network are generally fuzzified into linguistic terms so that fuzzy rules can be developed. The method of obtaining the corresponding output membership values from the "fired" fuzzy rule is called fuzzy logic reasoning. Many reasoning strategies have been developed, including Sup-bounded-product, Super-drastic-product, Sup-min and Sup-product [4]. Since it is not the intention of this paper to present a review of fuzzy logic reasoning strategies, the mentioned reasoning strategies are not further explained in this paper. In this paper, the Sup-product strategy is adopted due to its simplicity and relatively less calculation time.

After the fuzzification process with the generation of fuzzy rules, it is necessary to have a defuzzification process. The defuzzification process is a process of mapping from a space of inferred fuzzy control results to a space of non-fuzzy control action in a crisp form. In fact, a defuzzification strategy is aimed at generating a non-fuzzy control action that best represents the possibility distribution of the inferred fuzzy control results. The Mean of Maximum (MOM) and Centre of Area (COA) are two common defuzzification methods in fuzzy control systems, and the latter method is selected in this neural-fuzzy model to defuzzify the reasoned fuzzy output (the parameters value). Proposed parameter change is carried out and the dimensional outcome, resulting from the change is checked against the expected dimension.

Conclusion

This paper introduces a neural-fuzzy model for solving MIMO parameter-based control situation supplemented with a case example related to thermal system design in order to demonstrate the feasibility of this approach. The benefits of using two computational intelligence techniques including neural network and fuzzy logic reasoning to form an integrated model for handling heat transfer parameters are demonstrated. The test of this model indicates that it improves significantly the heat transfer situations although the results can be yet considered as perfect. Further research on the structural configuration of the model is needed in order to further enhance its benefits. In general, this model serves to enhance the progressive introduction of machine intelligence to the whole control system and provides a platform for further research in terms of intelligent control of heat transfer processes.

ACKNOWLEDGMENTS

The authors wish to thank the Research Committee of the Hong Kong Polytechnic University for the financial support of the project.

REFERENCES

[1] Driankov D, Hellendoorn H, Reinfrank M. An Introduction to Fuzzy Control. Springer, 149-163 (1996).

[2] Giarratano JC, Riley GD. Expert Systems: Principles and Programming. International Thompson Publishing (1993).

[3] Orchard RA. FuzzyCLIPS Version 6.02A User's Guide. National Research Council, Canada (1994).

[4] Mizumoto M. Fuzzy controls by product-sum-gravity method. In Advancement of fuzzy theory and systems in China and Japan, Proceeding of Sino-Japan Joint Meeting on Fuzzy Sets and Systems Oct. 15-18, Beijing, China, International Academic; 1-4 (1990).

Scenario Planning Using Fuzzy Cognitive Maps

Sebastian W. Khor
School of Information Technology
Murdoch University, Perth, Australia
s.khor@murdoch.edu.au

M. Shamim Khan
School of Information Technology
Murdoch University, Perth, Australia
s.khan@murdoch.edu.au

Abstract

A fuzzy cognitive map (FCM) is a directed graph representing concepts and their causal relationships in a given scenario. Application of FCMs as a simulation tool in scenario planning can aid in the visualisation and evaluation of possible scenarios in a problem domain.

Evaluation of a scenario is facilitated through the analysis of state changes that the factors undergo in the corresponding FCM at each time step. Its ability to learn from past experience enables an FCM to discover any missing causal links between factors in the scenario.

Keywords

Fuzzy cognitive map, scenario planning, strategic planning, scenario building system.

I. Introduction

The fuzzy cognitive map (FCM) was introduced by Kosko for modelling the causal relationship between concepts and analysing inference patterns [1]. An FCM is a directed graph representing concepts and their causal relationships in a given scenario. It has been used for decision-support and causal discovery in an environment of uncertainty and incomplete information, and for making predictions in different spheres of human life such as economy, politics sociology, and virtual reality simulation [2-4]. It has been also proposed as an alternative to knowledge-based expert systems for representing and analysing complex systems [5-7]. The attractiveness of the FCM lies in its relatively simple structure and operations, ease of implementation, and its adaptability in incorporating additional knowledge through Hebbian learning or merging with other FCMs. With the recent increase in global uncertainty, and turbulence in the business world, scenario simulations have become an important tool for identifying goals as well as threats, and for formulating counter measures. .

This paper proposes a methodology for effective scenario planning incorporating the use of FCMs for simulating and evaluating alternative scenarios. We explore how the likelihood of certain events as perceived by individual strategists (scenario planners) can be adopted for the whole organisation by augmenting and combining these individual strategies.

2. Scenario planning

Scenario planning has a proven track record in tapping the knowledge of a group of people with diverse perspectives to provide breakthrough insights and innovations. As a methodology, it has long been used by the military. Many people have ideas about where the future may be heading, but there is generally no established process for gathering such knowledge and putting it to good use. Scenario planning provides a concrete framework for sharing the insights of a broad cross-section of people in a way that often leads to fresh, new insights. The concrete outcome from scenario planning is a set of plausible future scenarios that can be used to evaluate opportunities and directions. With the identification of key external metrics, monitoring for early warning signs of changes is possible.

In a volatile situation, the future is often highly unpredictable and we are working from a limited range of expectations, our expectations will frequently be proved wrong. Scenario planning offers a framework for developing more resilient ecological policies to counter such situations where there is uncontrollable, irreducible uncertainty.

Scenario planning is especially useful in situations where, a high level of participation is required to create a common goal, such as in highly modernised military command and control structure where a large number of personnel are required to make collective strategic decisions, and in the competitive commercial world. It provides a useful process for pulling together all the major stakeholders in a strategic conversation that ultimately leads to shared vision and action. It is also extensively used in business organisations.

Herman Kahn [8] was an early founder of scenario-based planning in his work related to the possible scenarios associated with thermonuclear war. Interested readers are referred to books such as [9, 10] for further information on scenario planning.

2.1. Drawbacks of conventional scenario planning

Despite its merits and significance, little advance has been made in scenario planning. The following three significant facts may be observed:

- Most scenario planning practices lack time variant component, which is essential for yielding a more realistic scenario.
- Scenario planning is a time-consuming process. With world events spinning faster than ever before [11], the conventional scenario planning practice is lagging behind.
- Strategists rely heavily on the skills of the individuals to visualise how the different and often complex scenarios unfold. It is hard to imagine the inter-plays of the different factors at different time periods in the scenario.

The conventional scenario planning process relies very much on 'paper and pencil' to draft out the various scenarios. It is therefore very hard to visualise multiple time scales in the scenario models. However, such a time-variant capability is essential in decision-making because of fast changing, turbulent environments in recent times. Within the short time frames, the competitor's strategic activity may have changed.

Fuzzy cognitive map (FCM) simulation can intrinsically accommodate the time constraint. Instead of a static snap-shot of a time step, we are able to view the scenario over the entire time span as well as at any particular time step.

FCM aids the individual strategists in visualisation as the scenario unfolds and the states at each time step can be assessed and evaluated.

2.2. Scenario building procedure

We propose the following procedures for developing the scenario planning strategy:

1. Determine the time frame for the scenarios. This largely depends on the rate of change of all factors, past volatility, and uncertainty the organization faces, and the time required to develop new technology etc to counter the influences. Define the missions and purposes of the scenario plan.
2. Each scenario planner or group of planners, uncover the decisions to be made in the future that will affect the entity (the nation or organisation), using the missions and purposes of the scenario planning as a guide. That is, set the boundaries within which the organisation must act.
3. Identify the uncontrollable environmental variables and the unpredictable external forces that will influence the decision-making processes. The uncontrollable variables are the important trends and events that are certain to happen in the future. In other words, what one already knows – e.g. increase in insurance premium, faster computers, union strikes, etc. The external forces are those that are very unpredictable or uncertain. In other words, the unknown – e.g. how will global economy change in the next 10 years, the uncertainty of organic verses GM produce, etc.
4. Select two most important driving forces that are either uncontrollable or uncertain. Formulate three or four best plausible scenarios. Given that the impossibility of knowing precisely how the future will play out, a good decision or strategy to adopt is one such that each of these scenarios diverges markedly from one another. A scenario matrix similar to Table 1 may be used. For example, we may have outcomes A1 and B1 to be of more expected (normal) types whereas outcomes A2 and B2 are of the extreme types. Scenario 1 then is one with the presence of possible future outcomes A1 and B1; Scenario 2 is the presence of A2 and B1; and so on. The scenario or scenarios that are not plausible are dropped. If necessary, the selection process may have to be revised.

Table 1: Scenario matrix

			Uncontrollability / Uncertainty: Low	Uncontrollability / Uncertainty: High
			Variable A: Outcome A1	Variable A: Outcome A2
Uncontrollability / Uncertainty: Low	Variable B	Outcome B1	Scenario 1	Scenario 2
Uncontrollability / Uncertainty: High	Variable B	Outcome B2	Scenario 3	Scenario 4

5. Express each scenario as an FCM, where each driving force or factor is represented by a node, and each relationship between a pair of nodes is represented by an edge. This is further described in the next section.

6. Evaluate and review each scenario, using FCM simulation. Observe how the driving forces unfold over time. Identify the critical points along the path to determine under what conditions and how it unfolds. These critical points form the foundation for monitoring purposes.
7. Assess internal consistency and plausibility of each scenario.
8. Repeat steps 4 to 7 with other uncertainties and variables until all possible scenarios have been assessed.
9. Where scenarios are similar or that may be considered together, merge the FCMs.
10. Formulate strategies to counter the adversities in each scenario and encourage favourable conditions.
11. Monitor the real situation unfolding, recognise the scenario, and take necessary actions. If necessary, go back to beginning to restart the scenario planning process.

Steps 5, 6, and 9 are further described in Section 3.

Fig. 1 shows a schematic diagram of the proposed system.

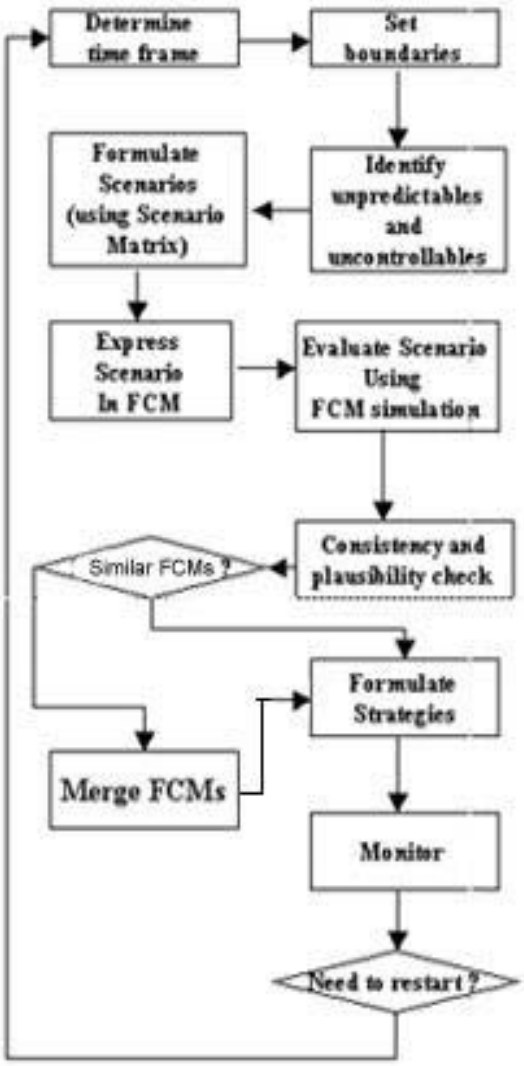

Figure 1: Proposed scenario planning system

3. Fuzzy Cognitive Map

In the scenario planning steps, there are a lot of "what if" questions being asked. A Fuzzy cognitive map (FCM) can play an important role in this respect. FCM can cope with uncertainties. Each factor in a scenario can be viewed as a concept and its effects on other concepts are the edges. Concepts can be abstract or real objects. Merging of similar scenarios can be accomplished by merging of the FCMs. These are explained in sub-sections 3.2 and 3.3 below.

A cognitive map [12] (CM) was originally used to represent knowledge in political and social sciences. It is well known for its simplicity in representing cause-effect relationships among elements in an interactive environment. It is a directed digraph with nodes representing the concepts or perceptions of the given environment and directed links or edges representing the causal relations between these nodes. FCMs were introduced to overcome the shortcomings of CMs which only allow basic symmetric and monotonic causal relations [13]. An FCM allows both the system concepts and relationships to be fuzzy. It is capable of dynamically modelling the world as a collection of concepts and causal relations between these concepts. Consider the case in Figure 2.

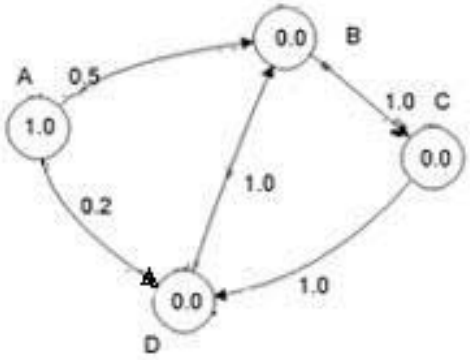

Figure 2: A simple FCM

Each node represents a concept and is linked to one or more other nodes via directed edges. As shown in Figure 2, node A has a positive causal link of strength of 0.5 leading into node B, and another positive causal link of strength of 0.2 to node D. The causal effect on a node (e.g. node D) or its output, is determined by computing the activation of the node due to other nodes influencing it, and then applying a transformation function to this activation. The output of a node C_i is given by the simple neuronal model: -

$$c_i(t+1) = S(\sum_{j=0}^{n-1} c_j(t) \bullet w_{ij}) \quad \text{(1}$$

where $S()$ is the transformation function,
w_{ij} is the weight of the edge from node j to node i.
t is a time step in a simulation model.

Several transformation functions exist and the commonly used ones are the step and the sigmoid functions, as shown in equations 2 and 3 respectively.

$$S(x) = \begin{cases} 0 & if \quad x \le 0 \\ 1 & if \quad x > 0 \end{cases} \quad \text{(2}$$

where x is the activation of a node.

$$S(x) = \frac{1}{1 + e^{-cx}} \quad \text{(3}$$

where x is the activation of a node, and c is a constant which decides the slop of the function.

3.1. FCM simulation

As can be seen in Fig. 2, Node A has a state value of 1, indicating that the node is 'on'. When this happens at the start of a simulation session, the effect is similar to asking the question: *What if concept (or variable) A happens?* Observing a simulation run gives the scenario planner insights into the interactions between the various nodes. The planner may also try out with other nodes or combination of nodes turned 'on'. The results of simulation of the FCM in Fig. 2 after time step 7 are as shown in Table 2. As can be seen, the states of the nodes form a fixed pattern of cyclically turning on the three nodes B, C, and D. With hard-limiting transformation function, different scenarios may have different limit cycles, or a fixed-point attractor [14] (a limit cycle of one). Using continuous transformation function such as the sigmoid function may also give rise to a situation known as chaotic attractor [5]. After reviewing and evaluating the different scenarios, the planners will be in a better position to decide which are the best scenarios for further evaluation.

Table 2: Results after 7 iterations

Time	A	B	C	D
0	1	0	0	0
1	0	1	0	1
2	0	1	1	0
3	0	0	1	1
4	0	1	0	1
5	0	1	1	0
6	0	0	1	1
7	0	1	0	1

3.2. Differential Hebbian Learning

Sometimes the planners may not be able to decide on the degrees of the causal effects of one node on another. In such cases, it is possible to let the FCM learn the causal weights by applying Differential Hebbian Learning (or DHL) [15] using a set of training data, which represents a record of the states of the nodes at a sequence of time steps. At each time step t, the weight value w_{ij} of an edge connecting concept nodes i to j, is given by the discrete version of the HDL:

$$w_{ij}(t+1) = \begin{cases} w_{ij}(t) + \mu_t[\Delta C_i(t) \bullet \Delta C_j(t) - w_{ij}(t)] & if \quad \Delta C_i(t) \neq 0 \\ w_{ij}(t) & if \quad \Delta C_i(t) = 0 \end{cases} \quad \text{(4}$$

where ΔC_i is the change in concept node i, $\Delta C = C_i(t) - C_i(t-1)$.

μ_t is the learning coefficient, which decreases over time, and is given by:

$\mu_1 = 0.1(1\text{-}t(1.1N))$, where t is the number of time steps, and N is a constant.

DHL thus provides a means of aiding the planner in determining the relationships between the nodes, provided the planner can provide the perceived sequence of events. However, DHL is not without problems. One major setback is that it's learning is a linear one, rather than a (biologically realistic) sigmoid learning curve. We are investigating the possibility to improve on this.

3.3. Merging of FCMs

Different scenario planners will come up with different scenarios and strategies. Merging of FCMs provides a simple yet effective means of combining the set of scenarios to give an overall picture of the possible scenario. By combining the FCMs to form a new FCM, which represents the collective experts' opinion on the particular scenario, the new FCM may be considered to have learnt from all the experts.

The FCMs are combined by summing the matrices of the edges of the FCMs [16, 17]. As not all the FCMs are having the same number of concept nodes, the missing concept nodes with default edge weight values of 0s are first appended to the respective FCMs. This is said to have the FCMs augmented to ensure conformity in the subsequent computation process. For example, we have two FCMs to be merged as depicted in Figures 3 and 4.

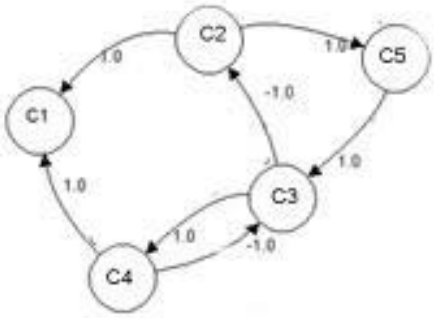

Figure 3: FCM# 1

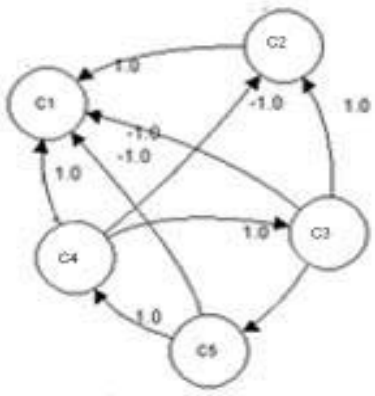

Figure 4: FCM# 2

The new FCM is given by:

$$E = \sum_{0}^{N-1} W_k E_k \quad \text{(5}$$

where E is the newly formed FCM,
E_k is the k^{th} FCM,
W_k is the credibility weighting, assigned to FCM E_k
N is the number of FCMs to be merged.

The weights of the edges of the new FCM is then normalised by dividing the weights by W, where W is the sum of the credibility weightings, i.e. $W = W_1 + W_2 \ldots + W_k$. It is possible that different planners may be given different credibility weighting to their FCMs [18]. That is, some planners' views are more credible than others.

The new augmented FCM is shown in Fig. 5.

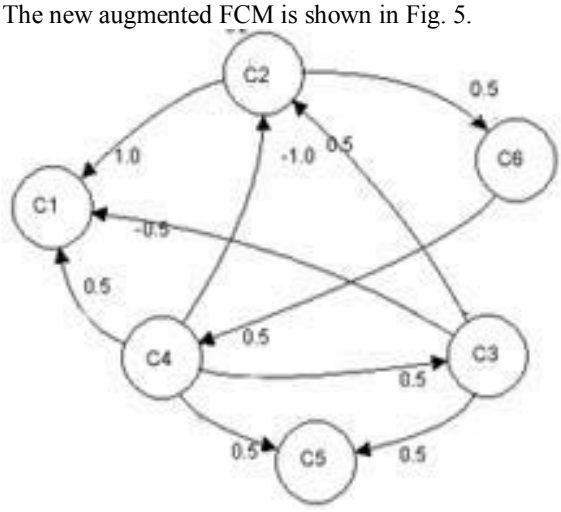

Figure 5: New augmented FCM

4. Conclusion

The Fuzzy Cognitive Map (FCM) has emerged as a powerful tool for modelling and simulation of events that are uncertain or uncontrollable. We have explored and shown how it is possible to use FCM to aid in the scenario planning process.

A system for scenario planning has been presented, with a demonstration of how FCMs can provide the essential visual aids often neglected in the past. By observing the states of each factor in an FCM at each time step, we have shown that it is possible to detect those factors that play an important role in the scenario. It is therefore possible to monitor these factors closely as the actual event unfolds.

FCMs can also be used to aid the scenario planners to discover missing causal links. However, Differential Hebbian Learning algorithm used in the FCM only provides an approximation of the causal links. We are currently investigating means of improving the algorithm.

REFERENCES

[1] B. Kosko, "Fuzzy Cognitive Maps," Int. Journal of Man-Machine Studies, vol. 24, pp. 65-75, 1986.

[2] C. D. Stylios and P. P. Groumpos, "Fuzzy cognitive map in modeling supervisory control systems," Laboratory for Automation and Robotics, Department of Electrical and Computer Engineering, University of Patras, Patras, Greece.

[3] R. Taber, "Fuzzy cognitive maps model social systems," AI Ex-pert, vol. 9, pp. 18-23, 1994.

[4] M. Parentho, P. Reignier, and J. Tisseau, "Put Fuzzy Cognitive-Maps to Work in Virtual Worlds," presented at 10th IEEE Int. Conf. on Fuzzy Systems (Fuzz-IEEE'01), Melbourne, Australia, 2001.

[5] M. S. Khan, A. Chong, and M. Quaddus, "Fuzzy Cognitive Maps and Intelligent Decision Support – a Review," presented at 2nd Western Australian Workshop on Information Systems Research (WAWISR 1999), Murdoch University, Perth, WA Australia, 1999.

[6] M. S. Khan, M. Quaddus, A. Intrapairot, and A. Chong, "Model-ling data warehouse diffusion using fuzzy cognitive maps - a comparison with the system dynamics approach," presented at 3rd Western Australian Workshop on Information Systems Re-search (WAWISR 2000), Edith Cowan University, 2000.

[7] K. Perusich, "Fuzzy Cognitive Maps for Policy Analysis," presented at International Symposium on Technology and Society (ISTAS'96), Purdue University, 1996.

[8] H. Kahn, On thermonuclear war. U.P: Princeton, 1961.

[9] P. Schwartz, The art of the long view : planning for the future in an uncertain world. New York: Wiley, 1996.

[10] M. Lindgren and H. Bandhold, Scenario planning : the link between NAFIPS-FLINT 2002, North American Fuzzy In-formation Processing Society, New Orleans, LA, 2002.

[14] A. Chong, M. S. Khan, and T. Gedeon, "Differential Hebbian Learning in Fuzzy Cognitive Map: A Methodological View in the Decision Support Perspective," presented at 3rd Australia-Japan Joint Workshop on Intelligent and Evolutionary Systems, Canberra, Australia, 1999.

[15] B. Kosko, "Differential Hebbian Learning," presented at American Institute of Physics Conf.: Neural networks for computing, Snowbird, Utah, 1986.

[16] B. Kosko, Neural Networks and Fuzzy Systems. Englewood Cliffs: Prentice Hall, 1992.

[17] B. Kosko, Neural networks and fuzzy systems : a dynamical systems approach to machine intelligence. New Jersey: Prentice Hall, 1992.

[18] B. Kosko, "Hidden Patterns in Combined and Adaptive Knowledge Networks," International Journal of Approximate Reasoning, vol. 2, pp. 377-393, 1988.

INTELLIGENT IMAGE PROCESSING & COMPUTER VISION II

(This page left blank intentionally)

The Correspondence Framework for Automatic Surface Matching

Birgit M. Planitz and Anthony J. Maeder
Cooperative Research Centre for Satellite Systems
Queensland University of Technology
GPO Box 2434 Brisbane, QLD 4001
{b.planitz, a.maeder}@qut.edu.au

John A. Williams
School of ITEE
University of Queensland
St Lucia, QLD 4072
jwilliams@itee.uq.edu.au

Abstract

Determining correspondence between sensed views of objects or scenes is a widely studied topic in computer vision. This paper examines correspondence, with particular focus on intrinsic rigid surface matching algorithms, where correspondences are generated using intrinsic surface properties. Many existing intrinsic correspondence algorithms use the same general approach to determine correspondences between surfaces. This paper details this general approach and shows how it forms the basis of the general correspondence framework. The framework is introduced as both a conceptual and an actual model that can be applied to a variety of correspondence tasks. Existing techniques are restructured to fit within the framework, and illustrate its generality. A novel algorithm is also constructed, to show how the framework facilitates innovation, that is, the synthesis of new techniques. Algorithms in the framework are tested to verify both generality and innovation. Future directions of the framework extend the potential testbed of the framework to incorporate a number of open computer vision correspondence issues.

1 Introduction

Correspondence is a fundamental task in computer vision, which typically precedes registration or a related task. In registration, correspondences between two or more views are used to compute the transformation parameters required to bring the views into alignment. A related task is stereo matching, where local correspondences between views are computed to determine the disparity between the left and right images of the same scene.

Formally, correspondence is the process of determining matching regions between views. In this paper, views are defined as renditions of objects or scenes, and regions are spatially consistent subsets of a view. An example of a view is a three dimensional (3D) surface, and region may be a small connected neighbourhood located on the surface.

This paper focuses on the problem of rigid 3D surface correspondence. This type of correspondence precedes the process of 3D surface registration. The problem where surfaces of the same object or view are acquired from different, unspecified viewpoints, is considered. The correspondence task is determining the matching surface regions to compute the registration parameters between them.

This paper specifically addresses *intrinsic* surface correspondence. Intrinsic correspondence refers to matching the intrinsic properties of regions between surfaces, rather than considering their spatial (*extrinsic*) differences. Because it relies only on surface properties, intrinsic correspondence is a powerful way of determining coarse matches between surfaces. Extrinsic methods are generally very good at refining the rough initial estimates. Therefore, surface correspondence methods are often intrinsic, followed by an extrinsic component (for examples, see [1, 8, 9]). The primary objective of this paper is to provide a framework for intrinsic correspondence methods, focusing on the rough initial correspondence estimates between views. Many suitable extrinsic methods exist, which can be used to refine the initial estimates (a popular example is [2]).

Determining initial correspondence estimates between surfaces is a challenging problem. This is primarily due to factors such as the unknown spatial relationships and unknown degrees of overlap between the surfaces. Existing correspondence algorithms combat these problems, but often suffer from weaknesses such as computational inefficiency [4], memory usage [8], and application specificity [9]. However, these problems are usually attributed to only one or two sections of the correspondence algorithms.

In this paper, the generalised correspondence framework is presented, which separates the task of intrinsic surface correspondence into five distinct components. By restructuring existing techniques to fit within the framework, it is easier to identify where the strengths and weaknesses of each method lie. The modular structure of the framework also allows for modules of different algorithms to be slotted into

an existing algorithm, to test or improve the algorithm. Finally, new components of algorithms can easily be synthesised and added to the library of components that already exists in the framework structure.

Formally, the primary objectives of the framework are:
Generality: to show that a wide variety of existing algorithms follow the same generic approach; and
Innovation: to synthesise new correspondence methods, using the interchangeable modules of the framework.

The objectives outlined above are addressed in this paper by first examining a general approach taken by existing intrinsic correspondence methods, in Section 2. This approach is then formalised in Section 3, where the correspondence framework is outlined and each stage of the model is explained in detail. This section also addresses the framework's objectives by first restructuring existing algorithms to fit within the framework, and then presenting a new method that combines components of existing algorithms. The coarse registration resulting from testing the restructured and new algorithms are presented in Section 4. Finally, future directions of the framework are discussed in Section 5, and Section 6 concludes the paper with some summary remarks.

2 Background

This section examines a general approach taken by many existing intrinsic rigid surface correspondence methods. First, some terminology, used to understand each algorithm in a common frame of reference, is presented. This is followed by outlining the general approach taken, and finally discussing four distinct algorithms with respect to the approach.

This section and the remainder of the paper focus on pairwise correspondence between surfaces. It is important to remember that the framework provides a guide for computing initial correspondence estimates between views. Once initial correspondence estimates have been determined, multiview methods, such as [11] can be employed to register all the surfaces simultaneously, refining the initial estimates.

2.1 Terminology

Terminology that is used throughout the remainder of the paper is presented in Table 1. These terms have been chosen to consist with common usage elsewhere in image processing, for example [7].

Term	Definition
view	rendition of an object/scene
region	spatially consistent subset of a view
feature	intrinsic attribute of a region
feature representation	functions of accumulated features, that are comparable using distance metrics
anchor	location of a region, feature or feature representation on a view
local match	distance measure used to compare feature representations
group	set of local correspondences
group match	intrinsic metric used to compare group properties between views
global match	extrinsic metric used to evaluate registrations resulting from group mappings

Table 1. Terminology.

2.2 A General Approach for Correspondence

Many existing intrinsic methods compute correspondence using a similar generic approach. In this section, two surfaces X and Y are considered. The aim is to determine the correspondences between X and Y, and compute a rough initial registration between the two surfaces. A general approach followed by a number of intrinsic correspondence methods begins by specifying regions on both surfaces. These regions are computed using either a segmentation algorithm, or by selecting points of interest on the surfaces, and constructing regions around the points. Each region contains at least one anchor, describing its position on its parent view.

The next stage of the general approach is to extract features from each region, and represent the features using functions that are comparable using distance metrics. The local matching from one surface to the next then occurs by matching each representation on X with each representation on Y. The best local matches are then selected and local correspondences are formed by pairing anchors from X and Y that form the best local matches.

The final stage of the general approach is a global match procedure. This procedure generally incorporates a grouping process where sets of local correspondences are grouped and tested. If a group contains anchors on X that contain sufficiently similar properties as the anchors on Y, the group is used to transform the two surfaces into a common coordinate system. The surfaces are final tested using an extrinsic global match. If a number of groups are tested, the one that results in the best registration is selected as the set of correspondences between X and Y. The following section reviews existing methods that follow the general procedure outlined here.

2.3 Existing Intrinsic Methods

Four significantly different algorithms, selected from the intrinsic correspondence literature, are presented in this section. These algorithms represent a wide variety of intrinsic surface correspondence methods. This section shows how

the algorithms relate to the approach discussed in the previous section. Examples of other algorithms that can be seen as following the same general approach are [6] and [12].

The four methods considered here are: spin-image [4], geometric histogram [1], Random Sample Consensus (RANSAC) based Data Aligned Rigidity Constrained Exhaustive Search (DARCES) [4] and intrinsic curve [9] matching. Spin-image [8] and geometric histogram [1] matching are similar techniques. Both methods build regions around interest points and use special 2D histogram feature representations to represent the regions. A set of pruned local correspondences is passed to each global match procedure. The match procedures vary, but both use a grouping and testing process.

The RANSAC-based DARCES method [4] does not extract feature information from regions. It initiates by computing point regions on one surface. The main component of the matching however occurs at the global match level, where collections of point regions on one surface are formed, and the second surface is searched for similar collections.

Intrinsic curve matching [9] extracts curvature information from regions, and then combines regions with similar curvature properties. Feature representations stem from these combined regions, and are matched from surface to surface. The global match procedure again relies on a grouping and testing scheme. This algorithm and the others outlined in this section are restructured to fit within the correspondence framework introduced next.

3 The Correspondence Framework

The correspondence framework is both a conceptual and an actual model that generalises the approach used by intrinsic surface correspondence outlined in the previous section. This section presents and details the five stages of the correspondence framework. It then re-casts four algorithms discussed in the previous section, to fit within the framework. A new algorithm is also presented, demonstrating how the framework facilitates the development of new correspondence methods.

3.1 A Model for Intrinsic Correspondence Computation

The correspondence framework consists of five stages: Region Definition, Feature Extraction, Feature Representation, Local Matching and Global Matching. Figure 1 illustrates the progression of a correspondence computation through these stages.

The function of each respective stage is:
Region Definition: The process of defining geometrically constrained regions on a surface. An example is constructing regions using neighbourhood information around anchors on surfaces [9].

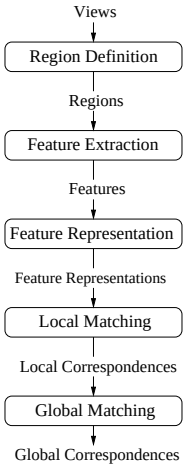

Figure 1. The correspondence framework.

Feature Extraction: The process of extracting geometric features inherent to each region. An example is extracting vertical and horizontal distances from the anchor to all surface points in the region [8].
Feature Representation: The process of representing the extracted features as functions that are comparable using distance metrics. An example is constructing special 2D histograms [1, 8].
Local Matching: The process of matching feature representations and culling bad matches. An example is comparing the Euclidean distance between intrinsic curvature signatures, and only accepting those signatures whose distance in difference fall below a preset threshold [9].
Global Matching: The process of grouping local correspondences, matching groups, and evaluating registrations derived from group anchors. An example is the RANSAC-based DARCES algorithm. This algorithm groups triplets of local match anchors based on the intrinsic distances between them. Registrations are applied to align the triplet pairs of the two surfaces. Finally, the registrations are evaluated by determining the number of closest points between the first surface and the registered second surface [4].

The following section examines the framework with respect to existing intrinsic methods.

3.2 Restructuring Existing Algorithms to Fit Within the Framework

The four algorithms outlined in Section 2.3 are revisited in this section. They are each modularised to fit within the correspondence framework. This modularisation demonstrates generality, implying that the framework is suitable for many intrinsic surface correspondence methods.

Figure 2 describes each stage of each algorithm. When modularised, the advantages and disadvantages of each algorithm outlined in Figure 2 are easier to identify. These are discussed below.

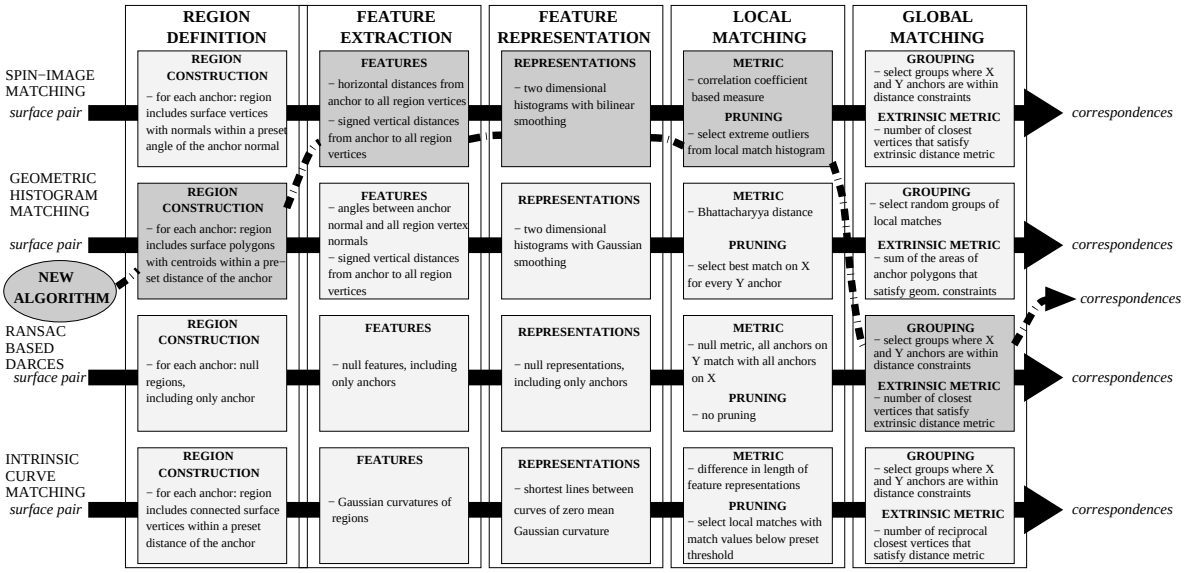

Figure 2. Existing intrinsic correspondence algorithms restructured to fit within the framework. The steps combined to construct the new correspondence algorithm are traced with the dotted line.

Spin-image matching [8] is a powerful algorithm using informative surface representations. It does however use large regions, which increase the storage space required to run the algorithm. The registration evaluation segment of the global matching process is also relatively slow, because it applies an iterative update scheme to each successful alignment.

Geometric histogram matching [1] uses smaller regions than spin-image matching, reducing the storage space required for the algorithm. The features extracted however, require that input surfaces are smooth, in order to retrieve accurate angle-between-normals data. The feature representations are 2D histograms, as in spin-image matching. The global match process selects random groups and tests their geometric consistency. This often requires a number of repetitions of the global match process, to achieve correct correspondences between two surfaces.

The computational effort in the RANSAC-based DARCES method [4] is reserved for the global match selection. The process relies on the random selection of the first point in each group, to build groups. Many iterations are required to achieve correct correspondence between the two surfaces. This process would operate much faster if fewer local correspondences were supplied to the algorithm.

Intrinsic curve matching [9] is relatively efficient. However, the feature representations are constructed from curves of zero mean Gaussian curvature. Surfaces without the curvature changes required to form the zero mean curvature curves, result in too few surface representations to achieve useful local and global matches.

3.3 Synthesising a New Algorithm

In the previous section, existing algorithms were decomposed into stages, to assist in the analysis of the algorithms. The best stages of each of these algorithms are now combined, to construct a new intrinsic correspondence method. The algorithm primarily combines the descriptive power of spin-image matching with the RANSAC-based DARCES global matching process. The steps used to construct the new algorithm are highlighted using the dotted and shaded path in Figure 2. Note that the local match path in Figure 2 does not show that both the spin-image matching and intrinsic curve matching pruning modules are combined to form the local match component of the new algorithm.

The new algorithm selects regions using the geometric histogram matching region selection process. This process ensures that regions are sufficiently large, but do not require as much storage space as spin-image regions. The feature extraction, feature representation and local match modules are all taken from the spin-image matching algorithm. As mentioned, spin-images generate powerful surface descriptions. The pruning section of the local correspondence algorithm uses the intrinsic curve pruning method, which reduces the number of best local matches passed to the global match module. The global match module then runs the RANSAC-based DARCES algorithm, which increases in speed dramatically, when using fewer local matches to achieve global correspondence.

The algorithm is presented below, with the sections incorporated from the four algorithms outlined labeled appropriately.

Region Definition: *geometric histogram matching*
regions defined by constricting the distance between the anchor and surrounding points
Feature Extraction: *spin-image matching*
features extracted are horizontal and signed vertical distances from anchor to surrounding region points
Feature Representation: *spin-image matching*
features are represented using 2D histograms
Local Matching: *spin-image matching*
representations are matched using a correlation-based coefficient
intrinsic curve matching
local matches with match values below a preset threshold are returned
Global Matching: *RANSAC-based DARCES*
groups are selected where the anchors on each surface fit the same distance constraints, and an extrinsic distance based measure is used to evaluate the registrations resulting from matched groups

The correspondence results achieved when using the modularised algorithms, including the new algorithm, are presented in the following section.

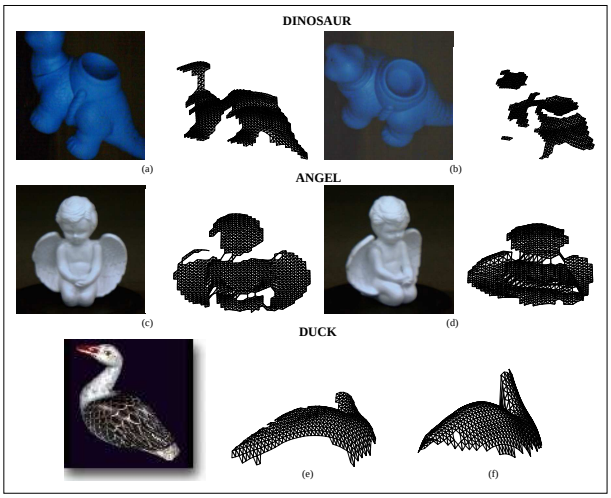

Figure 3. Surface pairs selected for testing: Dinosaur viewed at (a) 0 and (b) 36 degrees rotation, Angel viewed at (c) 0 and (d) 40 degrees rotation, and Duck viewed at two unspecified rotations (e) and (f).

4 Results

Each of the algorithms outlined in the previous section was tested using three test surface pairs. The test data are Dinosaur and Angel surface pairs [3], and a Duck surface pair [10]. The test surfaces and their corresponding 2D images are shown in Figure 3. The test surfaces are low resolution surfaces, averaging approximately 1000 vertices per surface.

The algorithms outlined in the previous section were tested, and each returned the best correspondences achieved between each surface pair. These correspondences were subsequently used to align each pair in the same coordinate frame. These registrations are shown in Figure 4. Each registration is a rough initial alignment, which is all that is required of an intrinsic method.

Figure 4 shows that spin-image matching results in correctly aligned surfaces for all three pairs. It must be reiterated however, that this technique is inefficient in terms of storage, as large regions are used to create the spin-images. The geometric histogram also resulted in correct alignments for the Dinosaur and Angel surface pairs. A slight misalignment of the Duck surface pair occurred, possibly due to insufficient information extracted, to clearly distinguish between corresponding regions. The intrinsic curve matching algorithm correctly aligned the Angel pair, slight misaligned the Dinosaur pair, and failed to correctly register the Duck pair. These results were expected, because the algorithm retrieves a greater number of intrinsic curves for surfaces with more curvature variation. The Angel surfaces produced more intrinsic curves then the Dinosaur or the Duck surfaces. The RANSAC-based DARCES correspondences correctly aligned all three surfaces. It did however, take longer to run then the other three algorithms.
The results of novel algorithm described in the previous section, are illustrated in the fifth row of Figure 4. All three surface pairs aligned correctly. The modules taken from the existing algorithms, which were combined to construct the new algorithm, performed as follows. The geometric histogram matching region selection module greatly reduced storage space required. The spin-image feature extraction, feature representation and local match modules applied the power of spin-image matching to the algorithm. The local match module also used the intrinsic curve matching culling process to reduce the number of local matches. Finally, the RANSAC-based DARCES global match module proved successful again, but ran much faster, as the number of local matches were supplied to it was greatly reduced.

The results in this section show that existing intrinsic algorithms perform as originally intended when re-cast in the proposed correspondence framework. They produce accurate results, and are easily combined to construct new algorithms. The new algorithm outlined shows how the framework facilitates the development of new and improved correspondence techniques.

5 Future Work

This paper focused on the correspondence framework for the purpose of rigid 3D surface correspondence. However, the correspondence framework is not limited to this domain.

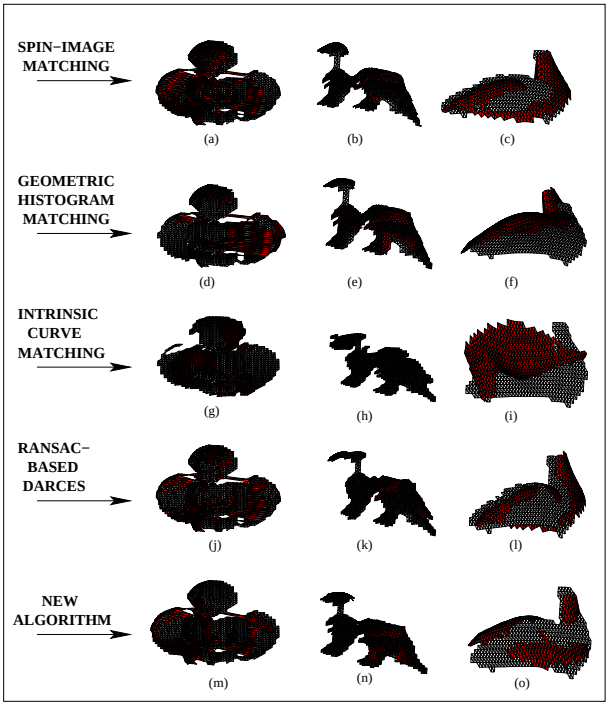

Figure 4. Registrations resulting from the best correspondences for the Angel (a,d,g,j,m), Dinosaur (b,e,h,k,n), and Duck surface pairs (c,f,i,l,o) using the algorithms indicated.

Correspondence algorithms for applications such as 2D image mosaicing can also be restructured to fit the framework.

A simple image mosaic algorithm has been implemented that first determines pairwise correspondence between images, before merging the set of images into a mosaic. Future work includes examining other domains, such as stereo matching, where the correspondence framework is applicable.

6 Conclusion

A correspondence framework was introduced in this paper, to provide a generic model for automatic surface correspondence. The framework was developed by examining the general approach to correspondence establishment, followed by many existing intrinsic rigid surface methods. The restructuring of algorithms, which were selected from a broad class of methods, to fit within the framework, demonstrated generality. Each algorithm produced correspondences that were the expected results for the method in question. A new algorithm was also developed and tested, showing how the framework facilitates the synthesis of new and improved correspondence methods. Finally, the expansion of the framework testbed was discussed, highlighting the framework's applicability to other open computer vision correspondence problems.

ACKNOWLEDGMENT: The Cooperative Research Centre for Satellite Systems is established and supported under the Australian Government's Cooperative Research Centres Program.

References

[1] A. Ashbrook, R. Fisher, C. Robertson, and N. Werghi. Finding surface correspondence for object recognition and registration using pairwise geometric histograms. In *Proc. European Conference on Computer Vision (ECCV98)*, pages 674–686, 1998.

[2] P. J. Besl and N. D. McKay. A method of registration of 3-D shapes. *IEEE Trans. on Pattern Analysis and Machine Intelligence*, 14(2):239–256, Feb. 1992.

[3] R. Campbell and P. Flynn. A WWW-accessible 3D image and model database for computer vision research. In K. Bowyer and P. Phillips, editors, *Empirical Evaluation Methods in Computer Vision*, pages 148–154. IEEE Computer Society Press, 1998.

[4] C. Chen and Y. Hung. RANSAC-Based DARCES: A new approach to fast automatic registration of partially overlapping range images. *IEEE Trans. on Pattern Analysis and Machine Intelligence*, 21(11):1229–1234, November 1999.

[5] Y. Chen and G. Medioni. Object modeling by registration of multiple range images. *Image and Vision Computing*, 10(3):145–155, Apr. 1992.

[6] K. Higuchi, M. Hebert, and K. Ikeuchi. Building 3-D models from unregistered range images. *Graphic AI Models and Image Processing*, 57(4):315–333, July 1995.

[7] B. Jaehne. *Practical handbook on image processing for scientific applications*. CRC Press LLC, Florida, USA, 1997.

[8] A. Johnson and M. Hebert. Surface registration by matching oriented points. *IEEE Proc. Int. Conf. on Recent Advances in 3-D Digital Imaging and Modeling*, pages 121–128, May 1997.

[9] P. Krsek, T. Pajdla, V. Hlavac, and R. Martin. Range image registration driven by hierarchy of surface differential features. In *Proceedings of the 22nd Workshop of the Austrian Association for Pattern Recognition*, pages 175–183, May 1998.

[10] Visual Information Technology, National Research Council of Canada, http://www.vit.iit.nrc.ca/VIT.html. Website, last visited: August 2003.

[11] J. A. Williams and M. Bennamoun. Simultaneous registration of multiple corresponding point sets. *Computer Vision and Image Understanding*, 81(1):117–142, Jan. 2001.

[12] J. V. Wyngaerd, L. V. Gool, R. Koch, and M. Proesmans. Invariant-based registration of surface patches. In *Proc. 7th IEEE International Conference on Computer Vision (ICCV '99)*, volume I, pages 301–306, Kerkyra, Greece, Sept. 1999.

Age Classification from Face Images by Neural Networks

Miyoko Nakano, Fumiko Yasukata
Fukuoka Prefectural University
Faculty of Nursing,
4395 Ita, Tagawa, Fukuoka,
825-8585 Japan
mnakano@fukuoka-pu.ac.jp

Shinobu Matsuo, Minoru Fukumi, Norio Akamatsu
University of Tokushima
Faculty of Engineering,
2-1, Minami-Josanjima,Tokushima,
770-8506 Japan
fukumi@is.tokushima-u.ac.jp

Abstract

In this paper, in order to achieve high-accurate age estimation, we paid attention to the edges that consist of all wrinkles in a face and also a neck. In particular, this method uses the value of gray scale in an edge image. Therefore, the feature values of gray scale are fed into input units of a neural network for age estimation. In order to show the effectiveness of the proposed method, the proposed age estimation method was applied to an age estimation system using real images. For the simulation results, the rate of a classification divided by age was approximately 90% *as the whole.*

1 Introduction

Human beings are sasily able to distinguish person's age from an image of the face. In some cases, we can discem even identical twins. This ability has not been realized at computer vision. If it can be mounted in a computer, it may be applicable to many fields. Research on " age estimation, gender estimation and expression estimation from face images " has increased recent years. In particular, its application to age estimation is expected. For example, it can think that it is one of the technologies which are useful for the marketing investigation of examining a purchaser and a passer-by and so on[1].

The next two information is important for gender estimation and age estimation from face images. One is shape information based on the frame of a face and the face muscle, and the other is texture information (such as soaks, the wrinkle and freckles) [2]. This method needs using the feature point extraction and carries out estimation paying attention to the form of portions which constitute faces, such as an eye, a nose, and a mouth. However, it is difficult to extract these portions with high accuracy. There is a method which uses Gabor characteristics and a line shape distinction analysis as the research of paying attention to the automation without giving it a characteristics point [3, 4]. However, it is not easy that an age is estimated from a face image such that 20-59 years old is handled as one generation.

Therefore, this research aims at age estimation in large application area. When shape characteristics are used, the child of 10 years old and under can be distinguished from the adult. Age estimation is tried toward the HOIP face image data base which collected face images of 15-64 years old. Density histogram in which the value of the edge intensity of the vertical direction in an image and the horizontal direction is more than 100 is computed by using the edge information, and feature data is produced.

Neural networks are advanced parallel systems, which are excellent especially in the problem related to pattern recognition. Therefore, NN is used in order to avoid the difficulty of the threshold value determination in many dimensions. By using neural networks, the differences of feature data between ages are clarified and are discriminated [5].

2 Image data

In this paper, we perform some simulations using the following databases of the face images.

2.1 HOIP data base of the face images

HOIP data base of the face images was built as a base of the research of face image processing in Human and Object Interaction Processing (HOIP) in Japan. The characteristics of this data base are that photography directions are fixed. 300 Japanese images of 15-65 years old are divided into the interval of 5 years, each of which is composed of 15 persons. An image is the BMP file which consists of 635 $\times$ 480 pixels. Moreover, photography conditions are set

Figure 1. The samples of HOIP's image data.

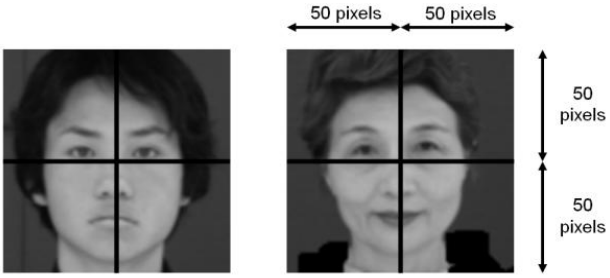

Figure 2. Normalization of the face image.

Figure 3. An edge extracted image.(Sobel filtering)

as fixed; that means the same lighting condition, subjects, and camera position. The sample image of the front face is shown in Fig. 1.

2.2 Normalization of an image data

In order to perform computer simulations, it is need to normalize original face images. The procedure of normalization is described in below.

At first, the center of a face image is adjusted at the intersection of two lines; the horizontal which passes along under the both eyes, and the vertical line which passes through the middle of the eyebrows are crossed as shown in Fig.2. The center of position of an image is extracted. Then the line joining both eyes is moved so that it may become parallel to the horizon. Next, in order to reduce information other than a face, an image is cut out as shown in Fig. fig:ndata. Then, it is changed into the size of 100 $\times$ 100 pixels.

3 Proposed method

The proposed method in this research is as follows:

1. A target image is normalized in the upper 100 $\times$ 100 pixel area from the neck as shown in Fig. 2.
2. The acquired face image is converted into a gray scale image.
3. Median filter is applied to the gray scale image, and a noise removal is done.
4. An edge is detected by the sobel filter as shown in Fig. 3.
5. A skin color area is extracted from the original image by the method of using threshold values (Fig. 4).
6. As for feature data are fed into the input units of NN, the pixels which have the value with edge intensity of more than 100 in the vertical direction and the horizontal direction are summed.

4 Computer simulations

4.1 Input data

This research is done by using the full color images of the BMP file. These subjects don't wear their glasses in an image to use this time. The total of the images is 252 sheets and another image of the same subject isn't contained. 10

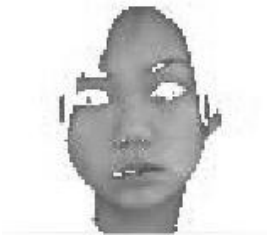

Figure 4. An skin color extracted image.

Figure 5. An image used as data.

sheets of total 120 sheets are used as the learning data for each age generation, and the remaining data are used as the test data of computer simulations (Table 1).

4.2 Structure of NN

A NN model used for the age estimation in this study is shown in Fig. 6. In this study, NN is used for age classification. It is a three-layered NN. BP method is adopted for learning. All data, the number of pixels, are used as input features in the input layer. The numbers of pixels are fed into the input units. The hidden layer has twenty units and the output layer has six units to classify six generations.

4.3 Experimental result

The result is shown in Table 3. The rate of an average accurate classification is 84.1%, which shows the classification of each age by using NN. In the details, the best rate of classification of 10's and 50's are 100.0%, and the worst rate of classification of 60's is 66.7%.

4.4 Comparative experiments 1

Simulation was done in the same way as a comparative experiment by using the image of only the face area. The example of an image to use in this simulation is shown in

Table 1. The details of the image data.

Gender	Age	Learning data	Test data
M	10's	10	5
M	20's	10	9
M	30's	10	12
M	40's	10	17
M	50's	10	9
M	60's	10	1
F	10's	10	5
F	20's	10	18
F	30's	10	17
F	40's	10	19
F	50's	10	18
F	60's	10	2
Total		120	132
		252	

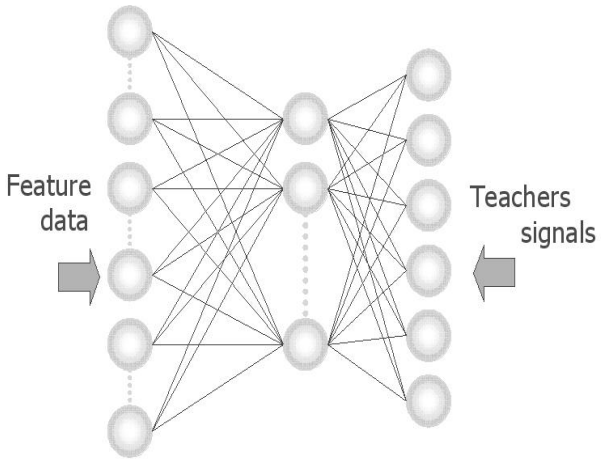

Figure 6. A NN model (Three-layer class type).

Table 2. Experimental condition.

Layer	The number of units
Input	100+100
Hidden	20
Output	6

Table 3. Experimental result

	10′s	20′s	30′s	40′s	50′s	60′s	Rate
10′s	100	0	0	0	0	0	100.0
20′s	11.1	70.1	18.5	0	0	0	70.4
30′s	0	6.9	89.7	3.4	0	0	89.7
40′s	0	0	11.1	75.0	13.8	0	75.0
50′s	0	0	0	0	100	0	100.0
60′s	0	0	0	0	33.3	66.7	66.7

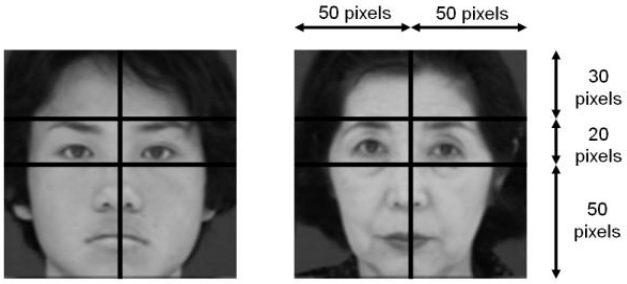

Figure 7. The sample image of comparative experiments 1.

Fig. 7. A result is shown in Table 4. The validity of the proposal method could be confirmed from this result as well.

4.5 Comparative experiments 2

On the other hand, an experiment was done by using the data on the different lighting condition. An experiment went by using 17 sheets of images in the 20's.

As shown in Table 5, an experimental result obtained the high recognition of 88.2%. It can be said that it is effective from this result even if it encounters the image in which a lighting condition is different.

5 Conclusion

The method in which an age was estimated at from the face images was proposed by using Neural Networks, and the verification of the validity was done by using the real image in this paper.

It paid attention to the wrinkle of the skin as the characteristics by which an age was estimated, an edge from

Table 4. The result of comparative experiments 1.

	10′s	20′s	30′s	40′s	50′s	60′s	Rate
10′s	90.0	10.0	0	0	0	0	90.0
20′s	0	81.5	18.5	0	0	0	81.5
30′s	0	3.4	89.7	10.3	0	0	89.7
40′s	0	2.7	2.8	91.7	2.8	0	91.7
50′s	0	0	0	7.4	81.5	11.1	81.5
60′s	0	0	0	0	33.3	66.7	66.7

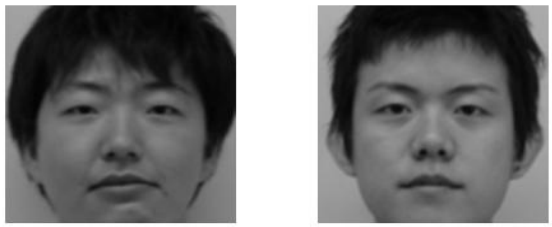

Figure 8. The sample image of comparative experiments 2.

Table 5. The result of comparative experiments 2.

	10's	20's	Rate(%)
20's	11.8	88.2	88.2

the face image was detected, and the value of edge intensity was made as characteristics data. It is shown that much amount of characteristics are contained in the part on the high value of the edge intensity from the experiment result. It was found out that the image which covered not only a face area but also a neck area was more effective. In conclusion, it is confirmed that the proposed method works very well.

From now on, age estimation from images with the emotion will be done in the next step, and also the gender estimation.

References

[1] S. Akamastu: “Computer Recognition of Human Face”, *IEICE Trans. on*, Vol.D-II-J80, No.8, pp.2031-2046, 1997. in Japanese

[2] H. Kwon, Niels da Vitioria Lobo: “Age Classification from Facial Images”, Computer Vision and Image Understanding, Vol.74, No.1, pp.1-21, 1999. *IEEE*, pp.861-864, 1990.

[3] B. Moghaddam and M. Yang, “Gender classification with support vector machne”, Proc. F&G2000, pp.306-311, Mar. 2000.

[4] M. Lyons, J. budynek, A. lane, and S. Akamatsu,“Classifying facial attributes using a 2-d gabor wavelet representation and discriminant analysis”, Proc. F&G2000, pp.202-207, Mar. 2000.

[5] S.Y.Kung: *Digital neural networks*, PTR Prentice-Hall (1993)

(This page left blank intentionally)

Protein 2D Gel Electrophoresis Images Matching with Maximum Relation Spanning Tree*

Daw-Tung Lin, Juin-Lin Kuo
Department of Computer Science and Information Engineering
Chung-Hua University
30 Tung Shiang, Hsinchu, Taiwan. R.O.C
dalton@chu.edu.tw, juinlin@mail2000.com.tw

En-Chung Lin, San-Yuan Huang
Divisions of Applied Biology and Biotechnology
Animal Technology Institute Taiwan
P.O. BOX 23, Chunan, Miaoli, Taiwan. R.O.C
eclin@mail.atit.org.tw,syhuang@mail.atit.org.tw

Abstract

The electrophoresis chromatography, a popular analysis tool, is able to separate different kinds of protein pro£les. In this paper, we present a robust comparative algorithm Maximum Relation Spanning Tree (MRST) for matching large scale and large sets of two dimensional protein gel electrophoresis (2DGE) chromatography images without the need of a priori landmark. The algorithm not only can handle the conditions of image rotation, shift and reverse, but also can handle fractional mapping problem. In the matching process, we apply fuzzy inference technique to conclude the £nal decision of mapping and location. The proposed system presents up to 94% correct matching performance for 225 2D gel test images. The additive value is the foundation of comparing small gel images to large format gel images and the constitution of searching scheme for a huge two dimensional gel electrophoresis chromatography image database.

1. Introduction

In the research of bio-informatics, proteomic technology plays an important role in protein expression study and analysis. Two dimensional gel electrophoresis (2DGE) chromatography is a popular tool for protein characteristics analysis. 2DGE images analysis is the £rst step of the whole study procedure. Issues of 2DGE images analysis have been discussed in some literatures. The problems can be categorized into the following topics: image registration, image distortion correction, spot detection, and spot matching. Image registration is widely used in biomedical imaging, which includes methods developed for automated image labelling and pathology detection in individuals and groups [1]. Image registration is equally important to biological systems, e.g. in proteomic research, 2DGE images is an important tool for investigating differential patterns of qualitative protein expression [2]. Spot detection is a basic procedure for 2DGE images analysis. We must locate the protein spots coordinates and then record or compare the attributes. There has been many methods proposed for protein spots detection, including Gaussian £tting [3], Laplacian £tting [4], Histogram [5] and Watershed Transformation [6, 7]. The common feature of those algorithms is spatial domain single processing. The aim of the segmentation process is to de£ne the location, true boundary and intensity for each spot. Image registration and spots detection are important procedure in the whole 2D gel image analysis scenario. Image registration and spot detection are common issues and has been studied thoroughly in the past.

Spot matching is a challenging problem in 2D gel comparison. We must £nd the different spots between standard gel and relative gel. A few algorithms have been proposed to solve this problem, for example Restriction Landmark Genomic Scanning (RLGS) [3, 8, 9] and Fuzzy Cluster [10]. RLGS compares the protein based on constructing of computer graphs and landmark. It has the drawback that users need to allocate the landmark manually. Fuzzy Cluster algorithm uses the relation between two protein spots and calculate the similarity. Fuzzy Cluster method also can calculate the similarity fast, but if there have hundreds or thousands protein spots in two gel images, this method will fail without using a large amount of features.

We have also investigated and implemented several methods to construct a framework of 2DGE image analysis system [11]. For spot detection, we choose the Watershed Algorithm to segment the protein spots for the sake of low intensity and process speed, and to adapt to local area

*This work was supported in part by the National Science Council, Taiwan, R.O.C. (NSC91-2745-E-216-001, NSC89-2313-B-059-045, NSC90-2313-B-059-002).

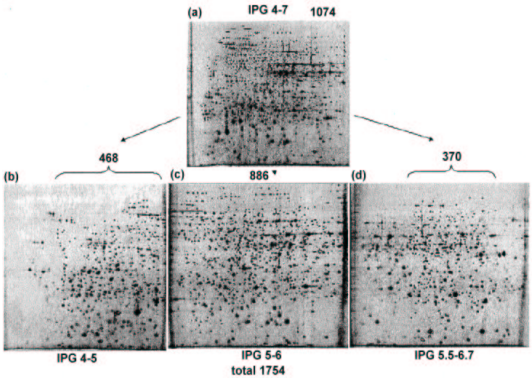

Figure 1. Illustration of gel images combination [12]: (a) IPG 4-7 gel image; (b) IPG 4-5 gel image; (c) IPG 5-6 gel image; (d) IPG 5.5-6.7 gel image.

intensity. We provide a novel Maximum Relation Spanning Tree (MRST) to overcome the problems of RLGS and Fuzzy cluster method. The algorithm not only can handle the rotation, shift and reverse condition, but also can handle fractional mapping problem. In the matching process, we apply fuzzy inference to correct the variation, which is generated from rotation, shift and reverse condition. In addition, this method doesn't need landmark allocated in a priori by users.

2. Features Extraction with Gabriel Graph and Relative Neighborhood Graph

In the early stages of the biological experiment with long range pH gradient, the protein spots were found usually too closed or overlap with each other. This is a major problem for protein purging. Therefore, the biologists would prefer processing with narrow range of pH gradient in the same gel areas separately and then compose several gel sub-images to analyze protein as a whole. As we can see in Fig. 1, the image on the top is composed from three partially overlapped images shown below it. We can use the combined gel image to identify more useful protein spots instead of using the overlapped and blurred protein spot in wide range IPG gel image. Due to this constraint, we provide a novel comparative method Maximum Relative Spanning Tree (MRST) for matching the small part of image with it's original gel image. Thus, we can use this method to £nd the original gel image form small and fractional images and allocate them by using this protocol.

Generally speaking, there is no £x model of protein spots distribution, nor £x size and could reside everywhere in the gel image. We cannot compare gels only by the information of protein spots location or by image intensity. According to the de£cient feature in gel image, we have to construct the unique feature of the protein spots. In this paper, we £rst apply the computer graphics theory to construct and to extract the features for gel images comparison [13, 14, 15, 16]. The proposed MRST algorithm is then utilized to compute the similarity between features with fuzzy inference rules We will discuss these issues in the following sections.

There have been several kind of graph computation methods studied by researchers and scientists such as minimum spanning tree (MST) [17], relative neighborhood graph (RNG) [18], Gabriel graph (GG),Delauney triangular graph (DT) [19] and etc.. These are simple, undirected, straight-lined, connected and planar graphs. Furthermore, these graphs will keep features unchanged no matter with the transformation of rotation, shift and reverse. Therefore, every point in the graph has a set of unique feature from graph viewpoint.
We have selected the Gabriel Graph (GG) and the Relative Neighborhood Graph (RNG) as feature constructive models because the variation of point's feature is more obvious than that of the others. We use two graph models GG and RNG to construct the features and to compare gel images. GG provides the major connection relation. We begin the de£nition of the theoretical and geometric terminologies in the next paragraph.

A graph $G = (V, E)$ consists of a £nite non empty set $V(G)$ of vertices, and a set $E(G)$ of unordered pairs of vertices known as edges. An edge $e \in E(G)$ consisting of vertices u and v and is denoted by $e = \overline{uv}$; u and v are called the endpoints of e and are said to be adjacent vertices or neighbors. The degree of a vertex $v \in V(G)$, denoted by $deg_G(V)$, is the number of edges of $E(G)$ which have v as an endpoint. A path in a graph G is a £nite non-null sequence $P = v_1v_2...v_k$ where the vertices $v_1v_2...v_k$ are distinct and $\overline{v_iv_{i+1}}$ is an edge for each $i = 1, ..., k-1$. The vertices v_1 and v_k are known as the endpoints of the path. A cycle is a path whose endpoints are the same. A graph is connected if, for each pair of vertices $u, v \in V$, there is a path from u to v . Gabriel Graph and Relative Neighborhood Graph are then de£ned in following sections:

2.1 Gabriel Graph

The Gabriel graph P , denoted by $GG(P)$, has its region of in¤uence the closed disk having segment $\overline{uv}$ as diameter. That is, two vertices $u, v \in S$ are adjacent if and only if

$$D^2(u,v) < D^2(u,w) + D^2(v,w) \quad , \; for\ all\ w \in S,\ w \neq u,\ v. \tag{1}$$

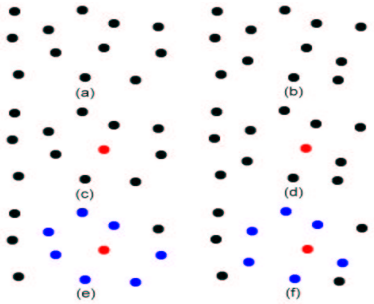

Figure 2. Illustration of major spots and satellite spots.

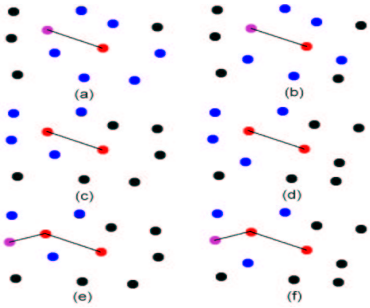

Figure 3. Illustration of maximum relation spanning tree matching pairs.

2.2 Relative Neighborhood Graph

Given a set P of points in R^2 , the relative neighborhood graph of P, denoted by $RNG(P)$, has a segment between points u and v in P if the intersection of the open disks of radius $D(u, v)$ centered at u and v is empty. This region of in¤uence is referred to as the lune of u and v . Equivalently, $u, v \in S$ are adjacent if and only if

$$D(u, v) \leq max[D(u, w), D(v, w)] \\ , for\ all\ w \in S, w \neq u, v. \quad (2)$$

2.3 Feature Extraction

After we have constructed the proximity graphs, we will continue to extract the features of the spots on protein gel images. In the above proximity graphs, we can obtain the following features:

- Degree of each protein spots,
- Angle of connected edges, and
- Distance between protein spots.

These features will not be changed in the circumstance of shift, rotation and reverse due to the advantage of graph properties. We will calculate the features for every protein spot based on these information and utilize them as a framework of spot matching comparison in the next section.

3 Fractional Spot Matching with Maximum Relation Spanning Tree

In order to compare the similarity between two gel images, we have developed the maximum relation spanning tree (MRST) a comparative framework for this task, as in which the minimum distance derived from the minimum spanning tree is replace by the maximum relation. We will calculate the relationship points as their features and £nd the maximum relation protein spot pair as basic information for image matching. The algorithm will be terminated if there is no referable pair in the spot pair sets. The illustration of the MRST algorithm is shown in Fig 2 and Fig. 3 and is discussed as follows.

The MRST algorithm is based on Gabriel graph. We use the connected condition of Gabriel graph to de£ne whether a spot can join and to be compared as shown in Fig. 2. Figure 2(a) and (b) denote two protein spots sets, (c) and (d) denote the initial comparative pair (plotted in red dots) found by global matching, (e) and (f) denoted the satellite spots (plotted in blue dots) found by Gabriel graph connected condition. We name the red spot and the blue spots as the major spot satellite spots, respectively. Starting from any two major spots in the standard gel image (target) and relative gel image (test sample), we will travel through all of the satellite spots in the standard gel image and calculate the relationship with all of the satellite spots in relative gel image. As illustrated in Fig. 3 with connected edges, we will £nd the maximum relation for every satellite spot pairs recursively. Figure 3(a) and (b) denotes the maximum relation matching pair between two images to be computed, (c) and (d) shows that the satellite spots are used as the center point and to £nd the next pair, (e) and (f) illustrates that recursive processing and £nd the next pair. From these pairs, we chose the maximum relation pair to be the major spot pair for comparison and store the rest of high relation pairs into the temporary stack. If we cannot £nd further major spot pair, choose the the largest relation pair in the temporary stack and process continuously. When all of the spots in the standard gel image have been traversed, the computation will be terminated and the matching results will be obtained. When we implement this algorithm, we separate the process into two parts: global matching and local matching.

3.1 Global matching

In this step, we need to £nd the initial comparative pair. We compare all possible pairs and £nd the maximum relation between each other. Euclidean distance of three different features (spot degree, angle, and distance as mentioned in Section 2.3) is computed as the similarity measure between spot pairs and then sort them by their relation values, then recorded into the temporary stack.

3.2 Local matching

After the searching of the similar pairs has been completed, we start to process the maximum relation spanning tree. The algorithm is elucidated as following:

$MRST()$
{
$If\ node\ tree\ is\ null.$
    $Inserting\ new\ comparative\ pair.$
    $MRST()$
$else\ if\ comparative\ pairs\ is\ not\ empty$
    $Find\ next\ comparative\ pair\ in\ the\ satellite\ spots.$
    $MRST()$
$else\ if\ temporary\ stack\ is\ empty$
    $Function\ will\ be\ terminated.$
}

3.3 Fuzzy Inference

Direct superimpose matching is not appropriate due to the imperfect 2D electrophoresis technique. 2D gel patterns usually present various kinds of transformations such as distortion, translation and the variation of protein properties. An adaptive decision method is essential to examine and conclude the similarity measure from the above-mentioned spot pair features. We decide to applying the fuzzy inference to develop our comparative framework. By transferring the crisp relation into fuzzy relation. Using fuzzy relation to compare satellite spots is more suitable.

Due to the difference in every local area, we use a stylized membership function. The feature of the spots in the standard gel image is de£ned as f^s and the feature of the spots in relative gel image is de£ned as f^r. Let the function be:

$$R(f_n^{S_a \to R_b}) = e^{-[\frac{(f_n^{S_a} - f_n^{R_b})}{2\sigma^2}]^2} \quad (3)$$

where R denotes the membership function and σ denotes the variance of the feature f_n between spots. The MRST algorithm utilizes this fuzzy inference system to compute the relations of every spots whether it is the neighbor of the center spot. With three different features, we calculate three different relations for these features and obtain the weighted average value [21]. The total relation R_{total} is de£ned as:

$$R_{total} = \frac{\omega_{f_1} \cdot R_{f_1} + \omega_{f_2} \cdot R_{f_2} + \omega_{f_1} \cdot R_{f_3}}{3} \quad (4)$$

w_{f_i} is the weight of the corresponding feature. Finally, we can choose the maximum relationship from the spot pairs and proceed to the next comparison procedure. This algorithm will be process recursively until all of the spot pairs produced by the Gabriel matching is completed. Through this process, we will £nd all similar spot pairs between two gel images. We will also label the matched spots corresponding to their relative spots and their matching area. As shown in Fig. 4, the left window displays the source image to be matched, the square on the right-hand side indicates the matched area in a large scale gel image. If no complete fractional match were available, this algorithm could present the possible match point pairs with corresponding matching labels as shown in Fig. 5. As we can observe in Fig 5, each spot in the rectangle area has two labels indicating the mapping relation between the standard (target) pattern and the corresponding spot label of the test pattern. The left label indicates the spot number in the target gel image. The right label followed by arrow sign denotes the matched spot label in the source (test) image.

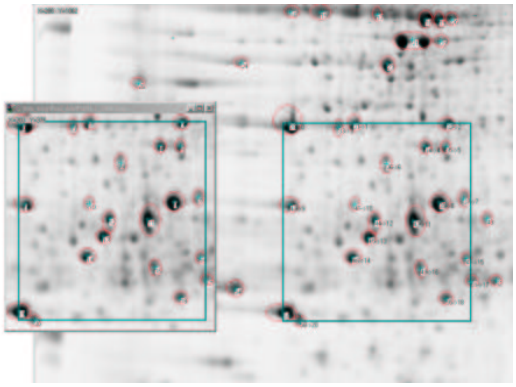

Figure 4. Result of fractional matching.

4 Simulation Results

We have implemented the proposed 2DGE images analysis system, and demonstrated the results of gel matching (global matching and fractional matching) in this section. We have obtained 15 gel images (1498 x 1544) from the Animal Technology Institute Taiwan (ATIT) as the test images. We utilized them to construct the experiment data set. The data set contains totally 225 gel images as illustrated in the following: 15 original gel images (1498 x 1544), 135 fractional gel images composed from

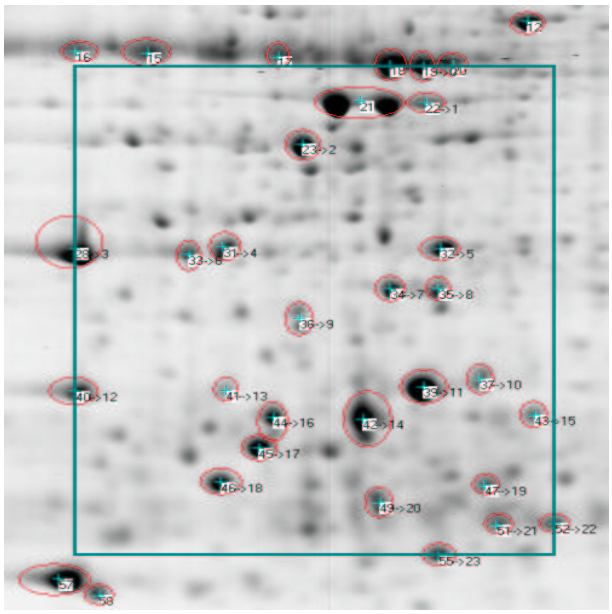

Figure 5. Relation of pattern mapping between two similar fractional gel images.

different sizes of fractional images (1000x1000, 900x900, 800x800,700x700, 600x600, 500x500, 400x400, 300x300 and 200x200) chopped randomly from each of 15 original gel images, and 75 rotated images: (1) 45 gel images obtained from the original gel images by rotating in $90°$, $180°$, and $270°$ degrees, respectively, and (2) 30 gel images obtained from the original gel images by ¤ipping horizontally and vertically, respectively. We have done two categories of experiments by using the data set as following:

- Fractional Matching: using various size of fractional image samples (135 images) to perform searching in the original gel images (15 images) and see if the proposed method can £nd the correct match.
- Spots Registration: using the rotated samples (75 images) to match the original gel images (15 images) and see if the proposed algorithm can £nd the correct registration without rotating the samples in *a priori*.

In order to obtain better performance, we tried to adjust two parameters - level of 'opening' and protein size threshold through extensive computer simulations. The 'opening' parameter ranges from 1 to 30, and the protein size threshold is between 0 and 1000. If the gel protein spots intensity in gel image is blurred, we must adjust the parameters to be low enough to retain the small protein spots for matching. On the other hand, if the image background is over-stained, we need to adjust the parameters as high as possible in order to delete the noise. The performance of fractional matching is raised to 94% after the adjustment. The detail results is shown in Table 1. In order to simulate the situations of input images rotation, reverse, and translation, we have tested 75 different modi£ed gel images with 5 situations as shown in Table 2 . The ratio of correct matching is about 80%.

Table 1. The results of fractional matching of different size of images with adapted parameters.

	Correct Matching Ratio
Original Images	100 %
1000x1000	100 %
900x900	100 %
800x800	100 %
700x700	100 %
600x600	100 %
500x500	100 %
400x400	100 %
300x300	86.7 %
200x200	53.3 %
Overall	94 %

Table 2. The result of registration for different rotation situations.

	Correct Registration Ratio
Rotated $90°$	80 %
Rotated $180°$	80 %
Rotated $270°$	80 %
Horizontal Reversal	86.7 %
Vertical Reversal	73.3 %
Overall	80 %

To further con£rm the capability of fractional matching, we have also used the rotated fractional gel images and to perform searching in the original large scale gel images (15 images) and see if the proposed method can £nd the correct match. One of the results is demonstrated in Fig. 6 where one fractional standard gel image of size of 200x200 is rotated or ¤ipped into £ve images with different conditions (rotated in $90°$, $180°$, $270°$, ¤ip horizontally ,and vertically) and these fractional images are shown on the left hand side in Fig. 6. By applying these six small images, we tried to search in the original large size 2D gel images and see if the proposed system can £nd exact match. The location of correct matching is identi£ed in the rectangle on the right hand side of Fig. 6.

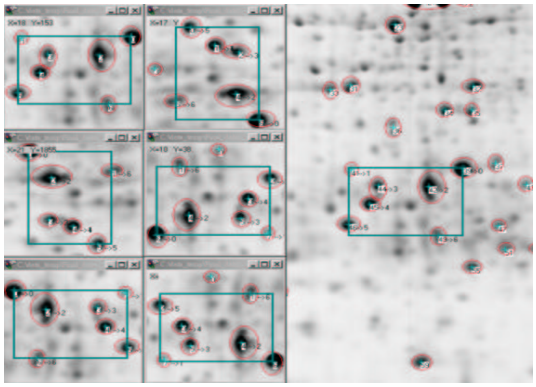

Figure 6. Result of fractional matching and allocation processing.

5 Conclusion

In this paper, we focused on the issues of fractional matching and relocation for the small fraction pattern in the large scale of 2D gel images. We have developed a fast, accurate and content-based image matching method Maximum Relation Spanning Tree (MRST). By using this algorithm, we can easily allocate the protein spots for the fractional images or warp images, and match the original gel images. After all, we can constitute the gel images and protein spots information into the database for further investigation. The proposed system archives up to 94% correct matching in large scale gel image searching scenarios. Most importantly, the proposed MRST matching algorithm does not require neither the landmarks manually set nor a prior information of gel image alignment.

References

[1] X. Y. Wang, D. D. Feng and H. Hong. "Novel Elastic Registration for 2-D Medical and Gel Protein Images". *In Proc. First Asia-Paci£c Bioinformatics Conference (APBC2003)*, Adelaide, Australia. Conferences in Research and Practice in Information Technology, 19. Chen, Y.-P. P., Ed. ACS. 223-226. .

[2] S. Veeser, M. J. Dunn and G. Z. Yang. "Multiresolution image registration for two-dimensional gel electrophoresis". *Proteomics 2001*, 1, 856-870.

[3] K. Takahashi, M. Nakazawa, Y. Watanabe and A. Konagaya. "Fully-Automated Spot Recognition and Matching Algorithms for 2-D Gel Electrophoretogram of Genomic DNA". *In Proc. of Genome Informatics Workshop*, pp.161-172, 1998. Dec.

[4] "Z3". http://www.compugen.co.il/.

[5] P. Culter, G. Heald, I. R. White and J. Ruan. "A novel approach to spot detection for two-dimensional gel electrophoresis images using pixel value collection". *Proteomics 2003*, 3, 392-401.

[6] L. Vincent and P. Soille. "Watersheds in Digital Spaces: An Ef£cient Algorithm Based on Immersion Simulations". *IEEE Transactions on Pattern Analysis and Machine Intelligence*, June 1991, Vol. 13, No. 6, pp. 583-598.

[7] S.Beucher. "The Watershed Transformation Applied to Image Segmentation". *Cambridge, UK, Scanning Microscopy International*, suppl. 6. 1992, pp. 299-314.

[8] K. Takahashi, M. Nakazawa, Y. Watanabe and A. Konagaya. "Automated Processing of 2-D Gel Electrophoretograms of Genomic DNA for Hunting Pathogenic DNA Melecular Changes". *In Proc. of Genome Informatics Workshop 1999*, pp121-132.

[9] T. Matsuyama, T. Abe, C. H. Bae, Y. Takahashi, R. Kiuchi, T. Nakano, T. Asami and S. Yoshida. "Adaptation of Restriction Landmark Genomic Scanning (RGLS) to Plant Genome Analysis". *Plant Molecular Biology Reporter 18*, 2000, 331-338.

[10] X. Ye, C.Y. Suen, M. Cheriet, E. Wang. "A Recent Development in Image Analysis of Electrophoresis Gels" *Vision Interface (VI'99)*, Trois-Rivieres, CA, 19-21 May 1999, pp. 432-438.

[11] J. L. Kuo, D. T. Lin, E. C. Lin and S. Y. Huang. "Image Analysis System for Protein Two Dimensional Gel Electrophoresis" *16th IPPR Conference on Computer Vision, Graphics, and Image Processing* (CVGIP 2003), pp. 139-146.

[12] H. J. Issaq, T. P. Conrads, G. M. Janini and T. D. Veenstra. "Methods for fractionation, separation and pro£ling of proteins and peptides". *Electrophoresis 2002*, 23, 3048-3061.

[13] A. Efrat, F. Hoffmann, K. Kriegel and C. Schultz. "Geometric Algorithms for the Analysis of 2D-Electrophoresis Gels". *Journal of Computational Biology*, 2002,9(2): 299-315.

[14] F. Hoffmann, K. Kriegel and C. Wenk. "Matching 2D Patterns of Protein Spots". *Symposium on Computational Geometry 1998*: 231-239.

[15] F. Hoffmann, K. Kriegel and C. Wenk. "An applied point pattern matching problem: comparing 2D patterns of protein spots". *Discrete Applied Mathematics 93 (1999)*, 75-88.

[16] Y. Watanabe, K. Takahashi and M. Nakazawa. "Automated Detection and Matching of Spots in Autoradiogram Images of Two-Dimensional Electrophoresis for High-speed Genome Scanning". *ICIP (3) 1997*: 496-499.

[17] D. R. Karger, P. N. Klein and R. E. Tarjan. "A Randomized Linear-Time Algorithm to Find Minimum Spanning Trees". *Journal of the ACM*, March 1995, 42(2):321-328.

[18] J. W. Jaromczyk and G. T. Toussaint. "Relative Neighborhood Graphs and Their Relatives". *Proc. IEEE* (1992), 80 (9):1502X1517.

[19] S. Fortune. "Voronoi Diagrams and Delauney Triangulations". *World Scienti£c, Singapore*, 2nd edition, 1995. Computing in Euclidean Geometry, volume 4 of Lecture notes series on Computing, pages 225–265.

[20] J. W. Jaromczyk and G. T. Toussaint. "Proximity Graphs for Nearest Neighbor Decision Rules: Recent Progress". *Technical Report, School of Computer Science, McGill University, Montreal, Canada*, June 2002, SOCS-02.5.

[21] G. J. Klir and B. Yuan. "FUZZY SETS AND FUZZY LOGIC - THEORY AND APPLICATION". *Prentice Hall International Editions*, 1995.

INTELLIGENT AGENTS

(This page left blank intentionally)

The Adaptation of Agent Configurations using Web Services as Components

D. Richards[1], S. van Splunter[2], F.M.T. Brazier[2], M. Sabou[2]

[1] Department of Computing
Macquarie University
Sydney, Australia
richards@ics.mq.edu.au

[2] Department of Computer Science
Vrije Universiteit Amsterdam
Amsterdam, The Netherlands
< marta, sander, frances>@cs.vu.nl

Abstract*: To support dynamic and reactive behaviour we have developed an Agent Factory which (re-)structures an agent configuration using existing components. In this paper we present our current work which uses Web services as the components. Our initial work has focused on configuring Web services to create a design artifact. This is achieved by reasoning about the requirements and the semantic descriptions of Web services in the DAML-S Web service description language and ontologies. We provide an example of the design process and our findings regarding DAML-S.*

Keywords: Applications, Intelligent agents, Ontology, Semantic Web, Web services

1. Introduction

The ability of agents to adapt according to changes in system requirements and the environment is important to enable dynamic and reactive behaviour. Following the use of compositionality in the major software engineering paradigms and based on the Factory design pattern [8], we have developed an Agent Factory (AF) architecture [1]. The approach is based on the use of components, the generic agent model and the DESIRE formal knowledge-level modeling and specification framework for multi-agent systems [3]. Our agent (re-)structuring approach [13] allows an agent to automatically adapt by reusing existing components. Our approach is a combination of process-oriented and object-oriented approaches by treating processes as the 'active' parts of our agent, which are our agent components, and classes as the 'passive' part of our agent, which are the data types used in the agent components.

Adaptation requires the identification of appropriate components. Determining what is 'appropriate' involves understanding of the requirements, the development of a design to meet those requirements, location of possible components and the ability to reason about those components. Reusable components must therefore be described syntactically and semantically to determine if a suitable component has been found and what changes, if any, are needed. There are a number of possible alternatives to using reusable components ranging from one extreme of creating your own closed library of components with well constrained specifications, languages, etc, or the other extreme of finding components "out there" which will require sophisticated matching and adaptation techniques. We have sought a middle position on this continuum. Our previous work has proposed an open architecture but our implementations have been restricted to the use of building blocks that we have developed our selves. Furthermore, the Agent Factory has been developed on the basis of a number of assumptions:

1. agents have a compositional structure
2. reusable parts can be identified
3. two levels of descriptions are used: conceptual and implementation
4. properties and knowledge of properties are available
5. no commitments are made to specific languages and/or ontologies.

Our current work is reviewing those assumptions through the application and extension of our approach by using Web services as components. Web services meet our first assumption as they exhibit modular behaviour [5]. The study described in this paper is particularly focused on addressing the second and fourth assumptions. Many agent approaches are based on similar assumptions and thus our work is of benefit to them. Further we believe that our architecture can be used to create composite Web services and address some of the issues facing the Web services and Semantic Web communities.

Additionally, the study reported in this paper seeks to take some of the key research efforts and defacto standards that are emerging for automated Web service usage and investigate their strengths and deficiencies. In the next section we provide some background to this project through review of a number of other adaptive agent approaches and current approaches to dynamic use of Web services. In section 3, we introduce the Agent Factory including a description of components, our architecture, the general agent model and assumptions. The fourth section describes the study we conducted. The final section gives our conclusions, future work and summary.

2. Background

To provide some background to our work we present an introduction to Web services and their semantic description in sections 2.1 and 2.2. Section 2.3 considers agent-based Web service research.

2.1 Web services

While a number of definitions of a Web service exist, the definition that most fits with our intended use of WSs as

components in the Agent Factory is given by the Stencil[i] group who define a WS as "loosely coupled, reusable software components that semantically encapsulate discrete functionality and are distributed and programmatically accessible over standard internet protocols". The three definitions offered differ in their emphasis on technology, business and software engineering but all encapsulate the self-contained, modular, composable and distributed nature of WS. These four characteristics of WS are well supported by a layered-architecture where the base is a well-established transport layer. In each layer we give an example of a major standard. In italics we position the work reported in this paper. The next layer up uses the Simple Object Access Protocol (SOAP) which is an XML-based communication protocol for exchanging data in

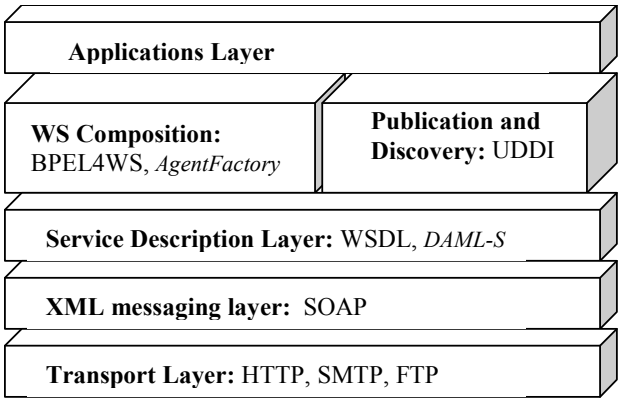

Figure 1: WS architecture (adapted from [14])

decentralized and distributed environments via typed message exchange and remote calls. The service description layer includes the XML-based Web Service Description Language (WSDL). The next layer is split into two main types of WS technologies: ones that support single service advertising and discovery and ones that support service composition. For service registration and discovery there is the Universal Description, Discovery and Integration (UDDI) (by IBM, Microsoft and Ariba) standard service repository. To provide some very basic semantics (such as identification via a product classification code) one or more tModel descriptions may be attached to a service. For service composition there are a myriad of possible solutions. Figure 1 includes the Business Process Execution Language for Web Services (BPEL4WS)[ii] which has grown out of the early offerings WS Flow Language (WSFL) (IBM)[iii] and XLANG (Microsoft)[iv] (an extension of the W3C's Web Services Description Language (WSDL)).

Academic research into WSs is seeking to provide compatibility and sufficient flexibility to support the emerging commercial standards while addressing current shortcomings in the 3rd and 4th layers. Since current technology only supports syntactic and static description and composition of WS having agents automatically find, compose and execute services is not a current reality.

2.2. Semantic description of Web Services

WSDL, SOAP and UDDI are seen as steps in the right direction but ones that will fail to achieve the goals of improved automation and interoperability, because they rely on *a priori* standardisation and require humans in the loop [9]. To support automated reasoning, knowledge representations (such as markup languages) will be needed that express both data and rules for reasoning. Ontologies will be used to enable definition and comprehension of meaningful content. These are the concerns of the Semantic Web community. Additionally, agents will be needed to interpret the content and transform user requests into optimized delivered solutions.

The ability to dynamically locate and compose Web services based on their semantic description will rely on the richness of the description and the robustness of the matching techniques used. The most significant work that has been done to describe Web services has been conducted by the DAML-S coalition [16].DAML-S is built on the AI-based action metaphor where each service is either an atomic/primitive or composite/complex action. Knowledge preconditions and knowledge effects are handled via the inputs and outputs of the Web service [10]. The matching of service providers and service requesters via semantic descriptions of the services are key goals of this work. DAML-S uses the DAML+OIL specification language (which extends the weak semantics of RDF(S)) to define four upper level ontologies that can be specifically used to describe Web services. The Service ontology is essentially a means of linking the three other ontologies that contain the what (ServiceProfile), the how it works (ServiceModel) and the how to use (ServiceGrounding). Matching is typically done at the Profile level. Execution monitoring is supported via the ServiceModel, also known as the Process Model. The ServiceGrounding definition maps the DAML-S Profile and Process models to a WSDL definition of the service. To provide further compatibility with other WS standards, each DAML-S parameter may be mapped to a UDDI tModel. In section 4.2 we use the DAML-S Profile and Grounding descriptions to configure a design artifact.

2.3. Agents and Web Services

To realize the potential of agents to manage interactions with Web services a number of research efforts are under way to bring semantics to Web service descriptions that will sit at layers above what is being offered commercially. A number of approaches (e.g. [5], Racing[v]). have been offered to provide Web services with agent-like behaviour through the use of agent wrappers. [6] use wrappers so that web sources can be queried in a similar manner to databases. Alternative agent-based approaches to Web services are provided by [7] and SWORD [11] who offer

model-based approaches and deductive reasoners to derive a composition. [17] use construction scripts and composite logic to define how the services in a component can be combined, synchronised and coordinated. Typical of many approaches to composition, these approaches focus on the latter half of the system development life cycle. In [11] and [10] the goal is to determine if a set of services fulfils the specification. In all three they use a reasoner to derive a plan.

This paper seeks to fill a gap in the current work by offering an approach that is truly automatic and spans the whole system development lifecycle from requirements specification to system execution. The building blocks are Web services. The emerging DAML-S standard is used as a description language to reason about WS. The main question to be addressed in this paper is whether DAML-S descriptions of web-services offer enough structure for automated configuration by the Agent Factory.

3. Agent Factory

In this section we provide an introduction to the Generic Design Model and the concepts of a component and template.

3.1 Generic Design Model

The configuration process of a software agent in the (re-)design centre is based on the Generic Design Model (GDM) presented in [2]. In short, the assumption behind this model is that both requirements and their qualifications, and the description of an artefact evolve during a design process. E.g., in practice often not all initial requirements can be satisfied. The artefact is designed to satisfy sets of these requirements. Design choices are influenced by high-level strategies, chosen on process objectives (e.g. deadlines, resources). As shown in Figure 2 this knowledge-based model of design distinguishes reasoning about requirements and their qualifications (Requirement Qualification Set (RQS) Manipulation), reasoning about the design artefact (Design Object Description (DOD) Manipulation), and reasoning about the design process itself (Design Process Co-ordination).

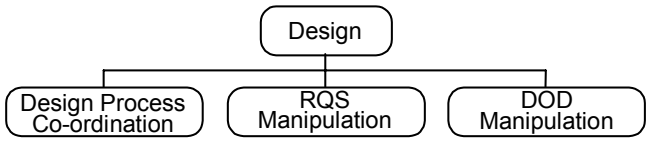

Figure 2. Main processes in GDM

The input and output of all four of these components is defined, together with the level of reasoning (meta-level) to which they pertain. Information exchange between components and potential control structures is also specified by the model as are the necessary control structures and a generic design ontology.

Design in the Agent Factory is conducted at two levels: the conceptual and implementation levels. Adaptation of an agent can involve redesign at both levels and thus requires the mapping between the two levels to be specified explicitly. The operational level includes implementation detail needed by the assembly process.

3.2 Components and Templates

A component has an interface which describes the input and output data types. Less conventionally, our components also contain slots to regulate the components configuration. Components themselves may be data types and thus may also have their own slots. Components are connected via the slots. Slots define an interface and what type of component or data type may be inserted. The use of slots provides a 'static' architecture for the agent. Templates are skeletons of components.

To support automatic agent adaptation we use two types of annotations: ontologies and co-ordination patterns. Ontologies are used to provide a shared understanding of concepts and relationships between concepts. Coordination patterns define the temporal sequence and dependencies between processes that combine to form a task. Annotations are associated with components and data types and may themselves be composed.

4. An Example

This section we provide and example of how the Agent Factory may be used for the composition of WSs in a specific domain. Section 4.1 describes the scenario. Section 4.2 follows a sample design trace of the configuration process.

4.1. The scenario

The example illustrates how the AF can be used to configure WS to create a portal containing bibliographic data.[vi].

The task of creating a portal from a given set of BibTex files is carried out by a set of web-services. First, each BibTex file is converted to RDF(S) using the BIB2RDF service then saved in a web-accessible RDF(S) repository and query engine, Sesame[vii], by the service ISESAME. The merger of all available data most often results in redundancies as different owners of the bibliographies use syntactically different resources to denote the same author. To deal with this issue the sets of redundant resources are labelled with the *sameIndividualAs* DAML tag. The task of finding and labelling redundant authors is performed by the SIA (SameIndividualAs) service. To determine the redundancies: all data is extracted from Sesame with the service ESESAME and sent to the SIA service. The results and extracted data are reinserted into Sesame using ISESAME. Finally, portal creator software creates the portals of publications by querying Sesame.

Table 1. Requirements

ID	Description
rq_i1	Create input for portal creator p_1
rq_i2	Input I_1 is generated from references in BibTex files

The initial requirement set is formulated for the design process is depicted in Table 1 Rq_i1 states that the user wants to use portal creator p_1 to create a portal on references BibTex files. This means that: the input I_1 of portal p_1 needs to be created from multiple BibTex files (rq_i2). Table 2 states the resulting additional requirements. Portal p_1 accesses the information for the portal creation from a Sesame repository (c1), which must contain references (c2), and p_1 should be able to access this information without worrying about authors being referenced differently (c3).

Table 2. Requirements of portal creator p_1

ID	Description
c1	Input I_{portal} must be in a SESAME repository
c2	Input I_{portal} contains set of references
c3	Input I_{portal} has one unique identifiers for each author

Some details that arise within the trace are in sequence:

- Sesame can handle double identifiers for the same instance if they are marked as being equal, this functional property is also stated in ISESAME.
- The input for ISESAME specified in its Profile is *data*, and *references* are a subtype of *data*. Note this relation is expressed in the ontology provided for this purpose.
- The input for ISESAME is specified in its Grounding as *rdf-stream*, which is no subtype of *data-stream.*
- A pre-condition of ISESAME is that its input needs to be tagged with sameIndividualAs before it can handle double identifiers.
- The output of is SIA specified in its Profile as *equal authors*.

4.2 An example of design

As described in Section 3.1, the Agent Factory uses the Generic Design Model as the basis for the design process. In this example reasoning about the design process (DPC), reasoning about requirements and their qualifications (RQSM), and reasoning about the design object description (DODM) are separated. Only the first part of the design trace is given. The design starts after the requirements and the constraints on portal creator p_1 have been communicated to the design process.

4.2.1. Step 1

DPC: The design process is started. The general strategy to be followed is a top-down approach: to identify a component that performs the required functionality.

RQSM: A relevant set of requirements must be compiled from the total set of requirements. The requirement rq_i1 to create input for portal p_1 is generalised to the requirement rq3. And c1, and c3 are combined to formulate requirements rq4 and rq5:

rq3 aggregate information in repository Rep_1
rq4 Rep_1 is a SESAME repository
rq5 Rep_1 identifies same instances with single identifier

This set of requirements is passed to DODM.

DODM: The first structural aspect considered is components. Functionally a web-service is sought that can store data in SESAME, and handle double identifiers for the same instance if they are marked as being equal. This functionality is covered by the web-service ISESAME. In the DAML-S profile the service category states that it stores data in a SESAME repository, and the repository can handle the DAML:sameIndividualAs-tag for identifying double instances.

4.2.2. Step 2:

DPC: Component for fulfilling requested functionality is found. Integrate this component for data-exchange.

RQSM: The relevant requirements on the data-exchange is rq_i2. This requirement is refined in rq6 and rq7.

rq6 Input are references
rq7 The input are BibTex files

The set of rq6 and rq7 are passed to DODM.

DODM: This step focuses on the structure data types. The input and output on both levels of abstraction of the component ISESAME are given in figure 3. In this figure functionality is shown with ovals for descriptions on the Profile-level, and the operational service is displayed in rectangles. On the conceptual level the data exchange poses no problems. ISESAME expects as input parameter in the DAML-S Profile *data*, which is a superclass of *references*.

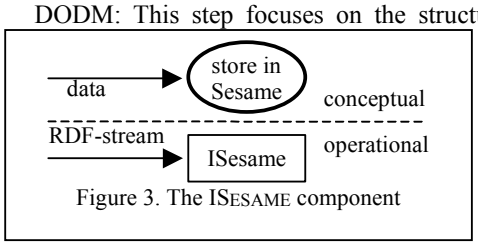

Figure 3. The ISESAME component

At the operational level there is, however a conflict. ISESAME expects an RDF-stream as input, specified in the DAML-S Grounding. However, rq7 states that the input should be BibTex files. BibTex is not of type *RDF-stream*. Therefore, to be able be used as input for ISESAME, the BibTex files should be translated into RDF. The web-

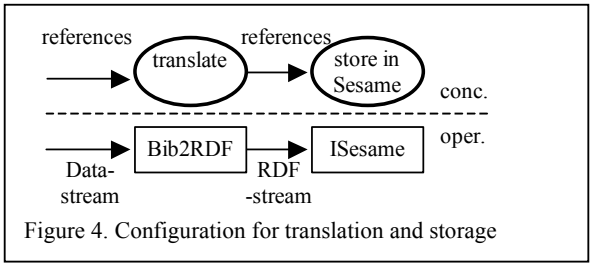

Figure 4. Configuration for translation and storage

service BIB2RDF is retrieved and included in the configuration. This web-service takes care of the translation at the operational level. In Figure 4 the result of this alteration is shown.

4.2.3. Step 3

DPC: Continue further integration of the components.

RQSM: Other requirements for checking the composition are temporal aspects. The requirement rq_i2 states that the input for the portal are gathered from multiple BibTex files. This is included in requirement rq8.

rq8 Input consists of multiple files

DODM: This step focuses on co-ordination patterns. For the creation of the portal multiple BibTex-files need to be aggregated. Therefore BIB2RDF and ISESAME need to be activated in sequence multiple times. This step results in a control construct (not depicted).

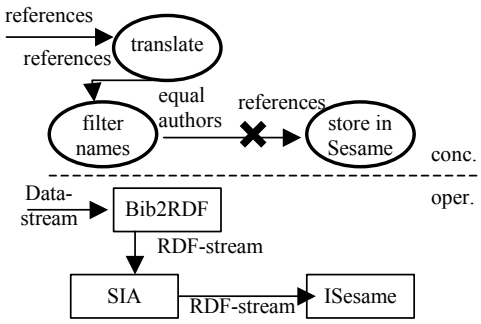

Figure 5. Configuration with error on conceptual data exchange

Further reasoning on behaviour, remaining preconditions and effects are checked for conflicts. There is one remaining conflict with respect to ISESAME, ISESAME has an additional pre-condition: to handle double instances, its input has to be tagged beforehand with the DAML:sameIndividualAs-tag. There is one web-service, which adds these tags for similar persons: SIA. This service needs to be integrated within the composition. Based on the operational in- and output, this service is activated between the BIB2RDF and ISESAME webservice.

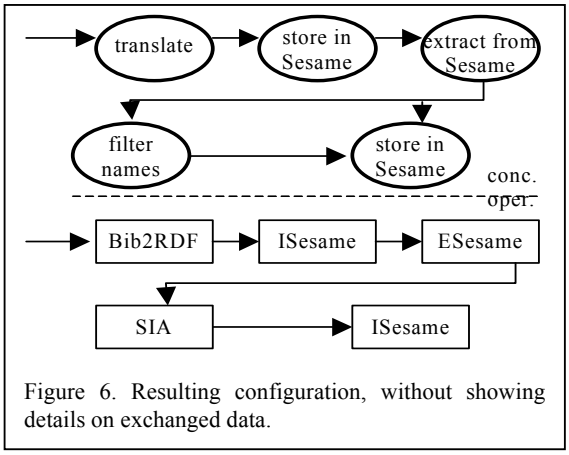

Figure 6. Resulting configuration, without showing details on exchanged data.

However, this results in a conflict on data exchange at the conceptual level. SameIndividualAs does not produce *references* as output, but *equal authors*, as shown in Figure 5. This difference does not show when only considering the XML-datatypes in the Grounding document. The solution to this problem involves multiple steps, which are not further elaborated. The resulting configuration is given, without the information flow for simplicity, in Figure 6. In this configuration, the references are translated and stored in the Sesame repository, until all files are handled, then the double author-names are filtered. The tags on equal author-names and the references are then stored together in a Sesame repository, this is the input for the portal as was requested by the user.

As shown, reasoning on function, data and behaviour is possible using DAML-S descriptions.

5. Discussion and Conclusion

Reasoning about requirements and configuring a set of components to satisfy those requirements is a novel approach to the configuration of web services. Most other work is based on workflow modeling and involves prespecification of a order and combination of WSs by a human making dynamic composition based on changing requirements impossible. Research using reusable components and patterns is not, however, unique to our work. The work by [7], which is also called the Agent Factory, is based on the notion of design patterns to assist the design of multi-agent systems. They have developed the PASSI methodology and an extended-UML CASE tool to help human designers design an agent. In the analysis/design phase, sequence diagrams are used to model protocol descriptions and class diagrams and OCL constraints are used to specify agent interactions and the knowledge agents have. The various diagrams may be compiled to generate an agent skeleton, database of patterns, reports and design documents. The Agent Factory allows the user to choose either the FIPA-OS or JADE platform. While there is much overlap at a superficial level between their work and ours, their approach aims to support developers to design agent systems while our approach is to automatically design agents. The use of the AF for Web services is a further distinguishing feature.

We note the following issues still to be resolved:

- The handling of parallel processes. We have only provided a solution which sequentially activates WSs. DAML-S does not have a means to express coordination of multiple services; DAML-S can only express control patterns within one service.
- The definition of complex services. While processes may be composed and described in the process model using DAML-S, the top level concept is a service and thus a set of services and the relationships between them cannot be

described. Szyperski [15] identifies that, today, services are almost completely self-contained, not revealing any dependencies on other services. This limits the reusability of these web-services in different contexts.

As stated in the introduction, the goal of the work reported in this paper was to review and evaluate the assumptions upon which the AF is based. Through the example, which we are currently implementing we have shown that Agent Factory can be used to automatically configure WS. We chose to test our assumptions using WS as they have many attractive features. First, they fit in the compositional view of our AF, they can easily be treated as agent components. Second, because they employ standard web protocols for interaction they are easy to integrate at the operational level. Further, the use of a semantic language for describing components at a conceptual level is promising. Our key next steps are to complete the implementation, making modifications to the process as necessary, and to further test the approach on various alternative scenarios.

Acknowledgements

The authors wish to thank the project Semantic Web at the Vrije Universiteit (SW@VU), for the usage of their developed web-services, N.J.E. Wijngaards for his work on the Agent Factory. This work is supported by the NLnet Foundation, http://www.nlnet.nl/.

References

[1] Brazier, F.M.T., Wijngaards, N.J.E. "Automated Servicing of Agents" *AISB Journal, Special Issue on Agent Technology*, 1:1 (2001) 5-20

[2] Brazier, F.M.T, Van Langen, P.H.G., Ruttkay, Zs. and Treur, J. "On formal specification of design tasks" *In Proc. of the AAAI Workshop on Artificial Intelligence and Manufacturing: State of the Art and Practice*, AAAI Press, 1994, 30-39.

[3] Brazier F.M.T., Dunin-Keplicz B.M., Jennings N.R., Treur J. "Formal specification of Multi-Agent Systems: a real-world case" In: Lesser V (ed.): *Proceedings of the First International Conference on Multi-Agent Systems, ICMAS'95*. Cambridge MA: MIT Press, 1995. p. 25-32.

[4] Brazier, F.M.T., Jonker, C.M., Treur, J. "Principles of Component-Based Design of Intelligent Agents". *Data and Knowledge Engineering* 41 (2002) 1-28.

[5] Bryson, J., Martin, D., McIlraith, S. and Stein, L.A., Agent-Based Composite Services in DAML-S: The Behavior-Oriented Design of an Intelligent Semantic Web http://www.cs.bath.ac.uk/ jjb/ftp/springer-daml.pdf.

[6] Buhler, P. A. and Vidal, J. M. "Semantic Web Services as Agent Behaviors" In B. Burg, J. Dale, T. Finin, H. Nakashima, L. Padgham, C. Sierra, and S. Willmott, eds., *Agentcities: Challenges in Open Agent Env.*, 25-31. Springer-Verlag, 2003

[7] Cossentino, M. Burrafato, P., Lombardo, S. and Sabatucci, L. 'Introducing Pattern Reuse in the Design of Multi-Agent Systems". *AITA'02 w'shop at NODe02* - 8-9 Oct. 2002 - Erfurt, Germany.

[8] Gamma, E., R. Helm, R. Johnson, J. Vlissides (1995). Design Patterns. Addison Wesley

[9] Lassila, O. "Serendipitous Interoperability", In Eero Hyvönen (ed.): *The Semantic Web Kick-Off in Finland - Vision, Technologies, Research, and Applications*, HIIT Publications 2002-001, University of Helsinki, 2002

[10] McIlraith, S. and Son, T., Adapting Golog for Composition of Semantic Web Services, Proceedings of the Eighth International Conference on Knowledge Representation and Reasoning (KR2002), Toulouse, France, April, 2002.

[11] Ponnekanti, S.H. and Fox, A. "SWORD: A Developer Toolkit for Web Service Composition" *In Proc. of 11th WWW Conf. (Web Eng. Track)*, Honolulu, Hawaii, May 7-11, 2002.

[12] Sabou, M., Richards, D. and van Splunter, S. An experience report on using DAML-S *Workshop on E-Services and the Semantic Web*, Budapest, Hungary, May 2003.

[13] Splunter, S. van, Wijngaards, N.J.E., Brazier, F.M.T., "Structuring Agents for Adaptation" In Alonso, E., Kudenko, D., Kazakov, D. (eds.) *Adaptive Agents and Multi-Agent Systems*, LNAI 2636, Springer-Verlag Berlin. 2003

[14] Staab, S., Benjamins, R., Bussler, C., Gannon, D., Sheth, A. and van der Aalst, W., Web services: Been there, Done that? IEEE Intelligent Systems, Trends & Controversies, 18(1), Jan/Feb 2003

[15] Szyperski, C. *Component Software - Beyond Object-Oriented Programming* – 2nd ed., Addison-Wesley & and ACM Press.

[16] The DAML Services Coalition "DAML-S: Web Service Description for the Semantic Web", *In Proc. of The First Int. Semantic Web Conference (ISWC)*, Sardinia (Italy), June, 2002.

[17] Yang, J. and Papazoglou, M. "Web Component: A Substrate for Web Service Reuse and Composition" *In Proc. of the 14th International Conference on Advanced Information Systems Engineering (CAiSE02)*, May, Toronto, LNCS, Vol. 2348, p21-36, Springer, 2002.

[i] www.stencilgroup.com/ideas_scope_200106wsdefined.html
[ii] http://xml.coverpages.org/bpel4ws.html
[iii] www-4.ibm.com/software/solutions/webservices/pdf/WSFL.pdf, 2001
[iv] www.gotdotnet.com/teaml/xml_wsspecs/xlang-c/default.htm
[v] http://www.zsu.zp.ua/racing/
[vi] See the SW@VU project at http://www.cs.vu.nl/~macklein/SW@VU/
[vii] http://sesame.aidministrator.nl

Intelligent Agent Framework for Modelling the Evolution of Small and Medium Sized Enterprises

Karen Blackmore
School of IT,
Charles Sturt University
Bathurst, NSW, Australia
kblackmore@csu.edu.au

Terry Bossomaier
School of IT,
Charles Sturt University
Bathurst, NSW, Australia
tbossomaier@csu.edu.au

Denise Jarratt
School of Marketing & Mgt,
Charles Sturt University
Bathurst, NSW, Australia
djarratt@csu.edu.au

Keith Nesbitt
School of IT,
Charles Sturt University
Bathurst, NSW, Australia
knesbitt@csu.edu.au

Abstract

Small and medium sized enterprises constitute a major component of the Australian economy. In fact in 2000-2001 they accounted for up to 91% of all businesses and provided 80% of all private sector employment [1]. Therefore many service industries are interested in the growth and potential of the small and medium business sector. However, modelling these enterprises is difficult because of their small size, and individual natures. One largely untried approach is to use agent-based modelling. Agent frameworks have become a powerful tool for modelling complex, interacting systems. This is a result of an agent-based systems capacity to handle nonlinear systems, their inherent flexibility and their ability to learn and adapt as the model evolves.

INTRODUCTION

The importance of small and medium sized enterprises (SMEs) to local, national and global economies is well understood. This is illustrated by the increasing amount of research aimed at understanding aspects of *organisational change* within the SME business sector [2, 3]. In particular this research studies the process of growth and innovation that an enterprise experiences as it evolves over time.

High-Level View

The agent framework presented in this paper focuses on the strategic behaviour of SMEs and the implications of different behaviour types, represented by a fuzzy logic ruleset, to information flows. This research is not an economic pricing model, rather, it is part of a larger project which aims to improve customer relationship management (CRM) practices by enabling more integrated marketing research and improving data mining practices within organisations servicing the SME sector. To this end, customer data on SMEs and measures of the economic environment form the two principle inputs to the over-arching agent-based system (figure 1). These data sources reflect the accent on customer relationships and the fact that SMEs are influenced by economic changes [4, 5]. The current agent-based framework model represents a component part of this over-arching framework. The framework will be extended to utilise commonly captured customer demographic data (about SMEs) that is often available in organisational data warehouses. The environmental condition indicators are also publicly available measures. Of course in the future, one might envision extending our agent-based framework so that mobile "information agents" proactively seek out their own data from electronic sources. However, currently the main agents we have modelled are SME-Agents. SME-Agents are designed to capture the concept, i.e., the needs and the behaviours of SMEs.

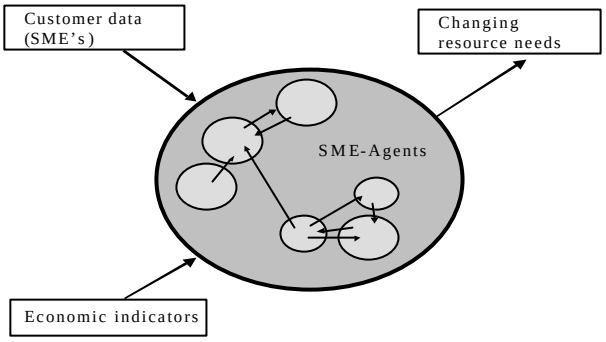

Figure 1. A high-level view of the agent system.

Current Model

As in the real-world, different SME-Agents have different beliefs, desires and intentions. Different businesses adopt different strategies of growth or survival. Some businesses operate in competition, while others may collaborate. SMEs consider not only broad environmental impacts, but also local spatialised competition and demands. For example, a local business may find it difficult to grow beyond its existing customer base. Perhaps, similar businesses may find themselves in direct competition if they are too closely situated. While the need to include spatial interaction is acknowledged, the inclusion of these dynamics will be left for future work.

A key success factor for businesses is the ability to align resources and strategies to changing environments. For example, computer or telecommunication needs change as a result of both environmental factors and the company's changing state in that environment. Importantly, a business may need to also change in response to customer needs. Our agent-based model is designed to allow for exploration of the role strategy and changing customer demands play in the telecommunications needs of an SME. The end goal is to predict changes in the resource needs of SMEs that result from change in the way a business employs strategies to compete under changing environmental conditions and customer demands.

STRATEGIC BEHAVIOUR

In today's business environment (exhibiting changing technology, economy, industry structure and participants, demand and supply), the barriers of economies of scale, differentiation, switching costs and distribution access have become obsolete. Consequently, strategy frameworks that address the fleeting nature of competitive advantage are argued to play a more dominant role [6]. The development of core competencies and capabilities, and strategies drawing on these resources, will be driven by the desired attainment of a future position. This presupposes that senior managers have a view about the future and, that their view is shaped through understanding all the relevant and appropriate developments that will drive the future. More particularly, it implies that their decisions will be shaped by a mental model that results in a consistent pattern of decision making.

Miles and Snow's Typology

Miles and Snow [7] described an organisational strategic orientation theoretical framework, based on the consistency of management decision patterns. This framework was subsequently validated across a breadth of domains, from health care markets [8] to electronic manufacturing [9]. Therefore this framework is adopted in our model as it also provides an appropriate segmentation basis to study resource change decisions.

Miles and Snow [7] define four categories, defender, prospectors, analysers and reactors. The typology views organisational patterns of strategic behaviour as an 'adaptive cycle', characterising behaviour using three strategic 'problem and solution' sets: (1) entrepreneurial problems focussing on the product-market domain; (2) engineering problems centring on the choice of technologies; and (3) administrative problems involving structure and processes. Each of the three problem sets involve multiple dimensions with a total of eleven distinctive strategic dimensions used to characterise the defender, analyser, prospector and reactor strategic types. Prospectors have been demonstrated to emphasise technology leadership, invest heavily in technology and exploit new product and market opportunities. Defenders, on the other hand are conservative, only investing in proven technology directly related to their line of business, producing a constrained product range for a narrowly defined market. Analysers are only willing to invest in new technologies following a detailed investigation of the issues surrounding its application and benefits, while Reactors are characterised by extreme organisational inertia [21, 12, 8]. These distinct behavioural orientations are argued to shape resource change decisions of managers as they respond to information on changes that occur in the economy, technology, industry structure, supply and demand.

Strategies define the purpose of organisations, the competitive domain of firms and the resource commitment these organisations make to achieve and sustain competitive advantage [12, 13, 14]. Hence, developing an appropriate strategy that fits the marketplace is one necessary ingredient for business success, which according to Miles and Snow, is 'achieving fit' between the firm and its environment. In operationalising the business strategy concept, Miles and Snow [7], Porter [15] and Miller and Friesen [16] as well as other researchers have done much in developing empirical and conceptual typologies of strategies. The typology as proposed by Miles and Snow remains one of the most popular approaches for defining and measuring the effectiveness of business level strategy [17]. It has been debated and supported by many researchers over the years [18, 19, 20, 17]. These studies have contributed significantly to the body of knowledge on strategic archetypes. The Miles and Snow typology has been demonstrated to predict 24% of the variance in overall organisational effectiveness [10]. Furthermore, the behavioural categories of this typology have been aligned with strategic aspects of product and service innovation and the degree and nature of market focus [11].

MODELLING AN SME AGENT

Holland [22] describes a complex adaptive system as an "*evolving perpetually novel world where there are many niches with no universal optimum of competitor, where innovation is a regular feature and equilibrium rare and temporary and where anticipations change the course of the system, even when they are not realized*". This description also seems well suited to describing a population of SMEs.

SMEs can also be conceptualised to fit John Casti's working definition of a complex adaptive system [23], comprising a population of "individual agents" who adapt their rules of behaviour over time. This could be interpreted to apply to a population of SMEs or the individuals who comprise them. If descriptions of SMEs are analogous to a complex adaptive system, then it follows that complexity theory may provide an understanding of the dynamic behaviour of SMEs, and assist in predicting changes in individual or populations of SMEs.

SMEs are not a homogeneous population, they vary considerably in size and sector activity, in their ownership, their location and the markets served. Some of the features of their domain are commonly shared, such as interaction with key economic stakeholders, such as banks and government agencies. Businesses operate in a regulated environment, providing at least some of the "rules" of behaviour. Financial resources represent the exogenous "energy", without which activities usually cease. Other resources, such as human and information and communications technology (ICT), are also requirements for operation.

One contribution that complexity theory makes to SME and entrepreneurship research is that it provides for multi-level views of both individual and populations of SMEs. It also provides concepts for making sense of changing patterns in the data. The notions of emergence, bifurcation and symmetry breaking in complexity are all notions of the "natural" formation of structures that behave with

different characteristics from the agents that constitute the structures. This may provide general propositions for why SMEs do not behave exactly like their owners.

It is suggested that the analogy of a complex adaptive system can provide a conceptual framework to understand or illuminate the dynamics of SMEs because:

i. Each business is different
ii. Each has its own "initial conditions" and each incurs a number of "events" in their temporal path.
iii. Given that entrepreneurs are "innovative", then many businesses will operate with their own "rules", as well as complying (more or less) to more general rules. There is a great deal of "replication" in the population as one SME copies another's ideas and government policy encourages SMEs to adopt "best practice".

The agent framework presented in the following section is a step toward a dynamic, multi-level analysis of SMEs at both the individual and population levels. By bringing together empirically validated rules of strategic behaviour typologies in a simulation environment, variations in emergent performance and communication flow can be analysed given differing levels of strategy types and consumer demands.

OVERVIEW OF THE AGENT FRAMEWORK

One of the objectives of this paper is to determine the minimum agent framework required to give rise to the Miles and Snow typology. In order to assess the validity of a fuzzy ruleset against Miles and Snow's strategic typology, a simple agent-based system (Figure 2) was constructed. In this system, SME-Agents operate in an artificial market place using fuzzy behaviour rules based on a subset of dimensions characterised by Defender, Analyser, Prospector and Reactor (DAPR) strategy types.

The model considers a retail scenario, where products are bought by SME-Agents for sale to consumers. The model accounts for only Business to Consumer (B2C) transactions and not Business to Business (B2B) and is parametrised using a chromosone like model (8 bits per parameter). The behaviour of SME-Agents is determined by using a fuzzy logic ruleset, which is discussed in detail in the following section.

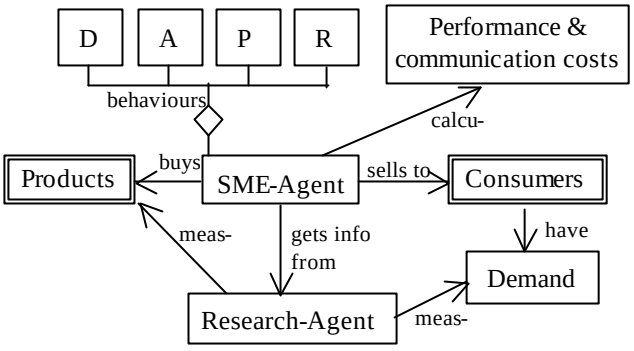

Figure 2. Agent framework with SME-Agents behaviour rules from Miles and Snow's strategic typology.

At each time step, SME-Agents decide whether to obtain customer demand information, how much of which products to buy. The model uses a pure data-push model, that is, consumers are presented with a full product list from which to select from. Changing products and obtaining demand information involve information flow, which is measured and tracked in the SME-Agent's state. A simple measure of SME-Agent performance, calculated by subtracting the amount spent on product from the amount received from sales to consumers, is also maintained in the agent's state.

SME-Agent Behaviour and Performance

The Miles and Snow four strategic types are employed to define the behavioural parameters of SME-Agents. Only the entrepreneurial problems and solutions adaptive cycle component was considered in this framework. This is a valid simplification as the current model focuses only on SME-Agent engagement with products and consumers. The behavioural parameters we model are:

i. Agressiveness (high, medium, low)
ii. ProductMix (high, medium, low)
iii. Awareness (high, medium, low)

SME-Agents maintain state parameters to be used for decision-making. These parameters consist of:

i. Cash level
ii. Stock ID
iii. Stock level
iv. Product longevity
v. Profits from last sale
vi. Average profit, and a
vii. Information flow measure.

A stock ID, level and longevity parameter is maintained for each type of product purchased by an SME-Agent for sale to consumers. The longevity parameter is incremented each iteration of the simulation to indicate the amount of time that an SME-Agent trades in a particular stock item. All trading costs are associated with an information flow.

Products

A simple product set is proposed, which are not agents, and at each time-step SME-Agents purchase one or a number of different products to sell to consumers. SME-Agents are initialised with equal financial resources to purchase products. Products are described using the following parameters:

i. ID
ii. Type
iii. Quality
iv. Cost per unit
v. Cost of entry

Consumer Demand and Growth/Decay

At the beginning of the simulation, the consumer set is initialised with equal demand in all product areas. Consumers are minimal agents with no adaptive behaviour and preferences are recorded using the following parameters:

i. ID
ii. product
iii. quality
iv. price
v. conservatism

In order for an SME-Agent to complete a sale, only the product preference of a consumer is fixed. A perfect match between the quality and price of products for sale and a consumers preferences is sought, however, an "acceptable tolerance" will allow consumers to purchase products closest to their preferences. Consumers are allowed buy requests until satisfied.

The consumer demand in the product areas will vary over time. This will enable a number of simulations using different consumer environment situations to be considered, namely:

1. Static
   In this scenario, consumer demand is fixed.
2. Turbulent
   A random replacement strategy is used to create a turbulent consumer environment. Once a consumer has made a successful purchase from an SME-Agent, the consumer are deleted from the set and randomly replaced.
3. Fashion/trend
   Trends in consumer demand are modelled using a growth and decay strategy. Each time a customer makes a successful purchase that customer will be deleted and replaced with a mutation. Thus the level of customers in the model remains constant, however, the types, quality and price of products they are willing buy vary in a trending scenario.

The conservatism parameter captures the preference a consumer has for buying products from an SME-Agent with longevity in a particular product. For example, a highly conservative consumer has a preference toward SME-Agents who have been selling the product of interest for the greatest amount of time, as measured by the stock longevity parameter. Conservativeness is measured as high, medium or low. High conservatism indicates that a consumer will rank by longevity then price, medium ranks by price followed by longevity, and low considers only price irrespective of longevity. In all situations, consumers will consider quality as the third ranking criteria by which to select SME-Agents to purchase products from.

Other Agents

The Research-Agent maintains information on consumer demands and changing trends. The Research-Agent maintains:

i. List of consumers and current preferences
ii. History of consumers and preferences

SME-Agents decide whether to poll the Research-Agent for information on consumer demands based on their behavioural rules. Obtaining information from the Research-Agent involves a communication flow and incurs a financial cost, the amounts of which are dependant on the type of information requested by an SME-Agent. The communication flow measure resulting from an information request is maintained in each SME-Agents state.

Fuzzy Logic Ruleset for SME-Agents

Through the use of fuzzy logic, rules can be organised and written to address the uncertainty and imprecision of business strategic decisions.

Decisions

Decisions are made based on the behaviour rules of SME-Agents and result in differentiations in information flows and profits. The outputs of defuzzification are crisp and relate to the following decisions:

i. ProductMix (add, delete)
ii. Buy (more, less)
iii. Research (getInfo, noInfo)

At various stages throughout the simulation, SME-Agents will make decisions about whether to add or delete products from their product mix, whether to buy more or less products in their chosen product mix and whether to buy research information about customers.

Rules of Engagement

The fuzzy rules aim to reproduce the Miles and Snow typologies. SME-Agents will evaluate the rules in the context of the current product mix, customer demand information and profits from previous sales. The following outlines the fuzzy ruleset and the implied strategy types.

Information

If Awareness = High THEN Research = getInfo ? Prospector

If ProductMix ? Low AND Awareness = Medium THEN Research = getInfo WHEN any profits < Avg ? Analyser

If ProductMix = Low AND Awareness = Medium THEN Research = getInfo WHEN any profits < Avg ? Defender

If Awareness = Low THEN Research = getInfo WHEN all profits < Avg ? Reactor

Buying and ProductMix

If Agressiveness = High AND ProductMix = Low THEN Buy = more WHEN profits >= Avg ? Defender

If Agressiveness = High AND ProductMix = Low THEN Buy = less WHEN profits < Avg AND customer demand >= Avg ? Defender

If Agressiveness = High AND ProductMix = Low THEN ProductMix = Add WHEN profits < Avg AND customer demand < Avg ? Defender

If Agressiveness ? Low AND ProductMix = High THEN ProductMix = add AND Buy = more WHEN profits >= Avg ? Prospector

If Agressiveness ? Low AND ProductMix = High THEN ProductMix = add AND Buy = less WHEN any profits <= Avg ? Prospector

If Agressiveness ? Low AND ProductMix = High THEN ProductMix = add AND ProductMix = Delete WHEN all profits <= Avg AND consumer demand < Avg ? Prospector

If Agressiveness ? Low AND ProductMix = Medium THEN Buy = more WHEN Profits >= Avg ? Analyser

If Agressiveness = Low AND ProductMix = Medium THEN ProductMix = add AND Buy = more WHEN profits >= Avg ? Reactor

If Agressiveness = Low AND ProductMix = Medium THEN ProductMix = delete AND Buy = less WHEN profits < Avg ? Reactor

The Miles and Snow typology differentiates strategies along the aggression, product mix and research dimensions, which are reflected in the fuzzy ruleset. Defenders are characterised by a narrow and carefully focussed product-market domain, which they aggressively defend. They exhibit prominence in their product market(s) and cautiously monitor activity in their domain. Prospectors can be conceptualised along an opposing axis to defenders (Figure 3). They are characterised by a broad and continuously expanding product-market domain, in which they are active initiators of change. They aggressively search for new opportunities. Analysers exhibit a mixture of both the defender and prospector behaviours. Analysers are characterised by a segmented and carefully adjusted product-market domain, maintaining core product(s) whilst "prospecting" in others. They are calculated followers of change and employ competitively oriented and thorough surveillance. Conventionally, reactors have been presented as a 'residual' type, lacking consistent characteristics. They exhibit uneven and transient product-market domain behaviour, characterised by opportunistic thrusts and coping postures. Reactors employ only sporadic and issue dominated surveillance [7].

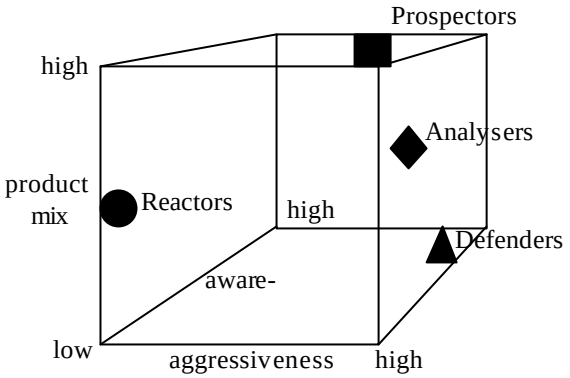

Figure 3. Characteristics of strategic types

The Simulation

1. Initialise product set, consumer set, SME-Agents and simulation count. Select consumer environment scenario.
2. Create random list of SME-Agent and Consumer IDs.
3. Research-Agent compiles list of consumer preferences. If simulation count ? 0, copy current consumer preferences to history list then create a list of all consumer IDs in the current simulation and their current preferences.
4. SME-Agents obtain information on products and can choose to obtain consumer demand information, depending upon rules (Decision: Research).
   a. Take the first SME-Agent ID from the randomised list and send product information request to Products. Update information flow parameter.
   b. Evaluate SME-Agent behaviour.
   If decision = obtain information, request consumer information from Research-Agent, update the cash level and communications flow parameters, else continue. Repeat (b) and (c) for all SME-Agent ID's in the randomised list.
5. SME-Agents buy products, update cash level and stock level (Decision: ProductMix, Buy). Take the first SME-Agent ID from the randomised list and determine SME-Agent behaviour. Update the SME-Agent cash level, stock level and communications flow parameters. Repeat for all SME-Agent IDs in the randomised list.
6. Update randomised list of SME-Agent IDs to include product information.
   a. Take the first SME-Agent ID from the randomised list and add product ID, amount, quality, and price variables to the randomised list.
   b. Update the product ID, longevity, amount and price variables in the randomised list from the matching SME-Agent. Update the quality variable in the randomised list from the Product details.
   c. If more than one product ID, add a row to the randomised list for each product ID. Repeat for all SME-Agent IDs in the randomised list.
7. Consumers obtain information on products for sale and select which products to buy from SME-Agents.
   a. Take the first consumer ID from the randomised list then search the randomised SME-Agent list for consumer preference and SME-Agent product for sale match. When a match is located, SME-Agent details are added to a temporary list of prospective sales for that consumer.
   b. List of prospective sales are sorted according to closest match of price, longevity and quality to consumers preference using the ranking criteria of the consumers conservatism measure.
   c. Sales occur, SME-Agents adjust cash and stock levels. Select first record in temporary list of prospective sales, reduce stock level of SME-Agent, add the value of sales to the cash level and retain the SME-Agent ID, with adjusted stock details, in the randomised list for future sales.
8. Consumer is replaced/reset depending on chosen consumer environment conditions (i.e. static, turbulent or fashion/trend) and simulation count is incremented.
9. Continue steps 2-8 until end.

DISCUSSION

When implemented, the agent-based model presented in this paper represents SME strategic behaviour and measures associated information flow. Simulations with different populations of SME-Agent strategy typologies and consumer demand scenarios will be used to assess variations in and responses to information flow. The model will be extended to incorporate:

1. emerging and evolving products;
2. other environmental conditions such as perceptions of the broader economic climate; and,
3. additional dimensions of the Miles and Snow typology, such as those in the engineering problem set, focusing on the adoption of technologies.

Finally, the proposed model, and its subsequent extensions, may provide insights into the structure of SME populations and the flows and responses to information within them. An analogy may exist between the flow of information, considered as a resource, and the interpretation of that information in a population of SMEs buying and selling products in a competitive environment, and the structure of ecological communities, commonly represented by food webs [24]

REFERENCES

[1] Australian Bureau of Statistics (2001). *Small Business in Australia (cat. no. 1321.0)*. (electronic). Available at http://www.abs.gov.au [18 July 2003].

[2] McMahon, Richard G. P. (2003) An exploratory study of under- and over-investment amongst manufacturing SMEs from Australia's business longitudinal survey. . *International Small Business Journal* **21** (1):29.

[3] Graham, Peter G. (1999) Small business participation in the global economy. *European Journal of Marketing* **33** (1/2):88

[4] Davidsson, P. and Henrekson, M. (2002) Determinants of the prevalence of start-ups and high-growth firms. *Small Business Economics* 19 (2):81

[5] Kirk, D. (1998) Entrepreneurial context and behaviour in SMEs An investigation of two contrasting manufacturing firms. *International Journal of Entrepreneurial Behaviour & Research* 4 (2):88

[6] Chakravarthy, Bala (1997) "A New Strategy Framework for Coping with Turbulence" *Sloan Management Review* Vol 38 (2) pp. 69-82

[7] Miles, Raymond E. and Snow Charles C. (1978) *Organizational Strategy, Structure and Processes*. McGraw-Hill, New York.

[8] Conant, Jeffrey S; Mokwa, Michael P; Varadarajan, P. Rajan (1990) Strategic Types, Distinctive Marketing Competencies and Organizational Performance: A Multiple Measures-Based Study. *Strategic Management Journal*, 11(5): 365-383.

[9] Smith, Ken G; Guthrie, James P; Chen, Ming-Jer (1989) Strategy, Size and Performance. *Organization Studies*, 10(1): 63-81.

[10] Doty, D Harold; Glick, William H; Huber, George P. (1993) Fit, equifinality, and organizational effectiveness: A test of two configurational theories. *Academy of Management Journal*, 36(6): 1196-1250.

[11] Floyd, Steven W; Wooldridge, Bill (1992) Middle Management Involvement in Strategy and Its Association with Strategic Type: A Research Note. *Strategic Management Journal*, 13(Summer): 153-167.

[12] Chandler, A. D., Jr. (1962) *Strategy and Structure: Chapters in the History of American Industrial Enterprise*, Cambridge, Massachusetts: MIT Press.

[13] Ansoff, H. I. (1965) *Corporate Strategy*, McGraw-Hill.

[14] Mintzberg, H. 1987. 'Five Ps For Strategy'. In Mintzberg, H. and Quinn. J., 1991. *The Strategy Process*. Prentice-Hall, Englewood Cliffs, N.J. 12-19

[15] Porter, M. 1985. *Competitive Advantage*. The Free Press. New York

[16] Miller, D., and P.H. Friesen (1983), Strategy-Making and Environment, The Third Link, *Strategic Management Journal*, 4, 221-235

[17] Zahra, S. and J. Pearce (1990), "Research Evidence on the Miles-Snow Typology", *Journal of Management*, 16, 751-768

[18] McDaniel, Stephen W. and James W. Kolari (1987), "Marketing Strategy Implications of the Miles and Snow Strategic Typology", *Journal of Marketing*, 51, 19-30

[19] Snow, Charles C. and Lawrence G. Hrebiniak (1980), "Strategy, Distinctive Competence, and Organizational Performance", *Administrative Science Quarterly*, 25, 317-335

[20] Hawes, J. and W. Crittenden (1984), "A Taxonomy of Competitive Retailing Strategies", *Strategic Management Journal*, 5, 275-287

[21] Dvir, Dov; Segev, Eli; Shenhar, Aaron (1993) Technology's varying impact on the success of strategic business units within the Miles and Snow typology. *Strategic Management Journal*, 14(2): 155-161.

[22] Holland, J. H. (1995). *Hidden order: How adaptation builds complexity*. New York: Addison-Wesley.

[23] Casti, John L. (1997) *Would-be worlds: How simulation is changing the frontiers of science.* New York: John Wiley & Sons.

[24] Garlaschelli D., Caldarelli G. & Pietronero L. (2003) Universal scaling relations in food webs. *Nature* 423:165-168.

Scrutable Programming By Demonstration for Email Management

Alex C. P. Lai
University of Sydney
Sydney, NSW, Australia
Email: imax_lai@hotmail.com

Abstract

Information overload is an increasing problem. A significant contributor is the large amount of email that people receive. It will be valuable if users can have assistance in managing email. The first stage in such a process is the classification of mail messages, which need to be treated alike into groups.

The IEMS [4] work is based upon machine learning for defining the rules. This project presumes that the user wishes to make use of this approach but then should be easily able to tune the rules. We also assume users want to be able to scrutinize the whole process so that they feel in control of the filtering rules or other mechanisms used to predict the classification of their mail.

1. Introduction

This paper describes the IEMS (Intelligent-Electronic Mail Sorter) [4] project which has the broad goal of improving our understanding of how to build systems which can assist users in managing email. In particular, we discuss work on automated support for classifying messages into appropriate folders. Choice of folder may depend on many factors including aspects such as the sender and nature of the email. For example, email from your supervisor may be filed into your "supervisor" folder.

Users can be assisted in the task of classifying email if they make use of filtering rules available within many widely used mail interfaces such as Netscape Messenger and Microsoft Explorer. These rules can be expressed in terms of strings appearing in different parts of an email message. To handle an email item, the rules are evaluated in order and the first rule that applies to the item triggers the email client to move the message into the associated folder.

The difficulty with rules is that the process of a rule is cognitively demanding and there is a real, potentially unacceptable risk of misfiling mail. Generally, users seem to avoid customizing software [8] [6]. In a recent study of user's management of email, the authors observe "Most of our users (17 interviewees, or 60 percent) say they don't use filters. Several simply haven't figured out how to use them, suggesting that either filters need to be simpler to use or that they are not that useful"

The motivation for rules is based on first, a belief these rules will relatively easy for end users to understand and modify, second, a suspicion that learning methods alone are not an adequate solution for categorization problems of this type. It seems likely that instead some mix of automatically and manually constructed classifiers will be necessary to account for the fact that both the user's interests and the distribution of message change (sometimes quite rapidly) over time. In many cases, the users themselves might have a better idea of the rules that would be appropriate for the applications they would like to build, so it would be useful for them to be able to specify new rules. For instance, at the time of this writing, the rules above may be accurate for messages I have received over the last few months; however at some point it will certainly become appropriate to modify it by replacing "Tutorial No: 05" with "Tutorial No: 06" and "Tutorial No: 5" with "Tutorial No: 6".

Our solution is to build a SPBD as an intelligent rule explorer that reduces the cognitive burden and the time required for easily understanding and customizing rules, to solve email classification into folder automatically in sort time. As we know rules make decisions based on a small number of keywords. Rules do not base classification decisions on word frequency, only on the presence or absence of a word. A problem with PBD has always been how to represent the rules to users, and how the users can come to feel in control the whole processes is becoming our major problem.

In this paper we will introduce our approach to solve the above problem. We use a system where the users can accept the rules given or view a pop up interface which gives them the opportunity to scrutinize the rule, and how it was derived, and then to modify it or to leave it as predicted by our system. It offers ease of use and flexibility to cater to users who wish to modify rules.

2. Previous Works

Most of the current systems have used simple rule-based inferencing for their generalizations. For example, the early Peridot system, developed in 1987 to create widgets by example uses about 50 hand-coded rules to infer the graphical layout of the objects from the example [9]. Each rule has three parts, one for testing, one for feedback, and one for the action. The test part checks the graphical objects to determine whether they match the rule. For example, the test part of a rule that aligns the centers of two rectangles checks whether the centers of the example rectangles are approximately centered. Because these rules allow some sloppiness in the drawing, and because multiple rules might apply, the feedback part of the rule asks the user whether the rule should be applied. For example, Peridot might ask something like: " Do you want the selected rectangle?" If the user answers yes, then the action part of the rule generates the code to maintain the constraint. The subsequent systems have used similar mechanisms, though often without the explicit list of rules we used in Peridot. For example, Tourmaline, which formats documents form example, contains rules that try to determine the role of different parts of a header in a text document, such as section number, title, author, and affiliation, as well as the formatting associated with each part. The results are displayed in a dialogue box for the user to inspect and correct.

Results have shown PBD has very high performance to solve classification problems based on rule-based inferencing, from different users (especially novices) by a series of very simple actions. As we know the purpose of PBD's characteristic is that it is easily understood. This characteristic led us alternative approach to encourage the users to solve email classification problem.

A variety of approaches have been taken to address the problem of automating email classification. Most of these can be split into two groups: filtering junk email; and general classification of email. At first glance, one might presume email classification was simply a special case of text categorization. However, even the seemingly similar work on the Reuters-21578 dataset is quite different from learning how to predict an individual user's classification of their own mail.

In any instance, it is desirable that any learning algorithm should produce useful results quite quickly, with small amounts of data: in our case, the learning is for a single user's filtering preferences and it is desirable that rules for automating this should be learnt from small numbers of example.

Further, the classification task may change with time. Changes in classifications might be due to changes in the user's activity: for example, a user who teaches a course in programming in one semester may not be involved in that type of activity in the next semester. This affects the task of a learner since it needs to recognize such changes. There are also many other changes that affect classifications. For example, if the user's supervisor changes or other personnel at work change their roles, a learner will need to adjust its classifications.

We note two other important aspects of this domain: user differences and differences in the difficulty in learning to predict the categorization for different mail classes. We know that different people use quite different mail management strategies, as noted, for example in [6]. We would expect that it is easier to learn the classifications applied by some users than would be the case for others.

On the matter of the varying difficulty of learning an individual users' different mail classes, Machine Learning and Information Retrieval approaches have demonstrated good performance can be achieved on spam/junk email. For example, SpamCop [10], using a Naïve Bayes approach achieved accuracy of 94%. Sahami *[14]* applied a Bayesian approach and achieved precision of 97.1% on junk and 87.7% on legitimate mail and recall of 94.3% on junk and 93.4% on legitimate mail. Katirai (1999) used a genetic classifier and its best run overall achieved a precision of 95% and a recall of 70%. Androutsopoulos *[1]* compared Naïve Bayes with a keyword approach. The keyword approach uses the keyword patterns in the anti-spam filter of Microsoft Outlook 2000 (which they believe to be hand constructed). They reported the keyword approach achieved precision of 95% and the Naïve Bayes approach 98%. On recall the corresponding performance was 53% and 78%. Androutsopoulos *[1]* also explored a memory based learning approach IiMBL (a simple variation of the K-Nearest Neighbour) showing similar performance to a Naïve Bayes classifier. Provost *[12]* also evaluated Naïve Bayes, comparing it with the RIPPER algorithm, showing 95% accuracy after learning on just 50 emails while RIPPER reached 90% accuracy only after learning on 400 emails.

One fairly strong result is described by Cohen *[3]*. He used the RIPPER learning algorithm to induce rules and reported 87%-94% accuracy. He also explored TF-IDF, and achieved 85%-94%. He observed that the rule based approach provided a more understandable description of the email filter. The iFile naïve Bayes classifier [13] was made available to several users to test on their own mail and this gave 89% accuracy. Grutlag (2000) assessed a Linear Support Vector Machine (SVM), reporting results from 70% to 90% correct and with the Unigram Language Model, 65% to 90%. They compared this against TF-IDF where they achieved 67% to 95%, depending on the store of email used.

The more general categorization task achieves weaker results than the levels achieved for two-category spam filtering employed by various researchers. Agent [2] explored learning in a two-class case, this time 'work' versus 'other'. Boone used a hybrid approach with TF-IDF to learn useful features and then both neural networks and nearest neighbour approaches. This gave 98% accuracy on

a datase where the standard IR approach had 91% accuracy.

This poorer result for general classification is unsurprising: useful email classification involves a user defining the class or classes within which they want to store a piece of email and this is a far less well defined task than distinguishing spam. When users make these classifications, there are many complex issues which define the process. For example, some users classify mail on the basis of the time by which they need to act upon it. Some classify mail according to the broad subject area as it relates to their work. In fact, the results summarized above seem very high for any realistic scenario where the user might have modest numbers of mail items in many of their mail folders.

The work described above does suggests that automated classification should be able to operate usefully in helping users create classification mechanisms for their email. The above work also indicates that some folder classifications will be far easier than others. It seems fruitful to explore approaches that can learn at least some classifications quickly. Even more importantly, it seems likely that a useful learner should be able to tell the user how well it performs so the user can decide whether that level of performance is good enough.

Previous work also suggests the need to build these classification mechanisms into an interface which proposes classifications rather than automatically acting on the mail. For example, the work on MailCat [15], using a TF-IDF approach initially had error rates of 20% to 40%. Since this was considered unacceptable, they took a different approach: MailCat recommended its three best predicted folders so that the user could archive email to one of these with a single click. This improved performance to acceptable levels.

Since several approaches seem to achieve good results in some studies, we can afford to explore the usefulness of a range of approaches that are simplest to explain to the user. Then the user should be able to understand any proposed classification rule and maintain a sense of control. This is the direction taken by Pazzani *[11]* who reported a study where users where asked to assess their preferences for different approaches for representing email filtering rules.

Our work is similar to previous work as PBD approach, and machine learning for defining the rules. The significant part of PBD is allowed user to explore the whole process and adjust the rules defined by the machine learning such as TFIDF, Sender, Keywords, DTree, and Naïve Gayes. After processed, it performs prediction as the presence or absence of a word.

3. Overview System

During our exploration, we found that there were many types of email client around the world, most of which come with email filtering (Microsoft Outlook, Hotmail, etc). Unfortunately, not many users apply this technology to deal with email classification problems. This result has been found in previous research. On the other hand, there are many researchers who believe that rule is a best solution to the issue of junk and email classification. Thus, a method to encourage users to customize and understand filter rules is fast becoming essential.

Cohen *[3]*, found that the problem with the use of keyword-spotting rules is based on first, a belief these rules were relatively easy for end users to understand and modify, and second, a suspicion that learning methods alone are not an adequate solution for categorization problems of this type. It seems likely that instead, some mix of automatically and manually constructed classifiers will be necessary to cater for the fact that both the user's interests and the distribution of messages change (sometimes quite rapidly) over time. For instance, at the time of this writing, the rule set above may be accurate for messages I have received over the last few months; however, at some point it will certainly become appropriate to modify it by replacing "Assignment No: 05" with "Assignment No: 06" and "Assignment No: 5" with "Assignment No: 6".

Our solution to the above problem is to combine two existing techniques: PBD and machine learning for defining the rules. In previous approaches in PBD, users demonstrate algorithms to the computer by operating the computer's interface just as they would if they weren't programming. The computer records the user's actions and can then reexecute them later on different inputs. PBD's most important characteristic is that it is accessible to everyone. PBD is not much different from or more difficult than using the computer normally. This characteristic led us to consider PBD as an alternative approach to infer the rules. This is a portion of work from the iems approach is based upon machine learning for defining the rules. We presume that the user wishs to make use of this approach but then should be easily able to adjust rules. We also presume the user wants to be able to explore whole process so that they feel in control of the filtering rules, or other mechanisms used to predict the classification of their mail.

Learners considered

The system of IEMS *[4]* has implemented in JAVA 1.3.1, which allows it to cross over to different platforms. We have explored the whole system, identified some of the most important classifications which include class of Gui, Store, RunLeanrer, LearnerSender, LearnerKeyword, LearnerTFIDF, MultiSet, and InvertTable. The Gui classification is to perform the graphical user interface, and convert user inputs to the relevant system event; The Store class is used to maintain the store

of all the messages, including training and classification; RunLearner is used to control which training algorithm is to be used, ie. Sender, keyword, or TFIDF algorithm; The class of LearnerTFIDF is going to train the set of folder used for learning and classification using the TFIDF algorithm. The classify function uses the standard first order classifier and places mail into proper folder. The induce function is going to train the set of folders used for learning. The reason function explains in word the reason for the particular classification, such as the particular mail message contains some keywords, that should be classified into a particular folder. The above functions must work with invertTable class; The class of InvertTable works in conjunction with the LearnerTFIDF class. When the "Next" button is enabled, this class evaluates the SIM4 similarity score of each of the folder with the next message and guesses the folder with the highest score for that message. The MultiSet class keeps track of the count of each word in a given message. It uses a HashMap to store "word as integer v.s. count" entries. Used by the various learner classes; The class of LearnerKeyword is going to train the set of folders used for learning and classification. The classify function uses the standard first order classifier with the hypothesis induced by the learner. It should place mail message into the proper folder. The reason function explains in word the reason for the particular classification; The class of LearnerSender is going to train the set of folders used for learning and classification. The main purpose is to look at the sender of email messages. A rule for each sender is created and this rule places anything new from that sender into the most commonly used folder they had been previously placed. The classify function uses the standard first order classifier and places mail into proper folder. The induce function is a simple hypothesis based on the Sender to achieve the goal. Note that the hypothesis is given in first order form. The reason function shows the clause as reason for the particular classification.

We would like to show a very high level description of a new algorithm as below, which would be able to accomplish our goal. See the Figure 1.

Figure 1. High level description of a new algorithm (SPBD)

Once a user has read a message, there are two possible courses of action. If they are happy with the classification, they can simply click on the Archive button. This is at the top left of the screen. This moves the message into that folder. In the case of the current message shown in Figure 2, the Archive button would move it to the PChardware folder.

Figure 2.

The other possibility is that the user is not happy with the classification. In that case, the user simply selects the MoveTo button followed by the name of the folder in the left panel. This moves the message to the correct folder. Meanwhile, it pops up the scrutable interface which tries to explain the rules particularly in highlighting some keywords, and waiting user to adjust the rules if they feel confident. This task is trying to encourage users to understand and adjust rules. In the case of the current message shown in Figure 3.

Figure 3.

This interface should help users to understand and customize filter rules faster, as well as encourage users to get involved with email classification tasks. If the system makes the correct classification, the user simply accepts it with a single click. If the system is wrong, the user does the sort of classification task (particular in adjusting rules) they would have had to do anyway. This should significantly reduce the cost of creating a filter rule while improving the accuracy for email classification.

4. Empirical Results

Below we describe the experiments that have been done so far. First, we conducted a 20 minute experiment and compared experience and non-experience users to see whether they could undertake the same task (creating a rule) or not. Second, we conducted a 4 month experiment and compared the Microsoft Outlook and iems system to see which one is easier to manage in terms of users email account. The last was a 4 month experiment conducted to see whether reconstructing the rules was a difficult task or not should disaster occur.

Experiment 1

We conducted this experiment in 20 minutes, setting up 10 computers with fully installed iems system, at a university computer laboratory. We arranged two groups called Group A, & Group B. Each group had 5 members, all students from university. We asked both groups to create a rule and compared how much time they took to customize a rule.

Group A had some experience in customize rules for email classification and group the emails into folders. Group B has no idea about rules, but they knew how to group the emails into folder.

From our observation, we found that most Group B's member only run the system directly without thinking, and they found that the system help them to predict a folder for each email. They could identify error of prediction from some emails, and the system enabled them to see the result of how system has been done so far, especially in highlighting some of most important keywords in green, based on the machine learning result and what the user input manually. Some users tried to add/delete some of keywords and clicked on the confirm button. They tried to test the system in order to see the different result produced.

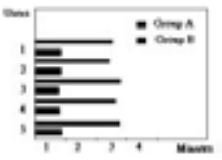

Figure 4.Group A & Group B

From the results, we believe that most Group B's members were able to create a rule in an average of 3 minutes. See Figure 4. Group A had good results as well, they could customize a rule on average in under 1 minute. It is very clear that both groups can perform and feel confident in customizing a rule for email classification in very a short time.

After this test, we gave them a questionnaires. The feedback was very positive. We found the Group A members were very happy with the SPBD technology as they felt it was easy to turn the rules, and believe they could customize a new rule in very a shout time. Group B members enjoyed creating a rule, because they could use their natural ability to identify error prediction easily. Meanwhile, they could change the rules as naturally without any stress.

Experiment 2

We set up another experiment, and conducted it over 4 months. First we looked at 10 users from university lectures. Currently they use Microsoft outlook filter to classify email into folder. The average amount of emails received in each day was 69 messages. We force them to use iems system to classify the emails, and then we compared the results to see which one gave a better performance.

After 3 months, we found very positive result such as the members continuing to use iems system to receive the emails from students and other staff. The reason given was that they could create/tune the rules in a very short space of time and only the system only required simple actions, compared with Microsoft Outlook.

Experiment 3

This experiment was conducted over 4 months. First we asked 10 users from university lectures to join our experiment. These students had been attacked by computer disaster, such as viruses, hard drive fault and operating system failure or other effects. They also had experience using Microsoft Express filters and know how to use rules to file emails into folders automatically. We asked them to use our new iems system instead of their current system.

After 4 months, we found very positive answers. They found iems system very powerful in creating rules in a very short time. They didn't feel that the system required much effort to use and they believed that if a disaster should happen again, they would not worry about re-creating the rules. One thing they worried about was how to back up the email files and it would seem that this is becoming another important task.

5. Conclusion

The SPBD approach is an easy-to-use personal assistant that helps users create a rule in a way more natural to them to solve their email classification problems. SPBD approach makes very few demands on users; they have nothing extra to learn when creating the rules and the only thing required is their natural ability. Users can identify the wrong prediction easily and move to the mail to the correct folder. Meanwhile it pops up with an interface to provide details and to ask them to modify it if

necessary. In the future, if the system detects a similar email coming in, it will predict a folder for this email. Users are required to do a final confirmation such as clicking on Achieve button.

The experiment results are very positive, as previous discussed. Experience and Non-Experience users can do the same task after 3 minutes. Some who have experience using Microsoft Outlook filters to classify their email into folder changed email reader from Microsoft Outlook to IEMS after 4 months. From the other experiment result, we see some are worry about. After 4 months, they believe this is the right technology to assist them in recovering rules in a very short time. This amounts to a significant qualitative enhancement that is likely to encourage users to file their mail using email filter by naturally ability.

While IEMS was developed for electronic mail the same technique can easily be used to organize other types of electronic documents such as disk files, audio, bookmarks, recordings, and other text-based documents that are placed into a hierarchy of folders.

ACKNOWLEDGMENTS

We would like to thank the people who contributed their email archives enabling us to conduct the expirical study. We also thank the reviewers for their valuable recommendations for improving this document.

References and Citations

[1] Androutsopoulos, I., Koutsias, J., Chandrinos, K., & Spyropoulos, C. An experimental comparison of naïve Bayesian and keyword-based anit-spam filtering with personal e-mail messages. Proceedings of the 23rd annual international ACM SIGIR conference on Research and development in information retrieval IN, 2000.

[2] Boone, G. Concept features in re:agent, an intelligent email agent. Second International Conference on Autonomous Agents, 1998.

[3] Cohen, W. Learning rules that classify e-mail. Papers from the AAAI Spring Symposium on Machine Learning in Information Access, pp. 18-25, 1996.

[4] Crawford, E., Kay, J., & McCreath, E. Automatic induction of rules for e-mail classification. In Proceeding of the Sixth Australiansian Document Computing Symposium, coffs Harbour, Australia, 2001.

[5] Cypher, A. Watch What I Do: Programming by Demonstration. MIT Press, Cambridge, Mass., 1993

[6] Ducheneaut, N., & Bellotti, V., Email as habitat: an exploration of embedded personal information management. Interactions, 8, 30-38, 2001.

[7] Lau, T., Weld, D. S., Programming by demonstration: An inductive learning Formulation, Intelligent User Interface, 145-152, 1999.

[8] Mackay, W., Triggers and barriers to customizing software. CHI'91 Conference on Human Factors in Computing Systems (pp. 153-160). New in Computing System. New Orleans, Louisiana. 1991.

[9] Myers, B. Creating user interfaces using programming by example, visual programming, and constraints. ACM Transact. Program Lang, Syst. 12, 2, 143-177, 1990.

[10] Pantel, P., & Lin, D., Spamcop: A spam classification & organization program. Proceedings of AAAI-98 Workshop on Learning for Text Categorization, (pp. 95-98), 1998.

[11] Pazzani, M. Representation of electronic mail filtering profiles: A user study. Proc. ACM Conf. Intelligent User Interfaces. ACM Press, 2000.

[12] Provost, J. Naïve-bayes vs. rule-learning in classification of email, 1999.

[13] Rennie, J. Ifile: An application of machine learning to e-mail filtering. KDD-2000 Text Mining Workshop, Boston, 2000.

[14] Sahami, M., Dumais, S., Heckerman, D., & Horvitz, E. A Bayesian approach to filtering junk email, AAAI-98 Workshop on learning for Text Categorization IN, 1998.

[15] Segal, R., & Kephart, M. Mailcat: An intelligent assistant for organizing e-mail. Proceedings of the Third International Conference on Autonomous Agents (pp. 276-282). Seattle, WA, 1999.

[16] Smith, D., Cypher, A. and Tesler, L., Novice programming comes of age, Communication of the ACM, 43(3):75-81, 2000.

MEDICAL APPLICATIONS II

(This page left blank intentionally)

KEYNOTE PRESENTATION

Hilbert, Poisson and other Relationships

Professor A G Constantinides
Imperial College London

The *Hilbert relationships or transforms* are well known and extensively used in Signal Processing. However the corresponding *Poisson relationships or transforms* are not as extensively known or used. In essence both Hilbert and Poisson transforms are concerned with minimum phase systems. The *Hilbert transforms* solve the following two problems

- Given the amplitude response, perhaps as a list of possibly equidistant numbers, to determine the phase response
- Given the phase response to determine the amplitude response

The *Poisson transforms* solve the following four problems

- Given the amplitude, or phase response, perhaps as a list of possibly equidistant numbers, to determine the phase or amplitude response possibly at some other contour

There are significant links between Hilbert and Poisson transforms and important extensions to both.

The talk will be focused on the development of the fundamental relationships involved in these transforms and their extensions. Some applications will also be outlined.

(This page left blank intentionally)

Detection of Brain Activity for Averaged Multiple-Trial Magnetoencephalography Data

Yoshio Konno
Sophia University
7-1 Kioicho, Chiyoda-ku, Tokyo, Japan
yo-konno@sophia.ac.jp

Jianting Cao
Saitama Institute of Technology
1690 Fusaiji, Okabe, Saitama, Japan
Brain Signal Processing, RIKEN
2-1 Hirosawa, Wako-shi, Saitama, Japan

Takayuki Arai
Sophia University
7-1 Kioicho, Chiyoda-ku, Tokyo, Japan

Tsunehiro Takeda
Graduate School of Tokyo University
7-3-1 Hongo, Bunkyo-ku, Tokyo, Japan

Abstract

Treating averaged multiple-trial data is a common approach in recent papers for applying independent component analysis (ICA) to neurobiological signal processing. Although averaging increases the signal-to-noise ratio (SNR), important information is lost, such as the strength of an evoked response and its dynamics. Alternatively, when averaging few-trial data, not much information is lost, but SNR is very poor. In this paper, we deal with averaged data of few as well as of many trials, and we demonstrate that not only the location, but also the direction vector and dipole moment of evoked fields (EFs) can be obtained by applying our method, even when the number of trials is small.

1. Introduction

Many researchers have applied independent component analysis (ICA) to electroencephalographic (EEG) or magnetoencephalographic (MEG) data to determine the behavior and localization of brain sources [1, 2, 3, 4, 6]. However, because the magnetic field of brain signals is weak, spontaneous and environmental noise makes it difficult to recognize brain signals in recorded data.

The most widely used technique for reducing instrumental and environmental noises, and for identifying the behavior and location of activities of interest, such as evoked field responses, is to take an average across many stimulation trials. In fact, when applying ICA to MEG data, most researchers have treated averaged data [1, 2, 4]. However, by taking an average, important information is lost, making it advantageous to decrease the number of averages across data trials. The disadvantage of having fewer averages is that because SNR is very poor, the decomposition of a low-power source signal from recorded data is still influenced by noise. In this paper, we deal with small numbers of trials (averaged 10-trials) and large numbers of trials (averaged 100-trials), and we demonstrate that evoked signals can be detected by applying our ICA approach in both cases.

When applying ICA to physiological data, most researchers have used real, measured, physiological data, with some individual responses evoked by stimuli, and their decomposed components are evaluated from a neuroscience perspective. In this study, we use a synthesized MEG data set, which includes an artificial evoked field and real, measured brain data. The behavior of our data set is similar to auditory evoked fields (AEFs). The main advantage of our data set is that dipole location of evoked responses and its dynamics are known in advance, which facilitates the evaluation of the decomposed components. In this paper, to evaluate the results of decomposition, we focus on not only the location but also the direction vector and dipole moment of evoked fields.

2. Data analysis model

In this section, we describe the model for applying ICA to MEG data. Based on the principle of MEG measurement, this problem can be formulated as

$$\mathbf{x}(t) = \mathbf{A}\mathbf{s}(t) + \mathbf{e}(t), \tag{1}$$

where $\mathbf{x}(t)$, $\mathbf{s}(t)$ and $\mathbf{e}(t)$ represent the transpose of m observations at time t, n unknown source components and additive noise, respectively. Since neither human tissue nor

skull attenuate magnetic fields in MEG, $\mathbf{A}$ can be represented by a numerical matrix whose element a_{ij} is simply a quantity related to the physical distance between the i-th sensor and the j-th source.

In the model, $\mathbf{s}(t)$, $\mathbf{e}(t)$, $\mathbf{A}$ and n are unknown but $\mathbf{x}(t)$ are accessible. It is assumed that the components of $\mathbf{s}(t)$ are mutually statistically independent, as well as being statistically independent of the noise components $\mathbf{e}(t)$. Moreover, the noise components $\mathbf{e}(t)$ themselves are assumed to be mutually independent.

3. Data analysis method

3.1. Robust pre-whitening technique

In this subsection, we describe our robust pre-whitening technique [1, 2, 3]. This technique is very capable of reducing the power of additive noise.

When the sample size is sufficiently large, the covariance matrix of the observed data in the mixing model $\mathbf{\Sigma}$ can be written as $\mathbf{\Sigma} = \mathbf{A}\mathbf{A}^T + \mathbf{\Psi}$, where $\mathbf{\Psi}$ is a diagonal matrix of the additive noise $\mathbf{e}$. Also the covariance matrix of the observed data recorded by sensors can be given by $\mathbf{C} = \mathbf{x}\mathbf{x}^T$.

For the robust pre-whitening technique, $\mathbf{A}$ can be estimated as

$$\widehat{\mathbf{A}} = \mathbf{U}_{\hat{n}}\mathbf{\Lambda}_{\hat{n}}^{\frac{1}{2}}, \tag{2}$$

by applying the standard PCA approach, where $\mathbf{\Lambda}_{\hat{n}}$ is a diagonal matrix whose elements are eigenvalues of $\mathbf{C}$, the columns of $\mathbf{U}_{\hat{n}}$ are the corresponding eigenvectors and $\widehat{n}$ is the estimated number of sources.

To estimate $\mathbf{\Psi}$, we fit $\mathbf{\Sigma}$ to $\mathbf{C}$ using the eigenvalue decomposition method. In this case, the cost function is obtained as $L(\mathbf{A}, \mathbf{\Psi}) = tr[\mathbf{\Sigma} - \mathbf{C}]^2$. And we minimize it by $\frac{\partial L(\mathbf{A},\mathbf{\Psi})}{\partial \mathbf{\Psi}} = 0$, whereby the estimate noise variance $\mathbf{\Psi}$ is obtained as

$$\widehat{\mathbf{\Psi}} = diag(\mathbf{C} - \widehat{\mathbf{A}}\widehat{\mathbf{A}}^T), \tag{3}$$

where the estimate $\widehat{\mathbf{A}}$ is obtained in the same manner as shown in Eq. (2). Using these estimates $\widehat{\mathbf{A}}$ and $\widehat{\mathbf{\Psi}}$, we can obtain the transform matrix for the robust pre-whitening technique as

$$\mathbf{Q} = [\widehat{\mathbf{A}}^T\widehat{\mathbf{\Psi}}^{-1}\widehat{\mathbf{A}}]^{-1}\widehat{\mathbf{A}}^T\widehat{\mathbf{\Psi}}^{-1}. \tag{4}$$

Using the above result, the new set of data transformed from the observations can be obtained by

$$\mathbf{z}(t) = \mathbf{Q}\mathbf{x}(t). \tag{5}$$

Note that the covariance matrix is $E\{\mathbf{z}\mathbf{z}^T\} = \mathbf{I}_{\hat{n}} + \mathbf{Q}\mathbf{\Psi}\mathbf{Q}^T$, which implies that the source signals in a subspace are decorrelated.

A similar noise reduction approach that applies factor analysis (FA) to the decomposition of MEG data has been reported in [4]. Both this method and ours take additive noises into account, but with our robust pre-whitening technique, the distribution of additive noises is not restricted. Therefore, our technique is more robust and effective for data with non-Gaussian noise such as the outlier.

3.2. JADE algorithm

It should be noted that the robust pre-whitening technique is needed to reduce the power of sensor noises and the number of parameters, but it is insufficient to obtain the independent components since an orthogonal matrix in general contains additional degrees of freedom. Therefore, the remaining parameters must be further estimated by using an ICA algorithm. In this study, we apply the JADE altorithm [5].

The JADE algorithm has two procedures termed orthogonalization in PCA and rotation. We did apply the rotation procedure in the JADE algorithm, described below, but instead of the orthogonalization in PCA, we applied the robust pre-whitening technique described in Section **3.1**.

The rotation procedure in JADE uses matrices $\mathbf{F}(\mathbf{M})$ formulated by the fourth-order cumulant tensor of the outputs with an arbitrary matrix $\mathbf{M}$ as

$$\mathbf{F}(\mathbf{M}) = \sum_{k=1}^{K}\sum_{l=1}^{L} \mathrm{Cum}(z_i, z_j, z_k, z_l) m_{lk}, \tag{6}$$

where the $\mathrm{Cum}(\cdot)$ denotes a standard cumulant and m_{lk} is the (l,k)-th element of matrix $\mathbf{M}$. The correct rotation matrix $\mathbf{W}$ can be obtained by diagonalizing the matrix $\mathbf{F}(\mathbf{M})$, i.e. $\mathbf{W}\mathbf{F}(\mathbf{M})\mathbf{W}^T$ approximates a diagonal matrix.

After performing the robust pre-whitening technique and rotation in JADE, the de-mixture matrix is $\mathbf{WQ}$. With it, we can calculate the decomposed sources $\mathbf{y} \in \mathbf{R}^n$ as

$$\mathbf{y}(t) = \mathbf{W}\mathbf{z}(t) = \mathbf{W}\mathbf{Q}\mathbf{x}(t). \tag{7}$$

3.3. Power of decomposed components

The robust pre-whitening and ICA techniques serve to filter the raw data, decreasing the power of the additive noises and decomposing the sources. The estimated behavior of the individual sources can be represented as Eq. (7). To better visualize the information, we projected the decomposed components onto the sensor space.

The virtual sensor signals coming from multiple components are obtained as

$$\widehat{\mathbf{x}}(t) = \widehat{\mathbf{A}}\mathbf{W}^{-1}\mathbf{y}(t). \tag{8}$$

To determine the information of the k-th individual components, we forced every element to be zero except the k-th

Table 1. Artificial evoked fields.

	peak time (sec.)	location x, y, z (mm)	vector az, dec (deg.)	moment Q (nAm)
Evoked Field 1	0.25	10, 50, 50	150, 108	20
Evoked Field 2	0.27	-40, 40, 40	250, 59	30

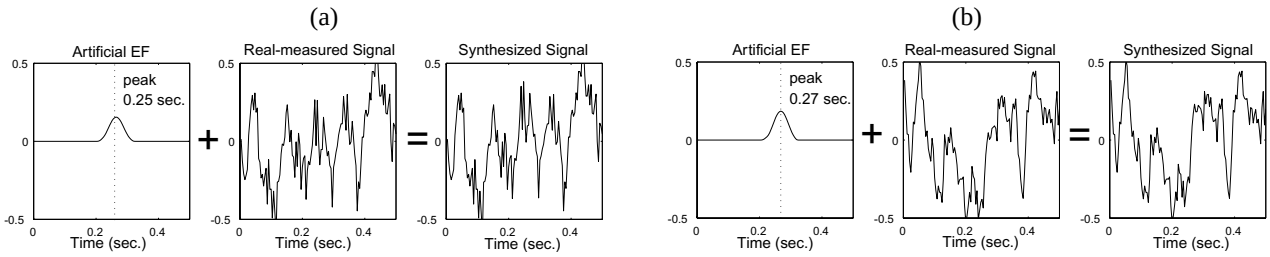

Figure 1. An example for data synthesizing: (a) Data synthesizing at sensor-L24, which detects signal EF1. (b) Data synthesizing at sensor-L44, which detects signal EF2. In each example, artificial EF signals (left), real measured MEG signals (middle), synthesized signals (right) are represented. The horizontal axis expresses time (sec.) and the vertical axis expresses amplitude (pT).

$(k = 1, \cdots, \widehat{n})$ of $\mathbf{y}(t)$ in Eq. (8). The virtual sensor signals coming from k-th individual components are obtained as

$$\widehat{\mathbf{x}}_k(t) = \widehat{\mathbf{A}}\mathbf{W}^{-1}[0 \cdots \mathbf{y}_k(t) \cdots 0]^T. \tag{9}$$

The relationship between virtual sensor signals from multiple $\widehat{\mathbf{x}}$ and k-th individual components $\widehat{\mathbf{x}}_k$ is $\widehat{\mathbf{x}}(t) = \sum_{k=1}^{\widehat{n}} \widehat{\mathbf{x}}_k(t)$. Note that some noises have been reduced in the estimated observation $\widehat{\mathbf{x}}_k(t)$.

In this paper, we define the total sum of each virtual sensor signal from the k-th individual component as:

$$\mathbf{v}_k(t) = \frac{1}{M} \sum_{i=1}^{M} \widehat{\mathbf{x}}_{k,i}(t) \tag{10}$$

to compare the power of decomposed components. In Eq. (10), M denotes the number of sensors and $\widehat{\mathbf{x}}_{k,i}$ denotes the k-th decomposed components of $\mathbf{y}(t)$ into the i-th sensor. Here $\mathbf{v}_k$ represents the total observation signals derived by the k-th decomposed signal, so that its amplitude is not ambiguous.

Using the above results, we define the power of the k-th decomposed components $\mathbf{v}_k$ as

$$P_{\mathbf{v}k} = \sum_{t=1}^{N} \mathbf{v}_k(t)\mathbf{v}_k^T(t), \tag{11}$$

where, N denotes the number of data samples. Applying $P_{\mathbf{v}k}$ as the power of the k-th decomposed components, we can compare the power of individual components decomposed by ICA.

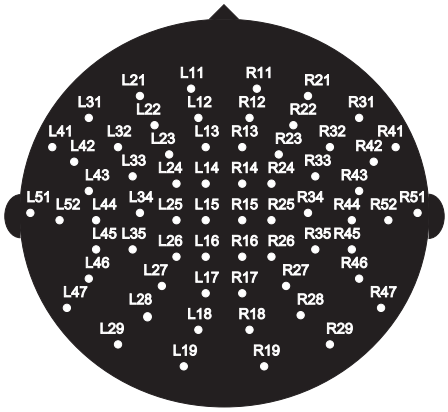

Figure 2. Sensor distribution.

4. Experimental results

4.1. Synthesized MEG data

In this subsection, we describe the synthesized MEG data set, used for simulation, which is similar to Auditory Evoked Fields (AEFs). As shown in Fig. 1, we synthesized an artificial signal and a real measured MEG signal which is recorded by using an Omega-64 (CTF Systems Inc., Canada). The sensor arrays consist of 64 channels and the sensor distribution is shown in Fig. 2. The sampling rate was 250 Hz with duration of 50 sec. for 12500 samples. The observed data $\mathbf{X}_{(64\times12500)}$ was segmented into 100 trials, so the duration of each trial $\mathbf{X}_{i(64\times125)}(i = 1, \cdots, 100)$ is 0.5 sec. and each trial has 125 samples, where i denotes the trial number.

The source signals in this data set include two different

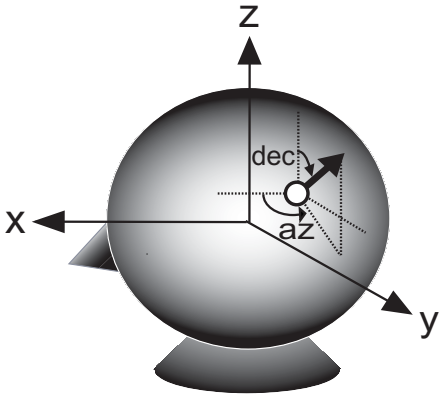

Figure 3. 3D frames of reference.

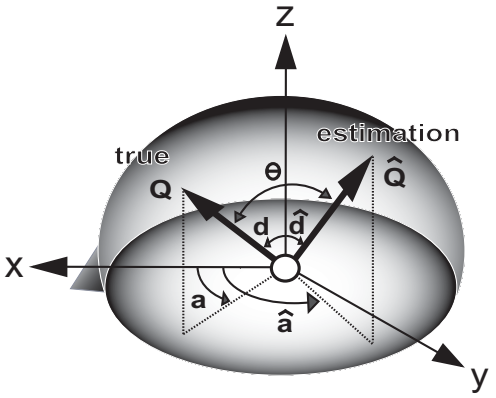

Figure 4. Angle Θ between the direction vector of true and estimated EFs, in case of uniting the starting point of two vectors (a : azimuth, d : declination).

evoked fields responses, EF1 and EF2, and include the 50 Hz electrical power interference and the α-wave component involved in the real measured MEG data. The signal EF1 was artificially evoked from 0.2 sec. to 0.3 sec. with a peak at 0.25 sec. and its strength (dipole moment) was $Q = 20$ nAm (see Fig. 1(a)). The signal EF2 was artificially evoked from 0.22 sec. to 0.32 sec. with a peak at 0.27 sec. and its strength was $Q = 30$ nAm (see Fig. 1(b)). The source of EF1 was located at $[x,\ y,\ z] = [10,\ 50,\ 50]$ mm and that of EF2 was located at $[x,\ y,\ z] = [-40,\ 40,\ 40]$ mm, where a head model presupposes a sphere with a radius of 75 mm and x, y, z axis are set according to Fig. 3. The direction vector, azimuth (az) and declination (dec), of EF1 was set at $[az,\ dec] = [150,\ 108]$ deg. and that of EF2 was set at $[az,\ dec] = [250,\ 59]$ deg. (see Table 1).

4.2. Automatic classification

In this subsection, we demonstrate the procedure for automatic classification of the decomposed components into signals EF1 and EF2. First, we calculated the power of each decomposed component in the time domain

$$P_{\mathbf{v}k} = \sum_{t=0}^{0.5} \mathbf{v}_k(t)\mathbf{v}_k^T(t), \tag{12}$$

where $\mathbf{v}_k(t)$ denotes the k-th decomposed component. To define the criterion for classifying the decomposed components into EF1 and EF2, we calculated the power of each decomposed component in the duration from 0.2 to 0.3 sec. $P'_{\mathbf{v}k}$ and from 0.22 to 0.32 sec. $P''_{\mathbf{v}k}$ as

$$\begin{aligned} P'_{\mathbf{v}k} &= \sum_{t=0.2}^{0.3} \mathbf{v}_k(t)\mathbf{v}_k^T(t), \\ P''_{\mathbf{v}k} &= \sum_{t=0.22}^{0.32} \mathbf{v}_k(t)\mathbf{v}_k^T(t). \end{aligned} \tag{13}$$

Using above results, we define the ratios

$$R'_{\mathbf{v}k} = \frac{P'_{\mathbf{v}k}}{P_{\mathbf{v}k}}, \quad R''_{\mathbf{v}k} = \frac{P''_{\mathbf{v}k}}{P_{\mathbf{v}k}}. \tag{14}$$

When $R'_{\mathbf{v}k} \geq k_{EF1}$, the decomposed component $\mathbf{v}_k$ is the signal EF1, since the signal EF1 was artificially evoked from 0.2 to 0.3 sec., where k_{EF1} is a positive constant. Similarly, when $R''_{\mathbf{v}k} \geq k_{EF2}$, the decomposed component $\mathbf{v}_k$ is the signal EF2, where k_{EF2} is a positive constant. Based on prior experience, for this experiment we set these parameters as $k_{EF1} = 0.6$, $k_{EF2} = 0.6$, respectively [2].

4.3. Evaluation methods

In this study, since the dipole locations, direction vectors and dipole moments of EF1 and EF2 were known in advance, we can compare them to the estimated ones. We used the standard spatio-temporal dipole fitting routine, MEG v3.3a (CTF System Inc., Canada), to find the dipole. Here we define the distance between true dipole location $[x,\ y,\ z]$ mm and estimated dipole location $[\widehat{x},\ \widehat{y},\ \widehat{z}]$ mm as

$$r = \sqrt{(x-\widehat{x})^2 + (y-\widehat{y})^2 + (z-\widehat{z})^2}. \tag{15}$$

When uniting the starting point of two vectors, we define the angle Θ between the direction vector of true and estimated EFs as

$$\Theta = \cos^{-1}[\sin(d)\sin(\widehat{d})\cos(a-\widehat{a}) + \cos(d)\cos(\widehat{d})], \tag{16}$$

where a and d denote azimuth and declination (deg.), respectively (see Fig. 4). We define the difference of true and estimated dipole moment ΔQ as

$$\Delta Q = |Q - \widehat{Q}|, \tag{17}$$

where Q and $\widehat{Q}$ denote the dipole moments (nAm) of the EFs and their estimates, respectively.

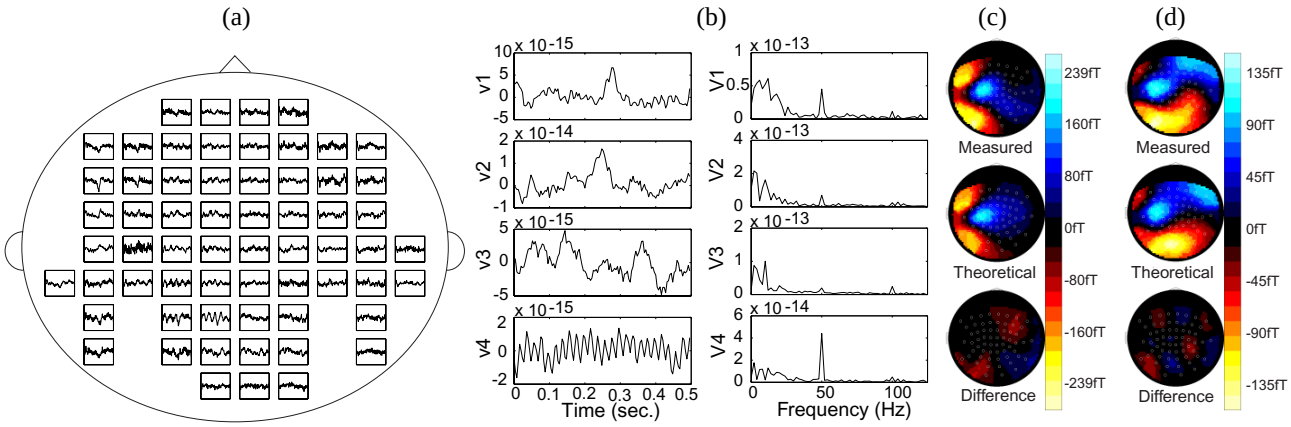

Figure 5. (a) Averaged of 10 trials data. (b) Result of ICA with the robust pre-whitening technique and its frequency contents. (c) Estimated map focus on EF1, (d) Estimated map focus on EF2.

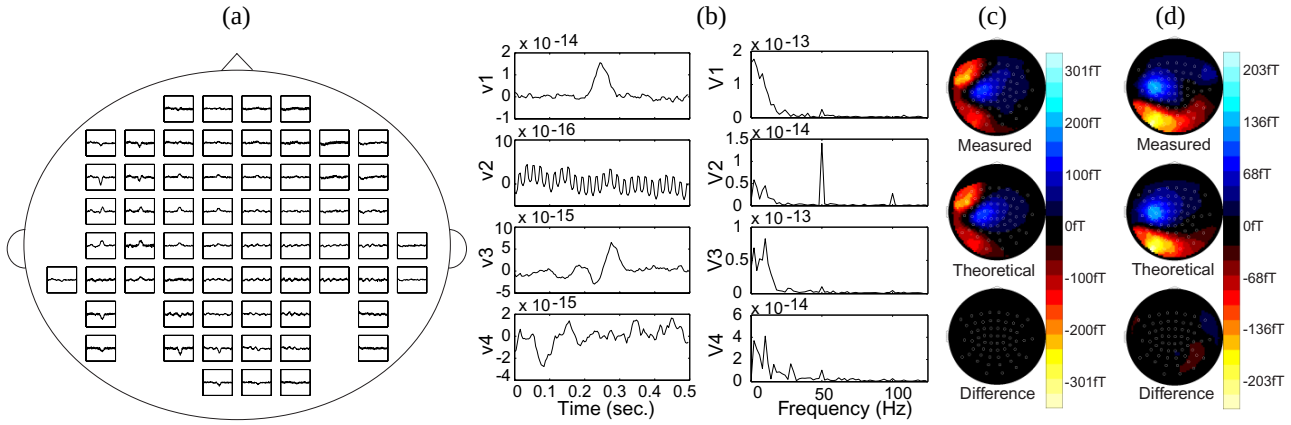

Figure 6. (a) Averaged of 100 trials data. (b) Result of ICA with the robust pre-whitening technique and its frequency contents. (c) Estimated map focus on EF1, (d) Estimated map focus on EF2.

4.4. Results for averaged 10-trials data

We demonstrate the results for the averaged 10-trial data, as shown in Fig. 5(a). In this figure, the horizontal axis and vertical axis express time from 0 to 0.5 sec. and amplitude from -0.5 to 0.5 pT, respectively. The results $\mathbf{v}(t)$ and these power spectrums $\mathbf{V}_k(f)$ are shown in Fig. 5(b). Applying the automatic classifying technique described in Sect. 4.2, $\mathbf{v}_1$ and $\mathbf{v}_2$ have satisfied the equations $R''_{\mathbf{v}1} \geq k_{EF2}$ and $R'_{\mathbf{v}2} \geq k_{EF1}$, respectively, and can thus be regarded as signals EF2, EF1, respectively.

The estimated maps of signals EF1 and EF2, derived by analyzing the average of 10-trials (after ICA), are shown in Fig. 5(c)(d), respectively. As for the result of EF1, note that the evoked response appears on the left-front area of the brain. For the result of EF2, the evoked response appears on the left-back area of the brain. The results of dipole estimation become $[\widehat{x},\ \widehat{y},\ \widehat{z}] = [-5.7,\ 46.4,\ 47.5]$ mm, $[\widehat{az},\ \widehat{dec}] = [145.1,\ 123.3]$ deg. and $\widehat{Q} = 50.0$ nAm for EF1 and $[\widehat{x},\ \widehat{y},\ \widehat{z}] = [-37.5,\ 24.1,\ 52.9]$ mm, $[\widehat{az},\ \widehat{dec}] = [293.6,\ 55.0]$ deg. and $\widehat{Q} = 30.6$ nAm for EF2. Using Eq. (15), (16) and (17), the difference between true and estimated dipole, r, Θ and ΔQ are $r = 16.3$ mm, $\Theta = 15.9$ deg. and $\Delta Q = 30.0$ nAm for EF1 and $r = 20.6$ mm, $\Theta = 36.5$ deg. and $\Delta Q = 0.6$ nAm for EF2, respectively (see Table 2).

Here, we describe the results of dipole estimation for averaged 10-trials data (before ICA). The results of dipole estimation for averaged 10-trials data become $[\widehat{x},\ \widehat{y},\ \widehat{z}] = [7.8,\ 16.5,\ 46.4]$ mm, $[\widehat{az},\ \widehat{dec}] = [167.2,\ 85.1]$ deg. and $\widehat{Q} = 119.8$ nAm for EF1 and $[\widehat{x},\ \widehat{y},\ \widehat{z}] = [-38.2,\ 12.5,\ 52.3]$ mm, $[\widehat{az},\ \widehat{dec}] = [299.8,\ 60.4]$ deg. and $\widehat{Q} = 41.1$ nAm for EF2. Therefore r, Θ and ΔQ are $r = 33.8$ mm, $\Theta = 28.5$ deg. and $\Delta Q = 99.8$ nAm for EF1 and $r = 30.2$ mm, $\Theta = 42.7$ deg. and $\Delta Q = 11.1$ nAm for EF2, respectively. The results show that by applying our ICA approach, we can obtain more accurate information about EFs.

Table 2. Comparison of true and estimated EFs

(a) Estimation of EF1.

		dipole location (mm)				direction vector (deg.)			moment (nAm)	
		x	y	z	r	az	dec	Θ	Q	ΔQ
true value		10.0	50.0	50.0	-	150.0	108.0	-	20.0	-
averaged 10-trials	after ICA	-5.7	46.4	47.5	16.3	145.1	123.3	15.9	50.0	30.0
	before ICA	7.8	16.5	46.4	33.8	167.2	85.1	28.5	119.8	99.8
averaged 100-trials	after ICA	8.9	47.0	50.9	3.4	149.5	107.6	0.6	24.3	4.3
	before ICA	5.6	57.3	48.1	8.7	141.5	123.0	16.8	13.4	6.6

(b) Estimation of EF2.

		dipole location (mm)				direction vector (deg.)			moment (nAm)	
		x	y	z	r	az	dec	Θ	Q	ΔQ
true value		-40.0	40.0	40.0	-	250.0	59.0	-	30.0	-
averaged 10-trials	after ICA	-37.5	24.1	52.9	20.6	293.6	55.0	36.5	30.6	0.6
	before ICA	-38.2	12.5	52.3	30.2	299.8	60.4	42.7	41.1	11.1
averaged 100-trials	after ICA	-37.1	37.0	36.3	5.6	259.6	50.7	11.4	33.0	3.0
	before ICA	-43.0	37.5	44.4	5.9	245.1	70.3	12.1	33.4	3.4

4.5. Results for averaged 100-trials data

Next, we describe the results of averaged 100-trials data, as shown in Fig. 6(a). The results $\mathbf{v}(t)$ and these power spectrums $\mathbf{V}_k(f)$ are shown in Fig. 6(b). Here, $\mathbf{v}_1$ and $\mathbf{v}_3$ have satisfied the equation $R'_{\mathbf{v}1} \geq k_{EF1}$ and $R''_{\mathbf{v}3} \geq k_{EF2}$, respectively, and can thus be regarded as EF1 and EF2, respectively.

The estimated maps of the EF1 and EF2 derived by analyzing the averaged 100-trials data (after ICA) are shown in Fig. 6(c)(d), respectively. In the results of EF1 and EF2, note that the evoked responses appear like the maps derived by analyzing the averaged 10-trials data. The results of dipole estimation are $[\widehat{x},\ \widehat{y},\ \widehat{z}] = [8.9,\ 47.0,\ 50.9]$ mm, $[\widehat{az},\ \widehat{dec}] = [149.5,\ 107.6]$ deg. and $\widehat{Q} = 24.3$ nAm at EF1 and $[\widehat{x},\ \widehat{y},\ \widehat{z}] = [-37.1,\ 37.0,\ 36.3]$ mm, $[\widehat{az},\ \widehat{dec}] = [259.6,\ 50.7]$ deg. and $\widehat{Q} = 33.0$ nAm at EF2. Therefore r, Θ and ΔQ are $r = 3.4$ mm, $\Theta = 0.6$ deg. and $\Delta Q = 4.3$ nAm for EF1 and $r = 5.6$ mm, $\Theta = 11.4$ deg. and $\Delta Q = 3.0$ nAm for EF2 (see Table 2).

The results of dipole estimation for averaged 100-trials data (before ICA) become $[\widehat{x},\ \widehat{y},\ \widehat{z}] = [5.6,\ 57.3,\ 48.1]$ mm, $[\widehat{az},\ \widehat{dec}] = [141.5,\ 123.0]$ deg. and $\widehat{Q} = 13.4$ nAm for EF1 and $[\widehat{x},\ \widehat{y},\ \widehat{z}] = [-43.0,\ 37.5,\ 44.4]$ mm, $[\widehat{az},\ \widehat{dec}] = [245.1,\ 70.3]$ deg. and $\widehat{Q} = 33.4$ nAm for EF2. Therefore r, Θ and ΔQ are $r = 8.7$ mm, $\Theta = 16.8$ deg. and $\Delta Q = 6.6$ nAm for EF1 and $r = 5.9$ mm, $\Theta = 12.1$ deg. and $\Delta Q = 3.4$ nAm for EF2.

Comparing the results of ICA and taking averages (before ICA), we conclude that not only dipole location, but also direction vector and dipole moment become more accurate by applying our ICA approach (see Table 2).

5. Conclusions

In this paper, we performed source decomposition of averaged multiple-trials MEG data using our ICA algorithm. Our results showed that the analysis of averaged data effectively determines not only dipole location but also direction vector and dipole moment of the evoked fields even when the number of averages is small. The authors hope these results will help neuroscientists to further their understanding of the temporal cortex.

References

[1] Y. Konno, J. Cao and T. Takeda, "Decomposition and Localization of MEG Brain Sources," Journal of Signal Processing, Vol. 6, No, 6, pp. 391-400, Nov 2002.

[2] Y. Konno, J. Cao, T. Arai and T. Takeda, "Visualization of Brain Activities of Single-Trial and Averaged Multiple-Trials MEG Data," IEICE Trans. on Fundamentals, Vol. E86-A, No. 9, pp. 2294-2302, Sep 2003.

[3] J. Cao, N. Murata, S. Amari, A. Cichocki and T. Takeda, "A robust approach to independent component analysis of signals with high-level noise measurements," IEEE Trans. on Neural Networks, Vol. 14, No. 3, pp. 631-645, June 2003.

[4] S. Ikeda, K. Toyama, "Independent component analysis for noisy data - MEG data analysis," Neural Networks 13, pp. 1063-1074, 2000.

[5] J. F. Cardoso and A. Souloumiac, "Jacobi angles for simultaneous diagonalization," SIAM J. Mat. Anal. Appl., Vol. 17, No. 1, pp. 145-151, 1996. Matlab code in WWW : http://sig.enst.fr/ cardoso/jointdiag.html

[6] Vigario, R., Sarela, J., Jousmiki, V., Hamalainen, M. and Oja, E, "Independent component approach to the analysis of EEG and MEG recordings," Biomedical Engineering, IEEE Transactions on, Vol. 47 Issue. 5, pp. 589-593, May 2000

Advanced Neural Network Learning Applied To Breast Cancer Detection

Zarita Zainuddin
School of Mathematical Sciences
Universiti Sains Malaysia, 11800 Minden, Malaysia
zarita@cs.usm.my

Computer Aided Diagnostics (CAD) in the form of neural networks (utilized for pattern recognition and classification) offer significant potential to provide an accurate and early automated diagnostic technology. This paper considers neural network training to detect breast cancer by analyzing the fine needle aspirates (FNA) of a breast mass. For enhanced learning, three gradient-based multi layer perceptron (MLP) training methods originated from optimization theory, namely, steepest-descent gradient search, conjugate-gradient and Levenberg Marquardt are considered. In addition, two newly proposed methods, the Dynamic Momentum Factor and Dynamic Learning Rate are discussed. The results presented show that significant improvements in convergence performance can be obtained through the integration of these acceleration methods whilst preserving the generalization capability of the networks.

INTRODUCTION

Breast Cancer is second only to lung cancer as a tumor-related cause of death in women. More that 180,000 new cases are reported annually in the US alone. Furthermore, the American Cancer Society estimates that at least 25% of these deaths could be prevented if all women in the appropriate age groups were regularly screened.

Although there exists reasonable agreement on the criteria for benign/malignant diagnoses using fine needle aspirate (FNA) and mammogram data, the application of these criteria are often quite subjective. Additionally, proper evaluation of FNA and mammogram sensor data is a time consuming task for the physician. Intra-and-inter-observer disagreement and/or inconsistencies in the FNA and mammogram interpretation further exacerbate the problem.

Consequently, C*omputer Aided Diagnostics* (CAD) in the form of neural networks (utilized for pattern recognition and classification) offer significant potential to provide an accurate and early automated diagnostic technology. This automated technology may well be useful in further assisting with other problems resulting from physical fatigue, poor mammogram image quality, inconsistent FNA discriminator numerical assignments, as well as other possible sensor interpretation problems.

Some practical results of CAD of breast cancer sensor data using neural networks are expected to be:

- Operational software which will aid the physician in making the diagnosis, quite possibly in real time, and once formulated and tested, they are always consistent, not prone to human fatigue or bias.
- Providing diagnostic assistance for the intra-and-inter-observability problems by ultimately minimizing the subjective component of the diagnostic process
- Providing an initial detection and/or classification process in the absence of a qualified physician
- Providing possible (and probably currently unknown) relationships between sensor environment discriminators and a correct diagnosis.

The efficient supervised training of neural networks (NNs) is a subject of considerable ongoing research and numerous algorithms have been proposed to this end. The backpropagation algorithm (BPA) [1] is one of the most common supervised training methods. It uses the gradient or steepest descent method to reduce

the error function where the weights are adjusted by the algorithm so as to make the error decreases along a descent direction. In doing so, the two parameters, learning rate (LR) and momentum factor (MF) are used to control the size of weight adjustment along the descent direction and for dampening oscillations of the iterations. In the conventional backpropagation algorithm (BPA), these two parameters are empirically chosen. In general, the MF should be less than unity to stabilize the BPA. When error oscillations happen, an MF close to unity is needed to smooth the error oscillations. As for the selection of the LR, it is more arbitrary due to the fact that the error surface usually consists of many flat and steep regions and behaves quite differently from application to application. A large LR is helpful to acceleration of the learning when the weight search crosses a plateau. Nevertheless, in the meanwhile, it increases the possibility that the weight search jumps over steep regions and moves into undesirable regions. When this happens, failure of the backpropagation learning may be caused. Therefore, an efficient BPA should be capable of dynamically varying its LR and MF in accordance with the regions the weight adjustment lies in. Research into the dynamic change of the LR and MF parameters has been carried out extensively by numerous authors including Becker & leCun [2], Battiti [3] and Yu et al. [4].

In this contribution, the performance of the Dynamic Momentum Factor (DMF) [5] and Dynamic Learning Rate (DLR) [6, 7] algorithms are evaluated and compared against the conventional BP and three other gradient based optimization methods - the steepest descent, conjugate gradient and Levenberg Marquardt methods [8] on the breast cancer detection problem using continuous-valued training data. This is accomplished by training a 30-6-4-2 MLP consisting of 30 input nodes, 6 first hidden layer nodes, 4 second hidden layer nodes and 2 output nodes. After being trained, the networks are tested on generalization capabilities on a testing set consisting of images outside the training set. The capabilities of the networks should at least be similar to the conventional BP trained network although lesser function evaluations are necessary to converge.

DESCRIPTION OF THE DATA SET

The data set used was obtained from the University of Wisconsin Breast Cancer problem [9]. Features were computed from a digitized image of a fine needle aspirate (FNA) of a breast mass. They describe characteristics of the cell nuclei present in the image. Ten real-valued features were computed for each cell nucleus: (a) radius (b) texture (c) perimeter (d) area (e) smoothness (f) compactness (g) concavity (h) concave points (i) symmetry (j) fractal dimension.

The mean, standard error, and "worst" or largest (mean of the three largest values) of these features were computed for each image, resulting in 30 features, from which one attribute, malignant or benign, must be detected.

TRAINING METHODS

In Evans [10], the reasons for the slow convergence of the backpropagation have been discussed. To date, many techniques have been proposed to deal with the inherent problems of backpropagation. These techniques can be divided roughly into two main categories; those referred to as global techniques that use global knowledge of the state of the entire network, such as the direction of the overall weight update vector. Most of these techniques have their roots in the well-explained domain of optimization theory. The simplest is a first-order method that uses the steepest-descent (SD) direction [1]. An alternative is the conjugate gradient (CG) method, which modifies the SD direction by conjugating it with the previously used direction [11]. Finally, the Levenberg – Marquardt (LM) method is a second – order method that approximates the second derivative using the first-order gradient [12].

In contrast, local adaptation strategies are based on weight specific information only, such as the temporal behavior of the partial derivative of the current weight. Two local adaptive learning rules are presented here, namely, the Dynamic Momentum Factor (DMF) [5] and Dynamic Learning Rate (DLR) [6].

Steepest Descent Method

The first method proposed by Rumelhart and McClelland [1] for training NNs is the SD method. The value of the weight update is calculated as follows:

$$\mathbf{w}(n+1) = \mathbf{w}(n) + \eta(n)\mathbf{p}(n) \quad (1)$$

$$\mathbf{p}(n) = -\frac{\partial E(n)}{\partial w(n)} + \alpha(n)\mathbf{p}(n-1) \quad (2)$$

where n is the iteration count, η is the step width (learrning rate), μ is the momentum factor, and $\mathbf{p}(n)$ is the step direction taken in the nth iteration step.

Conjugate Gradient Method

In optimization theory, the CG method has been known since Fletcher and Reeves [13]. Leonard and Kramer [11] introduced the original Fletcher – Reeves algorithm in the field of NN research. The method is, in some way, an extension to SD, introducing a formula for determining the momentum factor α in Eq. (2):

$$\alpha(n) = \frac{g^T(n+1)g(n+1)}{g^T(n)g(n)} \tag{3}$$

Levenberg Marquardt Method

The third commonly used minimization method is LM. It is directly applicable only when the error measure is a sum of squared errors:

$$E = \sum_{N,C}(y-d)^2 \tag{4}$$

Then, an approximate Hessian $\mathbf{H}$ can be written as

$$\frac{\partial^2 E(n)}{\partial w(n)^2} \approx \mathbf{H} = \left(\frac{\partial E}{\partial w}\right)^T \frac{\partial E}{\partial w} + \mu\mathbf{I} \tag{5}$$

where $\mathbf{I}$ is the identity matrix of dimension v and μ is a small scalar; this increment makes the matrix $\mathbf{H}$ to be invertible. The calculation of the weight update is then based on Eq. (1) and Eq. (2), using a square matrix $\mathbf{R}$, instead of the scalar η to premultiply the search – direction vector $\mathbf{p}$ with:

$$\mathbf{R} = \mathbf{H}^{-1} \tag{6}$$

and setting the momentum α in Eq. (2) to zero.

Dynamic Momentum

A momentum factor update rule, the basis of the Dynamic Momentum Factor (DMF) algorithm, which dynamically adapts the momentum factor with respect to the iteration number is given below. A complete analysis regarding momentum factor and a derivation of this rule has been presented in Evans and Zainuddin [5].

Momentum Constant Update Rule

Let $\Delta\alpha_{ji}(n,0)$ denote the positive adjustment applied at iteration n to the momentum constant at iteration 0, $\alpha_{ji}(0,0)$. We define $\Delta\alpha_{ji}(n,0)$ as

$$\Delta\alpha_{ji}(n,0) = \gamma_a^b + \alpha_{ji}(0,0) \tag{7}$$

for all $n \in [a,b]$ where $0 \le \gamma_a^b \le 1-\alpha_{ji}(0,0)$ and $\gamma_a^b > \gamma_c^d$ for a>c and b>d.

The constraint $0 \le \gamma_a^b \le 1-\alpha_{ji}(0,0)$ is imposed to ensure that $0<\alpha_{ji}(n)\le 1$ as the momentum constant α has to be in the range $0 \le |\alpha| \le 1$ to ensure convergence of the learning algorithm. The initial value of α, $\alpha_{ji}(0,0)$ can be chosen to be any small value in the interval [0,1]. Note that without loss of generality, we define $\Delta\alpha_{ji}(n,0)$ as a positive adjustment. If α is negative, then we will consider a negative adjustment but it is unlikely that a negative α would be used in practice.

The iteration number domain is partitioned into n intervals and a suitable value for the momentum constant is assigned for each respective interval. As n gets large, the momentum constant is incremented gradually making sure that $\alpha_{ji}(n)$ is less that or equals to 1. This method only requires n comparisons, where n is the number of iterations and no storage requirement is demanded at all.

Dynamic Adaptation of the Learning Rate

In Evans et al [10], we see that the convergence rate is crucially dependent on the optimal choice of the learning rate parameter. It is necessary to find a method that allows the parameters to be adjusted in the course of the learning procedure.

Presently, there exists many acceleration methods to overcome the slow convergence problem. There are methods that exploit the information contained in the second derivative of the cost function while others do not use higher-order derivatives [14, 15].

Below we present the learning rate update rule, which forms the basis of the Dynamic Learning Rate (DLR) method which dynamically adapts the learning rate parameter with respect to the magnitude of the partial derivative of the error surface with respect to the current weight, $w_{ji}(n)$, $\partial 1(n)/\partial w_{ji}(n)$. A derivation of the rule can be found in Zainuddin and Evans [6].

Learning Rate Update Rule

Let $\Delta\eta_{ji}(n)$ denote the adjustment applied at iteration n to the learning rate parameter at iteration 0, $\eta_{ji}(0)$. We define $\Delta\eta_{ji}(n)$ as

$$\Delta\eta_{ji}(n) = \lambda_{\delta b}^{\delta a} + \eta_{ji}(0) \tag{8}$$

for all $\delta = \left|\frac{\partial \xi(n)}{\partial w_{ji}(n)}\right| \in (\delta a, \delta b)$ and $\lambda_{\delta b}^{\delta a} < \lambda_{\delta d}^{\delta c}$ for $\delta a > \delta c$ and $\delta b > \delta d$.

In this learning rate adaptation method, the partial derivative domain is partitioned into n intervals (not necessarily of equal size) and a suitable value for the learning rate parameter is assigned for each respective interval.

If $\left|\frac{\partial \xi(n)}{\partial w_{ji}(n)}\right| \in (\delta a, \delta b)$ where δa and δb are small positive values, then $\lambda_{\delta b}^{\delta a}$ is large. On the other hand, if δa and δb are moderate, then $\lambda_{\delta b}^{\delta a}$ is moderate and if δa and δb are large, then $\lambda_{\delta b}^{\delta a}$ is small. The values of $\lambda_{\delta b}^{\delta a}$ are problem dependent. The values of the learning rate for each interval are assigned at the beginning of the learning procedure and they are kept fixed for the whole training process. The learning rate for each connection weight is adapted by determining which interval the gradient belongs to.

SIMULATIONS ON THE BREAST CANCER DETECTION PROBLEM

All the data set inputs have been scaled to the range –1 to 1 for the experiment. A 30-6-4-2 multi layer perceptron was used where the output nodes correspond to the 2 classification classes. The training set consists of 100 vector pairs while the testing set consists of 50 vector pairs. We have chosen the batch mode weight updating because results by other researchers [16], [17] suggest that in tasks where generalization is important, the pattern mode should be avoided, despite their faster training times. The weights and threshold values were initialized to values drawn at random with a uniform distribution between –1 and 1. The learning process was terminated when the sum of the square of the error reached $1*10^{-3}$.

The value of the learning rate was η = 2 and the momentum factor was chosen to be α = 0.9 in the first simulation (BP batch) while the DMF method was used for the second simulation. The partition of the iteration number domain and the α values for each interval is shown is Table 1. For the DLR method, the partition of the gradient domain and their respective η values chosen for each interval are shown in Table 2. Subsequently, the DLR, CG, LM and SD methods were employed. Table 3 shows the results of the simulations discussed above, which are the average of 10 trials. It can be observed that the DMF and DLR methods improved the convergence profoundly. A speedup of 97.08 % was obtained for the DMF method while a speedup of up to 97.27 % was obtained for the DLR method. The SD method gave 6 instances of no convergence. Although the CG method is able to provide a good convergence rate (99.19 %), it nevetheless, requires much more complexity and computation

TABLE 1. The chosen values of the momentum factor $\alpha(n)$ for the breast cancer detection problem using the Momentum Factor Update Rule.

Iteration number (n)	Value of $\alpha(n)$
$1 \le n < 100$	0.5
$100 \le n < 200$	0.6
$200 \le n < 300$	0.7
$300 \le n < 400$	0.8
$400 \le n < 500$	0.9
$500 \le n$	0.95

TABLE 2. The chosen values of η for the breast cancer detection problem using the Learning Rate Update Rule.

Gradient $\lvert\partial\xi/\partial w\rvert$	η
$10^{-2} \le \delta$	5
$5x10^{-3} \le \delta < 10^{-2}$	10
$10^{-3} \le \delta \le 5x10^{-3}$	15
$5x10^{-4} \le \delta < 10^{-3}$	20
$10^{-4} \le \delta \le 5x10^{-4}$	30
$10^{-5} \le \delta < 10^{-4}$	40
$10^{-6} \le \delta < 10^{-5}$	80
$\delta < 10^{-6}$	160

TABLE 3:The simulation results for the classification of iris plant using Batch Mode BP, DMF, DLR methods, Conjugate Gradient ,Steepest Descent and Levenberg – Marquardt methods.

per iteration than the other methods. The LM gave the best performance (99.90%). However, it involves a large number of computations and demands a huge storage requirement since it must store the approximate Hessian matrix. As for the DLR method, it was found that the η values change considerably during the learning process, providing the best progress in the reduction of the error function.

GENERALIZATION CAPABILITY OF THE MLP

Generalization is the ability of the network to respond to inputs it has not seen before and a network is said to generalize well when the output of the network is correct for input patterns that are never used in training the network. After being trained with the batch BP, DMF, DLR, CG, LM and SD methods respectively, the generalization capability of the MLPs on new vector pairs was tested.

The testing set for the breast cancer detection problem consists of 50 vector pairs. It should be emphasized here that these vector pairs were never used in training the network.

TABLE 4. Recognition rates of input patterns in the testing set.

Algorithm	Recognition Rate (%)
Batch BP	96
Dynamic MF	96
Dynamic LR	96
Conjugate Gradient	96
Levenberg-Marquardt	96
Steepest Descent	96

Table 4 shows the recognition rates of the MLP for input patterns in the testing sets. As can be seen, the DMF and DLR methods had similar generalization capability with the batch BP although lesser function evaluations were necessary to converge. It is important to note here that both the DMF and DLR methods demonstrated similar generalization capabilities when compared to the CG ,LM and SD methods.

The MLPs identified and categorized perfectly the input patterns on which they were trained. This is expected since the sum of squared errors for the Breast Cancer Detection problem, valued at $1*10^{-3}$ is a very small number. The recognition rate is as high as 96 % and similar errors occurred for the networks trained with the 5 different algorithms where these input patterns do not have many features in common with the input patterns used in the training set.

CONCLUSION

The acceleration methods namely, Dynamic Momentum Factor (DMF) and Dynamic Learning Rate (DLR), have proven to be very effective and superior in terms of convergence when tested and compared with the Batch BP on the Breast Cancer Detection problem. A speed up of up to 97.08 % and 97.27 % was obtained for the DMF and DLR methods respectively.

The Dynamic Momentum Factor method assigns an optimal value to the momentum factor for each individual weight at each iteration and this greatly enhanced the convergence rate. The main advantage of the DMF method is that the momentum factor is allowed to vary with time in the course of the learning. This in effect, stabilizes the network at the beginning of the learning process and accelerates the learning when the network is stable.

As for the Dynamic Learning Rate method, it was found that the η values changed considerably during the learning process, providing the best progress in the reduction of the error function. The conjugate gradient method has a much faster convergence rate than the other methods since it uses second order information to calculate the new direction, hence it entails more complexity and computation. The Levenberg – Marquardt method gave the best performance but it is suitable only for moderate numbers of network parameters since it involves a large number of computations and requires a huge storage requirement.

In terms of generalization capability, both the DMF and DLR showed similar generalization capability to the batch BP although lesser function evaluations are necessary to converge. In other words, the capability of the networks to recognize input patterns outside the training set is not impaired by the employment of these acceleration methods. Hence, these algorithms are promising in practical applications where generalization is important.

REFERENCES

[1] Rumelhart D.E. and McClelland J.L., eds., 1986, Parallel Distributed Processing: Explorations in the Microstructure of Cognition, Vol. 1, Cambridge, MA: MIT Press.

[2] Becker, S. & Le Cun, Y., 1988, Improving the convergence of back-propagation learning with second order methods. Technical Report CRG-TR-88-5, University of Toronto, Toronto, Canada.

[3] Battiti R., 1992, First and second order methods for learning: between steepest descent and Newton's method. Neural Computation, 4, 141-166.

[4] Yu, X.H., Chen, G.A. & Cheng, S.X., 1995, Dynamic learning rate optimization of the backpropagation algorithm. IEEE Transaction on Neural Networks, 6(3), 669-677.

[5] Evans D.J & Zainuddin Z., 1997, Acceleration of the backpropagation through dynamic adaptation of the momentum. Neural, Parallel & Scientific Computations, 5(3), 297-308. (see also Internal Report

No. 1028, PARC, Loughborough University of Tech., U.K. 1996).
[6] Zainuddin Z. & Evans D.J., 1997, Acceleration of the Back Propagation through dynamic adaptation of the learning rate, International Journal of Computer Mathematics, 334, 1-17. (see also Internal Report No. 1029, PARC, Loughborough University of Tech., U.K. 1996).
[7] Zainuddin, Z. & Evans, D.J., Human Face Recognition using Accelerated Multilayer Perceptrons, Int. J. of Computer Mathematics, 80 (2/3), 2003.
[8] Press, W.H., Flannery, B.P., Teukolsky, S.A., & Vetterling, W.T., 1986., "Numerical recipes : the art of scientific computing". Cambridge : Cambridge University Press.
[9] W. H. Wolberg, W. N. Street, and O. L. Mangasarian, 1995, Wisconsin Diagnostic Breast Cancer, University of Wisconsin, Computer Science Department:
http://www.cs.wisc.edu/~olvi/uwmp/mpml.html
[10] Evans, D.J. Ahmad Fadzil M.H. & Zainuddin, Z., 1997, Accelerating backpropagation in human face recognition, Proc. IEEE Int. Conf. on Neural Networks, IEEE Press, 1347-1352
[11] Leonard, J., & Kramer, M.A., 1990, Improvement to the back-propagation algorithm for training neural networks. Computers and Chemical Engineering, 14(3), 337-341.
[12] Chen, S., Billings, S.A., & Grant. P.M., 1990, Non-linear system identification using neural networks. International Journal of Control, 51(6), 1191-1215.
[13] Fletcher, R., & Reeves, C.M., 1964, Function minimization by conjugate gradients, Computer Journal, 7, 149-154.
[14] Van Der Smagt, P.P. & Krose, B.J.A., 1991, Acceleration of the backpropagation through dynamic adaptation of the learning rate, International Conf. on Artificial Neural Networks, p. 351-356, Espoo, Finland: Elsevier Science Publishers.
[15] Salomon R., 1996, Accelerating backpropagation through dynamic self-adaptation. Neural Networks, 9 (4), 589-602.
[16] Alpsan, D., Towsey, M., Ozdamar, O., Tsoi, A. & Ghista, D.N., 1994, Determining hearing threshold from brain stem evoked potentials. In IEEE Engineering in Medicine and Biology, 465-471.
[17] Cohn, D. & Tesauro, G., 1994, How tight are the Vapnik-Chervonenkis Bounds? Neural Computation, 4, 249-269.

SMART DEVICES & SIGNAL SENSING

(This page left blank intentionally)

Cigarette Brand Identification Using Intelligent Electronic Noses

Dehan Luo
Dept of Mechanical and Electrical Engineering, School of Economical and Technology, University of Science and Technology of China, Hefei, Anhui, China
luodehan@ustc.edu.cn

H. Gholam Hosseini
Dept of Electrotechnology, Faculty of Science and Engineering, Auckland University of Technology, Auckland, New Zealand
hgholamh@aut.ac.nz

John R. Stewart
School of Computer Science, Queen's University of Belfast, Belfast, Northern Ireland, UK
j.r.stewart@qub.ac.uk

Abstract
In this study we propose a practical approach to increase the performance of electronic noses (E-noses) in cigarette brand identification. A portable E-nose was employed to collect and classify aroma signals from different brands of cigarettes. Artificial neural networks (ANN) were employed and trained with raw data and extracted features from the data collected by the E-nose to identify the cigarettes. The Chinese cigarette industry is losing millions of dollars per year due to counterfeit cigarettes. Detecting illegal cigarettes in the field is difficult, but may be possible using portable E-noses. However, the differences between odours from counterfeit and genuine cigarettes are small and detection may prove difficult. This preliminary investigation succeeded in identifying four different types of cigarettes in the laboratory. The identification results obtained from the intelligent E-noise trained with an ANN using the extracted parameters were better than the ones obtained directly from the E-nose.

Keywords
Artificial Neural Network, Electronic Nose, Intelligent Instrumentation, Cigarette Brand Identification.

INTRODUCTION

The Chinese cigarette industry is currently suffering multi-million dollar annual lost revenues due to widespread production and sale of counterfeit cigarettes [1]. It would be a great advantage in combating this very widespread illegal activity if the authorities had access to simple, straightforward means of determining the legality or otherwise of suspect cigarettes and which could be used at the time and site of detection. It has proved to be almost impossible to identify counterfeit cigarettes either by visual inspection or by the aroma detectable by the human nose. Emissions of volatiles from cigarette tobacco comprise a wide range of chemical components making up a complex odour which makes discrimination between brands and/or counterfeit cigarettes difficult. One potential solution to the problem is the use of portable electronic nose devices.

While electronic nose technology has been available in bulky, laboratory-scale form for over twenty years, it is only since around 1999 that miniaturized, portable devices using various sensor technologies (conducting polymers, SAW, tin-oxide) have become available[2]-[4] and have gained renewed interest in both academic and industrial research areas [5,6]. There has been much recent research into the development of E-nose systems for odour detection and measurement [7]-[10].

In the human olfactory system there are around 10,000 sensors; these are non-selective but can be very sensitive to certain odours. Signals from these sensors, when they are exposed to a complex odour, are interpreted in the brain which identifies the characteristics of the odour. Recently, it has been shown that one odour sensor can recognise multiple odours but different odours are recognised by different combinations of odour sensors [11].

Electronic noses work in a similar manner to the human olfactory system. They usually consist of: an array of four to thirty two sensors which react in some repeatable way when exposed to an odour; a system (usually electrical) for polling and assembling the sensor responses; and, an associated computer program which interprets resulting signals. An e-nose system will typically comprise a number of different components including the sensors, pumps, valves, flow controller, air conditioner, control buttons and display panel. It will have software for monitoring the hardware, data pre-processing, statistic analysis, and other built in functions.

The tests described here were carried out using a Cyranose 320 electronic nose at the Queen's University of Belfast's QUESTOR environmental research centre. This device contains 32 carbon black/conducting polymer sensors. When the sensors are exposed to an odour the polymers swell to a greater or lesser extent, changing the physical separation of the particles of the carbon black surface coating, and hence their electrical resistance changes. The extent of such change depends on the materials used and the composition of the odours to which they are exposed. The E-nose will provide a characteristic "fingerprint" for odours arising from an individual chemical or from mixtures of chemicals. An E-nose built from broad response sensors can be trained or calibrated using characteristic samples of a potential odour source in air. When the E-nose is presented with an "unknown" odour some kind of pattern matching is used to determine if the fingerprint of the new odour matches one which is already known (i.e. on which the E-nose has already been trained). The recognition software should determine the best match with its li-

brary of known fingerprints and report the degree of confidence in the match. Provided the odour was caused by a known chemical, for which the sensor was appropriate, it should be possible to identify the chemical [12].

The human equivalent of the electronic nose is an olfactometry panel – a number of people selected for their ability to respond in a reasonably repeatable way when presented with various odour samples. Using humans in this way is subject to variations in the sense of smell between human beings and between individuals on different occasions, and for these reasons is not as objective as an electronic nose. However, in many cases humans are more sensitive and can detect odours at much lower concentrations than electronic noses. When artificial neural networks are trained with data from olfactometry panels there will be extra difficulties associated with the variations associated with human observers [13].

The application of portable E-noses in field conditions is more difficult than in a controlled laboratory environment. Variations in humidity, temperature and, especially, background odours and sample concentration mean that identification rate can be disappointingly low. It is, anyway, more difficult to correctly identify complex samples such as those from cigarettes which can be expected to show natural variation among batches and with age and storage conditions.

The aim of this work is to explore and improve the capability of a portable E-nose to identify different brands of cigarette. The sensor responses from the E-nose were analysed using artificial neural network (ANN) techniques. The data analysis were performed using MATLAB V6.5 and its neural network toolbox at the Electrotechnology Department, Auckland University of Technology (AUT), New Zealand. Data collected from the portable E-nose were used for feature extraction and principal component selection purposes. The extracted features and principal component selection were used to train the neural network providing an intelligent approach for identifying cigarettes [14]. The preliminary investigation described here was carried out on four brands of cigarettes under open laboratory conditions (no special atmospheric, humidity or temperature controls). We found that the rate of identification obtained using the neural network trained with extracted parameters was better than that obtained directly from the E-nose.

MATERIALS AND METHODS

Cigarette manipulation

The leaves of four different brands of cigarettes (with a total mass of about 10g each) were obtained from local suppliers and placed in different flasks. The flasks were closed tightly after introducing the tobacco and were held at room temperature (18 to 20 °C) for 6 hours before sampling.

The sample flasks were connected to the EDU inlet via a sample transfer line. The tobacco odours were collected onto the internal Tenax adsorbent tube, then desorbed to the Cyranose 320 E-nose via its detector line.

E-nose measurements

Figure 1 shows the experimental set-up for measuring and analysing cigarette odours using E-nose in the laboratory. The Cyranose 320 E-nose was coupled with an Airsense EDU pre-concentrator containing Tenax TA adsorbent.

The sample flasks were connected to the EDU inlet via a sample transfer line. The tobacco odours were collected onto the internal Tenax adsorbent tube, then desorbed to the Cyranose 320 E-nose via its detector line.

Figure 1 The E-nose and preconcentrator system in the laboratory.

The volatiles were thermally desorbed from the EDU and were pumped to the sensor array in the Cyranose 320. All measurements were performed at 30°C. The Cyranose 320 E-nose was set up as shown in Table 1.

Table 1 Cyranose 320 parameters set up for sampling cigarette volatile from Tenax tube

E-nose parameters		Run time (Sec)	Pump speed
Baseline Purge time		100	M
Sampling Time	Draw1	50	M
	Draw2	50	H
Purge Time	1st Air intake	15	M
	2nd Air intake	47	H
	2nd Air intake	28	M
Digital Filtering		On	
Substrate Heater Temperature		On	30 °C
Training Repeat count		10	
Identify Repeat Count		1	
Identification Quality		medium	
Algorithm		Canonical	

In Table 1, M and H stand for 'medium' and 'high' pump speed respectively.

Data acquisition and analysis

The raw sensor response data were acquired and formed the "fingerprints" shown in Figures 2 and 3. The data were

also saved into files for further analysis. The Cyranose 320 E-nose was trained with the sensor response data to obtain the patterns for each brand of cigarette which were then stored in its memory.

Figure 2 shows that the different brands of cigarette have very similar fingerprints – because the main odour components are similar. The result is that it would be difficult to discriminate them using the methods provided with E-nose software.

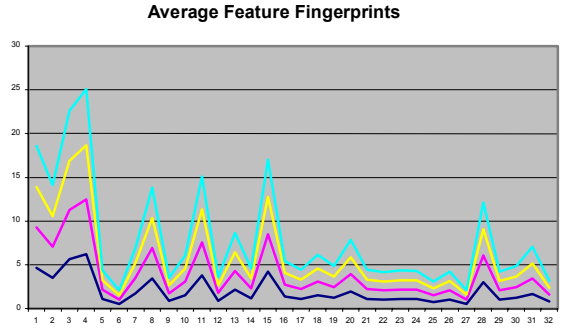

Figure 2 Fingerprints for four cigarette brands.

Figure 3 shows the average responses (from ten samples) from four brands of cigarette for each sensor. Note that all sensors, except S3, S4, S5, and S31, have very similar response data.

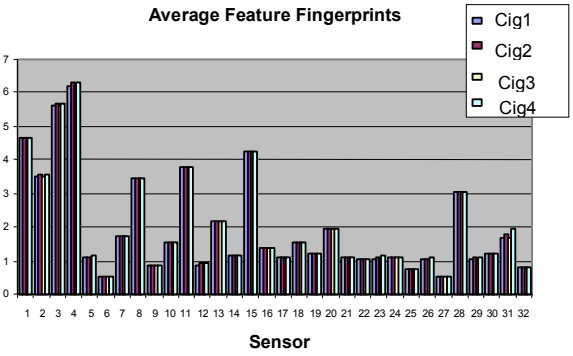

Figure 3 Average response for each brand.

Cigarette Identification using Cyranose 320 E-nose

The experimental tests for identifying the cigarettes were conducted in the laboratory one week after the Cyranose 320 E-nose had been trained. Identification samples were selected from the same packets of cigarettes as the training samples. Sampling time, desorption time and injection time were set to 100s, 80s and 60s respectively for EDU. The sampling time of Cyranose 320 was set to 100s. Each brand was sampled 10 times in order Cig1, Cig2, Cig3, and Cig4 with an interval of one day between test sets. The percentage correct identification rate is presented in Table 2. We can see that the E-nose canonical discrimination method has a poor discrimination rate, especially for Cig3 and Cig4 in this case.

Artificial Neural Networks (ANN)

In order to enhance the identification rate of cigarettes, a feed forward ANN has been used with the raw data from the E-nose. The nose has 32 sensors and collects 32 sets of data for each sample. These data were used to train our neural network for the purpose of comparing the identification rate. Several features were extracted from each sensor signal. They were the average (AVG), standard deviation (SD) and maximum response (MAX). As sensors S3, S4, S5, and S31 exhibited most resolution between the four brands, the output signals from these sensors were weighted for training purposes. All calculations and data evaluations were performed in MATLAB V.6.5 using the neural network toolbox.

The size of training data set and the number of extracted features was determined by the topology of the ANN. Figure 4 shows a two-layer log-sigmoid/log-sigmoid neural network. It has 32 or 35 inputs depending on using the additional three features with the 32 sensor signals. It has two neurons in its output layer to identify four classes. The number of neurons in its hidden layer was chosen to be eight. This number was selected by experience from other work.

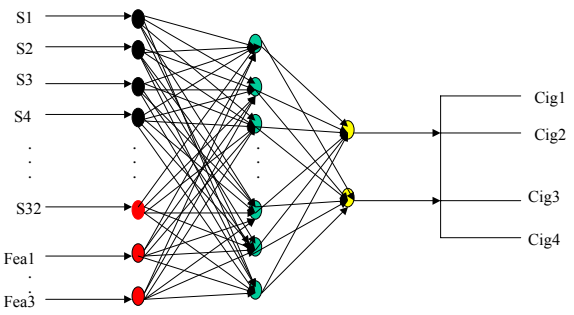

Figure 4 The network architecture with 32 inputs and 2 output neurons.

While altering the number of input neurons, the same transfer function and same parameters were used in the investigation. The log-sigmoid transfer function was chosen because its output range (0 to 1) is perfect for learning Boolean output values.

Four 32- or 35-element input vectors were defined as a matrix of input vectors for one sample to compare cigarette identification. The target vectors are two-element vectors to represent different classes. Each output vector corresponds to one class.

The same conditions were used to initialize networks with different architectures and the same parameters and learning functions were used to train them.

The Nguyen-Widrow initialization algorithm was used in this project. It has advantages over purely random weights and biases since few neurons are wasted (all the neurons are in the input space) and training works faster (each area of the input space has neurons). A log sigmoid transfer

function in layers calculates a layer's output from its net input. Learning occurs according to the defined gradient, learning rate and momentum constant.

RESULTS AND DISCUSSION

Feature extraction and training of the ANN

The proposed networks were trained under the same conditions in order to compare their performances. The training data sets were extracted from the data files of Cyranose 320. Four brands of cigarette with 160 samples for each were selected as basic signals to train the networks. The first network had 32 input signals and the second network had extra inputs for three extracted features AVG, SD and MAX. The third network was the same as the second one but S3, S4, S5, and S31 signals were weighted.

Training parameters were chosen carefully with maximum epoch of 3000, minimum gradient limited to 0.00001 and goal of 0.0001. Figure 5 shows the training performances of the neural networks. We can observe that the behaviours of the three networks in terms of training speed are different.

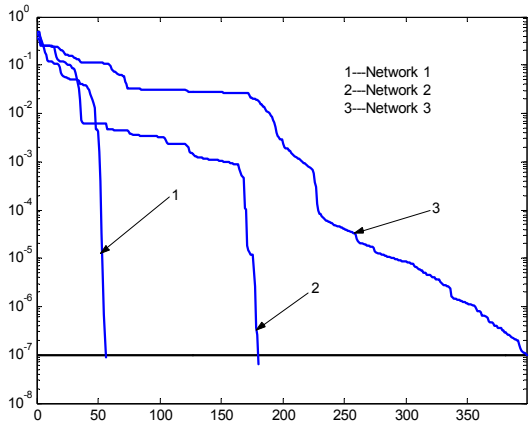

Figure 5 Training performance of the networks.

Test results

In comparing the performance of the ANN-based E-noses and Cyranose 320 E-nose, the same test data was used and each cigarette was tested 10 times. Each set of test data from the E-nose was preprocessed before submission to the ANNs for identification. Efficient features were extracted and some specific signals were weighted. The identification rate of each ANN-based E-nose is also shown in Table 2.

Table 2. Identification rates of cigarettes using Cyranose 320 and ANNs

Cyranose 320 E-nose	Cig1 (%)	Cig2 (%)	Cig3 (%)	Cig4 (%)
Without ANN	70	70	50	40
With ANN1	70	60	60	40
With ANN2	80	70	70	60
With ANN3	100	90	90	90

We can see the differences between results obtained by Cyranose 320 E-nose without and with three ANN networks. ANN1, with 32 input neurons, provides similar performance in correct identification of cigarettes as the Cyranose 320 E-nose without ANN. ANN2, which has 35 inputs (32 sensor signals plus three inputs for the extracted features) has better results than ANN1, but still its performance is rather low. ANN3, which uses weighted signals for S3, S4, S5 and S32 sensors, provides the best results. The identification rate has improved, especially for Cig1 and Cig4. Plainly, weighting the signals for specific sensors improves the identification rate.

Conclusions

In this work, we have demonstrated that artificial neural networks can improve E-nose classification performance for cigarette brand identification. In the experiments the performance of the Cyranose 320 E-nose was compared without and with utilising three ANNs in identifying four brands of cigarettes.

By utilising feature extraction techniques in combination with weighting sensitive signals from the E-nose and ANN, it is possible to improve E-nose identification performance. It is important to extract appropriate features from the raw data and apply them to the ANN for training and testing. The ANN input vector was formed by obtaining 32 sensor signals plus three features. Table 3 shows that there are different identification rates between ANNs with and without extracted features.

Significant improvement in successful discrimination between the brands was achieved by selecting specific sensors and applying extra weight to their signals during training and testing of the networks. The raw data from the Cyranose 320 indicated that signals from sensors S3, S4, S5 and S31 showed greater differences in their responses to the four different cigarette brands (than the other 28 sensors) and that S3 and S4 had the highest magnitude of response. Weighting these four signals was responsible for most of the advantage realised in the ANN tests.

The results from this study are sufficiently promising to justify further work with both legal and counterfeit cigarettes in China. The conditions used in the laboratory testing were not particularly controlled and the methods developed should be transferable to field analysis.

ACKNOWLEDGMENTS

Dehan Luo's visit to Queen's University and Auckland University of Technology (AUT) was funded by the China Scholarship Council. He acknowledges the support provided by the QUESTOR Centre at Queens and Electrotechnology Department at AUT. The E-nose used for the experimental work was supplied to the QUESTOR Centre by CyranoSciences Inc, USA.

REFERENCES

[1] State Tobacco Monopoly Administration (STMA) of China, 2001 Annual Report, *Proceedings of Annual*

Conference of Tobacco Supervision, Bejing, China, March, 2002.

[2] Lonergan, M. C., et al., "Array-Based Vapor Sensing Using Chemically Sensitive, Carbon Black-polymer Resistors," *Chem. Mater*, vol.8, 9, pp.2298-2312, 1996.

[3] Doleman, B. J., et al., "Quantitative Study of the Resolving Power of Arrays of Carbon Black –polymer Composites in Various Vapor Sensing Task," *Anal. Chem.* vol.70, 19, pp. 4177-4190, 1998.

[4] Natale, C. D., et al., "Electronic Nose and Sensorial Analysis: Comparison of Performances in Selected Case," *Sensors and Actuators*, B, vol. 50, pp. 246-252, 1998.

[5] Magan, N., et al., "Volatiles as an Indicator of Fungal Activity and Differentiation Between Species and the Potential Use of Electronic Nose Technology for Early Detection of Grain Spoilage," Journal of Stored Products Research, vol.36, pp. 319-340, 2000.

[6] Burl, M. C., et al., "Assessing the Ability to Predict Human Percepts of Odor Quality from the Detector Responses of a Conducting Polymer Composite-based Electronic Nose," *Sensors and Actuators*, B, vol.72, pp. 149-159, 2001.

[7] Misselbrook, T. H., et al., "Use of an Electronic Nose to Measure Odour Concentration Following Application of Cattle Slurry to Grassland," *Journal of Agricultural Engineering Research*, vol.66, pp. 213-220, 1997.

[8] Schaller, E., et al., "'Electronic Noses' and Their Application to food," *Lebensm.-Wiss. u.-Technol*., vol.31, pp. 305-316, 1998.

[9] Brezmes, J., et al, "Fruit Ripenness monitoring Using an Electronic Nose," *Sensors and Actuators*, B, vol. 69, pp. 223-229, 2000.

[10] Winquist, F., et al., "A Practical Use of Electronic Noses: Quality Estimation of Cod Fillet Bought Over the Counter," *Transducers '95 Eurosensors IX, The 8th International Conference on Solid-State Sensors and Actuators, and Eurosensors IX*, Stockholm, Sweden, vol. 1, pp. 695-697, June, 25-29, 1995.

[11] Doleman, B. J., et al., "Comparison of Odor Detection Thresholds and Odor Discriminablities of a Conducting Polymer Composite Electonic Nose Versus Mammalian Olfaction," *Sensors and Actuators*, B, vol.72, pp. 41-50, 2001.

[12] Cyrano Sciences Inc. USA, *The Cyranose 320 Electronic Nose User's Manual*, 3rd ed., (November 2000).

[13] Bockreis, A., et al., "Odour Monitoring by the Combination of Sensors and neural Network," *Environment Modeling & Software*, vol.14, pp. 421-426, 1999.

[14] Plaulsson, N., et al., "Extraction and Selection of Parameters for Evaluation of Breath Alcohol Measurement with an Electronic Nose," *Sensors and Actuators,* vol.84, pp. 187-197, 2000.

(This page left blank intentionally)

Nonlinear processing techniques for P-wave Detection and Classification: A review of current methods and applications

Adrian Diery
Griffith University
Biomonitioring Group
Kessels Rd, Brisbane, Qld.
Adrian.diery@student.gu.edu.au

David Rowlands
Griffith University
Biomonitioring Group
Kessels Rd, Brisbane, Qld
D.Rowlands@gu.edu.au

Daniel A James
Griffith University
Biomonitioring Group
Kessels Rd, Brisbane, Qld.
D.james@gu.edu.au

Tim Cutmore
Griffith University
Biomonitioring Group
Messines Ridge Rd. Brisbane
T.Cutmore@gu.edu.au

Abstract

In this paper we focus on the particular problem of extraction and classification of the P wave and the current techniques, both linear and nonlinear, which are employed. A brief description of the techniques is given along with specific examples of their application to the identification of Electrocardiographic P waves. Finally an analytical comparison of the sensitivity for each of these techniques is presented along with a discussion on their effectiveness and limitations.

1 Introduction

Heart disease is a major cause of death amongst Australians and New Zealanders and in 1999 caused almost 40% of all deaths in Australia and New Zealand [1][2]. Therefore research and development of technologies in the field of cardiology are of great interest and worth. In recent years many innovations in cardiac care have taken place, which have increased the tool base of modern cardiology. This has assisted the cardiologist in making more informed diagnosis thereby leading to prevention of serious conditions or the prescription of more beneficial treatment. Linear processing of biomedical signals have been implemented to great effect in the past [3,4,5], however current linear processing techniques are beginning to show limitations in their applications to the processing and analysis of biomedical signals. The limitations of linear processing techniques, such as the inability to discriminate between two signals of similar frequency content but difference phase information [6] can be overcome using relatively uncomplicated nonlinear methods of processing and analysis such as, nonlinear dynamics and representation, neural network analysis and non-linear filtering. In this paper several methods used to identify the p-wave are briefly described and their application to p-wave identification is then reviewed and a comparison of their effectiveness is presented. Finally a discussion of the relative merits and limitations of each method is offered.

1.1 The Electrocardiogram

The Electrocardiogram (ECG) is defined as the recordings made by the electrocardiograph, depicting the electrical activity of the heart [7]. Each segment or interval in the ECG signal (P-wave, QRS complex, ST segment) represents the electrical activity present in a specific part of the heartbeat cycle. The initial pulse formation in each section of the heart is conducted through the respective sections e.g. the Sinoatrial node provides the initial charge to the atria and the Atrioventricular node provides the initial charge to the ventricular mass, which comprises a number of separate sections. Arrhythmias arise when there is a disruption to the normal sequence of events of the electrical cycle. These disruptions may be due either to abnormalities in the pulse formation or in the electrical conduction. The abnormalities show up on the ECG signal as irregularities or anomalous events.

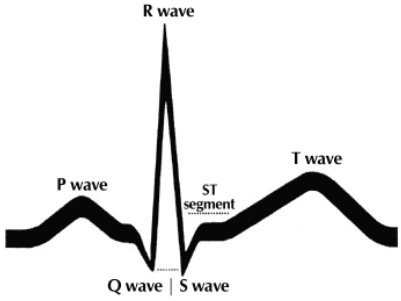

Figure 1 The ECG [10]

The ECG is usually represented on grided (1x1mm) paper. In the horizontal direction each grid represents 0.04 seconds whilst in the vertical direction each grid represents 100μV. The recording of the ECG is done by the use of the standard 12-Lead configuration, where the leads are grouped as the Limb (I,II,III), augmented Limb (aVL, aVR, aVF) and the precordial (V1,V2,V3,V4,V5,V6). The Limb and Augmented Limb leads are in the same axis on the front of the torso, whereas the precordial Leads move around the cardiac location from the front to the back of the torso.

1.2 The P-wave

The P-wave represents the depolarization of the atrium and is most prevalent in Lead II. The accurate identification and analysis of the P wave is of vital importance in early identification and diagnosis of many cardiac arrhythmias [10]. The P wave and PR interval are indicative of atrial fibrillation and other conduction problems in the atrium [10]. Abnormal P wave morphology is also indicative of atrial enlargement and congenital heart disease. The P wave can also become less pronounced with age and therefore more difficult to read and diagnose which

can make identification of the P wave, and consequently, diagnosis extremely difficult. Due to its relatively low amplitude, close proximity to the QRS complex and subtle changes in morphology, the P-wave presents a challenging problem in terms of identification, extraction or enhancement. This has lead to the popularity of non-linear signal processing techniques as a possible means of solving this problem.

2 Processing Techniques

Current linear processing techniques are beginning to show limitations in their applications to the processing of time-series data, in particular biomedical signal analysis. There also exist many inherent limitations of linear processing techniques, such as the inability to discriminate between two signals of similar frequency content but difference phase information [8]. This has lead to increased interest in non-linear processing techniques such as state-space dynamics and representation, neural network analysis and non-linear filtering. Linearity is the property displayed by a system when the output of the system is directly proportional to the system input. This property is reliant upon the functions of the components of the system being proportional to the overall system, of course this is unlikely to occur in any natural system [9].

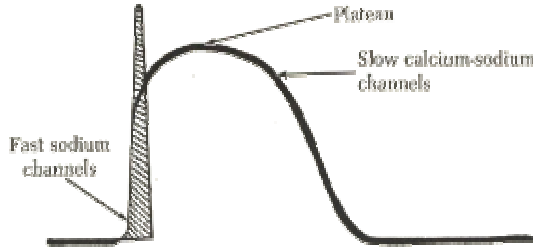

Figure 2 AV action potential (p 24 Boudreau-Conover [10])

Instead the components of the system are more likely to interact with each other and, from these interactions, produce outputs that are not proportional, and sometimes unrelated, to the original input, therefore creating a nonlinear system. For example the cardiac conduction cycle has nonlinear dependencies based upon the excitation patterns of the calcium channels present in the cardiac tissue, as shown in Figure 2. The different channels have differing conductivities and therefore produce a nonlinear reaction to their initial excitation. From this we can see that there is cause for examining the non linear dependencies of the ECG by using means other than linear time-series analysis. The obvious first choice for non-linear analysis is to examine the ECG in the frequency domain. This section examines the commonly used non-linear techniques of Wavelet processing (frequency domain), Artificial Neural Networks (classification/detection), numerical analysis including non-linear transformations, and non-linear dynamics analysis (Phase-Space portraits).

2.1 Wavelet Processing

Wavelet Processing techniques for signal processing and analysis have been well documented and widely employed for many applications including the processing and visualization of Electrocardiogram signals [11,12, 13, 14, 15]. The wavelet transform allows for the transform of linear time-series data into time-frequency levels. The continuous wavelet transform (CWT) represents the original data in a continuous frequency scale along a time axis. The cwt can be viewed as an image where the luminance or colour represents the amount of energy contained in a particular frequency at a particular time as shown in figure 3.

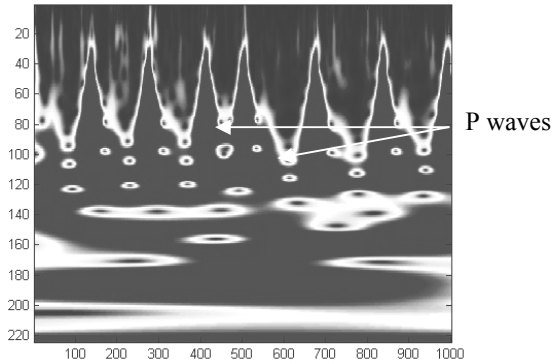

Figure 3 CWT image of an ECG signal [15]

The p-waves become evident in Figure 3 as clearly identifiable concentrations of energy preceding the QRS complex peaks as marked. Of more use in automated analysis and compression is the discrete wavelet transform. The DWT transforms the time series data into discrete time-frequency band coefficients. This allows analysis of the energy distribution of a signal of discrete narrow band frequencies.

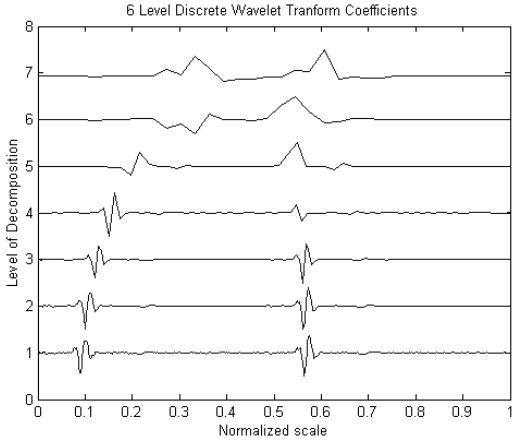

Figure 4 6-level DWT of 2 seconds of ECG data

In Figure 4, level one represents the upper half band of the original signal's frequency spectrum; each remaining lower band is split in half again so that the coefficients represent the upper half of each band. Level 7 represents the final lower half of band 6 and the coefficients of this level are called the detail coefficients, the other bands are

known as the approximation coefficients. The characteristic spikes present in the first three levels are related to the original QRS complex. By applying a threshold to these levels, thereby suppressing coefficients of low amplitude, peak detection can be applied to accurately detect and locate the QRS complex in the original signal. These QRS locations can then be used to suppress the QRS segments and search for other characteristics such as the P wave. The DWT also allows for reconstruction of the original signal from the detail and approximation coefficients which can be exploited for applications such as QRS detection [11] and data compression [14].

2.2 Artificial Neural networks

Artifical Neural Networks (ANN) are commonly used in signal processing for the classification, recognition, and detection of a required pattern. ANNs mimic the biological neural process, such as the brain, by modelling the neurological information processes by means of a mathematical paradigm [16]. In the last 50 years much work has been done applying ANN to practical applications and improving ANN structure for more effective and adaptable learning allowing for wider application of the technique [17].The common component of any Artificial Neural Network (ANN) is the McCulloch Pitts' Neuron Model [18] as shown in figure 5.

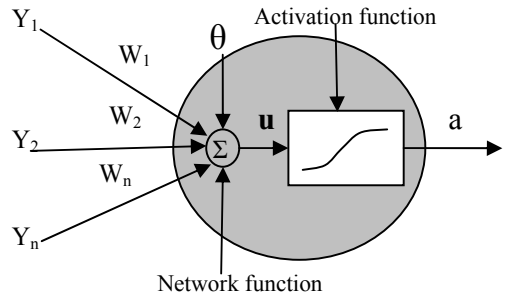

Figure 5 McCulloch and Pits neuron model [16]

The network function produces a weighted combination (**u**) of the input to the neuron, (Y_1, Y_2, Y_3….) which are usually the output of some nonlinear transformation of an original data set. Common nonlinear input transformations are covered in section 2.3. The network function may be either a linear summation or non-linear function; alternatively the network function can be the product of all the weighted inputs.

Equation 1 neuron output

$$a = f(u)$$

The actual function employed by the activation function can be graded slopes, thresholds or linear slopes; each has advantages for specific applications.

The main application for them in the ECG problem is in ECG characteristic identification or pattern recognition. The simplest method of implementing a neural network for pattern recognition makes use of the Perceptron network. The perceptron is a variation on the original neuron model where the weighting vector, $\underline{w} = \{w_1, w_2 \ldots w_N\}$ is indicative of the desired recognition pattern. In this manner, if the input data series, $\underline{x} = \{x_1, x2 \ldots x_N\}$, is similar to the weighting vector then their inner product should exceed an appropriately chosen threshold, determined by the activation function which is a discrete threshold function.

$$u = \sum_{j=1}^{N} Y_j . W_j + \theta$$

$$a = \begin{cases} 0 & u < 0 \\ 1 & u > 0 \end{cases}$$ **Increase size of {**

Where a=1 would be a detection.

A comparison of several ANN structures and learning algorithms for ECG classification in [19] found that a static ANN with principal component analysis input had the fastest training time when using a backpropagation training method. The relative simplicity of the backpropagation (BP) networks is an attractive feature and in addition to analysis of the ECG, BP networks can be adapted to also perform classification within the one network [20].

2.3 Numerical Analysis Techniques & Nonlinear Transformations

Many numerical transforms are used as the nonlinear transformation input to neural networks. These techniques are used to transform the data to provide more meaningful information sets for analysis. The following two techniques are principal component analysis and singular value decomposition. Both are common techniques used to efficiently represent data sets; however the discrete wavelet transform is also commonly used [39].

2.3.1 Principal Component Analysis (PCA)

PCA is a mathematical procedure whereby a dataset containing interrelated variables is collated into a correlation or covariance matrix. It is from this matrix the principal components are calculated such that the first component describes as much of the variability of the original data as possible, with each successive component describing as much of the residual variability as possible. In this way the dimensions of the original data set can be reduced by removing and expressing the interrelated data components in a more succinct form [21].

The application of PCA in signal processing can roughly be categorized into two applications where the goal is to reduce the original dimensions of data for compression or to extract meaningful characteristics of the original data so as to perform some form of classification or recognition. In terms of data dimensionality reduction PCA provides the optimum linear reduction and is often referred to as the Karhunen-Loeve expansion [16]. The PCA technique is primarily used as a pre-processor for Neural Networks which perform detection and classification, such as human identification through ECG analysis [22], face recognition [23] and Ischemia detection [24]. The latter uses a nonlinear PCA technique which will be discussed in section 2.3.3.

2.3.2 Singular Value Decomposition

Singular Value Decomposition (SVD), or eigenvalue decomposition, is a mathematical transform that can be used to reduce the amount of data required to represent a matrix. This allows for the efficient coding of images by means of lossy compression. The SVD of a matrix A of dimension (n x p), where n is the number of rows and p the number of columns, is given in equation 5:

Equation 2 Singular Value Decomposition

$$A = USV^T$$

where;

U and V are (n x r) and (p x r) matrices respectfully.

S is a (r x r) diagonal matrix.

S is an (r x r) diagonal matrix whose leading diagonal elements are known as the singular values. The matrices *U* and *V* are the left and right single value matrices and whose columns are orthonormal such that $U^TU = I_r = V^TV$. As previously mentioned SVD is used in signal processing applications primarily such as image compression [8] and noise removal by means of nonlinear filtering [25],[26] and also as an efficient algorithm for calculating principal components [21].

2.3.3 Nonlinear PCA

As mentioned earlier nonlinear PCA can provide a nonlinear mapping of the original data source by means of replacing the original data set x with a function of x [21]. There exist two models for creating a nonlinear PCA system, symmetric and hierarchical, of which the latter provides better classification through higher discrimination of significant features [27] [28] [29]. In [24] the non linear principal component analysis (NLPCA) is used to group and classify the nonlinear clusterings of normal and abnormal ischemic beats in a feature space. NLPCA provides a much more accurate characterisation of the clusterings then a normal PCA does.

2.4 Nonlinear Dynamics analysis through Phase-Space portraits

Nonlinear Dynamics is the term applied to the study of the complex behaviour of relatively simple systems [34] and as has been previously described in section 2 the heart represents such a system. The term state or phase space refers to the analysis of a system by its change in states and current state. This is often done by means of phase portrait representation as shown in figure 7. When applied to visualization of the ECG the phase portrait offers simple intuitive representations of the signal and easily highlights time varying properties of the ECG, such as increase in segment or complex duration. The true Phase-Space of an ECG cannot be reconstructed solely from the ECG signal; however a pseudo Phase Space, which is equivalent to the original phase space, may be reconstructed by the use of one of several methods. It can simply be presented as the original time series signal related to the first derivative of the time series, although in [30] the phase space derivation also includes a lag or delay term. The delay, or lag, used can be calculated using several methods; method of delays, trial and error, mutual information [31,32]. The most computationally simple method of calculating the optimum delay is the Takens' method of delays which ensures that the phase portrait is adequately decipherable [31]. That is, the ECG attractors are well spread allowing each characteristic loop of the ECG to be easily identified by visual inspection, such that the QRS loop is broad enough not to interfere with the other characteristic loops of the ECG. The attractors of a system describe its long term behaviour from starting conditions and maybe point, limit cycle (periodic) or chaotic (strange) in nature. Point attractors describe the system in equilibrium from any set of starting conditions after all motion has ceased. Limit cycle attractors describe the steady state oscillations of a system after the transients have subsided, however this state of steady oscillation may alter dependent upon initial conditions of the system. Finally chaotic attractors describe the aperiodic behaviour of the system [33] and their trajectories exhibit exponential divergence away from nearby paths [34].The mapping of the ECG time series data into this feature space phase portrait in Figure 7 shows each waveform of the ECG clearly distinguished and immediately apparent. Identifying the underlying attractors of the system means that the ECG can be still be a accurately analysed by such means as NLPCA [24] in the presence of temporal noise [34].

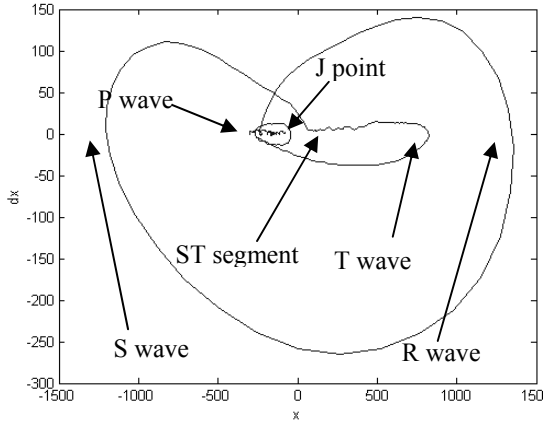

Figure 6 Phase Portrait of normal sinus rhythm

3 P Wave Detection Techniques

The common difficulties identified in relation to the identification of the P-wave are susceptibility to noise, low amplitude and merging with T waves in periods of tachycardia. The common solution to this problem is to implement some form of QRS complex suppression and then "search" for the P-wave. The methods used range from standard linear processing techniques to more complex applications of several non-linear processing techniques all with varying levels of success.

3.1 Linear Adaptive Signal Processing

In the field of Digital Signal Processing the term "adaptive" generally applies to systems which take into consideration that the processes which are being analysed

are non-stationary; that is the statistical characteristics of the processes vary with time and therefore the system must vary accordingly. In general non-adaptive systems work quite well when used for processing Electrocardiograms due to the generally consistent frequency content of the signal or pseudo-stationary behaviour of the ECG as a process; see Figure 8.

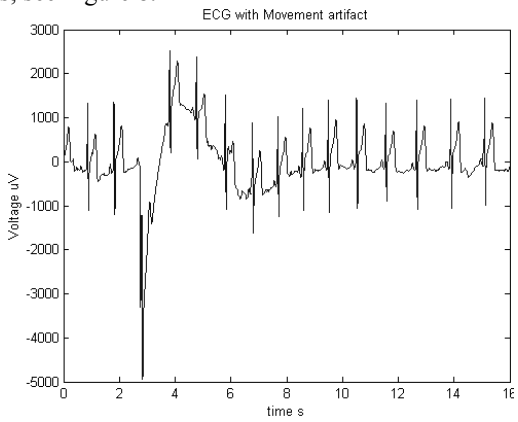

Figure 7 ECG signal containing movement artefact

The Power Spectral Density (PSD) estimate is a representation of the distribution of a signal across the original signal's frequency spectrum. The PSD shown in Figure 8 was calculated by cutting the ECG signal into blocks then performing the Burg PSD approximation on each block. The inadequacies of linear filtering become apparent when this approximation does not hold; the movement artefact present in Figure 7 is clearly evident in the PSD graph as the plot which deviates from the envelope created by all other frames of the signal. The noise is now spread across the frequency range inhabited by the normal ECG.

A simple first order filter accompanied with decision rules is implemented in [35] to detect onset of P and end of T waves. This algorithm has the advantage of being user defined, that is a cardiologist can initiate the algorithm with their definition of P wave onset and the end of the T wave. From these initial conditions an adaptive filtering constant μ is approximated and the ECG is filtered with a first order adaptive system utilizing this constant.

$$H(z) = \frac{1 - z^{-1}}{1 - (1 - \mu).z^{-1}}$$

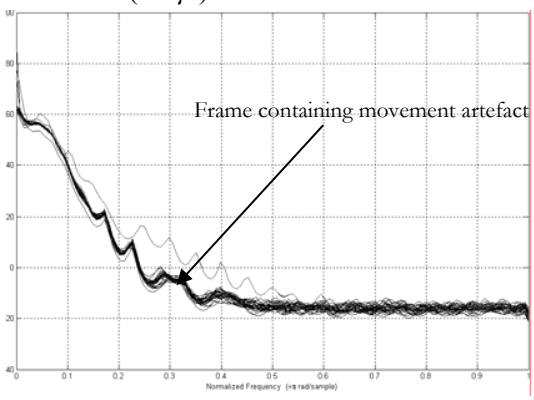

Figure 8 PSD estimate of ECG containing movement artefact

A second iteration of the constant approximation and filtering is performed and the first order discrete time derivative is taken. The points corresponding to zero are judged to be the P-wave onset and T-wave offset. A real-time filter based approach to ECG characteristic detection is developed and implemented in [36]. This method performs real-time analysis of the ECG and detects the onset and offset of each characteristic beat. The QRS complex is logically detected first and upon successful detection a search window is defined for the T wave which must follow the QRS. In the resulting window left between the detected T wave and QRS complex the P wave is searched for using the following rules.

The P wave is defined as:

- A positive slope followed by a negative slope
- Where both slopes have a magnitude greater than 0.004mV/s

The remaining characteristics such as RR, ST, PQ and QT intervals are derived from the wave locations as are the onset, peak and offset of each P wave detected.

3.2 Wavelet Techniques

Wavelet techniques for processing physiological signals, and in particular the ECG, have been well documented. Wavelet transforms are used in robust QRS detection to highlight the QRS complex and allow for easy location of each beat, when applied to the P-wave detection problem they are generally used to locate and suppress the QRS complexes [37]. The wavelet coefficients can also be used as the input to more complex pattern recognition techniques such as Hidden Markov Models [38] and back propagation neural networks [39]. In [38] a method of segmenting each beat in the ECG in order to extract and classify the P-waves is presented and discussed. The method is used to identify patients who are susceptible to Atrial Fibrillation (AF).

The steps involved in this algorithm are as follows

- Band limit ECG 0.01 – 40 Hz
- 4 level, multi resolution analysis using Haar wavelet transform.
- QRS detection and suppression
- Beat Segmentation by applying a Hidden Markov Model to each resolution level and correlating the results.

In [38] the ECG is first segmented into its various components so that the hidden Markov Model's states for the ECG can be determined. This creates a logical yet flexible pattern recognition model. The wavelet pre-processor is proven to be effective in decreasing the time or number of iterations required to train the ANN shown in [39].

3.3 Artificial Neural Networks

As previously mentioned ANN are primarily used in signal processing applications for pattern classification, pattern recognition or detection. They can then be thought of a as a dedicated form of classification where there exists only two output states; detection = true or false. However this binary definition is not held by Neuro-fuzzy networks [40] which employ a probabilistic approximation in terms of classification. The reduced emphasis on producing a definitive answer means that processing time needed to produce a result can be reduced; however this in turn means a reduction in accuracy of detection or rejection. To summarise, the Neuro-fuzzy network provides a quick and rough result based upon statistical properties obtained through training. The morphology of the P wave is also a factor which can alter detection rates and therefore the classification of this morphology would be of benefit to an ANN. Classification of the P wave into four groups, positive, negative, bi-phasic and M-shaped is achieved in [41] where the salient feature is the implementation of an asymmetric basis function which the authors claim produces higher classification results by improving the rate of classification for biphasic and M shaped P waves.

4 Comparison of P wave Detection methods

Most algorithms were tested using the MIT-BIH arrhythmia database; however a specific database dedicated to atrial fibrillation was compiled and used in [38], a database of healthy test patients was used in [40]. Most methods listed more than one measure of evaluation, such as sensitivity, positive predictivity, false detection, etc.

The sensitivity quality was chosen as the common denominator by which to compare the collated methods and the relative values for each method appear under the detection accuracy heading in Table 1. Unless otherwise specified these values relate to the sensitivity of the algorithm stated in the respective papers. Sensitivity is the proportion of actual positives that were predicted that way; here it describes the percentage of true positive P waves detected.

In some instances this information was not available, as in [35] where the positions of the detected P waves were compared to the onset and offsets as determined by a cardiologist. The highest rates of detection were associated with the adaptive filter system [36] and a neural network analysis system using a discrete wavelet transforms pre-processor [42]. In the case of the Adaptive filter proposed in [35] a cardiologist is required to mark the onset of the P waves and offset of the T waves, whilst this is useful due to the highly ambiguous nature of the P wave onset and the individual interpretation of it, it means that the system can not perform automated detection of the P waves. Automated detection would be desirable for long term monitoring but not essential for clinical monitoring. The authors also claim that baseline drift has no effect on the performance of the adaptive filter system. The flexibility of the Neural Networks to be applied to not only detection but classification of the P wave is an advantage over the adaptive signal processing techniques of [36] [35] which are dedicated solely to the detection of the P-wave. Results show that the choice of pre-processor has a significant impact upon the effectiveness and speed of the detector.

Table 1 Comparison of P wave Detection methods

System	Data base	Complexity	Position Accuracy	Detection Accuracy
Adaptive Signal Processing [35]	Healthy Database &. MIT-BIH segments containing 50 Beats	Simple, requires user input definitions, Training	2.31 +/- 4.57 ms [1]	-
Real time ECG characteristic detection with moving average filters [36]	QT database (MIT-BIH was used solely for QRS)	Simple moving average filters and rule book	-	69.3 % (onset) 73.8 % (peak) 77.6 % (offset) 73.6 % (mean)
Neural Network with Asymmetric Basis Function [41]	MIT-BIH recordings	Requires Training	-	Performs classification of the P-wave
Neuro fuzzy network [40]	Independent Data, Healthy test patients.	Requires Training	-	83.25%,
Wavelet transform and HMM analysis [38]	Brest University AF database		-	65-70%,
Wavelet decomposition for ANN analysis [42]		Requires Training	-	92% (relative to 96.19% QRS complexes detected).

The wavelet pre-processor applied to both the Neuro fuzzy network in [40] and the backpropagation ANN in [41] reportedly improves the speed of the networks training with both networks returning high levels of correct identification. The Wavelet transform fed HMM [38] in comparison has a much lower sensitivity for an increased level of complexity. Nonlinear dynamical analysis of the ECG has briefly been explored in [30] and [31] however a practical means of applying the dynamic analysis. The high degree of separation of the individual ECG waveforms provided by Figure 6 would suggest that the application of NLPCA to the phase space, similar to that which is applied to feature space data in [24], would provide a novel means of ECG characteristic identification, in particular the identification and enhancement of the P wave.

References

[1] Australian Bureau of Statistics, **"Cardiovascular Health 2002"** http://www.abs.gov.au/ausstats/abs@.nsf/0/D2A2D96DC505FD28CA256B35001586D4?Open, 2002, accessed 21/04/03

[1] Represents an average of the mean and standard deviation of the differences between the automatically detected and Cardiologist marked locations of the P wave onsets reported in [35]

[2] New Zealand Health Information Service, **"Mortality Rates"**, http://www.nzhis.govt.nz/stats/mortstats.html#01, 1999, accessed 21/04/03

[3] M.Kunt, H.Rey, A.Ligtenberg, **"Preprocessing of Electrocardiograms by digital Techniques"**, North Holland Publishing Group, Signal Processing 4, pp215-222,1982

[4] R. Nygaard, G. Melkinov, A.K. Katseggelos, **"A Rate Optimal ECG Coding Algorithm"**, IEEE Trans on Biomed Eng, Vol 48, No1, pp 28-40, January, 2001

[5] S. Jalaleddine, C.G. Hutchens, R.D Strattan, W.A. Coberly, **"A Unified Approach"** 1990, IEEE Trans. on Biomedical Eng., 37, 329-343

[6] Greg Morfill, Wolfram Bunk, **"New designs of complex systems"**, http://www.europhysicsnews.com/full/09/article1/article1.html, Europhysics News (2001) Vol. 32 No. 3, 2001

[7] G.S. Wagner, **"Marriot's Practical Electrocardiography"**, Tenth edition, Philadelphia, Lippincott Williams & Wilkins, 2001

[8] Greg Morfill, Wolfram Bunk, **"New designs of complex systems"**, http://www.europhysicsnews.com/full/09/article1/article1.html, Europhysics News (2001) Vol. 32 No. 3, 2001

[9] A.L. Goldberger, B.J. West, **"Chaos in Physiology: Health or Disease? "**, Proceedings of NATO Advanced Research Workshop on Chaos in Biological Systems, Dec 8-12, 1986, Cardiff, published by Plenum Press, "Chaos in Biological Systems", Series A, Vol 138, pp 1-4, 1987

[10] M. Boudreau-Conover**, "Understanding the Electrocardiogram: 12 lead"**, The C.V. Mosby Company, St. Louis, 1988

[11] C. Li, C. Zheng, C. Tai, **"Detection of ECG Characteristic Points Using Wavelet Transforms"**, IEEE Trans on Biomed Eng,Vol 42, No 1, pp 21-28, January, 1995

[12] P.S. Addison, J.N. Watson, G.R. Clegg, M. Holzer, G. Sterz, C.E. Robertson, **"Evaluating Arrhythmias in ECG Signals Using Wavelet Transforms"**, IEEE Engineering in Medicine and Biology, pp 104-109, Sept/Oct, 2000

[13] A.E. Cetin, A.H. Tewfik, Y. Yardimci, **"Coding of ECG Signals by Wavelet Transform Extrema"**, IEEE, 0-7803-2127-8/94, pp 544-547, Aug, 1994

[14] R.S.H. Istepanian, A.A. Pertrosian, **"Optimal Zonal Wavelet-Based ECG Data compression for a Mobile Telecardiology System**", IEEE Trans on Information Technology in Biomedicine, Vol 4, No 3, pp 200-211, Sept 2000

[15] R. Sedawie, **"ECG Visualization"**, Undergraduate Thesis, Griffith University, 2003

[16] Y. H. Hu, J. Hwang, **"Handbook of Neural Network Signal Processing"**, CRC Press, Boca Raton, 2002

[17] R.P. Lippmann, " An Introduction into Computing with Neural Nets",

[18] McCulloch W.S., Pitts W**. "A Logical Calculus of Ideas imminent in Nervous Activity"** Bulletin of Mathematical Biophysics, 5, pp 115-133, 1943

[19] R. Silipo, C. Marchesi**, "Artificial Neural Networks for Automatic ECG analysis"**, IEEE Transactions on Signal Processing, Vol 46, No 5, May, 1998

[20] S. Khursheed ul Hasnain, S. Muhammad Asim, "Artificial Neural Networks in Cardiology – ECG wave Analysis and Diagnosis Backpropagation Neural Networks",

[21] I.T. Joliffe, **"Principal Component Analysis",** Springer Verlag, New York, 1986

[22] L. Biel, O. Pettersson, L. Philipson, P. Wide**, "ECG Analysis: A New Approach in Human Identification"**, IEEE Transactions on Instrumentation and Measurement, Vol 50, No 3, June 2001

[23] W. S. Yambor, B. A. Draper, J. R. Beveridge, **"Analyzing PCA-based Face Recognition Algorithms: Eigenvector Selection and Distance Measures"**, Computer Science Department, Colorado State University, Fort Collins, CO, U.S.A 80523, July 1, 2000 available at: http://www.cs.colostate.edu/evalfacerec/papers/eemcvcsu.pdf

[24] T. Stamkopoulos, K. Dimantaras, N. Maglaveras, M. Strintzis, **"ECG Analysis Using Nonlinear PCA Neural Networks for Ischemia Detection"**, IEEE Transactions on Signal Processing, Vol 46, No 11, November, 1998.

[25] R.Vaccaro Ed., "SVD and Signal Processing II, Algorithms, Analysis and Applications", Elsevier, Amsterdam, 1991

[26] Per Christian Hansen, **"The Singular Value Decomposition"**, http://www.imm.dtu.dk/~pch/Projekter/tsvd.html, 26/05/2003

[27] M. Scholz, R Vagario "Nonlinear PCA: a new hierarchical approach",

[28] William W. Hsieh, **"Nonlinear principal component analysis by neural networks"**, Tellus, 2001, vol. 53A, pp 599 – 615 available @ : http://www.ocgy.ubc.ca/projects/clim.pred

[29] R.P.W. Duin, "Multi Class nonlinear feature extraction by nonlinear PCA",

[30] Zhenzhou Wang, Xinbao Ning, Yu Zhang, Gonghuan Du, **"Nonlinear dynamic characteristics Analysis of Synchronous 12-Lead ECG Signals"**, IEEE Engineering in Medicine and Biology, 0739-5175/00, September/October, 2000

[31] O. Fojt, J. Holcik, **"Applying nonlinear dynamics to ECG processing"**, IEEE Engineering In Medicine and Biology, 0739-5175/98, March/April 1998

[32] A.I. Karamavruc, N.N. Clark, J.S. Halow, "Application of Mutual Information theory to fluid bed temperature and differential pressure signal analysis", Elsevier Science, Powder Technology, 84, pp 247-257, 1995

[33] J.M.T. Thompson, H.B. Stewart, **"Nonlinear Dynamics and Chaos"**, Second Edition, Wiley, Chichester, 2002

[34] R. C. Hilborn, **"Chaos and Nonlinear Dynamics"**, Oxford University Press, New York, 1994

[35] E. Soria-Olivas, M. Martinez-Sober, J. Calpe-Maravilla, J.F. Guerrero-Martinez, J. Chorro-Gasco, J. Espi-Lopez, **"Application of Adaptive Signal Processing for Determining the Limits of P and T waves in an ECG"**, IEEE Transactions on Biomedical Engineering, Vol. 45, No. 8, August 1998.

[36] U. Kunzmann, G. von Wagner, J Schöchlin, A. Bolz, **"Parameter Extraction of ECG Signals in Real Time"**,

[37] S. Kadambe, R. Murray, G F. Boudreaux-Bartels, **"A Wavelet Transform-Based QRS Complex Detector"**, IEEE Transactions on Biomedical Engineering, Vol 46, No. 7, pp 838-848, July 1999

[38] R. Lepage, J-M Boucher, J-J Blanc, J-C Cornilly, **"ECG Segmentation and P-wave Feature Extraction: Application to Patients prone to Atrial Fibrillation"**, Proceedings 23rd annual Conf. IEEE/EMBS, Istanbul, Oct 25-28, 2001.

[39] K. S. Anwant, F. U. Dowla, G.H. Rodrigue, **"Detection of the electrocardiogram P-wave using wavelet analysis"**, Lawrence Livermore National Laboratory

[40] V. Pilla Jr., H. Silverio, **"Evolutionary Training of a Neurofuzzy Network for Detection of P wave of the ECG"**, Electronics Dept And Bioinformatics Laboratoy Federal Center of Technological Education of Parana, Curitaba, Brazil.

[41] E. de Azevedo Botter, C.L. Nascimento, Jr., T. Yoneyama, **"A Neural Network with Asymmetric basis functions for Feature Extraction of ECG P Waves"**, IEEE Transactions on Neural Networks, Vol 12, No. 5, September 2001.

[42] K. Sternickel, **"Automatic pattern recognition in ECG time series"**, Computer Methods and Programs in Biomedicine 68, pp109–115, (2002)

(This page left blank intentionally)

A Face Recognition System Using Neural Networks with Incremental Learning Ability

Soon Lee Toh and Seiichi Ozawa
Graduate School of Science and Technology, Kobe University
1-1 Rokko-dai, Nada-ku, Kobe 657-8501, JAPAN
den@frenchblue.scitec.kobe-u.ac.jp
ozawa@eedept.kobe-u.ac.jp

Abstract

This paper presents a fully automated face recognition system with incremental learning ability that has the following two desirable features: one-pass incremental learning and automatic generation of training data. As a classifier of face images, an evolving type of neural network called Resource Allocating Network with Long-Term Memory (RAN-LTM) is adopted here. This model enables us to realize efficient incremental learning without suffering from serious forgetting. In the face detection procedure, face localization is conducted based on the information of skin color and edges at first. Then, facial features are searched for within the localized regions using a Resource Allocation Network, and the selected features are used for in the construction of face candidates. After the face detection, the face candidates are classified using RAN-LTM. The incremental learning routine is applied to only misclassified data that are collected automatically in the recognition phase. Experimental results show that the recognition accuracy improves without increasing the false-positive rate even if the incremental learning proceeds. This fact suggests that incremental learning is a useful approach to face recognition tasks.

1. Introduction

Understanding how people process and recognize faces has been a challenging task in the field of object recognition for a long time. Many approaches have been proposed to simulate the human process, in which various adaptive mechanisms are introduced such as neural networks, genetic algorithms, and support vector machines [1].

Many of the proposed methods can achieve considerably good recognition results for available benchmark datasets. Several commercial products are also based on these methods, but in practice the recognition rates usually drop rather drastically as compared with the rates achieved for benchmark datasets. One primary reason for this failure in the existing commercial face recognition systems is that insufficient or inappropriate data have been used in the training of classifiers. Since human faces are prone to be changed in the course of time, it is quite difficult to collect all of the appropriate training data in advance.

A way to circumvent this problem is to introduce incremental learning [2, 3] into classifiers, much in the same way humans learn to recognize both unknown faces and known but varied faces. Most of the current commercial systems lack a learning ability to improve their performance automatically. Thus we think the concept of incremental learning is the essential factor to build a robust recognition system in real situations.

In this paper, we present a fully automated adaptive face recognition system in which the following two functions are realized for practical purposes by introducing two types of neural networks:

1. one-pass incremental learning,
2. automatic generation of training data.

In the one-pass incremental learning, each of the training data is given only once; that is, the previously given data will never be available in the future [3]. The largest benefit of introducing the one-pass incremental learning is that the system does not need so much large memory to enhance its performance; that is, the retraining of many training data is unnecessary. This property is very useful especially for small-scale systems. On the other hand, the second function is very important in the practical sense, because the incremental learning is carried out only after the actual recognition is done. That is to say, training data should be automatically generated based on the recognition results without any human intervention.

In Section 2, a brief explanation of our proposed incremental learning model is given. Section 3 describes the developed face recognition system in which face detection,

face recognition, and incremental learning are fully automatically carried out online for video streams. In Section 4, some recognition experiments are conducted to evaluate the incremental learning performance, and the concluding remarks are given in Section 5.

2. Incremental Learning Model

Disruption in neural networks, called "forgetting" or "catastrophic interference", often occurs during incremental learning. It is caused by the excessive adaptation of connection weights to new data. One way of overcoming this problem is that only representative training data are kept in memory and some of them are trained with newly given training data. To realize this, we have adopted a "Resource Allocating Network with Long-Term Memory (RAN-LTM)" using a fast learning algorithm based on the linear method [4] as our learning classifier.

2.1. Architecture of RAN-LTM

Figure 1 shows the architecture of RAN-LTM, which consists of two parts: Resource Allocating Network (RAN) [5] and Long-Term Memory (LTM). RAN is an extended model of the Radial Basis Function (RBF) network in which the automated allocation mechanism of hidden units is introduced. Hence, the information processing is almost the same as that in RBF except for the allocation of hidden units.

Let us denote the number of input units, hidden units, and output units as I, J, K, respectively. Moreover, let the inputs be $\boldsymbol{x} = \{x_1, \cdots, x_I\}'$, the outputs of hidden units be $\boldsymbol{y} = \{y_1, \cdots, y_J\}'$, and the outputs be $\boldsymbol{z} = \{z_1, \cdots, z_K\}'$. The calculation in the forward direction is given as follows:

$$y_j = \exp(-\frac{\|\boldsymbol{x} - \boldsymbol{c}_j\|^2}{2\sigma_j^2}) \quad (j = 1, \cdots, J), \tag{1}$$

$$z_k = \sum_{j=1}^{J} w_{kj} y_j + \xi_k \quad (k = 1, \cdots, K) \tag{2}$$

where $\boldsymbol{c}_j = \{c_{j1}, \cdots, c_{jI}\}'$ and σ_j^2 are respectively the center and variance of the jth hidden unit, w_{kj} is the connection weight from the jth hidden unit to the kth output unit, and ξ_k is the bias of the kth output unit.

The items stored in LTM are called "memory items" that correspond to the representative input-output data. These data can be selected from training samples, and they are trained with newly given training data to suppress forgetting. In the learning algorithm based on the linear method, a memory item is created when a hidden unit is allocated: that is, the RBF center and the corresponding output are stored in a memory item. As a result, the number of memory items is equivalent to the number of hidden units in this learning approach.

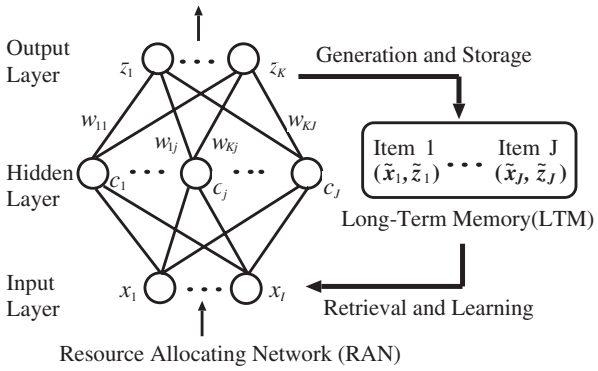

Figure 1. The architecture of RAN-LTM.

2.2. Learning Algorithm of RAN-LTM

The learning algorithm of RAN-LTM based on the linear method is divided into two phases: the dynamic allocation of hidden units (i.e., the selection of RBF centers in an incremental fashion) and the calculation of connection weighs between hidden and output units. The procedure in the former phase is almost the same as that in the original RAN [5], except that hidden units can be added after the update of connection weights (see Step 5 in the learning algorithm) and that memory items are generated at the same time. Once hidden units are allocated, the centers are fixed afterwards. Therefore, the connection weights $\boldsymbol{W} = \{w_{kj}\}$ are only parameters that are updated based on the output errors. To minimize the errors based on the least squares method, it is well known that the following linear equalities should be solved:

$$\boldsymbol{\Phi}\, \boldsymbol{W} = \boldsymbol{T} \tag{3}$$

where $\boldsymbol{T}$ is the matrix whose column vectors correspond to the target outputs. Suppose that a training sample $(\boldsymbol{x}, \boldsymbol{d})$ is given at time t and M memory items $(\tilde{\boldsymbol{x}}_m, \tilde{\boldsymbol{z}}_m)$ $(m = 1, \cdots, M)$ have already been created, then the target matrix $\boldsymbol{T}$ are formed as follows:

$$\boldsymbol{T} = \{\boldsymbol{d}, \tilde{\boldsymbol{z}}_1, \cdots, \tilde{\boldsymbol{z}}_M\}. \tag{4}$$

Furthermore, $\boldsymbol{\Phi}$ in Eq. (3) is calculated from these target vectors as follows:

$$\boldsymbol{\Phi} = \begin{bmatrix} \varphi_{11} & \cdots & \cdots & \cdots & \varphi_{1J} \\ \vdots & \ddots & & & \vdots \\ \vdots & & \varphi_{mj} & & \vdots \\ \vdots & & & \ddots & \vdots \\ \varphi_{M+1,1} & \cdots & \cdots & \cdots & \varphi_{M+1,J} \end{bmatrix}, \tag{5}$$

where

$$\varphi_{1j} = \exp(\frac{\|\boldsymbol{x}-\boldsymbol{c}_j\|}{\sigma_j^2}), \quad \varphi_{mj} = \exp(\frac{\|\tilde{\boldsymbol{x}}_m-\boldsymbol{c}_j\|}{\sigma_j^2}) \\ (j=1,\cdots,J;\ m=1,\cdots,M).$$

To solve $\boldsymbol{W}$ in Eq. (3), Singular Value Decomposition (SVD) can be used. The learning algorithm of RAN-LTM is summarized as follows:

[Learning Algorithm]

1. Find the nearest center $\boldsymbol{c}^*$ to an input $\boldsymbol{x}$ and then calculate the output error E.
2. If $E > \varepsilon$ and $\|\boldsymbol{x}-\boldsymbol{c}^*\| > \delta$, then allocate a hidden unit (i.e., $J \leftarrow J+1$) and create a memory item $(\tilde{\boldsymbol{x}}_M, \tilde{\boldsymbol{z}}_M)$ as follows:

   [Hidden Unit] $\boldsymbol{w}_J = \boldsymbol{d}-\boldsymbol{z}, \quad \boldsymbol{c}_J = \boldsymbol{x},$

   [Memory Item] $\tilde{\boldsymbol{x}}_m = \boldsymbol{x}, \quad \tilde{\boldsymbol{z}}_m = \boldsymbol{d}.$

   Then, go to Step 6. Otherwise, go to Step 3.
3. Calculate hidden outputs for the training sample $(\boldsymbol{x}, \boldsymbol{d})$ and memory items $(\tilde{\boldsymbol{x}}_m, \tilde{\boldsymbol{z}}_m)$ $(l=1,\cdots,M)$, and calculate $\boldsymbol{\Phi}$ in Eq. (3).
4. Using SVD, decompose $\boldsymbol{\Phi}$ as follows: $\boldsymbol{\Phi} = \boldsymbol{U}\boldsymbol{H}\boldsymbol{V}'$ where $\boldsymbol{U}$ and $\boldsymbol{V}$ are orthogonal matrices, and $\boldsymbol{H}$ is a diagonal matrix. Then, calculate the weight matrix as follows: $\boldsymbol{W} = \boldsymbol{V}\boldsymbol{H}^{-1}\boldsymbol{U}'\boldsymbol{T}$.
5. Give the input $\boldsymbol{x}$ to RAN-LTM again, and calculate the output error E. If $E > \varepsilon$, add a hidden unit and generate a memory item $(\tilde{\boldsymbol{x}}_M, \tilde{\boldsymbol{z}}_M)$ in the same way of Step 2.
6. If a new training sample is given, go back to Step 1.

3. Face Recognition System

3.1. Outline of Process Flow

The proposed fully automated face recognition system consists of the following four functions: face detection, face recognition, incremental learning, and a self-generation of training data. These functional components must be operated online without any human intervention. Figure 2 shows the overall process flow of the proposed system.

In the face detection part, at each time frame, face regions are localized based on the information of skin color and edges at first. Thereafter three types of facial features (eye, nose, mouth) are searched for within the localized regions through raster operations. In each raster operation, a small sub-image is extracted from a localized region, then the eigen-features of the sub-image are given to a Detection Neural Network (DNN) to verify if it corresponds to any one of the facial features. These eigen-features are obtained

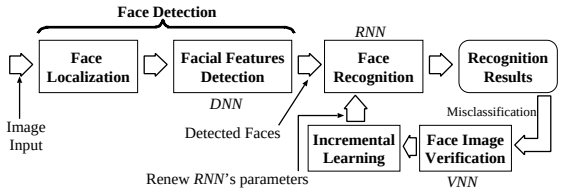

Figure 2. Block diagram of the process flow in the proposed face recognition system. Italic characters show the name of the three neural networks to be adapted.

using Principal Component Analysis (PCA). After all raster operations are done, face candidates are created by combining the identified facial features based on some geometrical constraints. The output of the face detection part is the center positions of the face candidates.

Next, in the face recognition part, the rectangular regions of the face candidates are first extracted from the original image, and then the extracted regions are applied to PCA in order to reduce their dimensions. These PCA features are given to Recognition Neural Network (RNN) as its input for classification. Note that RNN is implemented by RAN-LTM.

In the incremental learning part, misclassified images are collected from video clips as training data. However, there is a possibility that non-face images happen to be mixed into these training data because the perfect face detection is not ensured. Thus, another neural network called Verification Neural Network (VNN) is introduced into this part in order to filter out non-face images. After this verification process, the incremental learning for the misclassified face images is carried out by RNN.

3.2. Face Detection Part

Many approaches to the face detection have been proposed so far [6]. We adopt a common detection process that consists of the following two phases: face localization and face feature identification, and the results from each process are shown in Fig. 3.

3.2.1 Face Localization

To reduce time-consuming computations, facial regions are first localized for input images. This localization is done in the following procedure:

1. Perform the edge extraction by applying the MaxMin filter and Sobel horizontal filter to an input image. (See Fig. 3(a).)

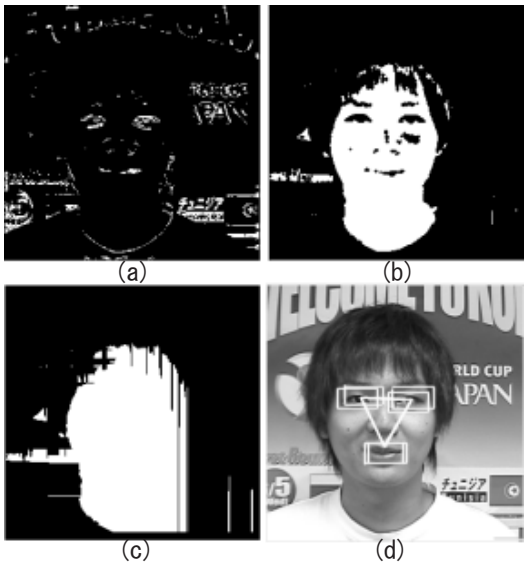

Figure 3. The results of applying (a) edge filter and (b) skin color filter to an input image. (c) A face region (in white) generated by combining the results in (a) and (b). (d) A final result of the face detection part (only one face detected in this case).

2. Calculate the projection (called skin-color features) of the input image to the skin-color axis. (See Fig. 3(b).)

3. Search for facial sub-regions using both the edge information and skin-color features, and extract the subregions from the original input image. (See Fig. 3(c).)

The skin-color axis is determined based on the least squares method to approximate the distribution of Japanese skin images in advance. In our preliminary experiment, this facial region extraction succeeded with 99% accuracy for a Japanese face image database.

3.2.2 Facial Feature Identification

Three types of facial features (i.e., eye, nose, mouth) are searched for within the facial regions extracted above at first. For the facial features, all of the combinations of these features are checked if they are satisfied with the defined facial geometric constrains. A minimum of three features must be found on the geometric template to identify as a face candidate. An example can be seen in Fig. 3(d) where the rectangular regions are the identified facial features and the inverted triangle marks the position of a face candidate. The center positions of all face candidates are sent to the next part.

To verify if the searched regions correspond to facial ones, the conventional RAN is adopted here as DNN. Note that there is no need for incremental learning of DNN because a large training data set is used and the features of the human eye, nose, and mouth are considered as invariant. The feature identification procedure is shown as follows:

1. Carry out the following raster operations on the region localized in the previous process:
   (a) Extract a 40×20 pixel sub-image from the localized region.
   (b) Carry out the dimension reduction for the extracted sub-image using PCA.
   (c) Check if the resultant 30-dimensional eigenfeature vector corresponds to one of the facial features using DNN.
2. For all of the identified facial features, construct possible face candidates based on the defined geometrical constraints.
3. Obtain the center positions of the identified face candidates, and send them to the next process.

3.3. Face Recognition Part

In this part, detected face candidates are differentiated between registered faces and non-registered ones. RNN implemented by RAN-LTM is used as the classifier to facilitate the later incremental learning. The eigenface approach [7] is adopted to reduce the dimensions of facial features. The eigen-features are sent to the RNN classifier. The recognition procedure is conducted in the following manner:

1. Extract 90×90 sub-images whose centers correspond to the centers of the face candidates.
2. Transform each of the sub-images into a 70-dimensional eigen-feature vector using PCA.
3. Perform the face recognition using RNN.

3.4. Incremental Learning Part

Suppose that the system is informed whether the classification was right or not. Then, the system can know what facial images should be learned to make correct decisions next time. This adaptation mechanism is realized by the incremental learning ability of RNN. The incremental learning procedure is carried out as follows:

1. If the classification is correct in the previous part, terminate this procedure. Otherwise, go to Step 2.
2. Obtain the misclassified eigen-features and then verify if they are face features using VNN. If they are non-face features, terminate this procedure. Otherwise, go to Step 3.

3. Store a pair of the misclassified eigen-features and the corresponding class label as a training sample into a memory device. If the number of stored training samples exceeds a certain value, go to Step 4. Otherwise, terminate this procedure.
4. Train VNN using all training samples stored in the memory based on the incremental learning algorithm described in Subsection 2.2.
5. Clear all training samples in the memory.

4. Experiments

4.1. Experimental Conditions and Evaluation Method

The largest benefit of introducing incremental learning is that the system does not need so much large memory to enhance its performance. This property is useful for small-scale systems rather than large-scale systems with high-performance servers. In this sense, we have intended to develop our face recognition system aimed for intelligent entrance control systems in residential environments. Hence, we can assume several conditions for the operating environments. The faces to be recognized are presumed to be frontal, allowing for slight rotations both laterally and longitudinally. The lighting conditions are changed to evaluate the robustness in both daylight and indoor conditions. Due to space constraints, we omit the detection results and focus on the recognition performance.

The evaluation dataset is divided into two sets. One is used for assessing the performance of incremental learning in RNN through an online recognition process (called "online dataset"). From the online dataset, images are given to the system one by one, and the recognition and incremental learning are carried out online. The other dataset is used for assessing the generalization performance of RNN (called "test dataset"). Hence, the images in this test dataset are not used for training.

These datasets contain video clips of seven people: four people (2 males and 2 females) are chosen as registered persons and the other three people are non-registered persons. The video clips have durations of $5 \sim 15$ seconds and they are taken over two weeks such that some changes in facial appearances are included. The online dataset consists of 654 images detected from the video clips of the first week; on the other hand, the test dataset consists of 499 images detected from the clips of the second week.

To simplify the evaluation procedure, the online dataset is further divided into six subsets separated by the time when the video is taken to simulate real-life consecutive learning. These subsets are given to the face recognition system in turn and the misclassified data are incrementally trained in RNN. The number of data in each subset is as follows: 139 (initial training set) $\rightarrow$ 107 $\rightarrow$ 75 $\rightarrow$ 98 $\rightarrow$ 106 $\rightarrow$ 129. Hence, five stages of incremental learning are carried out. Then the effectiveness of incremental learning is evaluated in terms of the recognition accuracy for all subsets given so far. Therefore, the number of evaluation data increases as the incremental learning stage proceeds: $139 \rightarrow 246 \rightarrow 321 \rightarrow 419 \rightarrow 525 \rightarrow 654$.

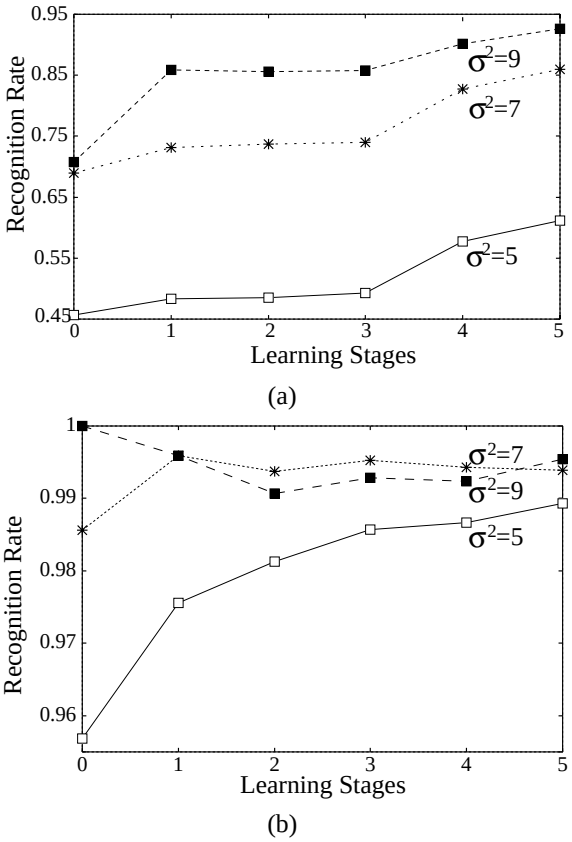

Figure 4. Time courses of recognition results for (a) test dataset and (b) online dataset.

As a security system, it is also important to evaluate the false-positive rate (the rate of the cases where non-registered or non-faces are classified as registered faces). To do this, we evaluate the recognition performance using another set of 3311 images, which consists of 1748 non-face images and 1536 non-registered faces. This dataset is referred to as the FP-dataset.

4.2. Experimental Results

Figure 4 shows the time courses of the recognition performance for two datasets through the five incremental learning stages. We compare the results of three RNNs whose radial bases have different variances ($\sigma^2 = 5, 7, 9$).

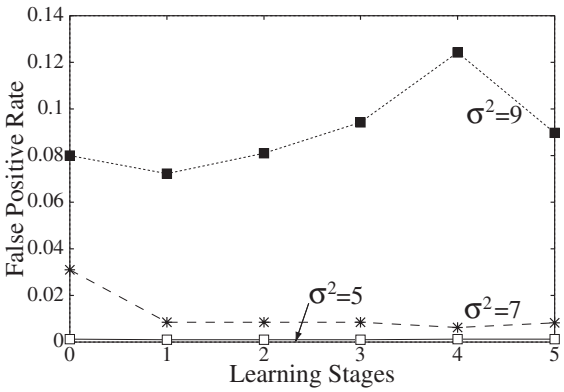

Figure 5. False-positive rate for the FP-dataset.

As seen from Fig. 4(a), the recognition rate for all three variance settings improves as the incremental learning stage proceeds. This result demonstrates that the incremental learning works effectively to enhance the generalization performance for unseen data. However, due to insufficient datasets, we cannot ascertain whether there is a ceiling for the recognition rate (i.e., whether further incremental learning is of use only up to a certain point).

The next important point to evaluate is whether destructive interference has occurred due to the incremental learning. To do this, we evaluate the recognition performance for the online dataset as stated in the previous subsection. The results are shown in Fig. 4(b). Although the recognition rate drops initially in one of the variance settings, overall we can say that the recognition performance stabilizes at an acceptable level. We can thereby conclude that the memory items recalled during incremental learning are effective in suppressing the destructive interference.

Figure 5 shows the false-positive performance for the FP-dataset. In the two variance settings ($\sigma^2 = 5, 7$), the false-positive rate is maintained below 1%. If the variance is set to a large value (e.g., $\sigma^2 = 9$), the base functions have wide response properties but there may be insufficient data initially to determine the connection weights properly. This is one of the reasons why the false-positive rate is rather high in the case of $\sigma^2 = 9$.

5. Conclusions and Further Work

In this paper, we have proposed an intelligent face recognition system with the following two desirable features: one-pass incremental learning and automatic generation of training data. This system can be implemented with limited hardware constraints and is suitable for the use in small devices where hardware capabilities are restricted such as home security systems. A memory-based learning approach (accumulating and retraining all previous data) may possibly obtain better recognition results but it is infeasible for large datasets like image streams. From the online recognition experiments, we can conclude that introducing the incremental learning function into the system is quite effective in the sense that the system can enhance its recognition performance automatically without any administrator intervention.

Several open questions still remain in our face recognition system. First, the face detection method introduced here is still rather immature in terms of the computation costs and accuracy. Moreover, the robustness for image variations in rotations, size, illumination, etc. must be improved. Here, we evaluated the recognition performance only for small datasets of Japanese people. From the aspect of security systems, such simple evaluations are useless. Hence, the evaluation on the robustness for the larger datasets is necessary in practical use.

Acknowledgment

The authors would like to thank Prof. Shigeo Abe, Dr. Motohide Yoshimura, and Shinji Kita for their useful discussions and comments. This research was supported by Matsushita Electric Works, Ltd. and the Ministry of Education, Science, Sports and Culture, Grant-in-Aid for Young Scientists (B).

References

[1] L. C. Jain, U. Halici, I. Hayashi, and S. B. Lee. *Intelligent Biometric Techniques in Fingerprint and Face Recognition.* CRC, 1999.

[2] J. L. Elman. Learning and Development in Neural Networks: The Importance of Starting Small. *Cognition*, 48: 71-99, 1993.

[3] N. Kasabov. *Evolving connectionist systems: Methods and applications in bioinformatics, brain study and intelligent machines.* Springer-Verlag, 2002.

[4] K. Okamoto, S. Ozawa, and S. Abe. A Fast Incremental Learning Algorithm of RBF Networks with Long-Term Memory. *Proc. Int. Joint Conf. on Neural Networks*, 102-107, 2003.

[5] J. Platt. A Resource-Allocating Network for Function Interpolation. *Neural Computation*, 3(2): 213-225, 1991.

[6] M. H. Yang, D. J. Kriegman, and N. Ahuja. Detecting Faces in Images: A Survey. *IEEE Trans. on Pattern Analysis and Machine Intelligence*, 24(1), 2002.

[7] M. Turk and A. Pentland. Eigenfaces for Recognition. *Journal of Cognitive Neuroscience*, 3(1): 71-86, 1991

SPEECH RECOGNITION & NATURAL LANGUAGE

(This page left blank intentionally)

Highlighted Technical Paper C

Spoken Sentence Retrieval Based on MPEG-7 Low-Level Descriptors and Two Level Matching Approach

Jhing-Fa Wang Po-Chuan Lin Jun-Jin Huang Li- Chang Wen

wangjf@csie.ncku.edu.tw tony178@ms24.hinet.net kjtom@icwang.ee.ncku.edu.tw lcw@icwang.ee.ncku.edu.tw

Department Of Electrical Engineering, National Cheng Kung University.

701 No.1, Ta-Hsueh Road, Tainan City Taiwan R.O.C.

Tel: 886-6-2746867, Fax: 886-6-2387092

ABSTRACT

In this paper, we propose a spoken sentence retrieval system based on MPEG-7 audio LLDs (Low-Level Descriptors). Our system retrieves the spoken sentence by a two-steps sentence matching method. First, we locate several possible segments that are similar with the user's query in spoken documents and retrieve top N from these candidate segments. Secondly, we rank the top N candidates with rank-based method. Without using the large-vocabulary recognizer, the computational power can be greatly reduced and be more suitable for hand-held devices by using our approach. Furthermore, the use of MPEG-7 based features has been proven comparable with the MFCCs. (Mel-Frequency Cepstrum Coefficients) in the experiment results.

Keywords

Speech retrieval, Matching algorithm, MPEG-7, Audio features

1. INTRODUCTION

With the development of electrical technology and Internet, we have lots of opportunities to access various kinds of multimedia data. Among them, spoken data is one of the most widespread information, such as broadcast radio, television programs, video tapes, digital libraries, course, and voice recordings and so on. Although parts of them have been digitalized, it still lacks efficient ways to retrieval them. About these demands, information retrieval technologies provide users a lot of methods [7].

Also, with the advances in speech process technology, most of works recently focus on integrating information retrieval and speech process, called SDR (Spoken Document Retrieval)[1][2][3]. In general, the methodology of SDR comprises mainly two levels, speech recognition and information retrieval. In the first level, queries and spoken documents are translated into a series of symbols, such as words, syllables, or phonemes. In the second level, the query transcripts are retrieved from those of spoken documents, where a lot of related information retrieval techniques can be utilized such as confusion matrix, document expansion and prosodic information.

However, there are still some researches about speech information retrieval without large-vocabulary recognizer [4] [5]. In [4], they implemented a system for user to search keywords in the speech database. In [5], a dynamic programming method was proposed to find the most frequent speech segments in the speech data and these segments were taken as indices to summarize the speech data.

As to MPEG-7 [6], officially called "Multimedia Content Description Interface", it defined lots of LLDs for multimedia. Audio LLDs are descriptors for audio data. There are two parts of MPEG-7 audio LLDs, audio spectrum descriptors and timbre descriptors. Audio spectrum descriptors describe several kinds of spectrum features of each audio frame, such as Spectrum Envelope, Centroid, Spread, and Flatness, etc. Timbre descriptors describe features of an entire audio segment, such as Harmonic spectral descriptors, SpectralCentriod, LogAttackTime, TempralCentroid, etc.

Most of the works about SDR [1] [2] [3] are engaged in retrieving data from a large amount of spoken data, such as broadcast news, TV programs, or speech recordings, etc. In [1], a database of 757 news recordings was considered. In [2] and [3], their databases take about 10 hours of speech signal. Although these systems have been proven effective, they need to construct lots of acoustic models and the language model. There is no denying that their computational complexity and memory requirement are very high. These stern conditions make them are not suitable for some embedded systems, such as handheld devices, which are limited on low power consumption and small memory size. In order to overcome these problems, we propose a multi-level matching method without the speech recognizer that may contain recognition errors and symbol boundary matching problems. Besides, we adopt MPEG-7 LLDs as speech features to study their retrieval performance.

This paper is organized as follows. In Section 2, MPEG-7 audio LLDs are introduced. In Section 3, our proposed method is described in details. The experiments about the discriminating capabilities of MPEG-7 audio LLDs and retrieval result of our retrieval system are discussed in

Section 4. Finally, we give the conclusions and future works in Section 5.

2. MPEG-7 AUDIO LOW-LEVEL DESCRIPTORS

2.1 Feature Descriptions

We adopt some of the audio low-level descriptors in MPEG-7 as our speech features. MPEG-7 audio low-level descriptors consist of a collection of simple, low complexity descriptors that are categorized into two parts, audio spectrum descriptors and timbre descriptors. We introduce the descriptors adopted in the paper as follows.

- **Audio spectrum centroid (ASC)** describes the center of gravity of the log-frequency power spectrum.
- **Audio spectrum spread (ASS)** describes the second moment of the log-frequency power spectrum.
- **Audio spectrum flatness (ASF)** describes the flatness properties of the spectrum of an audio signal within a given number of frequency bands.
- **Instantaneous harmonic spectral centroid (IHSC)** describes the amplitude weighted mean of the harmonic peaks of the spectrum.
- **Instantaneous harmonic spectral spread (IHSS)** describes the amplitude weighted standard deviation of the harmonic peaks of the spectrum, normalized by the harmonic spectral.

2.2 Computation Comparison between MPEG-7 LLDs and MFCCs

In this section, we analyze the computation complexity of spectrum and instantaneous harmonic descriptors (ASC+ASS+ASF+IHSC+IHSS) on the numbers of addition /subtraction, multiplication, division per frame. Furthermore, we compare these computational overloads with MFCCs [8] for one frame (240 samples, 8k sampling rate) From Table 2.1, we can find the low-complexity advantage of MPEG-7 LLDs.

Table 2.1 The Computation Loads of Extracting MPEG-7 LLDs and MFCCs for one frame

(240 samples, 8k sampling rate)

	Add./Sub.	Mult.	Div.
Total computations of the MPEG-7 LLDs	909	354	41
MFCCs	2768	2800	0

3. SYSTEM ARCHITECTURE OVERVIEW

An overview of our proposed system is depicted in Fig. 3.1, where the rectangular blocks stand for operation procedures.

We divide the retrieval processes into four procedures as follows. :

1) Audio/speech features extraction, in which MFCCs and MPEG-7 low-level descriptors are extracted.

2) **Similar frames tagging** for marking similar frames in database with query.

3) Possible segments extraction for verifying candidates corresponding to query.

4) Ranking these candidates and retrieve top N ones.

For all procedures above, we will describe them in the followed sections.

3.1 Speech feature extraction

For each frame of the speech data, we extract features including 13 MFCCs, 1 ASC, 1 ASS, 15 ASF, 1 IHSC, and 1HSS in the case of 8K sampling rate. The size of a frame is 30 ms (240 samples), while a frame is extracted with Hamming window-weighting every 10 ms (80 samples). These basic specifications are list in.

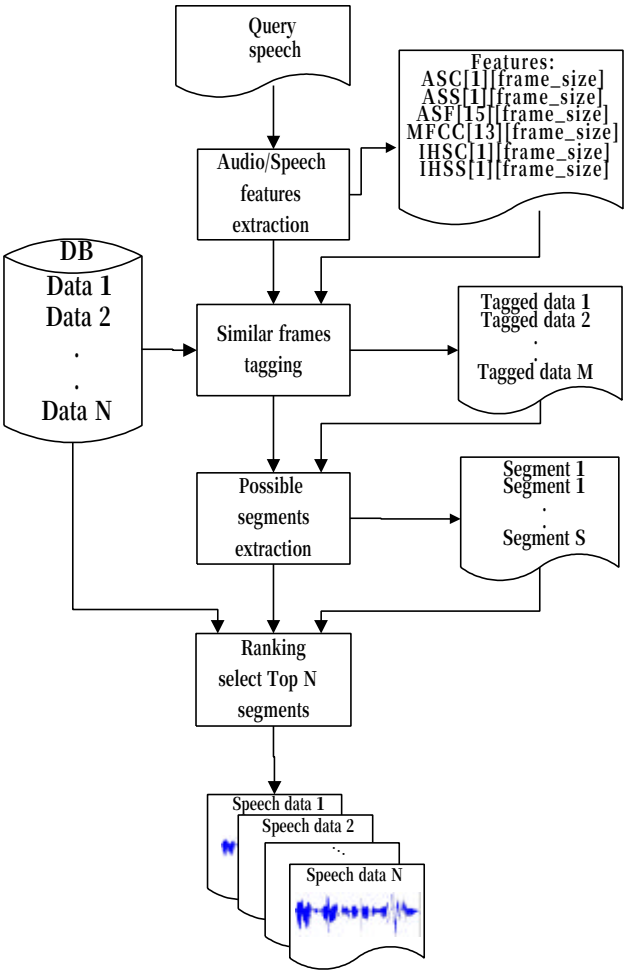

Figure 3.1 Overview of our retrieval system.

Table 3.1 Specifications of Feature Extraction

Sampling Rate	8 K/sec					
Frame Size	240 samples (30 ms)					
Frame Overlap	160 samples (20 ms)					
Features	ASC	ASS	ASF	IHSC	IHSS	MFCC
Feature Dimension	1	1	15	1	1	13

3.2 Similar frames tagging

It is a big overload for direct matching every frame interval. Therefore, we roughly tag the similar frames in speech data for help to allocate the possible segments. At first, we divide the query into several blocks with the length of 3 frames. The reasons we take a block as a processing unit are for reducing computations and no losing perception. Then, we calculate, block by block, the feature distance between the query and the sentences in database. If the distance is below our estimated threshold, $\boldsymbol{th_1}$, the block will be tagged with 1, otherwise 0. After calculating all block distances between query and each sentence, there will be an output data, ***tagged data*** for each sentence. In the same way, we get another ***tagged data*** by using the other features. Finally, we add those ***tagged data*** for different features as the ***final tagged data***.

3.3 Possible segment extraction

Here, we will extract several possible segments of speech data in the database based on the ***tagged data*** got in section 3.2. At first, we check the segments in each data if they are ***high-tagged***. Then, these ***high-tagged*** ones are extracted as candidates corresponding to the query.

Our implementation idea to check ***high-tagged*** segments is to utilize hamming window scanning method. First, we do convolution of ***tagged data*** with a Hamming window of query length to get a new data, $array_m$. And then, each local maximal value in $array_m$ is checked if it is greater than the threshold, th_2 for ***high-tagged***. These ***high-tagged*** segments, whose centers are the local maxima, are extracted. Finally, we check the next ***tagged data*** till check all of them. Fig. 3.2 shows the process of section 3.2 and section 3.3.

3.4 Ranking sentences output

After extracting these possible segments, we rank them by utilizing the DTW (Dynamic Temporal Warping) algorithm. Based on each feature, we can get the matching results and then we adopt the rank-based method, as described in (3.1), to integrate them. In (3.1), Rank is final rank output, while *i*, *j*, *f* are the indices for queries, data, descriptors respectively, and w_f is the weight for different features.

$$Rank(q_i, d_j) = \sum_{f=1,2,3,....} w_f \, rank_f(q_i, d_j) \qquad (3.1)$$

For example, we consider a segment whose rank for ASC is 3 while 5, 2, and 1 for ASS, ASF, and MFCC respectively. We will get a final rank, 1.68 by (3.1), where weight is 0.05, 0.05, 0.29, and 0.7.

Finally, according to the ranks of possible segments, the system outputs the sentences corresponding to the top N segments to the user. Fig. 3.3 displays the process of ranking possible segments and outputting corresponding sentences.

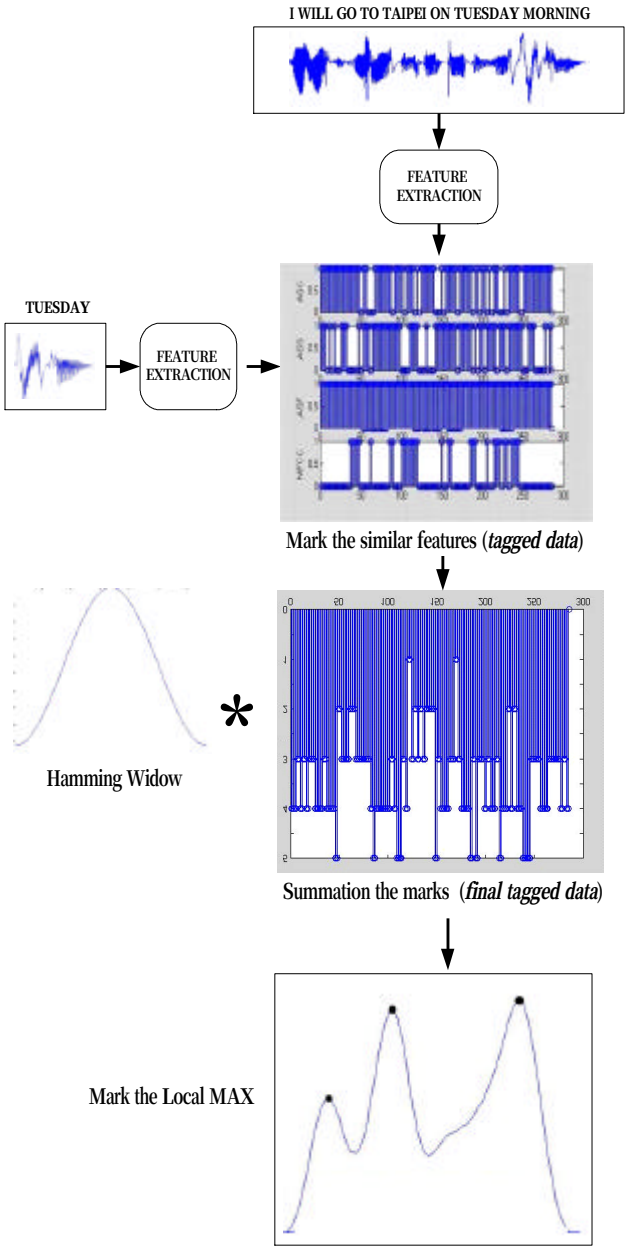

Figure 3.2 Process of similar frame tagging and possible segment extraction

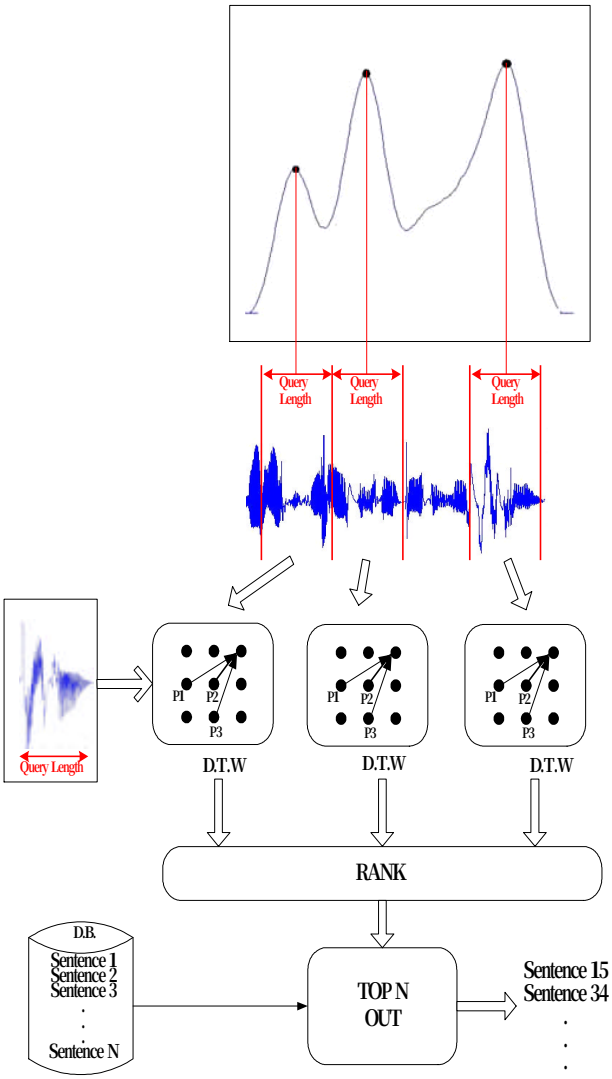

Figure 3.3 Process of ranking and output

3.5 Computational analysis of the direct matching method and our two level matching method.

In this section, we compare the computational load of our proposed method with direct matching method, which applies the DTW matching every frame interval [4] [5].

3.5.1 The direct matching method

We analyze the computation complexity from two main processes of DTW. First, we calculate the distance between frames of the query and the sentence. Secondly, we select the path whose cumulative distance is the shortest.

3.5.1.1 Local distance

Parts of total computation about local frame distance depends on the feature dimension, so we use ***O(local_dist_add)*** and ***O(local_dist_mul)*** to present the computation of additions and multiplications.

As shown in Fig. 3.4, N_q and N_d are frame numbers of query and sentence respectively. We need to compute the local distance N_q^2 times in one interval and the total shift number is about N_d-N_q. Therefore, the total computation loads are

Additions:

$N_q^2*(N_d-N_q)*O(local\_dist\_add)$, and

Multiplications:

$N_q^2*(N_d-N_q)*O(local\_dist\_mul)$

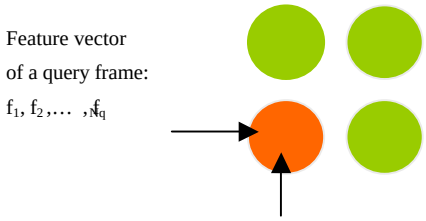

$$D = \sum_{i=1}^{N} (f_i - f_i')^2$$

N is the dimension of feature vectors

Figure 3.4 The Computation of Local Frame Distance

3.5.1.2 Path selections

As to the path selection, the type of DTW is shown in Fig. 3.5. It takes 4 additions,

3 addition operations to decide which is the last node and

1 addition to accumulate the path distance.

The same as above; the total counts for path selection are $N_q^2*(N_d-N_q)$. Since, the DTW path constraint factor is about **0.3**. Therefore, this part takes additions: $1.2*N_q^2*(N_d-N_q)$

$$m(k) = \min\left[f_x(k) - f_x(k-1), f_y(k) - f_y(k-1)\right] \qquad (3.2)$$

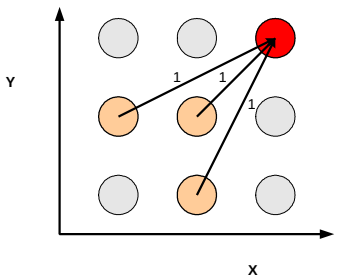

Figure 3.5 Path Selections

3.5.2 Our method

3.5.2.1 Similar frame tagging

We divide the query into several blocks with length of ***blocksize*** (3 frames) and compute local distance, block by block, and the shift interval is 2 frames, (N_{shift}).

The numbers of blocks are about $N_q/blocksize = N_q/3$.

Besides, each block needs S_N times for local distance computations,

$S_N = blocksize*(N_d - blocksize)/N_{shift}$

$= 3*(N_d-3)/2 \sim= 1.5*N_d$.

Therefore, we needs

Additions: $0.5*Nd*Nq*O(local\_dist\_add)$.

Multiplications $0.5*Nd*Nq*O(local\_dist\_mul)$.

3.5.2.2 Possible segment extraction

The main computation loads of this step are convolution between tagged data and a hamming window ($l_w = N_q$) .It takes about

Additions: N_q*N_d, and

Multiplications: N_q*N_d

3.5.2.3 Possible segment ranking

This part depends on the number of possible segments, $N_{possibleseg}$ that we extract for DTW. So it takes about

Additions:

local distance: $N_q^2*N_{possibleseg}*O(local\_dist\_add)$*+ path selections :* $1.2*N_q^2*N_{possibleseg}$

Multiplications:

local distance: $N_q^2*N_{possibleseg}*O(local\_dist\_mul)$.

3.5.3 Computational comparisons

For section 3.5.1 to 3.5.2, the totally analytic results are concluded in Table 3.2. As shown in Table 3.3, we see that the average numbers of possible segments, $N_{possibleseg}$, are usually far less than the average frames of sentences, N_d. Therefore, from Table3.2 and Table 3.3, since $N_q << N_d$, we find that the additions and multiplications are dominated by $N_q*N_d*O(local\_dist)$, while the parts of the direct matching (D.M.) method are dominated by $N_q^2*N_d*O(local\_dist)$. Comparing with the direct matching method, our method is about $1/N_q$ times of the computational load of them.

4 EXPERIMENT RESULTS

We perform the experiments to evaluate the retrieval performance of our proposed system. The object speech database in these experiments consists of 100 sentences (50 oral sentences and 50 news titles). Each data is uttered by a single person and is recorded twice. The sampling frequency is 8 KHz and the frame interval is 10 ms. MFCCs, ASC, ASS, ASF, IHSC, and IHSS are the features extracted from each frame. We use 50 spoken keywords as inputs totally and check if the retrieval spoken documents include them. Besides, we show the retrieval performance of the direct matching method as the baseline in the followed experiments.

Table 3.2 The Computation Loads of Our Method and the Direct Matching Method.

(The dominated terms are shown in boldface.)

	Add	Mul
D.M. [4],[5]	$N_q^2*(N_d-N_q)*$ $(1.2+O(local\_dist\_add))$	$N_q^2*(N_d-N_q)*O(local\_dist\_mul)$
Ours	$0.5*N_q*N_d*O(local\_dist\_add)$ $+N_q*N_d$ $+(1.2+0.3*N_q^2*N_{possibleseg})*$ $O(local\_dist\_add)$	$0.5*N_q*N_d*O(local\_dist\_mul)$ $+N_q*N_d$ $+0.3*N_q^2*N_{possibleseg}$ $*O(local\_dist\_mul)$

Table 3.3 The Average Numbers of Query Frames, Sentence Frames and Possible Segments

Avg. Nq	70.64
Avg. Nd	345.23
Avg. Npossibleseg	25.43

Table 4.1 shows the average retrieval accuracy and operational analysis by using a single feature. ASF has the best retrieval effects of the adopted MPEG-7 LLDs, while retrieval accuracy of the others are under 0.4. Additionally, the gaps between ASF and MFCC are about 0.03.

Table 4.2 shows the average retrieval accuracy and operational analysis by using the combination of features. We consider the combination of ASx (ASC+ASS+ASF), IHSx (IHSC+IHSS), LLDs (ASx+IHSx), and ALL (LLDs and MFCC). Besides, the performance of the combination of MPEG-7 LLDs meets 77.51%.

Comparing to the direct matching method, our proposed method degrades about 3% except instantaneous harmonic features. The decline is mainly from the extraction of possible segments. It may lose some possible segments else. However, as mention in 3.5, our matching method can reduce the computation overload greatly. Therefore, our method can provide a faster and little-degrading method.

5 CONCLUSIONS

This paper proposes a spoken sentence retrieval system. Instead of using traditional large-vocabulary recognizer, we adopt a two-level retrieval method to reduce the computational complexity. Besides, we choose the MPEG-7 audio LLDs as our features. They were proven comparable to the MFCC in our experiment result. Furthermore, the combination of MPEG-7 LLDs and MFCC has better performance than using them alone.

Table 4.1 The average retrieval accuracy and operational analysis by using a single feature between our method and direct matching method.

	ASC	ASS	ASF	IHSC	IHSS	MFCC
Ours.	0.413 /19 /76	0.391 /24 /83	0.760 /1.7 /74	0.220 /0.13 /0.3	0.301 /0.2 /1	0.7943 /4.7 /12
D.M.	0.420 /1923 /2081	0.427 /2438 /2254	0.809 /172 / 2004	0.441 /13 /7	0.577 /19 /27	0.821 /468 /340

Accuracy/Million Additions/Million Multiplications

Table 4.2 The average retrieval accuracy and operational analysis by using combination of features between our method and direct matching method.

	ASx	IHSx	LLDs	MFCC	ALL
Ours.	0.7599 /45.3 /233	0.3067 /0.336 /1.3	0.7751 /45.636 /234	0.7943 /4.7 /12	0.8076 /50 /246
D.M.	0.7687 /4532 /6340	0.5233 /32 /34	0.7979 /4564 /6374	0.821 /468 /340	0.8339 /4632 /6714

Accuracy/Million Additions/Million Multiplications

REFERENCES

[1] Berlin Chen; Hsin-min Wang; Lin-shan Lee; "Discriminating capabilities of syllable-based features and approaches of utilizing them for voice retrieval of speech information in Mandarin Chinese", Speech and audio Processing, IEEE Transactions on , Volume: 10 Issue: 5 , Jul 2002, Page(s): 303 -314

[2] Matthew A. Siegler, "Integration of Continuous Speech Recognition and Information Retrieval for Mutually Optimal Performance", Electrical and Computer

Engineering Carnegie Mellon University Pittsburgh, Pennsylvania 15213, 1999 December 15

[3] Ng, K, Zue, VW, "Phonetic recognition for spoken document retrieval", Acoustics, Speech, and Signal Processing, 1998. ICASSP'98. Proceedings of the 1998 IEEE International Conference on, Volume: 1 , 12-15 May 1998, Page(s): 325 -328 vol.1

[4] H.K Xie, "A Study on Voice Caption Search for Arbitrarily Defined Keywords." Master Thesis, National Taiwan University of Science and Technology, Taiwan, R.O.C., July 2000.

[5] Itoh, Y, "A matching algorithm between arbitrary sections of two speech data sets for speech retrieval"; Acoustics, Speech, and Signal Processing, 2001. Proceedings. (ICASSP '01). 2001 IEEE International Conference on, Volume: 1 , 2001 , Page(s): 593 -596 vol.1

[6] "ISO/IEC FDIS 15938-4 Multimedia Interface Description Interface Part 4 Audio"

[7] Richard.B, Berthier.R"Modern Information Retrieval", New York: ACM Press, 1999

[8] Y. S. Weng, "The chip design of Mel frequency cepstrum coefficient for HMM Speech Reconition," Master Thesis, National Cheng Kung University, Taiwan, R.O.C., June 1998.

A Novel Template-based Architecture for Spoken Language Translation on Personal Digital Assistants

Jhing-Fa Wang **Shun-Chieh Lin** **Hsueh-Wei Yang** **Fan-Min Li**
Dept. Electrical Engineering, National Cheng Kung University, Tainan, Taiwan, R.O.C.
email wangjf@csie.ncku.edu.tw

Abstract
Two major problems for an automatic spoken language translation on a handheld device are limited resources and real-time constraints. In this paper, we focus on developing techniques to overcome these problems based on our novel template-based approach. First is to derive demand translation templates for memory saving and translation capacity promoting. Second is to develop the fast template-based translation approach composed of crude template candidate selection, latent grammar understanding of templates, score normalization and ranking, and translation result generation. According to the experimental results, the proposed approach can averagely achieve about 76.5% translation understanding rate and 6.23 sec response time on 200MHz PDAs compared with 5 sec in traditional 1~2GHz PC-based approaches.

Keywords
Spoken Language Translation, Personal Digital Assistant, Template-based Architecture

INTRODUCTION

Automatic spoken language translation (SLT) has been one of prospective applications of the speech and language technology [1][2][3][4]. One common target application has been communication assistance for travelers in a foreign travel situation. In this situation, the user will want to carry the translation device and use it in an open space, rather than sit in a computer room in front of a display. An obvious approach is to build a stand-alone speech translation device that is compact enough to carry around, like personal digital assistants (PDAs) [4][5][6].

Currently, there are two main architectures of speech translation: conventional sequential architecture and fully integration architecture [7]. In the integrated architecture, speech feature models are integrated into translation models in the similar way as for speech recognition. According to this integration, the translation process can be efficiently performed by searching for an optimal path of states through the integrated network [8]. Therefore, we adopt the concept of the integrated architecture and revise to provide better quality and real-time response for spoken language translation that can run on resource-limited PDAs.

For translation models in the integrated architecture, one of the data-driven approaches, which has been proposed for the integrated architecture, is Statistical-based Machine Translation (SBMT)[9][10]. However, when the training data of SBMT is insufficient, the results obtained by the sequential architecture are better than the results obtained by the integrated architecture [8]. In addition, word reordering is still a thorny problem in SBMT, and present alignment models of SBMT for suboptimal solutions seem to be insufficient [11]. Another remarkable data-driven approach, Example-based Machine Translation (EBMT), does not require the database to be as large as in SBMT. Furthermore, the example-based approach can explore the alignments between word sequences and syntactic grammars for language translation. Various example-based speech translation methods have been widely used and their effectiveness for spoken language processing has been confirmed with the help of domain specificity [12]. For that reason, we adopt and further systematize the example-based approach for SLT.

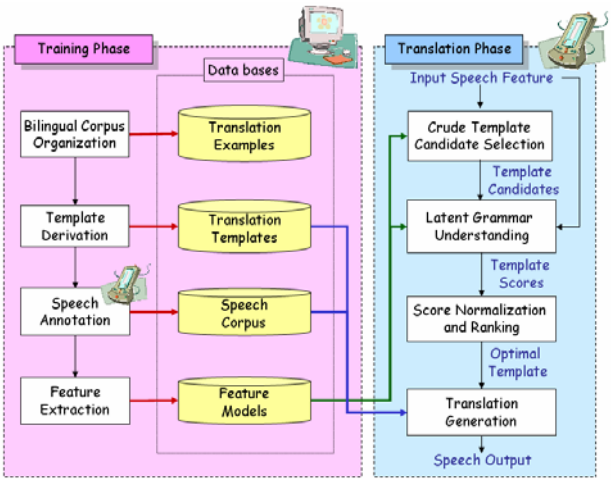

Figure 1. Architecture of the proposed system

The proposed framework involves two key components, the training phase and the translation phase, as shown in Fig. 1. The training phase is to derive four major required databases. During the translation phase, we use the derived databases to implement the spoken language translation on PDAs. The rest of the paper is organized as follows. First, discussing the construction of translation templates. Then, the proposed speech translation approach and the experimental results are presented in turn. Finally, we draw a generalized conclusion.

CONSTRUCTION OF TRANSLATION TEMPLATES

In this section, we will discuss three issues of our translation template construction underlying the example-based

approach. Starting with the organization for a database of examples, i.e. bilingual text corpora, we then derive the demand translation templates from the organized corpora, and finally, the related speech corpora are developed to apply for PDAs.

Bilingual text corpus organization

To deal with the speech translation, we have obtained the Taiwanese/English bilingual corpus[1]. By utilizing the corpus, we can acquire the alignments between word sequences and translation templates for language translation. However, there are a number of divergences, which make the straightforward mapping between languages impractical [13]. With regard to resource-limited handheld devices, these divergences also raise the cost of translation process and reduce the translation performance.

For Mandarin-English bilingual corpus, some divergence types, called thematic, structural, morphological, and conflational, are discussed [14]. On the other hand, Taiwanese and Mandarin both belong to the family of Chinese language [15], these divergences are also existed in the Taiwanese/English text corpus. Therefore, if the sentence pairs contain above a certain number of null mappings, the degree of alignment divergence comes into notice and the content of the sentence pairs has to be updated in order to improve the accuracy and effectiveness of the alignment execution and translation template derivation.

Translation template derivation

Figure 2 is an example of a simple translation template derived from one translated example indicating how a sentence in English (source language, SL) containing "Is there…" may be translated by a sentence in Taiwanese (target language, TL) containing "u…but"[2][16].

Example part: SL: *Is there* laundry service?
↔ TL: "*u* sea svaar e hogbu *but*"?
Alignment part: Is there E_p? ↔"u" T_p "but"?
alignments
Variable part: If $E_p \leftrightarrow T_p$,
laundry service ↔"sea svaar e hogbu"

Figure 2. A simple translation template

Functionality of such a simple template is like phrase books for travelers, which have fixed expressions and intentions, are often used as examples for translation with a replacement of the phrase variables. Besides, duplicate expressions can be projected into a unique template for memory saving. Therefore, we expect to expand more variable mappings for template flexibility and replacement rationality. An expansion strategy for multiform translation template generation [14] was developed and is adopted here. There are two levels of expansion: expansion within the intention class and expansion between intention classes. For the expansion within the intention class, the iterative procedure is shown as follows:

$$C_i \leftarrow C_i \oplus E_w(\chi_j, \chi_k), \quad \text{if } \tilde{\chi}_j = E_w(\chi_j, \chi_k) \text{ is classified correctly by } C_i\text{'}$$

where $E_w(\chi_j, \chi_k)$ expands template χ_j within template χ_k in class C_i with the variable mappings of template χ_k. For the expansion between the intention classes, the iterative procedure is as below:

$$C_i \leftarrow C_i \oplus E_b(\chi_j, C_k), \quad \text{if } \tilde{\chi}_j = E_b(\chi_j, C_k) \text{ is classified correctly by } C_i\text{'}$$

where $E_b(\chi_j, C_k)$ expands template χ_j between each template of its variable mappings in class C_k. After the expansion within and between the intention classes, the variable mappings in each template become more plentiful and reasonable for translation.

Speech data systemization

According to the derived translation templates, we now focus on how to efficiently record the information including speech data and feature models for promoting capacity of the templates. Within our proposed approach, we plan to unify the template-based linguistic translation knowledge and PDA-based speech features for spoken language translation. For feature extraction, we obtain the example speech and variable speech and are in chorus to reference model construction. The reference model v_i of one language is redefined as a two-layer model $v_i = \{v_i', v_i''\}$, where v_i' is an intention subspace of v_i and v_i'' is a variable subspace of v_i. The example of English is shown in Fig. 3. On the other hand, the obtained example speech and variable speech are also used for small-scale corpus-based speech generation. And the alignment information of translation templates is embedded in generation rules for speech replacement.

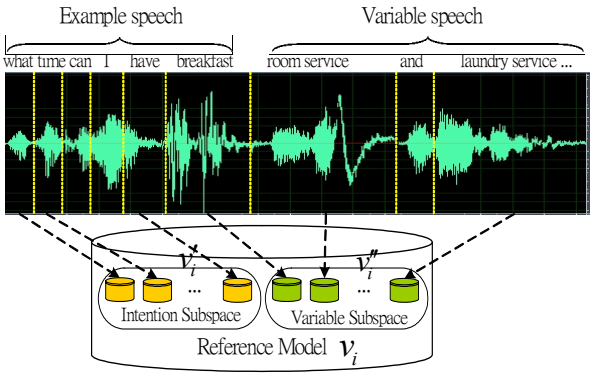

Figure 3. Speech annotation of data systemization

[1] The bilingual corpus is sentence-aligned and sentences are tokenized.

[2] Taiwanese words in phonetic transcription

SPOKEN LANGUAGE TRANSLATION

So far we have constructed the required translation templates with related speech data and feature models. In this section, according to the translation database, we propose to handle source speech input for real-time spoken language translation in the following way:

Crude template candidate selection

In order to speed up the determination of an optimal template, to preselect possible templates can achieve the requirement. Therefore, in the temporal fluctuation region between two speech spectra (source speech and intention speech), the range-limited dynamic time warping (DTW) solution is applied to measure efficiently the pattern dissimilarity with embedded time-normalization and alignment. In this paper, the pre-selection accuracy is estimated by the criterion that if the intention of source speech is located in the set of best N preselected templates. The criterion is best known as "TopN".

Latent grammar understanding for templates

Once the template candidates are retrieved, a one-stage based approach is applied to further segment the source speech input and to decide the optimal template with the two-layer model of each template candidate. In terms of searching for an optimal path of states through the two-layer model, the objective now is to measure the dissimilarity $d_i'^*$ of pair (s, v_i') of a fixed number of reference patterns, says N_i, for understanding the latent grammar in the intention subspace. (See Fig. 4) However, another problem is how to properly measure the dissimilarity score of pair (s, v_i') while adjudging the variable subspace v_i'' for segmenting the variable patterns of user's speech input.

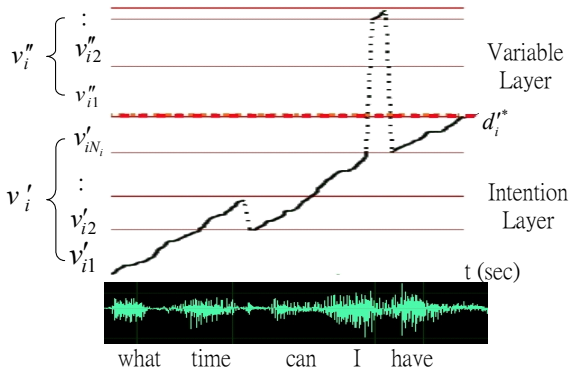

Figure 4. A one-stage based dissimilarity measurement

Referring to Fig 5., given two optimal matching paths of different preselected templates v_i and v_j, the scores used for comparing are the intention regions $D_i'^*$ and $D_j'^*$, where $D_i'^*$ is the dissimilarity measurement region of pair (v_i', s) and $D_j'^*$ is the dissimilarity measurement region of pair (v_j', s).

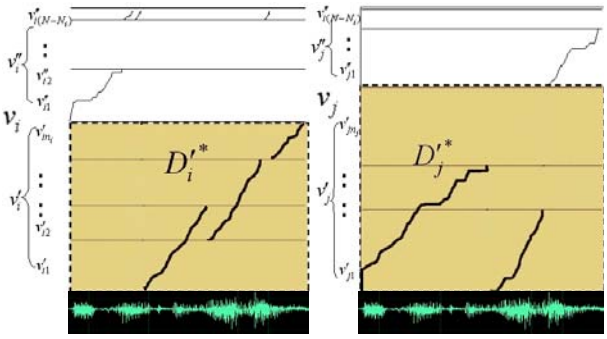

Figure 5. Search results of various reference models for speech input

For the consideration of the dissimilarity measurement between the intention layer and the variable layer, there are two additional types of search path registers for one-stage approach: 1) paths *between* v_i' and v_i'' and 2) paths *within* v_i' or v_i''. For the paths *between* v_i' and v_i'', a search block Z in the variable layer, which will be referred to a score-skip block while backtracking, contains more than one such path e connected by node u and node v. (See Fig. 6) Therefore, according to our proposed two-layer model, the one-stage based algorithm not only computes best paths to every reference pattern frame at every input frame, but also backtrack the desired score with giving the best word sequence.

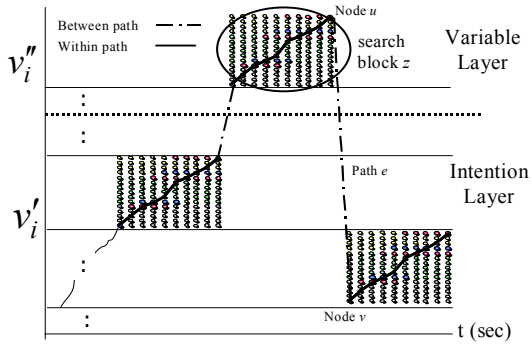

Figure 6. Additional search path registers for one-stage algorithm

Score normalization and ranking

Since the length of matching sequence can seriously affect the accumulative score of the dissimilarity measurement, a time-conditioned weight concept is further adopted to compensate for this defect. There are a number of similar ways to define the scoring methods with the length measurement of $\Delta(s, v_i')$ [17]:

$$\Delta(s, v_i') = \max(\|s\|, \|v_i'\|) (\text{or } \min(\|s\|, \|v_i'\|)) \quad (2)$$

$$\Delta(s, v_i') = \|s\| * \|v_i'\| \quad (3)$$

$$\Delta(s, v_i') = N(L, N_i) + F(L, N_i)/3, \quad (4)$$

where $\|s\|$ is the number of frames in speech input s, $\|v_i'\|$ is the number of total search frames in v_i', $N(L, N_i)$ is the number of frame comparison, and $F(L, N_i)$ is the number of frames that fail to get matched. In order to improve the flexibility of the dissimilarity measurement, an exponential definition for $\Delta(s, v_i')$ is described as follows:

$$\Delta(s, v_i') = \partial^{w_{v_i',s}}, \quad (5)$$

where ∂ is a weight factor, $w_{v_i',s} = \left(\|v_i'\| - \|s\|\right) \cdot \|s\|^{-1}$. Therefore, the modified dissimilarity measurement is given thereafter:

$$\tilde{d}_i'^{*} = d_i'^{*} \cdot \partial^{w_{v_i',s}} \quad (6)$$

The experimental analysis shows that the proper interval of ∂ is $[1.3-\delta, 1.3+\delta]$ to obtain the best accuracy of the dissimilarity measurement. Therefore, the value of ∂ chosen here is 1.3. After ranking all template candidates, the optimal template is decided by the one with minimum dissimilarity score.

Translation result generation

As soon as deciding the optimal template and smoothing the matching sequence of word patterns, we can exploit the gap between source speech input and the optimal template to generate the target speech. The generation process is straightforward as a corpus-based speech generation approach [15] by synthesizing example speech and variable speech. The process contains complete match, speech replacement, speech insertion and deletion, and composition in the example-based translation method [17].

EXPERIMENTAL RESULTS

A precision comparison test was performed to assess if the proposed template-based method translated on PDAs as well as on PC-based platform. Furthermore, the related experimental analysis of the proposed spoken language translation system is shown as follows.

The task and the corpus

The divergence between language pairs of bilingual corpus on unknown domain may be quite immeasurable when processing bilingual text corpus organization. Therefore, the bilingual corpus extended from specific domains is selected for experiments, covering simple travel conversations, about accommodation, transportation, restaurants, shopping, and other topics of interest to travelers. Additional important information was tagged to these sentences. From this bilingual corpus, we have derived basic travel mulitpotent templates that can be used for utterance recognition, understanding, and translation. In order to evaluate the system performance, a collection of 1,885 utterances for template derivation is speaker-dependent trained and 30 additional utterances of each language is collected for inside testing. Table 1 and Table 2 show the basic characteristics of the organized bilingual text corpus and the derived templates. All the utterances were sampled by a Taiwanese speaker and an English speaker at an 8 kHz sampling rate with a 16-bit precision on PCs and PDAs. The Taiwanese words in the corpus were obtained automatically by a Taiwanese morphological analyzer [15] and the English words were automatically tagged by LinkGrammar [18].

Table 1. Basic characteristics of the organized corpus

	Taiwanese	English
Number of sentences	2,084	2,114
Total number of words	14,317	11,648
Number of word entries	6,291	5,118
Average number of words per sentence	6.87	5.51

Table 2. Basic characteristics of the derived multipotent templates

Number of utterances	1,885
Number of templates	1,050
Total number of variables	5,500
Number of variable entries	1,260
Average number of variables per template	5.24

User interface

Figure 7 shows an example of the speech translation result, with: 1) the translation result by the decided optimal template and (2) the target speech output. Also, an agent is showing the status of the language templates in the upper windows. The user, first, selects the translation mode (the choices are Taiwanese=>English or English=>Taiwanese) and speaks to the system while pushing the "Speech Input" button. Then, the user can see the hypothesized template in the middle window and possible target text generation in the bottom window. The generated speech comes out when the user touches the "Output Replay" button. In Figure 7, there is an error in the speech segmentation result. However, even if the system makes the error, the window shows a possible generation because the system is using only the reliable keywords by measuring the intention region of the two-layer reference models.

Figure 7. An example of the speech translation result

Translation evaluations

The translation experiments were performed for both a PC-based platform and iPAQ PDAs. For the PC-based platform, the software simulations were done using Windows CE 3.0 on a Pentium® IV 1.8GHz, 1GB RAM, Windows® XP PC. For COMPAQ iPAQ PDAs, the system was implemented on StrongARM SA-1110 (200MHz), 32 MB SDRAM. Speech feature analysis was performed using 10 linear prediction coefficient cepstrum (LPCC) on a 32ms frame overlapped every 8ms. Figure 8 shows the precision results of crude template candidate selection, which intention segments of the source speech can be preselected correctly among the top 10 template candidates. According to the template candidates of top 10, the latent grammar understanding and score normalization are applied for further obtaining the target generation.

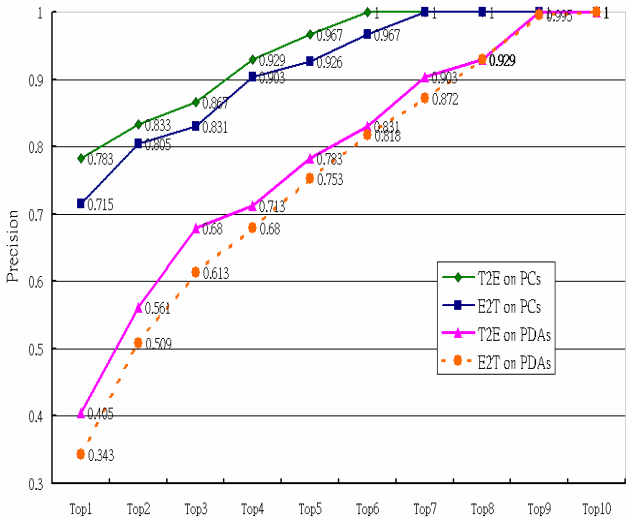

Figure 8. The results of template candidate selection

A bilingual evaluator classified the translation generation results into three categories [6]: *Good*, *Understandable*, and *Bad*. A *Good* generation should have no syntactic errors, and its meaning has to be correctly understood. *Understandable* generations may have some errors, but the main intention of source speech must be conveyed without misunderstanding. Otherwise, the translations are classified as *Bad*. With this subjective measure, the ratio of *Good* or *Understandable* generations with COMPAQ iPAQs was 79% for the Taiwanese-to-English (T2E) translation and 74% for the English-to-Taiwanese (E2T) translation. The ratio of *Good* generations was 70% for the T2E translation and 63% for E2T translation. Table 3 shows the average response time of 5 utterances with a duration of 1~3 seconds by the proposed template-based translation method on personal digital assistants. The proposed approach can achieve about 6.23 sec response time per source speech input on average compared with 5 sec in traditional 1~2GHz PC-based approaches [12].

Table 3. Average response time in the case of accommodation conversations for PDAs. (sec.)

Speech	Time
Yes, sir.	5.18
Is breakfast included?	5.42
What is the room rate per night?	6.30
Please wake me up at seven o'clock	7.02
I want to have breakfast tomorrow morning.	7.04

CONCLUSIONS

In this paper, we propose a novel template-based architecture for spoken language translation efficiently run on handheld devices. The proposed architecture is conducted with a mixture of utterance recognition, understanding, and translation. For the multipotent templates construction, which derives the translation database of spoken language, we blend with text-form translation templates and speech feature model for memory saving and translation capacity promoting. With the constructed templates, the proposed spoken language translation can be efficiently performed by crude template candidate selection, latent grammar understanding for templates, score normalization and ranking, and target speech generation. Experiments are conducted for the languages of Taiwanese and English on COMPAQ iPAQ Pocket PCs. According to the experimental results, our system can achieve about 76.5% translation understanding rate and 6.23 sec response time on average.

ACKNOWLEDGMENTS

The authors would like to thank the National Science Council, Taiwan, Republic of China, for its financial support of this work, under Contract No. NSC90-2215-E-006-009.

REFERENCES

[1] A. Lavie, A. Waibel, L. Levin, M. Finke, D. Gates, M. Gavalda, T. Zeppenfeld, and P. Zahn, "JANUS III: Speech-to-speech translation in multiple languages," Proc. ICASSP97, pp.99-102 (1997).

[2] F. Sugaya, T. Takezawa, A. Yokoo, and S. Yamamoto, "End-to-end evaluation in ATR-MATRIX: speech translation system between English and Japanese," Proc. Eurospeech-99, pp. 2431-2434 (1999).

[3] T. Watanabe, A. Okumura, S. Sakai, K. Yamabana, S. Doi, and K. Hanazawa, "An automatic interpretation system for travel conversation," Proc. ICSLP-2000, pp. IV 444-447 (2000).

[4] W. Wahlster, "Mobile speech-to-speech translation of spontaneous dialogs: an overview of the final Verbmobil system," in "Verbmobil: foundations of speech-to-speech translation," Ed. W. Wahlster, pp. 3-21, Springer (2000).

[5] R. Isotani, K. Yamabana, S. Ando, K. Hanazawa, S. Ishikawa, T. Emori, H. Hattori, A. Okumura, and T. Watanabe, " An automatic speech translation system on PDAs for travel conversation," Proc. ICMI-02, pp. 211-216 (2002).

[6] K. Yamabana, K. Hanazawa, R. Isotani, S. Osada, A. Okumura, and T. Watanabe, "A speech translation system with mobile wireless clients," Proc. ACL03 (2003).

[7] ATR Spoken Language Translation Research Laboratories research available at <http://www.slt.atr.co.jp/>

[8] Francisco Casacuberta, Enrique Vidal, and Juan Miguel Vilar, "Architectures for speech-to-speech translation using finite-state models," Proc. of the Workshop on Speech-to-Speech Translation: Algorithms and Systems, Philadelphia, pp. 39-44, (2002).

[9] Enrique Vidal, "Finite-State Speech-to-Speech Translation," Proc. ICASSP97, Vol. 1, pp: 111-114 (1997).

[10] F. Casacuberta, D. Llorens, C. Martinez, S. Molau, F. Nevado, H. Ney, M. Pastor, D. Pico, A. Sanchis, E. Vidal, J.M. Vilar, "Speech-to-Speech Translation Based on Finite-State Transducers," Proc. ICASSP2001, Vol. 1, pp: 613 –616, (2001).

[11] Herrmann Ney, Sonja Nießen, Franz Josef Och, Hassan Sawaf, Christoph Tillmann, and Stephan Vogel, "Algorithms for Statistical Translation of Spoken Language," IEEE Transaction on Speech and Audio Processing, Vol. 8, pp. 24-36, (2000).

[12] Kenji Matsui, Yumi Wakita, Tomohiro Konuma, Kenji Mizutani, Mitsuru Endo, and Masashi Murata, "An experimental multilingual speech translation system," Proc. PUI2001 (2001).

[13] Bonnie J. Dorr, Pamela W. Jordan and John W. Benoit, "A Survey of Current Paradigms in Machine Translation," In Advances in Computers, vol. 49, Academic Press (1999).

[14] Jhing-Fa Wang and Shun-Chieh Lin, "Bilingual Corpus Evaluation and Discriminative Sentence Vector Expansion for Machine Translation," Int. Conf. on Artificial Intelligence in Engineering and Technology (ICAIET-2002), Universiti Malaysia Sabah, Kota Kinabalu, Malaysia, 17-18 June 2002.

[15] Jhing-Fa Wang, Bao-Zhang Houg, and Shun-Chieh Lin, "A study for Mandarin text to Taiwanese speech system," Proc. ROCLING XII, pp. 37- 53 (1999).

[16] Yung-Ji Sher, Kao-Chi Chung, and Chung-Hsien Wu, "Establish Taiwanese 7-tones syllable –based synthesis units database for the prototype development of text-to-speech system," Proc. ROCLING XII, pp. 15- 35 (1999).

[17] Liu, J.N.K.; Lina Zhou, "A hybrid model for Chinese-English machine translation," IEEE International Conference on Systems, Man, and Cybernetics, Vol. 2, pp: 1201-1206 (1998).

[18] Davy Temperley, Daniel Sleator, and John Lafferty, Link Grammar Parser 4.1, available at <http://www.link.cs.cmu.edu/link/>

[19] Lawrence Rabiner and Biing-Hwang Juang, "" in "Fundamentals of Speech Recognition," pp. 211, Prentice-Hall, Inc. (1993)

An Accurate Speech Classification based on Fuzzy ARTMAP Neural Networks and Wavelet Packet

M.H. Radfar and K. Faez
Dept. of Electrical Eng., Amir Kabir Univ., Tehran, Iran
hradfar@aut.ac.ir | kfaez@aut.ac.ir

Abstract

This paper presents an accurate voiced/unvoiced/ transition/silence speech classifier that is used as an integral part of any toll quality speech coder. Due to ability of wavelet packet in decomposition of time–frequency plane with high resolution, first five discriminate features based on energy concentration of wavelet packet coefficients for each speech classes in time-frequency plane are extracted. Then a Fuzzy ARTMAP neural network classifier, which has been shown a powerful tool for non-stationary signal classification is employed. Experimental results show the proposed approach gives considerable performance improvements in some aspects with respects to the conventional methods

1. Introduction

In recent years emerging application for toll quality speech coder at low bit rate such as third generation of wireless networks has encouraged a lot of research in this area [1], [2]. Aim is to achieve a toll quality, and low bit rate speech coder simultaneously. Unfortunately, the two objectives are in contrast with each other. To cope with this dilemma, an adaptive hybrid-coding algorithm must be implemented for each speech class. Therefore, speech classifier is an inseparable part of any toll quality speech coder. Whatever a classifier is more accurate, more quality is achievable. Mainly low bit rate speech coders classify speech segments into voice/ unvoice source and encode each class with different methods, resulting in low bit rate vocoder especially below 2.4 kbps [3],[4]. However in order to preserve speech quality a more accurate classification than rough classification into voiced /unvoiced (V/U) is needed. Degradation of quality in low bit rate vocoder is mainly due to assumption of simple model for speech signal. Commonly, speech segments that have strong periodicity are identified as voices and unvoices are represented by noise model. Nevertheless transitional speech [6], [7], such as non periodic glottal pulse, onsets (transition from unvoice to voice) and plosives (b,t,g,k,q) don't follow these characteristics, and usually are misclassified by a speech classifier. Consequently need for an accurate multi speech classifier is manifested. Like other pattern recognition systems, speech classifiers consist of two parts, a feature extractor and a classifier. The most commonly speech classification features are zero crossing rates, first auto correlation coefficient, first LPC coefficient, speech peakiness and signal energy, which has been extensively used and developed by researchers [12].[22]. These parameters work properly when high level voice or unvoice are to be classified, but fail for transitional speech. Especially when auto correlation coefficients are used as classification parameters, non-periodic glottal pulses due to weak periodicity are classified as unvoiced but in fact the vocal cord is involved during constructing these sounds. Beyond these features, recently, multiresolution analysis with wavelet transform has been used widely, owing to its potential for dealing with non-stationary signal. Application of wavelet transform in speech classification and pitch detection was first introduced by Kadambe [18] who was inspired by Mallat [19] in which signal discontinuity are detected by decomposition of signal into wavelet scales and stable local maxima across several scales i.e. 3 through 5 are determined. These maxima identify edges or discontinuity in signals. Recently this approach has been developed by other contributions [8], [20]. However, most effort has been focused on event based-detection property of wavelet in speech signals where instances of glottal closure are determined by wavelet transform. Ability of wavelet transform in analysis of time-frequency plane has not been considered well up to now in speech area in compares with short time Fourier transform (STFT) and Mel frequency cepstral coefficients (MFCC). Among wavelet transform algorithms wavelet packet provides better resolution in time frequency domain while preserve computational complexity in comparison with MFCC and STFT .As will be shown, wavelet packet (WP) coefficients energy for each speech class is dispersed in different parts of time frequency plane. This favorite attribute makes WP coefficients a useful discriminated feature in speech classification.

In the second part of system, generally two strategies have been introduced. First by presenting a proper threshold, speech classes are determined [8], [9]. Second a neural network classifier such as Back propagation [10][14], self-organized map [11], and recurrent neural network [13] are employed to determine the corresponding class. Fuzzy ARTMAP neural network uses the class of adaptive resonance theory architecture designed for supervised learning, first introduced by Carpenter [15] and develops in other contributions [16], [17]. Fast and stable learning of large non-stationary databases has made Fuzzy ARTMAP as an outstanding candidate for classification problems.

The remainder of this paper organized as follows. First the procedure for extracting features is explained, and then a brief review of Fuzzy ARTMAP architecture will be presented. Finally experimental results are reported and compared with the conventional method.

2-Feature Extraction based on wavelet Packet

Aim of any feature extraction system is to choose those features, which are most effective for preserving the class separability and to prune non-relevance information.

As discussed before the objective is to classify each sub frame of speech signal (each frame contains 160 samples and is sampled in 8 KHz) as voice, unvoiced, transition, or silence. As it is proved in [21], if the scaling function and wavelets form an orthonormal basis (e.g. Daubechie mother wavelets), the Parsevall theorem relates energy of the signal to energy in each of components and their wavelet coefficients:

$$\int |g(t)|^2 dt = \sum_{j=-\infty}^{\infty} \sum_{k=-\infty}^{k=\infty} |d_j(k)|^2 \qquad (1)$$

Where the two-dimensional set of coefficients $d_j(k)$, are the discrete wavelet transform (DWT) of $g(t)$. According to this fact, we have a framework for describing the signal by wavelet coefficients in different parts of joint time-frequency domain of time frequency plane. We use dyadic wavelet packet transform, because the flexible tree structure makes it possible to have equivalent sub bands in the whole time frequency plane. In the corresponding wavelet packets situation, each detail coefficient vector is also decomposed into two parts using the same approach as in the approximation vector splitting. This offers the richest analysis of each frame. After examining various speech frames, we found the following partitioning of time frequency appropriate for our purposes. The time frequency plane is divided into different cells as illustrate in Fig 1.

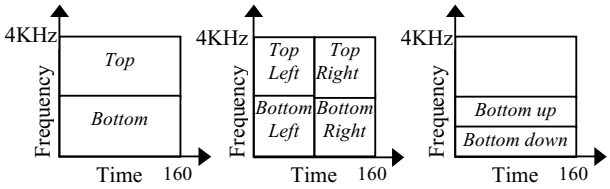

Figure 1-The time frequency plane is divided into different cells

Then the density of energy in each region is obtained by WP coefficients, and finally five sets of features are determined as follows. Decomposition of the wavelet packet tree is obtained in level three. After applying of wavelet packet with Daubechie 8 mother wavelet, the WP coefficient in level three i.e. 8 bands, with 8×160 coefficients, are obtained. We use the wavelet packet because it provides much finer and adjustable resolution. The features are extracted as follows. The term *E()* hereafter means the energy of WP coefficients in one of the indicated region in Fig 1, and is computed as follows

$$E(\text{desired reigon}) = \sum_{j\&k\in \text{desired..reigon}} \sum d^2{}_j(k) \qquad (2)$$

2-1 Voiced /Unvoiced/Silence Classification

As shown in Fig 2 (a) and (b), most parts of WP coefficients energy for a voiced frame are placed in low frequency part of time frequency plane and evenly distributed in time. In other hand, energy distribution for an unvoiced frame is evenly distributed in all over the time frequency plane. Therefore, we can define feature one by

$$feature1 = \frac{E(Bottom)}{E(Top)} \qquad (3)$$

Where for example, *E(Top)* means the WP coefficients energy in band 4through8 (2000Hz to 4000Hz).This parameter is especially useful to discriminate a reliable voiced subframe from unvoiced sub frame. In [8], they have proposed a similar parameter and introduced the threshold to make the relevance decision. However using the threshold solely provides good results, only when a reliable voice is to be classified. The term reliable voiced speech here means a voiced segment with strong periodicity and high energy. So, in order to separate unreliable voiced sub frame from unvoiced one, we consider the second feature that is defined by

$$feature2 = \frac{E(Bottom - down)}{E(Bottom - up)} \qquad (4)$$

If the value of feature 1 is not too high to make an explicit decision, then if the value of the second feature is high, the sub frame is voiced speech otherwise it is classified as unvoiced.

The above features perform well at distinguishing between voiced and unvoiced speech. However they do not enable to separate silence sub frames from voiced or unvoiced speech. A simple investigation shows the energy value of silence frame is too low in comparison with voiced/unvoiced speech. Thus the total energy of a frame is an appropriate feature to distingue silence segments as is expressed in equation 5.

$$feature3 = E(Total) \tag{5}$$

2-2 Transitional Classifications

Mainly transitional speech segments occur in the following situations:

First, in onsets where an unvoiced speech is ended and a voiced speech is started. Second, when a plosive sound is uttered such as p, t, b, q. The analysis of transitional speech, especially for onsets shows a transition occurs when a more rapidly waveform with low amplitude (i.e. with weak low frequency components) is followed by a slow varying waveform with high amplitude, (i.e. with dominant low frequency components). The above explanation makes clear that a transitional segment can be distinguished from a voiced or unvoiced speech by comparing the differences between the energy concentrations in bottom-left of time frequency plane to bottom-right of time frequency plane as has been illustrated in Figure 2 (c). Therefore we introduce the forth feature as:

$$feature4 = \frac{E(Bottom - Right) - E(Bottom - Left)}{E(Total)} \tag{6}$$

However, this criterion does not work well for all plosive sounds in which a transition happens during passing from a rapidly varying waveform to other rapidly varying waveform with a sudden change in amplitude. In these situations the differences between energy concentrations in top-left region to the top-right of the time frequency plane is a discriminated feature to classify these kinds of transitional sounds, as it has been illustrated in Figure 2 (d) and is expressed in equation 7. Table 1 illustrates the typical value of selected features for each class.

$$feature5 = \frac{E(Top - Right) - E(Top - Left)}{E(Total)} \tag{7}$$

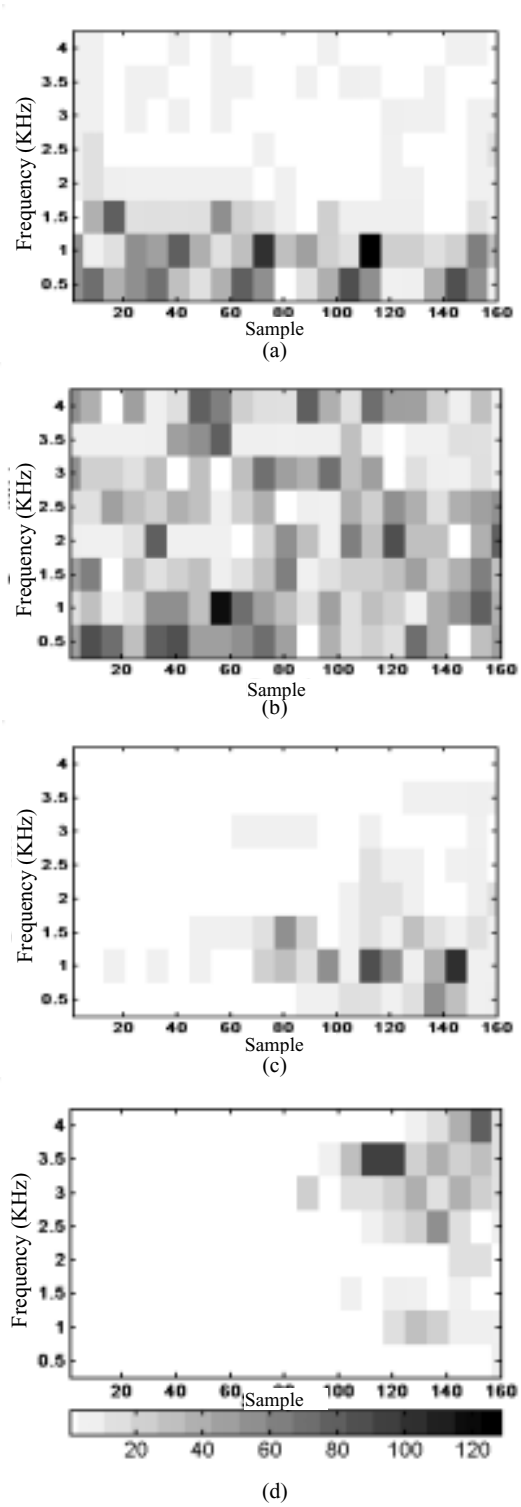

Figure 2: Energy distribution of WP coefficients for (a) voice (b) unvoice (c), (d) transitional segment;

Table 1: Typical value of proposed features for voiced/unvoiced/transition/silence segments

Feature	Silence	Voice	Unvoice	Transition
1	2.2983	9.2805	1.59	3.8321
2	1.757	1.5729	1.1686	2.2777
3	24.392	8055.94	623.903	4061.16
4	.1045	.07277	.027082	.82063
5	.1019	.029257	.078936	.075245

3. The Fuzzy ARTMAP Neural Network

A detailed description of the fuzzy ARTMAP neural network can be found in [15]. Here just a brief review is presented. The fuzzy ARTMAP neural network consists of two fuzzy ART modules, (ARTa, ARTb) as well as an extra inter ART module, shown in Figure 4. Each fuzzy Art is an extension of ART1 system to enable the network to handle the continuous inputs through the use of fuzzy AND operator ($\wedge$), instead of the logical intersection ($\bigcap$). In order to prevent category proliferation [15], input vectors are normalized by complementary coding where if $a \in [0,1]^M$ denotes original input, then the new F_0 layer input vector I ($I = (a, a^c) \in [0,1]^{2M}$, where $a^c = \{a_i^c\}$ and $a_i^c = 1 - a_i$) is fed into network.

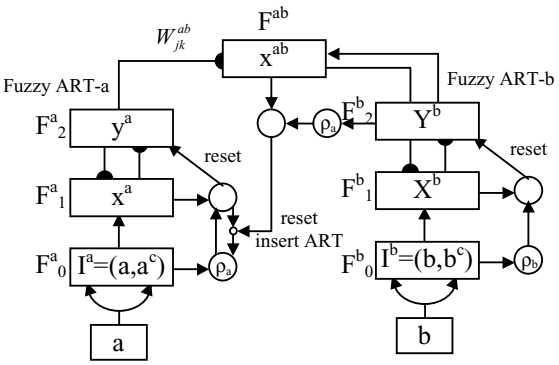

Figure 4: Fuzzy ARTMAP architecture

Thus, the complement coded input and W_j are of dimension 2M. During learning, the adaptive weights or the long term memory (LTM) are adjusted according to the winner take all rule i.e. at most one F2a node can become active at a given time. Map field realizes the match-tracking rule, whereby the vigilance parameter for ARTa increase in response to a miss match at ARTb. After each input in ARTa find a proper output in ARTb, the Map field weights and LTM in ARTa are trained. Thus the number of outputs nodes in ARTa, i.e. F2a, can be increased to some extends, while the number of the Map filed nodes are constant and are equal to the number of output classes. This property of Fuzzy ARTMAP is especially interesting when two input segments with different features belonging to one class are classified. Thus while we preserve generality, the error rate decreases too.

4. Experimental Results

In order to obtain a proper set of training data, twenty sentences from 10 male and 10 female of popular TIMIT database are selected. The sentences are divided into 10 msec (80 sample) sub frames and then are manually labeled as voice, unvoice, transition, and silence. The result of manual class decision is shown in table 2. Each entry shows the percentage of manual class decision.

Table 2: Manual Class decision

Voice	Unvoice	Transition	Silence
45	35	16.25	3.75

Then Daubechie 8 wavelet packet transform was performed on each frame. For restricting the effect of boundary at the frame edge, we extend each frame from left and right to 8 msec, however this amendment introduces 8 msec delays into system. In next step, five features are computed as discussed in pervious section. The features are normalized according to complementary coding as was discussed in section 3. Thus 10 inputs are fed into network. Fuzzy ARTMAP parameters are set as follows: choice parameter is set to zero, the ARTa based lined vigilance parameter, $\overline{\rho}_a$ is set to zero, the learning rate, β is set to one i.e. fast learning. Epsilon is set to 0.001, this value is added to ARTa vigilance parameter when a mismatch happens in F_{ab} , so a reset does not occur in ARTa. And finally the MAP field vigilance parameter ρ_{ab} is set to 0.95. The number of F^a_2 output nodes is initially set to 20. However due to representing the discriminating features just 12 nodes are used at the F_2^a output layer. In order to examine the reliability of features, a fixed set of 4000 chosen exemplars was normalized and presented to the Fuzzy ARTMAP system. After training the system, we test validation of the approach by presenting 4000 test samples. The neural network classification confusion matrix on the test database is presented in table 2 In order to evaluate the accuracy of method, five features (the signal energy, the first reflection coefficient, the rate of zero crossing, the first coefficient of the 10th order LPC and the peak amplitude of signal) that are extensively used in other contributions [12], [14], [5] are extracted from the

training data set (4000 exemplars as mentioned later) and fed into a back propagation neural network with 10 hidden layers and 4 outputs. After training, the confusion matrix is obtained by introducing of the test samples to the back propagation classifier. The method that is denoted by (a) in Table 3 demonstrates the results taken from WP-Fuzzy ArtMap classifier and the method (b) indicates the results from the Back propagation classifier. Each entry in the confusion matrix shows the percentage of the automatically detected class in comparison with manual class decision. As it is clear from the table 3, the error rate in the method b is somehow higher than those of the method a, especially for transitional speech. It must be mentioned here, in classifying the speech segments manually, the non-periodic glottal pulses were considered as an voiced speech rather than transitional speech, because naturally vocal cord is exited during the construction of non-periodic speech, although their residual signal exhibits weak periodicity, but the experiments show [6] when the non-periodic sounds are classified as voiced sounds, there is no or only slight degradation of perceived quality as long as the estimated pitch is not extremely high or low.

Table 3:Matrix confusion for proposed (a) WP-FuzzyArtMap classifier and (b) Back propagation

Manual	Methods	Unvoice	Voice	Transition	Silence
Unvoice	(a)	33	0.6	1.125	0.275
	(b)	31.8	0.5	1.979	0.721
Voice	(a)	0.35	43.7	0.75	0.2
	(b)	0.55	42.8	1.45	0.2
Transition	(a)	1.175	0.95	14.125	0
	(b)	2.575	1.55	11.9	0.225
Silence	(a)	0.45	0	0	3.3
	(b)	0.45	0	0	3.3

5. Conclusion

In this research, a more accurate speech classifier was presented. In comparison with other proposed methods, this approach uses a new set of features that appropriately characterize speech classes. Moreover, instead of using the thersholding to make the decision, like what was done in [9], a fast and stable neural network was employed to classify the proposed features. Flexibility of partitioning time-frequency plane into finer cells in addition to low computational complexity in comparison with short time Fourier transform and MFC coefficients, makes wavelet packet a powerful tool for the classification purposes. Furthermore reported results show that the accuracy of this model is comparable with other conventional model, and this method also performs a finer classification more than the voice/unvoice classification, that has been extensively used in other approaches. In the next step of this research we are going to evaluate the model accuracy in noisy environment.

References

[1] E. Shlomot, V. Cuperman, and A. Gersho, " Hybrid coding: combined harmonic and waveform coding of speech at 4 kb/s" Speech and Audio Processing, IEEE Transactions on, Volume: 9 Issue: 6, pp. 632 –646, Sept. 2001

[2] O. Gottesman, A. Gersho, "Enhanced waveform interpolative coding at low bit-rate "Speech and Audio Processing, IEEE Transactions on, Volume: 9 Issue: 8, pp. 786 – 798, Nov. 2001

[3] A. McCree, Kwan Truong, E.B. George, T.P. Barnwell and V. Viswanathan, "A 2.4 kbit/s MELP coder candidate for the new U.S. Federal Standard "Acoustics, Speech, and Signal Processing, 1996. ICASSP-96. Conference Proceedings, 1996 IEEE International Conference on, Volume: 1, pp. 200 -203, May 1996

[4] Tian Wang, K. Koishida, V. Cuperman, A. Gersho and J.S. Collura, "A 1200 bps speech coder based on MELP" Acoustics, Speech, and Signal Processing, 2000. ICASSP '00. Proceedings. 2000 IEEE International Conference on, Volume: 3, pp. 1375 - 1378, June 2000

[5] *J.A Marks,"* Real time speech classification and pitch detection", COMSIG 88. Southern African Conference on , 24 June 1988

[6] Jongseo Sohn, and Wonyong Sung, "A low resolution pulse position coding method for improved excitation modeling of speech transition" Acoustics, Speech, and Signal Processing, 1999. ICASSP '99. Proceedings, 1999 IEEE International Conference on, Volume: 1, pp. 265 -268, March 1999

[7] Li Chunyan and V. Cuperman, "Enhanced harmonic coding of speech with frequency domain transition modeling" Acoustics, Speech, and Signal Processing, 1998. ICASSP '98. Proceedings of the 1998 IEEE International Conference on, Volume: 2, pp. 581 –584, May 1998

[8] F.C.A. Brooks, L. Hanzo, "A multiband excited waveform-interpolated 2.35-kbps speech codec for bandlimited channels" Vehicular Technology, IEEE Transactions on, Volume: 49 Issue: 3, pp. 766 –777, May 2000

[9] J. Stegmann, G. Schroder, and Fischer, K.A., "Robust classification of speech based on the dyadic wavelet transform with application to CELP coding" Acoustics, Speech, and Signal Processing,. ICASSP-96. Conference Proceedings, 1996 IEEE International Conference on, Volume: 1, pp.546 -549 1,May

[10] Jiang Minghu, Yuan Baozong, and Lin Biqin, "The consonant/vowel (C/V) speech classification using high-rank function neural network (HRFNN)" Signal Processing, 1996, 3rd International Conference on, Volume: 2, 14-18 Oct. 1996 pp.1469 -1472
[11] P.P. Boda, "Robust voiced/unvoiced speech classification with self-organizing maps" Circuits and Systems, 1995. ISCAS '95, 1995 IEEE International Symposium on, Volume: 2, pp.1516 -1519, 28 April-3 May 1995
[12] A. Bendiksen, and K. Steiglitz, " Neural networks for voiced/unvoiced speech classification" Acoustics, Speech, and Signal Processing, 1990. ICASSP-90, 1990 International Conference on, pp.521 -524, April 1990
[13] Wei-Chen Chang, and A.W.Y. Su," A novel recurrent network based pitch detection technique for quasi-periodic/pitch-varying", Neural Networks, IJCNN '02, Proceedings of the 2002 International Joint Conference on, Volume: 1, pp. 816 –821,
[14] T. Ghiselli-Crippa, A. El-Jaroudi, "Voiced-unvoiced-silence classification of speech using neural nets", Neural Networks, 1991, IJCNN-91-Seattle International Joint Conference on, Volume: ii, 8-14 July 1991 pp. 851 -856 vol.2
[15] G.A. Carpenter, S. Grossberg, N. Markuzon, J.H. Reynolds and D.B. Rosen, " Fuzzy ARTMAP: A neural network architecture for incremental supervised learning of analog multidimensional maps" Neural Networks, IEEE Transactions on, Volume: 3 Issue: 5, pp. 698 –713, Sept. 1992
[16] I. Dagher, M. Georgiopoulos, G.L. Heileman, and G. Bebis, "An ordering algorithm for pattern presentation in fuzzy ARTMAP that tends to improve generalization performance" Neural Networks, IEEE Transactions on, Volume: 10 Issue: 4, pp. 768 –778, July 1999
[17] E. Gomez-Sanchez, Y.A. Dimitriadis, Cano-Izquierdo, J.M., and Lopez-Coronado, J., " μARTMAP: use of mutual information for category reduction in Fuzzy ARTMAP" Neural Networks, IEEE Transactions on, Volume: 13 Issue: 1, pp. 58 –69, Jan. 2002
[18] S. Kadambe, and G.F. Boudreaux-Bartels, "Application of the wavelet transform for pitch detection of spe ech signals", Information Theory, IEEE Transactions on, Volume: 38 Issue: 2, pp. 917 –924,March 1992
[19] S.J. Mallat and W.L. Hwang, "Singularity Detection and Processing with Wavelets", Information Theory, IEEE Transactions on, Volume: 38 Issue: 2, pp. 617 –642,March 1992
[20] S.H. Chen, and J.F. Wang, "Noise-robust pitch detection method using wavelet transform with aliasing compensation" Vision, Image and Signal Processing, IEE Proceedings-, Volume: 149 Issue: 6, pp. 327 -334, Dec. 2002
[21] S.G. Mallat, "A Wavelet Tour of Signal Processing", Academic Press, 2nd edition (September 15, 1999)
[22] R.P. Cohn, "Robust voiced/unvoiced speech classification using a neural net" Acoustics, Speech, and Signal Processing, 1991. ICASSP-91, 1991 International Conference on, vol.1, pp. 437 -440,April 1991

POSTER SESSION II

(This page left blank intentionally)

Autonomous Direct 3D Segmentation of Articular Knee Cartilage

Enrico Hinrichs
The Centre of Magnetic Resonance
CMR, The University of Queensland
Brisbane, Queensland, Australia, 4072
enrico@cmr.uq.edu.au

Brian C. Lovell
The Intelligent Real-Time Imaging and Sensing Group
ITEE, The University of Queensland
Brisbane Queensland, Australia, 4072
lovell@cmr.uq.edu.au

Ben Appleton
The Intelligent Real-Time Imaging and Sensing Group
ITEE, The University of Queensland
Brisbane, Queensland, Australia, 4072
appleton@itee.uq.edu.au

Graham John Galloway
The Centre of Magnetic Resonance
CMR, The University of Queensland
Brisbane, Queensland, Australia, 4072
gg@cmr.uq.edu.au

Abstract

The aim of the work presented here, is to speed up the entire evaluation process of articular knee cartilage and the associated medication developments for Osteoarthritis. To enable this, the development of an automated direct 3D segmentation is described that incorporates non-linear diffusion for efficient image denoising. Cartilage specific magnetic resonance imaging is used, which allows acquiring the entire cartilage volume as one 3D image. The segmentation itself is based on level sets for their accuracy, stability and topological flexibility. By using this kind of segmentation, it is hoped to improve the time efficiency and accuracy for quantitative and qualitative integrity evaluation of cartilage and to enable an earlier diagnosis and treatment of Osteoarthritis.

INTRODUCTION

Osteoarthritis (OA) occurs typically in the aged with a typical age range of 30 to 70 years, occurring earlier under extreme conditions such in as high-impact sports. It is a major cause of morbidity and causes significant health costs to communities. Much of the cost is associated with the treatment of late, symptomatic disease, especially joint replacement surgery. The work described here is part of the Brisbane Osteoarthritis Imaging Study (BOIS), a collaborative study between Pfizer and the University of Queensland, whose overall purpose is to develop a Phase II OA "Proof of Concept" clinical model by assessing changes in joint structure in knee OA in high risk patient cohorts using state-of-the-art magnetic resonance imaging (MRI). A significant advantage of using MRI is that it allows the acquisition of high-contrast cartilage images.
The purpose of segmentation for BOIS is to reliably extract the structure and pathological occurrences in cartilage from MR images. This will then form a basis for the detection of OA progression, which relies on quantitative and qualitative assessment of cartilage volume and thickness measurements.

There is currently no consensus on how to assess disease progression using MRI, and studies to date have generally focussed on cartilage volumes at their endpoints and incorporated segmentation with a high level of user interaction. Here we focus on the automation of the segmentation and the improvement of the accuracy of cartilage measurements in order to streamline further analysis and to enable an earlier detection of cartilage pathologies. A sensitive registration method for cartilage changes over a longer time period (e.g.: several month) will also be developed, based on segmentation fine-tuning for smaller diurnal changes.

The expected outcomes include:

- An autonomous segmentation method:
  - Accelerated drug trials
  - Simpler pre- and post-operative disease monitoring
- Early detection of Pathology-Associated Changes (thickness and volume changes)
  - Early diagnosis
- Detection of early onset OA (eg. due to sporting injuries)

This problem has been explored previously in [1]. They found that using only grey level features for the distinction of very similar cartilage contact zones was insufficient, and introduced a segmentation method in scale space. They formulated the problem as a hierarchical energy minimisation solved using a gradient descent scheme based on B-spline snakes. The use of a hierarchical scheme was found to produce relatively robust segmentations. Their automated algorithm failed to segment the cartilage between the patella and femoral cartilage and between the femoral and tibia cartilage and, therefore, required user interaction.

The solution of these drawbacks is the main objective of this work – to develop a fully automated 3D segmentation based on a level set approach [2] and non-linear diffusion (NLD). In order to do this we will overcome the distinction problem between very similar cartilage contact zones. Therefore, we apply NLD for an efficient image simplification and level sets for their improved stability, simple 3D implementation, accuracy and topological flexibility. Additionally, multispectral image information

will be considered to provide different contrast features for the distinction of similar tissues. The use of a 3D segmentation method is expected to give improvements over traditional 2D methods and assist in the automation of the method.

This paper is organized as follows: It starts explaining Osteoarthritis and segmentation relevant cartilage properties, and shows then the cartilage lesion classification system by Outerbridge in table 1. Furthermore, it is described how to overcome cartilage-imaging problems and advantages of 3D imaging are pointed out. Then current drawbacks for segmenting articular knee cartilage are explained. Subsequently, solutions as image simplification and the application of level sets for a 3D segmentation are proposed. In the discussion and results section two images containing the same information but with different contrasts are shown and their combination for multispectral segmentation described.

OSTEOARTHRITIS AND ARTICUALR CARTILAGE IN THE KNEE

The goal of our segmentation method is to extract the femoral and tibial articular cartilage. These cover the bone endings of the tibia and femur, which are part of the knee joint. The cartilage consists of a well-organized, multi-layered structure providing a high load-bearing capacity, high compressive stiffness and a smooth surface [3]. The smoothness of the cartilage surface and the additional lubrication provided by the synovial fluid allow low-friction gliding within the knee joint. Cartilage damage increases this friction and erodes the cartilage until femur and tibia come into direct contact, causing significant pain and eventually disability. Osteoarthritis and other types of arthritis are the second leading cause of disability in the United States [4].

MULTISPECTRAL IMAGING

For an automatic segmentation, current available MRI sequences are not sufficient to provide enough contrast between similar cartilage contact zones. To overcome this disadvantage we propose imaging with two different contrasts: fat- and non-fat-suppressed sequences. It is hoped that the combination of both sequences will allow better cartilage distinction than either allows individually.

CARTILAGE LESION CLASSIFICATION SYSTEM

Cartilage lesions of the knee may be characterised using the classification system of Outerbridge [5]. Currently available imaging sequences are sufficient for detecting grades 2-4 only and sequences to enable proper detection of grade 1 are under development. In this project thickening and softening detection will be enabled by incorporating sodium 23 nuclear MR imaging.

Table 1. Cartilage lesion classification system by Outerbridge

Grade	Symptom
1	Thickening and softening
2	Fissuring of the articular surface that does not extend to the underlying bone.
3+4	High-grade lesions with partial or full-thickness cartilage defect, respectively.

3D IMAGING

Traditional studies use 2D slice-based acquisition [1]. This often requires that each slice be aligned before processing, and introduces significant anisotropy into the image data. In this project we apply 3D imaging methods for improved spatial resolution and to avoid alignment problems. Therefore, the complete knee joint image is acquired as a monolithic volume.

In this study we use a water excited 3D DESS (Dual Echo Steady State) sequence. The imaging sequence enables high contrast between normal and abnormal cartilage, both in deep and superficial layers. It displays cartilage with an optimal contrast and high spatial resolution. Furthermore, volume calculations and 3D display are facilitated. The water excitation of the sequence enables cartilage selective display, whereas all other tissues appear darker. More over it provides high-quality multiplanar reconstruction (MPR), a strong T2 contrast and an improved signal to noise ratio. Despite its cartilage selectivity, the assessment of other joint structures is also possible.

SEGMENTATION

It is hypothesized that repeating a multispectral segmentation reveals differences in separation of pathological cartilage against the menisci. Here we intend to develop a fully automated segmentation method using NLD and level sets. Articular cartilage is difficult to segment because it is a thin structure (1-2mm). Its transmitted MRI signal intensity is proportional to its size and difficult to distinguish at low spatial resolutions. The problem of tissue differentiation becomes quite challenging and the main problem of automation is the distinction between deteriorated cartilage and its similar surroundings, such as the two menisci and the synovial fluid. At the end of the deterioration process the cartilage becomes indistinguishable from noise. To improve the signal to noise ratio, non-linear diffusion will be applied prior to segmentation.

Multispectral Segmentation

Another difficulty is that the given sequences cannot be used to reliably image early cartilage degeneration. To overcome the aforementioned problems we intend to consider a combination of more distinction properties for the segmentation by using multispectral images.

Manual Segmentation

As a reference for an accuracy validation a manual segmentation is performed first. Several 2D slices are printed out and an expert draws a line manually around the cartilage contour. These manual segmentations are then digitized and may then be used as templates to validate the results of automated segmentation.

Non-Linear Diffusion

First the acquired images are cropped to the area of interest, which includes the cartilage and its surroundings. Subsequently, the image is simplified to reduce noise and remove insignificant details. A standard method for this is to convolute the image with a Gaussian kernel. The disadvantage of this method is that due to its linearity, meaningful details such as edges are removed in the same manner as less important details. To overcome this disadvantage Non-Linear Diffusion (NLD) is used here. NLD enables image simplification while preserving meaningful features such as contiguous edges. Non-linearity is given by using a spatial-varying diffusity, which adapts to the image intensity gradient. Near significant edges the diffusivity reduces to zero and while in the interior of objects the diffusivity increases, allowing selective blurring.

The convolution of an image by a Gaussian kernel G_σ smoothes the image, reducing all image details equally. The scale σ of the kernel controls the amount of smoothing. Perona and Malik [6] recognized that this may be viewed as a linear diffusion:

$$I_t = \mathrm{div}(c \nabla I) \quad (1)$$

Here the diffusivity c is constant over the image plane. For a non-linear diffusion Perona and Malik [6] introduced spatially varying diffusion coefficients, such that the diffusivity is low on intensity gradients. Strong intensity gradients are typically associated with object edges. This choice of diffusivity function not only preserves large intensity discontinuities but sharpens the edges of objects. In the non-linear case we may rewrite the first equation 1 as:

$$I_t = \mathrm{div}\left(c\left(|\nabla I|\right)\nabla I\right) \quad (2)$$

Previous Work: B-Spline snakes

Deformable contour models or snakes that are based on the seminal work of Kass et al. [7] have been proven to be suitable for matching smooth surfaces such as the cartilage contour in MR images. The advantage of these models lies in the combination of external image forces, which are based on low level features that attract the initial contour toward the object boundaries and on internal forces such as the contour elasticity that preserves the smoothness of the contour. The previous work from [1] on knee cartilage segmentation uses B-Splines and a hierarchical energy minimization approach performed in scale space. The process starts at a coarse scale and reduces the scale in each step, while minimizing the energy function on each level. To let the algorithm start at a coarse scale assists contour attraction even if the initial contour is inaccurate, and minimises the attraction to noisy edges in the surrounding tissues. These properties are responsible for the stability of this algorithm. The semi-automated segmentation enabled by this method allowed a considerably higher reproducibility compared to a manual segmentation, which motivates developing the following automated segmentation.

Algorithm Development Using 3D Level Sets

Following mathematical descriptions are based on [2].

The cartilage surface S to segment, is represented in space R^3 as:

$$S : [\delta, \tau] \rightarrow \square$$

and embedded into the three dimensional level set function ϕ that maps to one dimension R:

$$\phi : \square \quad \rightarrow \square$$

such that S becomes an isosurface of ϕ

$$\phi(S) = 0 \, .$$

Now the level set function ϕ needs to be manipulated to match the cartilage contour and is represented as a partial differential level set equation:

$$\partial \phi / \partial t = - F \left| \nabla \phi \right| .$$

The gradient magnitude $|\nabla \phi|$ is multiplied with the speed function F that describes the normal velocity of the surface S. F is responsible to guide the surface and can be defined to allow a wide range of surface deformations in order to match the cartilage contour.

Advantages of Level Sets

The advantage is to have always control over the level set function ϕ, despite possible contortions of the embedded cartilage surface S. This property enables to handle easily breaking and merging for the segmentation process. Another benefit is that the technique trivially extends to three dimensions. Also, level sets allow establishing less complicated numerical schemes to approximate motion equations. The cartilage surface S matches the zero level set of the adjustable level set function ϕ. This allows starting the evolution process with a partial differential equation that is similar to the Hamilton–Jacobi equation. These conditions ease the evaluation of normals and curvatures and topological changes occur normally.

NLD, Level Sets and 3D Advantages for Automation

As above mentioned is one monolithic image volume acquired that is stored as a series of 2D-sliced DICOM images. The second focus – besides automation – of our work is to take advantage of the volumetric and singular property of the acquired data. Therefore, the series of 2D images is first reassembled to one 3D image. Subsequently, level sets are applied, to enable a segmentation of the complete three-dimensional cartilage contour at once. Level sets are the successor of snakes and offer a better stability, accuracy and topological flexibility. It is therefore hoped too gain improvements compared to the previous work [1] that uses the snake-splines approach. In addition to that, we use NLD in the first segmentation instance to efficiently denoise the image. It is hoped that combining NLD, level sets and multispectral image information enables automated cartilage segmentation.

Time Efficiency and Accuracy Improvements

All together there are three accuracy and two time efficiency improvements to expect.

We are using only one 3D image that contains all the information about the complete cartilage structure to segment. Using the one volume gives a better resolution, since "gaps" between 2D-acquired and 2D-segmented image slices—after assembling those to a volume—are avoided. The process will be faster, because everything will be directly 3D-segmented at once, and segmenting and combining of 2D slices becomes unnecessary. The direct 3D segmentation of the complete cartilage volume in one step and the automation feature are expected to speed up the entire segmentation process.

The three accuracy improvements are based on the better accuracy of level sets themselves, on the higher resolution as previously explained and that the automation avoids subjective decisions about tissue border distinctions.

It is also aimed to design a user-friendly GUI to reduce the familiarizing time and, therefore, the post-processing time.

DISCUSSION AND RESULTS

Based on the automatic segmentation described in this paper, it is intended to speed up drug development and to eventually improve OA medication. It is also aimed for an earlier OA treatment by detection of pathology-associated changes in cartilage as early as possible. This will be based on an automatic and more accurate segmentation and on Sodium 23 nuclear MR imaging, which will be considered for detecting abnormal cartilage changes as softening and thickening.

For comparison two images with different contrasts (fat- and non-fat-suppressed) are shown below and to the right. The image in figure one was acquired using the 3D DESS sequence with water excitation. Cartilage contains with 75% significantly more water than bones (22%). Therefore, mainly cartilage is visible, whereby bones containing fat appear dark (fat-suppressed).

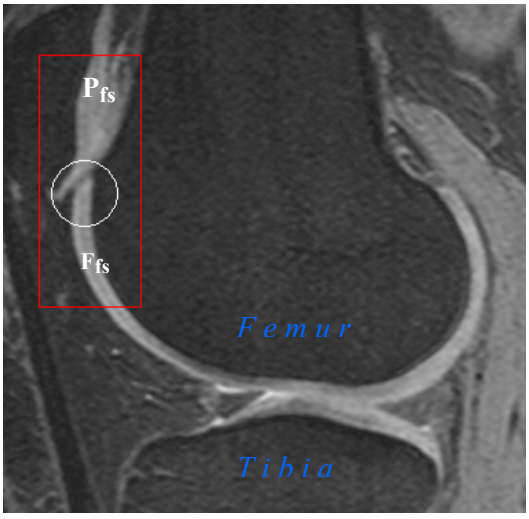

Figure 1. Knee joint in 2D view (fat– suppressed)

The image in figure two is acquired using a non-fat-suppressed sequence. Therefore, bones (containing bone marrow with fat cells) are better visualized as before. In both images P denotes cartilage belonging to the patella, F femoral cartilage and fs abbreviates fat-suppressed. The patello-femoral cartilage contact zone is within the white circle between P and F. As an example to enable better contrast, image parts around P_{fs} of figure one could be used to superpose or replace the same parts of the patella cartilage P in figure two. This would then result in a better contrast between P and F and support a distinction of both cartilage types.

The algorithm development is currently in the initial phase and more results will be provided soon.

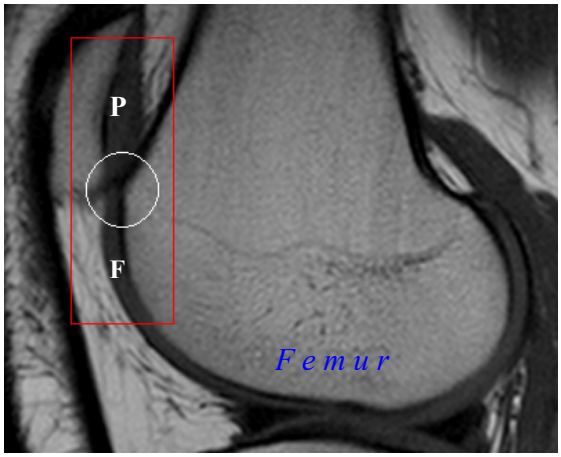

Figure 2. Knee joint (non– fat– suppressed)

ACKNOWLEDGMENTS

The authors are grateful to the University of Queensland, and the Wesley Hospital, Brisbane for enabling the acquisition of the knee joint MR images presented in this paper.

REFERENCES

[1] Stammberger T.; Eckstein, F., et al., Intraobserver Reproducibility Of Quantitative Cartilage Measurements: Comparison of B-Spline Snakes and Manual Segmentation, *Magnetic Resonance Imaging,* Vol. 17, No. 7, pp. 1033–1042, 1999

[2] Sethian, J., A., Level Sets Methods and Fast Marching Methods. Cambridge University Press, 1999

[3] Verstraete, K., L., Magnetic Resonance Imaging of Cartilage, Department of Radiology, Ghent University Hospital De Pintelaan 185, B-9000 Gent, Belgium

[4] Pfizer Inc, USA

[5] Outerbridge RE, The ethiology of chondromalacia patellae. J Bone Joint Surg Br. 1961, 4(34): 752–767

[6] Perona, P. and Malik, J., Scale-Space and Edge Detection Using Anisotropic Diffusion, *IEEE Transactions on Image Processing,* Vol. 12(7): 629–639, July 1990.

[7] Kass, M.; Witkin, A.; Terzopoulos, D. Snakes: Active contour models. Int. J. Comput. Vision 1:321–331; 1988

A Simulation Study On Transcellular and Transcapillary Fluid Shifts Induced By Hemodialysis

Amin Haddadzadeh
Department of Bio-Medical Engineering(Mechanics Department)
Iran University of Science & Technology
Management & Planning Organization
Tehran, Iran
No.24-Ladan St.-Northern Shirazi St.-Mollasadra St.-Vanak Sq.-Tehran-Iran-Tel.: +98-0913-234-4282(Mobile)-Email: a_hadadzadeh@hotmail.com- Telefax: +98-21-8086883,91

Abstract: *In this study, we developed a computer model to analyze body fluids volume variations, especially plasma volume changes. Also, serum sodium concentration and Blood Urea Nitrogen (BUN) changes were simulated using a combined model for transcapillary and transcellular fluid shift. Model predictions were found to be in good agreement with values which had been measured by Kimura et al[12,13]. Urea and sodium transfer across the dialyzer membrane and transcellular fluid shifts which occurs in response to the sodium and the other electrolytes transfer, were modeled. Tanscapillary fluid and proteins exchange occurs too, which influences hydrostatic and oncotic pressures in interstitial and capillary space due to ultrafiltration (UFR). With regard to that any of transcapillary and transcellular models itself cannot discuss fluids and electrolytes behavior in body, introducing lymphatic system, interstitial and capillary protein content as nonlinear behavior and transcellular electrolytes exchange, we simulated a new model. Using this model, it is possible to predict serum sodium concentration, blood osmolality, Blood Urea Nitrogen (BUN) after dialysis and plasma volume during dialysis in order to better hemodialysis therapy. Also, it is possible using model optimization and feedback blood volume controlling and monitoring systems to avoid hypotension. Using rational dialysate concentration with respect to serum sodium concentration changes can be used to reduce disequilibrium syndrome.*

Key Words: *transcapillary, transcellular*, Hemodialysis, Ultrafiltration, Electrolytes Exchange, Protein Exchange

Introduction

A person with renal failure has little or no kidney function. The signs and symptoms of renal failure, a state called uremia, are extremely diverse and frequently appear to point to disease of other organs. Failure to regulate the excretion of salt and water places the body at risk of fluid overload. Fluid may accumulate in the subcutaneous tissues as edema or in serous cavities as excess peritoneal fluid or pleural effusion. Peripheral edema is unsightly but harmless, whereas pulmonary edema can compromise gas exchange in the lungs, leading to shortness of breath, hypoxia and ultimately death[4].

Hemodialysis is a process whereby water and metabolic waste products are removed from the blood by an artificial kidney. During hemodialysis, blood circulates from an artery into a dialyzer and returns through a vein. Inside the dialyzer blood is separated from dialysate fluid by a semi-permeable membrane. Movement of solutes from the blood to the dialysate occurs by diffusion across the membrane. Concentration of solutes in the blood can be controlled by the composition of the dialysate. Excess body fluid is ultrafiltrated from the blood side of membrane due to negative pressure. A patient with renal failure uses an artificial kidney for several hours a day for a few days out of each week.

The incidence of intradialytic disequilibrium syndrome and symptomatic

hypotension has increased significantly among dialysis patients over the last ten years[2,12,13]. Also, It has been demonstrated that the use of dialysate with a high Na^+ concentration reduces these complications[12,13].

The model for transcapillary fluid exchange has been established for a long time[1,12]. It's impossible, however, to directly apply this model to hemodialysis therapy, because transcellular fluid exchange is also essential to simulate the change in plasma volume during hemodialysis.

In this work, the combination of these two models has been introduced to enable simulation of the change in plasma volume, serum sodium concentration and **BUN** during hemodialysis.

Model Assumptions

1. Body water is distributed in three uniformly mixed compartments approximating the intracellular(ICF), interstitial(ISF), and plasma(PL) volumes. The sum of the ISF and PL compartments forms the extracellular (ECF) compartment. The total body fluid (TBF) is the sum of the ICF and ECF volumes.
2. Water movement between the ICF and ECF compartments is analogous to movement across the cell membrane and is caused only by change in the concentration of osmotically active solutes in the ICF and ECF compartments [2,4,13].
3. The amount of osmotically active solutes in the ICF compartment doesn't change during dialysis. Water movement to or from the compartment causes changes in the concentration of osmotically active solutes in the ICF compartment[2,4,13].
4. Sodium diffuses freely across the capillary wall. Since sodium is contained mostly in the ECF compartment this assumption allows description of sodium kinetics during dialysis by a one-compartment model.
5. At the beginning of dialysis there is osmotic equilibrium. This allows calculation of the pre-dialysis concentration of osmotically active solutes from the pre-dialysis plasma sodium concentration.
6. Water movement between the ISF and PV is similar to movement across the capillary wall, which is proportional to the forces of capillary pressure, plasma oncotic pressure, interstitial hydrostatic pressure, and interstitial osmotic pressure[1,2,4,12].
7. Interstitial compliance is nonlinear[1].
8. Protein leaks across the capillary wall during dialysis with a certain content [16]. On the other hand, moves from ISF to capillary space with reabsorbsion with a certain content[16]. Proteins also moves from ISF to capillary compartment using lymph flow with a constant content[], so that lymph flow variations versus ISF pressure is nonlinear[1,16].
9. Osmotic pressure in PV and ISF compartments is nonlinear functions of their protein content[1,12].
10. PV and ISF protein content have nonlinear differential relations with their protein mass and compartments volume[16].
11. Protein mass variations in PV and ISF compartments are balanced with capillary filtration, reabsorbsion and lymph flow[1,12,14].

Figure1 is a schematic of combined model. As you see, filtration, reabsorbsion and lymph flow make fluid and protein to

move between ISF and PV. Water and electrolytes move between ECF and ICF through cell membrane by several mechanisms. As blood flows through dialyzer water and materials exchange occurs between plasma and concentrate.

The Mathematical Model

In order to establish the model, intracellular and extracellular volume changes were simulated using mathematical formulation during hemodialysis.
By combining this model with transcapillary model plasma volume was also obtained.

Landis-pappenheimer equations have been used as basic relations for establishing transcapillary models[12,14];

$$F_A(t)=L_A\times[H_A-H_T(t)-\Pi_{PL}(t)+\Pi_T(t)] \quad \underline{1}$$

$$R_V(t)=L_V\times[\Pi_{PL}(t)-\Pi_T(t)-H_V+H_T(t)] \quad \underline{2}$$

in which filtration F_A and reabsorbsion R_V are expressed as functions of hydrostatic arterial A, venous V, interstitial T pressures and oncotic plasma Π_{PL} and interstitial Π_T pressures and also hydrolic permeability coefficients L of vessels. The oncotic pressures are expressed as functions of plasma and interstitial spaces protein contents as below;

$$\Pi_{PL}(t)=2.1\times C_{PL}(t)+0.16\times C_{PL}^{2}(t)+0.009\times C_{PL}^{3}(t) \quad \underline{3}$$

$$\Pi_T(t)=2.8\times C_T(t)+0.18\times C_T^{2}(t)+0.012\times C_T^{3}(t) \quad \underline{4}$$

transcellular and transcapillary models are combined by the equation;

$$ISF(t)=ECF(t)-PV(t) \quad \underline{5}$$

in which ISF, ECF and PV are interstitial, extracellular and plasma volumes respectively. Plasma volume is also obtained by;

$$\frac{dPV(t)}{dt}=-[F_A(t)+UFR]+R_V(t)+Q_{rl}(t) \quad \underline{6}$$

in which UFR is ultrafiltration rate and Q_{rl} is lymph flow rate which are obtained using reference [1] relations.

Plasma and interstitial protein contents are expressed as nonlinear functions of protein mass in these spaces and their volumes instead of kimura linear functions as reference[16].

The following equations were also used for transcellular part of the model as had been introduced in reference[2];

$$\frac{d}{dt}[TBF(t)]=-UFR(t) \quad \underline{7}$$

$$TBF(t)=ICF(t)+ECF(t) \quad \underline{8}$$

$$ECF(t)=\frac{TBF(t)}{[1+\frac{M_{U,i}(t)+M''_{eq,i}(t)}{M_{Na,e}(t)+M_{U,e}(t)+M_{eq,e}(t)}]} \quad \underline{9}$$

so that TBF, ICF, $M_{U,i}$, $M_{U,e}$, $M_{Na,e}$ are total body fluid volume, intracellular fluid volume, amount of urea in the intracellular pool, amount of urea in extracellular pool, amount of sodium in ECF and $M''_{eq,i}$, $M_{eq,e}$ are amount of different solutes in ICF and ECF as has been described in reference [2].

Equations solution

The combined model for transcapillary and transcellular simulation contains a set of coupled linear and nonlinear differential equations. This set was processed using "simulink" toolbox of MATLAB software. In each test, initial conditions and constant values of certain group of patients were

used. In order to validate model outputs, experimental values of Kimura et al[12,13] were used. In their work, the values of parameters were had been measured in five patients who had been studied on hemodialysis at three different dialysate sodium concentration equal to 7% below and 7% above the predialysis serum sodium concentration.

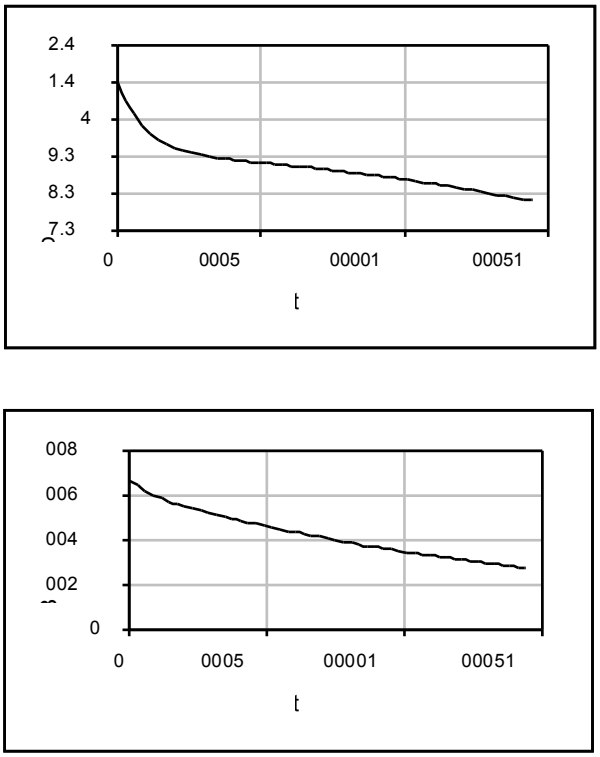

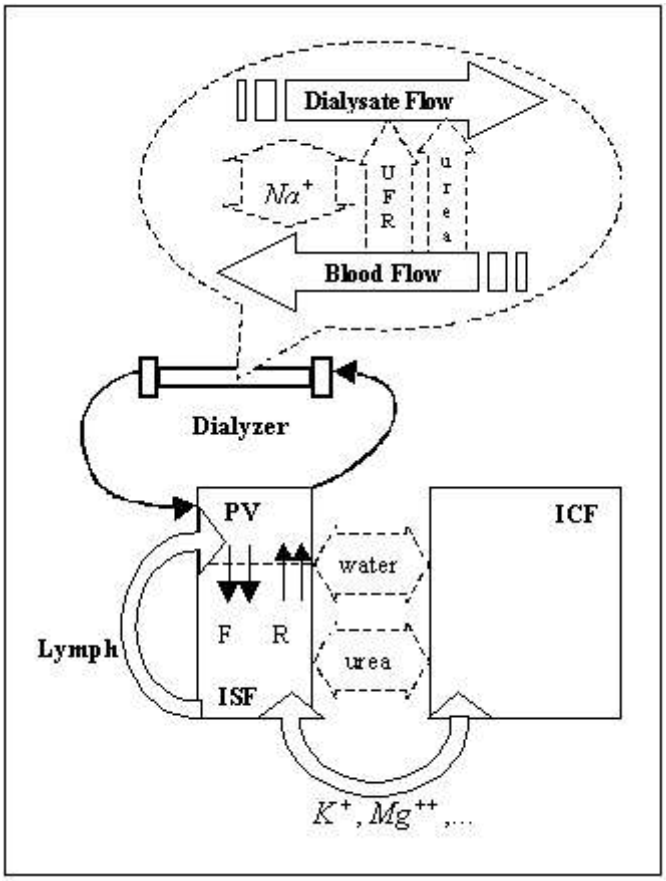

Fig1:Schematic diagram of combined simulated model.

Results

Figures 2 to 4 show plasma volume, serum sodium concentration and **BUN** changes during dialysis for the group of patients who were treated using high Na^+ concentrate as typical outputs.

Figures 2 and 3 show the trend, which is consistent with what the others obtained [1,3,4,5,8,12]. As we used average values of kimura et al, these trends are in excellent agreement with their results. Also, as you see in figure 4 the results of introduced model are in better agreement with measured data in comparison to kimura model.

In kimura model, there has been a significant difference in the value at 1 hr after the beginning of the high Na^+ hemodialysis. The present model can see the severe changes during first hour and cover them.

Fig3:BUN changes during dialysis with high sodium dialysate.

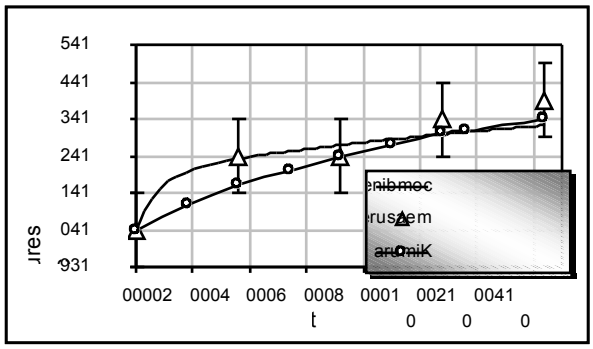

Fig4:A comparison between kimura model, combined model and measured values for serum sodium concentration.

Discussion and Conclusion

Several transcapillary and transcellular models have been proposed during past years. It is impossible; however, to directly apply these models to hemodialysis therapy, because transcapillary and transcellular fluid and materials exchanges occur together so that they are instantaneously engaged to each other. Also, some simplifications have been done in these models. Therefore, converting them into practical software and hardware in hemodialysis machines is a difficult problem.

The main goal of this study was to develop a combined biological model, which converge most of these models and experiences into one model using last researches in this field.

Based on literature survey, in recent researches[1] lymphatic system and interstitial compliance have been introduced as nonlinear behavior. Besides, fluid, sodium, and urea exchange across cell membrane and dialyzer membrane, also other electrolytes exchange across cell membrane had been considered as simplified behavior. But plasma and interstitial protein content changes, which had been considered before as linear behavior[4,12], has been introduced as nonlinear behavior, using Schneditz et al idea[8].

As you see, the model in some circumstances like serum sodium concentration changes in dialysis with high Na^+ concentrate had results better than Kimura model. In fact, severe extracellular osmolarity changes was hidden in the Kimura model point of view. On the other hand, in dialysis with normal and low concentrate, Kimura model introduced better results.

There have been some error resources for this simulation. Not to consider the other electrolytes exchange especially potassium except to sodium across dialyzer membrane is the most important one.

The present model can be optimized and examined by different experimental values and used to obtain the best UFR and dialysate profiles for individual convenient dialysis.

The use of the mathematical model allows us to obtain an approximate estimation of the amount of sodium (and probably the other electrolytes) which are actually removed during hemodialysis. The correct choice of the UFR and dialysate concentration profiles, able to remove a given amount of sodium per session is a difficult problem, the solution of which depends on several different simultaneous factors: mainly, the initial concentration of sodium and other solutes in the blood and in the extracellular pool, the UFR, dialysis operative conditions, and the duration of session. All these factors interact in complex nonlinear ways during treatment, thus making qualitative predictions of sodium and fluid extraction unreliable.

References

1. P.W.Chamney: " Fluid Balance Modeling in Patients with Kidney Failure ". J.Med.Eng. &Tech. (March/April 1999); P.45-52.
2. M.Ursino , L.Coli : " An Algorithm for the Rational Choice of Sodium Profile during Hemodialysis ". The Int.J.Art.Org.1997; Vol.20, no.12, P.659-672.
3. F.Lopot, P.Kotyk: " Computational Analysis Of Blood Volume Dynamics during Hemodialysis". The Int.J.Art.Org.1997; Vol.20, no.2, P.91-95.
4. Roger B.Winnett & Thomas C.: "Simulation of Blood Volume Change during Hemodialysis ". Conf.Proc.IEEE Southeastcon. 1995; P.450-453.
5. Mancini E. , Santoro A. : " Effect Of Automatic Blood Volume Control Over Interdialytic Hemodynamic Stability ". Int.J.Art.Organs. 1995; 18, 495-498.
6. G.Arrigo , R.Bucci : " Blood Volume Modeling and Refilling Rate Estimation in Hemodialysis by Continuous Hemoglobin Monitoring ". The Int.J.Art.Org. 1995; Vol.18, no.9, P.509-512.
7. J.P.P.M , De Vries , B.J.M Van Der Meer : " Combined Measurement Of Tissue Fluid, Blood Volume And Hemodynamics In Hemodialysis ". The Int.J.Art.Org. 1995; Vol.18, no.11, P.705-711.
8. D.Schneditz : " Nature and Rate of Vascular Refilling During Hemodialysis and Ultrafiltration". 1992; Vol.42, P.1425-1433.
9. Jermo C. & Thomas C. : " Output Sensitivity to Parameter Error in A Model of Blood Volume Change during Dialysis ". Annual Int.Conf.IEEE Eng.In Med.&Biology Soc. 1991; Vol.13 , no. 5, P.2276-2277.
10. James J.C. : " A Model of Blood Volume Change during Dialysis ". Proc.Conf. 1990; P.1876-1877.
11. Hendrik A. Koomans , Anton B. : " Plasma Volume Recovery after Ultrafiltration in Patients with Chronic Renal Failure ". Kidney Int. 1984; Vol.26 , P.848-854.
12. Kimura G. , Van Stone J.C. , Bauer J.H. : " Model Prediction of Plasma Volume Change Induced by Hemodialysis ". J.Lab.Clin.Med. 1984; 104 : 932-938.
13. Kimura G. , Van Stone J.C. , Bauer J.H. , Keshaviah P.R. : " A Simulation Study on Trancellular Fluid Shifts Induced by Hemodialysis ". Kidney Int. 1983; 24 : 542.
14. Landis E.M. , Pappenheimer J.R. : " Exchange of Substances through the Capillary Walls ". Hamilton W.F. , Dow P. , Eds. Handbook of Physiology. Vol.2 , Section 2 , Circulation. Washington , DC , 1963; American Physiological Society , P.961-1034.
15. A.Santoro , E.Mancini : "Clinical Significance of Intradialytic Blood Volume Monitoring". The International Journal of Artificial Organs. 1997 , Vol.20 , No.1 , 1-6.
16. A.Haddadzadeh : " A Model for Prediction of Plasma Volume, Serum Sodium Content and Urea Concentration During Dialysis". Supervisor: M.Navidbakhsh; A Thesis Submitted in Partial Fulfillment of Master of Science in Medical Eng.-Biomechanics; August2001.

Skull and Brain Visualization by Transcranial Sonography System

Takashi Shimizu[1], Kouki Nagamune[1], Syoji Kobashi[1], Katsuya Kondo[1], Yutaka Hata[1]
Yuri T. Kitamura[2], and Toshio Yanagida[2]
[1]Graduate School of Engineering
Himeji Institute of Technology
2167, Shosha, Himeji, 671-2201, Japan
[2]Graduate School of Frontier Biosciences
Osaka University
2-2, Yamadaoka, Suita, 565-0871, Japan
taka@comp.eng.himeji-tech.ac.jp

Abstract

In conventional transcranial sonography system, available window of skull in adults is limited to the temporal bone. However, by visualizing an intracranial tissue from all angles, it supports to diagnose the disease with high accuracy. Transcranial sonography system with placement free has not been developed. This paper describes skull and intracranial tissue visualization based on anatomical knowledge using ultrasound. Generally, it is difficult to visualize an intracranial tissue from frontal bone (3 - 6 mm) because of large attenuation in skull. To overcome this difficulty, we develop the system whose ultrasonic wave can penetrate the human frontal bone. In our system, we acquire data of an intracranial tissue in animal experiment model. This is made by cattle skull and goma-tofu (soft tissue) placed inside the skull. Using acquired data and this model knowledge, we image the skull and the soft tissue. As a result, our method could visualize skull and soft tissue surface in all data.

1. Introduction

Conventional transcranial sonography system can non-invasively image intracranial blood flow and brain tissue at real-time [1]-[3]. However, skull prevents ultrasound from disclosing a brain anatomy. The main factor is the acoustical mismatch between soft skin and the skull. The acoustic velocity in the skull is about 2800 - 3500 m/s whereas about 1600 m/s in soft skin [4][5]. Additionally, porous layer of the skull prevents ultrasound from penetrating to intracranial tissue. Due to this, the system is applicable to neonates whose skull is not developed. However, in adults, available window of skull is limited to the temporal bone [6]-[8]. Because of the limited size of the window, the obtained information is also limited. Any transcranial sonography system with placement free has not been developed. This paper describes intracranial tissue visualization with placement free. By visualizing shape of an intracranial tissue from all angles, it supports to diagnose the disease with high accuracy.

In Refs. [4], [9], and [10], we confirmed that ultrasonic wave penetrated the human frontal bone (3 - 6 mm) or artificial bone (12 mm).

In this paper, first, we acquire data of an intracranial tissue in animal experiment model. This model is made by cattle skull and *goma-tofu* (soft tissue). The soft tissue is placed inside the skull. The animal skull and the soft tissue imitate human skull and human brain tissue, respectively. The aim of this experiment is to recognize echoes of skull surface, skull bottom, and soft tissue surface, and to visualize the skull shape and the soft tissue surface. Second, we acquire the data of the model in a water bath. We determine each region position (skull surface, skull bottom, and soft tissue surface) using the anatomical knowledge. Finally, we image the skull and the soft tissue from these positions. As the result of applying it to the model, we could recognize echoes of skull surface, skull bottom and soft tissue surface. The shape of skull and the soft tissue in all data were obtained. Average error of the skull thickness was 0.43 mm, and the average error of water distance between skull bottom and soft tissue surface was 3.14 mm.

This paper organized as follows. Section 2 describes human brain model and overview of our experiment. Section 3 describes the visualization based on the anatomical knowledge. Section 4 shows the experimental result on cattle skull. In it, we could successfully visualize the shape of the skull and the soft tissue. Section 5 presents a summary of the technical results.

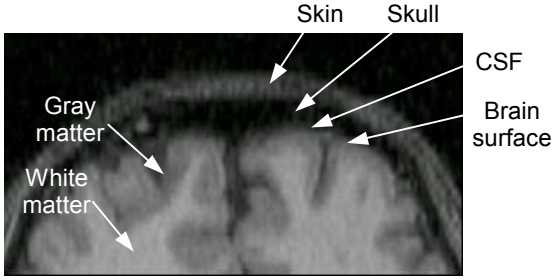

Figure 1. Human brain.

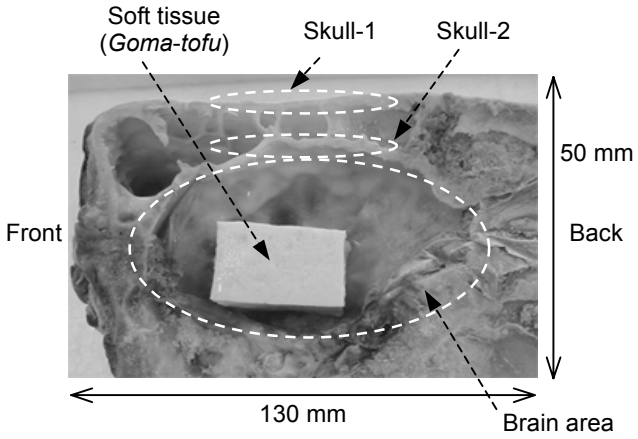

(a) Lateral view.

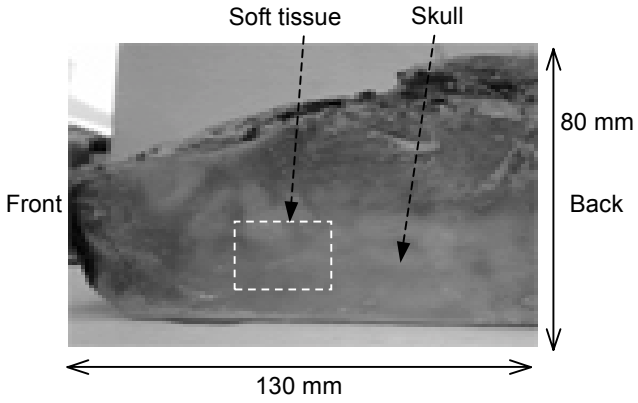

(b) Top view.

Figure 2. Animal experiment model.

2. Preliminary

2.1 Human brain model

Figure 1 shows MR image of the human brain. Information of the shape of brain surface in this figure is important to discriminate human disease. Additionally, the human brain consists of the skin (light white), the skull (black), cerebrospinal fluid (black), the gray matter (light black), the white matter (white). We construct animal experiment model using cattle skull and soft tissue. Constructed model is shown in Figure 2. Figure 2(a) shows the model of lateral view. Figure 2(b) shows the model of top view. As shown in Figure 2(a), brain portion is removed and a soft tissue is placed in it. In this model, the soft tissue (*goma-tofu*) is used instead of human brain. The aim of this experiment is to visualize the skull and the soft tissue. Cattle skulls were two layers: skull-1 denotes upper skull and skull-2 denotes lower skull. Skull thickness of the model varies from 2 to 5 mm.

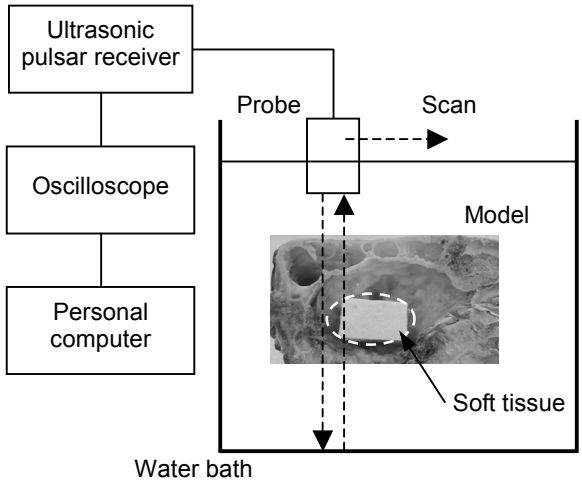

Figure 3. Overview of our experiment.

2.2 Overview of our experiment

The animal experiment model is placed into a water bath and we acquire data of the intracranial soft tissue. Figure 3 shows the overview of our experiment. The ultrasonic pulsar receiver (New Sensor Inc., NSI-PR2000L) transmits and receives ultrasonic waves via the probe. The data of ultrasonic waveform is acquired by the personal computer. The data obtained by this system includes the reflected wave from the skull surface, skull bottom, and intracranial soft tissue. Sampling interval is 10ns. We determined transmission frequency that is suitable for the skull penetration as 1MHz [4][9][10]. Additionally, in order to visualize intracranial soft tissue, we used ultrasonic focus probe (KGK, 1.0K14I/6I-F20) whose center frequency is 1MHz. We scan at interval of 1 mm using scanner equipment, and acquire data from above animal skull in each position. Scan field of probe is 60 mm and sixty-one data is acquired. An image consists of sixty-one data.

3. Visualization method based on the anatomical knowledge

This section describes model visualization method based on the anatomical knowledge. We perform visualization of human brain model by the following process.

(1) Determine each region position (skull-1 surface, skull-1 bottom, skull-2 surface, skull-2 bottom, and soft tissue surface) using the knowledge of model structure,
(2) Determine these positions considering the ultrasound velocity,
(3) Visualize these positions.

The detail of each process is as follows.

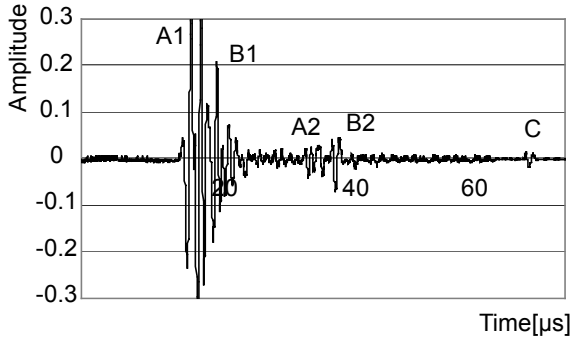

Figure 4. Ultrasonic waveform.

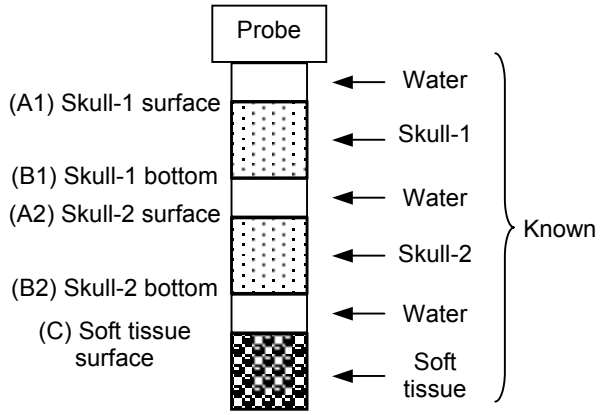

Figure 5. Model structure.

3.1 Determination of each region position

Figure 4 shows an example of ultrasonic waveform which is acquired in Figure 3. Path of each reflected wave (A1, B1, A2, B2, and C) is automatically determined. As shown in Figure 5, the model consists of layer structure in order: water, skull-1, water, skull-2, water, and soft tissue. We can therefore assume that these reflected waves are acquired in the order of skull-1 surface, skull-1 bottom, skull-2 surface, skull-2 bottom, and soft tissue surface. Therefore, in Figure 4, A1 represents reflected wave of skull-1 surface, B1 represents reflected wave of skull-1 bottom, A2 represents reflected wave of skull-2 surface, B2 represents reflected wave of skull-2 bottom, and C represents reflected wave of soft tissue surface. They are shown in Figure 5. Path of each reflected wave of sixty-one data is also automatically determined using the knowledge of model shape. The details are below.

Figure 6 shows the method of position determination of skull-1 surface. First, for first data of sixty-one data, we manually determine position of skull-1 surface as the initial position. A triangle function of the initial position is expressed by dotted line in Figure 6(a). The triangle function is shown in Figure 7. The function moves the range of threshold, *th*=3 μs. The triangle function is used

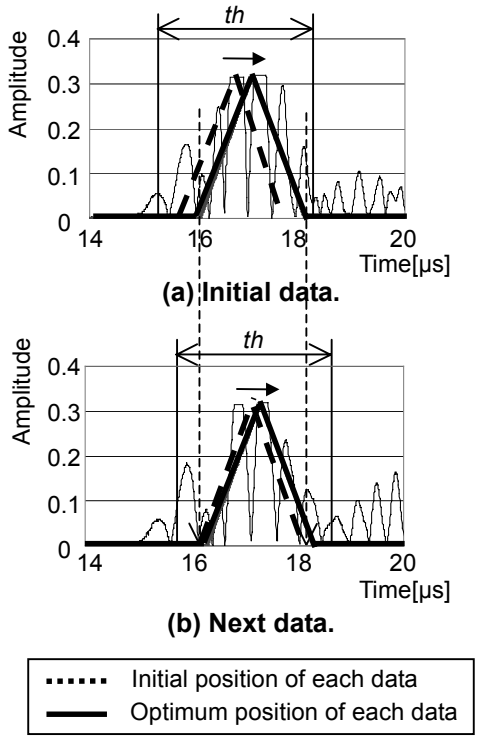

Figure 6. Position determination of region.

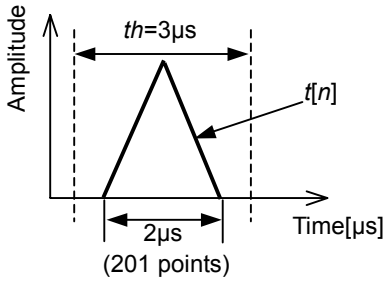

Figure 7. Triangle function.

for calculating the function S_i. The function S_i is defined by Equation (1).

$$S_i = \sum_{n=-100}^{100} x[n+i] \cdot t[n] \tag{1}$$

where, $x[n]$ denotes modulus of original signal, $t[n]$ denotes triangle function. We calculate S_i for all i $(15.0\ \mu s \le i \le 16.0\ \mu s)$. Position of triangle function with maximum S_i is determined as the optimum position of skull-1 surface of the first data. Triangle function of optimum position is expressed by solid line.

Second, as shown in Figure 6(b), the optimum position of initial data is applied to the initial position of next data (second data). This is why the region position is approximately same in the neighboring data. In the similar way, the triangle function is applied to the initial position, and S_i is calculated for every position i using

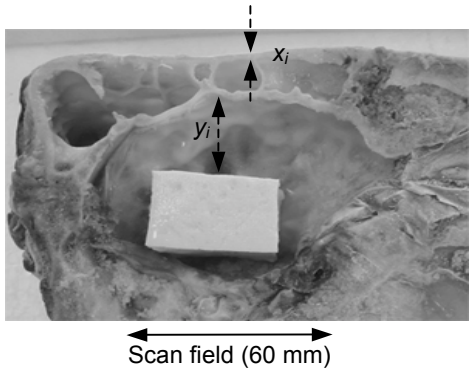

Figure 8. Calculation of real value (lateral view).

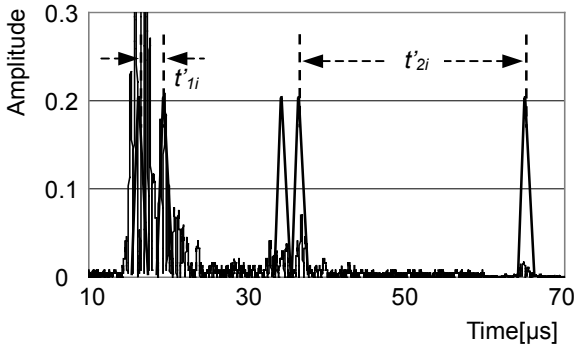

Figure 9. Time difference.

Equation (1). The optimum position of skull-1 surface for second data is determined. After performing above process to all sixty-one data in order, the positions of skull-1 surface are determined.

Finally, region position of skull-1 bottom, skull-2 surface, skull-2 bottom, and soft tissue surface are determined.

3.2 Determination of positions considering the ultrasound velocity

Horizontal axis of Figure 4 is time axis. We calculate distances from time-amplitude plane. First, we measure skull-1 thickness x_i and water distance y_i between skull-2 bottom and soft tissue surface in Figure 8. They are assumed as the real values. Second, we estimate skull-1 thickness x'_i and water distance y'_i between skull-2 bottom and soft tissue surface from positions of the determined triangle function, respectively. Suffix i denotes the number of scan data. As x'_i denotes skull-1 thickness, as shown in Figure 9, we calculate time difference t'_{1i} between skull-1 surface and skull-1 bottom. We define x'_i by Equation (2).

$$x'_i = \frac{1}{2} t'_{1i} \times v'_i \tag{2}$$

where, v'_i is acoustic velocity. We assume that ultrasound velocity in skull is 3100 m/s. On the other hand, time difference of y'_i is t'_{2i} between skull-2 bottom and soft tissue surface. We define y'_i by Equation (3).

$$y'_i = \frac{1}{2} t'_{2i} \times v'_i \tag{3}$$

We assume that ultrasound velocity in water is 1480 m/s [4][10][11]. We visualize these distances using this value x'_i and y'_i. Thus, we visualize points of all estimated distances.

4. Experimental results

In our experiment, we acquired data of three lines as shown in Figure 10. Sixty-one data is acquired in each line, and construct an image. These results are shown in Figure 11. In all figures, lines A1 and B1 represent skull-1 surface and skull-1 bottom, respectively. Line C represent soft tissue surface. We could recognize skull-1 surface and skull-1 bottom, and could confirm soft tissue surface form all image. Consequently, our system could visualize skull-1 shape and intracranial soft tissue from every position.

Figure 12 visualizes an overlapped image of Figures 2(a) and 11 (a). In it, extracted line exactly matched to the skull boundaries and soft tissue surface.

Figure 13 show a comparison between real thickness and calculated thickness for 1st line. The x_i is real value of skull-1 thickness and x'_i is the calculated value of skull-1 thickness by our method. The y_i is real value of water distance and y'_i is the calculated value of water distance by our method. Average of x_i was 3.52 mm and average of x'_i was 3.16 mm. The calculated value of skull thickness was smaller than real value. Average of y_i was 27.93 mm and average of y'_i was 29.47 mm. The calculated value of water distance was larger than real value. We could visualize the skull and soft tissue with average error 0.38 mm and 2.94 mm, respectively. Average error x_{err} of skull-1 thickness and y_{err} of water distance are calculated by Equations (4) and (5), respectively.

$$x_{err} = \sum_{i}^{n} \left| x_i - x'_i \right| / n \tag{4}$$

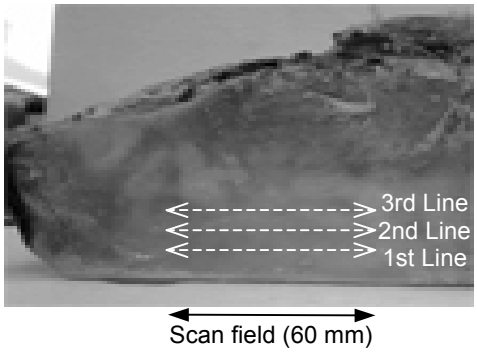

Figure 10. Data acquisition line (top view).

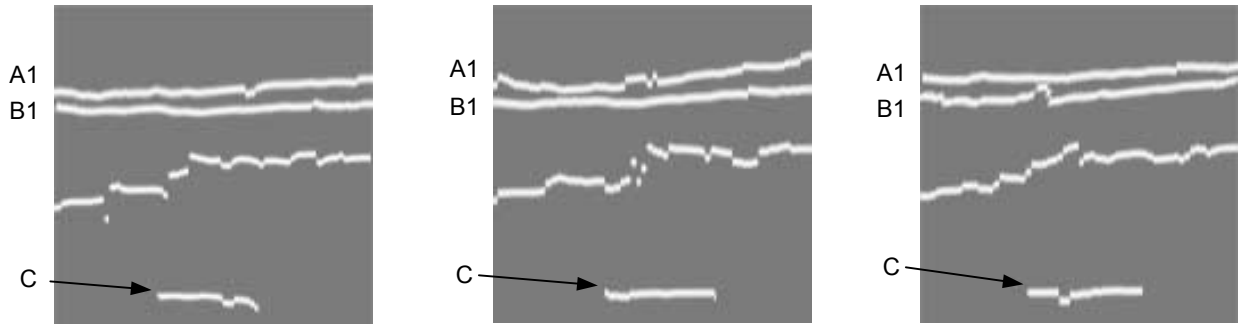

(a) 1st line. **(b) 2nd line.** **(c) 3rd line.**

Figure 11. Experimental result.

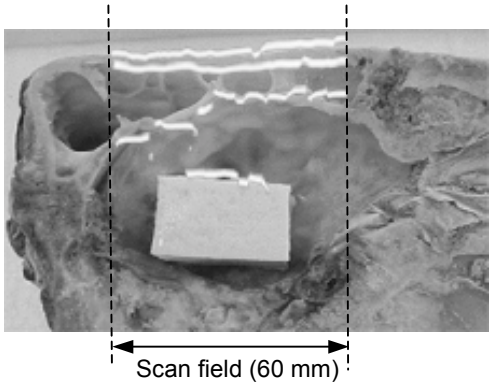

Figure 12. Overlapped result.

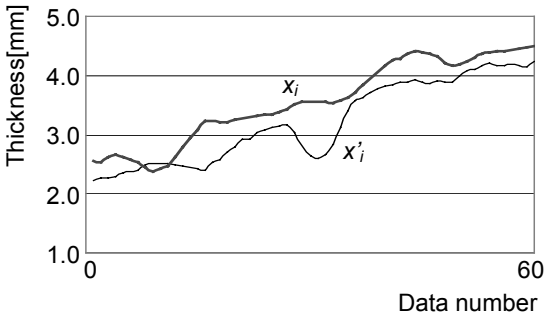

(a) Skull-1 thickness.

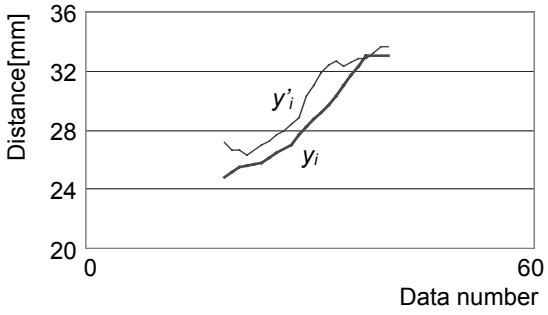

(b) Water distance.

Figure 13. Evaluation result of 1st example.

Table 1. Average error of all results.

Line	Animal skull thickness x_{err}		Water distance y_{err}	
	Average	Standard deviation	Average	Standard deviation
1	0.38	0.31	2.94	1.27
2	0.35	0.26	3.11	1.10
3	0.55	0.33	3.38	1.53
Average	0.43	0.59	3.14	1.30

(Unit [mm])

$$y_{err} = \sum_{i}^{n} \left| y_i - y'_i \right| / n \qquad (5)$$

where, n denotes number of data.

Table 1 tabulates average error in each line. In skull thickness, 2nd line has the lowest average error with 0.35 mm. In water distance, 1st line has the lowest average error with 2.94 mm. Average error of skull thickness is 0.43 mm and average error of water distance is 3.14 mm for all lines.

5. Conclusion

In this paper, we have proposed a visualization method of skull and brain tissue using ultrasound. In it, we constructed the human brain model using the cattle skull and soft tissue. This method employs that a path of each echo is uniquely derived from order of model structure. We applied this method to the cattle skull and soft tissue. This cattle skull thickness varies from 2 to 5 mm. We acquired three line data along different line. We could visualize the skull and the soft tissue for all lines. The average error of skull thickness and water distance were 0.43 mm and 3.14 mm, respectively. By considering thickness of the human skull is from 3 to 6 mm, our system could visualize human brain from all angles.

It remains as a future work to apply our method to human head.

Acknowledgement

This work was supported in part by the Ministry of Education, Culture, Sports, Science and Technology, Grant-in-Aid for Scientific Research (B) (KAKENHI 14370284) 2001.

References

[1] C. R. Levi, C. Selmes, and B. R. Chambers, "Transcranial Ultrasound Clinical Applications in Cerebral Ischaemia," *Australian Prescriber*, 24(6):137-140, 2001.

[2] G. Becker, "Perspectives of Cerebral Sonography in Neurology," *Electromedica*, 68:Neuro, 21-26, 2000.

[3] W. Hirsch, W. Hiebsch, H. Teichler, and A. SchIuter, "Transcranial Doppler Sonography in Children: Review of a Seven-Year Experience", *Clinical Radiology*, 57(6):492-497, June. 2002.

[4] K. Nagamune, S. Kobashi, K. Kondo, Y. Hata, Y. T. Kitamura, and T. Yanagida, "Challenge to the Development of a Transcranial Sonography System," *Proc. 6th Int. Conf. on Knowledge-Based Intelligent Information Engineering Systems & Allied Technologies*, 604-608, September. 2002.

[5] J. Ylitalo, and J. Koivukangas, "Ultrasonic Echo Tomography Trough Skullbone," *Ultrasonics Symposium*, 1019-1022, 1989.

[6] L. L. Berland, C. R. Bryan, and B. C. Sekar, "Sonographic Examination of the Adult Brain," *J. Clin. Ultrasound*, 337-345, 1988.

[7] G. Becker, A. Krone, D. Koulis, A. Lindner, E. Hofmann, W. Roggendorf, and U. Bogdahn, "Reliability of Transcranial Colourcoded Real-Time Sonography in the Assessment of Brain Tumors: Correlation between Ultrasound, Computerized Tomography and Biopsy Findings," *Neuroradiology*, 36:585-590, 1994.

[8] D. Berg, and G. Becker, "Perspectives of B-Mode Transcranial Ultrasound," *NeuroImage*, 15:463-473, 2002.

[9] Y. Hata, T. Shimizu, S. Kobashi, K. Kondo, Y. T. Kitamura, and T. Yanagida, "A Fuzzy Logic Approach to Transcranial Sonography System with Placement Free," *Proc. 1st Int. Conf. on Information Technology & Applications*, CD-ROM, November. 2002.

[10] T. Shimizu, K. Nagamune, S. Kobashi, K. Kondo, Y. Hata, Y. T. Kitamura, and T. Yanagida, "An Automated Ultrasound Discrimination System of Tissue under an Obstacle by Fuzzy Reasoning," *Joint. 1th Int. Conf. on Soft Computing and Intelligent Systems*, 83, October. 2002.

[11] J. Krautkramer, and H. Krautkramer, *Ultrasonic Testing of Materials*, *4th fully revised Edition*, 1990.

Reusable Software Components for Robots using Fuzzy Abstractions

Robert Smith
r2.smith@qut.edu.au

Glenn Smith
gp.smith@qut.edu.au

Aster Wardhani
a.wardhani@qut.edu.au

Centre for IT Innovation, Faculty of IT
Queensland University of Technology

Abstract

Mobile robots today, while varying greatly in design, often have a large number of similarities in terms of their tasks and goals. Navigation, obstacle avoidance, and vision are all examples. In turn, robots of similar design, but with varying configurations, should be able to share the bulk of their controlling software. Any changes required should be minimal and ideally only to specify new hardware configurations. However, it is difficult to achieve such flexibility, mainly due to the enormous variety of robot hardware available and the huge number of possible configurations. Monolithic controllers that can handle such variety are impossible to build.

This paper will investigate these portability problems, as well as techniques to manage common abstractions for user-designed components. The challenge is in creating new methods for robot software to support a diverse variety of robots, while also being easily upgraded and extended. These methods can then provide new ways to support the operational and functional reuse of the same high-level components across a variety of robots.

1. Introduction

Robotic control software has come along way since early sense, plan and execute systems [17] in the early 80s. Faster and more robust reactive styles were introduced [6], but were unable to execute complex plans. Deliberative systems that combine reactive and sense-plan-execute approaches have been built with varying degrees of success ([8], [11], [4], [2] and [16]). Decision-making and execution of robot activities are complex tasks to manage.

Hardware limitations and diversity have resulted in very specialised and inflexible software. Autonomous robots were traditionally faced with limitations in size, battery power, CPU speed, and memory. Hence controlling software was written to run as efficiently as possible to maximise the power of such hardware. The software had to focus on extracting the most from the hardware. This required very specialised solutions. In the past typical approaches to robot software construction produce monolithic systems using 'brute force' methods. This approach has made extensions, upgrades, and software reuse difficult.

Today, embedded processors are far more powerful. Autonomous robots with embedded CPUs are able to compute and react faster then ever before. This increased capacity reduces the need for low-level specialisation of software in order to gain critical speed optimisations. The increased capacity allows satisfactory computational speed to be achieved even when using more generic software.

This work leverages on the ability to use more generic software to address the need for more flexible and reusable robot code in the face of diverse hardware configurations. This is achieved via the specification and implementation of a framework that supports abstractions of robot hardware. The framework is constructed using component-based software techniques and the use of fuzzy logic enables a flexible and versatile manipulation of robot abstractions.

2. Issues

The most notable challenge with robot abstraction is that of the sheer diversity of robot hardware design. Secondly, the problem of moving code between systems is difficult as the translation is at best tedious or at worst impossible, even when the robot hardware can support all required functions of the code.

2.1. Diversity

The diversity among robots is extraordinary - both in their design (eg. hardware, size, shape) and their configuration (eg. orientation, position, facing). The matrix of possibilities creates a diversity that is unmanageable using existing techniques. There is very little standardisation between robots from different vendors. Even robots of the same type

can be easily altered and reconfigured - so there are no certainties in how their hardware is configured. The problem with this diversity is two-fold. Firstly, software support is required to interact with each piece of hardware. Usually a device specific driver is provided for this. Even though the device driver offers some level of abstraction from the hardware, there is no interface standardisation between drivers even when the driver is for the same type of device, such as a servo. Thus the use of drivers does not address the issue of diversity. Secondly, higher-level algorithms that combine different hardware elements to achieve an overall result still need to handle various and changing configurations. How can the algorithms be written and packaged to operate unchanged on different robots?

2.2. Software portability

Software development for robotic systems faces many difficulties. The diversity of hardware and performance constraints has made the production of satisfactory solutions difficult. Prior to the relatively recent improvements in processing capacity, software development could only afford to address the essential requirements. This has led to the use of software engineering practice that does not consider the need for software reuse. Even if software reuse were considered, the diversity of hardware and its configurations would have probably restricted reuse to a single robot. This situation does not provide the motivation to commit additional resources required to develop reusable software.

Software development for robots is relatively immature in both time and scale compared with software development for more established environments such as the desktop computer. The standardisation of desktop platforms and the sheer scale of development have expedited the improvement of the software development process. This has left the software development process used for robotics platforms lagging behind. More modern software processes use component-based techniques. It is proposed that the lack of use of such techniques hinders the portability of software for robots.

3. Proposed Solution

To address these problems the concept of a Virtual Robot Layer is introduced in this paper. The VRL has arisen to address these issues:

- the abstraction of hardware devices; and
- to manage the diverse variety of possible robot hardware and its configurations; and
- to act as a translator of a common instruction set to robots of different configurations.

The concept aims to provide a standard means of accessing a robots functionality, as well as providing a protocol for communicating between high-level software and low-level executions, allowing the high-level instructions to remain unchanged across different robots with different hardware or configurations. Note that the VRL concept is limited in that it can only extend its services to the group of robots that have been targeted by a particular VRL framework, such as mobile-wheeled robots for example. Other groups of robots (such as humanoid) can be subsequently targeted with VRLs designed for those groups.

4. Benefits

The VRL framework can provide the following benefits.

4.1. Portability

Methods for robot abstraction and creating independent robot software, will improve the system's portability. In operational terms, the components and abstraction framework will work on various robot run-time environments. In functional terms, the components will be able to control various robots using the same infrastructure and high level instructions.

4.2. Code Reuse

By making a set of software components that are completely portable, new robots could be quickly configured using existing software with minimal effort. These components can be shared between robots of similar types. They can even remain unchanged when the robot hardware is reconfigured (for instance a sensor is moved to a different position) as they will adapt with support from the architecture using the metadata available for the current configuration. More code reuse will then be possible and the configuration and deployment time of robots will be reduced.

5. Methods and Approaches

Here we describe the techniques used in the design.

5.1. Software Components

Technologies are emerging today that allow applications to be built from reusable components more than ever before. Component-Based Software Engineering (CBSE) has become recognised as a new sub-discipline of software engineering and should equally apply to robotics software.

The major goals of CBSE are the provision of support for the development of systems as assemblies of components,

the development of components as reusable entities, and the maintenance and upgrading of systems by customising and replacing their components [13].

Components, quite broadly speaking, are units for composition. In terms of software, a precise definition by Szyperski is frequently used today:

A software component is a unit of composition with contractually specified interfaces and explicit context dependencies only. A software component can be deployed independently and is subject to composition by third parties. [18]

We are using software components as, by definition, they bring modularity and well-defined interfaces and explicit context dependencies to the design and implementation of the abstraction framework and the sub-systems. The use of component-based software improves software development by enabling a design-by-composition environment and promoting software reuse [3].

5.2. Abstraction Principles

The essence of hardware abstraction is to decouple the users of the hardware from the non-essential details of its use. The user need only know how to manipulate the single abstraction, which in turn can be applied to a variety of hardware.

In software terms, hardware abstraction broadly means a separation of software from device dependencies or the complexities of underlying hardware. For instance, it enables programs to focus on a task, such as communications, instead of on individual differences between communications devices.

A hardware abstraction layer (HAL), in computing systems, is a layer of programming that allows a computer operating system to interact with a hardware device at a general or abstract level rather than at a detailed hardware level. Windows is one of several operating systems that include a hardware abstraction layer. The hardware abstraction layer can be called from either the operating system's kernel or from a device driver. In either case, the calling program can interact with the device in a more general way than it would otherwise.

In robot systems, the same approach is sometimes used. HALs exists for a few current robotic architectures ([10], [12], and [7]). The controlling software makes calls on hardware in only abstract terms, and the HAL then converts these calls into concrete signals to the hardware. To illustrate, a servo command such as `setspeed(byte speed)`, could be converted by the HAL to a series of ASCII characters to achieve that speed on the servo. When hardware is replaced or changed the HAL will also change the required signals, but the `setspeed(byte speed)` function call remains the same.

5.3. Degrees of Abstraction

Robotic software requires an even greater level of robot abstraction than provided by HALs. This is because robots interact with the real world. They are given commands that embody notions of position and direction, for example: `moveForward()`, and `turnRight()`. However, modern HALs have no information on relative placement of servos or sensors, making any abstraction involving location or direction impossible. This also precludes even higher levels of hardware abstraction to provide answers to questions such as:

- Is there an obstacle in that direction?
- How far away is the obstacle?
- Can I get through that gap in the wall?
- Where are my sensors pointing?

Most robot HALs only achieve the simpler level of hardware abstraction: the basic interface to the actual hardware. Higher-level algorithms still require built-in knowledge in to co-ordinate the hardware. It is far more useful (but complicated) to also abstract the configuration of hardware.

Most high-level algorithms use explicit knowledge of the hardware, such as where sensors are positioned and what the return values mean. This knowledge is usually encoded at a level higher than the HAL, which prohibits portability. For the higher-level algorithm to be portable, any such knowledge must be provided as a service from the HAL.

A HAL is useful because it allows code to be more portable. The more portable the code, the more diverse are the platforms on which it can be deployed. A HAL that supports even higher-level abstractions can remove platform dependence even further. This means that controlling software can run on different types of robots. How different the robots can be will depend on the sophistication of the HAL.

Even more sophisticated HALs in current robot architectures still only support robots from the same vendor, such as the ERP1 from Evolution Robotics [10]. Evolution Robotics has a proprietary robot architecture called ERSP [10]. This incorporates a HAL that uses XML specifications to support changes in the physical structure of their ER1 robot [9]. Hardware such as extra cameras and sensors can also be added. However, it is unable to support the abstraction of a completely different robot, such as the Khepera [15] for example.

The OROCOS project [7] also uses a hardware abstraction layer. They describe a layer between hardware and the framework, which translates calls from the framework to the present operation system and hardware drivers. OROCOS uses a suite of device drivers, which provide the hardware functions. There is no configuration specification or

means for understanding higher level instructions or semantics such as left, right or forward.

The Player/Stage [12] abstracts hardware using interfaces that use TCP/IP socket communication from controlling software to the robot client. As for OROCOS, the level of abstraction is at a low level with basic interface on device driver support for the hardware.

In computing terms, the extension of the HAL towards higher-level abstractions can be served by a 'virtual machine'. The equivalent concept in robotics would be a 'virtual robot'. The notion of a virtual robot as a translator for abstraction is new. Following is a broad description of this with respect to the traditional concept of a virtual machine.

5.4. The Virtual Robot

A virtual machine is a hypothetical computer, whose characteristics are defined by its machine language, or instruction set. In general, a real machine with the same characteristics could be constructed with hardware. In its popular use today, the virtual machine is a software emulation of a physical computing environment used to execute instructions on the real machine. The virtual machine is a level of abstraction even greater than a typical hardware abstraction layer. It defines a set of rules for what it can execute, and can provide feedback and results.

A natural extension of a virtual machine is a virtual robot. The virtual robot would be an abstraction of a notional robot. It would be configurable so it can change its virtual shape, size and accessories. It would define its virtual capabilities and return information from virtual sensors. It could reply to queries about its specification. Most importantly, it would also translate and execute instructions that make sense on a real robot. See section 6.1 for the elaboration on the idea of a virtual robot.

5.5. Fuzzy Mechanisms

The forms of the abstractions used by the VRL are fuzzy. In that, crisp (non-fuzzy) values acquired by the VRL from sensors, are fuzzified according to the specifications and membership profiles, and these are provided to the higher level components that make use of the values according to fuzzy rules that guide its navigation and other functions. Instructions to the VRL are usually in a fuzzy format and these are defuzzified for the hardware to use. The abstractions are described more fully in section 6.3.

6. System Design

The hardware abstraction problem has been partially addressed in some architectures ([7], [10], [14] and [19]), where hardware abstraction layers (HAL) have been designed to allow basic control functions to be ported to different robots. These control functions allow low-level abstractions such as setting a servo speed, or requesting a sensor value.

However, a high-level command to move forward, turn left, or scan an area, can have radically different implementations on different robots. A mechanism to provide consistent interpretation of these high-level commands on various robots would be useful. These high-level commands need to be defined in a fuzzy format to allow algorithms to manipulate them at their highest abstract level. Then the high-level functional components can be completely portable because they only deal with the fuzzy handlers. The lower level implications of the fuzzy manipulations are left to the abstraction mechanism (the VRL).

6.1. Virtual Robot Layer

The VRL is the layer that provides the interfaces of a 'virtual robot' for the high-level functional components to use - concealing how these commands are translated into hardware calls. The VRL will also reply to high-level queries about the robot's configuration. This is useful when initialising a component.

For example, a high-level `Navigation` component may plan a path based on sensory input. Then a low-level `Motion` component may manage the servos of the robot to achieve certain types of locomotion - for instance 'turn left', and 'set speed'. The `Navigation` component should not need to change between robots, yet the `Motion` component almost certainly would. The robotic framework's VRL will support this portability by:

- Translating high-level commands into a standard low-level protocol;
- Providing a specification of the configuration of the robot for any component to use; and
- Converting robot specific output or results into predefined standards used throughout the architecture.

To illustrate further, the VRL can convert infrared readings from the raw voltage value to a distance in centimetres. It specifies where the infrared sensors are and pointing. It also defines the size and extremities of the robot. It has information on the servo inputs required to achieve a particular speed profile. The VRL mediates communications between high-level and low-level components and systems as seen in Figure 1.

6.2. Operational and Functional Portability

To achieve cross-platform portability, a component must be portable in two (2) ways:

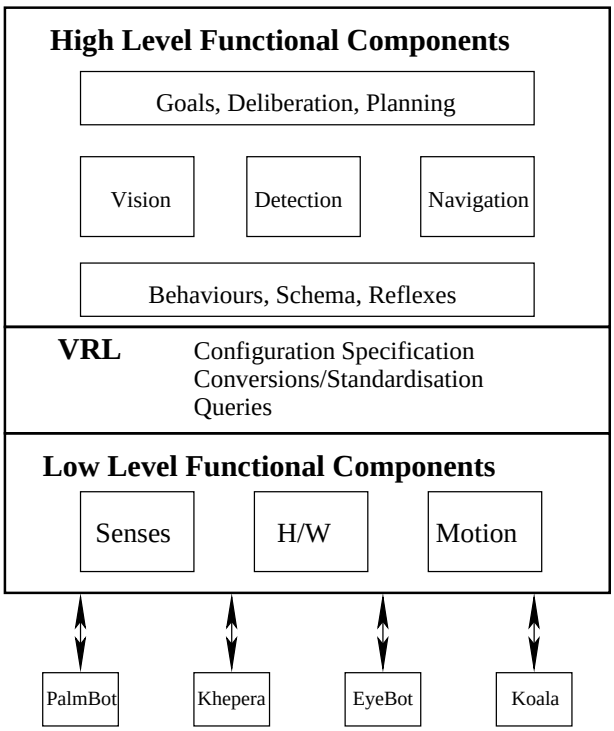

Figure 1. The VRL connects the high-level and low-level systems and components.

- Operationally - in that the component can be initialised and run using the new operating system or run-time environment; and
- Functionally - so that the control structures and algorithms that work in one robot (or configuration) continue to work on another.

In our prototype implementation, the robotic framework and the components are written in Java. This allows them to operate on any platform for which a suitable JVM is available. This provides the *operational* portability of the robot component. JVMs are run on any Windows or Linux OS based robot and can also be run on the Palm OS and there are even ports for the Motorola 68k series.

Furthermore, the *functional* portability of a component is supported by the VRL and operating infrastructure. Thus components can operate on any robot that has a VRL with a configuration that covers all required functionality.

It is important to note however, that not all components will work on all robots (even amongst those in the target group). For instance, before a particular component can initialised and run, sensors may be required in a certain direction. This preconditioning of operation precludes the component running on some configurations. Thus portability of code depends on some overlap in robot capability.

6.3. Fuzzy Abstractions

A simple illustration of the operation of the VRL will help identify the types of abstractions used. Take the pseudo-code for a Braitenberg styled obstacle avoidance algorithm as is shown in Figure 2.

```
while (true) {
        if (IRSensors(forward, blocked))
                Rotate(speed);
        else MoveForward(speed).
}
```

Figure 2. Simple pseudo-code for obstacle avoidance.

Even this simple algorithm requires the robotic framework to know the answers to questions such as:

- Which way is ‘forward’?
- What does ‘speed’ mean in the contexts of moving forward and rotation?
- How do I ‘rotate’?
- Where are the infrared sensors pointing?
- What infrared sensor reading means ‘blocked’?

These questions are answered by the VRL in terms of fuzzy abstractions and membership values of fuzzy sets. The current sets are:

- Direction - Front, Left, Right or Back
- Movement - Forward, RotateLeft, RotateRight or Reverse
- Speed - VeryFast, Fast, Medium, Slow, VerySlow or Stopped
- Distance - VeryFar, Far, Near or VeryNear
- Size - VerySmall, Small, Large or VeryLarge

These fuzzy constructs can then be used to describe hardware placement and orientation, the direction of obstacles or targets, speeds of travel and distances to the robot. All fuzzy terms are relative. By this we mean robot-centric. So an obstacle that is `Near` to a `Large` robot may only be `Far` to a `Small` robot. The VRL of course can be configured accordingly to make the correct interpretations.

The VRL is also configured with the appropriate hardware placements of sensors and cameras etc. Sensors can be grouped together to form zones of measuring (each group having its own membership function as to its direction from the robot). These details can be made available to the components on initialisation to check prerequisites as well as during run-time.

The VRL uses predefined standards within the system and these are built into the interface contracts. An example of this would be the `Speed` measurement, which is always available in cm/s before any fuzzification. Both the crisp and fuzzy value is available on demand. Other questions are translated by the VRL and queried or executed in the lower level components themselves. For instance, the motion component manages the rotation and movement of the robot. A VRL and associated low-level functional components are implemented uniquely for each robot. Again note, these particular components are not transferable between platforms as they are robot specific.

6.4. Configurability

The VRL provides data on the robot configuration including servo and sensor positioning and their signal input and output meanings. This function is loaded into the VRL from a configuration file, which is written once for each robot type and altered according to hardware changes. An configuration file using XML is very flexible, as used by [10] and [5]. We use XML configurations to completely specify our robots. This way the VRL can be easily modified with changes in the robot hardware or for entirely new robots.

7. Outcomes

The VRL concept has so far been implemented on three indoor mobile robots in our laboratory. These robots varied a great deal in size, performance and shape. From the small sized Khepera [15], to the larger Koala [15] with six wheels and many more sensors, to the Palmbot [1] with far fewer sensors and uses holonomic motion.

An obstacle avoidance component using infrared proximity measurements can operate completely unchanged on each of the three robots. The VRL would take the high level commands from the component and translate them into the appropriate robot level instructions. In future we hope to apply the VRL concept to humanoid and flying robots as well.

References

[1] Acroname. Palm Pilot Robot Kit. *www.acroname.com*, May 2002.

[2] R. Alami, R. Chatila, S. Fleury, M. Ghallab, and F. Ingrand. An architecture for autonomy. *International Journal of Robotics Research*, 17(4):315–337, April 1998.

[3] J. E. Beck, J. M. Reagin, T. E. Sweeny, R. L. Anderson, and T. D. Garner. Applying a component-based software architecture to robotic workcell applications. *IEEE Transactions on Robotics and Automation*, 16(3), June 2000.

[4] R. P. Bonasso. Experiences with an architecture for intelligent reactive agents. *Journal of Experimental and Theoretical AI*, 9(2), 1997.

[5] A. Bredenfeld. Behavior engineering with "dual dynamics" models and design tools. In *Sixteenth International Joint Conference on Artificial Intelligence IJCAI-99 Workshop ABS-4*, pages 57–62, Veloso, Manuela, 1999.

[6] R. A. Brooks. A robust layered control system for a mobile robot. *IEEE Journal on Robotiecs and Automation*, RA-2(1):14–23, March 1986.

[7] H. Bruyninckx. Open Robot Control Software: the OROCOS project. In *Proceedings of the 2001 IEEE International Conference on Robotics and Automation*, Seoul, Korea, May 21-26 2001. IEEE.

[8] C. Elsaesser and M. G. Slack. Integrating deliberative planning in a robot architecture. In *Proceedings of the AIAA/-NASA Conference on Intelligent Robots in Field, Factory, Service, and Space (CIRFFSS '94)*, pages 782–787, Houston, TX, 1994.

[9] Evolution Robotics. ER1 Robot. *www.evolution.com*, October 2002.

[10] Evolution Robotics. Robotic Architecture. *Technical White Paper*, www.evolution.com/product/oem/, January 2003.

[11] R. J. Firby. Programming CHIP for the IJCAI-95 robot competition. *AI Magazine*, Spring 1996.

[12] B. P. Gerkey, R. T. Vaughan, K. Sty, A. Howard, G. S. Sukhatme, , and M. J. Mataric. Most valuable player: A robot device server for distributed control. In IROS, editor, *Proceedings of the IEEE/RSJ International Conference on Intelligent Robots and Systems*, pages 1226–1231, Wailea, Hawaii, November 2001.

[13] G. Heineman and W. Councill. *Component-based Software Engineering, Putting the Pieces Together*. Addison Wesley, 2001.

[14] iRobot. Mobility Package. *www.irobot.com*, March 2003.

[15] K-Team. Mobile Robotics. *www.k-team.com*, July 2002.

[16] M. Lindstrom, A. Oreback, and H. Christensen. BERRA: A research architecture for service robots. In *International Conference on Robotics and Automation*. IEEE, 2000.

[17] N. J. Nilsson. *Principles of Artificial Intelligence*. Tioga Publishing Co., Palo Alto, CA, 1980.

[18] C. Szyperski. *Component Software Beyond Object-Oriented Programming*. Addison-Wesley Press, New York, 1998.

[19] R. Volpe, I. A. Nesnas, T. Estlin, D. Mutz, R. Petras, and H. Das. The CLARAty architecture for robotic autonomy. In *Proceedings of the 2001 IEEE Aerospace Conference*, Big Sky, Montana, March 2001.

Multi-step Independent Component Analysis for Removing Cardiac Artefacts from Back SEMG Signals

D Djuwari
SECE, RMIT University
RMIT City Campus, Swanston Street
Melbourne - Australia
s3001068@student.rmit.edu.au

D K Kumar
SECE, RMIT University
RMIT City Campus, Swanston Street
Melbourne - Australia
dinesh@rmit.edu.au

SC Ragupathy
SECE, RMIT University
RMIT City Campus, Swanston Street
Melbourne - Australia
s2116958@student.rmit.edu.au

B Polus
LS, RMIT University
RMIT Bundoora West Campus
Melbourne - Australia
barbara.polus@rmit.edu.au

Abstract

The Electromyogram (EMG) signals recorded from the back muscles often contain large electrocardiogram (ECG) artefacts. For better interpretation of these SEMG signals, it is essential to remove ECG artefacts. This paper reports research conducted to address the problem of removing ECG artefacts from SEMG recordings using new approach of Independent Component Analysis (ICA) called Multi-step ICA. The technique isolates the ECG artefact first and then removes the ECG artefact from each channel and solves permutation problem simultaneously. The results have been validated using standard deviation reduction of the normalised RMS amplitude of the data after separation process. The results demonstrate that this new proposed technique is successful in removing ECG artefacts from SEMG signals.

1. Introduction

Electromyogram (EMG) is the recording of the electrical activity of muscles. The EMG is usually recorded using monopolar or bipolar needle electrodes or surface electrodes. With needle EMG, it is possible to examine the activity of individual motor units while surface EMG (SEMG) is useful for examining the gross activity of a muscle or a group of muscles [6]. SEMG is a non-invasive technique and provides knowledge of the activation of the muscle of interest for a specific activity or posture and the relative strength of contraction [10]. One difficulty with SEMG is cross talk among the signals from adjacent electrodes and the recording of electrical activity from other sources. For accurate information of the activity of muscles it is important to ensure that SEMG is noise and artefact free and the recording represents the activity of the selected muscles.

SEMG of lumbar erector spine muscles (LESM) has been used frequently in applied physiology for the assessment of back muscle function during various activities [9]. Researchers have attempted to use the magnitude of the SEMG for the analysis of the relative

strength of contraction of the paraspinal muscles for the diagnosis of lumbar back ailments [1]. However, SEMG of lumbar paraspinal muscles may record the activity from several different muscles during static postures. Before the clinical and research utility of the SEMG for this task can be assessed, it is essential that issues of reliability and validity of the SEMG of lumbar paraspinal muscles be addressed. The ability of the SEMG to reliably record the relative strength of contraction of specific lumbar paraspinal muscles during the maintenance of a specific static posture is an important preliminary step in the validation procedure.

During SEMG recordings of multifidus muscle activity in different static postures the reliability of the SEMG signal is a major concern with issues such as electrode placement and high noise content in the recordings needing to be addressed. The development of a reliable objective measure of muscle activity would allow investigation into treatment outcomes and the role of muscle dysfunction in the maintenance or generation of LBP [9]. Recordings of SEMG from the back and abdomen muscles are contaminated by strong ECG signals making the raw signal unsuitable for analysis, confirming the findings of other researchers [11]. Therefore a technique to remove ECG artefact from SEMG recordings of the back is essential.

The commonly used techniques to remove noise such as high-pass filtering [13], spectral filtering [8], gating and cross-correlation subtraction [3] are not suitable. Each of these techniques has drawbacks that make them unsuitable for this application. Due to spectral overlap between ECG and SEMG, frequency filtering is unsuitable for this purpose. Gating, removing or deleting part of the SEMG that contains ECG adds discontinuities and makes the output unreliable since there must be some discontinuity in the joint point. Further, this technique is based on removing the QRS complex from the signal, often not the only source of contamination.

ECG and SEMG are statistically independent signals. Thus Independent Component Analysis (ICA) can be used to remove ECG artefact from SEMG recordings. ICA is a technique used to estimate two independent signals from a mixture of the two signals based on their independence to each other. It has been used to estimate and separate breathing artefacts from ECG recordings and results demonstrate the enhancement of cardiac signal quality with the use of ICA technique [16]. It has also been used to estimate and separate ECG artefact, noise and pure SEMG signal from synthetic mixture signals (one pure ECG signal and any two EMG signals that were linearly combined using 3x3 mixing matrix) using fixed-point algorithm but not with the real raw EMG signals from the recording [15]. A recently published paper reports success in the application of ICA to detect the underlying functional muscle activations during swallowing and successfully detect the presence of ECG and exclude it from the analysis. ICA was used to separate the 8 largest principle components of raw SEMG to obtain the signals representing each of the independent sources [11].

The ICA techniques described above were used in situations where the number of sources and recordings were the same. These methods are suitable where the prior knowledge of the type of independent component is known (such as pure ECG, abrupt signal and white noise) [14]. The other shortcoming of ICA is the ambiguity in permutation and amplitude [5]. Thus, ICA in the conventional form is not suitable for removing the ECG artefact from pre-recorded data where there is no extra channel that has simultaneously recorded ECG along with SEMG.

This paper presents a modification of ICA to overcome the shortcomings mentioned above. This technique successfully removes the ECG artefact from SEMG recordings from the muscles of the lumbar back. It overcomes the ambiguity of the permutation and amplitude and does not require an extra channel recording of ECG in parallel with SEMG. This is important for the analysis of the muscle activation for posture control.

1.1 Independent Component Analysis (a brief)

ICA was originally developed to deal with problems that are similar to the cocktail party problem. In a simplified situation, imagine 4 people are sitting together and talking to each other in a room that is equipped with 4 randomly distributed microphones. Each microphone will record a mixture of the 4 voices but with a different composition based on the relative location. The objective of ICA is to estimate the individual voice of each person, given only the recorded signals from those 4 microphones without having any knowledge about their location or their speech properties. Using ICA, the four recordings are separated to provide four sound signals that are independent to each other and thus are from each of the four speakers by suitably remixing the recordings.

ICA is based on some fundamental assumptions. Some of these have been listed below:

The first assumption is that the number of mixtures is greater than or equal to the number of independent sources.

The mixtures are linear combinations of the sources and there is no delay or external noise included.

The sources are stationary and are not moving during the recording process.

There is a constant effort by research groups to overcome the limitations of these assumptions.

A basic formulation of ICA can be expressed mathematically as [5]:

$$\begin{aligned} x_1(t) &= a_{11}s_1(t) + a_{12}s_2(t) \\ x_2(t) &= a_{21}s_1(t) + a_{22}s_2(t) \end{aligned} \quad (1)$$

or in general form (matrix notation)

$$\boldsymbol{x} = \boldsymbol{A}*\boldsymbol{s}, \quad (2)$$

where $\boldsymbol{x}$ is the vector of the mixtures, $\boldsymbol{A}$ is the unknown mixing matrix, and $\boldsymbol{s}$ is the vector of unknown independent components. The goal of ICA is finding an unmixing matrix $\boldsymbol{W}=\boldsymbol{A}^{-1}$ using neural networks.

Bell and Sejnowski have proposed a simple ICA algorithm based on an information maximization approach or minimization of mutual information among the outputs of neural network [4]. Mutual information is a natural measure of the dependence between random variables. The greater the mutual information, the more dependent are the variables. For this purpose, it is important to determine a suitable contrast function ***g(u)*** for the neurones of the network because the high density part of the probability density function (*pdf*) of $\boldsymbol{x}$ should be aligned with highly sloping part of ***g(u)***. Mutual information of the output vector **y** is defined as [5]:

$$I(y_1, y_2, ..., y_n) = \sum_{i=1}^{n} H(y_i) - H(y) \quad (3)$$

Bell and Sejnowski have shown that minimizing mutual information $\boldsymbol{I}(\boldsymbol{y})$ among the output components is equal to maximizing their joint entropy $\boldsymbol{H}(\boldsymbol{y})$ with respect to the weighting matrix, $\boldsymbol{W}$. The learning ruled derived by maximizing this joint entropy with respect to $\boldsymbol{W}$ is [7]:

$$\Delta W \propto \frac{\partial H(y)}{\partial W} W^T W = [I + \dot{p} u^T]W \quad (4)$$

where $\dot{p} = \frac{\partial}{\partial u_i} \ln \left| \frac{\partial y_i}{\partial u_i} \right|$ and $\boldsymbol{u} = \boldsymbol{W}*\boldsymbol{x}$.

If the contrast function $\boldsymbol{g}(\boldsymbol{u}) = \tanh(\boldsymbol{u})$ then:

$$\Delta W \propto \frac{\partial H(y)}{\partial W} W^T W = [I + 2\tanh(u)u^T]W \quad (5)$$

This is the learning rule used in the ICA algorithm to separate different sources from mixed recordings.

1.2 Multi-step ICA

The ICA technique has certain limitations such as lack of certainty of permutation and amplitude of the independent components. When applied to remove biosignal artefacts, the need for ICA to have as many channels as sources becomes a major limitation, as it requires an extra recording channel that would provide the information of the artefact. Thus it is not possible to apply ICA directly to remove the ECG artefact from 4 raw SEMG signals with the goal to obtain 4 clean SEMG signals. If the input of ICA algorithm is 4 raw EMG signals, the output will be 4 independent components where one of them is the ECG component while the other three are mixtures of the 4 EMG signals and are unsuitable for further analysis. Therefore, a new approach is needed in this situation to solve the problem.

The technique proposed here is called Multi-step ICA since it uses more than one step to get the clean EMG signals. The rationale of this is based on the fact that ECG is an independent signal that appears in each channel and identifying this would provide us information for the fifth channel. The detail description of this method is shown in figure 1. In the first step, the four raw SEMG signals from each channel are given as the input of ICA algorithm. The output of this separation process is 1 pure ECG signal and 3 SEMG mixture signals. Because of permutation problem of ICA, a short algorithm was used to get the pure ECG part for further processing. This algorithm discards the peak amplitude of abrupt noise by applying a 10-point moving average filter, detects the *R*-*S* value of the ECG that is much higher than any other part of the separated signals and gets the index of ECG signal. The ECG now becomes the first independent component that obtained from this ICA step.

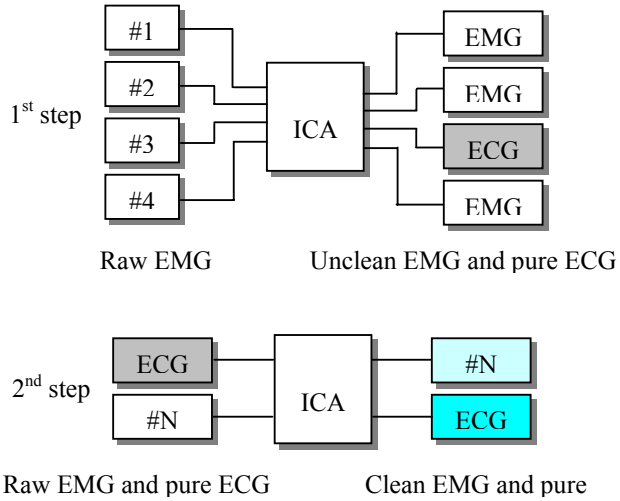

Figure 1: Cardiac artefact removal procedure by Multi-step ICA

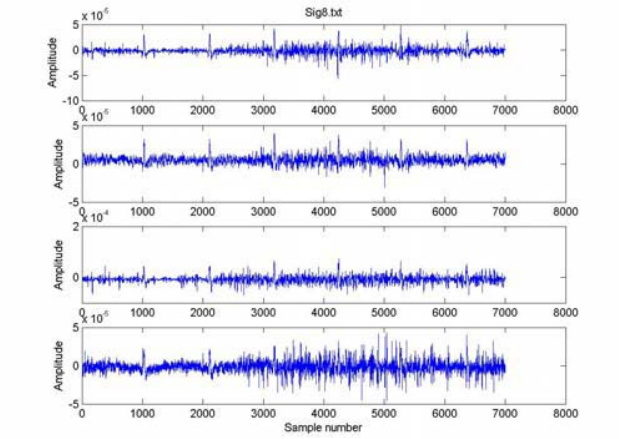

Figure 2: Four raw SEMG signals as an input to the first step ICA

The second step has one raw SEMG signal from a single channel and the ECG signal obtained from the previous process as the input to the ICA algorithm. The output of this process is 1 pure ECG and 1 clean SEMG for the particular channel. A similar algorithm as used in the previous step was used to detect the clean SEMG signal. This process is repeated for all the channels. Figure 2, 3 and 4 illustrate the waveform of the raw signals, first and second step ICA outputs respectively.

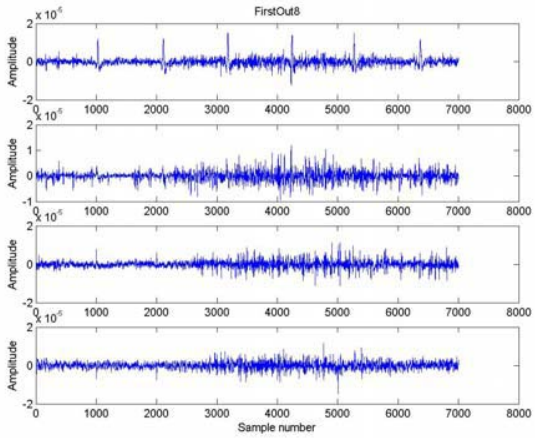

Figure 3: One ECG and three mixed SEMGs as the output of the first step ICA

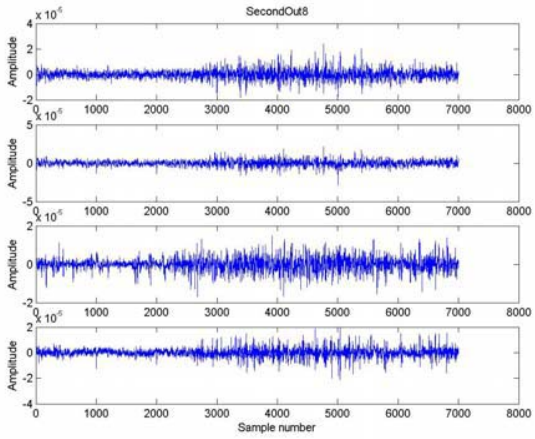

Figure 4: Four clean SEMGs as the output of the second step ICA

2. Materials And Methods

2.1 SEMG Recordings

SEMG recording was done using a 4-channel PowerLab data acquisition system (ADInstrument, Castle Hill, NSW, Australia) on 11 subjects on 2 days. The subjects were healthy males and females with ages ranging from 20 to 60 years old. The sampling rate was selected at 1000 sample/second and with antialiasing, high pass and notch filters having cut-off at 200 Hz, 3 Hz and 50 Hz respectively. The 4 channels were connected to 4 surface electrodes attached on the back muscles located on the left (ch.#3 and ch.#4) and right (ch.#1 and ch.#2) sides of the

spinal cord. The recording was done while the subjects were in specified normal sitting and standing positions. It was observed that most of the SEMG recordings were a mixture of SEMG and ECG. It was also observed that often the ECG (the artefact) strength was much greater than SEMG signal. A total of 31 recordings (containing 4 channels) were used for this experiment.

2.2 Signal Analysis

All SEMG recordings were saved in a *.txt format and then transferred to Matlab (Mathworks.Inc) for further processing. The ICA algorithm developed by Bell and Sejnowski [4] was used in the first and second step ICA calculation. The proposed technique Multi-step ICA explained above was applied to each SEMG recording to remove the ECG artefact. The outputs of this artefact removal process were saved again in the text format for further statistical analysis.

2.3 Validation of Results

SEMG, based on changes in amplitude and frequency, is a useful indicator for the strength of muscle contraction and muscle status. Comparison of SEMG magnitude from different locations of the back has been considered as a useful indicator of the relative contraction of the lumbar muscles and for information regarding posture control of the subject. Root Mean Square (RMS) is considered to be a good indicator of the strength of contraction of the muscles.

The RMS amplitude (energy) of a signal ***x(n)*** is defined as [2]:

$$RMS\{x(n)\} = \sqrt{\frac{1}{N-1}\sum_{0}^{N-1} x^2(n)} \qquad (6)$$

With the presence of ECG in the SEMG, the RMS of SEMG may have a very strong dependence on ECG and the information from this may not be reliable. But Melaku and Kumar have demonstrated that the RMS magnitude of the SEMG varies between subjects and between different recordings for the same subject and hence is not a suitable measure for improved reliability [12]. Thus, to determine any improvement in the reliability of the recordings using modified ICA for ECG removal, the reduction in the inter-recording variation is a suitable measure.

3. Results And Discussion

3.1 Results

RMS values of all raw SEMG recordings and clean SEMG signals after ECG artefact removal were calculated using (6). These values were then normalised by the value of the first channel of each recording to observe the relative muscles contraction for different postures. The mean, standard deviation and the ratio between standard deviation and mean of those normalised values were calculated. These are displayed in table 1 and tabel 2.

Table 1. Mean, STD and STD/mean values of the normalised data before and after separation for standing posture

	Raw SEMG signals				Multi-step ICA output			
	Ch1	Ch2	Ch3	Ch4	Ch1	Ch2	Ch3	Ch4
μ	*1.0000*	*0.5425*	*0.7342*	*0.4225*	*1.0000*	*1.0100*	*1.0169*	*1.0562*
σ	*0.0000*	*0.0870*	*0.2207*	*0.1299*	*0.0000*	*0.0558*	*0.1141*	*0.1077*
σ/μ	*0.0000*	*0.1603*	*0.3006*	*0.3075*	*0.0000*	*0.0552*	*0.1122*	*0.1019*

Table 2. Mean, STD and STD/mean values of the normalised data before and after separation for sitting posture

	Raw SEMG signals				Multi-step ICA output			
	Ch1	Ch2	Ch3	Ch4	Ch1	Ch2	Ch3	Ch4
μ	*1.0000*	*0.5698*	*0.9199*	*0.5593*	*1.0000*	*1.0111*	*0.9895*	*1.0041*
σ	*0.0000*	*0.3806*	*0.4459*	*0.2686*	*0.0000*	*0.0580*	*0.0502*	*0.1004*
σ/μ	*0.0000*	*0.6680*	*0.4848*	*0.4803*	*0.0000*	*0.0573*	*0.0507*	*0.1000*

3.2 Discussion

The analysis above provides evidence that ECG artefact removal using this new approach of ICA gives a convincing result. The decrease of standard deviation shows that after ECG artefact removal the variance of the signal is less then the raw SEMG. The ratio between standard deviation and mean demonstrates that the output of the separation has less Gaussian distribution. This means that the output signals are independent to each other.

This approach of ICA is suitable when there are fewer channels than sources and in situations where the signal / artefact that needs to be removed appears in all channels. The permutation ambiguity was also solved by applying ICA to each channel in turn while the magnitude ambiguity was equalised by a post processing step that makes the separated sources have unit variance. Thus, this technique gives more reliable SEMG signals for quality interpretation. With raw SEMG signals, it is hard to determine which muscles contribute more or less during a certain static posture.

The disadvantage of this technique is the increased computational time required to accomplish the separation task because of multi-step processing. Further, this technique is dependent on the artefact having a distribution that differs from the rest in the mixtures. The extension of this technique is to estimate a greater number of sources than the number of sensing channels.

4. Conclusion

From visual inspection of the output signals (Figure 4) and from the statistical analysis result, it is clear that this new approach of Multi-step ICA is able to remove the cardiac artefact from SEMG recording and give more reliable signal for clinical interpretation.

5. Acknowledgments

The authors want to thank Ken Mei who has contributed much in the SEMG recording and all-fellow researchers in the Biomedical Laboratory, School of Electronics and Computer Engineering, RMIT University for their support.

6. References

[1] Ambroz C, Scott A, Ambroz A and Talbott EO, “Chronic Low Back Pain Assessment Using Surface Electromyography”, JOEM, 42 (6), 660-669, 2000.

[2] Barney L and Gunnar A, “Selected Topics in Surface Electromyography for Use in the Occupational Setting: Expert Perspective”, DHHS (NIOSH) Publication, Chapter 5, No. 91-100, 1992.

[3] Bartolo A, C.R., R.Dz, and Goldman E, “Analysis of Diaphragm EMG signals: comparison of gating vs. subtraction for removal of ECG contamination”, American Physiological society, 1996.

[4] Bell AJ and Sejnowski TJ, "An information-maximization approach to blind separation and blind deconvolution", Neural Computation, Vol. 7, No. 6, 1129-1159, 1995.

[5] Hyvärinen A and Oja E, “Independent component analysis: algorithms and applications”, Neural Networks, 13 (4-5), 411-430, 2000.

[6] Kimura J, “Electrodiagnosis in diseases of nerve and muscle: principles and practice”, 2nd edition, Philadelphia: F.A Davis, 1989.

[7] Lee TW, Girolami M and Sejnowski TJ, “Independent Component Analysis Using an Extended Algorithm for Mixed Subgaussian and Supergaussian Sources”, Neural Computation, 11, 417-441, 1999.

[8] Levine S, J.G., Weiser P, Gillen M and Kwatny E, “Description and validation of an ECG removal procedure for EMG, Power Spectrum Analysis”, Journal of Applied Physiology, 60, 1073-1081, 1986.

[9] Marcarian D, “Surface EMG: Static vs. Dynamic Testing“, Canadian Chiropractor, 32-33, 1999.

[10] Marras W, “Selected Topics in Surface Electromyography for Use in the Occupational Setting: Expert Perspective”, DHHS (NIOSH) Publication, Chapter 1, No. 91-100, 1992.

[11] McKeown MJ, Torpey DC and Gehm WC, “Non-invasive monitoring of functionally distinct muscle activations during swallowing”, J. Clinical Neurophysiology, 113, 354-366, 2002.

[12] Melaku A, Kumar DK and Bradley AB, “Influence of Inter-Electrode Distance on The RMS of SEMG signal”, Electromyography and Clinical Neurophysiology, 41, 437-442, 2001.

[13] Redfern MS, Hughes RE and Chaffin DB, “High-pass filtering to remove electrocardiographic interference from torso EMG recordings”, Clinical Biomechanics, 8 (1), 44-48, 1993.

[14] Taigang H, Clifford G and Tarassenko L, “Application of ICA in Removing Artefacts from ECG”, Neural Computing and Applications, 2002.

[15] Wachowiak M, Smolikova R, Tourassi GD and Elmaghraby AS, “Separation of Cardiac Artefacts from EMG Signals with Independent Component Analysis”, Biosignal, 2002.

[16] Wisbeck JO, Barros AK and Ojeda R, “Application of ICA in the Separation of Breathing artefacts in ECG Signals”, Int. Conf. on Neural Information Processing (ICONIP’98), 1998.

Autonomous Land Vehicle Navigation using Artificial Neural Networks

Muthu Ganesh P.
R.M.K. Engineering College
Department of Information Technology
Chennai, Tamil Nadu, India
muthuganesh_p@hotmail.com

Sai Nithin Singh C.
R.M.K. Engineering College
Department of Information Technology
Chennai, Tamil Nadu, India
sainithin@hotmail.com

Abstract

Autonomous land vehicle navigation is used to assist the driver partially or completely with the help of modern technology in a non-intrusive manner. This work concerns with the addition of an additional neural network which works separately and takes care of the road signs and other such entities. It detects obstacles and tracks them till it is safely passed. The information about the obstacle is passed on to the driving network which deals with the obstacle by steering the vehicle away, or deciding some other means of avoiding the obstacle. Thus, the safety of the system is enhanced.

1. Introduction

1.1 Artificial Neural Networks (ANN):

Artificial Neural Networks, also called parallel distributed processing systems (PDPs) and connectionist systems, are intended for modeling the organizational principles of central nervous system, with the hope that the biologically inspired computing capabilities of the ANN will allow the cognitive and sensory tasks to be performed more easily and more satisfactorily than with conventional serial processors. In simple terms ANN is an attempt to mimic the functionality of the human neural network system (brain).

1.2 Autonomous Land Vehicle Navigation:

Autonomous land vehicle navigation is used to assist the driver partially or completely with the help of modern technology in a non-intrusive manner. Currently, the most discussed technology with respect to autonomous land vehicle navigation is the use of impregnated magnets along a path to guide the vehicle. But the drawback of this system is the cost and the practicality of implementation. Autonomous land vehicle navigation using ANN addresses all these drawbacks along with the added functionality of learning the different driving styles under different circumstances using on-the-fly training [1]. This system uses active sensors to interact with the environment and concurrently learn from the user using a non-intrusive gaze tracking system through ANN. The issues addressed by this system are:

- Rapidly Adapting the Lateral Position of the Vehicle.
- Kinematical Control of Vehicle using Simulated Highways for Intelligent Vehicle Algorithms.
- Inter-Vehicle Interaction using Visibility Estimation Techniques.
- Simultaneous Localization and Mapping with Detection and Tracking of Moving Objects.
- Path Intersection Detection and Traversal.
- Predicting Lane Position for Roadway Departure Prevention.
- Driving in traffic: Short-Range Sensing for Urban Collision Avoidance

1.3 Active Sensor Control for Autonomous Driving System:

The Autonomous Land Vehicle (ALV) is a neural network based system which has been successful in driving robot vehicles in a variety of situations. However, since ALV maintains no state information about the world, but processes each sensor frame individually, it can become confused on sharp curves when the field of view no longer displays the important features in the scene. A steerable sensor allows the perception system to select the desired field of view to maximize the information content of a sensor

frame. For a vision system that builds a map of the road, it is straightforward to point the camera in the desired direction, but ALV directly outputs a steering command, without generating an intermediate road representation. The system interprets this steering command as a point on the road and pans the camera in the desired direction. However since ALV is trained with a fixed sensor orientation, the position of the sensor during training is implicitly encoded in the weights and moving the camera results in the outputs of the network being invalid for the given configuration. The system solves this problem by post-processing the steering response of the neural network as a function of the current sensor configuration. A significant advantage of this approach is that existing networks can run under this new system without any modification or retraining.

The system's basic architecture is a three layered artificial neural network shown in figure. A reduced resolution camera image is fed into a 30x32 array of input units, which are fully connected to a hidden layer of 4 units. The hidden units are fully connected to a vector of 30 output units, and the steering response is given as a Gaussian activation level centered on the correct steering curvature. ALV's neural net is trained "on-the-fly", and the human driver's steering responses are used as the teaching signal. ALV is able to learn from this limited data by artificially expanding its training set. Each original image is shifted and rotated in software to create 14 additional images in which the vehicle appears to be situated differently in relation to the road. The training signal for each of these new images is calculated by assuming a pure pursuit model of driving and transforming the original steering response accordingly [1].

1.4 Inter-Vehicle Interaction using Visibility Estimation Techniques:

Reduced visibility is one of the key factors in many traffic accidents. It is very difficult to consistently find high contrast targets at various known ranges from a moving vehicle. This system overcomes this difficulty when detecting the position and curvature of the road ahead in camera images by utilizing whatever features are visible on the roadway, including lane markings, road/shoulder boundaries, tracks left by other vehicles, and even subtle pavement discolorations like the oil stripe down the lane center when necessary.

In order to estimate visibility the road feature should be detected. In this process an aerial image of the road is taken and a cross-section of the aerial image perpendicular to the road, called the road template is created.

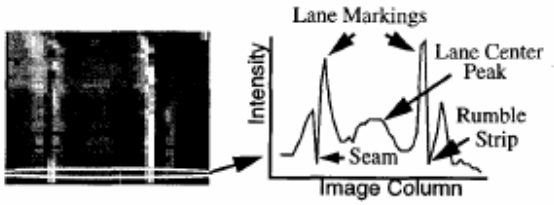

Fig. 1 – Image used to study the road using intensity as a parameter [4].

All the particulars necessary are taken from the road template and finds out the road ahead. The system adjusts the template left or to the right until it matches the particular row's cross-section. The amount of shift gives the lateral displacement.

1.5 Driving in traffic: Short-Range Sensing for Urban Collision Avoidance

This system addresses the issues involved in traffic driving. The requirements for an effective collision avoidance and warning system for urban environments, include the following as a minimum standard:

- Sensing
  - State of own vehicle
  - State of nearby objects
  - Environment
- Knowledge Base
  - Model of the own vehicle and driver
  - Model of other objects
  - Model of environment
  - Model of interaction between all of the above
- Processing and Algorithms
  - What situation we are in?
  - How likely is a collision?
  - How dangerous is the situation?
  - Is an action needed?
- System Response
  - Aware : Baseline Situational Awareness
  - Alert : Potential Obstacles
  - Warn : High Likelihood of Collision
  - Evade : Imminent Collision
  - Notify : Collision has occurred

One method of sensing the nearby objects in an urban environment is using a laser line striper shown in the figure below [2].

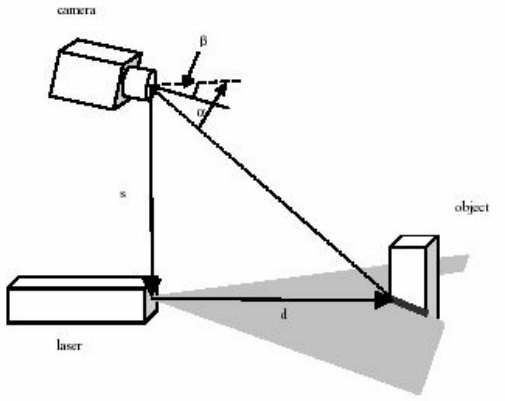

Configuration of laser and camera of the laser line striper.

Fig. 2 - Laser and Camera configuration used for short range detection of objects.

1.6 Overtaking Vehicle Detection

To detect vehicles, we do the following: first, we sample the image, perform edge detection, and use our planar parallax model to predict what that edge image will look like after traveling a certain distance. Next, we capture an image after traveling our assumed distance, and compare it to the prediction. For each edge point in the predicted image, we verify that there is a corresponding edge point in the actual image. If there is a match, then our prediction (based on a flat earth assumption) is verified. Otherwise, we know that the cause of the horizontal line in the predicted image was an obstacle (i.e., above the ground plane). There are 4 components to the system:

- Sampling and Preprocessing,
- Dynamic image Stabilization,
- Model-Based Prediction, and
- Obstacle Detection.

The figure 3 on the right is the difference image obtained by taking the difference of the images actually sampled and the image predicted by the system. When the noise is analyzed, the vehicle on the right easily stands out, since its predicted path of motion is varying greatly from its actual path of motion. Thus it is concluded that it is overtaking.

Fig. 3 - Rear View Road Image [3]

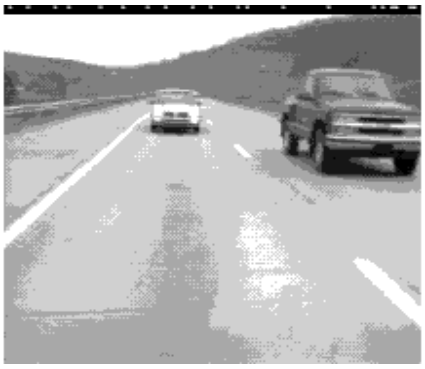

Fig. 4 - Same image after 120 ms [3]

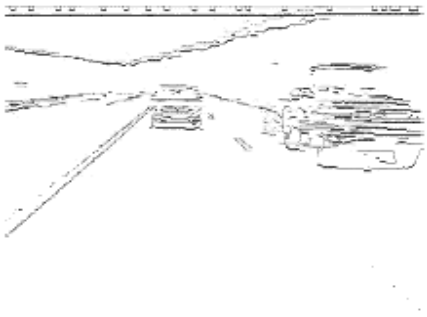

Fig. 5 - Difference Image [3]

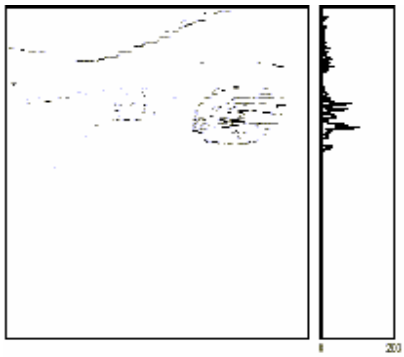

Fig. 6 - Obstacle Image [3]

2. Obstacle Tracking

Our work is extending the above working model developed by NAVLAB, Carnegie Mellon University by adding an obstacle tracking system. We have taken up a two dimensional case, for greater flexibility in case of contour changes on the road. With the initial positions of the obstacle and the autonomous vehicle, the bearing information is simulated using sensor simulator, the output of which is fed to the Least Square Estimator (LSE) filter which gives the estimated obstacle parameters. The errors between the estimated and the simulated obstacle parameters are compared. To reduce estimation error, the backpropogation neural network is incorporated with the LSE filter. The network is trained for a set of inputs and after testing, the network estimates the obstacle parameters. The errors between the simulated and the estimated values are compared with the errors obtained without the aid of the network.

2.1 Tracking Model Derivations

2.1.1 Mathematical Model:

System model at state k+1:

$$X(k+1) = A.X(k) + B.U(k) + W(k)$$

where

$$X(k) = \begin{bmatrix} r.x(k) \\ r.y(k) \\ v.x(k) \\ v.y(k) \end{bmatrix} = \text{State Vector}$$

$$= \begin{bmatrix} \text{Range in x-direction at time k} \\ \text{Range in y-direction at time k} \\ \text{Velocity in x-direction at time k} \\ \text{Velocity in y-direction at time k} \end{bmatrix}$$

$$U(k) = \begin{bmatrix} v.x(k) \\ v.y(k) \end{bmatrix}$$

$$= \begin{bmatrix} \text{Change in relative velocity in x-direction between time k and k+1.} \\ \text{Change in relative velocity in x-direction between time k and k+1.} \end{bmatrix}$$

W(k) = System Noise

$$A = \begin{bmatrix} 1 & 0 & kT & 0 \\ 0 & 1 & 0 & kT \\ 0 & 0 & 1 & 0 \\ 0 & 0 & 0 & 1 \end{bmatrix} = \text{State Transition Matrix}$$

$$B = \begin{bmatrix} 0 & 1 & 0 & 0 \\ 0 & 0 & 0 & 1 \end{bmatrix}^{-1} = \text{Input Matrix}$$

T = Sampling Period

k = Sample Number

U(k) is concerned with vehicle dynamics with respect to the obstacle. Since the vehicle is assumed to be moving with a uniform velocity within the infinitesimal period between k and k+1, B.U(k) term can be taken as zero for theoretical verification purposes. By assuming the system noise as zero, the system model becomes:

$$X(k+1) = A.X(k)$$

2.1.2 Measurement Model:

$$Y(k) = H.X(k) + \upsilon(k)$$

where,

Y(k) : Measured bearing at time k
H : [cos b -sin b 0 0]
: Measurement Matrix
b : Bearing
$\upsilon(k)$: Measurement noise component of the appropriate order.

2.1.3 System Dynamics Model:

The Cartesian state vector formulation is as follows:

Let 'k' be any arbitrary time instant,

$$X(k) = \begin{bmatrix} rx(k) \\ ry(k) \\ vx(k) \\ vy(k) \end{bmatrix}$$

$$rx(k) = rtx(k) - rox(k)$$
$$ry(k) = rty(k) - roy(k)$$

where,

rx and ry are relative ranges along x and y directions between the vehicle and the obstacle.
t : refers to the obstacle (target)
o : refers to the vehicle (observer)

The measurement process is described by non-linear elation:

$$b(k) = \arctan(rx/ry)$$

where,

b(k) represents the measured target (obstacle) bearing at the k^{th} instant of time and taking tan on both sides we have,

$$\tan(b(k)) = (rtx(k) - rox(k)) / (rty(k) - roy(k))$$

or,

$$\sin(b(k))\,(rty(k) - rox(k)) = \cos(b(k))\,(rtx(k) - rox(k))$$

but,

$$b(k) = bm(k) + v(k)$$

where,

bm(k) is the actual measured bearing at k^{th} instant and v(k) is the measurement noise at k^{th} instant.

This can be formulated as follows avoiding the subscript 'k':

$$(rtx - rox)\cos(bm) - (rty - roy)\sin(bm) = -rs(k).\sin(v(k))$$

where,

$$rs(k) = (rtx - rox)\sin(b) - (rty - roy)\cos(b)$$

i.e,

$$rox.\cos(bm) - roy.\sin(bm) = rtx.\cos(bm) - rty.\sin(bm) + rs(k).\sin(v(k))$$

In the above equation the left hand side denotes the measurement vector H(k), and is chosen as,

$$H(k) = [\cos(bm) \quad -\sin(bm) \quad 0 \quad 0]$$

Therefore the observation sequence is as follows,

$$z(k) = H(k).Xo(k) = H(k).Xt(k) + n(k)$$

i.e,

z(k) is the measurement at k^{th} instant,

Xo(k) is the observer(vehicle) state at the k^{th} instant,

Xt(k) is the target(obstacle) state at the k^{th} instant and

n(k) is the noise sequence at the k^{th} instant.

Hence the measurement scalar model

$$z(k) = H(k) \,.\, X(k) + n(k)$$

2.2 Backpropogation Neural Network Training

2.2.1 Forward Pass. Calculation in multilayer network is done layer by layer. The NET of each neuron in the first hidden layer is calculated as the weighted sum of all its neuron inputs. The activation function 'F' then squashes NET to produce the OUT value for each neuron in that layer. Once the set of outputs for a layer is found, it serves as the input for the next layer. The process is repeated , layer by layer, until the final set of network outputs is produced.

2.2.2 Backward Pass. The networks actual output from the forward pass is compared with the desired output and error estimates are computed for the output units. The weights connected to the output units are adjusted to reduce those errors. The error estimates of the output units are used to derive the error estimates for the units in the hidden layer. Finally, the errors are propagated back to the connections stemming from the input units.

Before starting the training process, all the weights must be initialized to small random numbers. This ensures that the network is not saturated by large values of weights.

2.3 Least Square Estimator Filter

The Least Square Estimator is one the methods providing Target Motion Analysis (TMA). We propose to incorporate this in our ALV model. Here instead of the target moving, the ALV model moves, and the obstacle remains stationary. The basic task is to estimate accurately to the extent possible, the relative position (Rx, Ry) and the relative velocities (Vx, Vy) of the obstacle, from either the Short Range Sensors or sonar noisy measurements of range and bearing. The obstacle can be a stone, a vehicle (parked or in motion), a signboard, etc. The state vector plays a key role in LSE diverging/converging cases.

The statistical characteristics of the noise depend upon the measuring equipment. It is observed that the LSE is optimum only for the

case of Gaussian noise. The LSE is an unbiased, stable, and optimal estimator with minimum variance, if the system is stochastically controllable and observable, with some noise assumptions being satisfied.

The recursive LSE is a linear, discrete time, finite-dimensional and sequential recursive system. It assumes the availability of a state model and an observational model. The input to the filter is a sensor or a sonar bearing contaminated with noise and the output is the obstacle parameters.

2.4 Block Diagram of Network Aided LSE

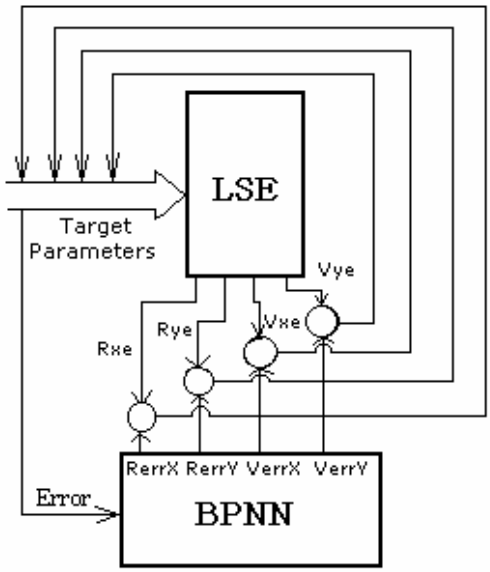

Fig. 7 - Block Diagram of Backpropogation Neural Network (BPNN) aided LSE (Least Square Estimator).

The block diagram shown above illustrates how the LSE functions in combination with the Backpropogation neural network. The compared results of the network and the LSE are fed back and thus the error is deducted.

3. Conclusion

Intelligent vehicles are beginning to appear on the market, but so far their sensing and warning functions only work on the open road. Functions such as run off road warning or adaptive cruise control are designed for the uncluttered environments of open highways. Current sensing/warning/controlling systems generally work only in relatively simple environments. Applications developed for open highways include Adaptive Cruise Control (ACC), which controls the throttle to keep a safe gap behind other vehicles; run-off-road collision warning systems, which alert a driver if the vehicle starts to drift out of its lane; and blind-spot sensors on heavy trucks to warn the driver if they start a lane change without seeing a car in the next lane. Some applications are also on the market for slow speed driving: rear-facing sensors as parking aids, for example. This work of ours gives a spin-off to further studies. Other neural networks such as the Hopfield network can be employed instead of the Backpropogation network.

The Autonomous Land Vehicle Navigation using Artificial Neural Networks puts forward a very promising technology which might change the very way vehicle navigation is perceived as of today. Although still under research, its results are very encouraging and in conjunction with other modern technologies like GPS, ACC, etc. can easily pull down the rate of causality which is very high in today's roadways. The future is very bright for Autonomous Land Vehicles. They have come here to stay and stay they will.

References

[1] Rahul Sukthankar, Dean Pomerleau and Charles Thorpe, Robotics Institute (NAVLAB) - Carnegie Mellon University. Panacea: An Active Sensor Controller for the ALVINN Autonomous Driving System.

[2] Mertz, C., Kozar, J., Miller, J.R., and Thorpe, C., Eye-safe Laser Line Striper for Outside Use. Paper submitted to: IV 2002, IEEE Intelligent Vehicle Symposium, June, 2002.

[3] Parag H. Batavia, Dean A. Pomerleau, Charles E. Thorpe, Robotics Institute, Carnegie Mellon University. Predicting Lane Position for Roadway Departure Prevention.

[4]. Dean Pomerleau, Carnegie Mellon University. Inter-Vehicle Interaction using Visibility Estimation Techniques.

A Study on the Content-Based Image Retrieval System for Medical Applications

Kien-Ping Chung, Lance Chun Che Fung and Hong Xie
School of Information Technology
Murdoch University
South Street, Murdoch
W.A. 6150, AUSTRALIA
{k.chung, l.fung, h.xie}@murdoch.edu.au

Abstract

The storage of images in databases is gaining popularity due to the rapid development of cheap and easy image capturing equipment. The principle of Content Based Image Retrieval (CBIR) system normally depends on specific features such as colour, texture, shape or semantic meaning of the image. On the other hand, content-based medical images retrieval (CBMIR) system presents different challenges. This paper discusses the comparison on the key features of a Content-Based Image Retrieval (CBIR) system and its potential adaptation as a content-based medical images retrieval (CBMIR) system. This will lead to subsequent studies and investigation in the prospective research areas.

1. Introduction

Over the last decade, there is an increasing trend of storing non text-based data in databases. Image in particular, has been gaining popularity as an alternative and sometime more viable option for information storage. While this presents a wealth of information, however, it also causes a great problem in retrieving appropriate and relevant information during searching. This has resulted in a growing interest and much active research on the subject of the extraction of relevant information from non text-based databases. Over the past few years, researchers have achieved certain degree of success in these fields. This is shown as evidence in the increasing number of commercially available search engines for images.

Content-based image retrieval (CBIR) system is a type of system which retrieves images based on their features such as colour, texture, shape or semantic meanings of the image. Upon reviewing the CBIR systems that have been reported, it was found that such systems can be grouped into two main categories, namely, *generic* and *domain-specific* systems. The generic retrieval systems like Yahoo Image Surfer and Lycos image library contain all types of different images. On the other hand, domain-specific retrieval systems only contain images that are closely related to a specific application area. A content-based medical image retrieval (CBMIR) system is a typical example of a domain-specific retrieval system.

During the past two decades, the development of new modalities such as Computed Tomography (CT), Magnetic Resonance Imagining (MRI), and Picture Archiving and Communication Systems (PACS) have resulted in an explosive growth in the number of images stored in databases. Until recently, textual index entries are mandatory to retrieve medical images from a hospital image archive system. However, the development of CBIR techniques has not only created new possible ways of retrieving images, but also opened out opportunities for other related applications.

It is however simplistic to consider that one can directly apply a generic CBIR system to a medical image database. In this study, it is considered that it will be of interest to readers the characteristics and the development trend of CBMIR systems from the perspective of one whose background is in the discipline of CBIR systems. In this paper, the applications of such technology are discussed. The development trend of CBMIR and when appropriate, comparisons between the two systems are also drawn. Finally, this paper concludes by summarizing the differences between the two systems.

2. Medical Image Database

First of all, three characteristics of a medical image database are identified. Each of these characteristics of the system presents a different challenge to the research community. The following sub-sections provide a detailed discussion on the characteristics of the CBMIR systems.

2.1 Heterogeneity

Medical image is only a general phrase many used to describe images which have captured information about the human body. It is actually a broad field that consists of image classes such as photography (e.g., endoscopy, histology, dermatology), radiographic (e.g., x-rays), and tomography (e.g., CT, MRI, ultrasound). It imposes

unique, image-dependent restrictions on the nature of features available for abstraction. Each of the image classes possesses its unique characters in terms of size, shape, colors and texture of the region of interest. Thus, the visual appearance of the same organ or part of the human body will be different under different modalities. Furthermore, it is also possible that the interest in the same image may be different by systems or users for different application. It is therefore not difficult to deduce that different approaches will be required for different modalities and systems for different applications. These approaches may include the design of user interface, indexing structure, feature extraction and query processing units.

2.2 Imprecision

Imprecision has been a problem for the CBIR systems. Likewise, CBMIR systems suffer the same problem. Tagare et al. [1] have identified three components in imprecision, i.e., semantic imprecision, feature imprecision, and signal imprecision. These imprecision are caused by the ambiguity of human language, disagreement in the observation of an image and quality of information captured in the image.

The three types of imprecision described by Tagare et al. [1] are very much similar to the problems experience by the general CBIR systems. One would argue that the semantic imprecision is similar to the problems of polysemy and synonymy occurring in terms of query processing. Feature imprecision also occurs in general CBIR system when users have different interpretation on the image, or the inability by the user to describe the semantic content of the image. This is a common problem in the CBIR system as the scope of the collected images are broader than images collected for medical field. Lastly, signal imprecision is quite common among images captured in the outdoor environment.

2.3 Dynamism of Indexing Structure

As described in the previous section, the human interpretation of a medical image may vary from person to person. The interpretation of an image from the same person may also change as the person gains more experience. Thus, the area of interest for the same image may change as the interpretation of the image changes. For systems that index images by their semantic contents or the visual features of the area of interest, such changes may result in a need to modify the indexing structure in order to adapt to the user's knowledge. However, traditional indexing structures reported so far are static. The process of re-organizing the indexing structure is mostly manually driven. Hence, a significant overhead is included. Ideally, the indexing structure for medical images should be dynamic while keeping the overhead for re-organizing the indexing structure to minimal. Preferably, very little manual interaction should be required.

2.4 Remark

All of the issues described above are not unique to CBMIR systems. As a matter of fact, these issues are also faced by CBIR systems. To a degree, the magnitude of some of these issues faced by CBIR is larger that what those in CBMIR systems. The reason is being that the scope of the medical images is bounded within the medical domain. Hence, certain assumptions can be made prior to analysing the images.

3. Applications

Medical imagery is an exciting field for researchers of CBIR. It not only contains vast amount of image resources that the researchers can work on, it also provides practical applications that research theories can be applied to. Due to these reasons, there has been a steady growth in developing medical applications with the use of CBIR techniques. The CBMIR systems are grouped into two categories mostly according to their input data format and to a certain extent, the domain scope of their applications.

Traditionally, there are two standard approaches in querying the system, namely, *query by keywords* or *image examples*. In query by example, the diagnostic system is one of the applications where researchers have been focusing on. As the name implies, the output from these systems is the diagnostic result derives from the system's input image. Until now, the systems reported have only been designed to support specific medical tasks such as retrieval of tumor shapes in mammograms [2], identification of lung disease from computed tomography [3], differentiation of Mantle Cell Lymphoma (MCL) from Chronic Lymphocytic Leukemia (CLL) or Follicular Center Cell Lyphoma (FCC) using pathology images [4], and retrieving of spine in the x-ray database [5]. All these systems are designed to query by image. The region of interest for the input image is partially or automatically selected by the system. Manual interrelation is required when the image resolution is low, or with an inability of applying image models to capture the visual features in interest. It is worth noting that some authors are quite cautious in using the term "diagnostic" for their proposed systems. Instead, these authors prefer to call them "decision support" systems.

In addition to the diagnostic systems, Liu et al. [6] have developed a teaching assistant system for the identification of lung diseases from tomographic images. This system allows the professor to select images with

similar texture but may be not belonging to the same disease. The objective is to teach interns to learn how to distinguish various disease images with similar texture.

Currently, the tradition picture and archiving image system (PACS) is used for searching medical images in many hospital or clinical systems. The images stored in the PACS system are normally organized according to their semantic content, or by patient's details, or, other related information. Systems that allow the users to retrieve images via the patient's details and other related information are normally based on the patients' history.

In summary, systems that browse or search images via the semantic content are mostly used for education or decision support purposes. The image grouping and organization is mostly manually driven, and these images are mostly indexed by a simple phrase or term.

4. Overall Framework

Figure 1 is a possible framework for CBIR systems. The communication between the modules is mostly bi-directional, implying this framework allows bi-direction interaction between users and the systems. This framework is an extension from Rui et al. [7]. It is felt that the query processing unit should be related to feature extraction unit, and the user should have a role in defining the image label.

The PACS systems discussed in the previous section are rather simple as a content-based retrieval system. At the minimum, a CBIR should consist of components as depicted in Figure 1. Clearly, the PACS systems lack the system module for feature selection, and quite possibly the images are indexed by a very simple one-dimensional structure grouped by the label given to the images.

Diagnostic systems reported so far are only designed for very specific application. It may not be possible for such systems to be transferred to other medical applications. The reason is obvious, different diagnostic system uses different visual features for identifying different medical cases. Thus, the feature extraction approach for each system will be different. Often, such systems are also static, implying that a significant overhead is required for a visual feature to be added, deleted or modified. Furthermore, the indexing structure applied for these systems are often not targeted for a large database and definitely not for image browsing.

Tagare et al [1] have identified several essential features for CBMIR systems: (a) non-textual indexing, (b) customized scheme, (c) dynamic modules, (d) similarity modules, (e) comparison modules, (f) iconic queries, (g) descriptive language, (h) multi-modality registration, (i) image manipulation. Researchers have generally viewed these necessities as the guideline for building a complete CBMIR system.

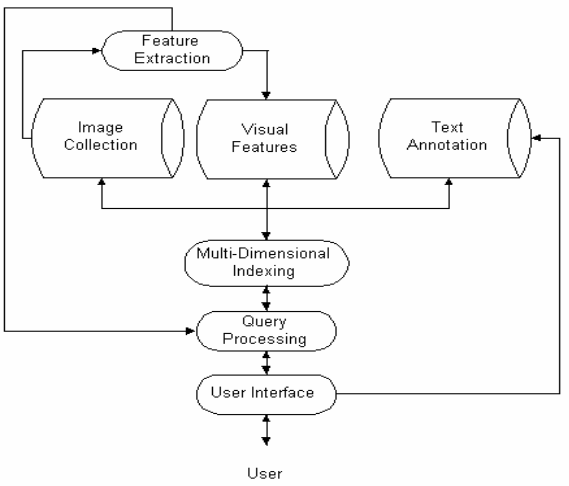

Figure 1. A possible framework for CBIR system.

Lehmann et al. [8] have proposed a medical image browsing and searching framework called Image Retrieval in Medical Application (IRMA). This framework has the potential of answering every system requirements as listed by Tagare et al [1]. IRMA is a multi-layer framework that provides separate layers which include: identification of image categories, extraction of image content and local features, indexing images based on their semantic content and image retrieval on the semantic level. The major difference between this framework and the more traditional CBIR framework [9] is that this framework uses prior knowledge of different medical modalities to determine the content of the images. This is however not possible for a general CBIR system.

5. User Retrieving Techniques

To date, much of the research effort for CBMIR systems has been spent on identifying features which uniquely identifying image, and the indexing structures for images in the system. Not much has been spent on the user interface of the system. It is true that most of the issues surrounding CBIR system in designing user interface are to do with limiting the domain scope of the input query, and to a degree, this is less of an issue for a narrow domain retrieval system such as CBMIR. However, most of the CBMIR systems reported are stilled targeted for trained personal, indicating that they are room for improvement.

The user interface for CBMIR system is based on the strategy adopted by the traditional CBIR system. The standard approach is query the system by image or keyword. As with any search engines, keywords have limited usefulness, in that it is difficult to assign keywords consistently and exhaustively to each image. In query by example, most of the systems provide users with editor for

manipulating the input image, and some may even allow the user to query by sketch. However, the issue facing most of these systems is that it is relatively difficult for the users to specify the appropriate combination of visual features for a particular search. Systems proposed by Liu et al. [6], Comaniciu et al. [4] and Shyu et al. [3] all require user to select the region of interest (ROI) area in an image for the system to construct the proper query. The users of this type of systems are usually the experts in the related fields. Automatic image extraction function however is relatively rare.

To solve these problems, in addition to the two query approaches using image or keyword, some systems also provide feedback strategies and ranking for refining the search query. The feedback strategies invite interactive inputs from the user to refine the query for subsequent retrieval. In addition to the relevant feedback, the ranking approach can also be incorporated to the user interface to provide a better capture on the relevancy of the result. In comparison to the CBIR systems, these approaches are simpler as the domain scope of CBMIR systems are better defined. Hence, the iteration cycles for the interaction between user and machine are less in CBMIR systems.

A popular approach for system such as MedPix is to use directory-like structure to guide user to construct a more accurate query. The advantage of this approach is the context of the query keywords are bounded by the directory entries established by the search engine site. In this way, the user is able to obtain more accurate search results.

6. Query Processing

Query processing, in any content-based retrieval systems, is a module between the user interface and the indexing structure. It acts as a module to bridge the semantic gap between the user's input and the actual query applied to the database. In short, it converts the user input into a feature vector to be applied for searching through the index tree. Thus, the approach applies to this component is tightly coupled with the design of the user interface and the image indexing structure employed by the system. Hence, the issues described in the previous section, that is, problems with keyword/s and image example, is mostly handled by this module.

6.1 Query by Keyword

One of the biggest challenges facing researchers in query with keywords is the ability to accurately represent the user input by the system-constructed query. One of the major reasons for the low accuracy of the search result is caused by miss-representation and the system's miss-interpretation of the user query. To a large degree, this is caused by the expressive nature of human language. Polysemy (word with multiple meanings), synonymy (different words with same meaning) and context sensitivity of a word or phrase are the primary reasons for the miss-interpretation of user inputs. In a narrow domain, these problems can be partly dealt with by applying techniques such as word dictionary, word stemming or thesaurus to reduce the ambiguity caused by the keywords. However, there is no CBMIR system to our knowledge that allows the user to construct more complex query such as "retrieve 5 images that looks 30% like the input image" or "red cat in the house".

6.2 Query by Image

In recent years, with the advancement of image processing techniques, query by image example has emerged as a preferred option for constructing searches in CBMIR systems. The reason being that query by image example can avoid the ambiguity issue surrounding with keyword query. Some systems also provide options for a user to specify the relative importance of each feature in the image, or functional features to let the user to manipulate the input image. All these extra options are designed for constructing queries that have a better representation of users' intention.

In query by image example, the query is constructed by extracting the relevant features from the input image and a search vector that uses these features. Weights can also be assigned to fine tune the importance of each element in the feature vector. Depending on the application, the weights of the feature vector can be explicitly assigned by users, or assigned by system through a system defined rule or relevance feedback from the user.

6.3 Relevance Feedback

The use of relevance feedback together with ranking is a means for the system to iteratively fine tune the feature vector through feedbacks from the user. It has not been found that any of the CBMIR systems are employing this technique. This may due to the fact that most of the CBMIR systems reported only apply to a very narrow scope domain. Nevertheless, if researchers are interested in integrating different medical modalities together, there is no doubt that such approach should have its place in CBMIR systems. Interested reader should refer to reference [10] for a comprehensive review on this technique.

7. Feature Extraction

Feature extraction is a core feature of any CBIR systems. This module is either directly or indirectly related

to all the different components in a CBIR system. In-fact, the selection of the indexing structure and design of the query processing unit is directly affected by this module. In the following paragraphs, the attention focuses on the discussion of visual features. A discussion on semantic feature is left to the subsequent section.

In the general CBIR systems, the standard approach for features extraction is to extract features such as colour, texture and shape. In the more advanced systems, the geometry information of the object/s in the image can also be extracted and analysed. The indexing structure is then constructed base on the combinations of these features information. These features in a general domain system are extracted and analysed by generic image-processing approaches. At the minimum, these image-processing approaches have to be robust and insensitive to the image size, viewing orientation and in some cases, object occlusion. For each of these visual features, there are various representations that represent the human perception of that feature from different perspectives. What features and representations to use will depend on the application, and sometimes, the selection process can be an art form in itself.

In comparison to the general domain retrieval system, the features selection process for CBMIR systems tends to be straightforward. Domain specific applications such as diagnostic systems [2, 3, 5] can apply their domain knowledge to assist the selection of important features required in identifying the disease, tumor or condition that the specialist is interested in.

8. Indexing

In order to make any CBIR systems truly scalable for large size image collection, the images are required to be indexed in a systematic manner. In a traditional database system, the data is indexed by a search key or combination of keys that uniquely identify an individual record. Often, a simple one dimensional data structure is adequate enough for indexing the data in such systems. However, images are more complex. Attempts to reflect this complexity usually results in images being represented by a set of values or attributes, commonly known as the feature vector. When represented in this manner, each value in the set becomes a point in an n-dimensional space, implying a multi-dimensional structure is required.

So far, the research efforts for indexing structures applied to CBMIR systems have been mostly revolved around two issues, and they are:

1. What data to be indexed?
2. How is the data organized?

These two issues are rather common in database and data structure communities. However, with the complexity of images and the high dimensionality of the visual features, the answers to these two questions may not be as trivial as it is for the traditional text database systems.

8.1 Indexing Value

In the previous section, we have discussed the possible visual features that can be used in indexing the image databases. However, visual features are only one of the possible features that can be used for indexing images. Depending on the application, image index structure can also be grouped by keywords, which is a great tool for capturing the semantic content of the images. In some cases, the image database may be better represented with the combination of semantic and visual features.

Cha and Chung [11] have proposed an approach that allows an image to be indexed by three separate indexing trees, and these index trees are: visual features, semantic and keyword indexing. The visual features are the combination of shape, color and texture. The semantic features of the system consist of a set of predefined attributes, and the keyword features are texts that are entered by users. The values of these attributes are stored in metadata format. These separate indexing structures provide the user with the flexibility to construct very complex query.

8.2 Indexing Structure

Indexing structure has been an interest for researchers for many years. This is mostly because it is essential to have a fast and efficient indexing structure for the database system to be scalable. As for CBMIR systems, many researchers have added two addition requirements to the system's indexing structure. The indexing structure has to be multi-dimensional and dynamic.

Multi-dimensional index is a structure that is often used in indexing large and complex data. These data include audios, videos, images and etc. Indexing tree is the most common used indexing structure for image database, and there are different types of indexing trees designed to accommodate different query requirements. Reader can refer to Reference [1] for a comprehensive review on the difference tree-based indexes available for image data.

One of the issues in applying indexing tree is the dimensionality of the index. The performance of the multi-dimensional indexing structure such as popular R-tree and R*-tree degenerates drastically with an increase in the dimensionality of the underlying feature space, this is mostly because the trees' fan-out decreases in inversely proportional to the dimensionality. To solve this problem, one promising approach is to first perform dimension reduction and then to use appropriate multidimensional indexing techniques for searching and retrieving images.

Even though the dimension of the feature vectors in most of the image retrieval systems is very high, not all the features posses the discriminatory power for being able to uniquely identify the images. There are various approaches in identifying the importance of an attribute in the feature space. Karhunen-Loeve transform (KLT), also known as principal component analysis (PCA), can be applied to identify the importance of the features in the principle component space. Different from KLT, Park et al. [12] used Quasi-Gabor Filter to reduce the dimensionality of the texture features.

Clustering is another powerful tool in performing dimension reduction. This approach cluster similar features together to perform recognition or grouping. This type of clustering is called row-wise clustering. Similarly, Zhang and Zhong [13] used self-organization map (SOM) neural networks as the tool for constructing the tree indexing structure. This approach provides the advantage of unsupervised learning ability, dynamic clustering nature, and the potential of supporting arbitrary similarity learning.

9. Conclusion and Remark

This paper briefly discussed the major components in the CBMIR systems, and a comparison is drawn with the generic CBIR systems wherever possible. Although the issues faced by both systems are common, the design approaches for the systems are quite dissimilar. Also, the approaches in designing the system components are vastly different. The strategies adopted in designing components such as user interface, query processing and the feature selection unit for the two systems are also vastly different. This is mostly because the scope of CBMIR systems is bounded by the systems' knowledge domain. Hence, certain assumptions can be made in CBMIR systems. It is recognised that CBMIR systems are still in an early stage of development. This is evidence in the lack of systems reported from the literatures. This should not be a surprise as the systems reported are only for diagnostic, decision support or teaching purpose. The application for these systems is very specific. The approach applied in these systems is also not generic enough to be transferred to other applications. Hence, there are ample rooms for future work in expanding the functionalities of both systems.

References

[1] H. D. Tagare, C. C. Jaffe, and J. Duncan, "Medical Image Databases: A Content-based Retrieval Approach," *Journal of the American Medical Informatics Association*, vol. 4(3), pp. 184-198, 1997.

[2] P. Korn, N. Sidiropoulos, C. Faloutsos, E. Siegel, and Z. Prtopaps, "Fast and Effective Retrieval of Medical Tumor Shapes," *IEEE Transactions on Knowledge and Data Engineering*, vol. 10, pp. 889-904, 1998.

[3] C.-R. Shyu, A. Kak, C. E. Brodley, and L. S. Broderick, "Testing for Human Perceptual Categories in a Physician-in-the-loop CBIR System for Medical Imagery," presented at IEEE Workshop on Content-Based Access of Image and Video Libraries, Fort Collins, Colorado, 1999.

[4] D. Comaniciu, P. Meer, D. Foran, and A. Medl, "Bimodal System for Interactive Indexing and Retrieval of Pathology Images," presented at 4th IEEE Workshop on applications of Computer Vision, Princeton, New Jersey, 1998.

[5] L. R. Long, S. K. Antani, and G. R. Thoma, "A Prototype Content-based Image Retrieval system for Spine X-rays," presented at 16th IEEE Symposium on Computer-Based Medical Systems, New York, New York, 2003.

[6] C. T. Liu, P. L. Tai, A. Y.-J. Chen, C.-H. Peng, and J. S. Wang, "A Content-based Medical Teaching File Assistant for CT Lung Image Retrieval," presented at The 7th IEEE International Conference on Electronics, Circuits and Systems, Lebanon, 2000.

[7] Y. Rui, T. S. Huang, and S.-F. Chang, "Image Retrieval: Current Techniques, Promising Directions, and Open Issues," *Journal of Visual Communication and Image Representation*, vol. 10, pp. 39-62, 1999.

[8] T. M. Lehmann, B. Wein, J. Dahmen, J. Bredno, F. Vogelsang, and M. Kohnen, "Content-Based Image Retrieval in Medical Applications: A Novel Multi-Step Approach," presented at Proceedings of SPIE, 2000.

[9] A. W. Smeulders, M. Worring, S. Santini, A. Gupta, and R. Jai, "Content-Based Image Retrieval at the End of the Early Years," *IEEE Transactions on Pattern Analysis and Machine Intelligence*, vol. 22(12), pp. 1349-1380, 2000.

[10] X. S. Zhou and T. S. Huang, "Relevance Feedback in Image Retrieval: A Comprehensive Review," *ACM Multimedia Systems*, vol. 8 No. 6, pp. 536 - 544, 2003.

[11] G.-H. Cha and C.-W. Chung, "An Indexing and Retrieval Mechanism for Complex Similarity Queries in Image Databases," *Journal of Visual Communication and Image Representation*, vol. 10, pp. 268-290, 1999.

[12] M. Park, J. S. Jin, and L. S. Wilson, "Fast Content-Based Image Retrieval Using Quasi-Gabor Filter and Reduction of Image Feature Dimension," presented at Fifth IEEE Southwest Symposium on Image Analysis and Interpretation, Santa Fe, New Mexico, 2002.

[13] H. J. Zhang and D. Zhong, "A Scheme for Visual Feature based Image Indexing," presented at Proceeding of SPIE Storage and Retrieval for Image and Video Databases, 1995.

Case Based Reasoning Models in Management Application

Fariba Shadabi
Division of Health, Design and Science,
University of Canberra, ACT 2601,
Australia

Mehrdad Khodai-Joopari
School of Computer Science, University of
New South Wales (ADFA campus), ACT 2600,
Australia

Abstract

In this study we investigate the need for Case-Based Reasoning (CBR) model calibration. This paper also presents some guidelines on building CBR model tailored to a specific management application. To address some of the practical issues associated with the use of case-based reasoning or estimation by analogy, we conducted an experiment on software effort estimation using a well-known project effort dataset, namely Albrecht. We found that pruning the irrelevant features can improve the performance of CBR applications and it is essential to calibrate the prediction model carefully.

1. Introduction

Over the years a variety of techniques have been purposed for management application such as loan evaluation and diagnosis programs. In recent years there has been great amount of interest on the application of case-based reasoning (CBR) [1], [2], [3]. This technique solves new problems by adapting solutions that were used to solve old problems.

The CBR approach is easy to understand and apply. The model can be used in conjunction with expert judgment. End-user can participate in the prediction process and use his or her judgment to modify (adopt) the prediction. However there are some important design decisions that must be made in order to generate a reasonably accurate estimation [1]. Such decisions include choice of distance metrics or similarity measures in order to measure the level of similarities between cases, number of most similar cases that need to be used to generate the estimation and choice of optimum feature set that gives the most accurate estimation. Studying the importance of these design decisions was the motivation for this paper.

Research shows that case-based reasoning or estimation by analogy can be successfully adapted in software effort or cost estimation domain [1], [4], [5], [6]. ANGEL [7] and CBR-Works [8] are two examples of CBR tools, which can make use of previous projects to estimate effort for a new project (see [9] for other CBR tools currently available on the market). The goal of this paper is to present some of the practical issues associated with the use of CBR models in cost estimation as a prototypical management application.

2. Research Method

The idea of effort estimation by analogy has been around for a long time, however this method has not been widely used. Shepperd and Schofield (1996) presented the idea of estimation by analogy in the form of detailed estimation methodology and developed a CBR tool [10], called ANGEL (ANaloGy Estimation tooL).

In order to investigate the effects of certain parameters in accuracy of CBR applications we used ANGEL [7], CBR-Works 4.0 [8] and a CBR system that was developed during this study. The CBR-Works tool can be used for the development and maintenance of management applications in a variety of domains and environments [11]. Throughout this study, we used a well-known dataset, namely Albrecht.

In this section, the Albrecht dataset and the measurements used to evaluate CBR modeling techniques will be briefly described.

2.1 Dataset

For our investigation we used the Albrecht dataset, which is a publicly available dataset [12], [13]. Albrecht is a relatively small (24 cases) software development project dataset. During this investigation it was decided to keep the original dataset as intact as possible.

A statistical summary of all the features (metrics) in the Albrecht dataset is presented in Table 1.

Table 1. Summary statistics for Albrecht dataset

Feature	Count	Min	Max	Mean	Median	St. Dev	Skewness
Effort	24	0.5	105	21.9	11.5	28.4	2.3
FP	24	100	1902	643.3	506	493	1.5
File	24	3	60	17.4	11.5	15.5	1.5
Input	24	7	193	40.3	33.5	36.9	3.3
Inquiry	24	0	75	16.9	13.5	19.3	2.1
Output	24	12	150	47.3	39	35.2	1.4
SLOC	24	3	318	61.1	51.7	63.7	3.1

2.2 Performance Evaluation

In order to study the accuracy of the estimation models, we adopted the jackknifing technique. This technique is also known as leave-one-out cross validation. Each completed project in turn was removed from the dataset and the remaining dataset was then used to estimate the effort for the removed project. MMRE (Mean Magnitude of Relative Error) and PRED (25) were computed from the jackknifing process [14]. MMRE is an error measurement method that has been used by various researchers [15], [16], [17]. Smaller MMRE value indicates better prediction model. MMRE is defined as:

$$100/n\sum_{i=1}^{n}\left(\frac{|\,ActualEffort-\Pr edictedEffort\,|}{ActualEffort}\right)_i$$

Where n represent the number of projects in the dataset.

Pred (25) measures the proportion of predictions that are within 25% of the actual values. Clearly, the higher this value is, the better.

3. Experiment Results

During this study we had to decide upon five parameters as follows:

Scaling or Standardization: All feature's values for the projects can be standardized between 0 and 1. By performing standardization we can ensure that all features have equal influences to the measure of similarity and the method is immune to the choice of units.

Feature set: All collected features may not be helpful in finding a good estimation. By the use of brute force algorithm, ANGEL can automatically determinate the best subset of features. However the brute force algorithm uses exhaustive search, so as the number of features increase the process gets slower [1]. Unlike ANGEL, CBR-Works cannot determine the best possible feature set for a particular dataset.

Similarity measure: Here the question is how much the new project is similar to the other projects in the available dataset. One good feature of CBR-Works is that it provides a variety of retrieval algorithms such as:

- Euclidean distance: The formula is similar to the one used in ANGEL. The CBR users can assign different weights to the features in order to reflect the relative importance of each feature.
- Average: The average similarity of all attributes defines the case similarity.
- Maximum: The highest feature similarity defines the case similarity.
- Minimum: The lowest feature similarity defines the case similarity.

Number of analogies: Number of analogies refers to the number of closest projects that can be used to generate estimation for the new case. The simplest way is to consider only the effort of the most similar case as estimation for the new case (1 analogy). However there are other alternative strategies that can be considered [18]. In this study we used 1,2 and 3 analogies similar to [1].

Analogy adaptation: When the analogy projects are selected, the question is what would be the best analogy adaptation technique so that the best estimation for the new case can be generated? We decided to choose the same adaptation process that have been used previously by Schofield [1] as outlined below:

- One analogy: Estimation for new case is the effort from the closest analogy.
- Two analogies: Estimation for new case is the average of efforts for the closest two analogies.
- Two analogies (Weighted): Estimation for new case is the average of efforts for the two closest analogies; however the closest analogy is weighted double.
- Three analogies: Estimation for new case is the average of efforts for the closest three analogies.

Table 2 shows the MMRE and Pred (25) results obtained for the following scenarios:

1. When the full features available in the dataset were used through CBR-Works.

2. When optimum combination of features was generated for use via ANGEL.

The results suggest that for the Albrecht dataset ANGEL outperforms CBR-Works. The results reveal that the performance of CBR-Works is poor because it is not calibrated correctly.

Table 2. Comparing ANGEL and CBR-Works models

Feature	Analogy	MMRE %	Pred (25) %
Full set of features (Using CBR-Works)	One	96	16
	Two	74	33
	Two (W)	129	21
	Three	85	21
Optimum features Subset (Using ANGEL)	One	67	33
	Two	66	37
	Two (W)	**61***	**41***
	Three	62	33

In configuring the CBR-Works we had to make decisions concerning similarity function, retrieval algorithm and pruning the feature set. We tried to find the best feature set that minimize the mean absolute relative errors by assigning different weights to the features, based on their relative importance.

Table 3. Comparison of distance measures

Dist. Metric	Analogy	MMRE %	Pred (25) %
Euclidean (Unweighted)	One	96.47	16.66
	Two	74.20	33.33
	Two (W)	129.47	20.83
	Three	85.01	20.83
Average (Unweighted)	One	97.40	16.36
	Two	**71.25***	**33.33***
	Two (W)	126.05	20.83
	Three	83.38	20.83
Euclidean (Weighted)	One	78.47	16.66
	Two	75.80	33.33
	Two (W)	118.86	20.83
	Three	75.18	29.16
Average (Weighted)	One	99.27	12.50
	Two	75.56	33.33
	Two (W)	128.74	16.66
	Three	87.00	20.83

An obvious choice to determine the degree of importance for each feature was to choose only features that have a strong statistical influence on effort. The results suggest that different configurations of CBR-Works may produce different levels of accuracy. As can be seen from Table 3, two analogies, with average retrieval algorithm (unweighted) was found to be the most accurate prediction by predicting 33% of projects within 25% of their actual effort and with MMRE of 71%.

3.1 Practical Advice

Many CBR tools are currently available on the market [9]. In this paper, CBR-Works, 4.0, was used to implement different CBR techniques for estimating the development effort.

The ANGEL is another CBR tool that previously was used by Schofield [1] for the purpose of software cost estimation. Both estimation tools are provided with an easy-to-use interface that can support the stage of data collection, effort prediction and adoption rule. However the functionality of collecting and pasting specific items were not provided in neither of them. These functionalities can be a great help for the person responsible for reviewing the model and ensuring its accuracy.

A tool for estimating the development effort, based on analogy can be easily implemented in any programming language. Readers who are building their first CBR system and are interested in most important issues in building and maintaining CBR systems should refer to [9], [19] and [20] for more information. Figure 1 shows the prototype for automatic software estimation that we developed using MATLAB[1]. The purpose of this tool is to help project managers make important decisions regarding certain parameters (e.g. number of analogies or distance metrics) when analogy based estimation is required. We named the tool "Calibration of the Analogy Procedure". This tool needs relatively little effort in order to generate useful results.

[1] MATLAB is a commercial (Matrix Laboratory) package. More information also can be found on: http://WWW.math.ufl.edu/help/matlab-tutorial/matlab-tutorial.html

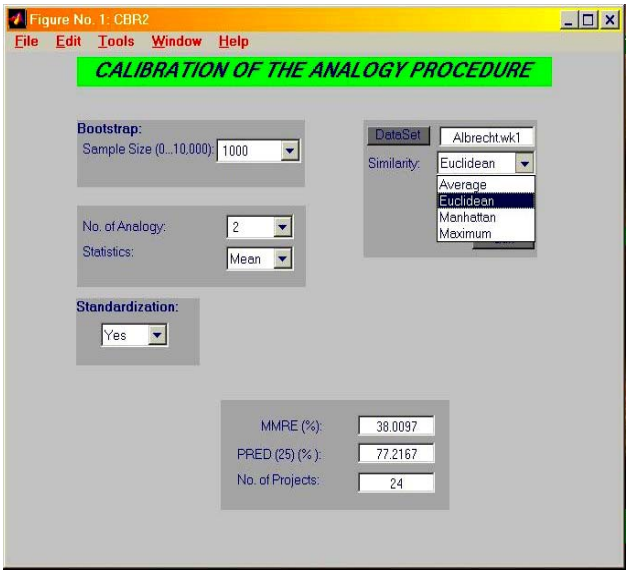

Figure 1. An example of Calibration of the Analogy Tool

The results in Table 4 have been obtained using four similarity measures, namely Euclidean (Un-weighted), Average (Un-weighted), Manhattan [18], Maximum, six choices for number of analogies (2,3,5,10,15 and 20), one choice of calculating the analogy (mean) and based on standardized (Std) /non-standardized feature values.

As can be seen from Table 4, two analogies, with average or Euclidean retrieval algorithm (non-normalized values) was found to be the most accurate prediction by predicting 67% of projects within 25% of their actual effort and with MMRE of 57%.

The results in Table 5 were generated with the help of a statistical simulation method, namely bootstrap in order to generate multiple samples for the accuracy indicators [18], [20]. This method can help the user to assess the accuracy of the tool or calibrate the analogy tool before its application to real projects. The results confirmed that two analogies, with average or Euclidean retrieval algorithm is the best choice.

Table 4. Comparison of various parameters in estimation by analogy

Distance	Analogy	Std	Statis-tic	MMRE (%)	PRED (25%)
Average	2	Yes	Mean	62.78	54.17
		No		**56.89**	**66.67**
	3	Yes	Mean	66.19	58.33
		No		66.18	58.33
	5	Yes	Mean	71.92	54.17
		No		83.48	20.83
Euclidean					
	2	Yes	Mean	62.78	54.17
		No		**56.89**	**66.67**
	3	Yes	Mean	66.19	58.33
		No		66.18	58.33
	5	Yes	Mean	71.92	54.17
		No		83.48	20.83
Manhattan					
	2	Yes	Mean	64.34	54.17
		No		62.02	58.33
	3	Yes	Mean	73.40	50
		No		73.96	50
	5	Yes	Mean	76.59	50
		No		83.77	25
Maximum					
	2	Yes	Mean	90.18	33.33
		No		62.02	58.33
	3	Yes	Mean	81.01	33.33
		No		73.96	50
	5	Yes	Mean	63.04	0
		No		83.77	25

Table 5. Comparison of various parameters in estimation by analogy (1000 bootstrap samples)

Distance	Analogy	Std	Statistic	MMRE (%)	PRED (25%)
Average	2	Yes	Mean	**38.12**	**76.72**
		No		40.65	75.21
	3	Yes	Mean	48.96	67.88
		No		52.14	61.45
	5	Yes	Mean	60.05	50.11
		No		70.66	51.34
Euclidean					
	2	Yes	Mean	**38.28**	**77.09**
		No		44.69	75.28
	3	Yes	Mean	49.09	67.64
		No		52.69	61.89
	5	Yes	Mean	59.95	49.70
		No		70.36	51.65
Manhattan					
	2	Yes	Mean	40.95	74.10
		No		43.19	73.33
	3	Yes	Mean	52.34	65.82
		No		54.21	59.30
	5	Yes	Mean	64.52	45.18
		No		71.38	52.37
Maximum					
	2	Yes	Mean	53	55.79
		No		42.99	73.19
	3	Yes	Mean	58.69	56.16
		No		54.54	59.37
	5	Yes	Mean	54.27	31.68
		No		70.93	50.67

Each organization applying analogy can design and implement a tool similar to the tool implemented in this study to meet their needs and generate useful results.

4. Conclusion and future work

Case-based reasoning or estimation by analogy is a relatively simple technique however it is essential to calibrate the prediction model carefully. Each organization applying analogy may design and implement a CBR tool tailored to their needs. Estimator should review the accuracy of CBR models at various time periods and configure the tool in best possible way (e.g. choosing the best combination of parameters). Clearly still there is a need for further investigation in this area.

As a continuation of our current work, we are currently developing a tool for predicting the outcomes of renal transplants and the type of graft rejection based on analogy. We also plan to compare the performance of CBR techniques in predicting medical outcomes against Artificial Neural Networks models.

References

[1] Schofield, C.: An Empirical Investigation Into Software Effort Estimation By Analogy**.** PhD thesis (1997)

[2] Kadoda, G., Cartwright M.: Issues on the effective use of CBR technology for software project prediction. Poole, UK, School of Design, Engineering Research Group, Bournemouth University (2001)

[3] Mendes, E., Watson, I.: A comparison of Development Effort Estimation Techniques for Web Hypermedia applications. International Software Metrics symposium (2002)

[4] Bisio, R., Malabocchia, F.: Cost Estimation of Software Projects Through Case Based Reasoning. International Conference on Case Based Reasoning, Sesimbra Portugal (1995)

[5] Finnie, G. R., Writtig, G. E.: A Comparison of Software Effort Estimation Techniques: Using Function Points with Neural Networks, Case-Based Reasoning and Regression Models. J.SYSTEMS SOFTWARE (1997) 281–289

[6] Walkerden, F., Jeffery R.: An Empirical Study of Analogy-based software effort Estimation. The University of New South Wales, Technical Report (1998)

[7] http://dec.bmth.ac.uk/ESERG/ANGEL/

[8] CBR-Works, 4.0 beta. Research group.: Artificial Intelligence-Knowledge-Based System, University of Kaiserslautern http://wwwagr.informatik.uni-kl.de/~lsa/CBRatUKL.html

[9] Watson. I: Applying Case-Based Reasoning: Techniques for Enterprise Systems. Morgan Kaufmann publishers Inc. (1997)

[10] Shepperd, M., Schofield C., Kitchenham, B.: Effort Estimation Using Analogies. Proceeding of 18th int. conference on software engineering, IEEE Com. Soc. Press (1996)

[11] Stefan, S.: CBR-Works - A State-of-the-Art Shell for Case-Based Application Building. Proceedings of the German Workshop on Case-Based Reasoning, GWCBR'99. Lecture Notes in Artificial Intelligence Springer-Verlag (1999)

[12] Albrecht, A. J.: Measuring Application Development Productivity. Proceedings of the IBM Applications Developments Symposium. (1979)

[13] Albrecht, A. J., Gaffney, J. E.: Software Function, Source Lines of Code, and Development Effort Prediction: A

Software Science Validation. IEEE Transactions on Software engineering 9(6) (1983) 639-648

[14] Conte, S., Dunsmore, H., Shen, V.Y.: Software Engineering Metrics and Models." Menlo Park, Calif.: Benjamin Cummings (1986)

[15] Low, G. C., Jeffery R.: Function Points in the Estimation and Evaluation of the Software Process. IEEE Transactions on Software engineering 16(1) (1990) 64-71

[16] Kemerer, C.: An Empirical Validation of Software Cost Estimation Models. ACM 30(5): (1987) 416-429

[17] Mukhopadhyay, t., Vicinaza, S. S., Prietula, M. J.: Examining the feasibility of a case-based reasoning model for software effort estimation." MIS Quarterly 16(2) (1992) 155–171

[18] Angelis, L., Stamelos, I.: A simulation Tool for Efficient Analogy Based Estimation. Empirical Software Engineering (2000) 35-68

[19] Heister, F., Wilke, W.: An Architecture for Maintaining Case-Based Reasoning Systems. Advances in Case-Based Reasoning, 221-232, Springer LNAI 1488, Berlin (1998)

[20] Efforn, B., Tibshirani, R.: An introduction to the Bootstrap (1998) New York: Chapman and Hall (1993) Gennari, J., et al., Templates for IEEE Proceedings, available at <http://www.sheridanprinting.com/ieee/ieee.htm>

EXPERT, FUZZY & NEURAL SYSTEMS III

(This page left blank intentionally)

Short Term Power System Forecasting Using an Adaptive Neural-Fuzzy Inference System

Cameron Potter
School of Engineering
University of Tasmania
Sandy Bay, Tasmania, Australia
Cameron.Potter@utas.edu.au

Michael Negnevitsky
School of Engineering
University of Tasmania
Sandy Bay, Tasmania, Australia
Michael.Negnevitsky@utas.edu.au

Abstract

This paper presents an application of an Adaptive Neural-Fuzzy Inference System (ANFIS) *to power forecasting problems. The need for accurate forecasts is increasing as power markets are becoming more competitive. This paper gives a brief overview of the issues facing power system forecasting and proposes the use of ANFIS to perform short term scheduling. Finally, it gives a comparison against other techniques that have been previously presented, highlighting ANFIS favourably.*

1. Introduction

The operation of a power system is usually divided into four different categories: long term, medium term, short term and real-time [1]. Long term forecasting is primarily associated with maintenance scheduling and generator lifespan. It considers time frames well over a year in advance. Medium term scheduling is used primarily for fuel planning and ensuring that the system will continue operations between maintenance checks and upgrades. It generally considers time frames from a week to a year ahead. Short term scheduling is the operation of a power system from anywhere between five-minute load schedules to week-ahead planning. It is the operation that ensures that loads are capable of being met and are being met in an efficient manner. Lastly is real-time scheduling, based on the operation of the machines themselves. Real-time scheduling focuses on supplying the energy to meet the goals that are set, while preserving operation limits on the machines.

This paper investigates short-term forecasting for a power system. However it especially centres on a sub-class referred to as *very* short term forecasting. Very short term forecasting is predominantly focussed on predicting the value of the next period of an applicable data set. In this instance, that period will be the operating cycle of the National Electricity Market of Australia.

2. Overview of the National Electricity Market

The National Electricity Market (NEM) is managed by an overseeing body called the National Electricity Market Management Company (NEMMCO). The NEM is a wholesale power pool to which the generators sell the power they produce and the distributors buy the power they need to sell to their clients. This form of power system is known as a "deregulated system". The generators make a bid to supply a certain amount of power at a chosen price and NEMMCO receives the generators' bids, ranks them according to price and accepts enough bids to satisfy the projected demand plus a safety margin. Usually this means that the last bid accepted is accepted as a partial amount. The highest accepted bid price is the price that each supplier receives for the power that they produce in that time period, regardless of their individual bid price. Finally, most generators and distributors have a majority of their power resources set in contracts. These contracts are unaffected by the spot price market so far as the customer is concerned. However, the generators can choose to buy power from the spot price market to fill their contracts if they either cannot make the contract themselves or it would be more economical to do so.

3. General Overview of Power System Operation

Short term scheduling is widely recognised as an essential element of power system operation [2]. It is a complex problem as there is no ideal solution. Certain generators operate better under different operating systems and schemes. Due to high production costs, small increases in efficiency also lead to large savings. This means that utilities are always in pursuit of a more efficient means of short term operation.

When considering short term scheduling and economic dispatch, accurate demand forecasts are essential [3]. The forecasts are used to try to reduce the difference between the power available and the power consumed. The use of forecasting techniques for load forecasting is a topic widely discussed in power engineering. Another less discussed, but no less useful, parameter is that of electricity prices. Traditionally, these "spot prices" have been difficult to predict and when investigated by a human, it is near impossible to discern any pattern in changes of spot price. This paper shows a way to overcome this issue.

4. Power System Specifics

In order to schedule a power system correctly, it is essential to know how that particular system operates and what

factors are most important to optimise. Generally, a system can be considered as fossil fuel-based or renewable, but even that distinction is somewhat blurred. However, for the purposes of this paper it will be convenient to use these two titles as all-encompassing categories. The fossil fuel based systems destroy the fuel they use, but can purchase more when needed. The renewable energy systems do not destroy the fuel, but the access to the fuel is limited.

4.1. Fossil Fuel Based Systems

Fuel based systems are diverse and include many variations that can solve most generation issues. Nuclear power has low running costs, but initial expenses are high. Gas power has low initial expenses, but running costs are relatively high. In the middle of these extremes is coal-fired generation. The coal-based and nuclear tend to have slow ramp-rates (rate at which the level of operation can be altered).

For a system that cannot be altered rapidly, once the system is turned on, it is committed to operation for a significant period of time. This means that the cheaper to operate systems, are also less flexible and sometimes even have to incur losses at low spot price periods in order to continue operations. To have a fossil fuel based power system that can rapidly respond to changes in demand, high-cost gas-fired stations must be used. The other alternative is to consider a renewable system.

4.2. Renewable Systems

Renewable systems also have diverse potential for generation. Hydro generation has the advantage of quick response, while wind and geothermal energy have the advantage of providing a non-exhaustible (within practical limits) supply of power. Furthermore, the energy sources used to produce the electricity are free. However, these systems do have their own shortcomings.

Renewable systems have a high installation cost and so have been prohibitively expensive to nations with closely limited resources. Wind and geothermal energy are not able to be stored in their own right. Hydro power, which can be stored, is not always available. If there is a drought, or even a period with less rain than forecast, this can cause problems with the operation of a hydro system. However, even with these negative aspects, in developed countries, most locations that could be used to generate renewable power (especially hydro) are being investigated or utilised [1]. Thus, most countries rich enough to afford the initial outlay agree that the advantages of free energy in the long term outweigh the negatives of renewable power – the fact it is environmentally sustainable is becoming more important as well.

5. Necessary Forecast Parameters

To efficiently operate a power system, it is important to have good predictions for the characteristics that determine the system's operation. For instance, unless the wind speed it accurately forecast, it becomes difficult to properly schedule any wind resources. This paper is based on very short term forecasting of demand (or load) and spot price data.

A typical load profile is relatively smooth and responds well to forecasting techniques. However, even the best predictions still tend to have significant errors associated with them.

Load forecasting has been approached in several ways, including weather dependent, weather independent and a combination of the two [3]. While, these have met with comparable levels of success, the weather independent models' main advantage is that there is no need to include another predicted variable (weather). This comes at the slight expense of accuracy. However, some power stations are very dependent upon the weather predictions for other operating parameters and thus the accuracy is more important as the weather predictions are already an integral part of the system.

Load forecasting is extremely important and has been researched quite extensively using traditional methods and in recent years, artificial intelligence techniques have also been applied to this field.

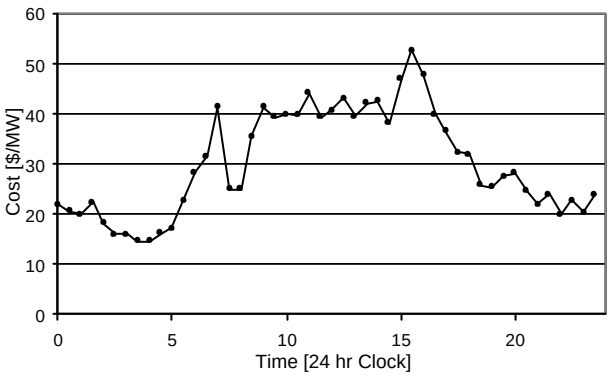

Figure 1: 20 February 2002. Typical summer day for Victoria, Australia. Data derived from NEMMCO site.

Spot price forecasting is a new area of research. Deregulation of power markets is still relatively new (beginning around 10 years ago) and the accurate forecasting of spot price data has had very little written

about it. The most likely reason for this is the difficultly in obtaining good results and the limited application of most techniques so far investigated.

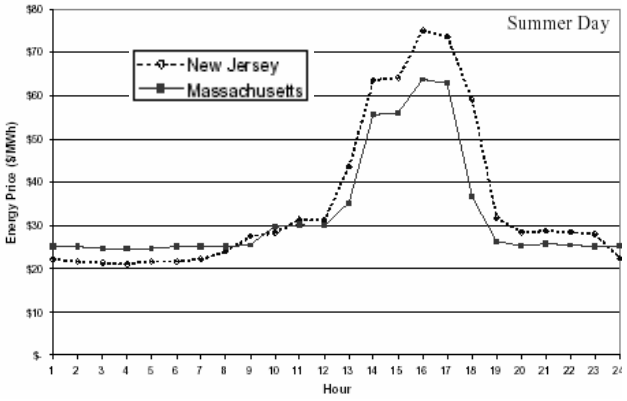

Figure 2: Typical summer day for large American spot price power pools. Tabors Caramanis and Associates developed this figure for a report [4].

Often an application is so site specific that there is no way that it can be used to forecast for another region. Furthermore, the very essence of the spot price data can vary greatly from region to region. Figure 1 shows a typical summer day's data from the Victorian (Australia) spot price energy pool and Figure 2 shows a typical summer day's data from New Jersey and Massachusetts (USA).

The two figures show that the smaller market (Victoria) is far more difficult to predict. A smaller market means load fluctuation has a more pronounced effect. This research applied new techniques to forecast this data.

6. Forecasting Technique

This paper proposes an application of a new forecasting technique that looks very promising. This technique was to use an Adaptive Neural-Fuzzy Inference System (ANFIS).

Traditionally, power systems operators have been focussed on load forecasting and used conventional mathematical procedures to try to predict future load values. There were several separate techniques applied from the mathematical domain [5]. Multiple linear regression (MLR) is used to derive the forecast value from other values that affect it. Stochastic time series (STS) forecasting works by creating a model, which essentially acts as a filter to a white noise input. There are numerous techniques that can be used as part of this encompassing heading. General exponential smoothing (GES) works by developing a fitting function to create a smooth transition from point-to-point (a likely behaviour of load). State space (SS) and Kalman filter is a general forecasting approach that utilises state space mathematics to combine several models to create a better overall system.

Then knowledge-based systems (KBS) started being investigated and were found to work well although were difficult, or even impossible (if there was no available expert), to implement. The next generation of forecasting measures was based on artificial neural networks (ANN). ANNs worked very well, but had the problem of over-fitting or "memorisation". As forecasting can include a very wide range of data with sharp spikes, a large amount of training data is necessary to be able to handle unusual events. Although, if too much information is used to train an ANN, the ANN will adjust to predict the training data very well, but not be able to handle new data.

6.1. The ANFIS model

ANFIS is a hybrid system that combines the low-level computation power of neural networks with the high-level reasoning capability of a fuzzy inference system [6, 7]. This research has been implemented using a version of ANFIS in the "Matlab Fuzzy Toolbox".

The easiest way to understand how the ANFIS model operates is to consider it in two steps. Once trained, the system operates as a fuzzy expert system would. Information is input, fuzzy rules are fired and a corresponding output is achieved. However, the training is more like that of a neural network (although not identical).

As with a supervised-learning neural network, the fuzzy system is trained with a set of data called a training set. This set is represented by several subsets of inputs and one desired output for each subset. Where it differs is in the selection of model parameters.

To use the ANFIS model, the user defines the number of inputs; the number of membership functions (MFs) and their type, and the number of epochs of training. One of the more unusual aspects of the ANFIS model is that changing even one of these parameters be the difference between a system that appears to be not working at all and a system that produces almost perfect results. This is exemplified in the *Results* section of this paper.

The number of inputs for this work was varied between 4 and 6 and it was found that the more inputs that were used, the better the result became. However, this also came at the cost of speed of training. When four inputs were used, it was possible to operate with three MFs, however, with six inputs, the number of MFs was limited to two (within reasonable training times). It was also noticed that in some cases, a system with four inputs and only two MFs outperformed a system with four inputs and three MFs.

This was due to a form of over-memorisation. The rules became too specific and could not handle a wide variety of test cases. Thus, for this example, it was found that six inputs and two MFs were the best combination.

The number of epochs is another factor that is very different from a standard ANN training regime. Generally an ANN will be trained for anywhere up to 1000 epochs (and is some cases even more). However, the ANFIS model trains in such a way that the number of epochs is of far less importance. Each epoch of an ANFIS model can take several minutes (or more) by itself and generally makes very little change after the first epoch, provided the training parameters are well chosen. Thus, the number of epochs for this work has been set to one.

The last of the parameters to be chosen was the type of MF. The type of MF is generally a "bell function", such as the Gaussian distribution function. This is a very good function for precise work and will function better if the system is relatively smooth and trained to cover all likely events. However, it does lack the robustness of some of the simpler membership functions.

6.2. Measures to Ensure Robustness

In the beginning sections of this work, the ANFIS was being trained with the bell function for its MF and was using a linear set of training data. When tested on intermediate sections between the test data, such as system gave almost perfect results. However, the results were less impressive for later test data and unusable for unusual and spikey test data. This showed the need for some added robustness to the ANFIS predictor.

The first step taken was to randomise the training data. For this project, the training set was initially chosen as every day in January 2002. To randomise the data, the training set was still selected in day-sized sections from the January data, however, now the sections began from different times of day and also occurred in a random order.

The next step to ensure robustness was to search the previous year (2001) for unusual events and randomly include these in the training data. This meant that the training set was "seeded" with large spikes so the model could accurately predict such events.

Another step that was taken was to change the input configuration. The inputs used were derived from previous data points, however, rather than simply taking the six points previous to the forecast point, it was found that taking a wider set of inputs improved the results. The final outcome was using the last, second last, third last, fifth last, seventh last and ninth last points gave the best results.

Even with these additions, it was found that the results were yet to reach an acceptable level on a consistent basis. Investigation showed that the ANFIS model was having difficulty in predicting the next point due to the coarse nature of the data. Figure 1 shows an example of spot price data and note the drop from 07:00 to 07:30.

With such rapid changes between data points, a successful forecast was almost impossible. Thus some attempt had to be made at bridging the gap between points. The first inclination is to use spline interpolation. However, interpolation is not possible between a known point and an unknown point (the point to be forecast). Thus, interpolation was used where possible in order to obtain input data, but another technique had to be used to obtain other the intermediary points leading to the desired forecast point. This was essentially a forecast to predict each intermediary point, which was in turn was used to predict the next point and so on, until the wanted prediction was reached. At that stage, the latest point was known again and interpolation was used to replace all the predicted intermediary points with real interpolated data. The actual time step that was used created 10 sub steps between each data point.

The last measure to ensure robustness was to try changing the MF type. Until this stage, large events still caused massive overshoot and undershoot as even with the seeded training set, the fuzzy rules were incapable of being trained to account for very rapid rises. This repetition of error lead to experimentation with other MFs. It was found that the more basic the MF was, the more robust the system was. However, the robustness did come at a slight cost of accuracy during the rest of the test data (see Table 4).

6.3. Predicting Difference to Improve Short Term Accuracy

One of the key features of the technique and results presented in this paper is using ANFIS to predict difference between points instead of raw data points themselves. The prediction of difference instead of the data points themselves presented some interesting problems. Difference data tends to be even more unpredictable than the data it is derived from. Thus, it is difficult to tune an ANFIS to predict the difference data correctly. However, when the difference data is properly predicted, the end results are improved and so is the robustness. During this work, difference data prediction was used and compared to similar systems that did not use difference prediction and those using the difference method were found to perform better. The reason for this is that while the difference data itself is more difficult to predict accurately, the prediction will be of smaller numbers, resulting in smaller total errors

in the true prediction data. Unfortunately, this technique is limited to very short term (or possibly short term) forecasting as the errors have a greater tendency to compound than with the more traditional techniques.

7. Results

Forecasts often have different time spans and can be performed on very different data, making good comparisons difficult to obtain. However, while it is difficult to objectively compare forecasting results, it is clear that the results obtained in this research were exemplary.

For the purposes of this paper, three papers were chosen as comparison cases. All three papers focussed on very short term forecasting. This means that the forecast values are likely to have similar errors. Reference [5] was chosen as it presented a good selection of techniques against which this paper can be compared. It was published in 1989 and is verging on being out of date, however, in order to compare artificial intelligence results with conventional techniques, it is necessary to go back that far. The other two references, [8, 9], were both published in 1999, both using ANNs. However Drezga and Rahman [8] looked at load forecasting and Szkuta, Sanabria and Dillon [9] looked at price forecasting. The price forecasting paper also used Australian market data, which limits another variable.

Moghram and Rahman [5] used conventional techniques and a knowledge-based technique to look at very short-term load forecasting (one hour ahead). They split the test values into summer and winter and achieved the results shown in Table 1.

Table 1: Absolute mean percentage errors from [5]

Algorithm	MLR	STS1	STS2	GES	SS	KBS
Summer %	2.78	0.54	0.51	2.12	1.57	1.22
Winter %	3.76	2.17	2.70	1.79	1.71	1.29
Total %	3.27	1.36	1.61	1.94	1.64	1.26

Drezga and Rahman [8] looked at several lead times and their results showed only a small difference in the errors, however, for the purposes of this paper, it is more appropriate to only look at the one hour ahead forecast. The results they obtained are shown in Table 2.

Table 2: Absolute mean percentage errors from [8]

Utility	Utility A				Utility B			
Month	Jan	Apr	Jul	Oct	Jan	Apr	Jul	Oct
Error	1.15	1.01	.8	1.04	1.59	1.23	.88	.99
Total	1.00				1.17			

Szkuta, Sanabria and Dillon [9] also were trying to predict the next data point (half hour values in this case) and reported their findings as a week worth of predictions and associated errors. The results are presented in Table 3. It also pays to note that the days used to test the ANN in this paper did not including the large spikes that can occur in the spot price market such as those included in Table 5.

Table 3: Absolute mean percentage errors from [9]

Date	14/5	15/5	16/5	17/5	18/5	19/5	20/5
Error	4.16	11.09	2.18	10.61	4.88	3.27	4.17
Total	5.77						

The results shown in Tables 1-3 demonstrate that ANNs represent a superior forecasting technique to the conventional techniques and that spot price data is much more difficult to forecast than load data.

The ANFIS model was trained on seeded January 2002 data and tested on February 2002 (summer) spot price data, June 2002 (winter) spot price data and retrained and tested for March 2002 demand data. Each of the test data sets was trained and tested for many combinations of parameters to ensure that near best results were being achieved and for this paper a comparison of results have been reported.

The data for February was the main thrust of this paper and received the most attention in ensuring good results. It was also much easier to get good results for the summer data than for the winter data as it did not have any large spikes. The results are shown in Table 4.

Table 4: Absolute mean percentage errors for spot price data during February 2002

MF	Bell Function MF		Triangular MF	
Data	Partial	Full	Partial	Full
Error %	0.43	2.30	0.75	0.73

The results show that the bell MF is superior to the triangular MF when given selected data from the seeded training set. If given the full seeded data set, it does not respond so well since it places too much emphasis on the spikes added to allow for unusual results. The bell function with the partial data set will work well for most months of the year, but will return large errors if used to try to predict the winter spikes. This is shown in Table 5. The triangular membership function did not respond quite so well, but was far more reliable at handling unusual events. This makes the triangular membership functions a safer option.

Table 5: Absolute mean percentage errors for spot price data during June 2002

MF	Bell Function MF		Triangular MF	
Data	Partial	Full	Partial	Full
Error %	1.72E09	1.27E07	35.23	10.73

The results shown in Table 5 seem alarmingly high, especially for the bell function. However, upon investigation it was clear that most points were very well predicted and the true data line was followed closely. However, when the data spiked upwards suddenly, the prediction completely overshot the result as it went to the full extent of the MF curve. For a bell function this is a very large number and so the errors were correspondingly large. To give an insight to the suddenness of a spike, in one period between predictions, the price rose from 235.79 to 3839.60. This kind of change is very difficult to properly predict.

The demand data test set was mainly done in order to compare the ANFIS system against a wider range of competition. Due to the vast differences in demand depending upon weather, season and day of the week, the training data was only used for weekdays. With more time spent on finetuning, the demand data could return even better results by using different inputs (such as using one input for weather values and one for day of the week). Even so, the results obtained clearly showed that ANFIS techniques are the best available. The results are presented in Table 6.

Table 6: Absolute mean percentage errors for demand data during Mar 2002

MF	Bell Function MF	Trapezoidal MF
Error %	925.52	0.084

As the training data set was not carefully selected, randomised and seeded, the bell function gave large errors at some stages as the ANFIS was not well trained to handle those particular values. However, by using the more robust trapezoidal MF an excellent result was obtained.

8. Further Research

One of the great advantages of a neuro-fuzzy system is that the operations of the system can be directly affected. This means that the rules can be altered manually to improve the results. The standing problem with this system is still founded in the spot price forecasting of large data spikes. Even with all the measures to improve robustness, the spikes still tend to be overshot by significant amounts. This could be corrected by adjusting the rules to create a cut-off. When the predicted difference might be clearly beyond reasonable expectations, the rules would limit the difference to some upper bound. This would need to be fine-tuned, but would stop the large overshoot and undershoot errors that are presently causing difficulties on the most severe days.

More work could also be done to improve the training set used for the demand data and with the better training set, longer forecasts are a strong possibility for this technique. Both load forecasting and price forecasting could be extended out to a six-hour forecast and maybe beyond.

9. Conclusion

The research shows that ANFIS is an excellent technique for power forecasting and is likely to work very well for other forecasting applications as well. In both instances (spot price and demand) the results obtained using ANFIS are approximately ten times better than the other research that was available. Especially impressive is the 10.73% error achieved for the spot price data of June. This data is almost impossible to predict and an error of around 10% is incredibly accurate.

10. Acknowledgments

The authors would like to thank Mr Mico Skoklevski, Mr Peter Clark and Dr Roger Allen for their assistance in focussing this paper and promised aid in the future. We would also like to thank Hydro Tasmania for their generous support of this project.

11. References

[1] B. M. Weedy, *Electric Power Systems*. Chichester: John Wiley and Sons, 1992.

[2] S. Li, S. M. Shahidehpour and C. Wang, "Promoting the Application of Expert Systems in Short Term Unit Commitment," *IEEE Trans. on Power Systems*, vol. 8, pp. 286-292, 1993.

[3] G. A. N. Mbamalu and M. E. El-Hawary, "Load Forecasting Via Suboptimal Seasonal Autoregressive Models and Iteratively Reweighted Least Squares Estimation," *IEEE Transactions on Power Systems*, vol. 8, pp. 343-348, 1993.

[4] A. Zobian, "Market Price Forecasting in Competitive Electricity Markets," Tabors Caramanis and Associates 7 February 2001.

[5] I. Moghram and S. Rahman, "Analysis and Evaluation of Five Short-Term Load Forecasting Techniques," *IEEE Trans. on Power Systems*, vol.4, no.4, pp. 1484-1491, 1989.

[6] Jang, J.-S.R., Sun, C.-T. and Mizutani, E. (1997). *Neuro-Fuzzy and Soft Computing: A Computational Approach to Learning and Machine Intelligence*, Prentice-Hall, New Jersey.

[7] M. Negnevitsky, *Artificial Intelligence: A Guide to Intelligent Systems*. Harlow: Pearson Education, 2002.

[8] I. Drezga and S. Rahman, "Short-Term Load Forecasting with Local ANN Predictors," *IEEE Trans. on Power Systems*, vol. vol.14, no.3, pp. 844-850, 1999.

[9] B. R. Szkuta, L. A. Sanabria and T. S. Dillon, "Electricity Price Short-Term Forecasting Using Artificial Neural Networks," *IEEE Trans. on Power Systems*, vol. vol.14, no.3, pp. 851-857, 1999.

Justification of HLabelSOM: Automatic Labelling of Self Organising Maps

Hiong Sen Tan
School of Computer and Information Science
University of South Australia
Adelaide, Australia
tan@cs.unisa.edu.au

Susan E. George
School of Computer and Information Science
University of South Australia
Adelaide, Australia
susan.george@unisa.edu.au

Abstract

HLabelSOM is a novel method to automatically label self organising maps. In this paper, we justify the method by defining the criteria of a good map. We first define the criteria of a good map for information retrieval, and then we justify the HLabelSOM for these criteria. We use medical documents retrieved from the web as experiment data to show the applicability of the HLabelSOM method. We also discuss other automatic labelling methods, LabelSOM and Lin's method, as comparison. Finally, we show that HLabelSOM outperforms other methods in producing good maps for information retrieval.

1. Introduction

In information retrieval, the common way to find documents is by entering keywords and hoping the system 'understands' the words we use in order to return the documents we expect relevant to our need. The key to success in this information retrieval mechanism is in the formulation of the keywords; this can be a problem for the users who are not very familiar with the domain.

One of the solutions to this keyword selection problem is to eliminate the necessity to provide a keyword in the information retrieval mechanism. We can give information about the document collection to the users and let them browse and explore, based on the information given, to get the documents they need. In this information retrieval mechanism, the users do not need to formulate the keywords as the keys are given.

The clustered map of self organising map (SOM) has been used on many occasions to retrieve the documents [1-4]. But, until now the information retrieval using a map is still not as popular as information retrieval by entering the keywords. One of the problems is due to the map itself, whether it is a good map in terms of being easy to understand, easy to use, and functional in its intended purpose as a browsing and exploration tool for information retrieval.

The SOM un-doubtedly can produce a good map. In fact, it can produce an accurate and ordered map. Several measures, such as quantisation error and topology preservation measures [5-6], justify the goodness of the map produced by the SOM technique. However, is the accuracy and the ordering, justified by the measures, of the map that the users are concerned about in information retrieval system? If it is not, what are the criteria of a good map from the users' points of view?

In this paper, we first define four properties a map should hold in order the map can be said 'good' for information retrieval. Then, we propose a novel method, HLabelSOM, to label automatically the SOM and last we justify that the HLabelSOM method is able to fulfil the criteria of a good map. We also discuss other automatic labelling methods, LabelSOM [2,7] and Lin's method [1], as comparison.

2. Document encoding

A document can be represented by a weighted vector or binary vector. The common way to weight the terms in the document is by using a frequency-based weighting function, known as inverse document frequency (IDF). Since not all the terms, e.g. 'a', 'the', and 'and', in the document are good for indexing purpose, the indexing process chooses only certain terms to be the keywords of the document. The IDF function then can be define as:

$$IDF_{ik} = \frac{\text{Frequency of keyword } k \text{ in document } i}{\text{Frequency of keyword } k \text{ in all documents}} \quad (1)$$

Using the IDF, a document D_i is represented by a vector $[IDF_{i1}, IDF_{i2}, \ldots, IDF_{iK}]$, where K is the number of keywords.

In contrast, the frequencies of the keywords are ignored in the binary vector. A document D_i will be represented by vector [0|1, 0|1, … , 0|1]. The given column is 1 if keyword k occurs in the document, and 0 otherwise. The binary presentation of the documents can only form a certain maximum number of patterns P, that is $P_{max} = 2^K$ or $P_{max} = 2^K - 1$ if we eliminate the zero

vector [0,0, …, 0]. For example, if we have $K = 3$ and k_1 = 'a', k_2 = 'b', and k_3 = 'c' then $P_{max} = 7$. All of them are P_1 = ['a'], P_2 = ['b'], P_3 = ['c'], P_4 = ['a', 'b'], P_5 = ['a', 'c'], P_6 = ['b', 'c'] and P_7 = ['a', 'b', 'c']. Also, $P_1 \subseteq P_1$, $P_1 \subseteq P_4$, $P_1 \subseteq P_5$, $P_1 \subseteq P_7$ and so on. We also can say if we have a document with an explicit pattern P_4 (for example), then implicitly we also have documents with the subsets of P_4, those are P_1, P_2, and P_4.

3. Exact match and approximate match

The subset relation of keywords plays an important role in information retrieval based on keywords. If we are looking for documents that have keywords 'a' and 'b', we expect the information retrieval system will return the documents with keywords 'a' and 'b', and we also do not mind if the system gives documents with keywords 'a', 'b', and 'c'. In our system, we call the former as an exact match and the later as an approximate match. It is an exact match if the hamming distance of two vectors, vector A represents the document and vector B represents the searched keywords, is equal to 0. The formula is as follows:

$$D_H(A,B) = \sum_{i=1}^{K} \|A_i - B_i\| \quad (2)$$

where K is the number of keyword.

To calculate the approximate match, the hamming distance is modified as follows:

$$D_{AH}(A,B) = \sum_{i=1}^{K} \begin{cases} 1, \text{ if } B_i > A_i \\ 0, \text{otherwise} \end{cases} \quad (3)$$

The approximate match is achieved if the distance is equal to 0. In HLabelSOM, the approximate match is used to map the documents to the nodes on the map. The approximate match function covers the exact match function as well since if it is an exact match then it is an approximate match.

4. Experiment data

The experiment data are 40 medical documents fetched from the web. After the indexing process using automatic indexing software, we found total 308 keywords in all the documents. We reduce the number of keywords by choosing only 12 keywords that have the most occurrences in all documents. Then, each document is transformed into a 12-element-keyword of binary vector. The list of keywords used can be found in table 1 column 1. The number of explicit patterns formed is 31.

5. The self organising map

The SOM is an artificial neural network that is able to perform data clustering. One of the most important aspects of the SOM is that it is primarily a visualisation method for the clustering. Unlike statistical methods or other ways of grouping data the SOM provides a topological ordering where the relationships between data items are made apparent. In fact, relationships between data of high-dimensionality are reduced to relationships on a two-dimensional surface.

The SOM has a two-dimensional matrix of processing elements (the output layer) and a scalar array of processing elements (the input layer). Each node in the output layer is connected to every node in the input layer by weights. A training process is necessary to change the initially random weights into values that respond to input data. Please refer to [8] for detail of the SOM and [9] for the practical version of the algorithm.

The two-dimensional output map effectively orders the input data once the training is complete. To make the ordering and the clusters apparent to the users we need to label the map. We can use a visualisation technique, such as U-matrix [10], cluster connection [11] and adaptive coordinate [12], or we can use an automatic labelling method, such as HLabelSOM that we propose in this paper, LabelSOM [2,7] and Lin's method [1].

6. The goodness of the map

The map is said to be good if the outputs represent accurately the inputs and the map has been in order. The accuracy can be measured by a quantisation error function as follows:

$$E_Q = \frac{1}{N} \sum_{i=1}^{N} \|x_i - m_c(x_i)\| \quad (4)$$

where N is the number of inputs and $m_c(x_i)$ is the output that have the closest distance from the input x_i.

The ordering of the map is how well the map keeps the relations in the input. It can be verified by using any topology preservation measures, such as topographic error [5] or a measure proposed by Kaski and Lagus [6].

7. Criteria of good map for information retrieval system

However, in information retrieval systems that use map display as a search tool to browse and explore the document collection, users will see the goodness of the map from different points of view. The users will be more concerned about whether the maps are easy to use, easy to understand, and function as their intended purpose rather than whether the maps are accurate and in order, justified by the measures mentioned above.

The map will help the users if after it is labelled, it holds these following properties:

Table 1. Keywords and their frequencies.

Keyword	F_{doc}	Frequency on 4 x 4 map				
		F_{eq}	F_{min}	F_{max}	F for λ =	
					0.50	0.41–0.45
arthritis	10	4.0	4	4	4	4
asthma	9	3.6	3	4	4	4
cancer	9	3.6	3	4	3	3
care	8	3.2	3	4	3	3
cause	11	4.4	4	5	5	5
diabetes	10	4.0	4	4	4	4
disease	12	4.8	4	5	5	5
health	11	4.4	4	5	4	4
joint	8	3.2	3	4	3	3
pain	8	3.2	3	4	2	3
patient	9	3.6	3	4	4	5
treatment	12	4.4	4	5	6	6
				DE =	0.17	0.17
				DD =	0.48	0.48

7.1. Continuity

A topology preservation measure guarantees that the map is in order. Therefore, regardless the labelling method used, the method should keep this continuity. What 'continuity' means here is that 'similar documents should be located close each other. The neighbouring nodes should be labelled by same patterns of keywords or share the common keywords to form clusters'. If the map does not hold this continuity, the map will be meaningless for browsing.

7.2. More and richer patterns on the map

The quantisation error measures how accurately the outputs represent the inputs. We probably cannot have all the explicit patterns in the input present on the map because the capability of showing all explicit patterns is limited by the map size (see the map size discussion below). But, of course we would like to have map(s) with more patterns and more keywords in the patterns, since the more patterns and the richer the keywords the patterns have, the easier it is for users to find specific documents. It is also possible that the map forms a zero pattern [0, 0, …, 0] and new patterns that are not present in the input, even though the new patterns are probably non-sense in some applications. For example, in animal domain a new pattern with keywords '4_legs' and 'fly' is a joke.

7.3. The equally keyword distribution

Given a labelled map, we probably conclude that if a keyword has higher or lower frequency than those of other keywords on the map then this keyword should have higher or lower frequency than those of other keywords in all documents. This is based on an equal distribution mechanism. The user will understand quite easily what the collection is about if the keyword frequencies in the input give equal distribution to the keyword frequencies in the output.

7.4. The smaller map size

We can show all the explicit patterns of the inputs by using a particular map size corresponding to the number of the input patterns. For example, if we have 31 explicit patterns of input, we probably can use 6 x 6 map (36 nodes) or bigger to make sure that all explicit patterns present in the output. But, it is not always a good solution since the space, i.e. computer screen resolution, is limited. And, even though we can use the scrolling function to move the screen window, we still prefer to see the smaller area as our working space. One of the solutions is to use hierarchical maps to reduce the working space.

In the next sections we will examine how the automatic labelling methods fulfil these criteria. In general, the automatic labelling method at least should hold the continuity property otherwise the map is meaningless. The more patterns and the richer the keywords the patterns have, the easier it is for users to find specific documents. The later two, the equally keyword distribution and the smaller map size, are not as essential as the formers, but they make the map easier to understand and use.

8. Automatic labelling

What we mean by automatic labelling of SOM here is a way to label to the nodes based on the weight values the nodes hold after the training. In this section, we will discuss HLabelSOM, the method we propose, LabelSOM and Lin's method.

8.1. HLabelSOM

Previously in HLabelSOM [13], we labelled a node with a keyword if the node weight value for a particular keyword is greater or equal to 0.5. The selection of value 0.5 as a threshold is based on the fact that the document vectors are binary vectors. If the final weight value is above or equal to 0.5, the node should have the keyword, otherwise it should not.

But, we still should justify whether 0.5 is the appropriate value for the threshold. If it is not, then what is the appropriate value? As a simple example, if we have input 0 and 1 and we train 1 x 1 SOM, what do we expect? We expect that the final weight is 0.5, but it isn't always the case, at least with the algorithm that we use,

the final weight values are not exactly 0.5, but about 0.5. There are several parameters of the SOM trainings influence the final weight, such as learning rate, neighbourhood function, and input sequences. We need an appropriate threshold that the value of it is between 0 and 1, and most probably about 0.5.

Since we label the node by comparing each weight, i.e. the weight of the keyword in each node, the selection of the threshold should have direct effect to the keyword distribution. Based on this fact, we should try to find a value of the threshold that makes the labelled map mirrors the keyword distribution most equally.

We apply the above idea into our experiment data. For example, if keyword 'arthritis' occurs 10 times in 40 documents, it should appear 4 times on 4 x 4 map (16 nodes) in order it can be said that it is equally distributed. If keyword 'asthma' occurs 9 times in 40 documents, it should appear 3.6 times (3 or 4 times) in 4 x 4 map. The complete frequencies of keywords in whole documents (F_{doc}), the equally distributed frequencies of keywords on the map (F_{eq}), minimum (F_{min}) and maximum (F_{max}) frequencies that are allowed, are given in table 1 column 2 to 5.

After the SOM is trained (and measured by some measures mentioned above to choose a 'good' map), the selection of the threshold value is undertaken before the HLabelSOM labelling method is applied. The distribution error (*DE*) values, which are the numbers of keywords that are not equally distributed, are calculated for all possible threshold values (λ) from 0.00 to 1.00. The *DE* is calculated and normalised as follows:

$$DE = \frac{1}{K}\sum_{i=1}^{K} \begin{cases} 0, & \text{if } F_{\min} <= F <= F_{\max} \\ 1, & \text{otherwise} \end{cases} \qquad (5)$$

where K is the number of keywords,

To extent the preciseness of the distribution error, we calculate distribution distance (*DD*) that is the distance from F to F_{eq}, as follows:

$$DD = \frac{1}{K}\sum_{i=1}^{K} \left\| F - F_{eq} \right\| \qquad (6)$$

Now, as we have *DE* and *DD* values for all possible threshold values between 0.00 and 1.00, we can choose the threshold value that most equally distributed the keywords, which is the threshold value with minimum *DE* (DE_{min}) or minimum *DD* (DD_{min}). For our experiment data, we found DE_{min} = 0.17 and DD_{min} = 0.48 for λ = 0.41, 0.42, 0.43, 0.44, 0,45 and 0.50. In this case, we choose the lowest λ, i.e. 0.41, since a low threshold increases the frequencies of the keywords that means more keywords in the patterns (see section 7.2 for the 'more and richer patterns on the map' discussion). The distributions of keyword frequencies for the above thresholds are shown in table 1 column 6 and 7. The result

cancer health	treatment	arthritis disease pain patient treatment	arthritis care cause joint pain
cancer patient treatment	cancer care cause disease health patient treatment	arthrits cause joint pain treatment	arthritis joint
asthma patient	asthma	diabetes	cause diabetes disease health treatment
asthma care cause disease health	asthma	diabetes	diabetes disease patient

Figure 1. The detail map. The map is labelled by using HLabelSOM with λ = 0.41.

map of applying HlabelSOM with λ = 0.41 is shown in figure 1.

As we refer to our novel method as the HLabelSOM, where H stands for Hierarchical, our purpose is to have a hierarchical visualisation. We believe in creating user interface that follows the information visualisation mantra: "overview first, zoom and filter, then details on demand" [14] can lead to an effective information retrieval system. A variation of the SOM, the HSOM [15, 16], will be able to achieve this purpose as well. But, using HSOM will require several trainings for different SOMs. We can also produce hierarchical maps by combining four adjacent nodes on the map into one node and naming the new node with the common keywords the four nodes share if the common keywords exist, otherwise with all keywords the four nodes have [17]. The absence of the common keywords in the four adjacent nodes leads to a drawback of this method because renaming a new node with all keywords that the four nodes have does not really represent the documents the node contains.

In the HLabelSOM method, the map is re-labelled to produce other maps. In the new maps the nodes are labelled with the keywords if the node weight value for the particular keyword is greater or equal to λ and only the n greatest weight values of keywords are selected. We can choose the values of n from 1 to a certain value that will lead to the production of the detail map (figure 1) as a result. Figure 2 shows the labelled map for λ = 0.41 and n = 1, this is an overview map. Since we have the overview map and the detail map now, we can always make intermediate maps between them, so called middle maps.

Figure 3 shows the middle map for λ = 0.41 and n = 2. We can now use the maps in figure 1, figure 3, and figure 2 as hierarchical maps: the detail map, more general (middle) map and most general (overview) map.

8.2. LabelSOM

LabelSOM [2,7] labels the nodes on the map based on the quantisation errors of all keywords that are accumulated distance between the weight vector elements of all input mapped to the nodes. The quantisation errors that are close to 0 or below a given threshold (λ_1) indicate the keywords best characterise the input mapped to the nodes. Further, we need another threshold, especially for the applications where we find a high number of input vectors that have values of 0, e.g. text documents. These zero values mean the keywords are not present in the particular input. The selected keywords should have weight vectors above the second threshold (λ_2). Figure 4 shows the result map when LabelSOM is used with λ_1=0.10 and λ_2 = 0.50.

For binary input vectors, we found out that the node can be labelled as follows: the node is labelled by all keywords of the document input if only one input is mapped to the node, and by the common keywords of the document inputs if more than one input mapped to the node. In this case, we do not need to calculate the accumulated quantisation error and define the thresholds.

8.3. Lin's method

Lin's method [1] labels the nodes by comparing each node to all unit vectors, which are vectors consisting of only one keyword, and labelling the node with the name of the winning keyword, which is a unit vector that has the closest distance to the node. As a result the areas on the map are continuous, shown in figure 2. The Lin's method gives the same result as HLabelSOM with n = 1 does.

The most important thing in the three automatic labelling methods above is the differences in the time and the method used of mapping the documents to the nodes on the map. In HLabelSOM, the mapping of the documents to the nodes is done after the map is labelled and the documents are mapped to the nodes for approximate matches. In LabelSOM, the mapping of the documents to the nodes is done before the map is labelled and the documents are mapped to the nodes that have minimum distances from the documents. In Lin's method, the documents are mapped to the nodes that have minimum distances as in LabelSOM, but the mapping can be done before or after the labelling since the inputs do not have any contribution to the labelling mechanism.

cancer	treatment	arthritis	arthritis
cancer	treatment	arthrits	arthritis
asthma	asthma	diabetes	diabetes
asthma	asthma	diabetes	diabetes

Figure 2. The overview map. The map is labelled by using HLabelSOM with λ = 0.41 and n = 1. Using Lin's method also produces this map.

cancer health	treatment	arthritis treatment	arthritis joint
cancer patient	cancer treatment	arthrits joint	arthritis joint
asthma patient	asthma	diabetes	diabetes disease
asthma health	asthma	diabetes	diabetes disease

Figure 3. The middle map. The map is labelled by using HLabelSOM with λ = 0.41 and n = 2.

cancer	treatment	arthritis disease pain patient treatment	arthritis cause joint pain
cancer patient	cancer disease treatment		arthritis joint
asthma patient			cause diabetes disease health treatment
asthma health	asthma	diabetes	diabetes disease

Figure 4. The map is labelled by using LabelSOM

9. Conclusion

We conclude the automatic labelling methods in respect to the properties of the good information retrieval map, which we defined above, should hold.

HLabelSOM, LabelSOM and Lin's method show the continuity on the map, neighbouring nodes are labelled by the same keywords or share the common keywords to form the clusters. The users will be able to utilise this continuity property to browse and explore the map to find the documents they need.

HLabelSOM, when more than one map is used, certainly has maps with more patterns and richer keywords in the patterns than LabelSOM and Lin's method do. The more patterns and the richer the keywords the patterns have, the easier it is for the users to find specific documents.

The selection of the threshold value used in HLabelSOM will lead to the production of the map towards the equally keyword distribution. We do not see any attempt to equally distribute the frequencies of the keywords in the input to the output in LabelSOM and Lin's method, as seen in table 2. The equal distribution of the keywords will give more clue to the users what the collection is about.

We do not need to worry about the map size by using the HLabelSOM because we can always stack the map hierarchically, to present more patterns, instead of making the map size bigger.

Now, we can say that the HLabelSOM outperforms the two other automatic labelling methods, LabelSOM and Lin's method, in respect to the four properties of a good information retrieval map. But, as we mentioned before, the continuity property, that the LabelSOM and Lin's method also posses, is sufficient for the map to be used for browsing and exploration in information retrieval. The LabelSOM is the most accurate method to map documents onto the nodes since the mapping is based on the quantisation errors of the inputs mapped to the nodes. Lin's method is always useful to give the overview of the collection without much detail and shows the continuity and the classification more clearly than other methods do since it labels the nodes with minimum number of keywords (mostly one keyword).

Table 2. Keyword frequency distribution on the 4 x 4 map using three different labelling methods.

Keyword	Frequency (*F*) on the map using		
	HlabelSOM	LabelSOM	Lin's method
arthritis	4	3	4
asthma	4	3	4
cancer	3	3	2
care	3	0	0
cause	5	2	0
diabetes	4	3	4
disease	5	2	0
health	4	2	0
joint	3	2	0
pain	2	2	0
patient	4	3	0
treatment	6	4	2
DE	0.17	0.67	0.75
DD	0.48	1.45	2.60

At the moment, to justify the wider applicability of the HLabelSOM method, we have been applying it onto a bigger collection of medical documents. The collection is about 6000 documents.

References

[1] X. Lin, D. Soergel and G. Marchionini. A self-organizing semantic map for information retrieval. Proc. of the 14th Annual Int'l ACM/SIGIR Conf. on Research and Development in Info. Retrieval, 1991.

[2] A. Rauber and D. Merkl. Automatic labeling of self-organizing maps for information retrieval. Journal of System Research Info. System, 10 (10): p.23-45, 2001.

[3] T. Kohonen et al. Self organization of a massive document collection. IEEE Trans. on Neural Networks, 11(3), 2000.

[4] A. L. Houston et al. Medical data mining on the internet: research on a cancer information system. Artificial Intelligence Review, 13: p. 437-466, 1999.

[5] K. Kiviluoto. Topology preservation in self-organizing maps. IEEE Conf. on Neural Networks, p.294-299, 1996.

[6] S. Kaski and K. Lagus. Comparing self-organizing maps. Proc of the Int'l Conf. of Artificial Neural Networks (ICANN96), 1996.

[7] A. Rauber. LabelSOM: on the labeling of self-organizing maps. Proc. of the Int'l Joint Conference on Neural Networks (IJCNN'99), Washington, 1999.

[8] T. Kohonen. Self-organizing map. 2nd Ed. Springer-Verlag, 1995.

[9] R. P. Lippmann. An introduction to computing with neural nets. IEEE Acoustics, Speech, and Signal Processing Society, p. 4-22, 1987.

[10] A. Ultsch. Self-Organizing neural networks for visualisation and classification. Information and Classification. Concepts, Methods and Applications. Springer: Berlin, 1993.

[11] D. Merkl and A. Rauber. Cluster connections: a visualzation technique to reveal cluster boundaries in self-organizing maps. Proc. of 9th Italian Workshop on Neural Nets (WIRN97), Vietri sul Mare, Italy, 1997.

[12] D. Merkl and A. Rauber. On the similarity of eagles, hawks, and cows: visualization of semantic similarity in Self-Organizing Maps. Proc. of Int'l Workshop Fuzzy-Neuro-Systems'97, Soest, Germany, 1997.

[13] H. S. Tan. HLabelSOM: Automatic Labelling of Self Organising Maps toward Hierarchical Visualisation for Information Retrieval. 16th Australian Joint Conference on Artificial Intelligence (AI'03), Perth, Australia, 2003.

[14] B. Shneiderman. The eyes have it: a task by data type taxonomy for information visualizations. Proc. of IEEE symposium on visual languages. Boulder, CO, USA, 1996.

[15] R. Miikkulainen. Script recognition with hierarchical feature maps. Connection Science, 2 (1) p.83-102, 1990.

[16] D. Merkl. Exploration of text collections with hierarchical feature maps. Proc. of the 20th Int'l ACM SIGIR Conf. on Research and Development in Info. Retrieval. 1997.

[17] H. S. Tan and S. E. George. Multi-media based web mining for an information resource. 3rd Int'l Conf. on Data Mining Methods and Databases for Engineering, Finance and Other Fields (Data Mining 2002), Bologna, Italy, 2002.

Convolution of Hyperplanes with Gaussian Kernals in a Differentially Fed Artificial Neural Network

Bangalore University
Manjunath.R, Dr K.S.Gurumurthy
Dept of EC & CSE, UVCE, Bangalore, INDIA
manju_r_99@yahoo.com

Abstract: The problem of function approximation to map a set of data with another is challenging When they are non linearly related. A variety of solutions based on Neural Networks are found in the literature. In this paper, a new class of Artificial neural networks with differential feedback are introduced. The different orders of differentials form a manifold of hyperplanes [2]. The spectral properties of these hyperplanes are explored

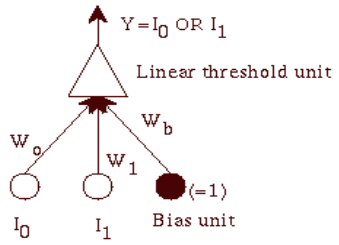

Figure.1. Artificial neural network

1 INTRODUCTION

Artificial neural network systems (ANN) are extremely helpful in modeling a system whose behaviour is unknown but for the enough non-linearly related input and output data.The structure of a simple Artificial neural network with two inputs is shown in the figure.1.The network has 2 inputs, and one output. All are binary.
The output is

$$1 \text{ if } W_0 * I_0 + W_1 * I_1 + W_b > 0$$
$$0 \text{ if } W_0 * I_0 + W_1 * I_1 + W_b <= 0 \quad (1)$$

The above network can learn Logical OR: output a 1 if either I_0 or I_1 is 1. The network adapts by changing the weight by an amount proportional to the difference between the desired output and the actual output.

$$\Delta w = \xi.(\text{error}).i \quad .(2)$$

here. i is the input driving the node.,ξ is the learning rate, The network functions as follows: Each neuron receives a signal from the neurons in the previous layer, andeach of those signals is multiplied by a separate weight value. The weighted inputs are summed, and passed through a limiting function (non linear in general) which scales the output to a fixed range of values.

A BP network learns by example. That is, a learning set has to be provided that consists of some input examples and the known-correct output for each case, like a look-up table. The network adapts.

The BP learning process works in small iterative steps: First, one of the example cases is applied to the network, and the network produces some output based on the current weights (initially, the output will be random). This output is compared to the known-good output, and a mean-squared error signal is calculated. The error value is then propagated backwards through the network, and small changes are made to the weights in each layer.(proportional to the error). The whole process is repeated for each of the example cases, then back to the first case again, and so on. The cycle is repeated until the overall error value drops to a predefined value. In section II differential feedback concept is developed.. In section III The spectral property of the hyperplanes is explained. The experimental results are demonstrated in section IV section V concludes

2. DIFFERENTIAL FEEDBACK METHOD

One of the major drawbacks of the conventional training methodology is that it is iterative in nature and takes a large number of cycles to converge to the prespecified error limit. By intuition, if more information is made to be

hidden with the data, it takes less No. of iterations to get stabilized to the pre defined error limit. Auto regressive Moving average (ARMA) model can be conveniently used in this direction. In a typical ARMA model, the output and input are related by

y(n)=a0*x(n)+a1*x(n-1)+…+b1*y(n-1)+… .(3)

The differentials of the output (& input) can be written in to similar linear combinations of present & previous outputs (inputs).

(dy/dt)=y(n+1)-y(n) . (4)

By (3) and (4) it is clear that

y(n)=f(x(n),x(n-1),..,dy/dtt=n,d^2y/dt^2t=n,) (5)

where the ANNs are made to learn this function. Here the ARMA output is subjected to non-linear function for the same reason as in ANN which makes it possible to learn non linear functions. The output y of a neural network but for the nonlinearities can be written as

y=Σwixi. (6)

Where xi are the inputs wi, the corresponding weights. The space spanned by weight vector for different inputs is a hyperplane. The important factor is weight cannot span the entire input space [1], whatever may be the training mode. Again the linearity of the output (1) may be viewed as a particular case of ARMA

y (n+1)=b0y(n)+b1y(n-1)+…..+a0xn+… (7)

Where b0.. and a0.. are constants. The auto regressive terms b0…bn may be realized using an implied differential feedback [3]. With differential feedback it has been found out[3] that the no of iterations required for training is reduced as shown in the table I.XOR gate is considered for simulation. Gaussian distributed random input with seed value 1000 is taken as input. With I order different feedback, the output may be written as:

Σwixi +b1y1 (8)

y1 being the I order differential. This equation once again represents a plane parallel to Σwixi. Thus the set of differentially fed ANNs form a manifold of parallel planes, with ∞ order feedback being the plane with zero error.Also, simulation results of table II show that two terms of II order differential feedback i.e., y2-y1 and y1-y0 can be replaced by a single equivalent plane represented by

Weq=(w1*iextra+w2*iextra1)/y0 (9)

In II order differential feedback system, the two differential terms can be replaced by a single term. Extending this principle, the ∞ terms of ∞ order differential feedback can be replaced by a single term. This is termed as eigen plane which is the practical way of generating lowest error. Now the differential feedback becomes

dy/dt+d^2y/dt^2+… (10)

Taking Z transform, & then the inverse,

yeq=IZT{Y(z)/(1-z)} (11)

3.CONVOLUTION OF HYPERPLANES

Let yk represent the kth hyperplane corresponding to kth order of differential feedback. Hence yk= a*y0+b*y1+…
=b1*yk-1+d/dtn(y0) c1 being a constant Here the incremental portion yΔ=c1*d/dt(0) will be approximated as the convolution of some function with y0.

Ie yΔ=y0*f (12)

F may be found out by pushing both sides of 12 to frequency domain. k*y(k)=y(k)*F(f) k being the frequency index of DFT.Thus F(f) should have a linear response over a range of indices as shown in fig 2.Its equivalent time domain signal may be expressed as. F=(sin**2(ax)/Ax *x)*exp-(Nt/2) since the triangle is delayed by N/2.N being the no. of points in DFT. The signal is shown in fig 3. As evident from the figure, over a very small duration, the result may be approximated to a Gaussian pulse of scale factor l where the Gaussian kernel with dilation parameter l is given by G(l,x) an exponential function. Analytically F decays as 1/t^2 =(1-t*t/k) . A Gaussian pulse exp(-t*t/k) also may be approximated as (1-t*t/k).Hence, the envelop of f is Gaussian if the peaks are too close ie sinc function function is large.

The table I shows that the gap between the hyperplanes decreases with increase in the order. I.e. the information content becomes more and more abstract. Hence the kernel which is convolved with the output y is scaled wth progressively increasing scale factor.

3.1.Working of the model

In the domain of learning, mixtures of Gaussians is a powerful tool for statistical modeling. Such a model can avoid the problem of overfitting if care is taken. For this class of generative models a complexity control scheme is presented in [4], to provide an effective means for avoiding the problem of over-fitting .The model calls for decrease in the variance at higher levels of resolution..

This constraint on the model is satisfied with higher order differential feedback. Table I shows that the error or variance gets reduced for a given number of iterations if differential feed back is given. The initialization problem [5], encountered with the fitting of Gaussian mixture models is remedied by choosing the zeroth ordered hyperplane as the initial approximation and giving more feedback to lift it towards the eigen plane or maximum likelihood estimator described in section I. It gradually deforms the objective function via deterministic annealing and progressively tracks the maximum likelihood solution across the decreasing noise levels as required by the model. The differential feedback architecture goes well with the model described in [4]. There the objective of model fitting is to exploit some subspace structure within the data, which often results from their concentration near some manifold of lower dimensionality. This gives rise to the following generative model

$$x=f(z)+u \qquad (13)$$

With an affine mapping $F(z)=Az+\mu$.All components of x are linear combinations of Gaussian random variables and thus the observable can be characterized by a multivariate normal density

$$g(x|\phi)=(2\pi)^{-d/2}|\Sigma|^{-1/2}\exp\{-\frac{1}{2}(x-\mu)^T\Sigma^{-1}(x-\mu)\} \qquad (14)$$

Since convolution with Gaussian function may be expressed as a linear combination of scaled and shifted Gaussians, the hyperplanes are expressible as a linear combination of Gaussian variables. Also, in sec II it has been observed that the hyperplanes are linearly transported.In order to reduce the complexity of such a model, the covariance model $\Sigma=\psi+2I\sigma$ is proposed[4].Thus the model has two parts- a data dependent signal part and a noise part which corresponds to the fixed part and differential parts of the proposed model. In the model in [4] as the variance reduces, more and more subspaces in the data become visible. This is true with the proposed model where outputs corresponding to higher levels include lower level planes.

To summarize, with differential feedback, the complexity of the model is automatically controlled making it resistant for overfitting and makes the observable data Gaussian.

4. SIMULATION

The differentially fed Artificial neural networks are made to learn the psd of random data .The Normal distributed data is generated using Matlab. The error after learning and the differentials of the error are stored. The normalised PSDs of convolution of outputs without feedback and Gaussian pulse and normalized PSD of the first derivatives with feedback are shown in the fig.4..It may be seen that the derivatives are formed by the convolution of the output with Gaussian functions of different scales

5. CONCLUSIONS

Differential feedback, when applied over a neural networks leads to a manifold of affinely transported hyperplanes. These hyper planes are actually formed by the convolution of the non feedback output with Gaussian kernels of different scales.

REFERENCES

1. S.Amari, 1995, Information Geometry of the EM and em algorithms for neural networks, Neural networks, 8,No.9
2. 7.S.Amari and H.Nagaoka, 2000, Methods of information geometry, AMS and Oxford University press.
3. Manjunath.R and K.S.Gurumurthy, Oct 2002, System design using differentially fed Artificial Neural networks, TENCON'02
4. Peter Meinicke and Helge Ritter. , 1999, Resolution based complexity control for Gaussian mixture models. Technical report, Faculty of Technology, University of Bielefeld.
5. McKenzie, P. and Alder. M. , 1994, Initializing the EM algorithm for use in Gaussian mixture modelling. In Gelsema, E. S. and Kanal, L. N., editors, *Pattern Recognition in Practice IV*, pages 91–105. Amsterdam:Elsevier.

.

Table 1.Performance with feedback

Order of differential	Square error	Iterations
No feedback	18	1156
I order	18	578
II order	18	289

Table 2..Performance with II order feedback

Order of differential	Square error	Iterations
II order Feedback	18	578
Equivalent Output feedback	18	578

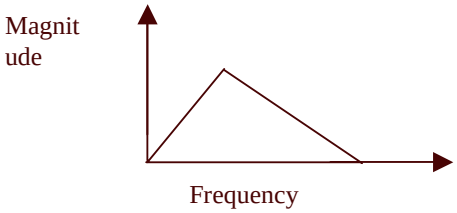

Figure 2.Desired linear response

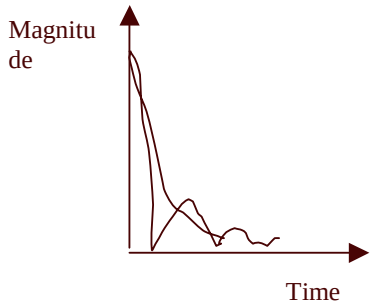

Figure.3. The time domain plot

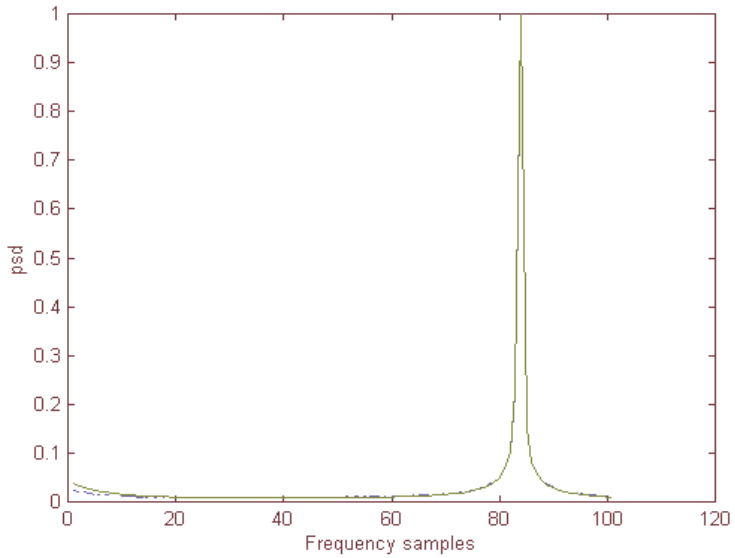

Legend: - PSD of non FB signal convolved with Gaussian pulse . –. PSD of the I order FB

Figure.4. PSDs of Differential signals and the convolved signals

A New Method for Explaining the Regression Output of a Multi-layer Perceptron Network with Real Valued Input Features

M.L.Vaughn, J.G.Franks
Cranfield University,
Defence Academy,
Swindon, UK
M.L.Vaughn@rmcs.cranfield.ac.uk

Abstract

In this paper, we present a new method for explaining the regression output of a MLP network with real valued input features. The application selected to demonstrate the method is the prediction of helicopter airframe load spectra from continuously valued flight parameter data. Two example regression outputs are studied - a high strain case and a low strain case. For each case the input channels are discovered that determine the output activation values. The underlying mechanism that drives the MLP regression output is determined.

INTRODUCTION

A full explanation facility has been developed by the first author [1-4] for interpreting the output on a case-by-case basis from any standard multi-layer perceptron (MLP) network that classifies binary input data in *n*-dimensional input space, using a sigmoidal activation function at the hidden layer and output layer neurons. The method represents a significant advance towards the goal of readily interpreting trained neural networks that solve real-world problems with a large number of input features [5].

This study adapts the MLP interpretation method developed for classification tasks to include MLP regression models that predict continuous variables from continuously valued input features. The need for such methods has been stated in [6] within the context of interpretation and knowledge extraction from trained artificial neural networks.

THE HELICOPTER MLP NETWORK

The aim in developing the helicopter MLP [7] was to predict component loads from easily measurable parameters without the use of strain gauges or other measuring equipment. The flight data was generated from flight tests using a Westland Lynx Helicopter. The total data consisted of 45 channels of flight parameter data and three channels of helicopter load spectra measured using strain gauges. The total flight data was in excess of four hours of flying time and represented 2 Gbytes of information. Each data channel was scaled between 0 and 1 before MLP development.

MLP Input and Output Channels

An 80 second sample was taken for MLP development [7], which included two cyclic 'pull-up' maneuvers and some non-transitional flight. A number of channels were omitted which were judged by experts not to affect the strain in the airframe or rotor-head. To simplify initial experiments, only one load channel was selected as the channel to be predicted. The final data set consisted of 21 channels of flight parameter data (F1 – F21) and one channel of load spectra (F0), measured using a strain gauge on the I-beam assembly, as shown in Table 1.

Table 1. MLP input channels and strain output channel

Input Channels	Description	Corr Coeff
F1	Collective Lever Position	+0.12
F2	Collective Servo Position	–0.07
F3	F/A Cyclic Stick Position	+0.10
F4	Lat Cyclic Stick Position	–0.05
F5	F/A Cyclic Servo Position	+0.79
F6	Lat Cyclic Servo Position	–0.01
F7	Tail Rotor Pitch Angle	–0.05
F8	Rudder Pedal Position	–0.13
F9	Barometric Altitude	–0.15
F10	Barometric Airspeed	+0.08
F11	Lateral 'G' at C of G	–0.04
F12	Main Rotor Speed	+0.04
F13	Outside Air Temperature	–0.00
F14	Pitch Attitude A/C System	+0.47
F15	Pitch Rate	+0.04
F16	Roll Attitude A/C System	–0.15
F17	Roll Rate	–0.32
F18	Aerodynamic Yaw	–0.06
F19	Normal 'G' at C of G	+0.53
F20	Yaw Rate	–0.18
F21	Main Rotor Hub Torque	–0.02
Output Channel	**Description**	
F0	Vertical Shear stbd STN 420A	

The correlation coefficient was evaluated between each of the input channels and the strain output channel F0, as shown in Table 1 [7]. It can be seen from Table 1 that the input channels with the highest correlation are F5, F14, F17 and F19.

MLP Selected for this Study

The first 40 seconds containing the first 'pull-up' maneuver were used for the MLP training. Data was sampled at 840 Hz and the 33,600 training vectors were presented in a random sequence during training. The following 40 seconds containing the second 'pull-up' maneuver were used for network testing with a further 33,600 test vectors.

A number of different MLP architectures were developed (using NeuralWare Professional II Plus™ on a Sun Sparc Workstation) with a range of hidden neurons from 5 to 25 and sigmoidal activation functions at hidden and output layer neurons. The MLP with 20 hidden neurons was found to have the minimum test mean absolute error of 0.021 at 250,000 cycles of training. The corresponding mean absolute error of the training data was 0.016. The 21-20-1 MLP was selected for this study.

The aim of this study is to explain how the helicopter MLP predicts the single strain channel, F0, from the 21 flight parameter data channels. This is achieved by interpreting two different cases – a high strain output value, and a low strain output value.

INTERPRETING THE HIGHEST STRAIN CASE

The training case with the maximum strain MLP output value of +0.7560 was the high strain case selected for interpretation. This was the training case with the maximum F0 target value of +0.7957 in the training set.

The interpretation begins at the MLP output neuron activation which, similar to a classifier output activation [1–4], is driven as high as possible by the MLP to meet the maximum target output. The high strain value of +0.7560 is sigmoid(+1.1309) where +1.1309 is the combined input sum from hidden neurons and the hidden bias to the single output neuron. The combined sum is made up of a positive part +1.9165 and a negative part –0.7760. The hidden bias contributes –0.0096.

Input Channels Driving the Positive Signal at the Regression Output Neuron

Following the same approach as the method that interprets classifier MLPs with binary inputs [1-4], the hidden layer feature detectors and the input channels are first discovered that drive the positive part of the combined input sum at the regression output high. This is then followed by the discovery of the input channels that drive the negative part of the combined input sum low.

Discovery of the Hidden Feature Detectors

In predicting a high strain output the MLP drives the *positive* part of the combined sum as *high* as possible to meet the maximum target output. This is achieved by the hidden neurons that provide all the *positive* part of the combined sum at the output neuron. The method defines these neurons as the *hidden layer feature detector* neurons [1–4].

Using sigmoidal activation functions, the feature detectors are hidden neurons connected with a *positive weight* to the regression output neuron. For the high strain case, 7 hidden neurons H_1, H_2, H_5, H_9, H_{13}, H_{19} and H_{20} are feature detectors, providing all the positive signal +1.9165 to the combined sum. It is of note that, for the high strain case, the only hidden neurons with activation >0.5 are H_1 and H_{19}, with activations of +0.5020 and +0.5383, respectively.

Ranking the Hidden Feature Detectors

Some positive feature detectors are more important to the MLP regression output than others. These are the positive feature detectors that contribute the highest positive combined input. In the high strain case, H_1, H_{19} and H_{13} together provide 97.4% of the total positive input at the strain output neuron, contributing 47.6%, 40.0% and 9.8% respectively.

Discovery of the Positive Input Channels

The positive input channels detected by each feature detector are the MLP inputs that provide the *positive* part of the combined input sum at each detector [1–4]. In this application, since all input channels have positive values, these are channels connected with positive weights to the detectors.

For example, the positive input channels detected by feature detector H_1 are channels F1, F3, F5, F6, F10, F11, F14, F15, F18, F19. All of the positive input channels detected by all 7 feature detector neurons are the 13 (out of 21) channels: F1, F3, F5, F6, F7, F8, F9, F10, F11, F14, F15, F18, F19.

Ranking the Positive Input Channels

The MLP is expected to use channels with high positive input values connected with high positive connection weights to drive the activation of the feature detectors, and subsequently the strain output, as high as possible. For this reason, the positive input channels can be ranked by forcing each channel in turn to its *minimum value* in the training set and presenting the new input vector to the MLP. The highest ranked channel is the one that produces the largest drop in activation at the MLP regression output neuron [1–4].

For the high strain case the highest ranked features are channels F5, F3, F14 and F15 with changes in the MLP output strain value of –18.0%, –11.5%, –6.5% and –3.2% respectively.

The Positive Input Channel Data Relationship

The positive input channel data relationship shows how the top ranked channels are related and provides the explanation of the positive activation of the highest strain case [1–4]. The data relationship is found by progressively *minimizing* each of the positive channels together *in ranked order*.

The results for the highest strain case are shown in Fig. 1, where the MLP strain value smoothly and gracefully degrades from a maximum of +0.7560 to a minimum of +0.4045. It can be seen from Fig. 1 that the positive activation in the highest strain case is driven mostly by the top 4 ranked channels F5, F3, F14 and F15 – and primarily by F5 and F3.

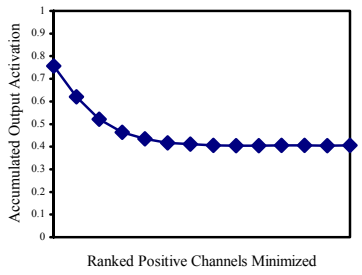

Fig. 1. Highest strain positive channel data relationship

Role of Not Feature Detector Hidden Neurons

In predicting a high strain output the MLP drives the *negative part* of the combined sum as *low* as possible so that the net sum is high enough to meet the maximum target output. The hidden neurons that provide the *negative part* of the combined sum at the output neuron are defined as the *not* feature detector neurons [1–4]. Using sigmoidal activation functions, these are hidden neurons connected with a *negative weight* to the output neuron. For the high strain case, 13 hidden neurons H_3, H_4, H_6, H_7, H_8, H_{10}, H_{11}, H_{12}, H_{14}, H_{15}, H_{16}, H_{17} and H_{18} are not feature detector neurons contributing –0.7760 to the combined sum, as previously stated.

Input Channels Reducing the Negative Signal at the Regression Output Neuron

The MLP drives the negative part of the combined sum at the regression output neuron as *low* as possible by *reducing* the activation of the not hidden feature detectors and by reducing the negative connection weights to the output neuron. For example, in the high strain case the activation of *all* not feature detectors is lower than all the feature detectors.

The reduction of a not feature detector activation is achieved in two ways, as follows.

By maximizing negative input at not feature detectors.

In the high strain case, it is discovered that *all input channels* are connected to the not feature detectors with negative weights. Since the MLP is expected to use *higher* channel values with higher *negative* weights to reduce the not feature detector activation, the channels are ranked by forcing each in turn to its *minimum value* in the training set and presenting the new input vector to the MLP. This is the same ranking procedure as used to find the ranked positive features.

For the highest strain case, the 9 highest ranked input channels reducing the not feature detector activation are discovered to be the same top ranked positive input channels. This demonstrates that the highest ranked input channels play a dual role in activating the hidden feature detectors and in de-activating the not feature detectors. The channel data relationship in this context is very similar to Fig. 1.

By minimizing positive input at not feature detectors

To reduce the not feature detector activation, the MLP is also expected to use *lower* channel values with lower *positive* weights. In this context, for the highest strain case, it is discovered that all input channels are used by the MLP for this purpose *except F3, F14* and *F15*, notably 3 of the top 4 ranked positive channels.

Since the MLP is expected to use *lower* channel values with lower *positive* weights, these channels are ranked by forcing each in turn to its *maximum value* in the training set and presenting the new input vector to the MLP. For the highest strain case, the de-activating channels *in highest ranked order* are found to be F17*, F21*, F16*, F8, F18, F20*, F2*, F12*, F4*, F7, F9, F13*, F5, F6, F1, F11, F19, F10, where starred channels are not also positive channels. However, all these channels have a minimal effect in this context since the output strain value of +0.7560 drops by a maximum value of –1.85% for highest ranked F17*.

In this context, the channel data relationship is found by progressively *maximizing* each of the channels together in ranked order. It is found that the accumulated output decreases smoothly from +0.7560 to a minimum of +0.7192 at F11*. This confirms that the de-activating channels in this context for the highest strain case have minimal effect, unlike results from binary input cases [1–4].

Summary of the Highest Strain Case Results

The analysis of the positive part of the combined input to the strain output neuron has discovered that 13 input channels (out of 21) positively activate 7 hidden layer feature detector neurons, which in turn positively activate the regression output neuron. The channel data relationship shown in Fig. 1 clearly demonstrates that channels F5, F3, F14 and F15 have a *major* control effect (in decreasing order) on the network during the 'pull-up' maneuver, but especially F5 and F3. When these two channels are minimized together, the strain output +0.7560 drops by 67% of

the maximum drop in activation. The additional effect of F14 causes the activation to drop by 83%.

INTERPRETING THE LOWEST STRAIN CASE

The training input case with the lowest strain MLP output value of +0.5518 was the low strain case selected for interpretation. This was the training case with the minimum F0 target value of +0.5006 in the training set.

Before commencing the interpretation, it must be emphasised that the regression output of the low strain case is no longer similar to the high output of a classifier MLP, as it was for the high strain output. In this situation the MLP is aiming to drive the regression output as *low* as possible.

The interpretation begins, as before, at the MLP output neuron. The lowest strain value of +0.5518 is sigmoid(+0.2080), where +0.2080 is the combined input sum from hidden neurons and the hidden bias to the single output neuron. The combined sum is made up of a positive part +1.1966 and a negative part –0.9790. This represents a decrease of +0.7199 (37.56%) in positive activation and an increase of –0.2030 (26.16%) in negative activation compared with the high strain case. The hidden bias still contributes –0.0096.

As before, the input channels that contribute to the positive part of the combined input sum at the regression output neuron are discovered first, followed by the input channels that contribute to the negative part of the combined sum.

Discovery of the Hidden Feature Detectors

For the lowest strain case, *exactly the same* 7 hidden neurons H_1, H_2, H_5, H_9, H_{13}, H_{19} and H_{20} are discovered to be feature detector neurons, providing all the positive signal +1.1966 to the combined sum at the regression output.

This was an unexpected result, meaning that the MLP must *decrease* the activation of the feature detectors and *increase* the activation of the not feature detectors to produce the low strain regression output.

Ranking the Hidden Positive Feature Detectors

In the lowest strain case, the highest ranked feature detectors are H_1, H_{19} and H_{13}, exactly the same ranked detectors as for the high strain case. These neurons together provide 96.2% of the total positive input at the strain output neuron, contributing 44.7%, 39.2% and 12.6% respectively. It is of note that now the activation of all hidden neurons is significantly below 0.5. (Feature detector H_{19} has the highest activation of +0.3297.)

Discovery of the Positive Input Channels

For the lowest strain case, the input channels connected to the 7 feature detector neurons with positive weights are *exactly the same* 13 channels as for the high strain case: F1, F3, F5, F6, F7, F8, F9, F10, F11, F14, F15, F18, F19. Again, this was an unexpected result.

Ranking the Positive Input Channels

In the lowest strain case, we have the opposite situation to the highest strain case. Here, the MLP is expected to use channels with *lower* positive input values connected with positive connection weights to decrease the activation of the positive feature detectors, and subsequently the strain output, as *low* as possible to meet the lowest target output.

This means that the positive channels for the lowest strain case are ranked by forcing each positive channel in turn to its *maximum value* in the training set and presenting the new input vector to the MLP. The highest ranked positive channel now produces the largest *increase* in activation at the MLP output neuron, in contrast to the largest *decrease* for the highest strain case (and classification applications [1-4]).

For the lowest strain case the highest ranked positive features are channels F5, F15, F3 and F14 with changes in the MLP output strain value of +23.9%, +14.0%, +11.4% and +6.7% respectively. This is similar to the ranked order of the top 4 channels in the high strain case except now F15 has risen to 2nd place.

The Positive Channel Data Relationship

For the lowest strain case, the data relationship is found by progressively *maximizing* each of the positive channels together in ranked order. The results for the lowest strain case are shown in Fig. 2, where the MLP strain value smoothly and gracefully degrades from a minimum of +0.5518 to a maximum of +0.8342.

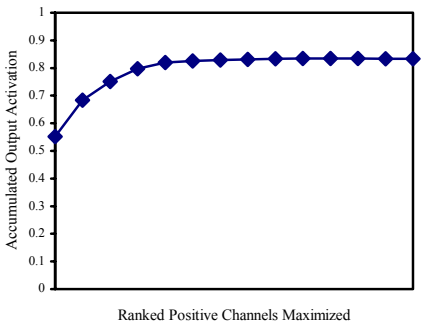

Fig. 2. Lowest strain positive channel data relationship

Input Channels Contributing to the Negative Signal at the Regression Output Neuron

For the low strain case, *exactly the same* 13 hidden neurons as for the high strain case are not feature detector neurons viz: H_3, H_4, H_6, H_7, H_8, H_{10}, H_{11}, H_{12}, H_{14}, H_{15}, H_{16}, H_{17} and H_{18}. These neurons contribute –0.9790 to the combined sum, which represents an increase in negative activation of 26.2%, as previously stated. As explained above, for the lowest strain case, the MLP increases the activation of the not hidden feature detectors so as to reduce the activation

of the regression output neuron. This increase is achieved in two ways:

By minimizing negative input at not feature detectors.

To achieve this, the MLP is expected to use lower channel values with lower negative weights. As for the high strain case, it is discovered that *all* input channels are connected to the not feature detectors with negative weights. In this context, channels are ranked by forcing each in turn to its *maximum value* in the training set.

The channels in highest ranked order are exactly the same as the highest ranked positive channels, showing that these channels play a dual role in activating the hidden feature detectors and in de-activating the not feature detectors. The channel data relationship is found by progressively *maximizing* each of the channels together in ranked order. As before, the relationship is very similar to the lowest strain positive relationship shown in Fig. 2.

By maximizing positive input at not feature detectors.
To achieve this, the MLP is expected to use higher channel values with higher positive weights. As for the highest strain case, it is discovered that all input channels *except F3, F14* and *F15* are used for this purpose in the low strain case, notably 3 of the top 4 ranked positive features.

In this context, the channels are ranked by forcing each in turn to its *minimum value* in the training set. The channels in highest ranked order are found to be F17*, F16*, F18, F8, F21*, F4*, F20*, F2*, F12*, F13*, F9, F10, F19, F7, F1, F11, F5, F6, where starred channels are not also positive channels. The output strain value of +0.5518 increases by a maximum value of +2.7%, for channel F17, the highest ranked input channel.

The channel data relationship is found by progressively *minimizing* each of the negative features together in ranked order. It is found that the accumulated output increases smoothly from +0.5518 to a maximum of +0.5882 at F19, confirming that the negative input channels in this context have minimal effect, as for the high strain case.

Summarizing the Lowest Strain Case Results

The analysis of the positive part of the combined input to the strain output neuron has discovered that the same 13 input channels as for the high strain case contribute *all* the positive part of the combined input sum to the strain output neuron. These 13 channels positively activate the same 7 hidden layer positive feature detector neurons as for the high strain case, which in turn positively activate the regression output neuron. It is highly significant that this is *exactly the same result* as for the highest strain case.

The positive channel data relationship graph shown in Fig. 2 clearly demonstrates that channels F5, F15, F3 and F14 have most influence (in decreasing order) on the low strain output, but especially F5 and F15. When these two channels are minimized together, the low strain output +0.5518 increases by +71% of the maximum increase in activation. The additional minimization of F3 causes an increase of +87% in activation.

MLP MECHANISM FOR PREDICTING THE STRAIN

Mechanism for Predicting the Highest Strain

Interpreting the highest strain output has shown that the helicopter MLP uses primarily 3 hidden positive feature detector neurons H_1, H_{13} and H_{19} to drive the *positive* part of the output combined sum as high as possible (to +0.7560) to meet the maximum target output of +0.7957. This is achieved by 13 (out of 21) input channels but primarily by the top ranked channels F5 and F3, as explained below.

The MLP uses the 13 hidden not feature detector neurons H_3, H_4, H_6, H_7, H_8, H_{10}, H_{11}, H_{12}, H_{14}, H_{15}, H_{16}, H_{17} and H_{18} to drive the *negative* part of the combined sum as low as possible to meet the maximum target output. This is achieved by all 21 input channels but primarily by the same top ranked input channels that drive the positive part of the regression output combined sum.

Mechanism for Predicting the Lowest Strain

Interpreting the lowest strain output has shown that the MLP uses the *same* positive feature detectors, the *same* not feature detectors and the *same* top ranked input channels to drive the positive part of the output combined sum as *low* as possible (to +0.5518) to meet the minimum target output of +0.5006.

The same top ranked input channels decrease the positive part of the high strain combined sum by 38% (through the positive feature detectors) and increase the negative part by 26% (through the not feature detectors) to lower the strain output to its minimum value of +0.5518. This is achieved primarily by the top ranked channels F5 and F3, as explained in the following section.

Explaining the Top Ranked Input Channels

For the highest strain case, the ranked order of the top ranked 4 channels is F5, F3, F14, and F15. In this case, the value of F5 is almost at its maximum in the training set, as shown in Table 2. It lies 0.20% of the F5 training set range below the maximum F5 value.

In the lowest strain case, the value of F5 lies 10.3% of the range above the minimum value in the training set. This means that F5 uses 89.5% of the F5 training set max/min range between the highest strain and lowest strain cases. F5 is possibly the highest ranked input channel in the high strain case because it has the *maximum decrease* (+0.1824) of *all* input channels between the highest and lowest strain values. It is of interest that F5 has the highest positive cor- relation (+0.79) with F0 in the training set, as shown in Table 1.

Table 2. Max/min training set values and high/low case values for 4 top ranked input channels

input channel	high case value	low case value	maximum value	minimum value
F3	0.5167	0.3493	0.5285	0.2350
F5	0.5628	0.3804	0.5632	0.3594
F14	0.5403	0.5631	0.7897	0.1835
F15	0.3528	0.3947	0.8131	0.1913

The value of F3 in the high strain case lies 4% of the training set range below its maximum value and lies 38.9% of the training set range above its minimum value in the low strain case. F3 is possibly the second highest ranked input channel in the high strain case because it has the *second* maximum decrease (+0.1674) of all input channels between the highest and lowest strain values.

It is highly significant that for the top 7 ranked channels in the high strain case F5, F3, F6, F19 and F11 have the maximum decrease of all input channels in the *same* descending ranked order between the highest and lowest strain values.

The high strain data relationship in Fig. 1 shows that when F5 and F3 are *together* switched to their minimum training set values the output strain channel F0 value drops from +0.7560 to +0.5208, a value *below* the minimum F0 lowest training set strain value of +0.5518. This indicates that channels F5 and F3 are the *main controlling channels* for the difference in the highest and lowest strain output values.

For the lowest strain case the ranked order of the top ranked 4 channels is F5, F15, F3 and F14. This is the same order of ranking for the highest strain case except for F15, which is now in 2nd place. It is possible that this ranking position is anomalously high due to F15 having the highest increase to its maximum value during the ranking process. This is confirmed by finding the ranked order from a weighted percentage contribution of the positive features to the positive combined input sum to the 3 top ranked positive feature detectors H_1, H_{19} and H_{13}. For both the highest and lowest strain cases the ranked order is then F5, F3, F14, and F15.

SUMMARY AND CONCLUSIONS

The interpretation of the highest and lowest strain cases has shown that the helicopter MLP uses the same mechanism to predict both the high strain and low strain output values. The MLP uses the same hidden feature detector neurons, the same hidden not feature detector neurons and the same top ranked input channels to lower the strain output from a maximum of +0.7560 to a minimum of +0.5518.

The top ranked input channels decrease the positive part of the high strain combined sum by 38% and increase the negative part by 26% to lower the strain output to its minimum value, and vice versa. This is achieved primarily by the top ranked channels F5 and F3 which are the main channels controlling the difference in the high and low strain output values. F5 and F3 are possibly the highest ranked channels because they have the maximum decrease between the highest and lowest strain values.

The analysis has shown that the top ranked input channels have a dual role. As well as driving the positive part of the combined sum at the regression output neuron sufficiently high they also drive the negative part sufficiently low.

It is expected that a MLP with more than one regression output neuron will have a different set of hidden feature detector neurons associated with each regression output. It is expected that the MLP will use a similar mechanism to that observed in this study in predicting each output value.

REFERENCES

[1] Vaughn M.L., Cavill S.J., Taylor S.J., Foy M.A., & Fogg A.J.B. "A full explanation facility for a MLP network that classifies low-back-pain patients and for predicting its reliability". In Abraham A., Koppen M. (eds*), Recent Advances in Intelligent Paradigms and Applications*, Physica Verlag, 2002.

[2] Vaughn M.L., Cavill S.J., Taylor S.J., Foy M.A., & Fogg A.J.B. "Direct explanations for the development and use of a multi-layer perceptron network that classifies low-back-pain patients", Special Issue International Journal of Neural Systems, Vol 11 No. 4, 335–347, 2001.

[3] Vaughn M.L. "Derivation of the weight constraints for direct knowledge discovery from the multilayer perceptron network". *Neural Networks*, Vol 12, pp. 1259 – 1271, 1999.

[4] Vaughn M.L., Cavill S.J., Taylor S.J., Foy M.A., Fogg A.J.B. (2000). "Direct explanations and knowledge extraction from a multilayer perceptron network that performs low back pain classification". In S.Wermter and R.Sun (Eds.), *Hybrid Neural Systems*. Springer, pp. 270 – 285.

[5] Craven M.W., & Shavlik J.W. "Using sampling and queries to extract rules from trained neural networks, in machine learning". *Proceedings of the Eleventh International Conference on Machine Learning*, Amherst, MA, USA. Morgan Kaufmann, pp. 73 – 80, 1994.

[6] Tickle A. B.., Andrews, R., Golea, M., & Diederich, J. "The truth will come to light: Directions and challenges in extracting the knowledge embedded within trained artificial neural networks". *IEEE Transactions on Neural Networks, 9, pp. 1057 – 1068,* 1998.

[7] A.C. Lison. *The prediction of helicopter airframe load spectra from flight parameter data using artificial neural networks*. Cranfield University (RMCS), MSc Dissertation, 1994.

INTELLIGENT IMAGE PROCESSING & COMPUTER VISION III

(This page left blank intentionally)

Learning Robust Object Recognition Strategies

Ilya Levner, Vadim Bulitko, Lihong Li, Greg Lee, Russell Greiner
University of Alberta
Department of Computing Science
Edmonton, Alberta, T6G 2E8, CANADA
ilya|bulitko|lihong|greglee|greiner@cs.ualberta.ca

Abstract

Automated image interpretation is an important task in numerous applications ranging from security systems to natural resource inventorization based on remote-sensing. Recently, a second generation of adaptive machine-learned image interpretation systems have shown expert-level performance in several challenging domains. While demonstrating an unprecedented improvement over hand-engineered and first generation machine-learned systems in terms of cross-domain portability, and design-cycle time, such systems have yet to be rigorously tested. This paper inspects the anatomy of the state-of-the-art Multi Resolution Adaptive Object Recognition framework (MR ADORE) and presents experimental results aimed at establishing the robustness of the system to real-world image perturbations. Tested in a challenging domain of forestry, MR ADORE is shown to be robust to changes in sun angle, camera angle and training signal accuracy.

Keywords: *Adaptive and Machine Learning, Intelligent Image Processing and Computer Vision.*

1 Introduction & Related Research

Image interpretation is an important and highly challenging problem with numerous practical applications. Hand engineering an image interpretation system requires a long and expensive design cycle as well as subject matter and computer vision expertise. Furthermore, hand-engineered systems are difficult to maintain, port to other domains, and tend to perform adequately only within a narrow range of operating conditions atypical of real world scenarios. In response to the aforementioned problems, various *automated* ways of constructing image interpretation systems have been explored in the last three decades [8].

Based on the notion of "goal-directed vision" [7], a promising approach for autonomous system creation lies with treating computer vision as a control problem over a space of image processing operators. Initial systems, such as the Schema system [7], had control policies consisting of *ad-hoc*, hand-engineered rules. While presenting a systemic way of designing image interpretation systems, the approach still required a large degree of human intervention. In the 1990's the second generation of control policy-based image interpretation systems came into existence. More than a systematic design methodology, such systems used theoretically well-founded machine learning frameworks for automatic acquisition of control strategies over a space of image processing operators. The two well-known pioneering examples are a Bayes net system [15] and a Markov decision process (MDP) based system [6].

Our research efforts have focused on automating the latter system, called ADaptive Object REcognition system (ADORE), which learned dynamic image interpretation strategies for finding buildings in aerial images [6]. As with many vision systems, it identified objects (in this case buildings) in a multi-step process. Raw images were the initial input data, while image regions containing identified buildings constituted the final output data; in between the data could be represented as intensity images, probability images, edges, lines, or curves. ADORE modelled image interpretation as a Markov decision process, where the intermediate representations were continuous state spaces, and the vision procedures were actions. The goal was to learn a dynamic control policy that selects the next action (i.e., image processing operator) at each step so as to maximize the quality of the final image interpretation.

As a pioneering system, ADORE proved that a machine learned control policy was much more adaptive that its hand-engineered counterparts by outperforming any hand-crafted sequence of operators within its library. In addition, the system was easily ported to recognize stationary (staplers, white-out, etc.) in office scenes and again was shown to outperform operator sequences designed by human domain experts [5]. In [13], such a system was used to identify individual trees from aerial images of forest plantation scenes, and was again shown to outperform *the best* static

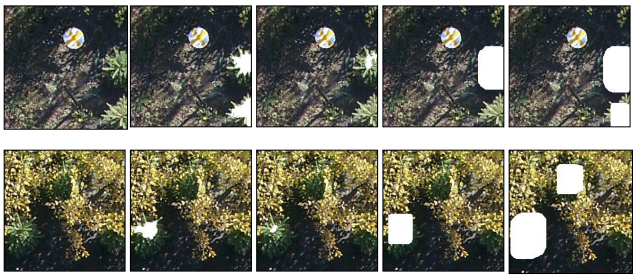

Figure 1. Each row from left to right: the original image, desired user-provided labeling (ground-truth), optimal off-line labeling, best static policy of length 4 labeling, best-first policy labeling. The adaptive policy used by MR ADORE has been observed to outperform best static policy (top row) and sometimes the human experts as well (bottom row).

sequence of operators. However, to date there have been no studies aimed at exploring the robustness of such systems. In response, this paper explores ability of the MR ADORE system to adapt to several perturbations typical of real-world scenarios. To evaluate the performance of MR ADORE, the test domain of forestry is used, which presents the following problems typical of other real-world domains. Special purpose algorithms designed to identify individual trees and their corresponding species class, have been known to be highly sensitive to the position of the camera and the angle of the sun with respect to the orientation of target objects (in this case trees) [4]. In addition, both forestry specific and general purpose vision systems, such as MR ADORE, require a set of training images (Figure 1). However, manual interpretation of aerial forest scenes is an error prone procedure [10]. Since training images are likely to contain annotation errors, the robustness of the system to labeling errors is of utmost interest. Hence, in addition to testing the robustness of the system to changes in sun angle and camera angle, this paper reports empirical evidence on robustness of the MR ADORE system to labeling errors.

The rest of the paper is organized as follows. First, we review the requirements and design of MR ADORE, in order to demonstrate the critical assumptions made and the resulting difficulties. Second, we briefly present the domain of forestry and outline the three challenges it presents. The paper then goes on to outline the experiments and their corresponding results and concludes with future research directions and closing comments.

2 MR ADORE Operation

MR ADORE starts with a Markov decision process (MDP) [16] as the basic mathematical model by casting the IPL operators as MDP **actions** and the results of their applications (i.e., data tokens) as MDP **states** (Figure 2).

First, the domain expertise is encoded in the form of

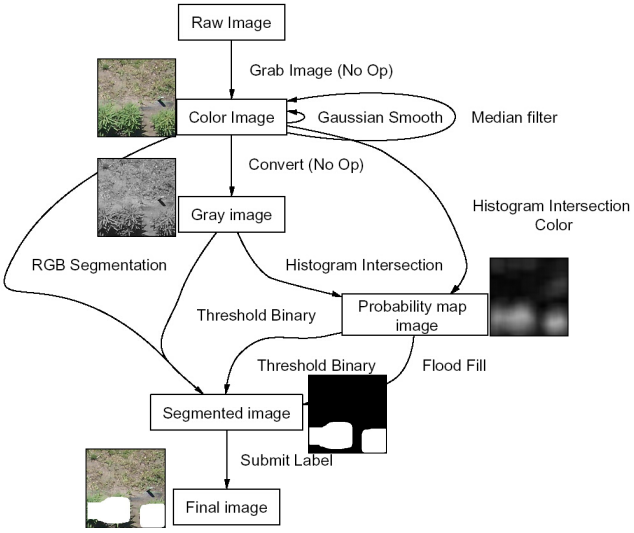

Figure 2. Partial operator graph for the domain of forest image interpretation. The nodes and the corresponding example images depict that data processing layers, which in turn describe the *type* of MDP states present with MR ADORE. The edges represent vision routines, typically ported from the Intel OpenCV and IPL libraries, that transform one state to another (i.e., the MDP actions).

training data. Each training datum consists of two images, the input image, and its user-annotated counterpart allowing the output of the system to be compared to the desired image labeling. Figure 1 (columns 1 - 2) demonstrates two training pairs (image and correct labeling) for the forestry image interpretation domain. Second, during the off-line stage the state space is explored via limited depth expansions of all training image pairs. Within a single expansion all sequences of IPL operators up to a certain user-controlled length are applied to a training image. Since training images are user-annotated with the desired output, terminal rewards can be computed based on the difference between the produced labeling and the desired labeling. System **rewards** are thus defined by creating a scoring metric that evaluates the quality of the final image interpretation with respect to the desired (used-provided) interpretation*. Then, dynamic programming methods [2] are used to compute the value function for the explored parts of the state space. We represent the value function as $Q : S \times A \rightarrow R$ where S is the set of states and A is the set of actions (operators). The true $Q(s, a)$ computes the maximum cumulative reward the

*For all experiments presented, the intersection over union scoring metric, $\frac{A \cap B}{A \cup B}$ is used. This pixel-based scoring metric computes the overlap between the set of hypothesis pixels produced by the system (A) and the set of pixels within the ground-truth image (B). If set A and B are identical then their intersection is equal to their union and the score/reward is 1. As the two sets become more and more disjoint the reward decreases, indicating that the produced hypothesis corresponds poorly to the ground-truth.

policy can expect to collect by taking action a in state s and acting optimally thereafter.

Features (f), used as **observations** by the on-line system component, represent relevant attributes extracted from the unmanageably large states (i.e., data tokens). Features make supervised machine learning methods practically feasible, which in turn are needed to extrapolate the sampled Q-values (computed by dynamic programming on the explored fraction of the state space) onto the entire space.

Finally, when presented with a novel input image, MR ADORE exploits the machine-learned heuristic value function $Q(f(s), a)$ over the abstracted state space, $f(S)$, in order to intelligently select operators from the IPL. The process terminates when the policy executes the action `Submit(`$\langle labeling \rangle$`)`, which becomes the final output of the system. Both the off-line and on-line processes are illustrated in Figure 3.

2.1 Adaptive Control Policies

The purpose of the off-line learning phase within MR ADORE is to construct an on-line control policy. While best-first policies are theoretically capable of much more flexibility than static policies, they depend crucially on (i) data token features for *all* levels and (ii) adequate amounts of training data to train the Q-functions for *all* levels. Feature selection/creation can be substantially harder for earlier data processing levels, where the data tokens exhibit less structure [8, 12]. Compounding the problem, a single user-labeled training image delivers exponentially larger numbers of training tuples, $\langle$ state, action, reward $\rangle$, at later processing levels. However, the first processing level gets the mere $|A_1|$ tuples per training image since there is only one data token (the input image itself) and $|A_1|$ actions. As a net result, best-first control policies have been shown to backtrack frequently [6] as well as produce highly suboptimal interpretations [3], due to poor decision making at the top processing layers.

Rather than making control decisions at every level based on the frequently incomplete information provided by imperfect features, the **least-commitment policies** postpone their decisions until more structured and refined data tokens are derived. That is, all operator sequences up to a predefined depth are applied and only then the machine-learned control policy is engaged to select the appropriate action. Doing so allows the control system to make decisions based on high-quality informative features, resulting in an overall increase in interpretation quality. As a side benefit, the machine learning process is greatly simplified since feature selection and value function approximation are performed for considerably fewer processing levels while benefiting from the largest amount of training data. In [13] such a policy was shown to outperform the *best* static policy.

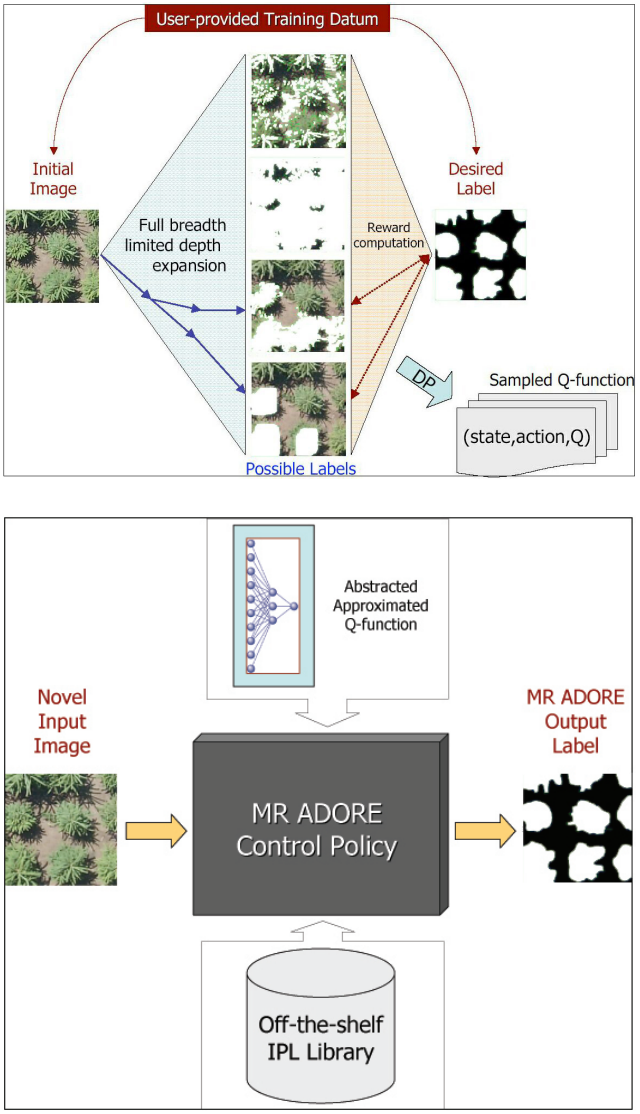

Figure 3. Top: Off-line training phase. Exploration of the state space is done by applying all possible operator sequences to a number of training images for which ground truth is provided. By comparing the interpretation resulting from an application of a sequence of operators to the ground truth, each hypothesis is assigned a quality measure (i.e., reward). The rewards are then propagated up the expansion tree in order to calculate q-values to the intermediate data tokens. Function approximators are trained on the features extracted from the data tokens produced during the exploration phase. **Bottom:** On-line operation. Using the machine leaned q-function approximators the on-line policy greedily selects the state-action pair expected to yield maximum reward. the process terminates then a interpretation hypothesis is submitted to the user.

3 Forestry Domain

Forest maps and inventories have become a critical tool for wood resource management (planting and cutting), ecosystem management and wild-life research. Canada alone has approximately 10^{11} harvestable trees, making manual forest inventorization completely infeasible. In order to automatically create forest inventories, an image interpretation system needs to measure the type (species), position, height, crown diameter, wood volume and age class for every tree in the survey area. This paper focuses on the tree labeling problem as a sub-process within a larger, complete system aimed at extracting the aforementioned parameters from individual trees. Namely, we consider the pixel-level labeling of aerial tree images and apply the adaptive object recognition approach that competes with previous state-of-the-art research methodologies and sometimes outperforms human interpreters as demonstrated in Figure 1.

A number of approaches have been proposed for extracting the aforementioned information about individual trees from aerial images. Model-free (image-based) approaches attempt to delineate individual trees, and subsequently classify each tree instance to a species class[10]. On the other hand, model-based approaches employ template matching methods to extract regions of interest and then delineate individual trees [11]. Regardless of the approach used, modern systems are highly sensitive to image variations, especially those resulting from sun angle and camera angle changes. For instance, the performance of image-based algorithms has been reported to degrade in proportion to the off-nadir view angle of a given forest scene. Likewise, off-midday sun angles negatively effect the performance of both the image-based and model based approaches [4]. Lastly, expert-annotated images, needed to train image-based, model-based, and MR ADORE-type systems, typically contain 10-40% miss-labeling errors when compared to ground-based forest surveys [9]. Thus, the use of MR ADORE is motivated by the inability of any single classical approach to perform adequately under the multitude of conditions typical of real-world scenarios within present-day remote sensing applications.

4 Empirical Evaluation

In order to test the feasibility of the MR ADORE in remote sensing applications three sets of experiments were carried out to test the robustness of the system to labeling errors, changes in overall illumination and changes in camera angle.

4.1 Labeling Errors Experiment

In Figure 1, a small pine tree was left unlabeled by the expert in row two, column two. However, the adaptive policy of MR ADORE was able to find it. To study the robustness of the off-line phase of the system, a synthetic forest

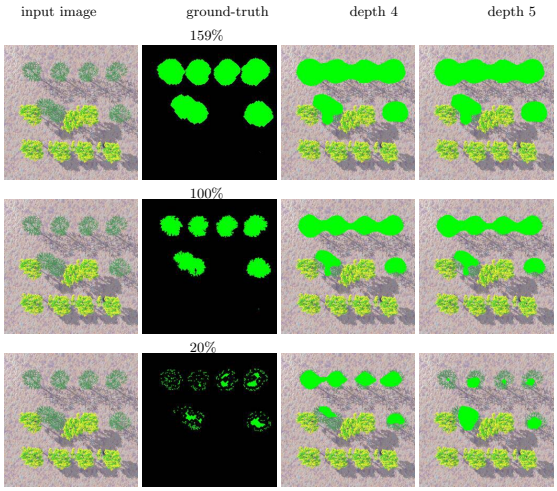

Figure 4. Column 1: Synthetic Input Image. **Column 2:** Ground-truth corresponding to the input image. Actual ground truth (100%, in row 2) is perturbed in rows 1 and 3 to simulate the error made by domain experts. **Columns 3 and 4:** Best interpretation found by MR ADORE during off-line expansion as a function of search depth.

scene and the corresponding ground truth were created. By spatially dilating/erroding the set of ground-truth pixels, labeling errors (false positives or false negatives respectively) were introduced into the expert labeled interpretation of the image as illustrated in Figure 4.

In order to assess performance degradation resulting from labeling errors, each interpretation (columns 3 and 4 in Figure 4) was re-evaluated against the true hypothesis (row 2 of Figure 4). The results are presented in Table 1.

The initial results indicate that adding pixels (i.e, false positives) to the ground-truth interpretation is less detrimental to performance than missing target class pixels (i.e. false negatives). Table 1 shows optimal results produced with respect to the erroneous interpretation but evaluated against the error-free ground-truth image.

4.2 Sun Angle Experiments

Changes in overall scene illumination were created by simulating various time of the day as shown in Figure 5. Table 2 shows the off-line performance on the sun angle experiment. Using the SNoW algorithm [1] in conjunction with local binary patterns serving as texture features [14], the on-line policy achieved an **89%** accuracy with respect to off-line optimal during the leave-one-out cross-validation experiment. In comparison, the best static sequence could only achieve a segmentation accuracy of **74%**. In essence, using a single sequence of operators cannot produce adequate results. Rather for each position of the sun there exists a specific sequence of operators that works best. Therefore in order to achieve robust performance an adaptive policy,

Table 1. Off-line robustness to noise. When maximal sequence length is set to four, the experimental results indicate a negligible performance degradation when false positives or false negatives are added to the ground-truth image. When maximal sequence length is set to five (and six), false positives appear less detrimental to the performance of the system when compared to false negatives. Middle row (highlighted) represents the base line performance given the correct ground-truth. Erroneously adding pixels to the set of target concept pixels appears to be less detrimental than omitting pixels belonging to the target concept for longer sequence lengths.

Pixels	%	depth 4 False Reward	depth 4 Real Reward	depth 5 False Reward	depth 5 Real Reward
12000	159%	0.77	0.554	0.77	0.554
10557	140%	0.74	0.592	0.74	0.592
8915	118%	0.703	0.622	0.703	0.622
7538	100%	0.639	0.639	0.64	0.64
4635	61%	0.455	0.606	0.458	0.592
2626	35%	0.267	0.553	0.308	0.389
1510	20%	0.147	0.553	0.2	0.284

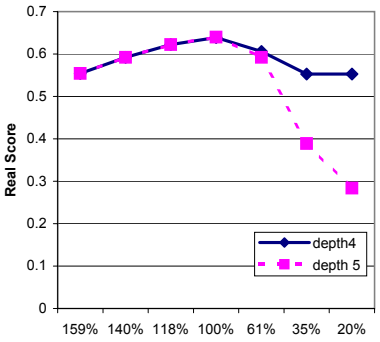

Table 2. Off-line performance on the Sun Angle experiment. The current library of operators appears to perform poorly in mid-day sun as the results indicate.

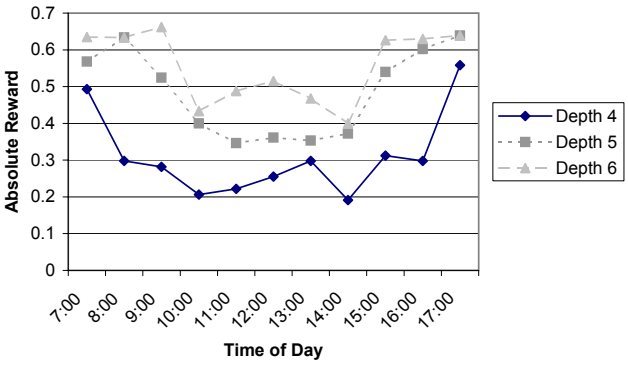

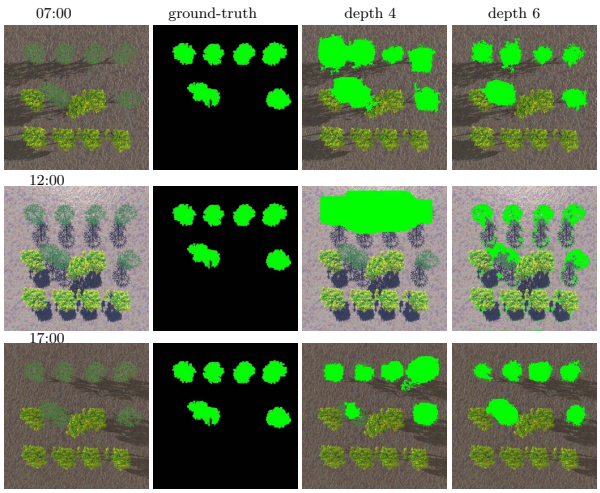

Figure 5. Various angles of the sun can produce vastly different image interpretations for a given scene. While sun positions at 07:00, 12:00, and 17:00 are shown in column one, a total of eleven images was used in the experiment containing sun angles between 07:00 and 17:00 hours at one hour increments. A static, expert labelled ground-truth image (column 2) is used to compare the hypotheses produced by MR ADORE at various search depths (columns 3 and 4).

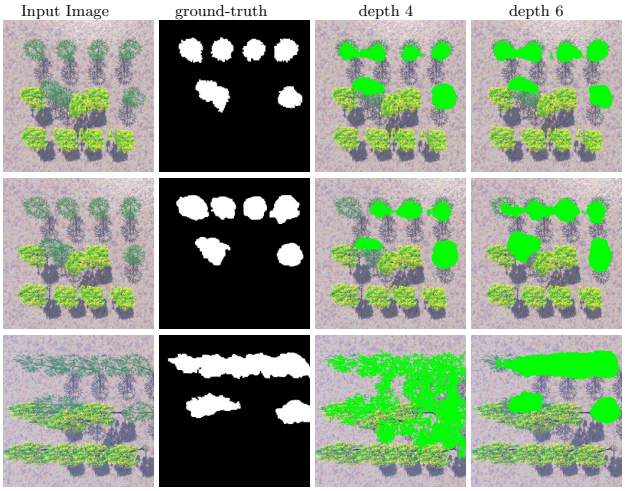

Figure 6. Various view angles produce different image interpretations for a given scene. The hypotheses produced by MR ADORE at various search depths (columns 3 and 4) are compared to ground-truth (column 2).

such as the least-commitment policy used by MR ADORE, is needed.

4.3 Camera Angle Experiments

To simulate changes in camera angle, the view of the synthetic image was altered by translating the camera

Table 3. Off-line performance on the View Angle experiment. Since the operator library uses a single template taken at nadir view angle, the interpretation quality gracefully degrades as the scene is viewed from larger off-nadir angles. At extreme view angles the best interpretation is increased by employing a significantly different sequence of operators from the previous 5 view angles.

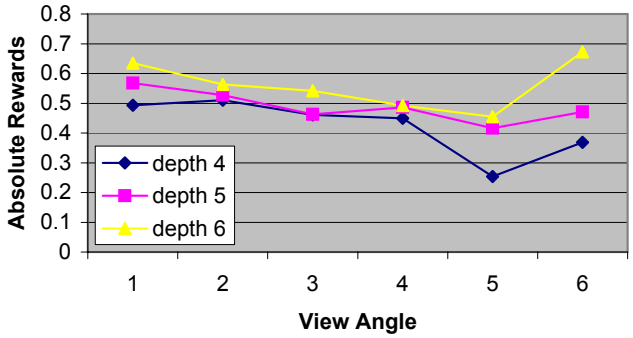

(0,10,20,40,80 or 160 units) left from the center of the scene and then rotating (pan) it back to view the center of the scene. Illustrated in Table 3, the system demonstrates a graceful degradation in performance as camera angle becomes more and more pronounced. The on-line performance unfortunately is not as successful as in the sun angle experiment. The best static sequence was able to achieve a 77% accuracy, while the least-commitment policy was only able to attain a 70% accuracy on the leave-one-out experiment. The exact causes for the rapid degradation of the online policy are currently under investigation.

5 Conclusion

This paper presented three sets of experiments aimed at determining the robustness of the MR ADORE system. First, effects of labeling errors were explored and the off-line system component was shown to be robust with respect to false positives but not false negatives. Next, the sun angle was varied for a static scene and corresponding ground-truth. The on-line component of the system learned to select near optimal interpretations demonstrating the system's robustness to changes in overall scene illumination. Respectively, the experiments varied the image or its ground-truth. By changing the camera angle in the final experiment, both the scene and the correct labeling were varied from one image to another. While the system gracefully degraded in its off-line performance, the on-line component was unable to cope with the changes in the test images. However, the poor performance of the on-line least-commitment policy may be the result of using a limiting set of training samples (5 images). Hence two main avenues of research still remain: (i) determining the cause of poor on-line performance on the view angle experiment and (ii) determining the on-line performance for the labeling errors experiment.

Acknowledgements

Bruce Draper participated in the initial MR ADORE design stage. Funding provided by University of Alberta, NSERC, and AICML.

References

[1] S. Agarwal and D. Roth. Learning a sparse representation for object detection. In *7th European Conference on Computer Vision*, volume 4, pages 113–130, Copenhagen, Denmark, 2002.

[2] A. G. Barto, S. J. Bradtke, and S. P. Singh. Learning to act using real-time dynamic programming. *Artificial Intelligence*, 72(1):81–138, 1995.

[3] V. Bulitko and I. Levner. Improving learnability of adaptive image interpretation systems. Technical report, University of Alberta, 2003.

[4] D. Culvenor. Tida: an algorithm for the delineation of tree crowns in high spatial resolution remotely sensed imagery. *Computers & Geosciences*, 28(1):33–44, 2002.

[5] B. Draper, U. Ahlrichs, and D. Paulus. Adapting object recognition across domains: A demonstration. In *Proceedings of International Conference on Vision Systems*, pages 256–267, Vancouver, B.C., 2001.

[6] B. Draper, J. Bins, and K. Baek. ADORE: adaptive object recognition. *Videre*, 1(4):86–99, 2000.

[7] B. Draper, A. Hanson, and E. Riseman. Knowledge-directed vision: Control, learning and integration. *Proceedings of the IEEE*, 84(11):1625–1637, 1996.

[8] B. A. Draper. From knowledge bases to Markov models to PCA. In *Proceedings of Workshop on Computer Vision System Control Architectures*, Graz, Austria, 2003.

[9] F. Gougeon. A crown-following approach to the automatic delineation of individual tree crowns in high spatial resolution meis images. *Canadian Journal of Remote Sensing*, 21(1):274–284, 1995.

[10] F. Gougeon and D. Leckie. Forest information extraction from high spatial resolution images using an individual tree crown approach. Technical report, Pacific Forestry Centre, 2003.

[11] M. Larsen. Individual tree top position estimation by template voting. In *Proceedings of the Fourth International Airborne Remote Sensing Conference and Exhibition*, 1999.

[12] I. Levner. Multi resolution adaptive object recognition system: A step towards autonomous vision systems. Master's thesis, Department of Computer Science, University of Alberta, 2003.

[13] I. Levner, V. Bulitko, G. Lee, L. Li, and R. Greiner. Towards automated creation of image interpretation systems. In *Australian Joint Conference on Artificial Intelligence (To appear)*, 2003.

[14] T. Ojala and M. Pietikinen. Unsupervised texture segmentation using feature distributions. *Pattern Recognition*, 32(3):477–486, 1999.

[15] R. Rimey and C. Brown. Control of selective perception using bayes nets and decision theory. *International Journal of Computer Vision*, 12:173–207, 1994.

[16] R. Sutton and A. Barto. *Reinforcement Learning: An Introduction*. MIT Press, 2000.

Accuracy and Speed Improvement in Lips Region Extraction

Takuya Akashi
Graduate School of Engineering
University of Tokushima
2-1 Minami-josanjima, Tokushima, Japan
akataku@is.tokushima-u.ac.jp

Minoru Fukumi
Faculty of Engineering
University of Tokushima
2-1 Minami-josanjima, Tokushima, Japan
fukumi@is.tokushima-u.ac.jp

Norio Akamatsu
Faculty of Engineering
University of Tokushima
2-1 Minami-josanjima, Tokushima, Japan
akamatsu@is.tokushima-u.ac.jp

Abstract

In this paper, a method for improvement of extraction accuracy and speed of lips region is described. In our previous study, we tried to extract lips region whose shape is varied by speech. Moreover, we want to apply this system in a mobile devices. Therefore, we think the condition is a nonrigid scene which is taken by a nonstationary camera. To solve these problem, we use template matching and the matching process is performed using a genetic algorithm. In addition, we think a characteristic shape and colour of the lips are effective for lips region extraction. Furthermore, to make the exploration of a genetic algorithm more efficient, we improve the fitness function and genetic operators. In our simulations, we obtain more efficient exploration, high accuracy and very short speed processing time. In this paper, these method of improvement and comparisons of results between our conventional method and improved method are described.

1. Introduction

Lately, the population that uses internet or e-mail by mobile devices, especially a cellular phone is increasing. However, the interface to input text is not convenient, because a cellular phone has only some key buttons for dialling. Therefore, we think that speech recognition is useful as an interface. In the field of speech recognition, there is a limit to recognize [4], in particular, a paragraph including a person name and a proper name. In the meantime, almost all cellular phones contains a small and high quality digital camera unit. Therefore, to improve the recognition rate, the system which we aim to achieve is translation of speech to text by using both speech and lips image data.

To make the process easy, the purpose of our study is to extract the lips region as a preprocessing of the system. However, this extraction process has some problems. The first is a nonrigid scene. Because the face move constantly and the camera is nonstationary and shake with the hand, the whole scene has considerable change. The second is the varying shape of lips by speech. The third is the processing time must be short. To solve these problems, we use template matching and the matching process is performed using a genetic algorithm with a characteristic shape and colour of the lips. In this paper, the method for improvement of our method [2] and comparisons of results between our conventional method and improved method are described.

2. Methodology

One of the earlier work is personal identification by using the feature of lips motion is described in [5]. This method calculates Mahalanobis distance from varying lips shapes by speech, but if the wrong feature points are detected, there is possibility of failure to recognize the lips shape. Also lipreading by using Eigen-template as the feature of the lips shape is reported in [8]. But, these works have a problem to being unadaptable for intensified geometric changes by a slope of a face or a camera and by a non-stable camera. That is the reason why one of the assumption is the camera and head of the subject are fixed.

On the other hand, to take the shape of the object into consideration, methods that use template matching have

been proposed [1, 3, 6, 10, 11]. In case the matching target has geometric changes that are parallel translation, scaling and rotation, the most basic approach is using multiple templates. But this approach has two problems. One, the more the number of templates used, the more template matching processing is required, which is time-consuming. Two, the fewer the number of the templates become, the less the extraction accuracy is, because few number of the templates means that the number of quantisation steps is large. For these problems, a template-matching method that constructs a parametric template space from a given set of template images is proposed [11]. But this method cannot apply to our study in terms of usefulness for our purpose, because a set of template images have to be prepared depending on the varying object shapes. To deal with the problems, a template matching using a genetic algorithm as a matching process is used in our proposed method. A large number of researches have been carried out into applications of the template matching using a genetic algorithm [3, 6, 10]. But, as far as we know, there is not a method that has invariance by only one template for shape deformations of lips that are an opened or closed mouth and showing or not showing any teeth, at the moment of speech.

Our conventional method [2] (SF-NPD: Static Fitness function with Normalised Pixel Difference) has invariance for an opened and closed mouth showing or not showing any teeth, and has high speed and high extraction accuracy using only one template by utilisation of the colour of lips and characteristics of shape deformations of lips during speech. Moreover, some distinctive inventions on a genetic algorithm make extraction processing relatively stable and high speed. In this paper, the proposed method (DF-PD: Dynamic Fitness function with Pixel Difference) which improves the SF-NPD method is described.

2.1. System Flow

As mentioned in 1, the lips region must be extracted notwithstanding heavy geometric changes and shape deformations in every frame of movie data. We, therefore, use template matching and the matching process is performed by a genetic algorithm. The system flow which we propose is as follows:

Step 1: Input a template and target image.

Step 2: Deform the template shape to a "square annulus".

Step 3: Generate a population of individuals of the first generation randomly.

Step 4: Measure fitness of individuals.

Step 5: Perform genetic operators.

Step 6: Output image which has extracted lips region.

In Step 1, image data is obtained from input images which are inputted on by one as test for our system. A x component (redness) of the Yxy colour space [7, 9] is used as this image data. The template shape is normal square in Step 1. By this normal square template can not support the varying lips shapes such as an opened or closed mouth and showing or not showing any teeth, at the moment of speech. Therefore, the template shape is deformed to a new shape called "square annulus" (refer to 3.1) in Step 2. From Step 3 to Step5, a genetic algorithm is performed. Step4 is described below in detail. Finally, a result of extraction is output on the target image in Step 6.

The procedure in Step 4 is as follows:

Step 4-1: Transform a template by using homogeneous coordinates.

Step 4-2: Control the template aspect ratio.

Step 4-3: Calculate a distance by the pixel difference between the template image and the target image.

Step 4-4: Penalize the distance according to the pixel difference.

Step 4-5:

SF-NPD: Calculate a fitness function and measure.

DF-PD: Calculate an objective function and a dynamic fitness function. and measure.

In Step 4-1, each individual parameters are obtained from informations based on the chromosome. These parameters are used for transforming the template by using homogeneous coordinates in Step 4-1. During the transformation, the aspect ratio of the template is controlled by Step 4-2. Then, in Step 4-3, a distance is calculated between the template image and the target image. And the distance is penalised according to the pixel difference in Step 4-4. This penalty is described in see 4.2. Then, in Step 4-5, in case of the SF-NPD method, fitness function is calculated using genetic operators. Then, the fitness value is measured (refer to 4.2). In the other case, the DF-PD method, at first an objective function is calculated using genetic operators. Next, fitness function is calculated and measured (refer to 4.2). The SF-NPD method has only a fitness function. This means that the objective function equals to the fitness function. This fitness value allows us to do a good exploration that the fitness approaches to 1. On the other hand, in the DF-PD method, an objective function and fitness function are distinguished.

3. Features of Varying Lips Shapes

To achieve invariance for shape deformations of lips, that is, an opened or closed mouth and showing or not showing any teeth, at the moment of speech, and to achieve high speed and high recognition accuracy by using only one template, we use some features of the varying shape of lips during speech. In this section, these methods are explained.

3.1. Shape of Template

In general, the typical template shape is a square. However, considering an application of the template matching to varying lips shapes, the square shape of template is unsuitable. This is because, at the moment of speech, the lips region has intense variations such as an opened or closed mouth and showing or not showing any teeth. In other words, the lips shape changes to other shapes constantly during speech. This is a serious problem in extraction of lips region by using only one template per user.

To solve this problem, we focus our attention on invariance under constantly varying shapes. Then, we find out that lips shapes (without buccal cavity, teeth, and a tongue and etc.) of opened mouth during speech have the same topological properties. In fact, they are homeomorphic. Thus, we use a new template shape illustrated in Figure 1 to cope with the ever-changing lips region. This shape is called "square annulus".

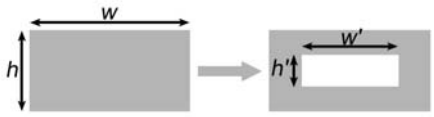

Figure 1. Square annulus

In Figure 1, w and h are the source square template's height and width. And w' and h' are the new square annulus template's width and height. In simulations (refer to Section 5), w' and h' are decided experientially. We performed preliminary examination to use this new template shape. In case of using the normal square template, the extraction accuracy rate is 10 [%], and in case of using the new square annulus template is 100 [%]. Thus, considering topology and using the square annulus is effective for lips extraction. And, the ignored $w' \times h'$ region reduces the accuracy is amount of calculated and makes the lips extraction high speed.

3.2. Control of Aspect Ratio

The aspect ratio of the template that can be transformed in matching processes such as scaling and rotation, is limited. The reason is, in some preliminary examinations, there are some failure that an extracted lips region is extracted using an impossible aspect ratio. This problem is caused by the redness of image data, the angle of light and the blushed part of face.

Therefore, we checked the aspect of varying lips at the moment of speech. The possible aspect ratio's range is shown in equation (1).

$$1.0 \leq \frac{w}{h} \leq 2.0 \tag{1}$$

where w and h are source square template's height and width, same values as in Figure 1.

The failure about the aspect ratio is eliminated by using this control.

4. Genetic Algorithm

4.1. Structure of Chromosome

A chromosome is an optimized solution. In other words, chromosomes are parameters which represent coordinates, scaling and rotation of an exploration object on the target image.

The solutions obtained by manual operations, is called true solution. Our method results are judged to be good or not good by comparison with true solutions. The comparison is performed by the following equations.

$$\begin{cases} C - 3 \leq c \leq C + 3 \\ M \leq m \leq 1.3 \times M \\ ANGLE - 5^\circ \leq angle \leq ANGLE + 5^\circ \end{cases} \tag{2}$$

where: capital letters are solutions obtained manually, and small letters are solutions by proposed method. c represents the x or y coordinate, m is scaling rate and $angle$ is rotation angle.

If a result satisfies these conditions, a good result for the speech recognition is obtained.

The Structure of Chromosome

Figure 2 shows the structure of chromosome before improvement. In Figure 2, c_x and c_y are coordinates after parallel translation, m_x and m_y are scaling rates, and $angle$ is rotation angle of lips shape. Each gene lengths are 8 bits and therefore, total chromosome length is 40 bits.

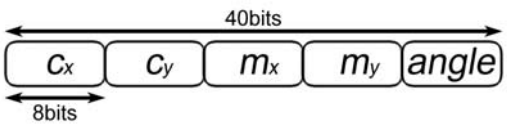

Figure 2. The new structure of chromosome

The lips region at the moment of speech is longer than the width or longer than the height. Thus, we use 2-dimensional scaling by m_x and m_y.

4.2. Fitness Function

In the SF-NPD method , we use only a fitness function which is normalised in range $[0, 1]$, because of reducing a dispersion of pixel differences whose pixel values are real values, x component of Yxy colour space. Moreover, this normalisation makes genetic algorithm process a simple maximisation problem. Against that, the DF-PD method does not normalise the pixel difference, and has an objective function and a dynamic fitness function. The objective function is a minimisation problem and the dynamic fitness function is a maximisation problem.

Pixel Difference

At first, parameters of geometric transformations are obtained from the chromosome. Then, the pixel difference is calculated by using equation (3)

$$D_{ij} = \begin{cases} \left|p^*_{ij} - p_{ij}\right| & \left(p^*_{ij} \in \text{target image}\right) \\ P_{\max} & \left(p^*_{ij} \notin \text{target image}\right) \end{cases} \quad (3)$$

where $P_{\max}$ is a maximum value of pixel, P is a point on the template image, and P^* is the point that corresponds to a transformed point P on the target image, p is a pixel value of a point P on coordinate (i, j) in the template image, p^* is a pixel value of a point P^* on coordinate (i, j) in the target image. D_{ij} is value of the pixel difference between p and p^*, however, in case of a point P^* is out of region template image, D_{ij} is worst $P_{\max}$.

Penalty

From preliminary examinations, we knew that the search efficiency is not very good and the result is unstable by using the fitness function mentioned below [1]. Therefore, the small pixel difference should not be ignored and the individual difference should be emphasised by introducing penalty for the pixel difference D_{ij}. Concretely speaking, if a pixel difference satisfies equation (4), D_{ij} is worst maximum value $P_{\max}$.

if

$$D_{ij} \geq TH \quad (4)$$

then

$$D_{ij} = P_{\max} \quad (5)$$

where TH is the threshold value to penalize.

This value is calculated by the following equation:

$$TH = \left(1 - \frac{S}{100}\right) \times P_{\max} \quad (6)$$

where S is the similarity per pixel, decided experientially and the unit is $[\%]$.

The more S increases, the stricter a condition becomes. In simulations, S is 90. Because, a probability of $100[\%]$ match is very low.

SF-NPD Method

A fitness value is calculated by using equation (7). The fitness is normalised and static.

$$\mathit{fitness} = 1.0 - \frac{\sum_{j=1}^{h}\sum_{i=1}^{w} D_{ij}}{(w \times h)\,(P_{\max})} \quad (7)$$

where the template size is w and h.

$fitness$ allows us to do a good exploration that the fitness approaches to 1.

DF-PD Method

An objective value and a fitness value is calculated by using equation (8) and (9). The fitness is not normalised and dynamic.

$$O = \sum_{j=1}^{h}\sum_{i=1}^{w} D_{ij} \quad (8)$$

where O is value of the objective function.

$$\mathit{fitness} = \max\{W_t, W_{t-1}, \ldots, W_{t-n}\} - O \quad (9)$$

where t is a current number of generation, W_t is a worst objective value of generation t, and n is a number of generation before.

This fitness function changes dynamically according to the worst objective value during n generations. Therefore, the selection pressure can be controlled automatically. O allows us to achieve good exploration that the value of the objective function approaches 0. In other words, $fitness$ allows us to do a good exploration that the fitness value becomes large. We use $n = 5$ in simulations.

5. Results and Discussions

5.1. Input Images

The template images are illustrated in Figure 3. Template image size of subject 1 and subject 2 is 18×8 [pixels], and subject 3 is 20×9 [pixels].

Figure 4 below shows examples (pronounce the vowel /e/) of target images. The images were captured using a

video camera include a face and background while each of three objects pronounce the vowels. Target images are then cut from the video streams. In consideration of use by mobile devices, target images have geometric changes based on the template image. The geometric changes are such as parallel translation, scaling, rotation. These value can be regarded as the true solution (refer to 4.1). All target images size are 240×180 [pixels].

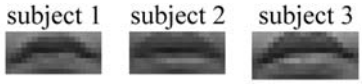

Figure 3. Template images

Figure 4. Target images

5.2. Configurations of System

A new structure chromosome is used in this demonstration (refer to 4.1). The parameters of genetic algorithms are: population size is 70, probability of crossover is 0.7, and probability of mutation is 0.05. The shape of template change parameters is $w'/w = 0.8$, $h'/h = 0.5$ (refer to Figure 1 in 3.1). Parameter S which decides a threshold of penalizing (refer to equations (4), (5) and (6) in 4.2) is set to 90. We use $n = 5$ in equation (9) of the DF-PD method. If the same fitness value continues until some generations, the solution is regarded as having converged and extraction is terminated. The more this value becomes large, the more the termination criterion becomes fair.

The machine speck which we use for simulation is Pentium4: 2[GHz].

5.3. Result of Simulation and Consideration

Figure 5 shows examples of results from the computer simulation. The rectangle region is the extracted lips region. The shape deformations of lips by speech are extracted exactly as shown in Figure 5.

Figure 5. Result images

Table 1 shows the true solution obtained manually for /e/ of subject 2 in Figure 4 and the solution obtained by the proposed method. It is found that these both solutions are similar.

Table 1. Example of solution of result (subject 2 /e/)

	coordinate		scaling [rate]		rotation
	x	y	x	y	[deg]
true solution	82	128	1.39	2.00	19.20
experimental result	81	131	1.68	2.51	17.33

The effectiveness of our method is demonstrated using 20 times simulations for each person (total is 60 times simulations per one vowel) being tested as shown in Tables 2, 3 and 4.

Table 2. Results of simulation (DF-PD method, tough criterion)

	/a/	/i/	/u/	/e/	/o/	total
acc [%]	95.00	93.33	95.00	91.67	98.33	94.67
time [sec]	0.198	0.203	0.199	0.197	0.199	0.199
gene	78.48	81.15	80.06	77.25	76.50	78.69

Table 3. Results of simulation (SF-NPD method, tough criterion)

	/a/	/i/	/u/	/e/	/o/	total
acc [%]	26.67	31.67	31.67	33.33	18.33	28.33
time [sec]	0.065	0.069	0.084	0.069	0.065	0.071
gene	55.52	63.24	75.41	60.84	57.42	62.49

Table 4. Results of simulation (SF-NPD method, fair criterion)

	/a/	/i/	/u/	/e/	/o/	total
acc [%]	98.33	96.67	91.67	93.33	91.67	94.33
time [sec]	0.323	0.318	0.332	0.299	0.329	0.320
gene	140.7	139.9	147.1	130.8	144.2	140.5

In Tables 2 and 3, the configuration of the simulations are described in 5.2. Table 4 is tested with another configuration and shows the conventional method result which is described in [2]. In case of Tables 2 and 3, their termination criterion value is 25 generations (refer to 5.2). Against that, in case of Table 4, it is 50 generations. In other words, Table 4 criterion is fairer than that in Tables 2 and 3.

In Tables 2, 3 and 4, "acc" means "extraction accuracy (only for correctly extracted lips region)", "time" means "processing time" and "gene" means "generation". Additionally, in Table 3, processing time and generation are not important, because their extraction accuracies are very low.

Comparing Table 3 with Table 4, they indicate that the SF-NPD method obtain high extraction accuracy on the fair

criterion, however on the tough criterion, it obtains low extraction accuracy. Against that, the DF-PD method works on the tough criterion in Table 2, and obtains better accuracy and speed.

Figures 6 and 7 illustrate a typical transition of the elite fitness and objective value with the SF-NPD method and the DF-PD method. Good results such as Figure 5 are obtained by these simulations. In Figure 6, the elite fitness changes with very small value and narrow range as opposed to Figure 7. This indicated that Figure 7 performed more efficient exploration. The reason is that the DF-PD method controls the selection pressure dynamically by equation (9).

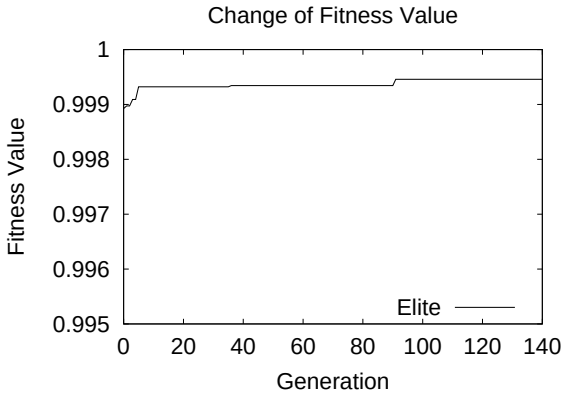

Figure 6. Transition of elite fitness (SF-NPD)

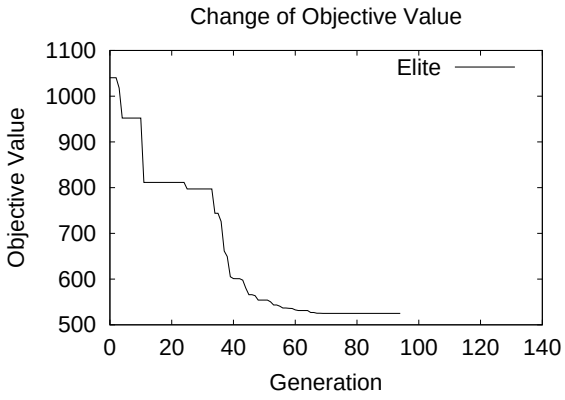

Figure 7. Transition of elite objective value (DF-PD)

6. Conclusion and Future Work

In this paper, a method for the improvement of lips extraction that has invariance for an opened and closed mouth showing or not showing any teeth, and has high speed and high recognition accuracy using only one template, is proposed. In Section 5, the results of these computer simulations indicate that the DF-PD method can perform more efficient exploration and has invariance for the varying shape, and higher extraction accuracy and a higher speed can be obtained in the extraction processing of all the vowels.

However, in the DF-PD method, some parameters have a lot to do with experiences. For example, S which decides the threshold of penalizing is set to 90 by trial and error (refer to 4.2), and the unconsidered region size w', h' of the square annulus is fixed (refer to 5.2). Moreover, parameter n of equation (9) in the DF-PD method is fixed to 5. Therefore, our future work needs improvement to decide all parameters automatically. Other future work is to apply this method to real-time processing. For this improvement, we hope to consider use of other feature of lips, such as another shape of the template except for the square annulus, will be effective.

References

[1] T. Akashi, M. Fukumi, and N. Akamatsu. Lips extraction with template matching by genetic algorithm. In *Knowledge-Based Intelligent Information Engineering systems and Allied Technologies*, pages 343–347, Crema, Italy, September 2002.

[2] T. Akashi, Y. Mitsukura, M. Fukumi, and N. Akamatsu. Genetic lips extraction method for varying shape. In *Computational Intelligence in Robotics and Automation*, Kobe, Japan, July 2003. (to appear).

[3] A. Hara and T. Nagao. Extraction of facial region of arbitrary directions from still images with a genetic algorithm. *Technical Report of IEICE*, HCS97-12, 97(262):37–44, December 1997.

[4] H. Kashiwazaki and S. Hirose. Extraction of issue for spoken language learning -using perceptual decision of spoken language and sound spectrograph-. In *The 17th Annual Meeting of the Japanese Cognitive Science Society*, pages 1–35, Japan, June 2000.

[5] M. Konda, M. Nishida, M. Ishii, and K. Sato. Application of the feature of lips motion in continuous image to personal identification. *T. IEE Japan*, 120-C(5):765–766, May 2000.

[6] S. Masunaga and T. Nagao. Extraction of human facial regions in still images using a genetic algorithm. *Technical Report of IEICE*, PRU95-160, 95(365):13–18, November 1995.

[7] L. Minolta Co. Story of color knowledge, 2002.

[8] Y. Nakata and M. Ando. Detection of mouth position using color extraction method and eigentemplate technique for lipreading. *Technical Report of IEICE*, PRMU2001-09, 101(303):7–12, September 2001.

[9] K. N. Plataniotis and A. N. Venetsanopoulos. *Color Image Processing and Applications*. Springer-Verlag, New York, USA, 2000.

[10] F. Saitoh. Pose recognition of gray-scaled template image using genetic algorithm. *T. IEE Japan*, 121-C(10):1500–1507, October 2001.

[11] K. Tanaka, M. Sano, S. Ohara, and M. Okudaira. Parametric template method and its application to high-accuracy robust matching. *T. IEICE Japan*, J83-D-II(4):1119–1130, April 2000.

Improving an Adaptive Image Interpretation System by Leveraging

Lihong Li Vadim Bulitko Russell Greiner Ilya Levner
University of Alberta
Department of Computing Science
Edmonton, Alberta, Canada T6G 2E8
{lihong|bulitko|greiner|ilya}@cs.ualberta.ca

Abstract

*Automated image interpretation is an important task in numerous applications ranging from security systems to natural resource inventorization based on remote-sensing. Recently, a second generation adaptive machine-learned image interpretation system (ADORE) has shown expert-level performance in several challenging domains. Its extension, MR ADORE, aims at removing the last vestiges of human intervention still present in the original design of ADORE. Both systems treat the image interpretation process as a finite-horizon non-discounted Markov decision process guided by a machine-learned heuristic value function. Therefore, the key task in automated development of such systems lies with acquiring the optimal control policy. This paper employs a new leveraging algorithm for regression (*RESLEV*) to improve the learnability of the optimal value function in MR ADORE. Experiments show that* RESLEV *improves the system's performance if the base learners are weak. More surprisingly, empirical evidence indicates that reducing the regression error can lead to worsening the overall performance of the system. We discuss this phenomenon thereby opening an exciting novel research direction.*

Keywords: adaptive image interpretation system, boosting, leveraging for value function regression, sequential decision making, reinforcement learning.

1. Introduction

Image interpretation is an important and highly challenging problem with numerous practical applications. Handcrafted image interpretation systems suffer from an expensive design cycle, a high demand for human expertise in both subject matter and computer vision, and the difficulties with portability and maintenance. Over the last three decades, various *automated* ways of constructing image interpretation systems have been explored [7].

One of the promising approaches to automatic acquisition of image interpretation systems lies with treating computer vision as a control problem over a space of image processing operators. Early attempts used the schema theory [2, 3]. While presenting a systemic way of designing image interpretation systems, the approach was still *ad-hoc* in its nature and required extensive manual design efforts [9].

In the 1990's the second generation of control policy based image interpretation systems came into existence. More than a systematic design methodology, such systems used theoretically well-founded machine learning frameworks for automatic acquisition of *control strategies* over a space of image processing operators. The two well-known representatives are a Bayes net system [21] and a Markov decision process (MDP) based system [8].

The latter system ADORE (ADaptive Object REcognition) [8] and its extension MR ADORE (Multi-Resolution ADaptive Object REcognition) [17] learn dynamic image interpretation strategies for finding target objects in images. As with many vision systems, they identify objects in a multi-step process. The input is a raw image, and the output is an interpretation identifying target objects in the image; in between, the data can be represented as intensity images, probability images, edges, lines, or curves. The systems model image interpretation process as a Markov decision process, where the intermediate representations are continuous state spaces, and the vision procedures are actions. The goal is to learn a dynamic control policy that selects the next action (i.e., image processing operator) at each step so as to maximize the quality of the final interpretation. Instead of learning the policy directly, the system *learns* the optimal value function as the heuristic for the MDP-based policy.

In this paper we consider the problem of ensemble learning (in particular, leveraging [20]) for the value function in MR ADORE. The task of recognizing tree canopies from aerial photographs (i.e., labeling pixels belonging to tree canopies in an input image) is used as the testbed.

The rest of the paper is organized as follows. Section 2 reviews the requirements and design of MR ADORE. Sec-

(a) Input image (b) Desired output

Figure 1. The left image is an original photograph. The right one is the corresponding desired labeling provided by an expert as a part of the training set.

tion 3 gives a brief overview of boosting/leveraging methods. Section 4 presents and discusses the experimental results. Finally, section 5 concludes the paper and points out several interesting future research directions.

2. MR ADORE design

MR ADORE was designed with the following objectives: (i) rapid system development for a wide class of image interpretation domains; (ii) low demands for subject matter, computer vision, and AI expertise on the part of the developers; (iii) accelerated domain portability, system upgrades, and maintenance; (iv) adaptive image interpretation wherein the system adjusts its operation dynamically to a given image; (v) user-controlled trade-offs between recognition accuracy and resources utilized (e.g., time required).

2.1. Overview

The objectives above favor the use of readily available off-the-shelf image processing operator libraries (IPL). However, the domain independence of such libraries requires an *intelligent policy* to control the application of library operators. Operation of such a control policy is a complex and adaptive process [5]. It is *complex* in the sense that there is rarely a one-step mapping from input images to their interpretations; instead, a series of operator applications are required to bridge the gap between raw pixels and semantic objects. Examples of the operators include region segmentation, texture filters, and the construction of 3D depth maps (see Figure 2 for a simplified example).

Image interpretation is an *adaptive* process in that there is no fixed sequence of actions that will work well for most images. For instance, the steps required to locate and identify isolated trees are different from the steps required to find connected stands of trees. Figure 3 demonstrates two specific forestry images that require significantly different operator sequences for satisfactory interpretation results.

The success of MR ADORE therefore depends on its control policy: given an input image, how to select a sequence of operators to interpret the image most effectively?

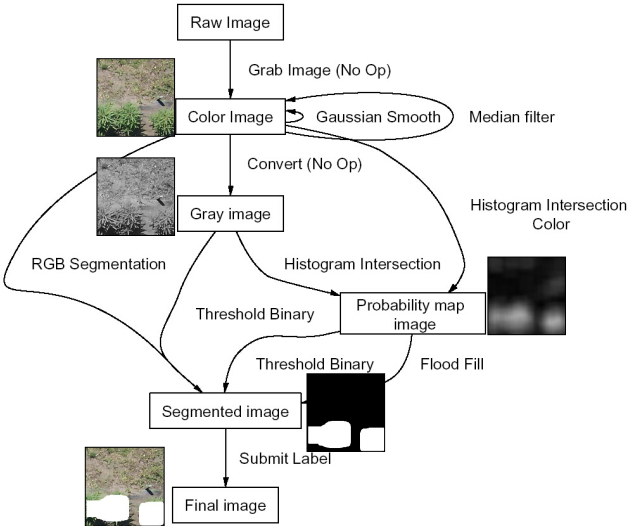

Figure 2. Data types (the boxes) and image processing operators (the arcs) in MR ADORE. Representatives of data tokens of each types are shown next to the nodes.

2.2. Learning control policies

MR ADORE starts with the Markov decision process (MDP) as the basic mathematical model by casting the IPL operators as the MDP actions and the results of their application as the MDP states. Then it learns an approximation to the optimal value function.

First, it uses training data (here, annotated images) to provide relevant domain information. Each training datum is a source image, annotated by an expert with the desired output. Figure 1 demonstrates a training datum in the forestry image interpretation domain.

Second, during the off-line stage the state space is explored via limited depth expansions of training images. Within a single expansion, all sequences of IPL operators up to a certain user-controlled length are applied to the training image. Since training images are user-annotated with the desired output, terminal rewards can be computed based on the difference between the produced labeling and the desired labeling. Then, dynamic programming methods [4] are used to compute the optimal value function for the explored parts of the state space. Note that MR ADORE does not use a discounting factor, making the entire problem a finite horizon non-discounted MDP. We represent the value function as $Q : S \times A \rightarrow \mathbb{R}$ where S is the set of states (image tokens) and A is the set of actions (IPL operators). The optimal $Q(s, a)$ computes the maximum cumulative reward the optimal policy can expect to collect by taking action a in state s and acting optimally thereafter [24]. As the raw state descriptions are on the order of mega-bytes each, we first abstract each state s into a set of features $f(s)$ using an abstraction function $f(\cdot)$. Then supervised ma-

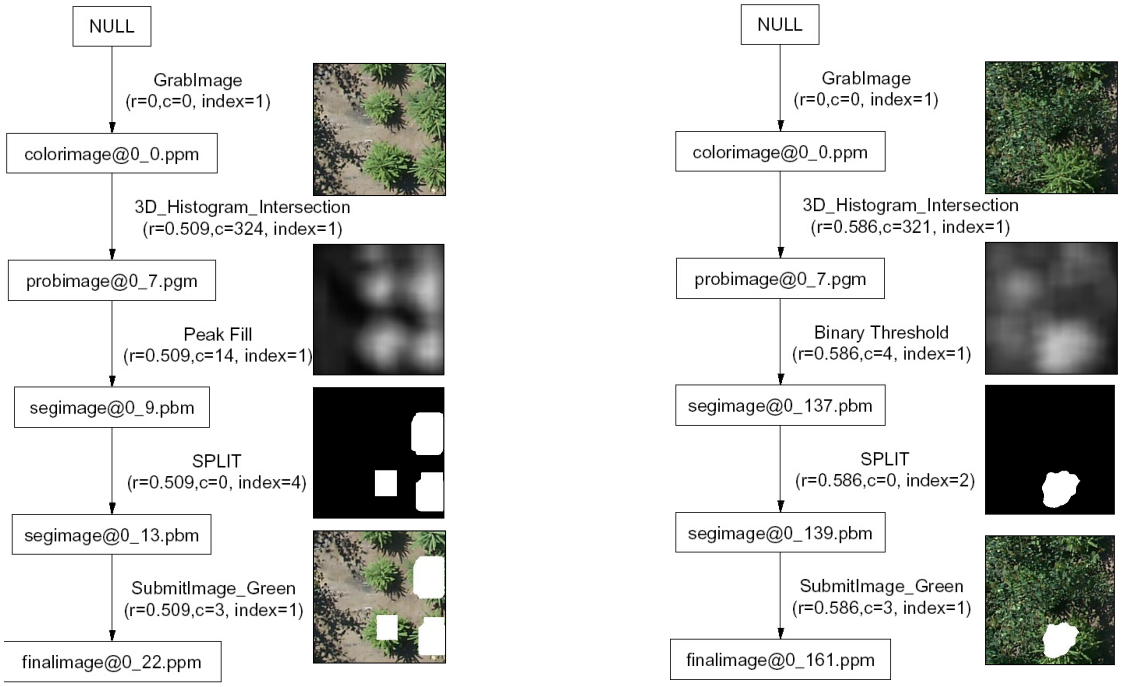

Figure 3. Adaptive nature of image recognition: two different input images require significantly different satisfactory operator sequences. Each node is labeled with its data type. Each arc between two data tokens is shown with the operator used.

chine learning extrapolates the sample Q^*-values computed by dynamic programming on the explored fraction of the state space onto the entire space.

Finally, when presented with a novel input image to interpret, MR ADORE first computes the abstracted version $f(s)$, then applies the machine-learned approximation to the value function $Q(\cdot,\cdot)$ to compute $Q(f(s),a)$ for each IPL operator a; it then performs the action $a^* = \arg_a \max Q(f(s),a)$. The process terminates when the policy executes action `submit(`⟨`labeling`⟩`)` where ⟨`labeling`⟩ becomes the system's output.

3. Boosting and leveraging methods

Boosting and leveraging have their roots in the PAC (Probably Approximately Correct) [25] learning model. A learner L_s for concept class $\mathcal{C}$ is a (*strong*) PAC learner, iff with an *arbitrarily high* probability, L_s produces a hypothesis h with *arbitrarily high* accuracy. The requirement of being arbitrarily accurate with an arbitrarily high probability is removed for weak learners. For example, a learner that produces hypotheses a little better than random guessing is a weak learner. An algorithm has the *PAC-boosting property* iff it can boost any weak PAC learner to a strong PAC learner [11].

Both boosting and leveraging methods work by repeatedly producing base hypotheses with modified training data, then using them to extend and modify the training data set, and then combining them into a final hypothesis that are better than any individual base hypothesis. While boosting methods provably have the PAC-boosting property, leveraging methods may or may not.

Since Schapire proposed the first provable polynomial time boosting algorithm [22], a number of boosting and leveraging algorithms have been developed [6, 10, 12, 13, 14, 16]. They are conceptually gradient-descent algorithms that iteratively increase the accuracy of the final hypothesis by decreasing some associated *potential functions*. Recently a simple and straightforward leveraging algorithm called ResLev (Figure 4) [19] has demonstrated the ability to improve the accuracy of a hypothesis by iteratively learning the previous ensemble hypothesis' residuals (i.e., errors) of predictions on training data. Experiments on the Friedman datasets [15] indicate the algorithm's effectiveness [18, 19].

Definitions: Given a hypothesis h and a set of training data

$$S = \{(x_1,y_1),(x_2,y_2),\cdots,(x_N,y_N)\}$$

the *sample error* of h on S is defined as:

$$\widehat{err}_S(h) = \frac{1}{N}\sum_{i=1}^{N}[y_i - h(x_i)]^2$$

Let $\mathcal{P}$ be a probability distribution on the whole instance space, the *generalization error* of h with respect to $\mathcal{P}$ is defined as:

$$err_{\mathcal{P}}(h) = \mathbf{E}_{\mathcal{P}}[y - h(x)]^2$$

RESLEV (S, R, T_{max})

Input: A set of training samples
$S = \{(x_1, y_1), (x_2, y_2), \cdots, (x_N, y_N)\}$;
A base regressor R;
Maximum number of iterations T_{max}

1. Initialize ensemble hypothesis $H_0 \equiv 0$
2. For $t = 1, \cdots, T_{max}$ Do
   (a) Apply R on S and produce a base hypothesis h_t
   (b) $H_t = H_{t-1} + h_t$
   (c) Modify data in S: $\forall i, y_i = y_i - h_t(x_i)$
3. Output final ensemble hypothesis $H_{T_{max}}$

Figure 4. RESLEV: Residual Leveraging

where (x, y) is drawn randomly according to $\mathcal{P}$.

The following theorem gives a *sufficient* condition under which RESLEV will decrease the sample error, based on the relation between the training data and the sample error.

Theorem 1 [19] *Given any training set* $T = \{(u_1, v_1), (u_2, v_2), \cdots, (u_M, v_M)\}$, *if the learner* L *produces a hypothesis* h *that satisfies*

$$\sum_{i=1}^{M} v_i^2 \quad > \quad \sum_{i=1}^{M} (v_i - h(u_i))^2 = M \cdot \widehat{err}_T(h) \qquad (1)$$

then RESLEV *reduces the sample error with the learner* L.

RESLEV reduces sample error by repeatedly reducing the residuals of predictions over the training data. Assuming that the training data and test data are both drawn from an unknown distribution $\mathcal{P}$, it is expected that a small sample error implies a small generalization error [1], provided that the ensemble hypothesis is sufficiently simple [1].

4. Empirical evaluation

We applied RESLEV to learning the optimal value function $Q(\cdot, \cdot)$ in MR ADORE. Multi-layer feed-forward neural networks were used as the base learners/regressors. Common sets of features including RGB-HISTOGRAM, HSV-HISTOGRAM, HSV-MEAN, textural features, etc. were used. Experiments were run with combinations of different features and neural network topologies, as shown in Figure 5 and 6. Three measures: sample and generalization errors in the Q-function and the value of the resulting MR ADORE control policy were computed.[2]

Thirty two forestry aerial images with user-annotated labeling were used in our experiments. Since the training data are quite limited, leave-one-out cross-validation was employed for evaluation. In each run, one image was selected for testing while the other thirty one images were used to train MR ADORE (i.e., to learn the function $Q(\cdot, \cdot)$). The three performance measures were then averaged over all the thirty two runs.

Figure 5 shows the experimental results [3]. For comparison, experiments with the random policy (i.e., the system randomly selects an operator to apply on the current token) were tried and an average relative reward of 26.3% was attained. Obviously, learning in all experiments increases the system's performance: the average relative reward ranges from 53% to 85%.

Several observations are in order. First, the leveraging process reduces the regression errors in the Q-function when the base learners are weak (e.g., SET#4). On the other hand, it can actually *increase* the errors when the base learners are strong to begin with (e.g., SET#3 and #5). An investigation of this phenomenon revealed that with stronger base learners condition (1) of Theorem 1 is often violated.

Second, leveraging can often improve the value of the policy while *decreasing* the regression accuracy (e.g., with SET#2). The reverse phenomena takes place as well. Furthermore, such a divergence between the effects of leveraging on regression errors and the performance of the control policy was recorded even with boosting algorithms such as SQUARELEV.R [12] [18]. These observations provide empirical support for the following claim:

Claim: *decision-making problems behave differently from regression problems in terms of boosting/leveraging methods applied to the value function.*

Note that if the optimal value function can be learned with an arbitrary precision then the resulting control policy can be made arbitrarily close to the optimal policy (cf. [23] for an analysis of discounted cases). In practice, however, the complexity of sequential decision-making frequently does not allow to learn the optimal value function arbitrarily well. This paper demonstrate that in such cases and in the absence of discounting leveraging/boosting methods can have opposite effects on regression error vs. value of the resulting control policy. Therefore, it is of interest to develop leveraging and boosting methods that optimize the control policy value *directly*.

5. Conclusions and future directions

Future Work: As discussed in previous sections, primary future directions include: (i) employing other base regression algorithms so that the condition (1) in Theorem 1 is satisfied and thus RESLEV can be of help; (ii) investigation of the generalization error of RESLEV, and whether it has the PAC-boosting property. (iii) comparing the ef-

[1] The risk of overfitting increases with the complexity of the hypothesis.

[2] The control policy value was computed as the ratio of the cumulative reward collected by the resulting control policy to the optimal reward.

[3] Detailed and up-to-date results are available at [18].

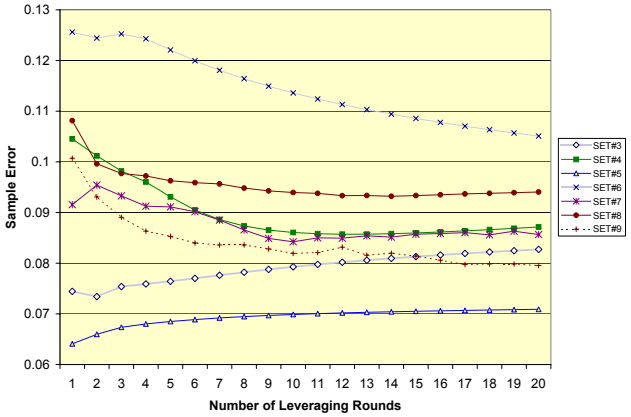

(a) Sample errors on $Q(\cdot,\cdot)$

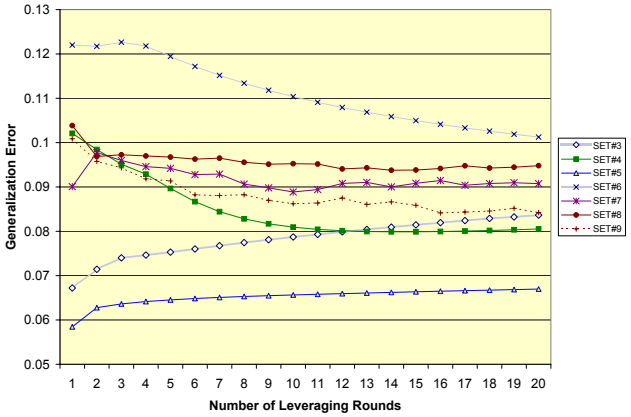

(b) Generalization errors on $Q(\cdot,\cdot)$

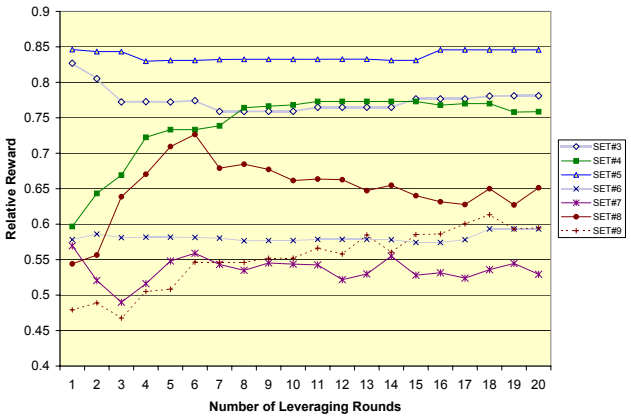

(c) Value of the resulting control policy

Figure 5. Experiments on MR ADORE using RESLEV. Different combinations of features and neural network topologies were tried, and three performance measures (sample/generalization errors and average relative reward) were adopted.

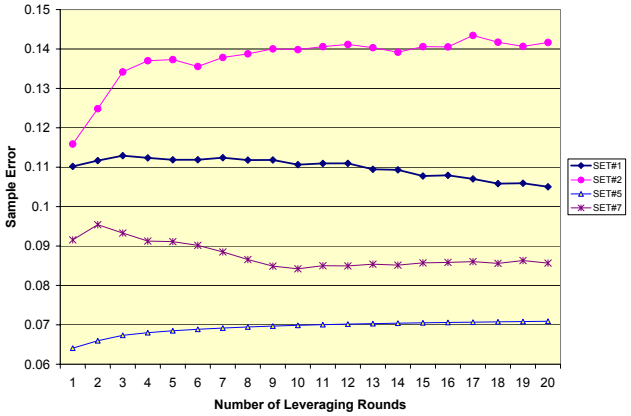

(a) Sample errors on $Q(\cdot,\cdot)$

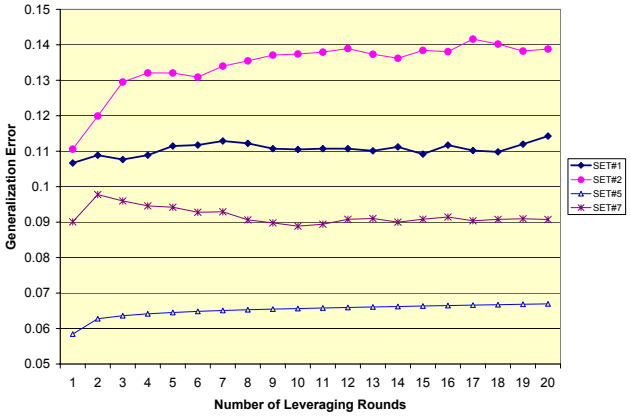

(b) Generalization errors on $Q(\cdot,\cdot)$

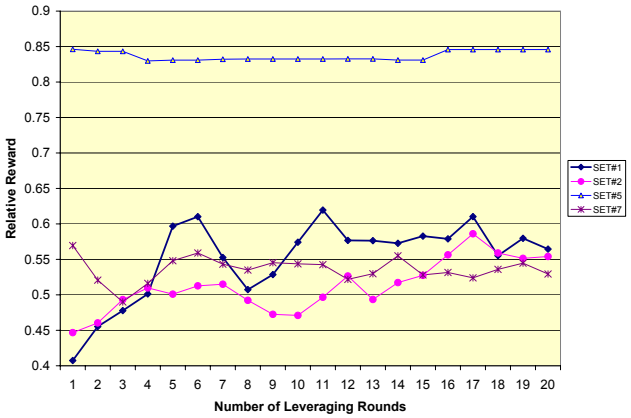

(c) Value of the resulting control policy

Figure 6. Contradictions among different measures exist in these experiments, which suggest the different behaviors between a regression problem and a decision-making problem in terms of boosting/leveraging methods applied to the value function.

fectiveness of RESLEV to that of other boosting/leveraging algorithms; (iv) developing new boosting/leveraging algorithms that directly optimize the *overall* decision-making performance as opposed to the regression error (such as sample/generalization errors) of the value function.

Contributions: In this paper we consider a state-of-the-art adaptive image interpretation system that casts vision as a non-discounted finite-horizon MDP control problem over a library of image processing operators. The key learning task in such systems is automated acquisition of the optimal control policy. We apply two recent leveraging algorithms, RESLEV and SQUARELEV.R, to learning the optimal value function. Experiments in the real-life domain of forest image interpretation indicate that (i) leveraging is indeed useful in improving complex sequential decision-making policies, and (ii) reducing the regression error in the value function can actually *decrease* the overall interpretation performance (i.e., the value of the resulting control policy). Consequently, the paper opens a novel research direction of developing boosting/leveraging algorithms that target reducing the control policy value directly.

Acknowledgements

Bruce Draper participated in the initial MR ADORE design stage. Terry Caelli, Li Cheng, Joan Fang, Ken Greenway, Dorothy Lau, Omid Madani, Rongzhou Man, David McNabb, and Guanwen Zhang have contributed in various ways. We are grateful for the funding from the Alberta Ingenuity Center for Machine Learning, the University of Alberta, and NSERC.

References

[1] M. Anthony and P. L. Bartlett. *Neural Network Learning: Theoretical Foundations*. Cambridge University Press, Cambridge, 1999.

[2] M. Arbib. *The metaphorical brain: An introduction to cybernetics as artificial intelligence and brain theory*. Wiley-Interscience, New York, 1972.

[3] M. Arbib. Segmentation, schemas, and cooperative computation. In S. Levin, editor, *MAA studies in Mathematics*, pages 118–155. 1978.

[4] A. G. Barto, S. J. Bradtke, and S. P. Singh. Learning to act using real-time dynamic programming. *Artificial Intelligence*, 72(1):81–138, 1995.

[5] V. Bulitko, L. Li, G. Lee, R. Greiner, and I. Levner. Adaptive image interpretation : A spectrum of machine learning problems. In *ICML-03 Workshop on the Continuum from Labeled to Unlabeled Data in Machine Learning and Data Mining*, Washington D.C., August 2003.

[6] T. G. Dietterich. An experimental comparison of three methods for constructing ensembles of decision trees: Bagging, boosting, and randomization. *Machine Learning*, 40(2):139–157, 2000.

[7] B. Draper. From knowledge bases to Markov models to PCA. In *Workshop on Computer Vision System Control Architectures (held in conjunction with ICVS)*, Graz Austria, March 2003.

[8] B. Draper, J. Bins, and K. Baek. ADORE: Adaptive object recognition. In *International Conference on Vision Systems*, Spain, 2000.

[9] B. Draper, A. Hanson, and E. Riseman. Knowledge-directed vision: Control, learning and integration. In *Proceedings of the IEEE*, volume 84, pages 1625–1637, 1996.

[10] H. Drucker. Improving regressors using boosting techniques. In D. H. Fisher, editor, *Proc. Fourteenth International Conference on Machine Learning (ICML-97)*, pages 107–115. Morgan-Kaufmann, 1997.

[11] N. Duffy and D. Helmbold. Potential boosters? In K.-R. M. Sara Solla, Todd Leen, editor, *Advances in Neural Information Processing Systems (NIPS-99)*, volume 12, pages 258–264. MIT Press, 2000.

[12] N. Duffy and D. Helmbold. Boosting methods for regression. *Machine Learning*, 47:153–200, 2002.

[13] Y. Freund and R. Schapire. A decision-theoretic generalization of on-line learning and an application to boosting. *Journal of Computer and System Sciences*, 55(1):119–139, 1997.

[14] Y. Freund and R. E. Schapire. Experiments with a new boosting algorithm. In *Proceedings of the Thirteenth International Conference on Machine Learning (ICML-96)*, pages 148–156, 1996.

[15] J. Friedman. Multivariate adaptive regression splines. *Annals of Statistics*, 19:1–141, 1991.

[16] J. Friedman. Greedy function approximation: A gradient boosting machine. Technical report, Department of Statistics, Stanford University, CA, March 2000.

[17] I. Levner, V. Bulitko, L. Li, G. Lee, and R. Greiner. Towards automated creation of image interpretation systems. In *Proceedings of the Sixteenth Australian Joint Conference on Artificial Intelligence (AI-03)*, Perth, Australia, December 2003.

[18] L. Li. Experimental results of RESLEV, 2003. Available at http://www.cs.ualberta.ca/∼lihong/research/reslev/reslev.htm.

[19] L. Li. ResLev: A leveraging method for regression. Technical report, Department of Computing Science, University of Alberta, Edmonton, Alberta, Canada, July 2003. Available at http://www.cs.ualberta.ca/∼lihong.

[20] R. Meir and G. Rätsch. An introduction to boosting and leveraging. In S. Mendelson and A. Smola, editors, *Advanced Lectures on Machine Learning*, LNCS, pages 119–184. Springer, 2003.

[21] R. Rimey and C. Brown. Control of selective perception using Bayes nets and decision theory. *International Journal of Computer Vision*, 12:173–207, 1994.

[22] R. E. Schapire. The strength of weak learnability. *Machine Learning*, 5(2):197–227, 1990.

[23] S. P. Singh and R. C. Yee. An upper bound on the loss from approximate optimal-value functions. *Machine Learning*, 16(3):227–233, 1994.

[24] R. S. Sutton and A. G. Barto. *Reinforcement Learning: An Introduction*. MIT Press, Cambridge, MA, March 1998.

[25] L. G. Valiant. A theory of the learnable. *Communications of the ACM*, 27(11):1134 – 1142, Nov. 1984.

Calculating the Similarity of Textures using Wavelet Scale Relationships

Andrew Busch, Wageeh W. Boles & Sridha Sridharan
Research Centre in Speech, Audio, Image and Video Technology
School of Electrical and Electronic Systems Engineering
Queensland University of Technology
a.busch@qut.edu.au, w.boles@qut.edu.au, s.sridharan@qut.edu.au

Abstract

Texture is an important property of many types of images, and has been widely used in a number of applications to describe, classify and index images. In this paper we propose a novel technique for characterising texture by modelling the relationships between the high and low frequency bands of its wavelet decomposition, which have been experimentally shown to provide information which is not available when considering such bands independently. A similarity measure using the recently proposed earth mover's distance is formulated, and the results of using this measure for retrieval of textures from a database presented.

1 Introduction

The wavelet transform has emerged over the last two decades as a powerful new theoretical framework for the analysis and decomposition of signals and images at multiple resolutions [1]. One of the most common forms of the transform used for image analysis applications is the separable two dimensional wavelet transform, defined as

$$A_j = [H_x * [H_y * A_{j-1}]_{\downarrow 2,1}]_{\downarrow 1,2} \quad (1)$$

$$D_{j1} = [G_x * [H_y * A_{j-1}]_{\downarrow 2,1}]_{\downarrow 1,2} \quad (2)$$

$$D_{j2} = [H_x * [G_y * A_{j-1}]_{\downarrow 2,1}]_{\downarrow 1,2} \quad (3)$$

$$D_{j3} = [G_x * [G_y * A_{j-1}]_{\downarrow 2,1}]_{\downarrow 1,2} \quad (4)$$

where G and H are the high and low-pass filters along the subscripted axis, $*$ is the convolution operator, j is the resolution level, and $\downarrow a, b$ represents downsampling along the x and y axes by factors of a and b respectively. The resulting images A_j and $D_{ji},\ i \in \{1, 2, 3\}$ are known as the approximation and detail coefficients respectively.

The coefficients of the wavelet transform have been shown to provide an excellent basis for identifying and segmenting textured images, and have been used in many applications to date [2, 3, 4]. The first and simplest of the features extracted from the wavelet coefficients were the so-called wavelet energy signatures, which were a representation of the energy contained within each band of the decomposition. Extending this, the mean deviation and other higher order moments have also been used for the purposes of texture classification and segmentation. Such features have been shown to provide good characterisation of textures in certain environments, and typically outperform single resolution techniques such as grey-level co-occurrence matrix features.

More recently, a number of new algorithms for extracting features from the coefficients of the wavelet transform have been proposed in the literature. Kim and Udpa propose a new non-separable set of wavelet filters for characterising texture which are shown to outperform the more commonly used separable DWT [5]. Tabesh uses the zero-crossings of a wavelet frame representation to extract texture features, and has shown experimentally that these features contain information not contained within the energy signatures [6]. By combining these two feature sets, overall accuracy is improved by up to 70%. Van de Wouwer *et. al.* have proposed a set of features based on second-order statistics of the wavelet coefficients, calculated using co-occurrence matrices [7]. Numerous methods of extracting texture features using the wavelet packet transform have been proposed [8, 9, 10].

In each of the feature extraction techniques listed above, the coefficients of each band are analysed separately, with the correlations between bands of the same and different resolution levels ignored, even though it is well-known that strong relationships between neighbouring bands exists. Portilla and Simoncelli have shown that without knowledge of these correlations accurate reconstruction of the texture is not possible, indicating that this information is significant for characterising the texture [11].

This paper proposes a novel method for indexing and retrieving textures based on *wavelet scale co-occurrence matrices*, which capture information about the relationships between each band of the transform and the low frequency

approximation at the corresponding level. A theoretical description of scale co-occurrence matrices is first presented, and is then used to formulate a metric for measuring the similarity of two texture samples. The *earth mover's distance* (EMD), a recently proposed metric for measuring the distance between two distributions, is used for this purpose, as it has been shown to provide a more robust measure in many applications. Results from retrieval experiments conducted using this metric on a set of textures from the Brodatz album [12] are presented.

2 Limitations of Independent Wavelet Features

Initial experiments conducted by Julesz in the field of visual texture led him to conjecture that such images could be completely characterised by their second-order statistics [13]. Eventually, this was shown to be false, with many counter-examples presented showing visually distinct textures with identical second-order statistics. Recently, the main focus of much texture analysis research has centered around multi-scale filtering, with Gabor filters and the WT used to good effect. Common WT-based texture analysis techniques extract features from each band of the wavelet decomposition, measuring statistical information or modelling these coefficients via some parametric form. In this section, we show that it is possible for markedly different textures to have identical such statistics, indicating that they do not completely characterise texture. Examples of synthetic textures are provided to illustrate this point.

Wavelet energy signatures are one of most commonly used texture features in many applications, and can be calculated from the coefficients of the separable FWT by

$$E_{jl} = \frac{1}{MN} \sum_{m=1}^{M} \sum_{n=1}^{N} D_{jl}(m,n)^2 \qquad (5)$$

where D_{jl} are the wavelet detail coefficients are resolution level j, $l \in \{1,2,3\}$ indicates which of the detail images is being analysed, and M and N are the dimensions of the coefficient matrix. Such features have been shown to perform well in various texture analysis applications, however they are not sufficient to fully characterise a texture, and the performance of these features is generally not for any segmentation, classification or retrieval task.

In order to improve upon the performance of the first-order energy features, a method of modelling textures using both the first and second order statistics of wavelet detail coefficients has been proposed by Van de Wouwer *et. al.* [7]. Co-occurrence matrices are generated from each band of a redundant wavelet frame decomposition, and a set of eight standard co-occurrence features extracted to represent the second-order statistics of the texture. While this set of features improves performance compared to energy signatures, figure 1 shows that such a representation is still insufficient to completely characterise a texture. The synthetic image is generated having equal first and second order statistics of wavelet coefficients for the first 4 decomposition levels, and using the same low resolution approximation image. Clearly, these two textures are easily distinguishable by any observer, proving that the second order statistics of wavelet coefficients are insufficient to fully characterise texture. Without information to describe the relationships between each band of the WT, visual artifacts of the texture which contain elements at numerous scales are not adequately represented.

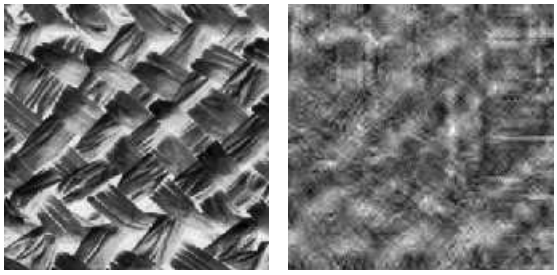

(a) (b)

Figure 1. Example showing the limitations of second-order statistics of wavelet coefficients as a texture descriptor. The natural texture (a) and synthesised texture (b) have identical first and second-order wavelet statistics of wavelet coefficients, yet are clearly distinguished by human observers.

3 Wavelet Scale Co-occurrence Matrices

From the examples shown in the previous section, it is clear that features obtained independently from each band of the wavelet decomposition are not sufficient to fully characterise textured images. Portilla and Simoncelli have shown that relationships between direction and scale bands of the wavelet transform are in many cases critical for adequate reconstruction of a textured image [11, 14], and use the correlations between the coefficients of a complex steerable pyramid decomposition to characterise texture for the purpose of synthesis. These features quantitatively measure the correlation between each orientation band at a given resolution level j, as well as between each detail image and the detail images at neighbouring resolution resolution levels. These parameters are then used, along with autocorrelation features of both the magnitude and raw coefficient values

and various statistics of the grey-level values, to generate synthetic texture images by restraint enforcement.

In order to capture the relationships between bands of the wavelet transform, we propose the *scale co-occurrence matrix* $S(k,l)$, which is defined as the probability of a detail coefficient $D(x,y)$ having a quantised value k while the approximation coefficient $A(x,y)$ at the same spatial position has a quantisedvalue of l. For an image of size $N \times M$, this can be expressed as

$$S_{ji}(k,l) = \frac{|\{(u,v) : q_1(D_{ji}(u,v)) = k, q_2(A_j(u,v)) = l\}|}{NM} \tag{6}$$

where A_j is the approximation image at resolution level j, D_{ji} are the three detail images, and $q_1(x)$ and $q_2(x)$ are the quantisation functions for the detail and approximation coefficients respectively. An overcomplete wavelet frame decomposition is used in our experiments in order to provide translation invariance and a higher robustness against nose, give higher spatial resolution, and avoid an overly sparse matrix at the lower resolutions.

The scale co-occurrence captures first order statistics of both the detail and approximation coefficients, and can be seen to fully encompass the wavelet mean deviation signatures. More importantly, by defining the relationships between the low and high frequency information at each scale, much information regarding structural components of the texture such as lines and edges can be extracted. The scale co-occurrence matrices overcome many of the limitations of features modelling the first and second order statistics of wavelet coefficients, as can be seen in figure 2, which shows two of the scale co-occurrence matrices extracted from the textures of figure 1, which have identical first and second order statistics. These matrices are clearly distinguishable, and provide the discrimination power lacking in other wavelet texture features. Previous work has shown that features extracted from the scale co-occurrence representation of texture are extremely powerful when used for classification and segmentation tasks [15].

4 Scale Co-occurrence Matrices for Similarity Measure

Using the scale co-occurrence matrices defined previously, it is possible to calculate a similarity measure between two textures

$$SM = \frac{1}{\sum_{j=1}^{J}\sum_{i=1}^{3} w_{ji} d(S1_{ji}, S2_{ji})} \tag{7}$$

where $d(x)$ is a distance metric used to determine the difference of the two distributions $S1$ and $S2$, and w_{ji} are weighting constants satisfying $\sum_j \sum_i w_{ji} = 1$. Such a similarity measure can then be used in image retrieval tasks, and also in classification and segmentation problems, where a candidate image is assigned to the class with the highest similarity measure. A number of choices for the distance metric $d(x)$ are available, ranging from the computationally inexpensive mean-squared error to more sophisticated techniques. We have chosen the earth mover's distance for this application as it has been experimentally shown to give a more accurate and stable measure of the difference between two scale co-occurrence representations that other metrics.

4.1 Earth Mover's Distance

The earth mover's distance (EMD) is a relatively new metric for representing the distance between two distributions in which the minimum amount of *work* required to transform one distribution to the other is calculated, given a set of ground distances between each point of the matrix [16]. Calculating this minimum amount can be viewed as a case of the *network transportation problem*, where one distribution is considered as a set of suppliers, and the other as a set of consumers. For the case of the scale co-occurrence matrix, each element of the matrix corresponds to a supplier or consumer.

Formally, the earth mover's distance can then be expressed as the minimum of the cost function of a set of weighted flows f_{ij} given by

$$EMD = \min \sum_{i \in \mathcal{I}} \sum_{j \in \mathcal{J}} c_{ij} f_{ij} \tag{8}$$

where $\mathcal{I}$ and $\mathcal{J}$ are the sets of suppliers and consumers, and c_{ij} is the ground distance between bins i and j. To ensure a valid solution, the following restraints are also applied:

$$f_{ij} \geq 0 \tag{9}$$

$$\sum_{i \in \mathcal{I}} f_{ij} = y_j \tag{10}$$

$$\sum_{j \in \mathcal{J}} f_{ij} = x_i \tag{11}$$

where x_i is the total supply the supplier i and y_j the total capacity of consumer j, which in our case are represented by the values of each element of the scale co-occurrence matrices.

A solution to the transportation problem of finding f_{ij} can be achieved using the simplex algorithm [17], an iterative method which will eventually converge to a local minimum. Russell has proposed an algorithm to determine a near-optimal starting point for this algorithm, which is used to ensure that the final value is close to the global minimum.

Using the earth mover's distance on the full scale co-occurrence matrices of two textures involves solving a transportation optimisation problem, which is of computational complexity $O(N^2)$, for more than 1000 suppliers and

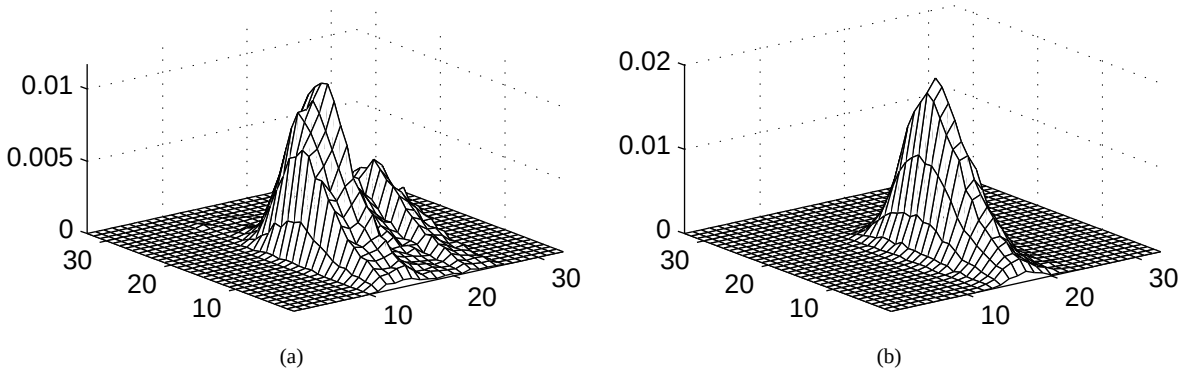

Figure 2. Examples of wavelet scale co-occurrence matrices for each of the textures of figure 1, showing considerable differences. (a) shows the horizontal and scale co-occurrence matrices respectively for the first level decomposition of the texture of figure 1(a), while (b) shows the same for figure 1(b).

consumers. Even for a relatively low number of iterations, this computational time can easily become excessive in all but the most trivial of applications. To improve this performance, it is necessary to significantly reduce the size of the flow optimsation problem without adversely affecting the accuracy of the distance metric. This can be accomplished by using *signatures* to represent the scale co-occurrence data rather than the traditional matrix form. Signatures, rather than representing fixed intervals, model a distribution using a set of clusters, and are defined as [16]

$$\{\vec{s}_i = (\vec{m}_i, v_i)\} \tag{12}$$

where $\vec{m}_i$ are the means of each cluster, and v_i the weightings. If sufficient clusters are used, it is possible to represent any distribution with arbitrary accuracy. It can also be shown that the histogram or matrix representation is actually a special case of a signature in which the clusters are set at fixed equidistant intervals in the underlying space. In fact, because of the possibility the each bin mean is not the mean of the distribution within it, a signature in this case will give a more accurate representation than the corresponding histogram form.

Calculating the signature of a distribution can be easily done by any one of a number of data clustering techniques. Using the k-means clustering algorithm has shown to produce acceptable results using approximately 50 clusters. More sophisticated techniques for approximating the modality of a distribution can be used for this purpose, but are beyond the scope of this paper.

The optimal flows f_{ij} and thus the final value of the EMD is highly dependent on the set of ground distances c_{ij}. Generally, these values are expressed as a function of (i, j), which in our case are the indices (k, l) of the scale co-occurrence matrices S_1 and S_2, and thus a two-dimensional vector. One commonly used metric for the ground distance between 2D points is the Euclidean distance

$$d(k_1, l_1, k_2, l_2) = \sqrt{(k_1 - k_2)^2 + (l_2 - l_2)^2} \tag{13}$$

where (k_1, l_1) and (k_2, l_2) are the indices of the scale co-occurrence matrices S_1 and S_2 respectively. Other metrics include the city block or Manhattan distance

$$d(k_1, l_1, k_2, l_2) = |k_1 - k_2| + |l_2 - l_2| \tag{14}$$

which is a summation of the distance of each dimension, and the maximum distance

$$d(k_1, l_1, k_2, l_2) = \max(|k_1 - k_2|, |l_2 - l_2|) \tag{15}$$

which considers only the greatest of the differences over all dimensions. Experimentally, a weighted Euclidean distance defined by

$$d(k_1, l_1, k_2, l_2) = \sqrt{a_k(k_1 - k_2)^2 + a_l(l_2 - l_2)^2} \tag{16}$$

where a_k and a_l are the weights for each dimension, has been found to give the most robust distance metric. Values of $a_k = 2$ and $a_l = 1$ are used in our experiments, meaning that differences in the detail coefficients are considered more important than a similar difference in the approximation coefficients.

4.2 Computational Considerations

The wavelet scale co-occurrence signature representation is quite small, less than 1kb for an image, making

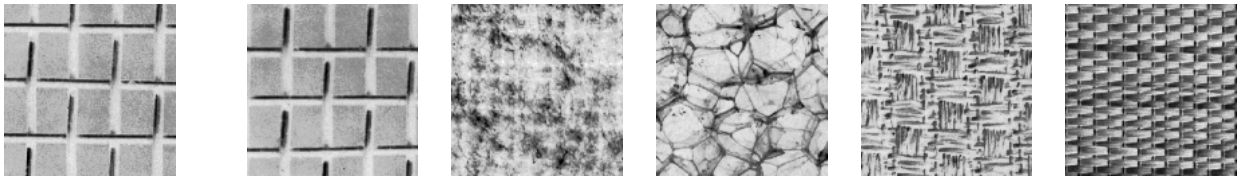

Figure 3. Results of a query using the scale co-occurrence similarity measure and the EMD. Query image (left) and top 5 matches, with distance measures of 42.7, 264, 274, 347.1 and 495.4 respectively.

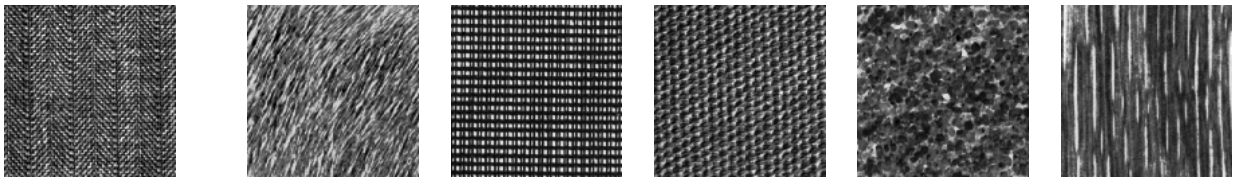

Figure 4. Retrieved images when using texture not present in the database. Query image (left) and top 5 matches, with distance measures of 196.8, 207.8, 226.7, 401.2 and 457.1 respectively.

it suitable for indexing large collections of textures. This size can be further reduced by traditional compression algorithms, which generally perform quite well given the relatively sparse nature of the data. Calculation of the similarity measure using the mean squared error is very fast, with more than 1000 comparisons performed per second on a 1700MHz workstation. Using the signatures rather than the full co-occurrence matrices provides a significant improvement to the efficiency of calculating this distance metric, reducing the computation time by many orders of magnitude, resulting in over 100 comparisons per second in most cases. On large databases or when computation speed is of critical importance, however, it may be necessary to further improve the computational efficiency of the search.

A suggested technique for pruning the search tree in large databases is to estimate a lower bound of the EMD, and use this estimate to remove unlikely match candidates. One such estimate of this lower bound is the distance between the centroids of the distributions, given using the notation of (8)-(11) as [16]

$$\min(EMD) = \left\| \sum_{i \in \mathcal{I}} x_i p_i - \sum_{j \in \mathcal{J}} y_j q_j \right\| \qquad (17)$$

where p_i and q_j are the coordinates of each cluster in the signatures $\mathcal{I}$ and $\mathcal{J}$ respectively. Such a lower bound is significantly faster to computer than the EMD, and by setting a suitable adaptive threshold a large proportion of the total candidates can be removed from the search without compromising the final result.

Another computational improvement can be realised by using a tree structured search algorithm, whereby the lowest resolution matrices or signatures are first compared, and processing continued for only those samples with the highest partial similarity measure. By combining these two methods of searching, the computation time for a typical search is reduced by approximately 95% with no noticeable affect on the quality of the retrieved matches.

4.3 Texture Retrieval Results

Using the distance metrics shown above, texture retrieval experiments were conducted using a small database of 50 images from the Brodatz album. The scale co-occurrence signature representations in of each of these images is extracted to 4 levels of wavelet decomposition, and used to create an index into the database. A test set of 200 images was the selected from the same 50 images, 4 from each class. In all cases, the training and test images were extracted from separate parts of the image such that no overlap between the two sets of possible. The top 5 matches for each of these test cases were then found in the database using the proposed similarity measure using the EMD metric. Overall, an image of the same class as the test case was returned as the most similar image in 97% with only 8 samples returning another class of image as the most likely. The results of a typical query for such an image is shown in figure 3.

In order to show the robustness of the proposed measure, a selection of textures which were not present in the database were searched for, with the results for a few such

examples shown in figure 4. It can be seen from these examples that the textures retrieved from the database are visually similar to the candidate image, indicating that the scale co-occurrence matrices provide a good characterisation of the visual appearance of texture.

5 Conclusions and Future Work

In this paper we have proposed a novel representation of texture which models the relationships between bands of the wavelet transform decomposition. Such a representation has been empirically shown to provide better characterisation of many textures than statistics extracted independently from each band. Using the earth mover's distance, a similarity measure for comparing two textures based on this representation has been presented, with results from texture retrieval experiments showing excellent performance on a set of natural textures. Future work will aim to further improve the modelling of the scale co-occurrence distributions in a parametric form, and to study the types of textures for which the proposed representation provides the best representation. The proposed representation is also being investigated for the purposes of texture classification using both the distance metric and via a set of features extracted from the scale co-occurrence matrices.

References

[1] M Vetterli and J Kovacevic. *Wavelets and Subband Coding*. Prentice Hall, Englewood Cliffs, New Jersey, 1995.

[2] T. Chang and C. C. Kuo. Texture segmentation with tree-structured wavelet transform. In *Proceedings of IEEE International Symposium on Time-Frequency and Time-Scale Analysis*, volume 2, page 577, 1992.

[3] S. Fukuda and H. Hirosawa. A wavelet-based texture feature set applied to classification of multifrequency polarimetric sar images. *IEEE Transactions on Geoscience and Remote Sensing*, 37(5):2282–2286, 1999.

[4] H. Greenspan, S. Belongie, R. Goodman, and P. Perona. Rotation invariant texture recognition using a steerable pyramid. In *Proceedings of 12th International Conference on Pattern Recognition*, volume 2, pages 162–167, Jerusalem, Israel, 1994.

[5] Sam-Deuk Kim and S. Udpa. Texture classification using rotated wavelet filters. *IEEE Transactions on Systems, Man and Cybernetics*, 30(6):847–852, 2000.

[6] A. Tabesh. Zero-crossing rates of wavelet frame representations for texture classification. *Electronics Letters*, 38(22):1340–1341, 2002.

[7] G. Van de Wouwer, P. Scheunders, and D. Van Dyck. Statistical texture characterization from discrete wavelet representations. *IEEE Transactions on Image Processing*, 8(4):592–598, 1999.

[8] T. Chang and C. C. J. Kuo. Texture analysis and classification with tree-structured wavelet transform. *IEEE Transactions on Image Processing*, 2:429–441, 1993.

[9] A. Laine and J. Fan. Texture classification by wavelet packet signatures. *IEEE Transactions on Pattern Analysis and Machine Intelligence*, 15(11):1186–1191, 1993.

[10] C.-M. Pun and M.-C. Lee. Rotation-invariant texture classification using a two-stage wavelet packet feature approach. *IEE Proceedings - Vision, Image and Signal Processing*, 148(6):422–428, 2001.

[11] Javier Portilla and Eero. P. Simoncelli. A parametric texture model based on joint statistics of complex wavelet coefficients. *International Journal of Computer Vision*, 40(1):49–71, 2000.

[12] Phil Brodatz. *Textures: A Photographic Album for Artists and Designers*. Dover Publications Inc., New York, 1966.

[13] B. Julesz, E. N. Gilbert, L. A. Shepp, and H. L. Frisch. Inability of humans to discriminate between visual texture that agree in second-order statistics - revisited. *Perception*, 2:391–405, 1973.

[14] E. P. Simoncelli and J. Portilla. Texture characterization via joint statistics of wavelet coefficient magnitudes. In *Proceedings of International Conference on Image Processing*, volume 1, pages 62–66, 1998.

[15] A. Busch and W. W. Boles. Texture classification using wavelet scale relationships. In *Proceedings of IEEE International Conference on Acoustics, Speech and Signal Processing*, volume 4, pages 3484–3487, 2002.

[16] Y. Rubner, C. Tomasi, and L. J. Guibas. A metric for distributions with applications to image databases. In *Proceedings of IEEE International Conference on Computer Vision*, pages 59–66, Bombay, India, 1998.

[17] F. S. Hillier and G. J. Liberman. *Introduction to mathematical programming*. McGraw-Hill, 1990.

AUTHOR INDEX